



ISOTOPE GEOCHEMISTRY

William M. White

Isotope Geochemistry

Isotope Geochemistry

William M. White

Department of Earth & Atmospheric Sciences
Cornell University
Ithica, New York, USA

WILEY Blackwell

This edition first published 2015 © 2015 by John Wiley & Sons Ltd,

Registered office: John Wiley & Sons, Ltd, The Atrium, Southern Gate, Chichester, West Sussex, PO19 8SQ, UK

Editorial offices: 9600 Garsington Road, Oxford, OX4 2DQ, UK
The Atrium, Southern Gate, Chichester, West Sussex, PO19 8SQ, UK
111 River Street, Hoboken, NJ 07030-5774, USA

For details of our global editorial offices, for customer services and for information about how to apply for permission to reuse the copyright material in this book, please see our website at www.wiley.com/wiley-blackwell.

The right of the author to be identified as the author of this work has been asserted in accordance with the UK Copyright, Designs and Patents Act 1988.

All rights reserved. No part of this publication may be reproduced, stored in a retrieval system, or transmitted, in any form or by any means, electronic, mechanical, photocopying, recording or otherwise, except as permitted by the UK Copyright, Designs and Patents Act 1988, without the prior permission of the publisher.

Designations used by companies to distinguish their products are often claimed as trademarks. All brand names and product names used in this book are trade names, service marks, trademarks or registered trademarks of their respective owners. The publisher is not associated with any product or vendor mentioned in this book.

Limit of Liability/Disclaimer of Warranty: While the publisher and author(s) have used their best efforts in preparing this book, they make no representations or warranties with respect to the accuracy or completeness of the contents of this book and specifically disclaim any implied warranties of merchantability or fitness for a particular purpose. It is sold on the understanding that the publisher is not engaged in rendering professional services and neither the publisher nor the author shall be liable for damages arising herefrom. If professional advice or other expert assistance is required, the services of a competent professional should be sought.

Library of Congress Cataloging-in-Publication Data

White, William M., 1948-

Isotope geochemistry / William M. White.

pages cm

Includes bibliographical references and index.

ISBN 978-0-470-65670-9 (pbk.)

1. Isotope geology. 2. Geochemistry. 3. Earth sciences. I. Title.

QE501.4.N9W55 2015

551.9 – dc23

2014029372

A catalogue record for this book is available from the British Library.

Wiley also publishes its books in a variety of electronic formats. Some content that appears in print may not be available in electronic books.

Cover image: L. Sue Baugh/Wild Stone Arts™ © 2002

Set in 11/12pt Sabon by Laserwords Private Limited, Chennai, India

1 2015

Contents

Preface	xi
About the companion website	xiii
Chapter 1: Atoms and nuclei: their physics and origins	1
1.1 Introduction	1
1.2 Physics of the Nucleus	2
1.2.1 Early development of atomic and the nuclear theory	2
1.2.2 Some definitions and units	3
1.2.3 Nucleons, nuclei, and nuclear forces	3
1.2.4 Atomic masses and binding energies	4
1.2.5 The liquid-drop model	6
1.2.6 The shell model of the nucleus	7
1.2.7 Collective model	11
1.3 Radioactive Decay	12
1.3.1 Gamma decay	12
1.3.2 Alpha decay	13
1.3.3 Beta decay	13
1.3.4 Electron capture	14
1.3.5 Spontaneous fission	15
1.4 Nucleosynthesis	16
1.4.1 Cosmological nucleosynthesis	18
1.4.2 Stellar nucleosynthesis	18
1.4.3 Explosive nucleosynthesis	25
1.4.4 Nucleosynthesis in interstellar space	27
1.4.5 Summary	28
Notes	29
References	29
Suggestions for Further Reading	30
Problems	30
Chapter 2: Decay systems and geochronology I	32
2.1 Basics of Radioactive Isotope Geochemistry	32
2.1.1 Introduction	32
2.1.2 The basic equations	33
2.1.3 A special case: the U-Th-Pb system	35
2.2 Geochronology	36
2.2.1 Isochron dating	36
2.2.2 Calculating an isochron	37

2.3	The K-Ar-Ca System	39
2.3.1	Diffusion, cooling rates, and closure temperatures	40
2.3.2	^{40}Ar - ^{39}Ar dating	43
2.4	The Rb-Sr System	47
2.4.1	Rb-Sr chemistry and geochronology	48
2.4.2	Sr isotope chronostratigraphy	49
2.5	The Sm-Nd System	50
2.5.1	Sm-Nd model ages and crustal residence times	55
2.6	The Lu-Hf System	56
2.7	The Re-Os System	61
2.7.1	The Re-Os decay system	61
2.7.2	Re-Os geochronology	63
2.7.3	The ^{190}Pt - ^{186}Os decay	65
	Notes	66
	References	66
	Suggestions for Further Reading	68
	Problems	69
Chapter 3:	Decay systems and geochronology II: U and Th	72
3.1	Introduction	72
3.1.1	Chemistry of U, Th, and Pb	72
3.1.2	The ^{238}U / ^{235}U ratio and uranium decay constants	73
3.2	Pb-Pb Ages and Isochrons	74
3.2.1	Total U-Pb isochrons	76
3.2.2	Th/U ratios	77
3.3	Zircon Dating	77
3.4	U-decay Series Dating	83
3.4.1	Basic principles	84
3.4.2	^{234}U - ^{238}U dating	86
3.4.3	^{230}Th - ^{238}U dating	88
3.4.4	^{231}Pa - ^{235}U dating	91
3.4.5	^{226}Ra dating	93
3.4.6	^{210}Pb dating	93
3.4.7	^{210}Po - ^{210}Pb dating	95
	Notes	96
	References	97
	Suggestions for Further Reading	98
	Problems	98
Chapter 4:	Geochronology III: other dating methods	101
4.1	Cosmogenic Nuclides	101
4.1.1	Cosmic rays in the atmosphere	101
4.1.2	^{14}C dating	102
4.1.3	^{10}Be , ^{26}Al , and ^{36}Cl	106
4.1.4	Cosmogenic and bomb-produced radionuclides in hydrology	108
4.1.5	<i>In-situ</i> produced cosmogenic nuclides	110
4.2	Fission Tracks	114
4.2.1	Analytical procedures	115
4.2.2	Interpreting fission track ages	117
4.2.3	Interpreting track length	119
	Notes	121
	References	122
	Suggestions for Further Reading	123
	Problems	123

Chapter 5: Isotope cosmochemistry	125
5.1 Introduction	125
5.2 Cosmochronology	126
5.2.1 Conventional methods	126
5.2.2 Extinct radionuclides	129
5.2.3 Extinct radionuclides in the Earth	136
5.2.4 Origin of short-lived nuclides	145
5.3 Stardust and Isotopic Anomalies in Meteorites	146
5.3.1 Neon alphabet soup and “pre-solar” noble gases in meteorites	146
5.3.2 Isotopic composition of pre-solar grains	148
5.3.3 Other exotic components in meteorites	151
5.4 Oxygen Isotope Variations and Nebular Processes	151
5.5 Exposure Ages of Meteorites	154
Notes	154
References	155
Suggestions for Further Reading	158
Problems	159
Chapter 6: Radiogenic isotope geochemistry of the mantle	161
6.1 Introduction	161
6.1.1 Definitions: time-integrated and time-averaged	162
6.2 Isotope Geochemistry of the Earth’s Mantle	163
6.2.1 The Sr-Nd-Hf picture	163
6.2.2 The Pb picture	166
6.3 Balancing Depleted Mantle and Crust	172
6.4 Mantle Plume Reservoirs	179
6.4.1 Mantle plumes and the mantle zoo	179
6.4.2 The evolution of mantle geochemical reservoirs	180
6.5 Geographic Variations in Mantle Isotopic Composition	187
6.6 The Subcontinental Lithosphere	189
6.7 U-Series Isotopes and Melt Generation	193
6.7.1 Spiegelman and Elliot model of melt transport	194
Notes	198
References	201
Suggestions for Further Reading	203
Problems	204
Chapter 7: Radiogenic isotope geochemistry of the continental crust and the oceans	205
7.1 Introduction	205
7.2 Growth of the Continental Crust Through Time	205
7.2.1 Mechanisms of crustal growth	205
7.2.2 The Hadean eon and the earliest continental crust	206
7.2.3 Subsequent growth of the crust	212
7.2.4 Nd and Hf isotopic approaches to crustal evolution	215
7.3 Isotopic Composition of the Continental Crust	217
7.3.1 Sediments and rivers as samples of the upper crust	218
7.3.2 Isotopic composition of the lower crust	221
7.3.3 Pb isotope ratios and the Th/U ratio of the crust	223
7.4 Other Approaches to Crustal Composition and Evolution	224
7.5 Subduction Zones	226
7.5.1 Geochemistry of two-component mixtures	226
7.5.2 Isotopic compositions of subduction-related magmas	228
7.6 Radiogenic Isotopes in Oceanography	231
7.6.1 Oceanographic circulation and geochemical cycling	232
7.6.2 Nd, Hf, Os, and Pb in the modern ocean	233

7.6.3	Radiogenic isotopes in paleoceanography	236
Notes		240
References		240
Suggestions for Further Reading		244
Problems		244
Chapter 8: Stable isotope geochemistry I: Theory		246
8.1	Introduction	246
8.2	Notation and Definitions	246
8.2.1	The δ notation	246
8.2.2	The fractionation factor	247
8.3	Theory of Mass Dependent Isotopic Fractionations	247
8.3.1	Equilibrium fractionations	249
8.3.2	Kinetic fractionation	258
8.4	Mass Independent Fractionation	260
8.5	Hydrogen and Oxygen Isotope Ratios in the Hydrologic System	262
8.6	Isotope Fractionation in the Biosphere	265
8.6.1	Carbon isotope fractionation during photosynthesis	265
8.6.2	Nitrogen isotope fractionation in biological processes	269
8.6.3	Oxygen and hydrogen isotope fractionation by plants	271
8.6.4	Carbon and hydrogen isotopic composition of organic matter in sediments	271
8.6.5	Biological fractionation of sulfur isotopes	273
Notes		274
References		274
Suggestions for Further Reading		275
Problems		276
Chapter 9: Stable isotope geochemistry II: High temperature applications		277
9.1	Introduction	277
9.2	Equilibrium Fractionations Among Minerals	277
9.2.1	Compositional and structural dependence of equilibrium fractionations	277
9.2.2	Geothermometry	279
9.3	Stable Isotope Composition of the Mantle	282
9.3.1	Oxygen	283
9.3.2	Carbon	284
9.3.3	Hydrogen	286
9.3.4	Nitrogen	287
9.3.5	Sulfur	288
9.4	Oxygen Isotopes in Magmatic Processes	288
9.4.1	Oxygen isotope changes during crystallization	289
9.4.2	Combined fractional crystallization and assimilation	291
9.4.3	Combining radiogenic and oxygen isotopes	291
9.4.4	Sediment subduction versus assimilation	292
9.4.5	Stable isotopes as indicators of crust-to-mantle recycling	296
9.5	Oxygen Isotopes in Hydrothermal Systems	298
9.5.1	Ridge crest hydrothermal activity and metamorphism of the oceanic crust	298
9.5.2	Meteoric geothermal systems	301
9.5.3	Water-rock reaction: Theory	301
9.5.4	The Skaergaard intrusion	303
9.5.5	Oxygen isotopes and mineral exploration	304
9.6	Sulfur Isotopes and Ores	305
9.6.1	Introduction	305

9.6.2	Sulfur isotope fractionations in magmatic processes	306
9.6.3	Sulfur isotope fractionation in hydrothermal systems	307
9.6.4	Isotopic composition of sulfide ores	309
Notes		312
References		312
Suggestions for Further Reading		314
Problems		315
Chapter 10: Stable isotope geochemistry III: Low temperature applications		316
10.1	Stable Isotopes in Paleontology, Archeology, and the Environment	316
10.1.1	Introduction	316
10.1.2	Isotopes and diet: You are what you eat	316
10.1.3	Carbon isotopes and the evolution of horses and grasslands	318
10.1.4	Isotopes, archeology, and paleodiets	321
10.1.5	Carbon isotopes and the earliest life	323
10.1.6	Tracing methane contamination in drinking water	325
10.2	Stable Isotopes in Paleoceanography	326
10.2.1	Introduction	326
10.2.2	The record of climate change in deep sea sediments	327
10.2.3	The quaternary $\delta^{18}\text{O}$ record	327
10.2.4	The cause of quaternary glaciations	329
10.2.5	Carbon isotopes, ocean circulation, and climate	332
10.2.6	The tertiary marine $\delta^{18}\text{O}$ record	334
10.2.7	Continental isotopic records	336
10.2.8	Vostok and EPICA Antarctic ice cores	337
10.2.9	Ice records from Greenland: GRIP, GISP, and NGRIP	338
10.2.10	Speleotherm and related climate records	340
10.2.11	Soils and paleosols	341
10.3	The Carbon Cycle, Isotopes, and Climate	342
10.3.1	The short-term carbon cycle and anthropogenic impacts	342
10.3.2	The quaternary carbon isotope record and glacial cycles	347
10.3.3	The long-term carbon cycle	351
Notes		359
References		359
Suggestions for Further Reading		362
Problems		363
Chapter 11: Unconventional isotopes and approaches		364
11.1	Introduction	364
11.2	Applications of Isotopic Clumping	365
11.3	Mass Independent Isotope Fractionations	368
11.3.1	Mass-independent fractionation of oxygen in the atmosphere	368
11.3.2	Mass independent sulfur isotope fractionation and the rise of atmospheric oxygen	369
11.4	Isotopes of Iron and Molybdenum	370
11.4.1	Fe isotopes and the great oxidation event	371
11.4.2	Mo isotopes and oxygenation of the oceans	374
11.5	Isotopes of Copper and Zinc	377
11.5.1	Cu isotopes	377
11.5.2	Zn isotopes	380
11.6	Isotopes of Boron and Lithium	383
11.6.1	Boron isotopes	384
11.6.2	Li isotopes	389
11.7	Isotopes of Magnesium and Calcium	392
11.7.1	Mg isotopes	392

11.7.2 Calcium isotopes	396
11.8 Silicon Isotopes	400
11.9 Chlorine Isotopes	404
Notes	407
References	408
Suggestions for Further Reading	416
Problems	416
Chapter 12: Noble gas isotope geochemistry	418
12.1 Introduction	418
12.1.1 Noble gas chemistry	418
12.1.2 Noble gases in the Solar System	419
12.2 Helium	422
12.2.1 He in the atmosphere, crust, and oceans	422
12.2.2 He in the mantle	424
12.3 Neon	426
12.3.1 Neon in the solid earth	428
12.4 Argon	429
12.5 Krypton	431
12.6 Xenon	432
12.7 Implications of Noble Gas Isotope Ratios for the Origin and Evolution of the Earth	436
12.7.1 Mantle reservoirs of noble gases in the modern Earth	436
12.7.2 Formation of the Earth and evolution of the atmosphere	443
Notes	447
References	448
Suggestions for Further Reading	452
Problems	452
Appendix: Mass spectrometry	453
A.1 Sample Extraction and Preparation	453
A.2 The Mass Spectrometer	453
A.2.1 The ion source	454
A.2.2 The mass analyzer	455
A.2.3 The detector	457
A.3 Accelerator Mass Spectrometry	458
A.4 Analytical Strategies	459
A.4.1 Correcting mass fractionation	459
A.4.2 Deconvolution of results	461
A.4.3 Isotope dilution analysis	461
Notes	462
References	463
Problems	463
Index	465

Preface

Over the past half century or so, isotope geochemistry has touched virtually every subfield of the earth sciences, from petroleum exploration to paleontology, climatology, and study of the Earth's deep interior, the latter being one of my principal fields of interest. Consequently, nearly every earth scientist needs some exposure to, if not fluency in, isotope geochemistry. The intent of this book is to provide that fluency. It assumes a background knowledge of geochemistry more or less equivalent to that contained in my earlier book, *Geochemistry*, also published by Wiley-Blackwell.

This text is based on a course in *Isotope Geochemistry* that I have taught at Cornell University for the past 25 years. It began as lecture notes, initially copied and handed out and later posted electronically on the Internet. The notes, and eventually the book draft, increased in length over the years and the book is now longer than I imagined it would be. That said, it remains an incomplete treatment of the topic. Although isotope geochemistry is a very small fraction of the range of human knowledge, I have come to realize that no single person can know everything about it, much less write it all down. In part, this is because of the velocity at which the field has expanded and continued to expand. When I began teaching this course, stable isotope geochemistry was restricted to the five "traditional" elements, H, C, N, O, and S; today it encompasses a fair fraction of the entire Periodic Table. Radiogenic isotope geochemistry and geochronology were restricted to K-Ar, Rb-Sr, Sm-Nd, and U-Th-Pb. Although I was involved in the early development of the field, I would have had to admit that Lu-Hf was more a curiosity than a useful tool; this was even truer of Re-Os. Data on cosmogenic isotopes beyond ^{14}C was scarce and only a few decay products of extinct radionuclides had been identified in meteorites and, with the exception of ^{129}Xe , none in the Earth. Mass independent fractionation was a laboratory curiosity and isotope "clumping" had yet to be explored. Except for helium, there was essentially no data on the isotopic composition of mantle noble gases. Thus, a good part of the book describes discoveries of the last 25 years. The rate of discovery is accelerating rather than decelerating and it is thrilling to think about how much we will learn in the next 25 years. It is, at the same time, intimidating, in part because some of what we now think to be true (including material in this book) will prove to be wrong and in part because it will be even more difficult for any one person to comprehend it all.

I am grateful to the students in my courses for asking questions that inspired me to expanding my own range knowledge and expertise and also for pointing out the inevitable errors in drafts of the book. Once posted on the Internet, readers around the world found the lecture notes and provided feedback as well. I am grateful to them (there are too many to list here). I would, however, like to specifically thank Jeff Vervoort, Kyle Trostle, Dave Graham, and Bill McDonough for their critical reading of late drafts of parts of the text. And thanks too, to the fine people at Wiley-Blackwell who will be working in the coming months to transform this typescript to an actual book.

Bill White.
Ithaca, NY
December, 2013

About the companion website

This book is accompanied by a companion website:

www.wiley.com/go/white/isotopegeochemistry

The website includes:

- Powerpoints of all figures from the book for downloading
- PDFs of tables from the book

Chapter 1

Atoms and nuclei: their physics and origins

1.1 INTRODUCTION

Isotope geochemistry has grown over the last 50 years to become one of the most important fields in the earth sciences as well as in geochemistry. It has two broad subdivisions: *radiogenic isotope geochemistry* and *stable isotope geochemistry*. These subdivisions reflect the two primary reasons why the relative abundances of isotopes of some elements vary in nature: radioactive decay and chemical fractionation.¹ One might recognize a third subdivision: cosmo-genic isotope geochemistry, in which both radioactive decay and chemical fractionation are involved, but additional nuclear processes can be involved as well.

The growth in the importance of isotope geochemistry reflects its remarkable success in attacking fundamental problems of earth science, as well as problems in astrophysics, physics, and biology (including medicine). Isotope geochemistry has played an important role in transforming geology from a qualitative, observational science to a modern quantitative one. To appreciate the point, consider the Ice Ages, a phenomenon that has fascinated geologist and layman alike for more than 150 years. The idea that much of the Northern Hemisphere was once covered by glaciers was first advanced by Swiss zoologist Louis Agassiz in 1837. His theory was based on observations of geomorphology and modern glaciers. Over the next 100 years, this theory advanced very little,

other than the discovery that there had been more than one ice advance. No one knew exactly when these advances had occurred, how long they lasted, or why they occurred. Stable and radiogenic isotopic studies in the last 50 years have determined the exact times of these ice ages and the exact extent of temperature change (about 3°C or so in temperate latitudes, more at the poles). Knowing the timing of these glaciations has allowed us to conclude that variations in the Earth's orbital parameters (the Milankovitch parameters) and resulting changes in insolation have been the direct cause of these ice ages. Comparing isotopically determined temperatures with CO₂ concentrations in bubbles in carefully dated ice cores leads to the hypothesis that atmospheric CO₂ plays an important role in amplifying changes in insolation. Careful U-Th dating of corals has also revealed the detailed timing of the melting of the ice sheet and consequent sea level rise. Comparing this with stable isotope geothermometry shows that melting lagged warming (not too surprisingly). Other isotopic studies revealed changes in the ocean circulation system as the last ice age ended. Changes in ocean circulation may also be an important feedback mechanism affecting climate. Twenty-five years ago, all this seemed very interesting, but not very relevant. Today, it provides us with critical insights into how the planet's climate system works. With the current concern over potential global warming and greenhouse gases, this information is extremely "relevant".

Some isotope geochemistry even seeps into public consciousness through its application to archeology and forensics. For example, a recent *National Geographic* television documentary described how carbon-14 dating of 54 beheaded skeletons in a mass grave in Dorset, England revealed they were tenth century and how strontium and oxygen isotope ratios revealed they were those of Vikings executed by Anglo-Saxons and not visa versa, as originally suspected. Forensic isotopic analysis gets occasional mention in both in shows like *CSI: Crime Scene Investigation* and in newspaper reporting of real crime investigations.

Other examples of the impact of isotope geochemistry would include such diverse topics as ore genesis, mantle dynamics, hydrology, and hydrocarbon migration, monitors of the cosmic ray flux, crustal evolution, volcanology, oceanic circulation, environmental protection and monitoring, and paleontology. Indeed, there are few, if any, areas of geological inquiry where isotopic studies have not had a significant impact.

One of the first applications of isotope geochemistry remains one of the most important: geochronology and cosmochronology: the determination of the timing of events in the history of the Earth and the Solar System. The first “date” was obtained in 1907 by Bertram Boltwood, a Yale University chemist, who determined the age of uranium ore samples by measuring the amount of the radiogenic daughter of U, namely Pb, present. Other early applications include determining the abundance of isotopes in nature to constrain models of the nucleus and of nucleosynthesis (the origin of the elements). Work on the latter problem still proceeds. The origins of stable isotope geochemistry date to the work of Harold Urey and his colleagues in the 1940s. Paleothermometry was one of the first applications of stable isotope geochemistry as it was Urey who recognized the potential of stable isotope geochemistry to solving the riddle of the Ice Ages.

This book will touch on many, though not all, of these applications. We'll focus first on geochronology and then consider how radioactive isotopes have been used to understand the origin and evolution of the Earth. Next, we consider the fundamental principles underlying stable isotope geochemistry and then

examine its applications to fields as diverse as paleoclimate, paleontology, archeology, ore genesis, and magmatic evolution. In the final chapters, we'll see how the horizons of stable isotope geochemistry have broadened from a few light elements such as hydrogen, carbon, and oxygen to much of the periodic table. Finally, we examine the isotope geochemistry of the noble gases, whose isotopic variations are due to both nuclear and chemical processes and provide special insights into the origins and behavior of the Earth.

Before discussing applications, however, we must build a firm basis in the nuclear physics. We'll do that in the following sections. With that basis, in the final sections of this chapter we'll learn how the elements have been created over the history of the Universe in a variety of cosmic environments.

1.2 PHYSICS OF THE NUCLEUS

1.2.1 Early development of atomic and the nuclear theory

John Dalton, an English schoolteacher, first proposed that all matter consists of atoms in 1806. William Prout found that atomic weights were integral multiples of the mass of hydrogen in 1815, something known as the *Law of Constant Proportions*. This observation was strong support for the atomic theory, though it was subsequently shown to be only approximate, at best. J. J. Thomson of the Cavendish Laboratory in Cambridge developed the first mass spectrograph in 1906 and showed why the *Law of Constant Proportions* did not always hold: those elements not having integer weights had several *isotopes*, each of which had mass that was an integral multiple of the mass of H. In the meantime, Rutherford, also of Cavendish, had made another important observation: that atoms consisted mostly of empty space. This led to Niels Bohr's model of the atom, proposed in 1910, which stated that the atom consisted of a nucleus, which contained most of the mass, and electrons in orbit about it.

It was nevertheless unclear why some atoms had different masses than other atoms of the same element. The answer was provided by W. Bothe and H. Becker of Germany and James Chadwick of England: the neutron. Bothe and Becker discovered the particle, but mistook it for radiation. Chadwick won the Nobel

Prize for determining the mass of the neutron in 1932. Various other experiments showed the neutron could be emitted and absorbed by nuclei, so it became clear that differing numbers of neutrons caused some atoms to be heavier than other atoms of the same element. This bit of history leads to our first basic observation about the nucleus: it consists of protons and neutrons.

1.2.2 Some definitions and units

Before we consider the nucleus in more detail, let's set out some definitions: N : the number of neutrons, Z : the number of protons (same as atomic number since the number of protons dictates the chemical properties of the atom), A : Mass number ($N + Z$), M : Atomic Mass, I : Neutron excess number ($I = N - Z$). *Isotopes* have the same number of protons but different numbers of neutrons; *isobars* have the same mass number ($N + Z$); *isotones* have the same number of neutrons but different number of protons.

The basic unit of nuclear mass is the unified atomic mass unit (also known as the *dalton* and the atomic mass unit or amu), which is based on $^{12}\text{C} \equiv 12$ unified atomic mass units; that is, the mass of ^{12}C is 12 unified atomic mass units (abbreviated u²). The masses of atomic particles are:

$$\begin{aligned} \text{proton: } & 1.007276467 \text{ u} = 1.67262178 \\ & \times 10^{-27} \text{ kg} = 938.2720 \text{ MeV/c}^2 \\ \text{neutron: } & 1.008664916 \text{ u} \\ \text{electron: } & 0.0005485799 \text{ u} = 9.10938291 \\ & \times 10^{-31} \text{ kg} = 0.5109989 \text{ MeV/c}^2 \end{aligned}$$

1.2.3 Nucleons, nuclei, and nuclear forces

Figure 1.1 is a plot of N versus Z showing which nuclides are stable. A key observation in understanding the nucleus is that not all combinations of N and Z result in stable nuclides. In other words, we cannot simply throw protons and neutrons (collectively termed nucleons) together randomly and expect them to form a nucleus. For some combinations of N and Z , a nucleus forms but is unstable, with half-lives from $>10^{15}$ yrs to $<10^{-12}$ sec. A relative few combinations of N and Z result in stable nuclei. Interestingly, these stable nuclei generally have $N \approx Z$, as Figure 1.1 shows. Notice also that for small A , $N = Z$, for large A , $N > Z$. This is another important

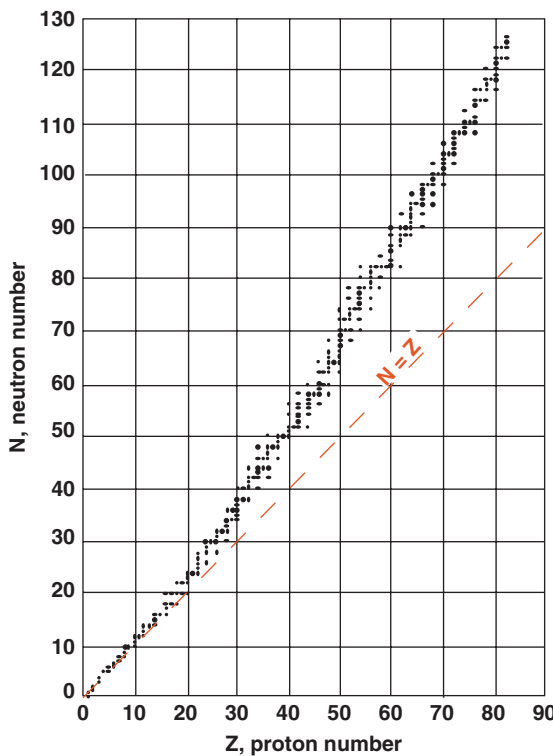


Figure 1.1 Neutron number versus proton number for stable nuclides. (Source: White (2013). Reproduced with permission of John Wiley & Sons.)

observation that will lead us to the first model of the nucleus.

A significant portion (about half) of the nucleus consists of protons, which obviously tend to repel each other by coulombic (electrostatic) force. From the observation that nuclei exist at all, it is apparent that another force must exist that is stronger than coulomb repulsion at short distances. It must be negligible at larger distances; otherwise all matter would collapse into a single nucleus. This force, called the *nuclear force*, is a manifestation of one of the fundamental forces of nature (or a manifestation of the single force in nature if you prefer unifying theories), called the *strong force*. If this force is assigned a strength of 1, then the strengths of other forces are: electromagnetic 10^{-2} ; weak force (which we'll discuss later) 10^{-5} ; gravity 10^{-39} . Just as electromagnetic forces are mediated by a particle, the photon, the nuclear force is mediated by the *pion*. The photon carries one quantum of electromagnetic force field; the pion carries

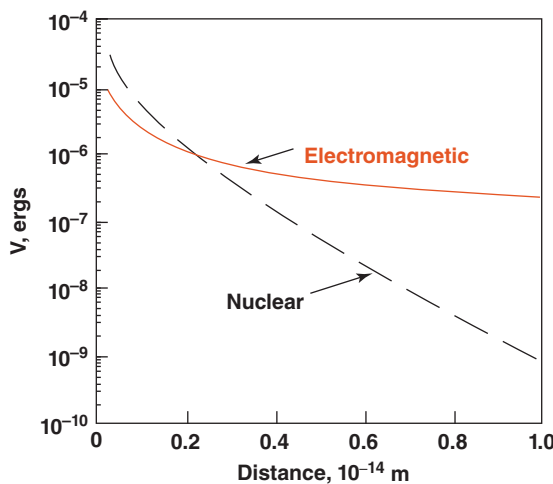


Figure 1.2 The nuclear and electromagnetic potential of a proton as a function of distance from the proton.

one quantum of nuclear force field. A comparison of the relative strengths of the nuclear and electromagnetic forces as a function of distance is shown in Figure 1.2.

1.2.4 Atomic masses and binding energies

The carbon-12 atom consists of six neutrons, six protons, and six electrons. But using the masses listed here, we find that the masses of these 18 particles sum to more than 12 u, the mass of ^{12}C atom. There is no mistake, they do not add up. What has happened to the extra mass? The mass has been converted to the energy binding the nucleons. It is a general physical principle that the lowest energy configuration is the most stable. We would expect that if ^4He is stable relative to two free neutrons and two free protons, ^4He must be a lower energy state compared to the free particles. If this is the case, then we can predict from Einstein's mass-energy equivalence:

$$E = mc^2 \quad (1.1)$$

that the mass of the helium nucleus is less than the sum of its constituents. We define the *mass decrement* of an atom as:

$$\delta = W - M \quad (1.2)$$

where W is the sum of the mass of the constituent particles and M is the actual mass of

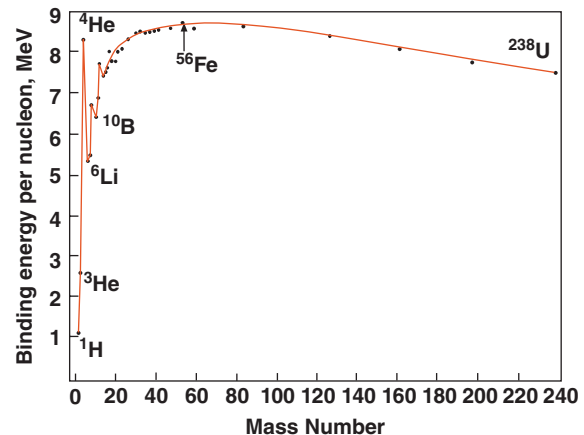


Figure 1.3 Binding energy per nucleon versus mass number. (Source: White (2013). Reproduced with permission of John Wiley & Sons.)

the atom. For example, W for ^4He is $W = 2m_p + 2m_n + 2m_e = 4.03298u$. The mass of ^4He is $4.002603u$, so $\delta = 0.0306767u$. Converting this to energy using Eqn. 1.1 yields 28.28 MeV. This energy is known as the *binding energy*. Dividing by A , the mass number, or number of nucleons, gives the *binding energy per nucleon*, E_b :

$$E_b = \left[\frac{W - M}{A} \right] c^2 \quad (1.3)$$

This is a measure of nuclear stability: those nuclei with the largest binding energy per nucleon are the most stable. Figure 1.3 shows E_b as a function of mass. Note that the nucleons of intermediate mass tend to be the most stable. This distribution of binding energy is important to the life history of stars, the abundances of the elements, and radioactive decay, as we shall see.

Some indication of the relative strength of the nuclear binding force can be obtained by comparing the mass decrement associated with it to that associated with binding an electron to a proton in a hydrogen atom. The mass decrement we calculated previously for He is of the order of 1%, one part in 10^2 . The mass decrement associated with binding an electron to a nucleus of the order of one part in 10^8 . So, bonds between nucleons are about 10^6 times stronger than bonds between electrons and nuclei.

Pions and the nuclear force

As we noted, we can make an *a priori* guess as to two of the properties of the nuclear force: it must be very strong and it must have a very short range. Since neutrons as well as protons are subject to the nuclear force, we may also conclude that it is not electromagnetic in nature. What inferences can we make on the nature of the force and the particle that mediates it? Will this particle have a mass, or be massless like the photon?

All particles, whether they have mass or not, can be described as waves, according to quantum theory. The relationship between the wave properties and the particle properties is given by the *de Broglie Equation*:

$$\lambda = \frac{h}{p} \quad (1.4)$$

where h is Planck's constant, λ is the wavelength, called the *de Broglie wavelength*, and p is momentum. Eqn. 1.2 can be rewritten as:

$$\lambda = \frac{h}{mv} \quad (1.5)$$

where m is mass (relativistic mass, not rest mass) and v is velocity. From this relation we see that mass and de Broglie wavelength are inversely related: massive particles will have very short wavelengths.

The wavefunction associated with the particle may be written as:

$$\frac{1}{c^2} \frac{\partial^2 \psi}{\partial t^2} - \nabla^2 \psi(x, t) = -\left(\frac{mc}{\hbar}\right)^2 \psi(x, t) \quad (1.6)$$

where ∇^2 is simply the LaPlace operator:

$$\nabla^2 \equiv \frac{\partial^2}{\partial x^2} + \frac{\partial^2}{\partial y^2} + \frac{\partial^2}{\partial z^2}$$

The square of the wavefunction, ψ^2 , describes the probability of the particle being found at some point in space x and some time t . In the case of the pion, the wave equation also describes the strength of the nuclear force associated with it.

Let us consider the particularly simple case of a time-independent, spherically symmetric solution to Eqn. 1.4 that could describe the pion field outside a nucleon located at the origin. The solution will be a potential function $V(r)$, where r is radial distance from the origin and V is the strength of the field. The condition of time-independence means that the first term on the left will be 0, so the equation assumes the form:

$$\nabla^2 V(r) = -\left(\frac{mc}{\hbar}\right)^2 V(r) \quad (1.7)$$

r is related to x , y , and z as:

$$r = \sqrt{x^2 + y^2 + z^2} \quad \text{and} \quad \frac{\partial r}{\partial x} = \frac{x}{r}$$

Using this relationship and a little mathematical manipulation, the LaPlace operator in 1.7 becomes:

$$\nabla^2 V(r) = \frac{1}{r^2} \frac{d}{dr} \left(r^2 \frac{dV(r)}{dr} \right) \quad (1.8)$$

and 1.7 becomes:

$$\frac{1}{r^2} \frac{d}{dr} \left(r^2 \frac{dV(r)}{dr} \right) = -\left(\frac{mc}{\hbar}\right)^2 V(r)$$

Two possible solutions to this equation are:

$$\frac{1}{r} \exp\left(-r\frac{mc}{\hbar}\right) \quad \text{and} \quad \frac{1}{r} \exp\left(+r\frac{mc}{\hbar}\right)$$

The second solution corresponds to a force increasing to infinity at infinite distance from the source, which is physically unreasonable, thus only the first solution is physically meaningful. Our solution, therefore, for the nuclear force is

$$V(r) = \frac{C}{r} \exp\left(-r\frac{mc}{\hbar}\right) \quad (1.9)$$

where C is a constant related to the strength of the force. The term mc/\hbar has units of length⁻¹. It is a constant that describes the effective range of the force. This effective range is about 1.4×10^{-13} cm. This implies a mass of the pion of about 0.15 u. It is interesting to note that for a massless particle, equation 1.7 reduces to

$$V(r) = \frac{C}{r} \quad (1.10)$$

which is just the form of the potential field for the electromagnetic force. Thus, both the nuclear force and the electromagnetic force satisfy the same general Eqn. 1.9. Because pion has mass while the photon does not, the nuclear force has a very much shorter range than the electromagnetic force.

A simple calculation shows how the nuclear potential and the electromagnetic potential will vary with distance. The magnitude for the nuclear potential constant C is about 10^{-18} erg-cm. The constant C in Eqn. 1.10 for the electromagnetic force is e^2 (where e is the charge on the electron) and has a value of 2.3×10^{-19} erg-cm. Using these values, we can calculate how each potential will vary with distance. This is just how Figure 1.2 was produced.

1.2.5 The liquid-drop model

Why are some combinations of N and Z more stable than others? The answer has to do with the forces between nucleons and how nucleons are organized within the nucleus. The structure and organization of the nucleus are questions still being actively researched in physics, and full treatment is certainly beyond the scope of this text, but we can gain some valuable insight to nuclear stability by considering two of the simplest models of nuclear structure. The simplest model of the nucleus is the *liquid-drop model*, proposed by Niels Bohr in 1936. This model assumes all nucleons in a nucleus have equivalent states. As its name suggests, the model treats the binding between nucleons as similar to the binding between molecules in a liquid drop. According to the liquid-drop model, the total binding energy of nucleons is influenced by four effects: a volume energy, a surface energy, an excess neutron energy, and a coulomb energy. The variation of three of these forces with mass number and their total effect is shown in Figure 1.4.

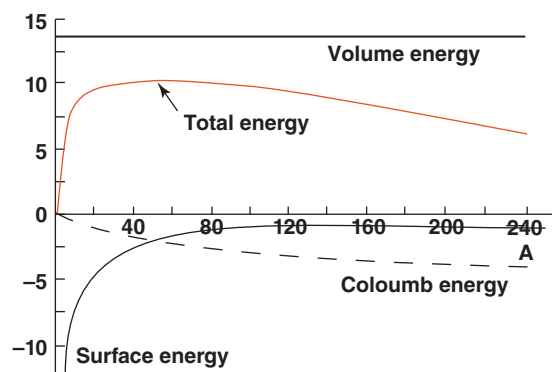


Figure 1.4 Variation of surface, coulomb, and volume energy per nucleon versus mass number. (Source: White (2013). Reproduced with permission of John Wiley & Sons.)

In the liquid-drop model, the binding energy is given as a function of mass number, A , and neutron excess number, $I (= N - Z)$, as:

$$B(A, I) = a_1 A - a_2 A^{2/3} - a_3 I^2 / 4A - a_4 Z^2 / A^{1/3} + \delta \quad (1.11)$$

where:

a_1 : heat of condensation (volume energy \propto

$$A) = 14 \text{ MeV}$$

a_2 : surface tension energy = 13 MeV

a_3 : excess neutron energy = 18.1 MeV

a_4 : coulomb energy = 0.58 MeV

δ : even-odd fudge factor. Binding energy greatest for even-even and smallest for odd-odd.

Some of the nuclear stability rules here can be deduced from Eqn. 1.11. Solutions for Eqn. 1.11 at constant A, that is, for isobars, result in a hyperbolic function of I as illustrated in Figure 1.5. In other words, for a given number of protons, there are an optimal number of neutrons: either too many or too few results in a higher energy state. For odd A, one nuclei will lie at or near the bottom of this function (energy well). For even A, two curves result, one for odd-odd, and one

for even-even. The even-even curve will be the one with the lower (more stable) one. As we shall see, nuclei with either too many or too few neutrons tend to decay to nuclide with the optimal number of neutrons.

1.2.6 The shell model of the nucleus

1.2.6.1 Odd-even effects, magic numbers, and shells

Something that we have alluded to and which the liquid-drop model does not explain is the even-odd effect, illustrated in Table 1.1. Clearly, even combinations of nuclides are much more likely to be stable than odd ones. This is the first indication that the liquid-drop model does not provide a complete description of nuclear stability. Another observation not explained by the liquid-drop model are the so-called *Magic Numbers*. The *Magic*

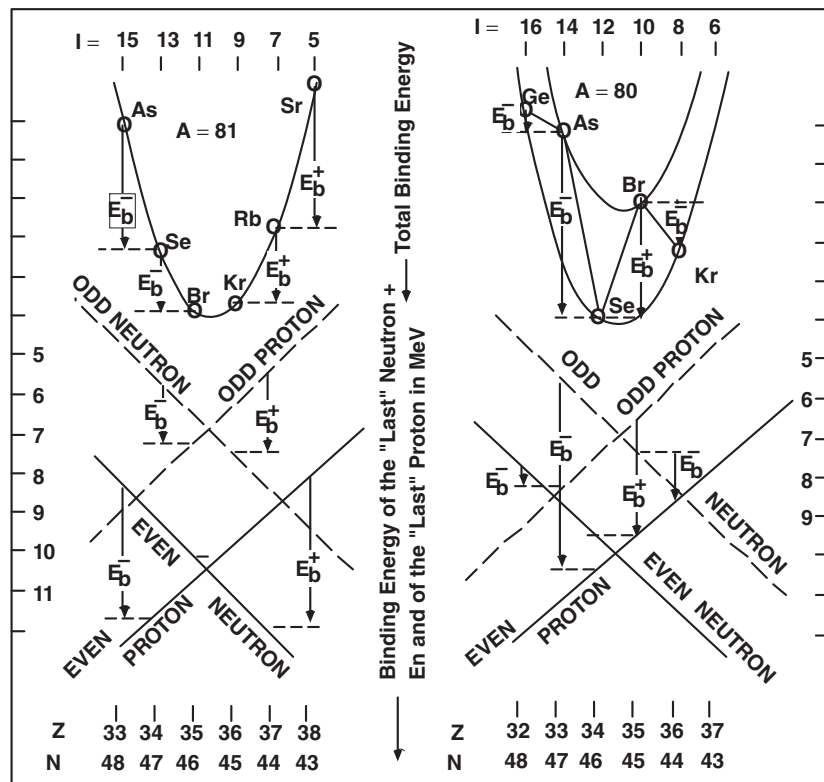


Figure 1.5 Graphical illustration of total binding energies of the isobars of mass number $A = 81$ (left) and $A = 80$ (right). Energy values lie on parabolas, a single parabola for odd A and two parabolas for even A . Binding energies of the ‘last’ proton and “last” neutrons are approximated by the straight lines in the lower part of the figure. (Source: Suess (1987). Reproduced with permission of John Wiley & Sons.)

Table 1.1 Numbers of stable nuclei for odd and even Z and N.

Z	N	A	Number of stable nuclei (Z + N)	Number of very long-lived nuclei
odd	odd	even	4	5
odd	even	odd	50	3
even	odd	odd	55	3
even	even	even	165	11

Numbers are 2, 8, 20, 28, 50, 82, and 126. Some observations about magic numbers:

1. Isotopes and isotones with magic numbers are unusually common (i.e., there are a lot of different nuclides in cases where N or Z equals a magic number).
2. Magic number nuclides are unusually abundant in nature (high concentration of the nuclides).
3. Delayed neutron emission occurs in fission product nuclei containing $N^* + 1$ (where N^* denotes a magic number) neutrons.
4. Heaviest stable nuclides occur at $N = 126$ (and $Z = 83$).
5. Binding energy of last neutron or proton drops for $N^* + 1$.
6. Neutron-capture cross sections for magic numbers are anomalously low.
7. Nuclear properties (spin, magnetic moment, electrical quadrupole moment, metastable isomeric states) change when a magic number is reached.

The electromagnetic spectra emitted by electrons are the principal means of investigating the electronic structure of the atom. By analogy, we would expect that the electromagnetic spectra of the nucleus should yield clues to its structure, and indeed it does. However, the γ spectra of nuclei are so complex that not much progress has been made interpreting it. Observations of magnetic moment and spin of the nucleus have been more useful (nuclear magnetic moment is also the basis of the nuclear magnetic resonance, or NMR, technique, used to investigate relations between atoms in lattices and the medical diagnostic technique nuclear magnetic imaging).

Nuclei with magic numbers of protons or neutrons are particularly stable or “unreactive.” This is clearly analogous to chemical

properties of atoms: atoms with filled electronic shells (the noble gases) are particularly unreactive. In addition, just as the chemical properties of an atom are largely dictated by the “last” valence electron, properties such as the nucleus’s angular momentum and magnetic moment can often be accounted for primarily by the “last” odd nucleon. These observations suggest the nucleus may have a shell structure similar to the electronic shell structure of atoms, and leads to the shell model of the nucleus.

In the shell model of the nucleus, the same general principles apply as to the shell model of the atom: possible states for particles are given by solutions to the Schrödinger Equation. Solutions to this equation, together with the Pauli Exclusion Principle, which states that no two particles can have exactly the same set of quantum numbers, determine how many nucleons may occur in each shell. In the shell model, there are separate systems of shells for neutrons and protons. As do electrons, protons and neutrons have intrinsic angular momentum, called *spin*, which is equal to $1/2\hbar$ ($\hbar = h/2\pi$, where h is Planck’s constant and has units of momentum, $h = 6.626 \times 10^{-34}$ joule-sec). The total nuclear angular momentum, somewhat misleadingly called the nuclear spin, is the sum of (1) the intrinsic angular momentum of protons, (2) the intrinsic angular momentum of neutrons, and (3) the orbital angular momentum of nucleons arising from their motion in the nucleus. Possible values for orbital angular momentum are given by ℓ , the orbital quantum number, which may have integral values. The total angular momentum of a nucleon in the nucleus is thus the sum of its orbital angular momentum plus its intrinsic angular momentum or spin: $j = \ell \pm 1/2$. The plus or minus results because the spin angular momentum vector can be either in the same

Table 1.2 Nuclear spin and odd-even nuclides.

Number of nucleons	Nuclear spin
Even-even	0
Even-odd	1/2, 3/2, 5/2, 7/2 ...
Odd-odd	1, 3

direction or opposite direction of the orbital angular momentum vector. Thus nuclear spin is related to the constituent nucleons in the manner shown in Table 1.2.

Let's now return to magic numbers and see how they relate to the shell model. The magic numbers belong to two different arithmetic series:

$$n = 2, 8, 20, 40, 70, 112 \dots$$

$$n = 2, 6, 14, 28, 50, 82, 126 \dots$$

The lower magic numbers are part of the first series, the higher ones part of the second. The numbers in each series are related by their third differences (the differences between the differences between the differences). For example, for the first of the previous series:

2	8	20	40	70	112
Difference	6	12	20	30	42
Difference	6	8	10	12	
Difference	2	2	2		

This series turns out to be solutions to the Schrödinger equation for a three-dimensional harmonic oscillator (Table 1.3). (This solution

is different from the solution for particles in an isotropic coulomb field, which describes electron shells.)

1.2.6.2 Magnetic moment

A rotating charged particle produces a magnetic field. A magnetic field also arises from the orbital motion of charged particles. Thus, electrons in orbit around the nucleus, and also spinning about an internal axis, produce magnetic fields, much as a bar magnet. The strength of a bar magnet may be measured by its magnetic moment, which is defined as the energy needed to turn the magnet from a position parallel to an external magnetic field to a perpendicular position. For the electron, the spin magnetic moment is equal to 1 Bohr magneton ($\mu_e = 5.8 \times 10^{-9} \text{ eV/gauss}$). The spin magnetic moment of the proton is 2.79 nuclear magnetons, which is about three orders of magnitude less than the Bohr magneton (hence nuclear magnetic fields do not contribute significantly to atomic ones). Surprisingly, in 1936 the neutron was also found to have an intrinsic magnetic moment, equal to -1.91 nuclear magnetons. Because magnetism always involves motion of charges, this result suggested there is a non-uniform distribution of charge on the neutron, which was an early hint that neutrons and protons were composite particles rather than elementary ones.

Total angular momentum and magnetic moment of pairs of protons cancel because the vectors of each member of the pair are aligned in opposite directions. The same holds true for neutrons. Hence, even-even nuclei have 0 angular momentum and magnetic

Table 1.3 Particles in a three-dimensional harmonic oscillator (solution to the Schrödinger Equation).

N	1	2		3			4			
ℓ	0	1		0	2		1	3		
j	1/2	1/2	3/2	1/2	3/2	5/2	1/2	3/2	5/2	7/2
State	s ⁺	p ⁻	p ⁺	s ⁺	d ⁻	d ⁺	p ⁻	p ⁺	f ⁻	f ⁺
No.	2	2	4	2	4	6	2	4	6	8
Σ	2	6		12				20		
Total	(2)	(8)		(20)				(40)		

N is the shell number; No. gives the number of particles in the orbit, which is equal to $2j + 1$; Σ gives the number of particles in the shell or state, and total is the total of particles in all shells filled. Magic numbers fail to follow the progression of the first series because only the f state is available in the fourth shell.

moment. Angular momentum, or nuclear spin, of odd-even nuclides can have values of $1/2$, $3/2$, $5/2$, and non-zero magnetic moment (Table 1.2). Odd-odd nuclei have integer value of angular momentum or “nuclear spin.” From this we can see that the angular momentum and magnetic moment of a nucleus are determined by the last nucleon added to the nucleus. For example, ^{18}O has eight protons and 10 neutrons, and hence

zero angular momentum and magnetic moment. Adding one proton to this nucleus transforms it to ^{19}F , which has angular momentum of $1/2$ and magnetic moment of ~ 2.79 . For this reason, the shell model is also sometimes called the single-particle model, since the structure can be recognized from the quantum-mechanical state of the “last” particle (usually). This is a little surprising since particles are assumed to interact.

Aside: Nuclear magnetic resonance

Nuclear magnetic resonance (NMR) has no application in isotope geochemistry (it is, however, used in mineralogy), but it has become such an important and successful medical technique that, as long as we are on the subject of nuclear spin, a brief examination of the basics of the technique seems worthwhile. In brief, some nuclei can be excited into higher nuclei spin energy states by radio frequency (RF) radiation – the absorption of this radiation can be detected by an appropriate RF receiver and the frequency of this absorbed radiation provides information about the environment of that nucleus on the molecular level.

In more detail, it works like this. As we have seen, even-odd and odd-odd nuclei have a nuclear spin. A nucleus of spin j will have $2j + 1$ possible orientations. For example, ^{13}C has a spin $1/2$ and two possible orientations in space of the spin vector. In the absence of a magnetic field, all orientations have equal energies. In a magnetic field, however, energy levels split and those spin orientations aligned with the magnetic field have lower energy levels (actually, spin vectors precess around the field vector) than others. There will be a thermodynamic (i.e., a Boltzmann) distribution of nuclei among energy states, with more nuclei populating the lower energy levels. The energy difference between these levels is in the range of energies of RF photons (energies are of the order of $7 \times 10^{-26}\text{ J}$, which corresponds to frequencies around 100 MHz). When a nucleus absorbs a photon of this energy, it will change its spin orientation to one having a higher energy level. The precise energy difference between spin states, and hence the precise RF frequency that must be absorbed for the transition to occur, depends on the strength of the applied magnetic field, the nature of the nucleus, and also the atomic environment in which that nucleus is located. The latter is a consequence of magnetic fields of electrons in the vicinity of the nucleus. Although this effect is quite small, it is this slight shift in energy that makes NMR particularly valuable as it allows a non-destructive method of probing the molecular environments of atoms. Non-destructivity is often an advantage for many analytical problems, but, as you can easily imagine, it is particularly important when the sample is a person!

The three-dimensional harmonic oscillator solution explains only the first three magic numbers; magic numbers above that belong to another series. This difference may be explained by assuming there is a strong spin-orbit interaction, resulting from the orbital magnetic field acting upon the spin magnetic moment. This effect is called the Mayer–Jensen coupling. The concept is that the energy state of the nucleon depends strongly on the orientation of the spin of the particle relative to the orbit, and that parallel spin-orbit orientations are energetically favored, that is, states with higher values of j

tend to be the lowest energy states. This leads to filling of the orbits in a somewhat different order; that is, such that high spin values are energetically favored. Spin-orbit interaction also occurs in the electron structure, but it is less important.

1.2.6.3 Pairing effects

In the liquid-drop model, it was necessary to add a “fudge factor,” the term δ , to account for the even-odd effect. The even-odd effect arises from a “pairing energy” that exists between two nucleons of the same kind. When

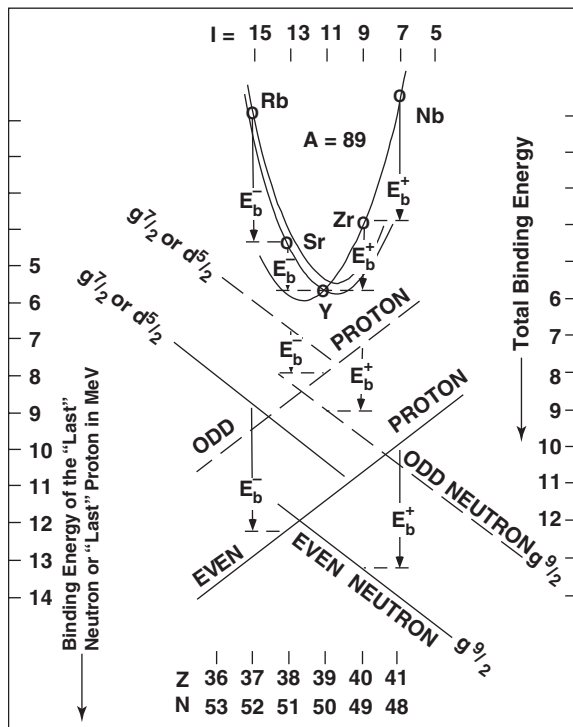


Figure 1.6 Schematic of binding energy as a function of I , neutron excess number in the vicinity of $N = 50$. (Source: Suess (1987). Reproduced with permission of John Wiley & Sons.)

proton-proton and neutron-neutron pairing energies are equal, the binding energy defines a single hyperbola as a function of I (e.g., Figure 1.5). When they are not, as is often the case in the vicinity of magic numbers, the hyperbola for odd A splits into two curves, one for even Z , the other for even N . An example is shown in Figure 1.6. The empirical rule is: *Whenever the number of one kind of nucleon is somewhat larger than a magic number, the pairing energy of this kind of nucleon will be smaller than the other kind.*

1.2.6.4 Capture cross sections

Information about the structure and stability of nuclei can also be obtained from observations of the probability that a nucleus will capture an additional nucleon. This probability is termed the *capture cross section*, and has units of area. Neutron capture cross sections are generally of greater use than proton capture cross sections, mainly because they are much larger. The reason for this is simply that a proton must overcome the repulsive coulomb forces to be captured, whereas a

neutron, being neutral, is unaffected electrostatic forces. Neutron-capture cross sections are measured in barns, which have units of 10^{-24} cm^2 , and are denoted by σ . The physical cross section of a typical nucleus (e.g., Ca) is of the order of $5 \times 10^{-25} \text{ cm}^2$, and increases somewhat with mass number (more precisely, $R = r_0 A^{1/3}$, where A is mass number and r_0 is the nuclear force radius, $1.4 \times 10^{-13} \text{ cm}$). While many neutron capture cross sections are of the order of 1 barn, they vary from 0 (for ${}^4\text{He}$) to 10^5 for ${}^{157}\text{Gd}$, and are not simple functions of nuclear mass (or size). They depend on nuclear structure, being for example, generally low at magic numbers of N . Capture cross sections also dependent on the energy of the neutron, the dependence varying from nuclide to nuclide.

1.2.7 Collective model

A slightly more complex model is called the collective model. It is intermediate between the liquid-drop and the shell models. It emphasizes the collective motion of nuclear matter, particularly the vibrations and rotations, both

quantized in energy, in which large groups of nucleons can participate. Even-even nuclides with Z or N close to magic numbers are particularly stable with nearly perfect spherical symmetry. Spherical nuclides cannot rotate because of a dictum of quantum mechanics that a rotation about an axis of symmetry is undetectable, and in a sphere every axis is a symmetry axis. The excitation of such nuclei (that is, when their energy rises to some quantum level above the ground state) may be ascribed to the vibration of the nucleus as a whole. On the other hand, even-even nuclides far from magic numbers depart substantially from spherical symmetry and the excitation energies of their excited states may be ascribed to rotation of the nucleus as a whole.

1.3 RADIOACTIVE DECAY

As we have seen, some combinations of protons and neutrons form nuclei that are only “metastable.” These ultimately transform to stable nuclei through the process called radioactive decay. This involves emission of a particle or particles and is usually accompanied by emission of a photon as well. In some cases, the photon emission is delayed and the daughter nuclide is left in an excited state. Just as an atom can exist in any one of a number of excited states, so too can a nucleus have a set of discrete, quantized, excited nuclear states. The behavior of nuclei in transforming to more stable states is somewhat similar to atomic transformation from excited to more stable states, but there are some important differences. First, energy level spacing is much greater; second, the time an unstable nucleus spends in an excited state can range from 10^{-14} sec to 10^{11} years, whereas atomic lifetimes are usually about 10^{-8} sec. Like atomic transitions, nuclear reactions must obey general physical laws, conservation of momentum, mass-energy, spin, and so on, and conservation of nuclear particles.

Nuclear decay takes place at a rate that follows the law of radioactive decay. There are two extremely interesting and important aspects of radioactive decay. First, the decay rate is dependent only on the nature and energy state of the particular nuclide; it is independent of the history of the nucleus, and essentially independent of external influences such as temperature, pressure, and so on. It

is this property that makes radioactive decay so useful as a chronometer. Second, it is completely impossible to predict when a given nucleus will decay. We can, however, predict the probability of its decay in a given time interval. The probability of decay in some infinitesimally small time interval, dt is λdt . Therefore, the rate of decay among some number, N , of nuclides is:

$$\frac{dN}{dt} = -\lambda N \quad (1.12)$$

The minus sign simply indicates N decreases. Equation 1.12 is a first-order rate law known as the *basic equation of radioactive decay*. Essentially, all the significant equations of radiogenic isotope geochemistry and geochronology can be derived from this simple expression.

1.3.1 Gamma decay

A gamma ray is simply a high-energy photon (i.e., electromagnetic radiation). Just as an atom can be excited into a higher energy state when it absorbs photon, nuclei can be excited into higher energy states by absorption of a much higher energy photon. Both excited atom and nuclei subsequently decay to their ground states by emission of a photon. Photons involved in atomic excitation and decay have energies ranging from the visible to the X-ray part of the electromagnetic spectrum (roughly 1 eV to 100 keV); gamma rays involved in nuclear transitions typically have energies greater than several hundred keV. Although nuclei, like atoms, generally decay promptly from excited states, in some cases nuclei can persist in metastable excited states characterized by higher nuclear spin for considerable lengths of time.

The gamma ray frequency is related to the energy difference by:

$$\hbar\nu = E_u - E_l \quad (1.13)$$

where E_u and E_l are simply the energies of the upper (excited) and lower (ground) states and \hbar is the reduced Planck's constant ($h/2\pi$). The nuclear reaction is written as:



Gamma emission usually, but not invariably, accompanies alpha and beta decay as a consequence of the daughter being left in an excited state. Decay generally occurs within 10^{-12} sec of the decay, but, as noted here, can be delayed if the daughter persists in a metastable state.

1.3.2 Alpha decay

An α -particle is simply a helium nucleus. Since the helium nucleus is particularly stable, it is not surprising that such a group of particles might exist within the parent nucleus before α -decay. Emission of an alpha particle decreases the mass of the nucleus by the mass of the alpha particle, and also by the kinetic energy of the alpha particle and the remaining nucleus (because of the conservation of momentum, the remaining nucleus recoils from the decay reaction). The α particle may leave the nucleus with any of several discrete kinetic energy levels, as is illustrated in Figure 1.7.

The escape of the α particle is a bit of a problem, because it must overcome a very substantial energy barrier, a combination of the strong force and the coulomb repulsion, to get out. For example, α particles fired at in ^{238}U with energies below 8 Mev are scattered from the nucleus. However, during α decay of ^{238}U , the α particle emerges with an energy of

only about 4 Mev. This is an example of an effect called *tunneling* and can be understood as follows. We can never know exactly where the α particle is (or any other particle, or you or I for that matter), we only know the probability of its being in a particular place. This probability is given by the particle's wavefunction, $\psi(r)$. The wave is strongly attenuated through the potential energy barrier, but has a small but finite amplitude outside the nucleus, and hence a small but finite probability of its being located there.

The escape of an alpha particle leaves a daughter nucleus with mass $<\text{A}-4$; the missing mass is the kinetic energy of the alpha and remaining nucleus. The daughter may originally be in an excited state, from which it will decay by γ -decay. Figure 1.7 shows an example energy-level diagram for such decay. Note that the sum of the kinetic energy of the α and the energy of the γ is constant.

Alpha-decay occurs in nuclei with mass above the maximum in the binding energy curve (Figure 1.3), which occurs at ^{56}Fe . Possibly all such nuclei are unstable relative to alpha-decay, but most of their half-lives are immeasurably long.

1.3.3 Beta decay

Beta decay is a process in which the charge of a nucleus changes, but the number of nucleons

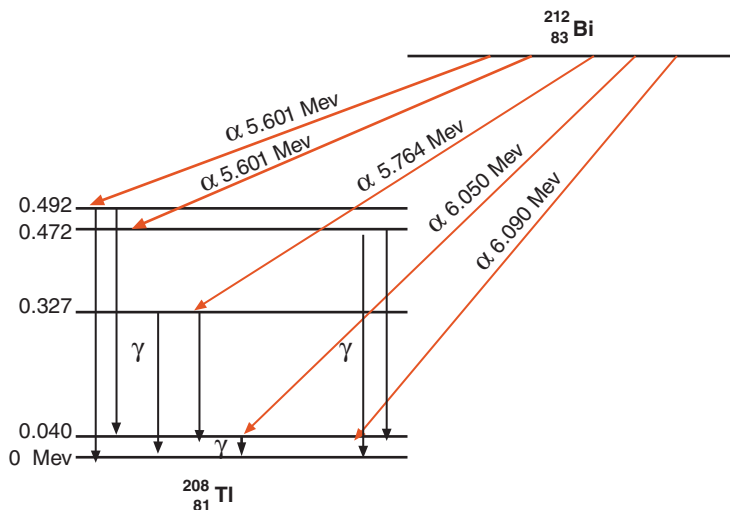


Figure 1.7 Nuclear energy-level diagram showing decay of bismuth-212 by alpha emission to the ground and excited states of thallium-208. (Source: White (2013). Reproduced with permission of John Wiley & Sons.)

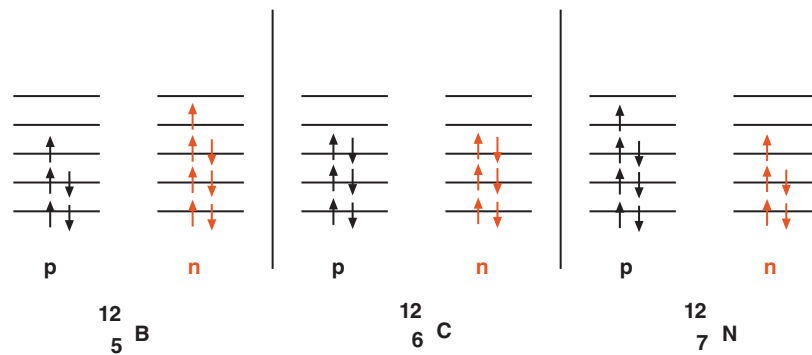


Figure 1.8 Proton and neutron occupation levels of boron 12, carbon 12, and nitrogen 12. (Source: White (2013). Reproduced with permission of John Wiley & Sons.)

remains the same. If we plotted Figure 1.1 with a third dimension, namely energy of the nucleus, we would see the stability region forms an energy valley. Alpha-decay moves a nucleus down the valley axis; beta decay moves a nucleus down the walls toward the valley axis. Beta-decay results in the emission of an electron or positron, depending on which side of the valley the parent lies. Consider the three nuclei in Figure 1.8 (these are isobars, since they all have 12 nucleons). From what we have learned of the structure of nuclei, we can easily predict the ^{12}C nucleus is the most stable. This is the case. ^{12}B decays to ^{12}C by the creation and emission of a β^- particle and the conversion of a neutron to a proton. ^{12}N decays by emission of a β^+ and conversion of a proton to a neutron.

Here, physicists had a problem. Angular momentum must be conserved in the decay of nuclei. The ^{12}C nucleus has integral spin as do ^{12}B and ^{12}N . But the beta particle has 1/2 quantum spin units. An additional problem is that rather than having discrete kinetic energies, β particles exhibit a spectrum of kinetic energies, although there is a well-defined maximum energy. Thus beta decay appeared to violate both conservation of momentum and energy. The solution, proposed by Enrico Fermi, was the existence of another, nearly massless particle,³ called the neutrino, having 1/2 spin and variable kinetic energy. Thus in beta decay, a neutrino is also released and the sum of the kinetic energy of the beta and neutrino, plus the energy of any gamma, is constant.

Beta decay involves the weak force, or weak interaction. The weak interaction transforms

one flavor of quark into another and thereby a charged particle (e.g., a proton) into a one neutral (e.g., a neutron) and vice versa. Both the weak and the electromagnetic forces are thought to be simply a manifestation of one force, called electroweak, that accounts for all interactions involving charge (in the same sense that electric and magnetic forces are manifestations of electromagnetism). In β^+ decay, for example, a proton is converted to a neutron, giving up its +1 charge to a neutrino, which is converted to a positron. This process occurs through the intermediacy of the W+ particle in the same way that electromagnetic processes are mediated by photons. The photon, pion, and W particles are members of a class of particles called bosons that mediate forces between the basic constituents of matter. However, the W particles differ from photons in having a very substantial mass (around 80 GeV or almost 2 orders of magnitude greater mass than the proton). Interestingly, *Nature* rejected the paper in which Fermi proposed the theory of beta decay involving the neutrino and the weak force in 1934!

1.3.4 Electron capture

Another type of reaction is electron capture. This is sort of the reverse of beta decay and has the same effect, more or less, as β^+ decay. Interestingly, this is a process in which an electron is added to a nucleus to produce a nucleus with less mass than the parent! The missing mass is carried off as energy by an escaping neutrino, and in some cases by a γ . In some cases, a nucleus can decay by either electron capture, β^- , or β^+ emission. An

example is the decay of ^{40}K , which decays to ^{40}Ca by β^- and ^{40}Ar to by β^+ or electron capture. We should point out that electron capture is an exception to the environmental independence of nuclear decay reactions in that it shows a very slight dependence on pressure.

β decay and electron capture often leaves the daughter nucleus in an excited state. In this case, it will decay to its ground state (usually very quickly) by the emission of a γ -ray. Thus, γ rays often accompany β decay (as well as α decay). A change in charge of the nucleus necessitates a rearrangement of electrons in their orbits. This is particularly true in electron capture, where an inner electron is lost. As electrons jump down to lower orbits to occupy the orbital freed by the captured electron, they give off electromagnetic energy. This produces X-rays from electrons in the inner orbits.

1.3.5 Spontaneous fission

This is a process in which a nucleus splits into two or more fairly heavy daughter nuclei. In nature, this is a very rare process, occurring only in the heaviest nuclei, ^{238}U , ^{235}U , and ^{232}Th (it is, however, most likely in ^{238}U). It also occurs in ^{244}Pu , an extinct radionuclide (we use the term “extinct radionuclide” to refer to nuclides that once existed in the Solar System, but which have subsequently decayed away entirely). The liquid-drop model perhaps better explains this particular phenomenon than the shell model. Recall that in the liquid-drop model, there are four contributions to total binding energy: volume energy, surface tension, excess neutron energy, and coulomb energy. The surface tension tends to minimize the surface area while the repulsive coulomb energy tends to increase it. We can visualize these nuclei as oscillating between various shapes. It may very rarely become so distorted by the repulsive force of 90 or so protons, that the surface tension cannot restore the shape. Surface tension is instead minimized by the splitting the nucleus entirely.

Since there is a tendency for N/Z to increase with A for stable nuclei, the parent is much richer in neutrons than the daughters produced by fission (which may range from $Z = 30$, zinc, to $Z = 65$, terbium). Thus fission generally also produces some free neutrons in addition to two nuclear fragments (the

daughters). The daughters are typically of unequal size, the exact mass of the two daughters being random. The average mass ratio of the high to the low mass fragment is about 1.45. Even though some free neutrons are created, the daughters tend to be too neutron-rich to be stable. As a result, they decay by β^- to stable daughters. It is this decay of the daughters that results in radioactive fallout in bombs and radioactive waste in reactors (a secondary source of radioactivity is production of unstable nuclides by capture of the neutrons released).

Some non-stable heavy nuclei and excited heavy nuclei are particularly unstable with respect to fission. An important example is ^{236}U . Imagine a material rich in U. When ^{238}U undergoes fission, one of the released neutrons can be captured by ^{235}U nuclei, producing ^{236}U in an excited state. This ^{236}U then fissions producing more neutrons, and so on. This is the basis of nuclear reactors and bombs (the latter can also be based on Pu). The concentration of U is not usually high enough in nature for this sort of thing to happen. But it apparently did at least once, 1.5 billion years ago in the Oklo U deposit in Africa. This deposit was found to have an anomalously high $^{238}\text{U}/^{235}\text{U}$ ratio (227 versus 137.82), indicating some of the ^{235}U had been “burned” in a nuclear chain reaction. Could such a natural nuclear reactor happen again? Probably not, because there is a lot less ^{235}U around now than there was 1.7 billion years ago. With equations we’ll introduce soon, you should be able to calculate just how much less.

Individual natural fission reactions are less rare. When fission occurs, there is a fair amount of kinetic energy produced (maximum about 200 MeV), the nuclear fragments literally flying apart. These fragments damage the crystal structure through which they pass, producing “tracks”, whose visibility can be enhanced by etching. This is the basis of fission-track dating, which we’ll describe in Chapter 4.

Natural fission also can produce variations in the isotopic abundance of elements among the natural, ultimate product. Xenon is an important product, as we’ll learn in Chapter 12. Indeed, the critical evidence showing that a nuclear chain reaction had indeed occurred in the Oklo deposit was the discovery that fission product elements, such as Nd and Ru, had

anomalous isotopic compositions. Analysis of the isotopic composition of another fission product, Sm, has led to a controversy over whether the fine scale constant, α , has changed over time. α is related to other fundamental constants as:

$$\alpha = \frac{e^2}{\hbar c} \quad (1.15)$$

where e is the charge of the electron (and \hbar is the reduced Planck constant and c is the speed of light). A change in the fine scale constant thus raises the possibility of a change in c . The change, if it occurred, is quite small, less than 1 part in 10^7 , and could be consistent with some observations about quasars and the early universe.

1.4 NUCLEOSYNTHESIS

A reasonable starting point for isotope geochemistry is a determination of the abundances of the naturally occurring nuclides. Indeed, this was the first task of isotope geochemists (although those engaged in this work would have referred to themselves simply as physicists). This began with Thomson, who built the first mass spectrometer and discovered that Ne consisted of two isotopes (actually, it consists of three, but one of them, ^{21}Ne , is very much less abundant than the other two, and Thomson's primitive instrument did not detect it). Having determined the abundances of nuclides, it is natural to ask what accounts for this distribution, and even more fundamentally, what process or processes produced the elements. This process is known as nucleosynthesis.

The abundances of naturally occurring nuclides are now reasonably well known – at least in our Solar System. We also have what appears to be a reasonably successful theory of nucleosynthesis. Physicists, like all scientists, are attracted to simple theories. Not surprisingly then, the first ideas about nucleosynthesis attempted to explain the origin of the elements by single processes. Generally, these were thought to occur at the time of the Big Bang. None of these theories was successful. It was really the astronomers, accustomed to dealing with more complex phenomena than physicists, who successfully produced a theory of nucleosynthesis that involved a number of processes. Today, isotope geochemists continue to be involved in refining

these ideas by examining and attempting to explain isotopic variations occurring in some meteorites; two recent examples are papers by Jadhav et al. (2013) and Haenecour et al. (2013).

The origin of the elements is an astronomical question, perhaps even more a cosmological one. To understand how the elements formed we need to understand a few astronomical observations and concepts. The Universe began about 13.8 Ga⁴ ago with the Big Bang. Since then the Universe has been expanding, cooling, and evolving. This hypothesis follows from two observations: the relationship between red-shift and distance and the cosmic background radiation, particularly the former. This cosmology provides two possibilities for formation of the elements: (1) they were formed in the Big Bang itself, or (2) they were subsequently produced. As we shall see, the answer is both.

Our present understanding of nucleosynthesis comes from three sorts of observations: (1) the abundance of isotopes and elements in the Earth, Solar System, and cosmos (spectral observations of stars), (2) experiments on nuclear reactions that determine what reactions are possible (or probable) under given conditions, and (3) inferences about possible sites of nucleosynthesis and about the conditions that would prevail in those sites. The abundances of the elements in the Solar System are shown in Figure 1.9.

Various hints came from all three of these observations. For example, it was noted that the most abundant nuclide of a given set of stable isobars tended to be the most neutron-rich one. We now understand this to be a result of shielding from β -decay (see the discussion of the r-process next).

Another key piece of evidence regarding formation of the elements comes from looking back into the history of the cosmos. Astronomy is a bit like geology in that just as we learn about the evolution of the Earth by examining old rocks, we can learn about the evolution of the cosmos by looking at old stars. It turns out that old stars (such old stars are most abundant in the globular clusters outside the main disk of the Milky Way) are considerably poorer in heavy elements than are young stars. This suggests much of the heavy element inventory of the galaxy has been produced since these stars formed (some

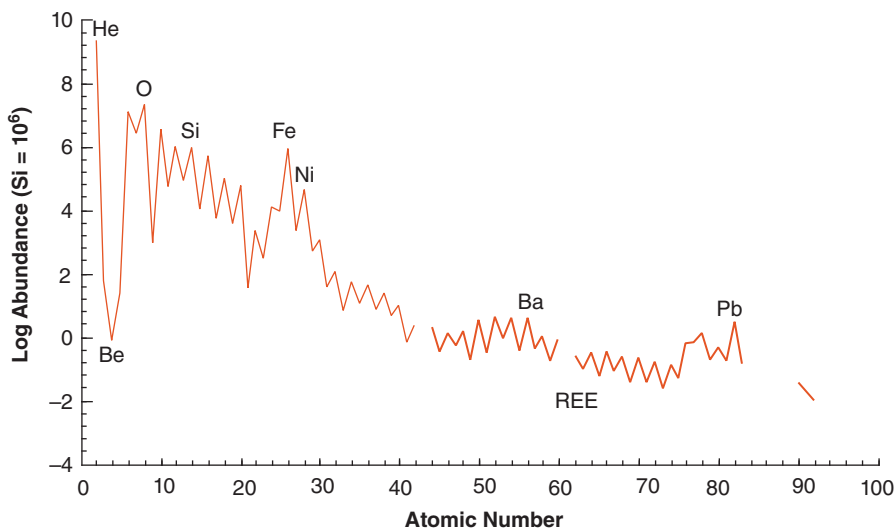


Figure 1.9 Solar System abundance of the elements relative to silicon as a function of atomic number.
(Source: White (2013). Reproduced with permission of John Wiley & Sons.)

10 Ga ago). On the other hand, they seem to have about the same He/H ratio as young stars. Indeed ${}^4\text{He}$ seems to have an abundance of 24–28% in all stars. Another key observation was the identification of technetium emissions in the spectra of some stars. Since the most stable isotope of this element has a half-life of about 100,000 years and for all intents and purposes it does not exist in the Earth, it must have been synthesized in those stars. Thus the observational evidence suggests (1) H and He are everywhere uniform implying their creation and fixing of the He/H ratio in the Big Bang and (2) subsequent creation of heavier elements (heavier than Li, as we shall see) by subsequent processes.

As we mentioned, early attempts (\sim 1930 – 1950) to understand nucleosynthesis focused on single mechanisms. Failure to find a single mechanism that could explain the observed abundance of nuclides, even under varying conditions, led to the present view that relies on a number of mechanisms operating in different environments and at different times for creation of the elements in their observed abundances. This view, often called the polygenetic hypothesis, is based mainly on the work of Burbidge, Burbidge, Fowler and Hoyle. Their classic paper summarizing the theory, “Synthesis of the elements in stars” was published in *Reviews of Modern Physics* in 1957. Interestingly, the abundance of trace

elements and their isotopic compositions were perhaps the most critical observations in development of the theory. An objection to this polygenetic scenario was the apparent uniformity of the isotopic composition of the elements. But variations in the isotopic composition have now been demonstrated for many elements in some meteorites. Furthermore, there are quite significant compositional variations in heavier elements among stars. These observations provide strong support for this theory.

To briefly summarize it, the polygenetic hypothesis proposes four phases of nucleosynthesis. *Cosmological nucleosynthesis* occurred shortly after the Universe began and is responsible for the cosmic inventory of H and He, and some of the Li. Helium is the main product of nucleosynthesis in the interiors of normal, or “main sequence” stars. The lighter elements, up to and including Si, but excluding Li and Be, and a fraction of the heavier elements may be synthesized in the interiors of larger stars during the final stages of their evolution (*stellar nucleosynthesis*). The synthesis of the remaining elements occurs as large stars exhaust the nuclear fuel in their interiors and explode in nature’s grandest spectacle, the supernova (*explosive nucleosynthesis*). Finally, Li and Be are continually produced in interstellar space by interaction of cosmic rays with matter (*galactic*

nucleosynthesis). In the following sections, we examine these nucleosynthetic processes as presently understood.

1.4.1 Cosmological nucleosynthesis

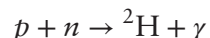
Immediately after the Big Bang, the Universe was too hot for any matter to exist – there was only energy. Some 10^{-11} seconds later, the Universe had expanded and cooled to the point where quarks and anti-quarks could condense from the energy. The quarks and anti-quarks, however, would also collide and annihilate each other. So a sort of thermal equilibrium existed between matter and energy. As things continued to cool, this equilibrium progressively favored matter over energy. Initially, there was an equal abundance of quarks and anti-quarks, but as time passed, the symmetry was broken and quarks came to dominate. The current theory is that the hyper-weak force was responsible for an imbalance favoring matter over anti-matter. After 10^{-4} seconds, things were cool enough for quarks to associate with one another and form nucleons: protons and neutrons. After 10^{-2} seconds, the Universe has cooled to 10^{11} K. Electrons and positrons were in equilibrium with photons, neutrinos, and antineutrinos were in equilibrium with photons, and antineutrinos combined with protons to form positrons and neutrons, and neutrinos combined with neutrons to form electrons and protons:



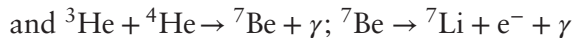
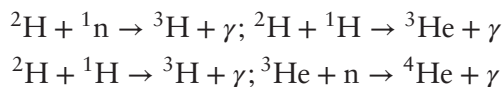
This equilibrium produced about an equal number of protons and neutrons. However, the neutron is unstable outside the nucleus and decays to a proton with a half-life of about 15 min. So as time continued passed, protons became more abundant than neutrons.

After a second or so, the Universe had cooled to 10^{10} K, which shut down the reactions above. Consequently, neutrons were no longer being created, but they were being destroyed as they decayed to protons. At this point, protons were about three times as abundant as neutrons.

It took another 3 min to for the Universe to cool to 10^9 K, which is cool enough for ^2H , created by



to be stable. At about the same time, the following reactions could also occur:



One significant aspect of this event is that it began to lock up neutrons in nuclei where they could no longer decay to protons. The timing of this event fixes the ratio of protons to neutrons at about 7:1. Because of this dominance of protons, hydrogen is the dominant element in the Universe. About 24% of the mass of the Universe was converted to ^4He in this way; less than 0.01% was converted to ^2H , ^3He , and ^7Li (and there is good agreement between theory and observation). Formation of elements heavier than Li was inhibited by the instability of nuclei of masses 5 and 8. Shortly thereafter, the universe cooled below 10^9 K and nuclear reactions were no longer possible.

Thus, the Big Bang created H, He and a bit of Li ($^7\text{Li}/\text{H} < 10^{-9}$). Some 300,000 years or so later, the Universe had cooled to about 3000 K, cool enough for electrons to be bound to nuclei, forming atoms. It was at this time, called the “recombination era” that the Universe first became transparent to radiation. Prior to that, photons were scattered by the free electrons, making the Universe opaque. It is the radiation emitted during this recombination that makes up the cosmic microwave background radiation that we can still detect today. Discovery of this cosmic microwave background radiation, which has the exact spectra predicted by the Big Bang model, represents a major triumph for the model and is not easily explained in any other way.

1.4.2 Stellar nucleosynthesis

1.4.2.1 Astronomical background

Before discussing nucleosynthesis in stars, it is useful to review a few basics of astronomy. Stars shine because of exothermic nuclear reactions occurring in their cores. The energy released by these processes results in thermal expansion that, in general, exactly balances gravitational collapse. Surface temperatures are very much cooler than temperatures in stellar cores. For example, the Sun, which is

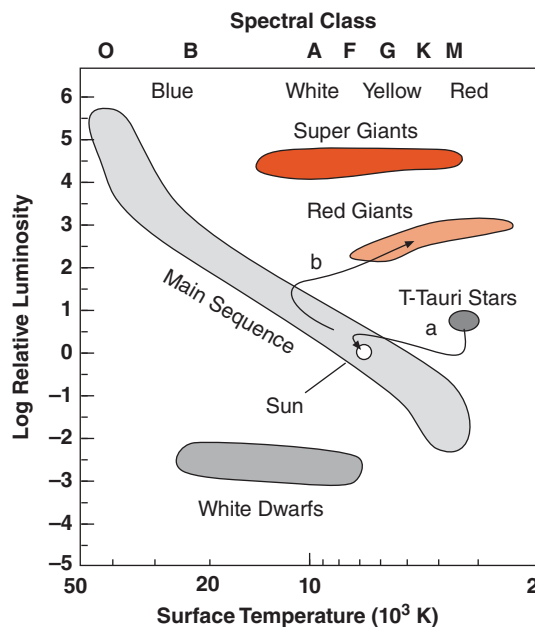


Figure 1.10 The Hertzsprung–Russell diagram of the relationship between luminosity and surface temperature. Arrows show evolutionary path for a star the size of the Sun in pre- (a) and post- (b) main sequence phases. (Source: White (2013). Reproduced with permission of John Wiley & Sons.)

in many respects an average star, has a surface temperature of 5700 K and a core temperature thought to be 14,000,000 K.

Stars are classified based on their color (and spectral absorption lines), which in turn is related to their temperature. From hot to cold, the classification is: O, B, F, G, K, M, with subclasses designated by numbers, for example, F5. (The mnemonic is “*O Be a Fine Girl, Kiss Me!*”). The Sun is class G. Stars are also divided into Populations. Population I stars are second or later generation stars and have greater heavy element contents than Population II stars. Population I stars are generally located in the main disk of the galaxy, whereas the old first generation stars of Population II occur mainly in globular clusters that circle the main disk.

On a plot of luminosity versus wavelength of their principal emissions (i.e., color), called a Hertzsprung–Russell diagram (Figure 1.10), most stars (about 90%) fall along an array defining an inverse correlation between these two properties. Since wavelength is inversely related to temperature, this correlation means simply that hot stars are more luminous and give off more energy than cooler stars. Mass and radius are also simply related to

temperature and luminosity for these so-called “main sequence” stars;⁵ hot stars are big, small stars are cooler. Thus O and B stars are large, luminous, and hot; K and M stars are small, cool, and (comparatively speaking) dark. Stars on the main sequence produce energy by “hydrogen burning,” fusion of hydrogen to produce helium. Since the rate at which these reactions occur depends on temperature and density, hot, massive stars release more energy than smaller ones. As a result, they exhaust the hydrogen in their cores much more rapidly. Thus there is an inverse relationship between the lifetime of a star and its mass. The most massive stars, up to 100 solar masses, have life expectancies of only about 10^6 years or so, whereas small stars, as small as 0.01 solar masses, remain on the main sequence more than 10^{10} years.

The two most important exceptions to the main sequence stars, the red giants and the white dwarfs, represent stars that have burned all the H fuel in their cores and have moved on in the evolutionary sequence. When the H in the core is converted to He, it generally cannot be replenished because the density difference prevents convection between the core and outer layers, which are still H-rich. The interior

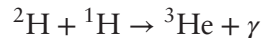
part of the core collapses under gravity. With enough collapse, the layer immediately above the He core will begin to “burn” H again, which again stabilizes the star. The core, however, continues to collapse until T and P are great enough for He burning to begin. At the same time, energy from the interior is transferred to the outer layers, causing the exterior to expand; it cools as it expands, resulting in a *red giant*; a star that is over-luminous relative to main sequence stars of the same color. When the Sun reaches this phase, in perhaps another 5 Ga, it will expand to the Earth’s orbit. A star will remain in the red giant phase for of the order of 10^6 – 10^8 years. During this time, radiation pressure results in a greatly enhanced solar wind, of the order of 10^{-6} to 10^{-7} , or even 10^{-4} , solar masses per year. For comparison, the present solar wind is 10^{-14} solar masses/year; thus, in its entire main-sequence lifetime, the Sun will blow off 1/10,000 of its mass through solar wind.

The fate of stars after the red giant phase (when the He in the core is exhausted) depends on their mass. Nuclear reactions in small stars cease and they simply contract, their exteriors heating up as they do so, to become *white dwarfs*. The energy released is that produced by previous nuclear reactions and released gravitational potential energy. This is the likely fate of the Sun. White Dwarfs are underluminous relative to stars of similar color on the main sequence. They can be thought of as little more than glowing ashes. Unless they blow off sufficient mass during the red giant phase, stars larger than 8 solar masses die explosively, in supernovae (specifically, Type II supernovae). (Novae are entirely different events that occur in binary systems when mass from a main sequence star is pull by gravity onto a white dwarf companion.) Supernovae are incredibly energetic events. The energy released by a supernova can exceed that released by an entire galaxy (which, it will be recalled, consists of on the order of 10^9 stars) for a period of days or weeks!

1.4.2.2 Hydrogen, helium, and carbon burning in main sequence and red giant stars

For quite some time after the Big Bang, the Universe was a more or less homogeneous, hot gas. More or less turns out to be critical wording. Inevitably (according to fluid dynamics),

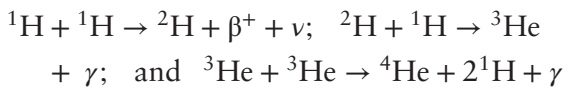
inhomogeneities in the gas developed. These inhomogeneities enlarged in a sort of run-away process of gravitational attraction and collapse. Thus were formed protogalaxies, thought to date to about 0.5–1.0 Ga after the Big Bang. Instabilities within the protogalaxies collapsed into stars. Once this collapse proceeds to the point where temperatures reach 1 million K, deuterium burning can begin:



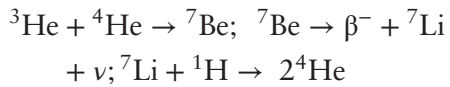
This occurs while pre-main stars are still accreting mass and growing and temporarily stabilizes the star against further collapse. This may continue for several million years in smaller stars such as the Sun. (In low mass objects that will never reach temperatures and pressures for hydrogen burning to initiate, known as brown dwarfs, deuterium burning can occur and continue for hundreds of millions of years before the deuterium is exhausted. This requires a mass at least 13 times that of Jupiter to occur.)

When deuterium is exhausted and the stellar core reaches a density 6 g/cm and temperature 10–20 million K, *hydrogen burning*, or the *pp process* begins and continues through the main sequence life of the star. There are three variants,

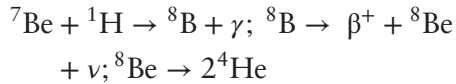
PP I:



PP II:



and PP III:



Which of these reactions dominates depends on temperature, but the net result of all is the production of ^4He and the consumption of H (and Li). All main sequence stars produce He, yet over the history of the cosmos, this has had little impact on the H/He ratio of the Universe. This in part reflects the observation that for small mass stars, the He produced remains hidden in their interiors or their white dwarf remnants and for large mass stars, later

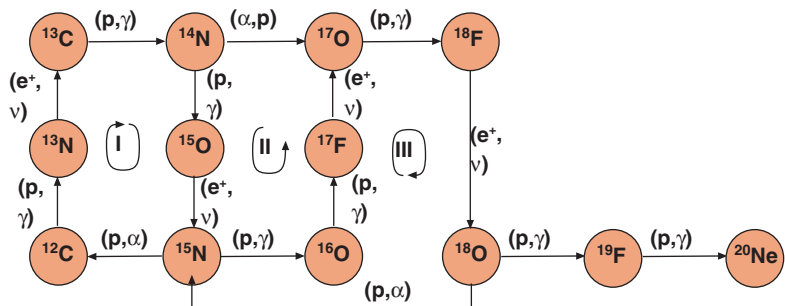
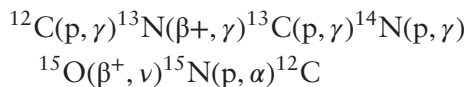


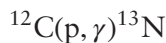
Figure 1.11 Illustration of the CNO cycle, which operates in larger second and later generation stars.

reactions consume the He produced in the main sequence stage.

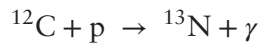
Once some carbon had been produced by the first generation of stars and supernovae, second and subsequent generation stars could synthesize He by another process as well, the CNO cycle:



Here we are using a notation commonly used in nuclear physics. The reaction:



is equivalent to:



It was subsequently realized that this reaction cycle is just part of a larger reaction cycle, which is illustrated in Figure 1.11. Since the process is cyclic, the net effect is consumption of four protons and two positrons to produce a neutrino, some energy, and a ^4He nucleus. Thus, to a first approximation, carbon acts as a kind of nuclear catalyst in this cycle: it is neither produced nor consumed. When we consider these reactions in more detail, not all of them operate at the same rate, resulting in some production and some consumption of these heavier nuclides. The net production of a nuclide can be expressed as:

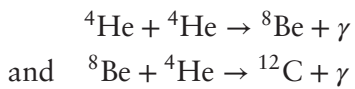
$$\frac{dN}{dt} = (\text{creation rate} - \text{destruction rate}) \quad (1.16)$$

Reaction rates are such that some nuclides in this cycle are created more rapidly than they are consumed, while for others the opposite is true. The slowest of the reactions in Cycle I is

$^{14}\text{N}(p, \gamma)^{15}\text{O}$. As a result, there is a production of ^{14}N in the cycle and net consumption of C and O. The CNO cycle will also tend to leave remaining carbon in the ratio of $^{13}\text{C}/^{12}\text{C}$ of 0.25. This is quite different than the Solar System (and terrestrial) abundance ratio of about 0.01. Because of these rate imbalances, the CNO cycle may be the principle source of nitrogen in the Universe.

The CNO cycle and the PP chains are competing fusion reactions in main sequence stars. Which dominates depends on temperature. In the Sun, the PP reactions account for about 98–99% of the energy production, with the CNO cycle producing the remainder. But if the Sun were only 12–30% more massive (and consequently a few million K hotter), the CNO cycle would dominate energy production.

Once the H is exhausted in the stellar core, fusion ceases, and the balance between gravitational collapse and thermal expansion is broken. The interior of the star thus collapses, raising the star's temperature. The increase in temperature results in expansion of the exterior and ignition of fusion in the shells surrounding the core that now consists of He. This is the *red giant* phase. Red giants may have diameters of hundreds of millions of kilometers (greater than the diameter of Earth's orbit). If the star is massive enough for temperatures to reach 10^8K and density to reach 10^4 g/cc in the He core, *He burning*, (also called the triple alpha process) can occur:



The catch in these reactions is that the half-life of ^8Be is only 7×10^{-16} sec, so three

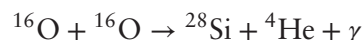
He nuclei must collide nearly simultaneously (this reaction is sometimes called the triple alpha process for this reason), hence densities must be very high. Depending on the mass of the star, the red giant phase can last for as much as hundred million years or as little as a few hundred thousand years, as a new equilibrium between gravitational collapse and thermal expansion sets in. Helium burning also produces ^{16}O through fusion of ^4He with ^{12}C . Upon the addition of further He nuclei, ^{20}Ne and ^{24}Mg can be produced. ^{14}N created by the CNO cycle in second generation stars can be converted to ^{22}Ne ; however, production rates of nuclei heavier than ^{16}O is probably quite low at this point. Also note that Li, Be, and B have been skipped: they are not synthesized in these phases of stellar evolution. Indeed, they are actually consumed in stars, in reactions such as PP II and PP III.

Evolution for low-mass stars, such as the Sun, ends after the Red Giant phase and helium burning. Densities and temperatures necessary to initiate further nuclear reactions cannot be achieved because the gravitational force is not sufficient to overcome coulomb repulsion of electrons. Thus nuclear reactions cease and radiation is produced only by a slow cooling and gravitational collapse. Massive stars, those greater than about four solar masses, however, undergo further collapse and further evolution. Evolution now

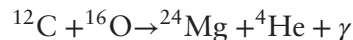
proceeds at an exponentially increasing pace (Figure 1.12), and these phases are poorly understood. But if temperatures reach 600 million K and densities $5 \times 10^5 \text{ g/cc}$, carbon burning becomes possible:



The carbon-burning phase marks a critical juncture in stellar evolution. As we mentioned, low mass stars never reach this point. Intermediate mass stars, those with 4–8 solar masses can be catastrophically disrupted by the ignition of carbon burning. The outer envelope of the star is ejected, leaving an O-Ne-Mg white dwarf. But in large stars, those with more than 8 solar masses, the sequence of production of heavier and heavier nuclei continues. After carbon burning, there is an episode called Ne burning, in which ^{20}Ne “photodisintegrates” by a (γ, α) reaction. The α s produced are consumed by those nuclei present, including ^{20}Ne , creating heavier elements, notably ^{24}Mg . The next phase is oxygen burning, which involves reactions such as:



and



A number of other less abundant nuclei, including Na, Al, P, S, and K are also synthesized at this time.

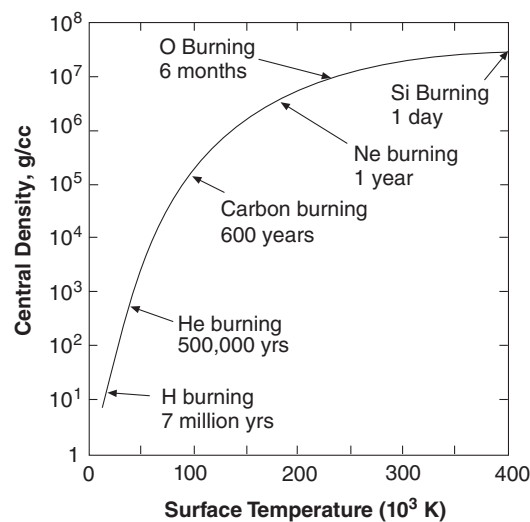
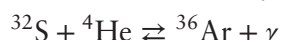
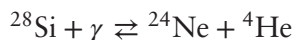


Figure 1.12 Evolutionary path of the core of a 25 solar mass star (after Bethe and Brown, 1985). Note that the period spent in each phase depends on the mass of the star: massive stars evolve more rapidly. (Source: ©Ian Worpole. Reproduced with permission.)

During the final stages of evolution of massive stars, a significant fraction of the energy released is carried off by neutrinos created by electron-positron annihilations in the core of the star. If the star is sufficiently oxygen-poor that its outer shells are reasonably transparent, the outer shell of the red giant may collapse during last few 10^4 years of evolution to form a *blue supergiant*.

1.4.2.3 The e-process

Eventually, a new core consisting mainly of ^{28}Si is produced. At temperatures above 10^9K and densities above 10^7 g/cc a process known as *silicon burning*, or the *e process*, (for equilibrium) begins, and lasts for only day or so, again depending on the mass of the star. These are reactions of the type:



While these reactions can go either direction, there is some tendency for the build up of heavier nuclei with masses 32, 36, 40, 44, 48, 52, and 56. Partly as a result of the e-process, these nuclei are unusually abundant

in nature. In addition, because of a variety of nuclei produced during C and Si burning phases, other reactions are possible, synthesizing a number of minor nuclei. The star is now a cosmic onion of sorts (Figure 1.13), consisting of a series of shells of successively heavier nuclei and a core of Fe. Though temperature increases toward the interior of the star, the structure is stabilized somewhat with respect to convection and mixing because the each shell is denser than the one overlying it.

Fe-group elements may also be synthesized by the e-process in Type I supernovae. Type I supernovae occur when white dwarfs of intermediate mass (3–10 solar masses) stars in binary systems accrete material from their companion. When their cores reach the Chandrasekhar limit, C burning is initiated and the star explodes. This theoretical scenario has been confirmed in recent years by space based optical, gamma-ray, and X-ray observations of supernovae, such as the Chandra X-ray observatory image in Figure 1.14.

1.4.2.4 The s-process

In second and later generation stars containing heavy elements, yet another nucleosynthetic process can operate. This is the slow

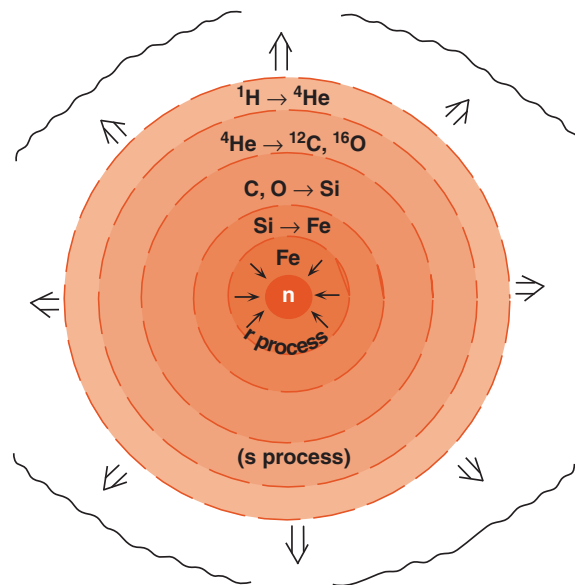


Figure 1.13 Schematic diagram of stellar structure at the onset of the supernova stage. Nuclear burning processes are illustrated for each stage. (Source: White (2013). Reproduced with permission of John Wiley & Sons.)

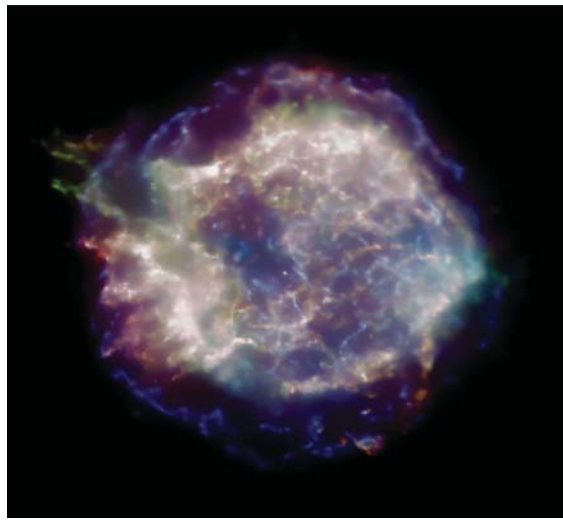
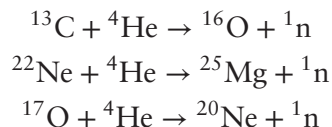


Figure 1.14 Chandra X-ray image of the supernova remnant Cassiopeia A (Cas A). The original Chandra X-ray image of the supernova remnant Cassiopeia A has red, green, and blue regions that show where the intensity of low, medium, and high energy X-rays, respectively, is greatest. The red material on the left outer edge is enriched in iron, whereas the bright greenish white region on the lower left is enriched in silicon and sulfur. In the blue region on the right edge, low and medium energy X-rays have been filtered out by a cloud of dust and gas in the remnant. (Source: Photo: NASA.)

neutron capture or *s*-process. It is so-called because the rate of capture of neutrons is slow, compared to the *r*-process, which we will discuss next. It operates mainly in the red giant phase (as evidenced by the existence of ^{99}Tc and enhanced abundances of several s-process elements) where neutrons are produced by reactions such as:



(but even H burning produces neutrons; one consequence of this is that fusion reactors will not be completely free of radiation hazards). These neutrons are captured by nuclei to produce successively heavier elements. The principal difference between the r- and s-process (discussed in the following) is the rate of capture relative to the decay of unstable isotopes. In the s-process, a nucleus may only capture a neutron every thousand years or so. If the newly produced nucleus is not stable, it will decay before another neutron is captured. As a result, instabilities cannot be bridged as they can in the r-process discussed next. In the s-process, the rate of formation of stable

species is given by

$$\frac{d[A]}{dt} = f[A - 1]\sigma_{A-1} \quad (1.17)$$

where $[A]$ is the abundance of a nuclide with mass number A, f is a function of neutron flux and neutron energies, and σ is the neutron capture cross section. Note that a nuclide with one less proton might contribute to this build up of nuclide A, provided that the isobar of A with one more neutron is not stable. The rate of consumption by neutron capture is:

$$\frac{d[A]}{dt} = -f[A]\sigma_A \quad (1.18)$$

From these relations we can deduce that the creation ratio of two nuclides with mass numbers A and $A - 1$ will be proportional to the ratio of their capture cross sections:

$$\frac{[A]}{[A - 1]} = \frac{\sigma_{A-1}}{\sigma_A} \quad (1.19)$$

Here, we can see that the s-process will lead to the observed odd-even differences in abundance since nuclides with odd mass numbers tend to have larger capture cross sections than even mass number nuclides. The s-process also

explains why magic number nuclides are particularly abundant. This is because they tend to have small capture cross sections and hence are less likely to be consumed in the s-process. The r-process, which we discuss next, leads to a general enrichment in nuclides with N up to 6–8 greater than a magic number, but not to a build up of nuclides with magic numbers. That the s-process occurs in red giants is confirmed by the overabundance of elements with mainly s-process nuclides, such as those with magic N, in the spectra of such stars. On the other hand, such stars appear to have normal concentrations of elements with $25 < A < 75$, and show normal abundances of r-only elements. Some, however, have very different abundances of the lighter elements, such as C and N, than the Sun.

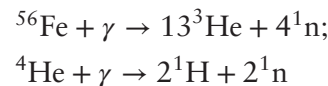
1.4.3 Explosive nucleosynthesis

1.4.3.1 *The r-process*

The e-process stops at mass 56. In an earlier section, we noted that ^{56}Fe had the highest binding energy per nucleon, that is, it is the most stable nucleus. Fusion can release energy only up to mass 56; beyond this the reactions become endothermic, that is, they absorb energy. Thus, once the stellar core has been largely converted to Fe, a critical phase is reached: the balance between thermal expansion and gravitation collapse is broken. The stage is now set for the most spectacular of all natural phenomena: a supernova explosion, the ultimate fate of large stars. The energy released in the supernova is astounding: supernovae can emit more energy than an entire galaxy (the recent supernova SN2011fe in the Pinwheel Galaxy, M101, provides an example; at its peak brightness, the supernova was visible with a small telescope, even though the galaxy was not).

When the mass of the iron core reaches 1.4 solar masses (the Chandrasekhar mass), further gravitational collapse cannot be resisted, even by coulomb repulsion. The supernova begins with the collapse of this stellar core, which would have a radius similar to that of the Earth's before collapse, to a radius of 100 km or so. This occurs in a few tenths of a second, with the inner iron core collapsing at 25% of the speed of light. As matter in the center 40% of the core is compressed beyond the density of nuclear matter

($3 \times 10^{14} \text{ g/cc}$), it rebounds, colliding with the outer part of the core, which is still collapsing, sending a massive shock wave back out less than a second after the collapse begins. As the shock wave travels outward through the core, the temperature increase resulting from the compression produces a break down of nuclei by photodisintegration, for example:



This results in the production of a large number of free neutrons (and protons). The neutrons are captured by those nuclei that manage to survive this hell. In the core itself, the reactions are endothermic, and thermal energy cannot overcome the gravitational energy, so it continues to collapse. If the mass of the stellar core is less than 3–4 solar masses, the result is a neutron star, in which all matter is compressed into neutrons. Supernova remnants of masses greater than 3 solar masses can collapse to produce a singularity, where density is infinite. A supernova remnant having the mass of the Sun would form a neutron star of only 15 km radius. A singularity of similar mass would be surrounded by a black hole; a region whose gravity field is so intense even light cannot escape, with a radius of 3 km.

Another important effect is the creation of huge numbers of neutrinos by positron-electron annihilations, which in turn had “condensed” as pairs from gamma rays. The energy carried away by neutrinos leaving the supernova exceeds the kinetic energy of the explosion by a factor of several hundred, and exceeds the visible radiation by a factor of some 30,000. The neutrinos leave the core at nearly the speed of light (and may contribute to the explosive rebound of the star). Although neutrinos interact with matter very weakly, the density of the core is such that their departure is delayed slightly. Nevertheless, they travel faster than the shock wave and are delayed less than electromagnetic radiation. Thus, neutrinos from the 1987A supernova arrived at Earth (some 160,000 years after the event) a few hours before the supernova became visible.

The shock wave eventually reaches the surface of the core, and the outer part of the star is blown apart in an explosion of unimaginable

violence. Amidst the destruction new nucleosynthetic processes are occurring.

This first of these is the *r* process (rapid neutron capture), and is the principle mechanism for building up the heavier nuclei. In the *r*-process, the rate at which nuclei with mass number $A + 1$ are created by capture of a neutron by nuclei with mass number A can be expressed simply as:

$$\frac{dN_{A+1}}{dt} = f N_A \sigma_A \quad (1.20)$$

where N_A is the number of nuclei with mass number A , σ is the neutron capture cross section and f is the neutron flux. If the product nuclide is unstable, it will decay at a rate given by λN_{A+1} . It will also capture neutrons itself, so the total destruction rate is given by

$$\frac{dN_{A+1}}{dt} = -f N_{A+1} \sigma_{A+1} - \lambda N_{A+1} \quad (1.21)$$

An equilibrium distribution occurs when nuclei are created at the same rate as they are destroyed, that is:

$$N_A \sigma_A f = \lambda N_{A+1} + N_{A+1} \sigma_{A+1} f \quad (1.22)$$

Thus, the equilibrium ratio of two nuclides A and $A + 1$ is:

$$N_A/N_{A+1} = (\lambda + \sigma_{A+1} f)/\sigma_A f \quad (1.23)$$

Eventually, some nuclei capture enough neutrons that they are not stable even for short periods (in terms of Equation 1.23, λ becomes large, hence N_A/N_{A+1} becomes large). They β^- decay to new elements, which are more stable and capable of capturing more neutrons. This process reaches a limit when nuclei beyond $Z = 90$ are reached. These nuclei fission into several lighter fragments. The *r*-process is thought to have a duration of 100 sec during the peak of the supernova explosion. Figure 1.15 illustrates this process.

During the *r*-process, the neutron density is so great that all nuclei will likely capture a number of neutrons. And in the extreme temperatures, all nuclei are in excited states, and relatively little systematic difference is expected in the capture cross sections of odd and even nuclei. Thus, there is no reason why the *r*-process should lead to different abundances of stable odd and even nuclides.

The fact that the *r*-process occurs in supernovae is confirmed by the observation of γ -rays from short-lived radionuclides.

1.4.3.2 The *p*-process

The *r*-process tends to form the heavier isotopes of a given element. The *p*-process

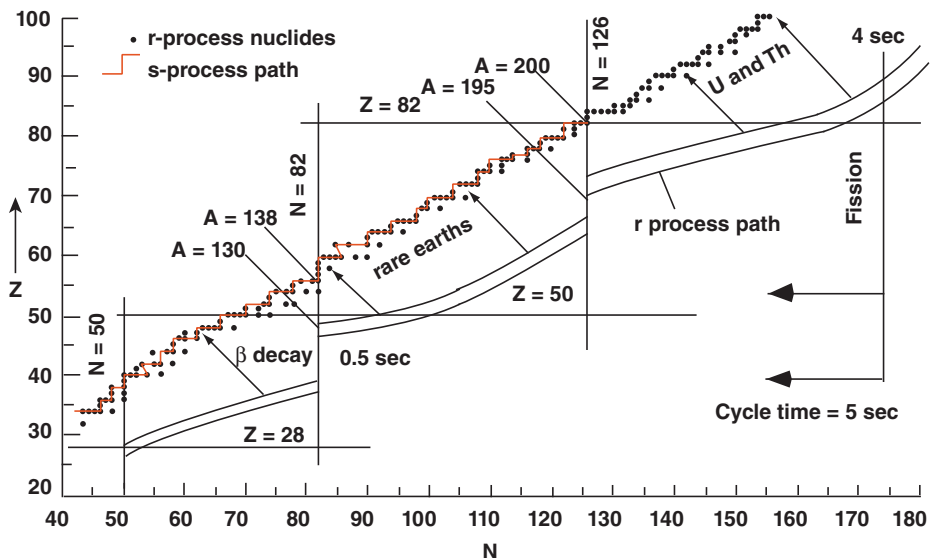


Figure 1.15 Diagram of the *r* process path on a Z versus N diagram. Dashed region is *r*-process path; solid line through stable isotopes shows the *s*-process path. (Source: White (2013). Reproduced with permission of John Wiley & Sons.)

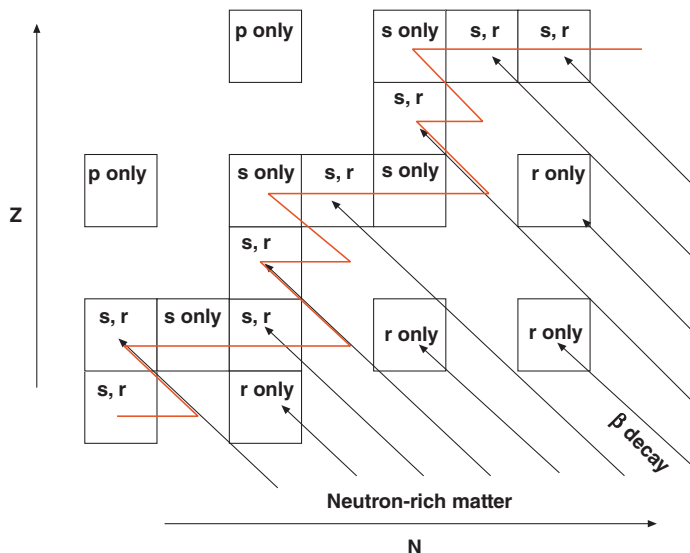


Figure 1.16 Z versus N diagram showing production of isotopes by the r-, s- and p-processes. Squares are stable nuclei; black lines are beta-decay path of neutron-rich isotopes produced by the r-process; solid red line through stable isotopes shows the s-process path. (Source: White (2013). Reproduced with permission of John Wiley & Sons.)

(proton capture) also operates in supernovae and is responsible for the lightest isotopes of a given element. The probability of proton capture is much less likely than neutron capture and hence it contributes negligibly to the production of most nuclides. The reason should be obvious: to be captured the proton must have sufficient energy to overcome the coulomb repulsion and approach to within 10^{-13} cm of the nucleus where the strong nuclear force dominates over the electromagnetic one. Since the neutron is uncharged, there is no coulomb repulsion and even low energy neutrons can be captured. Some nuclides, however, particularly the lightest isotopes of elements, can only be produced by the p-process. These p-process-only isotopes tend to be much less abundant than those created by the s- or r-process.

Figure 1.16 illustrates how the s-, r- and p-processes create different nuclei. Note also the shielding effect. If nuclide X has an isobar (nuclide with same mass number) with a greater number of neutrons, that isobar will “shield” X from production by the r-process. The most abundant isotopes will be those created by all processes; the least abundant will be those created by only one, particularly by only the p-process.

1.4.3.3 SN 1987A

The discussion previously demonstrates the importance of supernovae in understanding the origin of the elements that make up the known Universe. On February 23, 1987, the closest supernova (Figure 1.17) since the time of Johannes Kepler appeared in the Large Magellanic Cloud, a small satellite galaxy of the Milky Way visible in the Southern Hemisphere. This provided the first real test of models of supernovae as the spectrum could be analyzed in detail. Overall, the model presented earlier was reassuringly confirmed. The very strong radiation from ^{56}Co , the daughter of ^{56}Ni and parent of ^{56}Fe was particularly strong confirmation of the supernova model. There were of course, some minor differences between prediction and observation (such as an overabundance of Ba), which provided the basis for refinement of the model.

1.4.4 Nucleosynthesis in interstellar space

Except for production of ^7Li in the Big Bang, Li, Be, and B are not produced in any of the earlier situations. One clue to the creation of these elements is their abundance in galactic cosmic rays: they are over abundant by a factor of 10^6 , as is illustrated in Figure 1.18. They

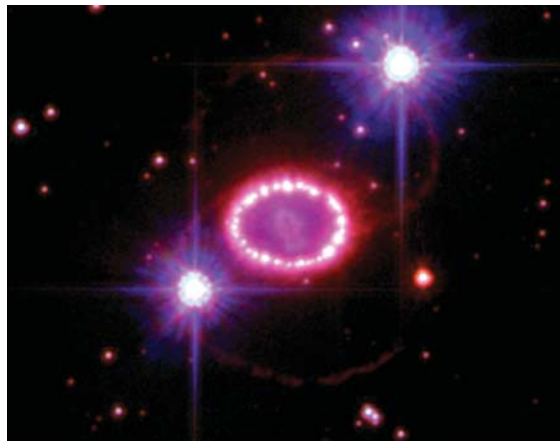


Figure 1.17 Rings of glowing gas surrounding the site of the supernova explosion named Supernova 1987A photographed by the Hubble Space Telescope in 2006. The shock wave produced by the supernova explosion is slamming into the ring, about a light-year across, that was probably shed by the star about 20,000 years before it exploded. (Source: NASA photo.)

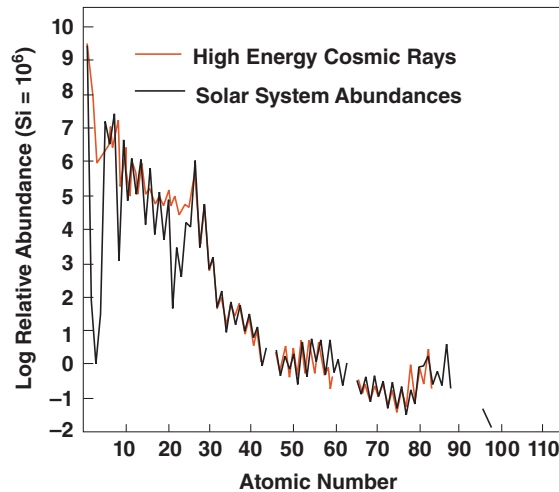


Figure 1.18 Comparison of relative abundances in cosmic rays and the solar system. (Source: White (2013). Reproduced with permission of John Wiley & Sons.)

are believed to be formed by interactions of cosmic rays with interstellar gas and dust, primarily reactions of ${}^1\text{H}$ and ${}^4\text{He}$ with carbon, nitrogen and oxygen nuclei. These reactions occur at high energies (higher than the Big Bang and stellar interiors), but at low temperatures where the Li, B, and Be can survive.

1.4.5 Summary

Figure 1.19 is a part of the Z versus N plot showing the abundance of the isotopes of elements 56 through 62. It is a useful region

of the chart of the nuclides for illustrating how the various nucleosynthetic processes have combined to produce the observed abundances. First we notice that even number elements tend to have more stable nuclei than odd numbered ones – a result of the greater stability of nuclides with even Z, and, as we have noted, a signature of the s-process. We also notice that nuclides “shielded” from β^- decay of neutron-rich nuclides during the r-process by an isobar of lower Z are underabundant. For example, ${}^{147}\text{Sm}$ and ${}^{49}\text{Sm}$ are more abundant than ${}^{148}\text{Sm}$, even though the

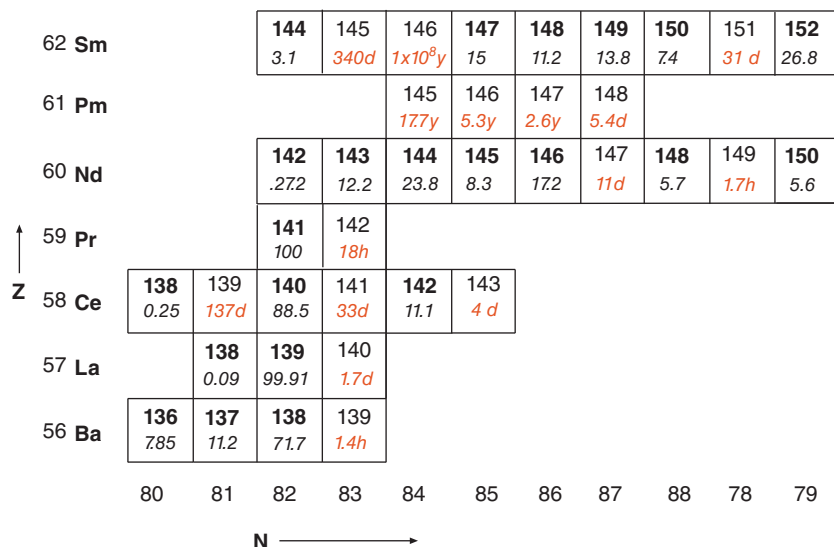


Figure 1.19 View of part of chart of the nuclides. Mass numbers of stable nuclides are shown in bold, their isotopic abundance is shown in italics as percentages. Mass numbers of short-lived nuclides are shown in plain text with their half-lives also given.

former have odd mass numbers and the latter an even mass number. ^{138}La and ^{144}Sm are rare because they “p-process only” nuclides: they are shielded from the r-process and also not produced by the s-process. ^{148}Nd and ^{150}Nd are less abundant than ^{146}Nd because the former are r-process only nuclides while the latter is by both s- and p-processes. During the s-process, the flux of neutrons is sufficiently low that any ^{147}Nd produced decays to ^{147}Sm before it can capture a neutron and become a stable ^{148}Nd .

NOTES

1. We define “fractionation” as any process in which two substances, in this case two isotopes of the same element, behave differently. Thus, fractionation is a process that causes the relative abundances of these substances to change.
2. u has been the internationally accepted symbol for this unit since 1961. However, the older abbreviation, *amu* is still often used (even though its defined value is slightly different).

Dalton is a newer, but still not fully accepted, name for this unit now commonly used by biochemists and likely to be officially adopted in the future.

3. The mass of the neutrino remains a subject of active research in physics. Results of the most recent experiments indicate that it is non-zero, but extremely small; no more than a few electron volts. By comparison, the mass of the electron is about 0.5 MeV.
4. Ga is an abbreviation for giga-annum or 10^9 years. Other such abbreviations we will use in this book are a, years, Ma, 10^6 years, and ka, 10^3 years.
5. It was originally believed that stars evolved from hot and bright to cold and dark across the diagram, hence the term “main sequence.” This proved not to be the case. Stars do, however, evolve somewhat to hotter and brighter during the main sequence part of these lives. The Sun is now about 30% brighter than it was when it first reached the main sequence; this, however, is small compared to the orders of magnitude range in luminosity.

REFERENCES

- Burbidge, E. M., Burbidge, G. R., Fowler, W. A., and Hoyle, F. 1957. Synthesis of the elements in stars, *Reviews of Modern Physics*, 2: 547–650.

- Haenecour, P., Zhao, X., Floss, C., Lin, Y. and Zinner, E. 2013. First laboratory observation of silica grains from core collapse supernovae. *The Astrophysical Journal Letters*, 768: L17, doi: 10.1088/2041-8205/768/1/L17.
- Jadhav, M., Zinner, E., Amari, S., Maruoka, T., Marhas, K. K. and Gallino, R. 2013. Multi-element isotopic analyses of presolar graphite grains from Orgueil. *Geochimica et Cosmochimica Acta*, 113: 193–224, doi: 10.1016/j.gca.2013.01.018.
- Suess, H. E. 1987. *Chemistry of the Solar System*. New York: John Wiley & Sons, Inc.
- White, W. M. 2013. *Geochemistry*. Oxford: Wiley-Blackwell.

SUGGESTIONS FOR FURTHER READING

- Cowley, C. R. 1995. *Cosmochemistry*. Cambridge: Cambridge University Press.
- Dickin, A. 1995. *Radiogenic Isotope Geochemistry*. Cambridge: Cambridge University Press.
- Faure, G. 1986. *Principles of Isotope Geology*. New York: John Wiley & Sons, Inc.
- McSween, H. Y. and Huss, G. R. 2010. *Cosmochemistry*. Cambridge: Cambridge University Press.
- Prantzos, N., Vangioni-Flam, E. and Cassé, M. (eds) 1993. *Origin and Evolution of the Elements*. Cambridge: Cambridge University Press.
- Rolfs, C. E. and Rodney, W. S. 1988. *Cauldrons in the Cosmos*. Chicago: Chicago University Press.
- Wasserburg, G. J., Busso, M., Gallino, R. and Raiteri, C. M. 1994. Asymptotic giant branch stars as a source of short-lived radioactive nuclei in the solar nebula. *Astrophysical Journal*, 424: 412–428.

PROBLEMS

Useful facts for these problems:

Avagadro's number is 6.02252×10^{23} (mole) $^{-1}$

Speed of light: $c = 2.997925 \times 10^8$ m/sec

$1\text{ eV} = 1.60218 \times 10^{-19}\text{ J}$; $1\text{ J} = 1\text{ kg m}^2/\text{sec}^2$; $1\text{ J} = 1\text{ VC}$

electron charge: $q = 1.6021 \times 10^{-19}\text{C}$ (coloumb)

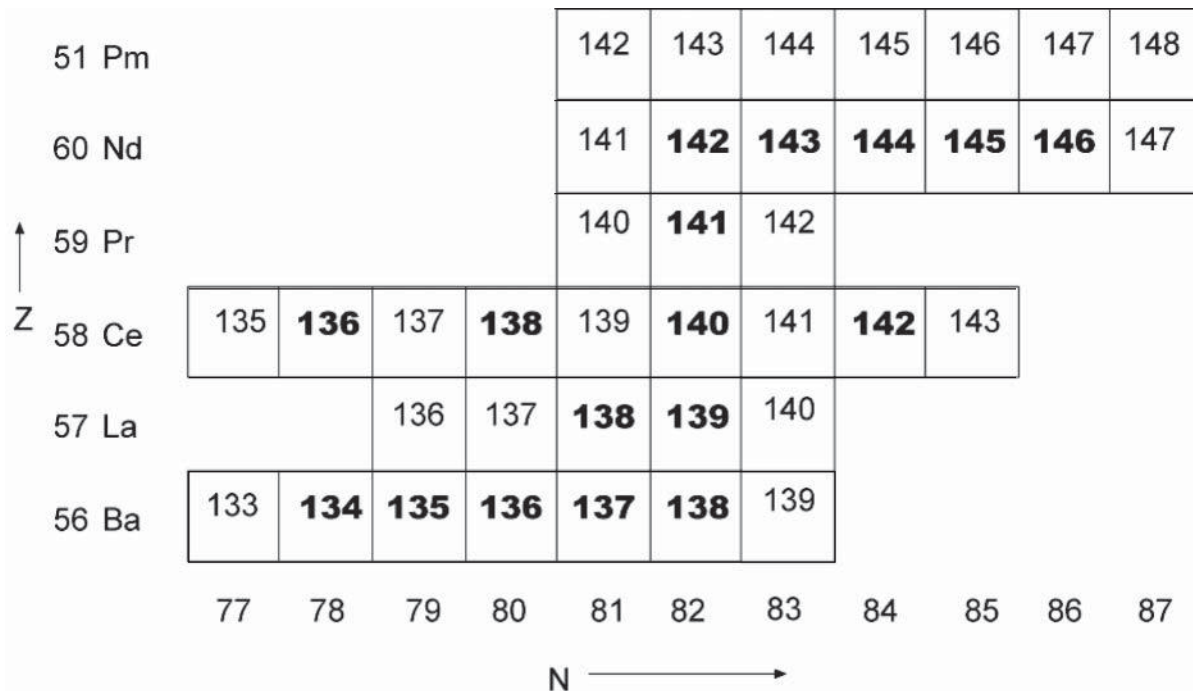
$1\text{ u} = 1.660541 \times 10^{-27}\text{ kg}$

$1\text{ Gauss} = 2.997925 \times 10^4\text{ J/mC}$

1. (a) How many moles of Nd (AW = 144.24 u; u is unified atomic mass units) are there in 50 g of Nd_2O_3 (AW of oxygen is 15.999 u)?
 (b) How many atoms of Nd in this?
2. Given an electron and positron of equal energy, how much more energy is the positron capable of depositing in a detector?
3. What are the binding energies per nucleon of ^{87}Sr (mass = 86.908879u) and ^{143}Nd (mass = 86.90918053u)?
4. What is the total energy released when ^{87}Rb (mass = 86.909183) decays to ^{87}Sr (mass = 86.908879 u)?
5. Using the equation and values for the liquid-drop model, predict the binding energy per nucleon for ^4He , ^{56}Fe , and ^{238}U (ignore even-odd effects).
6. How many stable nuclides are there with $N = 82$? List them. How many with $N = 83$? List them too. Why the difference?
7. Calculate the maximum β^- energy in the decay of ^{187}Re to ^{187}Os . The mass of ^{187}Re is 186.9557508 u; the mass of ^{187}Os is 186.9557479 u.
8. 28% of ^{228}Th atoms decay to ^{224}Ra by emitting an alpha of 5.338 MeV. What is the recoil (kinetic) energy of the ^{224}Re atom? Is the ^{224}Ra in its ground state? If not, what is nuclear energy in excess of the ground state? (Mass of ^{228}Th 228.0288 u, mass of ^{224}Ra is 224.0202 u, mass of alpha is 4.002603 u).

9. A section of the chart of the nuclides is shown next. Mass numbers of stable isotopes are shown in bold; unstable nuclides, shown in plain typeface, can be assumed to be short-lived. The chart shows all nuclides relevant to the questions next.

- Show the s-process path beginning with ^{134}Ba .
- Identify all nuclides created, in part or in whole, by the r-process.
- Identify all nuclides created *only* by the p-process.
- Which of the stable nuclides shown should be least abundant and why?
- Which of the cerium (Ce) isotopes shown would you expect to be most abundant and why? (Your answer *may* include more than one nuclide in d and e.)



Detailed information on the nuclides can be found on a web version of the Chart of the Nuclides maintained by Brookhaven National Laboratory Site (www.nndc.bnl.gov/chart/).

- Both ^{122}Te and ^{123}Te are created only in the s-process. ^{122}Te constitutes 2.55% of Te and ^{123}Te constitutes 0.89% of Te. What was the ratio of capture cross sections of these nuclides during the s-process? (Your answer might differ from capture cross sections listed in tables as the probability of neutron capture varies with neutron energy.)
- What is the recoil energy of ^{208}Tl (mass = 207.9820187 u) in the 5.601 MeV alpha decay illustrated in Figure 1.7?
- A certain radionuclide emits radiation at the rate of 15.0 μW at one instant of time and at 1.0 μW (microwatts) 1 h latter. What is its half-life?

Chapter 2

Decay systems and geochronology I

2.1 BASICS OF RADIOACTIVE ISOTOPE GEOCHEMISTRY

2.1.1 Introduction

We can broadly define two principal applications of radiogenic isotope geochemistry. The first is *geochronology*. Geochronology makes use of the constancy of the rate of radioactive decay to measure time. Since a radioactive nuclide decays to its daughter at a rate independent of everything, we can determine a *time* simply by determining how much of the nuclide has decayed. We will discuss the significance of this *time* at a later point. Geochronology is fundamental to our understanding of nature and its results pervade many fields of science. Through it, we know the age of the Sun, the Earth, and our Solar System, which provides a calibration point for stellar evolution and cosmology. Geochronology also allows us to trace the origins of culture, agriculture, and civilization back beyond the 5000 years of recorded history, to date the origin of our species to some 200,000 years, the origins of our genus to nearly 2 million years, and the origin of life to at least 3.5 billion years. Most other methods of determining time, such as so-called molecular clocks, are valid only because they have been calibrated against radiometric ages.

The history of geochronology begins with Yale University chemist Bertram Boltwood. In collaboration of Ernest Rutherford (a New Zealander working at Cambridge University),

Boltwood had deduced that lead was the ultimate decay product of uranium. In 1907, he analyzed a series of uranium-rich minerals, determining their U and Pb contents. He found that the Pb/U ratio in these minerals was same when minerals were from the same geologic period (the *relative* geologic time-scale, more or less as we know it today, had been worked out by the mid-nineteenth century) and increased with apparent geologic age. From laboratory experiments, he had calculated that 1 g of Pb was produced per year for every 10 billion grams of uranium; based on this he calculated ages for his samples ranging from 410 to 2200 million years. These ages meant that the Earth was far older than Lord Kelvin (William Thomson) had estimated a decade earlier from cooling of the Earth, which was about 20–40 million years. Boltwood's ages turn out to be too old by almost a factor of two. There are a variety of reasons for this. For one thing, he was unaware that there were two isotopes of uranium decaying to two isotopes of lead at different rates. Indeed, isotopes had not yet been discovered: it would be five more years before J. J. Thompson of Cambridge University would demonstrate their existence. The main reason was perhaps his failure to account for thorogenic Pb; although he was aware that thorium was radioactive, he did not know that Pb was its ultimate decay product.

Physicists at first resisted this new age, but geologists felt vindicated as they had felt that Kelvin's age was too young. As it turns out,

radioactivity also helps explain why Kelvin's age was wrong: the radioactive decay of U, Th, and K heat the Earth, providing much of the energy for geological processes. The great age of the Earth also required some new, as yet unknown energy source for the Sun and the stars, which Hans Bethe later deduced to be nuclear fusion.

The other application of radiogenic isotope geochemistry is *tracer studies*. These studies make use of the differences in the ratio of the radiogenic daughter isotope to other isotopes of the element. This approach, which when combined with geochronology, provides insights into the formation and evolution of the Earth, its parts, and its sister planets. This will be the subject of Chapters 5 through 8 and again in Chapter 12.

The elements of interest here are all experience chemical isotopic fractionations. That is to say, their isotopic ratios vary because of slight differences in the chemical behavior of those isotopes. We will discuss the underlying physics and chemistry of these isotopic fractionations in Chapter 8. We can ignore these effects in this chapter for several reasons. First, natural chemical fractionations for the elements of interest are generally quite small. For example, Krabbenhöft et al. (2010) documented variations in the $^{86}\text{Sr}/^{88}\text{Sr}$ ratio of less than $1/2$ per mil in rivers, carbonate rocks, and the ocean. Second, Sr, Nd, Hf, and Os isotope ratios are routinely corrected for

such fractionation by measuring the extent to which the ratio of a pair of non-radiogenic isotopes (e.g., ^{86}Sr and ^{88}Sr or ^{146}Nd and ^{144}Nd) differs from an accepted value and applying a correction for fractionation, assuming the magnitude of the fractionation depends on the masses of the isotopes of interest. The details of this correction are explained in the appendix. This correction is essential because fractionations occurring in the mass spectrometer can be much larger than natural ones (1% or more in the case of the $^{86}\text{Sr}/^{88}\text{Sr}$ ratio). Correction for fractionation in this manner is not possible for Pb isotopes because there is only one non-radiogenic isotope. As a consequence, it has traditionally not been possible to measure Pb isotope ratios with the precision of those of other elements (on the other hand, variations tend to be greater, so less precision is required). In the last decade or so, several techniques have been come in to wide use to correct Pb isotope ratios for fractionation, leading to much greater precision than in the past.

2.1.2 The basic equations

Table 2.1 lists the principal decay systems used in geology; these are also illustrated in Figure 2.1. As is suggested by the various footnotes, decay constants continue to be a field of active research (and note that in this text we will be using some recently determined

Table 2.1 Geologically useful long-lived radioactive decay schemes.

Parent	Decay mode	λ	Half-life	Daughter	Ratio
^{40}K	β -, e.c., β^+	$5.5492 \times 10^{-10} \text{ yr}^{-1}$ *	$1.28 \times 10^9 \text{ yr}$	$^{40}\text{Ar}, ^{40}\text{Ca}$	$^{40}\text{Ar}/^{36}\text{Ar}$
^{87}Rb	β^-	$1.42 \times 10^{-11} \text{ yr}^{-1}$ ^f	$48.8 \times 10^9 \text{ yr}$	^{87}Sr	$^{87}\text{Sr}/^{86}\text{Sr}$
^{138}La	β^-	$2.67 \times 10^{-12} \text{ yr}^{-1}$	$2.59 \times 10^{11} \text{ yr}$	$^{138}\text{Ce}, ^{138}\text{Ba}$	$^{138}\text{Ce}/^{142}\text{Ce}, ^{138}\text{Ce}/^{136}\text{Ce}$
^{147}Sm	α	$6.54 \times 10^{-12} \text{ yr}^{-1}$	$1.06 \times 10^{11} \text{ yr}$	^{143}Nd	$^{143}\text{Nd}/^{144}\text{Nd}$
^{176}Lu	β^-	$1.867 \times 10^{-11} \text{ yr}^{-1}$	$3.6 \times 10^{10} \text{ yr}$	^{176}Hf	$^{176}\text{Hf}/^{177}\text{Hf}$
^{187}Re	β^-	$1.64 \times 10^{-11} \text{ yr}^{-1}$	$4.23 \times 10^{10} \text{ yr}$	^{187}Os	$^{187}\text{Os}/^{188}\text{Os}, (^{187}\text{Os}/^{186}\text{Os})$
^{190}Pt	α	$1.54 \times 10^{-12} \text{ yr}^{-1}$	$4.50 \times 10^{11} \text{ yr}$	^{186}Os	$^{186}\text{Os}/^{188}\text{Os}$
^{232}Th	α	$4.948 \times 10^{-11} \text{ yr}^{-1}$	$1.4 \times 10^{10} \text{ yr}$	$^{208}\text{Pb}, ^4\text{He}$	$^{208}\text{Pb}/^{204}\text{Pb}, ^4\text{He}/^4\text{He}$
^{235}U	α	$9.8571 \times 10^{-10} \text{ yr}^{-1}$ ^g	$7.07 \times 10^8 \text{ yr}$	$^{207}\text{Pb}, ^4\text{He}$	$^{207}\text{Pb}/^{204}\text{Pb}, ^4\text{He}/^4\text{He}$
^{238}U	α	$1.55125 \times 10^{-10} \text{ yr}^{-1}$	$4.47 \times 10^9 \text{ yr}$	$^{206}\text{Pb}, ^4\text{He}$	$^{206}\text{Pb}/^{204}\text{Pb}, ^4\text{He}/^4\text{He}$

Note: the branching ratio, i.e., ratios of decays to ^{40}Ar to total decays of ^{40}K is 0.1037 according to Renne et al. (2010); the conventional value is 0.117. ^{147}Sm and ^{190}Pt also produce ^4He , but a trivial amount compared to U and Th.

*This is the value recently suggested by Renne et al. (2010). The conventional value is $5.543 \times 10^{-10} \text{ yr}^{-1}$.

^fThe officially accepted decay constant for ^{87}Rb is that shown here. However, recent determinations of this constant range from $1.421 \times 10^{-11} \text{ yr}^{-1}$ by Rotenberg (2005) to $1.393 \times 10^{-11} \text{ yr}^{-1}$ by Nebel et al. (2011).

^gThis is the value recommended by Söderlund et al. (2004).

^hValue suggested by Mattinson (2010). The conventional value is $9.8485 \times 10^{-10} \text{ yr}^{-1}$.

The periodic table shows the following color coding for elements:

- Red boxes (radioactive parents):** Sm, Os, Rn, Fr, Ra, Ac, La, Ce, Pr, Nd, Pm, Sm, Eu, Gd, Tb, Dy, Ho, Er, Tm, Yb, Lu.
- Orange boxes (radiogenic daughters):** H, Be, Li, Mg, K, Ca, Sc, Ti, V, Cr, Mn, Fe, Co, Ni, Cu, Zn, Ga, Ge, As, Se, Br, Kr, Rb, Sr, Y, Zr, Nb, Mo, Tc, Ru, Rh, Pd, Ag, Cd, In, Sn, Sb, Te, I, Xe, Cs, Ba, La, Hf, Ta, W, Re, Os, Ir, Pt, Au, Hg, Tl, Pb, Bi, Po, At, Rn.
- Grey boxes (both):** H, Be, Li, Mg, K, Ca, Sc, Ti, V, Cr, Mn, Fe, Co, Ni, Cu, Zn, Ga, Ge, As, Se, Br, Kr, Rb, Sr, Y, Zr, Nb, Mo, Tc, Ru, Rh, Pd, Ag, Cd, In, Sn, Sb, Te, I, Xe, Cs, Ba, La, Hf, Ta, W, Re, Os, Ir, Pt, Au, Hg, Tl, Pb, Bi, Po, At, Rn.

Figure 2.1 Periodic Table showing the elements having naturally occurring radioactive isotopes and the elements produced by their decay.

values that have not yet become the official ones). All of these decay systems obey the basic equation of radioactive decay, which is:

$$\frac{dN}{dt} = -\lambda N \quad (2.1)$$

λ is the decay constant, which we define as the probability that a given atom would decay in some time dt . It has units of time⁻¹. Each radioactive nuclide has a unique decay constant governing its probability of decay. With the minor exception of electron capture that we noted in Chapter 1, decay constants are true constants: their value is the same throughout all space and all time. All other equations that we'll introduce in this and subsequent chapters are derived from this one equation.

Let's rearrange Eqn. 2.1 and integrate:

$$\int_{N_0}^N \frac{dN}{N} = \int_0^t -\lambda dt \quad (2.2)$$

where N_0 is the number of atoms of the radioactive, or parent, isotope present at time $t = 0$. Integrating, we obtain:

$$\ln \frac{N}{N_0} = \lambda t \quad (2.3)$$

This can be expressed as:

$$\frac{N}{N_0} = e^{-\lambda t} \quad \text{or} \quad N = N_0 e^{-\lambda t} \quad (2.4)$$

Suppose we want to know the amount of time for the number of parent atoms to decrease to half the original number, that is, t when $N/N_0 = 1/2$. Setting N/N_0 to 1/2, we can rearrange Eqn. 2.3 to get:

$$\ln = -\lambda t_{1/2} \quad \text{or} \quad \ln 2 = \lambda t_{1/2}$$

and finally:

$$t_{1/2} = \frac{\ln 2}{\lambda} \quad (2.5)$$

This is the definition of the *half-life*, $t_{1/2}$.

Now the decay of the parent produces a daughter, or *radiogenic*, nuclide. The number of daughter atoms produced, D^* , is simply the difference between the initial number of parents and the number remaining after time t :

$$D^* = N_0 - N \quad (2.6)$$

Rearranging 2.4 to isolate N_0 and substituting that into 2.06, we obtain:

$$D^* = N e^{\lambda t} - N = N(e^{\lambda t} - 1) \quad (2.7)$$

This tells us that the number of daughters produced is a function of the number of

parents present and time. Since in general there will be some atoms of the daughter nuclide around to begin with, that is, when $t = 0$, a more general expression is:

$$D = D_0 + N(e^{\lambda t} - 1) \quad (2.8)$$

where D is the total number of daughters and D_0 is the number of daughters originally present.

As an aside, we'll note that there is a simple linear approximation of this function for times short compared to the inverse of the decay constant. An exponential function can be expressed as a Taylor Series expansion:

$$e^{\lambda t} = 1 + \lambda t + \frac{(\lambda t)^2}{2!} + \frac{(\lambda t)^3}{3!} + \dots \quad (2.9)$$

Provided $\lambda t \ll 1$, the higher order terms become very small and can be ignored; hence for times that are short compared to the decay constant inverse (i.e., for $t \ll 1/\lambda$), Eqn. 2.8 can be written as:

$$D \cong D_0 + N\lambda t \quad (2.10)$$

Let's now write Eqn. 2.8 using a concrete example, such as the decay of ^{87}Rb to ^{87}Sr :

$$^{87}\text{Sr} = ^{87}\text{Sr}_0 + ^{87}\text{Rb}(e^{\lambda t} - 1) \quad (2.11)$$

As it turns out, it is generally much easier, and usually more meaningful, to measure the ratio of two isotopes than the absolute abundance of one. We therefore measure the ratio of ^{87}Sr to a non-radiogenic isotope, which by convention is ^{86}Sr . Thus the useful form of 2.11 is:

$$\frac{^{87}\text{Sr}}{^{86}\text{Sr}} = \left(\frac{^{87}\text{Sr}}{^{86}\text{Sr}} \right)_0 + \frac{^{87}\text{Rb}}{^{86}\text{Sr}}(e^{\lambda t} - 1) \quad (2.12)$$

Similar expressions can be written for other decay systems.

It must be emphasized that $^{87}\text{Rb}/^{86}\text{Sr}$ ratio in Eqn. 2.12, which we will call the “parent-daughter ratio,” is the ratio at time t , that is, *present* ratio. If we need this ratio at some other time, we need to calculate it using equation 2.4.

2.1.3 A special case: the U-Th-Pb system

The U-Th-Pb system is somewhat of a special case as there are three decay schemes

producing isotopes of Pb. In particular two U isotopes decay to two Pb isotopes, and since the two parents and two daughters are chemically identical, combining the two provides a particularly powerful tool.

Let's explore the mathematics of this. First some terminology. The $^{238}\text{U}/^{204}\text{Pb}$ ratio is called μ (mu) the $^{232}\text{Th}/^{238}\text{U}$ is called κ (kappa). The ratio $^{238}\text{U}/^{235}\text{U}$ is constant, or nearly so,¹ at any given time in the Earth and today is 137.82. Now, we can write two versions of Eqn. 2.8:

$$\begin{aligned} ^{207}\text{Pb}/^{204}\text{Pb} &= (^{207}\text{Pb}/^{204}\text{Pb})_0 \\ &+ \frac{\mu}{137.82}(e^{\lambda_{235}t} - 1) \end{aligned} \quad (2.13)$$

and

$$^{206}\text{Pb}/^{204}\text{Pb} = (^{206}\text{Pb}/^{204}\text{Pb})_0 + \mu(e^{\lambda_{238}t} - 1) \quad (2.14)$$

These can be rearranged by subtracting the initial ratio from both sides and calling the difference between the initial and the present ratio Δ . For example, Eqn. 2.13 becomes

$$\Delta^{207}\text{Pb}/^{204}\text{Pb} = \frac{\mu}{137.82}(e^{\lambda_{235}t} - 1) \quad (2.15)$$

Dividing by the equivalent equation for $^{238}\text{U}-^{206}\text{Pb}$ yields:

$$\frac{\Delta^{207}\text{Pb}/^{204}\text{Pb}}{\Delta^{206}\text{Pb}/^{204}\text{Pb}} = \frac{(e^{\lambda_{235}t} - 1)}{137.82(e^{\lambda_{238}t} - 1)} \quad (2.16)$$

Notice the absence of the μ term. The equation holds for any present-day ratio of $^{207}\text{Pb}/^{204}\text{Pb}$ and $^{206}\text{Pb}/^{204}\text{Pb}$ we measure and thus for all pairs of ratios. The left-hand side is simply the slope of a series of data points from rocks or minerals formed at the same time (and remaining closed systems since time t) on a plot of $^{207}\text{Pb}/^{204}\text{Pb}$ vs. $^{206}\text{Pb}/^{204}\text{Pb}$. This means we can determine the age of a system without knowing the parent-daughter ratio. The bad news is that Eqn. 2.16 cannot be solved for t . However, we can guess a value of t , plug it into the equation, calculate the slope, compare the calculated slope with the observed one, revise our guess of t , calculated again, and so on. Pretty laborious, but making “educated guesses” of t and using a computer, this is pretty easy. In fact, using simple minimization algorithms we can generally converge to a high degree of accuracy after a few iterations.

2.2 GEOCHRONOLOGY

2.2.1 Isochron dating

Let's rewrite Eqn 2.12 in more general terms

$$R = R_0 + R_{P/D} (e^{\lambda t} - 1) \quad (2.17)$$

where R_0 is the initial ratio and $R_{P/D}$ is the parent/daughter ratio at time t . Measurement of geologic time is most often based this equation, or various derivatives of it. We'll refer to it as the *isochron equation*. First let's consider the general case. Given a measurement of an isotope ratio, R , and a parent-daughter ratio, $R_{P/D}$, two unknowns remain in Eqn. 2.17: t and the initial ratio. In general, we can calculate neither from a single pair of measurements. In the special case where the initial concentration of the daughter is very small, we can neglect R_0 or, if $R \gg R_0$, simple assumptions about R_0 may suffice. But in the general case, we must measure R and $R_{P/D}$ on a second system for which we believe t and R_0 are the same. Then we have two equations and two unknowns and subtracting the two equations yields

$$\Delta R = \Delta R_{P/D} (e^{\lambda t} - 1) \quad (2.18)$$

which eliminates R_0 from the equation and allows us to solve for t . This can be rearranged as:

$$\frac{\Delta R}{\Delta R_{P/D}} = e^{\lambda t} - 1 \quad (2.19)$$

In practice, one measures many pairs and solving for $\Delta R/\Delta R_{P/D}$ by regression (indeed, geochronologists would not generally accept an age based on only two measurements), t may be then be solved for as:

$$t = \frac{\ln(\Delta R / \Delta R_{P/D} + 1)}{\lambda} \quad (2.20)$$

For a given value of t , Eqn. 2.17 has the form $y = a + bx$, where y is R , a is R_0 , b is $e^{\lambda t} - 1$, and x is $R_{P/D}$. This is, of course, an equation for a straight line on a plot of R vs. $R_{P/D}$ with slope $b = e^{\lambda t} - 1$, and intercept $a = R_0$. Thus on such a plot, the slope of the line depends only on t (since λ is a constant for any given decay system). A line whose slope depends only on t is known as an *isochron*.

Note that on a plot of $^{207}\text{Pb}/^{204}\text{Pb}$ versus $^{206}\text{Pb}/^{204}\text{Pb}$, a line may also be an isochron, since its slope depends only on t .

Regression is simply a statistical method of calculating the slope of a line. Regression treatment yields both a slope and an intercept. The latter is simply the initial ratio since, as may be seen from 2.17, $R = R_0$ when $R_{P/D} = 0$. The geochronological information is contained in the slope, since it depends on t , but important information can also be obtained from the value of the intercept, the initial ratio, since it gives some information about the history prior to time $t = 0$ of the system being investigated.

There are two important assumptions, or conditions, built into the use of Eqn. 2.20:

1. The system of interest was at isotopic equilibrium at time $t = 0$. Isotopic equilibrium in this case means the system had a homogeneous, uniform value of R_0 .
2. The system as a whole and each analyzed part of it was closed between $t = 0$ and time t (usually the present time). By "closed" we mean there has been no transfer of the parent or the daughter element into or out of the system.

Violation of these conditions is the principal source of error in geochronology. Other errors arise from errors or uncertainties associated with the analysis. If the range in variation in measured R and $R_{P/D}$ is small, the analytical errors can be the limiting factor in the determination of an age. Note that both R and $R_{P/D}$ must be known accurately.

Finally, of course, we must also know λ accurately. Decay constants are not fundamental constants that can somehow be deduced from the fundamental laws; instead each must be measured and there are limits to the accuracy with which they have been measured. As technology advances and analytical precision increases, the accuracy of radiometric ages is increasingly limited by how well the decay constants are known. Decay constants can be determined in three ways, which we will refer to as counting, accumulation, and calibration. In counting, a known amount of the nuclide of interest is placed in a detector of known efficiency and the number of α , β , or γ rays emitted in a fixed time are counted. In accumulation, a known mass of highly

purified parent nuclide is allowed to sit for a fixed amount of time (decades in some cases), after which the daughter nuclide is extracted and its mass determined. In the calibration approach, isotope ratios and parent-daughter ratios of two systems, for example, Lu-Hf and U-Pb, are determined in rocks or minerals that are known to meet the previous two conditions. The age is determined using the system whose decay constant is well known, and then Eqn. 2.19 is solved for λ for the second system, using t determined in the first. Decay constants for U, Th, and K are now known within an uncertainty of considerably better than 1% (but even at this level, uncertainty in decay constants can limit the precision of age determinations and revisions to the ^{235}U decay constant have recently been suggested). Decay constants for Rb, Lu, and Re are less well known and continue to be active research topics, and there have been a number of recent suggested revisions to these values, as Table 2.1 indicates. These nuclides emit relatively low energy β s and no γ s, so the counting approach has proved problematic. Indeed, two recent attempts to determine the ^{87}Rb decay constant by accumulation and calibration disagree by 1.5%. The situation for ^{176}Lu was even worse in the early part of this century, with values determined over the last 15 years varying by 6%. However, the most recent determinations by counting and calibration agree within 1%.

The requirement of a closed and initially homogeneous system described here suggests a meaning for the nature of the *event* dated by radiogenic isotope geochemistry, and a meaning for *time* in the first paragraph of this chapter. In general, the *event* is the last time the system was open to complete exchange of the parent and daughter elements between the various subsystems we sample and analyze, that is, the last point in time that the system had a homogeneous, uniform value of R . Since the rate at which diffusion and chemical reactions occur increases exponentially with temperature, this event is generally a thermal one: that is, the last time the system was hot enough for such exchange between subsystems to occur. Exactly what temperature is implied can vary widely, depending on the nature of our samples and the particular decay system we are using. Minerals

such as biotite and hornblende will lose Ar at temperatures of a few hundred degrees. On the other hand, minerals such as pyroxene can remain closed to Sm and Nd exchange up to nearly 1000°C. The “closure” temperatures of various isotope systems in various minerals can be used to advantage: in some cases, an analysis of a variety of decay systems on a variety of sample types has recorded entire cooling histories.

The process accomplishing isotopic homogenization of a “system” usually involves diffusion, the rate of which, like other reaction rates, increases exponentially with temperature. Diffusion rates will vary depending on the element and the properties of the material through which the element diffuses. We can nevertheless make the general observation that the greater the length scale, the greater will be the time (or the higher the temperature required) for isotopic homogenization to be achieved. For the same temperature and duration of a thermal event, diffusion will more readily achieve isotopic homogenization on a small scale than on a large one. Thus, if our samples or subsystems are “whole rocks” collected meters or perhaps kilometers apart, the event dated will generally be a higher temperature one than an event dated by analysis of individual minerals from a rock specimen whose scale is only a few centimeters.

2.2.2 Calculating an isochron

The idea of *least squares regression* is to minimize the *squares* of the deviations from the function relating one variable to another (i.e., deviations from a line on a graph of the two variables). In the simplest case, the relationship is assumed to be linear, as it is in the isochron equation. The quantity to be minimized is the sum of the squares of deviations:

$$\sum_{i=1}^n e^2 = \sum_{i=1}^n (y - a - bx)^2 \quad (2.21)$$

where y is the observed value, $a + bx$ is the predicted value, and e is the difference between the observed and predicted value, that is, the *deviation*.

The use of the squares of the deviations means that large deviations will affect the calculated slope more than small deviations.

By differentiating Eqn. 2.21, it can be shown that the minimum value for the left side occurs when the slope is:

$$b = \frac{\sum (x_i - \bar{x})(y_i - \bar{y})}{\sum (x_i - \bar{x})^2} \quad (2.22)$$

where \bar{x} and \bar{y} are the means of x and y respectively, and x_i and y_i are the i^{th} pair of observations of x and y respectively. We can see from 2.22 that the regression slope is the sum of the cross products of the deviations of x and y from the means divided by the sum of the square of the deviations of x from the mean of x . A more convenient computational form of 2.22 is:

$$b = \frac{\sum x_i y_i - \frac{\sum y \sum x}{n}}{\sum x_i^2 - \bar{x}^2 n} \quad (2.23)$$

The intercept is then given by:

$$a = \bar{y} - b\bar{x} \quad (2.24)$$

The error on the slope is:

$$\sigma_b = \sqrt{\left[\sum y_i^2 - \bar{y}^2 n - \frac{\left(\sum (x_i y_i) - \bar{y} \bar{x} n \right)^2}{\sum x_i^2 - \bar{x}^2 n} \right] \times \left[\frac{1}{(n-2)(\sum x_i^2 - \bar{x}^2 n)} \right]} \quad (2.25)$$

The error on the intercept is:

$$\sigma_a = \sqrt{\left[\sum y_i^2 - \bar{y}^2 n - \frac{\left(\sum (x_i y_i) - \bar{y} \bar{x} n \right)^2}{\sum x_i^2 - \bar{x}^2 n} \right] \times \left[\frac{1}{n} + \frac{\bar{x}^2}{(\sum x_i^2 - \bar{x}^2 n)} \right] \left[\frac{1}{n-2} \right]} \quad (2.26)$$

Statistics books generally give an equation for linear least squares regression assuming one dependent and one independent variable where the independent variable is assumed to be known absolutely. While it is true that

in the isochron equation R is a function of $R_{P/D}$ in a geologic sense and hence may be considered the dependent variable, in practice both R and $R_{P/D}$ are measured quantities and neither is known absolutely: both have errors of measurement associated with them. These must be taken into account for a proper estimate of the slope and the errors associated with it. In some cases, the errors in measurement of x and y can be correlated, and this must also be taken into account. The so-called *two-error regression* algorithm takes account of these errors. This is, however, considerably less straightforward than that mentioned previously. The approach is to weight each observation according to the measurement error (the weighting factor will be inversely proportional to the estimated analytical error – so that observations with larger errors are less important than those with small ones). A solution was published by York (1969), among others. The regression slope is:

$$b = \frac{\sum \left[\frac{Z_i^2 (y_i - \bar{y})}{\omega(y_i)} + \frac{b(y_i - \bar{y})}{\omega(x_i)} + \frac{r_i(y_i - \bar{y})}{\alpha_i} \right]}{\sum \left[\frac{Z_i^2 (x_i - \bar{x})}{\omega(y_i)} + \frac{b(y_i - \bar{y})}{\omega(x_i)} + \frac{br_i(y_i - \bar{y})}{\alpha_i} \right]} \quad (2.27)$$

where $\omega(x_i)$ is the weighting factor for x_i (generally taken as the inverse of the square of the analytical error), $\omega(y_i)$ is the weighting factor for y_i , r_i is the correlation between the error of measurement of x_i and y_i , $\alpha = \sqrt{\omega(x_i)\omega(y_i)}$, $\bar{x} = \sum Z_i x_i / \sum Z_i$, $\bar{y} = \sum Z_i y_i / \sum Z_i$ (weighted means), and Z_i is:

$$Z_i = \frac{\alpha_i^2}{\omega(y_i) + \omega(x_i) - 2bra_i}$$

Note that the expression for b contains b . This requires an iterative solution: not something you want to do in your head, but reasonably easy with a computer. For example, the first estimate of b could be made using Eqn. 2.23. The difference between this method and the standard one is not great, so convergence is generally quick. The intercept

is calculated as in Eqn. 2.24. Calculating the errors associated with a and b is fairly complex, but approximate solutions are given by:

$$\sigma_b = \sqrt{\frac{1}{\sum Z_i(x_i - \bar{x})^2}} \quad (2.28)$$

$$\sigma_a = \sqrt{\frac{\sigma_b}{\sum Z_i}} \quad (2.29)$$

From the error on the slope, the error on the age can be derived by simple algebra. The error so derived, however, does not include uncertainty in the value of the decay constant, which may or may not be significant.

A useful measure of the fit of the data to the regression line (isochron) is the mean squared weighted deviations (MSWD). If, as is usual, the weight factors are taken as the inverse square of the estimated analytical errors and assuming errors are uncorrelated, the MSWD is calculated as (Wendt and Carl, 1991):

$$MSWD = \frac{\sum_i^N \frac{(y_i - bx_i - a)^2}{(b^2 \sigma_{x_i}^2 + \sigma_{y_i}^2)}}{N - 2} \quad (2.30)$$

where σ_{xi} and σ_{yi} are the errors on x_i and y_i , respectively. An MSWD value less or equal than 1 indicates the deviations from perfect linear correlation between x and y are less than or equal to those attributable to associated analytical errors; an MSWD greater than 1 indicates other (geological) factors have contributed to the deviations from linearity and suggest that conditions (1) and (2) earlier have been violated.

Today, there are programs available that implement these equations, so there is no need to code them anew. One of the most popular and useful is *ISOPLOT*, a Visual Basic Add-in for Microsoft's Excel® written by Ken Ludwig of the Berkeley Geochronology Center (BGC) and obtainable at http://bgs.org/isoplot_etc/isoplot.html. This software is useful for a wide variety of other geochronological problems that we will explore in this and subsequent chapters, including concordia diagrams and $^{40}\text{Ar}/^{39}\text{Ar}$ dating. Some of the problems in this book require the use of this or similar software. Since its use is well documented in the user's manual, we will not delve further into it here.

2.3 THE K-AR-CA SYSTEM

We have now discussed many of the basic aspects of radiogenic isotope geochemistry and we can now consider how it is applied to solving questions about the Earth. We will begin by discussing geochronology, because this aspect is basic to other aspects of isotope geochemistry. To understand the more chemical and geological aspects of isotope geochemistry, we must first learn to tell time, so to speak. We will consider the various decay systems separately. Many of these have special aspects, but all share a common foundation based on Eqn. 2.1; *the basic equation of radioactive decay*.

Two aspects of the K-Ar-Ca system make it special. First, it is a branched decay: a ^{40}K nucleus (an odd-odd nuclide) may decay to either a ^{40}Ca by β^- or to a ^{40}Ar atom by electron capture (or much more rarely by positron emission – which is just as well for us). It is impossible to predict how a given ^{40}K atom will decay, just as it is impossible to predict when it will decay. We can predict quite accurately what proportion of a large number of ^{40}K atoms will decay in each way, however. The ratio of electron captures to beta decays is called the *branching ratio* and is defined as:

$$R = \frac{\lambda_{ec}}{\lambda_\beta} \quad (2.31)$$

where the two lambdas are the decay constants (i.e., the probability of decay) for each mode. According to recent work by Renne et al. (2010), the branching ratio is 0.1037, $\lambda_{ec} = 0.5755 \times 10^{-10} \text{ a}^{-1}$, $\lambda_\beta = 4.9737 \times 10^{-10} \text{ a}^{-1}$. The total decay constant for ^{40}K is:

$$\lambda = \lambda_\beta + \lambda_{ec} = 5.5492 \times 10^{-10} \text{ a}^{-1} \quad (2.32)$$

We need to take account of this branched decay in our equation, because while a K atom decaying to Ca does not produce radiogenic Ar, it is no longer available for ^{40}Ar production. Thus our equation for radiogenic daughter production (Eqn. 2.7) becomes:

$$^{40}\text{Ar}* = \frac{\lambda_e}{\lambda} {}^{40}\text{K}(e^{\lambda t} - 1) \quad (2.33)$$

where the asterisk indicates radiogenic ^{40}Ar (designating the *radiogenic* atoms of an

element with an asterisk is a widely used convention and we will follow it in this book). Note we can write a similar equation for ${}^{40}\text{Ca}^*$ by substituting λ_β for λ_e .

Most, although not all, of the work on the K-Ca-Ar system has focused on Ar because the ${}^{40}\text{K}/{}^{40}\text{Ca}$ ratio is usually small. ${}^{40}\text{K}$ is the least abundant of the K isotopes (0.01167%), whereas ${}^{40}\text{Ca}$ is the most abundant ${}^{40}\text{Ca}$ isotope (96.92%), and Ca is a more abundant element than K (${}^{40}\text{Ca}$ is even-even, ${}^{40}\text{K}$ is odd-odd). As a result, variations in the ${}^{40}\text{Ca}/{}^{42}\text{Ca}$ ratio resulting from radioactive decay are quite small and difficult to measure (indeed, there is usually more variation in this ratio due to other causes, which we will discuss in Chapter 11). Only in very favorable circumstances, such as halide salt deposits, is geochronology practical.

As one might expect, particularly in view of the previous discussion, *one of the most important criteria for a useful radiometric chronometer is that the variations in the radiogenic isotope be large relative to the precision and accuracy with which they can be measured.* In this respect, a short half-life is advantageous, and K has one of the shortest half-lives of the long-lived radioactive nuclides. Because of the volatility of Ar, the Earth either lost much of its Ar during its formation, or never acquired much, giving the Earth a rather high K/Ar ratio. Furthermore, much of the Ar the Earth retained is now in the atmosphere (as we'll learn in Chapter 12). As a result, ${}^{40}\text{K}/{}^{40}\text{Ar}$ ratios in the solid Earth tend to be quite high. Because of the high ${}^{40}\text{K}/{}^{40}\text{Ar}$ ratios and the relatively short half-life of ${}^{40}\text{K}$, *the K-Ar system is often the one of choice when the task at hand is to date very young events.* Meaningful ages (meaning the uncertainty is small relative to the age) of less than 30,000 years have been determined in favorable circumstances. Much of what we know of the timing of the evolution of our species is based on ${}^{40}\text{K}/{}^{40}\text{Ar}$ dating (including ${}^{40}\text{Ar}/{}^{39}\text{Ar}$ dating that we will discuss shortly).

Much of what is special about K-Ar derives from Ar being a noble gas and its resulting refusal to be chemically bound in crystal lattices. Ar in rocks and minerals is simply trapped there. It has difficulty escaping because the atoms of the lattice block its escape path, but it does not form chemical bonds with other atoms in the lattice. Thus

when a mineral crystallizes from a lava, it will generally, although not always, do so with very little Ar. Pillow basalts formed on the seafloor are one example of exceptions to this rule. The combination of relatively high pressure and rapid transition from the liquid to the solid state can result in trapping of substantial amounts of Ar. Similarly, minerals crystallizing from plutonic rocks may also retain Ar.

In favorable circumstances, essentially no Ar will be trapped in a mineral crystallizing from lava. The great advantage of this, from a geochronological viewpoint, is we have only one unknown, namely t , and we can use Eqn. 2.33 to solve for it by measuring the ${}^{40}\text{K}$ and ${}^{40}\text{Ar}$ in one sample. Actually, one need not assume that no "initial" Ar whatsoever is present. Indeed, in detail, this would seem a poor assumption since a mineral crystallizing in contact with the atmosphere can be expected to absorb a small but finite amount of atmospheric Ar. This atmospheric Ar is readily corrected for since the atmosphere has a uniform ratio ${}^{40}\text{Ar}/{}^{36}\text{Ar}$ of 296.16. By measuring the amount of ${}^{36}\text{Ar}$ present, we can deduce the amount of atmospheric ${}^{40}\text{Ar}$ initially present. Our age equation (Eqn. 2.17) becomes simply:

$$\frac{{}^{40}\text{Ar}}{{}^{36}\text{Ar}} = 296.16 + \frac{\lambda_e}{\lambda} \frac{{}^{40}\text{K}}{{}^{36}\text{Ar}} (e^{\lambda t} - 1) \quad (2.34)$$

If we suspect that the composition of "initial" Ar differs significantly from atmospheric, it is then necessary to employ the isochron approach, measuring K and Ar in a number of cogenetic samples and solving simultaneously for t and the initial ${}^{40}\text{Ar}/{}^{36}\text{Ar}$ ratio.

2.3.1 Diffusion, cooling rates, and closure temperatures

Because Ar is not chemically bound in lattices, the K-Ar clock will generally be reset more readily than other systems. We concluded earlier that an event that "resets" a radiometric clock is generally a thermal one. In the case of K-Ar, we might guess that the system would be reset whenever temperatures are high enough to allow Ar to diffuse out of the rock or mineral of interest. It is worth considering this on a slightly more quantitative level.

It can be shown both theoretically and experimentally that the rate at which a species

will diffuse through a medium is related exponentially to temperature:

$$D = D_0 e^{-E_A/RT} \quad (2.35)$$

where D is the diffusion coefficient, D_0 is the “frequency factor,” E_A is the activation energy, R is the gas constant and T is thermodynamic, or absolute, temperature, (i.e., Kelvin). The diffusion “flux” is then related to the concentration gradient by:

$$J = -D \left(\frac{\partial C}{\partial x} \right) \quad (2.36)$$

where C is the concentration and x is distance. Figure 2.2 shows a plot of experimentally determined values of D for Ar in biotite plotted against the inverse of temperature. The point to be made here is that relatively small increases in temperature result in large increases in the diffusion coefficient. For example, increasing the temperature from 600 to 700°C results in a 2-orders-of-magnitude increase of the diffusion coefficient, and, for a given concentration gradient, of the Ar diffusion flux. Using the values of E_A

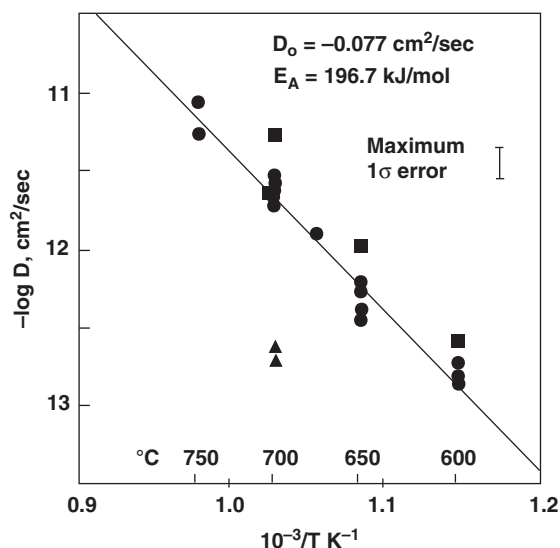


Figure 2.2 Log of the diffusion coefficient for argon in biotite against the inverse of thermodynamic temperature. Circles and squares indicate different size fractions of biotite used in 1 kbar experiments. Triangles are 14 kbar experiments. (Source: Adapted from Harrison et al. (1985). Reproduced with permission of Elsevier.)

and D_0 given in the figure, we can calculate the diffusion coefficient for temperatures not shown in the graph. The value of R is 8.314 J/Kelvin-mole (1.987 cal/Kelvin-mole). For a temperature of 300 K (27°C), D would be $4 \times 10^{-36} \text{ cm}^2/\text{sec}$. For any reasonable concentration gradient, there would be no significant Ar loss from biotite, even over extremely long times. At 600 K (327°C), we obtain $D = 6 \times 10^{-19} \text{ cm}^2/\text{sec}$, which implies a slow, but significant diffusion rate. At 700°C, however, loss of Ar would be quite rapid: about 1/3 of the Ar would be lost from biotites of 97 μ radii in 2–3 weeks (you can understand then why the experiments were done at these temperatures and not lower ones).

The following equation (from Crank, 1975) is of use in interpreting diffusion coefficients. The equation gives the fraction of the species lost as a function of time (t), diffusion coefficient, and the diffusion radius (a).

$$f \cong \frac{4}{\pi^{1/2}} \left(\frac{Dt}{a^2} \right)^{1/2} - \frac{Dt}{a^2} - \frac{1}{3\pi^{1/2}} \left(\frac{Dt}{a^2} \right)^{3/2} \quad (2.37)$$

The equation assumes radial diffusion in a cylinder of infinite length and radius a . We can use this equation to understand how Ar loss will vary with temperature.² We assume a value for a of 150 μ, and use the D_0 and E_A values given in Figure 2.2. Figure 2.3 shows the results of this calculation performed for various times (and at various temperatures: D is a function of temperature, of course).

Let's consider the geological implications of this diagram. Imagine a body of rock, either igneous or metamorphic, cooling from high temperature, a temperature high enough so that all Ar is lost. Let's pick up the story when the body is still 400°C and cooling at a rate of 100°C/Ma. At this temperature, the biotite would be just beginning to retain radiogenic Ar; that is, it is not being lost quite as fast as it is being created. After the first additional million years, it would have cooled to 300°C, and biotite would be retaining most of its radiogenic Ar (loss rate of about 10% per Ma). If cooling continues at this rate for another million years (in the real world, it is unlikely cooling rates would be so constant), biotite would be losing Ar at a rate of only a tenth of a percent per Ma, a fairly insignificant rate. If the body then cooled completely, and

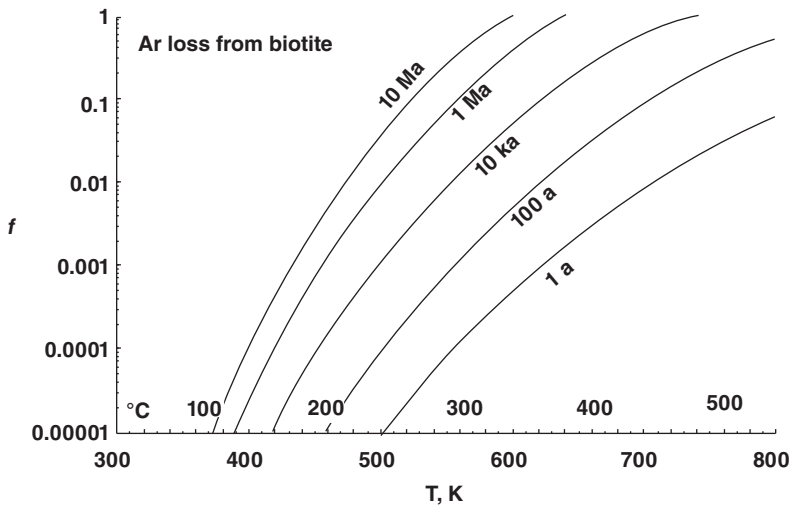


Figure 2.3 Fraction of Ar lost from a 150μ cylindrical crystal as a function of temperature for various heating times. All Ar is lost in 10 Ma at 340°C , or in 1 Ma at 380°C .

if we sampled biotite for K-Ar dating some 100 Ma later, assuming the biotite was not reheated, the “age” we would calculate would refer to that 2 Ma period when the biotite cooled from 400 to 200°C , and probably closer to the time it passed from 400 to 300°C . We say the biotite “closed” at that time, and we can estimate the closure temperature at between 300 and 400°C .

Suppose cooling was slower, say $10^\circ/\text{Ma}$. In this case, 10 Ma would be required to cool from 400 to 300°C , and 20 Ma to cool to 200°C . A much smaller fraction of the radiogenic Ar produced while the biotite was in the 200 – 400°C range would have been retained. The “age” we would calculate using Eqn. 2.33 would be younger than in the example previously. It would thus seem that under these circumstances, the “closure temperature” would depend on the cooling rate. This is indeed the case.

Dodson (1973) derived an equation for closure temperature (also sometimes called blocking temperature) as a function of diffusion parameters, grain size and shape, and cooling rate:

$$T_c = \frac{E_A}{R \ln \left(-\frac{ART_c^2 D_0}{a^2 E_A \tau} \right)} \quad (2.38)$$

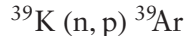
where τ is the cooling rate, dT/dt (for cooling, this term will be negative), a is the

characteristic diffusion dimension (e.g., radius of a spherical grain), and A is a geometric factor (equal to 55 for a sphere, 27 for a cylinder, and 9 for a sheet) and temperatures are in Kelvin. Unfortunately, this is not directly solvable since T_c occurs both in and out of the log, but it can be solved by indirect methods.³

There are several important notions we can come away with. First, a closure temperature is a useful concept, but a mineral will not suddenly stop loosing Ar, or any other radiogenic component, at its closure temperature. Closure temperature reflects a tradeoff between loss and creation of the radiogenic component. Second, there are some ultimate geological limitations on the meaning of an age of a slowly cooled rock, such as a large intrusion or regionally metamorphosed body of rock. We might also expect the age we obtain will depend on the mineral we use for dating (since the diffusion coefficient will vary), and perhaps on its composition (there is in fact some compositional dependence of the Ar diffusion coefficient on the Fe/Mg ratio in biotite; but apparently none in hornblende). Finally, we get the sense that it might be rather easy for K-Ar mineral age to be *partially* reset. This is certainly the case. We discuss next a technique that can at least identify partially reset minerals, and in favorable cases, provide a reasonable estimate of the original “age.”

2.3.2 ^{40}Ar - ^{39}Ar dating

If you look at a table of isotopes you'll see ^{39}Ar has a half-life of 269 years and does not occur naturally. You might justifiably wonder how it could be used for dating. The so-called *40–39 method* is actually ^{40}K - ^{40}Ar dating but employing a somewhat different analytical technique for the potassium first described by Merrihue and Turner (1966). The key is the production of ^{39}Ar by a nuclear reaction on ^{39}K , the most abundant of potassium's three isotopes:



The reaction is produced by irradiating a sample with fast neutrons in a reactor. It is important to distinguish this reaction from simple neutron capture, but we can nevertheless define a reaction cross section. The amount of ^{39}Ar produced is then a function of the amount of ^{39}K present, the reaction cross section, the neutron flux, and the irradiation time. Since the $^{40}\text{K}/^{39}\text{K}$ ratio in the Earth is constant (at any given time), the amount of ^{40}K can be calculated from ^{39}Ar . In practice, the situation is more complex because the reaction cross section is a function of neutron energy and there typically is a spectrum of energies present. The production of ^{39}Ar from ^{39}K can be expressed as:

$$^{39}\text{Ar} = ^{39}\text{K}\tau \int \phi_e \sigma_e de \quad (2.39)$$

where e is the neutron energy, ϕ_e is the flux of neutrons with energy e , and σ_e is the capture cross section for that energy, and τ is irradiation time. The $^{40}\text{Ar}^*/^{39}\text{Ar}$ is then:

$$\frac{^{40}\text{Ar}^*}{^{39}\text{Ar}} = \frac{\lambda_e}{\lambda} \frac{^{40}\text{K}(e^{\lambda t} - 1)}{^{39}\text{K}\tau \int \phi_e \sigma_e de} \quad (2.40)$$

In practice, the analysis is performed by simultaneously irradiating and analyzing a standard of known age. The flux, capture cross section, and decay constant terms will be the same for the standard as for the unknown sample. We can combine them into a single term, C , as:

$$C = \frac{\lambda_e}{\lambda} \frac{1}{\tau \int \phi_e \sigma_e de} \quad (2.41)$$

and Eqn. 2.40 becomes:

$$\frac{^{40}\text{Ar}^*}{^{39}\text{Ar}} = C \frac{^{40}\text{K}(e^{\lambda t} - 1)}{^{39}\text{K}} \quad (2.42)$$

The value of C can be determined from analysis of the standard, so that 2.42 can be solved for the age.

Another problem is the production of both ^{39}Ar and ^{40}Ar by other reactions that include $^{40}\text{K}(\text{n}, \text{p})^{40}\text{Ar}$, $^{40}\text{Ca}(\text{n}, \text{n}\alpha)^{36}\text{Ar}$, and $^{42}\text{Ca}(\text{n}, \alpha)^{39}\text{Ar}$. Corrections for these must be made. Generally, ^{37}Ar , produced by $^{40}\text{Ca}(\text{n}, \alpha)^{37}\text{Ar}$, is used to make these corrections.

In conventional K-Ar dating, Ar is released from samples by fusing in vacuum. However, we might guess from our knowledge of diffusion that a sample will begin to lose Ar before it reaches its melting temperature. If the ratio of radiogenic ^{40}Ar to K (and therefore to ^{39}Ar) were distributed uniformly throughout the sample, a sample of gas taken before the sample fused would produce the same age as for total fusion. We might guess, however, that some parts of a crystal will preferentially lose Ar through diffusion during the initial cooling of the crystal, or perhaps during some subsequent reheating event. Since the diffusion rate is proportional to the concentration gradient, we can anticipate that diffusion will be faster from the rims of crystals where the concentration gradient is higher than in the interior of crystals. So we might expect crystal rims to experience Ar loss at lower temperatures than crystal interiors. The rims would then record younger ages. As we heat the sample, we would also expect rims to start to give up their Ar at the lowest temperatures, partly for this reason, and partly because the Ar has less distance to go to get out. The lower $^{40}\text{Ar}/^{39}\text{Ar}$ of the gas in the rim would be seen as a lower age (which may or may not have significance). As we increased the temperature, the more retentive parts of the crystal would release their gas, and we could expect the $^{40}\text{Ar}/^{39}\text{Ar}$ and the apparent age to increase. If some parts of the crystals have lost no gas, their $^{40}\text{Ar}/^{39}\text{Ar}$ ratios would record the “correct” age, even though the crystal as a whole has suffered some loss. Figure 2.4 is an Ar release diagram for a biotite exhibiting this sort of behavior. Conventional K-Ar dating would have produced

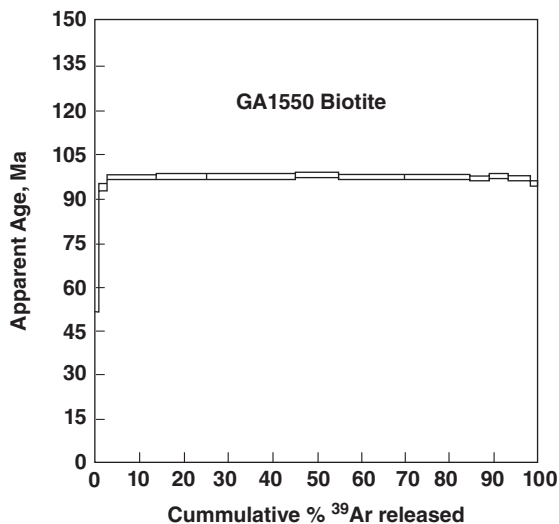


Figure 2.4 $^{40}\text{Ar}/^{39}\text{Ar}$ age spectrum produced by step heating of a biotite from a granitic gneiss. (Source: Tetley, 1978.)

an age intermediate between the “correct” age and the apparent young age of those parts of crystal that have suffered loss of radiogenic ^{40}Ar . Thus, the combination of the $^{40}\text{Ar}/^{39}\text{Ar}$ method with step-heating provides a means of retrieving useful geochronological information from samples whose value would have otherwise been compromised because of diffusional loss. In a certain sense, we are relaxing our requirement that the system must have remained closed: with $^{40}\text{Ar}/^{39}\text{Ar}$ dating, we require only that some part of the system have remained closed.

Most Ar release spectra are not so simple as that in Figure 2.4. Figure 2.5 shows Ar release spectra for a series of hornblende samples taken at varying distances from the contact with an intrusive granodiorite. All show significant Ar loss as a result of heating from the intrusion. None retain, even at the highest release temperature, the true age of 367 Ma.

2.3.2.1 Other complications affecting $^{40}\text{Ar}-^{39}\text{Ar}$ spectra

In the previous section, we saw two examples of $^{40}\text{Ar}/^{39}\text{Ar}$ release spectra: one where there was only minor loss of Ar from the rims, and another where significant fractions of the total Ar had been lost due to metamorphic

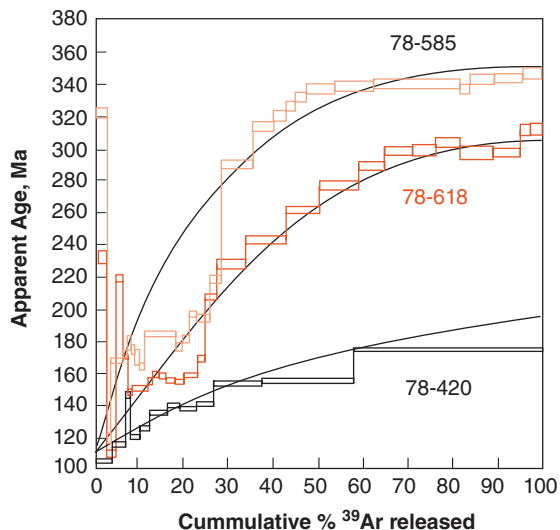


Figure 2.5 Ar release spectra for hornblendes taken from varying distance from a 114 million year old intrusion. The crystallization age of the samples is 367 Ma. Curves show calculated release spectra expected for samples that lost 31, 57, and 78% of their argon. (Source: Adapted from Harrison and McDougall (1980). Reproduced with permission of Elsevier.)

heating. Figure 2.4 showed spectra that almost perfectly match theoretical patterns for diffusional loss. Such examples are uncommon; many spectra are more complex. For example, some samples that have been reheated show false plateaus that correspond to ages intermediate between the crystallization age and the reheating age. An additional problem in interpreting such spectra is that samples that have not been subjected to reheating events but cooled slowly originally can show release spectra that mimic those of reheated samples in Figure 2.5.

Recoil of ^{39}Ar produced by the $^{39}\text{K}(\text{n},\text{p})^{39}\text{Ar}$ reaction during irradiation can also produce problems. The recoil results in loss of ^{39}Ar from sites near the mineral surface. For large grains, this is largely insignificant, but for small grains, this can lead to significant ^{39}Ar loss, leading in turn to erroneously old apparent ages.

In most case, the Ar present in a sample will not be pure radiogenically produced Ar. Non-radiogenic argon is often called *excess* Ar. $^{40}\text{Ar}/^{39}\text{Ar}$ ratios used to calculate ages

in release spectra are typically corrected for the presence of atmospheric Ar by measuring the $^{40}\text{Ar}/^{36}\text{Ar}$ ratio. Atmospheric argon has a constant $^{40}\text{Ar}/^{36}\text{Ar}$ ratio of 296.16.⁴ Only ^{40}Ar present in excess of this ratio is considered radiogenic and used to calculate the $^{40}\text{Ar}/^{39}\text{Ar}$ ratio. Nevertheless, some samples can have “initial” $^{40}\text{Ar}/^{36}\text{Ar}$ ratios greater than the atmospheric ratio; this will lead to too old an age if not properly accounted for. It is this “excess” argon that is of greatest concern.

Excess Ar can have two sources. First, it can arise when minerals crystallize under a finite partial pressure of Ar. For example, mantle-derived submarine basalts have been shown in some cases to have initial $^{40}\text{Ar}/^{36}\text{Ar}$ ratios of up to 40,000. The high $^{40}\text{Ar}/^{36}\text{Ar}$ ratio reflects production of ^{40}Ar by decay of ^{40}K within the mantle. Minerals crystallizing in the presence of this gas will trap some of this ^{40}Ar , which will result in anomalously old age upon analysis. This is referred to as *inherited* Ar. Second, during a thermal event, ^{40}Ar diffusing out of some minerals may be taken up by other minerals. Since this ^{40}Ar is diffusing into the mineral grain, its concentration will be highest in the exterior of grains and thus will tend to be released at the lowest temperatures. An example is shown in Figure 2.6.

When excess Ar is held in more than one crystallographic site, for example different minerals in the analyzed sample, release spectra can reveal a saddle shape. An example is shown in Figure 2.7. This sample is a calcic plagioclase from Broken Hill in Australia. The true metamorphic age is approximately 1600 Ma. Even the minimum values in the bottom of the saddle are too old. Electron microscopy of the plagioclase revealed that it had exsolved into a Ca-rich and Na-rich plagioclase. The saddle shape results because Ar in one of the phases diffuses readily and is thus released at low temperature, and diffuses more slowly in the other, resulting in release at high temperature.

A new technique, developed only in the last 20 years, involves releasing Ar from small areas of a sample through laser ablation. This allows release of Ar from areas with diameters less than a millimeter, and provides the possibility of spatial resolution of Ar diffusional loss.

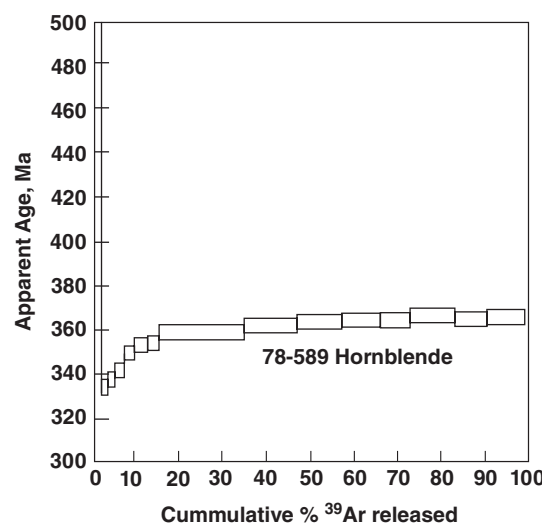


Figure 2.6 Ar release spectrum of a hornblende in a Paleozoic gabbro reheated in the Cretaceous by the intrusion of a granite. Anomalously old apparent ages in the lowest temperature release fraction results from diffusion of radiogenic Ar into the hornblende during the Cretaceous reheating. (Source: Adapted from Harrison and McDougall (1980). Reproduced with permission of Elsevier.)

2.3.2.2 $^{40}\text{Ar}-^{39}\text{Ar}$ isochrons

The data from various temperature release steps are essentially independent observations of Ar isotopic composition. Because of this, they can be treated much the same as in conventional isochron treatment. The isochron equation, written for the K-Ar system is:

$$\frac{^{40}\text{Ar}}{^{36}\text{Ar}} = \left(\frac{^{40}\text{Ar}}{^{36}\text{Ar}} \right)_0 + \frac{^{40}\text{K}}{^{36}\text{Ar}} (e^{\lambda t} - 1) \quad (2.43)$$

When $^{40}\text{Ar}/^{36}\text{Ar}$ data from a series of samples are plotted against $^{40}\text{K}/^{36}\text{Ar}$, the slope of the resulting line will be proportional to age, and the intercept gives the initial $^{40}\text{Ar}/^{36}\text{Ar}$ ratio. Since for all release fractions of a sample the efficiency of production of ^{39}Ar from ^{39}K is the same and $^{40}\text{K}/^{39}\text{K}$ ratios are constant, we may substitute $^{39}\text{Ar} \times C$ for ^{40}K :

$$\frac{^{40}\text{Ar}}{^{36}\text{Ar}} = \left(\frac{^{40}\text{Ar}}{^{36}\text{Ar}} \right)_0 + \frac{^{39}\text{Ar}}{^{36}\text{Ar}} C (e^{\lambda t} - 1) \quad (2.44)$$

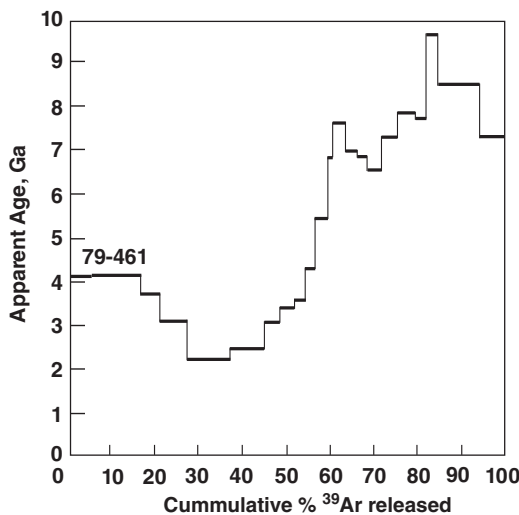


Figure 2.7 Ar release spectrum from a calcic plagioclase from Broken Hill, Australia. Low temperature and high temperature fractions both show erroneously old ages. This peculiar saddle shaped pattern, which is common in samples containing excess Ar, results from the excess Ar being held in two different lattice sites. (Source: Adapted from Harrison and McDougall (1980). Reproduced with permission of Elsevier.)

C is a constant that depends on the efficiency of ^{39}Ar production during irradiation. Thus when $^{40}\text{Ar}/^{36}\text{Ar}$ ratios from a series of release fractions are plotted against $^{39}\text{Ar}/^{40}\text{Ar}$, the slope of the resulting line will be proportional to the age of the sample, as is illustrated in Figure 2.8.

The use of the isochron diagram can help to identify excess Ar and its nature (e.g., atmospheric, inherited, etc.). It also provides a crucial test of whether ages obtained in release spectra are meaningful or not. A drawback of this diagram is that ^{36}Ar , which is the denominator in both the ordinate and abscissa, is often present in only trace amounts and is difficult to measure precisely. Because it appears in both ordinate and abscissa, errors in its measurements can produce correlations that imitate isochrons.

An alternative is to use a plot of $^{36}\text{Ar}/^{40}\text{Ar}$ against $^{39}\text{Ar}/^{40}\text{Ar}$ (Figure 2.9), often called an *inverse isochron plot*. We can think of the Ar in a sample as a mixture of a trapped component and a radiogenic component. As such, the data for various release fractions

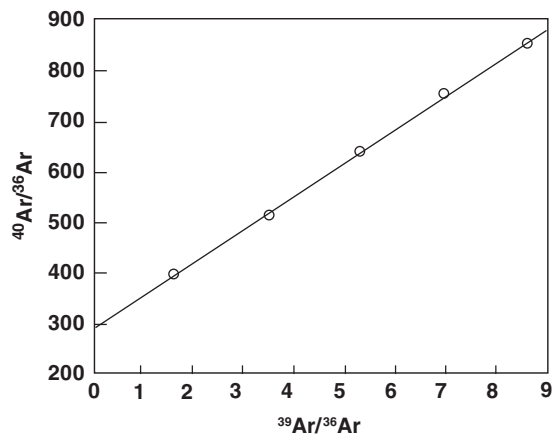


Figure 2.8 Hypothetical $^{40}\text{Ar}-^{39}\text{Ar}$ isochron diagram. The slope is proportional to the age and the intercept gives the initial $^{40}\text{Ar}/^{36}\text{Ar}$ ratio, which is commonly atmospheric, as is illustrated here.

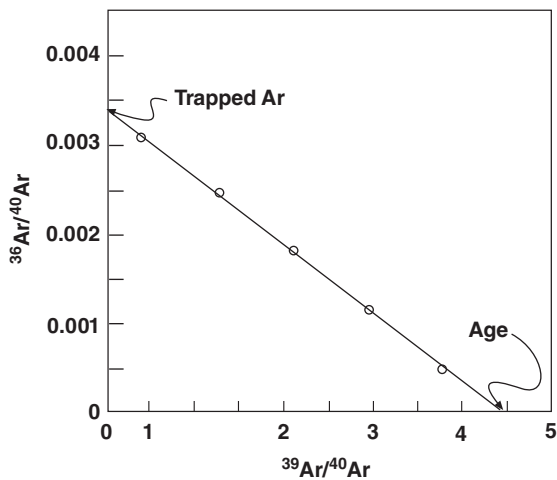


Figure 2.9 Plot of $^{36}\text{Ar}/^{40}\text{Ar}$ vs $^{39}\text{Ar}/^{40}\text{Ar}$, also called an inverse isochron diagram. Age is obtained from the value of $^{39}\text{Ar}/^{40}\text{Ar}$ corresponding to $^{36}\text{Ar}/^{40}\text{Ar} = 0$.

should plot as a straight line on such a plot. The radiogenic component has a $^{36}\text{Ar}/^{40}\text{Ar}$ ratio of 0 (because ^{36}Ar is not produced by radioactive decay), whereas the trapped, non-radiogenic component can be found by extrapolating to a $^{39}\text{Ar}/^{40}\text{Ar}$ ratio of 0 (corresponding to a $^{39}\text{K}/^{40}\text{Ar}$ ratio of 0; since ^{39}K is proportional to ^{40}K , this also corresponds to a $^{40}\text{K}/^{40}\text{Ar}$ ratio of 0). Thus the age may be computed from the $^{39}\text{Ar}/^{40}\text{Ar}$ ratio obtained by

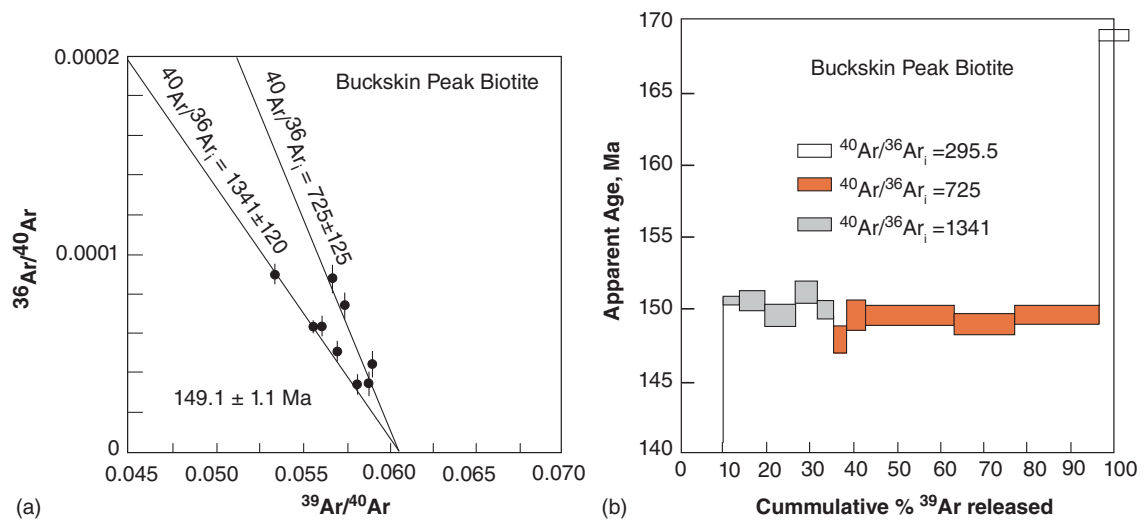


Figure 2.10 (a) Inverse isochron diagram revealing the presence of two excess Ar components. (b) Ar release spectrum for the same sample after correction for non-atmospheric excess Ar. (Source: Adapted from Heizler and Harrison (1988). Reproduced with permission of Elsevier.)

extrapolating the correlation line to $^{36}\text{Ar}/^{40}\text{Ar}$ to 0, and the composition of the trapped component by extrapolating to $^{39}\text{Ar}/^{40}\text{Ar}$ of 0.

Figure 2.10 provides an example of how the inverse isochron plot may be used to identify trapped components. The original release data showed a disturbed pattern and lacked a plateau (not shown). The inverse isochron plot (Figure 2.10a) revealed two correlations suggesting the presence of two distinct trapped components. The lower intercept yielded an age of 149.1 Ma. When the data were corrected for the trapped component and replotted on a release spectrum, they produced a plateau corresponding to the same age as the isochron age. The book by McDougall and Harrison (1999) provides much greater detail on $^{40}\text{Ar}/^{39}\text{Ar}$ geochronology.

2.4 THE RB-SR SYSTEM

The K-Ar system is exceptional in that we can sometimes ignore or readily correct for initial Ar. In the systems we'll discuss in the remainder of this chapter, both the initial ratio and the age are always unknown, meaning we must solve for both simultaneously through the isochron method. Consequently, this is an opportune time to briefly review and summarize the conditions that must be met to obtain a meaningful isochron.

1. *The ratio of parent to daughter should be large.* When this is the case, variations in the isotopic composition of the daughter will be large relative to our ability to measure them. Under the best of circumstances, isotope ratios can be measured with a precision of a few ppm. If the total amount of radioactively produced daughter is small relative to the amount present initially, for example if the proportion of radiogenically produced daughter is only a few tens of ppm or less of the total amount of daughter, accuracy of “ages” will be compromised.
2. *The parent/daughter should have a large range.* A large range in parent/daughter ratio leads to a large range in isotope ratios in the daughter. The error on the regression slope, and ultimately the age, is a function of the range of values used in the computation. So, given similar analytical precisions, we will obtain a more precise date with a decay system where the variations in parent-daughter ratio are large than with one where these variations are small.
3. *Deviations from closed system behavior must be minimal* subsequent to the event we are attempting to date. This should be considered when choosing both the decay system and the samples we plan to analyze. As we shall see, some elements

tend to be more mobile than others, and some minerals are less reactive than others. Size also plays some role. A large sample is more likely to meet the closed system requirement than a small one (the elements have further to diffuse). Often, metamorphism will disturb a system on the scale of mineral grains, but not a scale of “whole rock” samples taken hundreds of meters apart (however, whole rocks will generally show less variation in parent/daughter ratios than minerals). One must also bear in mind that an atom created by radioactive decay will generally be a misfit in the lattice site it occupies (since the site was originally occupied by the parent). Furthermore, the decay process may damage the site. Such damage is more likely in the case of alpha decay than beta decay or electron capture because of the high energy of the alpha (typically 4 MeV), and the kinetic recoil energy of the daughter nucleus. These factors all lead to higher mobility of the daughter.

4. *The isotopic composition of the daughter must have been homogeneous at the time of the event we wish to date. On a small scale, homogenization takes place through diffusion, which, as we have seen, is highly temperature dependent. The higher the temperatures obtained during the “event,” the more rapidly and completely the system will be homogenized. On scales larger than 10 m or so, homogenization can only be achieved through convective-driven advective transport. This effectively means homogenization requires the presence of a liquid. This might be a magma or a hydrous fluid circulating through rocks undergoing metamorphism. In any case, both convection and diffusion will be more efficient at higher temperatures, so homogenization is more likely to be achieved at high temperatures than at low ones. Finally, the larger the range in parent/daughter ratios, and hence isotopic composition at the time we measure them, the less important will be any initial variations in isotopic composition.*

We will now continue with our consideration of the various decay systems.

Rb-Sr geochronology does not differ in principle from Sm-Nd geochronology or Re-Os geochronology, however. Thus, our discussion will focus mainly on the geochemistry of these elements and the behavior of these systems with reference to the four points listed previously.

2.4.1 Rb-Sr chemistry and geochronology

Both Rb and Sr are trace elements in the Earth: their concentrations are generally measured in ppm. Rb is an alkali element (Group 1) with a valence of +1. Like other alkalis, it is generally quite soluble in water and hydrous fluids. As a result, it is among the more mobile elements. Rb has an ionic radius of 148 pm. This large ionic radius means it is excluded from many minerals: it is simply too large to fit in the sites available. Hence, it is among the most *incompatible* elements. However, its radius is sufficiently similar to that of potassium (133 pm) that it substitutes readily for K in K-bearing minerals such as mica and K-feldspar. As a result, no Rb minerals occur in nature: that is, it is not a stoichiometric component of any mineral. Because of its incompatible nature, it is strongly concentrated in the Earth’s crust and depleted in its mantle.

Sr is an alkaline earth element (Group 2) with a valence of +2. The alkaline earths are also reasonably soluble in water and hydrous fluids, but not as soluble as the alkalis. Sr is therefore a moderately mobile element. Its ionic radius is 113 pm, which is still sufficiently large for it to be excluded from many minerals, and it is also an incompatible element, but not a highly incompatible one. It substitutes for Ca (ionic radius 99 pm) to varying degrees. It is quite comfortable in the Ca site in plagioclase, the solid/liquid partition⁵ coefficient being about 2. It seems to be considerably less comfortable in the Ca site in clinopyroxene; the Sr partition coefficient being only about 0.1. Thus in most igneous and high-grade metamorphic rocks, most Sr will be in plagioclase (which typically constitutes about 50% of mafic igneous rocks). Sr can also substitute for Ca in other minerals such as calcite, apatite, gypsum, titanite (CaTiSiO_5 , also known as sphene), and so on. Sr is also concentrated in the crust relative to the mantle, but not to the degree that Rb is.

The Rb/Sr in the Earth as a whole is in the range of 0.021–0.029; we do not know this ratio exactly.⁶ The ratio is lower in the mantle, and much higher in the crust. Mantle-derived rocks such as basalts also have low Rb/Sr ratios. Low ratios such as these violate condition 1 previously; as a result, it is often difficult to obtain good Rb/Sr ages on mafic⁷ and ultramafic rocks. However, igneous differentiation tends to increase the Rb/Sr ratio because Sr is removed by fractional crystallization of plagioclase while Rb remains in the melt. In felsic or silicic igneous rocks, the Rb/Sr ratio often exceeds 1 (a Rb/Sr ratio of 1 corresponds to a $^{87}\text{Rb}/^{86}\text{Sr}$ ratio of 2.9, depending somewhat on the $^{87}\text{Sr}/^{86}\text{Sr}$ ratio). As a result, Rb/Sr dating can often be applied successfully to felsic igneous rocks. A large range in Rb/Sr ratio is also reasonably common. It may occur in whole rock samples when the whole rocks represent various members of a comagmatic differentiation suite, or in mineral samples when both K- and Ca-bearing minerals are present. Rb-Sr geochronology can also be applied to metamorphic rocks, provided K-bearing, Rb-rich minerals are present, as they typically are. Figure 2.11 shows an example isochron of a meteorite.

A serious disadvantage of the Rb-Sr system is the mobility of these elements, particularly Rb. Because of their solubilities, Rb and Sr are readily transported by fluids, and may be moved into or out of the system. Furthermore, some K-bearing minerals such

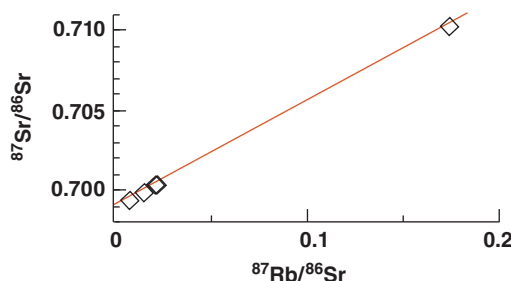


Figure 2.11 A Rb-Sr isochron. Five analyses from a clast in the Bholghati meteorite fall on an isochron, whose slope is related to the age of the system. The age in this case is 4.54 Ga. Data from Nyquist et al. (1990). (Source: White (2013). Reproduced with permission of John Wiley & Sons.)

as micas are comparatively reactive, in the sense that some or much of the Rb may be present in exchangeable sites. These minerals are also subject to metamorphic resetting or partial resetting at relatively low temperatures. Thus, *Rb-Sr is a good system for dating acid igneous rocks where no intervening metamorphism or alteration has occurred, and for metamorphic rocks.*

Rb-Sr dating can in special instances be applied to sedimentary rocks. Sedimentary rocks are generally difficult to date by any method because of the lack of the high-temperatures necessary for homogenization of initial Sr isotope ratios. But minerals crystallizing from a homogeneous solution, such as seawater, will all have identical initial ratios. Thus dates have been obtained using minerals such as authigenic celadonite (a K- and Rb-rich mineral) and calcite (a Rb-poor, Sr-rich mineral). An additional advantage is that the evolution of $^{87}\text{Sr}/^{86}\text{Sr}$ in seawater is known. Thus a reasonable assumption about the initial $^{87}\text{Sr}/^{86}\text{Sr}$ ratio may be made if the approximate age is known. However, successful dates of sediments are certainly rare.

2.4.2 Sr isotope chronostratigraphy

Sr isotope ratios can, however, be used to date sediments in another way. Sr has a long residence time in the oceans, a consequence, in part, of its relatively high solubility. Consequently, it is uniformly mixed in the open ocean. As a result of that, its concentration and isotopic composition in the modern ocean is uniform. Its isotopic composition has, however, changed over geologic time. The change over the Phanerozoic is illustrated in Figure 2.12.

Since seawater $^{87}\text{Sr}/^{86}\text{Sr}$ is geographically uniform at any time yet varies through time, the isotopic composition of material precipitated from seawater will be a function of time. Sr is concentrated in calcite and aragonite, which many organisms, most notably mollusks, corals, and foraminifera, precipitate to form shells. By comparing the $^{87}\text{Sr}/^{86}\text{Sr}$ of a particular shell with the seawater curve in Figure 2.12, we can determine its age. This dating technique is called *Sr isotope chronostratigraphy*. There are, however, several caveats. First, $^{87}\text{Sr}/^{86}\text{Sr}$ is

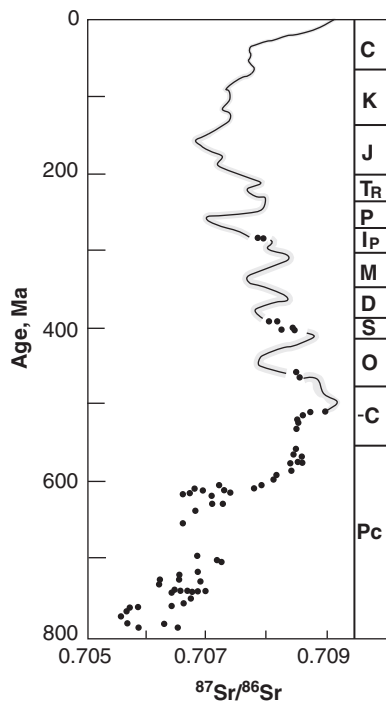


Figure 2.12 $^{87}\text{Sr}/^{86}\text{Sr}$ in seawater through Phanerozoic time determined from the analysis of phosphate and carbonate fossils. (Source: Adapted from McArthur et al., 2001).

uniform only in the open ocean; it can vary in coastal areas due to continental inputs. Thus, for example, oyster shells would not be useful because oysters grow in brackish water. Second, while the ratio in a pristine shell should reflect the composition of the water it precipitates from, this ratio may change as a result of interaction with pore water. Finally, a given value of $^{87}\text{Sr}/^{86}\text{Sr}$ does not necessarily correspond to a unique age. For example, the value of 0.7080 occurred during Ordovician, Devonian, Mississippian, Permian, and Cenozoic time. Thus, the age of the fossil being dated needs to be approximately known before Sr isotope chronostratigraphy can be applied usefully. Finally, the accuracy of this technique depends on how accurately the $^{87}\text{Sr}/^{86}\text{Sr}$ value of seawater is known for any given time. For much of the Cenozoic, particularly the late Cenozoic, these values are very well known. Consequently, Sr isotope chronostratigraphy provides useful and accurate ages for these times. Values are much less well known for the Paleozoic.

The change in seawater $^{87}\text{Sr}/^{86}\text{Sr}$ shown in Figure 2.12 has been very non-linear. Indeed, there have been times, such as the Permian and the Jurassic, when $^{87}\text{Sr}/^{86}\text{Sr}$ has actually decreased in seawater. This is perhaps initially surprising since the decay of ^{87}Rb to ^{87}Sr occurs at a constant rate. This reflects the *open system* nature of the oceans. Salts are continuously added and removed from seawater; consequently, the oceans inventory of Sr is constantly, albeit slowly, renewed. Thus, the isotopic composition of seawater Sr reflects the isotopic composition of Sr added to seawater, that is, the isotopic composition of the *sources* of Sr in seawater. We can broadly divide these sources into “continental” and “mantle.” The continental source is dominantly the riverine input, and secondarily wind-blown and glacially derived particles that dissolve or partly dissolve when they reach the sea. The isotopic composition of the continental source will vary with the nature of continental material undergoing erosion at any time as well as with the rate of erosion. The mantle source consists primarily of hydrothermal fluids of mid-ocean ridge hydrothermal systems. Secondary sources include erosion and weathering (both subareal and submarine) of young, mantle-derived basalts. We’ll discuss this further in Chapter 7.

2.5 THE SM-ND SYSTEM

^{147}Sm decays to ^{143}Nd by alpha decay with a half-life of 106 Ga ($\lambda = 6.54 \times 10^{-12} \text{ a}^{-1}$). Because the half-life is so long, the resulting variations in Nd isotopic composition are small and require precise measurement. Sm and Nd are both intermediate rare earth elements (Figure 2.13). The distinctive feature of the rare earth elements is that inner electron shells (specifically the 4f and 5d shells) are being filled as atomic number increases. Normally an electron is added to the outermost shell when atomic number increases. It is the outer electron shells that dictate the chemical behavior of elements. Since the outer electron shells of the rare earths have identical configurations, we would expect them to behave quite similarly. This is indeed the case. The rare earths generally have a +3 valence, the most important exceptions being Eu, which is +2 under some conditions, and Ce, which is +4 under some conditions. The primary

The Rare Earth Elements

H																	He
Li	Be																
Na	Mg																
K	Ca	Sc	Ti	V	Cr	Mn	Fe	Co	Ni	Cu	Zn	Ga	Ge	As	Se	Br	Kr
Rb	Sr	Y	Zr	Nb	Mo	Tc	Ru	Rh	Pd	Ag	Cd	In	Sn	Sb	Te	I	Xe
Cs	Ba	La	Hf	Ta	W	Re	Os	Ir	Pt	Au	Hg	Tl	Pb	Bi	Po	At	Rn
Fr	Ra	Ac															
La	Ce	Pr	Nd	Pm	Sm	Eu	Gd	Tb	Dy	Ho	Er	Tm	Yb	Lu			
Ac	Th	Pa	U														

Figure 2.13 Periodic Table highlighting the rare earths (gray background) and Nd and Sm.

chemical difference between the rare earth elements is the ionic radius, which shrinks systematically from 115 pm for La ($A = 57$) to 93 pm for Lu ($A = 71$). Since the rare earths form predominately ionic bonds with oxygen in the solid Earth, their ionic radius is a key factor in their geochemical behavior. Thus there is a systematic variation in their abundances in rocks, minerals, and solutions (see Box 2.1 on rare earth plots). The ionic radii of Sm and Nd, which are separated by Pm (an element that has no stable or long-lived isotope), differ by only 4 pm (Nd = 108, Sm = 104). The ionic radii and relatively high charge of the rare earths make them fairly unwelcome in many mineral lattices: they can be considered moderately incompatible, with Nd being slightly more incompatible than Sm. Ce is generally the most abundant rare earth and forms its own phase in rare instances. Some rare earths, particularly the heavier ones, are accommodated in lattice structures of common minerals; for example, the partition coefficient of Lu in garnet is in the range of 4–10 (depending on the composition of the magma and the garnet). In mafic minerals, the lighter rare earths, which have the largest ionic radii, tend to be excluded more than the heavies, but in plagioclase, the heavies are the most excluded (though partition coefficients generally are less than 0.1). The high valence state of the rare earths results in relatively

strong bonds. This, together with their tendency to hydrolyze (i.e., surround themselves with OH^- radicals), results in relatively low solubilities and low mobilities.

Although absolute concentrations vary significantly, the rare earths have very nearly the same *relative* abundances (that is, ratios to each other) in all classes of chondritic meteorites and they all exhibit flat patterns on rare earth plots such as Figure 2.15 (see Box 2.1). This suggests that the rare earths were not fractionated in the solar nebula, the cloud of gas and dust from which solar system bodies, including the parent bodies of meteorites and the Earth, formed. This is also true of other refractory⁸ elements, such as Lu, Hf, Th, and U, but it is not true of elements that condense at lower temperatures. Much of the chemical variation among chondritic meteorites relates to volatility, and hence is apparently due to elements evaporating or condensing from nebular gas. That the relative abundance of refractory elements does not vary suggests nebular temperatures were never hot enough for significant fractions of these elements to evaporate.

Since the relative concentrations of rare earths in chondrites are uniform and identical (within analytical error) to those in the Sun, the nebular dust from which the Earth formed should also have had those same relative concentrations of Sm and Nd. Thus, until recently it was widely assumed that the Earth

Box 2.1 Rare Earth Plots

The systematic contraction in the ionic radii of the rare earth elements leads to systematic variation in their behavior. This is best illustrated by viewing their abundances on rare earth, or Masuda–Coryell, plots. The plots are constructed by first “normalizing” the concentrations of the rare earth; that is, dividing by the concentration of the element in a standard. Generally, this standard is the abundance in chondritic meteorites, but other values are also used (for example, rare earths in sediments and seawater are often normalized to average shale). This normalizing process removes the sawtooth pattern that results from odd-even nuclear effects, and also the effect of decreasing concentration with atomic number. Those concentration variations, illustrated in Figure 2.14, reflect differences in nuclear stability and the nucleosynthetic process, and therefore affect the abundances of rare earths in all matter. Removing these effects by normalization highlights differences in concentration due to geochemical processes. After normalizing, the log of the abundance of each element is plotted against atomic number, as is illustrated in Figure 2.15.

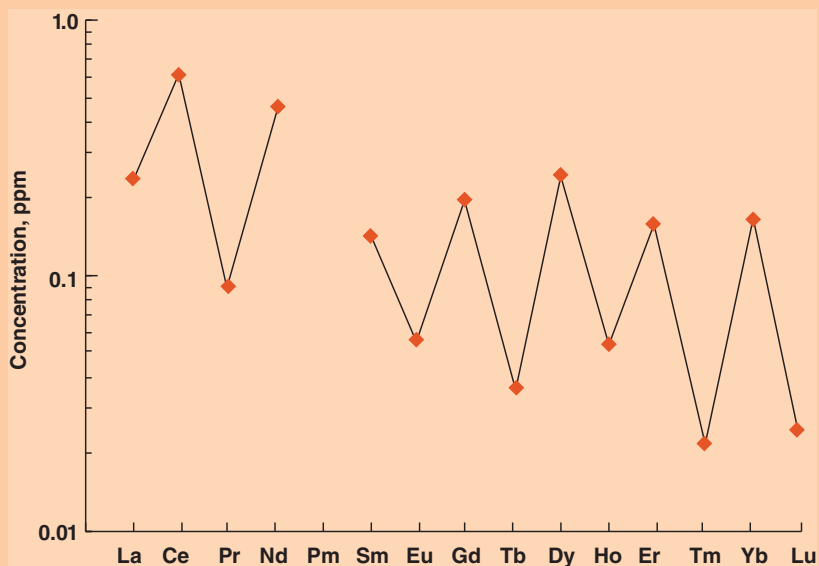


Figure 2.14 Rare earth concentrations in the CI carbonaceous chondrite Orgueil. (Source: White (2013). Reproduced with permission of John Wiley & Sons.)

also has chondritic relative abundances of the rare earth elements. Consequently, the $^{147}\text{Sm}/^{144}\text{Nd}$ ratio of the Earth was assumed to be equal to the mean chondritic value of 0.1960–0.1967 (corresponding to a Sm/Nd of about 0.325; uncertainty in this number reflects the small variation observed in chondrites and in determining a mean value). Assuming further that the solar nebula was isotopically homogeneous, we could also infer that the initial $^{143}\text{Nd}/^{144}\text{Nd}$ ratio of the Earth should be identical to the initial $^{143}\text{Nd}/^{144}\text{Nd}$ ratio of chondrites. If the initial $^{143}\text{Nd}/^{144}\text{Nd}$ ratio and the Sm/Nd ratio of Earth are the same as chondrites, then the

present $^{143}\text{Nd}/^{144}\text{Nd}$ should also be the same as the present ratio in chondrites.

These observations and assumptions led to a useful notation, namely ϵ_{Nd} (epsilon-Nd), which is the relative deviation from the chondritic value (DePaolo and Wasserburg, 1976). These deviations are small, so we write them in deviations in parts in 10,000. Thus ϵ_{Nd} is defined as follows:

$$\epsilon_{\text{Nd}} = \left[\frac{^{143}\text{Nd}/^{144}\text{Nd}_{\text{sample}}}{^{143}\text{Nd}/^{144}\text{Nd}_{\text{CHUR}}} - 1 \right] \times 10000 \quad (2.45)$$

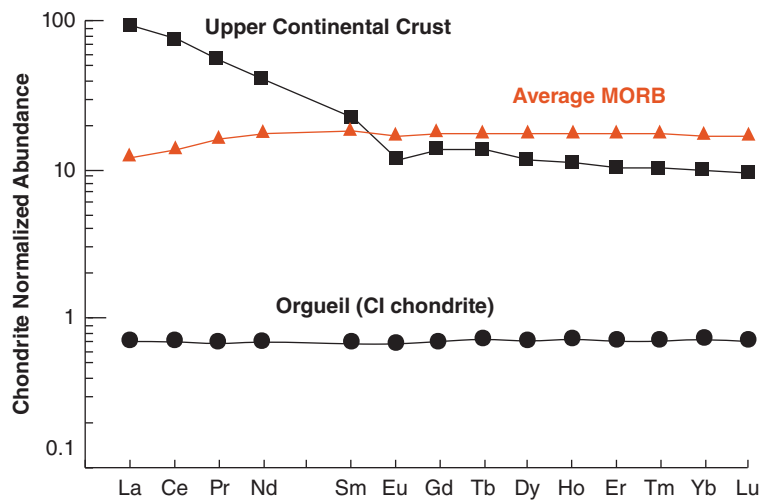


Figure 2.15 A rare earth plot showing rare earth patterns for Orgueil, average upper continental crust, and average mid-ocean ridge basalt (MORB). (Source: White (2013). Reproduced with permission of John Wiley & Sons.)

where CHUR stands for *chondritic uniform reservoir*; that is, $(^{143}\text{Nd}/^{144}\text{Nd})_{\text{CHUR}}$ is the value of the ratio in chondrites. We can calculate an ϵ_{Nd} for any point in time. For the present, the value of $(^{143}\text{Nd}/^{144}\text{Nd})_{\text{CHUR}}$ is 0.512630 or 0.512638 when $^{146}\text{Nd}/^{144}\text{Nd} = 0.7219^9$ and $^{147}\text{Sm}/^{144}\text{Nd}$ is 0.1960 or 0.1966, respectively (Jacobsen and Wasserburg, 1984; Bouvier et al., 2008). To calculate ϵ_{Nd} for any other time, we need to use the chondritic value at that time. One advantage of this notation is that ϵ_{Nd} are small numbers of only two or three significant digits, with the range in ϵ_{Nd} among most terrestrial rocks being +14 to -20. This same range corresponds to $^{146}\text{Nd}/^{144}\text{Nd}$ from 0.5116 to 0.5132.

Recent work on the $^{142}\text{Nd}/^{144}\text{Nd}$ ratio has provided reason to question the assumption that the Sm/Nd ratio of the Earth is chondritic. ^{142}Nd is produced by decay of ^{146}Sm , which has a half-life of 68 Ma. Because of its short half-life, ^{146}Sm no longer exists in the Solar System, but it did when the Solar System first formed. Its decay led to variations in the $^{142}\text{Nd}/^{144}\text{Nd}$ ratio. Most notably, nearly all terrestrial materials have $^{142}\text{Nd}/^{144}\text{Nd}$ ratio about 0.2 epsilon units (0.002%) higher than the chondritic value (Boyett and Carlson, 2005), the only exceptions being some early Archean rocks (>3.5 Ga) that show variable $^{142}\text{Nd}/^{144}\text{Nd}$ ratios (e.g., Boyett et al., 2003, O’Neil et al., 2008). This implies the

$^{147}\text{Sm}/^{140}\text{Nd}$ ratio of the Earth is about 6–8% higher than the chondritic one (about 0.208), corresponding to an ϵ_{Nd} of about +7.

Why the Earth should not have a chondritic Sm/Nd ratio is unclear. These two elements are very similar to each other in chemical behavior, having identical configurations of electrons in bonding orbitals, and are both refractory lithophile elements. Indeed, Nd and Sm have 50% condensation temperatures of 1602 and 1590 K, respectively. It is difficult to see how processes operating in the solar nebula could have fractionated these elements significantly. Two primary hypotheses have been proposed to explain this; both involve formation of an early primitive, incompatible element-enriched, and therefore low Sm/Nd, crust by crystallization of a terrestrial magma ocean. Boyet and Carlson (2006) suggested that this enriched crust (what they call the “Early Enriched Reservoir”) subsequently sank to the deep mantle where it remains. The complimentary “Early Depleted Reservoir” is the part of the mantle sampled by volcanism and gave rise to the present continental crust. In this model, the bulk Earth does have chondritic Sm/Nd, although the “observable” part does not.

Alternatively, Caro et al. (2008) and Caro and Bourdon (2010) proposed that the primitive incompatible element-enriched crust was lost from the Earth by “collisional erosion”;

as the Earth accreted from nebular material, very large impacts of protoplanetary bodies blasted the proto-crust into space. In support of this view, they point out that the Moon, itself thought to have formed when a large protoplanet impacted Earth, appears to have the same non-chondritic Sm/Nd as the Earth, as may Mars (although the case for non-chondritic Sm/Nd is weaker for Mars). A third proposed explanation is heterogeneous distribution of ^{142}Nd or, particularly, ^{144}Sm in the solar nebula. There is indeed some evidence of isotopic heterogeneity in the solar system and we will consider this in more detail in Chapter 5.

Figure 2.16 illustrates how $^{143}\text{Nd}/^{144}\text{Nd}$ has evolved in the Earth. If the Earth indeed has chondritic Sm/Nd, it evolves along the line labeled “CHUR.” If the $^{147}\text{Sm}/^{144}\text{Nd}$ is higher (0.208), it evolves along a steeper trajectory labeled “Bulk (Observable) Silicate Earth.” In either case, differentiation of the Earth into a light rare earth-enriched crust and light rare earth-depleted mantle results in the mantle evolving along a steeper (high Sm/Nd) trajectory, and crust evolving along a less steep one (low Sm/Nd). Converting $^{143}\text{Nd}/^{144}\text{Nd}$ to ε_{Nd} (Figure 2.16b) the CHUR value remains constant at $\varepsilon_{\text{Nd}} = 0$ while the observable Earth evolves toward an ε_{Nd} value of about +7. The mantle evolves toward even more positive ε_{Nd} while the crust evolves toward negative ε_{Nd} .

Perhaps the greatest advantage of Sm/Nd is the lack of mobility of these elements. *The Sm-Nd chronometer is therefore relatively robust with respect to alteration and low-grade metamorphism.* Thus the Sm-Nd system is often the system of choice for mafic rocks and for rocks that have experienced metamorphism or alteration. An additional advantage is relatively high closure temperatures for this system making it useful for dating peak metamorphism.

There also are several drawbacks to the use of the Sm-Nd system in geochronology. First, the half-life of ^{147}Sm is relatively long, leading to relatively small variation in $^{143}\text{Nd}/^{144}\text{Nd}$ and imprecise ages, particularly for young rocks. The second is the limited variation in Sm/Nd. As things turn out, however, Sm-Nd complements Rb-Sr nicely. Sm/Nd variations tend to be largest in mafic and ultramafic rocks and smallest in acid rocks, exactly the

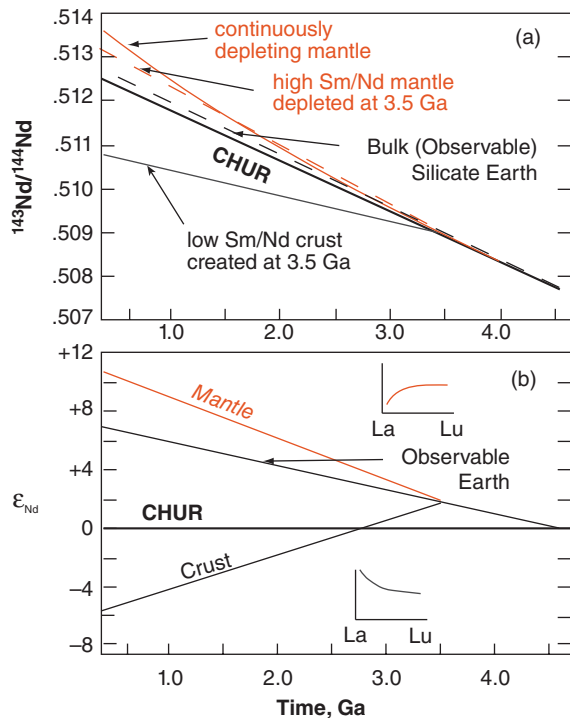


Figure 2.16 (a) Nd isotope evolution in CHUR, the chondritic uniform reservoir (bold line), a bulk observable Earth with higher Sm/Nd than CHUR (dashed), and crust and residual mantle produced at 3.5 Ga, and the evolution of a continuously depleted mantle. (b) Evolution of bulk (observable) silicate earth, crust, and mantle when $^{143}\text{Nd}/^{144}\text{Nd}$ is transformed to ε_{Nd} . Also shown are cartoons of the corresponding rare earth patterns. (Source: White (2013). Reproduced with permission of John Wiley & Sons.)

opposite of Rb/Sr. One application that has been highly successful has been to use the Sm-Nd isotope system to date garnet bearing rocks. Garnets incorporate HREE over LREE as they grow, which lead to very high Sm/Nd ratio in these minerals. Therefore, garnet bearing rocks such as eclogites can be dated to relatively high precision with the Sm-Nd system. Figure 2.17 is an example of a Sm-Nd isochron of a garnet-bearing granite from the Qinling–Tongbai–Dabie–Sulu ultrahigh-pressure (UHP) metamorphic belt in China (Cheng et al., 2011). The 394 Ma age is younger than the 434 ± 7 Ma zircon age of the granite. The garnets likely formed from incongruent breakdown of biotite.

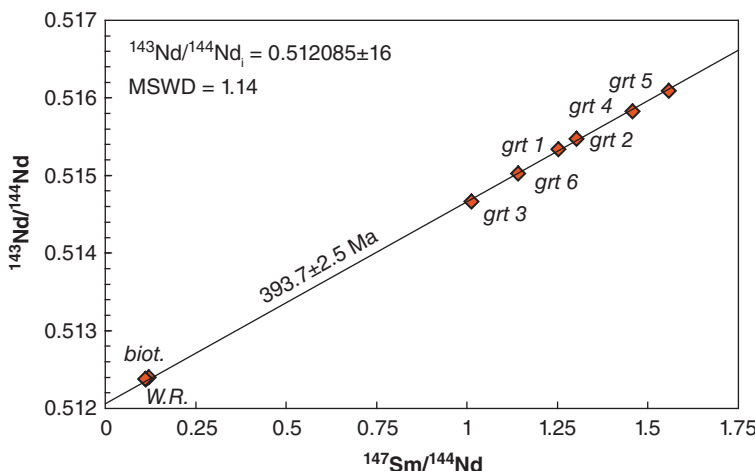


Figure 2.17 Sm-Nd isochron based on six garnet fractions, two whole rocks and a biotite fraction from the Qinling metamorphic belt in China. Errors are smaller than the symbols. (Source: Adapted from Cheng et al. (2011). Reproduced with permission of Elsevier.)

The age reflects time the granite cooled through the closure Sm-Nd temperature, in this case some 40 million years after crystallization, suggesting it remained deeply buried.

2.5.1 Sm-Nd model ages and crustal residence times

A general assumption about the Earth is that the continental crust has been created from the mantle by magmatism. When a piece of crust is first created, it will have the $^{143}\text{Nd}/^{144}\text{Nd}$ ratio of the mantle, though its Sm/Nd ratio will be lower than that of the mantle (a consequence of Nd being more incompatible and partitioning more into the melt than Sm). Let's make the simplistic assumption that the mantle has the same Nd isotopic history as CHUR. This means a piece of crust will have the same $^{143}\text{Nd}/^{144}\text{Nd}$ as the mantle and as CHUR when it is created, that is, $\varepsilon_{\text{Nd}} = 0$. If we know the present-day Sm/Nd and $^{143}\text{Nd}/^{144}\text{Nd}$ ratio of this piece of crust, we can estimate its age. Figure 2.18 illustrates how this is done graphically; let's see how this is done mathematically. What we want to find is the intersection of line describing the evolution of the sample and that describing the evolution of the mantle. To do so, we simply need to subtract one equation from the other.

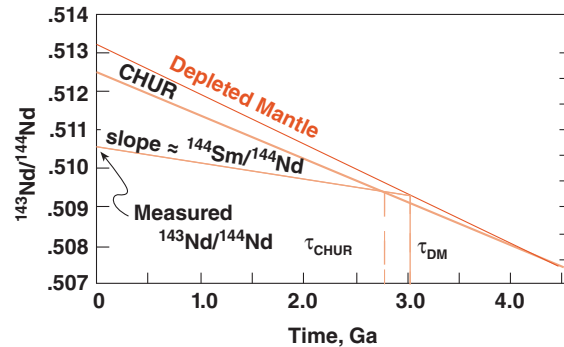


Figure 2.18 Sm-Nd model ages. The $^{143}\text{Nd}/^{144}\text{Nd}$ is extrapolated backward (slope depending on Sm/Nd) until it intersects a mantle or chondritic growth curve. (Source: White (2013). Reproduced with permission of John Wiley & Sons.)

The closed system isotopic evolution of any sample can be expressed as:

$$\begin{aligned} {}^{143}\text{Nd}/{}^{144}\text{Nd}_{\text{sam}} &= {}^{143}\text{Nd}/{}^{144}\text{Nd}_0 \\ &\quad + {}^{147}\text{Sm}/{}^{144}\text{Nd}_{\text{sam}}(e^{\lambda t} - 1) \end{aligned} \quad (2.46)$$

The chondritic evolution line is:

$$\begin{aligned} {}^{143}\text{Nd}/{}^{144}\text{Nd}_{\text{CHUR}} &= {}^{143}\text{Nd}/{}^{144}\text{Nd}_0 \\ &\quad + {}^{147}\text{Sm}/{}^{144}\text{Nd}_{\text{CHUR}}(e^{\lambda t} - 1) \end{aligned} \quad (2.47)$$

The CHUR model age of a system is the time elapsed, $t = \tau$, since it had a chondritic

$^{143}\text{Nd}/^{144}\text{Nd}$ ratio, assuming the system has remained closed. We can find τ by subtracting Eqn. 2.47 from 2.46, which yields:

$$\begin{aligned} & ^{143}\text{Nd}/^{144}\text{Nd}_{\text{sam}} - ^{143}\text{Nd}/^{144}\text{Nd}_{\text{CHUR}} \\ & = \{ ^{147}\text{Sm}/^{144}\text{Nd}_{\text{sam}} - ^{147}\text{Sm}/^{144}\text{Nd}_{\text{CHUR}} \} \\ & \times (e^{\lambda\tau} - 1) \end{aligned} \quad (2.48)$$

Another way of thinking about this problem is to imagine a $^{143}\text{Nd}/^{144}\text{Nd}$ versus time plot: on that plot, we extrapolate the sample's evolution curve back to the chondritic one. In terms of these equations, this intersection occurs at $(^{143}\text{Nd}/^{144}\text{Nd})_0$.

Solving eqn. 2.48 for τ :

$$\tau_{\text{CHUR}} = \frac{1}{\lambda} \ln \left(\frac{\frac{^{143}\text{Nd}/^{144}\text{Nd}_{\text{sam}}}{-^{143}\text{Nd}/^{144}\text{Nd}_{\text{CHUR}}}}{\frac{^{147}\text{Sm}/^{144}\text{Nd}_{\text{sam}}}{-^{147}\text{Sm}/^{144}\text{Nd}_{\text{CHUR}}}} + 1 \right) \quad (2.49)$$

An age obtained in this way is called an *Nd model age* (the model is that of chondritic evolution of the mantle), or a *crustal residence age*, because it provides an estimate of how long this sample of Nd has been in the crust. Note that we explicitly assume the sample has remained a closed system, in the sense of no migration in or out of Sm or Nd. Because of the immobility of these elements, the assumption often holds, although generally only approximately.

We can obtain somewhat better model ages by making more a sophisticated assumption about the Nd evolution of the mantle. Since the crust is enriched in Nd relative to Sm, the mantle must be depleted in Nd relative to Sm (analyses of mantle-derived rocks confirm this) and the mantle should evolve along a line steeper than chondritic. Once we decide on Sm/Nd and present-day $^{143}\text{Nd}/^{144}\text{Nd}$ ratios for this "depleted-mantle" (the latter can be estimated from the $^{143}\text{Nd}/^{143}\text{Nd}$ of MORB, mid-ocean ridge basalts), we can calculate a model age relative to the depleted mantle by substituting the depleted-mantle terms for the CHUR terms in 2.47 and 2.48.

To calculate the depleted mantle model age, τ_{DM} , we use the same approach, but this time we want the intersection of the sample evolution line and the depleted mantle

evolution line. So Eqn. 2.49 becomes:

$$\tau_{\text{DM}} = \frac{1}{\lambda} \ln \left(\frac{\frac{^{143}\text{Nd}/^{144}\text{Nd}_{\text{sam}}}{-^{143}\text{Nd}/^{144}\text{Nd}_{\text{DM}}}}{\frac{^{147}\text{Sm}/^{144}\text{Nd}_{\text{sam}}}{-^{147}\text{Sm}/^{144}\text{Nd}_{\text{DM}}}} + 1 \right) \quad (2.50)$$

The depleted mantle (as sampled by mid-ocean ridge basalts) has an average ϵ_{Nd} of about 9, or $^{143}\text{Nd}/^{144}\text{Nd} = 0.51310$. The simplest possible evolution path, and the one we shall use, would be a closed system evolution since the formation of the Earth, 4.55 Ga ago (i.e., a straight line on a $^{143}\text{Nd}/^{144}\text{Nd}$ vs. time plot). This evolution implies a $^{147}\text{Sm}/^{144}\text{Nd}$ of 0.213.

Because the Sm/Nd ratio is so little affected by weathering, and because these elements are so insoluble, Sm/Nd ratios in fine-grained sediments do not generally differ much from the ratio in the precursor crystalline rock. Thus, the system has some power to "see through" even the process of making sediment from crystalline rock. The result is we can even compute crustal residence times from Nd isotope ratio and Sm/Nd measurements of fine-grained sediments. This generally does not work for coarse-grained sediments though because they contain accessory minerals whose Sm/Nd ratios can be quite different from that of the whole rock.

2.6 THE LU-HF SYSTEM

Lu is the heaviest rare earth element, with a valence of +3 and an ionic radius of 93 pm. It has two isotopes, ^{175}Lu (97.4%) and ^{176}Lu (2.6%). As an odd-odd nuclei, ^{176}Lu is unstable relative to both ^{176}Yb and ^{176}Hf . However, there is some uncertainty as to whether the decay to ^{176}Yb occurs at all, and it certainly constitutes less than 3% of the decay. Hf is a member of the group IVB elements, which include Ti and Zr. As members of the same periodic group, the three elements show chemical similarity and this similarity is quite strong in the case of Zr and Hf. Hf has an ionic radius of 71pm in 6-fold coordination (0.83 in 8-fold coordination) and a valence of +4. The particularly strong similarity between Hf and Zr results in part from the similarity of ionic radii: the radius of Zr^{4+} is 72pm in 6-fold and 84 pm in 8-fold coordination; the radius of Ti^{4+} is much

smaller: 61pm. Lu can be considered a slightly to moderately incompatible element; Hf is moderately incompatible (its incompatibility is very similar to that of Sm).

The Lu-Hf system shares many of the advantages of the Sm-Nd system: both are relatively insoluble and immobile elements, both are refractory and hence we have reason to believe that the Lu/Hf ratio is the same as in chondrites. Indeed, we can define an ϵ_{Hf} value in a manner exactly analogous to the ϵ_{Nd} :

$$\epsilon_{Hf} = \left[\frac{\left(^{176}\text{Hf}/^{177}\text{Hf} \right)_{\text{sample}}}{\left(^{176}\text{Hf}/^{177}\text{Hf} \right)_{\text{Chon}}} - 1 \right] \times 10000 \quad (2.51)$$

Isotopic analysis of Hf is made difficult by its extremely limited aqueous solubility and its nearly identical chemical behavior to Zr (indeed, its chemical similarity to Zr is one reason why Hf was the very last stable element to be discovered and isolated – it was discovered in X-ray spectra in 1923 and the metal first purified in 1925). Although laborious, standard techniques are available for Hf purification. An additional problem is that the temperatures required for ionization are extremely high; as a result the ionization efficiency by thermal ionization is low, making analysis difficult by this method. This problem has been overcome with the development of multiple-collector magnetic sector inductively coupled plasma mass spectrometers (MC-ICP-MS), in which the analyte is ionized in an Ar plasma rather than thermally. Secondary ion mass spectrometry, in which the Hf is ionized by an ion beam while being heated (hot SIMS), has also been used with some success but has now been abandoned in favor of MC-ICP-MS Hf analysis, which enjoys widespread use.

As the analytical problems with the Lu-Hf system were overcome, other problems emerged that needed to be resolved. Perhaps most importantly, there was a worrisome amount of uncertainty of the value of the decay constant. Determining the decay rate of a nuclide that decays as slowly as ^{176}Lu is not easy. As we noted earlier, there are several possible approaches. These approaches produced results that did not agree as well as one would

hope. Counting experiments performed since 1975 have yielded a range of decay constants ranging from $1.70 \times 10^{-11}\text{ a}^{-1}$ to $1.93 \times 10^{-11}\text{ a}^{-1}$, a 14% range. The “calibration” approach has also produced a range of values. Tatsumoto et al. (1981) calculated a decay constant of $1.94 \times 10^{-11}\text{ a}^{-1}$ from a Lu-Hf isochron on eucrite meteorites assuming an age of 4.55 Ga. Scherer et al. (2001) performed a calibration experiment by obtaining U-Pb and Lu-Hf isochrons on four rock suites ranging in age from 0.91 to 2.06 Ga and using the U-Pb ages to determine a decay constant for ^{176}Lu of $1.865 \pm 0.015 \times 10^{-11}\text{ a}^{-1}$. Söderlund et al. (2004) calculated a decay constant of $1.867 \pm 0.008 \times 10^{-11}\text{ a}^{-1}$ by comparing Lu-Hf and U-Pb isochrons of Proterozoic dolorites from Sweden and Finland. Bizzarro et al. (2003) determined a decay constant of $1.983 \times 10^{-11}\text{ a}^{-1}$ from an isochron on chondritic and eucritic meteorites and an assumed age of 4.56 Ga. Although the Bizzarro age was based on an isochron that mixed different classes of meteorites with different histories, it seemed that one value of the decay constant applied to meteorites and another to terrestrial samples, which hardly seemed likely.

Subsequent studies of meteorites appear to have resolved this issue in favor of the “terrestrial” decay constant of Söderlund and Scherer ($1.867 \times 10^{-11}\text{ a}^{-1}$ is the currently accepted value). Amelin (2005) carried out a calibration study using phosphates (such as apatite) in the Acapulco and Richardton meteorites. Phosphates have the useful property that they concentrate both U and the rare earths, such as Lu while excluding Pb and Hf. The resulting high U/Pb and Lu/Hf ratios lead to good chronometers (unfortunately, phosphates are also rather soluble, hence isochrons are potentially easily disturbed, although they were not in this study). Comparing Lu-Hf isochrons with previously determined U-Pb ages of 4556.5 ± 1.3 Ma and 4550.7 ± 2.6 Ma, Amelin (2005) found decay constants of $1.864 \pm 0.016 \times 10^{-11}\text{ a}^{-1}$ and $1.832 \pm 0.029 \times 10^{-11}\text{ a}^{-1}$, in good agreement with the previously determined decay constants from terrestrial samples. Subsequent work by Bouvier et al. (2008) found that the least thermally metamorphosed chondrites (petrologic classes 1–3) showed much less scatter on an Lu-Hf

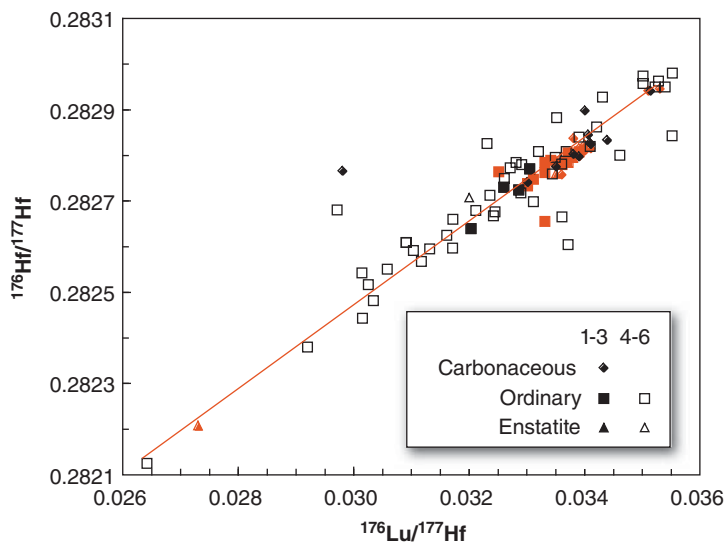


Figure 2.19 Lu-Hf systematics of chondrite meteorites. Data of Bouvier et al. (2008) in gray, data from Blichert-Toft and Albarede (1997), Bizzarro et al. (2003), and Patchett et al. (2004) in black. Petrologic classes 4-6 (open symbols) considered “equilibrated” while classes 1-3 (closed symbols) are considered “unequilibrated.” Red line is the isochron of Bouvier et al. (2008). The scatter is likely due to thermal and shock metamorphism and Lu mobility in phosphate compounds on the meteorite parent bodies.

isochron plot than metamorphosed or “equilibrated” chondrites (Figure 2.19). Using only the most precise data and assuming an age of 4568.5 Ma, they calculated a ^{176}Lu decay constant of $1.884 (\pm 0.060) \times 10^{-11} \text{ a}^{-1}$, in good agreement with the value obtained in studies of terrestrial rocks.

In addition to questions about the decay constant, there have also been questions about the $^{167}\text{Lu}/^{177}\text{Hf}$ ratio and the present and initial $^{176}\text{Hf}/^{177}\text{Hf}$ ratio of chondrites. A good part of the problem is that there is a 28% variation in the $^{167}\text{Lu}/^{177}\text{Hf}$ ratio in chondrites (compared to only 3% variation in the Sm/Nd ratio). Bouvier et al. (2008) found that when only the least thermally metamorphosed chondrites are considered the scatter in $^{167}\text{Lu}/^{177}\text{Hf}$ ratio reduces to only 3%, comparable to that observed for Sm/Nd. They argued the problem likely relates to the presence of phosphate phases in meteorites. These can have very high $^{167}\text{Lu}/^{177}\text{Hf}$ ratios and easily mobilized and recrystallized during thermal metamorphism. Using only the least thermally metamorphosed chondrites, Bouvier et al. calculate a mean $^{176}\text{Lu}/^{177}\text{Hf}$ ratio of 0.0336 ± 1 and a mean $^{176}\text{Hf}/^{177}\text{Hf} = 0.282785 \pm 11$, corresponding to an initial $^{176}\text{Hf}/^{177}\text{Hf} =$

0.27978 ± 0.00004 . However, the question of the initial $^{176}\text{Hf}/^{177}\text{Hf}$ of the Solar System persists. For example, Bizzarro et al. (2012) reported a $^{176}\text{Lu}-^{176}\text{Hf}$ internal isochron age of 4869 ± 34 Ma for a pristine achondritic meteorite (the angrite SAH99555), which had been precisely dated by U-Pb to 4564.58 ± 0.14 Ma. Thus the Lu-Hf age is roughly 300 Ma too old. Their isochron yields an initial $^{176}\text{Hf}/^{177}\text{Hf}$ of 0.279685 ± 0.000019 , 3.4 ϵ_{Hf} units lower than Bouvier et al.’s value, which they argue is the initial ϵ_{Hf} of the Solar System. We’ll discuss this question in more detail in the context of events of the early Solar System in further detail in Chapter 5. In this book we will continue to use the Bouvier et al. (2008) value of the chondritic $^{176}\text{Hf}/^{177}\text{Hf}$ for calculation of ϵ_{Hf} . Nevertheless, there is some uncertainty in the ϵ_{Hf} of the silicate Earth, perhaps several epsilon units, just as there is for the ϵ_{Nd} of the silicate Earth.

The Lu-Hf system has several advantages, in principle at least, over the Sm-Nd system. First, because the half-life of ^{176}Lu is shorter than that of ^{147}Sm (37 Ga versus 106 Ga) and because the range of Lu/Hf ratios in common rocks and minerals is greater than that of Sm/Nd, the variations in $^{176}\text{Hf}/^{177}\text{Hf}$

and ε_{Hf} are larger than of $^{143}\text{Nd}/^{144}\text{Nd}$ and ε_{Nd} . Second, because of the chemical similarity of Hf to Zr, Hf is concentrated in zircon, a very robust mineral that also concentrates U and can be dated using the U-Pb system.

The general similarity between the Lu-Hf system and the Sm-Nd system is demonstrated by Figure 2.20, which shows that ε_{Hf} and ε_{Nd} are well correlated in crustal rocks of all ages. It also shows that the variations in ε_{Hf} are about half again as large as those of ε_{Nd} . The correlation holds for “terrigenous,” that is marine continent-derived sediments, but breaks down for “hydrogenous” sediments that contain a significant component derived from seawater, which define a shallower “seawater array.” This results from two effects. The first is the “zircon effect” (Patchett et al., 2004). When continental rocks are weathered, the rare earths, including Sm, Nd, and Lu concentrate in clays, but a significant fraction of unradioactive Hf remains concentrated in zircons, which resist both chemical and mechanical weathering. The zircons tend to remain in coarser-grained sediments on the continents or continental shelves, thus the Hf flux to the oceans from the continents

is more radiogenic than the continents themselves. Secondly, Hf is extremely insoluble in stream and ocean water, but less so in hydrothermal solutions where it forms soluble complexes with fluorine (Bau and Koschinsky, 2006). As a result, the flux of radiogenic Hf to seawater from the oceanic crust is larger compared to the hydrothermal Nd flux (White et al., 1986). One consequence of the different behaviors of Hf and Nd during weathering is that there would be little point to calculating Lu-Hf crustal residence times analogous to Sm-Nd residence times. We can, however, use initial ε_{Hf} values of detrital zircons to trace crustal evolution. We will return to all of these topics in Chapter 7.

One important difference between Lu-Hf and Sm-Nd is that whereas Sm/Nd ratios usually do not change much in the weathering of a crystalline rock to form a sediment, Lu/Hf ratios do. In both cases, the elements are reasonably insoluble, and little is carried away by solution. Most of the rare earths end up in clays, but much of the Hf in felsic crystalline rocks of the continental crust is in zircon (ZrSiO_4), which, as we have already noted, is very resistant

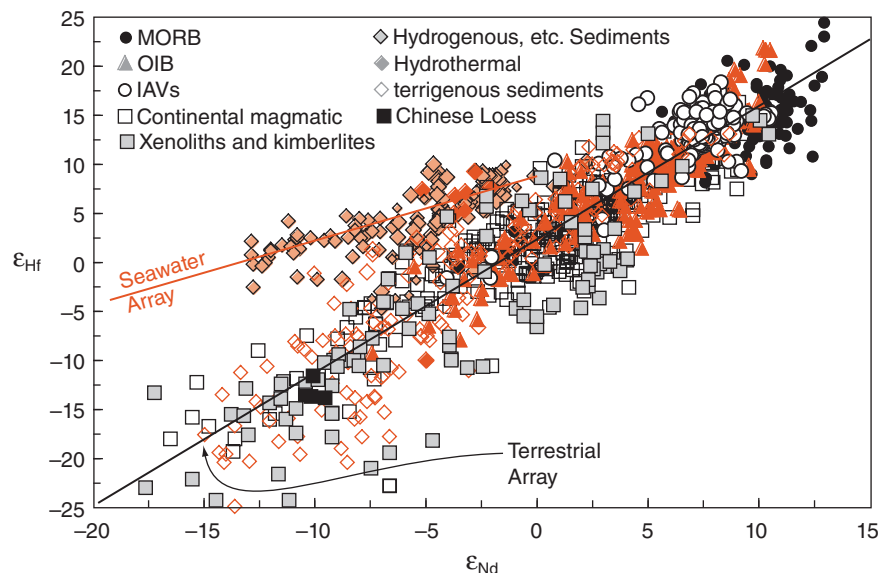


Figure 2.20 ε_{Hf} and ε_{Nd} in the Earth. The ε_{Hf} and ε_{Nd} in magmatic rocks of the continental and oceanic crust define the “terrestrial array” ($\varepsilon_{\text{Hf}} = 1.21 + 1.55\varepsilon_{\text{Nd}}$; Vervoort and Blachert-Toft, 1999; Vervoort et al., 2011). Terrigenous sediments also lie on this array. Hydrothermal and hydrogenous sediments, including Mn-Fe crusts and nodules, define a shallower array, called the seawater array by Albarède et al. (1998) described by the equation $\varepsilon_{\text{Hf}} = 7.1 + 0.55\varepsilon_{\text{Nd}}$ (Vervoort et al., 2011). From the database kindly provided by J. D. Vervoort.

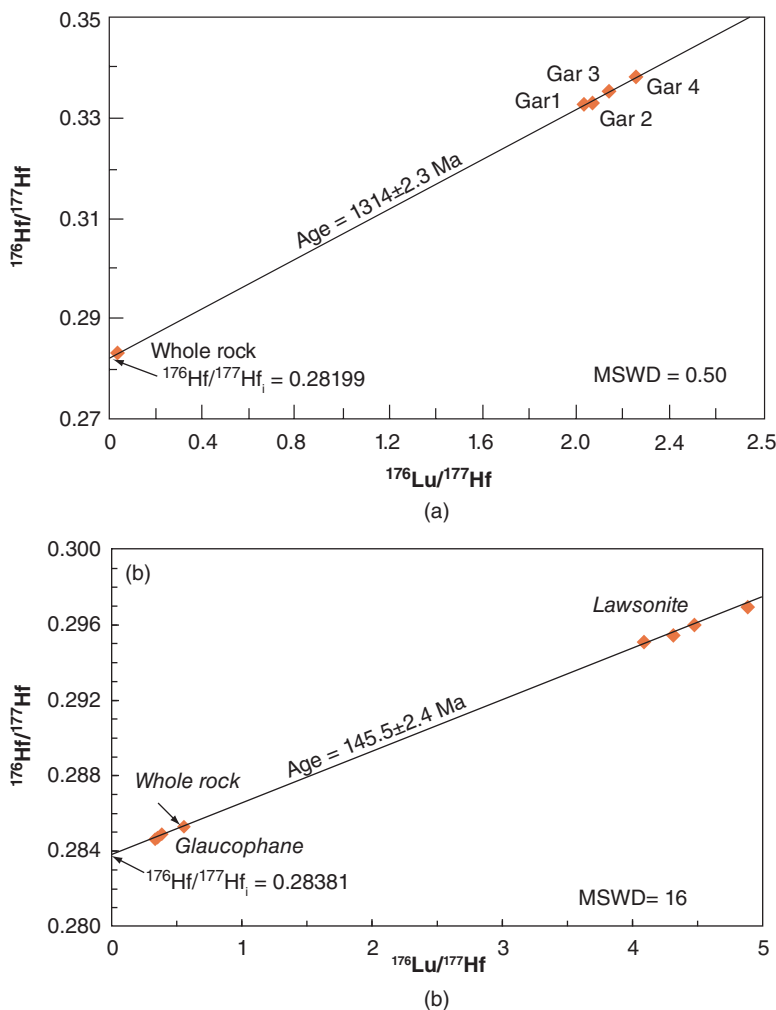


Figure 2.21 (a) Lu-Hf isochron for a garnet-mica schist from northern Idaho. The low MSWD indicates a good fit. (Source: Adapted from Nesheim et al. (2012). Reproduced with permission of Elsevier.) (b) Lu-Hf age for a blueschist from the Franciscan of California. The high MSWD indicates the isochron fits the data poorly and suggests either open system behavior or the effect of zircon inclusions. (Source: Adapted from Mulcahy et al., 2009.)

to both chemical and mechanical weathering. The clays are, of course, quite fine and can be carried great distances from their source. Zircon remains in the coarse (and hence less mobile) sand fraction. As a result, there are large differences between Lu/Hf ratios in fine and coarse sediments.

Figure 2.21 illustrates two recent examples of Lu-Hf geochronology. The first (Figure 2.21a) is a garnet-mica schist from Snow Peak in northern Idaho. Garnets strongly concentrate Lu, as well as the other heavy rare earths, while excluding Hf, making garnet-bearing rocks good targets for Lu-Hf

geochronology, as they are for Sm-Nd geochronology. Nesheim et al. (2012) analyzed four garnet fractions and a whole rock, with the data defining an age of metamorphism $1314 \pm 2.3 \text{ Ma}$. The low MSWD indicates that all variation from the isochron can be explained by analytical error alone. The second example is blueschist facies metamorphic rocks from the Ring Mountain on the Tiburon Peninsula in California (which projects into San Francisco Bay). Blueschist facies metamorphic rocks are formed in the high pressure, low temperature regime of subduction zones and have been

difficult to date by methods other than K-Ar. Among their characteristic minerals are glaucophane ($\text{Na}_2\text{Mg}_3\text{Al}_2\text{Si}_8\text{O}_{22}(\text{OH})_2$), which gives blueschist facies rocks their characteristic blue color, and lawsonite, ($\text{CaAl}_2\text{Si}_2\text{O}_7(\text{OH})_2 \cdot \text{H}_2\text{O}$). The latter can, in some cases, incorporate heavy rare earths such as Lu, while glaucophane preferentially incorporates Hf. The ages reflect closure of these to diffusion; the closure temperatures are not known but are probably high relative to the conditions typical of blueschist facies metamorphism. Mulcahy et al. (2009) analyzed lawsonite and glaucophane separates, as well as whole rock samples, and obtained the isochron shown in Figure 2.21(b). In this case, the MSWD is rather high, indicating the misfit to the isochron is greater than expected from estimated analytical errors alone. This may be a consequence of open system behavior – the lawsonite formed under retrograde conditions while the rocks were being exhumed – or, in this case, inclusion of Hf-rich phases within the separates, such as titanite. The age nevertheless agrees well with other ages from the Tiburon Peninsula, which range from 157 to 141 Ma.

2.7 THE RE-Os SYSTEM

2.7.1 The Re-Os decay system

After early efforts by Hirt et al. (1963), the Re-Os system was largely ignored due to the analytical challenges it presented. The problems are two-fold: (1) Os is an extremely rare element, rarely present at concentrations above the part per billion level (and often much lower) and (2) Os metal is extremely refractory, evaporating and ionizing only at extremely high temperatures. This was been overcome through analysis of the negative ion of OsO_3^- , which, in contrast to the metal, evaporates and ionizes at quite low temperature. This technique has proved to be extremely sensitive, making it possible to determine Os isotope ratios on extremely small amounts of Os (Creaser et al., 1991). Consequently, the Re-Os system has become a useful geochronological tool over the past two decades, although the applications are somewhat limited. Up to now, most of the elements of the decay systems we have discussed have been *lithophile* (derived from Greek words for “rock” and “love”) elements (the exception

is Pb, which is chalcophile). Lithophile means simply that, given the choice, the element prefers a silicate or oxide phase (in fact a better term would be oxyophile) to a sulfide or metal phase. *Chalcophile* elements would choose the sulfide phase and *siderophile* elements would choose a metal phase given the same choices (a final group is the *atmophile* elements: those elements preferring a gas phase). Re and Os are both *siderophile* elements, though both also have some *chalcophile* tendencies. Their siderophile nature accounts for their low concentrations in the crust and mantle: most of the Earth’s Re and Os are in the core. Os is one of the platinoid, or platinum-group, elements (the second and third transition series members of Group VIII elements) that include Ru, Rh, Pd, and Ir and well as Os and Pt. Like the rare earths, these elements behave coherently, though their valences and ionic radii differ. The usual valence state of Os is +4 at the Earth’s surface; its ionic radius is 0.69. The valence of Re is also +4; its ionic radius is 0.63. However, in the mantle and in magmas, these elements are likely in +1 or 0 valence states. Re is a moderately incompatible element whereas Os is highly compatible one: it partitions into a melt only very sparingly. Hence, the crust has a much lower Os concentration than the mantle (the core, of course, should have a higher concentration than both).

The older convention for Os isotope ratios, established by Hirt et al. (1963) reports the isotope ratio as $^{187}\text{Os}/^{186}\text{Os}$ (normalized for fractionation to $^{192}\text{Os}/^{188}\text{Os}$ of 3.08271). The difficulty is with this normalization is that ^{186}Os is itself radiogenic, being the product of α -decay of ^{190}Pt . ^{190}Pt is sufficiently rare and its half-life sufficiently long (450 billion years) that in most cases the amount of radiogenic ^{186}Os is insignificant. However, measurable amounts of radiogenic ^{186}Os have been observed, as discussed next. This discovery prompted a shift in the convention and now all laboratories report Os isotope analyses as $^{187}\text{Os}/^{188}\text{Os}$. $^{187}\text{Os}/^{186}\text{Os}$ ratios may be converted to $^{187}\text{Os}/^{188}\text{Os}$ ratios by multiplying by 0.12035.

Figure 2.22 illustrates the evolution of Os isotope ratios in the crust and mantle. As expected from the difference in compatibilities of Re and Os, much higher $^{187}\text{Os}/^{188}\text{Os}$ ratios are found in the crust than in the mantle.

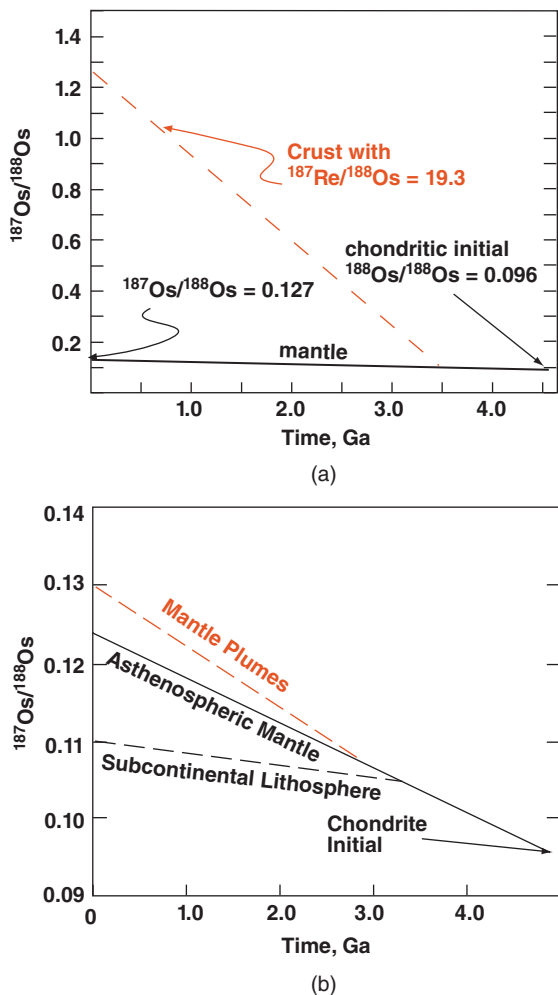


Figure 2.22 (a) Schematic evolution of Os isotope ratios in the mantle and crust. (b) $^{187}\text{Os}/^{188}\text{Os}$ evolution in the mantle. The mantle root of continents (lithospheric mantle) appears to have been particularly strongly depleted in Re by melt extraction. (Source: White (2013). Reproduced with permission of John Wiley & Sons.)

Interestingly, the Re/Os ratio of the mantle, and therefore presumably the silicate Earth, is nearly chondritic (Allégre and Luck, 1980), but unlike the Sm-Nd and Lu-Hf system, there is no theoretical expectation that it should be. This is a bit surprising if most of Re and Os have been extracted to the core. If the core and mantle are in equilibrium, then mantle concentrations will be determined by metal-silicate partition coefficients, which are large for both elements. Since the partition coefficients of these two elements are different,

the ratio of the two in the mantle should be quite different from chondritic. The approximately chondritic Re/Os ratio of the mantle is, however, consistent with models in which core formation is complete before the Earth entirely accretes. In these models, the highly siderophile elements, such as Re and Os, are quantitatively extracted by core formation. The inventory of highly siderophile elements in the crust and mantle comes from the last 1% of material to accrete to the Earth, which occurs after core formation. An alternative explanation has been proposed by Snow and Schmidt (1998). They argue that the nearly chondritic Re-Os ratio of the mantle results from mixing of a small fraction of the outer core back into the mantle.

Since the silicate Earth appears to have a near-chondritic $^{187}\text{Os}/^{188}\text{Os}$ ratio, it is useful to define a parameter analogous to ϵ_{Nd} and ϵ_{Hf} that measures the deviation from chondritic. Walker et al. (1989) defined γ_{Os} as:

$$\gamma_{\text{Os}} = \frac{\left(^{187}\text{Os}/^{188}\text{Os} \right)_{\text{sample}} - \left(^{187}\text{Os}/^{188}\text{Os} \right)_{\text{Chon}}}{\left(^{187}\text{Os}/^{188}\text{Os} \right)_{\text{Chon}}} \times 100 \quad (2.52)$$

(The present day chondritic $^{187}\text{Os}/^{188}\text{Os}$ is taken to be 0.1270.) Thus, the gamma parameter is exactly analogous to the epsilon one, but where the latter is deviations in parts per 10,000, the former is percentage deviations.

Since the mantle $^{187}\text{Os}/^{188}\text{Os}$ evolution curve is known, at least to a first approximation, an estimate of age, or model age, analogous to Sm-Nd model ages, can be obtained simply by comparing the measured $^{187}\text{Os}/^{188}\text{Os}$ ratio with the mantle evolution curve. Platinoid metal deposits association with mantle-derived ultramafic rocks would be one example of where such model ages could be obtained. The PGM's (platinum group metals) occur as very fine (down to a μm or so) metal alloys and sulfides. Os occurs principally as osmiridium (OsIr) and laurite ($\text{Ru}[\text{Os},\text{Ir}]_2$). These minerals have Re/Os close to zero. As a result the $^{187}\text{Os}/^{188}\text{Os}$ ratio ceases to change once these minerals form (a model age would still be possible even if a small correction for radiogenic growth of ^{187}Os were necessary).

There has also been considerable interest in the Os isotope composition of seawater.

The $^{187}\text{Os}/^{188}\text{Os}$ ratio of modern seawater is about 1.07. Like that of $^{87}\text{Sr}/^{86}\text{Sr}$, $^{187}\text{Os}/^{188}\text{Os}$ depends on the balance of continental fluxes (e.g., rivers, with $^{187}\text{Os}/^{188}\text{Os} \sim 1.4$) and oceanic crustal fluxes (e.g., hydrothermal activity, with $^{187}\text{Os}/^{188}\text{Os} \sim 0.13$). In addition, however, cosmic fluxes ($^{187}\text{Os}/^{188}\text{Os} \sim 0.13$), which include both cosmic dust, which continually settles through the atmosphere into the oceans, and large meteorite impacts, may be significant for Os. Variations in the proportions of these fluxes have resulted in systematic changes in the $^{187}\text{Os}/^{188}\text{Os}$ ratio through time. We'll return to this topic and discuss these changes in Chapter 7.

2.7.2 Re-Os geochronology

Because of the differences in compatibility, Re/Os variations are huge, at least by comparison to the other systems we have considered. The mantle has a Re/Os ratio on the order of 0.1 whereas the crustal materials can have Re/Os ratios of 100 or even more. The $^{187}\text{Os}/^{188}\text{Os}$ ratio of the mantle is about 0.128 whereas the crustal ratio is thought to be between 1.1 and 1.3. Despite these large variations, strictly geochronological applications of Re-Os are limited because of the very low concentrations of Os in most minerals. Yet in specialized circumstances, such as iron meteorites, a variety of ore deposits, hydrocarbons, and for some ultramafic rocks such as komatiites (komatiites are very MgO-rich lavas that occur almost exclusively in the Archean, i.e., before 2.5 Ga), Re-Os geochronology has proved quite valuable. Figure 2.23 is an example of an isochron obtained on a komatiite from Monro Township in Ontario. Re is strongly concentrated in some sulfides and arsenides, making the system ideal for dating a variety of ore deposits, including sulfides and gold deposits (e.g., Arne et al., 2001). Let's consider a few examples.

2.7.2.1 Re-Os dating of diamonds

One novel application of the Re-Os system is dating diamonds by dating sulfide inclusions within them. Since Re and Os are somewhat chalcophile, they can be concentrated in mantle sulfide minerals such as pyrrhotite (FeS), chalcophyrite (CuFeS_2), and

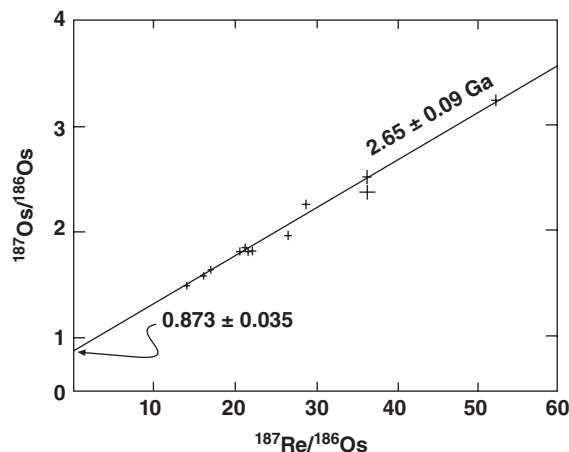


Figure 2.23 Re-Os isochron for a komatiite from Monro Township. (Notice this uses the older convention of $^{187}\text{Os}/^{186}\text{Os}$.) (Source: Adapted from Walker et al. (1988). Reproduced with permission of Elsevier.)

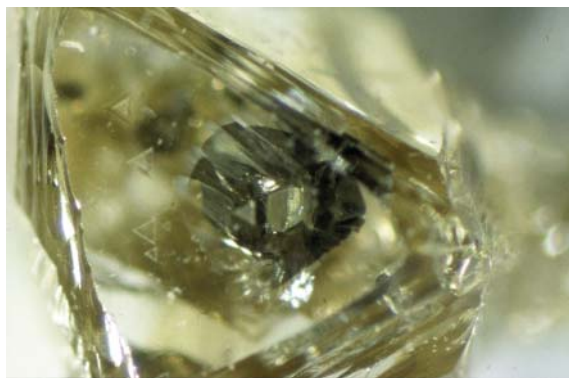


Figure 2.24 A sulfide inclusion in diamond. Fractures result because the sulfide expands more than the diamond as it is decompressed during ascent in the kimberlite eruption. Carnegie Institution of Washington. (Source: Photo J. W. Harris. Reproduced with permission.)

pentlandite ($(\text{Fe},\text{Ni})_9\text{S}_8$). These minerals are sometimes found as small inclusions in diamond (Figure 2.24). Encapsulated in diamond, individual inclusions become closed systems and accumulate ^{187}Os in proportion to the amount of ^{187}Re they contain. Figure 2.25 shows a 2.9 Ga Re-Os isochron derived from inclusions in diamonds from the Kimberley mine in South Africa. Studies such as these have shown that diamond formation in the

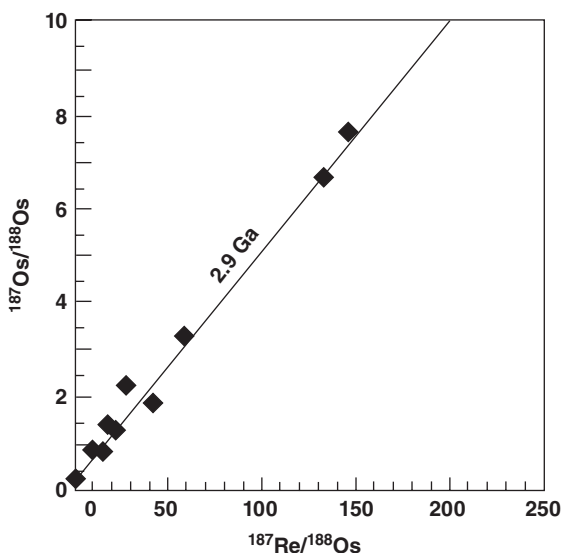


Figure 2.25 2.9 Ga Re-Os isochron from high-Os sulfide inclusions in diamonds from the Kimberley mine, South Africa. (Source: Adapted from Richardson et al., 2001.)

mantle occurs in discrete events, most likely related to subduction (Shirey et al., 2004).

2.7.2.2 Re-Os dating of hydrocarbons

There is, perhaps, no geologic material that is as essential to modern society as petroleum. Petroleum, however, consists almost exclusively of hydrocarbons, that is, compounds of C and H, making its formation a challenge to date. Economic petroleum deposits can form if a series of conditions are met: an environment in which relatively high concentrations of organic matter are preserved in sediment as kerogen during deposition of the *source rock*; subsequent burial and conversion of the kerogen to hydrocarbons through gentle heating, and migration and concentration of the petroleum thus produced in a sufficiently porous *reservoir rock*. Through a variety of methods (some of which involve isotopic analysis), it is often possible to identify the source rock, and standard correlation techniques can determine the age of source rock deposition. The age of other steps in the process, particularly the timing of generation and migration, have been much harder to determine. Researchers have recently had some success in dating hydrocarbon migration using Re-Os.

Perhaps surprisingly, noble metals, and Re and Os in particular, can be present in *relatively* high concentrations in petroleum. Work by Selby et al. (2007) found that Re and Os are primarily present in *asphaltene* fraction of petroleum. Asphaltenes are heavy (molecular masses around 750 u) polycyclic aromatic hydrocarbons. Although detailed studies have not been done, it seems likely that Re and Os are bound in porphyrins in the asphaltene fraction. Porphyrins are rings of pyrrole and pyrrolidine groups (five-sided hydrocarbon rings containing N or NH) that can complex a metal ion in the center of the ring. Such organometallic complexes play vital biological roles. In the chlorophyll porphyrin, essential for harvesting photic energy in plants, Mg occupies this site; in the porphyrin structure that is part of the hemoglobin protein, essential for oxygen transport in blood, Fe occupies this site. Porphyrins in hydrocarbons can have high concentrations (up to a ppm or so) of transition metals such as Ni, V, and Mo. Re concentrations in petroleum can be as high as 50 ppb, and it is more strongly concentrated than Os, whose concentration reaches only 300 ppt. Consequently, $^{187}\text{Rb}/^{188}\text{Os}$ ratios can exceed 1000, and that in turn results in high $^{187}\text{Os}/^{188}\text{Os}$ ratios.

Selby and Creaser (2005) used Re-Os to “date” petroleum of the Western Canada Sedimentary Basin (WCSB). As may be seen in Figure 2.26, *apparent* isochrons yield ages of 111–121 Ma, depending on which samples are included. We say “apparent” isochrons because the mean square weighted deviation (MSWD) is greater than 1, indicating that not all deviations from regression can be accounted for by analytical error. In other words, there is real *geologic* variation from the isochron model. Selby and Creaser (2005) argue that, given the regional scale involved, this is more likely due to incomplete homogenization of the initial isotope ratio than to subsequent disturbances of Re/Os ratios. Precisely what event is being dated here is, however, somewhat unclear. Hydrocarbons in the WCSB are thought to have been derived from source rocks on the western side of the basin and then migrated east. It seems reasonable that hydrocarbon generation and migration could homogenize $^{187}\text{Os}/^{188}\text{Os}$ ratios, although perhaps imperfectly, but it is unclear what

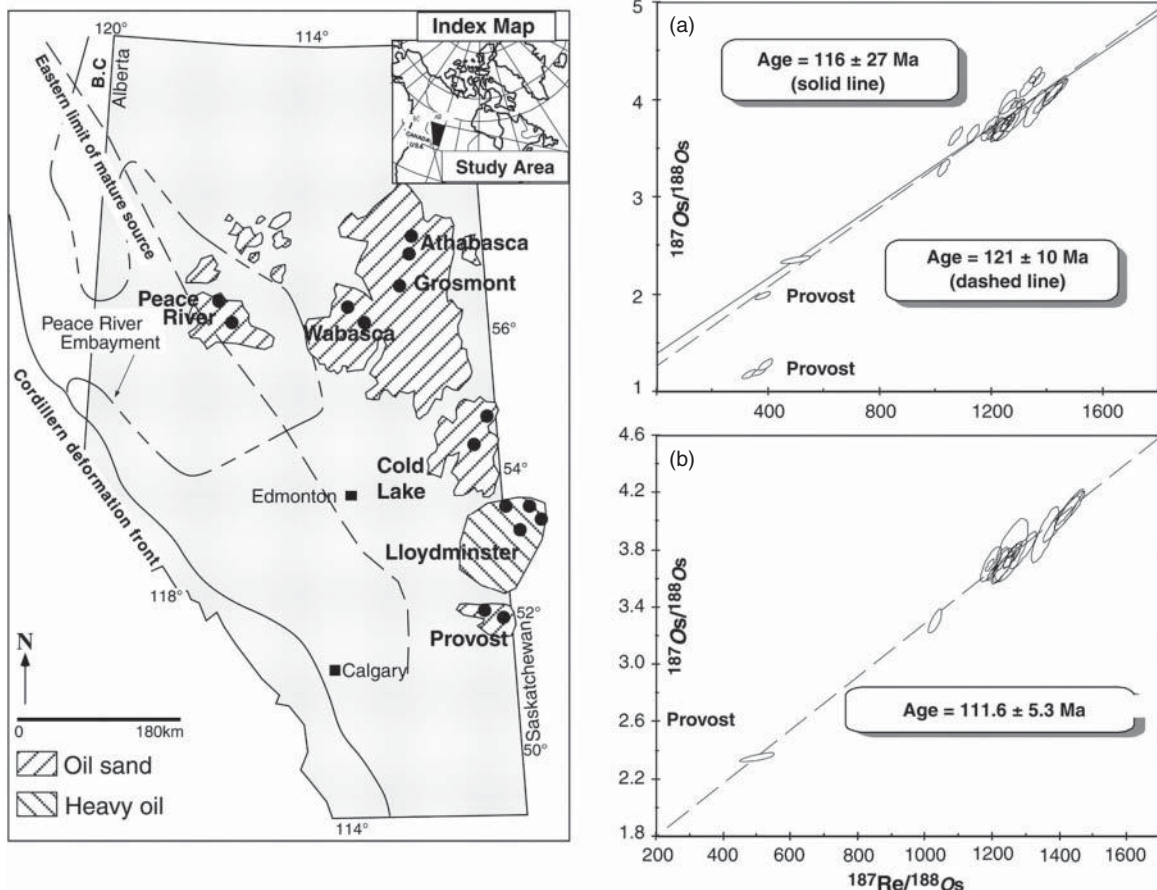


Figure 2.26 (a) Re-Os isochron diagram for 24 samples of oil from the WCSB. The slope when all data are included corresponds to an age of 116 ± 27 Ma. A slightly older but more precise age is obtained when the Provost data is excluded. (b) Including just those samples whose calculated $^{187}\text{Os}/^{188}\text{Os}$ at 110 Ma is 1.4 to 1.5 yields a yet more precise age of 111.6 ± 5.3 Ma. (c) Location map for samples. (Source: Selby and Creaser (2005). Reproduced with permission of AAAS.)

mechanism produced the high $^{187}\text{Re}/^{188}\text{Os}$ ratios observed. Selby and Creaser (2005) noted the high initial $^{187}\text{Os}/^{188}\text{Os}$ compared to $^{187}\text{Os}/^{188}\text{Os}$ in Mesozoic seawater suggests that the source rocks are of Paleozoic age.

2.7.3 The $^{190}\text{Pt}-^{186}\text{Os}$ decay

As noted earlier, ^{186}Os is the decay product of ^{190}Pt . Significant amounts of radiogenic ^{186}Os were first observed by Walker et al. (1991) in copper ores from Sudbury, Ontario. The chondritic $^{186}\text{Os}/^{188}\text{Os}$ ratio is 0.119828 ± 6 ; the value in most terrestrial materials is indistinguishable from this value. In Sudbury sulfide copper ore, however, Walker et al. (1991) measured a $^{186}\text{Os}/^{188}\text{Os}$ ratio of

greater than 0.3. This is a result of the strongly chalcophile nature of Pt, and its consequent concentration in sulfides; Os by contrast, is only weakly chalcophile. More recently, Brandon et al. (1998) have reported measurable variations in the $^{186}\text{Os}/^{188}\text{Os}$ ratio in mantle materials. They found that most mantle materials have $^{186}\text{Os}/^{188}\text{Os}$ ratios indistinguishable from the chondritic value, but samples of komatiite (a rare ultramafic lava type) and a xenolith from Kilbourne Hole, Colorado had ratios as high as 0.119842. Excess ^{186}Os has also been found in some Hawaiian basalts, prompting the suggestion that the Hawaiian plume might contain a small core-derived component (Brandon et al., 1998).

NOTES

1. We'll discuss the small variations that occur in this ratio in the next chapter.
2. Note that this equation implies that diffusional loss will be inversely related to crystal size: larger crystals will lose less.
3. The *Solver*, an add-in tool available for Microsoft *Excel*TM can be used to solve problems such as this. Programs such as *Mathematica*TM and *MatLab*TM also have tools for indirect solution built-in.
4. This is the newly determined value (Mark et al., 2011). The older, more widely accepted value is 295.5.
5. The solid-liquid partition (or distribution) coefficient is a useful parameter in igneous trace element geochemistry. It is defined simply as the equilibrium ratio of the concentration of the element in the solid phase (e.g., a mineral such as plagioclase) to the concentration in the magma. The partition coefficient provides a means of quantifying the term "incompatibility": the lower the partition coefficient, the higher the incompatibility.
6. A reasonable compositional model for the Earth is that of chondritic meteorites, which we consider representative of the concentrations of non-gaseous elements in the solar system. However, the Earth is demonstrably depleted in the more volatile of the non-gaseous elements, so that this model of the Earth is valid only for the more refractory elements. The alkalis, including Rb are among the volatile elements, for which this model is not valid.

7. Mafic rocks are those rich in magnesium and iron (the term *mafic* comes from "MAgnesium and Ferric or Ferrous (*fer* being the Latin root meaning iron). Ultramafic rocks are simply very rich in magnesium and iron. Basalt, the composition typical of many lavas, is mafic. The Earth's mantle is composed of peridotite, an ultramafic rock.
8. Here we define a refractory element as one that condenses from a gas phase at high temperature or forms compounds (usually oxides) that condense at high temperature.
9. The isotope ratios of Sr, Nd, Hf, and Os are corrected for mass fractionation occurring during analysis by "normalizing" the ratio of interest to an assumed "true" ratio of two non-radiogenic isotopes of the element of interest, for example, Sr isotope ratios are always corrected to $^{86}\text{Sr}/^{88}\text{Sr} = 0.11940$. Unfortunately, two normalization schemes evolved for Nd. The "Cal Tech" normalization is to $^{146}\text{Nd}/^{142}\text{Nd} = 0.636151$. Using this scheme, the present-day $^{143}\text{Nd}/^{144}\text{Nd}$ chondritic value is 0.511847. This normalization is now uncommon (in part due to the demonstration of radiogenic ^{142}Nd), but there is still considerable data in the literature based on it. The most common normalization is to $^{146}\text{Nd}/^{144}\text{Nd} = 0.7219$. The value of $\varepsilon_{\text{Nd}}^{144}$ for a given rock should be the same, however, regardless of normalization. We'll discuss the issue of mass fractionation in a subsequent chapter.

REFERENCES

- Albarède, F., Simonetti, A., Vervoort, J. D., Blichert-Toft, J. and Abouchami, W. 1998. A Hf-Nd isotopic correlation in ferromanganese nodules. *Geophysical Research Letters*, 25: 3895–3898, doi: 10.1029/1998gl900008.
- Allégre, C. J., and Luck, J. M. 1980. Osmium isotopes as petrogenic and geologic tracers, *Earth and Planetary Science Letters*, 48: 148–154.
- Amelin, Y. 2005. Meteorite phosphates show constant ^{176}Lu decay rate since 4557 million years ago, *Science*, 310: 839–841.
- Arne, D. C., Bierlein, F. P., Morgan, J. W., and Stein, H. J. 2001. Re-Os dating of sulfides associated with gold mineralization in central Victoria, Australia, *Economic Geology*, 6: 1455–1459.
- Bau, M. and Koschinsky, A. 2006. Hafnium and neodymium isotopes in seawater and in ferromanganese crusts: The "element perspective." *Earth and Planetary Science Letters*, 241: 952–961, doi:10.1016/j.epsl.2005.09.067.
- Bizzarro, M., Baker, J. A., Haack, H., Ulfbeck, D. and Rosing, M. 2003. Early history of Earth's crust-mantle system inferred from hafnium isotopes in chondrites. *Nature*, 421: 931–933.
- Bizzarro, M., Connelly, J. N., Thrane, K. and Borg, L. E. 2012. Excess hafnium-176 in meteorites and the early Earth zircon record. *Geochemistry, Geophysics, Geosystems*, 13: Q03002, doi: 10.1029/2011gc004003.
- Blichert-Toft, J. and Albarède, F. 1997. The Lu-Hf isotope geochemistry of chondrites and the evolution of the mantle-crust system. *Earth and Planetary Science Letters*, 148: 243–258, doi 10.1016/S0012-821X(97)00040-X.
- Boltwood, B. B. 1907. Ultimate disintegration products of the radioactive elements; Part II, Disintegration products of uranium. *American Journal of Science*, Series 4, 23: 78–88, doi:10.2475/ajs.s4-23.134.78.

- Bouvier, A., Vervoort, J. D. and Patchett, P. J. 2008. The Lu-Hf and Sm-Nd isotopic composition of CHUR; constraints from unequilibrated chondrites and implications for the bulk composition of terrestrial planets. *Earth and Planetary Science Letters*, 273: 48–57.
- Boyett, M. and Carlson, R. L. 2005. ^{142}Nd evidence for early (>4.3 Ga) global differentiation of the silicate Earth, *Science*, 309: 576–581.
- Boyett, M. and Carlson, R. L. 2006. A new geochemical model for the Earth's mantle inferred from ^{146}Sm - ^{142}Nd systematics, *Earth and Planetary Science Letters*, 250: 254–268.
- Boyett, M., Blichert-Toft, J., Rosing, M., Storey, M., Telouk, P. and Albarede, F. 2003. ^{142}Nd evidence for early Earth differentiation, *Earth and Planetary Science Letters*, 214: 427–442.
- Brandon, A. D., Walker, R. J., Morgan, J. W., Norman, M. D. and Prichard, H. M. 1998. Coupled ^{186}Os and ^{187}Os evidence for core-mantle interaction, *Science*, 280: 1570–1573.
- Caro, G. and Bourdon, B. 2010. Non-chondritic Sm/Nd ratio in the terrestrial planets: Consequences for the geochemical evolution of the mantle crust system, *Geochimica et Cosmochimica Acta*, 74: 3333–3349.
- Caro, G., Bourdon, B., Halliday, A. N. and Quitte, G. 2008. Super-chondritic Sm/Nd ratios in Mars, the Earth, and the Moon. *Nature*, 452: 336–339, doi: 10.1038/nature06760.
- Cheng, H., Zhang, C., Vervoort, J. D., Li, X., Li, Q., Zheng, S. and Cao, D. 2011. Geochronology of the transition of eclogite to amphibolite facies metamorphism in the North Qinling orogen of central China. *Lithos*, 125: 969–983, doi: 10.1016/j.lithos.2011.05.010.
- Crank, J. 1975. *The Mathematics of Diffusion*. Oxford Press, 2nd edn, 414 pp.
- Creaser, R. A., Papanastassiou, D. A. and Wasserburg, G. J. 1991. Negative thermal ion mass spectrometry of osmium, rhenium, and iridium, *Geochimica et Cosmochimica Acta*, 55: 397–401.
- DePaolo, D. and Wasserburg, G. 1976. Inferences about magma sources and mantle structure from variations of $^{143}\text{Nd}/^{144}\text{Nd}$. *Geophysical Research Letters*, 3: 743–746, doi: 10.1029/GL003i005p00249.
- Dodson, M. H. 1973. Closure temperature in cooling geochronological and petrological systems, *Contributions to Mineralogy and Petrology*, 40: 259–274.
- Harrison, T. M. and McDougall, I. 1980. Investigations of an intrusive contact, northwest Nelson, New Zealand-II. Diffusion of radiogenic and excess ^{40}Ar in hornblende revealed by $^{40}\text{Ar}^{39}\text{Ar}$ age spectrum analysis. *Geochimica et Cosmochimica Acta*, 44: 2005–2020, doi: 10.1016/0016-7037(80)90199-4.
- Harrison, T. M. and McDougall, I. 1981. Excess ^{40}Ar in metamorphic rocks from Broken Hill, New South Wales: implications for $^{40}\text{Ar}/^{39}\text{Ar}$ age spectra and the thermal history of the region. *Earth and Planetary Science Letters*, 55: 123–149, doi: 10.1016/0012-821X(81)90092-3.
- Harrison, T. M., Duncan, I. and McDougall, I. 1985. Diffusion of ^{40}Ar in biotite: temperature, pressure and compositional effects, *Geochimica et Cosmochimica Acta*, 49: 2461–2468.
- Heizler, M. T. and Harrison, T. M. 1988. Multiple trapped argon isotope components revealed by $^{40}\text{Ar}^{39}\text{Ar}$ isochron analysis. *Geochimica et Cosmochimica Acta*, 52: 1295–1303, doi: 10.1016/0016-7037(88)90283-9.
- Hirt, B., Herr, W. and Hoffmester, W. 1963. Age determinations by the rhenium-osmium method. In: *Radioactive Dating*, pp. 35–44. Vienna: Internation. Atom Energy Agency.
- Jacobsen, S. B. and Wasserburg, G. J. 1984. Sm-Nd isotopic evolution of chondrites and achondrites, II. *Earth and Planetary Science Letters*, 67: 137–150, doi: 10.1016/0012-821X(84)90109-2.
- Krabbenhöft, A., Eisenhauer, A., Böhm, F., Vollstaedt, H., Fietzke, J., Liebetrau, V., andet al. 2010. Constraining the marine strontium budget with natural strontium isotope fractionations ($^{87}\text{Sr}/^{86}\text{Sr}^*$, $\delta^{88}/^{86}\text{Sr}$) of carbonates, hydrothermal solutions and river waters. *Geochimica et Cosmochimica Acta*, 74: 4097–4109, doi: 10.1016/j.gca.2010.04.009.
- Mark, D. F., Stuart, F. M. and de Podesta, M. 2011. New high-precision measurements of the isotopic composition of atmospheric argon. *Geochimica et Cosmochimica Acta*, 75: 7494–7501, doi: 10.1016/j.gca.2011.09.042.
- Mattinson, J. M. 2010. Analysis of the relative decay constants of ^{235}U and ^{238}U by multi-step CA-TIMS measurements of closed-system natural zircon samples. *Chemical Geology*, 275: 186–198, doi: 10.1016/j.chemgeo.2010.05.007.
- McArthur, J. M., Howarth, R. J. and Bailey, T. R. 2001. Strontium isotope stratigraphy: LOWESS Version 3: Best fit to the marine Sr-isotope curve for 0–509 Ma and accompanying look-table for deriving numerical age. *The Journal of Geology*, 109: 155–170.
- McDougall, I. and Harrison, T. M. 1999. *Geochronology and Thermochronology by the $^{40}\text{Ar}/^{39}\text{Ar}$ Method*. 2nd edn. New York: Oxford University Press, 269 p.
- Merrihue, C. and Turner, G. 1966. Potassium-argon dating by activation with fast neutrons. *Journal of Geophysical Research*, 71: 2852–2857, doi: 10.1029/JZ071i011p02852.
- Mulcahy, S. R., King, R. L. and Vervoort, J. D. 2009. Lawsonite Lu-Hf geochronology: A new geochronometer for subduction zone processes. *Geology*, 37: 987–990, doi: 10.1130/g30292a.1.
- Nebel, O., Scherer, E. E. and Mezger, K. 2011. Evaluation of the ^{87}Rb decay constant by age comparison against the U-Pb system. *Earth and Planetary Science Letters*, 301: 1–8, doi: 10.1016/j.epsl.2010.11.004.
- Nesheim, T. O., Vervoort, J. D., McClelland, W. C., Gilotti, J. A. and Lang, H. M. 2012. Mesoproterozoic syntectonic garnet within Belt Supergroup metamorphic tectonites: Evidence of Grenville-age metamorphism and deformation along northwest Laurentia. *Lithos*, 134–135: 91–107, doi: 10.1016/j.lithos.2011.12.008.

- Nyquist, L. E., Bogard, D. D., Wiesmann, H., Bansal, B. M., Shih, C.-Y. and Morris, R. M. 1990. Age of a eucrite claste from the Bholghati howardite. *Geochimica et Cosmochimica Acta*, 54: 2195–2206.
- O’Neil, J., Carlson, R. L., Francis D. and Stevenson, R. K. 2008. Neodymium-142 evidence for Hadean mafic crust, *Science*, 321: 1828–1831.
- Patchett, P. J., Vervoort, J. D., Söderlund, U. and Salters, V. J. M. 2004. Lu-Hf and Sm-Nd isotopic systematics in chondrites and their constraints on the Lu-Hf properties of the Earth. *Earth and Planetary Science Letters*, 222: 29–41, doi: 10.1016/j.epsl.2004.02.030.
- Renne, P. R., Mundil, R., Balco, G., Min, K. and Ludwig, K. R. 2010. Joint determination of ^{40}K decay constants and $^{40}\text{Ar}^*/^{40}\text{K}$ for the Fish Canyon sanidine standard, and improved accuracy for $^{40}\text{Ar}/^{39}\text{Ar}$ geochronology, *Geochimica et Cosmochimica Acta*, 74: 5349–5367, 10.1016/j.gca.2010.06.017.
- Richardson, S. H., Shirey, S. B., Harris, J. W. and Carlson, R. L. 2001. Archean subduction recorded by Re-Os isotopes in eclogitic sulfide inclusions in Kimberley diamonds, *Earth and Planetary Science Letters*, 191: 257–266.
- Rotenberg, E., Davis, D. W. and Amelin, Y. 2005. Determination of the ^{87}Rb decay constant by ^{87}Sr accumulation, *Geochimica et Cosmochimica Acta*, 69 supplement: A326.
- Scherer, E., Munker, C. and Mezger, K. 2001. Calibration of the Lutetium-Hafnium Clock, *Science*, 293: 683–686.
- Selby, D. and Creaser, R. A. 2005. Direct radiometric dating of hydrocarbon deposits using rhenium-osmium isotopes. *Science*, 308: 1293–1295, doi: 10.1126/science.1111081.
- Selby, D., Creaser, R. A. and Fowler, M. G. 2007. Re-Os elemental and isotopic systematics in crude oils. *Geochimica et Cosmochimica Acta*, 71: 378–386, doi:10.1016/j.gca.2006.09.005.
- Shirey, S. B., Richardson, S. H. and Harris, J. W. 2004. Integrated models of diamond formation and craton evolution, *Lithos*, 77: 923–944.
- Snow, J. E., and Schmidt, G. 1998. Constraints on Earth accretion deduced from noble metals in the oceanic mantle, *Nature*, 391: 166–169.
- Söderlund, U., Patchett, P. J., Vervoort, J. D. and Isachsen, C. E. 2004. The ^{176}Lu decay constant determined by Lu–Hf and U–Pb isotope systematics of Precambrian mafic intrusions. *Earth and Planetary Science Letters*, 219: 311–324.
- Tatsumoto, M., Unruh, D. M. and Patchett, P. 1981. U-Pb and Lu-Hf systematics of Antarctic meteorites, *Mem. Nat. Inst. Polar. Res. Tokyo, Spec. Issue*, 20: 237–249.
- Tetley, N. W. 1978. *Geochronology by the $^{40}\text{Ar}/^{39}\text{Ar}$ Method Using the HIFAR Reactor*. PhD dissertation, Australian National University, Canberra.
- Vervoort, J. D. and Blichert-Toft, J. 1999. Evolution of the depleted mantle; Hf isotope evidence from juvenile rocks through time. *Geochimica et Cosmochimica Acta*, 63: 533–556.
- Vervoort, J. D., Plank, T. and Prytulak, J. 2011. The Hf–Nd isotopic composition of marine sediments. *Geochimica et Cosmochimica Acta*, 75: 5903–5926, doi:10.1016/j.gca.2011.07.046.
- Walker, R. J., Morgan, J. W., Naldrett, A. J., Li, C. and Fassett, J. D. 1991. Re-Os isotope systematics of Ni-Cu sulfide ores, Sudbury igneous complex, evidence for a major crustal component. *Earth and Planetary Science Letters*, 105: 416–429.
- Walker, R. J., Carlson, R. W., Shirey, S. B. and Boyd, F. R. 1989. Os, Sr, Nd, and Pb isotope systematics of southern African peridotite xenoliths: implications for the chemical evolution of the subcontinental mantle. *Geochimica et Cosmochimica Acta*, 53: 1583–1595.
- Walker, R. J., Shirey, S. B. and Stecher, O. 1988. Comparative Re-Os, Sm-Nd and Rb-Sr isotope and trace element systematics for Archean komatiite flows from Munro Township, Abitibi Belt, Ontario. *Earth and Planetary Science Letters* 87: 1–12.
- Wendt, I. and Carl, C. 1991. The statistical distribution of the mean squared weighted deviation. *Chemical Geology: Isotope Geoscience Section*, 86: 275–285, doi: 10.1016/0168–9622(91)90010-T.
- White, W. M., Patchett, P. J. and Ben Othman, D. 1986. Hf isotope ratios of marine sediments and Mn nodules: evidence for a mantle source of Hf in seawater. *Earth and Planetary Science Letters*, 79: 46–54,
- York, D. 1969. Least squares fitting of a straight line with correlated errors, *Earth and Planetary Science Letters*, 5: 320–324.

SUGGESTIONS FOR FURTHER READING

- Albarède, F. 2003. The thermal history of leaky chronometers above their closure temperature, *Geophysical Research Letters*, 30(1): 1015, doi: 10.1029/2002GL016484.
- Brooks, C., Hart, S. R. and Wendt, I. 1972. Realistic use of two-error regression treatments as applied to rubidium-strontium data. *Reviews of Geophysics*, 10: 551–577, doi: 10.1029/RG010i002p00551.
- DePaolo, D. J. 1988. *Neodymium Isotope Geochemistry, an Introduction*, Berlin: Springer-Verlag.
- Dickin, A. 1995. *Radiogenic Isotope Geochemistry*. Cambridge: Cambridge University Press.
- Duchene, S. 1997. The Lu-Hf dating of garnets and the ages of the Alpine high-pressure metamorphism, *Nature*, 387: 586–589.
- Ehlers, K. E. and Powell, R. 1994. An empirical modification of Dodson’s equation for closure temperature in binary systems, *Geochimica et Cosmochimica Acta*, 58: 241–248.

- Onstott, T. C. and Peacock, M. W. 1987. Argon retentivity of hornblendes: a field experiment in a slowly cooled metamorphic terrane, *Geochimica et Cosmochimica Acta*, 51: 2891–2904.
- Patchett, P. J. 1983. Importance of the Lu-Hf isotopic system in studies of planetary chronology and chemical evolution, *Geochimica et Cosmochimica Acta*, 47: 81–91.
- Thrane, K., Connelly, J. N., Bizzarro, M., Meyer, B. S. and The, L.-S. 2010. Origin of Excess ^{176}Hf in Meteorites. *The Astrophysical Journal*, 717: 861–867, doi: 10.1088/0004-637X/717/2/861.
- Vervoort, J. D., Patchett, P. J., Gehrels, G. E. and Nutmann, A. P. 1996. Constraints on early differentiation from hafnium and neodymium isotopes, *Nature*, 379: 624–627.

PROBLEMS

1. Use Dodson's equation (Eqn. 2.38) to calculate the closure temperatures of biotite for the cases of a slowly cooled intrusion discussed in Section 2.3.1, namely at $10^\circ/\text{Ma}$ and $100^\circ/\text{Ma}$. Use the data given in Figure 2.1, which correspond to $E_A = 196.8 \text{ kJ/mol}$ and $D_0 = -0.00077 \text{ m}^2/\text{sec}$. Assume $a = 140 \mu\text{m}$ and $A = 27$. The value of R is 8.314 J/K-mol . If we were to do K-Ar dating on these biotites long after they cooled (say 100 Ma later), how much different would the two ages be assuming the intrusion cooled at these rates from an initial temperate of 600°C ? (*Hint, you can easily do this in Excel, either using the solver, or iterating manually following an initial guess of the closure temperature – you can base that on the discussion in the text. Be careful to use consistent units*).
2. You measure the following K_2O and ^{40}Ar on minerals from a small pluton. Calculate the age for each. What do you think the ages mean? Use the following branching ratio is 0.1157 , $\lambda_e = 0.58755 \times 10^{-10} \text{ yr}^{-1}$, $\lambda_{\text{total}} = 5.5492 \times 10^{-10} \text{ yr}^{-1}$. (These are newly recommended values.)
 $^{40}\text{K}/\text{K} = 0.0001167$, atomic weight of K is 39.03983 .

	K_2O (wt. %)	Radiogenic ^{40}Ar , mole/g
biotite	8.45	6.016×10^{-10}
hornblende	0.6078	0.4642×10^{-10}

Are the ages the same? If not, speculate on why not?

3. Use following data to answer this question:
 $\lambda_{\text{Rb}} = 1.42 \times 10^{-11} \text{ y}$; $^{86}\text{Sr}/^{88}\text{Sr} = 0.11940$; $^{84}\text{Sr}/^{88}\text{Sr} = 0.006756$, $^{85}\text{Rb}/^{87}\text{Rb} = 2.59265$, atomic weight of Rb: 85.46776
 Atomic masses of Sr:

^{88}Sr : 87.9056
 ^{87}Sr : 86.9088
 ^{86}Sr : 85.9092
 ^{84}Sr : 83.9134

Calculate the abundances of the isotopes and atomic weight of Sr given that $^{87}\text{Sr}/^{86}\text{Sr} = 0.7045$.

4. The following $^{40}\text{Ar}^*/^{39}\text{Ar}$ ratios were measured in step-heating of lunar Basalt 15555 from Hadley Rile. The flux monitor had an age of $1.062 \times 10^9 \text{ yrs}$ and its $^{40}\text{Ar}^*/^{39}\text{Ar}$ ratio after irradiation was 29.33. The $^{40}\text{K}/^{39}\text{K}$ ratio is 0.000125137. Calculate the age for each step and plot the ages versus percentage of release. From this release spectrum, estimate the age of the sample.

Cumulative % Ar released	$^{40}\text{Ar}^*/^{39}\text{Ar}$
3	58.14
10	61.34
27	72.77
61	80.15
79	83.32
100	79.80

5. The following data were obtained on three minerals from a pegmatite. Calculate the age of the rock using the isochron method (you may use conventional regression for this problem). The data and approach used in Problem 3 will prove useful.

	Rb, ppm	Sr, ppm	$^{87}\text{Sr}/^{86}\text{Sr}$
Muscovite	238.4	1.80	1.4125
Biotite	1080.9	12.8	1.1400
K-feldspar	121.9	75.5	0.7502

6. The following data were measured on phlogopites (P) and phlogopite leaches (LP) from a kimberlite from Rankin Inlet area of the Hudson Bay, Northwest Territories, Canada. What is (1) the age of the rock, (2) the uncertainty on the age, (3) the initial $^{87}\text{Sr}/^{86}\text{Sr}$ ratio, and (4) the uncertainty on the initial ratio? The relative uncertainty on the $^{87}\text{Sr}/^{86}\text{Sr}$ is 0.005% and that of the $^{87}\text{Rb}/^{86}\text{Sr}$ is 1%. (*Hint: this is best accomplished using the Isoplot.xls Excel add-in written by Ken Ludwig and available at <http://bgs.org/isoplot/etc/isoplot.html>.*)

Sample	$^{87}\text{Rb}/^{86}\text{Sr}$	$^{87}\text{Sr}/^{86}\text{Sr}$
P1	46.77	0.848455
P2	40.41	0.828490
P3	34.73	0.810753
P4	33.78	0.807993
P5	0.1829	0.706272
P6	0.1373	0.705616
P7	1.742	0.710498

7. The following were measured on a coarse grained metagabbro from Cana Brava complex in central Brazil. Plot the data on an isochron diagram, calculate the age, errors on the age, and the initial ϵ_{Nd} and the error on the initial. The errors on the $^{147}\text{Sm}/^{144}\text{Nd}$ are all 0.0001 (2 sigma absolute). Two sigma errors on the $^{143}\text{Nd}/^{144}\text{Nd}$ shown below are in the fifth digit.

	$^{147}\text{Sm}/^{144}\text{Nd}$	$^{143}\text{Nd}/^{144}\text{Nd}$
pyroxene	0.1819	0.51234 ± 2
plagioclase	0.0763	0.51183 ± 4
whole rock	0.1678	0.51227 ± 4
plagioclase	0.0605	0.51173 ± 4
biotite	0.1773	0.51232 ± 4

8. The following data apply to whole rocks and separated minerals of the Baltimore Gneiss. Interpret these data by means of suitable isochron diagrams. Determine dates and initial $^{87}\text{Sr}/^{86}\text{Sr}$ ratios and errors on both using simple linear regression. Speculate on the geologic history of these rocks and minerals.

	$^{87}\text{Rb}/^{86}\text{Sr}$	$^{87}\text{Sr}/^{86}\text{Sr}$
Rock 1	2.244	0.7380
Rock 2	3.642	0.7612
Rock 3	6.59	0.7992
biotite	289.7	1.969
K feldspar	5.60	0.8010
plagioclase	0.528	0.7767
Rock 4	0.2313	0.7074
Rock 5	3.628	0.7573
biotite	116.4	1.2146
K feldspar	3.794	0.7633
plagioclase	0.2965	0.7461

9. The following data were obtained on a Egyptian diorite:

	$^{87}\text{Rb}/^{86}\text{Sr}$	$^{87}\text{Sr}/^{86}\text{Sr}$
plagioclase	0.05124	0.705505
amphibole	0.13912	0.706270
biotite	0.95322	0.713847
alkali feldspar	0.58489	0.710418
whole rock	0.33975	0.708154

Assume that the analytical error on the $^{87}\text{Sr}/^{86}\text{Sr}$ ratio was 0.006% and that the analytical error on the $^{87}\text{Rb}/^{86}\text{Sr}$ ratio was 0.1% in each case, and that these errors are uncorrelated. Use the two-error regression method to calculate the age and initial ratio and the errors on both.
(HINT: this is best accomplished using the Isoplot.xls Excel add-in.)

10. A sample of granite has $^{143}\text{Nd}/^{144}\text{Nd}$ and $^{147}\text{Sm}/^{144}\text{Nd}$ of 0.51196 and 0.12990, respectively. The present chondritic $^{143}\text{Nd}/^{144}\text{Nd}$ and $^{147}\text{Sm}/^{144}\text{Nd}$ are 0.512638 and 0.1967, respectively. The decay constant of ^{147}Sm is $6.54 \times 10^{-12} \text{ a}^{-1}$. Calculate the τ_{CHUR} , that is, crustal residence time relative to a chondritic mantle, for this granite.
11. The following data were obtained on sulfide inclusions in diamonds from the Keffiefontein mine in South Africa. Calculate the age of the diamonds assuming all analyzed samples are cogenetic.

	$^{187}\text{Re}/^{188}\text{Os}$	$^{187}\text{Os}/^{188}\text{Os}$
K310	104	2.19
K309	5.24	0.346
K308	116	2.28
K307	6.31	0.411
K305	80.6	1.78

Chapter 3

Decay systems and geochronology II: U and Th

3.1 INTRODUCTION

The U-Th-Pb system is certainly the most powerful tool in the geochronologist's tool chest. While we can use the three decay systems independently, the real power comes in using them in combination, particularly the ^{235}U - ^{207}Pb and ^{238}U - ^{208}Pb systems, as it allows a check of the fidelity of the age calculated and, in some circumstances, to obtain accurate ages despite disturbances to the system that violate the conditions we discussed in Chapter 2. We'll begin by discussing U-Th-Pb dating, which is useful on a wide range of time scales, from hundreds of thousands to billions of years. Indeed, as we will see in this and subsequent chapters, U-Pb dating provides the definitive ages of the Solar System and the oldest rocks on Earth. Without question, it is the "gold standard" of geochronology.

Rather than decaying directly to lead, uranium and thorium decay through a chain of intermediate daughters, some of which have half-lives of tens or hundreds of thousands of years. Measuring the ratios of intermediate radioactive parents and daughters enables an entirely new set of geochronological tools for use on those time-scales. We'll devote the second half of this chapter to uranium decay series geochronology.

3.1.1 Chemistry of U, Th, and Pb

U and Th are, strictly speaking, rare earth elements, although they belong to the actinide

series instead of the lanthanide series. The other rare earths we have met so far, Lu, Nd and Sm, are lanthanides. As in the lanthanide rare earths, an inner electron shell is being filled as atomic number increases in the actinides. Both U and Th generally have a valence of +4, but under oxidizing conditions, such as at the surface of the Earth, U has a valence of +6. In 6-fold coordination, U^{4+} has an ionic radius of 89 pm¹ (100 pico meters = 1 Å); U^{6+} has an ionic radius of 73 pm in 6-fold and 86 pm in 8-fold coordination. Th⁴⁺ has an ionic radius of 94 pm. These radii are not particularly large, but the combination of a somewhat large radius and high charge is not readily accommodated in crystal lattices of most common rock-forming minerals, so both U and Th are highly incompatible elements. Th is relatively immobile under most circumstances. In its reduced form, U^{4+} is insoluble and therefore fairly immobile, but in the U^{6+} form, which is stable under a wide range of conditions at the surface of the Earth, U forms the soluble oxyanion complex, UO_4^{2-} . As a result, U can be quite mobile. U and Th can form their own phases in sedimentary rocks, uraninite and thorite, but they are quite rare. In igneous and metamorphic rocks, U and Th are either dispersed as trace elements in major phases, or concentrated in accessory minerals (when they are present) such as zircon (ZrSiO_4) that concentrates U more than Th, and monazite ($[\text{La}, \text{Ce}, \text{Th}] \text{PO}_4$) that concentrates Th more than U. These elements may be also

concentrated in other accessory phases such as apatite ($\text{Ca}_5(\text{PO}_4)_3(\text{OH})$), xenotime (YPO_4) and titanite (or sphene, CaTiSiO_5). However, zircon is by far and away the most important from a geochronological perspective.

U and Th are refractory elements, and we can therefore expect the Th/U ratio of the Earth to be the same as chondrites or nearly so. There is, however, some debate about the exact terrestrial Th/U ratio, and we can be no more precise than to say it is 4 ± 0.2^2 . This ratio is 3.8 in the CI chondrite Orgueil, but may be low due to mobility of U in hydrous fluid in the CI parent body.

The geochemical behavior of Pb is more complex than that of the elements we have discussed so far and consequently, less well understood. It is a relatively volatile element, so its concentration in the Earth is certainly much lower than in chondrites. It is also a *chalcophile* element. If the core contains, as some believe, substantial amounts of S, it is possible that a significant fraction of the Earth's Pb is in the core (it is, however, difficult to distinguish loss of Pb from the Earth due to its volatility from loss of Pb from the silicate portion of the Earth due to extraction into the core). Pb can exist in two valence states, Pb^{2+} and Pb^{4+} . Pb^{2+} is by far the most common state; the Pb^{4+} state is rare and restricted to highly alkaline or oxidizing solutions. The ionic radius of Pb^{2+} is 119 pm in 6-fold coordination and 129 pm in 8-fold coordination. As a result of its large ionic size, Pb is an incompatible element, though not as incompatible as U and Th (incompatibility seems to be comparable to the light rare earths). The most common Pb mineral is galena (PbS). In silicates, Pb substitutes readily for K (ionic radius 133 pm) in potassium feldspar, but less so in other K minerals such as biotite. Most naturally occurring compounds of Pb are highly insoluble under most conditions. As a result, Pb is usually reasonably immobile. However, under conditions of low pH and high temperature, Pb forms stable and somewhat soluble chloride and sulfide complexes, so that Pb can sometimes be readily transported in hydrothermal solutions.

Although Pb is clearly less incompatible than U and Th, these three elements have been extracted from the mantle and concentrated in the crust to *approximately* the same degree. The reason for this is not yet completely

understood, and we will discuss this problem in more detail in Chapter 6.

3.1.2 The $^{238}\text{U}/^{235}\text{U}$ ratio and uranium decay constants

Until the last few years, it had been assumed that the $^{238}\text{U}/^{235}\text{U}$ ratio was constant. In this case, the $^{207}\text{Pb}^*/^{206}\text{Pb}^*$ ratio is a function only of time (and the decay constants). The conventionally accepted value of this ratio was 138.88 (Jaffey et al., 1971; Steiger and Jäger, 1977). However, as precision in isotopic measurements has improved, it became apparent (1) that this value varied somewhat, and (2) that mean value in terrestrial materials is actually a little lower (e.g., Stirling et al., 2007; Weyer et al., 2008; Amelin et al., 2010; Martinson, 2010; Hiess et al., 2012). Stirling et al. (2007) found a range of about 4 per mil in this ratio in natural terrestrial materials, while Weyer et al. (2008) found a range of about 1.4 per mil. Hiess et al. (2012) demonstrated a variation of 5 per mil in uranium-bearing minerals commonly analyzed in geochronological work (zircon, apatite, monazite, xenotime, baddeleyite, titanite), but this range is defined by relatively few "outliers" and almost all zircons fell within a much smaller range of 137.77 to 137.91, a 0.1 per mil variation. These variations result in slight differences in bond strength and diffusivity that result from the mass differences of the two U isotopes. We will postpone discussion of the causes of isotopic variations resulting from chemical effects such as these until Chapter 8, where we will discuss them at length. Somewhat greater variations occur in meteorites as a consequence of very slight chemical and isotopic heterogeneity in the solar nebula and the decay of the short-lived, and now extinct, radionuclide ^{247}Cm (more on that in Chapter 5).

Amelin estimated the mean terrestrial $^{238}\text{U}/^{235}\text{U}$ to be 137.821 ± 0.014 ; Hiess et al. (2012) estimated it to be 137.818 ± 0.045 . There is excellent agreement between these two values, but both differ from the conventional value. Goldmann et al. (2013) have proposed a slightly lower value of 137.79 ± 0.03 based on measurements of meteorites. In this text, we will adopt a value for the $^{238}\text{U}/^{235}\text{U}$ of 137.82 and we will assume the value to be constant. However, you should

Table 3.1 Parameters of the U-Th-Pb system.

Parent	Decay Mode	λ	Half-life	Daughter	Ratio
^{232}Th	α, β	$4.948 \times 10^{-11} \text{y}^{-1}$	$1.4 \times 10^{10} \text{y}$	$^{208}\text{Pb}, 8 \ ^4\text{He}$	$^{208}\text{Pb}/^{204}\text{Pb}, \ ^3\text{He}/^{4}\text{He}$
^{235}U	α, β	$9.8571 \times 10^{-10} \text{y}^{-1*}$	$7.07 \times 10^8 \text{y}$	$^{207}\text{Pb}, 7 \ ^4\text{He}$	$^{207}\text{Pb}/^{204}\text{Pb}, \ ^3\text{He}/^{4}\text{He}$
^{238}U	α, β	$1.55125 \times 10^{-10} \text{y}^{-1}$	$4.47 \times 10^9 \text{y}$	$^{206}\text{Pb}, 6 \ ^4\text{He}$	$^{206}\text{Pb}/^{204}\text{Pb}, \ ^3\text{He}/^{4}\text{He}$

*Value recommended by Mattinson (2010). “Official” Steiger and Jäger value is $9.8485 \times 10^{-10} \text{y}^{-1}$

be aware that, at least as of this writing, a value of 137.88 remains the “official” value (the one recommended by the IGC Subcommission on Geochronology) and that almost all the ages in the literature are based on that value. Furthermore, the highest precision geochronology may require in the analysis of the $^{238}\text{U}/^{235}\text{U}$ as well as Pb isotope ratios. Finally, this value of 137.82 is the *present-day value*; it changes through time as a result of the two isotopes decaying at different rates. If we need to know the ratio at some other time (e.g., Problem 1), we need to calculate it based on Eqn. 2.4.

As Mattinson (2010) noted, a change in the accepted value of the $^{238}\text{U}/^{235}\text{U}$ ratio will require a re-evaluation of U half-lives, particularly that of ^{235}U , hence further refinement of these values can be expected in the future.

3.2 PB-PB AGES AND ISOCHRONES

Table 6.1 summarizes this decay system. If the “Mad Men” of Madison Avenue were given the task of selling the U-Th-Pb system, they would probably say that you get four dating methods for the price of one. We can calculate three ages using the conventional isochron approach, one for each for the $^{238}\text{U}-^{206}\text{Pb}$, $^{235}\text{U}/^{207}\text{Pb}$, and $^{232}\text{Th}/^{208}\text{Pb}$ systems. This proceeds exactly as for the decay systems we discussed in Chapter 2. However, we can also combine the ^{238}U and ^{235}U decays to calculate an additional age, known as a *Pb-Pb age*. If you bought the Madison Avenue sales pitch, you would probably discover that the conventional isochron approach for the first two systems mentioned was not particularly powerful, at least in comparison to either the Pb-Pb technique or when several approaches are used in combination. The reason for the power is simply that there are three parents decaying to three isotopes of Pb, and in particular, there are two isotopes of U which decay to Pb with very different half-lives. This

is important because chemical processes will generally not change the ratio of the two U isotopes to each other significantly and will not change the ratio of the two Pb daughter isotopes to each other. The point is best illustrated as follows. First we write the decay equation for each of the two U decay systems:

$$^{207}\text{Pb}^* = ^{235}\text{U}(e^{\lambda_{235}t} - 1) \quad (3.1)$$

$$^{206}\text{Pb}^* = ^{238}\text{U}(e^{\lambda_{238}t} - 1) \quad (3.2)$$

where the asterisk designates *radiogenic* ^{206}Pb and ^{207}Pb (we will use the same designation in subsequent equations), and λ_{235} and λ_{238} are the decay constants for ^{235}U and ^{238}U respectively. If we divide 3.1 by 3.2, we have:

$$\frac{^{207}\text{Pb}^*}{^{206}\text{Pb}^*} = \frac{^{235}\text{U}(e^{\lambda_{235}t} - 1)}{^{238}\text{U}(e^{\lambda_{238}t} - 1)} \quad (3.3)$$

Let’s consider this in more detail. Assuming the present day $^{238}\text{U}/^{235}\text{U}$ ratio is indeed constant, Eqn. 3.3 can be written as:

$$\frac{^{207}\text{Pb}^*}{^{206}\text{Pb}^*} = \frac{(e^{\lambda_{235}t} - 1)}{137.82(e^{\lambda_{238}t} - 1)} \quad (3.4)$$

The nice thing about Eqn. 3.4 is that the only variable on the right hand side is time; in other words the $^{207}\text{Pb}^*/^{206}\text{Pb}^*$ is a function only of time.

In practice what this means is that the age is independent of the parent/daughter ratio; that is, we do not need to measure the parent/daughter ratio. We shall see that this property actually allows us to somewhat relax our requirement that the system remain closed. We can also see that although we could write an equation similar to 3.3 using ^{232}Th and ^{208}Pb instead of ^{235}U and ^{207}Pb , there would be little advantage to doing so because Th and U are different elements and could well be lost or gained in different proportions.

The Pb-Pb method, as it is called, can be quite useful when applied independently,

particularly where there is reason to believe that there has been some recent change in the parent/daughter ratio.

The slope on a plot of $^{207}\text{Pb}/^{204}\text{Pb}$ vs. $^{206}\text{Pb}/^{204}\text{Pb}$ is proportional to age since:

$$\frac{\Delta(^{207}\text{Pb}/^{204}\text{Pb})}{\Delta(^{206}\text{Pb}/^{204}\text{Pb})} = \frac{(e^{\lambda_{235}t} - 1)}{137.82(e^{\lambda_{238}t} - 1)} \quad (3.5)$$

Equation 3.5 is very similar to Eqn. 3.4. We would use 3.4 when either the initial Pb is insignificant, or the amount of initial Pb is sufficiently small that we can make a reasonable estimate of its isotopic composition and make a correction for it. We would use 3.5 when initial Pb is present in significant quantities and has an unknown composition. Figure 3.1 shows an example of a Pb-Pb isochron that yielded a reasonably precise age based on Eqn. 3.5. Unlike a conventional isochron, the intercept in the Pb-Pb isochron has no significance, and the initial isotopic composition cannot be determined without some additional information about parent/daughter ratios. As in the isochron approaches we discussed in Chapter 2, the slope is determined by regression.

There are a couple of reasons why we might suspect U/Pb ratios have changed, and hence might prefer the Pb-Pb approach to a conventional U-Pb isochron approach. First, the solubility of U under oxidizing conditions

often leads to mobility (open-system behavior) in the zone of weathering. It has often been found that U-Pb ages are spurious, yet Pb-Pb ages seem correct. This circumstance appears to result from recent U mobility as erosion brings a rock into the weathering zone. A second situation where parent/daughter ratios would have experienced recent change is in magma generation. When melting occurs, the U and Pb isotope ratios in the magma will be identical to those in the source (because the isotopes of an element are chemically identical), but the U/Pb ratio (and Th/Pb) ratio will change, as the chemical behaviors of U and Pb differ. So, conventional dating schemes cannot generally provide useful geochronological information about sources of magmas. However, the Pb-Pb dating method can, at least in principle, provide useful information, because the Pb isotope ratios of a magma are representative of the source and the method does not depend on parent/daughter ratios. Essentially, what we are doing is allowing volcanism to “sample” the source, generally the mantle, but sometimes the lower continental crust. The sample is representative of the isotopic composition of the source, but not representative of the elemental chemistry of the source. The relationship between Pb isotope ratios in mantle-derived magmas has led to the conclusion that heterogeneities in the mantle must have existed for times on the order of 1–2 Ga.

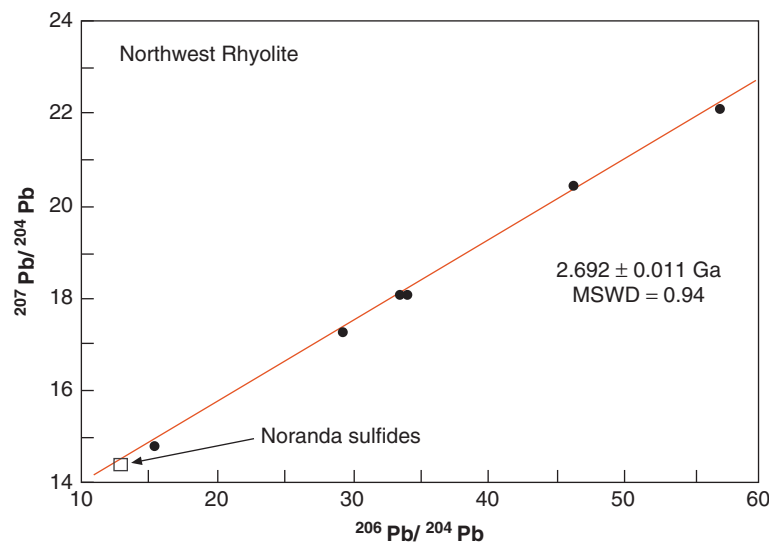


Figure 3.1 A Pb-Pb isochron obtained on volcanic rocks hosting the Noranda (Quebec) Cu-Zn sulfide deposit. Data from Vervoort et al. (1993).

This is an extremely important constraint not only on the chemical evolution of the mantle, but also on its dynamics.

3.2.1 Total U-Pb isochrons

The U-Pb system achieves its greatest power when we use the ^{238}U - ^{206}Pb , ^{235}U - ^{207}Pb , and ^{207}Pb - ^{206}Pb methods in combination. In the ideal case where the system was isotopically homogeneous at time 0 and has remained closed since, the ^{238}U - ^{206}Pb , ^{235}U - ^{207}Pb , and ^{207}Pb - ^{206}Pb ages should agree. In this case, the age obtained is said to be “concordant.” Even when the three ages do not agree, it can be possible to “see through” open system behavior and obtain an age of initial crystallization. In this section, we’ll consider an approach that is useful when the amount of initial Pb, often referred to as “common lead,” is significant. Since ^{204}Pb is non-radiogenic, this is the case where significant amounts of ^{204}Pb are present and ^{206}Pb / ^{204}Pb and ratios are ^{207}Pb / ^{204}Pb relatively low. We’ll consider the case where nearly all the Pb is radiogenic in the subsequent section on zircon geochronology.

Tera and Wasserburg (1972), working with lunar samples, developed a graphical approach to evaluate the degree to which

^{238}U - ^{206}Pb and ^{207}Pb / ^{206}Pb ages agree, that is, are concordant. On a *Tera-Wasserburg diagram*, or as Ludwig (1998) calls it, a *semi-total Pb isochron diagram*, measured ^{207}Pb / ^{204}Pb ratios are plotted against ^{238}U / ^{206}Pb ratios. Ratios are corrected for any contribution from analytical blank, but not for initial, or common, Pb. On such a diagram (Figure 3.2), purely radiogenic Pb will have unique $^{207}\text{Pb}^*/^{206}\text{Pb}^*$ and $^{238}\text{U}/^{206}\text{Pb}^*$ ratios at any given time and hence define the black “concordia” curve in Figure 3.2. If we measure a series of samples with different U/Pb values containing common Pb and if those samples meet the conditions of (1) isotopic homogeneity at time 0 and (2) no disturbance since, they will plot along a straight line that intercepts the “concordia” curve at a point where $^{207}\text{Pb}/^{206}\text{Pb}$ and $^{238}\text{U}/^{206}\text{Pb}$ ages are equal. The intercept of the regression line is the initial $^{207}\text{Pb}/^{206}\text{Pb}$ (because a sample with a $^{238}\text{U}/^{206}\text{Pb}$ ratio of 0 will retain its initial Pb isotopic composition).

The equation for the concordia line can readily be derived from Eqn. 3.1 through 3.4 (see Problem 2) and is:

$$\frac{^{207}\text{Pb}^*}{^{206}\text{Pb}^*} = \frac{(e^{\lambda_{235}t} - 1)}{137.82(^{238}\text{U}/^{206}\text{Pb}^*)} \quad (3.6)$$

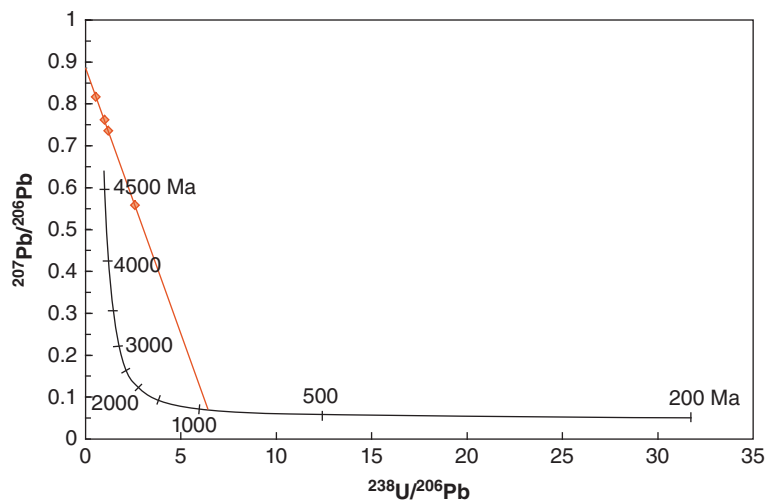


Figure 3.2 The *Tera-Wasserburg*, or *Semi-Total Lead Isochron Diagram*. The black line is the concordia curve where the $^{207}\text{Pb}^*/^{206}\text{Pb}^*$ age equals the $^{238}\text{U}/^{206}\text{Pb}^*$ age, with ticks indicating the ages. A hypothetical data set with an age of 935 Ma and $(^{207}\text{Pb}/^{206}\text{Pb})_I = 0.8857$ is illustrated. The initial $^{207}\text{Pb}/^{206}\text{Pb}$ ratio is given by the y-intercept while the age is given by the intersection of the slope and the concordia curve and by the slope of the line (Eqn. 3.7).

The slope of the line through the data, which in practice would be determined by regression, is:

$$\begin{aligned} b &= \frac{d(207\text{Pb}/206\text{Pb})}{d(238\text{U}/206\text{Pb})} \\ &= \frac{235\text{U}}{238\text{U}} (e^{\lambda_{235}t} - 1) - \left(\frac{207\text{Pb}}{206\text{Pb}}\right)_i (e^{\lambda_{238}t} - 1) \end{aligned} \quad (3.7)$$

(Tera and Wasserburg, 1972). Thus this line is an isochron since its slope depends on t . The goodness of fit of the data to a straight line, of which the MSWD is a measure, depends on the degree to which conditions (1) and (2) here have been met. An analogous and more complete approach involves computing $207\text{Pb}/206\text{Pb}$, $238\text{U}/206\text{Pb}$, and $235\text{U}/207\text{Pb}$ isochrons simultaneously, which Ludwig (1998) calls *total Pb/U isochrons*. It is, however, difficult to represent this graphically, both because it is three-dimensional and because the relationship between $207\text{Pb}/206\text{Pb}$ and $235\text{U}/207\text{Pb}$ is non-linear (however, the $206\text{Pb}/207\text{Pb}$ – $235\text{U}/207\text{Pb}$ relationship is linear). Ludwig (1998) explains that approach in detail.

3.2.2 Th/U ratios

Provided Th/U ratios are constant and known in a set of samples we wish to date, we can calculate ages from $208\text{Pb}/204\text{Pb}$ – $206\text{Pb}/204\text{Pb}$ isochrons just as we can using 207Pb and 206Pb . However, although U and Th are geochemically similar and the Th/U ratio is not likely to vary much, it would not be prudent to assume the ratio is actually constant for geochronological purposes. Furthermore, there is little reason to do so, since we can already compute the age using 207Pb and 206Pb . But it may be useful in some circumstances to turn the problem around and compute the Th/U ratio from the age and the slope of the data on a plot of $208\text{Pb}/204\text{Pb}$ versus $206\text{Pb}/204\text{Pb}$. The basis of this is as follows. We write the usual growth equations for 206Pb and 208Pb ,

$$\begin{aligned} 206\text{Pb}/204\text{Pb} &= (206\text{Pb}/204\text{Pb})_0 + 238\text{U}/204\text{Pb} (e^{\lambda_{238}t} - 1) \end{aligned} \quad (3.8)$$

$$\begin{aligned} 208\text{Pb}/204\text{Pb} &= (208\text{Pb}/204\text{Pb})_0 + 232\text{Th}/204\text{Pb} (e^{\lambda_{232}t} - 1) \end{aligned} \quad (3.9)$$

Subtracting the initial ratio from each side of each equation and dividing 3.9 by 3.8 we have

$$\frac{\Delta(208\text{Pb}/204\text{Pb})}{\Delta(206\text{Pb}/204\text{Pb})} = \frac{232\text{Th}/204\text{Pb} (e^{\lambda_{232}t} - 1)}{238\text{U}/204\text{Pb} (e^{\lambda_{238}t} - 1)} \quad (3.10)$$

$$\text{or } \frac{\Delta(208\text{Pb}/204\text{Pb})}{\Delta(206\text{Pb}/204\text{Pb})} = \frac{\kappa(e^{\lambda_{232}t} - 1)}{(e^{\lambda_{238}t} - 1)} \quad (3.11)$$

where κ is used to designate the $232\text{Th}/238\text{U}$ ratio. Using μ to designate the $238\text{U}/204\text{Pb}$ ratio, the parent-daughter ratio of the Th-Pb system is the product $\mu\kappa$.

Equation 3.11 tells us that the slope of a line on a plot of $208\text{Pb}/204\text{Pb}$ versus $206\text{Pb}/204\text{Pb}$ is proportional to time and κ , provided that κ does not vary. If we can calculate t from the corresponding $207\text{Pb}/204\text{Pb}$ – $206\text{Pb}/204\text{Pb}$ slope, we can solve 3.11 for κ . If, however, κ varies linearly with μ , a straight line will still result on the $208\text{Pb}/204\text{Pb}$ versus $206\text{Pb}/204\text{Pb}$ plot and our estimate of κ will be incorrect.

3.3 ZIRCON DATING

Zircon (ZrSiO_4) is a mineral with a number of properties that make it extremely useful for geochronologists (Figure 3.3). First of all, it is very hard (hardness $7\frac{1}{2}$), which means it is extremely resistant to mechanical weathering. Second, it is extremely resistant to chemical weathering and metamorphism. For

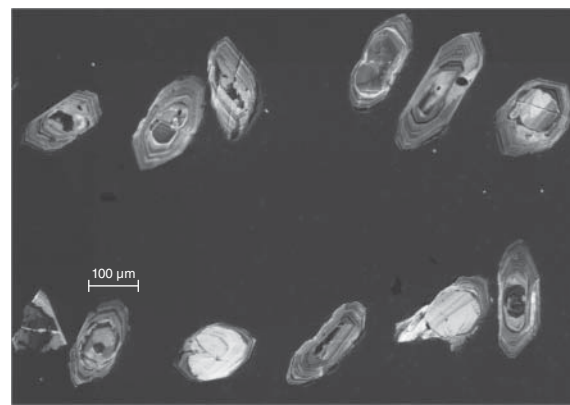


Figure 3.3 Zircon grains viewed under cathode luminescence, which reveals zoning. (Source: Photograph by J. D. Vervoort, Washington State University. Reproduced with permission.)

geochronological purposes, these properties mean it is likely to remain a closed system. Third, it concentrates U (and Th to a lesser extent) and excludes Pb, resulting in typically very high $^{238}\text{U}/^{204}\text{Pb}$ ratios. It is quite possibly nature's best clock. Finally, it is reasonably common as an accessory phase in a variety of intermediate to siliceous igneous and metamorphic rocks.

The very high $^{238}\text{U}/^{204}\text{Pb}$ ratios in zircon (and similar high μ minerals such as titanite and apatite) provide some special geochronological opportunities and a special diagram, the *concordia diagram*, first introduced by Wetherill (1956), was developed to take advantage of them. The discussion that follows can be applied to any other minerals with extremely high $^{238}\text{U}/^{204}\text{Pb}$ ratios, but in practice, zircons constitute the most common target for Pb geochronologists.

A concordia diagram is simply a plot of $^{206}\text{Pb}^*/^{238}\text{U}$ versus $^{207}\text{Pb}^*/^{235}\text{U}$; that is, the ratios of the number of atoms of radiogenic daughter produced to the number of atoms of radioactive parent. You should satisfy yourself that both of these ratios are proportional to time. In essence, the concordia diagram is a plot of the $^{238}\text{U}-^{206}\text{Pb}$ age against the $^{235}\text{U}-^{207}\text{Pb}$ age. The concordia curve on such a diagram that is the locus of points where the $^{238}\text{U}-^{206}\text{Pb}$ age equals the $^{235}\text{U}-^{207}\text{Pb}$ age. Such ages are said to be *concordant*. Figure 3.4 is an example of a concordia diagram.

The best way to think about evolution of Pb/U ratios is to imagine that the diagram itself evolves with time, along with its axes, while the actual data point stays fixed. Let's take a 4.0 Ga old zircon as an example. When it first formed, or "closed," it would have plotted at the origin, because had anyone been around to analyze it, they would have found the $^{207}\text{Pb}^*/^{235}\text{U}$ and $^{206}\text{Pb}^*/^{238}\text{U}$ ratios to be 0. Initially, $^{207}\text{Pb}^*/^{235}\text{U}$ would have increased rapidly, while the $^{206}\text{Pb}^*/^{238}\text{U}$ would have been increasing only slowly. This is because 4.0 Ga ago there was a lot of ^{235}U around (recall that ^{235}U has a short half-life). As time passed, the increase in $^{207}\text{Pb}^*/^{235}\text{U}$ would have slowed as the ^{235}U was "used up." So imagine that the diagram initially "grows" or "expands" to the left, expanding downward only slowly. Had someone been around 3.0 Ga ago to determine "zircon" ages, they would have drawn it as it appears in Figure 3.5 (of course, they would have labeled the 3.0 Ga point as 0, the 4.0 Ga point as 1.0, etc.).

In a zircon that has remained as a completely closed system since its crystallization the $^{206}\text{Pb}^*/^{238}\text{U}$ versus $^{207}\text{Pb}^*/^{235}\text{U}$ will change as a function of age in such a way that it will always plot on the concordia line. What happens when a zircon gains or loses U or Pb? Let's take the case of Pb loss, since that is the most likely type of open-system behavior in zircons. The zircon must lose ^{207}Pb and ^{206}Pb in exactly the proportions they exist in the

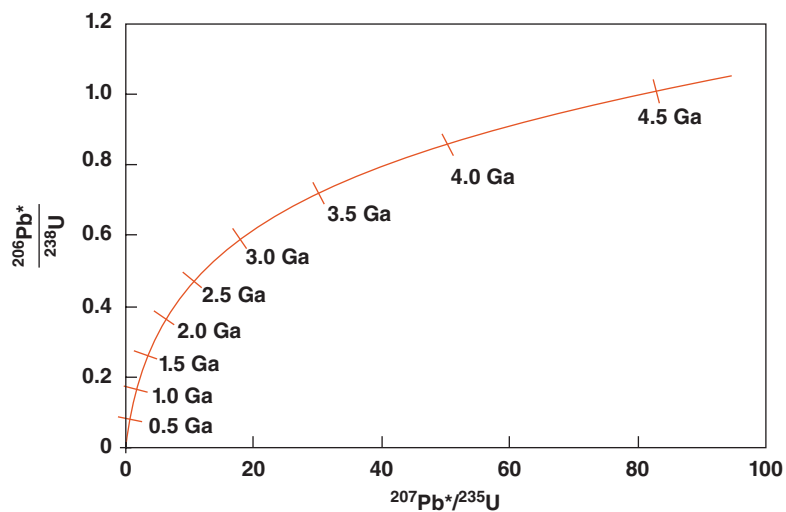


Figure 3.4 The concordia diagram. We use the asterisk to denote *radiogenic* Pb. In many concordia plots, the asterisk is not used, but it is nevertheless only radiogenic Pb in these ratios.

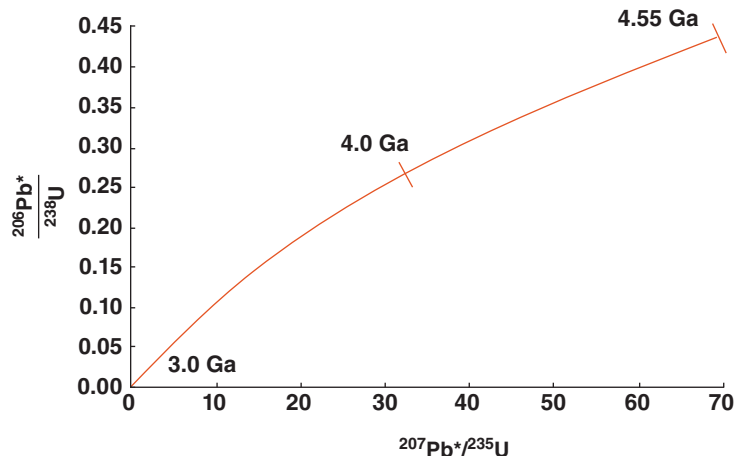


Figure 3.5 A concordia diagram as it would have been drawn at 3.0 Ga.

zircon because the two are chemically identical. In other words, a zircon will not lose ^{206}Pb in preference to ^{207}Pb or vice versa.

Let's take the specific case of a 4.0 Ga zircon that experienced some Pb loss during a metamorphic event at 3.0 Ga. If the loss were complete, the zircon would have been reset and would have plotted at the origin in Figure 3.5. We could not distinguish it from one that formed 3.0 Ga. Suppose now that that zircon had lost only half its Pb at 3.0 Ga. Because ^{206}Pb and ^{207}Pb would have been lost in the same proportions in which they were present in the zircon, both the $^{206}\text{Pb}/^{238}\text{U}$ and $^{207}\text{Pb}/^{235}\text{U}$ would have both decreased by half.

Consequently, the point would have migrated half way along a straight line between its original position and the origin. At 3.0 Ga, therefore, it would have plotted on a "cord," that is, a straight line, between its initial position on the concordia curve, the 4.0 Ga point, and the origin at 3.0 Ga. Had other zircons lost some other amount of Pb, say 30% or 80%, they would have plotted on the same cord, but further or nearer the origin and our concordia plot would appear as it does in Figure 3.6(a). The line is straight because the loss of ^{207}Pb is always directly proportional to the loss of ^{206}Pb . The origin in Figure 3.6(a) corresponds to the 3.0 Ga point on the concordia in

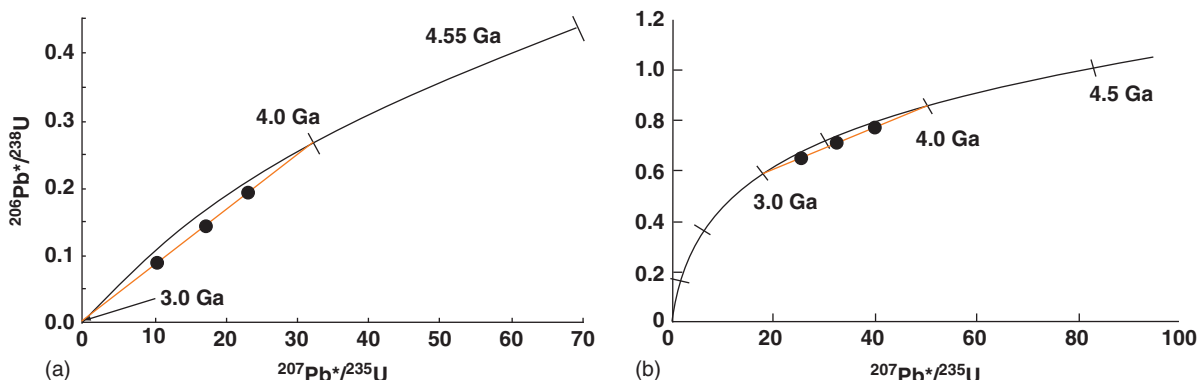


Figure 3.6 (a) Concordia diagram as it would have appeared at 3.0 Ga. Three zircons that experience variable amounts of Pb loss move from the 4.0 Ga point on the concordia curve (their crystallization age) toward the origin. (b) The same three zircons as they would plot at present. The three define a cord between 3.0 and 4.0 Ga. A possible interpretation of this result would be that 4.0 Ga is the crystallization age and 3.0 Ga is the metamorphic age.

Figure 3.6(b), which shows how those zircons would plot today assuming they had remained closed subsequent to the Pb loss at 3 Ga. So, in Figure 3.6(b), the zircons would lay on a cord between the 4.0 Ga and the 3.0 Ga point. We would say these are “discordant” zircons.

The intercepts of this cord with the concordia give the ages of initial crystallization (4.0 Ga) and metamorphism (3.0 Ga). So if we can determine the cord on which this discordant zircon lies, we can determine the ages of both events from the intercepts of that cord with the concordia. Unfortunately, if our only data point is a single zircon, we can draw an infinite number of cords passing through this point, so the ages of crystallization and metamorphism are indeterminate. However, we can draw only one line through two points. So by measuring two zircons (or populations of zircons) that have the same crystallization ages and metamorphism ages, but have lost different amounts of Pb, and hence plot on different points on the same cord, the cord can be determined. The closure age and partial resetting ages can then be determined from the intercepts. As usual in geochronology, however, we are reluctant to draw a line through only two points since any two points define a line; so at least three measurements are generally made. In practice, different zircon populations are selected based on size, appearance, magnetic properties, color, etc. While zircon

is generally a trace mineral, only very small quantities, a few milligrams, are needed for a measurement. Indeed, it is possible to analyze single zircons and even parts of zircons.

U gain, should it occur, would affect the position of zircons on the concordia diagram in the same manner as Pb loss; the two processes are essentially indistinguishable on the concordia diagram. U loss, on the other hand, moves the points away from the origin at the time of the loss (Figure 3.7). In this case, the zircons lie on an extension of a cord above the concordia. As is the case for Pb loss, the upper intercept of the cord gives the initial age and the lower intercept gives the age of U loss. Such U loss is far less common than Pb loss, however. This is true for two reasons. First, U is compatible in the zircon, Pb is not. Second, Pb occupies a site damaged by the alpha decay process, particularly the recoil of the atom as it undergoes alpha decay, making diffusion out of this site easier. Radiation damage to the crystal lattice is a significant problem in zircon geochronology, and one of the main reasons ages can be imprecise. U-rich zircons are particularly subject to radiation damage. Heavily damaged crystals are easily recognized under the microscope and are termed *metamict*.

Pb gain in zircons is not predictable because the isotopic composition of the Pb gained need not be the same as the composition of the Pb in the zircon. Thus Pb gain would destroy any age relationships. However, Pb gain is much

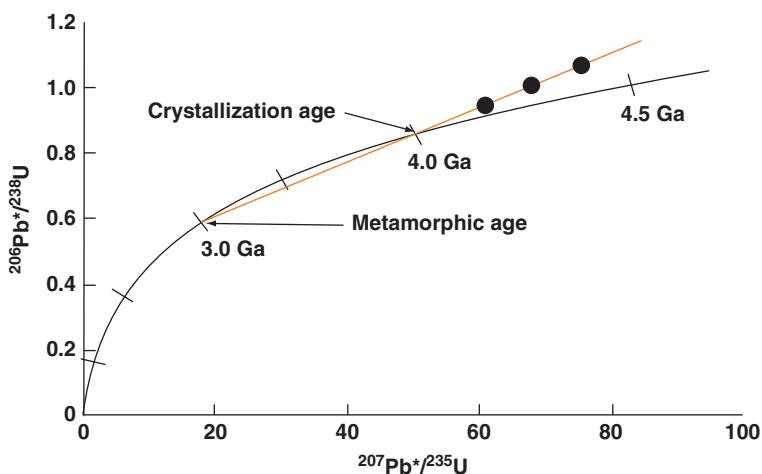


Figure 3.7 A concordia plot showing hypothetical zircons that crystallized at 4.0 Ga and lost U during metamorphism at 3.0 Ga.

less likely than other open system behaviors, of which Pb loss is by far the most common.

Zircons that have suffered multiple episodes of open system behavior will have U-Pb systematics that are difficult to interpret and could be incorrectly interpreted. For example, zircons lying on a cord between 4.0 and 3.0 Ga that subsequently lose Pb and move on a second cord toward the 2.0 Ga could be interpreted as having a metamorphic age of 2.0 Ga and a crystallization age of between 4.0 and 3.0 Ga.

Continuous Pb loss from zircons can also complicate the task of interpretation. The reason is that in continuous Pb loss, zircons do not define a straight-line cord, but rather a slightly curved one. Again imagining that the concordia diagram grows with time, a zircon losing Pb will always move toward the origin. However, the position of the origin relative to the position of the zircon moves with time in a non-linear fashion. The result is a non-linear evolution of the isotopic composition of the zircon.

Krogh (1982) showed that metamict regions of zircons could be removed abrasively using small air abrasion chambers designed and built expressly for this purpose. He demonstrated that abraded zircons were typically much more concordant than unabraded ones. Consequently, age uncertainties were considerably reduced. In addition to physical abrasion, numerous attempts have been made to “chemically abrade,” or leach, zircons, the idea being to remove the radiation damaged regions of the crystal. The most successful of these methods has been that of Mattinson (2005), which involves first annealing the crystals at 800–1000°C for 48 h (this repairs the radiation damage) before step-wise partial dissolution in acid at progressively higher temperatures. This step-wise dissolution allows for an approach similar to step-wise heating in ^{40}Ar - ^{39}Ar dating, as illustrated in Figure 3.8. The uncertainty in this age is less than 0.1%, a level of accuracy otherwise unattainable. Figure 3.9 shows another example of how this technique improves accurate determination of crystallization ages. Three different fractionations of untreated zircons from a Finnish tonalite are discordant, but define a cord with an upper concordia intercept of about 1870 Ma. The chemically abraded zircon fraction is nearly concordant at this age,

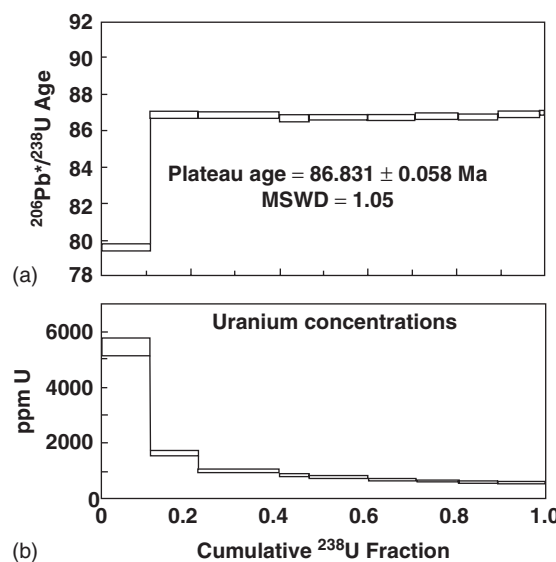


Figure 3.8 (a) Ages calculated from step-wise dissolution of zircons from the Sierra Nevada batholith that had been abraded, then annealed at 850°C for 48 h. (b) Corresponding U concentrations in the step-wise dissolution. The outer zones of the zircons are the most U-rich and consequently the most radiation-damaged and discordant. (Source: Mattinson (2005). Reproduced with permission of Elsevier.)

allowing a much more precise determination. In this diagram, the analyses are plotted by ellipses in order to represent analytical errors. The analytical errors in on the $^{207}\text{Pb}/^{235}\text{U}$ and $^{206}\text{Pb}/^{238}\text{U}$ ratios are highly correlated, hence the elliptical shape. This “chemical abrasion” technique is now widely used in conventional thermal ionization analysis of zircons.

A variety of analytical methods have evolved for zircon analysis. The oldest is thermal ionization mass spectrometry (TIMS), in which U and Pb concentrations are determined by isotope dilution along with their isotope ratios (these techniques are discussed in the appendix). Chemical abrasion is routinely done in connection with this method. This produces the most precise analyses. However, the technique lacks spatial resolution so ages can be less precise if the zircons are zoned (although it is possible to analyze grain fragments of zircon crystals).

Multi-collector secondary ionization mass spectrometers (MC-SIMS) work by firing an ion beam at the polished surface of a sample.

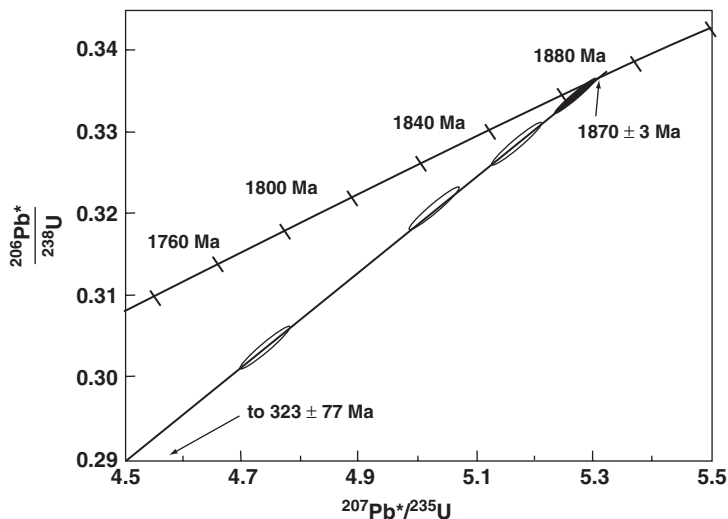


Figure 3.9 Concordia diagram for zircons from Tiirismaa tonalite in Finland. Untreated zircon analyses are shown as open error ellipses, while the chemically abraded zircon analysis is shown as a filled error ellipse. The elliptical shape of the error representation results from the correlation in analytical errors of $^{207}\text{Pb}/^{235}\text{U}$ and $^{206}\text{Pb}/^{238}\text{U}$ ratios. (Source: Lahtinen and Nironen (2010). Reproduced with permission of Elsevier.

Atoms on the surface are ionized and swept into a double-focusing mass spectrometer (see Appendix) for isotopic analysis. Both U and Pb can be analyzed simultaneously on spots $\sim 30\ \mu\text{m}$ in diameter and $2\text{--}3\ \mu\text{m}$ deep. Isotope ratios are measured less precisely than with TIMS, but ages are often more precise because a single zone of the zircon can be analyzed. There are only a handful of laboratories around the world doing this work due to the expense and complexity of these instruments.

The newest technique is laser-ablation inductively coupled mass spectrometry (LA-ICP-MS), in which a laser is fired at a small spot on the zircon, ablating the surface. The ablated material is then swept into a mass spectrometer and analyzed. LA-ICP-MS has somewhat less spatial resolution, but is faster and cheaper than SIMS instruments and provides reasonable precision. The availability of these instruments has resulted in an explosion of zircon dating in the past decade.

U-Pb dating has now improved to the point where uncertainty in decay constants now constitutes a major part of the uncertainty in zircon ages. Because it is far less abundant, the decay constant for ^{235}U is the most uncertain. Based on highly concordant zircon analyses obtained through the chemical

abrasion technique, Mattinson (2010) has recently proposed that the ^{235}U decay constant should be revised from the conventionally accepted value of $0.98485 \pm 0.00135 \times 10^{-9}\text{yr}^{-1}$ to $0.98571 \pm 0.00012 \times 10^{-9}\text{yr}^{-1}$.

Given the mechanical and chemical stability of zircon, it should not be surprising that the oldest terrestrial material yet identified is zircon. Work published in 1989, revealed that the Acasta gneisses of the Slave Province (Northwest Territories, Canada) are 3.96 Ga old (Bowring et al., 1989). These ages were determined using an ion probe to date the cores of zircon crystals extracted from these gneisses. The next oldest rocks are those of the Isua gneisses in Greenland. These are roughly 3850 Ma old.

Zircons having ages in the range of 4100–4260 Ma have been identified in quartzites in the Jack Hills of the Yilgarn craton in Western Australia (e.g., Compston and Pidgeon, 1986). The Jack Hills are located in the Narryer terrane a geologically complex, multiply metamorphosed region. The depositional age of the old zircon-bearing quartzites is constrained to be between 2.65 Ga, the U-Pb age of metamorphic monazite in the quartzite, and the 3.08 Ga age of the youngest detrital zircons (Rasmussen et al., 2010). The first >4.0 Ga zircons were analyzed by a specially

built secondary ionization mass spectrometer at the Australian National University nicknamed “SHRIMP.” Its success led to instruments of this type becoming commercially available and installed in several other laboratories around the world. As we noted, the great advantage of these instruments over conventional analysis is spatial resolution so that small areas the zircons can be analyzed. As can be seen in Figure 3.3, zoning in zircon is not uncommon and this zoning often reflects multiple episodes of growth. This was the case with the Jack Hills zircons, which had complex histories suffering multiple metamorphic events between 4260 and 2600 Ma. The principal effect was the growth of rims of new material on the older cores around 3500 Ma. Conventional analysis of these zircons would not have recognized the older ages. The cores of these zircons, however, proved to be nearly concordant at the older ages. These determined by ion probe ages were initially highly controversial. By and large, however, the community has come to accept them as reliable, when performed carefully.

Subsequently even older zircons (would be more correct to say parts of zircons) were discovered in the Jack Hills of Australia (Wilde, et al., 2001). Ion probe ages of one of these zircons, including one area giving an age of 4.404 ± 0.008 Ga, are shown in Figure 3.10.

Thus the oldest known terrestrial materials are approaching the oldest ages from other planetary bodies, including the Moon, Mars, and asteroids (as represented by meteorites). They remain, however, significantly younger than the age of the Solar System, which is 4.568 Ga. Nevertheless, these very old ages seem to demonstrate that it is zircons, not diamonds that “are forever.”

3.4 U-DECAY SERIES DATING

Up to now, we have been discussing decay schemes that are based on measuring the amount of a stable daughter nuclide relative to the amount of the radioactive parent. Since the decay of the parent takes place at an invariant rate, this ratio of daughter to parent is proportional to time (in a closed system). In addition to Pb, decay of U and Th also produces ${}^4\text{He}$, and thus the accumulation of ${}^4\text{He}$ in crystals can also be used for dating. Since ${}^4\text{He}$ is a noble gas and not chemically bound in minerals, it begins to diffuse out at low temperatures, that is, the “closure temperatures” for the U-Th-He system is quite low. Consequently, it is often used in combination with fission track dating and K-Ar dating to determine cooling and erosion rates, a field known as thermochronology (Reiners and Brandon, 2006), which we’ll discuss in

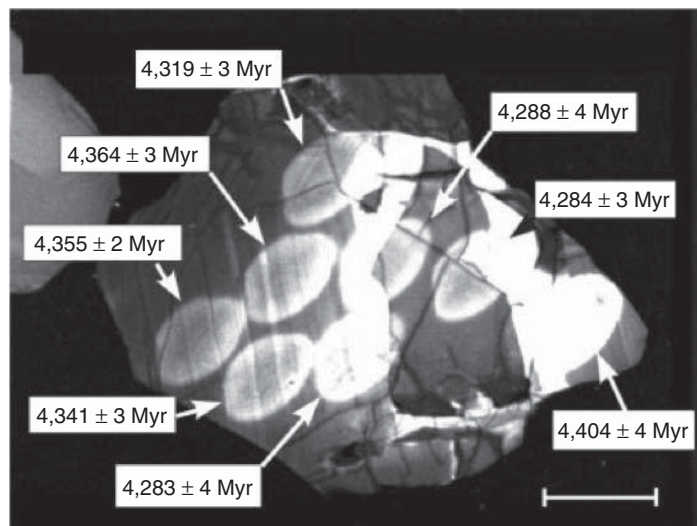


Figure 3.10 Photomicrograph of the oldest zircon known. Light areas are regions of ion probe analysis. Ages determined on these areas are shown. (Source: Wilde et al. (2001). Reproduced with permission of Nature Publishing Group.)

the following chapter. In the remainder of this chapter, we will consider a method of dating based on the intermediate decay products of U and Th and where both parent and daughter are radioactive. U-decay series dating differs in a very fundamental way from the conventional techniques we have been discussing. It does, however, share two features. First, the time we are measuring is the time since the system closed, and second, an accurate date requires the system to have remained closed. U-decay series are also useful in inferring the rate and extent of melting in the mantle. We'll examine that application in a later chapter.

3.4.1 Basic principles

The fundamental principal involved in U decay series dating is that, *in a closed system, the ratio of parent to daughter will tend toward an equilibrium state in which the rate of decay of the parent is equal to the rate of decay of the daughter. A closed system will approach this equilibrium state at a predictable rate with the ratio of the parent to daughter being proportional to time*, provided equilibrium has not been reached. Once equilibrium has been achieved, the ratio of parent to daughter no longer depends on the time elapsed, and we can calculate only a minimum age.³

U and Th do not decay directly to Pb; rather the transition from U and Th to Pb passes through many intermediate radioactive daughters (Figure 3.11). Most of these daughters have very short half-lives, ranging from milliseconds to hours, and are of little use in study of the Earth. However, a number of the intermediate daughters have half-lives ranging from days to hundreds of thousands of years and do provide useful information about geological processes. Of these, the U decay chains are of greatest interest because the longest lived ²³²Th product, ²²⁸Ra, has a half-life of only 5.75 years. Table 3.2 lists half-lives and decay constants of some of the most useful of these isotopes. As one might guess from the short half-lives, U-decay series isotopes are used to date relatively recent events.

The half-lives of all of these daughter nuclides are short enough so that any atoms present when the Earth formed have long since decayed (to Pb). They exist in the Earth

(and in all other bodies of the Solar System) only because they are continually produced by the decay of the long-lived isotopes of U and Th. The abundance of such a nuclide depends on the balance between its own radioactive decay and the rate at which it is produced by the decay of its parent:

$$\frac{dN_D}{dt} = \lambda_P N_P - \lambda_D N_D \quad (3.12)$$

where subscripts *P* and *D* refer to parent and daughter respectively. *This equation says simply that the rate of change of the abundance of the daughter isotope is equal to the rate of production less the rate of decay.* This can be integrated to give:

$$N_D = \frac{\lambda_P}{\lambda_D - \lambda_P} N_P^o (e^{-\lambda_P t} - e^{-\lambda_D t}) + N_D^o e^{-\lambda_D t} \quad (3.13)$$

Scientists dealing with the intermediate daughters of U and Th (it is the daughters of ²³⁸U that are of the most interest), generally work with *activities* rather than atomic abundances. By activity, we mean rate of decay, dN/dt , measured in disintegrations per unit time.⁴ One reason for this is that the abundance of these isotopes was traditionally determined by detecting their decay. Today, abundances of the longer-lived nuclides can be measured by mass spectrometry, but the shorter-lived ones are so rare that they are still most readily detected by their decay. The other reason we work with activities will become apparent shortly. We will follow the standard convention of denoting activities by enclosing the isotope or isotope ratio in parentheses. Thus, (²³⁰Th) denotes the activity of ²³⁰Th, and (²³⁰Th/²³⁸U) denotes the ratio of activities of ²³⁰Th and ²³⁸U. Activities are related to atomic (or molar) abundances by the basic equation of radioactive decay:

$$\frac{dN}{dt} = -\lambda N \quad (1.12)$$

Hence if we know the activity, the molar abundance can be calculated and vice versa.

The *radioactive equilibrium* state of the daughter and the parent is the condition where their *activities* are equal, that is:

$$\frac{dN_D}{dt} = \frac{dN_P}{dt} \quad (3.14)$$

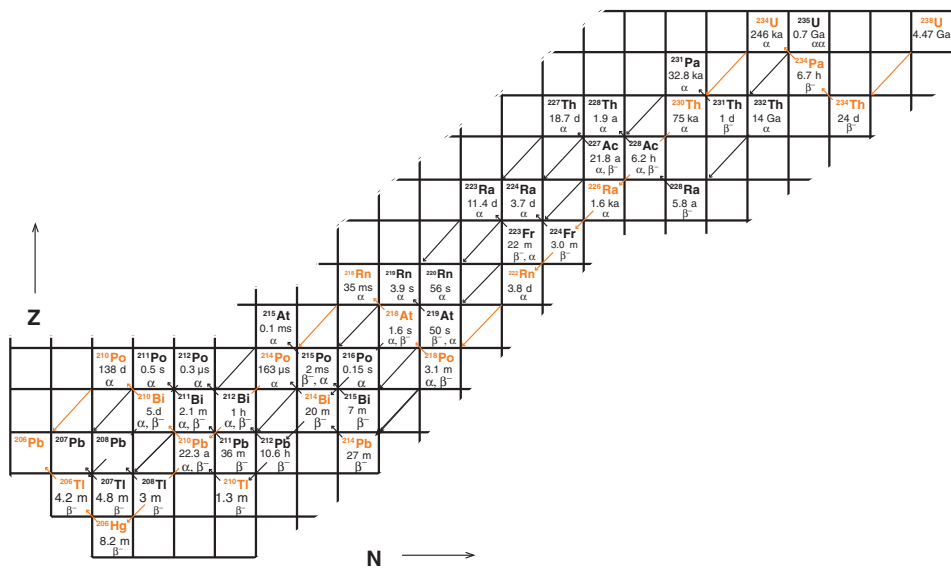


Figure 3.11 Part of the chart of the nuclides showing the series of decays that occur as ^{238}U , ^{235}U , and ^{232}Th are transformed to ^{206}Pb , ^{207}Pb , and ^{208}Pb , respectively.

Table 3.2 Half-lives and decay constants of long-lived U and Th daughters.

Nuclide	Half-life, yrs	Decay constant, yr^{-1}	Series
^{234}U	245,250	2.826×10^{-6}	^{238}U
^{231}Pa	32,670	2.116×10^{-5}	^{235}U
^{230}Th	75,690	9.158×10^{-6}	^{238}U
^{226}Ra	1600	4.332×10^{-4}	^{238}U
^{228}Ra	6.7	1.06×10^{-1}	^{232}Th
^{210}Pb	22.23	3.118×10^{-2}	^{238}U
^{210}Po	0.3789	1.829	^{238}U

Source: ^{234}U and ^{230}Th from Cheng et al. (2000); others are from Laboratoire National Henri Becquerel (www.nucleide.org)

This is the state that will be eventually achieved by any system if it is not perturbed (remains closed).

We can demonstrate that this is so in two ways. The first is a simple mathematical demonstration. The equilibrium state is the steady state where the abundance of the daughter does not change, that is, where the left hand side of 3.12 is zero:

$$0 = \lambda_P N_P - \lambda_D N_D \quad (3.15)$$

We substitute the dN/dt for the λN terms in 3.14, rearrange and we obtain 3.15; *QED*.

The second demonstration is a thought experiment. Imagine a hopper, a grain hopper for example, with an open top and a door in the bottom. The door is spring-loaded such that the more weight placed on the door, the wider it opens. Suppose we start dropping marbles into the hopper at a constant rate. The weight of marbles accumulating in the hopper will force the door open slightly and marbles will start falling out at a slow rate. Because the marbles are falling out more slowly than they are falling in, the number and weight of marbles in the hopper will continue to increase. As a result, the door will continue to open. At some point, the door will be open so wide that marbles are falling out as fast as they are falling in. This is the steady, or equilibrium, state. Marbles no longer accumulate in the hopper and hence the door is not forced to open any wider. The marbles falling into the door are like the decay of the parent isotope. The marbles in the hopper represent the population of daughter isotopes. Their decay is represented by their passing through the bottom

door. Just as the number of marbles passing through the door depends on the number of marbles in the hopper, the activity (number of decays per unit time) of an isotope depends on the number of atoms present.

If the rate of marbles dropping into the hopper decreases for some reason, marbles will fall out of the hopper faster than they fall in. The number of marbles in the hopper will decrease, as a result the weight on the door decreases and it starts to close. It continues to close (as the number of marbles decreases) until the rate at which marbles fall out equals the rate at which marbles fall in. At that point, there is no longer a change in the number of marbles in the hopper and the position of the door stabilizes. Again equilibrium has been achieved, this time with fewer marbles in the hopper, but nevertheless at the point where the rate of marbles going in equals the rate of marbles going out. The analogy to radioactive decay is exact.

Thus when a system is disturbed by addition or loss of parent or daughter, it will ultimately return to equilibrium. The rate at which it returns to equilibrium is determined by the decay constants of the parent and daughter. If we know how far out of equilibrium the system was when it was disturbed, we can determine the amount of time that has passed since it was disturbed by measuring the present rate of decay of the parent and daughter.

In the past, activities were measured by alpha-counting and fairly large quantities of material were necessary. But improvements in mass spectrometry over the past several decades have made it possible to measure the longer-lived radionuclides, including ^{234}U , ^{230}Th , and ^{231}Pa by mass spectrometry on small quantities of material and with better precision than by α counting, although the shorter-lived nuclides, such as ^{210}Pb are still measured by decay counting. Over the last decade or so, it has become possible to also measure these radionuclides on the scale of tens of microns using the kinds of ion microprobes used for zircon dating.

3.4.2 ^{234}U - ^{238}U dating

The equilibrium, or more precisely the lack thereof, between ^{234}U and ^{238}U can be used to date carbonates precipitated from seawater. As it turns out, (^{234}U) and (^{238}U) in seawater

are not in equilibrium, that is, the $(^{234}\text{U}/^{238}\text{U})$ ratio is not 1. It is uniform,⁵ however, with a ratio of about 1.145 ± 0.03 . The reason the ratio is higher than 1 is that ^{234}U is preferentially leached from rocks because ^{234}U is located in crystals of rocks in damaged lattice sites. It occupies the site of a ^{238}U atom that has undergone α -decay. The α -particle and the recoil of the nucleus damage this site. Since it occupies a damaged site, it is more easily removed from the crystal by weathering than ^{238}U . The oceans collect this “leachate,” hence they are enriched in ^{234}U . When U precipitates from seawater into, for example, the calcium carbonate in a coral skeleton, it will initially have the same $(^{234}\text{U}/^{238}\text{U})$ as seawater, but ^{234}U will decay faster than it is created by decay of ^{238}U , so $(^{234}\text{U}/^{238}\text{U})$ will slowly return to the equilibrium condition where $(^{234}\text{U}/^{238}\text{U}) = 1$. Deviations of the $(^{234}\text{U}/^{238}\text{U})$ ratio from the equilibrium value (1) are usually expressed in per mil units and denoted as $\delta^{234}\text{U}$. Thus a $(^{234}\text{U}/^{238}\text{U})$ value of 1.145 would be expressed as $\delta^{234}\text{U} = 145$.

Let's see how we can take advantage of this to determine geologic time. We can divide the activity of ^{234}U in a sample into that which is supported by ^{238}U , that is, that amount in radioactive equilibrium with ^{238}U and that amount which is excess, that is, unsupported by ^{238}U :

$$(^{234}\text{U}) = (^{234}\text{U})_s + (^{234}\text{U})_u \quad (3.16)$$

where we are using parentheses to denote activity and subscripts *s* and *u* denote *supported* and *unsupported* abundances respectively. The activity of the excess ^{234}U decreases with time according to equation 2.04, which we can rewrite as:

$$(^{234}\text{U})_u = (^{234}\text{U})_u^o e^{-\lambda_{234}t} \quad (3.17)$$

where the superscript *o* denotes the initial activity (at time $t = 0$). We can also write:

$$(^{234}\text{U})_u^o = (^{234}\text{U})^o - (^{234}\text{U})_s \quad (3.18)$$

which just says that the initial unsupported activity of ^{234}U is equal to the total initial activity of ^{234}U less the (initial) supported activity of ^{234}U . Since to a very good approximation the activity of the parent, ^{238}U , does not change over times on the order of the half-life of ^{234}U or even 10 half-lives of ^{234}U , the present ^{238}U activity is equal

to the activity at $t = 0$ (we make the usual assumption that the system is closed). And by definition the supported activity of ^{234}U is equal to the activity of ^{238}U , both now and at $t = 0$. Hence, 3.16 can be expressed as:

$$(^{234}\text{U}) = (^{238}\text{U}) + (^{234}\text{U})_u \quad (3.19)$$

and 3.18 becomes

$$(^{234}\text{U})_u^o = (^{234}\text{U})^o - (^{238}\text{U}) \quad (3.20)$$

Substituting 3.20 into 3.17 yields:

$$(^{234}\text{U})_u = [(^{234}\text{U})^o - (^{238}\text{U})] e^{-\lambda_{234}t} \quad (3.21)$$

Substituting 3.21 into 3.19, we have:

$$(^{234}\text{U}) = (^{238}\text{U}) + [(^{234}\text{U})^o - (^{238}\text{U})] e^{-\lambda_{234}t} \quad (3.22)$$

Just as for other isotope systems, it is generally most convenient to deal with ratios rather than absolute activities (among other things, this allows us to ignore detector efficiency provided the detector is equally efficient at all energies of interest⁶), hence we divide by the activity of ^{238}U :

$$\left(\frac{^{234}\text{U}}{^{238}\text{U}} \right) = 1 + \left\{ \frac{(^{234}\text{U})^o - (^{238}\text{U})}{(^{238}\text{U})} \right\} e^{-\lambda_{234}t} \quad (3.23)$$

or since $^{238}\text{U} = ^{238}\text{U}^o$:

$$\left(\frac{^{234}\text{U}}{^{238}\text{U}} \right) = 1 + \left\{ \left(\frac{^{234}\text{U}}{^{238}\text{U}} \right)^o - 1 \right\} e^{-\lambda_{234}t} \quad (3.24)$$

Thus, the present activity ratio can be expressed in term of the initial activity ratio, the decay constant of ^{234}U , and time. For material such as a coral, in (isotopic) equilibrium with seawater at some time $t = 0$, we know the initial activity ratio was 1.14. Carbonates, for example, concentrate U. If we measure the $(^{234}\text{U}/^{238}\text{U})$ ratio of an ancient coral, and assume that the seawater in which that coral grew had $(^{234}\text{U}/^{238}\text{U})$ the same as modern seawater (1.14), the age of the coral can be obtained by solving Eqn. 3.22 for t . The age determined is the time since the material last reached isotopic equilibrium with seawater.

The application of $^{234}\text{U}/^{238}\text{U}$ has been largely restricted to corals. It is not generally useful for freshwater carbonates because of uncertainty in the initial activity ratio. Mollusk shells and pelagic biogenic carbonate (e.g., foraminiferal ooze) often take up U after initial deposition of the carbonate and death of the organism, thus violating our closed system assumption. The technique is typically useful up to about four times the half-life of ^{234}U when alpha spectrometry is the analytical method, but can be applied to longer times with mass spectrometry because of higher precision.

3.4.3 $^{230}\text{Th}-^{238}\text{U}$ dating

The $^{244}\text{U}-^{238}\text{U}$ technique does not have high temperature applications, because at high temperature, ^{234}U and ^{238}U do not fractionate as they do at low temperature. The reason is that radiation damage, which is the reason ^{234}U is removed in weathering more easily than ^{238}U , anneals quite rapidly at high temperature. Disequilibrium between ^{230}Th (the daughter of ^{234}U) and its U parents can, however, provide useful geochronological and geochemical information in both high- and low-temperature systems. We start with an equation analogous to Eqn. 2.4:

$$\left(\frac{^{230}\text{Th}}{^{232}\text{Th}}\right)_u = \left(\frac{^{230}\text{Th}}{^{232}\text{Th}}\right)_u^0 e^{-\lambda_{230}t} \quad (3.25)$$

As is the usual practice, we normalize to a non-radiogenic isotope:

$$\left(\frac{^{230}\text{Th}}{^{232}\text{Th}}\right)_u = \left(\frac{^{230}\text{Th}}{^{232}\text{Th}}\right)_u^0 e^{-\lambda_{230}t} \quad (3.26)$$

(^{232}Th , although non-radiogenic, is radioactive, of course. However, with a half-life of 14 Ga, its abundance will not change on time scales comparable to the half-life of ^{230}Th .)

In seawater, and in its oxidized state generally, U is quite soluble. Th, however, is quite insoluble: its seawater residence time is 300 years or less compared to about 500,000 year for U. (It should be noted here that solubility in seawater does not control concentrations or residence times. Nevertheless solubility is a good guide to both of these.) Once a ^{234}U atom decays to ^{230}Th , it is quickly absorbed onto particles that in

turn are quickly incorporated into sediment. As a result, relatively high concentrations of unsupported ^{230}Th can be removed (by leaching) from some sediments (mainly relatively slowly accumulating ones). In cases where the amount of leached ^{234}U is negligible and where the $(^{230}\text{Th}/^{232}\text{Th})^0$ is known (from, for example, zero-age sediment at the seawater-sediment interface), Eqn. 3.26 can be used to determine the age of the sediment.

Let's consider a specific example. The tops of manganese nodules grow by precipitation of Mn – Fe oxides and hydroxides from seawater. They are known to grow very slowly, but how slowly? If we assume the rate of growth is constant then depth in the nodule should be proportional to time. If z is the depth in the nodule, and s is the growth (sedimentation) rate, then:

$$t = z/s \quad (3.27)$$

and 3.26 becomes:

$$\begin{aligned} \left(\frac{^{230}\text{Th}}{^{232}\text{Th}}\right) &= \left(\frac{^{230}\text{Th}}{^{232}\text{Th}}\right)^0 e^{-\lambda_{230}z/s} \\ &+ \left(\frac{^{238}\text{U}}{^{232}\text{Th}}\right) (1 - e^{-\lambda_{230}z/s}) \end{aligned} \quad (3.28)$$

At the surface of the nodule, $z = 0$, so the exponential terms both go to 1 and the measured activity ratio is initial activity ratio. Having a value for $(^{230}\text{Th}/^{232}\text{Th})^0$, Eqn. 3.29 can then be solved for s , the growth rate if measurements are made at some other depth.

In practice, however, it is difficult to obtain a sample exactly at the surface: a finite amount of material is required for analysis, and this often translates into a layer several millimeters thick. Equation 3.28 is solved in that instance by less direct means. For example, consider the data shown in Figure 3.12 on a Pacific manganese nodule reported by Huh and Ku (1984). In this plot of $\log(^{230}\text{Th}/^{232}\text{Th})$ versus depth, the initial ratio is the intercept of the best-fit line through the data. A growth rate was obtained by obtaining an initial guess of the initial $(^{230}\text{Th}/^{232}\text{Th})$, then iteratively refining the solution to 3.28 by minimizing the difference between computed and observed activity ratios. A growth rate of 49.5 mm/Ma

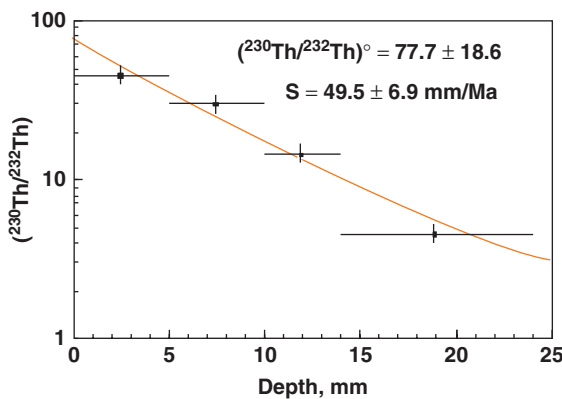


Figure 3.12 $^{230}\text{Th}/^{232}\text{Th}$ as a function in depth in a manganese nodule from MANOP Site H. (Source: Adapted from Huh and Ku (1984). Reproduced with permission of Elsevier.)

and a $(^{230}\text{Th}/^{232}\text{Th})$ of 77.7 was found to best fit the observations.

Some of the most successful applications of ^{230}Th dating have been in determining the age of carbonates, such as corals, mussel shells, and speleothems (carbonates precipitated from water moving through limestone caves including stalactites, stalagmites, and flowstone). As we noted, carbonates concentrate U and exclude Th. This leads to $(^{230}\text{Th}/^{238}\text{U})$ ratios much smaller than 1 (the equilibrium value); indeed, $(^{230}\text{Th}/^{238}\text{U})$ in many modern carbonates approaches 0. However, the problem of determining ages, specifically the mathematics, is complicated by the disequilibrium that will generally exist between ^{234}U and ^{238}U . The relevant equation, which we give without derivation, is:

$$\left(\frac{^{230}\text{Th}}{^{234}\text{U}} \right) = \frac{1 - e^{-\lambda_{230}t}}{(^{234}\text{U}/^{238}\text{U})} + \frac{\lambda_{230}}{\lambda_{230} - \lambda_{234}} \times \left[1 - \frac{1}{(^{234}\text{U}/^{238}\text{U})} \right] \times \left(1 - e^{-(\lambda_{230} - \lambda_{234})t} \right) \quad (3.29)$$

(see Ivanovich et al., 1992 for the derivation). This is yet another example of an equation that must be solved indirectly. This equation assumes that the initial $(^{230}\text{Th}/^{238}\text{U})$ ratio was 0 (rarely the actual case). One can correct for any ^{230}Th initially present by measuring

the ^{232}Th assuming an initial value of $(^{230}\text{Th}/^{232}\text{Th})$; for example, a value equal to the modern value of the solution from which the calcite precipitated, such as modern seawater or modern cave water.

Studies of speleothems have provided useful paleoclimatic information as the rate and composition of water flowing through caves has varied with past climate. Caves are also interesting because they contain some of the oldest examples of art. The ability to produce and appreciate art seems to be a uniquely human trait, and one that apparently developed rather late in our evolution. The question of how late is where geochronology comes in. Where the pigment is an organic substance such as charcoal, carbon-14 dating can be used. But many cave painting are done with mineral pigments such as red ochre, which cannot be so dated. Pike et al. (2012) sampled thin layers of calcite flowstone that precipitated over Paleolithic cave paintings and engravings in a variety of caves in northern Spain and found ages ranging from 22,000 to 41,000 years (see Problem 7). The age of the flowstone coating provides a minimum age of the painting that it covers. The 41,000 year age is the oldest example of art in Europe and likely dates the arrival of modern humans in Spain, as the artistic achievements of the indigenous Neanderthals appear to have been quite limited.

^{230}Th dating of fossil reef corals has proved extremely useful in a number of ways; for example, it has been used to calibrate the ^{14}C time-scale (we'll discuss ^{14}C dating and why it must be calibrated in the next chapter) and has provided a time scale for Pleistocene climate change. One of the most important aspects of Pleistocene climate change has been the rise and fall of sea level driven by retreating and advancing glaciers. These are, of course, driven by climate change, which we will discuss extensively in Chapter 10. Since sea level changes are directly driven by climate change, placing a time-scale on sea level allows us to place a time-scale on climate change. Reef-building corals contain photosynthetic symbiotic algae, which require they grow near the ocean surface to maximize light. Thus, dating reef corals allows us to date change in sea level. This approach was pioneered by Edwards et al. (1987) and many other groups of scientists have expanded on this work (e.g.,

Bard et al., 1990; Fairbanks et al., 2005). One of the more recent is that of Peltier and Fairbanks (2006) who produced a late Pleistocene sea level curve by dating coral samples recovered from drill cores on the island of Barbados. These studies have revealed that the last glacial maximum occurred around 26,000 years ago when sea level was 140 m below the present one, that the glacial episode began to end around 14,000 years ago and was briefly interpreted by the Younger Dryas event at around 12,000 years ago, and that sea level has been comparatively stable over the last few millennia. We'll return to the topic of Pleistocene climate in Chapter 10.

In systems where we can assume $(^{234}\text{U}) = (^{238}\text{U})$, high-temperature systems for example, the mathematics simplifies somewhat. With this assumption, we can treat the production of ^{230}Th as if it were the direct decay product of ^{238}U . We write an equation analogous to 3.13 and from it derive:

$$\left(\frac{^{230}\text{Th}}{^{232}\text{Th}} \right) = \left(\frac{^{230}\text{Th}}{^{232}\text{Th}} \right)^0 e^{-\lambda_{230}t} + \left(\frac{^{238}\text{U}}{^{232}\text{Th}} \right) (1 - e^{-\lambda_{230}t}) \quad (3.30)$$

(the tricks to this derivation are to make the approximations $\lambda_{230} - \lambda_{238} = \lambda_{230}$ and $e^{-\lambda_{238}t} = 1$; that is, assume $\lambda_{238} \approx 0$; this is the mathematical equivalent of assuming the activity of ^{238}U does not change with time). The first term on the right describes the decay of unsupported ^{230}Th while the second term describes the growth of supported ^{230}Th . Note that this equation has the form of a straight line in $(^{230}\text{Th}/^{232}\text{Th}) - (^{238}\text{U}/^{232}\text{Th})$ space, where the first term is the intercept and $(1 - e^{-\lambda_{230}t})$ is the slope. This is illustrated in Figure 3.13.

Now let's consider an example of a high temperature application. Imagine a crystallizing magma with homogeneous $(^{230}\text{Th}/^{232}\text{Th})$ and $(^{238}\text{U}/^{232}\text{Th})$ ratios. Th and U will partition into different minerals to different degrees. The minerals will have homogeneous $(^{230}\text{Th}/^{232}\text{Th})$, (assuming crystallization occurs quickly compared to the half-life of Th) since these two isotopes are chemically identical, but variable $(^{238}\text{U}/^{232}\text{Th})$ ratios. Thus the minerals will plot on a horizontal line

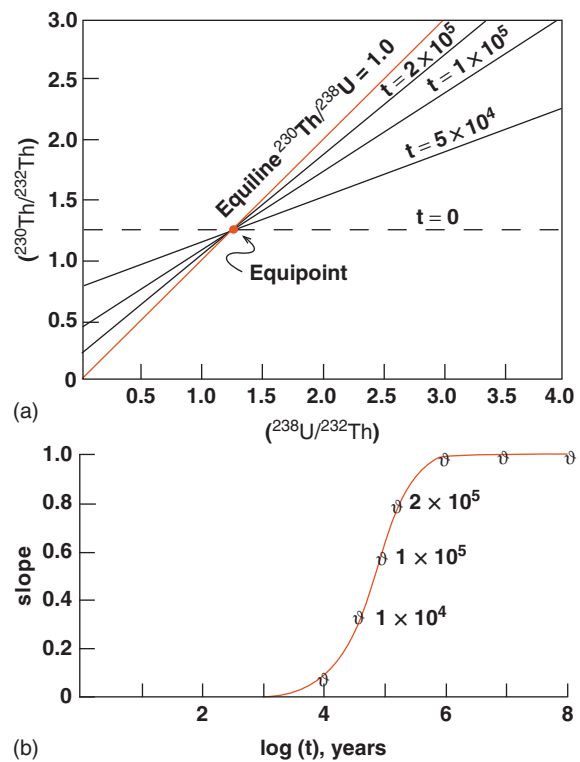


Figure 3.13 (a) $^{230}\text{Th} - ^{238}\text{U}$ isochron diagram. The $(^{238}\text{U}/^{232}\text{Th})$ of the source is given by the intersection of the isochron with the equiline. (b) shows how the slope changes as a function of time. (Source: Faure (1986). Reproduced with permission of John Wiley & Sons.)

in Figure 3.13. After the system closes, ^{238}U and ^{230}Th will begin to come to radioactive equilibrium (either ^{230}Th will decay faster than it is produced or vice versa, depending on whether $(^{230}\text{Th}/^{238}\text{U})$ is greater than or less than 1, the equilibrium value). Thus, the original horizontal line will rotate, as in a conventional isochron diagram. The rotation occurs about the point where $(^{230}\text{Th}/^{232}\text{Th}) = (^{238}\text{U}/^{232}\text{Th})$ known as the *equipoint*. As t approaches infinity, the exponential term approaches 1 and:

$$\lim_{t \rightarrow \infty} \left(\frac{^{230}\text{Th}}{^{232}\text{Th}} \right) = \left(\frac{^{238}\text{U}}{^{232}\text{Th}} \right) \quad (3.31)$$

Thus, the *equilibrium* situation, the situation at $t = \infty$, is $(^{230}\text{Th}/^{232}\text{Th}) = (^{238}\text{U}/^{232}\text{Th})$. In this case, all the minerals will fall

on a line, having a slope of 1. This line is known as the *equiline*.

Figure 3.14 shows a ^{230}Th - ^{238}U mineral isochron obtained on a peralkaline lava from the African Rift Valley in Kenya (Black et al., 1997) yields an age of $36,200 \pm 2600$ years. However, the eruption age of this lava is constrained by stratigraphy and ^{14}C dating to be less than 9000 years. Other lavas in the area yielded similarly precise, but anomalously old, U-Th ages. Black et al. interpreted the ages to reflect the time of crystallization of the phenocrysts, which in this case predates eruption by $>25,000$ years.

In most cases, however, concentrations of Th and U are so low that accurate measurement of Th-U disequilibria on mineral separates remains challenging. Some minerals, however, such as zircon, allanite ($(\text{Ca},\text{Ce},\text{Y},\text{La})_2(\text{Al},\text{Fe}^{+3})_3(\text{SiO}_4)_3(\text{OH})$), pyrochlore ($\text{Na},\text{Ca})_2\text{Nb}_2\text{O}_6(\text{OH},\text{F})$), and baddeleyite (ZrO_2), concentrate uranium and/or thorium sufficiently that they can be analyzed with the ion microprobe and U-Th ages determined not only on individual grains, but also of individual zones of mineral grains. The zones develop as a consequence of changing conditions during crystallization; in igneous minerals cooling and fractional crystallization as well as injection of new magma and associated heating can produce zonation. How long does this go on? What is the residence time of magma in a magma chamber?

One of the largest eruptions over the period of human existence was the eruption of Toba volcano in Sumatra, Indonesia, 73,000 years ago, which erupted 3000 km^3 of magma. The resulting caldera, now filled by Lake Toba, is enormous, $100 \times 30 \text{ km}$. How long had that magma resided in the magma chamber? Using ion probe ^{230}Th - ^{238}U dating of allanite crystals from in the pyroclastic products of the 73 Ka BP eruption, Vazquez and Reid (2004) found that allanite cores had crystallized between 100 and 225 thousand years ago, whereas most rims had ages identical with error of the eruption age. Simultaneous chemical analysis of the allanite zones revealed that between 255 ka and 110 ka, allanite composition, and therefore magma composition, was relatively restricted. Subsequent to that time, compositions became much more diverse. Vazquez and Reid interpreted this as less efficient magma mixing as the reservoir increased in size and suggested that merging of magma in the Toba reservoir could have catalyzed the cataclysmic eruption.

3.4.4 ^{231}Pa - ^{235}U dating

As Figure 3.11 shows, ^{231}Pa is the granddaughter of ^{235}U , but the intervening nuclide ^{231}Th has a sufficiently short half-life that we can always assume it is in equilibrium with its parent and hence can ignore it. Protactinium is typically in the 5+ valence state with

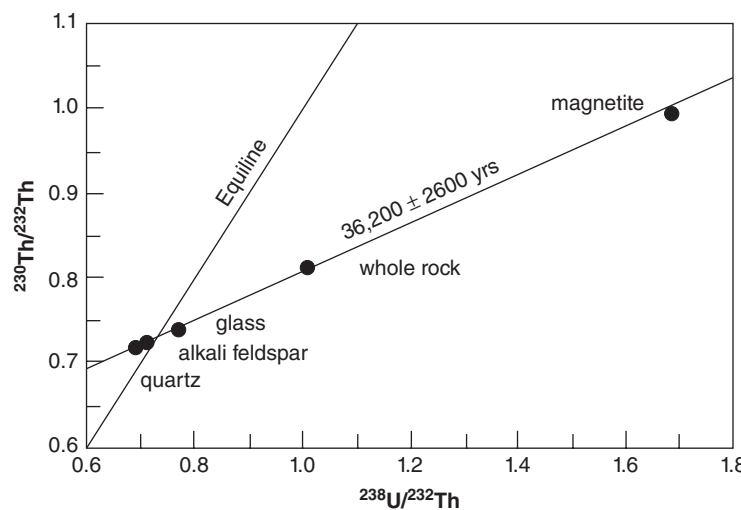


Figure 3.14 ^{230}Th - ^{238}U mineral isochron on a commondite lava from Kenya. (Source: Black et al. (1997). Reproduced with permission of Oxford University Press.)

ionic radii of 92 pm and partitions readily into the same igneous and metamorphic accessory minerals that concentrate U and Th, but like Th, it is excluded from carbonates. Also like Th and unlike U, Pa is generally immobile. Precisely the same principles apply to ^{231}Pa - ^{235}U dating as to ^{238}U decay series dating. We can derive the following relationship of the dependence of the ($^{231}\text{Pa}/^{235}\text{U}$) ratio on age from Eqn. 3.13:

$$\begin{aligned} \left(\frac{^{231}\text{Pa}}{^{235}\text{U}}\right) &= \frac{\lambda_{231}}{\lambda_{231} - \lambda_{235}} (e^{-\lambda_{235}t} - e^{-\lambda_{231}t}) \\ &\quad + \left(\frac{^{231}\text{Pa}}{^{235}\text{U}}\right)^0 e^{-\lambda_{231}t} \end{aligned} \quad (3.32)$$

In almost all instances, we can take λ_{235} to be 0, so that 3.32 simplifies to:

$$\left(\frac{^{231}\text{Pa}}{^{235}\text{U}}\right) = (1 - e^{-\lambda_{231}t}) + \left(\frac{^{231}\text{Pa}}{^{235}\text{U}}\right)^0 e^{-\lambda_{231}t} \quad (3.33)$$

Compared to dating based on the ^{238}U to ^{230}Th decay series, the ^{231}Pa - ^{235}U decay has a few advantages: there is no long-lived intermediate comparable to ^{234}U , the half-life of ^{235}U is less than a sixth of that of ^{238}U and thus it decays more rapidly, and ^{231}Pa decays more rapidly than ^{230}Th . These are outweighed by a number of disadvantages: the abundance

of ^{235}U is less than 1% of that of ^{238}U , ^{231}Pa is less abundant than ^{230}Th , ^{231}Pa decay constant is less well known than that of ^{234}U or ^{230}Th , and the short half-life means it is useful over a smaller range of time. So why would anyone bother?

The answer is that, just as for the ^{235}U - ^{207}Pb chronometer, its power comes not from using it in isolation, but by using it in combination with the ^{238}U decay chain (Edwards et al., 1997; Grün et al., 2010). Just as was the case for U-Pb, we expect ages based on the ^{235}U decay to be the same as those based on the ^{238}U decay if the system is undisturbed. Indeed, we can create a diagram (Figure 3.15) that has many similarities to the concordia diagram in Figure 3.4. The curved line on Figure 3.15 is the concordia curve, the locus of points where the $^{231}\text{Pa}^*/^{235}\text{U}$ age equals the $^{230}\text{Th}^*/^{234}\text{U}$ age (as is the case in the concordia diagram in Figure 3.4, the ratio is corrected for any initially present daughter). The $^{231}\text{Pa}^*/^{235}\text{U}$ - $^{230}\text{Th}^*/^{234}\text{U}$ concordia diagram is similar to the $^{207}\text{Pb}^*/^{235}\text{U}$ - $^{206}\text{Pb}^*/^{238}\text{U}$ one in that U-loss will move points away from the origin and U-gain will move them toward the origin. However, Pa and Th need not be lost or gained in proportions in which they are present in the specimen, so loss or gain of daughters can result in points moving in any direction. However, at low temperature at

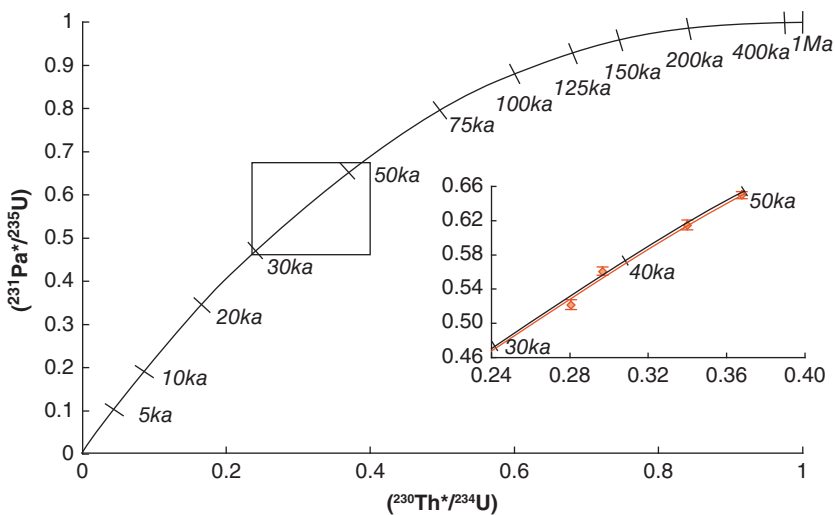


Figure 3.15 A $^{231}\text{Pa}^*/^{235}\text{U}$ - $^{230}\text{Th}^*/^{234}\text{U}$ concordia diagram. The line is the locus of points where the $^{231}\text{Pa}^*/^{235}\text{U}$ age equals the $^{230}\text{Th}^*/^{234}\text{U}$ age. Inset is the rectangular region blown up and shows a black concordia curve for $(^{234}\text{U}/^{238}\text{U})^0 = 1.0$ and a red one $(^{234}\text{U}/^{238}\text{U})^0 = 1.145$. Also shown are coral data from Araki Island from Chiu et al. (2006).

least, U is more mobile than either Pa or Th, so U-disturbance is probably the most likely form of open system behavior.

One other difference with the U-Pb concordia diagram is that the concordia curve depends on the $(^{234}\text{U}/^{238}\text{U})$ initial ratio, because the $^{230}\text{Th}^*/^{234}\text{U}$ age depends on it. This is illustrated in the inset in Figure 3.15: the black curve is for a $(^{234}\text{U}/^{238}\text{U})^0 = 1.0$, as might be relevant to a magmatic system, while the gray curve is drawn for a $(^{234}\text{U}/^{238}\text{U})^0 = 1.145$, relevant to carbonates precipitated from seawater, such as corals. The difference is not great; indeed, at the scale of the larger diagram, the two curves are virtually indistinguishable.

The key feature of the diagram is that Pa-Th-U ages should, if undisturbed, plot on the concordia curve. Shown in the inset are data from corals from the Araki Island, Vanuatu, New Hebrides archipelago, analyzed by Chiu et al. (2006). The data plot within error on the concordia diagram, assuring us that the corals are likely undisturbed and the ages accurate. To date, there are still few examples of combined $^{231}\text{Pa}^*/^{235}\text{U}$ – $^{230}\text{Th}^*/^{234}\text{U}$ dating, largely because of the challenges of measuring ^{231}Pa accurately. As analytical techniques continue to improve, however, we can expect to see these systems used in combination more commonly.

3.4.5 ^{226}Ra dating

^{226}Ra is another relatively long-lived nuclide ($\tau_{1/2} = 1600$ yr) that has proved useful in dating igneous rocks. The fundamentals are precisely analogous to those we have discussed for ^{234}U and ^{230}Th , with one exception. Unfortunately, Ra has no stable isotope to which one can ratio ^{226}Ra , so the assumption is made that Ra behaves as Ba (which sits directly above Ra in the periodic table), and the abundance of Ba is used to form a ratio.

Figure 3.16 shows a ^{226}Ra – ^{230}Th whole rock isochron obtained on a sequence of trachytic lavas from Longonot volcano in the Gregory Rift of Kenya. The samples represent roughly 5 km^3 of lava. The degree of igneous fractionation increases upward in the sequence, resulting in a range of whole rock compositions and Th/Ba ratios. The age of 4274 years dates this igneous differentiation and falls within the range of eruption ages,

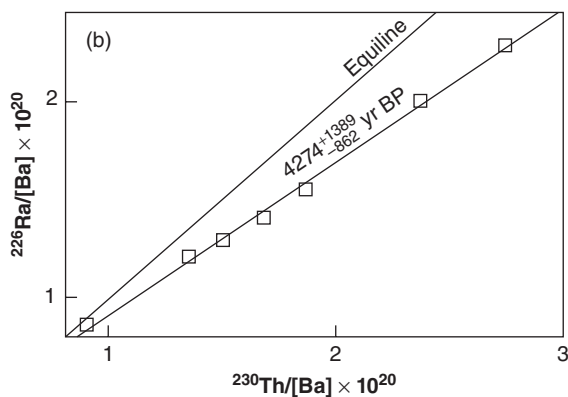


Figure 3.16 ^{226}Ra – ^{230}Th whole rock isochron on trachyte lavas from Longonot volcano in Kenya. (Source: Hawkesworth et al. (2000). Reproduced with permission of Oxford University Press.)

5650 to 3280 years BP, inferred from ^{14}C dating.

3.4.6 ^{210}Pb dating

^{210}Pb has a much shorter half-life (22.3 yrs) than the nuclides we have discussed thus far, so it is useful for much shorter time intervals. It is the great, great . . . granddaughter (six intermediate nuclides) of ^{226}Ra , but all the intermediate nuclides are quite short-lived, ^{222}Rn , with a half-life of 3 days being the longest-lived. Its existence in the decay chain is significant because it is a noble gas and hence can diffuse out of soils and into the atmosphere. ^{210}Pb , produced by decay of atmospheric radon, will quickly be removed from the atmosphere by absorption onto aerosols and find its way into sediments, either through wet or dry deposition. Consequently, young sediments commonly have ^{210}Pb activities in excess of that in equilibrium with its long-lived parent, ^{226}Ra . The decay of this “excess” or “unsupported” ^{210}Pb thus provides a convenient means of dating young sediments (including snow and ice), that is, those less than 100–200 years old. Because its abundance is low, its activity is always determined by counting rather than mass spectrometry. Because its pathway into sediments can differ from that of stable Pb, it is not useful to ratio ^{210}Pb to one of the other isotopes of Pb.

We can write an equation analogous to the one equation we wrote for unsupported ^{230}Th (3.25):

$$(^{210}\text{Pb})_u = (^{210}\text{Pb})^0 e^{-\lambda t} \quad (3.34)$$

We might continue by using the same simple approach we used in the case of ^{230}Th dating of a manganese nodule, but there are several reasons why we should not. First, detrital sediments, unlike chemical ones such as manganese nodules, inevitably undergo compaction as they accumulate, meaning that density will increase downward in a core and hence the sedimentary mass above a given depth, say z_i , will not be a linear function of z . Thus, in attempting to calculate ages or sedimentation rates of accumulating detrital sediments, we need to correct for compaction by measuring and take account of down-core changes in density (or, equivalently, porosity). To correct for compaction, we replace depth, z , with a function called mass-depth, which has units of depth per unit area. We define Δm_i as the mass of sediment in the core in depth interval Δz_i and the mass-depth, m_i , at depth z_i as the total mass (per cross-sectional area of the core) above z_i .

Next, we need to think about how ^{210}Pb accumulates in sediment. In the case of the manganese nodules previously, we assumed a constant sedimentation rate and a constant flux of ^{230}Th to the surface of the nodule. These might be reasonable assumptions in this case, because the process of Mn nodule growth is one of chemical precipitation and adsorption and occurs in the remote areas of the deep ocean where environmental conditions are constant. Accumulation of ^{210}Pb in detrital sediments in lakes and coastal areas might not meet those conditions. For example, if the ^{210}Pb in the sediment derived entirely or nearly so from dry or wet deposition of atmospheric ^{210}Pb on the surface of the lake, we might assume that the flux of ^{210}Pb to the sediment surface is constant and independent of the rate at which sedimentary mass accumulates. This is known as the *Constant Flux* or *Constant Rate of Supply* model. Alternatively, if Pb absorbed onto sedimentary particles carried into the lake by streams was the primary ^{210}Pb source, we might assume that these particles always had the same concentration of ^{210}Pb . This is known as the *Constant Activity*

or *Constant Initial Concentration* model. Yet another possibility is that the sedimentary flux (mass accumulation rate) is constant, but the Pb flux varies, known as the *Constant Sedimentation* model (Sanchez-Cabeza and Ruiz-Fernandez, 2012). Yet another possibility is the *Constant Flux–Constant Sedimentation* model. This is the simplest model because it predicts a simple exponential decrease of activity with depth, once compaction has been accounted for. The advantages and disadvantages of these approaches have been discussed by a number of workers over the years (e.g., Appleby and Oldfield, 1983; Sanchez-Cabeza and Ruiz-Fernandez, 2012). Let's briefly review them in a bit more detail.

In the *Constant Activity* model, the activity at the surface, $(^{210}\text{Pb})^0$, is constant, so that the activity in any layer i at depth is given by eqn. 3.34, and the age of that layer may be calculated as:

$$t_i = \frac{1}{\lambda} \ln \frac{(^{210}\text{Pb})^0}{(^{210}\text{Pb})_i} \quad (3.35)$$

(In this and subsequent equations we will explicitly state we are interested only in unsupported activity and we will drop the u subscript.) The initial activity can be found by regressing $\ln(^{210}\text{Pb})$ versus (compaction-corrected) depth and finding the intercept at 0 depth.

In the *Constant Flux* model, we assume that the flux of ^{210}Pb to the surface of the sediment, f , is constant and independent of the mass accumulation rate, r . Thus, at the time of deposition of layer i , the total accumulated ^{210}Pb in the sediment column below it, $A(0)$, will be constant, where $A(0)$ is defined as:

$$A(0) = \int_0^\infty (^{210}\text{Pb}) dm \quad (3.36)$$

where m is mass-depth as defined above. The total activity below layer i is then:

$$A(i) = \int_{m_i}^\infty (^{210}\text{Pb})_i dm_i \quad (3.37)$$

It follows that:

$$A(i) = A(0) e^{-\lambda t_i} \quad (3.38)$$

and the age of layer i is then:

$$t_i = \frac{1}{\lambda} \ln \frac{A(0)}{A(i)} \quad (3.39)$$

This model requires determining the entire inventory of ^{210}Pb in the core. In practice, this would mean over the last 100–200 years (depending on the sensitivity of the analytical method used). If the this entire interval is not sampled, it may be possible to extrapolate to the depth where $(^{210}\text{Pb})_u$ is 0.

In the *Constant Flux–Constant Sedimentation* model, the initial concentration is assumed to be constant and activity will decrease exponentially with mass-depth. With r as the mass accumulation rate and m as mass-depth, in a manner analogous to Eqn. 3.27, we let $t = m/r$, we have:

$$(^{210}\text{Pb}) = (^{210}\text{Pb})^0 e^{-\lambda_{210}m/r} \quad (3.40)$$

Thus we would expect the unsupported ^{210}Pb to decay exponentially with depth. Taking the log of both sides, we have:

$$\ln (^{210}\text{Pb})_i = \ln (^{210}\text{Pb})^0 + \frac{-\lambda_{210}}{r} m_i \quad (3.41)$$

Equation 3.40 is the equation of a straight line on a plot of $\ln (^{210}\text{Pb})$ versus mass-depth, where $\ln (^{210}\text{Pb})^0$ is the intercept and $-\lambda_{210}/r$ is the slope. Applying linear regression to the data in this form, we can determine both the slope and the intercept. From the slope, we can easily solve for r , the mass accumulation rate.

Let's consider an example from Sanchez-Cabeza and Ruiz-Fernandez (2012) based on the data of Ruiz-Fernandez (2010). Figure 3.17 shows the measured unsupported or excess ^{210}Pb as function of mass and mass-depth. The data clearly do not show a simple exponential decrease in depth and suggest at least two times when sedimentation rates changed significantly. Using the constant flux model, Sanchez-Cabeza and Ruiz-Fernandez (2012) date the changes to about 1972 and 1930. Breaking the core into three sections applying the constant flux-constant sedimentation model to each Sanchez-Cabeza and Ruiz-Fernandez (2012) calculated mass accumulation rates of 0.66, 0.22, and 0.11 g/cm²-yr for the upper, middle, and lower sections of the core. Ruiz-Fernandez et al. (2011) attribute these changes in sedimentation rates to significant changes in land use, demographic changes and channelization of the Tehuantepec River over this time.

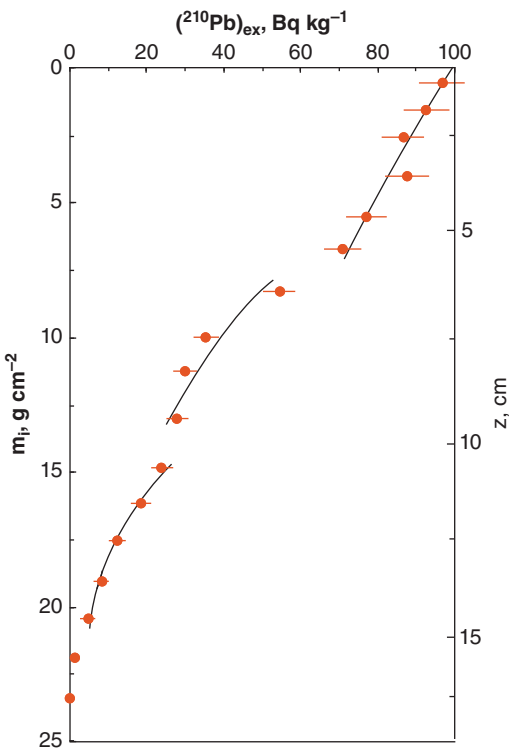


Figure 3.17 Unsupported ^{210}Pb activity measured on sediment samples from Tehuantepec Gulf, Mexico as a function of mass depth (depth is shown on the right). Three mass accumulation rates for three parts of the core calculated using the constant flux-constant sedimentation model are shown as solid lines. Data from Ruiz-Fernandez et al. (2009); model from Sanchez-Cabeza and Ruiz Fernandez (2012).

3.4.7 ^{210}Po - ^{210}Pb dating

^{210}Pb , β -decays through ^{210}Bi ($t_{1/2} = 5$ days) to ^{210}Pb , which then α -decays to ^{206}Pb with a half-life of 138.4 days or 0.379 years, sufficiently short that it has few geological applications. It has proved useful in dating unobserved submarine eruptions when those eruptions occurred shortly before sample collection. ^{210}Po is quite volatile and appears to be nearly quantitatively lost through degassing during eruption (probably as halide species such as PoCl_3). We can write the following equation:

$$\frac{(^{210}\text{Po})}{(^{210}\text{Pb})} = (1 - e^{-\lambda_{210}\text{Po}t}) + \frac{(^{210}\text{Po})^0}{(^{210}\text{Pb})} e^{-\lambda_{210}\text{Po}t} \quad (3.42)$$

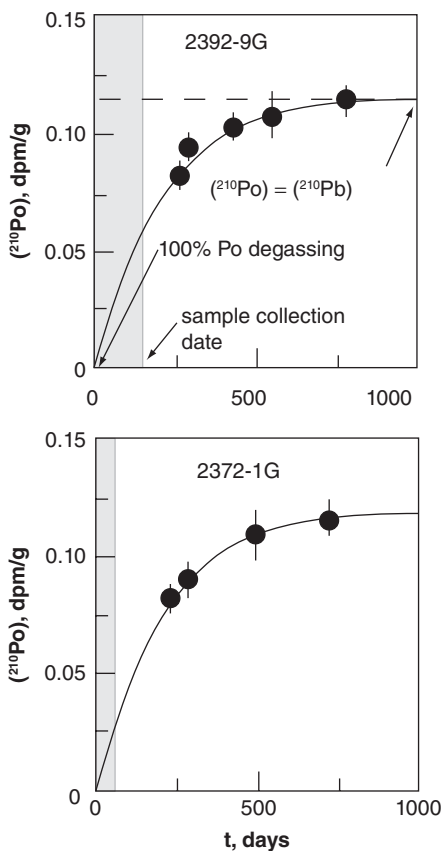


Figure 3.18 Measured ^{210}Po activities as a function of time for two samples from the East Pacific Rise. A curve through the data shows the best fit assuming $(^{210}\text{Po})^0 = 0$. The intersection gives the maximum age; the collection date gives the minimum age. (Source: Rubin et al. (1994). Reproduced with permission of Nature Publishing Group.)

To determine t_0 , the eruption age, we need to know $(^{210}\text{Po}/^{210}\text{Pb})^0$, the initial polonium-lead disequilibrium, and we do not. A simple assumption is that it is 0, which corresponds to complete degassing. An age calculated on this assumption will be a maximum. Rubin et al. (1994; 1998) made a series of measurements of (^{210}Pb) over a period of years following sample collection, then using non-linear regression to fit the data under the assumption that $(^{210}\text{Po}/^{210}\text{Pb})^0 = 0$. The minimum age is, of course, the date of sample collection, but Rubin et al. (1994) considered the most likely “eruption window” corresponded to 75–100% degassing of Po. Figure 3.18 shows the data for two samples

collected from 9°N on the East Pacific Rise in 1991 and analyzed in this way. The results in these cases indicate the eruptions occurred within 3–4 months prior to collection. Interesting, these samples were collected from the same area about a month apart, yet their “eruption windows” don’t overlap, suggesting two separate eruptions occurred in the area. Subsequently, several other recent eruptions, most recently in 2005–2006, occurred in this area. Po dating of samples collected after that event also suggested several eruptions occurred over a period of 6 months or so (Tolstoy et al., 2006).

NOTES

1. In 8-fold coordination, the effective ionic radius of U^{4+} is 1.00 Å. In zircon, a mineral which highly C, U, U is in 8-fold coordination. This is probably a pretty good indication that 8-fold coordination is the preferred configuration. The figure for 6-fold coordination is given for comparison to other radii, which have been for 6-fold coordination. Th has a radius of 1.05 Å in 8-fold coordination.
2. The uncertainty results from the mobility of U. The CI carbonaceous chondrites experienced mild alteration in hydrous conditions on the parent body. U was mobilized under these conditions and thus the U/Th ratio varies in these meteorites. For this reason, they cannot be used to precisely determine the U/Th ratio of the Solar System and the Earth.
3. In principle, a system will approach equilibrium asymptotically, and will only achieve equilibrium after an infinite amount of time. In practice, an effective equilibrium is achieved when the difference between the measured ratio of parent to daughter is less than the analytical uncertainty of the measurement. This typically will occur after a maximum of 5–10 half-lives of the nuclide with the shortest half-life.
4. The SI, and therefore official, unit of radioactivity is the Becquerel (abbreviated Beq), and is equal to one disintegration per second. An older and still used unit is the Curie (abbreviated Ci) equal to 3.7×10^{10} disintegrations per second. Because concentrations of these elements in nature are generally low, activity is often expressed in disintegrations per minute (dpm).

5. The ratio is uniform in space, but there is evidence to suggest it has varied slightly with time, particularly between glacial and interglacial periods.
6. In the case of ^{238}U and ^{234}U the α energies are quite similar (4.2 and 4.7 MeV). Interestingly,

the energies of α particles are approximately inversely proportional to half-life. From our discussion of α decay, you should be able to surmise why.

REFERENCES

- Amelin, Y., Kaltenbach, A., Iizuka, T., Stirling, C. H., Ireland, T. R., Petaev, M. and Jacobsen, S. B. 2010. U-Pb chronology of the Solar System's oldest solids with variable $^{238}\text{U}/^{235}\text{U}$. *Earth and Planetary Science Letters*, 300: 343–350, doi: 10.1016/j.epsl.2010.10.015.
- Appleby, P. G. and Oldfield, F. 1983. The assessment of ^{210}Pb data from sites with varying sediment accumulation rates. *Hydrobiologia*, 103: 29–35, doi: 10.1007/bf00028424.
- Bard, E., Hamelin, B., Fairbanks, R. G. and Zindler, A. 1990. Calibration of the ^{14}C timescale over the past 30,000 years using mass spectrometric U-Th ages from Barbados corals. *Nature*, 345: 405–410.
- Black, S., MacDonald, R. and Kelly, M. R. 1997. Crustal origin for peralkaline rhyolites from Kenya: Evidence from U-series disequilibria and Th-isotopes. *Journal of Petrology*, 38: 277–297, doi: 10.1093/petroj/38.2.277.
- Bowring, S. A., Williams, I. S. and Compston, W. 1989. 3.96 Ga gneisses from the Slave province, Northwest Territories, Canada. *Geology*, 17: 971–975.
- Cheng, H., Edwards, R. L., Hoff, J., Gallup, C. D., Richards, D. A. and Asmerom, Y. 2000. The half-lives of uranium-234 and thorium-230. *Chemical Geology*, 169: 17–33, doi: 10.1016/S0009-2541(99)00157-6.
- Chiu, T.-C., Fairbanks, R. G., Mortlock, R. A., Cao, L., Fairbanks, T. W. and Bloom, A. L. 2006. Redundant $^{230}\text{Th}/^{234}\text{U}/^{238}\text{U}$, $^{231}\text{Pa}/^{235}\text{U}$ and ^{14}C dating of fossil corals for accurate radiocarbon age calibration. *Quaternary Science Reviews*, 25: 2431–2440, doi: 10.1016/j.quascirev.2006.01.025.
- Compston, W. and Pidgeon, R. T. 1986. Jack Hills, evidence of more very old detrital zircons in Western Australia. *Nature*, 321: 766–769.
- Edwards, R. L., Chen, J. H., Ku, T.-L. and Wasserburg, G. J. 1987. Precise timing of the last interglacial period from mass spectrometric determination of thorium-230 in corals. *Science*, 236: 1547–1553, doi: 10.1126/science.236.4808.1547.
- Edwards, R. L., Cheng, H., Murrell, M. T. and Goldstein, S. J. 1997. Protactinium-231 dating of carbonates by thermal ionization mass spectrometry: implications for quaternary climate change. *Science*, 276: 782–786, doi: 10.1126/science.276.5313.782.
- Fairbanks, R. G., Mortlock, R. A., Chiu, T.-C., Cao, L., Kaplan, A., Guilderson, T. P., et al. 2005. Radiocarbon calibration curve spanning 0 to 50,000 years BP based on paired $^{230}\text{Th}/^{234}\text{U}/^{238}\text{U}$ and ^{14}C dates on pristine corals. *Quaternary Science Reviews*, 24: 1781–1796, doi: 10.1016/j.quascirev.2005.04.007.
- Faure, G., 1986. *Principles of Isotope Geology*, 2nd edn, New York: John Wiley & Sons, 589 p.
- Goldmann, A., Brennecke, G. A., Noordmann, J., Weyer, S. and Wadhwa, M. 2013. $^{238}\text{U}/^{235}\text{U}$ of the Earth and the Solar System. *Mineralogical Magazine*, 77: 1118, doi: 10.1180/minmag.2013.077.5.1.
- Grün, R., Aubert, M., Hellstrom, J. and Duval, M. 2010. The challenge of direct dating old human fossils. *Quaternary International*, 223: 224, 87–93, doi: 10.1016/j.quaint.2009.10.005.
- Hawkesworth, C. J., Blake, S., Evans, P., Hughes, R., MacDonald, R., Thomas, L. E., et al. 2000. Time scales of crystal fractionation in magma chambers – Integrating physical, isotopic and geochemical perspectives. *Journal of Petrology*, 41: 991–1006, doi: 10.1093/petrology/41.7.991.
- Hiess, J., Condon, D. J., McLean, N. and Noble, S. R. 2012. $^{238}\text{U}/^{235}\text{U}$ systematics in terrestrial uranium-bearing minerals. *Science*, 335: 1610–1614, doi: 10.1126/science.1215507.
- Huh, C.-A. and Ku, T.-L. 1984. Radiochemical observations on manganese nodules from three sedimentary environments in the north Pacific. *Geochim. Cosmochim. Acta*, 48: 951–964.
- Ivanovich, M., Latham, A. G. and Ku, T.-L. 1992. Uranium-series disequilibrium applications on geochronology. In: *Uranium-Series Disequilibrium Applications to Earth, Marine and Environmental Sciences*, 2nd edn. Ivanovich, M. and Harmon, R. S. (eds). Oxford: Oxford University Press, pp. 62–94.
- Jaffey, A. H., Flynn, K. F., Glendenin, L. E., Bentley, W. C. and Essling, A. M. 1971. Precision measurement of the half-lives and specific activities of ^{235}U and ^{238}U . *Physical Review C*, 4: 1889–1906.
- Krogh, T. E. 1982. Improved accuracy of U-Pb zircon ages by the creation of more concordant systems using an air abrasion technique. *Geochimica et Cosmochimica Acta*, doi: 46:637–649, 10.1016/0016-7037(82)90165-x.
- Lahtinen, R. and Nironen, M. 2010. Paleoproterozoic lateritic paleosol-ultra-mature/mature quartzite-meta-arkose successions in southern Fennoscandia – intra-orogenic stage during the Svecofennian orogeny. *Precambrian Research*, 183: 770–790, doi: 10.1016/j.precamres.2010.09.006.
- Ludwig, K. R. 1998. On the Treatment of Concordant Uranium-Lead Ages. *Geochimica et Cosmochimica Acta*, 62: 665–676, doi: 10.1016/S0016-7037(98)00059-3.

- Mattinson, J. M. 2005. Zircon U-Pb chemical abrasion (“CA-TIMS”) method: Combined annealing and multi-step partial dissolution analysis for improved precision and accuracy of zircon ages. *Chemical Geology*, 220: 47–66, doi: 10.1016/j.chemgeo.2005.03.011.
- Mattinson, J. M. 2010. Analysis of the relative decay constants of ^{235}U and ^{238}U by multi-step CA-TIMS measurements of closed-system natural zircon samples, *Chemical Geology*, 275: 186–198, doi: 10.1016/j.chemgeo.2010.05.007.
- Peltier, W. R. and Fairbanks, R. G. 2006. Global glacial ice volume and Last Glacial Maximum duration from an extended Barbados sea level record. *Quaternary Science Reviews*, 25: 3322–3337, doi: 10.1016/j.quascirev.2006.04.010.
- Pike, A. W. G., Hoffmann, D. L., García-Diez, M., Pettitt, P. B., Alcolea, J., De Balbín, R., et al. 2012. U-Series Dating of Paleolithic Art in 11 Caves in Spain. *Science*, 336: 1409–1413, doi: 10.1126/science.1219957.
- Rasmussen, B., Fletcher, I. R., Muhling, J. R. and Wilde, S. A. 2010. *In situ* U-Th-Pb geochronology of monazite and xenotime from the Jack Hills belt: Implications for the age of deposition and metamorphism of Hadean zircons. *Precambrian Research*, 180: 26–46, doi: 10.1016/j.precamres.2010.03.004.
- Reiners, P. W. and Brandon, M. T. 2006. Using thermochronology to understand orogenic erosion. *Annual Review of Earth and Planetary Sciences*, 34: 419–466, doi: 10.1146/annurev.earth.34.031405.125202.
- Rubin, K. H., Macdougall, J. D. and Perfit, M. R. 1994. ^{210}Po - ^{210}Pb dating of recent volcanic eruptions on the sea floor. *Nature*, 368: 841–844.
- Rubin, K. H., Smith, M. C., Perfit, M. R., Christie, D. M. and Sacks, L. F. 1998. Geochronology and geochemistry of lavas from the 1996 North Gorda Ridge eruption. *Deep Sea Research Part II*, 45: 2571–2597, doi: 10.1016/S0967-0645(98)00084-8.
- Ruiz-Fernández, A. C., Hillaire-Marcel, C., de Vernal, A., Machain-Castillo, M. L., Vásquez, L., Ghaleb, B., et al. 2009. Changes of coastal sedimentation in the Gulf of Tehuantepec, South Pacific Mexico, over the last 100 years from short-lived radionuclide measurements. *Estuarine, Coastal and Shelf Science*, 82: 525–536, doi: 10.1016/j.ecss.2009.02.019.
- Sanchez-Cabeza, J. A. and Ruiz-Fernández, A. C. 2012. ^{210}Pb sediment radiochronology: An integrated formulation and classification of dating models. *Geochimica et Cosmochimica Acta*, 82: 183–200, doi: 10.1016/j.gca.2010.12.024.
- Steiger, R. H. and Jäger, E. 1977. Subcommission on geochronology: conventions on the use of decay constants in geochronology and cosmochronology. *Earth and Planetary Science Letters*, 36: 359–362.
- Stirling, C. H., Andersen, M. B., Potter, E.-K. and Halliday, A. N. 2007. Low-temperature isotopic fractionation of uranium. *Earth and Planetary Science Letters*, 264: 208–225, doi: 10.1016/j.epsl.2007.09.019.
- Tera, F. and Wasserburg, G. J. 1972. U-Th-Pb systematics in three Apollo 14 basalts and the problem of initial Pb in lunar rocks. *Earth and Planetary Science Letters*, 14: 281–304, doi: 10.1016/0012-821X(72)90128-8.
- Tolstoy, M., Cowen, J. P., Baker, E. T., Fornari, D. J., Rubin, K. H., Shank, T. M., et al. 2006. A sea-floor spreading event captured by seismometers. *Science*, 314: 1920–1922, doi: 10.1126/science.1133950.
- Vazquez, J. A. and Reid, M. R. 2004. Probing the accumulation history of the voluminous toba magma. *Science*, 305: 991–994, doi: 10.1126/science.1096994.
- Vervoort, J. D., White, W. M., Thorpe, R. I. and Franklin, J. M. 1993. Postmagmatic thermal activity in the Abitibi Greenstone Belt, Noranda and Matagami Districts: evidence from whole rock Pb isotope data. *Economic Geology*, 88: 1598–1614.
- Wetherill, G. W. 1956. Discordant U-Pb ages. *Transactions of the American Geophysical Union*, 37: 320.
- Weyer, S., Anbar, A. D., Gerdes, A., Gordon, G. W., Algeo, T. J. and Boyle, E. A. 2008. Natural fractionation of ^{238}U / ^{235}U . *Geochimica et Cosmochimica Acta*, 72: 345–359, doi: 10.1016/j.gca.2007.11.012.
- Wilde, S. A., Valley, J. W., Peck, W. H. and Graham, C. M. 2001. Evidence from detrital zircons for the existence of continental crust and oceans on the Earth 4.4 Gyr ago, *Nature*, 409: 175–178.

SUGGESTIONS FOR FURTHER READING

- Blichert-Toft, J., Zanda, B., Ebel, D. S. and Albarède, F. 2010. The Solar System primordial lead. *Earth and Planetary Science Letters*, 300: 152–163, doi: 10.1016/j.epsl.2010.10.001.
- Dickin, A. 1995. *Radiogenic Isotope Geochemistry*. Cambridge: Cambridge University Press.
- Kirchner, G. 2011. ^{210}Pb as a tool for establishing sediment chronologies: examples of potentials and limitations of conventional dating models. *Journal of Environmental Radioactivity*, 102: 490–494, doi: 10.1016/j.jenvrad.2010.11.010.
- Volpe, A. M. and Hammond, P. E. 1991. ^{238}U - ^{230}Th - ^{226}Ra disequilibria in young Mount St Helens rocks: time constraint for magma formation and crystallization, *Earth and Planetary Science Letters*, 107: 475–486.

PROBLEMS

- Assuming present ratio of ^{238}U to ^{235}U in the Earth is 137.82, what was this ratio 1.7 billion years ago when the Oklo natural reactor was operating?

2. Derive Eqn. 3.6.
3. The following were measured on whole rock samples from the Seminoe Mountains of Wyoming. Plot the data on an isochron diagram and calculate the age and errors on the age. Assume that the errors on both isotope ratios are 0.1% and that there is a 50% correlation in the errors.

$^{206}\text{Pb}/^{204}\text{Pb}$	$^{207}\text{Pb}/^{204}\text{Pb}$
30.09	18.03
31.49	18.30
32.02	18.40
32.20	18.43
34.04	18.86
36.80	19.41

4. The following data were reported on zircons separated from a Paleozoic granite that gave a Rb-Sr age of 542 million years. The granite is located in Archean terrane that was reactivated in the early Paleozoic/late Precambrian. Calculate the age using a concordia diagram. You should obtain both a lower and an upper intercept with concordia. What is your interpretation of the ages?

(Hint: you will need to correct for the initial Pb isotopic compositions shown here).

Zircon	$^{206}\text{Pb}/^{204}\text{Pb}$	$^{238}\text{U}/^{204}\text{Pb}$	$^{207}\text{Pb}/^{204}\text{Pb}$	$^{235}\text{U}/^{204}\text{Pb}$
1	796	6800	88.46	49.3
2	1563	6649	257.1	48.2
3	1931	6432	340.1	46.6
4	2554	6302	481.7	45.7
5	2914	6250	560.3	45.3
Initial ratios	16.25		15.51	

5. The following data were reported for zircons from the felsic norite of the Sudbury Intrusive complex. Using these data, calculate the crystallization age and the error on the age of the intrusion. Also determine the age of the lower intercept.

Sample	Fraction	$^{207}\text{Pb}^*/^{235}\text{U}$	2σ	$^{206}\text{Pb}^*/^{238}\text{U}$	2σ	Error Correl.
DWD5538	eq, 1 h HF	0.4385	0.0036	0.028	0.0001	0.61098
DWD5537	frag, 5h Hf	3.1073	0.0096	0.1991	0.0006	0.92907
AD5	eq, 1h HF-HCl	2.4352	0.0205	0.1561	0.0013	0.99179
AD4	anneal 2h HF-HCl	2.8698	0.024	0.1841	0.0015	0.99165
AD3	anneal 2h HF-HCl	4.0724	0.0189	0.2614	0.0012	0.97925
AD1	anneal 1h HF-HCl	3.0066	0.0093	0.1932	0.0004	0.84911
AD2	anneal 1h HF-HCl	2.0764	0.008	0.1343	0.0004	0.83521

6. The ^{210}Pb data shown were measured on a core from coastal pond. Determine the sedimentation rate.

Depth, cm	(^{210}Pb) , pCi
0–2	3.9
4–6	3.7
8–10	3.3
14–16	2.6
18–20	2.2
24–26	1.8
28–30	1.8

7. Pike et al. (2012) measured the following activity ratios on flowstone covering two examples of Paleolithic art from the El Castillo cave in northern Spain. Calculate the ages of the two flowstones.

Sample	$(^{234}\text{U}/^{238}\text{U})$	$(^{230}\text{Th}/^{234}\text{U})$
O-87	2.7432	0.29052
O-69	2.7072	0.27748

8. Given the following data on a Mt St Helens lava flow, calculate the age. You may use either simple linear regression in obtaining your solution, or the Isoplot Excel plug-in.

	$(^{238}\text{U}/^{232}\text{Th})$	$(^{230}\text{Th}/^{232}\text{Th})$
Whole rock	1.245	1.184
Plagioclase	1.128	1.126
Magnetite	1.316	1.205
Groundmass	1.335	1.214

Chapter 4

Geochronology III: other dating methods

4.1 COSMOGENIC NUCLIDES

4.1.1 Cosmic rays in the atmosphere

As the name implies, cosmogenic nuclides are produced by cosmic rays colliding with atoms in the atmosphere and the surface of the solid Earth. Nuclides so created may be stable or radioactive. Radioactive cosmogenic nuclides, like the U decay series nuclides, have half-lives sufficiently short that they would not exist in the Earth if they were not continually produced. Assuming that the production rate is constant through time, then the abundance of a cosmogenic nuclide in a reservoir isolated from cosmic ray production is simply given by:

$$N = N_0 e^{-\lambda t} \quad (4.1)$$

Hence, if we know N_0 and measure N , we can calculate t . Table 4.1 lists the radioactive cosmogenic nuclides of principal interest. As we shall see, cosmic ray interactions can also produce rare stable nuclides, and their abundance can also be used to measure geologic time.

A number of different nuclear reactions create cosmogenic nuclides. “Cosmic rays” are high-energy (several GeV up to 10^{19} eV!) atomic nuclei, mainly of H and He (because these constitute most of the matter in the universe), but nuclei of all the elements have been recognized. To put these kinds of energies in perspective, the previous generation of accelerators for physics experiments, such as the Cornell Electron Storage Ring produce

energies in the tens of GeV (10^{10} eV); while CERN’s Large Hadron Collider, mankind’s most powerful accelerator, located on the Franco-Swiss border near Geneva produces energies of ~ 10 TeV range (10^{13} eV). A significant fraction of cosmic rays originates in the Sun, although these are mainly of energies too low to generate cosmogenic nuclides. The origin of the remainder is unclear; most likely originate in supernovae or similar high-energy environments in the cosmos.

The cosmic ray flux decreases exponentially with depth in the atmosphere as these particles interact with matter in the atmosphere. This observation has an interesting history. Shortly after the discovery of radioactivity, investigators noticed the presence of radiation even when no known sources were present. They reasonably surmised that this resulted from radioactivity in the Earth. In 1910, an Austrian physicist named Victor Hess carried his detector (an electroscope consisting of a pair of charged gold leaves: the leaves would be discharged and caused to collapse by the passage of charged particles) aloft in a balloon. To his surprise, the background radiation increased as he went up rather than decreased. It thus became clear that this radiation originated from outside, rather than inside, the Earth.

The primary reaction that occurs when cosmic rays encounter the Earth is *spallation*, in which a nucleus struck by a high energy particle shatters into two or more pieces, including stable and unstable nuclei, as well as protons

Table 4.1 Data on cosmogenic nuclides.

Nuclide	Half-life, years	Decay constant, yr^{-1}
^{14}C	5730	1.209×10^{-4}
^3H	12.33	5.62×10^{-2}
^{10}Be	1.500×10^6	4.62×10^{-7}
^{26}Al	7.16×10^5	9.68×10^{-5}
^{36}Cl	3.08×10^5	2.25×10^{-6}
^{32}Si	276	2.51×10^{-2}

and neutrons. Short-lived particles such as muons, pions, and so on are also created. The interaction of a cosmic ray with a nucleus sets off a chain reaction of sorts as the secondary particles and nuclear fragments, which themselves have very high energies then strike other nuclei producing additional reactions of lower energy. ^{14}C is actually produced primarily by reactions with secondary particles, mainly by the $^{14}\text{N}(\text{n}, \text{p})^{14}\text{C}$ reaction involving relatively slow neutrons.

4.1.2 ^{14}C dating

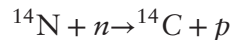
Carbon-14 is by far the most familiar and useful of the cosmogenic dating schemes. Its usefulness results from its relatively short half-life, a relatively high production rate, and the concentration of carbon in biological material. The short half-life has the advantage of producing accurate dates of young (geologically speaking) materials and events and easy determination by counting the decays. The traditional method of ^{14}C determination is counting of the β rays produced in its decay. ^{14}C decays without emitting a gamma, which is unfortunate because γ -rays are more readily detected. Difficulties arise because the rate of decay of a reasonable sample of carbon (a few grams) is low. One of the first problems that had to be solved was eliminating “counts” that arose from cosmic rays rather than the decay of the carbon sample. This is done with a combination of shielding and “coincidence counting.”¹ Counting techniques make use of either liquid scintillation counters or gas proportional counters. A gas proportional counter is simply a metal tube containing a gas, with a negatively charged wire (the anode) running through it. The emitted beta particle causes ionization of the gas, and the electrons released in this way drift to the wire (the anode), producing a measurable pulse

of current. In this technique, carbon in the sample is converted to CO_2 , and purified (in some cases it is converted to methane) and then admitted into the counting chamber. Several grams of carbon are generally required. In liquid scintillation counting, the carbon is extracted from a sample and converted into CO_2 , purified, and eventually converted to benzene (C_6H_6) and mixed with a liquid scintillator (generally an organic liquid). When a carbon atom decays, the beta particle interacts with the scintillator, causing it to give off a photon, which is then detected with a photomultiplier, and the resulting electrical pulse sent to a counter. Liquid scintillation is the new and more sensitive of these two techniques and it has now largely replaced gas proportional counting. Liquid scintillation analysis can be done with less than 1 g of carbon.

In the last 30 years or so, a newer method, accelerator mass spectrometry (AMS), has been used with considerable success. Greater accuracy is achieved with considerably less sample (analysis requires a few milligrams to tens of milligrams). Initially, this work was done with accelerators built for high-energy physics experiments, but subsequently accelerators have been designed and built exclusively for radiocarbon dating. Although these instruments are expensive, there are now dozens of them in the world. While most radiocarbon dating is still done by beta counting, use of AMS is increasing.

Because of the way in which it was traditionally measured, ^{14}C is generally reported in units of *specific activity*, or disintegrations per minute per gram carbon rather than as a ratio to ^{12}C or ^{13}C (in SI units, 1 unit of specific activity is equal to $1/60 = 0.017 \text{ Beq/g C}$). Atmospheric carbon and carbon in equilibrium with the atmosphere (carbon in living plant tissue and the surface of the oceans) has a specific activity of 13.56 dpm/g. This is, in effect, the value of N_0 in Eqn. 4.1. By historical convention, radiocarbon ages are reported in years before 1950 (the year the first ^{14}C age determination; the abbreviation BP thus means not *before present*, but before 1950) and assuming a half-life of 5568 years (instead of the currently accepted value of 5730 years).

The actual reaction that produces ^{14}C is:



This is a charge exchange reaction in which the neutron gives up unit of negative charge to a proton in the nucleus and becomes a proton. The neutron involved comes from a previous interaction between a cosmic ray and a nucleus in the atmosphere; in other words, it is a *secondary* particle. As charged particles, cosmic rays interact with the Earth's magnetic field and are deflected by it (but not those with energies above 10^{14} eV). Consequently, the production rate of ^{14}C is higher at the poles. However, because the mixing time of the atmosphere is short compared to the residence time of ^{14}C in the atmosphere, the ^{14}C concentration in the atmosphere is uniform.

Can we really assume, however, that the atmosphere specific activity today is the same as in the past? From Eqn. 4.1, we can see that knowing the initial specific activity is essential if an age is to be determined. To investigate the variation of the specific activity of ^{14}C with time in the atmosphere, the specific activity of ^{14}C in wood of old trees has been examined. The absolute age of the wood is determined by counting tree rings, a procedure known as dendrochronology. The result of such studies shows that the specific activity has indeed not been constant, but has varied with time (Figure 4.1). There are a number of effects involved. Since 1945 injection of bomb-produced ^{14}C into the atmosphere has raised the specific activity. Then, over the past 200 years, the specific activity has decreased because of addition of "old" (i.e., ^{14}C -free) carbon in CO_2 produced by fossil fuel burning

(*the Suess effect*). Similar variations occurred further back in time. Indeed, between 33,000 and 45,000 years ago, atmospheric specific activity appears to have been twice what it was in 1950 (Beck et al., 2001). These changes in atmospheric specific activity almost certainly occurred as a consequence of the changing balance between CO_2 in the atmosphere and the ocean. Far more CO_2 is dissolved in the ocean, particularly in deep water, than in the atmosphere. Shifting CO_2 from the atmosphere to the ocean increases the specific activity of ^{14}C in the atmosphere. These are termed *reservoir effects*.

There are also century-scale variations in ^{14}C , known as the *deVries events* that result from variation in the cosmic ray flux that in turn result from variations in solar activity. Changes in solar activity, whose most obvious manifestation is the sunspot cycle, produce changes in the intensity of the solar wind, particles (again, mainly H and He nuclei and electrons) blown off the surface of the Sun. At the height of the sunspot cycle, the solar wind is greatly enhanced, up to a factor of 10^6 . The solar wind in turn modulates the solar magnetosphere, which deflects galactic cosmic rays at the outer edge of the solar system (the heliopause). A stronger solar wind results in few high-energy cosmic rays reaching the Earth. On longer time-scales, variation in the Earth's magnetic field also affect the cosmic ray flux and consequently cosmogenic nuclide production. As Figure 4.2 shows, as the geomagnetic field increased between 40,000 and

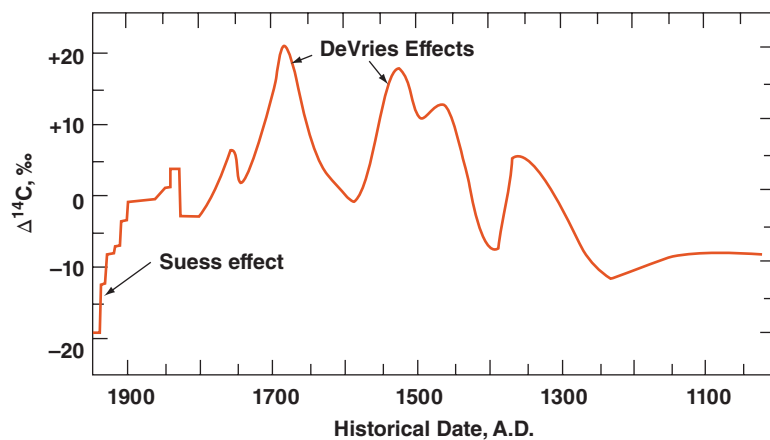


Figure 4.1 Variation of initial specific activity of ^{14}C in the past 1000 years. (Source: Faure (1986). Reproduced with permission of John Wiley & Sons.)

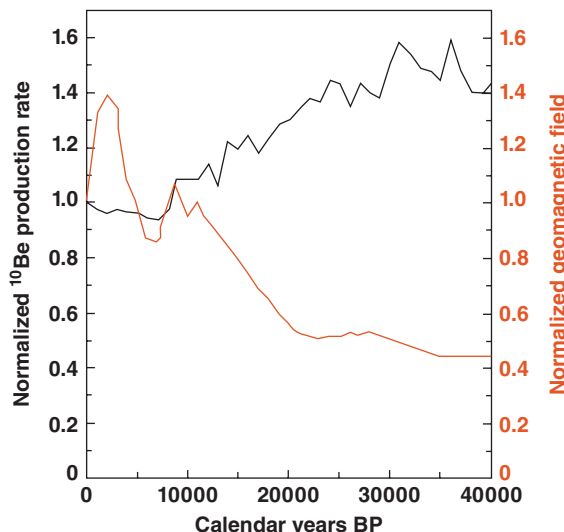


Figure 4.2 Low latitude ($<60^\circ$) production rate of ^{10}Be (black line) compared with geomagnetic field strength (red line) over the last 40,000 years. Magnetic field intensity based on paleomagnetic intensity measurements of volcanic rocks compiled by McElhinny and Senanayake (1982). ^{10}Be production rates based on Frank et al. (1997). (Source: Adapted from Bard (1998). Reproduced with permission of Elsevier.)

10,000 years ago, production of ^{10}Be at low latitudes declined (there was no apparent decline at the pole) as the increasing strength of Earth's magnetic field deflected a greater fraction of cosmic rays.

Because of these variations in the specific activity of atmospheric carbon, a correction must be applied to ^{14}C dates because of the variation in initial specific activity with time. Calibration of ^{14}C through dendrochronology has now been done over the last 11,000 years using waterlogged oaks in swamps and bogs of Germany and Ireland and bristlecone pines in the US and has been extended to 45,000 years through comparison of ^{14}C and $^{238}\text{U}/^{230}\text{Th}$ ages, for example in corals, as we'll discuss shortly. Computer programs are available for converting radiocarbon ages to calendar years, for example, the CALIB program available from the Queen's University Belfast (<http://calib.qub.ac.uk/calib/>).

The variation in initial specific activity makes the conversion from radiocarbon

ages to calendar years somewhat complex. Figure 4.3 illustrates the case of a hypothetical radiocarbon age of 3000 years BP with a 1σ uncertainty of 30 years. On the left, is shown the uncertainty histogram in gray. The pair of nearly parallel black curves encloses the uncertainty on the calibration between radiocarbon age and calendar years. The black histogram on the bottom shows the probable correspondence of calendar dates to this radiocarbon age. The irregularity of the histogram reflects the irregularity of the calibration curve, which in turn reflects the variation in reservoir effects, cosmic ray flux, and so on mentioned previously. In this case, the 2σ uncertainty encompasses a range of calendar dates from 1390 BC to 1130 BC.

On longer time scales, carbon-14 ages have been calibrated to U-Th ages of carbonates, primarily corals and speleothems, as we discussed in Chapter 3. Figure 4.4 shows the data and calibration curve of Fairbanks et al. (2005), which extends the calibration back 45,000 years. As may be seen in this figure, carbon-14 and U-Th ages diverge increasing backward in time, due to the reservoir and magnetic field effects discussed above. At 45,000 years, C-14 ages are almost 4000 years too young. A web-based radiocarbon to calendar age conversion for this calibration is available at www.radiocarbon.LDEO.columbia.edu/.

Most of the applications of ^{14}C dating are probably in archaeology, but geological applications include volcanology (^{14}C dating is an important part of volcanic hazard assessment), Holocene stratigraphy, paleoclimatology, and oceanography. It is also used extensively in paleoseismology to determine the time of prehistoric earthquakes, and thus part of earthquake hazard assessment. Knowing the frequency of past earthquakes is useful in predicting future earthquake probabilities. In oceanography, the age of bottom water (age meaning the time since the water last equilibrated with the atmosphere) can be determined with ^{14}C . Typically, this age is of the order of 1000 yrs.

One oceanographic application, which utilizes accelerator mass spectrometry, is the determination of paleo-bottom water ages. The ice ages affected ocean circulation, but the exact nature of the effect is still uncertain. Of particular interest are the changes

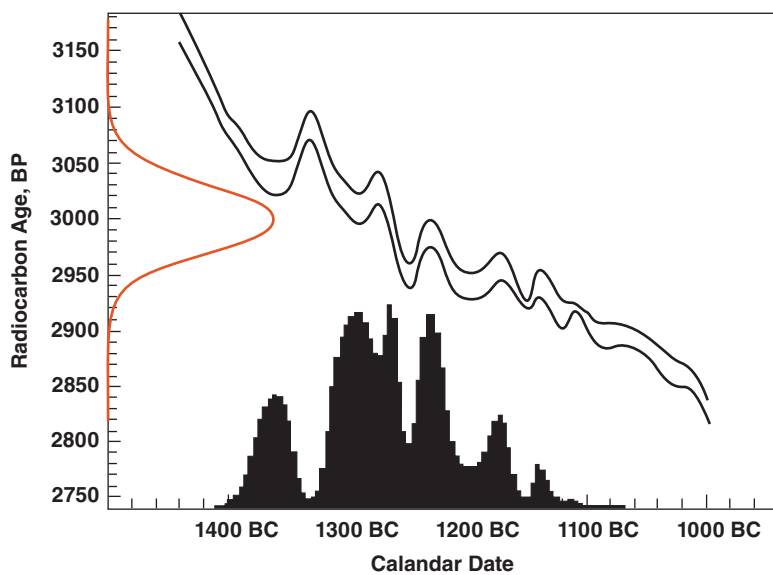


Figure 4.3 Conversion of radiocarbon dates to calendar years. The gray curve at left shows the uncertainty histogram for a radiocarbon age of 3000 ± 30 (1σ) years BP. The set of curves shows the calibration between radiocarbon age and calendar date. The black histogram at the bottom shows the probably corresponding calendar date for this radiocarbon age.

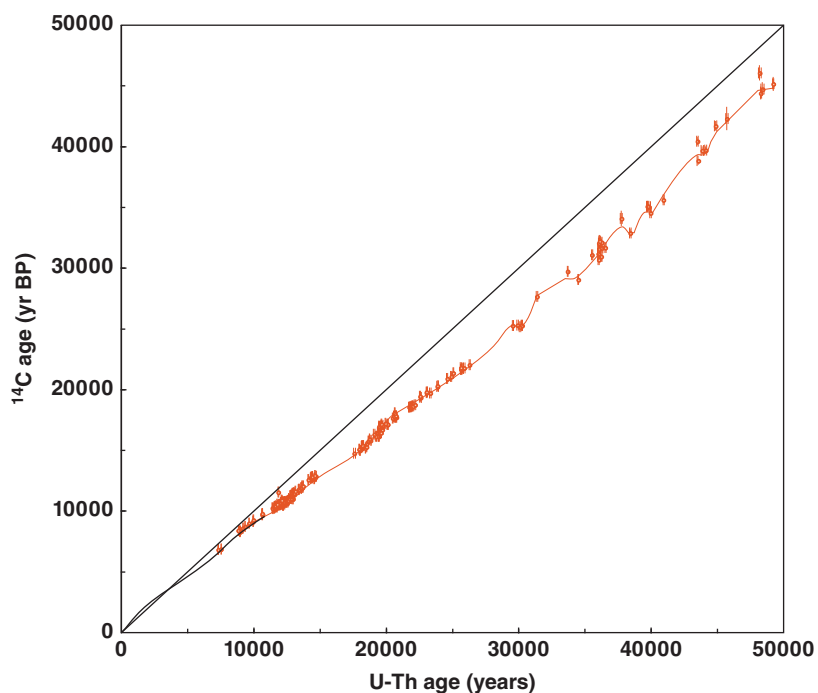


Figure 4.4 Comparison of ^{14}C and U-Th ages of Fairbanks et al. (2005) based on dating of corals from Barbados, Kiritimati Atoll in the central equatorial Pacific, and from Araki Island in the southwest Pacific. Red line is the calibration of Fairbanks et al. (2005); black line is the tree ring calibration. Data from Fairbanks et al. (2005).

in the ocean circulation pattern that occurred as the last glaciation ended. Because planktonic foraminifera live in the upper part of the ocean, which is in equilibrium with the atmosphere, one can date a sedimentary stratum by measuring ^{14}C in planktonic foraminiferal tests. Benthic foraminifera live at the bottom of the ocean, and build their tests from CO_2 dissolved in bottom water. Thus a ^{14}C date of a modern benthic foram would give the age of the bottom water. By comparing the ^{14}C ages of planktonic and benthic foraminifera, one may determine the “ages” of bottom waters in the past. This in turn reveals something of paleocirculation patterns.

4.1.3 ^{10}Be , ^{26}Al , and ^{36}Cl

We now consider some of the other nuclides produced by cosmic ray interactions with atmospheric gases. These include ^{10}Be , ^{26}Al , and ^{36}Cl . These nuclides have much longer half-lives than ^{14}C and thus are best applied to longer time-scale problems, such as Pleistocene chronology and dating of groundwater. Of these, ^{10}Be has been the most extensively utilized, for several reasons. First, its production rate is higher (10^{-2} – 10^{-3} atoms/ cm^2/sec versus 10^{-5} – 10^{-6} for ^{26}Al and ^{36}Cl). Second, it has the advantage over ^{36}Cl that, once absorbed onto clays, it is relatively immobile, and third, while a small amount of ^{36}Cl will be produced within the earth by neutron capture on ^{35}Cl (with neutrons arising from fission of U, as well as secondary neutrons produced by (α, n) reactions), there is effectively no internal “nucleogenic” production of ^{10}Be in the Earth.

^{10}Be is created by spallation reactions between cosmic rays and N and O nuclei. Since these are the most abundant nuclei in the atmosphere, the production rate of ^{10}Be is comparatively high. ^{26}Al is produced by spallation of ^{40}Ar , and ^{36}Cl is produced by $^{40}\text{Ar}(\text{p}, \alpha)^{36}\text{Cl}$ reactions (probably mainly with secondary protons). Unlike carbon, Be, Cl, and Al do not form gases under ambient conditions at the surface of the Earth,² so residence time of ^{10}Be , ^{26}Al , and ^{36}Cl in atmosphere are quite short. Once they form, they are quickly extracted from the atmosphere by rain. Since we know the cosmic ray flux varies latitudinally, we might expect latitudinal variation in, for example, the ^{10}Be production rate

and flux to the surface of the Earth. Subareal variations ^{10}Be show the expected latitudinal dependence. However, the distribution in oceans is uniform because ^{10}Be spends sufficient time in oceans that its distribution is homogenized (the residence time of Be is somewhat uncertain, but seems to be about 4000 years). Be is readily scavenged and absorbed by clay particles, both subareally and in the oceans. The concentration in soils is quite high. In the oceans ^{10}Be is extracted from seawater by adsorption on suspended clay particles. Because of its low activity, ^{10}Be is analyzed primarily by accelerator mass spectrometry. The applications include dating marine sediments, paleosols, Mn nodules, and so on.

Let's now consider some examples of how these nuclides can be used for geochronology. We will begin with ^{10}Be dating of sediments and they go on to show how ages can be improved if we use both ^{10}Be and ^{26}Al . We will then consider how ^{36}Cl and bomb-produced ^{3}H are used in hydrology.

Let's now see how ^{10}Be can be used for age determination. The relevant equation is

$$^{10}\text{Be} = ^{10}\text{Be}_0 e^{-\lambda t} \quad (4.2)$$

For simplicity, we start by assuming the flux of ^{10}Be to the sediment, f , is constant, hence,

$$[^{10}\text{Be}] \propto f e^{-\lambda t} \quad (4.3)$$

where λ is the flux of ^{10}Be to the sediment surface and the bracket denotes the number of atoms of ^{10}Be . Even if the flux is constant, the concentration of ^{10}Be in a given amount of sediment may nonetheless vary because it can be variably diluted depending on how fast other components in the sediment are deposited. In other words, we must also consider the sedimentation rate. The amount of ^{10}Be in a given amount of sediment then becomes:

$$[^{10}\text{Be}] = \frac{f}{s} e^{-\lambda t} \quad (4.4)$$

where s is the sedimentation rate. If both the flux and sedimentation rate are constant, then the depth, z , of a given horizon in the sediment is given by

$$z = s \times t \quad (4.5)$$

$$\text{and } t = \frac{z}{s} \quad (4.6)$$

We can substitute Eqn. 4.6 into 4.4 to obtain:

$$[{}^{10}\text{Be}] = \frac{f}{s} e^{-\lambda z/s} \quad (4.7)$$

Figure 4.5 shows some actual data from the western tropical Pacific illustrating this exponential decrease with time in ${}^{10}\text{Be}$ concentration. Taking the log of both sides, we have:

$$\ln [{}^{10}\text{Be}] = \ln \left(\frac{f}{s} \right) - \frac{\lambda}{s} z \quad (4.8)$$

From this we can see that the slope of a plot of $\ln[{}^{10}\text{Be}]$ versus depth will be inversely related to sedimentation rate (see Problem 1).

In a more general case, the sedimentation rate will not be constant, but will be a function of time. A general equation will then be

$$[{}^{10}\text{Be}] = \frac{f}{s(t)} e^{-\lambda t(z)} \quad (4.9)$$

In a sedimentary sequence such as a piston core, we do not necessarily know t (indeed, that is what we wish to determine), but we do know the depth in the core, which we know is some function of time. It is convenient then to transform Eqn. 4.8 to a function of depth rather than time:

$$[{}^{10}\text{Be}] (z) = \frac{f}{s(z)} e^{-\lambda t(z)} \quad (4.10)$$

The sedimentation rate s is simply

$$s = \frac{d(z)}{dt(z)} \quad (4.11)$$

Substituting for s and integrating, we obtain:

$$\int_0^z [{}^{10}\text{Be}] (z) dz = -\frac{f}{\lambda} (e^{-\lambda t(z)} - 1) \quad (4.12)$$

This equation in turn can be solved for $t(z)$:

$$t(z) = -\frac{1}{\lambda} \ln \left[1 - \frac{\lambda}{f} \int_0^z [{}^{10}\text{Be}] (z) dz \right] \quad (4.13)$$

The integral is simply the sum of the concentration of ${}^{10}\text{Be}$ down the core to any depth z . Like many rare radionuclides, the amount of ${}^{10}\text{Be}$ is sometimes expressed in activity rather than atoms or moles. Expressed in terms of activity, Eqn. 4.13 is:

$$t(z) = -\frac{1}{\lambda} \ln \left[1 - \frac{1}{f} \int_0^z ({}^{10}\text{Be}) (z) z \right] \quad (4.14)$$

This method has been used successfully to date sediments. However, since there are a number of ways of determining the age of young marine sediments, a more interesting application is determination of growth rates of manganese nodules, for which age determination is quite difficult.

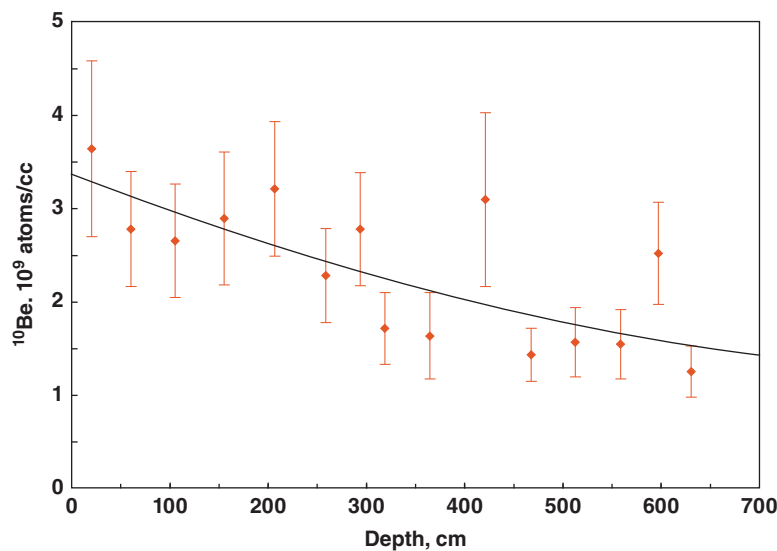


Figure 4.5 ${}^{10}\text{Be}$ as a function of depth in a sediment core from the western tropical Pacific. Black line shows the expected exponential decrease in ${}^{10}\text{Be}$ for a constant sedimentation rate. Data from Tanaka and Inoue (1979).

In the previous, we have assumed a constant production rate for ^{10}Be , but Frank et al. (1997), as we saw in Figure 4.2, derived the production rate curve by calibrating ^{10}Be dates against ^{230}Th dates in marine sediments. One can account for variation in production rate by replacing Φ in the Eqn. 4.14 with a function $\Phi(t)$ that describes this variation.

An alternative is to remove the production rate term altogether. This can be done by simultaneously using two cosmogenic nuclides. For example, ^{10}Be and ^{26}Al . In this case we can write two equations:

$$^{10}\text{Be} = ^{10}\text{Be}_0 e^{-\lambda t} \quad (4.2)$$

$$^{26}\text{Al} = ^{26}\text{Al}_0 e^{-\lambda t} \quad (4.15)$$

Dividing one by the other, we obtain

$$\frac{^{26}\text{Al}}{^{10}\text{Be}} = \left(\frac{^{26}\text{Al}}{^{10}\text{Be}} \right)_0 e^{(\lambda_{10} - \lambda_{26})t} \quad (4.16)$$

The advantage of this approach is that the initial $^{26}\text{Al}/^{10}\text{Be}$ ratio should be independent of the cosmic ray flux. Although this method is, in principle, quite attractive, it has not been applied because of the difficulty of simultaneous measurement of ^{26}Al . Exploratory studies suggest that it could be used in the future (e.g., Shibata et al., 2000).

4.1.4 Cosmogenic and bomb-produced radionuclides in hydrology

Determining the age of water in underground aquifers is an important problem because of the increasing demands placed in many parts of the world on limited water resources. A prudent policy for water resource management is to withdraw from a reservoir at a rate no greater than the recharge rate. Determination of recharge rate is thus prerequisite to wise management. Cosmogenic radionuclides are swept out of the atmosphere by rain and into the groundwater system. If we know the concentration of a radionuclide in rainwater whose initial activity is also known and if we can assume that it is not produced within the Earth or lost from solution (this is our closed system requirement), then the “age” of water in an aquifer is determined simply from Eqn. 4.1, where we define age as the time since the water left the atmosphere and entered the groundwater system. This term can be

misleading, however. As Bethke and Johnson (2008) emphasize, water may enter an aquifer at different points along a flow path; consequently water within an aquifer can be a mixture of water added to it at different times. Consequently, a short-lived radionuclide such as ^{14}C can be present and indicate one age, while a longer-lived one such as ^{36}Cl can indicate an older age. It is perhaps best to think in terms of “residence time,” the average time a molecule has resided in an aquifer.

In addition to cosmogenic production, ^3H and other radionuclides were produced in significant quantities during atmospheric thermonuclear tests between 1952 and 1963. The pulse of ^3H in precipitation during this period is illustrated in Figure 4.6. Tritium is readily detected by beta counting, and therefore bomb-produced tritium is potentially useful for tracing precipitation that fell during the 1950s and 1960s through groundwater systems. There are limitations on using it as a geochronological tool because the precipitation history of ^3H is not well known in most areas. In most cases, tritium has been used simply to distinguish pre-bomb from post-bomb waters. Older ground waters would be essentially free of atmospherically produced ^3H because of its short half-life (12.3 years), but contain some ^3H produced *in situ* by fission-generated neutrons. The usefulness of this approached has diminished significantly, however, as most of the bomb-produced tritium has now decayed.

^{14}C has been used successful for dating groundwater for decades. Since the concentration of ^{14}C in the atmosphere is uniform, its concentration in precipitation is also uniform. However, there are several problems with ^{14}C dating. The first is that ^{14}C is present in water principally as HCO_3^- and CO_3^{2-} . Both isotopic exchange reactions with carbonates in soils and the aquifer matrix and precipitation and dissolution of carbonates will alter the concentration of ^{14}C in groundwater. This, of course, violates the closed-system requirement. A second disadvantage is its relatively short half-life, which restricts the use of ^{14}C dating to waters less than 25,000 years old. While this is sufficient for shallow, localized groundwater systems, regional systems often contain much older water.

In contrast to ^{14}C , ^{36}Cl is essentially conservative in groundwater solutions, and has a

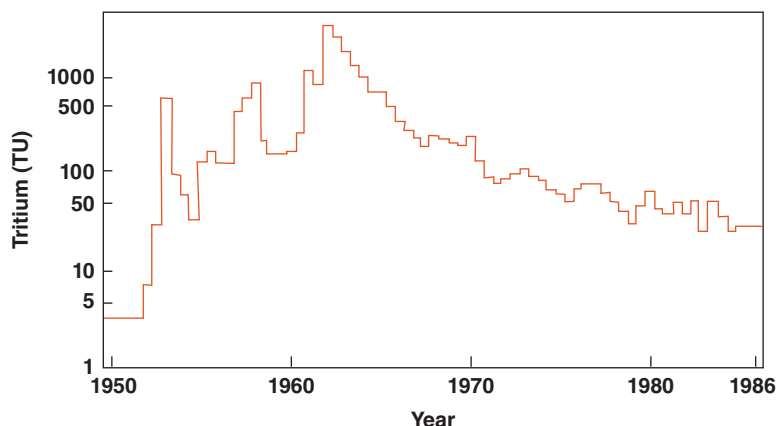


Figure 4.6 ${}^3\text{H}$ in precipitation recorded at Ottawa, Canada from 1950 to 1986. Vertical scale is in “Tritium Units,” which are 10^{-18} atoms ${}^3\text{H}/\text{atom} {}^1\text{H}$.

half-life suitable for dating water in regional aquifers as old as 1 Ma. The disadvantage is that it has a much lower production rate in the atmosphere than ${}^{14}\text{C}$, and its analysis requires accelerator mass spectrometry.

In the atmosphere, the primary means of production of ${}^{36}\text{Cl}$ are spallation of ${}^{40}\text{Ar}$ and neutron capture by ${}^{36}\text{Ar}$. The former process has been estimated to produce about 11 atoms $\text{m}^{-2}\text{-s}^{-1}$, while the latter produces about half that, for a total production of about 15 atoms $\text{m}^{-2}\text{-s}^{-1}$. The residence time of ${}^{36}\text{Cl}$ in the atmosphere (about 1 week) is not long enough to homogenize its concentration, so the fallout varies with latitude as shown in Figure 4.7.

As usual, dealing with just the number, or concentration, of ${}^{36}\text{Cl}$ atoms can have disadvantages, and can be misleading. Evaporation, for example, would increase the number of ${}^{36}\text{Cl}$ atoms. Thus the ${}^{36}\text{Cl}/\text{Cl}$ ratio (Cl has two stable isotopes: ${}^{35}\text{Cl}$ and ${}^{37}\text{Cl}$) is generally used. Stable chlorine can be leached from rocks. This chlorine will be nearly, but not entirely, free of ${}^{36}\text{Cl}$. Some ${}^{36}\text{Cl}$ is produced naturally by ${}^{35}\text{Cl}$ capturing neutrons generated by fission and (α, n) reactions on light elements. Further complications arise from the bomb-produced ${}^{36}\text{Cl}$. Dissolved chlorine can also capture neutrons. Thus ${}^{36}\text{Cl}$ will build up in groundwater water according to:

$$[{}^{36}\text{Cl}] = \frac{\phi_n f [{}^{35}\text{Cl}]}{\lambda_{36}} (1 - e^{-\lambda_{36} t}) \quad (4.17)$$

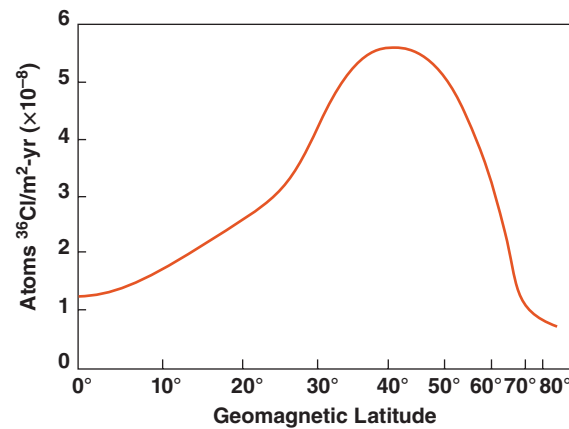


Figure 4.7 Latitudinal dependence of the fallout of atmospheric ${}^{36}\text{Cl}$. (Source: Adapted from Bentley et al. 1986). Reproduced with permission of John Wiley & Sons.)

where $[{}^{36}\text{Cl}]$ is the ${}^{36}\text{Cl}$ concentration (number of ${}^{36}\text{Cl}$ atoms per mole), $[{}^{35}\text{Cl}]$ is the concentration of ${}^{35}\text{Cl}$ target atoms, ϕ_n is the neutron flux, and f is the fraction of neutrons captured by ${}^{35}\text{Cl}$. The secular equilibrium value, that is, the concentration at $t = \infty$, is simply:

$$\frac{[{}^{36}\text{Cl}]}{[\text{Cl}]} = 0.7576 \times \frac{\phi_n f}{\lambda_{36}} \quad (4.18)$$

where 0.7576 is the fraction of Cl that is ${}^{35}\text{Cl}$. This *in situ* production must be taken into account.

Stable Cl derived from sea spray is also present in the atmosphere and in precipitation. Its concentration decreases exponentially from coasts to continental interiors. Thus, the initial $^{36}\text{Cl}/\text{Cl}$ ratio in precipitation will be variable and must be determined or estimated locally before groundwater ages can be estimated. The age of groundwater may then be determined from:

$$t = \frac{-1}{\lambda} \ln \left\{ \frac{[\text{Cl}] \left(^{36}\text{Cl}/\text{Cl} - ^{36}\text{Cl}/\text{Cl}_{se} \right)}{[\text{Cl}]_0 \left(^{36}\text{Cl}/\text{Cl}_0 - ^{36}\text{Cl}/\text{Cl}_{se} \right)} \right\} \quad (4.19)$$

where $[\text{Cl}]$ is the chloride concentration and the subscripts “0” and “se” denote initial and secular equilibrium values respectively.

Bentley et al. (1986) used this approach to determine the age of groundwater in the Great Artesian Basin aquifer. The Great Artesian Basin aquifer is one of the largest artesian aquifers in the world and underlies about a fifth of Australia (Figure 4.8). The primary aquifer is the Jurassic Hooray sandstone, which outcrops and is recharged along the eastern edge of the basin. Bentley et al. (1986) sampled 28 wells from the system. They estimated an initial $^{36}\text{Cl}/\text{Cl}$ ratio of 110×10^{-15} and a secular equilibrium value of 9×10^{-15} atoms per liter. Some well samples showed evidence of ^{36}Cl addition, probably from upward

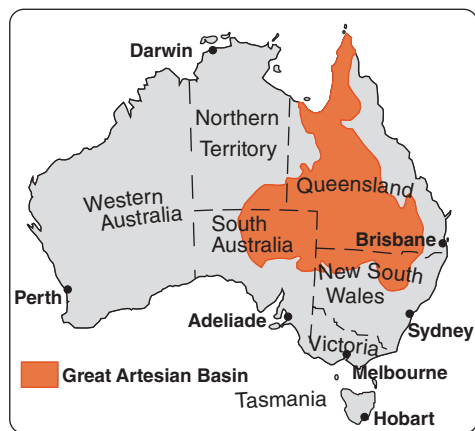


Figure 4.8 Extent of the Great Artesian Basin aquifer in Australia. (Source: Adapted from Bentley et al. 1986). Reproduced with permission of John Wiley & Sons.)

leakage of water from evaporate-bearing Devonian sediments beneath the aquifer. Other wells, particularly those in the recharge area, showed evidence of evaporation, which increases Cl concentrations before the water penetrated the groundwater system, not surprising in an arid environment. On the whole, however, ^{36}Cl ages were comparable to calculated hydrodynamic ages, as illustrated in Figure 4.9.

^4He data can provide a useful compliment to ^{36}Cl studies. ^4He accumulates in rocks as a consequence of α -decay. Instead of decaying, we expect ^4He to accumulate linearly with time. Assuming that water flows uniformly through an aquifer as though it were pushed along by a piston (“piston-flow”), accumulation of ^4He may be described by:

$$[^4\text{He}] = [{}^4\text{He}]_0 + \frac{R_\alpha t}{\phi} \quad (4.20)$$

where $[{}^4\text{He}]_0$ is the initial concentration, R_α is the production rate (a function of the Th and U concentration), ϕ is the aquifer porosity (volume fraction of the aquifer not occupied by rock), and t is time. In the Great Artesian Aquifer, however, Torgensen et al. (1992) found that ^4He appears to accumulate non-linearly, as in Figure 4.10(a). Bethke and Johnson (2008) explain this with a model in which ^4He diffuses into the aquifer from underlying crystalline basement (Figure 4.10b). Beds of fine-grained, low porosity rocks within the aquifer (which consists mainly of sandstone as noted previously), limits the upward mobility of ^4He , resulting in a strong vertical gradient within the aquifer. Eventually upwelling of water near the downstream end of the aquifer allows the ^4He to be mixed vertically.

4.1.5 *In-situ* produced cosmogenic nuclides

A few cosmic rays and secondary particles manage to pass entirely through the atmosphere where they interact with rock at the surface of the Earth. These interactions produce a great variety of stable and unstable nuclei. Because the atmosphere is a very effective cosmic ray shield, these cosmogenic nuclides are rare and difficult to detect, so most of the nuclides of interest are unstable ones that otherwise do not occur in the Earth.

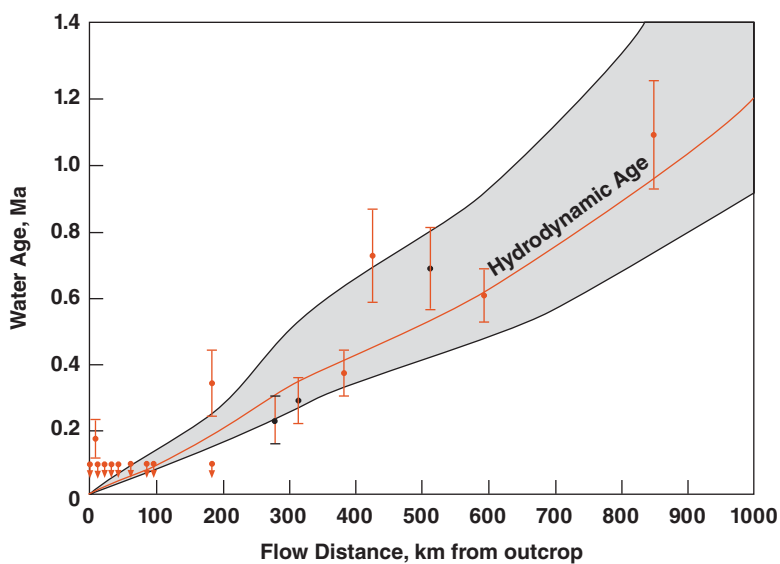


Figure 4.9 Comparison of ^{36}Cl ages with “hydrodynamic age,” that is, the age estimated from hydrologic flow parameters. (Source: Adapted from Bentley et al. 1986). Reproduced with permission of John Wiley & Sons.)

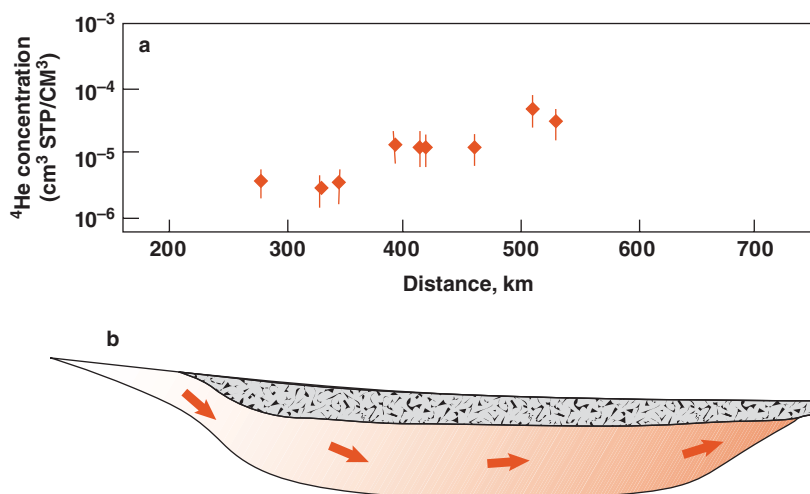


Figure 4.10 (a) Concentration of ^4He measured by Torgersen et al. (1992) as a function of distance from source in the Great Artesian Aquifer of Australia. Rather than the linear increase predicted by water ages shown in Figure 4.8, concentrations appear to increase exponentially. (b) Model of ^4He concentrations in the Great Artesian Aquifer (red shading). ^4He diffuses in from below, and then is confined to the bottom of the aquifer until water upwells toward the surface. (Source: Adapted from Bethke et al. (1999). Reproduced with permission of John Wiley & Sons.)

Those nuclides that are geologically useful are listed along with approximate production rates in Table 4.2. The most important of these are ^{36}Cl , ^{26}Al , and ^{10}Be . In addition to cosmic ray-induced spallation, these nuclides

can be produced by reactions with lower energy secondary particles, including neutrons, muons, and alpha particles. The most important of these reactions are also listed in Table 4.2. Stable cosmogenic nuclides can

Table 4.2 Isotopes with appreciable production rates in terrestrial rocks.

Isotope	Half-life (years)	Spallation		Thermal neutrons		Capture of μ^- Target
		Target(s)	Rate (atoms/g-yr)	Target	Reaction	
${}^3\text{He}$	stable	O, Mg, Al, Si, Fe	100–150	${}^6\text{Li}$	(n, α)	
${}^{10}\text{Be}$	1.6×10^6	O, Mg, Al, Si, Fe	6	—	—	${}^{10}\text{B}$, C, N, O
${}^{14}\text{C}$	5730	O, Si, Mg, Fe	20	${}^{14}\text{N}$, ${}^{17}\text{O}$	(n, p), (n, α)	N, O
${}^{21}\text{Ne}$	stable	Mg, Al, Si, Fe	80–160	—	—	Na, Mg, Al
${}^{26}\text{Al}$	7.1×10^5	Mg, Al, Si, Fe	35	—	—	Si, S
${}^{36}\text{Cl}$	3.0×10^5	K, Ca, Cl	10	${}^{35}\text{Cl}$, ${}^{39}\text{K}$	(n, γ), (n, α)	K, Ca, Sc
${}^{129}\text{I}$	1.6×10^5		$\ll 1$	${}^{128}\text{Te}$	(n, γ)	${}^{130}\text{Te}$, Ba

also provide useful geological information. To be of use, the cosmogenic production must be large relative compared to the background abundance of such nuclides. Thus, only ${}^3\text{He}$ and ${}^{21}\text{Ne}$ have been studied to date. In the following examples, we will see how the cosmogenic production of a rare stable nuclide, ${}^3\text{He}$, can be used to estimate erosion rates, and how ${}^{36}\text{Cl}$ can be used to determine the time material has been exposed to cosmic rays.

4.1.5.1 Determining erosion rates from cosmogenic ${}^3\text{He}$

The penetration of cosmic rays decays exponentially with depth according to:

$$e^{-z\rho/l} \quad (4.21)$$

where z is depth, l is a constant that depends on the nature and energy of the particle and on the material it penetrates, and ρ is the density. For the nucleonic component of cosmic rays, l is approximately 160 g/cm^2 . For a material, such as a typical rock, having a density of 2.5 g/cc , the ratio ρ/l is about 64 cm^{-1} . Thus, at a depth of 64 cm the cosmic ray flux would be $1/e$ or 0.36 times the flux at the surface. This is referred to as the characteristic penetration depth. For the μ (muon)³ component, l is about 1000 g/cm^2 , and for neutrinos l is nearly infinite (because neutrinos interact so weakly with matter). Most of the cosmic ray interactions are with the nucleonic component. The meaning of all this is that cosmogenic nuclides will be produced only on the surface (the top meter or two) of a solid body. As in the atmosphere, cosmic ray interactions produce both stable and unstable nuclei. If we consider the case of the production of a stable nucleus, the number

of stable nuclei produced at the surface of the body over some time t is simply given by:

$$N = P t \quad (4.22)$$

where P is the production rate at the surface, which is in turn a function of the cosmic ray flux, depth, elevation, geomagnetic latitude, and reaction cross section. If we know the production rate, we can solve 4.19 for t , the length of time the surface has been exposed to cosmic rays.

Despite being the second most abundant element in the cosmos, He is very rare on Earth because it is too light to be retained – it escapes from the atmosphere readily. Of helium's two isotopes, ${}^3\text{He}$ is some 7 orders of magnitude less abundant than ${}^4\text{He}$. This is partly because ${}^4\text{He}$ is continually produced by α -decay. Hence the Earth's supply of ${}^4\text{He}$ is continually replenished, whereas ${}^3\text{He}$ is not.⁴ In 1986 M. D. Kurz found extraordinarily high ${}^3\text{He}/{}^4\text{He}$ ratios in basalts from Hawaii. The origin proved to be cosmogenic (Kurz, 1986a). Most of the ${}^3\text{He}$ is produced by spallation of abundant elements such as O, Mg, and Si, with a minor component produced by ${}^6\text{Li}(n, \alpha)$ and ${}^7\text{Li}(\mu, \alpha)$ reactions. Figure 4.11 shows the decrease in cosmogenic ${}^3\text{He}$ with depth in a core from Haleakala (Maui, Hawaii) compared with the predicted decrease for $l = 165\text{ g/cm}^2$. The dashed line show the depth dependence of the μ stopping rate needed to explain the discrepancy between the predicted and observed depth dependence. Ignoring the small contribution from muon interactions, the concentration of ${}^3\text{He}$ as a function of depth, z , and exposure time, t , is given by:

$$C(z, t) = \int_0^t P e^{-z(t)\rho/l} dt \quad (4.23)$$

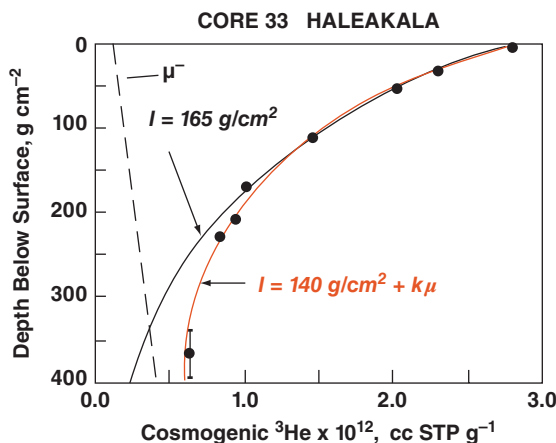


Figure 4.11 Variation of cosmogenic ${}^3\text{He}$ with depth in a core from Haleakala volcano in Hawaii. (Source: Kurz (1986). Reproduced with permission of Elsevier.)

If the depth is not a function of time, this simply integrates to

$$C(z, t) = Pe^{-z\rho/l} \quad (4.24)$$

If erosion occurs, then z will be a function of t . We obtain the simplest relationship between time and depth by assuming the erosion rate is time-independent:

$$z = z_0 - \varepsilon t \quad (4.25)$$

where ε is the erosion rate and z_0 is the original depth. Substituting for z in Eqn. 4.23 and integrating, we have

$$C(z, t) = P \frac{l}{\varepsilon\rho} e^{-z_0\rho/l} (e^{t\varepsilon\rho/l} - 1) \quad (4.26)$$

Substituting $z_0 = z + \varepsilon t$, Eqn. 4.26 simplifies to:

$$C(z, t) = P \frac{l}{\varepsilon\rho} e^{-z\rho/l} (1 - e^{-\varepsilon t\rho/l}) \quad (4.27)$$

For a sample at the surface, $z = 0$ and this equation reduces to:

$$C_0 = P \frac{l}{\varepsilon\rho} (1 - e^{-\varepsilon t\rho/l}) \quad (4.28)$$

Neither 4.28 nor 4.27 can be solved directly. However, if the age of the rock, t , is known, one can measure a series of values, C , as function of depth and make a series of guesses of the erosion rate until a curve based on 4.27 fits the data. Using this procedure, Kurz estimated an erosion rate of 10 m/Ma for

Haleakala (Kurz noted that for higher erosion rates, it would be necessary to take account of the muon-produced ${}^3\text{He}$).

4.1.5.2 Erosion rates from radioactive cosmogenic nuclides

For a radioactive nuclide such as ${}^{26}\text{Al}$ or ${}^{36}\text{Cl}$ we need to consider its decay as well as its production. The concentration of such nuclide as a function of time and depth is given by:

$$C(z, t) = \frac{Pe^{-z\rho/l}}{\lambda + \varepsilon\rho/l} (1 - e^{(-\lambda + \varepsilon\rho/l)t}) \quad (4.29)$$

where λ is the decay constant and t is age of the rock. If the rock is much older than the half-life of the nuclide (i.e., $\lambda t \gg 1$; for ${}^{36}\text{Cl}$, for example, this would be the case for a rock >3 Ma old), then the last term tends to 1. Eventually, production of the nuclide, its decay, and erosion will reach steady-state (assuming cosmic ray flux and erosion rate are time-independent). In this case, the concentration at the surface will be given by:

$$C_0 = \frac{P}{\lambda + \varepsilon\rho/l} \quad (4.30)$$

Since this equation does not contain a time term, we cannot deduce anything about time in this situation. However, knowing the penetration depth, λ , and the production rate, we can deduce the erosion rate.

4.1.5.3 ${}^{36}\text{Cl}$ dating of glacial deposits

Let us next consider the build-up of a radioactive nuclide in a rock where the erosion rate can be ignored. For a nuclide being both produced by cosmic ray bombardment and lost by radioactive decay, our basic equation becomes:

$$\frac{dN}{dt} = P - \lambda N \quad (4.31)$$

To obtain the abundance, N , of the radionuclide at some time t , we simply integrate 4.27:

$$N = \frac{P}{\lambda} (1 - e^{-\lambda t}) \quad (4.32)$$

For $t >> \lambda$; that is, after many half-lives, a steady-state is reached where:

$$N = \frac{P}{\lambda} \quad (4.33)$$

For shorter times, however, we can solve Eqn. 4.32 for t . In this case, t is the time the rock has been exposed to cosmic rays. Since the penetration of cosmic rays is so limited, this is the time the rock has been exposed at the surface of the Earth. This particular problem is of some interest in dating rock varnishes and glacial moraines. All moraines except those from the most recent glaciation will be too old for ^{14}C dating, but virtually the entire Pleistocene glacial history is an appropriate target for dating with ^{26}Al or ^{36}Cl .

Since ^{36}Cl is a fairly heavy nuclide, only a few specific cosmic ray-induced nuclear reactions yield ^{36}Cl . The principle modes of production are thermal neutron capture by ^{35}Cl (the most abundant of chlorine's two stable isotopes), spallation reactions on ^{39}K and ^{40}Ca , and muon capture by ^{40}Ca (Phillips et al., 1986). In effect, this means the composition of the sample, in particular the concentrations of Cl, K, and Ca, must be known to estimate the production rate. Phillips et al. (1986) showed that the build-up of ^{36}Cl in rocks can be reasonably predicted from these concentrations by determining ^{36}Cl in a series of well-dated lavas and tuffs. In addition to rock composition, it is also necessary to take into consideration (1) latitude, (2) elevation, and (3) non-cosmogenic production of ^{36}Cl . As we saw in the last section, spontaneous fission of U and Th will produce neutrons that will result in some production of ^{36}Cl by neutron capture by ^{35}Cl .

Philips et al. (1990) determined ^{36}Cl ages for boulders taken from a series of moraines in Bloody Canyon of Mono Basin, California. They were careful to sample only boulders from moraine crests as these were most likely to remain above the snow during winter and less likely to have rolled. Their results are shown graphically in Figures 4.12. The youngest moraines correspond to glacial maxima of the most recent glaciation and yield ages in good agreement with ^{14}C dating. Older moraines show considerably more scatter. In addition to analytical errors, factors that might account for the larger scatter include: ^{35}Cl inherited from earlier exposure, preferential leaching of ^{35}Cl , erosion of the rock surface, gradual exposure as a result of erosion of till matrix, and snow cover. Most of these factors will result in the age being too young, so that maximum ages were preferred

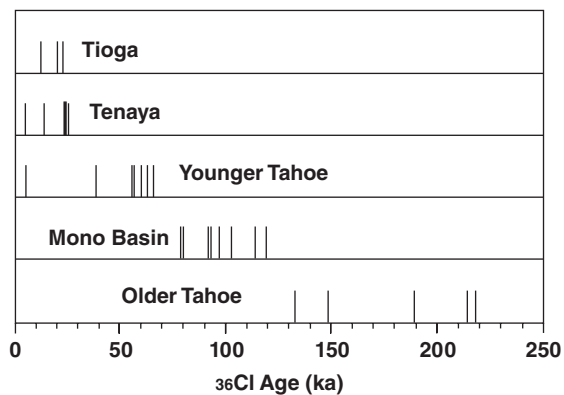


Figure 4.12 ^{36}Cl ages of moraine boulders from Bloody Canyon, eastern Sierra Nevada. (Source: Adapted from Phillips et al. (1990). Reproduced with permission of AAAS.)

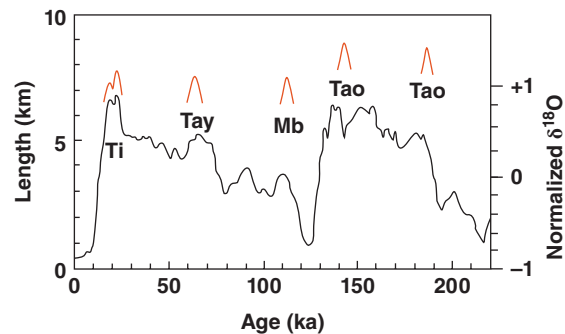


Figure 4.13 Comparison of best-estimated ^{36}Cl ages of moraine boulders from Bloody Canyon with the marine $\delta^{18}\text{O}$ record. There is a reasonably good correspondence with the moraine ages and glacial maxima inferred from ^{18}O . (Source: Adapted from Phillips et al. (1990). Reproduced with permission of AAAS.)

for the older moraines. The best estimates of moraine ages are compared with the marine O isotope record, which in this case is used as a proxy for global temperature history (Chapter 10), in Figure 4.13. Generally, the moraines correspond in time to high $\delta^{18}\text{O}$ in the oceans, which corresponds to cold temperatures. This is just what we expect: maximum extent of the glaciers occurred during cold climatic episodes.

4.2 FISSION TRACKS

As we have already noted, a fraction of uranium atoms undergo spontaneous fission

rather than alpha decay. The sum of the masses of the fragments is less than that of the parent U atom: this difference reflects the greater binding energy of the fragments. The missing mass has been converted to kinetic energy of the fission fragments. Typically, this energy totals about 200 MeV, a considerable amount of energy on the atomic scale. The energy is deposited in the crystal lattice through which the fission fragments pass by stripping electrons from atoms in the crystal lattice. The ionized atoms repel each other, disordering the lattice and producing a small channel, something like several nm (10^{-9} m) in width, and a wider stressed region in the crystal. The damage is visible as tracks seen with an electron microscope operating at magnifications of 50,000 \times or greater. However, the stressed region is more readily attacked and dissolved by acid; so the tracks can be enlarged by acid etching to the point where they are visible under the optical microscope. Figure 4.14 is an example.

Because fission is a rare event in any case, fission track dating generally uses uranium-rich minerals. Most work has been done on apatites and zircon, but other minerals such as sphene are also used.

Fission tracks will *anneal*, or self-repair, over time. The rate of annealing is vanishingly small at room temperature, but increases with temperature and becomes significant at geologically low to moderate temperatures. In the absence of such annealing, the number of tracks is a simple function of time and the

uranium content of the sample:

$$F_s = (\lambda_f / \lambda_\alpha) [^{238}\text{U}] (e^{\lambda_\alpha t} - 1) \quad (4.34)$$

where F_s is the number of tracks produced by spontaneous fission, $[^{238}\text{U}]$ is the number of atoms of ^{238}U , λ_α is the α decay constant for ^{238}U , and λ_f is the spontaneous fission decay constant, the best estimate for which is $8.46 \pm 0.06 \times 10^{-17} \text{ yr}^{-1}$. Thus about 5×10^{-7} U atoms undergo spontaneous fission for every one that undergoes α -decay. Equation 4.34 can be solved directly for t simply by determining the number of tracks and number of U atoms per volume of sample. In this case, t is the time elapsed since temperatures were high enough for all tracks to anneal. This is the basis of fission-track dating. The temperatures required to anneal fission damage to a crystal are lower than those required to isotopically homogenize the crystal. Thus fission track dating is typically used to “date” lower temperature events than conventional geochronometers. It is part of a suite of chronometers, which also include previously discussed ^{40}Ar - ^{39}Ar and U-Th-He dating, that are reset over a range of temperatures (mostly fairly low) that are used in the field of *thermochronology*.

4.2.1 Analytical procedures

Determining fission track density involves a relatively straightforward procedure of polishing and etching a thin section or grain mount, and then counting the number of tracks per unit area. A number of etching procedures have been developed for various substances. These are listed in Table 4.3. Track densities of up to several thousand per cm^2 have been recorded. A minimum density of 10 tracks per cm^2 is required for the results to be statistically meaningful. A fission track, which is typically 10 μm long, must intersect the surface to be counted. Thus Eqn. 4.34 becomes:

$$\rho_s = F_s q = (\lambda_f / \lambda_\alpha) [^{238}\text{U}] (e^{\lambda_\alpha t} - 1) q \quad (4.35)$$

where ρ_s is the track density, q is the fraction of tracks intersecting the surface, and $[^{238}\text{U}]$ is now the concentration of ^{238}U per unit area.

The second step is determination of the U concentration of the sample. This is usually



Figure 4.14 Fission tracks in a polished and etched zircon. (Source: Photo by J. M. Bird. Reproduced with permission.)

Table 4.3 Etching procedures for fission track dating.

Mineral etching	Solution	Temperature (°C)	Duration
Apatite	5% HNO ₃	25	10–30 s
Epidote	37.5M NaOH	159	150 min
Muscovite	48% HF	20	20 min
Sphene	Conc. HCl	90	30–90 min
Volcanic glass	24% HF	25	1 min
Zircon	100M NaOH	270	1.25 h

done by neutron irradiation and counting of the tracks resulting from neutron-induced fission. There are variations to this procedure. In one method, spontaneous fission tracks are counted, then the sample is heated to anneal the tracks, irradiated and recounted (this is necessary because irradiation heats the sample and results in partial annealing). Alternatively, a “detector,” either a U-free muscovite sample or a plastic sheet, is placed over the surface of the polished surface that has previously been etched and counted. The sample together with the detector is irradiated, and the tracks in the detector counted. This avoids having to heat and anneal the sample. This latter method is more commonly employed.

Whereas ²³⁸U is the isotope that fissions in nature, it is actually ²³⁶U, produced by neutron capture by ²³⁵U that undergoes neutron-induced fission. The number of ²³⁵U fission events induced by thermal neutron irradiation is:

$$F_i = [{}^{235}\text{U}] \phi\sigma \quad (4.36)$$

where ϕ is the thermal neutron dose (neutron flux times time) and σ is the reaction cross section (about 580 barns for thermal neutrons). The induced track density is:

$$\rho_i = F_i q_i = [{}^{235}\text{U}] \phi\sigma q \quad (4.37)$$

Dividing Eqn. 4.35 by 4.37 we have:

$$\frac{\rho_s}{\rho_i} = \frac{\lambda_f}{\lambda_a} \frac{137.82}{\phi\sigma} (e^{\lambda_a t} - 1) \quad (4.38)$$

In the detector method, Eqn. 4.38 must be modified slightly to become:

$$\frac{\rho_s}{\rho_i} = \frac{\lambda_f}{\lambda_a} \frac{137.82}{2\phi\sigma} (e^{\lambda_a t} - 1) \quad (4.39)$$

The factor of two arises because surface-intersecting tracks produced by spontaneous fission originate both from U within the sample and from that part of the sample removed from etching. However, tracks in the detector can obviously only originate in the remaining sample. This is illustrated in Figure 4.15.

One of the most difficult problems in this procedure is correctly measuring the neutron dose. This is usually done by including a gold or aluminum foil and counting the decays of the radioisotope produced by neutron capture. Nevertheless, the neutron flux can be quite variable within a small space and it remains a significant source of error.

We can readily solve Eqn. 4.39 for t :

$$t = \frac{1}{\lambda_a} \ln \left[1 + \frac{\rho_s}{\rho_i} \frac{\lambda_a}{\lambda_f} \frac{2\phi\sigma}{137.82} \right] \quad (4.40)$$

and thus determine the time since the tracks last annealed.

Yet another alternative method is the *zeta method*, which involves comparison of spontaneous and induced fission track density

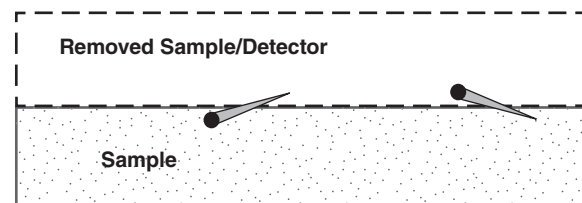


Figure 4.15 Geometry of the fission tracks in the detector method of U determination. Spontaneous fission tracks in the sample surface could have originated from either the existing sample volume, or the part of the sample removed by polishing. Tracks in the detector can only originate from the existing sample volume.

against a standard of known age. The principle involved is no different from that used in many methods of analytical chemistry, where comparison to a standard eliminates some of the more poorly controlled variables. In the zeta method, the dose, cross section, and spontaneous fission decay constant, and U isotope ratio are combined into a single constant:

$$\zeta = \frac{\phi\sigma^{235}U}{\lambda_f^{238}U\rho_d} = \frac{\phi\sigma}{\lambda_f 137.88\rho_d} \quad (4.41)$$

where ρ_d is the density of tracks measured in a U-doped glass standard. The value of ζ is determined by analyzing standards of known age in every sample batch. ζ is determined from:

$$\zeta = \frac{e^{\lambda_a t} - 1}{\lambda_a (\rho_s / \rho_i) \rho_d} \quad (4.42)$$

The age is then calculated from:

$$t = \frac{1}{\lambda_a} \ln \left(1 + \frac{\zeta \lambda_a \rho_s \rho_d}{\rho_i} \right) \quad (4.43)$$

Standards used in the zeta method include zircon from the Fish Canyon Tuff (27.9 Ma), the Tardree rhyolite of Ireland (58.7 Ma), and South African kimberlites (82 Ma).

Usually, fission track ages on a number of grains must be measured for the results to be significant. The results are often presented as histograms. Alternatively, when the errors are also considered, the results may be presented as a probability density diagram, such as Figure 4.16. Yet another approach is to plot the spontaneous track density (ρ_s) versus the induced track density (ρ_i), such as in Figure 4.17. From Eqn. 4.38, we see that the slope on such a diagram is proportional to time. Thus, these kinds of plots are exactly analogous to conventional isochron diagrams. There is a difference, however. On a plot of ρ_s vs. ρ_i the intercept should be 0.

4.2.2 Interpreting fission track ages

Fission tracks will anneal at elevated temperatures. As is typically the case for chemical reaction rates, the temperature dependence of the annealing rate, da/dt , can be expressed by the *Arrhenius relation*:

$$\frac{da}{dt} \propto A e^{-E_A/RT} \quad (4.44)$$

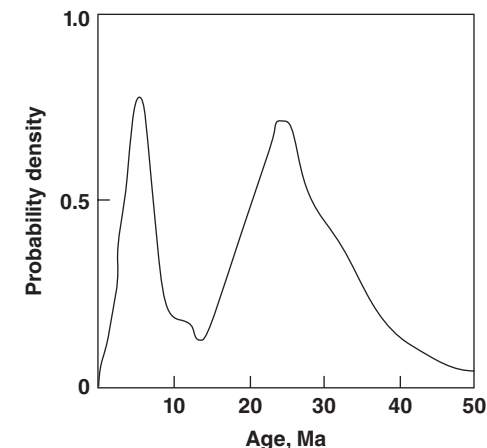


Figure 4.16 Probability density plot of fission track ages of 30 detrital zircon grains from the reworked El Ocote tephra from Mexico. The data show a bimodal distribution. (Source: Adapted from Kowallis et al. (1986). Reproduced with permission of the Geological Society of America.)

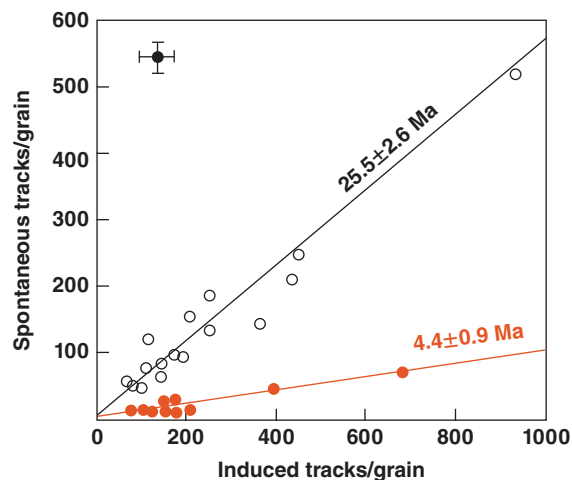


Figure 4.17 Spontaneous track density versus induced track density for the same set of zircon grains as in Figure 4.16. On this plot, the slope of the correlation is proportional to time. (Source: Adapted from Walter (1989). Reproduced with permission of Elsevier.)

where T is thermodynamic temperature (kelvins), A is a constant, R is the gas constant (some equations use k , Boltzmann's constant, which is proportional to R), and E_A is the activation energy. Estimates of activation energies for fission track annealing

range from 140 to 190 kJ/mol for apatite to 200–325 kJ/mol for zircon (Reiners and Brandon, 2006). In detail, activation energies depend on the composition of the mineral, crystallographic direction, and, at least in the case of zircon, radiation damage, with metamict zircons annealing faster than those without radiation damage. Experiments suggest that the annealing rate also depends on the extent of annealing, such that the rate accelerates as it proceeds and can be expressed as:

$$\frac{da}{dt} = Ae^{-E_A/RT}(1 - a)^n \quad (4.45)$$

where n has a value around –3 or –4 (Laslett et al., 1987).

Thus, as is the case for conventional radiometric dating, fission track dating measures the time elapsed since some thermal episode, which may not necessarily be the same time as the formation of the crystal. Annealing results in the track shrinking from both ends, but in detail the process is somewhat irregular, with the morphology of the track becoming ragged and gaps developing before annealing is complete. The constants k and E_A will vary from mineral to mineral (and indeed even with crystallographic axis), so that each mineral will close at different rates. In laboratory experiments, apatite begins to anneal around 70°C and anneals entirely on geologically short times at 175°C. Sphene (or titanite,

CaTiSiO_5), on the other hand, only begins to anneal at 275°C and does not entirely anneal until temperatures of 420°C are reached. At higher temperatures, these minerals anneal very quickly in nature: no fission tracks are retained. Figure 4.18 shows the experimental relationship between the percentage of tracks annealed, temperature, and time.

Consider a U-bearing mineral cooling from metamorphic or igneous temperatures. At first, tracks anneal as quickly as they form. As temperature drops, tracks will be partially, but not entirely preserved. As we discussed in the context of K-Ar dating, the apparent closure temperature is a function of cooling rate. Figure 4.19 illustrates this and compares fission track closure temperatures with those of K-Ar and U-Th-He. Because different methods of etching attack partially annealed tracks to different degrees, etching must be done in the same way for closure temperature determination.

As may be seen in Figure 4.19, fission track closure temperatures are low, so they more useful in determining cooling histories than crystallization ages. When combined with estimates of geothermal gradients, fission track ages, particularly if ages for a variety of minerals are determined, are a useful tool in studying uplift and erosion rates. Let's see how this works. Consider a layer of crust L km thick undergoing erosion at a rate ε . Let the

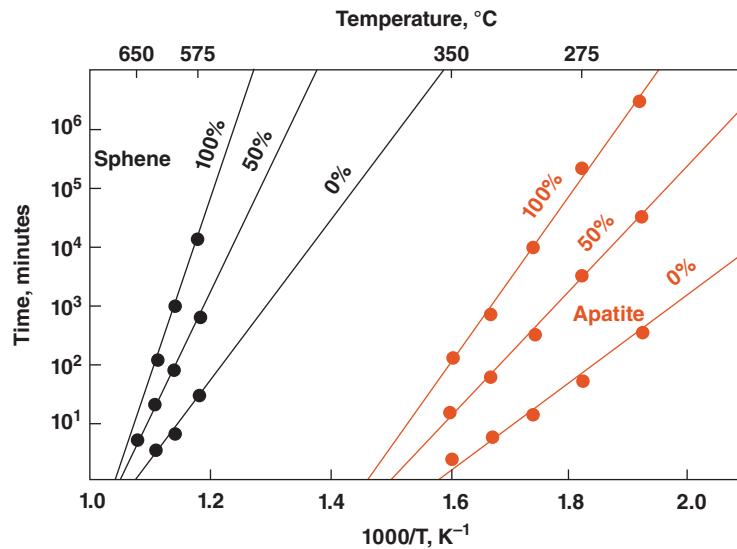


Figure 4.18 Relationship between the percentages of tracks annealed (lines labeled 100%, 50%, and 0%), temperature, and time for apatite and sphene.

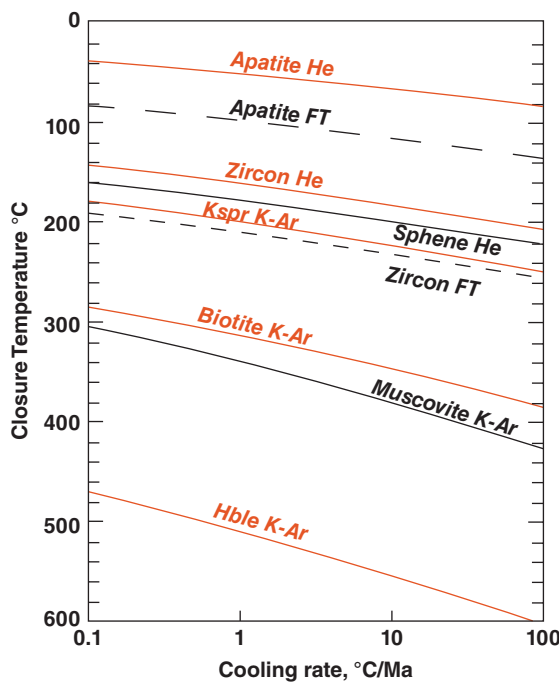


Figure 4.19 Comparison of apparent closure temperatures of fission tracks, U-Th-He, and K-Ar as a function of cooling rate for a variety of minerals. (Source: Reiners and Brandon (2006). Reproduced with permission of Annual Reviews, Inc.)

temperature at the base and top of the layer (the surface) be T_L and T_S , respectively, that internal radiogenic heat production provides heating of H_T °C/Ma, and that the thermal conductivity is κ . Temperature as a function of depth is then given by:

$$T(z) = T_S + \left(T_L - T_S + \frac{H_T L}{\kappa} \right) \times \frac{1 - e^{-\varepsilon z / \kappa}}{-e^{-\varepsilon L / \kappa}} - \frac{H_T z}{\kappa} \quad (4.46)$$

When erosion rates are high, this results in non-linear geothermal gradients, as can be seen in Figure 4.20. When erosion rates are small the exponential terms disappear and the gradient is nearly linear. To determine erosion rates, what we really wish to know is the closure depth, rather than closure temperature. By iteratively simultaneously solving Eqn. 4.46 as well as Dodson's closure temperature equation (Eqn. 2.37), Reiners and Brandon (2006) determined the "closure depths"

for several minerals shown by the bold lines in Figure 4.20.

Let's consider a simple example. We measure an apatite fission track age of 12.5 Ma. We chose 10°C/Ma for a first order estimate of cooling rate and determine the closure temperature from Figure 4.19 to be 120°C. Assuming an average surface temperature of 10°C, we calculate the cooling rate to be:

$$\frac{dT}{dt} = \frac{120 - 10}{12.5} = 8.8^\circ\text{C/Ma} \quad (4.47)$$

We could iteratively refine our result value by recalculating the closure temperature based on previously calculated cooling rate and obtain a rate of 8°C/Ma. If we assume the geothermal gradient to be 30°C/km, we can calculate the exhumation rate to be:

$$\begin{aligned} \frac{dz}{dt} &= \frac{dT/dt}{dT/dz} \\ &= \frac{8^\circ\text{C/Ma}}{0.030^\circ\text{C/m}} = 267\text{m/Ma} \end{aligned} \quad (4.48)$$

Using this approach, exhumation rates have been estimated as 500 m/Ma over the past 10 Ma for the Alps and 800 m/Ma for the Himalayas. Figure 4.21 shows an example of the results of one such study of the Himalayas from northern India (Kashmir). A plot of ages versus the altitude at which the samples were collected indicates an exhumation rate of 0.35 mm/a or 350 m/Ma over the last 7 million years.

4.2.3 Interpreting track length

As fission tracks anneal, they become shorter. Thus when a grain is subjected to elevated temperature, both the track density and the mean track length will decrease. As a result, problems of partial annealing of fission tracks can to some degree be overcome by also measuring the length of the tracks. Because (1) tracks tend to have a constant length (controlled by the energy liberated in the fission), (2) tracks become progressively shorter during annealing, and (3) each track is actually a different age and has experienced a different fraction of the thermal history of the sample, the length distribution records information about the thermal history of the sample. Figure 4.22 illustrates how track lengths are expected to vary for a variety of

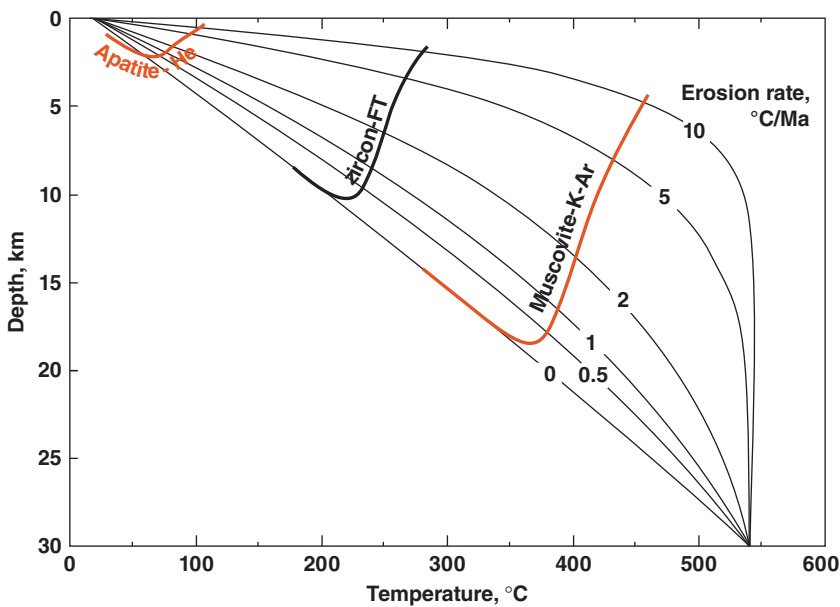


Figure 4.20 Geothermal gradients calculated from Eqn. 4.46 for $T_S = 14^\circ\text{C}$, $T_L = 540^\circ\text{C}$, $\kappa = 27 \text{ km/Ma}$, and $H_T = 4.5^\circ\text{C/Ma}$. Bold lines show the “closure depths” for three mineral chronometers. (Source: Reiners and Brandon (2006). Reproduced with permission of Annual Reviews, Inc.)

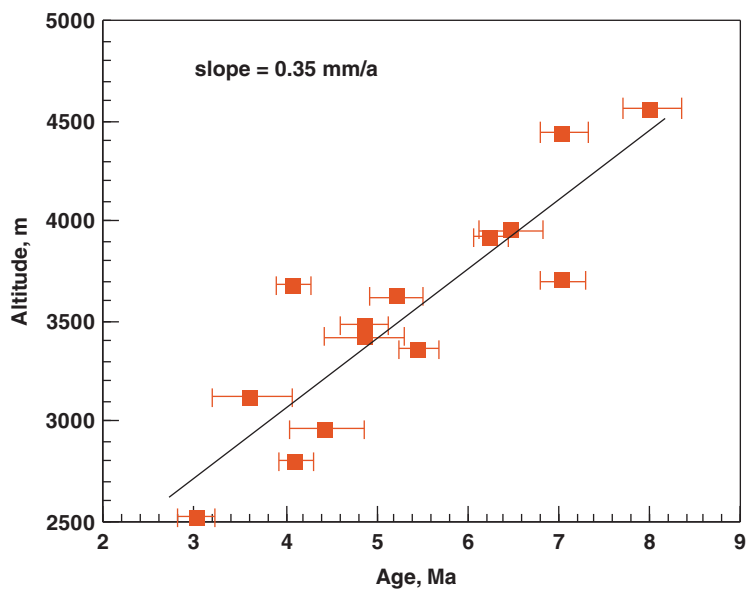


Figure 4.21 Apatite fission track ages vs. altitude for metamorphic rocks of the Higher Himalaya Crystalline belt of Kashmir. The correlation coefficient is 0.88. The slope indicates an uplift rate of 350 m/Ma. (Source: Kumar et al. (1995). Reproduced with permission of the Geological Society of India.)

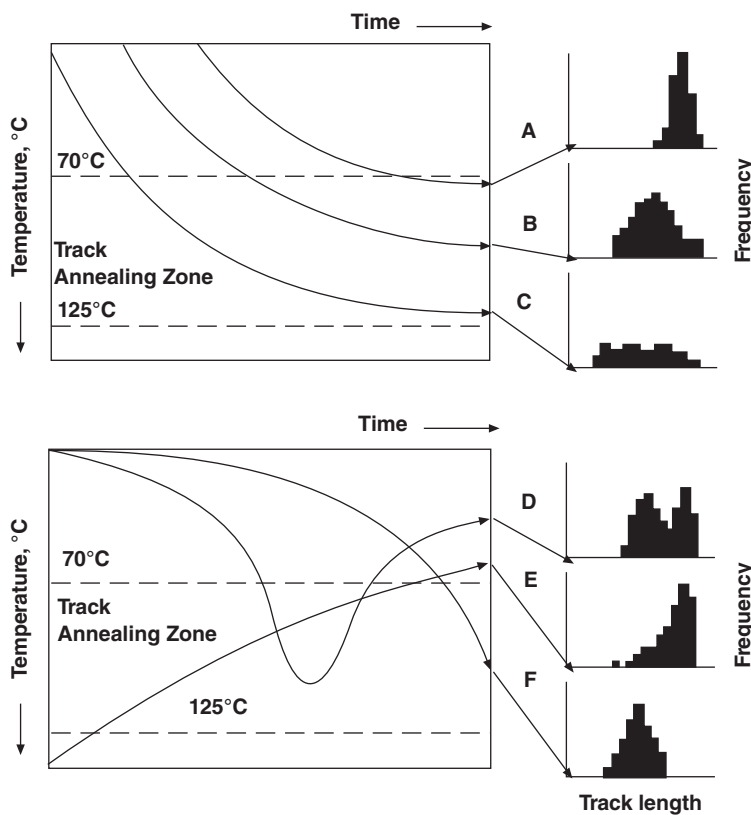


Figure 4.22 Hypothetical time-temperature paths and the distribution of track lengths that should result from these paths. (Source: Ravenhurst and Donelick (1992). Reproduced with permission of the Mineralogical Association of Canada.)

hypothetical time-temperature paths. Uniform track lengths suggest a simple thermal history of rapid cooling and subsequent low temperatures (such as might be expected for a volcanic rock), while a broad distribution of track lengths suggests slower cooling. A skewed distribution suggests initial slow cooling and subsequent low temperatures.

One problem with the approach is that both etching rates and annealing rates, and therefore track lengths, depend on crystallographic orientation. As a result, track length measurements should be only on tracks having the same crystallographic orientation.

NOTES

- Beta detectors are subject to electronic and other noise – in other words pulses that originate from something other than a beta particle. Coincidence counting is a technique that

employs two detectors. Only those pulses that are registered on both detectors are counted – other pulses are considered noise.

- In the laboratory, elemental chlorine is, of course, a gas, but it is so reactive that it quickly reacts with electropositive atoms (e.g., alkalis, metals) in nature to form chlorides.
- The μ particle belongs to the family of particles known as *leptons*, the most familiar members of which are the electron and positron. Like the electron, it may be positively or negatively charged and has a spin of $1/2$. However, its mass is about 100 MeV, more than 2 orders of magnitude greater than that of the electron, and about 1 order of magnitude less than the proton. It is produced mainly by decay of pions, which are also leptons and are created by high-energy cosmic ray interactions. Muons are unstable, decaying to electrons and positrons and ν_u (muonic neutrino) with an average lifetime of 2×10^{-6} s. Because muons are leptons, they are not affected by the

- strong force, and hence interact more weakly with matter than the nucleonic component of cosmic rays.
4. This is not strictly true. ^3He is produced by ${}^6\text{Li}(\text{n},)^3\text{He}$ from spontaneous fission-produced neutrons. However, we might guess that this is a rather improbable reaction. First of all, U is a rare element, and furthermore it rarely fissions. Secondly, Li is a rare element, with typical concentrations of a few tens of ppm. The probability of a fissogenic neutron finding a ${}^6\text{Li}$ nucleus before it is captured by some other nucleus will therefore not be high. Not surprisingly then, the ${}^3\text{He}$ production rate can be considered insignificant in most situations.

REFERENCES

- Bard, E. 1998. Geochemical and geophysical implications of the radiocarbon calibration. *Geochimica et Cosmochimica Acta*, 62: 2025–2038, doi: 10.1016/S0016-7037(98)00130-6.
- Beck, J. W., Richards, D. A., Edwards, R. L. et al. 2001. Extremely large variations of atmospheric ${}^{14}\text{C}$ concentration during the last glacial period. *Science*, 292: 2453–2458.
- Bentley, H. W., Phillips, F. M., Davis, S. N., Habermehl, M. A., Airey, P. L., Calf, G. E. et al. 1986. Chlorine-36 dating of very old groundwater 1. The Great Artesian Basin, Australia. *Water Resources Research*, 22: 1991–2001.
- Bethke, C. M., Zhao, X. and Torgersen, T. 1999. Groundwater flow and the ${}^4\text{He}$ distribution in the Great Artesian Basin of Australia. *Journal of Geophysical Research: Solid Earth*, 104: 12999–13011, doi:10.1029/1999JB900085
- Bethke, C. M. and Johnson, T. M. 2008. Groundwater Age and Groundwater Age Dating. *Annual Review of Earth and Planetary Sciences*, 36: 121–152, doi: doi:10.1146/annurev.earth.36.031207.124210.
- Fairbanks, R. G., Mortlock, R. A., Chiu, T.-C., Cao, L., Kaplan, A., Guilderson, T. P., et al. 2005. Radiocarbon calibration curve spanning 0 to 50,000 years BP based on paired ${}^{230}\text{Th}/{}^{234}\text{U}/{}^{238}\text{U}$ and ${}^{14}\text{C}$ dates on pristine corals. *Quaternary Science Reviews*, 24: 1781–1796, doi: 10.1016/j.quascirev.2005.04.007.
- Frank, M., Schwarz, B., Baumann, S., Kubik, P. W., Suter, M. and Mangini, A. 1997. A 200 kyr record of cosmogenic radionuclide production rate and geomagnetic field intensity from ${}^{10}\text{Be}$ in globally stacked deep-sea sediments. *Earth and Planetary Science Letters*, 149: 121–129, doi: 10.1016/S0012-821X(97)00070-8.
- Kowallis, B. J., Heaton, J. S. and Bringhurst, K. 1986. Fission-track dating of volcanically derived sedimentary rocks. *Geology*, 14: 19–22, doi:10.1130/0091-7613(1986)14<19:fdovds>2.0.co;2.
- Kumar, A., Lal, N., Jain, A. K. and Sorkhabi, R. B. 1995. Late Cenozoic-Quaternary thermo-tectonic history of Higher Himalaya Crystalline (HHC) in Kishtwar-Padar-Zanskar region, NW Himalaya: evidence from fission track ages. *Journal of the Geological Society of India*, 45: 375–391.
- Kurz, M. D. 1986a. Cosmogenic helium in a terrestrial rock. *Nature*, 320: 435–439, doi:10.1038/320435a0.
- Kurz, M. D. 1986b. *In Situ* production of terrestrial cosmogenic helium and some applications to geochronology. *Geochim. Cosmochim. Acta*, 50: 2855–2862.
- Laslett, G. M., Green, P. F., Duddy, I. R. and Gleadow, A. J. W. 1987. Thermal annealing of fission tracks in apatite 2. A quantitative analysis. *Chemical Geology*, 65: 1–13, doi: 10.1016/0168-9622(87)90057-1.
- McElhinny, M. W. and Senanayake, W. E. 1982. Variations in the geomagnetic dipole in the past 50,000 years. *Journal of Geomagnetism and Geoelectricity*, 34: 39–51.
- Phillips, F. M., Leavy, B. D., Jannik, N. O., Elmore, D. and Kubik, P. W. 1986. The accumulation of cosmogenic chlorine-36 in rocks: a method for surface exposure dating, *Science*, 231: 41–43.
- Phillips, F. M., Zreda, M., Smith, S. S., Elmore, D., Kubik, P. W. and Sharma, P. 1990. Cosmogenic chlorine-36 chronology for glacial deposits at Bloody Canyon, Eastern Sierra Nevada, *Science*, 248: 1529–1531.
- Ravenhurst, C. E. and Donelick, R. A. 1992. Fission Track Thermochronology. In: *Short Course Handbook on Low Temperature Thermochronology*, M. Zentilli and P. H. Reynolds (eds). pp. 21–42. Nepean, Ontario: Mineralogical Society Canada.
- Reiners, P. W. and Brandon, M. T. 2006. Using thermochronology to understand orogenic erosion. *Annual Review of Earth and Planetary Sciences*, 34: 419–466, doi: 10.1146/annurev.earth.34.031405.125202.
- Shibata, Y., Tanaka, A., Yoneda, M., Uehiro, T., Kawai, T., Morita, M. and Kobayashi, K. 2000. ${}^{26}\text{Al}/{}^{10}\text{Be}$ method for dating of sediment core samples from Lake Baikal. *Nuclear Instruments and Methods in Physics Research Section B: Beam Interactions with Materials and Atoms*, 172: 827–831, doi: 10.1016/S0168-583X(00)00133-6.
- Tanaka, S. and Inoue, T. 1979. ${}^{10}\text{Be}$ dating of North Pacific sediment cores up to 2.5 million years B.P. *Earth and Planetary Science Letters*, 45: 181–187, doi: 10.1016/0012-821X(79)90119-5.
- Torgersen, T., Habermehl, M. A. and Clarke, W. B. 1992. Crustal helium fluxes and heat flow in the Great Artesian Basin, Australia. *Chemical Geology*, 102: 139–152, doi: 10.1016/0009-2541(92)90152-U.
- Walter, R. C. 1989. Application and limitation of fission-track geochronology to quaternary tephras. *Quaternary International*, 1: 35–46, doi: 10.1016/1040-6182(89)90007-4.

SUGGESTIONS FOR FURTHER READING

- Dickin, A. 1995. *Radiogenic Isotope Geochemistry*. Cambridge: Cambridge University Press.
- Elmore, D. and Phillips, F. M. 1987. Accelerator mass spectrometry measurements of long-lived radioisotopes. *Science*, 236: 543–550.
- Faure, G. 1986. *Principles of Isotope Geology*. New York: John Wiley & Sons, Inc.
- Kurz, M. D. and Brook, E. J. 1994. Surface exposure dating with cosmogenic nuclides. In: *Dating in Surface Context*, Beck, C. (ed.), pp., Albequerque: University New Mexico Press, pp. 139–159.
- Lal, D. 1988. *In situ*-produced cosmogenic isotopes in terrestrial rocks, *Annual Reviews of Earth and Planetary Science*, 16: 355–388.
- Majer, J. R. 1977. *The Mass Spectrometer*. London: Wykeham Publications.
- Nishizumi, K., Kohl, C. P., Arnold, J. R., Klein, J., Fink, D. and Middleton, R. 1991. Cosmic ray produced ^{10}Be and ^{26}Al in Antarctic rocks: exposure and erosion history, *Earth and Planetary Science Letters*, 104: 440–454.
- Tagami, T. and O'Sullivan, P. B. 2005. Fundamentals of Fission-Track Thermochronology. *Reviews in Mineralogy and Geochemistry*, 58: 19–47, doi: 10.2138/rmg.2005.58.2.
- Zentilli, M. and Reynolds, P. H. (eds) 1992. *Short Course Handbook on Low Temperature Thermochronology*. Nepean, Ontario: Mineralogical Society of Canada.

PROBLEMS

- Suppose you determine that a sample of bone from southern England has a specific carbon-14 activity of $11.85 \pm 0.7 \text{ dpm/g}$.
 - Use Eqn. 4.1 to determine the radiocarbon age and the associated error on the age.
 - Use the Calib program (<http://calib.qub.ac.uk/calib/>) to convert this age to calendar years and produce a probability graph similar to Figure 4.3 (ignore inputs for deltas and fractionation factors).
 - An archeologist judges from artifacts found with the bones that the bones is pre-Norman (i.e., pre-1066 AD). Is he wrong?
- Using the data in the Table from core KH711–11 from Tanaka and Inoue (1979), calculate the sedimentation rate assuming constant flux and constant sedimentation. (This is the data set plotted in Figure 4.5.)

Core interval, cm	mean depth, cm	^{10}Be atoms/ $\text{cc} \times 10^9$	\pm
0–40	20	3.64	0.94
40–80	60	2.78	0.62
80–130	105	2.65	0.61
130–180	155	2.89	0.71
180–233	206.5	3.21	0.72
233–284	258.5	2.28	0.50
284–303	293.5	2.78	0.61
303–332	318.5	1.71	0.38
332–397	364.5	1.63	0.46
397–445	421	3.09	0.93
445–490	467.5	1.43	0.28
490–535	512.5	1.56	0.37
535–582	558.5	1.54	0.37
582–612	597	2.51	0.55
612–649	630.5	1.25	0.27

- Using the values for ε , ρ , and l given in the text and a concentration of $2.76 \times 10^{-13} \text{ cc STP/g}$ for the cosmogenic ^3He in the surface sample from Core 33 (Figure 4.11) and an age of 650,000 years, calculate the production rate (your answer will be in cc STP/g).

4. A series of apatite U-Th-He ages were measured on samples from a variety of elevations in southeastern Alaska are listed in the Table. Assuming that the erosion rates exactly balance uplift rates so that the surface of the present landscape would have risen through a flat closure isotherm (Figure), with lower elevations passed through the isotherm most recently.

Elevation, m	Age, Ma
300	17
600	21
900	26
1200	30
2000	38

- (a) Use the data to estimate the uplift/erosion rate.
 (b) Assuming a geothermal gradient of 30°C/km, calculate the cooling rate, and use this to estimate the apatite He closure temperature from Figure 4.19.
5. Suppose you have data such as the series of elevations and ages in Figure 4.22 that suggest an uplift rate of 50 m/Ma. Assume a geothermal gradient of 30°C/Ma, an activation energy, E_A , of 170 kJ/mol, a frequency factor, D_o , of 0.46 cm² / sec, a radius of 60 µm, a geometric factor of 27, and R = 8.314 J/K-mol.
- (a) Calculate the zircon fission track closure temperature from Eqn. 2.37 using Figure 4.19 for the initial guess. Iterate this procedure as necessary. (*HINT: convert temperatures to kelvins and convert all the values above to consistent units; iterative calculations are easiest done in a spreadsheet*).
- (b) Suppose the fission track age is 3 Ma. Assuming a surface temperature of 10°C, the same geothermal gradient, and the closure temperature you calculated earlier, estimate a new uplift rate as described in Section 4.2.2. Iterate calculation of the closure temperature and uplift rate until your answer converges.

Chapter 5

Isotope cosmochemistry

5.1 INTRODUCTION

Meteorites are our primary source of information about the early Solar System. Chemical, isotopic, and petrological features of meteorites reflect events that occurred in the first few tens of millions of years of Solar System history. Observations on meteorites, together with astronomical observations on the birth of stars and the laws of physics, are the basis of our ideas on how the Solar System, and the Earth, formed.

Meteorites can be divided into two broad groups: *primitive meteorites* and *differentiated meteorites*. The chondrites constitute the primitive group: most of their chemical, isotopic, and petrological features resulted from processes that occurred in the cloud of gas and dust that we refer to as the solar nebula. They are far more commonly observed to fall than differentiated meteorites.¹ All chondrites, however, have experienced at least some metamorphism on “parent bodies,” the small planets (diameters ranging from a few km to a few hundred km) from which meteorites are derived by collisions. The differentiated meteorites, which include the achondrites, stony irons, and irons, were so extensively processed in parent bodies, by melting and brecciation, that information about nebular processes has largely been lost. On the other hand, the differentiated meteorites provide insights into the early stages of planet formation. We’ll provide only a brief overview here. More details of meteoritics (the study

of meteorites) can be found in McSween and Huss (2010) and White (2013).

Chondrites are so called because they contain “chondrules,” small (typically a few mm diameter) round bodies that were clearly once molten (Figure 5.1). The other main constituents of chondrites are the matrix, which is generally very fine-grained, amoeboid olivine aggregates (AOAs), and refractory calcium-aluminum inclusions (generally called CAIs). These last two groups formed by a variety of mechanisms, some of which appear to be complex, but we can generalize and say that all these are grains or aggregates of grains that equilibrated with nebular gas at high temperature through condensation and/or evaporation. As we’ll see, the CAIs were the first objects formed in the Solar System and their ages are used to define the birth of the Solar System, that is, time 0.

Most chondrites can be divided into carbonaceous (C), ordinary, and enstatite classes.² The carbonaceous chondrites are, as their name implies, rich in carbon (as carbonate, graphite, organic matter, and, rarely, microdiamonds) and other volatiles and are further divided into classes CI, CV, CM, CO, CR, CH, and CB. The CI chondrites lack chondrules and are considered the compositionally the most primitive of all objects. The ordinary chondrites, so-called because they are by far the most common type, are divided into classes H, L, and LL based on iron content. Enstatite chondrites can be subdivided into EH and EL, also based on iron content.

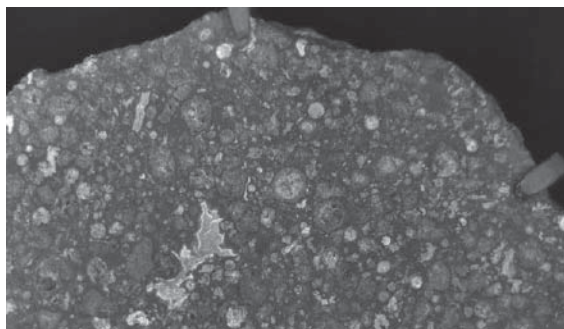


Figure 5.1 Photograph of the meteorite Allende, which fell in Mexico in 1969. Circular/spherical features are chondrules. Irregular white patches are CAIs. (Source: Photograph by NASA.)

It is thought that each class of chondrites is likely derived from a single asteroidal parent body. Chondrites are further assigned a petrographic grade on the basis of the extent of metamorphism they have experienced in parent bodies. Grades 4, 5, and 6 have experienced increasing degrees of high-temperature metamorphism, while grades 1 and 2 experienced low-temperature aqueous alteration. Grade 3 is the least altered.

The various groups of differentiated meteorites can be further subdivided as well. Achondrites are in most cases igneous rocks, some roughly equivalent to terrestrial basalt; others appear to be cumulates. Other achondrites are highly brecciated mixtures. Irons, as they name implies, consist mainly of Fe-Ni metal (Ni content around 5%). Stony-irons are, as their name implies, mixtures of iron metal and silicates. Among achondrites, the *Acapulcoites*, *Lodranites*, *Winonaites*, and *Urelites* are referred to as *primitive achondrites* because they retain some similarity in composition and mineralogy to chondrites. The *diogenites*, *eucrites*, and *howardites*, collectively called the HED meteorites, were long known to be related and thought to come from the asteroid 4 *Vesta*. NASA's DAWN mission orbited Vesta from 2011 to 2012 and confirmed this inference based on spectroscopic measurements of Vesta's surface (DAWN departed Vesta in 2012 for 1 *Ceres*, the largest asteroid). The diogenites are intrusive igneous rocks, the eucrites extrusive ones (lavas), while the howardites are highly brecciated mixtures of both. The *angrites*

constitute another group of achondrites likely derived from a single parent body; they are considerably rarer than the HED group. They too include both intrusive and extrusive igneous rocks, which appear to be derived from a chondritic parent by partial melting under highly oxidizing conditions. They are highly depleted in moderately volatile elements such as Na, which has led to speculation that they might come from Mercury. Based on their reflectance spectra, the small asteroids 239 *Nenetta* and 3819 *Robinson* are also parent body candidates. The SNC meteorites, a group that includes the *Shergottites*, *Nakhlites*, and the meteorite *Chassigny*, derived from Mars, and a few achondrites are derived from the Moon. The irons are divided based on composition into a dozen or so groups. Most of these, referred to as the *magmatic irons*, represent cores of disrupted asteroids. A few, which includes the IAB, IIICD, and IIE irons are referred to as *non-magmatic irons*, but the term is misleading because they too solidified from liquid iron. However, rather than coming from cores, they probably formed as pools of iron liquid segregated from a silicate matrix.

In this chapter, we focus on the question of the age of meteorites and variations in their isotopic composition, and what that can tell us about the early history of our Solar System and the Earth.

5.2 COSMOCHRONOLOGY

5.2.1 Conventional methods

The oft-cited value for the age of the Solar System is 4.567 Ga and is based on dating of meteorites, or more precisely, their components. Before we discuss meteorite ages further, we need to consider the question of precisely what event is being dated by radiometric chronometers. Radioactive clocks record the last time the isotope ratio of the daughter element, for example, $^{87}\text{Sr}/^{86}\text{Sr}$, was homogenized. This is usually some thermal event. In the context of what we know of early Solar System history, the event dated might be (1) the time solid particles were removed from a homogeneous solar nebula, (2) thermal metamorphism in meteorite parent bodies, or (3) crystallization (in the case of chondrules and achondrites), or (4) impact

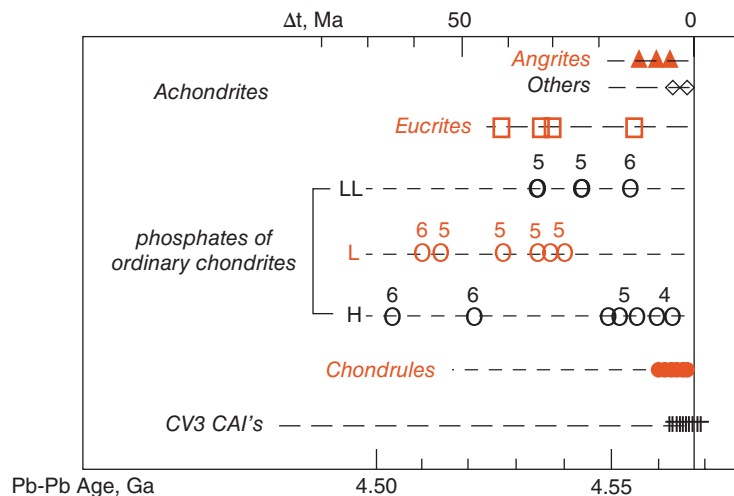


Figure 5.2 Summary of U-Pb ages of chondritic and achondritic meteorites.

metamorphism of meteorites or their parent bodies. In some cases, the nature of the event being dated is unclear.

The most precise ages of meteorites have been obtained using the U-Pb chronometer (Figure 5.2). Advances in analytical techniques have remarkably improved precision over the last decade or so, to the point that ages with uncertainties of only a few 100,000 years can be obtained. However, some of the issues that traditionally plague geochronology come into focus, including lack of complete initial isotopic homogeneity and deviations from closed system behavior. In addition, new issues arise, including uncertainties in half-lives of the parents and uncertainty in, as well as variation of, the $^{238}\text{U}/^{235}\text{U}$ ratio (Amelin et al., 2009). Progress is being made in resolving these issues, but further research remains necessary.

As Figure 5.2 shows, the oldest objects are CAIs; CAIs are good U-Pb dating targets since they are rich in refractory elements like U and depleted in volatile elements like Pb; they are largest (1 mm) and most abundant in CV chondrites, but have been found in all chondrites except the CI group. The oldest high-precision date of a CAI is 4568.67 ± 0.17 Ma for a CAI from the CV3 meteorite NWA2364³ calculated using the “canonical” $^{238}\text{U}/^{235}\text{U}$ ratio of 137.88 (Bouvier et al., 2010). The next oldest age is a CAI from *Allende*, also CV3 meteorite, whose age, calculated using the canonical $^{238}\text{U}/^{235}\text{U}$ value,

is 4567.59 ± 0.11 Ma (Bouvier et al., 2007). Less precise ages ranging from 4567.4 to 4568.6 have been reported for other *Allende* inclusions. Amelin et al. (2009) reported a high precision Pb-Pb age of 4567.11 ± 0.16 Ma for a CAI from the CV3 meteorite *Efremovka*. The accuracy of these dates has, however, been thrown into question by Brennecke et al.’s (2010) discovery of variable $^{238}\text{U}/^{235}\text{U}$ ratios in CAIs from Allende, which range from 137.409 ± 0.039 to 137.885 ± 0.009 , compared to the “canonical” value of 137.88. The age of the NWA2364 CAI decreases to $4,568.22 \pm 0.17$ Ma if a value of 137.84 is used for that ratio and Bouvier et al. (2010) speculated that the $^{238}\text{U}/^{235}\text{U}$ of the CAI might be as low as 137.81, which would make the age 0.3 Ma younger.

Brennecke et al. (2010) concluded that the cause of the $^{235}\text{U}/^{238}\text{U}$ variability was decay of ^{247}Cm , which decays to ^{235}U with a half-life of 13.6 Ma. Amelin et al. (2010) calculated an age for one *Allende* CAI using the $^{238}\text{U}/^{235}\text{U}$ measured in that CAI (137.876) and obtained an age of 4567.18 ± 0.50 Ma. Using measured $^{238}\text{U}/^{235}\text{U}$ ratios in three CAIs from *Efremovka*, which ranged from 137.27 to 137.83, Connelly et al. (2012) found that Pb ages fell within the narrow range of 4567.23 ± 0.29 to 4567.38 ± 0.31 . Connelly et al. noted that while CAIs have variable $^{238}\text{U}/^{235}\text{U}$, this ratio appears to be uniform in chondrules and achondrites, an observation inconsistent with ^{247}Cm decay. They

argued that the cause was mass dependent fractionation instead.

Chondrules in carbonaceous chondrites have Pb-Pb ages that range from 4562.7 ± 0.5 for a *Gujba* (CB3) to 4567.32 ± 0.42 Ga for *Allende* and are thus generally slightly younger than the CAIs. These ages assume the canonical $^{238}\text{U}/^{235}\text{U}$ value. Amelin et al. (2010) found that the *Allende* whole rock and chondrules had a low $^{238}\text{U}/^{235}\text{U}$, 137.747 ± 0.017 , which implies earlier reported ages of the chondrules were too old by about 1.4 Ma. Connelly et al. (2012) found that chondrules from *Allende* and NWA 5697 (an L3 ordinary chondrite) were identical within analytical error with a mean of 137.786 ± 0.013 . Using this $^{238}\text{U}/^{235}\text{U}$ value, they found that ages of five chondrules from these two meteorites ranged from 4564.71 ± 0.30 to 4567.32 ± 0.42 . The range in ages of 3 million years contrasts with the ages of CAIs, which are nearly indistinguishable within analytical error.

Phosphates also have high U/Pb ratios and these were analyzed by Göpel et al. (1994) to obtain high precision ages of a variety of equilibrated (i.e., petrologic classes 4–6) ordinary chondrites, whose ages range from 4.563 to 4.502 Ga. The phosphates are thought to have formed during metamorphism, thus these ages represent the age of metamorphism of these meteorites. The oldest of these meteorites was H4 chondrite *Ste. Marguerite*. Bouvier et al. (2007) subsequently reported a Pb-Pb isochron age of 4562.7 Ma, in excellent agreement with the age determined by Göpel et al. (1994). The age of CAIs from CV3 meteorites thus seems 3 Ma older than the oldest precise ages obtained on ordinary chondrites. No attempt has been made at high precision dating of CI chondrites, as they are too fine-grained to separate phases.

Among achondrites, the chronology of the angrites is perhaps best documented. The oldest high precision Pb-Pb age is 4564.58 ± 0.14 Ma for the angrite SAH99555 (Connelly et al., 2008). An age nearly as old, 4563.37 ± 0.25 was reported for the angrite *D'Orbigny* (Amelin, 2008; Brennecka and Wadhwa, 2012). *Angra dos Reis*, the type meteorite of the class, has a Pb-Pb age of 4557.65 ± 0.13 Ma, and *Lewis Cliff 86010*, a coarse grained “plutonic” angrite, has an age of 4558.55 ± 0.15 Ma. Thus differentiation,

cooling, and crystallization of the angrite parent body apparently lasted some 6 million years. Wadhwa et al. (2009) reported an age of 4566.5 ± 0.2 Ma for unusual basaltic achondrite, *Asuka 881394*. Bouvier et al. (2011) determined an age of 4562.89 ± 0.59 Ma for another unusual basaltic achondrite, NWA2976. *Ibitira*, a unique unbreciated eucrite, has an age of 4556 ± 6 Ma. Perhaps surprisingly, these ages are similar to those of chondrites. This suggests that the parent body of these objects formed, melted, and differentiated, and the outer parts crystallized within a very short time interval. Not all achondrites are quite so old, however. A few other high precision ages (those with quoted errors of less than 10 Ma) are available and they range from this value down to 4.529 ± 0.005 Ga for *Nuevo Laredo* and 4.510 ± 0.004 Ga for *Bouvante*. Thus, the total range of the few high precision ages in achondrites is about 50 million years. Iron meteorites appear to be similarly old. Smoliar et al. (1996) reported Re-Os ages of 4558 ± 12 and 4537 ± 8 Ma for IIIA and IIA irons, respectively; ages of other iron groups range from 4506 to 4569 Ma, but are of lower precision and are not significantly different from the IIIA and IIA ages. As can be seen in Figure 5.2, there is no obvious relationship between meteorite class and age. H chondrites do seem a bit older than other ordinary chondrites and Göpel et al. (1994) did find an inverse correlation between petrologic type and age (the least metamorphosed are oldest), but this does not appear to be true of chondrites in general. Furthermore, there appears to be little difference in age between chondrites and achondrites. The present state of conventional meteorite chronology may be summarized by saying that it appears the meteorite parent bodies formed around 4.567 ± 0.001 Ga, and there is some evidence that high-temperature inclusions and chondrules in carbonaceous chondrites may have formed a few Ma earlier than other material. Sm-Nd, Lu-Hf, and Rb-Sr ages are less precise than the U-Pb ages and are often a bit younger, and perhaps date peak metamorphism of chondrite parent bodies, and melting or metamorphism on achondrite parent bodies.

In contrast to the tightly clustered ages for the chronometers discussed previously, K-Ar (including ^{40}Ar - ^{39}Ar) ages show a much wider

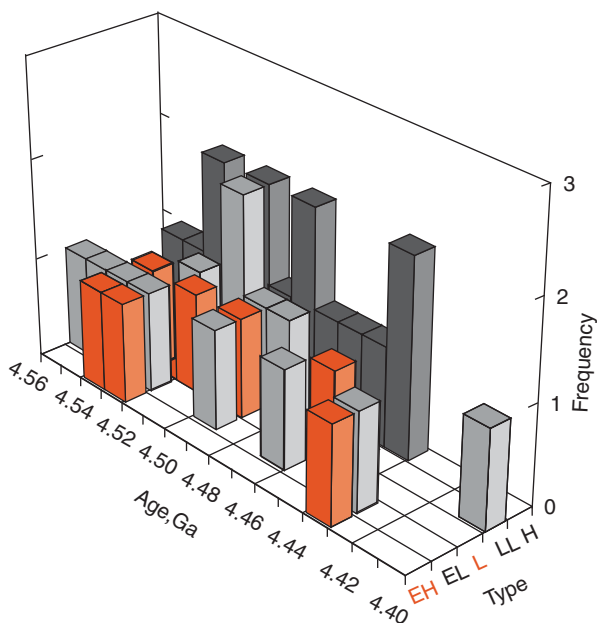


Figure 5.3 Histogram illustrating ^{40}Ar - ^{39}Ar ages of ordinary and enstatite chondrites. Data from the summary of Bogard (2photo 2011).

range. As we found in Chapter 2, closure temperatures for K-Ar are generally much lower than for other chronometers, so these younger ages could reflect the time required to cool to lower closure temperature or heating events resulting from impacts. Figure 5.3 summarizes K-Ar ages of ordinary and enstatite chondrites, which range down to more than 100 Ma after formation of the Solar System and the parent bodies of these meteorites. The parent bodies were initially hot due to (1) gravitation energy release during their accretion, and (2) heating by short-lived radionuclides that were present in the early Solar System (and which we will discuss in the following section). Based on these ages, the size of the parent bodies can be estimated to be ~ 100 km. For some chondrites, notably some H-chondrites, younger ages are associated with the higher metamorphic grade, suggesting we are seeing a depth profile in the parent body, with increasing metamorphic temperatures and longer cooling times at greater depths within the parent body (Bogard, 2011). Some chondrites have ^{40}Ar - ^{39}Ar ages of less than 1 Ga, including many L chondrite ages that cluster around 0.5 Ga. These ages reflect resetting during impact heating

on the chondrite parent bodies, demonstrating that large collisions have occurred in the asteroid belt throughout Solar System history.

Other groups of meteorites yield a variety ^{40}Ar - ^{39}Ar ages. Some primitive achondrites, (acapulcoites and lodranites) have ages that tightly cluster around 4.51 Ga. Silicate from IAB irons (which are among the so-called non-magmatic irons) give a continual distribution of ages between 4.53–4.32 Ga. Eucrites (from Vesta), many of which are brecciated, yield a wide range ages with peaks in the distribution occurring at 4.48 Ga, 4.0 to 3.7 Ga and 3.45–3.55 Ga, which date heating from large impacts on the surface of Vesta, and the view of Vesta from the DAWN spacecraft (Figure 5.4) certainly shows there have been many of those.

5.2.2 Extinct radionuclides

There is evidence that certain short-lived nuclides once existed in meteorites. This evidence consists of the anomalous abundance of nuclides, ^{129}Xe , for example, known to be produced by the decay of short-lived radionuclides, such as ^{129}I , and correlations between the abundance of the radiogenic *isotope* and the parent *element*. Consider, for example,



Figure 5.4 A mosaic image of Vesta based on photographs taken by the DAWN spacecraft as it orbited Vesta from 2011 to 2012. Two very large craters in the southern hemisphere appear to be less than 2 Ga, the largest and most recent of which, the Rheasilvia Basin, may have been the impact that launched the HED meteorites into Earth-crossing orbits. (Source: Photograph by NASA.)

^{53}Cr , which is the decay product of ^{53}Mn . The half-life of ^{53}Mn , only 3.7 million years, is so short that any ^{53}Mn produced by nucleosynthesis has long since decayed. If ^{53}Mn is no longer present, how do we know that the anomalous ^{53}Cr is due to decay of ^{53}Mn ? We reason that the abundance of ^{53}Mn , when and if it was present, should have correlated with the abundance of other isotopes of Mn. ^{55}Mn is the only stable isotope of Mn. So we construct a plot similar to a conventional isochron diagram (isotope ratios versus parent/daughter ratio), but use the stable isotope, in this case ^{55}Mn , as a proxy for the radioactive one, ^{53}Mn . An example is shown in Figure 5.5.

Starting from our basic equation of radioactive decay, we can derive the following equation:

$$D = D_0 + N_0(1 - e^{-\lambda t}) \quad (5.1)$$

This is similar to the isochron equation we derived earlier, Eqn. 2.8, but not identical. In particular, notice 5.1 contains N_0 , the initial abundance of the parent, whereas 2.8 contains the present abundance of the parent. Notice also that the term in parenthesis on the right is

different. Written for the example of the decay of ^{53}Mn to ^{53}Cr , we have:

$$\frac{^{53}\text{Cr}}{^{52}\text{Cr}} = \left(\frac{^{53}\text{Cr}}{^{52}\text{Cr}} \right)_0 + \left(\frac{^{53}\text{Mn}}{^{52}\text{Cr}} \right)_0 (1 - e^{-\lambda t}) \quad (5.2)$$

where as usual the subscript naught denotes the initial ratio. The problem we face is that we do not know the initial $^{53}\text{Mn}/^{52}\text{Cr}$ ratio. We can, however, measure the $^{55}\text{Mn}/^{53}\text{Cr}$ ratio. Assuming that initial isotopic composition of Mn was homogeneous in all the reservoirs of interest; that is, $^{53}\text{Mn}/^{55}\text{Mn}_0$ is constant, the initial $^{53}\text{Mn}/^{52}\text{Cr}$ ratio is just:

$$\left(\frac{^{53}\text{Mn}}{^{52}\text{Cr}} \right)_0 = \left(\frac{^{55}\text{Mn}}{^{52}\text{Cr}} \right)_0 \left(\frac{^{53}\text{Mn}}{^{55}\text{Mn}} \right)_0 \quad (5.3)$$

Of course, since ^{55}Mn and ^{52}Cr are both non-radioactive and non-radiogenic, the initial ratio is equal to the present ratio (i.e., this ratio is constant through time). Substituting 5.3 into 5.2, we have:

$$\begin{aligned} \frac{^{53}\text{Cr}}{^{52}\text{Cr}} &= \left(\frac{^{53}\text{Cr}}{^{52}\text{Cr}} \right)_0 + \left(\frac{^{55}\text{Mn}}{^{52}\text{Cr}} \right)_0 \left(\frac{^{53}\text{Mn}}{^{55}\text{Mn}} \right)_0 \\ &\quad \times (1 - e^{-\lambda t}) \end{aligned} \quad (5.4)$$

Finally, for a short-lived nuclide like ^{53}Mn , the term λt is very large after 4.56 Ga, so the term $e^{-\lambda t}$ is 0 (this is equivalent to saying all the ^{53}Mn has decayed away). Thus, we are left with:

$$\frac{^{53}\text{Cr}}{^{52}\text{Cr}} = \left(\frac{^{53}\text{Cr}}{^{52}\text{Cr}} \right)_0 + \left(\frac{^{55}\text{Mn}}{^{52}\text{Cr}} \right)_0 \left(\frac{^{53}\text{Mn}}{^{55}\text{Mn}} \right)_0 \quad (5.5)$$

On a plot of $^{53}\text{Cr}/^{52}\text{Cr}$ versus $^{55}\text{Mn}/^{52}\text{Cr}$, the slope is proportional not to time, as in a conventional isochron diagram, but to the initial $^{53}\text{Mn}/^{55}\text{Mn}$ ratio. Thus, correlations between isotope ratios such as these are evidence for the existence of extinct radionuclides.

In this way, many extinct radionuclides have been identified in meteorites from variations in the abundance of their decay products. The most important of these are listed in Table 5.1. On a cosmic scale, nucleosynthesis is a more or less continuous process – roughly once every second a supernova explodes somewhere in the Universe. So we might expect that interstellar dust might contain some of the longer-lived of these nuclides at low,

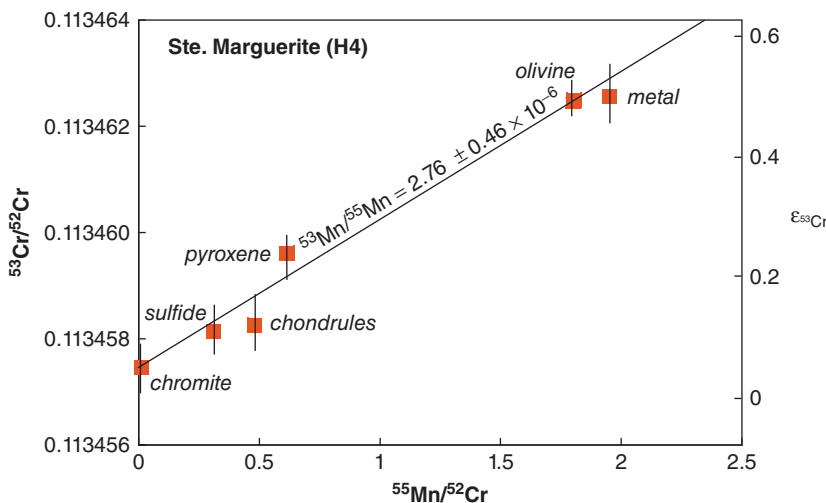


Figure 5.5 Correlation of the $^{53}\text{Cr}/^{52}\text{Cr}$ ratio with $^{55}\text{Mn}/^{52}\text{Cr}$ ratio in components of the ordinary chondrite St. Marguerite. (Source: Trinquier et al. (2008). Reproduced with permission of Elsevier.)

Table 5.1 Important short-lived radionuclides in the early Solar System.

Radio-nuclide	Half-life Ma	Decay	Daughter	Initial abundance Ratio
^{10}Be	1.5	β	^{10}B	$^{10}\text{Be}/^9\text{Be} \sim 7.5 \times 10^{-4}$
^{26}Al	0.72	β	^{26}Mg	$^{26}\text{Al}/^{27}\text{Al} = 5.2 \times 10^{-5}$
^{36}Cl	0.301	β	$^{36}\text{Ar}/^{36}\text{S}$	$^{36}\text{Cl}/^{35}\text{Cl} \sim 1.6 \times 10^{-4}$
^{41}Ca	0.15	β	^{41}K	$^{41}\text{Ca}/^{40}\text{Ca} \sim 1.5 \times 10^{-8}$
^{53}Mn	3.7	β	^{53}Cr	$^{53}\text{Mn}/^{55}\text{Mn} \sim 1 \times 10^{-5}$
^{60}Fe	1.5	β	^{60}Ni	$^{60}\text{Fe}/^{56}\text{Fe} \sim 5.8 \times 10^{-8}$
^{107}Pd	9.4	β	^{107}Ag	$^{107}\text{Pd}/^{108}\text{Pd} \sim 5.9 \times 10^{-4}$
^{129}I	15.7	β	^{129}Xe	$^{129}\text{I}/^{127}\text{I} \sim 1.35 \times 10^{-4}$
^{146}Sm	68 ± 7	α	^{142}Nd	$^{146}\text{Sm}/^{144}\text{Sm} \sim 0.0094$
^{182}Hf	9	β	^{182}W	$^{182}\text{Hf}/^{180}\text{Hf} \sim 9.7 \times 10^{-5}$
^{244}Pu	82	α, SF	Xe	$^{244}\text{Pu}/^{238}\text{U} \sim 0.0068$
^{247}Cm	15.6	α, SF	^{235}U	$^{247}\text{Cm}/^{235}\text{U} \sim 6 \times 10^{-5}$

near-steady state concentrations. However, such events are much rarer on a local scale (fortunately for us), and the shorter-lived of these nuclides must have been synthesized nearby shortly before the Solar System formed.

To understand why these short-lived radionuclides require a nucleosynthetic event, consider the example of ^{53}Mn . Its half-life is 3.7 Ma. Hence 3.7 Ma after it was created only 50% of the original number of atoms would remain. After two half-lives, or 7.4 Ma, only 25% would remain, after four half-lives, or 14.8 Ma, only 6.125% of the original ^{53}Mn would remain, and so on. After 10 half-lives, or 37 Ma, only $1/2^{10}$ (0.1%) of the original amount would remain. The

correlation between the Mn/Cr ratio and the abundance of ^{53}Cr indicates some ^{53}Mn was present when the meteorite, or its parent body, formed. From this we can conclude that an event that synthesized ^{53}Mn occurred not more than roughly 30 million years before the meteorite formed. The shorter-lived nuclides provide even tighter constraints on this time scale. We'll return to this later in the chapter.

5.2.2.1 ^{129}I - ^{129}Xe and ^{244}Pu

The first of these short-lived radionuclides discovered was ^{129}I , which decays to ^{129}Xe . Figure 5.6 shows the example of the analysis of the meteorite LL5 chondrite *Tuxtuac*. In this case, the analysis is done in a manner very

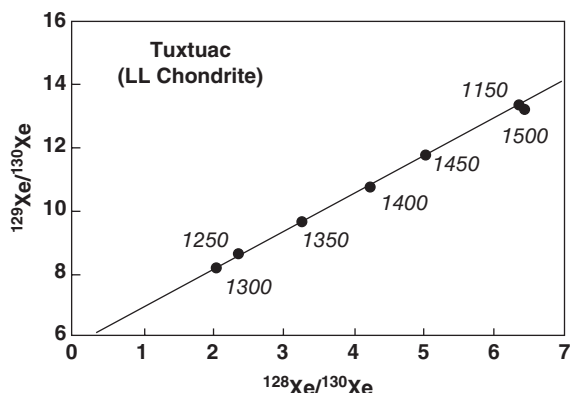


Figure 5.6 Correlation of $^{129}\text{Xe}/^{130}\text{Xe}$ with $^{128}\text{Xe}/^{130}\text{Xe}$. The ^{128}Xe is produced from ^{127}I by irradiation in a reactor, so that the $^{128}\text{Xe}/^{130}\text{Xe}$ ratio is proportional to the $^{127}\text{I}/^{130}\text{Xe}$ ratio. Numbers adjacent to data points correspond to temperature of the release step ($^{\circ}\text{C}$). (Source: Adapted from Bernatowicz et al. (1988).)

analogous to $^{40}\text{Ar}-^{39}\text{Ar}$ dating: the sample is first irradiated with neutrons so that ^{128}Xe is produced by neutron capture by ^{127}I creating ^{128}I , which subsequently decays to ^{128}Xe . The amount of ^{128}Xe produced is proportional to the amount of ^{127}I present (as well as the neutron flux and reaction cross section). The sample is then heated in vacuum through a

series of steps and the Xe released at each step analyzed in a mass spectrometer. As was the case in Figure 5.5, the slope is proportion to the $^{129}\text{I}/^{127}\text{I}$ ratio at the time the meteorite formed.

In addition to ^{129}Xe produced by decay of ^{129}I , the heavy isotopes of Xe are produced by fission of U and Pu. ^{244}Pu is of interest because it another extinct radionuclide. Fission does not produce a single nuclide, rather a statistical distribution of many nuclides. Each fissionable isotope produces a different distribution. The distribution produced by U is similar to that produced by ^{244}Pu , but the difference is great enough to demonstrate the existence of ^{244}Pu in meteorites, as is shown in Figure 5.7. Fission tracks in excess of the expected number of tracks for a known uranium concentration are also indicative of the former presence of ^{244}Pu .

These extinct radionuclides provide a means of relative dating of meteorites and other bodies. Figure 5.8 shows relative ages based on this $^{129}\text{I}-^{129}\text{Xe}$ decay system. These ages are calculated from $^{129}\text{I}/^{127}\text{I}$ ratios, which are in turn calculated from the ratio of excess ^{129}Xe to ^{127}I . I-Xe ages are often reported relative to the age of the *Shallowater* aubrite (achondrite). Whitby et al. (2000) determined the initial Solar System $^{129}\text{I}/^{127}\text{I}$ from halite in the H chondrite *Zag* to be 1.35×10^{-4} .

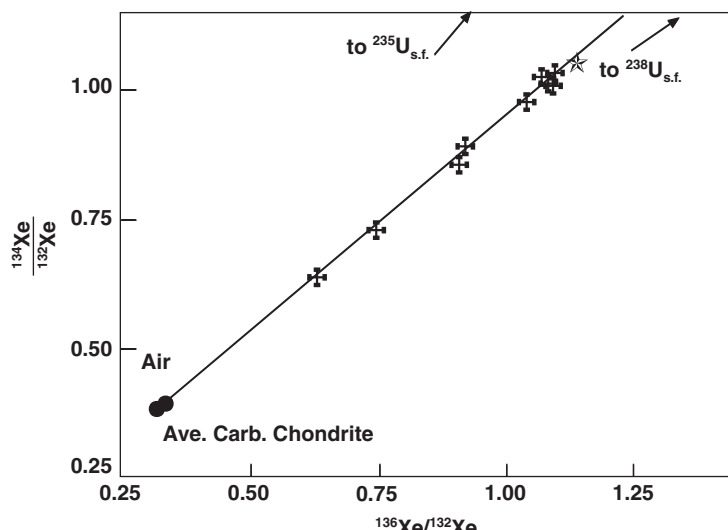


Figure 5.7 Variation of $^{134}\text{Xe}/^{132}\text{Xe}$ and $^{136}\text{Xe}/^{132}\text{Xe}$ in meteorites (5). The isotopic composition of fission products of man-made ^{244}Pu is shown as a star (\star). (Source: Adapted from Lewis (1975).)

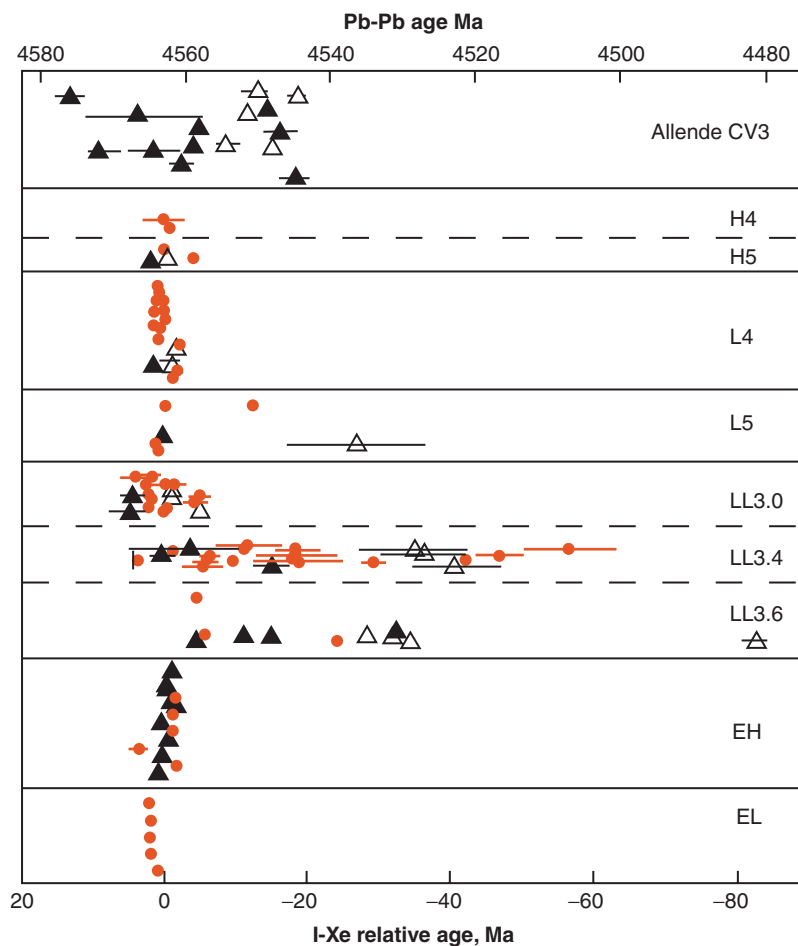


Figure 5.8 Summary of I-Xe ages of meteorites relative to Bjurböle Shallowater. Solid gray symbols are “whole rock” ages, open triangles are chondrules with low release temperature I-Xe isochrons, solid triangles are chondrules with high temperature isochrons. (Source: Adapted from Hohenberg and Pravdivtseva 2008. Reproduced with permission of Elsevier.)

That, together with I-Xe dating of phosphates also dated by Pb-Pb, allows I-Xe ages to be calibrated to an absolute time scale (Brazzle et al., 1999, Gilmour et al., 2006). On this time scale, the absolute age of *Shallowater* is 4563.3 ± 0.4 Ma.

Because both I and Xe are mobile elements, the I-Xe system is readily disturbed. Consequently, they more likely date processes occurring on meteorite parent bodies rather than nebular events. Most chondrules have I-Xe ages that are no more than a few million years younger than the age of CAIs, although some, particularly those with low-temperature Xe release patterns are, however, tens of millions of years younger. Differentiated meteorites show a similar spread of ages, with some, such as the aubrite *Shallowater* and the acopulcite

Acopulco, being only a few million years younger than CAIs.

5.2.2.2 $^{107}\text{Pd}-^{107}\text{Ag}$

The existence of variations in isotopic composition of silver, and in particular variations in the abundance of ^{107}Ag that correlate with the Pd/Ag ratio in iron meteorites indicates that ^{107}Pd was present when the irons formed. The half-life of ^{107}Pd is 9.4 million years; hence the irons must have formed within a few tens of millions of years of synthesis of the ^{107}Pd . This in turn implies that formation of iron cores within small planetary bodies occurred within a few tens of millions of years of formation of the Solar System.

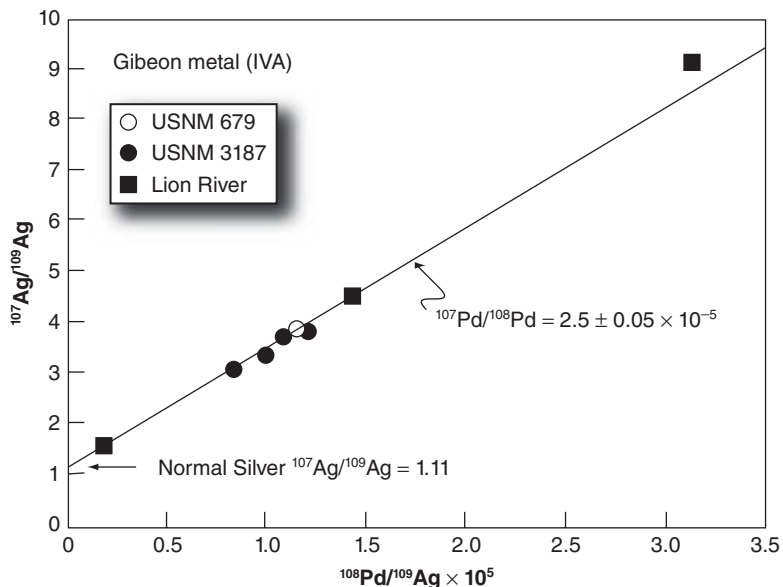


Figure 5.9 Correlation of $^{107}\text{Ag}/^{109}\text{Ag}$ with $^{108}\text{Pd}/^{109}\text{Ag}$ in various samples of the Group IVA iron meteorite Gibeon, demonstrating the existence of ^{107}Pd at the time these irons formed. (Source: Chen and Wasserburg (1990). Reproduced with permission of Elsevier.)

Fractions of metal from the meteorite *Gibeon* (IVA iron) define a fossil isochron indicating an initial $^{107}\text{Pd}/^{108}\text{Pd}$ ratio of 2.5×10^{-5} (Chen and Wasserburg, 1990). Other IVA irons generally fall along the same isochron (Figure 5.9). IIAB and IIAB irons, as well as several anomalous irons show $^{107}\text{Ag}/^{109}\text{Ag}$ - $^{108}\text{Pd}/^{109}\text{Ag}$ correlations that indicate $^{107}\text{Pd}/^{108}\text{Pd}$ ratios between 1.5 and 2.4×10^{-5} . Assuming these differences in initial $^{107}\text{Pd}/^{108}\text{Pd}$ are due to time and the decay of ^{107}Pd , all of these iron meteorites would have formed no more than 10 million years after *Gibeon* (Chen and Wasserburg, 1996).

5.2.2.3 ^{26}Al - ^{26}Mg

Perhaps the most significant extinct radionuclide is ^{26}Al . Because of its short half-life (0.717 Ma), it provides much stronger constraints on the amount of time that could have passed between nucleosynthesis and processes that occurred in the early Solar System. Furthermore, the abundance of ^{26}Al was such that its decay could have been a significant source of heat, and it was likely to have played a role in heating, melting, and metamorphism of meteorite parent bodies. ^{26}Al decays to ^{26}Mg : Two examples

of the correlation between $^{26}\text{Mg}/^{24}\text{Mg}$ and $^{27}\text{Al}/^{24}\text{Mg}$ are shown in Figure 5.10.

Because of the relatively short half-life of ^{26}Al and its potential importance as a heat source, considerable effort has been devoted to measurement of Mg isotope ratios in meteorites. Much of this work has been carried out with ion microprobes, which allow the simultaneous measurement of $^{26}\text{Mg}/^{24}\text{Mg}$ and $^{27}\text{Al}/^{24}\text{Mg}$ on spatial scales as small as $10\text{ }\mu\text{m}$. As a result, there are more than 1500 measurements more than 60 meteorites reported in the literature, mostly on CAIs, because CAIs, with their high Al/Mg ratios should produce higher $^{26}\text{Mg}/^{24}\text{Mg}$ ratios, which allows for high temporal resolution.

Figure 5.11 shows that the highest inferred $^{26}\text{Al}/^{27}\text{Al}$ ratios are found in CAIs and that, with some exceptions, chondrules and other objects have lower inferred $^{26}\text{Al}/^{27}\text{Al}$ ratios or lack evidence of ^{26}Al altogether, suggesting they formed at least several million years later, after ^{26}Al had largely decayed. Advances in analytical technology have allowed higher precision measurements have recently revealed that there are systematic variations in inferred $^{26}\text{Al}/^{27}\text{Al}$ ratios even among CAIs. MacPherson et al. (2012) found

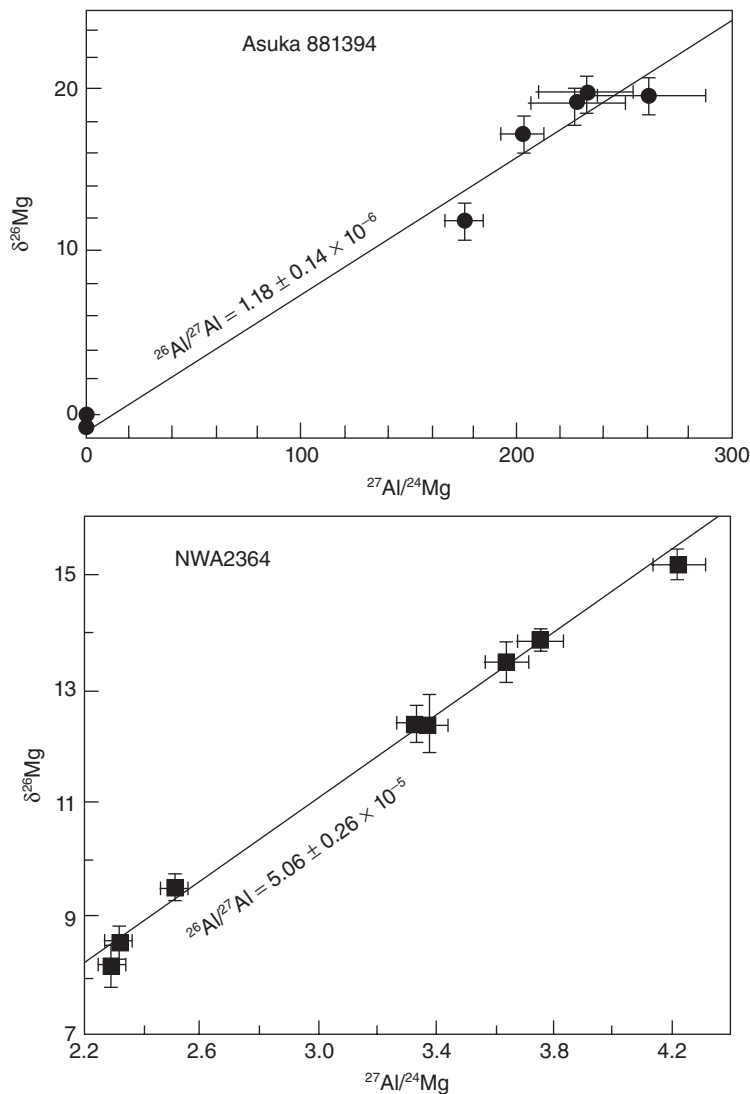


Figure 5.10 Comparison of Al-Mg isotope systematics for two different meteorites. The lower diagram shows minerals separated from a CAI in CV3 NWA2364, one of the oldest objects in the solar system (Bouvier and Wadhwa, 2010). The upper diagram shows plagioclase and pyroxene separates from the eucrite Asuka 881394 (Nyquist et al., 2003). The later has an initial $^{27}\text{Al}/^{26}\text{Al}$ more than 40 times lower than NWA2364, implying it is some 4 million years younger.

that primitive, unmelted CAIs have initial $^{26}\text{Al}/^{27}\text{Al}$ ratios of 5.2×10^{-5} , melted CAIs range from 5.17×10^{-5} to 4.24×10^{-5} , and one single CAI has an range of 4.77 to 2.77×10^{-5} . The entire range is thus a factor of 2 and corresponds to time span of ~ 0.7 Ma, presumably the time span during which the inner Solar System was hot enough for CAI formation and reprocessing. Higher precision analyses are also revealing more details of the timing of chondrule formation. Most

chondrules have inferred $^{26}\text{Al}/^{27}\text{Al}$ ratios of less than 1×10^{-5} , but a significant fraction have values ranging as high as 2×10^{-5} , suggesting chondrule formation began as early as 1 million years after the start of CAI formation (time 0) and continued for another 2–3 million years after that (e.g., Villeneuve et al., 2009). These higher inferred ratios are consistent with Pb-Pb ages discussed in Section 5.2.1 indicating that at least some chondrules are as old as CIAs. Nevertheless, the majority appears to be younger.

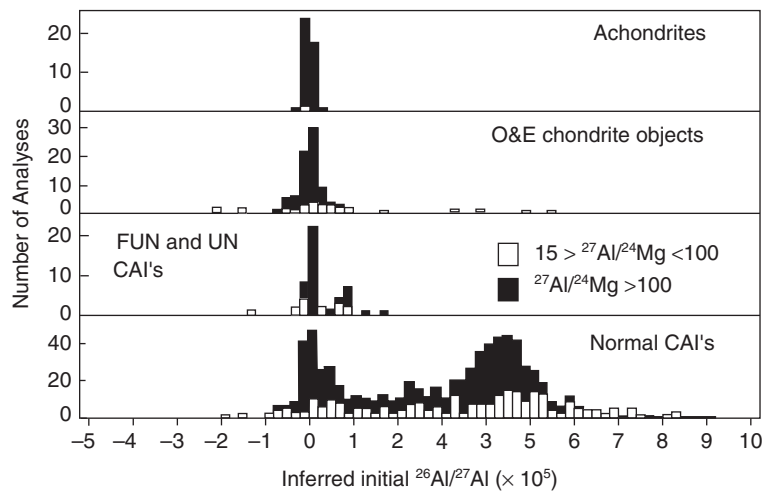


Figure 5.11 Inferred initial $^{26}\text{Al}/^{27}\text{Al}$ for all available meteoritic data. “O&E objects” are chondrules and other constituents of ordinary and enstatite chondrites; FUN and UN refers to CAI’s with “fractionated and unknown nuclear” isotopic anomalies. Source: MacPherson et al. 1995. Reproduced with permission of John Wiley & Sons.

There has been some debate as to whether differences in inferred $^{26}\text{Al}/^{27}\text{Al}$ ratios reflected a heterogeneous distribution of recently synthesized ^{26}Al in the solar nebula. Under that theory, CAIs formed in a ^{26}Al -rich region while chondrules formed in a ^{26}Al -poor one. Most of the presently available evidence suggests that $^{26}\text{Al}/^{27}\text{Al}$ ratios in the solar nebula were homogeneous within about 10%, implying differences in inferred initial $^{26}\text{Al}/^{27}\text{Al}$ do in fact reflect differences in formation ages (Bouvier and Wadhwa, 2010; Villeneuve, et al., 2009; Boss, 2012), although some types of CAIs found in CM, CO, and CH chondrites may have different initial ratios (Krot et al., 2009) and the question of heterogeneous distribution of ^{26}Al remains debated.

Amebiolal olivine aggregates (AOAs) found in chondrites are likely to be direct condensates from nebular gas. Anorthite inclusions in them have $^{26}\text{Al}/^{27}\text{Al}$ ratios up to 4×10^{-5} , suggesting they formed only slightly later than CAIs and before most chondrules (Nagashima et al., 2013).

Extinct radionuclides alone provide only a relative chronology of early Solar System events. An absolute chronology can be established by calibrating relative ages determined from extinct radionuclides with high precision Pb-Pb ages. For the earliest objects, the short-lived nuclides ^{53}Mn and

^{26}Al have proved most useful. Figure 5.12 illustrates such a time-scale, anchored on objects dated by both Pb-Pb and ^{26}Al or ^{53}Mn . The chronology begins with the CAI from NWA2364. Objects such as *Lewis Cliffs* 86010, *St. Marguerite*, and *D’Orbigny* provide other anchors. Objects such as *Orgueil*, which has not been dated by conventional radiometric methods, can be placed on the time scale based on their apparent initial $^{26}\text{Al}/^{27}\text{Al}$ or $^{53}\text{Mn}/^{55}\text{Mn}$ ratios.

5.2.3 Extinct radionuclides in the Earth

Several of the short-lived radionuclides listed in Table 5.1 have half-lives sufficiently long that they should have been present in the early Earth. Of greatest interest are ^{129}I , ^{182}Hf , and ^{146}Sm . The decay products of these nuclides are ^{129}Xe , ^{182}W , and ^{142}Nd , an atmophile, a siderophile, and a lithophile element, respectively. Their distribution can tell us about the early evolution of the Earth’s atmosphere, core, and mantle. Here, we’ll consider ^{182}Hf and ^{146}Sm ; we’ll discuss ^{129}I in Chapter 12.

5.2.3.1 $^{182}\text{Hf}-^{182}\text{W}$ constraints of the age of the Moon and the Earth’s Core

The Hf-W pair is particularly interesting because Hf is lithophile while W is moderately siderophile. Thus the $^{182}\text{Hf}-^{182}\text{W}$

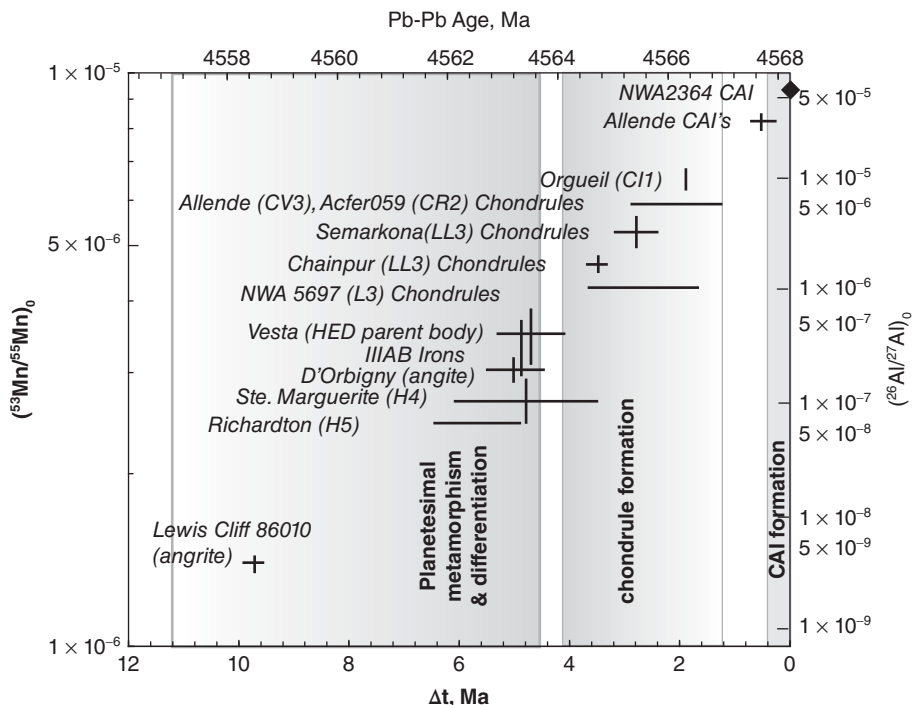


Figure 5.12 Time scale of events in the early solar system based on calibrating ^{53}Mn and ^{26}Al extinct radionuclide chronology to Pb-Pb ages. Based on data in Trinquier et al. (2008), Nyquist et al. (2009), Bouvier and Wadhwa (2010), and Connelly et al (2012).

decay system should be useful in “dating” silicate-metal fractionation, including core formation in the terrestrial planets and asteroids. Both are highly refractory elements, which have the advantage that a first order assumption is that bodies such as the Earth should have a chondritic Hf/W ratio. These observations have led to a series of measurements of W isotope ratios on terrestrial materials, lunar samples, and a variety of meteorites, including those from Mars. The conclusions have evolved as new measurements have become available. Among other things, the story of Hf-W illustrates the importance of the fundamental dictum in science that results need to be independently replicated before they are accepted.

Because the variations in $^{182}\text{W}/^{183}\text{W}$ ratio are quite small, they are sometimes presented and discussed in the same ϵ notation used for Nd and Hf isotope ratios or in μ notation, which is deviations in parts per million. There is a slight difference, however; ϵ_{W} or μ_{W} are deviations in parts per 10,000 or 1,000,000, respectively, *from a terrestrial tungsten standard*, and $f_{\text{Hf/W}}$ is the fractional

deviation of the Hf/W ratio from the chondritic value. Assuming that the silicate Earth has a uniform W isotope composition identical to that of the standard then the silicate Earth has ϵ_{W} of 0 by definition. The basic idea this: if the $^{182}\text{W}/^{183}\text{W}$ ratio in the silicate Earth is higher than in chondrites, it would mean that much of the Earth’s tungsten had been sequestered in the Earth’s core before ^{182}Hf had entirely decayed. Since the half-life of ^{182}Hf is 9 Ma and using our rule of thumb that a radioactive nuclide is fully decayed in 5–10 half-lives, this would mean the core must have formed within 45–90 million years of the formation of the Solar System (which we take as the age of the CAIs). If on the other hand, the $^{182}\text{W}/^{183}\text{W}$ ratio in the silicate Earth was the same as in bulk chondrites, which never underwent silicate-metal fractionation, this would mean that at least 45–90 million years must have elapsed (enough time for ^{182}Hf to fully decay) between the formation of chondrites and the formation of the Earth’s core. As we’ll see, the reality is likely more complex than either of these simply scenarios.

“Anomalous” W isotopic compositions were first found in the IA iron *Toluca* by Harper et al. (1991). They found the $^{182}\text{W}/^{183}\text{W}$ ratio in the meteorite was 2.5 epsilon units (i.e., parts in 10,000) lower than in terrestrial W. This value was revised to -3.9 epsilon units by subsequent, more precise, measurements (Jacobsen and Harper, 1996). Essentially, the low $^{182}\text{W}/^{183}\text{W}$ ratio indicates *Toluca* metal separated from Hf-bearing silicates before ^{182}Hf had entirely decayed. At this point, however, no measurements had yet been made on chondritic meteorites, so it was unclear how rapidly the Earth’s core had formed. Chondrites are undifferentiated Solar System material, and therefore the reference to which other materials must be compared.

Lee and Halliday (1995) reported W isotope ratios for two carbonaceous chondrites (*Allende* and *Murchison*), two additional iron meteorites and a lunar basalt. They found the iron meteorites showed depletions in ^{182}W ($\epsilon_{\text{W}} = -4.5$ and -3.7 for *Arispe* and *Coya Norte*, respectively) that were similar to that observed in *Toluca* by Jacobsen and Harper (1996). The chondrites, however, had ϵ_{W} values that were only slightly positive, about $+0.5$, and were analytically indistinguishable from “terrestrial” W, as was the lunar basalt. Lee and Halliday (1995) inferred an initial $^{182}\text{Hf}/^{180}\text{Hf}$ for the solar nebula of 2.6×10^{-4} , much higher than the ratio assumed by Jacobsen and Harper (and the present best estimate listed in Table 5.1). Based on this similarity of isotopic compositions of chondritic and terrestrial W, Lee and Halliday (1995) concluded that the minimum time required for formation of the Earth’s core was 62 million years.

Subsequently, Lee and Halliday (1998) reported ϵ_{W} values of $+32$ and $+22$ in the achondrites *Juvina*s and ALHA78132. These large differences in W isotopic composition meant that metal-silicate fractionation, that is, core formation, occurred quite early in the parent bodies of achondritic meteorites (*Juvina*s and ALHA78132 are eucrites and their parent body, Vesta, is known to have an iron core based on density determined by the DAWN mission). In other words, asteroids or “planetesimals” must have differentiated to form iron cores and silicate mantles very early, virtually simultaneous with the formation of the Solar System. This is consistent with other evidence discussed above for very

little age difference between differentiated and undifferentiated meteorites. Lee and Halliday (1998) also reported ϵ_{W} values in the range of $+2$ to $+3$ in three SNC meteorites thought to have come from Mars. These data indicated that the Martian core formed relatively early and the heterogeneity in tungsten isotopes indicates in Martian mantle was never fully homogenized. Lee et al. (1997) reported that the W isotope ratio of the Moon was about 1.2 epsilon units higher than that of terrestrial W.

At that point, the Earth appeared to be puzzlingly anomalous among differentiated planetary bodies in that silicate-metal differentiation appeared to have occurred quite late. Subsequently two groups, working independently, found that chondrites had ϵ_{W} significantly lower than reported by Lee and Halliday (1995), Yin et al. (2002) reported W isotope measurements carried out in two laboratories, Harvard University and the Ecole Normale Supérieure de Lyon, which showed that the chondrites *Allende* and *Murchison* had W isotope ratios 1.9 to 2.6 epsilon units lower than the terrestrial standard (Figure 5.10). Yin et al. (2002) also analyzed separated metal and silicate fractions from two ordinary chondrites (*Dhurmsala* and *Dalgety Downs*) that allowed them to estimate the initial $^{182}\text{Hf}/^{180}\text{Hf}$ of the Solar System as $\sim 1 \times 10^{-4}$. In the same issue of the journal *Nature*, Kleine et al. (2002) reported similarly low ϵ_{W} (i.e., -2) for the carbonaceous chondrites *Allende*, *Orgueil*, *Murchison*, *Cold Bokkeveld*, *Nogoya*, *Murray*, and *Karoonda* measured in a third laboratory (University of Münster). They inferred a similar estimate of the Solar System initial $^{182}\text{Hf}/^{180}\text{Hf}$. Furthermore, Kleine et al. (2002) analyzed a variety of terrestrial materials and found they all had identical W isotopic composition (Figure 5.13). It thus appears that the original measurements of Lee and Halliday (1995) were wrong. The measurement error most likely relates to use of what was at the time an entirely new kind of instrument, namely the multi-collector ICP-MS.

Using the revised initial $^{182}\text{Hf}/^{180}\text{Hf}$ and previously published data on HED and SNC achondrites, Kleine et al. (2002) estimated the age of the core of Vesta as 4.2 ± 1.3 Ma, that of Mars as 13.0 ± 2.0 Ma and that of Earth as 33 ± 2 Ma after the start of the Solar

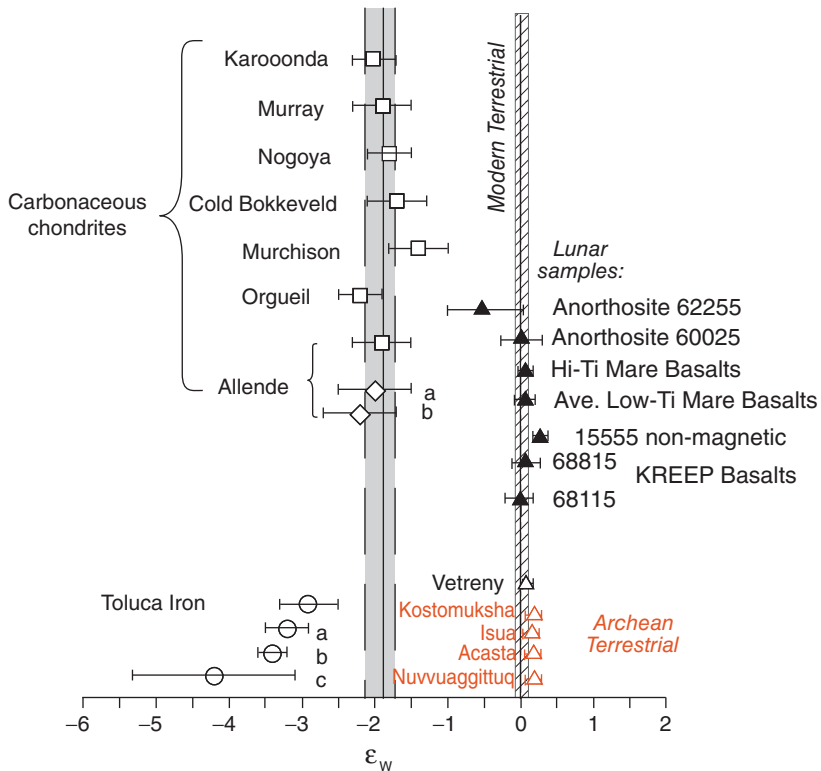


Figure 5.13 W isotope ratios measured in chondrites, the iron meteorite Toluca, and terrestrial materials. (Source: Adapted from Kleine et al. 2002.)

System, and noted that the time-scale for core formation increases with size of the planet. Yin et al. (2002) considered two scenarios for the formation of the core. In the first, which they call the two-stage model in which the Earth first accretes (stage 1) and then undergoes core formation (stage 2), induced by the giant impact that forms the Moon. In this scenario, core formation occurs 29 million years after formation of the Solar System. In the second scenario, which they believed more likely, metal segregates continuously from a magma ocean. In this continuous model, the mean age of core formation is 11 million years. In contrast, they concluded that Vesta underwent core formation within 3 million years of formation of the Solar System.

The next twist in the story came when it was recognized that ^{182}W could be produced by beta decay of ^{182}Ta which in turn is produced cosmogenically through the reaction $^{181}\text{Ta}(n,\gamma)^{182}\text{Ta}$. Because the Earth's surface is largely shielded from cosmic rays by the

atmosphere, this reaction is entirely trivial for the Earth. However, the Moon has no atmosphere. Furthermore, the lack of lunar geologic activity means that materials are exposed at the surface for very long times (hundreds of millions of years and more) and so far we have sampled only this material at the surface. Consequently, the cosmogenic production of nuclides in lunar materials can be significant. Early studies failed to appreciate this or to fully correct for this effect. Touboul et al. (2007), working with W-rich, Ta-poor metal grains separated from lunar samples, showed that previous high ϵ_W values in lunar samples were due to cosmogenic effects and when these were eliminated the Moon has an isotopically homogeneous W isotopic composition that is identical to that of the silicate Earth – about 2 epsilon units higher than chondrites.

The homogeneous isotopic composition of lunar materials, including samples with highly variable Hf/W ratios such as anorthosites from the ancient lunar crust and mare basalts formed by later melting of the lunar mantle,

implies that ^{182}Hf had effectively decayed completely before the Moon formed (or at least before its magma ocean solidified). Given the analytical precision with which W isotopes can be measured, this implies an age of the Moon of greater than 60 Ma after the beginning of the Solar System (the age of Allende CAIs). The minimum age of the Moon is constrained by Sm-Nd ages of the lunar anorthositic crust. This age is 4.456 ± 0.040 Ga, or about 100 Ma after the beginning of the Solar System. Touboul et al. (2007) thus estimate an age for the Moon of $62 + 90/-10$ Ma after the start of the Solar System.

There is a very broad consensus among scientists that the Moon formed as a result of a collision between a nearly full-sized Earth and a second body (sometimes called *Thera*) about the size of Mars. This is known as the *Giant Impact Hypothesis*. Debris thrown into orbit about the Earth as a result of the impact subsequently coalesced to form the Moon. A collision between bodies of these sizes releases enormous amounts of energy; depending on how efficiently the gravitational-kinetic energy is converted to heat, potentially enough energy to entirely melt the Earth. At the very least, one expects significant melting would have occurred on the Earth and one of the virtues of the hypothesis is that it explains the extensive melting experienced by the Moon. (Because it has remained geologically active, all evidence of a magma ocean on the Earth has been erased; because it quickly became geologically inactive, evidence of extensive early melting on the Moon has been preserved.) The significance of this is that such an impact would have provided a last opportunity for the metal to segregate from the mantle and sink into the core (a process that almost certainly requires the metal, if not also the silicate, to be liquid). We expect therefore, that the Moon-forming giant impact should also be the time of final separation of the core.

If, however, the core formed in a single event 60–100 Ma after the start of the Solar System, we would that the silicate Earth would have a W isotopic composition very close to chondritic; instead the terrestrial value is 2 epsilon units higher than chondritic. Furthermore, if, as both tungsten and silver isotopes clearly reveal, cores of asteroids formed within 10 Ma of the start of the Solar System (and

likely even earlier), why was core formation on the Earth so delayed? We can reconcile these observations if we assume that core formation was a more or less continuous process that began very early and only ended with the giant impact. In essence, the scenario goes like this: Once planetesimals exceed a few tens of km in radius, heating, either from ^{26}Al or release of gravitational energy in collisions, caused melting that allowed and metal and silicate to separate, with the metal sinking to form cores of the planetesimals. As the bodies grew into larger ones through collision with other planetesimals, enough energy was released to allow the cores of colliding bodies to merge. This process, known as *oligarchic growth*, continued to build larger and larger planetary embryos. As the embryos merged through collision, fewer and fewer embryos remained and the collisions were less frequent, slowing the planetary growth process. But the collisions that did occur were far more energetic. The process, in the case of the Earth, culminates when the last two bodies in the Earth's orbital neighborhood (or “feeding zone”) collide in the giant impact that forms the Moon. Thus metal that ultimately formed the Earth's core actually segregated from silicate far earlier, in the much smaller planetesimals, when ^{182}Hf was still live. The giant impact then marks only the end of the process.

The exact age deduced for this event then depends on the difference in ϵ_W and Hf/W ratio between the Earth and the Moon. This is illustrated in Figure 5.14. This lead to an estimate of the age of the Moon (and completion of the Earth's core) of 50–90 Ma.

The latest episode of this story was the recent discovery of heterogeneous ϵ_W values in Archean rocks. The interpretation is that these variations reflect inhomogeneous distribution of a “late accretionary veneer” of chondritic material added to the Earth after final segregation of the core. We'll discuss this in more detail in Chapter 7.

5.2.3.2 $^{146}\text{Sm}-^{142}\text{Nd}$

As we have mentioned, geochemists generally assume that rare earth and other refractory elements have the same *relative* concentrations in the Earth as they have in chondrites. If so, the Sm/Nd ratio of the Earth should be

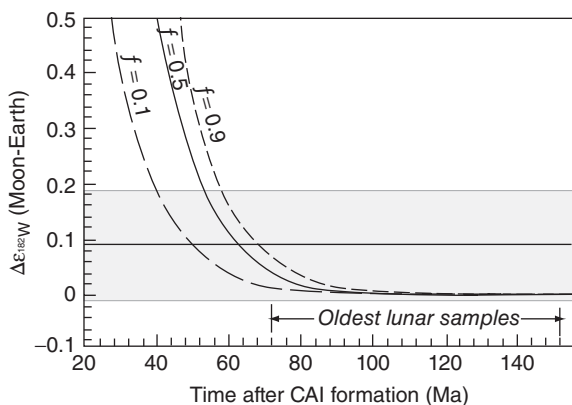


Figure 5.14 Difference between ϵ_W of Earth and Moon (Δ) versus the age the giant impact (and presumably final core formation in the Earth). f is the relative difference in Hf/W ratios between the silicate part of the Earth and the silicate part of the Moon (i.e., $(\text{Hf}/\text{W}_{\text{Moon}} - \text{Hf}/\text{W}_{\text{Earth}})/\text{Hf}/\text{W}_{\text{Earth}}$). The grey area shows the best value of $\Delta\epsilon_W(0.09 \pm 0.10)$. The Hf/W ratio of the Earth's mantle is estimated at 18 and that of the Moon is 26.5, corresponding to an f of 0.47 (solid line). (Source: Touboul et al. 2007. Reproduced with permission of Nature Publishing Group.)

chondritic, and by extension the $^{147}\text{Sm}/^{144}\text{Nd}$ ratio of the present Earth should be chondritic and the $^{146}\text{Sm}/^{144}\text{Nd}$ of the early Earth should also have been chondritic. Thus the $^{143}\text{Nd}/^{144}\text{Nd}$ and $^{142}\text{Nd}/^{144}\text{Nd}$ of the bulk Earth should also be chondritic. However, recent studies of the $^{142}\text{Nd}/^{144}\text{Nd}$ ratio in chondrites and terrestrial materials suggest that this may not be the case, at least for that part of the Earth accessible to sampling. This is surprising to say the least. These two elements are very similar to each other in chemical behavior, having identical configurations of electrons in bonding orbitals, and are both refractory lithophile elements. Indeed, Nd and Sm have 50% condensation temperatures of 1602 and 1590 K, respectively. It is difficult to see how processes operating in the solar nebula could have fractionated these elements significantly. The total range of high precision Sm/Nd ratio measurements in chondrites varies by less than 3%, which would seem to confirm that these elements were not fractionated in the solar nebula.

^{142}Nd is the product of α -decay of ^{146}Sm , a nuclide with a half-life of 68 million years.

As Table 5.1 shows, the initial $^{146}\text{Sm}/^{144}\text{Sm}$ ratio of the Solar System is about 0.0094, a value deduced from $^{142}\text{Nd}/^{144}\text{Nd}$ variations in meteorites using procedures discussed earlier. ^{144}Sm is the least abundant isotope of Sm, comprising only 3% of natural Sm, so even initially, ^{146}Sm would have only constituted 0.025% of Sm. Because of this and because the range of Sm/Nd ratios in nature is small, any variations in the $^{142}\text{Nd}/^{144}\text{Nd}$ ratio should be quite small, no more than a few tens of ppm. Detecting such small variations is analytically challenging, and indeed was nearly impossible before the 1990s. Furthermore, because the half-life of ^{146}Sm is short, any variation in $^{142}\text{Nd}/^{144}\text{Nd}$ must be the result of fractionation occurring in at most the first few hundred million years of Solar System or Earth history. However, considerable variation in the $^{142}\text{Nd}/^{144}\text{Nd}$ ratio had been detected in SNC meteorites, which suggested early mantle differentiation on Mars. It thus seemed reasonable to look for such variations on Earth.

Geochemists focused their initial attention on early Archean rocks from the Isua area in Greenland. A study by Harper and Jacobsen (1992) reported a 33 ppm excess of ^{142}Nd in one 3.8 Ga old metavolcanic rock from Isua compared to laboratory standards; the latter was assumed to have the same $^{142}\text{Nd}/^{144}\text{Nd}$ ratio as chondrites. Other workers initially failed to find any excesses in other rocks from Isua, so these results were controversial. Subsequent work by Caro et al. (2003) and Boyet et al. (2003), however, eventually confirmed the original findings of Harper and Jacobsen. This means that these early parts of the crust formed from a mantle reservoir that had a high Sm/Nd ratio – and importantly, that this reservoir formed very early, most likely within the first 100 Ma. Subsequently, other $^{142}\text{Nd}/^{144}\text{Nd}$ “anomalies” were found in other early Archean rocks, including ones from Australia and Labrador (Bennett et al., 2007; O’Neil et al., 2008).

A yet more surprising result came when Boyet and Carlson (2005) analyzed the $^{142}\text{Nd}/^{144}\text{Nd}$ ratios of meteorites and found that modern terrestrial igneous rocks had $^{142}\text{Nd}/^{144}\text{Nd}$ ratios that average 20 ppm or 0.2 epsilon units higher than ordinary chondrites, and most eucrites as well (Figure 5.15). This implies that the modern mantle has a significantly higher Sm/Nd ratio than

chondrites. How much higher depends on when the increase occurred. If the increase occurred 5 million years after the beginning of the Solar System (taken as the age of CAIs), the Sm/Nd ratio of the accessible Earth would have to be $\sim 6\%$ higher than chondrites; if the increase occurred at 30 million years, it would have to be $\sim 10\%$ higher. If the increase occurred later, the Sm/Nd ratio would have to be even higher. This increase in Sm/Nd might seem small, yet this small difference is very important in interpretation of Nd isotope systematics. For the two scenarios mentioned previously, 5 Ma and 30 Ma, Boyet and Carlson (2005) calculated that the ϵ_{Nd} of the accessible Earth would be +6.9 and +11 respectively, assuming a half-life for ^{146}Sm of 103 million years. These values fall within the range of values of mid-ocean ridge basalts. Subsequently, the half-life was found to be only 68 Ma (Kinoshita et al., 2012), which would imply slightly higher ϵ_{Nd} for the Earth. Recalling that the Isua samples have a 30 ppm excess in ^{142}Nd relative to a *terrestrial standard*⁴ this means that the Isua samples have a 50 ppm excess in ^{142}Nd relative to chondrites.

How might these isotopic differences come about? Three possible answers have been proposed. First, it is possible that the early Solar System was isotopically heterogeneous. As we'll see in a subsequent section, some isotopic heterogeneity existed in the early Solar System. More significantly, small variations in the isotopic composition of Nd and Sm (and Ba and Sr as well) have been found in chondrites (Andreasen and Sharma, 2006; Carlson et al. 2007; Gannoun et al., 2011; Qin et al., 2011; Boyet and Gannoun, 2013). Indeed, carbonaceous, ordinary, and enstatite chondrites each appear to have different $^{142}\text{Nd}/^{144}\text{Nd}$ despite identical Sm/Nd (Figure 5.15). Both ^{146}Sm and ^{144}Sm are p-process-only nuclides produced exclusively in supernova explosions while ^{142}Nd is primarily an s-process nuclide produced in red giants, with a small fraction (<5%) produced by the p-process (see Chapter 1 for an explanation of these processes). Incomplete mixing of material from different stellar sources thus could result in variations in $^{142}\text{Nd}/^{144}\text{Nd}$ in the early Solar System. Indeed, Qin et al. (2011) found that excesses in ^{148}Nd , an r-process nuclide produced

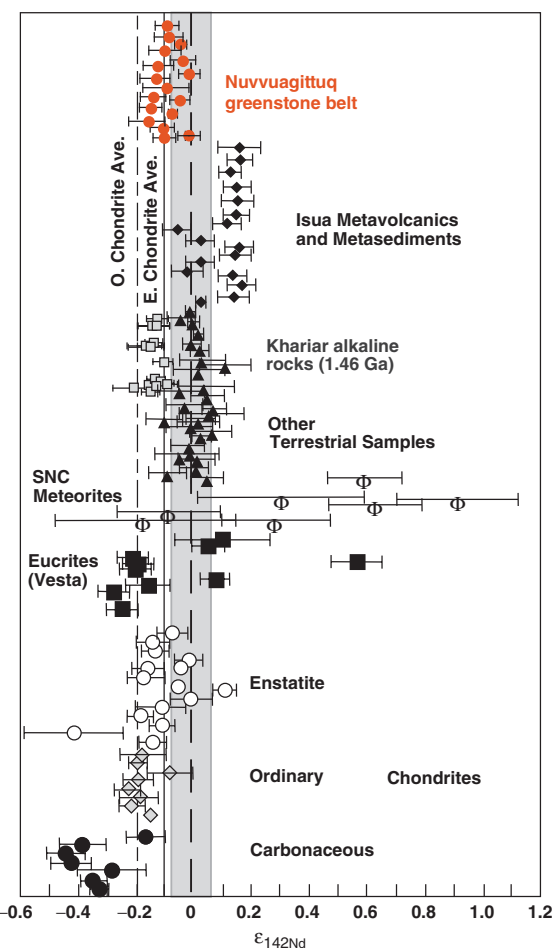


Figure 5.15 Variation in $\epsilon_{142}\text{Nd}$ in the Earth and meteorites. Gray region is the range measurements of laboratory standards derived from terrestrial Nd. All other terrestrial materials plot within this range with the exception of some samples from Isua, Greenland. Chondrites have, on average, $\epsilon_{142}\text{Nd}$ of -0.2 relative to terrestrial standards. Data from Caro et al. (2003), Boyet and Carlson (2005), Boyet and Carlson (2006), O'Neil et al (2008), and Upadhyay et al., 2009. SNC data from the compilation of Halliday (2001).

in supernovae, correlated with deficits of ^{142}Nd (Figure 5.16). The correlation could be explained by incomplete mixing of material from different stellar sources. Both Qin et al. (2011) and Boyet and Gannoun (2013) also performed step-wise dissolution experiments that demonstrated internal isotopic heterogeneity in meteorites. In both cases, the most

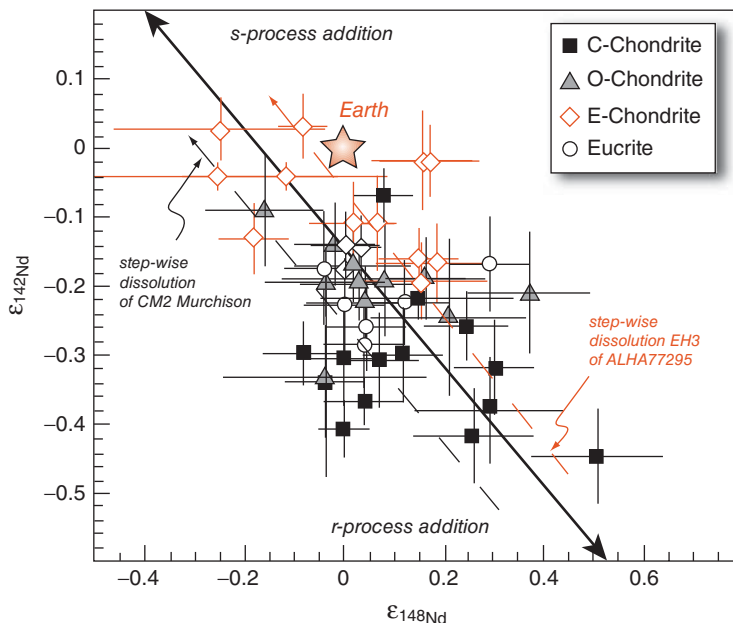


Figure 5.16 Variation of $^{142}\text{Nd}/^{144}\text{Nd}$ and $^{148}\text{Nd}/^{144}\text{Nd}$ (in epsilon units) in meteorites. The two isotope ratios are anti-correlated, suggesting incomplete mixing of s- and r-process nuclides in these materials. Also shown are the trajectories of step-wise dissolution experiment of carbonaceous chondrite Murchison (Qin et al., 2011) and enstatite chondrite ALHA77295 (Boyett and Gannoun, 2013). (Source: Adapted from Qin et al. 2011.)

resistance fractions were enriched in s-process nuclides (and deficient in r-process nuclides). Although neither study identified the carrier phase, it is most likely silicon carbide, which, as we will see in the next section, has been identified as the carrier of s-process isotopes of noble gases and other elements. And as we'll see in that section, there is some evidence for a late addition of supernova debris to the solar nebula – incomplete mixing of that material could explain much of the isotopic variation seen in Figure 5.16. However, as Andreasen and Sharma (2006) and Qin et al. (2011) concluded, while the observed isotopic heterogeneity could explain some or much of $^{142}\text{Nd}/^{144}\text{Nd}$ variations observed among chondrites, it does not appear that it can entirely explain the difference between chondrites and the Earth, which plots off the correlation in Figure 5.16. Furthermore, Yokoyama et al. (2013) analyzed two ordinary, one R-type, and one carbonaceous chondrite using a higher temperature (240°C) dissolution technique that included sulfuric acid not used in previous studies and found that all four meteorites

had homogeneous $^{142}\text{Nd}/^{144}\text{Nd}$ that was 20 ± 3 ppm (0.2 epsilon units) lower than the modern terrestrial value with $^{145}\text{Nd}/^{144}\text{Nd}$, $^{148}\text{Nd}/^{144}\text{Nd}$, and $^{150}\text{Nd}/^{144}\text{Nd}$ being indistinguishable from the terrestrial ratios. As they point out, this suggests that the Nd isotopic composition of the solar nebular was homogeneous and that Nd isotopic variations in observed chondrites reflects a failure to completely digest isotopically heterogeneous presolar grains present in the meteorites. If so, then the difference between chondritic and terrestrial $^{142}\text{Nd}/^{144}\text{Nd}$ must reflect a difference in the Sm/Nd ratio.

A second possibility was suggested by Boyett and Carlson (2005). They suggested that Earth underwent early differentiation forming an *early-enriched reservoir* (EER) such as a primordial crust that sank into the deep mantle and has not been sampled since. Alternatively, crystallization of a terrestrial magma ocean might have left a layer of residual melt, similar to the KREEP⁵ source on the Moon. Boyett and Carlson (2005) noted that if it were rich in Fe and Ti, as is the lunar KREEP reservoir is, once crystallized, the EER could have

sunk into the deep mantle, where it remains because of its high density.

A third possibility, “collisional erosion,” has been suggested by Caro et al. (2008) and O’Neill and Palme (2008). As noted earlier, planetary bodies are thought to form through the process of oligarchic growth, the later stages of which involve infrequent, energetic collisions between large bodies. Sufficient energy is released in these collisions that the growing planet extensively melts. Between collisions, one might reasonably expect a primitive basaltic crust to form through crystallization at the surface. Caro et al. (2008), O’Neill and Palme (2008), and Caro and Bourdon (2010) suggest that a substantial fraction of this crust was blasted away in these collisions, leaving the Earth depleted in elements that were concentrated in that crust, namely incompatible elements like Nd and Sm.

Common to both the latter hypotheses is the idea that planetary melting and consequent differentiation begins during, rather than after, planet accretion. Both hypotheses rely on the idea of formation, through melting and fractional crystallization, of a primitive crust enriched in incompatible elements. Such a crust would have a low Sm/Nd ratio, leaving the remainder of the planet with a higher Sm/Nd ratio than the material from which it accreted. In the Boyet and Carlson (2005) hypothesis, this early crust sinks into the deep mantle where it remains as an isolated reservoir. In collisional erosion hypothesis, this early crust is lost to space.

An additional important observation is that the Moon, and possibly Mars, also appear to have $^{142}\text{Nd}/^{144}\text{Nd}$ ratios higher than chondritic. All lunar rocks are ancient, so not surprisingly, they have variable $^{142}\text{Nd}/^{144}\text{Nd}$ ratios. When these ratios are plotted against $^{147}\text{Sm}/^{144}\text{Nd}$ they display a correlation indicating the bulk Moon has $^{142}\text{Nd}/^{144}\text{Nd}$ about 17 ppm higher than the ordinary chondrite value, identical, within uncertainty, to the modern terrestrial value (Boyet and Carlson, 2008). These lunar data are particularly significant. First, the similarity of $^{142}\text{Nd}/^{144}\text{Nd}$ in the Earth and Moon imply that the Sm/Nd ratio of the Earth-Moon system was fixed before the giant impact that formed the Moon. One reaches the same conclusion when one

considers the timing of the Moon-forming event. As we saw in the previous section, tungsten isotope ratios of the lunar rocks are uniform and indistinguishable from those of the Earth, indicating the Moon-forming event occurred at least 50 and as much as 150 million years after the start of the Solar System. Unreasonably high Sm/Nd ratios would be required to explain the $^{142}\text{Nd}/^{144}\text{Nd}$ of the Earth and Moon if the fractionation occurred that late. Thus the early-enriched reservoir hypothesized by Boyet and Carlson must predate the giant impact. Whether this reservoir could have survived this event without being remixed into the mantle is a matter of current debate.

$^{142}\text{Nd}/^{144}\text{Nd}$ and $^{147}\text{Sm}/^{144}\text{Nd}$ ratios in shergottites (meteorites from Mars) suggest the Martian $^{142}\text{Nd}/^{144}\text{Nd}$ ratio is, like the Earth and Moon, 10 to 20 ppm higher than chondritic and Caro et al., (2008) argue that this suggests that all planetary objects in the inner Solar System have Sm/Nd ratios higher than chondritic. Other Martian meteorites, the nakhlites and *Chaussigny* plot above this correlation. Caro et al. (2008) explain this by suggesting that the Martian mantle source of these meteorites underwent later differentiation. However, since there are multiple possible interpretations of the data, the Martian evidence must be considered equivocal at best on this point.

There are geophysical arguments both for and against the early-enriched reservoir hypothesis. If this reservoir formed by igneous processes it would have to contain at least 40% of the Earth’s inventory of highly incompatible lithophile elements to explain the 6% increase in Sm/Nd in the remaining mantle. This group of elements includes the heat-producing elements K, U, and Th. Thus the early-enriched reservoir at the base of the mantle would be responsible for some 40% of the heat production in the Earth, and 70% or more of the heat production in the mantle, leaving the remaining mantle particularly depleted in heat producing elements. That would appear to be inconsistent with fluid dynamic models of the Earth. Convecting fluids heated mainly from below are dominated by plumes that initiate as instabilities at the base of the layer (Davies, 2009). While some plumes do form at the base of the mantle and rise through it, the

dominant form of convection in the Earth's mantle is plate tectonics, which is the kind of convection expected in systems heated from within (lava lakes, for example, convect in a way similar to plate tectonics). On the other hand, seismologists have identified two large low shear wave velocities provinces (LLSVPs) in the lower mantle, one beneath Africa, the other beneath the Pacific. The LLSVPs cover 50% of the core–mantle boundary and rise 400–1000 km above it. The low velocities may reflect either higher temperatures or higher densities, or both; beyond that their nature is enigmatic, with several possible interpretations. One possibility is that they are dense Fe-rich regions that have existed since the Earth's formation (Garnero and McNamara, 2008) and thus represent a plausible candidate for Boyet and Carlson's early enriched reservoir.

Regardless of which of the latter two explanations is correct and whether an early-formed crust was eroded by collisions or sunk into the deep mantle, the implications of the non-chondritic Sm/Nd ratio of the Earth are profound. Both hypotheses imply that at least the observable Earth is depleted in the incompatible elements that would have been concentrated in that early crust. This would include the heat producing elements, K, U, and Th, so there are geodynamic implications as well.

As a final point, we note that the three hypotheses explored previously are not mutually exclusive. For example, the Earth has other isotopic similarities to enstatite chondrites and the difference between the average enstatite chondrite $^{142}\text{Nd}/^{144}\text{Nd}$ and modern terrestrial value is only 10 ppm (as opposed to the 20 ppm difference from ordinary chondrites). If we take the initial isotopic composition of the Earth to be that of enstatite chondrites, a much smaller mass fraction would have to be lost to space in the collisional erosion hypothesis or a smaller fraction hidden in the deep Earth in the “early-enriched reservoir” hypothesis. Finally, as we noted, the latter two ideas both involve a primitive low Sm/Nd crust. It is possible some was lost to space and some stored in the deep mantle.

We'll return to this topic when we explore the implications of $^{142}\text{Nd}/^{144}\text{Nd}$ variations in early Archean rocks for the early history of the Earth in Chapter 7.

5.2.4 Origin of short-lived nuclides

There is some debate over exactly how the short-lived radionuclides were synthesized. As we saw earlier in this chapter, heavy element nucleosynthesis occurs mainly in red giant stars and in supernovae. Anomalous isotopic compositions of stable elements, which we discuss in the following section, provide clear evidence that meteorites contain some material synthesized in both these environments. However, they provide no constraints on *when* this happened. Only with the unstable nuclides can we address the question of when. On galactic scales of time and space, red giants and supernovae continually inject newly synthesized elements into the interstellar medium. Those nuclides that are unstable will steadily decay away. These two competing processes will result in steady-state abundance of these nuclides in the interstellar medium. The abundances of ^{107}Pd , ^{129}I , and ^{182}Hf listed in Table 5.1 roughly match the expected steady-state galactic abundances and hence do not require a specific synthesis event. However, the abundances of shorter-lived ^{10}Be , ^{26}Al , ^{41}Ca , ^{53}Mn , or ^{60}Fe in the early Solar System requires synthesis of these nuclides at the time of, or just before, Solar System formation.

The conventional view is that these nuclides were synthesized in a nearby red giant and/or a supernova shortly before Solar System formation began. Some of these elements, such as ^{26}Al are most efficiently synthesized in red giants; others, such as ^{60}Fe , are most efficiently synthesized in supernovae. Thus most models invoke both environments, which may or may not have been the same star at different times. From an astronomical perspective, nucleosynthesis shortly before the Solar System formed is not surprising: stars usually form in clusters in large clouds of gas and dust known as nebulae. The Great Nebula in Orion is a good example. Some of the stars formed in these stellar nurseries will be quite large and have short lifetimes, ending their existence in supernova explosions. Thus stellar death, including the red giant and supernova phases, goes on simultaneously with star birth in these nebulae. Indeed, one popular hypothesis is that the formation of the Solar System was actually triggered by a supernova shock wave. Boss and Vanhala (2001) provide a good discussion of this view.

Evidence of the existence of ^{10}Be in some CAIs has led to an alternative hypothesis, namely that many of the short-lived extinct radionuclides were produced by spallation within the Solar System as it was forming. As we have seen, Be is not synthesized in stars, hence its presence in CAIs and other primitive chondritic components is problematic for the red giant/supernova injection hypothesis. Another key observation is that young protostars emit X-rays. X-rays are produced by accelerating charged particles. Hence, some have suggested that near the surface of the accreting protosun, magnetic reconnection events could produce flares that accelerate ions up to very high energies – essentially creating cosmic rays. Spallation would occur when the accelerated particles encounter dust grains – the CAIs – that happen to be close to the forming Sun (within 0.1 AU). According to this theory, some of these irradiated CAIs would have been carried back out to the vicinity of the asteroid belt by the energetic “X-winds” that are associated with these protostars. This theory can readily account for the abundances of ^{10}Be , ^{26}Al , ^{41}Ca , and ^{53}Mn observed. If it is correct, it provides an alternative explanation for the difference in $^{26}\text{Al}/^{27}\text{Al}$ ratios between CAIs and chondrules: that CAIs formed in an ^{26}Al rich environment near the Sun while chondrules formed further out in a region lacking spallation-produced ^{26}Al .

Proponents of the red giant/supernova injection hypothesis point out that the spallation hypothesis cannot explain the presence of ^{60}Fe , which cannot be produced by spallation. They concede that spallation is the only way to produce ^{10}Be , but argue that it can be produced by collisions with particles accelerated in the enhanced solar winds of red giants and/or in the expanding envelopes of supernovae. Although some debate on this subject continues, but there is something close to a consensus that most short-lived radionuclides detected so far were mainly produced in stars and nucleosynthesis but spallation may account for some nuclei such as ^{10}Be . They also note that chronologies deduced from short-lived radionuclides appears to agree well with high precision Pb ages (Figure 5.12), indicating homogeneous distribution of these nuclides in the solar nebula.

5.3 STARDUST AND ISOTOPIC ANOMALIES IN METEORITES

In addition to the isotopic anomalies that resulted from decay of short-lived radionuclides, there are other isotopic anomalies in meteorites that are not due to such *in situ* decay. Many of these anomalies, like those created by decay of extinct radionuclides, may reflect the injection of newly synthesized material into the cloud of dust and gas from which the Solar System ultimately formed. Others, however, may reflect isotopic inhomogeneity within this cloud, and the variable abundance of exotic gas and grains of material synthesized at various times and places in the galaxy. Still other isotopic anomalies may reflect chemical fractionations within this cloud. It is these anomalies we focus on in this section.

5.3.1 Neon alphabet soup and “pre-solar” noble gases in meteorites

Noble gases were the first group of elements in which isotopic variations were identified, and these variations occur in virtually all of the carbonaceous chondrites that have not experienced extensive metamorphism. Much of the isotopically distinct noble gas is contained in the matrix that accreted at low temperature (below 100–200°C), specifically in highly unreactive carbon species, including organic carbon, graphite, diamond, and silicon carbide. Noble gases are present in meteorites at concentrations that are often as low as 1 part in 10^{10} . Although they can be isolated and analyzed at these concentrations, their isotopic compositions are nonetheless partly sensitive to change due to processes such as radioactive decay (for He, Ar, and Xe), spallation and other cosmic-ray induced nuclear processes, and solar wind implantation. In addition, mass fractionation can significantly affect the isotopic compositions of the lighter noble gases (He and Ne). Up to the late 1960s, it was thought that all isotopic variations in meteoritic noble gases were related to these processes. For example, Ne isotopic variations could be described as mixtures of three components, “Neon A” or “planetary” (similar in composition to the Earth’s atmosphere), “Neon B,” or solar, and “Neon S,” or spallogenic (cosmogenic) (Figure 5.17). In

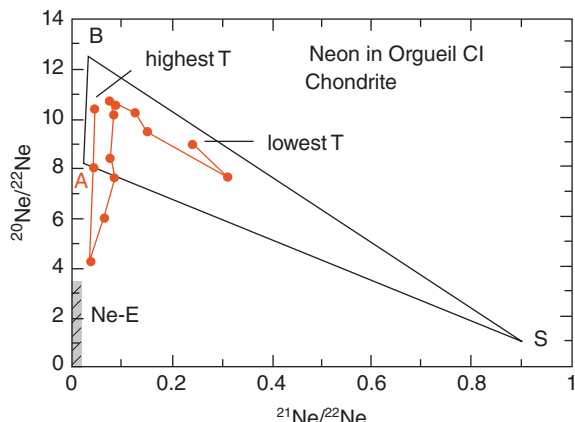


Figure 5.17 Neon isotopic compositions in a step-heating experiment on Orgueil CI chondrite, which produced the first evidence of “pre-solar” or exotic Ne. The points connected by the line show the changing Ne isotope ratios with increasing temperature. Shaded area was the original estimate of the composition of the pure Ne-E component. Also shown are the compositions of Ne-A (“planetary”), Ne-B (“solar”), and Ne-E (“spallogenic”). (Source: Adapted from Black 1972.)

1969, evidence of a ^{22}Ne -rich component, named “Neon E” was found in the high temperature (900–1100°C) release fractions of six carbonaceous chondrites. Its release at high temperature indicated it was efficiently trapped in a phase that breaks down only at high temperature.

The carrier of Neon-E proved difficult to identify. Many scientists participated in an intensive search over nearly two decades for the carrier phase of these components. The search quickly focused on the matrix, particularly that of CM2 chondrites. But the fine-grained nature of the matrix, together with the abundance of sticky and refractory organic compounds, made work with the groundmass difficult. In the late 1980s, E. Anders and his colleagues at the University of Chicago (e.g., Tang and Anders, 1988) found that Neon-E is associated with fine-grained (<6 µm) graphite and SiC (silicon carbide) of the matrix. Ne-E actually consists of two isotopically distinct components: Ne-E(L), which was released at low temperature and ultimately found to reside in graphite, and Ne-E(H) which is released at high temperature

resides in SiC. The $^{20}\text{Ne}/^{22}\text{Ne}$ ratio of Ne-E(H) is less than 0.01, while that of Ne-E(L) is less than 0.2.

The origin of Ne-E, and Ne-E(L), which is almost pure ^{22}Ne , posed something of a mystery. It was originally thought that it was a decay product of ^{22}Na , which has a half-life of 2.6 years, produced in red giants. Na could readily separate from Ne and other noble gases by condensation into grains. However, this hypothesis has now largely been rejected. For one thing, Huss et al. (1997) found that SiC grains in Orgueil (CI), had far too little Na to account for the observed amount of ^{22}Ne . More detailed analytical work (Lewis et al., 1990) found that the Ne isotopic abundances actually match rather well that expected for nucleosynthesis in the He-burning shells of low mass, carbon-rich, thermally pulsing red giants called *Asymptotic Giant Branch* (AGB) stars.⁶ ^{22}Ne is synthesized from ^{14}N , which is synthesized from C, N, and O nuclei during the previous hydrogen burning phase, through the sequence $^{14}\text{N}(\alpha, \gamma)^{18}\text{F}(\beta^+, \nu)^{18}\text{O}(\alpha, \gamma)^{22}\text{Ne}$ (Gallino et al., 1990).

The other key noble gas in this context was xenon. Having nine isotopes rather than three and with contributions from both ^{129}I decay and fission of various heavy elements, isotopic variation in xenon are bound to be much more complex than those of Ne. On the other hand, its high mass minimizes mass fractionation effects, so “solar” (more properly solar wind) and “planetary” Xe are less isotopically dissimilar than Ne. The first evidence of isotopic variations in Xe came in the early 1960s, but these variations were thought to be fissogenic (at one time it was argued they were produced by fission of short-lived superheavy elements). Subsequently, several isotopically distinct Xe components were identified. One of these is associated with Ne-E(H) in SiC and is enriched in the s-process-only isotopes of Xe (^{128}Xe and ^{130}Xe) and is called, appropriately enough, Xe-S. The isotopic pattern of Xe-S is shown in Figure 5.18. This is most likely synthesized in red giants. Indeed, there is a striking similarity of the isotopic abundances to the calculated production of s-process nuclides in AGB stars. Comparison of the isotopic composition of Kr, which is also anomalous in the SiC, with theoretical calculations further narrows the site of synthesis to low-mass AGB stars, consistent with the inferences made for ^{22}Ne .

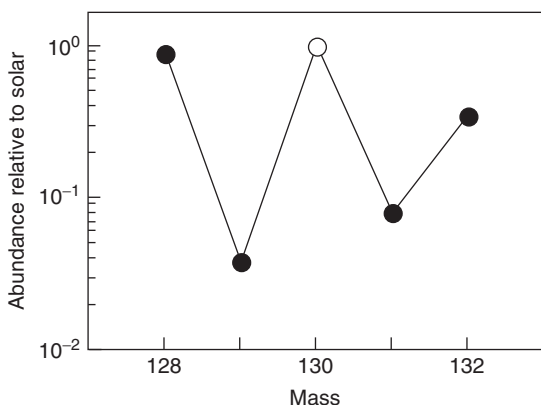


Figure 5.18 Isotopic composition of Xe-S (relative to normal solar Xe with $^{130}\text{Xe} \equiv 1$). Xe-S is found in silicon carbide and associated with Ne-E(H). ^{128}Xe and ^{130}Xe are synthesized only in the s-process, hence the most likely site for its synthesis is red giants. (Source: Adapted from Anders (1988).)

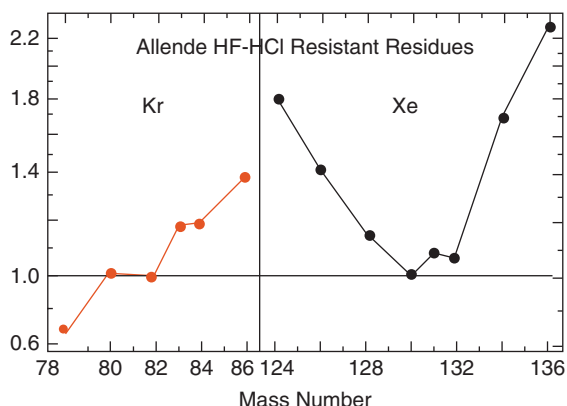


Figure 5.19 The isotopic composition of Kr and Xe of the “Xe-HL” component in the matrix of the Allende CM-2 carbonaceous chondrite. Xe-HL is characteristically enriched in both the light and heavy isotopes, while the lighter noble gases show enrichment only in the heavy isotopes. (Source: Adapted from Lewis et al., 1975).

synthesis. SiC grains (Figure 5.19) are thus apparently condensates from material ejected from red giant stars, which have very strong solar winds. Thus, in a very real sense, these grains are truly stardust.

The Ne in the SiC is a little richer in ^{21}Ne than the predicted products of AGB stars. This is presumably due to cosmogenic production

of ^{21}Ne . If so, some 130 Ma of cosmic ray irradiation would be required to produce the observed ^{21}Ne , indicating the grains predate meteorite parent body formation by this amount of time (Lewis et al., 1994). If they had been degassed, however, the grains could be much older.

Another isotopically distinct component, identified in acid-dissolution residues of Allende (CV3) named Xe-HL because it is enriched in both heavy and light Xe isotopes, was released in the 700–1000°C temperature step. This particular enrichment pattern can be produced only by a combination of the p- and r-processes (Figure 5.19). As we found in Chapter 1, these processes operate only in supernovae. Unlike Ne-E, Xe-HL is accompanied by the other noble gases, of which Ne, Ar, and Kr all show enrichment in their heavier isotopes. Eventually, Anders’ group identified the carrier of Xe-HL as microdiamonds. These diamonds are extraordinarily fine, averaging only 1 nm in diameter and containing typically only 10^3 or so atoms. Roughly one in every four atoms is at the surface. As a result, the properties of this material differ significantly from normal diamond, which considerably complicated the effort to isolate it.

5.3.2 Isotopic composition of pre-solar grains

Analysis of the noble gases in the SiC, graphite and diamond by step-heating was comparatively easy, since each of these decomposes at distinct temperatures. Identifying the carriers proved more difficult. However, once the carrier grains were identified and isolated, it became possible to analyze the isotopic composition of other elements. The isotopic compositions of other elements have also proved to be anomalous to varying degrees. The noble gas, C and N isotopic compositions are summarized in Table 5.2. Also shown in the table is the abundance of these phases, which is quite low.

Many of the SiC and graphite grains are large enough to image with the scanning electron microscope. The grains have several different morphologies; a cauliflower-like morphology SiC grain is shown in Figure 5.20. Other grains have onion-like layered morphologies, suggesting discontinuous, layer-by-layer growth; still others appear

Table 5.2 Isotopic characteristics of presolar grains in CM2 chondrites. (Source: Adapted from Anders and Zinner 1993. Reproduced with permission of John Wiley & Sons.)

Phase	Diamond	SiC	Graphite	Amorphous C
Noble gas component	Xe-HL	Xe-S, Ne-E(H)	Ne-E(L)	no noble gases
Enriched in isotopes	$^{124}\text{Xe}, ^{136}\text{Xe}$	$^{128}\text{Xe}, ^{130}\text{Xe}$, ^{22}Ne	^{22}Ne	^{12}C
Nuclear process	p, r	s, $^{22}\text{Na}(\beta^+, \nu)^{22}\text{Ne}$	$^{14}\text{N} + 2\alpha \rightarrow ^{22}\text{Ne}$	
Grain Size, μ	0.001–0.0025	0.03–20	0.8–20	0.2–2
Abundance, ppm	400	7	<2	100
$(^{13}\text{C}/^{12}\text{C})/(^{13}\text{C}/^{12}\text{C})_{\odot}$	0.96	0.03–50	0.012–50	0.95
$(^{15}\text{N}/^{14}\text{N})/(^{15}\text{N}/^{14}\text{N})_{\odot}$	0.66	0.015–20	0.55–6.7	
Stellar environment	Supernova	AGB	Nova, Supernova, AGB	Supernova

(Source: Adapted from Anders and Zinner 1993. Reproduced with permission of John Wiley & Sons. Adapted from Lodders & Amari 2005.)

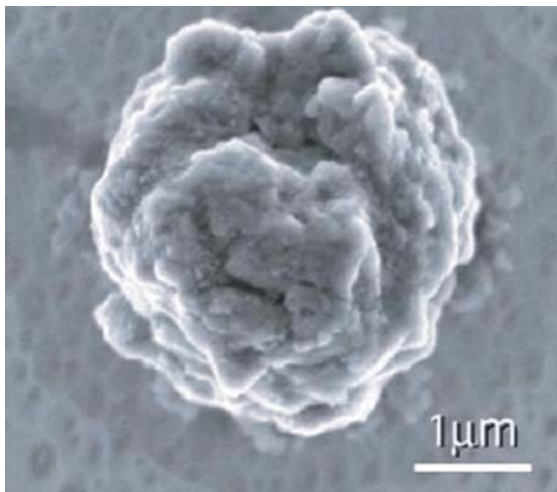


Figure 5.20 A presolar SiC grain. (Source: Nittler 2003. Reproduced with permission of Elsevier.)

euhedral with distinct crystal faces. The isotopic compositions of individual grains can be analyzed by ion probe. These analyses (e.g., Figure 5.21) reveal a diversity of isotopic compositions as well as correlations between grain size and isotopic composition. Clearly, the SiC grains do not form a single population, but represent a number of populations of grains, each produced in a different astronomical environment. The majority of grains have isotopically heavy C and light N (relative to solar), which are the compositions expected from production in the CNO cycle (Chapter 1). However, compositions produced by other mechanisms are also represented. Si isotopic compositions are also anomalous. Anomalies have also been identified in the isotopic compositions

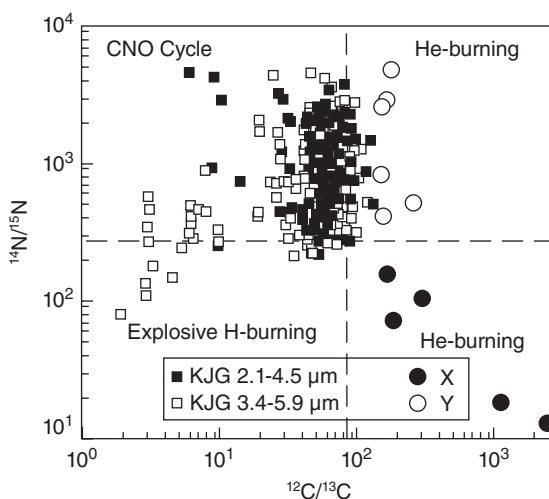


Figure 5.21 Isotopic composition of C and N in SiC from Murchison (CM2) meteorite. Dashed lines show the isotopic composition of normal Solar System C and N. Populations X and Y, which are anomalous here, are anomalous in other respects as well. (Source: Anders and Zinner (1993). Reproduced with permission of John Wiley & Sons.)

of Ti, Sr, Zr, Mo, Ba, Nd, Sm, and Dy in these grains. These have further helped to identify the stellar production environments of these grains (Figure 5.22). For example, graphite and most SiC grains display enrichment in ^{96}Mo , which is an s-process isotope. This enrichment pattern is that expected for s-process nucleosynthesis in the He-burning shell of AGB stars. A subset of the SiC grains, the so-called SiC X grains, show enrichment in ^{95}Mo and ^{97}Mo , which are r-process isotopes, and were likely produced in the neutron burst of supernovae.

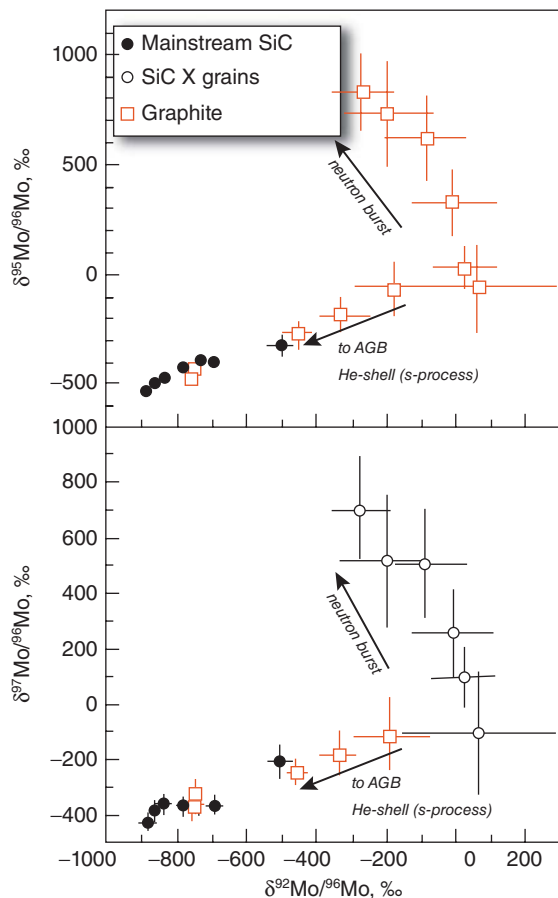


Figure 5.22 Mo isotope anomalies in SiC and graphite interstellar grains in meteorites. The “mainstream” SiC and graphite are enriched in ^{96}Mo , while the SiC X grains are enriched in ^{95}Mo and ^{97}Mo . (The two groups of SiC grains are defined on the basis of their Si and C isotopic compositions.) (Source: Nittler 2003. Reproduced with permission of Elsevier.)

Mg isotopic compositions in both graphite and SiC are also anomalous. A fourth refractory phase identified in the groundmass (but poor in noble gases) is corundum (Al_2O_3). The graphite, SiC, and corundum have inferred initial $^{26}\text{Al}/^{27}\text{Al}$ ratios of 5×10^{-5} to 1×10^{-1} . In contrast, we found in the previous section that CAIs had inferred initial $^{26}\text{Al}/^{27}\text{Al}$ ratios up to 5×10^{-5} , and that most other meteoritic materials showed no excess ^{26}Mg .

Diamond, graphite, and silicon carbide were the first presolar phases to be discovered largely because of the approaches used to isolate them: acid digestion that dissolved most other phases. Furthermore, these

phases are quite refractory and resist reaction with hydrous alteration that affected many primitive meteorites. The initial focus was on a few primitive CV and CM meteorites for which large amounts of material were available to researchers. Subsequent studies have identified these and other minerals in nearly all classes of unequilibrated (that is, petrologic grade less than 4) chondrites and they are most abundant in CI chondrites such as Orgueil. The inventory of presolar grains includes Si_3N_4 , corundum (Al_2O_3), spinel (MgAl_2O_4), hibonite ($\text{CaAl}_{12}\text{O}_{19}$), a variety of metal carbides, Fe-Ni metal, and perhaps TiO_2 . Some of these occur as inclusions in other grains. Presolar grains have also been identified among interplanetary dust particles (IDPs) collected by spacecraft and high-altitude aircraft. Up until 2004, however, all were non-silicates. This puzzled cosmochemists as spectroscopic observations of young stars revealed that silicates are abundant, meaning they should be abundant in molecular clouds like the one in which the Solar System formed. In 2004, several research groups reported not only finding silicates (olivine, pyroxene, and SiO_2) with highly anomalous O isotope ratios, hence indicating a presolar provenance, they reported that that presolar silicates were actually more abundant than non-silicate presolar grains. In the exceptionally primitive (i.e., unmetamorphosed) carbonaceous chondrite *Acfer* (CH3), Nagashima et al. (2004) and Nguyen and Zinner (2004) found presolar silicates were present in the groundmass at an abundance of about 30–40 parts per million, compared to 14 parts per million for presolar SiC.

5.3.2.1 A late injection of supernova debris?

Bizzarro et al. (2007) found a subset of early-formed differentiated meteorites, including the angrites, urelites, and some irons and pallasites (stony-irons thought to be asteroidal core-mantle boundaries), have ^{60}Ni deficits of around 25 ppm (0.2 epsilon units) compared to terrestrial material, enstatite and ordinary chondrites, and a Martian meteorite. Carbonaceous chondrites have ^{60}Ni excesses of 33 ppm. ^{60}Ni is the daughter of ^{60}Fe , which has a half-life of 1.5 Ma. Bizzarro et al. found that ^{26}Al and ^{60}Fe abundances are uncorrelated, which might not be what one would

expect if the source of the ^{60}Fe were a Type II core collapse supernova. As we noted, ^{26}Al is synthesized in the red giant phase of stars. But whereas red giant stars of 8–30 solar masses go on to explode as Type II supernovae, particularly massive stars throw off their ^{26}Al -containing outer regions before exploding as Type Ib/c supernovae (in which ^{60}Fe is synthesized). Thus, in this type of stellar evolution injection of ^{26}Al and ^{60}Fe would be decoupled.

Brenneka et al. (2013) documented (small) isotopic variations in Sr, Mo, Ba, Nd, and Sm isotopic compositions of CAIs that can be explained by deficits or excesses of r-process nuclides. While Sr, Mo, and Ba generally have excesses of r-process nuclides, Nd and Sm exhibit r-process deficits. They argue material from multiple supernovae are necessary to explain these observations and that an injection of supernova material occurred into a reservoir untapped by CAIs, implying it occurred after CAI formation.

Another line of evidence of a possible supernova in the vicinity of the solar nebula arises from anomalously old Lu-Hf ages of many, but not all, meteorites and their components (discussed in Section 2.6). Albarède et al. (2006) proposed that these anomalous ages are a consequence of excitation of the ^{176}Lu nucleus by absorption of γ -radiation into an excited state energy state, from which it decays to ^{176}Hf with a half-life of 3.7 h. They proposed that the γ -rays originated from a nearby supernova. The difficulty with this hypothesis is that gamma rays have very limited penetrating power through solids: this would affect only material on the surface of meteorite parent bodies. Alternatively, either neutrinos or cosmic rays can excite the ^{176}Lu nucleus (Thrane et al., 2010). Supernovae do produce prodigious numbers of neutrinos, but a supernova close enough to produce the necessary neutrino flux would have completely disrupted the solar nebula, so that possibility can also be ruled out (Thrane et al., 2010). Thrane et al. (2010) and Bizzarro et al. (2012) suggested instead that ^{176}Lu was excited by high-energy cosmic rays, which have more penetrating power than γ -rays and these are also produced in abundance by supernovae. However, Bouvier and Boyet (2013) obtained an age of 4560 ± 190 s Ma for Allende CAIs, with an initial $^{176}\text{Hf}/^{177}\text{Hf}$ of 0.27985 ± 15 ,

in excellent agreement with other ages of CAIs and the initial $^{176}\text{Hf}/^{177}\text{Hf}$ of Bouvier et al. (2007). Certainly these early-formed small objects would have been affected by any radiation penetrating the chondrite parent bodies. As yet, no consensus has been reached on this matter.

5.3.3 Other exotic components in meteorites

Besides isotopic anomalies apparently produced by decay of short-lived radionuclides such as ^{26}Al , ^{129}I , and ^{244}Pu , and those associated with the interstellar grains in the matrix, other isotopic anomalies have been identified in CAIs. Some of these have been observed only in a few CAIs from *Allende*: Ca, Ba, Sm, Nd, and Sr. They have been termed FUN anomalies: fractionation and unknown nuclear. A systematic search by G. Lugmair and colleagues at the University of California at San Diego revealed that isotopic variations of the iron peak elements (elements clustered around the cosmic abundance peak at Fe), Ca through Zn, are ubiquitous in many CAIs (Shuloyukov and Lugmair, 1993). Variations are up to per mil size relative to terrestrial isotope ratios, and are characterized by over-abundance of the most neutron-rich nuclides (^{48}Ca , ^{50}Ti , ^{54}Cr , ^{64}Ni , and ^{66}Zn), often accompanied by under-abundance of the most neutron-poor isotopes. In some instances, isotopic variations within single mineral grains have been observed with the ion microprobe. In general, these isotopic variations are most readily explained if the inclusions contain an admixture of neutron-rich e-process material from a supernova.

Although recent research has turned up many examples of isotopic heterogeneity, mainly large variations on very fine scales and very small variations on larger scales, and undoubtedly will continue to do so as analytical precision improves, the overall picture of the solar nebula is of isotopic homogeneity, indicating that it was well mixed. The most notable exception is oxygen, which we discuss next.

5.4 OXYGEN ISOTOPE VARIATIONS AND NEBULAR PROCESSES

Another element commonly showing isotopic variations is O. Until 1973, O isotope variations in meteorites were thought to be simply

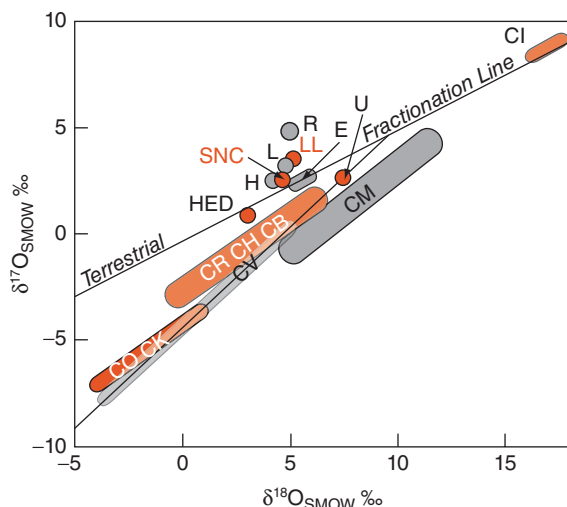


Figure 5.23 Variation of O isotope ratios in meteorites CO, CK, and so on: carbonaceous chondrites; H, L, LL: ordinary chondrites; HED: howardites, eucrites, diogenites; U: ureilites; SNC: Shergottites, naklites, Chassigny; E: enstatite chondrites. The Earth, Moon, and aubrites have the same isotopic composition as enstatite chondrites. (Source: Adapted from Clayton, 1993).

the result of fractionation, as they generally are on Earth. But when R. Clayton of the University of Chicago went to the trouble of measuring ^{17}O (0.037% of O) as well as ^{18}O and ^{16}O , he found that these variations were not consistent with simple mass-dependent fractionation. This is illustrated in Figure 5.23, which presents $^{17}\text{O}/^{16}\text{O}$ and $^{18}\text{O}/^{16}\text{O}$ ratios in delta notation, which are deviations in parts per thousand from a standard (standard mean ocean water or SMOW, in this case; see Chapter 8 for more details). In a plot of $\delta^{17}\text{O}$ versus $\delta^{18}\text{O}$, variations created by mass-dependent fractionation (we'll explain this more fully in Chapter 8) should plot along a line with slope of $\sim 1/2$. Terrestrial and lunar samples do indeed define such a line, but other meteorites or their components, carbonaceous chondrites and CAIs in particular, fall along a line with slope = 1. One interpretation is that this reflects mixing between a more or less pure ^{16}O component, such as might be created by helium burning, and a component of “normal” isotopic composition. However, Thiemens and Heidenreich (1983) conducted experiments in which ozone produced by

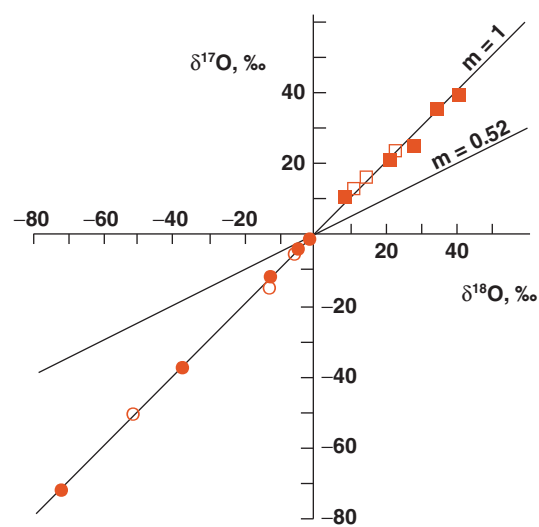


Figure 5.24 Mass independent fractionation during the production of ozone from molecular oxygen. Squares are ozone, dots are oxygen. (Source: Thiemens and Heidenreich 1983. Reproduced with permission of AAAS.)

a high frequency electric discharge showed “mass independent fractionation,” that is, where the ozone was equally enriched in ^{17}O and ^{18}O (Figure 5.24) relative to ^{16}O . The experiment demonstrates that a slope of 1 on the $\delta^{17}\text{O} - \delta^{18}\text{O}$ diagram could be produced by chemical processes. Thiemens suggested this kind of fractionation results from a kinetic fractionation mechanism, which arises because non-symmetric (e.g., $^{16}\text{O}^{17}\text{O}$ or $^{18}\text{O}^{16}\text{O}$) molecules have more available energy levels than symmetric (e.g., $^{16}\text{O}^{16}\text{O}$) molecules (as we will see in Chapter 8, symmetry enters into the partition function, which governs isotope fractionation).

Subsequent to Thiemens and Heidenreich’s work, mass-independent fractionations have been discovered in atmospheric ozone as well as in Archean sulfides. In the case of sulfur, photodissociation of atmospheric sulfur compounds appears to have been cause mass-independent fractionation. We’ll return to this in subsequent chapters.

The explanation for mass-independent O fractionation in the solar nebula may also involve photodissociation. Thiemens and Heidenreich (1983) and Clayton (2002) suggested that the anomalies arose through radiation self-shielding in the solar nebula. In this model, ultraviolet radiation from the

early proto-Sun dissociated carbon monoxide, which would have been among the most abundant gases in the solar nebula. Because C^{16}O rather than C^{17}O or C^{18}O was the dominant oxygen-bearing species, the radiation of the wavelength necessary to dissociate C^{16}O would have been quickly absorbed as it traveled outward from the Sun. At greater distance from the Sun, radiation of the frequency necessary to dissociate C^{16}O would have been absent, while that needed to dissociate C^{17}O and C^{18}O would still be available. Thus, at these distances, C^{17}O and C^{18}O are preferentially dissociated, and equally so, making ^{17}O and ^{18}O preferentially available for reaction to form silicates and other meteorite components. Since the solar nebula would have been fairly opaque at this time, this isotopic fractionation would have occurred in the inner part of the nebula, near the forming star, and then expelled back out by the “X-wind.” The implication of this is that most of the solid matter that makes up the Earth and its neighbors must have cycled through this inner region at one point. Clayton’s model also predicts that the Sun itself should be poor in ^{18}O and ^{17}O compared to meteorites and the Earth – closer in composition to the CAIs. This prediction has been confirmed, initially based on analysis of solar wind implanted in lunar soil (Hashizume and Chaussidon, 2005) and subsequently by the analysis of solar wind collected by NASA’s Genesis mission. Some mass fractionation occurs in the Genesis collectors and after correction for this, McKeegan et al. (2011) estimate the oxygen isotopic composition of the solar wind as $\delta^{18}\text{O} = -102.3 \pm 3.3\text{‰}$ and $\delta^{17}\text{O} = -80.8 \pm 5\text{‰}$, so that it would plot well off to the lower left of Figure 5.22. There is reason to believe that mass fractionation occurs in generation of the solar wind, and that the Sun’s photosphere is not as depleted in light O isotopes as the solar wind. McKeegan et al. (2011) estimate the composition of the solar photosphere as $\delta^{18}\text{O} = -58.5$, $\delta^{17}\text{O} = -59.1\text{‰}$ which would place it on carbonaceous chondrite line in Figure 5.22 (but still well off the plot). The ^{16}O -rich nature of the Sun compared to the Earth and nearly all planetary materials would appear to confirm Clayton’s self-shielding hypothesis, although some problems persist with the self-shielding model, as Thiemens (2006) points out.

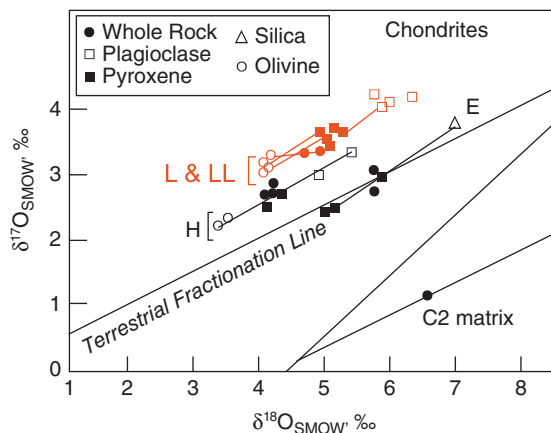


Figure 5.25 O isotope variations among minerals of various meteorite classes. (Source: Clayton et al., 1976). Reproduced with permission of Elsevier.)

As Figure 5.25 shows, while variations *between* classes are mostly mass-independent, variations *within* groups of meteorites fall along mass-dependent fractionation lines. This strongly suggests that, for the most part, different meteorite groups probably formed in different parts of the presolar nebula. There are a few exceptions: IIE irons fall on a mass-dependent fractionation line (MDFL) with H-chondrites, IVA irons plot on a MDFL with L and LL chondrites, basaltic and hypersthene achondrites plot on a MDFL with IAB irons and some stony-irons, and the moon and the Earth plot on a MDFL together with enstatite chondrites and achondrites. This suggests a genetic relationship between these objects, perhaps derivation from a single a single parent body in some cases.

Oxygen isotope compositions of the minerals of the FUN inclusions of Allende are erratic and do not fall on any line. These are certainly nuclear effects.

Mass-independent effects have not been found among isotopes of other elements such as Si, S, and Mg in meteorites (except in some inclusions, groundmass phases, and chondrules as noted previously), although large mass-dependent fractionations are ubiquitous. Thus, oxygen appears unique. The reason may be related to the partition of oxygen between the gaseous and solid phases of the presolar nebula. Over a large temperature range, only about 17% of oxygen will condense, the remainder being in the

gas, principally as CO and H₂O. Hydrogen and carbon have only two stable isotopes so mass-dependent and mass-independent effects cannot be distinguished.

5.5 EXPOSURE AGES OF METEORITES

Cosmogenic nuclides have been used for many years to determine cosmic-ray exposure ages of meteorites. Meteorites experience a much higher cosmic ray flux because they have no atmospheres to shield them. Unstable and stable nuclides are sometimes used together to determine such ages. The rate of change of abundance of an unstable cosmogenic nuclide is given by:

$$\frac{dN}{dt} = P - \lambda N \quad (5.6)$$

where P is the production rate. If we consider the case of the production of a stable nucleus, the number of stable nuclei produced at the surface of the body over some time t is simply given by:

$$N = Pt \quad (5.7)$$

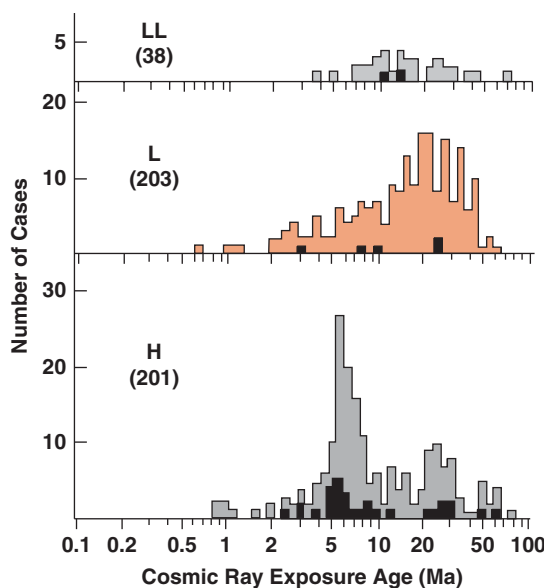


Figure 5.26 Cosmic ray exposure ages for three classes of ordinary chondrites. Filled histogram is for meteorites with regolith histories (i.e., brecciated meteorites). (Source: Crabb and Schultz 1981. Reproduced with permission of Elsevier.)

Combining these equations, we may obtain an expression for t that is independent of variations production

$$N = \frac{N_s}{N_u} \left(\frac{P_s}{P_u} \right) \frac{t}{\lambda} \quad (5.8)$$

Cosmic ray exposure ages of meteorites have been found to be on the order of millions or tens of millions of years for stony meteorites and hundreds of millions of years for iron meteorites. Ages for the three classes of ordinary chondrites are shown in Figure 5.26. These ages are much less than their formation ages as determined by conventional radiometric dating. This implies that through most of their histories, meteorites must have been shielded from cosmic rays. Hence, they must have come from much larger bodies that were broken up by collisions. The similarity of exposure ages for all meteorites of a given class is consistent with the idea that individual meteorite classes are derived from single parent bodies.

NOTES

1. Among so-called “finds,” meteorites found but not associated with an observed fireball, irons are more common because they are more likely to be recognized as meteorites.
2. In the last decade or two, additional classes have been added that are defined by rarer meteorites.
3. NWA stands for Northwest Africa. This is one of many meteorites found in the Sahara desert over the last couple of decades.
4. The two standards commonly used in Nd isotope ratios measurements are the “La Jolla” standard and the “Ames” standard. Both are solutions created from industrially purified Nd.
5. So named because magma derived from it are rich in potassium, rare earths, and phosphorus.
6. More specifically, AGB stars are low to moderate mass stars (i.e., 0.6 to 10 solar masses) that have completed the He-burning phase of their post-main sequence evolution. They have enormously strong stellar winds, enough to lose 50–70% of their mass during this phase.

REFERENCES

- Albarède, F., Scherer, E. E., Blichert-Toft, J., Rosing, M., Simionovici, A. and Bizzarro, M. 2006. γ -ray irradiation in the early Solar System and the conundrum of the ^{176}Lu decay constant. *Geochimica et Cosmochimica Acta*, 70: 1261–1270, doi: 10.1016/j.gca.2005.09.027.
- Amelin, Y. 2008. U-Pb ages of angrites. *Geochimica et Cosmochimica Acta*, 72: 221–232, doi: 10.1016/j.gca.2007.09.034.
- Amelin, Y., Connelly, J., Zartman, R. E., Chen, J. H., Göpel, C. and Neymark, L. A. 2009. Modern U-Pb chronometry of meteorites: Advancing to higher time resolution reveals new problems. *Geochimica et Cosmochimica Acta*, 73: 5212–5223, doi: 10.1016/j.gca.2009.01.040.
- Amelin, Y., Kaltenbach, A., Iizuka, T., Stirling, C. H., Ireland, T. R., Petaev, M. and Jacobsen, S. B. 2010. U-Pb chronology of the Solar System's oldest solids with variable $^{238}\text{U}/^{235}\text{U}$. *Earth and Planetary Science Letters*, 300: 343–350, doi: 10.1016/j.epsl.2010.10.015.
- Anders, E. and Zinner, E. 1993. Interstellar grains in primitive meteorites: diamond, silicon carbide, and graphite. *Meteoritics*, 28: 490–514.
- Anders, E. 1988. Circumstellar material in meteorites: noble gases, carbon and nitrogen. In: *Meteorites and the Early Solar System*, J. F. Kerridge and M. S. Matthews (eds). Tucson: University of Arizona Press.
- Andreasen, R. and Sharma, M. 2006. Solar nebula heterogeneity in p-process samarium and neodymium isotopes, *Science*, 314: 806–809.
- Bennett, V.C., Brandon, A.D. and Nutman, A. P. 2007. Coupled $^{142}\text{Nd}-^{143}\text{Nd}$ isotopic evidence for Hadean mantle dynamics. *Science*, 318: 1907–1910.
- Bernatowicz, T. J., Podosek, F. A., Swindle, T. D. and Honda, M. 1988. I-Xe systematics in LL chondrites. *Geochimica et Cosmochimica Acta*, 52: 1113–1121, doi: 10.1016/0016-7037(88)90265-7.
- Bizzarro, M., Connolly, J. N., Thrane, K. and Borg, L. E. 2012. Excess hafnium-176 in meteorites and the early Earth zircon record. *Geochemistry, Geophysics, Geosystems*, 13: Q03002, doi: 10.1029/2011gc004003.
- Bizzarro, M., Ulfbeck, D., Trinquier, A., Thrane, K., Connolly, J. N. and Meyer, B. S. 2007. Evidence for a late supernova injection of ^{60}Fe into the protoplanetary disk, *Science*, 316: 1178–1181.
- Black, D. C. and Pepin, R. O. 1969. Trapped neon in meteorites – II. *Earth and Planetary Science Letters*, 6: 395–405, doi: 10.1016/0012-821X(69)90190-3.
- Bogard, D. D. 2011. K-r ages of meteorites: Clues to parent-body thermal histories. *Chemie der Erde*, 71: 207–226, doi: 10.1016/j.chemer.2011.03.001.
- Boss, A. P. 2012. Mixing and transport of isotopic heterogeneity in the early Solar System. *Annual Review of Earth and Planetary Sciences*, 40: 23–43, doi: 10.1146/annurev-earth-042711-105552.
- Boss, A. P. and Vanhala, H. A. T. 2001. Injection of newly synthesized elements into the protosolar cloud. *Philosophical Transactions of the Royal Society London*, 359: 2005–2017.
- Bouvier, A. and Boyet, M. 2013. Lu-Hf and Sm-Nd systematics of the first solids in the Solar System. *Mineralogical Magazine*, 77: 754.
- Bouvier, A. and Wadhwa, M. 2010. The age of the Solar System redefined by the oldest Pb-Pb age of a meteoritic inclusion. *Nature Geoscience*, 3: 637–641, doi: 10.1038/ngeo941.
- Bouvier, A., Blichert-Toft, J., Moynier, F., Vervoort, J. D. and Albarede, F. 2007. Pb-Pb dating constraints on the accretion and cooling history of chondrites. *Geochimica et Cosmochimica Acta*, 71: 1583–1604, doi: 10.1016/j.gca.2006.12.005.
- Bouvier, A., Spivak-Birndorf, L. J., Brennecka, G. A. and Wadhwa, M. 2011. New constraints on early Solar System chronology from Al-Mg and U-Pb isotope systematics in the unique basaltic achondrite Northwest Africa 2976. *Geochimica et Cosmochimica Acta*, 75: 5310–5323, doi: 10.1016/j.gca.2011.06.033.
- Boyet, M. and Carlson, R. W. 2007. A highly depleted moon or a non-magma ocean origin for the lunar crust? *Earth and Planetary Science Letters*, 262: 505–516, 10.1016/j.epsl.2007.08.009.
- Boyet, M. and Gannoun, A. 2013. Nucleosynthetic Nd isotope anomalies in primitive enstatite chondrites. *Geochimica et Cosmochimica Acta*, 121: 652–666, doi: 10.1016/j.gca.2013.07.036.
- Boyet, M. and Carlson, R. L. ^{142}Nd evidence for early (>4.3 Ga) global differentiation of the silicate Earth, *Science*, 309: 576–581, 2005.
- Boyet, M., Blichert-Toft, J., Rosing, M., Storey, M., Telouk, P. and Albarede, F. 2003. ^{142}Nd evidence for early Earth differentiation, *Earth and Planetary Science Letters*, 214: 427–442.
- Brazzle, R. H., Pravdivtseva, O. V., Meshik, A. P. and Hohenberg, C. M. 1999. Verification and interpretation of the I-Xe chronometer. *Geochimica et Cosmochimica Acta*, 63: 739–760, doi: 10.1016/S0016-7037(98)00314-7.
- Brennecka, G. A. and Wadhwa, M. 2012. Uranium isotope compositions of the basaltic angrite meteorites and the chronological implications for the early Solar System. *Proceedings of the National Academy of Sciences*, 109: 9299–9303, doi: 10.1073/pnas.1114043109.
- Brennecka, G. A., Weyer, S., Wadhwa, M., Janney, P. E., Zipfel, J. and Anbar, A. D. 2010. $^{238}\text{U}/^{235}\text{U}$ variations in meteorites: extant ^{247}Cm and implications for Pb-Pb dating. *Science*, 327: 449–451, doi: 10.1126/science.1180871.

- Brennecke, G., Borg, L. and Wadhwa, M. 2013. Evidence for supernova injection into the solar nebula and the decoupling of r-process nucleosynthesis. *Mineralogical Magazine*, 77: 768.
- Carlson, R. W., Boyet, M. and Horan, M. 2007. Chondrite barium, neodymium, and samarium isotopic heterogeneity and early earth differentiation. *Science*, 316: 1175–1178, doi: 10.1126/science.1140189.
- Caro G. and Bourdon B. 2010. Non-chondritic Sm/Nd ratio in the terrestrial planets: Consequences for the geochemical evolution of the mantle crust system. *Geochimica et Cosmochimica Acta* 74: 3333–3349.
- Caro, G., Bourdon, B., Halliday, A. N. and Quitte, G. 2008. Super-chondritic Sm/Nd ratios in Mars, the Earth, and the Moon, *Nature*, 452: 336–339.
- Caro, G., Bourdon, B., Birck, J.-L. and Moorbath, S. 2003. ^{146}Sm - ^{142}Nd evidence from Isua metamorphosed sediments for early differentiation of the Earth's mantle, *Nature*, 423: 428–432.
- Chen, J. H. and Wasserburg, G. J. 1990. The isotopic composition of Ag in meteorites and the presence of ^{107}Pd in protoplanets, *Geochimica et Cosmochimica Acta*, 54: 1729–1743.
- Chen, J. H. and Wasserburg, G. J. 1996. Live ^{107}Pd in the early Solar System and implications for planetary evolution. In: *Earth Processes: Reading the Isotope Code*, Vol. 95, S. R. Hart and A. Basu. (eds), pp. 1–20. Washington: AGU.
- Clayton, R. N. 1993. Oxygen isotopes in meteorites. *Annual Review of Earth and Planetary Sciences*, 21: 115–149, doi:10.1146/annurev.ea.21.050193.000555.
- Clayton, R. N., Onuma, N. and Mayeda, T. K. 1976. A classification of meteorites based on oxygen isotopes, *Earth and Planetary Science Letters*, 30: 10–18.
- Clayton, R. N. 2002. Self-shielding in the solar nebula, *Nature*, 415: 860–861.
- Connelly, J. N., Bizzarro, M., Krot, A. N., Nordlund, Å., Wielandt, D. and Ivanova, M. A. 2012. The absolute chronology and thermal processing of solids in the solar protoplanetary disk. *Science*, 338: 651–655, doi:10.1126/science.1226919.
- Connelly, J. N., Bizzarro, M., Thrane, K. and Baker, J. A. 2008. The Pb-Pb age of Angrite SAH99555 revisited. *Geochimica et Cosmochimica Acta*, 72: 4813–4824, doi: 10.1016/j.gca.2008.06.007.
- Crabb, J., and Schultz, L. 1981. Cosmic-ray exposure ages of the ordinary chondrites and their significance for parent body stratigraphy, *Geochimica et Cosmochimica Acta*, 45: 2151–2160.
- Davies G. F. 2009. Effect of plate bending on the Urey ratio and the thermal evolution of the mantle. *Earth and Planetary Science Letters*, 287: 513–518.
- Gallino, R., Busso, M., Picchio, G. and Raiteri, C. M. 1990. On the astrophysical interpretation of isotope anomalies in meteoritic SiC grains. *Nature*. 348: 298–302.
- Gannoun, A., Boyet, M., Rizo, H. and El Goresy, A. 2011. ^{146}Sm - ^{142}Nd systematics measured in enstatite chondrites reveals a heterogeneous distribution of ^{142}Nd in the solar nebula. *Proceedings of the National Academy of Sciences*, 108: 7693–7697, doi:10.1073/pnas.1017332108.
- Garnero, E. J. and McNamara, A. K. 2008. Structure and dynamics of Earth's lower mantle. *Science*, 320: 626–628, doi:10.1126/science.1148028.
- Gilmour, J. D., Pravdivtseva, O. V., Busfield, A. and Hohenberg, C. M. 2006. The I-Xe chronometer and the early Solar System. *Meteoritics and Planetary Science*, 41: 19–31, doi: 10.1111/j.1945-5100.2006.tb00190.x.
- Göpel, C., Manhès, G. and Allègre, C. 1994. U-Pb systematics of phosphates from equilibrated ordinary chondrites. *Earth and Planetary Science Letters*, 121: 153–171,
- Halliday, A. N., Wanke, H., Birck, J.-L. and Clayton, R. N. 2001. The accretion, composition, and early differentiation of Mars, *Space Science Reviews*, 96: 197–230.
- Harper, C. L. and Jacobsen, S. B. 1992. Evidence from coupled ^{147}Sm - ^{143}Nd and ^{146}Sm - ^{142}Nd systematics for very early (4.5-Gyr) differentiation of the Earth's mantle, *Nature*, 360: 728–732.
- Harper, C. L., Volkening, J., Heumann, K. G., Shih, C.-Y. and Wiesmann, H. 1991. ^{182}Hf - ^{182}W : New cosmochronometric constraints on terrestrial accretion, core formation, the astrophysical site of the r-process, and the origins of the Solar System. *Lunar and Planetary Science Conference Abstracts*. 22: 515–516.
- Hashizume, K. and Chaussidon, M. 2005. A non-terrestrial ^{16}O -rich isotopic composition of the protosolar nebula, *Nature*, 434: 619–622.
- Hohenberg, C. M. and Pravdivtseva, O. V. 2008. I-Xe dating: From adolescence to maturity. *Chemie der Erde - Geochemistry*, 68: 339–351, doi: 10.1016/j.chemer.2008.06.002.
- Huss, G. R., Hutcheon, I. D. and Wasserburg, G. J. 1997. Isotopic systematics of presolar silicon carbide from the Orgueil (CI) chondrite: implications for Solar System formation and stellar nucleosynthesis. *Geochimica et Cosmochimica Acta*. 61: 5117–5148.
- Jacobsen, S. B. and Harper, C. L. 1996. Accretion and early differentiation history of the Earth based on extinct radionuclides. In: *Earth Processes: Reading the Isotope Code*, Vol. 95, S. R. Hart and A. Basu. (eds), pp. 47–74. Washington: AGU.
- Kinoshita, N., Paul, M., Kashiv, Y., Collon, P., Deibel, C. M., DiGiovine, B., et al. 2012. A shorter ^{146}Sm half-life measured and implications for ^{146}Sm - ^{142}Nd chronology in the Solar System. *Science*, 335: 1614–1617, doi: 10.1126/science.1215510.

- Kleine, T., Münker, C., Mezger, K. and Palme, H. 2002. Rapid accretion and early core formation on asteroids and the terrestrial planets from Hf-W chronometry, *Nature*, 418: 952–954, doi: 10.1038/nature00982.
- Krot, A. N., Amelin, Y., Bland, P., Ciesla, F. J., Connelly, J., Davis, A. M., et al. 2009. Origin and chronology of chondritic components: A review. *Geochimica et Cosmochimica Acta*, 73: 4963–4997, doi: 10.1016/j.gca.2008.09.039.
- Lee, D. C. and Halliday, A. N. 1995. Hafnium-tungsten chronometry and the timing of terrestrial core formation. *Nature*, 378: 771–774.
- Lee, D. C. and Halliday, A. N. 1998. Hf-W evidence for early differentiation of Mars and the Eucrite parent body. *Lunar Planet. Sci. Conf. Absts.* 28: 79.
- Lee, D.-C., Halliday, A. N., Snyder, G. A. and Taylor, L. A. 1997. Age and origin of the Moon. *Science*, 278: 1098–1103, doi:10.1126/science.278.5340.1098.
- Lewis, R. S., Srinivasan, B. and Anders, E. 1975. Host phase of a strange xenon component in Allende. *Science*, 190: 1251–1262, doi:10.2307/1741803.
- Lewis, R. S., Amari, S. and Anders, E. 1990. Meteorite silicon carbide: pristine material from carbon stars. *Nature*, 348: 293–298.
- Lewis, R. S., Amari, S. and Anders, E. 1994. Interstellar grains in meteorites: II. SiC and its noble gases. *Geochimica et Cosmochimica Acta*, 58: 471–494.
- Lodders, K. and Amari, S. 2005. Presolar grains from meteorites: Remnants from the early times of the Solar System. *Chemie der Erde - Geochemistry*, 65: 93–166, doi:10.1016/j.chemer.2005.01.001.
- MacPherson, G. J., Davis, A. and Zinner, E. 1995. The distribution of aluminum-26 in the early Solar System-A reappraisal. *Meteoritics*, 30: 365–385.
- MacPherson, G. J., Kita, N. T., Ushikubo, T., Bullock, E. S. and Davis, A. M. 2012. Well-resolved variations in the formation ages for Ca-Al-rich inclusions in the early Solar System. *Earth and Planetary Science Letters*, 331: 43–54, doi: 10.1016/j.epsl.2012.03.010.
- McKeegan, K. D., Kallio, A. P. A., Heber, V. S., Jarzebinski, G., Mao, P. H., Coath, C. D., et al. 2011. The oxygen isotopic composition of the sun inferred from captured solar wind. *Science*, 332: 1528–1532, doi: 10.1126/science.1204636.
- McSween, H. Y. and Huss, G. R. 2010. *Cosmochemistry*, Cambridge: Cambridge University Press.
- Nagashima, K., Krot, A. N. and Yurimoto, H. 2004. Stardust silicates from primitive meteorites, *Nature*, 428: 921–924.
- Nagashima, K., Krot, A. and Park, C. 2013. Mineralogy, petrology, O and Mg-Isotope compositions of AOAs from CH carbonaceous chondrites. *Mineralogical Magazine*, 77: 1822.
- Nguyen, A. N. and Zinner, E. 2004. Discovery of ancient silicate stardust in a meteorite, *Science*, 303: 1496–1499.
- Nyquist, L. E., Kleine, T., Shih, C. Y. and Reese, Y. D. 2009. The distribution of short-lived radioisotopes in the early Solar System and the chronology of asteroid accretion, differentiation, and secondary mineralization. *Geochimica et Cosmochimica Acta*, 73: 5115–5136.
- Nyquist, L. E., Reese, Y., Wiesmann, H., Shih, C. Y. and Takeda, H. 2003. Fossil ^{26}Al and ^{53}Mn in the Asuka 881394 eucrite: evidence of the earliest crust on asteroid 4 Vesta. *Earth and Planetary Science Letters*, 214: 11–25, doi:10.1016/s0012-821x(03)00371-6.
- O’Neil J., Carlson, R. L., Francis, D., and Stevenson, R. K. 2008. Neodymium-142 evidence for Hadean mafic crust. *Science* 321: 1828–1831.
- O’Neill, H. S. C. and Palme, H. 2008. Collisional erosion and the non-chondritic composition of the terrestrial planets. *Philosophical Transactions of the Royal Society A: Mathematical, Physical and Engineering Sciences*, 366: 4205–4238, doi:10.1098/rsta.2008.0111.
- Podosek, F. and Swindle, T. D. 1989. Extinct Radionuclides. In: *Meteorites and the Early Solar System*, 1093–1113. Tuscon: University of Arizona Press.
- Qin, L., Carlson, R. W. and Alexander, C. M. O. Å. 2011. Correlated nucleosynthetic isotopic variability in Cr, Sr, Ba, Sm, Nd and Hf in Murchison and QUE 97008. *Geochimica et Cosmochimica Acta*, 75: 7806–7828, doi: 10.1016/j.gca.2011.10.009.
- Shuloyukov, A., and Lugmair, G. W. 1993. ^{60}Fe in eucrites, *Earth and Planetary Science Letters*, 119: 159–166.
- Smoliar, M. I., Walker, R. J. and Morgan, J. W. 1996. Re-Os ages of group IIA, IIIA, IVA, and IVB iron meteorites. *Science*, 271: 1099–1102, doi:10.1126/science.271.5252.1099.
- Swindle, T. D., Caffee, M. W., Hohenberg, C. M. and Lindstrom, M. M. 1983. I-Xe studies of individual Allende chondrules. *Geochimica et Cosmochimica Acta*, 47: 2157–2177, doi:10.1016/0016-7037(83)90040-6.
- Tang, M. and Anders, E. 1988. Isotopic anomalies of Ne, Xe, and C in meteorites. II. Interstellar diamond and SiC: Carriers of exotic noble gases. *Geochimica et Cosmochimica Acta*, 52: 1235–1244.
- Thiemens, M. H., and Heidenreich, J. E. 1983. The mass independent fractionation of oxygen – A novel isotopic effect and its cosmochemical implications, *Science*, 219: 1073–1075.
- Thiemens, M. 2006. History and applications of mass-independent isotope effects, *Annual Review of Earth and Planetary Sciences*, 34: 217–262.

- Thrane, K., Connelly, J. N., Bizzarro, M., Meyer, B. S. and The, L.-S. 2010. Origin of excess ^{176}Hf in meteorites. *The Astrophysical Journal*, 717: 861–867, doi: 10.1088/0004-637X/717/2/861.
- Touboul, M., Kleine, T., Bourdon, B., Palme, H. and Wieler, R. 2007. Late formation and prolonged differentiation of the Moon inferred from W isotopes in lunar metals. *Nature*, 450: 1206–1209.
- Touboul, M., Kleine, T., Bourdon, B., Palme, H. and Wieler, R. 2009. Tungsten isotopes in ferroan anorthosites: Implications for the age of the Moon and lifetime of its magma ocean. *Icarus*, 199: 245–249.
- Touboul, M., Puchtel, I. S. and Walker, R. J. 2012. ^{182}W evidence for long-term preservation of early mantle differentiation products. *Science*, 335: 1065–1069, doi:10.1126/science.1216351.
- Trinquier, A., Birck, J. L., Allègre, C. J., Göpel, C. and Ulfbeck, D. 2008. ^{53}Mn –Cr systematics of the early Solar System revisited. *Geochimica et Cosmochimica Acta*, 72: 5146–5163, doi: 10.1016/j.gca.2008.03.023.
- Upadhyay, D., Scherer, E. E. and Mezger, K. 2009. ^{142}Nd evidence for an enriched Hadean reservoir in cratonic roots. *Nature*, 459: 1118–1121, doi: 10.1038/nature08089.
- Villeneuve, J., Chaussidon, M. and Libourel, G. 2009. Homogeneous distribution of ^{26}Al in the Solar System from the Mg isotopic composition of chondrules. *Science*, 325: 985–988, doi: 10.1126/science.1173907.
- Wadhwa, M., Amelin, Y., Bogdanovski, O., Shukolyukov, A., Lugmair, G. W. and Janney, P. 2009. Ancient relative and absolute ages for a basaltic meteorite: Implications for timescales of planetesimal accretion and differentiation. *Geochimica et Cosmochimica Acta*, 73: 5189–5201, doi: 10.1016/j.gca.2009.04.043.
- Whitby, J., Burgess, R., Turner, G., Gilmour, J. and Bridges, J. 2000. Extinct ^{129}I in halite from a primitive meteorite: evidence for evaporite formation in the early Solar System. *Science*, 288: 1819–1821, doi:10.1126/science.288.5472.1819.
- Whitby, J. A., Gilmour, J. D., Turner, G., Prinz, M. and Ash, R. D. 2002. Iodine-Xenon dating of chondrules from the Qingzhen and Kota Kota enstatite chondrites. *Geochimica et Cosmochimica Acta*, 66: 347–359, doi: 10.1016/S0016-7037(01)00783-9.
- White, W. M. 2013. *Geochemistry*, Oxford: Wiley-Blackwell, 672 p.
- Yin, Q., Jacobsen, S. B., Blichert-Toft, Y. K., J. Télouk, P. and Albarède, F. 2002. A short timescale for terrestrial planet formation from Hf-W chronometry of meteorites, *Nature*, 418: 949–951.
- Yokoyama, T., Takahashi, H. and Yamazaki, H. 2013. ^{142}Nd isotope anomaly in chondrite revisited. *Mineralogical Magazine*, 77: 2561.

SUGGESTIONS FOR FURTHER READING

- Amelin, Y. and Krot, A. N. 2007. Pb isotopic age of the Allende chondrules, *Meteoritics and Planetary Science*, 42: 1321–1335.
- Amelin, Y., Krot, A. N., Hutcheon, I. D. and Ulyanov, A. A. 2002. Lead isotopic ages of chondrules and calcium-aluminum-rich inclusions, *Science*, 297: 1678–1683.
- Baker, J., Bizzarro, M., Wittig, N., Connolly, J. N. and Haack, H. 2005. Early planetesimal melting from an age of 4.5662 Gyr for differentiated meteorites, *Nature*, 436: 1127–1131.
- Benz, W., Slattery, W. L. and Cameron A. G. W. 1988. Collisional stripping of Mercury's mantle. *Icarus*, 74: 516–28.
- Chen, J. H. and Wasserburg, G. J. 1983. The least radiogenic Pb in iron meteorites. *Fourteenth Lunar and Planetary Science Conference*, Abstracts, Part I, Lunar and Planetary Science Institute, Houston, pp. 103–104.
- Corgne, A. and Wood, B. J., 2004. Trace element partitioning between majoritic garnet and silicate melt at 25 GPa. *Physics of the Earth and Planetary Interiors*. 143–144: 407–419.
- Corgne, A., Liebske, C., Wood, B. J., Rubie, D. C. and Frost, D. J. 2005. Silicate perovskite-melt partitioning of trace elements and geochemical signature of a deep perovskitic reservoir, *Geochimica et Cosmochimica Acta*, 69: 485–496.
- Jacobsen, S. B. and Wasserburg, G. J. 1984. The Sm-Nd evolution of chondrites and achondrites, II. *Earth and Planetary Science Letters*, 67: 137–50.
- Jacobsen, S. and Wasserburg, G. J. 1980, Sm-Nd isotopic evolution of chondrites, *Earth and Planetary Science Letters*, 50: 139–155.
- Lee, T. D. A. Papanastassiou and G. J. Wasserburg, 1976. Demonstration of 26Mg excess in Allende and evidence for 26Al, *Geophysical Research Letters*, 3: 41–44.
- Nittler, L. R. 2003. Presolar stardust in meteorites: recent advances and scientific frontiers. *Earth and Planetary Science Letters*, 209: 259–273.
- Papanastassiou, D. A. and Wasserburg, G. J. 1969. Initial strontium isotopic abundances and the resolution of small time differences in the formation of planetary objects. *Earth and Planetary Science Letters*, 5: 361–376.
- Podosek, F. A., 1970. Dating of meteorites by high temperature release of iodine correlated ^{129}Xe , *Geochimica et Cosmochimica Acta*, 34: 341–365.
- Ranen, M. C. and Jacobsen, S. B. 2006. Barium isotopes in chondritic meteorites: implications for planetary reservoir models, *Science*, 314: 809–812.
- Tatsumoto, M., Knight, R. J. and Allègre, C. J. 1973. Time differences in the formation of meteorites ad determined from the ratio of lead-207 to lead-206. *Science*, 180: 1279–1283.

PROBLEMS

- One calcium-aluminum inclusion in the Allende meteorite has $\delta^{26}\text{Mg}$ values which imply a $^{26}\text{Al}/^{27}\text{Al}$ ratio of 0.46×10^{-5} at the time of its formation. A second inclusion apparently formed with a $^{26}\text{Al}/^{27}\text{Al}$ ratio of 1.1×10^{-5} . The half-life of ^{26}Al is 7.2×10^5 years. Assuming both these inclusions formed from the sample cloud of dust and gas and that the $^{26}\text{Al}/^{27}\text{Al}$ ratio in this cloud was uniform, how much earlier did the second inclusion form than the first?
- The calculated initial $^{27}\text{Al}/^{26}\text{Al}$ of the basaltic achondrite NWA2976 is 3.94×10^{-7} . Using a half-life of 7.16×10^5 years and assuming an initial $5.05 \times 10^{-5} \text{ }^{27}\text{Al}/^{26}\text{Al}$ at the start of the Solar System, what is the age of this meteorite?
- Suppose you measure the $^{129}\text{Xe}/^{130}\text{Xe}$ and I/Xe ratios in two chondritic meteorites in step-heating gas release experiments. From the first, you deduce a $^{129}\text{I}/^{127}\text{I}$ ratio of 0.53×10^{-4} at the time of formation. In the second, you deduce a $^{129}\text{I}/^{127}\text{I}$ ratio of 1.47×10^{-4} at the time of formation. How much time elapsed between formation of these meteorites, and which formed first?
- Bouvier et al. measured the following data on the H4 meteorite *St Margarite*:

	$^{206}\text{Pb}/^{204}\text{Pb}$	$^{207}\text{Pb}/^{204}\text{Pb}$
Whole-rock R0	41.6593	30.4466
L0	24.8906	20.0734
Chondrule R0	35.8299	26.8506
L0	18.5585	16.0838
Px + Ol R2	47.2008	33.9302
L1	20.3812	17.2259
L2	21.9916	18.2169

Calculate the $^{207}\text{Pb}/^{204}\text{Pb}$ age of this meteorite assuming a $^{238}\text{U}/^{235}\text{U}$ ratio of 137.88. Then calculate the age assuming a $^{238}\text{U}/^{235}\text{U}$ ratio of 138.79.

- The initial $^{206}\text{Pb}/^{204}\text{Pb}$ and $^{207}\text{Pb}/^{204}\text{Pb}$ ratios of the Solar System at 4.567 Ga are 9.307 and 10.294, respectively. If the value of $^{238}\text{U}/^{204}\text{Pb}$ in the solar nebula was 0.14, calculate the evolution of $^{206}\text{Pb}/^{204}\text{Pb}$ and $^{207}\text{Pb}/^{204}\text{Pb}$ of the solar nebula at 100 Ma intervals from 4.567 to at 4.45 Ga. (Hint: this calculation is a little trickier than you might think.)
- In which cosmic environments could the following short-lived radionuclides be made? Justify your answer.
 - ^{182}Hf
 - ^{146}Sm
 - ^{107}Pd
 - ^{129}I
 - ^{247}Cm
- Excesses of ^{135}Ba , ^{137}Ba , and ^{138}Ba have been found in several chondrites. How would you explain these in terms of the different nucleosynthetic processes occurring in different stellar environments? (Hint: look at a Chart of the Nuclides and refer to Chapter 1.)
- The following data were measured on the ungrouped basaltic achondrite NWA 2976. Calculate the initial $^{26}\text{Al}/^{27}\text{Al}$ using the isochron method (adapt Eqn. 5.5 for the $^{26}\text{Al}-^{26}\text{Mg}$

decay). Assuming the $^{26}\text{Al}/^{27}\text{Al}$ abundance ratio listed in Table 5.1 was the initial ratio of the Solar System, what is the age of this meteorite relative to that initial time?

	$^{27}\text{Al}/^{24}\text{Mg}$	$^{26}\text{Mg}/^{24}\text{Mg}$
WR5	1.87	0.13979
PX3	0.67	0.13979
PL3	513.60	0.13999
PL4	143.00	0.13984
PL5	121.60	0.13984
PL6	82.27	0.13983

Chapter 6

Radiogenic isotope geochemistry of the mantle

6.1 INTRODUCTION

The initial use of radioactive and radiogenic isotopes in geology was directed exclusively toward geochronology. The potential geochemical applications became apparent only later. One of the first to recognize the potential of radiogenic isotope studies was Paul Gast, who was a student of Al Nier, who invented the magnetic sector mass spectrometer. In what was one of the first papers to apply radiogenic isotopes to a geochemical problem (the composition of the mantle), Gast (1960) described the principles of Sr isotope geochemistry as follows:

In a given chemical system the isotopic abundance of ^{87}Sr is determined by four parameters: the isotopic abundance at a given initial time, the Rb/Sr ratio of the system, the decay constant of ^{87}Rb , and the time elapsed since the initial time. The isotopic composition of a particular sample of strontium, whose history may or may not be known, may be the result of time spent in a number of such systems or environments. In any case the isotopic composition is the time-integrated result of the Rb/Sr ratios in all the past environments. Local differences in the Rb/Sr will, in time, result in local differences in the abundance of ^{87}Sr . Mixing of material during processes will tend to homogenize these local variations. Once homogenization occurs, the isotopic composition is not further affected by these processes. Because of this property and because of the time-integrating effect, isotopic compositions lead to useful inferences concerning the Rb/Sr ratio of the crust

and of the upper mantle. It should be noted that similar arguments can be made for the radiogenic isotopes of lead, which are related to the U/Pb ratio and time.

We can add the study of isotope systems subsequently developed, namely Nd, Hf, and Os, to that list.

Gast's first sentence is simply a statement of the radiogenic growth equation for the Rb-Sr system:

$$\frac{^{87}\text{Sr}}{^{86}\text{Sr}} = \left(\frac{^{87}\text{Sr}}{^{86}\text{Sr}} \right)_0 + \frac{^{87}\text{Rb}}{^{86}\text{Sr}} (e^{\lambda t} - 1) \quad (6.1)$$

Gast's statement remains a valid and succinct summary of the principles of radiogenic isotope geochemistry.

A principal objective of geology is to understand how the Earth evolved from its initial state to its present one. Radiogenic isotope geochemistry is uniquely suited for this sort of study because an isotope ratio such as $^{87}\text{Sr}/^{86}\text{Sr}$ is a function not only of the differentiation processes that fractionate Rb from Sr, it is also a function of the time at which the fractionation occurred. On a continuously evolving Earth, ancient features tend to be destroyed by subsequent processes. For example, erosion of rock to form a new sedimentary rock destroys information about the large-scale structure of the pre-existing rock. If the sediment is sufficiently coarse-grained, some information about the fine-scale structure of parent rock will be preserved. If the sediment produced is fine-grained, such as

shale, no structural information is preserved. Some chemical information might be preserved in this case, although often very little. Isotopic ratios of the shale, however, preserve information not only about the chemistry of the parent, but also about its age of formation. Similarly, melting of the sediment to form granite destroys all structural information, but considerable chemical information is often preserved. Isotope ratios, however, preserve, albeit incompletely, information about both chemistry and time.

As Gast said, the $^{87}\text{Sr}/^{86}\text{Sr}$ ratio is a function of the time-integrated Rb/Sr. Ultimately, we can draw much broader inferences than merely the time-integrated Rb/Sr ratio. Rb and Sr are both trace elements, and together account for only a few ppm of the mass of the Earth. However, Rb and Sr share some of their properties with other elements of their group: Rb with the alkalis, Sr with the alkaline earths. So Rb/Sr fractionations tell us something about alkali/alkaline earth fractionations. In addition, since Rb is highly incompatible and Sr only moderately so, Rb/Sr fractionations tell us something about the fractionation of incompatible elements from less incompatible elements. Similarly Sm/Nd variations are related to variations between light and heavy rare earths, as well as incompatible/less incompatible element variations. We have some knowledge of the processes that fractionate the alkalis and alkaline earths and the light and heavy rare earths. Thus knowledge of variations in these element ratios allows us to limit the range of possible processes occurring within the Earth; the time parameter in Eqn. 6.1 allows us the limit the range of possible times at which this fractionation occurred.

6.1.1 Definitions: time-integrated and time-averaged

Gast stated that the $^{87}\text{Sr}/^{86}\text{Sr}$ is a function of the *time-integrated* Rb/Sr ratio. What did he mean by “time-integrated”?

Suppose the $^{87}\text{Rb}/^{86}\text{Sr}$ ratio evolves in some reservoir in some complex way. Let's allow the $^{87}\text{Rb}/^{86}\text{Sr}$ to be an arbitrary function of time such as $^{87}\text{Rb}/^{86}\text{Sr} = t + \sin(5t/\pi) + 1$. This is shown plotted in Figure 6.1a. If we integrate $^{87}\text{Rb}/^{86}\text{Sr}$ with respect to time, we get the area under the curve, of course. From that, we can

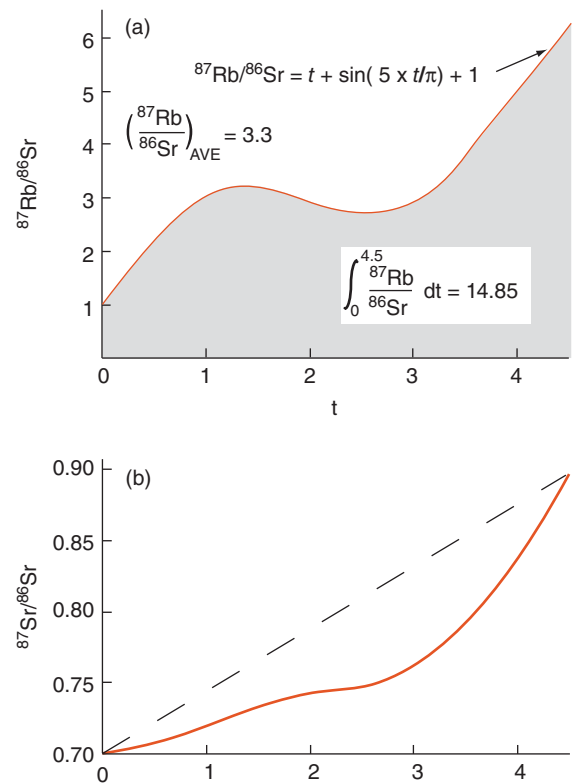


Figure 6.1 (a) $^{87}\text{Rb}/^{86}\text{Sr}$ is shown as changing in a hypothetical reservoir as some arbitrary function of time. The average $^{87}\text{Rb}/^{86}\text{Sr}$ may be calculated by integrating $^{87}\text{Rb}/^{86}\text{Sr}$ with respect to time, and then dividing by $(t - t_0)$. (b) Evolution of $^{87}\text{Sr}/^{86}\text{Sr}$ for the case where $^{87}\text{Rb}/^{86}\text{Sr}$ is a function of time as shown in (a). The dashed line shows the growth of $^{87}\text{Sr}/^{86}\text{Sr}$ if $^{87}\text{Rb}/^{86}\text{Sr}$ is constant and equal to 3.3.

find the average $^{87}\text{Rb}/^{86}\text{Sr}$ simply by dividing the area under the curve by $(t - t_0)$, which is 3.3. The $^{87}\text{Sr}/^{86}\text{Sr}$ would evolve as shown by the solid line in Figure 6.1b. Just as we can calculate the average $^{87}\text{Rb}/^{86}\text{Sr}$ ratio from the area under the curve in Figure 6.1(a), we can deduce the average $^{87}\text{Rb}/^{86}\text{Sr}$ in a reservoir if we know the initial and final values of t and $^{87}\text{Sr}/^{86}\text{Sr}$. It is in this sense that $^{87}\text{Sr}/^{86}\text{Sr}$ yields a *time-integrated* value of $^{87}\text{Rb}/^{86}\text{Sr}$.

Notice that the same final $^{87}\text{Sr}/^{86}\text{Sr}$ value in Figure 6.1b would have been reached if $^{87}\text{Rb}/^{86}\text{Sr}$ had a constant value of 3.3 ($^{87}\text{Sr}/^{86}\text{Sr}$ evolves along the dashed line). It could have been reached by an infinite other number of paths as well. Thus, while we can deduce the time-averaged $^{87}\text{Rb}/^{86}\text{Sr}$ of a

reservoir over its history from the $^{87}\text{Sr}/^{86}\text{Sr}$, we cannot decipher the details of the evolution (i.e., the exact path) of the $^{87}\text{Rb}/^{86}\text{Sr}$ ratio. An interesting feature of the U-Pb system is that we can constrain, though not specify exactly, the evolutionary path. This is because the two isotopes of U have very different half-lives.

We will begin our study of isotope geochemistry with an examination of mantle geochemistry. In the next chapter, we will then turn to the geochemistry of the continental crust. The two problems are closely related, so ultimately, we will attempt to understand the relationship between chemical evolution of the crust and of the mantle. At the end of that chapter, we'll examine how isotope ratios are used to constrain how the ocean circulate today and in the past, and isotope ratios of material precipitating from seawater help reveal how the surface of the Earth has evolved through time.

6.2 ISOTOPE GEOCHEMISTRY OF THE EARTH'S MANTLE

The mantle constitutes two-thirds of the mass of the Earth and very nearly the entire mass of the silicate Earth. The relative abundances of many elements in the mantle, therefore, should be close to that of the Earth as a whole, most particularly for those elements that do not partition into either the core or the crust. We will begin with a working hypothesis that the crust, which constitutes only 0.5% of the mass of the Earth, has been created by partial melting of the mantle. This is one of only two possible alternatives: either the crust was formed at the same time as the Earth or it grew out of the mantle. There is no *a priori* reason why either of these two must be the case; we simply arbitrarily chose the second (in due course we will see that isotopic data substantiate our choice). Doing so allows us to define a reservoir that we shall call *primitive mantle* and is *equivalent to the composition of the bulk Earth less the composition of the core*. Thus *primitive mantle* is synonymous with *bulk silicate Earth*. In mathematical notation, then:

$$m_{PM}[\text{E}]_{PM} = m_E[\text{E}]_E - m_C[\text{E}]_C \quad (6.2)$$

where m denotes mass, the subscripts PM , E , and C denote primitive mantle, bulk Earth, and core respectively, and $[\text{E}]$ is a 1×92

matrix containing the concentrations of the elements in the reservoir. The *relative* abundances of lithophile elements (those elements for which $[\text{E}]_C = 0$) in the primitive mantle are the same as in the bulk Earth. The average modern mantle composition is then equal to the primitive mantle less the present composition of the crust:

$$m_M[\text{E}]_M = m_{PM}[\text{E}]_{PM} - m_K[\text{E}]_K \quad (6.3)$$

where the subscript K denotes continental crust and M the mantle. Our formulation implicitly assumes the core was formed before the crust. Again this is a somewhat arbitrary choice, but we have seen that deviation of terrestrial $^{182}\text{W}/^{183}\text{W}$ from chondritic suggests the core formed early. Similar mass balance equations may be written for isotope ratios and ratios of elements, but this requires slightly more complex mass balance equations.

The mantle is not generally accessible for direct sampling, so geochemists must resort to indirect samples. Much of the information we have about the geochemistry of the Earth's mantle comes from studies of mantle-derived magmas; other samples of the mantle include peridotite¹ massifs and xenoliths² in magmas. The utility of the peridotite massifs is limited by their rarity and metamorphic and metasomatic processes associated with emplacement in the crust; information from xenoliths is limited both by their rarity and their small size; the information from basalts is limited because all structural information is lost and much of the chemical information is "distorted" by the partial melting process. But all three types of samples have particular advantages as well. Together, they provide a picture of the composition and structure of the mantle complimentary to the information derived from geophysical observations such as seismic waves, free oscillations, and so on.

6.2.1 The Sr-Nd-Hf picture

Figure 6.2 shows the Sr and Nd isotopic characteristics of the Earth's major silicate reservoirs. We begin by focusing on the picture of the mantle provided by isotopic compositions of basalts³ derived from the suboceanic mantle. There are two reasons for this initial focus on oceanic basalts: (1) many are contaminated by the continental crust through which they

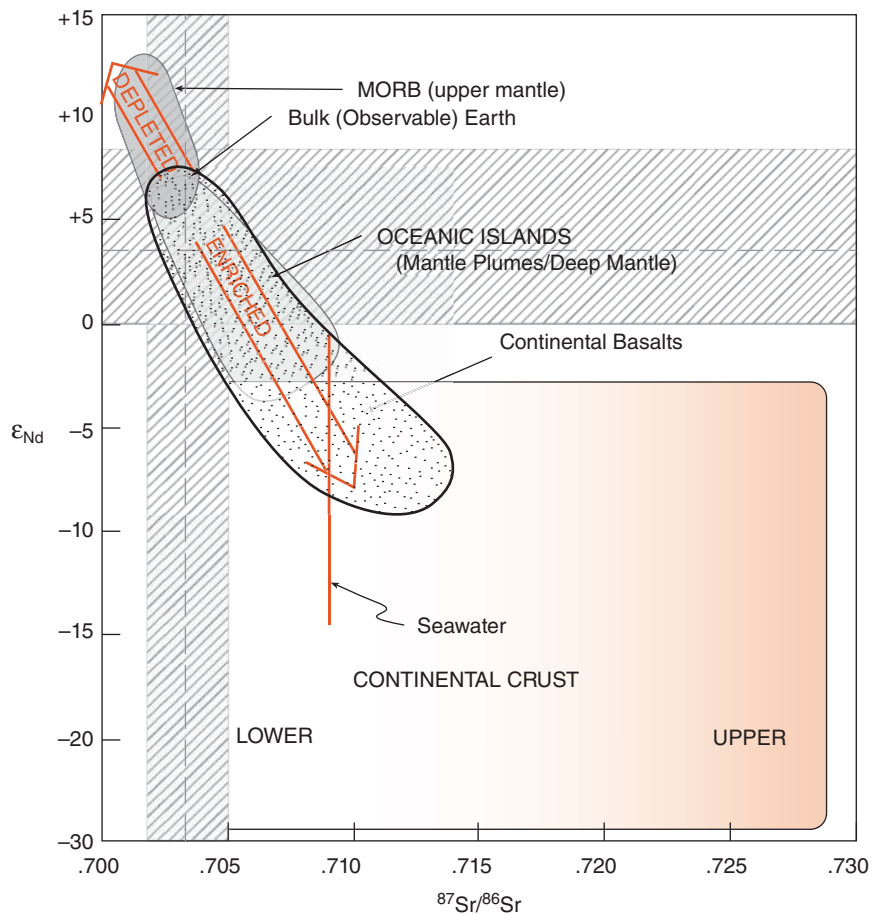


Figure 6.2 Sr and Nd isotopic systematics of the crust and mantle. Oceanic island basalts and MORB sample major reservoirs in the mantle. Continental basalts represent mixtures of various components, including mantle plumes, subcontinental lithosphere, and continental crust. Horizontal and vertical hashed bands are the estimated ϵ_{Nd} and $^{87}\text{Sr}/^{86}\text{Sr}$ of the *observable Earth* of Caro and Bourdon (2010).

ascend and (2) the subcontinental lithosphere, from which some of the continental basalts are derived, does not convect and hence, many not be as well mixed and as representative of the mantle as oceanic basalts derived from the convecting mantle. We will later consider continental basalts and what they can tell us about the mantle lithosphere.

Figure 6.3 shows the isotopic compositions of oceanic basalts – mid-ocean ridge basalts and oceanic island basalts in detail. Mid-ocean ridge basalts (MORB) are those erupted at plate boundaries along the Earth's 50,000 km mid-ocean ridge system. Oceanic island basalts (OIB) are those that erupt on oceanic island volcanoes, such as the Hawaiian ones, and include oceanic islands, such as Iceland, that lie on mid-ocean ridges. The

first observation is that Nd and Sr isotope ratios are inversely correlated and the region occupied by the oceanic basalt data is often referred to as the “mantle array.” The second observation is that, although there is overlap, MORB have the lower $^{87}\text{Sr}/^{86}\text{Sr}$ ratios and higher ϵ_{Nd} than OIB. Variations in radiogenic isotope ratios in basalts result from variations in parent-daughter ratios in the mantle over great lengths of time. For example, to create a 1 ϵ_{Nd} variation in $^{143}\text{Nd}/^{144}\text{Nd}$ would require a variation in $^{147}\text{Sm}/^{144}\text{Nd}$ of 0.02, or about 10%, which existed for 1.4 Ga. We infer MORB come from a source with lower time-integrated $^{87}\text{Rb}/^{86}\text{Sr}$ and higher $^{147}\text{Sm}/^{144}\text{Nd}$ than OIB.

Nd isotopes systematics can help put the relative differences between MORB and

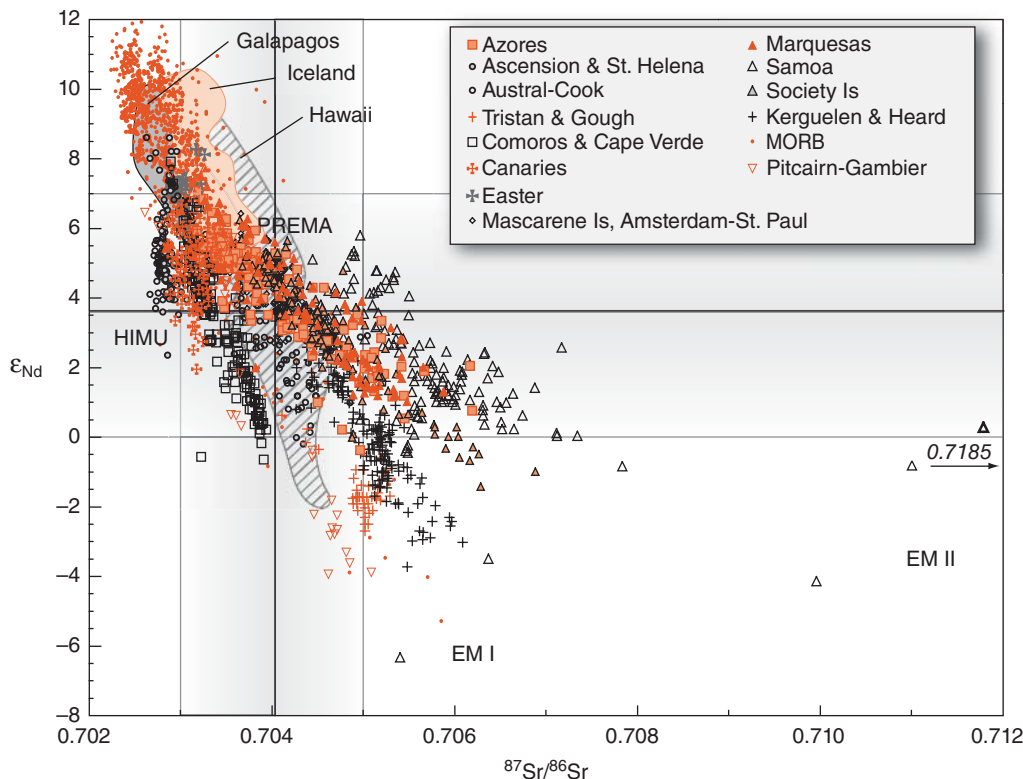


Figure 6.3 Sr and Nd isotope ratios of oceanic island basalts. The gradient in the MORB field indicates data density: the vast majority of MORB plot at the high ϵ_{Nd} end of the spectrum. Lines and hashed regions are the estimated composition of the observable Earth. (Source: Adapted from White, 2010.)

OIB in context because $^{142}\text{Nd}/^{144}\text{Nd}$ ratios provide some constraints on the Sm/Nd ratio of the silicate Earth and primitive mantle. As we saw in the last chapter, $^{142}\text{Nd}/^{144}\text{Nd}$ ratios of all modern terrestrial materials are about 18 ppm higher than those of ordinary chondrites and 10 ppm higher than enstatite chondrites. How different the Sm/Nd ratio of the Earth must be from chondritic depends somewhat on the very early history of the Earth, but Caro and Bourdon (2010) estimate the $^{147}\text{Sm}/^{144}\text{Nd}$ ratio of the bulk Earth as 0.2082 ± 25 compared to a chondritic value in the range of 0.1960–0.1966, about a 6% difference. This would mean that the bulk silicate Earth, or at least the observable part of it (if a hidden low $^{147}\text{Sm}/^{144}\text{Sm}$ reservoir exists), has $\epsilon_{\text{Nd}} = 6.9 \pm 1.9$. If instead we assume that the Earth has a $^{142}\text{Nd}/^{144}\text{Nd}$ initial ratio similar to that of enstatite chondrites, only a 3% difference in Sm/Nd is required and the present ϵ_{Nd} of the silicate Earth would be about +3.6. Assuming the bulk silicate

(observable) Earth lies on the “mantle array” in Figure 6.3, Caro and Bourdon estimated the $^{87}\text{Sr}/^{86}\text{Sr}$ of the bulk (observable) silicate Earth as 0.7030 ± 0.004 ; using the lower value of 3.6 for the ϵ_{Nd} of the silicate Earth implies a $^{87}\text{Sr}/^{86}\text{Sr}$ of about 0.70404. These values are illustrated on Figures 6.2 and 6.3 as hashed bands. On average, MORB have $\epsilon_{\text{Nd}} = 8.53$ and $^{87}\text{Sr}/^{86}\text{Sr} = 0.70289$; so-called “normal MORB”, those that are light rare earth-depleted, have $\epsilon_{\text{Nd}} = 9.25$ and $^{87}\text{Sr}/^{86}\text{Sr} = 0.70273$ (White and Klein, 2013). Thus MORB have higher time-integrated $^{147}\text{Sm}/^{144}\text{Nd}$ and lower $^{87}\text{Rb}/^{86}\text{Sr}$ than bulk Earth – one that is relatively depleted in more incompatible elements, such as Rb and Nd compared to more compatible ones such as Sr and Sm. For this reason, we often speak of MORB as being derived from a “depleted,” meaning incompatible element-depleted, reservoir.

Although we tend to think of MORB and OIB as being isotopically distinct, there is

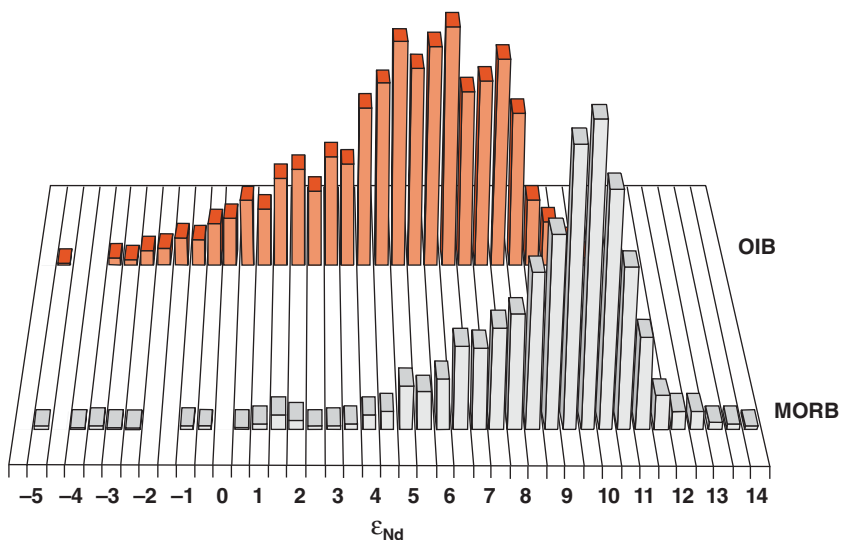


Figure 6.4 Comparison of Nd isotope ratio analyses of 1679 MORB and 2380 OIB from the PetDB and GEOROC databases. While distributions overlap, the two groups have different means and different spreads, with these differences being highly statistically significant.

in fact considerable overlap in the isotopic compositions of these groups. This is illustrated in Figure 6.4 for ϵ_{Nd} . Nevertheless, the means of the two are quite different, 8.5 and 5.0, respectively. MORB also clearly have a more uniform isotopic compositions with less dispersion than OIB, implying the reservoir from which MORB are derived is less heterogeneous.

In the previous discussion, we have transformed the isotopic information into information about parent-daughter ratios. The next step is to consider those processes that can fractionate, or change, the parent-daughter ratios. Rb is more incompatible than Sr, while Nd is more incompatible than Sm. This suggests the mantle has been affected by a process that removes the more incompatible elements. Partial melting and extraction of the melt is such a process. If, as we supposed earlier, the crust has formed by extraction of the mantle, then the depleted isotopic signature of the mantle might just reflect formation of the continental crust. The source of MORB appears to have been more depleted, perhaps having lost a greater melt fraction, than the source of OIB. There are, however, other explanations for the difference between MORB and OIB, which we will consider later.

Figure 6.5 shows $^{176}\text{Hf}/^{177}\text{Hf}$ ratios plotted against Nd isotope ratios. As we expect

from what we know of the behavior of the parents relative to the daughters, ϵ_{Hf} is negatively correlated with $^{87}\text{Sr}/^{86}\text{Sr}$ and positively correlated with ϵ_{Nd} . From the intersection of the $\epsilon_{\text{Hf}}-\epsilon_{\text{Nd}}$ array with $\epsilon_{\text{Nd}} = 3.6$, we estimate the $^{177}\text{Hf}/^{176}\text{Hf}$ ratio of the bulk (observable) silicate Earth as 0.28287, compared to a chondritic value of 0.282786, corresponding to an ϵ_{Hf} of +6.4. MORB have average ϵ_{Hf} of 14.2, implying they come from a reservoir with higher time-integrated Lu/Hf than the bulk silicate Earth. Because Hf is more incompatible than Lu, this is entirely consistent with the inference of incompatible element-depletion of the MORB source made from the Sm-Nd and Rb-Sr systems.

6.2.2 The Pb picture

Pb is by far the most powerful of the isotopic tools available to us because three parents decay to three isotopes of Pb. We have seen that the two U decay systems make Pb isotopes particularly useful in geochronology. The same is true in isotope geochemistry. Let's consider the special features of the Pb isotope system. We noted earlier that the slope on a plot of $^{207}\text{Pb}/^{204}\text{Pb}-^{206}\text{Pb}/^{204}\text{Pb}$ is proportional to time. Since Pb is a volatile element, and also somewhat siderophile and chalcophile, the U/Pb ratio of the silicate Earth

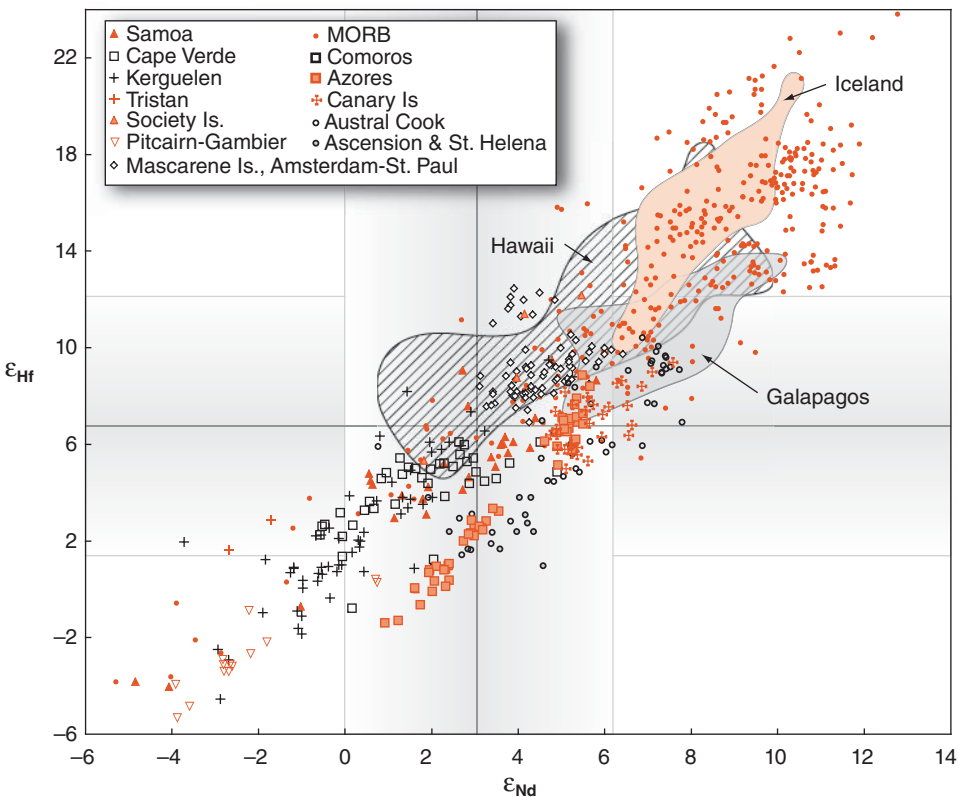


Figure 6.5 Hf and Nd isotope ratios of the suboceanic mantle as sampled by oceanic basalts. Gray bands show the inferred isotopic composition of the bulk silicate Earth. Data from GEOROC database.

is unlikely to be the same as the chondritic one. Indeed, it is demonstrably not. Hence the Pb isotope ratios of the bulk Earth are not readily constrained from chondritic values. Pb isotope ratios are, however, constrained by the assumptions that (1) the solar nebula has a uniform Pb isotopic composition when it formed, which we take to be equal to the composition of Pb in troilite in the *Nantan* (IAB-IICD) iron meteorite (Blichert-Toft et al., 2010) and (2) the Earth formed from this nebula 4.56 Ga ago. Thus the $^{207}\text{Pb}/^{204}\text{Pb}$ and $^{206}\text{Pb}/^{204}\text{Pb}$ ratios of the Earth today must lie on a unique isochron, called the *Geochron*, whose slope corresponds to 4.56 Ga and which passes through *Nantan* initial Pb (Figure 6.6; Table 6.1). Indeed, all planetary bodies that formed from the solar nebula at that time (4.56 Ga ago), and have remained closed system since then must plot on this isochron.

While there are no good grounds to question assumption 1, while assumption 2 might

be questioned in detail. The Solar System certainly formed 4.567 Ga ago, but the accretion of the inner planets may have required a significant amount of time. Indeed, computer models of planetary accretion suggest the process may take as much as 100 Ma. In this case, the Earth might be as young as 4.45 Ga, and would have begun with slightly different initial Pb isotope ratios, because of growth of radiogenic Pb over this 100 Ma period. The W isotope evidence we discussed in Chapter 5 together with the age of the oldest rocks on the Moon suggests the Earth is at least 50 million years younger, and perhaps 100 million years younger, than the 4.567 Ga age of the solar system. The point is that we cannot be quite certain that bulk Earth Pb isotope ratios must lie on the Geochron shown in Figure 6.6, but it certainly must lie close to it.

The U/Pb ratio of chondrites is quite low, so that Pb isotopes evolve slowly in a chondritic reservoir such as the solar nebula. Thus when the Earth first formed, its Pb isotope ratios

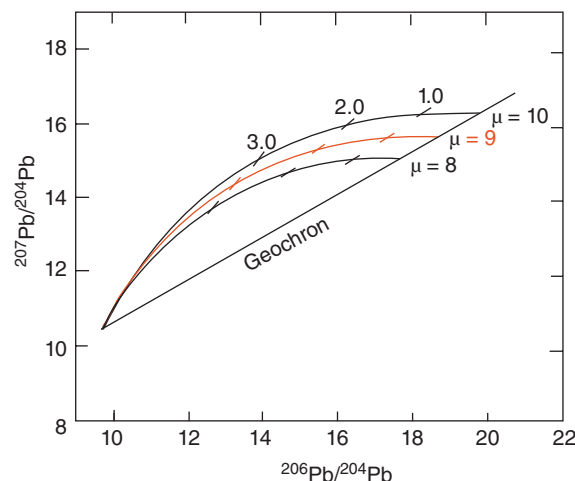


Figure 6.6 Evolution of Pb isotope ratios. The curve lines represent the evolutionary paths for systems having μ values of 8, 9, and 10. The hash marks on the evolution curves mark Pb isotope compositions 1.0, 2.0, and 3.0 Ga ago. (Source: White (2013). Reproduced with permission of John Wiley & Sons.)

Table 6.1 Pb isotope ratios in Nantan troilite.

$^{206}\text{Pb}/^{204}\text{Pb}$	9.306
$^{207}\text{Pb}/^{204}\text{Pb}$	10.307
$^{208}\text{Pb}/^{204}\text{Pb}$	29.532

should have been similar as that of the Nantan iron. Once the Earth formed with its high U/Pb ratio, $^{207}\text{Pb}/^{204}\text{Pb}$ and $^{206}\text{Pb}/^{204}\text{Pb}$ ratios increased as ^{235}U and ^{238}U decayed. At first, the $^{207}\text{Pb}/^{204}\text{Pb}$ ratio increased rapidly because there was about as much ^{235}U as ^{238}U around and ^{235}U was decaying to Pb more rapidly than ^{238}U . But as the ^{235}U was consumed, the rate of increase of $^{207}\text{Pb}/^{204}\text{Pb}$ slowed until the present when there is very little ^{235}U left to produce additional ^{207}Pb . Thus, growth of Pb isotope ratios through time in any system follows a curved path, such as those in Figure 6.6, which depends on the $^{238}\text{U}/^{204}\text{Pb}$ ratio (μ). For a system that has remained closed (no change in μ) for the entire 4.56 Ga, it starts at Nantan and ends (at present) at some point on the Geochron determined by its $^{238}\text{U}/^{204}\text{Pb}$ ratio.

With this in mind, we can now consider the available Pb isotopic data on the mantle,

which is shown in Figure 6.7. Perhaps somewhat surprisingly, almost all oceanic basalts plot to the high $^{206}\text{Pb}/^{204}\text{Pb}$ side of the Geochron. Taken together, these basalts likely represent the isotopic composition of the convecting mantle. As we shall see in next chapter, the average isotopic composition of the bulk continental crust also plots to the high $^{206}\text{Pb}/^{204}\text{Pb}$ side of the Geochron (average lower continental crust probably plots slightly to the low $^{206}\text{Pb}/^{204}\text{Pb}$ side). Thus the terrestrial reservoirs available to us, the *accessible* Earth, seems to have a mean isotopic composition falling off the Geochron. Halliday (2004) compiled 10 estimates of the Pb isotopic composition of the bulk silicate Earth (BSE). These estimates vary widely, from $^{206}\text{Pb}/^{204}\text{Pb} = 17.44$ and $^{207}\text{Pb}/^{204}\text{Pb} = 15.16$ to $^{206}\text{Pb}/^{204}\text{Pb} = 18.62$ and $^{206}\text{Pb}/^{204}\text{Pb} = 15.565$, reflecting our uncertainty in this BSE Pb isotopic composition. However, all of these estimates plot significantly to the high $^{206}\text{Pb}/^{204}\text{Pb}$ side of the Geochron. The mean of these estimates, 18.1 and 15.5, is shown in Figure 6.7. If this is indeed the BSE isotopic composition, it means that the silicate Earth must be significantly younger (50–100 Ma younger) than 4.56 Ga.

The U/Pb ratio in carbonaceous chondrites, and thus presumably in the solar nebula, was so low that any increase in $^{206}\text{Pb}/^{204}\text{Pb}$ and $^{207}\text{Pb}/^{204}\text{Pb}$ during the time Pb spent in the solar nebula would have been negligible. The silicate Earth has a much higher U/Pb ratio than carbonaceous chondrites, and the Pb-Pb age of the Earth reflects the timing of this change in U/Pb ratio. The change could be due either to Pb loss to its volatility or sequestering of Pb in the core. It is possible, if not likely, that both played a role. If the latter stages of Earth's formation involved violent collisions between large proto-planets, this would have provided energy to vaporize Pb. And we saw in the previous chapter that growth of the Earth's core probably occurred in parallel with accretion of the Earth. The relatively young Pb-Pb age of the Earth is more or less consistent with evidence of W isotope for relatively late formation of the Earth that we discussed in the last chapter. Yet another possibility is that the apparently ^{206}Pb -rich nature of the observable silicate Earth reflects differentiation of the Earth into early enriched and depleted reservoirs as suggested by Boyet and

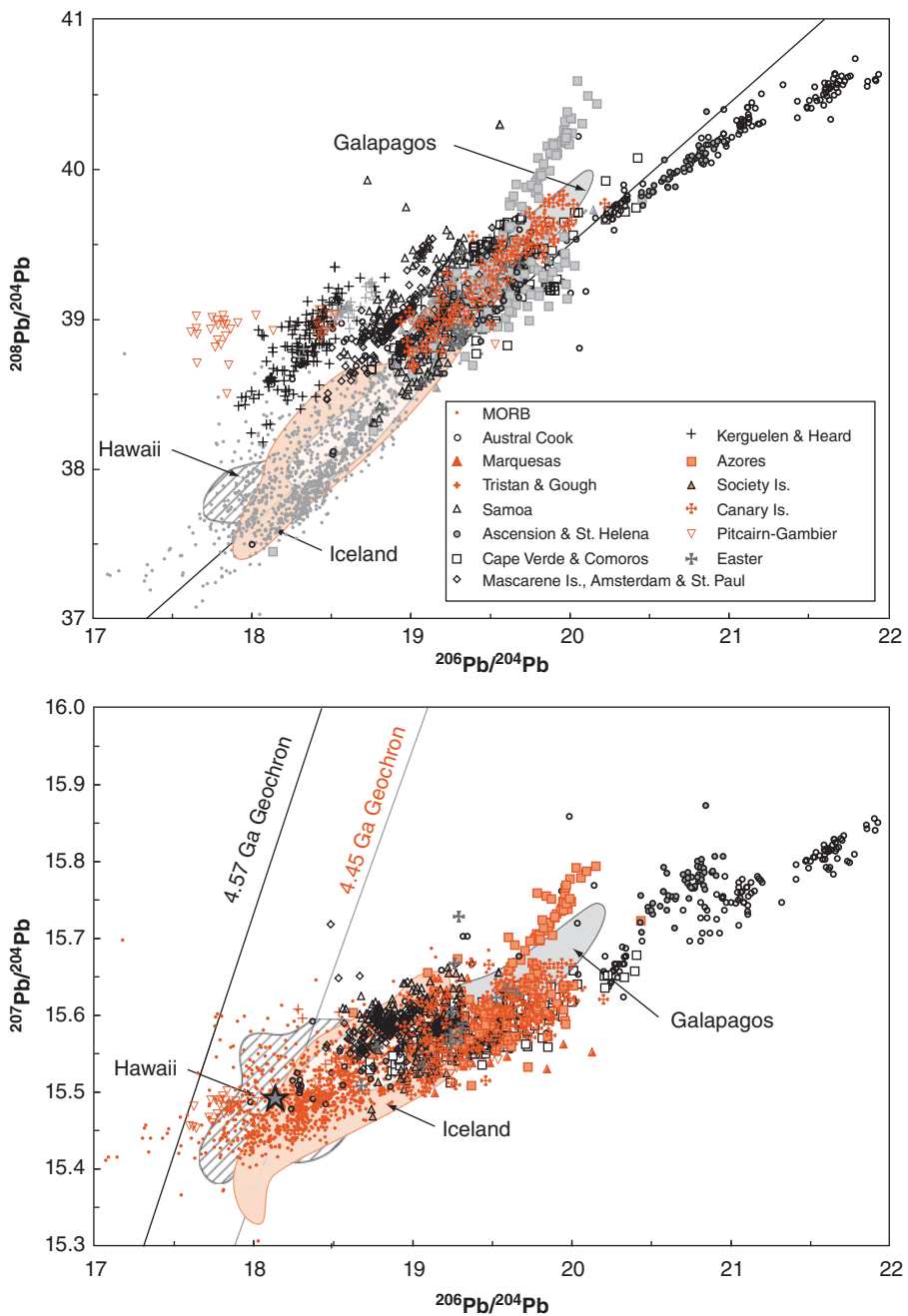


Figure 6.7 Pb isotope systematics of oceanic basalts on the $^{207}\text{Pb}/^{204}\text{Pb}$ – $^{206}\text{Pb}/^{204}\text{Pb}$ and $^{208}\text{Pb}/^{204}\text{Pb}$ – $^{206}\text{Pb}/^{204}\text{Pb}$ diagrams. The \star is the mean of 10 estimates of BSE compiled by Halliday (2004). The line in the $^{208}\text{Pb}/^{204}\text{Pb}$ – $^{206}\text{Pb}/^{204}\text{Pb}$ diagram is calculated for an age of 4.568 Ga and the chondritic κ of 3.814.

Carlson (2005). Perhaps the early-enriched reservoir plots to the low $^{206}\text{Pb}/^{204}\text{Pb}$ side of the Geochron. We simply don't know if this is the case because we do not know the nature of this early-enriched reservoir, if it exists.

While the Earth has remained a closed system with respect to Pb since its formation (indeed, a reasonable definition of the "age" of the Earth is the time since it became a closed system), but no reservoir within the Earth

need have remained closed for this period. Systems that have experienced a net increase in μ over the past 4.56 Ga will plot today to the high $^{206}\text{Pb}/^{204}\text{Pb}$ side of the Geochron. This is because U/Pb would be high in later parts of the system's history, when there was still a lot of ^{238}U around but not much ^{235}U , leading to high $^{206}\text{Pb}/^{204}\text{Pb}$ ratios relative to $^{207}\text{Pb}/^{204}\text{Pb}$ ratios. Conversely, a system experiencing a net decrease in μ at some time later than 4.56 Ga would plot to the low $^{206}\text{Pb}/^{204}\text{Pb}$ side of the Geochron (note that changes in μ at 4.56 Ga affect only the ultimate position of the system on the Geochron – they do result in the system plotting off the Geochron). Thus, despite our lack of knowledge about the Earth's U/Pb ratio, we can still draw inferences about changes in μ in any subsystem or reservoir within the Earth relative to the Earth as a whole. U is more incompatible than Pb, so increases in μ should accompany increases in Rb/Sr and decreases in Sm/Nd and Lu/Hf. Th is slightly more incompatible than U.

Looking at Figure 6.7, we see that Pb isotope ratios in OIB are generally, though not uniformly, higher than in MORB. This is what we expect if Pb is more compatible than U. On the other hand, there is a lot more overlap between MORB and OIB than for the other decay systems, suggesting greater complexity of the U-Pb system. Figure 6.7 also shows the relationship between $^{208}\text{Pb}/^{204}\text{Pb}$ and $^{206}\text{Pb}/^{204}\text{Pb}$. The two ratios are reasonably well correlated, implying U and Th have behaved rather similarly.

Since slopes on $^{207}\text{Pb}/^{204}\text{Pb}$ – $^{206}\text{Pb}/^{204}\text{Pb}$ plots are proportional to time, we can associate an age with the overall slope of the array in Figure 6.7. The slope corresponds to an age of about 1.68 Ga (White, 2010). Exactly what this age means, if indeed it is meaningful at all, is unclear. The array in Figure 6.7 can be interpreted as a mixing line between components at each end, in which case the age is only the minimum time that the two components must have been isolated. Alternatively, the age may date a single differentiation event, or represent the average age of a series of differentiation events, with the latter case being the most likely.

Sm-Nd, Lu-Hf, and Rb-Sr all appear to be behaving in a generally coherent manner in the mantle, but one or all of U, Th, and Pb appear

to behave “anomalously.” Pb isotope ratios generally show only poor correlations with other isotope ratios, for example, $^{206}\text{Pb}/^{204}\text{Pb}$ versus ϵ_{Nd} shown in Figure 6.8. We know that the $^{207}\text{Pb}/^{204}\text{Pb}$ and $^{206}\text{Pb}/^{204}\text{Pb}$ ratios provide information about the time-integrated U/Pb ratio, or μ , and $^{208}\text{Pb}/^{204}\text{Pb}$ provides information about time-integrated Th/Pb. The Pb isotope system can also provide information about the time-integrated Th/U ratio, or κ . This is done as follows. We can write two equations:

$$^{208}\text{Pb}^* = ^{232}\text{Th}(e^{\lambda_{232}t} - 1) \quad (6.4)$$

$$\text{and} \quad ^{206}\text{Pb}^* = ^{238}\text{U}(e^{\lambda_{238}t} - 1) \quad (6.5)$$

where, as usual, the asterisks denotes the radiogenic component. Dividing 6.4 by 6.5, we obtain:

$$\frac{^{208}\text{Pb}^*}{^{206}\text{Pb}^*} = \frac{^{232}\text{Th}}{^{238}\text{U}} = \kappa \frac{(e^{\lambda_{232}t} - 1)}{(e^{\lambda_{238}t} - 1)} \quad (6.6)$$

Thus, the ratio of radiogenic ^{208}Pb to radiogenic ^{206}Pb is proportional to the time-integrated value of κ . This ratio may be computed as:

$$\frac{^{208}\text{Pb}^*}{^{206}\text{Pb}^*} = \frac{^{208}\text{Pb}/^{204}\text{Pb} - (^{208}\text{Pb}/^{204}\text{Pb})_i}{^{206}\text{Pb}/^{204}\text{Pb} - (^{206}\text{Pb}/^{204}\text{Pb})_i} \quad (6.7)$$

where the subscript i denotes the initial ratio. By substituting a value for time in Eqn. 6.6, and picking appropriate initial values for Eqn. 6.7, we can calculate the time-integrated value of κ over that time. For example, picking $t = 4.56$ Ga and initial ratios equal to Nantan, we calculate the time-averaged κ over the past 4.56 Ga.

Now let's see how $^{208}\text{Pb}^*/^{206}\text{Pb}^*$, and hence κ relates to other isotope ratios, and hence other parent-daughter ratios. Figure 6.9 shows ϵ_{Nd} plotted against $^{208}\text{Pb}^*/^{206}\text{Pb}^*$. We can see that the two are reasonably well correlated, implying the fractionations of Sm from Nd and U from Th in the mantle have been closely related. From this, we conclude that the lack of correlation of “first-order” Pb isotope ratios with Sr, Nd, and Hf isotope ratios is due to “anomalous” behavior of Pb.

We have seen that there are systematic differences in isotopic composition between MORB and OIB. Thus, there are at least two major reservoirs in the mantle – although

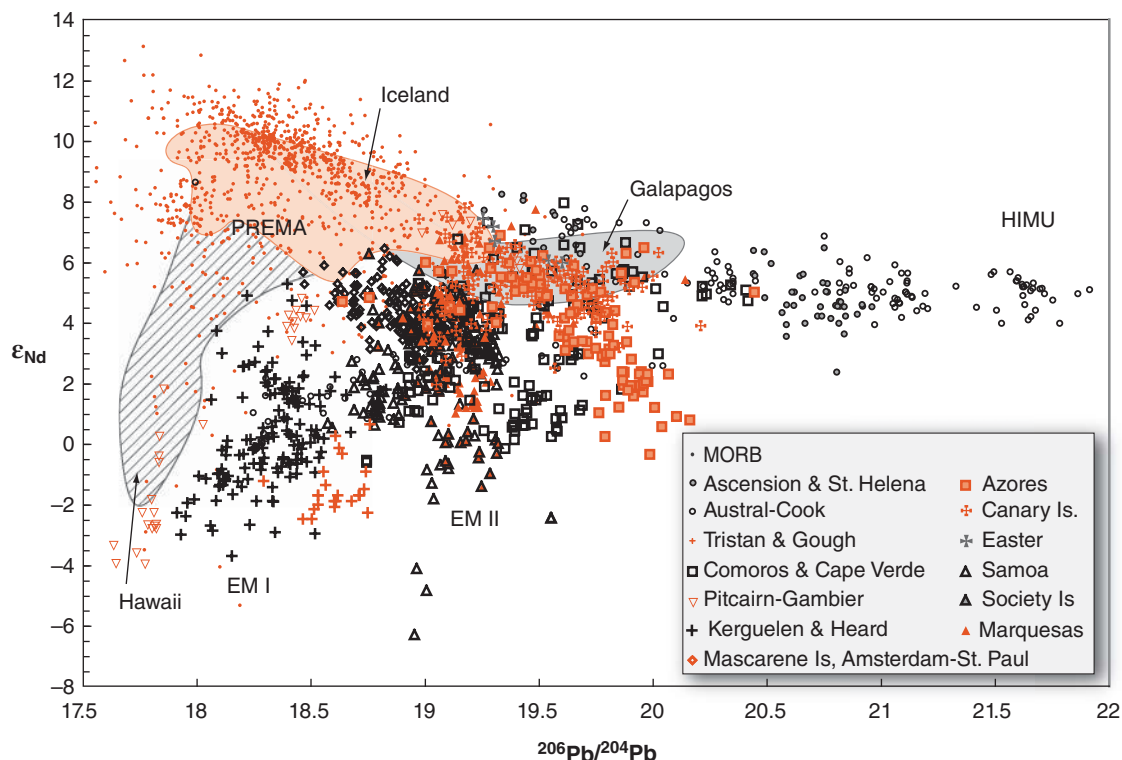


Figure 6.8 ϵ_{Nd} versus $^{206}\text{Pb}/^{204}\text{Pb}$ ratios of the suboceanic mantle as sampled by oceanic basalts.

deducing the physical relationship between these reservoirs is more problematic. The conventional interpretation is that MORB are derived from the uppermost mantle, which we can see is the most depleted of the reservoirs sampled by oceanic volcanism. Oceanic islands are thought to be surface manifestations of mantle plumes, which rise from, and therefore “sample,” the deeper mantle. A standard interpretation would, thus, be of a layered mantle. However, this interpretation encounters the difficulty that there is little or no geophysical evidence for a layered mantle. Seismic tomography, in particular, has imaged subducted oceanic lithosphere extending to near the core-mantle boundary, suggesting free communication between deep and shallow mantle. Furthermore, there is no convincing evidence of reflections or seismic velocity discontinuities that would be expected from a boundary between distinct and isolated mantle layers, with the possible exception of the D” region occupying the lowermost 200 km of the mantle. The large slow-shear wave velocity (LLSVPs) mentioned in Chapter 5,

although not layers, do represent possibly distinct mantle reservoirs. The magma flux of mantle plumes is, however, small compared to the magmatic flux at mid-ocean ridges. Thus the volume required of a plume reservoir could be quite small, perhaps no bigger than the seismically distinct D” layer or the LLSVPs.

The idea of early enriched and depleted reservoirs in the mantle, derived from the non-chondritic nature of the terrestrial $^{142}\text{Nd}/^{144}\text{Nd}$ ratio, encounters similar problems. The hypothesis of Boyet and Carlson (2005) effectively requires that the early-enriched reservoir remain isolated, not just for a couple of billion years, but throughout Earth’s history. As we noted in the previous chapter, such a reservoir would contain a significant fraction of the Earth’s radiogenic heat production, and it seems particularly unlikely that such an energy-rich reservoir would remain isolated. The difficulty in associating “reservoirs” deduced from isotope geochemistry with physical features in the mantle remains one of the most pressing

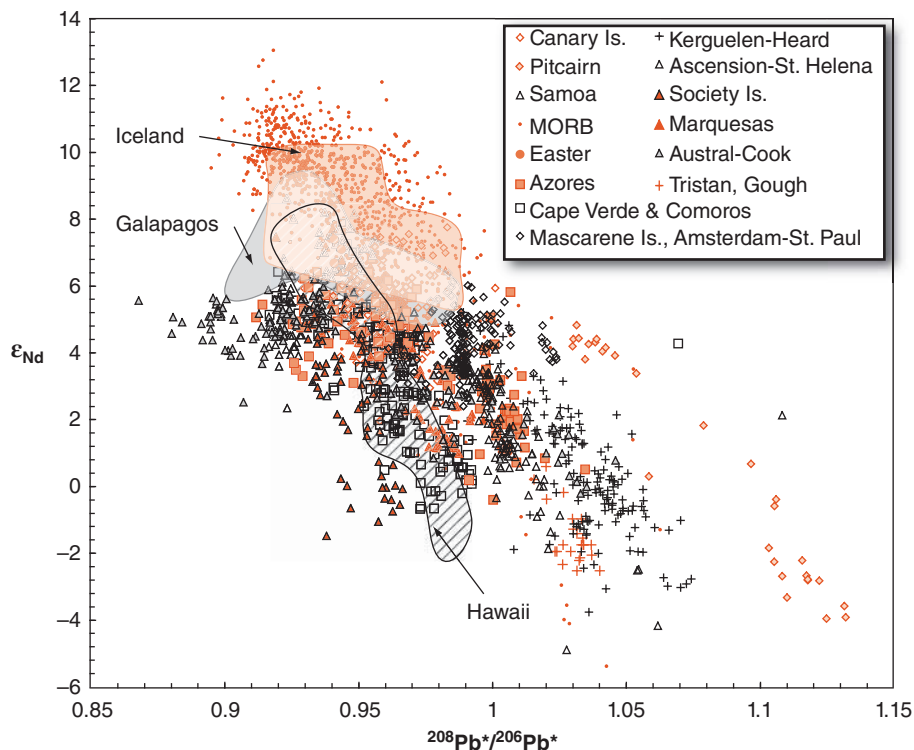


Figure 6.9 ϵ_{Nd} versus $^{208}\text{Pb}^*/^{206}\text{Pb}^*$ ratios of the suboceanic mantle as sampled by oceanic basalts.

problems in understanding the Earth's deep interior, although both D" and the LLSVPs are possibilities.

Most of the geochemistry of the MORB source can be described in terms of depletion in incompatible elements due to partial melting and removal of the melt. But how are we to interpret the OIB data? There are a number of possible interpretations. One of the earliest was OIB sources were mixtures of lower *primitive* mantle, as we defined it earlier, and upper depleted mantle. Such an interpretation does not explain those OIB with negative ϵ_{Hf} and ϵ_{Nd} , and it is completely at odds with the Pb data. If this interpretation were correct, OIB should lie between MORB and the Geochron, but they clearly do not. An interpretation that OIB sources are simply less depleted than the MORB source also does not account for those OIB with negative ϵ_{Hf} and ϵ_{Nd} . A final possibility is that OIB sources are depleted mantle that has experienced some incompatible element re-enrichment. These alternative hypotheses are not mutually exclusive, all may

have affected all OIB reservoirs, or each of the alternatives may exclusively account for a portion of OIB sources. Our next step is to consider the OIB data and seek any regularities in it that might suggest a process or processes to explain their isotopic compositions. Before we do so, however, let's attempt to estimate the fraction of the mantle occupied by the depleted MORB-source reservoir.

6.3 BALANCING DEPLETED MANTLE AND CRUST

The crust of the Earth is enriched in incompatible elements. This is true of both the oceanic and continental crust, although the continental crust is much more incompatible element-enriched than the oceanic crust. This is entirely consistent with our hypothesis that the crust was created through partial melting of the mantle. We can then ask, from what fraction of the mantle have these incompatible elements been extracted to account for

their abundance in the crust? Since the ocean crust is ephemeral, on average only 60 million years old, let's ignore it for the moment and just focus on continental crust. We have seen that MORB have "depleted" Nd, Sr, and Hf isotopic compositions – let's assume that the MORB source is residual mantle remaining after extraction of the continental crust. How much undepleted mantle would remain?

This is essentially a problem mass balance among a number of reservoirs, so following DePaolo (1980) we begin by writing a series of mass balance equations. The first is mass of the reservoirs:

$$\sum_j M_j = 1 \quad (6.8)$$

where M_j is the mass of reservoir j as a fraction of the total mass of the system, in this case the silicate Earth. We can also write a mass balance equation for any element i as:

$$\sum_j M_j C_j^i = C_0^i \quad (6.9)$$

where C_0^i is the concentration of i in the silicate Earth.

For an isotope ratio, R , of element i , or for an elemental ratio of which element i is the denominator, the mass balance equation is:

$$\sum_j M_j C_j^i R_j^i = C_0^i R_0^i \quad (6.10)$$

Our problem assumes the existence of three reservoirs: the continental crust, the mantle depleted by crust formation, and the undepleted, or primitive, mantle (we explicitly ignore any enriched mantle reservoirs at this point). These mass balance equations can be combined to solve for the mass ratio of continental crust to depleted mantle:

$$\frac{M_{DM}}{M_{CC}} = \frac{C_{CC}^i (R_{CC}^i - R_{DM}^i)}{C_0^i (R_0^i - R_{DM}^i)} - 1 \quad (6.11)$$

where the subscripts DM and CC refer to depleted mantle and continental crust, respectively. A number of solutions to the mass balance equations are possible, but we choose this form because it does not contain the concentration term for the depleted mantle. We

can judge the isotopic composition of mantle sources because the magmas they produce have the same isotopic composition, but this is not true of elemental concentrations. Once we have solved for the mass of depleted mantle, however, it is straightforward to solve for the depleted mantle concentration term:

$$C_{DM}^i = \frac{C_0^i (M_{DM} + M_{CC}) - M_{CC} C_{CC}^i}{M_{DM}} \quad (6.12)$$

Another difficulty arises with the isotopic composition of the continental crust, which is not well known. On the other hand, there are a number of estimates of elemental composition of the continental crust based on compilations of data, as well as on the age of the crust. With some assumptions, however, we can combine the information that we do have to arrive at an estimate of the volume of mantle depleted by crust formation.

The Nd isotope system is perhaps best suited for this question since $^{142}\text{Nd}/^{144}\text{Nd}$ ratios constrain the Nd isotopic composition of the Earth and, being a refractory lithophile element, its concentration in the bulk silicate Earth is also constrained (though not precisely). The Nd concentration and the Sm/Nd ratio of the continental crust are also better constrained than many other elements. The Sm/Nd ratio and $^{143}\text{Nd}/^{144}\text{Nd}$ of the crust are related through isotopic evolution, specifically:

$$\begin{aligned} ^{143}\text{Nd}/^{144}\text{Nd} &= (^{143}\text{Nd}/^{144}\text{Nd})_0 \\ &\quad + ^{147}\text{Sm}/^{144}\text{Nd}(e^{\lambda t} - 1) \end{aligned} \quad (6.13)$$

Because the half-life of ^{147}Sm is long compared to the age of the Earth and because we do not need the level of precision necessary for geochronology, we can linearize this equation as:

$$\begin{aligned} ^{143}\text{Nd}/^{144}\text{Nd} & \\ &= ^{143}\text{Nd}/^{144}\text{Nd}_0 + ^{147}\text{Sm}/^{144}\text{Nd} \lambda t \end{aligned} \quad (6.14)$$

Let's assume for simplicity that the some fraction of silicate Earth differentiated in a single event into a continental crust and depleted mantle at some time T . This is certainly not

the case, as we shall see, but because of the linearity of the Eqn. 6, even if the crust formed through similar events over a range of times, our approach is still valid if T is the average age of the crust. At time T , the continental crust and depleted mantle both had the same isotopic composition as undepleted mantle; that is, the composition of the undepleted mantle becomes the initial ratio in versions of 6.13 written for depleted mantle and continental crust. For the continental crust:

$$(^{143}\text{Nd}/^{144}\text{Nd})_{CC} = (^{143}\text{Nd}/^{144}\text{Nd})_{PM}^T + (^{147}\text{Sm}/^{144}\text{Nd})_{CC}\lambda T \quad (6.15)$$

where the superscript T denotes the value at time T . We can calculate that value from the present-day $^{143}\text{Nd}/^{144}\text{Nd}$ and $^{147}\text{Sm}/^{144}\text{Nd}$ of primitive mantle. Substituting, we have:

$$(^{143}\text{Nd}/^{144}\text{Nd})_{CC} = (^{143}\text{Nd}/^{144}\text{Nd})_{PM} + [(^{147}\text{Sm}/^{144}\text{Nd})_{CC} - (^{147}\text{Sm}/^{144}\text{Nd})_{PM}]\lambda T \quad (6.16)$$

The value thus calculated can then be used in Eqn. 6.11 to calculate the mass fraction of depleted mantle.

Now let's assign some values to these equations. The mass of the continental crust as a fraction of the mass of the silicate Earth, M_{CC} , is about 0.0055. For the $^{143}\text{Nd}/^{144}\text{Nd}$ value of the depleted mantle, we'll choose 0.51310 (equal to the median value for MORB listed in Table 11.05, $\epsilon_{\text{Nd}} \approx +9$). Based on assessments of the composition of continental crust, a good estimate for the $^{147}\text{Sm}/^{144}\text{Nd}$ ratio of the continental crust is 0.123. We can use these values to calculate the mass of depleted mantle as a fraction of the silicate Earth as a function of the other parameters in Eqn. 6.11, namely the ratio of Nd concentration in the crust to primitive mantle, C_{CC}/C_0 the average age of the continents, T , and the $^{143}\text{Nd}/^{144}\text{Nd}$ of the silicate Earth (expressed in epsilon units). Figure 6.10 shows the results. A good estimate of C_{CC}/C_{PM} is about 19, but there is considerable uncertainty. A good estimate of T is about 2 Ga, but there is easily 10% uncertainty in this value. If the Sm/Nd ratio is chondritic, Figure 6.10 suggests that the depleted mantle constitutes 40% or less, and more likely only

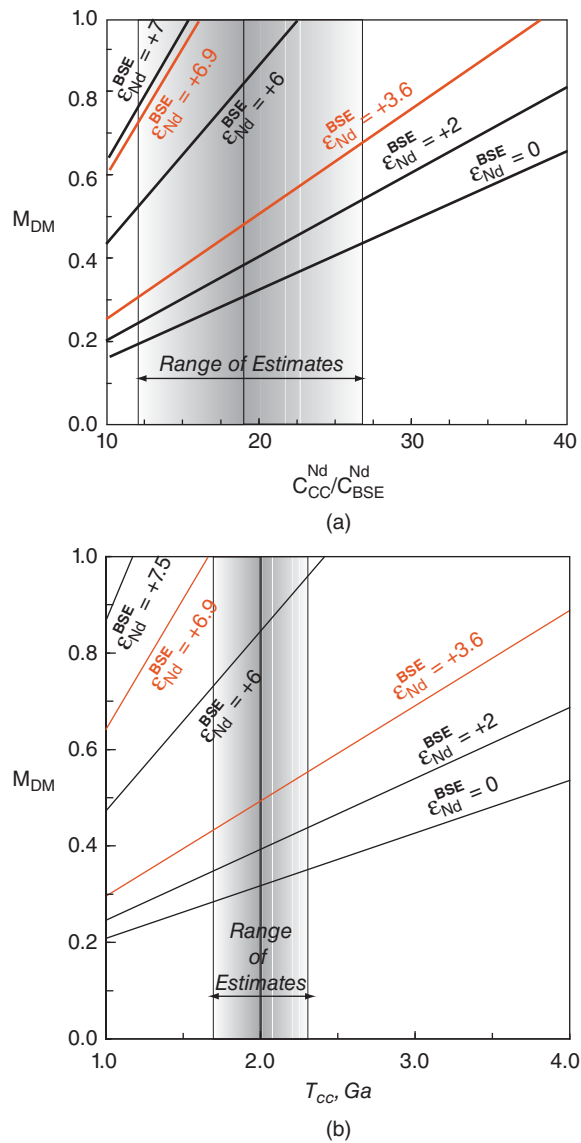


Figure 6.10 Mass fraction of the depleted mantle (DMM) calculated from Eqn. 6.11. Top graph shows this for a variety of values of ϵ_{Nd} for the silicate Earth and a range of C_{CC}/C_{PM} assuming an average age of the continents of 2 Ga. Lower graph shows the same thing for $C_{CC}/C_{PM} = 19$ and a range for the average age of the continents. (Source: White (2013). Reproduced with permission of John Wiley & Sons.)

about 25% of the mantle. That result tended to favor two-layer convection models, and implied only the mantle above the 660 km discontinuity was involved in crust production. However, as we have seen, the $^{142}\text{Nd}/^{144}\text{Nd}$ of

terrestrial materials suggests the Sm/Nd ratio is non-chondritic. If the terrestrial Sm/Nd ratio is 3% greater than chondritic, then the ϵ_{Nd} value of the Earth is +3.6 and the depleted mantle constitutes 40–60% of the mantle. If the Sm/Nd ratio of the Earth is 6% greater than chondritic, as Caro and Bourdon (2010) argue, then the ϵ_{Nd} of the Earth is +6.9, then the mantle depleted by crust extraction constitutes at least 70% of the entire mantle and possibly all of it. We assumed that there are no incompatible-enriched reservoirs in the mantle, which is clearly not the case. The existence of such reservoirs, as manifested by OIB with negative ϵ_{Nd} and ϵ_{Hf} , means that our estimates of the volume of depleted mantle must be minimum values. Although we don't know with certainty, the volumes of such incompatible-enriched reservoirs in the mantle is probably fairly small, so our estimates are likely not too far off.

This is quite a different picture of the mantle from the one that has prevailed for the last 30 years or so derived from assumption that the Earth has chondritic Sm/Nd and therefore $\epsilon_{\text{Nd}} = 0$. Mass balance calculations such as those of Jacobsen and Wasserburg (1979), O'Nions et al. (1979), and DePaolo (1980) concluded that the mass of the depleted mantle was only 25–50% of the total mass of the mantle, and therefore that a large “primitive mantle” reservoir existed. The lower end of this range corresponds to the mass fraction of mantle above the 660 km seismic discontinuity. This coincidence led to models of the mantle in which a depleted reservoir occupied the upper mantle, the region above the 660 km discontinuity, and the region below it, the lower mantle, consisted of primitive mantle. Maintaining two distinct reservoirs for the age of the Earth in turn implied that convection in the mantle was layered and that the 660 km discontinuity represented a boundary to mass transport. Eventually, however, new evidence from other branches of earth science raised questions about this model. Experimental studies revealed that increase in seismic velocity at 660 km depth resulted from a phase change resulting from a fundamental change in silicate structure, and that while the phase change might retard mass transport across the boundary, it probably did not prohibit it. The development of seismic

tomography in the 1990s confirmed that subducting lithosphere did, at least sometimes, pass through the 660 km discontinuity into the lower mantle, and in some cases could be traced nearly to the core-mantle boundary. Thus, isotope geochemistry, which seemed to support two-layered convection in the mantle, was at odds with geophysics and mineral physics, which favored whole mantle convection. This conflict is resolved if the Earth is non-chondritic and has a high ϵ_{Nd} . Any surviving “primitive mantle” reservoir would be small; most of the mantle likely consists of the kind of depleted mantle that produces MORB. This accords with the observation that no mantle or mantle-derived materials having $\epsilon_{\text{Nd}} = 0$ and other chemical and isotopic characteristics expected of primitive mantle have been identified.

A different view of the mantle was taken in papers by Galer and O’Nions (1985) and White et al. (1993). The models we have discussed thus far assume that isotope ratios in mantle reservoirs reflect the time-integrated values of parent-daughter ratios in those reservoirs. Indeed, we devoted some time to the concept of time-integrated parent-daughter ratios discussed at the beginning of this chapter. Wasn’t this, after all, what Gast said, that (among other things) an isotope ratio reflects the *time-integrated* parent-daughter ratio?

Indeed, what did Gast say? He said,

The isotopic composition of a particular sample of strontium ... may be the result of time spent in a number of such environments. In any case, the isotopic composition is the time-integrated result of the Rb/Sr ratios in all past such environments.

If, for example, a sample of Sr from the depleted upper mantle (we’ll adopt the acronym DUM⁴ for this reservoir) had spent the past 4.55 Ga in that reservoir, its isotopic composition should indeed reflect the time-integrated Rb/Sr in that reservoir. But suppose that sample of Sr had spent only the last few hundred million years in the DUM? Its isotopic composition will be more of a reflection of the Rb/Sr ratios in the previous environments than in DUM. This is exactly the point made by Galer and O’Nions (1985).

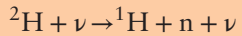
Geoneutrinos, heat production, and composition of the Earth

In addition to their importance in geochronology, U, Th, and K are also important sources of energy in the Earth. Indeed, except for residual heat left over from accretion of the Earth, radioactive decay is the *only* source of energy to drive processes such as mantle convection, which in turn drives plate tectonics, volcanism, faulting, folding, and mountain building. Decay of potassium presently accounts for ~19% of radioactive heat production, thorium 42%, and uranium 39%. To know how much heat the Earth is producing, we need to know the concentrations of these elements. Knowing the concentrations of U and Th is important for another reason: these elements are refractory lithophile elements, a group of elements whose relative concentrations in chondritic meteorites vary little. Many models of the composition of the Earth (e.g., McDonough and Sun, 1995; Palme and O'Neill, 2003) are built from the assumption that the relative concentrations of these elements in the Earth is the same as in chondrites. Independently determining the concentrations of U and Th thus provides a test of these models (Bellini et al., 2013a).

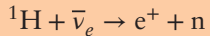
As we found in Chapter 1, β^+ -decay also produces neutrinos. β^+ decay produces an electron neutrino, ν_e , as does electron capture, while β^- decay produces an electron antineutrino, $\bar{\nu}_e$. Six electron antineutrinos are produced in the decay of ^{238}U to ^{206}Pb , while four are produced in both the decay of ^{235}U to ^{207}Pb and of ^{232}Th to ^{208}Pb . Most ^{40}K decays to ^{40}Ca with the production of an electron antineutrino while roughly 10% decays to ^{40}Ar and produce an electron neutrino. Assuming the U, Th, and K terrestrial concentrations of McDonough and Sun (1995), the Earth produces something like 5.5×10^{25} *geoneutrinos* per second. If we could detect those geoneutrinos and determine their rate of production, we could determine the concentrations of radioactive elements in the Earth.

That's easier said than done. Neutrinos, having no electric charge and with virtually no mass, interact so weakly with matter that essentially all pass through the Earth unnoticed. Indeed, Wolfgang Pauli, having proposed the existence of the neutrino to solve the beta decay spin and energy conservation conundrums (Chapter 1) lamented. "I have done a terrible thing, I have postulated a particle that cannot be detected." To make matters worse, neutrinos are also produced by the p-p and other fusion processes in stars, including the Sun. Something like 7.7×10^{28} solar neutrinos pass through the Earth every second. Neutrinos are also produced by cosmic ray interactions at the surface of the Earth and in the atmosphere and are produced in enormous numbers in supernovae and other extreme environments in the cosmos. Making things even more complicated is the ability of neutrinos to oscillate between three flavors: electron, tau, and muon.

There is, however, a very small probability of a neutrino interacting with matter through the weak nuclear force, which provides an opportunity for their detection. One such reaction is the so-called *neutral current reaction*, in which the neutrino dissociates the deuterium and continues on with somewhat less energy:



The reaction can be detected by the gamma radiation given off when the neutron is captured by another nucleus. All flavors of neutrinos participate in this reaction. Another interaction is the so-called *inverse beta decay* reaction:



Only electron antineutrinos participate in this reaction.

There are a number of experiments around the world actively detecting neutrinos, but at present only two of these, KamLAND in Japan and Borexino in Italy, are detecting geoneutrinos. In addition, the SNO+ detector in Sudbury, Ontario, should come on-line in 2014. These detectors, located deep underground to shield against cosmic rays, are designed to detect the flash of energy resulting from the almost instantaneous annihilation of the positron produced by the above inverse beta, reaction the energy being approximately equal to the energy equivalent of the mass of the positron-electron pair (~1.02 MeV) plus most of the kinetic energy of the neutrino; hence energy of the neutrino can be determined from the energy this radiation. A small fraction of the energy is carried off as kinetic energy by the neutron, which is subsequently captured by a proton to form deuterium. The latter

reaction produces a 2.2 MeV γ -ray. Since the neutron must lose some of its kinetic energy before being captured, the neutron capture typically follows the positron annihilation by $\sim 200\text{ }\mu\text{s}$, during which time the neutron has moved only about a meter. This double burst of energy in a small volume provides a nearly unambiguous signal of the inverse beta reaction. The detectors consist of large volumes of transparent hydrocarbon fluid spiked with wavelength shifting organic compounds (scintillators) and surrounded by large numbers of photomultiplier tubes. When gamma rays are produced in these reactions, they cause the liquid scintillator to produce a pulse of light that is then detected by the photomultiplier tubes.

There are some limitations and complications:

First, only neutrinos with energies above 1.8 MeV can produce inverse beta decay. Unfortunately, the maximum neutrino energy of ^{40}K decay is only 1.3 MeV and all neutrinos emitted in the decay chain of ^{235}U are also below this energy threshold. Thus the method is limited to detecting neutrinos from the ^{238}U and ^{232}Th decay chain, and less than 10% of those exceed the 1.8 MeV threshold.

Second, the flux of geoneutrinos of appropriate energy at the surface of the Earth is of the order of $10^6\text{ cm}^{-2}\text{ sec}^{-1}$ and the reaction cross section is $\sim 10^{-44}\text{ cm}^2$ so a large numbers of protons are necessary to provide useful detection rates. One thousand tons of detector fluid (whose composition is approximately CH_2) contains $\sim 10^{32}$ hydrogens and results in a geoneutrino detection rate of ~ 10 geoneutrinos per year assuming 100% detector efficiency (Dye, 2012). The KamLAND detector employs 1000 tons of liquid scintillator surrounded by 1879 large photomultiplier tubes (Figure 6.11)

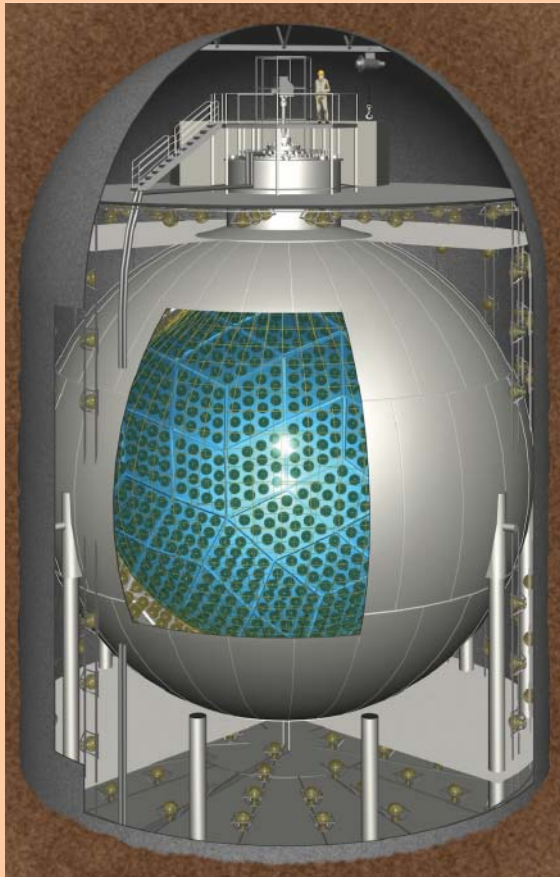


Figure 6.11 A 3D view of the KamLAND neutrino detector. (Source: Reproduced with permission of Lawrence Berkeley National Laboratory.)

and Borexino employs 300 tons and 1800 photomultiplier tubes. SNO+ will employ 780 tons of fluid and 9500 photomultiplier tubes.

Third, nuclear reactors produce large fluxes of electron antineutrinos, the energy spectrum of which overlaps with the geoneutrino spectrum.

Finally, because U and Th are concentrated in the continental crust, much of the detected neutrino flux comes from the local region; hence a correction based on local geology must be made in estimating the total geoneutrino flux and the terrestrial U and Th inventory (Huang et al., 2013; Šrámek et al., 2013).

The Borexino detector captured 14.3 ± 4.4 geoneutrinos over 1353 days of operation (up to August, 2012), from which they estimate a neutrino flux of $4.4 \pm 0.7 \times 10^6 \text{ cm}^{-2} \text{ sec}^{-1}$ (Bellini et al., 2013b) KamLAND captured 116 ± 28 between 2002 and 2012, from which they calculate a neutrino flux of $3.4 \pm 0.8 \times 10^6 \text{ cm}^{-2} \text{ sec}^{-1}$ (Gando et al., 2013). After correcting for the neutrino energy spectrum, flavor oscillation and local geology, the estimated Borexino flux corresponds to a U and Th concentrations of 22 ± 4 and 86 ± 14 ppb, respectively, in good agreement with estimates of McDonough and Sun (1995) and Palme and O'Neill (2003). The lower flux estimated by the KamLAND experiment would correspond to somewhat lower U and Th concentrations of 15 ± 4 and 60 ± 14 ppb, respectively. These are consistent with U and Th concentrations predicted by the collisional erosion model of O'Neill and Palme (2008). Uncertainties in two estimated fluxes overlap, so both compositional models remain possible. Both estimates, however, imply total radioactive heat production in the Earth of between 15 and 27 terawatts (TW), which is substantially less than heat loss, which is estimated at 46 TW. Thus, the ratio of terrestrial heat production to heat loss, known as the Urey ratio, is most likely less than 0.5 and less than the value assumed in many geodynamic models.

The time integrated Th/U ratio is recorded by the $^{208}\text{Pb}^*/^{206}\text{Pb}^*$ ratio. Galer and O'Nions (1985) found that the average $^{208}\text{Pb}^*/^{206}\text{Pb}^*$ in MORB corresponded to a time-integrated Th/U ratio of about 3.75. The chondritic Th/U ratio, according to several compilations, is about 3.9. Since Th and U are both refractory elements, the ratio of the bulk Earth should be similar to this as well. According to the compilation made by Galer and O'Nions, κ in DUM, based on Th isotope ratios in MORB, is about 2.5. That the present ratio is lower than the chondritic one makes perfect sense because Th is more incompatible than U, so we would expect this ratio to be low in DUM. Assuming the upper mantle started out with a chondritic κ of 3.9 at 4.55 Ga, and has decreased through time to 2.5, the time-integrated ratio should be somewhere in between these two values. Indeed, it is. However, the time-integrated value of 3.75 is surprisingly close to the initial value. This would imply in a simple evolutionary model of the mantle that the depletion in Th relative to U must have occurred relatively recently. Indeed, as illustrated in Figure 6.12, this depletion must have occurred only 600 Ma ago. This is

a surprising result, and one that is inconsistent with other evidence. If the depleted mantle is the complimentary reservoir to the continental crust, time-integrated parent-daughter ratios should indicate a depletion age of about 2–2.5 Ga.

Galer and O'Nions (1985) concluded that something was very wrong with conventional views of the mantle. They suggested that Pb now in the upper mantle had not resided there for long, that it was ultimately derived from a lower mantle reservoir that had a primitive (i.e., chondritic) Th/U ratio. In other words, the upper mantle had not evolved simply by losing melt fractions to the continental crust, but was a completely open system, with fluxes into it as well as out of it. They argued that the apparent depletion time of 600 Ma was in reality simply the residence time⁵ of Pb in the upper mantle. Galer and O'Nions may have underestimated the value of κ in the Earth; it is very possible that the value for the bulk Earth is higher than 3.9, perhaps in the range of 4.0–4.2. However, this only extends the residence time to about 1–1.2 Ga, still much less than the average age of continents, so their point remains valid.

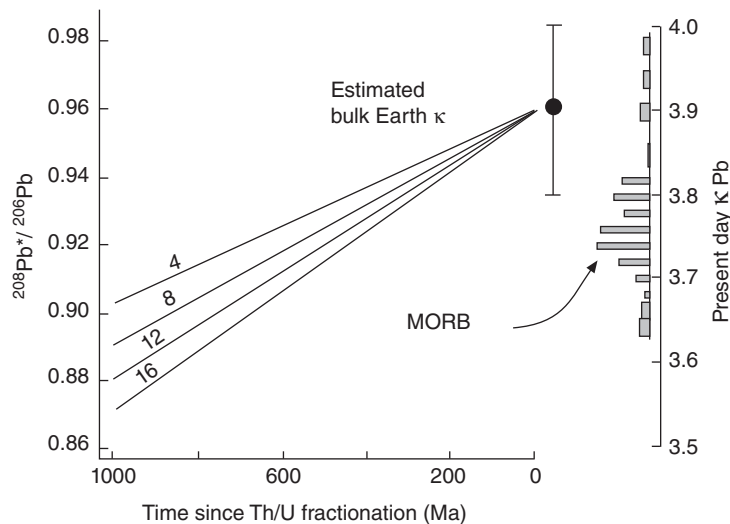


Figure 6.12 Evolution of $^{208}\text{Pb}^*/^{206}\text{Pb}^*$ is a system with $\text{Th}/\text{U} = 2.5$ assuming a starting Th/U of 3.9. κ_{Pb} is the time-integrated value of κ . Lines indicate values of μ ranging from 4–16. Histogram on the right shows the values of $\bar{\kappa}_{\text{Pb}}$ in MORB. Comparison of these values with the evolution lines suggests a residence time for Pb in the upper mantle of 600 ± 200 Ma. (Source: Galer and O’Nions (1985). Reproduced with permission of Nature Publishing Group.)

Since oceanic crust is continually extracted from the DUM, it either must become progressively more depleted in incompatible elements with time, or it must be resupplied. As we'll see, the evidence suggests it has not become progressively more depleted, so it must be resupplied. Thus the Galer and O’Nions view of an open system seems correct. Galer and O’Nions implicitly assumed that the DUM was resupplied by primitive mantle. This, however, is inconsistent with several observations, most notably the Pb isotope systematics in Figure 6.7. Mixing in of primitive mantle should pull the DUM toward the Geochron, which does not seem to be the case. White et al. (1993) and Phipps Morgan (2000) suggested it was resupplied by mantle plumes. As we'll discuss in the next section, mantle plumes rise into the upper mantle where they melt to produce oceanic island basalts. The melting residues plus and melt not extracted becomes part of the upper mantle, so there is a good physical basis for this idea. Mixing of oceanic island basalt-like material should pull the DUM away from the Geochron toward higher $^{206}\text{Pb}/^{204}\text{Pb}$ and $^{207}\text{Pb}/^{204}\text{Pb}$ composition. This can explain why MORB and OIB appear lie on the same array with overlapping compositions.

6.4 MANTLE PLUME RESERVOIRS

6.4.1 Mantle plumes and the mantle zoo

It is now widely, albeit not universally, accepted that chains of oceanic volcanoes form as lithosphere moves over melting zones or “hot spots” as Wilson (1963) called them, which are the near surface manifestation of “mantle plumes” (Morgan, 1971). Morgan envisioned mantle plumes as columns of hot mantle rising buoyantly and melting once they reach the upper hundred kilometers or so of mantle. Noting that they are roughly stationary relative to one and other,⁶ he proposed that they arise from the very deep mantle, perhaps the core-mantle boundary. Subsequent numerical and laboratory modeling confirmed at least the plausibility of Morgan’s plume model, and calculations of their “buoyancy flux,” which in turn relates to their advective heat flux, approximately matched the expected heat coming from the Earth’s core (e.g., Davies, 1988; Sleep, 1990). Later, seismic studies revealed anomalously slow seismic velocities beneath many of these hot spots that extend well into the deep mantle and the core-mantle boundary in some cases (Montelli, et al., 2004). Consequently,

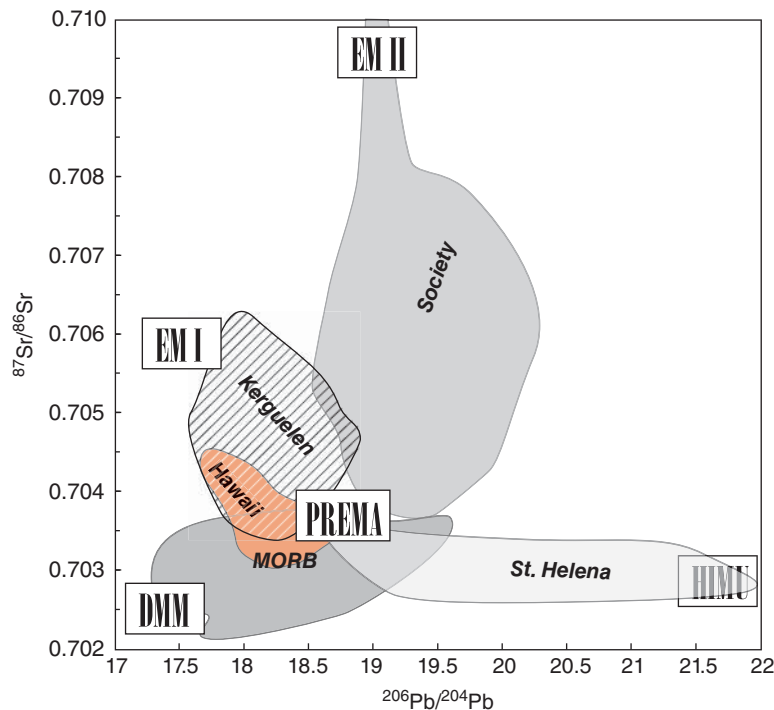


Figure 6.13 Five reservoir types of White (1985) and the components of Zindler and Hart (1986). They are essentially identical, except for Hawaii and PREMA (prevalent mantle). Other Zindler and Hart acronyms stand for high- μ (HIMU), enriched mantle I and II (EM I and EM II), and depleted MORB mantle (DMM).

we consider that oceanic islands sample geochemical reservoirs in deep mantle carried to the near surface by mantle plumes.

DePaolo and Wasserburg (1976) termed the linear correlation originally observed between Sr and Nd isotope ratios the “mantle array.” Even though it is now clear that mantle Sr and Nd isotope ratios do not always plot on the linear array, the term has survived, and is useful for reference. If we consider where individual oceanic islands or island chains plot on various isotope ratio plots, we can see that there are some systematic features. For example, several islands, including St. Helena Island in the Atlantic and the Austral Chain in the Pacific, plot on Figure 6.3 slightly below the main Sr-Nd mantle array with $^{87}\text{Sr}/^{86}\text{Sr}$ about 0.7029, which is well within the range of MORB, although slightly higher than the average. Basalts from these same islands also plot below the Hf-Nd isotope correlation (Figure 6.5). In addition, they have remarkably radiogenic Pb, with $^{206}\text{Pb}/^{204}\text{Pb} > 20$ (Figure 6.7 and 6.8). Based on observations such as these, White (1985) grouped oceanic

island basalts into five groups named MORB, *St. Helena*, *Kerguelen*, *Society*, and *Hawaii* shown in Figures 6.13 and 6.14 (A. Hofmann has called this the *mantle zoo*). It is reasonable to suppose that this reflects the existence of five reservoirs, or perhaps more accurately, five *types* of reservoirs, each type having followed a similar evolutionary path, within the mantle. Although this need not necessarily be the case, the idea has been accepted as a working hypothesis by mantle geochemists (although it is unclear exactly how many classes there are, some prefer 4 or 6).

6.4.2 The evolution of mantle geochemical reservoirs

The next question to ask is what processes have led to the distinct identities of these reservoirs. For the MORB reservoir, this question is relatively easy to answer: extraction of partial melts, with those melts forming the Earth’s crust. The remaining reservoirs are, at least for the most part, enriched in incompatible elements relative to primitive

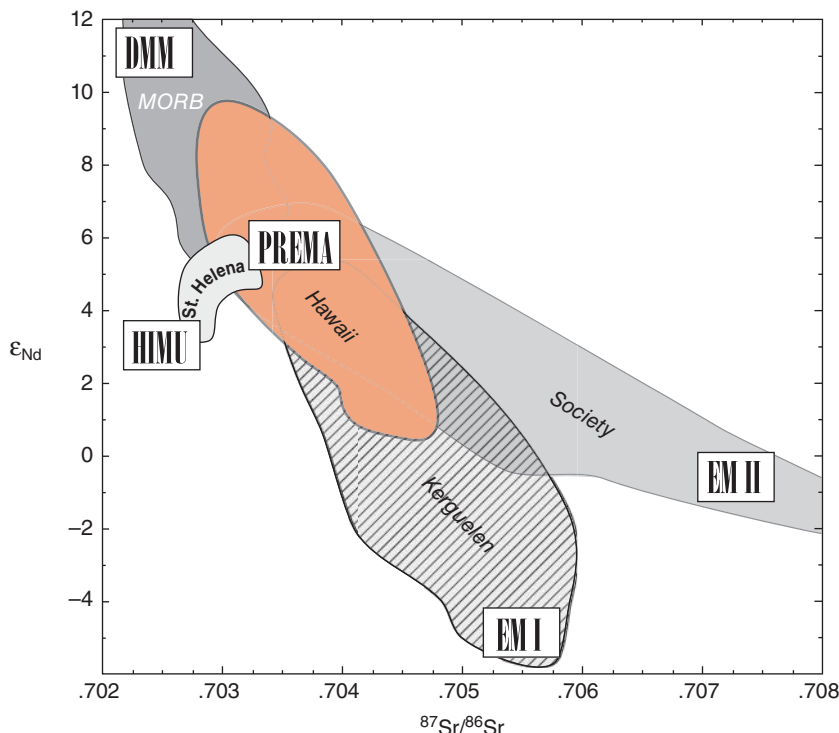


Figure 6.14 Five isotopic reservoirs of White (1985) and the components of Zindler and Hart (1986) in a plot of ϵ_{Nd} versus $^{87}\text{Sr}/^{86}\text{Sr}$.

mantle (or, equivalently, bulk silicate Earth). Differences in the major and compatible element chemistry between the MORB and mantle plume reservoirs are difficult to demonstrate (although there has been some suggestion that such differences exist; e.g., Hauri, 1996; Sobolev et al., 2005); the differences are mainly in incompatible elements and isotope ratios (the latter reflecting long term differences in parent-daughter ratios such as Rb/Sr and, consequently, also incompatible element enrichment). This suggests that melting is also involved in the genesis of mantle plume reservoirs. For the most part, melting in the Earth seems restricted to the upper few hundred kilometers of the mantle, and mostly within the upper 100 km: this is where temperatures can exceed the solidus temperature. Ultra-low s-wave velocities in some regions of the deepest mantle suggest melting may locally occur there as well. However, high-pressure melting experiments show that melting in the deep mantle produces elemental fractionations quite different from those in the upper mantle (e.g., Kato et al., 1988; Corrige et al., 2005). The incompatible enrichment

patterns in oceanic island basalts match those created by melting processes in the upper mantle. Thus, while mantle plumes sample deep mantle reservoirs, their geochemical characteristics were acquired in the upper mantle. There is wide agreement on this point.

We might also ask when these signatures were acquired. While no firm answer can be given, the overall slope of the data on $^{207}\text{Pb}/^{204}\text{Pb}$ – $^{206}\text{Pb}/^{204}\text{Pb}$. We must be careful not to attach too much age significance to this slope, which can arise in a variety of ways. With that caveat, we note that slope corresponds to an age of 1.5–2 billion years. This age is much older than, for example, the age of even the oldest oceanic crust, but much younger than the age of the Earth and comparable to, although slightly younger than, the average age of the continents. As we noted earlier, it most likely reflects an average age of many events rather than a single event. It is likely that mantle chemical heterogeneity has been created and destroyed throughout Earth's history.

Hofmann and White (1982) suggested mantle plumes obtain their unique geochemical

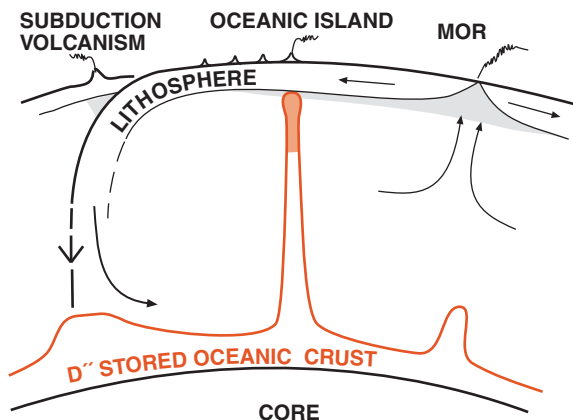


Figure 6.15 Cartoon illustrating the oceanic crustal recycling model of Hofmann and White (1982). Oceanic crust is transformed into eclogite and post-eclogite assemblages upon subduction. It separates from the less dense underlying lithosphere and sinks to the deep mantle where it accumulates. Eventually, it becomes sufficiently hot to form plumes that rise to the surface, producing oceanic island volcanism. (Source: Hofmann and White (1982). Reproduced with permission of Elsevier.)

signature through deep recycling of oceanic crust (Figure 6.15). Partial melting at mid-ocean ridges creates oceanic crust that is enriched in incompatible elements relative to its depleted mantle source. The oceanic crust is apparently inevitably subducted as virtually none is preserved at the surface, so it clearly is recycled back into the mantle. The question is, what becomes of it? Hofmann and White noted that once oceanic crust reaches depths of about 60 km it converts to eclogite, which is denser than peridotite. Because it is rich in Fe and garnet-forming components, it remains denser than peridotite at all greater depths (except, perhaps, near the 660 discontinuity due to the negative Clapeyron slope). Thus, it will sink to the base of the convecting region. If the mantle is chemically stratified, with a Fe-rich lower mantle, oceanic crust would sink to a thermal boundary layer at the 660 discontinuity. If the entire mantle convects as a single unit, that is if it is not chemically stratified, ocean crust will sink to base of the mantle. Hofmann and White originally suggested radioactive heating would ultimately cause it to become buoyant. However, heat

conducted into it from below, from either the lower mantle or the core, is likely a more important heat source. In any case, upon sufficient heating, it rises, melting near the surface to create intraplate volcanoes.

Sediment appears to be always subducted along with the igneous oceanic crust. This subducted sediment also potentially contributes to incompatible element enrichment of plumes. Varying amounts, types, and ages of subducted sediment may be responsible for some of the geochemical variety displayed by plumes. Since sediment is ultimately derived from the continents, recycling of oceanic crust, continental crust, mantle plumes, and oceanic island basalts may all be part of a grand geochemical cycle. Tectonic erosion of continental crust in subduction zones and delamination of continental crust may be alternative mechanisms for deep recycling of continental crust.

Because the major element chemistry of OIB is often similar to that of MORB, it seems unlikely plumes could be composed entirely of recycled oceanic crust. Presumably, they consist primarily of peridotite, with a subordinate fraction of oceanic crust. However, because the oceanic crust and sediment has much higher incompatible element concentrations than peridotite, it provides most of the isotopic and incompatible element “flavor” of plumes.

An alternative origin for mantle plumes was proposed by McKenzie and O’Nions (1983). They noted the common evidence for incompatible element enrichment in the subcontinental lithosphere, a consequence of a process called *mantle metasomatism*, which we will discuss in a subsequent section, and suggested this material may, because it is cold, occasionally founder and sink to the deep mantle. As in the case of the Hofmann and White model, it would be stored in a thermal boundary layer, heated, and rise in the form of mantle plumes. However, as we shall see in the next section, recent studies have shown that the Os isotope composition of the subcontinental lithosphere is quite distinctive, and quite different from that of mantle plumes. This suggests that “delaminated” subcontinental lithosphere does not contribute significantly to mantle plumes. Because mantle plumes come in several geochemical varieties, it is possible that both mechanisms operate. Indeed, other

as yet unknown processes may be involved as well.

Workman and Hart (2004) noted the mantle xenoliths from oceanic regions also show evidence of metasomatic enrichment and suggested that incompatible element-enriched oceanic lithosphere, which is inevitably subducted, might later rise as mantle plumes. It is hard to rule out this process, although it is hard to imagine that oceanic lithospheric enrichment is great enough and widespread enough to account for that seen in mantle plumes.

Foundering of lower continental crust (often mislabeled as “delamination”) provides a way of transferring incompatible element-enriched crustal material into the mantle. Lower crustal foundering occurs when continental crust is over-thickened in orogenies, such as the Himalayas and dense garnet-bearing lithologies form in the deep crust. The crust can then become denser than underlying mantle and sink (Kay and Kay, 1991), perhaps into the deep mantle where it is incorporated into mantle plume source regions. Lower crust can also be removed and carried into the mantle through the process of subduction erosion. In subduction zones where there is little sediment atop the oceanic crust, there is good geophysical evidence that the margin of the upper plate is being abraded and eroded by the subducting plate (e.g., von Huene et al., 1991). This material can be carried into the deep mantle where it may contribute to mantle plume sources. Paul et al. (2002) found they could model the evolution of Pb isotope ratios in the mantle only if lower crust as well as upper crust were recycled into it. Although not definitive, this certainly supports the idea foundering or subduction erosion of lower continental crust has been important in the chemical evolution of the Earth.

Can we associate some of these processes with specific reservoirs shown in Figures 6.14 and 6.15? White and Hofmann (1982) suggested that the Society group, termed enriched mantle 2 or EM II by Zindler and Hart (1986), was produced by subduction of oceanic crust and sediment. Subsequent evidence certainly points to recycling of oceanic crust and continent-derived sediment as the source of the EM II reservoir. Trace elements ratios, particularly the Pb/Ce ratio, can be

useful indicator of the presence of sediment for several reasons. First, the Pb/Ce ratio is comparatively uniform in MORB and many OIB. Second, the Pb/Ce ratio is an order of magnitude higher in sediments than in the mantle (typically, Pb/Ce is greater than 0.3 in sediments and <0.04 in MORB). Third, sediments have two orders of magnitude higher concentrations of Pb (typically 20 ppm or more) than the mantle (less than 0.05 ppm). Although some Pb is removed from sediment and oceanic crust during subduction, mass balance calculations indicate that the subducted package retains most of its Pb and its high Pb/Ce signature (Porter and White, 2009), so that addition of even small amounts of sediment to mantle shifts the Pb/Ce ratio. Finally, the near constancy of Pb/Ce in most basalts suggests this ratio is not significantly changed in by magmatic processes such as partial melting and fractional crystallization. The $^{207}\text{Pb}/^{204}\text{Pb}$ ratio is also a good indicator of a crustal component because, as we shall see in the next chapter, $^{207}\text{Pb}/^{204}\text{Pb}$ is consistently higher in the crust than in the mantle (whereas this is not true of $^{206}\text{Pb}/^{204}\text{Pb}$). Basalts from both the Society and Samoan Islands have Pb/Ce ratios well above the mantle background level. As Figure 6.16 shows, the relationship between $^{207}\text{Pb}/^{204}\text{Pb}$

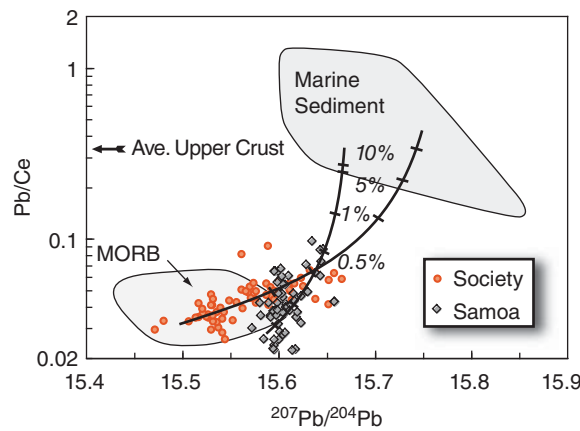


Figure 6.16 Pb/Ce and $^{207}\text{Pb}/^{204}\text{Pb}$ in basalts from the Society Island and Samoan Islands. Two calculated mixing lines between a MORB-like depleted mantle and sediment passes through the data. Data from White and Duncan (1996), Jackson et al. (2007) and the GEOROC database.

and Pb/Ce is consistent with mixing between recycled sediment and mantle. Extremely high $^{87}\text{Sr}/^{86}\text{Sr}$ (>0.72) and low ϵ_{Nd} (~ -7) values in some volcanics from the Samoan chain provide further strong evidence that the Society-like isotopic compositions (i.e., EM II compositions) reflect recycling of continental material, most likely through sediment subduction (Jackson et al., 2007).

There is broad consensus on the origin of the MORB and EM II mantle reservoirs, but little consensus on the remaining evolution of the remaining groups. The following discussion of the evolution of the remaining reservoirs is thus merely biased speculation.

White and Hofmann (1982) suggested EM I reservoir might be created by recycling of oceanic crust alone, but it is unclear whether oceanic crust is ever subducted without sediment. Porter and White (2009) found that no oceanic crust currently being subducting into the deep mantle that would evolve toward EM I compositions. Similarly, Chauvel et al. (2008) found that Hf-Nd isotopic systematics of the mantle array could not be generated by subduction and recycling of oceanic crust alone and that recycling of continental

material and sediments must also be involved. Others have suggested that the EM I reservoir is sourced in subcontinental lithosphere. Willbold and Stracke (2010) argued that the EM I component was produced by recycling of lower continental crust, either through subduction erosion or lower crustal floundering. They point out that while EM II basalts typically have Eu anomalies⁷ less than 1, while EM I basalts generally have Eu anomalies greater than 1. Eu anomalies arise because some fraction of Eu can be in the 2+ valence state and as such it partitions more readily into plagioclase. Because plagioclase can be present in the solid residue during partial melting of the continental crust, differentiation of the continental crust has led to an upper crust with a negative Eu anomaly and lower crust with a positive Eu anomaly. As can be seen in Figure 6.17, EM II basalts trend toward negative Eu anomalies and very high $^{87}\text{Sr}/^{86}\text{Sr}$, consistent with upper crustal compositions, while EM I trend toward positive EU anomalies and more moderate $^{87}\text{Sr}/^{86}\text{Sr}$ consistent with lower crustal compositions. The generally low $^{206}\text{Pb}/^{204}\text{Pb}$ of EM I compositions is also consistent with a lower continental

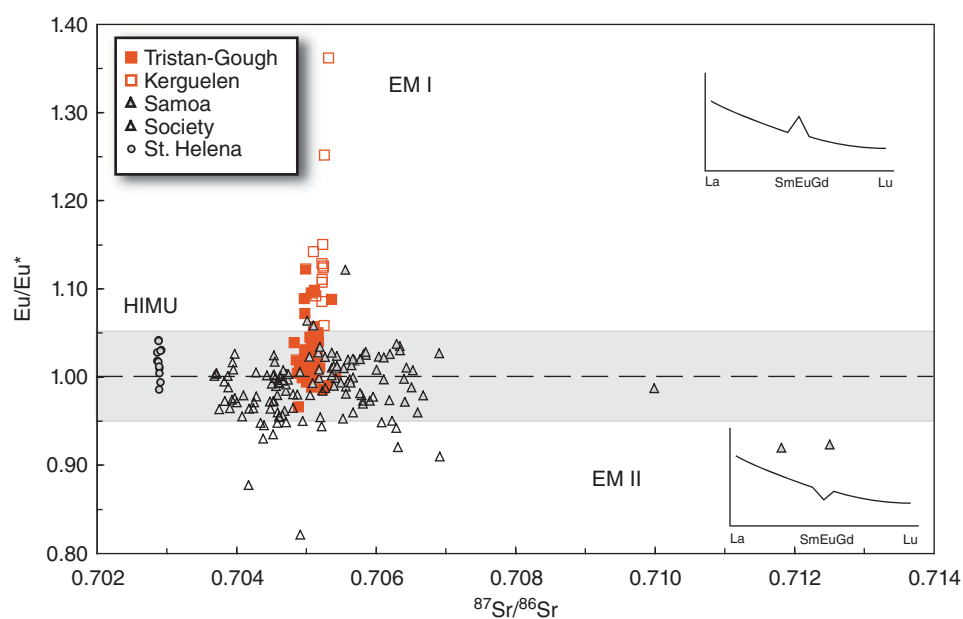


Figure 6.17 Eu/Eu* and $^{87}\text{Sr}/^{86}\text{Sr}$ in some oceanic island basalts. HIMU basalts have average Eu/Eu* ratios close to 1, EM I generally have Eu/Eu* > 1 and EM II generally have Eu/Eu* < 1 . Cartoon rare earth patterns illustrate positive and negative Eu anomalies. St. Helena, Tristan da Cunha, and Gough data from Willbold and Stracke (2010); remaining data from the GEOROC database.

crustal source as the lower crust typically has low μ and low $^{207}\text{Pb}/^{204}\text{Pb}$.

Many studies have suggested the St Helena reservoir type, whose most distinctive characteristic is high Pb isotope ratios, and which Zindler and Hart (1986) called HIMU (for high- μ), has also been produced by recycling of the oceanic crust. The basis for this argument is the effects of ridge-crest hydrothermal activity, which apparently removes Pb from the oceanic crust, but transfers seawater U (which is ultimately of continental crustal derivation) to the oceanic crust, effectively increasing its μ (Chauvel et al., 1992). However, Pb is extremely insoluble in seawater and most Pb removed from the oceanic crust precipitates in the immediate vicinity of hydrothermal vents, and that which does not is removed by particle absorption, with the particles then settling onto the oceanic crust and sediment. Enrichment of oceanic crust in U occurs because U, which is fairly abundant in seawater as the soluble oxianion UO_4^- , is reduced to insoluble U^{4+} in the hydrothermal systems. However, the deep oceans were reducing until at least the late Proterozoic, and consequently would have been U-poor. Thus U-enrichment of the oceanic crust is likely a process restricted to the last 500 to 1000 million years of Earth's history, whereas Pb isotopes suggest this reservoir is much older than that (Section 6.2.2). An alternative possibility is that the high- μ character is acquired as a consequence of Pb removal as oceanic crust and sediment is subducted beneath island arcs. Porter and White (2009) used a mass balance approach to determine the extent subduction zone processing affects parent-daughter ratios in subducting oceanic lithosphere. While Pb is removed and the U/Pb ratio increased by this process, the effect is generally small. They found that no modern residual subducted lithosphere would evolve to Sr-Nd-Pb isotopic compositions similar to either HIMU or EM I.

The HIMU reservoir characterizes only a couple of relatively small mantle plumes, so the mass of this reservoir may be quite small. This, as well as the well-defined end-member Pb and Sr isotopic compositions suggest it may be the product of a relatively rare event or events in Earth's history.

Hart et al. (1992) plotted oceanic basalt isotope data in three dimensions, with axes of $^{87}\text{Sr}/^{86}\text{Sr}$, $^{143}\text{Nd}/^{144}\text{Nd}$, and $^{206}\text{Pb}/^{204}\text{Pb}$

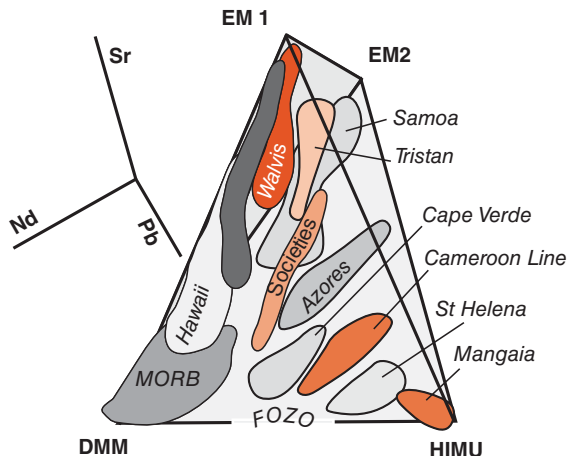


Figure 6.18 Three-dimensional plot of $^{87}\text{Sr}/^{86}\text{Sr}$, $^{143}\text{Nd}/^{144}\text{Nd}$, and $^{206}\text{Pb}/^{204}\text{Pb}$. Most oceanic basalt data plot within a tetrahedron defined by the composition of EM1, EMII, HIMU, and DMM components. Oceanic islands and island chains tend to form elongate isotopic arrays, many of which seem to point toward a focal zone (FOZO) at the base of the tetrahedron. (Source: Adapted from Hart et al. (1992).)

(Figure 6.18). Principal component analysis confirmed that 97.5% of the variance in the oceanic basalt isotope data could be accounted for by these ratios (leaving 2.5% to be accounted for by $^{207}\text{Pb}/^{204}\text{Pb}$, $^{208}\text{Pb}/^{204}\text{Pb}$, and $^{176}\text{Hf}/^{177}\text{Hf}$). They found that most of the data plotted within a tetrahedron defined by the hypothetical end members EM1, EM2, HIMU, and DMM. They also noticed that many arrays were elongated toward the base of this tetrahedron on the DMM-HIMU join. From this they concluded that in many, if not most cases, mantle plumes appear to mixing with a previously unidentified component, which they named "FOZO" (an acronym for Focal Zone), that has the approximate isotopic composition of $^{87}\text{Sr}/^{86}\text{Sr} = 0.7025$, $\epsilon_{\text{Nd}} = +9$, and $^{206}\text{Pb}/^{204}\text{Pb} = 21.5$. They suggested that FOZO is the isotopic composition of the lower mantle and that plumes rising from the core-mantle boundary entrain and mix with this lower mantle material. It is unclear, however, whether such a composition for the lower mantle can be fitted to reasonable isotopic mass balances for the Earth.

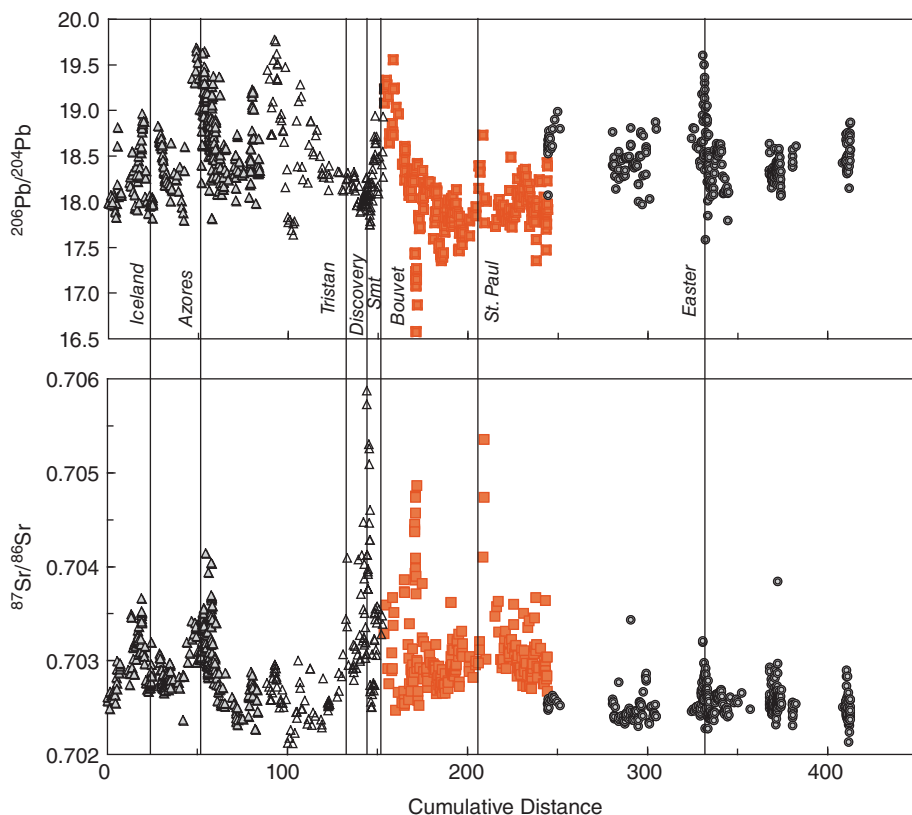


Figure 6.19 Variation of Sr and Pb isotope ratios with angular distance along the mid-ocean ridge system. The “0” point is the location of the northernmost sample site of the Gakkel Ridge at 85.64°N, 85.05°E. Filled triangles: N. Atlantic MORB, open triangles: S. Atlantic MORB, squares: Indian MORB, and circles: Pacific MORB. (Source: White and Klein (2013). Reproduced with permission of Elsevier.)

A rather similar idea was presented by Farley et al. (1992), who point out that this additional component, which they called “PHEM,” seems to be associated with high $^3\text{He}/^4\text{He}$. Hanan and Graham (1996) used Pb and He isotope ratios to deduce yet another potential *common* component of plumes, which they called “C.” The “C” composition of Hanan and Graham is similar to the PHEM of Farley et al. (1992) and may be just another name for the same thing. “C” and “PHEM” occur in the interior of the tetrahedron shown in Figure 6.19. Hanan and Graham (1996) argued that “C” is the principal component of plumes, the other components just add “flavor.” The “C” and PHEM compositions would have ϵ_{Nd} of about +5. This is fairly close the revised value for the bulk silicate Earth, or the observable part

of it, judging from the Earth’s $^{142}\text{Nd}/^{144}\text{Nd}$ (Section 6.2.1). This is also close to the modal (i.e., most common) value of ϵ_{Nd} for oceanic island basalts (Figure 6.4). That and the high $^3\text{He}/^4\text{He}$ ratios in this reservoir suggest it may be something approximating a mantle composition that has been minimally modified since either the Earth formed or it initially differentiated and may be quite abundant in the deep Earth. In other words, it might be something close to “primitive mantle.”

We should note that the existence of multiple reservoirs in the mantle does not necessarily invalidate the mass balance models discussed earlier if the mass of the various OIB reservoirs is small. Since the volume of OIB is small compared to MORB, this is certainly a possibility. Mass balance models also neglect the mass of the subcontinental

mantle lithosphere. Although significant parts of the subcontinental lithosphere appear highly incompatible element enriched, other parts appear to be extremely incompatible element depleted and it is probably not a significant reservoir of incompatible elements.

6.5 GEOGRAPHIC VARIATIONS IN MANTLE ISOTOPIC COMPOSITION

Can geographic variations in mantle chemistry be identified on a larger scale than that of individual volcanic island chains? The answer turns out to be yes. The first such variation observed was on the Mid-Atlantic Ridge by J.-G. Schilling and colleagues. Sr and Pb isotope ratios in MORB were observed to decrease with distance from Iceland and the Azores. Hart et al. (1973) and White et al. (1976) interpreted this as outflow from the Iceland and Azores mantle plumes mixing with upper mantle asthenosphere. Somehow, the rising mantle plume mixes with asthenosphere through which it ascends, with the effect on isotopic compositions being noticeable up to 1000 km from the center of the plume. Subsequent studies showed similar effects even when a ridge is located in proximity to a hot spot or mantle plume, including Easter Island, the Galapagos, and several of the islands in the South Atlantic and Indian Oceans (Schilling, 1985). These variations can be seen in Figure 6.19. Other variations along the ridge, however, do not appear to be directly related to mantle plumes.

Is there evidence for larger scale geochemical provinces in the mantle, comparable to say tectonic provinces of the continents? The answer is again yes. Perhaps the first such “province” to be identified was the Indian Ocean geochemical province. Data published as early as the early 1970s suggested MORB from the Indian Ocean were distinct from those of the Pacific and the Atlantic, having higher $^{87}\text{Sr}/^{86}\text{Sr}$ ratios. However, the scarcity and poor quality of data on Indian Ocean MORB left the issue in doubt for more than a decade. It was resolved with a flood of data on Indian Ocean MORB, beginning with a paper by Dupré and Allègre (1983). Dupré and Allègre found Indian Ocean MORB has higher $^{87}\text{Sr}/^{86}\text{Sr}$ ratios but lower $^{206}\text{Pb}/^{204}\text{Pb}$ ratios compared to MORB from

other oceans. They also have high $^{207}\text{Pb}/^{204}\text{Pb}$ and $^{208}\text{Pb}/^{204}\text{Pb}$ ratios for a given value of $^{206}\text{Pb}/^{204}\text{Pb}$ than other MORBs. This is can be seen in Figure 6.7. The Indian Ocean MORBs have low ϵ_{Nd} as well. Subsequent work has showed that isotopic distinctions exist between North and South Atlantic, and Pacific Ocean MORB as well. Pacific MORB have lower $^{87}\text{Sr}/^{86}\text{Sr}$ ratios for a given ϵ_{Nd} than do either group of Atlantic MORB, while high $^{208}\text{Pb}/^{204}\text{Pb}$ for a given $^{206}\text{Pb}/^{204}\text{Pb}$ and low ϵ_{Nd} and ϵ_{Hf} relative to $^{87}\text{Sr}/^{86}\text{Sr}$ distinguish S. Atlantic from N. Atlantic MORB (e.g., Meyzen et al., 2007; White and Klein, 2013).

Boundaries between these domains can be sharp or diffuse (Figure 6.19). The Indian-Pacific boundary is located at a small discontinuity of the Southeast Indian Ridge (SEIR) within the Australian-Antarctic Discordance and manifests a very sharp change in isotopic characteristics (Klein et al., 1988; Pyle et al., 1992). By contrast, the boundary between the South Atlantic and Indian domains, which occurs west of the Andrew Bain Fracture Zone (the Antarctic-Nubian-Somalian triple junction) located at 30°E on the Southwest Indian Ridge (SWIR), is gradual (Meyzen et al., 2007). The boundary between the North and South Atlantic provinces, located near 23°S, is also diffuse.

Hart (1984) noticed that oceanic basalts with high $^{207}\text{Pb}/^{204}\text{Pb}$ and $^{208}\text{Pb}/^{204}\text{Pb}$ ratios for a given value of $^{206}\text{Pb}/^{204}\text{Pb}$ come mainly from a belt centered at about 30°S. Hart named this feature the DUPAL anomaly (after Dupré and Allègre). He defined the DUPAL isotopic signature as having higher ΔSr ($\Delta\text{Sr} = [^{87}\text{Sr}/^{86}\text{Sr} - 0.7030] \times 10^4$) and high $\Delta 8/4$ and $\Delta 7/4$. The value of $\Delta 8/4$ and $\Delta 7/4$ are percent deviations from what Hart defined as the *Northern Hemisphere Regression Line*, regression lines through the $^{208}\text{Pb}/^{204}\text{Pb} - ^{206}\text{Pb}/^{204}\text{Pb}$ and $^{207}\text{Pb}/^{204}\text{Pb} - ^{206}\text{Pb}/^{204}$ arrays for northern hemisphere data:

$$\begin{aligned} \Delta 8/4 &= [^{208}\text{Pb}/^{204}\text{Pb} - ^{208}\text{Pb}/^{204}\text{Pb}_{\text{NHRL}}] \times 100 \\ \Delta 7/4 &= [^{207}\text{Pb}/^{204}\text{Pb} - ^{207}\text{Pb}/^{204}\text{Pb}_{\text{NHRL}}] \times 100 \end{aligned} \quad (6.17)$$

$$\begin{aligned} \Delta 8/4 &= [^{208}\text{Pb}/^{204}\text{Pb} - ^{208}\text{Pb}/^{204}\text{Pb}_{\text{NHRL}}] \times 100 \\ \Delta 7/4 &= [^{207}\text{Pb}/^{204}\text{Pb} - ^{207}\text{Pb}/^{204}\text{Pb}_{\text{NHRL}}] \times 100 \end{aligned} \quad (6.18)$$

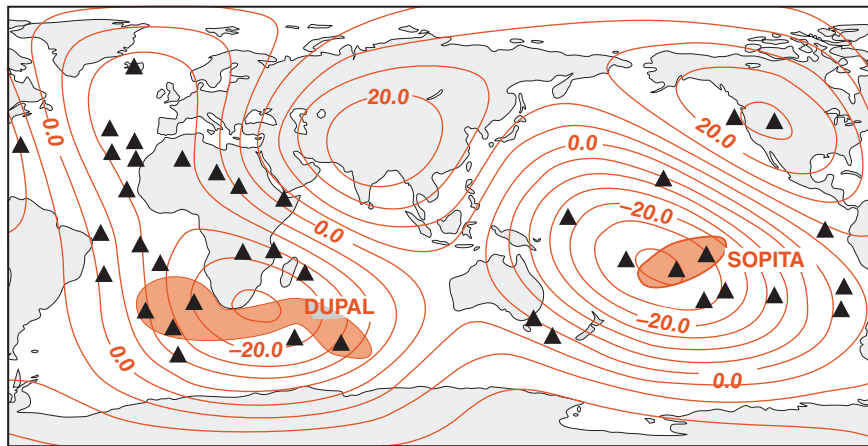


Figure 6.20 Map showing the distribution of mantle plumes (triangles), P-wave velocity anomalies (m/sec) averaged over the whole lower mantle (red lines), and location of the DUPAL and SOPITA isotope anomalies (red shaded regions). Mantle plumes are located in regions of slow lower mantle seismic velocities, implying high temperatures. (Source: Castillo (1989). Reproduced with permission of Nature Publishing Group.)

where

$$\begin{aligned} {}^{208}\text{Pb}/{}^{204}\text{Pb}_{\text{NHRL}} \\ = 15.627 + 1.209 {}^{206}\text{Pb}/{}^{204}\text{Pb} \end{aligned} \quad (6.19)$$

and

$$\begin{aligned} {}^{207}\text{Pb}/{}^{204}\text{Pb}_{\text{NHRL}} \\ = 13.491 + 0.1804 {}^{206}\text{Pb}/{}^{204}\text{Pb} \end{aligned} \quad (6.20)$$

Subsequently, Castillo (1989) suggested that Hart's "DUPAL anomaly" actually consisted of two separate regions: the DUPAL in the Indian Ocean, and the "SOPITA" (South Pacific Isotope and Thermal Anomaly) in the South Pacific and pointed out they correspond to regions of slow seismic velocities in the deep mantle, which in turn imply high mantle temperatures. Castillo's map is shown in Figure 6.20.

Interestingly, the DUPAL characteristic is shared by both Indian Ocean OIB and MORB, but this does not seem to be the case in the Atlantic and Pacific. The DUPAL signature has not been observed in Atlantic or Pacific MORB, except in the immediate vicinity of the Tristan da Cunha mantle plume in the South Atlantic. An additional question relates to sampling coverage. Nearly two-thirds of oceanic islands occur in the DUPAL belt, so it is not surprising that a particular chemistry is often found there. Nevertheless, it is clear

that there is something anomalous about this region.

The Galapagos Archipelago provides another example of geographic variation of isotope composition in the mantle. The Galapagos provide an unusually favorable opportunity for producing a geochemical map of the mantle because they consist of 20 or so volcanoes that have all been active over the past 2 or 3 million years. Combining Nd isotope ratio determined on basalts from these volcanoes as well as data from previous geochemical studies of the Galapagos Spreading Center (GSC) just to the north, White et al. (1993) produced the contour map of Nd isotope ratios shown in Figure 6.21. The contours reflect regional geochemical variations in the mantle below.

The contouring reveals a horseshoe-shaped region around the western, northern, and southern periphery of the archipelago in which low ϵ_{Nd} values occur, and a region in the center of the archipelago in which high ϵ_{Nd} values occur. The high ϵ_{Nd} values are more typical of MORB than of oceanic island basalts. This pattern was unexpected. From what was observed along the MAR (Figure 6.19), one might expect ϵ_{Nd} to decrease radially from the center of the archipelago. The pattern in the Galapagos most likely reflects the fluid dynamics of plume-asthenosphere interaction. Laboratory

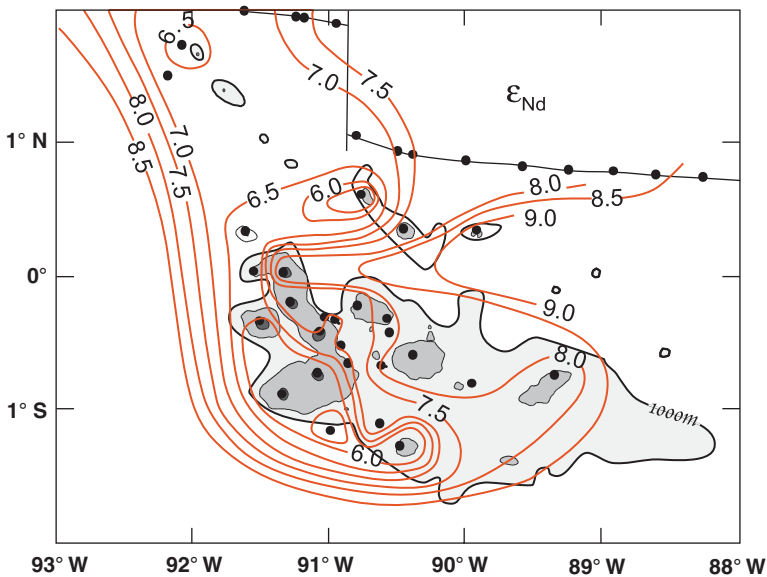


Figure 6.21 Contour map of ϵ_{Nd} variation in the mantle beneath the Galapagos. Contouring is based on average ϵ_{Nd} from 21 volcanoes, whose locations are shown by solid dots (locations were corrected for plate motion since time of eruption). (Source: White et al. (1993). Reproduced with permission of John Wiley & Sons Ltd.)

experiments have shown that a thermal plume (i.e., one that rises because it is thermal buoyant rather than chemically buoyant) will entrain surrounding asthenosphere if it is bent by asthenospheric motion. This is because the surrounding asthenosphere is heated by the plume, as a result, it also begins to rise.

While much of the geographic variation in the Galapagos appears to reflect processes in the upper mantle, geographic variation in Hawaii may reflect deep mantle spatial heterogeneity. The Hawaiian archipelago consists of two geochemically distinct chains: Loa and Kea (named for the two “type” volcanoes, Mauna Loa and Mauna Kea). Despite close proximity, these chains have maintained distinct isotopic identities for over 5 million years (e.g., Tatsumoto et al., 1978; Stille et al., 1983). The Hawaiian plume, projected downward into the deep mantle appears to overlie a seismological boundary between typical Pacific lower mantle and a sharply defined layer of low seismic shear velocities on the Loa side of the plume (Weis et al., 2011). Weis et al. argued that the Tristan da Cunha and Kerguelen plumes overlie similar anomalous low-velocity zones at the core–mantle boundary.

6.6 THE SUBCONTINENTAL LITHOSPHERE

Figure 6.22(a) shows Sr and Nd isotopic variations in continental basalts. The data span a much larger range than oceanic basalts. Some, but not all, of this variation reflects the effects of assimilation of continental crust on the isotopic signatures of the mantle-derived magmas. Assimilation effects can be avoided by considering only the data on peridotite xenoliths in continental basalts, the data for which is shown in Figure 6.22(b). As may be seen, the range of values is reduced, but nevertheless much greater than that observed in oceanic basalts. One needs be cautious in directly comparing the heterogeneity observed in xenolith data to basalt data because the two represent different scales of sampling of the mantle. Basalts are created by melting of regions that have characteristic scales of tens of kilometers and more. The magma generation process undoubtedly averages out very small-scale heterogeneities. Xenoliths, on the other hand, have characteristic dimensions of centimeters. Thus variations in isotope ratios in basalts reflect large-scale heterogeneity in the mantle, while xenoliths reflect small-scale

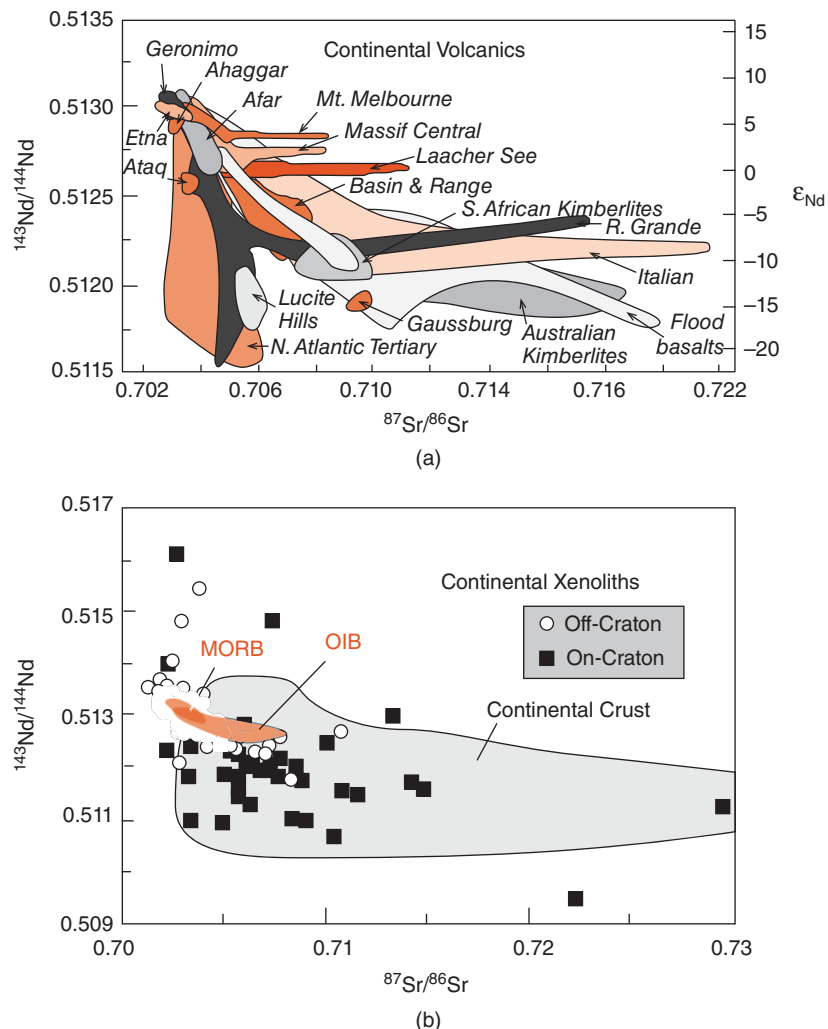


Figure 6.22 (a) top. Sr and Nd isotope ratios in continental basalts. (Source: Adapted from Wörner et al. (1986). Reproduced with permission of Elsevier.) (b) bottom. Sr and Nd isotope ratios in peridotite xenoliths from the subcontinental mantle lithosphere. (Source: Adapted from Pearson et al. (2003). Reproduced with permission of Elsevier.)

heterogeneity. Despite this, it appears that the subcontinental lithosphere is more heterogeneous, even on relatively large scales, than is the suboceanic mantle.

It appears that the subcontinental lithosphere can be quite old, and, at least in some cases, has the same age as the crust it underlies. As we saw Chapter 2, studies of xenoliths and inclusions in diamond from South African kimberlites suggests the mantle is 3–3.5 Ga old in this region, ages similar to that of the South African craton. The greater isotopic heterogeneity of the subcontinental lithosphere probably reflects its long-term stability, which allows variations in

parent-daughter ratios to be expressed in variations in radiogenic isotope ratios. Convective mixing in the suboceanic mantle will tend to destroy heterogeneity in it.

Though many xenoliths have isotopic compositions indicating incompatible-element enrichment, others xenoliths show parts of the subcontinental lithosphere can be extremely incompatible-element depleted. ϵ_{Nd} values of +500 have been recorded in garnets in eclogites from the Roberts Victor mine kimberlite. These eclogites appear to be rafts of subducted oceanic crust stranded in the subcontinental lithosphere over 3 Ga ago, an interpretation supported by highly variable

oxygen isotope ratios in the eclogites. They apparently suffered extreme LRE depletion around that time, perhaps by a small degree of melting or dehydration after subduction. Much of the subcontinental lithosphere may consist of mantle from which partial melts have been extracted to form the continental crust. Interesting, when the upper mantle undergoes melting both the melt and residual solid will have a density that is less than the original material. This residue is less dense because garnet, a very dense phase, is preferentially removed during melting. Thus both the crustal and mantle parts of the continental lithosphere have relatively low density, which may help to explain its stability.

If the subcontinental lithosphere is residual material from which melts have been extracted, why are xenoliths and basalts with “enriched” isotopic signatures so common? What process or processes could have produced this incompatible element enrichment of many parts of the subcontinental lithosphere? One possibility, first suggested by Brooks et al. (1976), is that partial melts from mantle plumes migrate upward into the lithosphere, where they freeze. The extent to which upwelling mantle can melt will depend on the depth to which it rises. Where continental lithosphere prevents plumes from rising above 200 km depth or so, the degree of melting is likely to be quite small, meaning the melts would be quite incompatible-element enriched. These melts could then migrate upward into the lithosphere, reacting with it, freezing, and enriching it in incompatible elements. Yet another possibility is that hydrous fluids released during dehydration of subducting oceanic lithosphere may migrate into the continental lithosphere and react with it (Hawkesworth et al., 1990). Judging from studies of island arc magmas, such fluids appear to be particularly enriched in soluble incompatible elements, such as the alkalis and alkaline earths. These processes in which lithosphere reacts with melts or fluids is known as *mantle metasomatism*.⁸ Petrographic studies of some xenoliths clearly reveal features, such as the secondary growth of hydrous minerals such as phlogopite (Mg-rich mica) and richterite (an alkali-rich amphibole) indicative of such metasomatism.

Studies of Os isotope ratios in xenoliths from the subcontinental lithosphere have

been particularly enlightening. Most xenoliths derived from below regions of old continental crust have low Os isotope ratios, which imply that low Re/Os ratios were established long ago. The low Re/Os ratios are consistent with the idea that this material undergone partial melting in the past, since Re is moderately incompatible, and would partition into the melt, while Os is highly compatible, and would remain in the solid. Despite their low $^{187}\text{Os}/^{188}\text{Os}$ ratios, many of these same xenoliths have quite low ε_{Nd} (Figure 6.23). The low ε_{Nd} suggests incompatible element enrichment, and hence would appear to be inconsistent with the high $^{187}\text{Os}/^{188}\text{Os}$ ratios. The explanation of this paradox appears to be that Os was not affected by the metasomatism that enriched these regions in incompatible elements and decreased Sm/Nd ratios (e.g., Carlson and Irving, 1994). Apparently, neither Re nor Os are transported effectively by metasomatic fluids. If the fluids are aqueous, this is perhaps not surprising, since these elements have low solubilities under reducing conditions. If the fluids are silicate melts, it is unclear why they do not transport Re. The answer may have to do with dependence of the Re partition coefficient on composition and oxygen fugacity.

Regardless of why they arise, these unusual Os-Nd isotope systematics provide the continental lithosphere with a distinctive isotopic signature and geochemists with a means of identifying continental lithosphere. In an earlier section, we discussed the hypothesis of McKenzie and O’Nions that subcontinental lithosphere can delaminate and sink to the bottom of the mantle where it is incorporated into mantle plumes. The distinctive isotope signatures of mantle plumes on the one hand and subcontinental lithosphere on the other (Figure 6.24) are inconsistent with this hypothesis.

Continental flood basalts provide another interesting example. These are huge outpouring of basaltic lava that apparently occurred within relatively short time intervals, a few million years and possibly less in some cases. The great oceanic plateaus, such as Ontong-Java and Kerguelen, are the marine equivalents. A number of continental floods basalts can be clearly associated with mantle plumes. For example, the Deccan Traps erupted 65 million years ago when

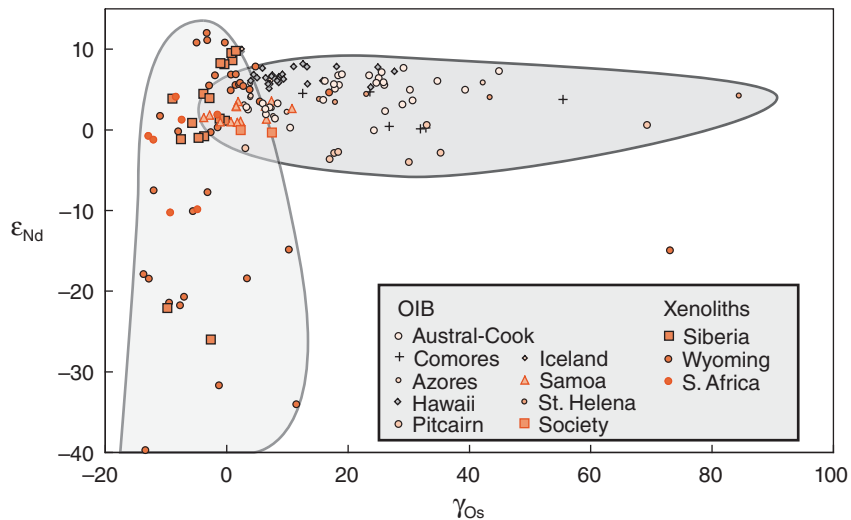


Figure 6.23 ε_{Nd} versus γ_{Os} in xenoliths from the subcontinental lithosphere and oceanic island basalts. Despite low and variable ε_{Nd} , the subcontinental lithosphere appears to be characterized by systematically low γ_{Os} (γ_{Os} is the percent deviation of the $^{187}\text{Os}/^{188}\text{Os}$ ratio from the chondritic value). (Source: White, 2010).

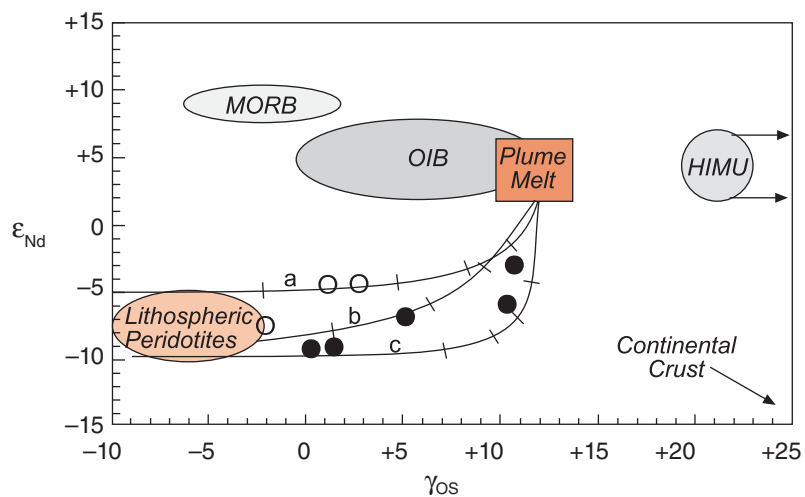


Figure 6.24 ε_{Nd} of picritic basalts from the Karroo flood basalts plotted against γ_{Os} . They fall between the fields of OIB and subcontinental lithosphere. Three lines, illustrating three mixing models (different concentrations of Os and Nd in the end-members), connect the fields of xenoliths from the subcontinental lithosphere and oceanic island basalts (i.e., mantle plumes). The data fall close to these lines, suggesting they are mixtures of melts of lithosphere and a mantle plume. (Source: Ellam et al. (1992). Reproduced with permission of Nature Publishing Group.)

India lay directly over the Reunion mantle plume, and the Parana in Brazil and Etendeka in Namibia were erupted 130 million years ago over the Tristan da Cunha mantle plume when Africa and South America were rifting.

These observations have given rise to the idea that continental flood basalts are produced when new mantle plumes arrive at the surface. Fluid dynamic experiments and simulations show that new plumes will have large bulbous

heads. When the heads arrive in the upper mantle, they melt, producing a pulse of volcanism. Others, however, have argued on geochemical grounds that continental flood basalts are produced by melting of the continental lithosphere. Because mantle plumes and continental lithosphere have such different Os and Nd isotope signatures, Os-Nd systematics provide a means of discriminating between these possibilities. Because of the difficulties in determining Os isotope ratios in basalts, only one such study has been carried out thus far. In it, Ellam et al. (1992) found that the Karroo flood basalts, erupted in South Africa 190 million years ago, have Os and Nd isotope compositions that lie on mixing lines connecting mantle plume compositions and continental lithosphere compositions (Figure 6.23). Thus at least in this case, both a mantle plume and continental lithosphere appear to have contributed to the magmas. The data also demonstrate the assimilation of continental crust cannot explain the low ϵ_{Nd} observed in these basalts.

6.7 U-SERIES ISOTOPES AND MELT GENERATION

We introduced the concepts of activity and radioactive equilibrium in Chapter 4. We noted that when a system has remained undisturbed for a sufficiently long time, a condition such that:

$$a_p = a_d$$

where a is the radioactivity (more often simply called activity) and the subscripts p and d refer to parent and daughter respectively. This is the condition of radioactive equilibrium. Measurement of U series isotopes in young volcanic rocks reveals that radioactive disequilibrium among U decay series nuclides is common, particularly for the $^{230}\text{Th}/^{238}\text{U}$ pair, but also for $^{231}\text{Pa}/^{235}\text{U}$ and $^{226}\text{Ra}/^{230}\text{Th}$. Figure 6.25 shows the data for Hawaii and MORB. The disequilibrium is not entirely surprising, since we expect radioactive equilibrium will be disturbed by the melting process if parent and daughter are partitioned between solid and melt differently. The magnitude of the disequilibrium proves, however, to be surprising indeed. The $^{230}\text{Th}/^{238}\text{U}$ ratio in MORB can be as high as 1.38, although the mean value is somewhat lower, 1.17. Similar disequilibrium is observed in Hawaiian basalts.

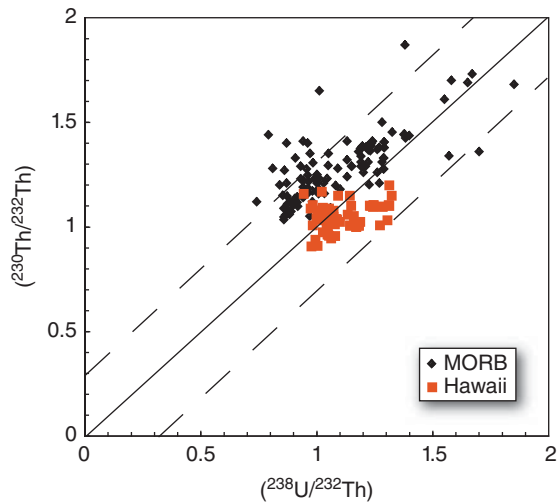


Figure 6.25 $(^{230}\text{Th}/^{232}\text{Th})$ versus $(^{238}\text{U}/^{232}\text{Th})$ ratios for MORB and Hawaiian basalts. Dashed lines show the limits of 30% disequilibrium. Data from the GEOROC and PETDB databases.

These numbers correspond to excesses of Th of 38% and 17% respectively. Let's consider what is required to produce this kind of disequilibrium.

The simplest model of melting is *batch melting*, in which a fraction of melt, F , is created, and remains in contact and in equilibrium with the solid until melting is complete (melt fraction reaches F). Only then is the melt extracted. For this situation, we may write the following mass balance equation:

$$c_i^o = c_i^s(1 - F) + c_i^\ell F \quad (6.21)$$

where c is the concentration of element i , F is the fraction of melt by weight, and the superscripts o , s , and ℓ refer to the original solid (=system as a whole), the solid, and the melt respectively. The partition, or distribution coefficient is defined as:

$$D_i^{s/\ell} = c_i^s / c_i^\ell \quad (6.22)$$

Substituting this into 6.21, we have:

$$c_i^o = D_i c_i^\ell (1 - F) + c_i^\ell F \quad (6.23)$$

Upon rearranging, we have:

$$\frac{c_i^\ell}{c_i^o} = \frac{1}{D_i(1 - F) + F} \quad (6.24)$$

Since the activity of i is simply $a_i = \lambda_i c_i$, this same equation holds equally well for activities:

$$\frac{a_i^\ell}{a_i^o} = \frac{1}{D_i(1 - F) + F} \quad (6.25)$$

If we assume that the system was in radioactive equilibrium before melting occurs, then:

$$a_P^o = a_D^o \quad (6.26)$$

Then the activity ratio of the parent and daughter in the melt is given by:

$$\frac{a_D^\ell}{a_P^\ell} = \frac{D_P(1 - F) + F}{D_D(1 - F) + F} \quad (6.27)$$

From this, we can easily solve for F . Thus, if we know the values of the partition coefficients, we can determine the necessary extent of batch melting to produce the observed activity ratio. Table 6.2 lists solid/liquid partition coefficients for U and Th for major mantle minerals determined by Beattie (1993). The bulk partition coefficient, which we want to use here, is simply the average for each element weighted by the fraction of the mineral in the solid (i.e., weighted by the mineral mode):

$$\bar{D}_i = \sum_{\chi} m_{\chi} D_i^{\chi/\ell} \quad (6.28)$$

where m_{χ} is the modal abundance of phase χ . Assuming, somewhat arbitrarily, a mantle of 60% olivine, 20% orthopyroxene, 12% clinopyroxene, and 8% garnet, the bulk partition coefficients for U and Th are 0.00114 and 0.00024 respectively. To produce 38% disequilibrium between ^{238}U and ^{230}Th with simple batch melting requires the extent of melting be 0.2%. While such low extents of melting might be reasonable under some circumstances, they certainly are not at mid-ocean ridges. The oceanic crust is

typically 6 km thick. To produce it by 0.2% melting requires efficient extraction of melt from $6/0.002 = 3000$ km of mantle – the entire mantle! Clearly, if our partition coefficients are correct (there is certainly plenty of variability in partition coefficients – but even the most favorable ones would suggest <1% melting), then the simple model of batch melting must be wrong. Fortunately, plausible models of melting and melt extraction can provide an explanation for the large disequilibrium observed. Let's now consider those.

6.7.1 Spiegelman and Elliot model of melt transport

The problem of large disequilibrium between ^{230}Th and ^{238}U was first addressed theoretically by McKenzie (1985). He concluded that the large disequilibrium observed required slow melting compared to the half-life of ^{230}Th and no more than a few percent melt present in the mantle at any time. He also concluded that the melting region beneath mid-ocean ridges was more than 100 km wide. Navon and Stopler (1987) argued that rapid disequilibrium melting could explain the isotopic disequilibrium observed. Spiegelman and Elliot (1993) developed a more complete model of melting and showed that large isotopic disequilibrium can result from differences in transport velocities of the different elements, which in turn results from continued solid-melt equilibria and exchange as melt percolates upward through the melting column.

To begin with, let's consider the physics of melting beneath mid-ocean ridges (the physics are similar for mantle plumes). Melting occurs at mid-ocean ridges as a consequence of decompression. Because the slope of the solidus is steeper than that of the adiabat (Figure 6.26), rising mantle eventually crosses the solidus. Melting begins at the point the mantle reaches the solidus and continues as the mantle continues to rise until it reaches the depth where temperature decreases due to conductive cooling. As melt is created, it will rise out of the mantle because it is less dense than the solid. However, surface tension will force some fraction of melt remain in the solid, resulting in a small but finite porosity of the solid. Melts streaming upward out of the mantle will eventually aggregate and mix in crustal magma chambers before erupting.

Table 6.2 Partition coefficients for Th and U. (Source: Beattie, 1993. Reproduced with permission of Elsevier.)

	Cpx	Gnt	Opx	Ol
Th	0.00047	0.0021	0.00003	0.00001
U	0.00036	0.0135	0.00004	0.00001

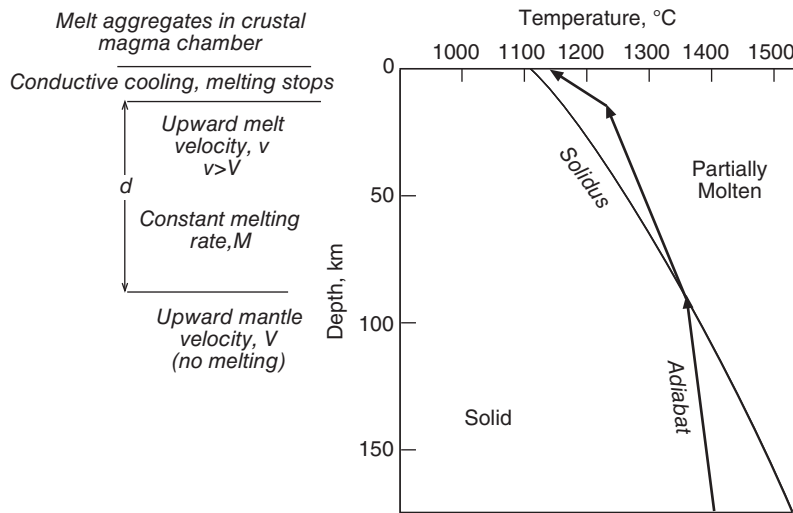


Figure 6.26 Schematic model of decompression melting beneath mid-ocean ridges and oceanic islands.

Spiegelman and Elliot (1993) begin by writing a conservation equation for each parent-daughter pair as:

$$\begin{aligned} & \frac{\partial[\phi\rho_m + (1-\phi)\rho_s D_i]}{\partial t} c_i^m \\ & + \nabla \cdot [\rho_m \phi v + \rho_s (1-\phi) D_i V] c_i^m \\ & = \lambda_{i-1} [\rho_m \phi + \rho_s (1-\phi) D_{i-1}] c_{i-1}^m \\ & - \lambda_i [\rho_m \phi + \rho_s (1-\phi) D_i] c_i^m \end{aligned} \quad (6.29)$$

where the subscript i denotes the element, c^m is the concentration of the element of interest in the melt, ∇ is the gradient, ρ_m is the density of the melt, ρ_s is the density of the solid, v is the velocity of the melt, V is the velocity of the solid, D is the partition coefficient, ϕ is the melt *volume* fraction, and, as usual, λ is the decay constant. The first nuclide in the chain, ^{238}U , has no parent, so that $\lambda_0 = 0$. In a one-dimensional steady-state system, the melt flux is simply the melt density times porosity times velocity:

$$\rho_m \phi v \quad (6.30)$$

The mid-ocean ridge is approximates such a one-dimensional (vertical) system, and for simplicity, we will restrict ourselves to one dimension. In this case, the melt flux is simply:

$$\rho_m \phi v = \dot{M}_0 z \quad (6.31)$$

where \dot{M}_0 is the (constant) melting rate and z is height above the base of the melting column. Equation 6.31 is simply a statement that for

a constant melting rate, the melt flux must increase linearly with height. Mass balance then requires that upward flux of solid is given by:

$$\rho_s (1-\phi) V = \rho_s V_0 - \dot{M}_0 z \quad (6.32)$$

where V_0 is the initial upwelling velocity of the solid (i.e., at the base of the melting column). Since melting is driven by decompression, the melting rate depends on velocity. We are assuming a constant melting rate, \dot{M}_0 , which can be expressed as:

$$\dot{M}_0 = \frac{\rho_s V_0 F_{\max}}{d} \quad (6.33)$$

where F_{\max} is the maximum extent of melting (which occurs at the top of the column) and d is the height over which melting occurs (height of the melting column). The extent of melting at any height z is just:

$$F = F_{\max} \frac{z}{d} \quad (6.34)$$

From these relationships, we can derive the following relationship between melt velocity and porosity:

$$v = V_0 \frac{\rho_s F}{\rho_m \phi} \quad (6.35)$$

Spiegelman and Elliot used Darcy's law to determine the relationship between porosity

and depth:

$$\phi(v - V) = \frac{k_0}{\mu} \phi^n (1 - \phi) (\rho_s - \rho_m) g \quad (6.36)$$

where k_0 is the permeability, g is the acceleration of gravity, μ is melt viscosity. The exponent n depends on melt distribution, and is 2 if the melt is distributed in tubes and 3 if it is in veins and sheets.

Using these equations, we can express the porosity as a function of height as:

$$\frac{\rho_m}{\bar{\rho}} [\phi + A \phi^n (1 - \phi)^2] = \frac{F_{\max} z}{d} \quad (6.37)$$

where ϕ_{\max} is the maximum porosity at the top of the column, $\bar{\rho}$ is the mean density at ϕ_{\max} , and A is:

$$A = \frac{1}{\phi_{\max}^{n-1} (1 - \phi_{\max})^2} \left[\frac{\bar{\rho} F_{\max}}{\rho_m} - 1 \right] \quad (6.38)$$

Thus, if ϕ_{\max} and F_{\max} are chosen, then the distribution of ϕ is fixed throughout the column (we can readily solve for ϕ using indirect methods, for example, using the Solver in Microsoft Excel™).

Equation 6.29 may now be rewritten as:

$$\begin{aligned} \frac{dc'_i}{d\zeta} &= c'_i \frac{(D_i - 1) F_{\max}}{D_i + (1 - D_i) F_{\max}} \\ &+ \lambda_i d \left[B(\zeta) \frac{c'_{i-1}}{v'_{eff}^{i-1}} - \frac{c'_i}{v'_{eff}^i} \right] \end{aligned} \quad (6.39)$$

where

$$B(\zeta) = \frac{D_i [D_{i-1} + (1 - D_{i-1}) F_{\max} \zeta]}{D_{i-1} [D_i + (1 - D_i) F_{\max} \zeta]}$$

c' is the concentration of the element relative to its *initial* concentration in the melt, $\zeta = z/d$, the fractional height in the column, and v'_{eff} is the *effective velocity* of the element through the melting column:

$$\begin{aligned} v'_{eff} &= \frac{\rho_m \phi v + \rho_s (1 - \phi) D_i V}{\rho_m \phi + \rho_s (1 - \phi) D_i} \\ &\approx V + \frac{v - V}{1 + D_i / \phi} \end{aligned} \quad (6.40)$$

The effective velocity of an element is the just average of the velocity of the melt and the solid, weighted by the fraction of the

element in each. We can see from Eqn. 6.40 that if $D_i \ll \phi$, then most of the element will be in the melt and the effective velocity will approach that of the melt velocity. For an element with $D_i \gg \phi$, then most of the element will be in the solid and the effective velocity will approach that of the solid. Thus elements travel upward at different velocities depending on the partition coefficient. Very incompatible elements travel up through the melting column at near the velocity of the melt; very compatible elements travel upward at velocities near the solid velocity.

Assuming equilibrium between melt and solid, the initial concentration of an element in the melt, c_0^m is readily assessed from Eqn. 6.25 by setting $F = 0$. In that case, we see that:

$$\frac{c_{i0}^m}{c_i^0} = \frac{1}{D_i}$$

Equation 6 forms a system of ordinary differential equations that can be solved numerically for the concentration of each element i . In practice, a web-based calculator is available, *Usercalc*, and is described in Spiegelman (2000). The user specifies F_{\max} , ϕ_{\max} , upwelling velocity, pressure gradient (depends on bulk density), the value of the permeability coefficient, n , the partition coefficients, and the pressure range over which melting occurs. The model has provision for two layers where the partition coefficients and permeability can differ (to take account of phase changes in the melting region: for example, melting can begin in the garnet peridotite facies and end in the spinel peridotite facies).

Let's consider an example in which F_{\max} is 20% and melting begins at 4 GPa (40 kb, 123.56 km) and ends at 0 GPa. Using the mineral partition coefficients in Table 6.1, the bulk partition coefficients for U and Th are 0.0011 and 0.00024 respectively in the garnet peridotite facies, and both are 0.00033 in the spinel peridotite facies. (We use the program's default partition coefficients for Ra and Pa, which are 2×10^{-5} and 1×10^{-5} in both facies.) The phase transition occurs at 2 GPa. We set the remaining parameters to their default values ($V = 3 \text{ cm/yr}$, $\phi_{\max} = 0.008$, $n = 2$). Figure 6.27 is the output of the program, showing the variation of melt fraction, porosity, and the activity ratios with depth. The result is a $(^{230}\text{Th}/^{238}\text{U})$

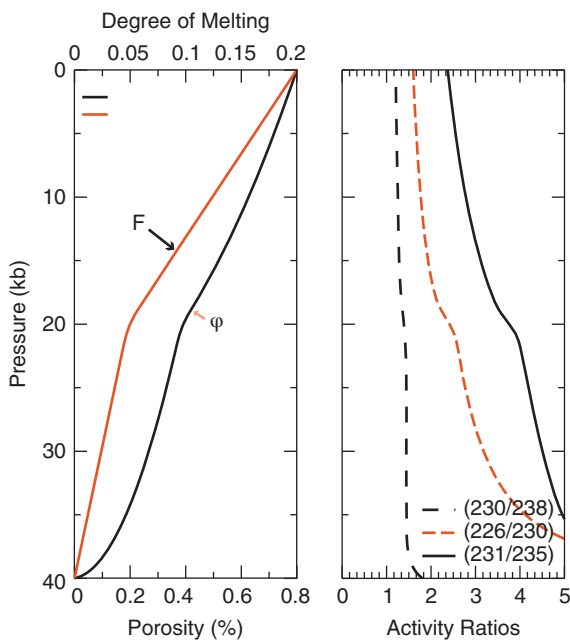


Figure 6.27 Prediction of Spiegelman’s *Usercalc* program for conditions specified in the text. Kinks in the curves reflect the phase change from garnet to spinel peridotite at 20 kb. $^{230}\text{Th}/^{238}\text{U}$ of the melt flowing out the top is 1.113. *Usercalc* is available on the web at (www.ledo.columbia.edu/~mspieg/UserCalc/).

ratio of 1.113 for the melt flowing out of the system – in other words, a 11.3% excess of ^{230}Th .

Considering the corresponding $(^{230}\text{Th}/^{232}\text{Th})$ versus $(^{238}\text{U}/^{232}\text{Th})$ diagram (Figure 6.28) helps to elucidate what is occurring. As melting begins, Th is partitioned into the melt relative to U, so the $(^{238}\text{U}/^{232}\text{Th})$ is low relative to the initial solid while that of the residual solid is high. With further melting, the $(^{238}\text{U}/^{232}\text{Th})$ of the melt increases – this effect is just what is expected from simple melting models (for example, the batch melting equations). The $(^{238}\text{U}/^{232}\text{Th})$ ratio in the solid also increases, as ^{232}Th is increasingly stripped from the solid.

Interestingly, the $(^{230}\text{Th}/^{232}\text{Th})$ ratio in both solid and melt, which are both initially equal to the value of the ratio before melting, also increase as melting proceeds, and, more importantly, as time passes. After melting begins the $(^{230}\text{Th}/^{238}\text{U})$ ratio in the solid is lower than the equilibrium ratio (which is 1); it therefore increases as a consequence of

radioactive decay of ^{238}U . Because ^{232}Th is not being produced, the $(^{230}\text{Th}/^{232}\text{Th})$ in solid must increase. Chemical equilibrium dictates that $(^{230}\text{Th}/^{232}\text{Th})_{\text{melt}} = (^{230}\text{Th}/^{232}\text{Th})_{\text{solid}}$ so long as solid and melt remain in equilibrium. Therefore, $(^{230}\text{Th}/^{232}\text{Th})$ in the melt also increases.

The effect depends on the relative effective velocities (Eqn. 6.40) of parent and daughter through the melting column. In this example, the melt velocity is 88 cm/yr, or 29.46 times greater than the mantle upwelling velocity. Within the spinel peridotite facies, the effective velocity of Th is 90% of the melt velocity, while that of U is only 66% of the melt velocity. In other words, the upward velocity of Th is 36% greater than that of U. The longer residence time of U in the column leads to an excess of the daughter nuclide.

The times required for solid and melt to traverse the melting zone are 4 Ma and 0.136 Ma, respectively. The latter time approaches two half-lives of ^{230}Th . In the time required for ^{230}Th to traverse the melting column, only 32% of the ^{230}Th atoms originally present still remain – 68% have decayed in this time. What this means is that most of the ^{230}Th present in the melt at the top of the melting column have been produced during the melting process.

In this example, the partition coefficients for Th and U are identical in the spinel facies, so once that is crossed, $(^{238}\text{U}/^{232}\text{Th})$ of both solid and melt begin to decrease. This occurs because once garnet is no longer present, the solid is oversaturated with U, which begins to partition into the melt. As U is lost from the solid, the $(^{230}\text{Th}/^{238}\text{U})$ ratio increases toward the equilibrium value, so there is less “excess” ^{230}Th in the solid. In this example, there is only a 13% excess of ^{230}Th . However, the melt at the garnet-spinel transition, had it been sampled, would have had a 30% excess of ^{230}Th .

Data has also become available for ^{226}Ra (half-life 1622 years) and ^{231}Pa (half-life 32480 years). Although there is less data for these nuclides than for ^{230}Th , the available data show even greater excesses of ^{226}Ra and ^{231}Pa . Both of these elements are less compatible than their parents (^{230}Th and ^{235}U respectively), but again, the extent of disequilibrium is greater than can be predicted by simple melting models. Figure 6.29 shows histograms for $(^{226}\text{Ra}/^{230}\text{Th})$ and $(^{231}\text{Pa}/^{235}\text{U})$

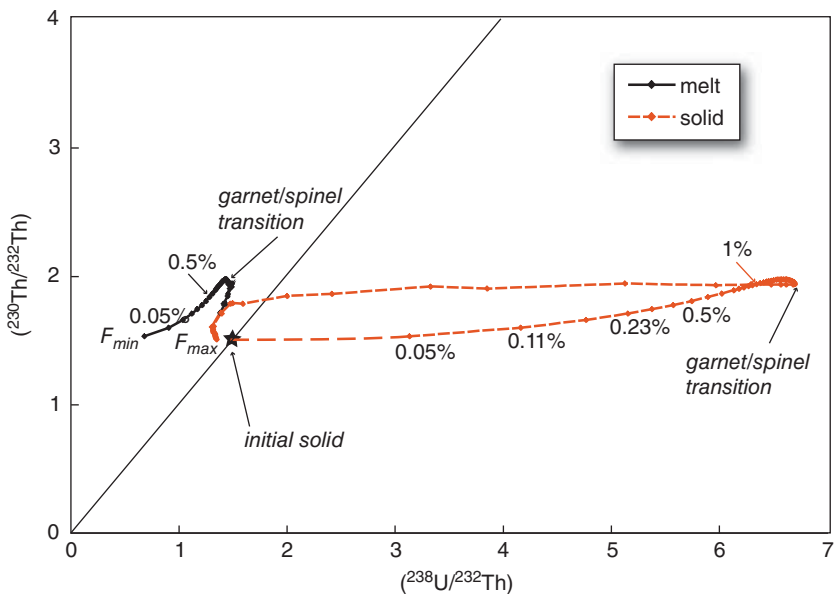


Figure 6.28 $(^{230}\text{Th}/^{232}\text{Th})$ versus $(^{238}\text{U}/^{232}\text{Th})$ plot for the melting model discussed in the text. Initial solid plots on the equiline with $(^{230}\text{Th}/^{232}\text{Th}) = (^{238}\text{U}/^{232}\text{Th}) = 1.5$.

for MORB and Hawaii. The MORB data show particularly great dispersion, with mean $(^{226}\text{Ra}/^{230}\text{Th})$ and $(^{231}\text{Pa}/^{235}\text{U})$ of 1.63 and 2.38, respectively. The Hawaiian data show less dispersion, with means of 1.16 and 1.40 for $(^{226}\text{Ra}/^{230}\text{Th})$ and $(^{231}\text{Pa}/^{235}\text{U})$, respectively.

Since these nuclides have half-lives that are short compared to the time required for them to traverse the melting region, it is useful to consider them as well. In our example, *Usercalc* predicts $(^{226}\text{Ra}/^{230}\text{Th}) = 1.05$ and $(^{231}\text{Pa}/^{235}\text{U}) = 1.17$. Now let's consider how these results depend on the values of ϕ , and V chosen for the model. Recall that we set $V_0 = 3 \text{ cm/yr}$, and $\phi_{max} = 0.008$ in this particular model. Using contour plots available in *Usercalc*, we can see how the results depend on these parameters. We'll set the target values to the mean values for the Hawaiian data set, namely $(^{230}\text{Th}/^{238}\text{U}) = 1.15$, $(^{226}\text{Ra}/^{230}\text{Th}) = 1.15$, and $(^{231}\text{Pa}/^{235}\text{U}) = 1.5$. Clearly, a valid model for melting under Hawaii must simultaneously reproduce all of these ratios. Figure 6.30 shows that while the specific values of V and ϕ chosen do not reproduce the mean Hawaiian values, there is a region in $V_0 - \phi$ space where all these target values can be approximately reproduced,

namely the region $V_0 = 0.5$ to 1.5 cm/yr and $\phi = 0.0015$ to 0.003 . We can also see from these plots that $(^{226}\text{Ra}/^{230}\text{Th})$ is essentially independent of upwelling velocity and strongly dependent on porosity. Indeed, assuming our partition coefficients are correct, the model tightly constrains porosity under Hawaii to be about 0.0025. The $(^{230}\text{Th}/^{238}\text{U})$ and $(^{231}\text{Pa}/^{235}\text{U})$ ratios depend on both upwelling velocity and porosity over most of the $V_0 - \phi$ space, but at small ϕ , and large V_0 , the $(^{230}\text{Th}/^{238}\text{U})$ and $(^{231}\text{Pa}/^{235}\text{U})$ ratios become independent of porosity and depend only on upwelling velocity. Thus, the U-series isotopes provide constraints on important parameters in mantle melting, notably upwelling velocity and porosity.

NOTES

1. Peridotite is a rock that consists of greater than 50% olivine, $[\text{Mg},\text{Fe}]_2\text{SiO}_4$; the term peridotite comes from the gem name of olivine, peridot. Various lines of evidence, including density, seismic velocities, and the assumption of an approximately chondritic Earth, indicate the mantle must consist of peridotite. Other essential minerals in the upper mantle are clinopyroxene ($[\text{Mg},\text{Fe}]\text{CaSi}_2\text{O}_6$)

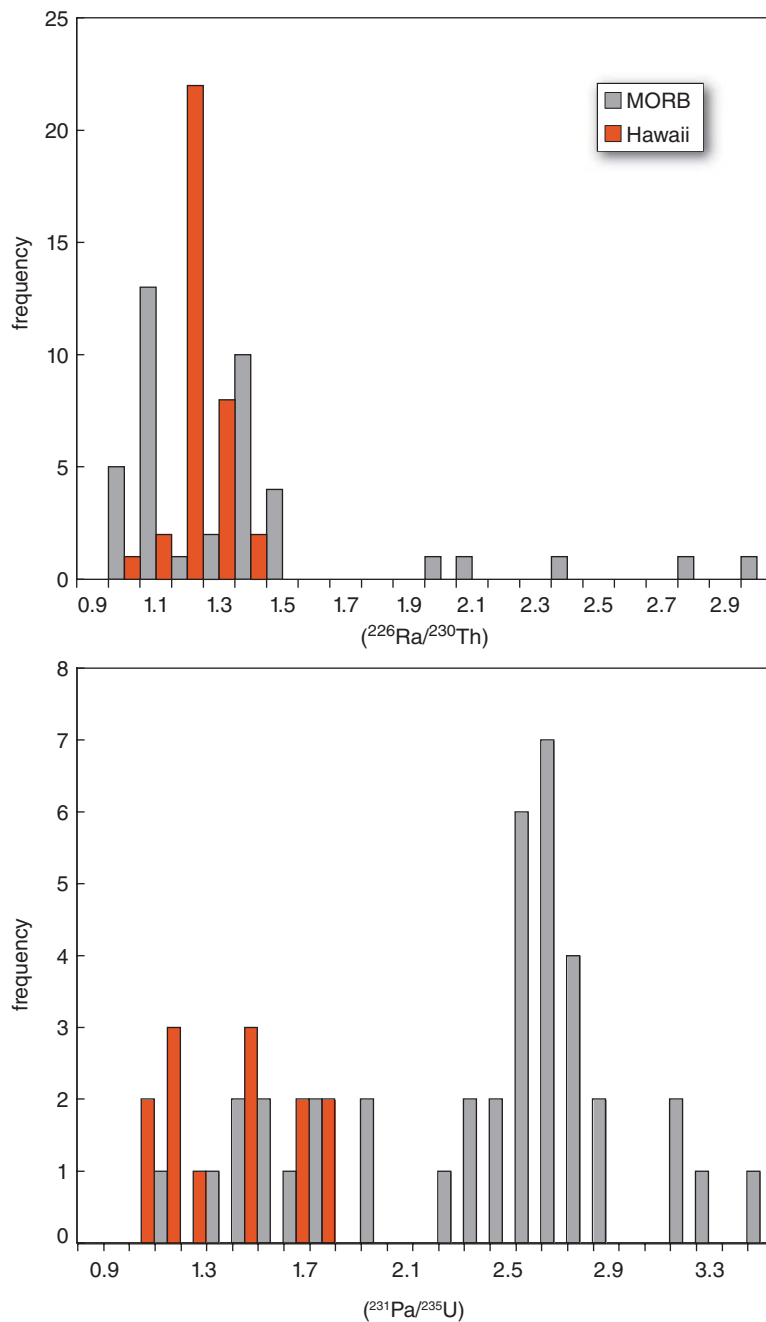


Figure 6.29 Histograms of $(^{226}\text{Ra}/^{230}\text{Th})$ and $(^{231}\text{Pa}/^{235}\text{U})$ in MORB and Hawaii. Data from the PetDB and GEOROC databases.

and orthopyroxene ($[\text{Mg},\text{Fe}]\text{SiO}_3$), and an aluminous phase, either plagioclase ($\text{CaAl}_2\text{Si}_2\text{O}_8$), spinel (MgAlSiO_4), or garnet ($[\text{Mg},\text{Fe},\text{Ca}]_3\text{Al}_2\text{Si}_2\text{O}_{12}$) depending on pressure. Most other elements will be dissolved in these four phases. In the lower mantle, this assemblage is replaced by one consisting

primarily of Mg-perovskite ($(\text{Mg},\text{Fe},\text{Ca})\text{SiO}_3$) and magnesiowüstite ($(\text{Mg},\text{Fe})\text{O}$).

2. A xenolith is any foreign rock found in an igneous rock. Xenoliths of peridotite in igneous rocks are often pieces of mantle that have been carried to the surface by ascending magma.

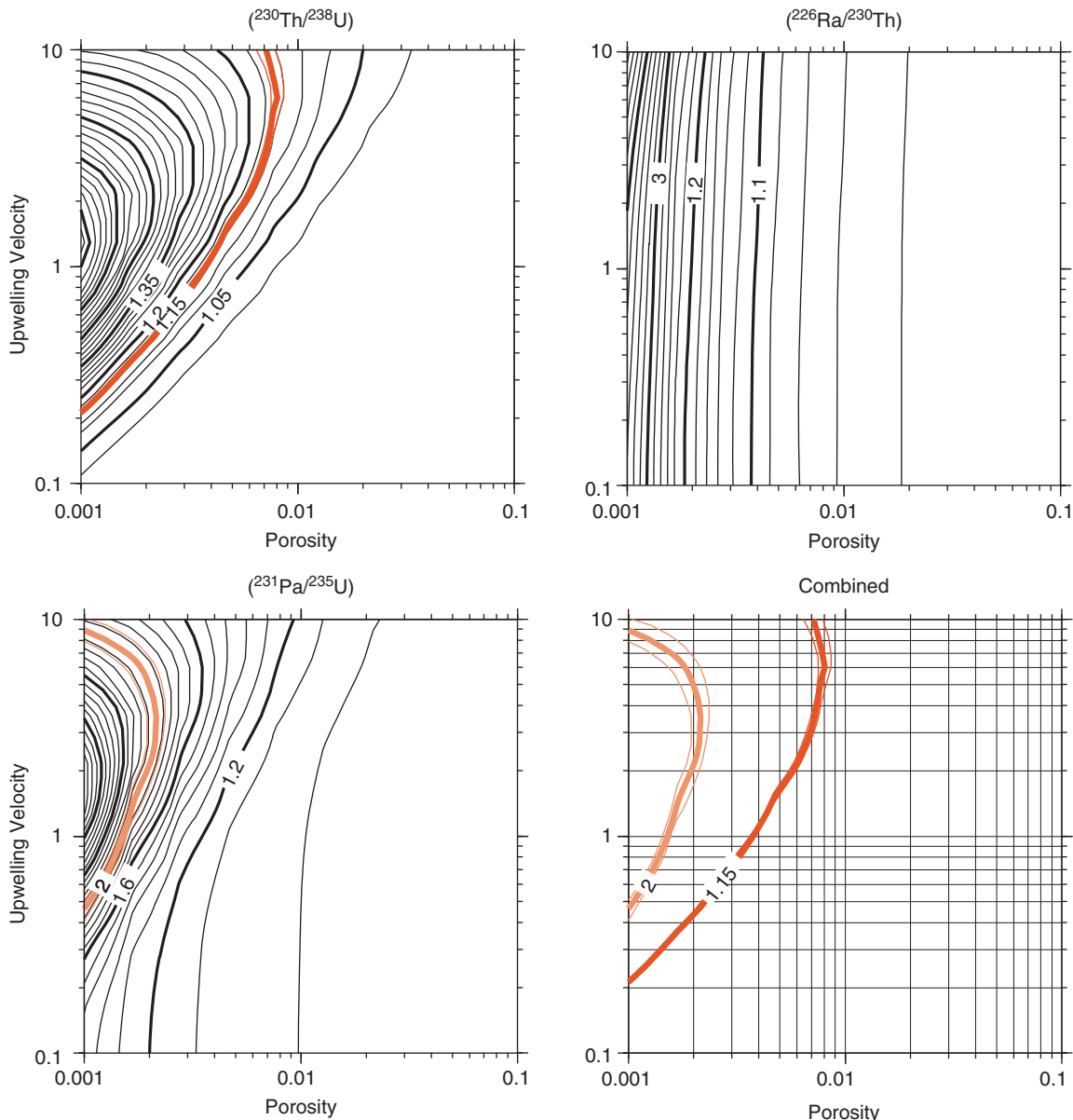


Figure 6.30 Contour plots illustrating the sensitivity of U-series disequilibria to porosity and upwelling velocity (the latter is in cm/yr). Colored lines show the combination of porosity and upwelling velocity needed to reproduce the “target values,” which are $(^{230}\text{Th}/^{238}\text{U}) = 1.15$, $(^{226}\text{Ra}/^{230}\text{Th}) = 1.15$, and $(^{231}\text{Pa}/^{235}\text{U}) = 1.5$. Panel in the lower right shows contours for the three ratios combined.

3. By definition, basalt is an extrusive igneous rock (i.e., lava) with less than 52% SiO_2 . Basalt is the primary product of melting of the mantle. Mid-ocean ridge basalts are simply those lavas erupted at mid-ocean ridge spreading centers, that is, divergent plate boundaries.
4. You may get the impression that to really succeed in mantle isotope geochemistry you

need to be good at thinking up acronyms. As near as I can tell, this is true. This acronym is due to Claude Allègre.

5. Residence time of some element i in a reservoir is defined as: $\tau = \frac{C_i M_i}{f_i}$ where τ is the residence time, C_i is the concentration of element i in the reservoir, M is the mass of the reservoir, and f_i is the flux of i into or out of the reservoir. The

- residence time of Pb in the depleted mantle is the average time an atom of Pb will spend there between entering and leaving.
6. Subsequent work has shown that these hot spots are not completely fixed: they do move slowly relative to one and other. This, however, is readily explained by the rising plumes being influenced by convection currents in the mantle through which they rise, as smoke plumes are bent by wind. Indeed, plume motions are consistent with predictions of mantle convection models (e.g., Steinberger and O'Connell, 1998).
 7. The “Eu anomaly” is defined as the ratio of the chondrite-normalized Eu concentration to its predicted chondrite-normalized concentration based on the concentrations of the two adjacent rare earths, Sm and Gd. It is often expressed as Eu/Eu* where Eu* is the predicted concentration calculated as $(Sm_{N}xGd_{N})^{1/2}$ where the subscript “N” is the chondrite normalized concentration. A Eu/Eu* > 1 is referred to as a positive anomaly, while Eu/Eu* < 1 constitutes a negative anomaly.
 8. Metasomatism is defined in metamorphic petrology as a subsolidus process that results in a net change in the composition of the metamorphic rock. Usually this is accomplished by the flow of aqueous solutions through the rock. The term “mantle metasomatism” is widely used to refer to reaction between rock and silicate liquid as well as between rock and aqueous solution.

REFERENCES

- Beattie, P. 1993. Olivine-melt and orthopyroxene-melt equilibria, *Contributions to Mineralogy and Petrology*, 115: 103–111.
- Bellini, G., Ianni, A., Ludhova, L., Mantovani, F. and McDonough, W. F. 2013a. Geo-neutrinos. *Progress in Particle and Nuclear Physics*, 73: 1–34, doi: 10.1016/j.ppnp.2013.07.001.
- Bellini, G. and the Borexino Collaboration 2013b. Measurement of geo-neutrinos from 1353 days of Borexino. *Physics Letters B*, 722: 295–300, doi: 10.1016/j.physletb.2013.04.030.
- Blichert-Toft, J., Zanda, B., Ebel, D. S. and Albarède, F. 2010. The Solar System primordial lead. *Earth and Planetary Science Letters*, 300: 152–163, doi: 10.1016/j.epsl.2010.10.001.
- Boyett, M. and Carlson, R. L. 2005. ^{142}Nd evidence for early (>4.3 Ga) global differentiation of the silicate Earth, *Science*, 309: 576–581.
- Brooks, C., James, D. E. and Hart, S. R. 1976. Ancient lithosphere: its role in young continental volcanism. *Science*, 193: 1086–1094.
- Carlson, R. W. and A. J. Irving. 1994. Depletion and enrichment history of subcontinental lithospheric mantle *Earth and Planetary Science Letters*, 126: 457–472.
- Caro, G. and Bourdon, B. 2010. Non-chondritic Sm/Nd ratio in the terrestrial planets: Consequences for the geochemical evolution of the mantle crust system, *Geochimica et Cosmochimica Acta*, 74: 3333–3349.
- Castillo, P. 1989. The Dupal anomaly as a trace of the upwelling lower mantle. *Nature*. 336: 667–670.
- Chauvel, C., Hofmann, A. W. and Vidal, P. 1992. HIMU-EM: The French Polynesian connection. *Earth and Planetary Science Letters*, 110: 99–119.
- Chauvel, C., Lewin, E., Carpentier, M., Arndt, N. T. and Marini, J.-C. 2008. Role of recycled oceanic basalt and sediment in generating the Hf-Nd mantle array. *Nature Geoscience*, 1: 64–67, doi: 10.1038/ngeo.2007.51.
- Corgne, A., Liebske, C., Wood, B. J., Rubie, D. C. and Frost, D. J. 2005. Silicate perovskite-melt partitioning of trace elements and geochemical signature of a deep perovskitic reservoir. *Geochimica et Cosmochimica Acta*, 69: 485–496.
- Davies, G. F. 1988. Ocean bathymetry and mantle convection, 1, large-scale flow and hotspots. *Journal of Geophysical Research*, 93: 10467–10480.
- DePaolo, D. and Wasserburg, G. 1976. Inferences about magma sources and mantle structure from variations of $^{143}\text{Nd}/^{144}\text{Nd}$. *Geophysical Research Letters*, 3: 743–746, doi:10.1029/GL003i012p00743.
- DePaolo, D. J. 1980. Crustal growth and mantle evolution: inferences from models of element transport and Nd and Sr isotopes. *Geochimica et Cosmochimica Acta*, 44: 1185–1196.
- Dupré, B. and Allègre, C. J. 1983. Pb-Sr isotope variations in Indian Ocean basalts and mixing phenomena. *Nature*, 303: 142–146.
- Dye, S. T. 2012. Geoneutrinos and the radioactive power of the Earth. *Reviews of Geophysics*, 50: RG3007, doi: 10.1029/2012rg000400.
- Ellam, R. M., Carlson, R. W. and Shirey, S. B. 1992. Evidence from Re-Os isotopes for plume-lithosphere mixing in Karoo flood basalt genesis. *Nature*. 359: 718–721.
- Farley, K. A., Natland, J. H. and Craig, H. 1992. Binary mixing of enriched and undegassed (primitive?) mantle components (He, Sr, Nd, Pb) in Samoan lavas. *Earth and Planetary Science Letters* 111: 183–199.

- Galer, S. J. G. and O’Nions, R. K. 1985. Residence time of thorium, uranium and lead in the mantle with implications for mantle convection. *Nature*, 316: 778–782.
- Gando, A., and the KamLAND collaboration. 2013. Reactor on-off antineutrino measurement with KamLAND. *Physical Review D*, 88: 033001, doi: 10.1103/PhysRevD.88.033001.
- Gast, P. W. 1960. Limitations on the composition of the upper mantle. *Journal of Geophysical Research*, 65: 1287–1297.
- Halliday, A.N. 2004. Mixing, volatile loss and compositional change during impact-driven accretion of the Earth, *Nature*, 427: 505–509.
- Hanan, B. B. and Graham, D. W. 1996. Lead and helium isotope evidence from oceanic basalts for a common deep source of mantle plumes, *Science*, 272: 991–995.
- Hart, S. R. 1984. The DUPAL anomaly: A large-scale isotopic mantle anomaly in the Southern Hemisphere. *Nature*, 309: 753–757.
- Hart, S. R., Hauri, E. H., Oschmann, L. A. and Whitehead, J. A. 1992. Mantle Plumes and entrainment: isotopic evidence, *Science*, 256: 517–520.
- Hart, S. R., Schilling, J. G. and Powell, J. L. 1973. Basalts from Iceland and along the Reykjanes Ridge: Sr isotope geochemistry, *Nature Physical Science*, 246:104–107.
- Hauri, E. 1996. Major element variability in the Hawaiian Mantle Plume. *Nature*, 382: 415–419.
- Hawkesworth, C. J., Kempton, P. D., Rogers, N. W., Ellam, R. M. and van Calsteren, P. W. 1990. Continental mantle lithosphere, and shallow level enrichment processes in the Earth’s mantle, *Earth and Planetary Science Letters*, 96: 256–268.
- Hofmann, A. W. and White, W. M. 1982. Mantle Plumes from ancient oceanic crust, *Earth and Planetary Science Letters*, 57: 421–436.
- Huang, Y., Chubakov, V., Mantovani, F., Rudnick, R. L. and McDonough, W. F. 2013. A reference Earth model for the heat-producing elements and associated geoneutrino flux. *Geochemistry, Geophysics, Geosystems*, 14: 2003–2029, doi:10.1002/ggge.20129.
- Jackson, M. G., Hart, S. R., Koppers, A. A. P., Staudigel, H., Konter, J., Blusztajn, J., et al. 2007. The return of subducted continental crust in Samoan lavas. *Nature*, 448@ 684–687.
- Jacobsen, S. B. and Wasserburg, G. J. 1979. The mean age of mantle and crustal reservoirs., *Journal of Geophysical Research*, 84: 7411–7427.
- Kato, T., Ringwood, A. E. and Irfune, T. 1988. Experimental determination of element partitioning between silicate perovskites, garnet and liquids: constraints on early differentiation of the mantle. *Earth and Planetary Science Letters*, 89: 123–145,
- Kay, R. W. and Kay, S. M. 1991. Creation and destruction of lower continental crust. *Geologisches Rundschau*, 80: 259–278.
- Klein, E. M., Langmuir, C. H., Zindler, A. and H. Staudigel, B. H. 1988. Isotope evidence of a mantle convection boundary at the Australian-Antarctic Discordance. *Nature*, 333: 623–629.
- McDonough, W. F. and Sun, S.-S. 1995. The composition of the Earth. *Chemical Geology*, 120: 223–253.
- McKenzie, D. P. and O’Nions, R. K. 1983. Mantle reservoirs and ocean island basalts, *Nature*, 301: 229–231.
- McKenzie, D.P. 1985. ^{230}Th - ^{238}U disequilibrium and the melting processes beneath ridge axes *Earth and Planetary Science Letters*, 72: 149–157.
- Meyzen, C. M., Blichert-Toft, J., Ludden, J. N., Humler, E., Mevel, C. and Albarede, F. 2007. Isotopic portrayal of the Earth’s upper mantle flow field. *Nature*, 447: 1069–1074,
- Montelli, R., Nolet, G., Dahlen, F. A., Masters, G., Engdahl, R. and Hung, S.-H. 2004. Finite-frequency tomography reveals a variety of plumes in the mantle. *Science*, 303:, 338–343, doi: 10.1126/science.1092485.
- Morgan, W. J. 1971. Convection plumes in the lower mantle. *Nature*, 230: 42–43.
- Navon, O. and Stolper, E. 1987. Geochemical consequences of melt percolation: the upper mantle as a chromatographic column. *Journal of Geology*, 95: 285–307.
- O’Neill, H. S. C. and Palme, H. 2008. Collisional erosion and the non-chondritic composition of the terrestrial planets. *Philosophical Transactions of the Royal Society A*, 366: 4205–4238, doi: 10.1098/rsta.2008.0111.
- O’Nions, R. K., Evensen, N. M. and Hamilton, P. J. 1979. Geochemical modelling of mantle differentiation and crustal growth. *Journal of Geophysical Research*, 84: 6091–6101.
- Palme, H. and O’Neill, H. S. C. 2003. Cosmochemical Estimates of Mantle Composition. In: *The Mantle and Core*. Heinrich, D. H. and Karl, K. T. (eds). Amsterdam: Elsevier.
- Paul, D., White, W. M. and Turcotte, D. L. 2002. Modelling the Pb isotopic composition of the Earth. *Philosophical Transactions of the Royal Society of London A*, 360: 2433–2474.
- Pearson, D. G., Canil, D. and Shirey, S. B. 2003. Mantle samples included in volcanic rocks: xenoliths and diamonds. In: *Treatise on Geochemistry v.2 The Mantle and Core*. Carlson, R. L. (ed.). Amsterdam: Elsevier.
- Phipps Morgan, J. 2000. Isotope topology of individual hotspot basalt arrays: Mixing curves or melt extraction trajectories? *Geochemistry, Geophysics, Geosystems*, 1: 1003, doi: 10.1029/1999gc000004.

- Porter, K. A. and White, W. M. 2009. Deep mantle subduction flux. *Geochemistry, Geophysics, Geosystems*, 10: Q12016, doi: 10.1029/2009gc002656.
- Pyle, D., Christie, D. M. and Mahoney, J. J. 1992. Resolving an isotopic boundary within the Australian-Antarctic Discordance. *Earth and Planetary Science Letters*, 112: 161–178,
- Schilling, J.-G. 1985. Upper mantle heterogeneities and dynamics. *Nature*, 314: 62–67.
- Sleep, N. H. 1990. Hotspots and mantle plumes: some phenomenology. *Journal of Geophysical Research*, 95: 6715–6736,
- Sobolev, A. V., Hofmann, A. W., Sobolev, S. V. and Nikogosian, I. K. 2005. An olivine-free mantle source of Hawaiian shield basalts. *Nature*, 434: 590–597, doi: 10.1038/nature03411.
- Spiegelman, M. 2000. Uservcalc: A web-based uranium series calculator for magma migration problems. *Geochemistry Geophysics, Geosystems*, 1: paper number 1999GC00030.
- Spiegelman, M. and Elliot, T. 1993. Consequences of melt transport for uranium series disequilibrium in young lavas, *Earth and Planetary Science Letters*, 118: 1–20.
- Srámek, O., McDonough, W. F., Kite, E. S., Lekifá, V., Dye, S. T. and Zhong, S. 2013. Geophysical and geochemical constraints on geoneutrino fluxes from Earth's mantle. *Earth and Planetary Science Letters*, 361: 356–366, doi: 10.1016/j.epsl.2012.11.001.
- Steinberger, B. and O'Connell, R. J. 1998. Advection of plumes in mantle flow: implications for hotspot motion, mantle viscosity and plume distribution. *Geophysical Journal International*, 132: 412–434.
- Stille, P., Unruh, P. M. and Tatsumoto, M. 1983. Pb, Sr, Nd and Hf isotopic evidence of multiple sources for Oahu basalts, Hawaii. *Nature*, 304: 25–29.
- Tatsumoto, M. 1978. Isotopic composition of lead in oceanic basalt and its implication to mantle evolution. *Earth and Planetary Science Letters*, 38: 63–87.
- von Huene, R. and Scholl, D. W. 1991. Observations at convergent margins concerning sediment subduction, subduction erosion, and the growth of continental crust. *Reviews of Geophysics*, 29: 279–316.
- Weis, D., Garcia, M. O., Rhodes, J. M., Jellinek, M. and Scoates, J. S. 2011. Role of the deep mantle in generating the compositional asymmetry of the Hawaiian mantle plume. *Nature Geoscience*, 4: 831–838, doi: 10.1038/ngeo1328.
- White, W. M., 1985. Sources of oceanic basalts: radiogenic isotope evidence, *Geology*, 13: 115–118.
- White, W. M. and Duncan, R. A. 1996. Geochemistry and geochronology of the Society Islands: new evidence for deep mantle recycling. In: *Earth Processes: Reading the Isotope Code*. Hart, S. R. and Basu, A. (eds). Washington: AGU.
- White, W. M. and Klein, E. M., 2013. The composition of the oceanic crust. In: *Treatise on Geochemistry v. 2: The Crust*. Rudnick, R. (ed). Amsterdam: Elsevier.
- White, W. M., 2010. Oceanic island basalts and mantle plumes: The geochemical perspective, *Annual Review of Earth and Planetary Sciences*, 38: 133–160, doi: 10.1146/annurev-earth-040809-152450.
- White, W. M., McBirney, A. R. and Duncan, R. A. 1993. Petrology and geochemistry of the Galapagos: Portrait of a pathological mantle plume. *Journal of Geophysical Research*, 93: 19533–19563.
- White, W. M. and Hofmann, A. W. 1982. Sr and Nd isotope geochemistry of oceanic basalts and mantle geochemistry, *Nature*, 296: 821–825.
- Willbold, M. and Stracke, A. 2010. Formation of enriched mantle components by recycling of upper and lower continental crust. *Chemical Geology*, 276: 188–197, doi: 10.1016/j.chemgeo.2010.06.005.
- Wilson, J. T. 1963. Evidence from islands on the spreading of the ocean floors. *Nature*, 197: 536–538.
- Workman, R., Hart, S. R., Jackson, M., Regelous, M., Farley, K. A., Blusztajn, J., et al. 2004. Recycled metasomatized lithosphere as the origin of the Enriched Mantle II (EM2) end member: Evidence from the Samoan Volcanic Chain. *Geochemistry Geophysics, Geosystems*, 5: doi: 10.1029/2003GC000623.
- Wörner, G., Zindler, A., Staudigel, H. and Schmincke, H. U. 1986. Sr, Nd, and Pb isotope geochemistry of tertiary and quaternary alkaline volcanics from West Germany. *Earth and Planetary Science Letters*, 79: 107–119.
- Zindler, A. and Hart, S. R. 1986. Chemical Geodynamics, *Annual Review of Earth and Planetary Sciences*, 14: 493–571.

SUGGESTIONS FOR FURTHER READING

- Keppie, D. F., Currie, C. A. and Warren, C. 2009. Subduction erosion modes: Comparing finite element numerical models with the geological record. *Earth and Planetary Science Letters*, 287: 241–254.
- Menzies, M. A. and Hawkesworth, C. J. (eds) 1987. *Mantle Metasomatism*. London: Academic Press.
- Wasserburg, G. J. and DePaolo, D. J. 1977. Models of earth structure inferred from neodymium and strontium isotopic abundances. *Proceedings of the National Academy of Sciences of the United States*, 74: 3594–3598.

PROBLEMS

- Assume that the depleted mantle has a $\varepsilon_{\text{Nd}} = +8$, that the Earth is 4.56 billion years old and that the depleted mantle has evolved with constant $^{147}\text{Sm}/^{144}\text{Sm}$ since that time. What is the value of that $^{147}\text{Sm}/^{144}\text{Nd}$ ratio? Chondritic $^{143}\text{Nd}/^{144}\text{Nd}$ and $^{147}\text{Sm}/^{144}\text{Nd}$ are 0.51268 and 0.1966, respectively.
- Assume that the depleted mantle has a $^{87}\text{Sr}/^{86}\text{Sr} = 0.7029$, that the Earth is 4.56 billion years old and has that the depleted mantle evolved with constant $^{87}\text{Rb}/^{86}\text{Sr}$ since that time, and that its initial $^{87}\text{Sr}/^{86}\text{Sr} = 0.7000$. What is the value of that $^{87}\text{Rb}/^{86}\text{Sr}$ ratio?
- Plot the evolution of a reservoir that has $\mu = 8$ from 4.456 to 2.7 Ga and a $\mu = 10$ from 2.7 Ga to the present on a $^{207}\text{Pb}/^{204}\text{Pb}$ - $^{206}\text{Pb}/^{204}\text{Pb}$ diagram. Assume a present $^{238}\text{U}/^{235}\text{U}$ of 137.82. Also plot the 4.456 Ga Geochron on this diagram. (*Hint: μ is defined as the present $^{238}\text{U}/^{204}\text{Pb}$ ratio. The latter changes with time due to radioactive decay. Equations such as 3.8 describe Pb isotope ratios in terms of present parent daughter ratios – you will have to modify them for this problem.*)
- Assuming the following: the concentration of Nd in the bulk silicate Earth is 1 ppm, that of the continental crust is 22 ppm, the $^{147}\text{Sm}/^{144}\text{Nd}$ of the continents is 0.12, average age of the continents is 2.2 Ga, the present chondritic $^{143}\text{Nd}/^{144}\text{Nd}$ is 0.51268, the present chondritic $^{147}\text{Sm}/^{144}\text{Nd}$ is 0.1966, the ε_{Nd} of the depleted mantle is +8, mass of the continents is 0.5% of the mass of the silicate Earth. Calculate mass of the depleted mantle as a fraction of the mass of the silicate Earth assuming the silicate Earth has $\varepsilon_{\text{Nd}} = 0$ and $\varepsilon_{\text{Nd}} = +4$.
- The most extreme HIMU Pb isotope compositions are about $^{206}\text{Pb}/^{204}\text{Pb} = 22$ and $^{208}\text{Pb}/^{204}\text{Pb} = 40.5$. What is the corresponding $^{208}\text{Pb}^*/^{206}\text{Pb}^*$ ratio? What is the time-integrated value of κ ?
- Using the default values in UserCalc (www.ldeo.columbia.edu/~mspieg/UserCalc/), calculate activity ratios ($^{230}\text{Th}/^{238}\text{U}$), ($^{226}\text{Ra}/^{230}\text{Th}$), and ($^{231}\text{Pa}/^{235}\text{U}$) and produce a 1D column plot similar to Figure 6.26. If this basalt has a $^{232}\text{Th}/^{238}\text{U}$ atomic ratio (i.e., κ), where would it plot on Figure 6.24?
- Assume that the HIMU reservoir with present $^{206}\text{Pb}/^{204}\text{Pb} = 21$ and $^{207}\text{Pb}/^{204}\text{Pb} = 15.85$ evolved by a single differentiation event (a single change in μ) from the bulk silicate Earth, whose present $^{206}\text{Pb}/^{204}\text{Pb} = 18.1$ and $^{207}\text{Pb}/^{204}\text{Pb} = 15.5$. When would this hypothetical differentiation event have occurred?

Chapter 7

Radiogenic isotope geochemistry of the continental crust and the oceans

7.1 INTRODUCTION

The continental crust is the most accessible part of the Earth and, therefore, certainly the part we know most about. That, however, is not to say that we know it well; there is still uncertainty about the overall composition, age, and evolution of the crust. This is to say that there is still much work left for future generations of earth scientists, and geochemists in particular. This is because the continental crust is remarkably complex tapestry of terrains with different histories. In the previous chapter we assumed that the crust has been created through time (rather than all at the beginning, as the core was). In this chapter we will review the evidence that this was indeed the case. Isotope geochemistry is a particularly powerful tool in unraveling crustal genesis, precisely because the crust has evolved and changed over time. The Earth has, of course, two kinds of crust: continental and oceanic. The continental crust is thick, low density, and persistent. The oceanic crust is thin, dense, and ephemeral, continually being created and destroyed such that its average age is only 60 million years. It consists almost entirely of mid-ocean ridge basalts and related intrusive rocks. It is compositionally and structurally simple in comparison to continental crust. In this chapter, we will focus on continental crust, which, being thicker and more persistent, better qualifies and an important terrestrial reservoir.

Erosion products of the continents are carried to the oceans by rivers and winds.

Hydrothermal systems at mid-ocean ridges and elsewhere also add radiogenic elements, most notably Sr, to seawater. This processes lead to isotopic variations in seawater in space and time. In the latter part of this chapter, we will see how radiogenic isotope ratios in seawater and sediments precipitated from seawater are used to trace the evolution of the Earth's surface through time as well to trace changing patterns of ocean circulation.

7.2 GROWTH OF THE CONTINENTAL CRUST THROUGH TIME

7.2.1 Mechanisms of crustal growth

There is unanimous agreement the crust has formed through magmatism: partial melting of the mantle followed by buoyant rise of those melts to the surface. There is less agreement on the details. Furthermore, the composition of the continental crust is problematic in the context of this hypothesis because it does not have the composition of a mantle-derived magma. This suggests that evolution of the crust is more complex than simple melt extraction from the mantle. We can identify a number of possible mechanisms that would result in the creation of new continental crust. Most of these mechanisms suffer from the problem that they result in a more mafic crust than that observed.

- *Accretion of oceanic crust and oceanic plateaus.* The oceanic crust is generally subducted and returned to the mantle.

It might in unusual situations be thrust upon or under continental crust. Subsequent melting of the basalt could produce granite. Thick oceanic plateaus produced by mantle plumes such as Ontong-Java and Iceland would be subducted less readily than normal oceanic crust. Their isotopic composition would be less depleted.

- *Underplating.* Because of the low density of the continental crust, magmas have difficulty rising through it and may become trapped at the crust-mantle boundary. This produces new basaltic lower crust, which upon remelting would produce a granitic upper crust.
- *Continental volcanism.* For example, flood basalts have occasionally been erupted in tremendous volumes. Volcanism and underplating may occur simultaneously.
- *Subduction-related volcanism.* Volcanism is usually present along active continental margins. Most of the magma is of mantle derivation. Accretion of intra-oceanic island arcs to continents is a closely related mechanism.

It is clear that at present, and almost certainly throughout the Phanerozoic, the last mechanism has produced the greatest additions to continental crust. It is tempting to assume this has been the case throughout geologic time, but this has not been demonstrated unequivocally. Because subduction zones appear to play such a key role in the evolution of the crust and mantle, we will discuss them in more detail in a subsequent section. In all the previously-mentioned mechanisms, there must be some additional mechanism by which the crust loses a mafic component. The most probable is lower crustal foundering; the lower crust, under some circumstance becomes so dense that it sinks into the mantle. In addition, weathering and erosion tend to remove Mg in preference to Si and Al. Rivers then carry Mg to the ocean where hydrothermal activity transfers it into the oceanic crust.

7.2.2 The Hadean eon and the earliest continental crust

The Hadean eon is defined as the time of Earth's formation and preceding the geologic record. The oldest surviving continental crust

is the 3.92 Ga Acasta gneiss in Canada's Northwest Territory, and thus marks beginning of the geologic record and the end of the Hadean eon (defined as the time before the oldest rocks). One zircon from the Acasta gneisses has a 4.20 ± 0.06 Ga core surrounded by a rim with an age of 3.8 to 3.9 Ga (Iizuka et al., 2006) indicating these gneisses formed from even older, Hadean crustal protoliths. Even older zircon cores, with ages of up to 4.4 Ga, have been found in mid- to late-Archean quartzite (metamorphosed sandstone) from the Jack Hills of Western Australia. The Acasta and Jack Hills zircons are the only known survivors of the Earth's Hadean eon. As we will see, however, isotope ratios of rocks from the subsequent Archean eon provide insights into this earliest part of Earth's history.

7.2.2.1 Evidence of a late accretionary veneer?

As we found in Chapter 5, ^{182}Hf (half-life 9 Ma) was present in the early Solar System and the silicate Earth's $^{182}\text{W}/^{184}\text{W}$ is about 2 epsilon units higher than chondrites. The difference reflects sequestration of W in the Earth's core (or, more likely, the cores of the planetary embryos that accreted to form the Earth) before ^{182}Hf completely decayed, leaving the silicate Earth and Moon enriched in ^{182}W . Subsequently, increased precision has led to the discovery of small variations in ϵ_{W} in Archean rocks. Willbold et al. (2011) reported an average ϵ_{W} of $+0.13 \pm 0.04$ (2σ) for seven samples of 3.8 Ga Isua (southwest Greenland) including gneisses, metabasalts, and metasediments (individual samples were identical within analytical error). The positive values imply the source of these rocks had a higher Hf/W ratio than modern Earth materials. How can we explain this? The hint is that the silicate Earth is richer in siderophile elements such as W, Re, and Os than one would expect from equilibrium partitioning between a metal core and silicate mantle (see Section 2.7). A long-standing hypothesis to explain this is addition of a "late veneer" of chondritic material that accreted to the Earth after final segregation of the core in the Moon-forming giant impact (Chou, 1978; Wänke et al., 1984). A later veneer is consistent with the cratering history of the Moon, which culminates in a "late heavy bombardment" at about

3.9 Ga as well as with computer simulations of planetary accretion. An amount of chondritic material equaling less than 1% of the mass of Earth would explain the high siderophile abundances in the silicate Earth. If this late veneer were undifferentiated chondritic material it would have ϵ_W of -2 (Figure 5.13), so adding it would decrease the ϵ_W of the Earth. If the Earth today has ϵ_W of 0, it must have had a higher value before the addition of the late accretionary veneer. This is just what Willbold et al. (2011) proposed, namely that the Isua samples retain a memory of the Earth's ϵ_W before addition of the late accretionary veneer. The decline of Earth's ϵ_W from +0.13 to 0 is consistent with addition of just under 0.5% by mass of chondritic material. The data do not directly constrain the timing of the addition, but are most easily explained if the addition occurred after ^{182}Hf was effectively extinct, or more than ~50 million years after the start of the Solar System. All the analyzed rocks display excesses in ^{142}Nd that, as we discuss in the next section, implying they formed from precursor material that had differentiated from the primitive mantle within ~200 million years or less of the start of the Solar System.

The following year, Touboul et al., (2012) reported ϵ_W averaging $+0.15 \pm 0.05$ in 2.8 billion year old komatiites (which are ultramafic lava flows) from Kostomucksha in the Karelia region the Baltic Shield of northeastern Russia. Several interpretations are possible: that metal separated from the mantle source region of these lavas earlier than the rest of the Earth's mantle; that silicate differentiation of the mantle fractionated Hf/W ratios subsequent to core formation; or that the lavas are derived from a part of the mantle into which the late veneer has not been mixed. Touboul et al. also reported that 3.5 billion year old komatiites from Komati, South Africa, have normal tungsten isotopic composition. Willbold et al. (2013) reported ϵ_W values comparable to those found in rocks from the Isua supracrustal belt in the 3.92 Ga Acasta gneisses of the Northwest Territories of Canada and Touboul et al. (2013) reported that the 3.8 Ga Nuvvuaggittuq supracrustals of Labrador have ϵ_W of +0.15, similar to the Isua supracrustals and Kostomucksha komatiites. They also found that much younger 2.4 Ga Vetreny komatiites, located to the southeast of the Karelia region

in Russia have slight ^{182}W excesses, averaging ϵ_W of $+0.062 \pm 4.5$ ppm (2σ , $n = 5$). In contrast, they found that the 3.3. Ga Barberton komatiites of South Africa have tungsten isotopic compositions similar to the modern Earth (i.e., $\epsilon_W \approx 0$). As may be seen in Figure 5.13, these variations are small compared to those observed in extraterrestrial materials.

Thus, the silicate Earth appears to have had a heterogeneous tungsten isotopic composition in the Archean, perhaps because convection had not yet succeeded in mixing the late accretionary veneer into the mantle or to fully homogenize the mantle following crystallization of a magma ocean. The uniform ϵ_W in the three early Archean localities, Isua, Acasta, and Nuvvuaggittuq, however, is consistent with the idea that mantle that had an initially homogeneous ϵ_W of about +0.15 and that ϵ_W subsequently decreased to 0 as a late veneer of chondritic material was slowly mixed into the mantle. Subsequent convection apparently homogenized the mantle such that only a hint of the initial higher ϵ_W remained by the early Proterozoic and no trace of that remains today as all modern mantle-derived rocks have uniform ϵ_W .

7.2.2.2 ^{142}Nd evidence of Hadean crust formation

In addition to the Acasta gneisses, early Archean crust of approximately 3.7 Ga and older has been found in Greenland, Labrador, Western Australia, and India. The total volume of this crust, however, is quite small. This raises some profound questions: how and when did the earliest crust form? Did only a small volume form initially, or did a much larger volume form, with only a small fraction of that surviving to the present?

$^{142}\text{Nd}/^{144}\text{Nd}$ ratios along with $^{176}\text{Hf}/^{177}\text{Hf}$ and $^{143}\text{Nd}/^{144}\text{Nd}$ are beginning to provide fairly clear evidence that differentiation of the Earth began early (Figure 7.1). As we found in Chapter 5, modern terrestrial samples have $^{142}\text{Nd}/^{144}\text{Nd}$ that is about 20 ppm, or 0.2 epsilon units, higher than chondritic. However, samples from the early Archean Amitsoq Complex of West Greenland have $^{142}\text{Nd}/^{144}\text{Nd}$ that is up to an additional 20 ppm higher than that (Caro et al., 2003, Boyet et al. (2003), Bennett et al., 2007, Rizo

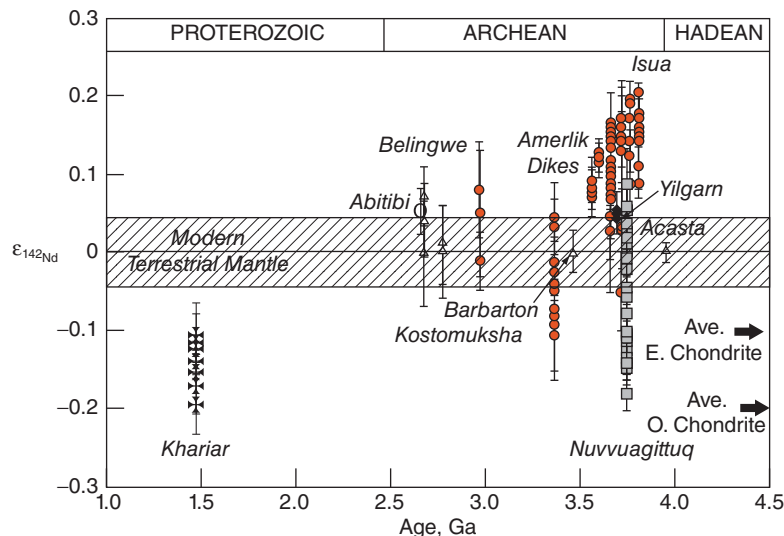


Figure 7.1 $^{142}\text{Nd}/^{144}\text{Nd}$ (expressed in epsilon units from a terrestrial standard) as a function of age in terrestrial samples. Circles are from Greenland, gray squares from Labrador, black diamonds from Western Australia, and crosses from Khariar, India, black circle from Theo's Flow, Canada. (Source: Adapted from Bennett et al. (2007) and Rizo et al. (2012).)

et al. 2013). $^{142}\text{Nd}/^{144}\text{Nd}$ excess of 5 ppm were also found in two 3.7 Ga tonalites¹ from the Yilgarn block Western Australia (Bennett et al., 2007). The $^{142}\text{Nd}/^{144}\text{Nd}$ excesses indicate that these early crustal rocks were derived from a mantle reservoir having a Sm/Nd ratio higher than chondritic and higher than modern bulk silicate (observable) Earth. High Sm/Nd ratios are indicative of trace element depletion, indicating these rocks were derived from mantle that had experienced even earlier episodes of crust creation. An early incompatible element-enriched crust that formed either by fractional crystallization of a primordial magma ocean or by partial melting of the mantle, would leave part of the mantle incompatible element-depleted. Early Archean crust formed by subsequent melt extraction from that depleted mantle would have high $^{142}\text{Nd}/^{144}\text{Nd}$. Thus, some of the oldest rocks on Earth suggest crust formation began even earlier – well before 4.0 Ga and arguably before 4.4 Ga. On this point there is no debate. The crucial question, and one that is debated, is how much?

A particularly interesting twist to this was reported by O’Neil et al. (2008). They found negative $\epsilon_{142\text{Nd}}$ values in amphibolites from the Nuvvuagittuq Belt of northwestern Labrador and this has recently been confirmed

by additional analyses of O’Neil et al. (2012) and Roth et al. (2013). There is a strong correlation between $^{142}\text{Nd}/^{144}\text{Nd}$ and $^{147}\text{Sm}/^{144}\text{Nd}$ in a subset of rocks from the area, cummingtonite amphibolites (Figure 7.2). As we found in Chapter 5, when an extinct radionuclide is involved, the slope of the line on plots such as this is proportional to the parent isotope ratio, in this case $^{146}\text{Sm}/^{144}\text{Sm}$, at the time the rocks formed. Using both the data from O’Neil et al. and Roth et al., the slope in the case for the cummingtonite amphibolites corresponds to $^{146}\text{Sm}/^{144}\text{Sm} = 0.00116$. Using a ^{147}Sm half-life of 68 Ma and the Solar System initial $^{146}\text{Sm}/^{144}\text{Nd}$ of 0.0094, the apparent age is 4.36 Ga. Other suites of rocks from the region yield $^{142}\text{Nd}/^{144}\text{Nd}$ – $^{147}\text{Sm}/^{144}\text{Nd}$ pseudo-isochrons corresponding to ages ranging from 4.31–4.41 Ga (O’Neil et al., 2012). However, a $^{147}\text{Sm}/^{144}\text{Nd}$ – $^{143}\text{Nd}/^{144}\text{Nd}$ isochron for the cummingtonite amphibolites gives an age of only 3.89 Ga with considerable uncertainty and other suites in the area give even younger ages. There are no zircons in the mafic rocks, but crystallization age of zircons in felsic rocks as well as detrital zircons in metasediments give ages that range from 3.75–3.78 Ga, which is likely the maximum age of the Nuvvuagittuq supracrustal belt (Cates, 2013).

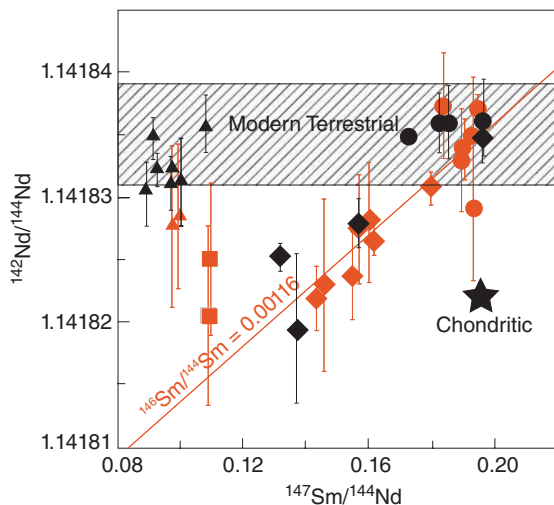


Figure 7.2 $^{142}\text{Nd}/^{144}\text{Nd}$ versus $^{147}\text{Sm}/^{144}\text{Nd}$ for rocks from the Nuvvauqittuq Belt of northwestern Labrador. The slope of the line corresponds to a $^{146}\text{Sm}/^{144}\text{Nd}$ ratio of 0.00116. If this line is interpreted as an isochron, it implies a formation age of 4.36 Ga. Triangles: felsic gneisses, diamonds, cummingtonite amphibolite, circles: hornblende amphibolites. Square symbols from O'Neil et al. (2008); diamond symbols from Roth et al. (2013). (Source: Adapted from O'Neil et al., 2008 and Roth et al., 2013.)

An alternative interpretation is that the Nuvvauqittuq $^{142}\text{Nd}/^{144}\text{Nd}$ – $^{147}\text{Sm}/^{144}\text{Nd}$ correlations are mixing lines resulting from assimilation of early crust by a much later basaltic magma rising from the mantle. Modeling done by Cates et al. (2013) suggests this assimilated crust could have formed at 4.5 Ga, and that metamorphism of the amphibolites (which they speculate were originally pyroclastic rocks) formed around 3.8 Ga, resulted in decoupling of the $^{142}\text{Nd}/^{144}\text{Nd}$ and $^{143}\text{Nd}/^{144}\text{Nd}$ ages. While the amphibolite is much younger (3.8–4.0 Ga) in this interpretation, the $^{142}\text{Nd}/^{144}\text{Nd}$ – $^{147}\text{Sm}/^{144}\text{Nd}$ correlation nevertheless provides evidence of an early-formed incompatible element-enriched crust with low Sm/Nd.

Rizo et al. (2012) subsequently reported ^{142}Nd deficits in the 3.4 Ga mafic Amerlik dikes, which intrude the early Archean Isua supracrustals and surrounding gneisses. They argue these magmas were derived from a low Sm/Nd reservoir that formed before 4.47 Ga

either as a result of crystallization of a magma ocean or an early mafic protocrust.

The largest $^{142}\text{Nd}/^{144}\text{Nd}$ anomalies are found in the earliest Archean rocks. Variations in $^{142}\text{Nd}/^{144}\text{Nd}$ appear to decline through the Archean, and most rocks younger than 3.5 Ga have $\epsilon_{142\text{Nd}}$ whose errors overlap the range of the modern terrestrial mantle ($\epsilon_{142\text{Nd}} = 0 \pm 0.05$). One exception is Theo's flow, a komatiitic lava flow from the 2.7 Ga Abitibi belt in Quebec that has $^{142}\text{Nd}/^{144}\text{Nd}$ ratios ($\epsilon_{142\text{Nd}} = 0.07 \pm 0.03$) barely outside the modern mantle range (Debaillé et al., 2013). Again, this positive $\epsilon_{142\text{Nd}}$ is the signature of mantle depleted in Nd relative to Sm by melting extraction in the first 100 Ma or so of Earth history, implying that remnants of this early depleted mantle persisted at least locally through much of the Archean. Debaille et al. (2013) point out that this is surprising since we would expect convective mixing to scale with heat production, which decreases exponentially with time. They suggest the persistence of heterogeneity implies a convective style that lacked subduction and plate tectonics and that was less efficient at mixing out mantle heterogeneity in the Archean. A variety of studies carried out with increasing precision have found that the modern mantle has a homogeneous $^{142}\text{Nd}/^{144}\text{Nd}$ (e.g., Jackson and Carlson, 2012), implying these heterogeneities were eventually erased.

The only case of ^{142}Nd anomalies in post-Archean rocks is the 1.48 Ga Khariar nepheline syenites from southeastern India, which have $\epsilon_{142\text{Nd}}$ as low as –0.13. Upadhyay et al. (2009) interpret these igneous rocks have having sampled a very ancient incompatible element-enriched reservoir that survived in the lithospheric mantle beneath the Bastar craton of India until 1.5 Ga. These data suggest that some parts of the mantle managed to avoid mixing processes that have homogenized isotopic and chemical heterogeneities that were present in the early mantle. That some heterogeneity survived for 3 billion years may be less surprising than the opposite observation: nearly all initial heterogeneity in the Earth's mantle has been eliminated by mixing. The Khariar syenites intruded into the Archean Bastar (or Bhandara) craton that include 3.5-Ga-old gneisses. Upadhyay et al. (2009) suggest that the Khariar syenites were derived from the lithospheric root beneath

the ancient Bastar craton. Because the lithosphere does not experience convective mixing, ancient chemical and isotopic heterogeneity can survive. The Khariar results are presently somewhat controversial. As analytical precision improves, however, we may see additional examples of rocks with resolvable $^{142}\text{Nd}/^{144}\text{Nd}$ anomalies will be found, particularly in mid-to late Archean rocks.

Could the Archean $^{142}\text{Nd}/^{144}\text{Nd}$ heterogeneity, like that of $^{182}\text{W}/^{184}\text{W}$, be due to a late accretionary veneer? The answer is no. First, the difference in $^{142}\text{Nd}/^{144}\text{Nd}$ between the silicate Earth and chondrites is more than an order of magnitude smaller than for $^{182}\text{W}/^{184}\text{W}$. Second, the mantle is richer in Nd than are chondrites, while chondrites have five to six times greater W concentrations than does the mantle. Thus, small addition of chondritic material affects the mantle's $^{182}\text{W}/^{184}\text{W}$, it has virtually no effect on its $^{142}\text{Nd}/^{144}\text{Nd}$.

7.2.2.3 Evidence of Hadean crust from zircons and ϵ_{Hf}

A few tiny detrital (that is, eroded from their original rocks and deposited in sediments) zircon crystals are all that remain of Hadean crustal rocks that once must have existed in Australia. The Jack Hills zircons occur in a metasedimentary conglomerate thought to be about 3 billion years old. The metasediments are surround by the Narryer gneisses (3.65–3.3 Ga), which were intruded by granites at 2.65 Ga. The majority of zircon crystals are about 3.6–3.8 billion years old, but a small fraction are older than 4 billion years and the oldest date is 4.4 billion years (Figure 3.10). Despite the extremely small volume of this material, new micro-analytical techniques are providing a wealth of information on crust from which these crystals were eroded. The zircons have complex histories, and the very old ages were only discovered by analyzing individual zones with the ion micro-probe (Froude et al., 1983; Compston and Pidgeon, 1986). More recently, it has become possible to determine Pb-Pb ages using laser ablation multi-collector inductively coupled plasma mass spectrometry (LA-MC-ICP-MS). This technique can also determine other isotope ratios and elemental abundances on regions as small as 50 μm in diameter. Hf is

strongly concentrated in zircon so that Lu/Hf ratios are quite low. Consequently, initial Hf isotopic compositions are quite readily determined. Several groups had studied the Hf isotopic compositions of the zircons. However, interpretation is difficult because the zircons are often zoned with overgrowths as young as 3.3 Ga (Harrison et al., 2005). Blichert-Toft and Albarède (2008) determined both Pb-Pb ages and Hf isotopic compositions by bulk analysis using MC-ICP-MS. They found a nearly Gaussian distribution of ages with a mode of about 4.1 Ga. Initial ϵ_{Hf} calculated for this time show range of values, with a mode of about -3. The negative values imply the zircons formed in rocks derived from an older incompatible element-enriched precursor. The problem with bulk analyses of zircons having complex histories is that it integrates diverse age and Hf isotope ratio in a single analysis, which can produce mixtures that are at best impossible to deconvolve.

Kemp et al. (2010) simultaneously determined both Hf isotope compositions and Pb-Pb ages on the Jack Hills detrital zircons as well as from the surrounding Narryer gneisses and intrusive granites. The new results reveal a much simpler picture of early crustal evolution than earlier studies. The data scatter about a relatively simple ϵ_{Hf} evolutionary path of increasingly negative ϵ_{Hf} with time (Figure 7.3), in contrast to the much greater scatter of earlier data. Recall that in a plot such as this of an isotope ratio versus time, slopes are proportional to the parent-daughter ratio. The slope of the least disturbed detrital Jack Hills zircons corresponds to a $^{176}\text{Lu}/^{177}\text{Hf}$ ratio of about 0.019 and project back to $\epsilon_{\text{Hf}} = 0$ at 4.46 ± 0.12 Ga. This Lu/Hf ratio is typical of mafic (i.e., basaltic) rocks. In Kemp et al.'s (2010) interpretation, the zircons were derived from granitic rocks produced by partial melting of an enriched, dominantly mafic protolith that was extracted from primordial mantle at 4.4–4.5 Ga. The lowest ϵ_{Hf} in zircons from younger meta-igneous Narryer gneisses plot near an extension of the ϵ_{Hf} – time array defined by the Hadean detrital zircons (Figure 7.4). From this, Kemp et al. argue that Hadean crust may have contributed substantially to the younger Archean magma. Vervoort et al. (2013) caution, however, that ancient Pb loss in these old complex zircons

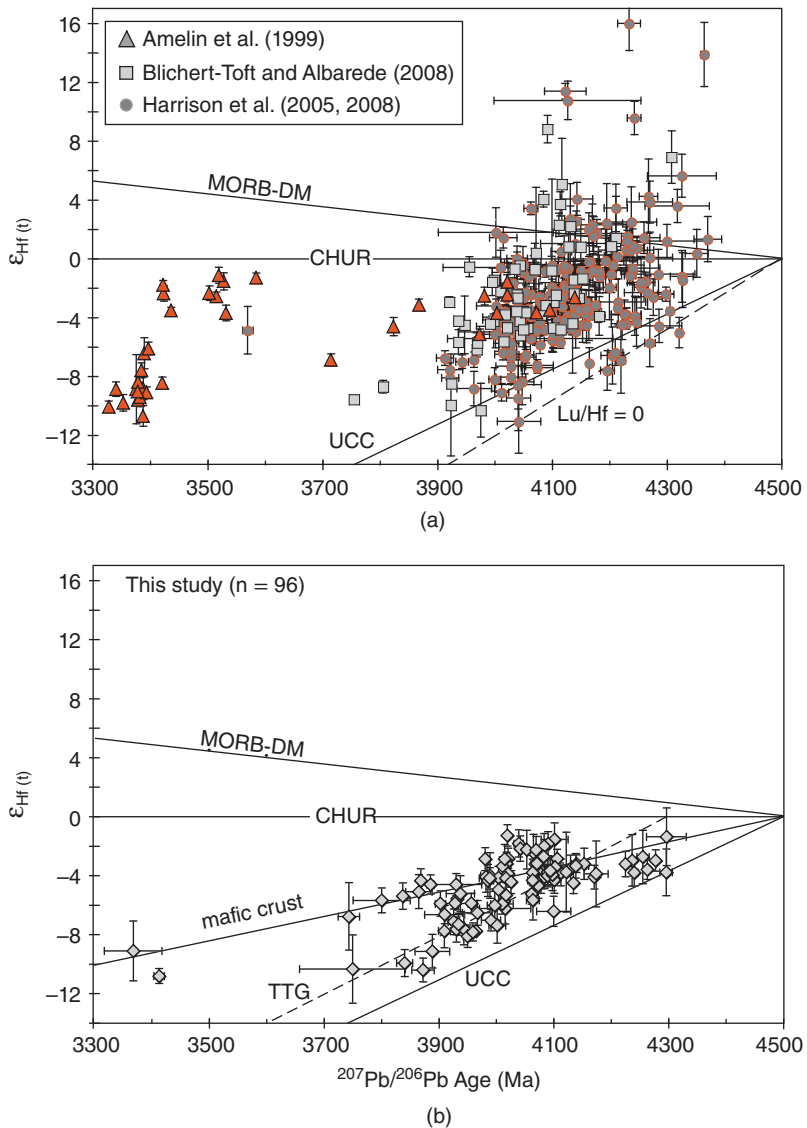


Figure 7.3 Hf isotope evolution plots for the Jack Hills detrital zircons comparing (a) previously published datasets with (b) data obtained during by Kemp et al. (2010). The isotope trajectories of upper continental crust, mafic crust and tonalite-tronjhemite granite suites (TTG) (formed at 4.3 Ga with $^{176}\text{Lu}/^{177}\text{Hf} = 0.005$, Blichert-Toft and Albarède, 2008) are shown for reference as is a depleted mantle-MORB evolution curve (MORB-DM). (Source: Adapted from Kemp et al. (2010). Reproduced with permission of Elsevier.)

can produce younger apparent ages that are unrelated to crustal reworking. They further argue that the depleted mantle evolution curve (shown in Figures 7.3 and 7.4) for Hf is poorly constrained and may not diverge from CHUR until nearly 3.8 Ga. The implication of this is that large-scale crustal formation may have not begun prior to 3.8 Ga.

Remarkably, the Jack Hills zircons plot along the same evolutionary path displayed by

zircons from Apollo 14 lunar breccias (Taylor et al., 2009). From this Kemp et al. speculate that the mafic protolith may have formed during the solidification of a terrestrial magma ocean analogous to the lunar one.

As Figure 7.4 shows, data from early Archean rocks from Greenland, Acasta, and the Baltic plot along trajectories with slopes implying slightly higher $^{176}\text{Lu}/^{177}\text{Hf}$ than the Jack Hills data and intersecting the CHUR or

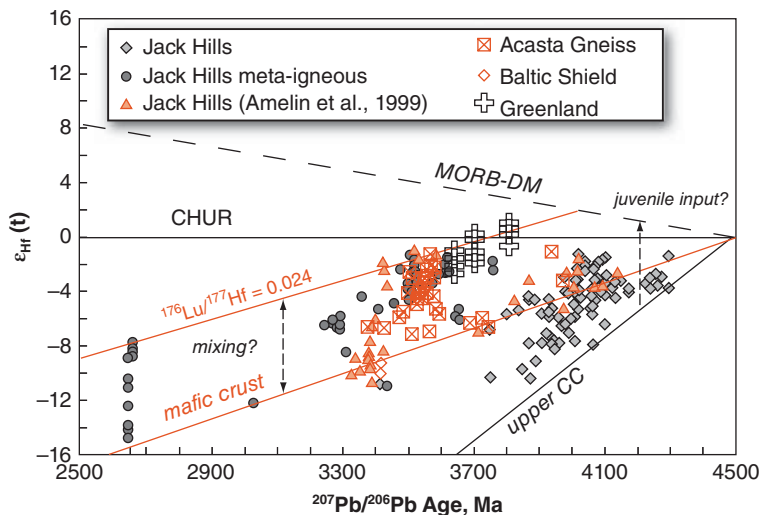


Figure 7.4 Hf isotope composition of zircons from the Jack Hills meta-igneous rocks in comparison to data from the detrital Jack Hills zircons, Greenland, the Acasta Gneisses, and the Baltic Shield. (Source: Adapted from Kemp et al. (2010). Reproduced with permission of Elsevier.)

depleted mantle evolution curves somewhat later, but nevertheless before 4.0 Ga. That would in turn imply that these rocks may also have been derived from Hadean protoliths. The implied Lu/Hf higher relative to modern upper continental crust suggests early Archean crust may have been more mafic. Indeed, it is likely thick felsic crust could not have survived long in the Archean because much higher radioactive heat production would have caused it to melt.

There is also some Pb isotope evidence that differentiation of the silicate Earth began very early. Figure 7.5 shows initial Pb isotope ratios from sulfide ores associated with submarine volcanic rocks that erupted in the Abitibi Belt of Canada around 2.7 Ga ago. The data plot virtually along the 2.7 Ga Geochron (the Geochron as it was 2.7 Ga ago). The most straightforward interpretation of this data is that it reflects heterogeneity in the mantle that dates from the time the Earth formed, or shortly thereafter.

We may summarize by saying that there is now clear evidence from geochronology and from $^{176}\text{Hf}/^{177}\text{Hf}$ and $^{142}\text{Nd}/^{144}\text{Nd}$ for the existence of Hadean crust but the question of the volume of that crust remains the subject of vigorous debate, because none of this crust has survived. Reworking of this Hadean crust may have given rise to some of the earliest

Archean rocks. Thus, we can conclude that the process of crust formation began very early in Earth's history, but certainly did not end in Hadean/Early Archean time.

7.2.3 Subsequent growth of the crust

If the crust has grown through time, at what rate and by what processes has it done so? We listed possible mechanisms at the start of the chapter; all undoubtedly operate, but which is dominant? While there is as yet no definitive answer to this question, it certainly has been given considerable study. Perhaps the first quantitative attempt to determine continental evolution rate was by Hurley and others (1962). They compiled radiometric ages (mainly Rb-Sr) of rocks in the North American continent to produce a map that looked similar to that shown in Figure 7.6. Hurley et al. recognized that age provinces in Figure 7.6 could be produced by either tectonic reworking (melting, metamorphism, etc.) of preexisting crust or new additions to crust. They also recognized they could distinguish reworked crust from new crust by initial Sr isotope ratios. They argued that because the crust has a higher Rb/Sr ratio than the mantle, new additions to crust should have lower initial $^{87}\text{Sr}/^{86}\text{Sr}$ ratios than material produced by reworking old crust. From consideration of

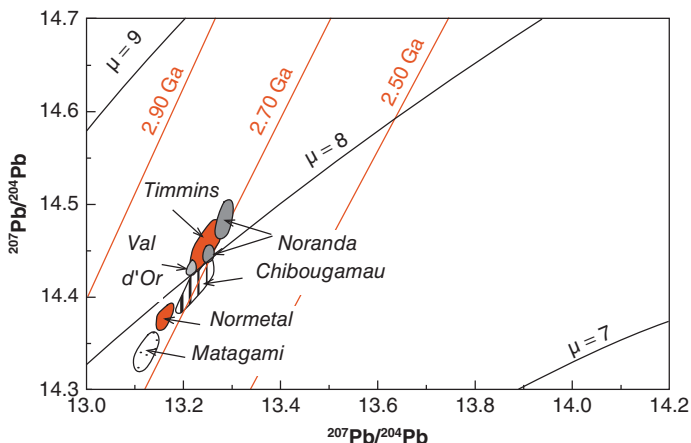


Figure 7.5 $^{207}\text{Pb}/^{204}\text{Pb}$ – $^{206}\text{Pb}/^{204}\text{Pb}$ plot showing Pb isotopic fields for volcanogenic massive sulfide deposits from the Abitibi greenstone belt. Also shown are single-stage Pb growth curves corresponding to μ values of 7, 8, and 9 and geochrons at 2.5, 2.7, and 2.9 Ga assuming an age for the Earth of 4.52 Ga. (Source: Vervoort, et al., 1994.)

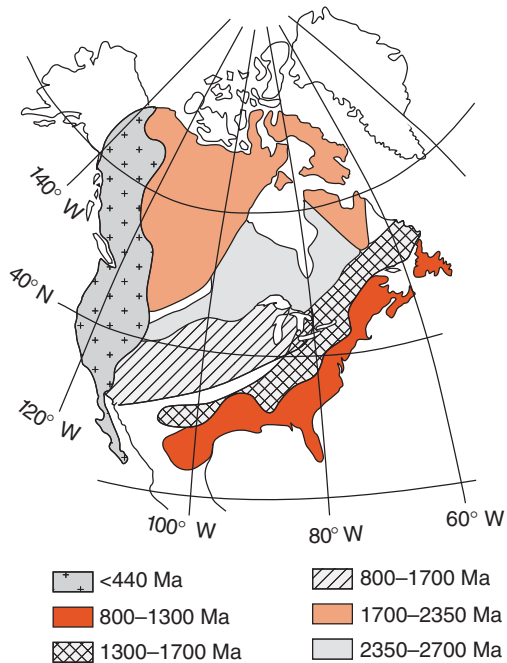


Figure 7.6 Age provinces of the North American continent (after Hurley and Rand, 1969). (Source: Adapted from Hurley et al., 1962.)

both age and initial isotopic composition, they argued that the crust had grown at a more or less steady rate through geological time.

The Rb-Sr system is particularly subject to resetting during metamorphism, so this is

certainly not the best geochronological system to determine the times at which new magmas were added to the continental crust. Condie (1998) and subsequently Condie and Aster (2010) compiled zircon ages, which are shown in Figure 7.7. There are several important results from this study. First, zircon ages are concentrated at 2700, 1870, 1000, 600, and 300 Ma, with the number of zircon ages in these peaks decreasing through time (there are sufficient numbers of age determinations, ~40,000, to guarantee that these peaks are not random artifacts). If these ages represent new additions to crust, then overall, crustal growth rates have slowed through time. A generally decreasing rate is what we might expect since the Earth is cooling and heat, both initial and radiogenic heat, is the source of energy for magmatism and tectonic activity. The peaks in the age histograms appear to coincide with supercontinent formation and the minima with supercontinent breakup.

Figure 7.7 also shows a variety of estimates of how crustal growth rates have varied through time, which are framed by the extreme estimates by Hurley and Rand (1969) and Armstrong (1981). As discussed earlier, the Hurley estimate was based on Rb-Sr geochronology and very likely overestimates the amount of young crust. Armstrong argued for a steady-state crustal mass. In his model the continental crust reached more or less its present mass in the early Archean and its mass

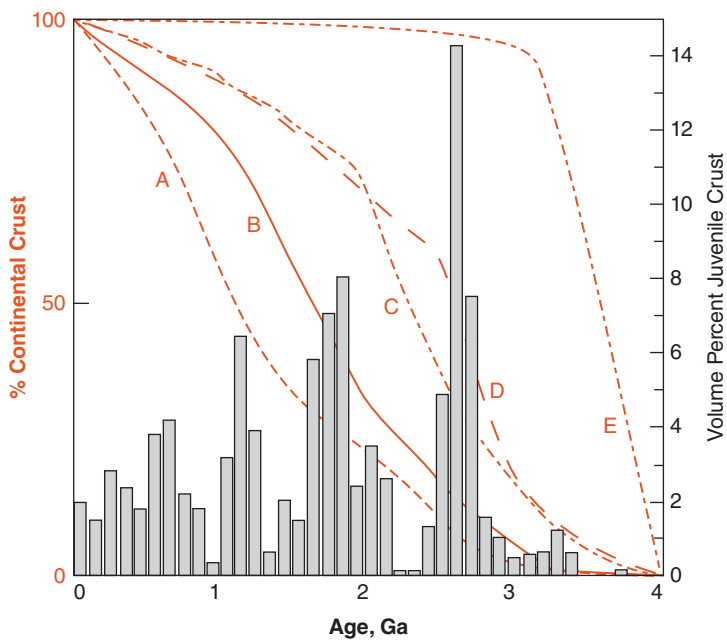


Figure 7.7 Histogram of U/Pb ages of juvenile igneous rocks (from Condie and Aster, 2010) compared with curves representing different models for changing volumes of stable continental crust through time. Curve A is Hurley and Rand (1969), B is based on Nd isotopes in shales (Allegré and Rousseau, 1984), C from Pb isotope modeling (Kramers and Tolstikhin, 1997) and D from Taylor and McLennan (1995) and E from Armstrong (1981). (Source: Replace with Adapted from Hawkesworth and Kemp (2006). Reproduced with permission of Elsevier.)

has remained approximately constant because new additions to crust have been balanced by losses as a result of erosion, sedimentation, and subduction. At least at present, this seems to be the case. Scholl and von Huene (2009) estimate the amount of continental crust being transported into the mantle (a combination of sediment subduction and subduction erosion) at $3.2 \text{ km}^3/\text{yr}^2$ and the rate of additions to crust through subduction zone magmatism at $2.8\text{--}3.0 \text{ km}^3/\text{yr}$; in other words crustal production and destruction are currently roughly in balance. The distribution of zircon crystallization ages shown in Figure 7.7 cannot rule out Armstrong's hypothesis because zircons can only record the ages of crust that has survived.

Nevertheless, in view of the comparatively large amount of surviving late Archean crust, the lack of surviving early Archean crust is surprising if Armstrong's hypothesis is correct. While the full crustal mass may not have been established by 4 Ga, Armstrong's steady-state model could survive in modified form, however, as Hawkesworth et al. (2010) suggest

that the present continental crust mass was established by 2–3 Ga.

Do the zircon crystallization ages shown in Figure 7.7 record new additions to crust or something else? Condie and Aster (2010) interpret the zircon age histogram as “probably related chiefly to preservation of juvenile crust in orogens during supercontinent assembly.” Hawkesworth et al. (2010) concur, suggesting that the peaks are artifacts of preservation marking the times of supercontinent formation. Hawkesworth et al. (2010) point out that magmatism associated with continental collisions (such as India and Asia) is dominated by remelting of older crust and granitic magmas, which are what dominate the upper continental crust). They also suggest that detritus, including detrital zircons, eroded from the collisional orogenic belts in the cores of supercontinents are more likely to be preserved than detritus from subduction zone volcanism. Thus, they argue that,

... that the record of magmatic ages is likely to be dominated by periods when supercontinents assembled, not because this is a major

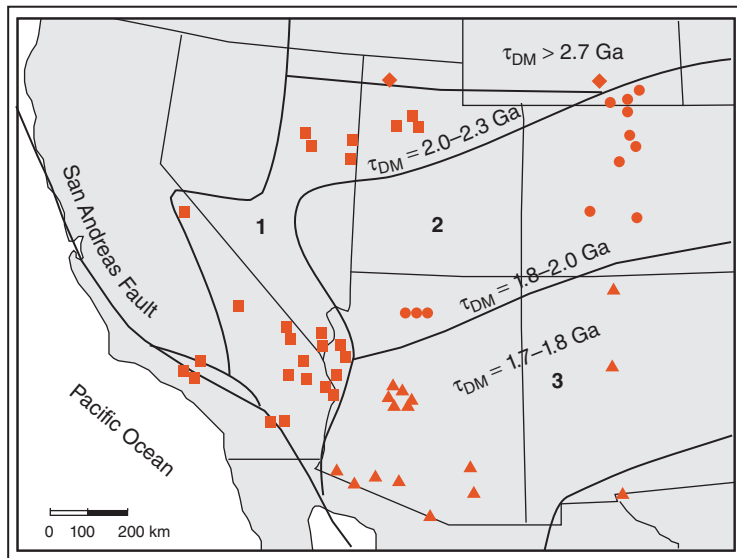


Figure 7.8 Isotopic provinces, based on crustal residence times (τ_{DM}) of the Western USA. (Source: Adapted from Bennett and DePaolo, 1987.)

phase of crust generation but because it provides a setting for the selective preservation of crust. The preservation potential, particularly for crystallization ages of zircons, is greater for late-stage collisional events as the supercontinents come together, rather than for subduction- and extension-related magmatism,

whereas it is the latter processes that predominantly create new continental crust. The record shown in Figure 7.7 is that much of that initially created crust does not long survive. Initial Nd and Hf isotope ratios and model ages provide approaches that can get around issue of preferential preservation, and we explore them next.

7.2.4 Nd and Hf isotopic approaches to crustal evolution

Nd isotope systematics provides a wonderful tool for examining the evolution of the continental crust. We have already discussed the concept of the Nd model ages, or crustal residence times (Section 2.5.1). Hf model ages can be calculated in an exactly analogous manner, although one must be cautious since Lu and Hf are relatively easily fractionated within the crust, unlike Sm and Nd. Here we will see how model ages can be used to infer when crustal material was first derived from the mantle. We

begin by examining the work of Bennett and DePaolo in the Western USA.

Figure 7.8 is a map of Western USA showing contours of crustal residence times (τ_{DM}). The data define three distinct provinces and suggest the existence of several others. There is a general similarity to Hurley's map, but the Nd work shows greater detail, and the ages are often older. Figure 7.9 shows the initial ϵ_{Nd} values of the granites from the three numbered provinces plotted as a function of crystallization age. Only in province three do we find rocks, tholeiitic and calc-alkaline greenstones, whose crustal residence time is equal to their crystallization ages. In the other regions, the oldest rocks have initial ϵ_{Nd} values that plot below the depleted mantle evolution curve. This suggests they contain significant amounts of preexisting crust. We should emphasize at this point that the crustal residence time gives the average crustal residence time of Nd in the material. Thus, if a continental rock formed at 1.0 Ga contained Nd derived in equal proportions from the mantle and 2.0 Ga crust, its crustal residence time would be 1.5 Ga. In each province there have been subsequent episodes of magmatism, but in those subsequent episodes there have been no new additions of crust (they plot along the same evolutionary array as the older material in the province).

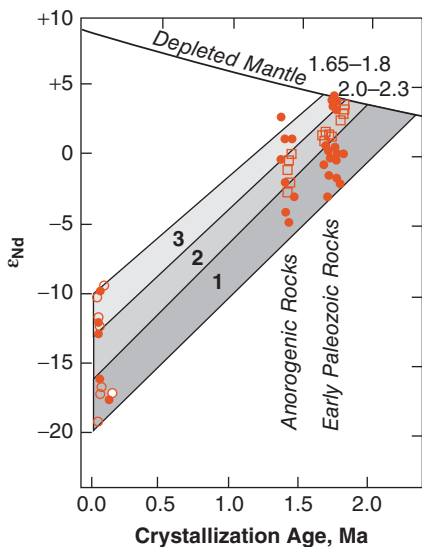


Figure 7.9 ϵ_{Nd} (initial) as a function of crystallization age of Western USA. Groupings 1, 2, and 3 refer to provinces shown in Figure 7.8. (Source: Adapted from Bennett and DePaolo, 1987.)

All three provinces apparently formed between 1.8 and 1.65 Ga, though rocks from province 1 may be slightly older. A scenario suggested by DePaolo that is consistent with the observations is successive accretion or growth of island arcs to the pre-existing Archean craton to the north. The earliest formed arcs, or at least those closest to the craton received a substantial component of older crust from the craton. This could have occurred through erosion and subduction, or, if the arc was built directly on the continent, through assimilation of crust. As new Proterozoic crust was built outward from the continent, it screened subsequent arcs from the contribution of material from the Archean crust. A similar effect has been observed in the Proterozoic provinces of Canada.

The Paleozoic Lachlan Fold Belt of southeastern Australia provides another interesting case study. Chappell and White (1974) divided the granites of this region into I- and S-types, introducing what has become a widely used terminology. The I- (for igneous) type are metaluminous ($(\text{Ca} + \text{Na} + \text{K})/\text{Al}_{\text{atomic}} > 1$) to weakly peraluminous, with high CaO and Ca/Na, and usually contains hornblende and are thought to be derived by melting of a meta-igneous protolith. The S (for

sedimentary) types are strongly peraluminous ($(\text{Ca} + \text{Na} + \text{K})/\text{Al}_{\text{atomic}} < 1$), typically cordierite-bearing and have generally lower abundances of seawater soluble elements (Na, Ca, and Sr), and are thought to be derived by melting of a metasedimentary protolith. Despite the difference in origin, the trace element compositions are similar and they define a single overlapping array on an $\epsilon_{\text{Nd}}-\delta^{18}\text{O}$ diagram. As a result, in contrast to the Southwestern USA discussed earlier, it has not been possible to resolve whether the low ϵ_{Nd} of some of the I-type granites reflect contamination by melts of metasediments or derivation from meta-igneous protoliths of different crustal residence ages.

Hawkesworth and Kemp (2006) combined LA-MC-ICP-MS to determine ages and Hf isotopic compositions of zircons with ion microprobe analysis to determine O isotope ratios on two suites of I-type granites. As we'll learn in Chapter 9, $\delta^{18}\text{O}$ values of the mantle and purely mantle-derived magmas are uniform at values around +5 to +6. Higher values indicate that rocks have interacted with water on the surface or within the crust. Both suites show a range of $\delta^{18}\text{O}$ values extending down to mantle-like values. In one suite, the O- ϵ_{Hf} relationship suggested mixing between a juvenile mantle magma and melts of a sedimentary protolith; in the other suite, it suggested mixing between mafic crust that has evolved to lower ϵ_{Hf} and a sedimentary protolith (Figure 7.10). Hawkesworth and Kemp (2006) also analyzed detrital zircons from the metasediments of the Lachlan Fold Belt (Figure 7.11). The crystallization age spectra of the detrital zircons are dominated by peaks at 450–600 Ma and 0.9–1.2 Ga. Hf model ages of zircons, which were calculated assuming the zircons crystallized from magmas with Lu/Hf ratios similar to average bulk continental crust (0.08), are much older, showing peaks around 1.7–1.9 and 2.9–3.1 Ga. Those with the most mantle-like O isotope ratios ($\delta^{18}\text{O} < 6.5$) tend to have the older ages, while zircons with higher $\delta^{18}\text{O}$ tend to have the younger ages. Presumably, the zircons with the lower $\delta^{18}\text{O}$, and older Hf model ages, and represent reworking or melting of deeper crustal material that had never interacted with water at low and moderate temperatures. The important result from this study

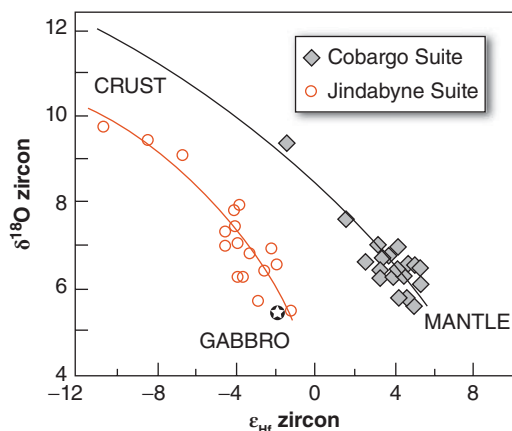


Figure 7.10 $\delta^{18}\text{O}$ versus ϵ_{Hf} for two I-type granite suites from the Lachlan fold belt. They define two distinct mixing curves with a “sedimentary” (high $\delta^{18}\text{O}$) material. The average Hf and O isotope (zircon) composition of a gabbro that is spatially associated with the Jindabyne Suite is shown by the star symbol. (Source: Hawkesworth and Kemp (2006). Reproduced with permission of Elsevier.)

is that even the zircon ages may date times when older crust was being reworked rather than new crust being formed.

We should also recognize that rate at which the volume of the continental crust has grown could be different from the rate at which new material has been added to it. This is because crust can also be destroyed. Three mechanisms seem possible. The most easily demonstrated is erosion and subduction of the resulting sediment. A second is subduction erosion, a process in which lower continental crust is essentially abraded away by plate subducting beneath it. A third mechanism is foundering or delamination, particularly of lower crust. The latter process would occur when mafic lower crust becomes dense and mobile enough to sink into the mantle. One possibility would be where the rates of continent creation and destruction are equal, resulting in a steady state volume of continental crust. This is just the situation envisioned by Armstrong (1968, 1971). He argued that although there had been continuing additions to continental crust through geologic time, these additions were balanced by destruction and recycling of continental crust into the mantle so that there had been no net growth of the crust since very early in Earth's history. Armstrong's

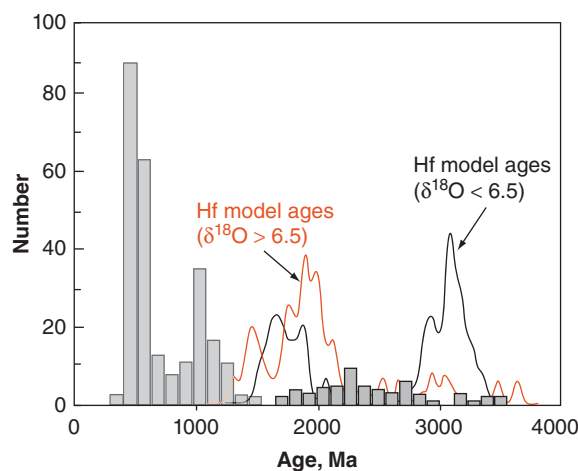


Figure 7.11 Comparison of the crystallization age histogram of detrital zircons from the Lachlan Fold Belt, Australia, as established by ion microprobe U–Pb dating with the distribution of Hf model ages for inherited and detrital zircons with low and approximately mantle-like $\delta^{18}\text{O}$ values ($<6.5\text{\textperthousand}$) and zircons with high $\delta^{18}\text{O}$ values ($>6.5\text{\textperthousand}$). Zircons for which Hf and O isotope data are available are from only S-type granites, and two samples of Ordovician metasedimentary rock. (Source: Hawkesworth and Kemp (2006). Reproduced with permission of Elsevier.)

idea, and that of Hurley and Rand, frames the range of estimates of the rate of growth of continental crust illustrated in Figure 7.7. To this day, it has not been possible to distinguish unequivocally between these alternatives. The most likely answer, however, lies somewhere between the two extremes.

7.3 ISOTOPIC COMPOSITION OF THE CONTINENTAL CRUST

Isotope systems have particular value in studies of mantle geochemistry because of the difficulty of obtaining direct, representative samples of mantle. The upper crust is largely accessible to direct sampling, so we are less dependent on isotopic composition in geochemical studies of the continental crust. Knowing the isotopic composition of the continental crust is nevertheless useful for (1) establishing the isotopic signature of the continental crust so we can recognize it elsewhere (such as the oceans, atmosphere and mantle) and (2) in mass balance calculations to

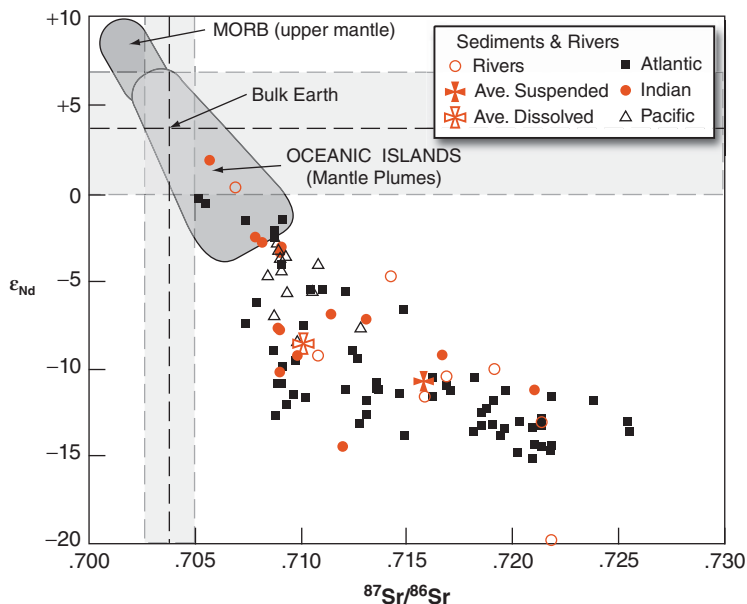


Figure 7.12 Sr and Nd isotope ratios in modern marine sediments (from Ben Othman et al., 1989). Also shown are data on the isotopic composition of suspended loads of rivers (from Goldstein and Jacobsen, 1988), and their estimated global river average ($^{87}\text{Sr}/^{86}\text{Sr} = 0.716$; $\varepsilon_{\text{Nd}} = -10.4$).

establish the size of various geochemical reservoirs in the Earth. We now turn our attention to assessing the average isotopic composition of the continental crust.

7.3.1 Sediments and rivers as samples of the upper crust

The Earth is a big place and obtaining a representative sample of the continental crust is therefore a difficult job. Just as we let nature do some of the work of sampling the mantle for us (by bringing magmas and xenoliths to the surface), we can take advantage of nature's sampling of the crust. Weathering and erosion are constantly removing material from the continents and depositing it in the oceans as sediment. Thus, to the isotope geochemist, sediment is a sort of premixed, homogenized, and pre-powdered sample of the continental crust. Figures 7.12 and 7.13 show Sr, Nd, and Pb isotopic compositions of marine sediments from the world oceans. The data provide some indication of the composition of the crust. As may be seen, $^{87}\text{Sr}/^{86}\text{Sr}$ ratios are much higher and $^{143}\text{Nd}/^{144}\text{Nd}$ isotope ratios much lower than those of the mantle. This is precisely what we expect since we know that Rb and Nd are enriched in the crust relative to Sr and Sm.

U, Th, and Pb should also be enriched in the crust in the order Th>U>Pb. Somewhat surprisingly, we find that $^{206}\text{Pb}/^{204}\text{Pb}$ ratios in the crust overlap the MORB range considerably. $^{207}\text{Pb}/^{204}\text{Pb}$ ratios are, however, systematically higher. For a given value of $^{206}\text{Pb}/^{204}\text{Pb}$, $^{208}\text{Pb}/^{204}\text{Pb}$ ratios in the crust are also systematically higher than in MORB (which are shown in these figures primarily to represent the isotopic composition of the upper mantle), indicating a higher Th/U ratio in the crust as expected. The $^{207}\text{Pb}/^{204}\text{Pb}$ ratio is an indicator of U/Pb ratios in the early part of Earth's history: the ^{235}U present in the Earth today is only about 2% of the ^{235}U the Earth had at its start: 98% of ^{235}U has already decayed to ^{207}Pb . Half of the ^{235}U had already decayed by 3.8 Ga. So the high $^{207}\text{Pb}/^{204}\text{Pb}$ of the crust relative to $^{206}\text{Pb}/^{204}\text{Pb}$ tells us that in the early part of Earth's history, crustal rocks, or their precursors, had a higher U/Pb ratio than the mantle. The half-life of ^{238}U is about the same as the age of the Earth, so $^{206}\text{Pb}/^{204}\text{Pb}$ has grown more linearly over Earth's history. The similarity of $^{206}\text{Pb}/^{204}\text{Pb}$ ratios in crust and upper mantle suggests the average U/Pb ratios of the two have been roughly similar over all of Earth's history.

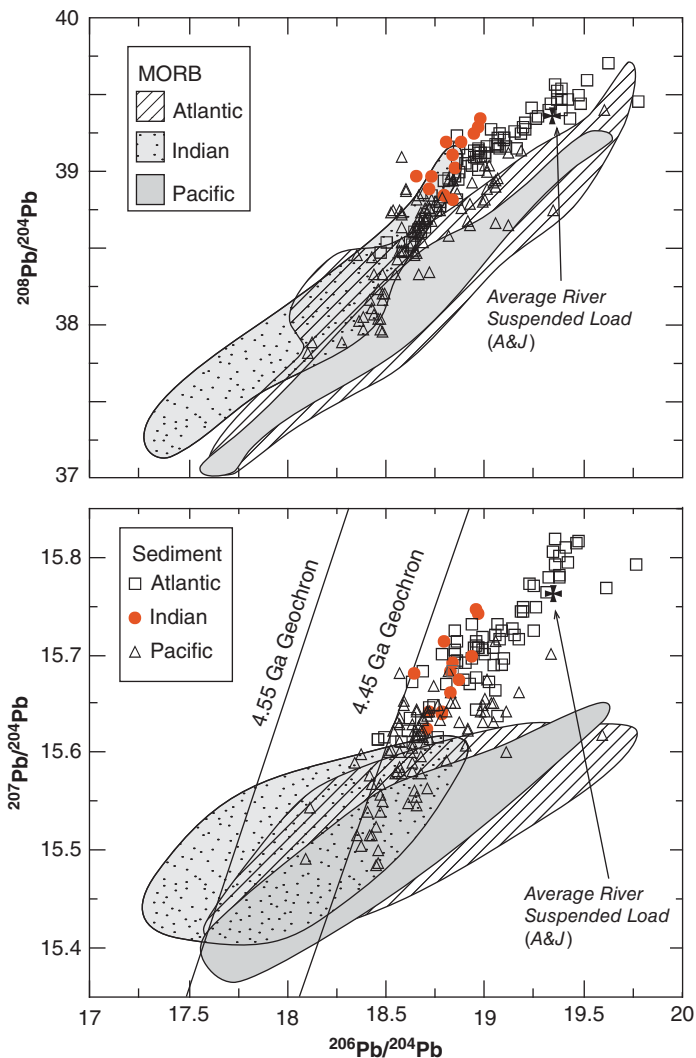


Figure 7.13 Pb isotope ratios in modern marine sediments. Asmeron and Jacobsen's (1993) estimate of the average riverine suspended load is also shown.

It is appropriate at this point to consider just how representative of the continents the isotopic compositions of marine sediments are. Sediments are only representative of those parts of the crust undergoing erosion. This excludes almost the entirety of the lower crust. So it is therefore proper to consider sediments as representative of only the upper crust. Furthermore, it is likely to be a biased sample of the upper crust. Elevated regions erode faster and therefore generate more sediment than low plains. Tectonically active areas are typically elevated relative to stable areas. By and large, new additions to crust occur exclusively in tectonically active areas and are more likely to be eroded. (By the way, it is exactly this

tendency of young igneous crust to be eroded and carried into the oceans that may explain the bias in the zircon data towards zircons created by supercontinent assembly.) In essence, this means sediments will be biased toward younger crust, and will have lower Sr and higher Nd isotope ratios. This biased sampling is to some degree apparent when the data are considered ocean by ocean. The Pacific Ocean is surrounded by tectonically active continental margins, and as we might expect, Sr, Nd, and Pb isotope ratios are lower in Pacific sediments than in those from the Atlantic and Indian. Finally, we need to assure ourselves that when a rock weathers and erodes, the erosion products carried to the sea have isotopic

compositions of the rock as a whole. This is probably the case for Nd because it ends up primarily in the clay fraction. A larger fraction of Sr may be carried to the sea as dissolved load; this eventually precipitates in carbonates. However, Sr in seawater is derived in part from the oceanic crust (entering seawater through hydrothermal activity); furthermore carbonates weather easily and much of the riverine and seawater Sr is derived from earlier marine carbonates. Thus, the total composition of marine sediments, including both carbonates and detrital fractions is probably not entirely representative of the continental crust.

It is also probable that the Hf carried to the deep ocean is not isotopically representative of the composition of the eroding rock (Patchett et al., 1984; White et al., 1986). This is because much of the Hf in crustal rocks is contained in zircon, which is extremely resistant to weathering. As a result, it is not readily transported great distances from its source. It will typically be retained on the continents in sands and sandstones. That which does reach the sea is mostly deposited on the continental shelf. The Lu/Hf ratio of zircon is lower than that of the bulk rock, so that Hf that does reach the sea may have higher $^{177}\text{Hf}/^{176}\text{Hf}$ ratios than the eroding rock. Similarly, while much of the ^{204}Pb is probably in phases such as feldspars that break down readily to form clays, the radiogenic isotopes will, to some degree, be retained in zircon. On the other hand, bedloads of streams, and even the suspended loads, can be biased toward unradioactive Pb (Garçon et al., 2013), with this material ultimately being retained in the continents. Thus, Pb isotope ratios of marine sediment may underestimate $^{206}\text{Pb}/^{204}\text{Pb}$, $^{207}\text{Pb}/^{204}\text{Pb}$, and $^{208}\text{Pb}/^{204}\text{Pb}$ (less so the latter) ratios of the eroding rock. Finally, some of the Pb in marine sediments is also derived from the oceanic crust through hydrothermal activity. In summary, sediments do provide a sample of the continental crust, but it is a biased one. They can nevertheless provide useful information on the composition of the crust today, as well as a perspective on the evolution of the crust through time.

A slightly different, but closely related way of estimating crustal composition is to measure the isotopic composition of dissolved or suspended loads in rivers. Rivers carry most of the weathering products from the continents

to the oceans (other material is carried by winds and glaciers); hence this strategy is similar to that of sampling oceanic sediments. By using the river samples, we avoid the problem of hydrothermal contributions to sediment. Furthermore, we can calculate weighted averages, based either on the flux of the rivers or the area they drain, to come up with a more accurate estimate of crustal composition than using marine sediments. Goldstein and Jacobsen (1988) measured the riverine Sr and Nd isotopic fluxes by measured isotopic compositions of *suspended load* in a subset of rivers (mainly North American) and attempting to extrapolate their results to obtain a global average (shown in Figure 7.12). They estimated the $^{87}\text{Sr}/^{86}\text{Sr}$ and ε_{Nd} of the continental crust exposed to weathering as 0.716 and -10.6 respectively. However, they had no data on a number of major rivers, notably the Brahmaputra, Ganges, and Yangtze. In a related study Goldstein and Jacobsen (1987) also attempted to estimate the global average Sr and Nd isotopic composition of the *dissolved load* of rivers and estimated these as $^{87}\text{Sr}/^{86}\text{Sr} = 0.7101$ and $\varepsilon_{\text{Nd}} = -8.4$ respectively. The much lower Sr isotope ratios in the dissolved load reflects dissolving carbonate sediments. Palmer and Edmond (1989) did a more thorough job of measuring the Sr isotopic compositions of the dissolved load of rivers and obtained an average $^{87}\text{Sr}/^{86}\text{Sr}$ of 0.7119, but did not measure the Nd isotopic composition. Given the more thorough sampling done by Palmer and Edmond, their estimate is probably more accurate. Since Goldstein and Jacobsen's estimate of average and suspended loads are based on the same rivers sampled at the same locations, it possible, and perhaps likely, that their estimate of the isotopic composition of the suspended load is also a bit low. It is nevertheless the best estimate available.

As we noted earlier, a small but significant fraction of the Sr in rivers is in dissolved form, whereas the amount of dissolved Nd is insignificant compared to that in the suspended load. Goldstein and Jacobsen (1988) also calculated the bulk load (dissolved plus suspended) carried by rivers. Their estimate of the $^{87}\text{Sr}/^{86}\text{Sr}$ of the bulk load was 0.7133. The lower $^{87}\text{Sr}/^{86}\text{Sr}$ in the dissolved fraction reflects the influence of dissolving carbonates, which have lower $^{87}\text{Sr}/^{86}\text{Sr}$ than silicate

rocks because their Rb/Sr is low and seawater, from which they precipitate, is influenced by hydrothermal activity at mid-ocean ridges.

Asmeron and Jacobsen (1993) estimated the Pb isotopic composition of the crust by measuring Pb isotope ratios in the suspended load of sediments, and then estimating the global average from the correlation between Pb isotope ratios and ϵ_{Nd} in suspended loads. Their estimated composition of the upper crust exposed to weathering is $^{206}\text{Pb}/^{204}\text{Pb} = 19.32$, $^{207}\text{Pb}/^{204}\text{Pb} = 15.76$, and $^{208}\text{Pb}/^{204}\text{Pb} = 39.33$. This mean value is shown in Figure 7.13.

Esser and Turekian (1993) measured the Os isotopic composition of river sediments and from this estimated the average $^{187}\text{Os}/^{186}\text{Os}$ of the continental crust exposed to weathering at 10.5 ($\gamma_{\text{Os}} = 895$). Pegram et al. (1994) measured the isotopic composition of leachable Os in river sediments. The isotopic composition of the leachable fraction presumably reflects isotopic composition of dissolved Os (which was in too low a concentration to measure directly). $^{187}\text{Os}/^{186}\text{Os}$ ranged from 10.1–21.5.

Using riverine suspended load eliminates the influence of hydrothermal activity on marine sediments, but the other problems with using sediments to estimate continental material remain: at best we can only estimate the composition of the crust exposed to weathering.

7.3.2 Isotopic composition of the lower crust

Like the mantle, the lower continental crust is not generally available for sampling. While much can be learned about the lower crust through remote geophysical means (seismic waves, gravity, heat flow, etc.), defining its composition and history depends on being able to obtain samples of it. As with the mantle, three kinds of samples are available: terrains or massifs that have been tectonically emplaced in the upper crust, xenoliths in igneous rocks, and magmas produced by partial melting of the lower crust. All these kinds of samples have been used and each has advantages and disadvantages similar to mantle samples. We will concentrate here on xenoliths and terrains.

Figure 7.14 summarizes Sr and Nd isotopic compositions of lower crustal xenoliths. Initial Sr and Nd isotopic studies of the lower crust indicated it had similar ϵ_{Nd} to the

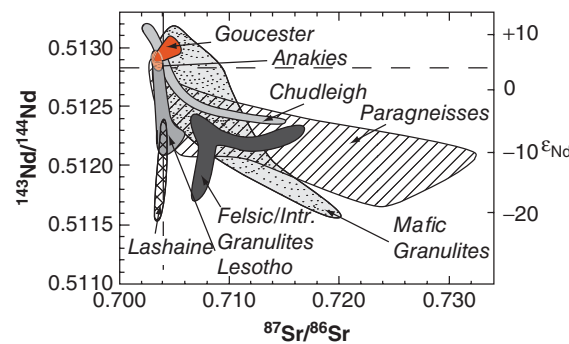


Figure 7.14 Sr and Nd isotopic composition of granulite* xenoliths in volcanic rocks. Chudleigh, Gloucester, and Anakies are in Australia, Lashaine is in Tanzania, and Lesotho is in South Africa. (Source: Replace with Adapted from Rudnick (1992). Reproduced with permission of Elsevier.)

upper crust, but low $^{87}\text{Sr}/^{86}\text{Sr}$. It is clear from Figure 7.14 that while this may be true in some instances, the lower crust is quite heterogeneous in its isotopic composition and is not easily characterized by a single isotopic composition. Some lower crustal xenoliths have very radiogenic Sr.

The Pb isotopic composition of the lower crust is a particularly important question because it bears on the question of the composition of the bulk silicate Earth and its age. The upper crust, the upper mantle, and mantle plumes all have Pb isotopic compositions lying to the right of the 4.5 Ga Geochron. If the Earth is this old, mass balance requires a significant reservoir of unradiogenic Pb, that is, Pb that plots to the left of the Geochron somewhere in the Earth. Some early studies of granulite terrains, such as the Scourian in Scotland, suggested the lower crust might be characterized by unradiogenic Pb. Furthermore, the lower crust is known to have a low heat production, implying low concentrations of U and Th.

Rudnick and Goldstein (1990) found that while most Archean lower crustal terrains did indeed have very unradiogenic Pb, post-Archean ones did not. This is summarized in Figure 7.15. Furthermore, many lower crustal xenoliths have radiogenic Pb (Figure 7.16). Rudnick and Goldstein concluded that unradiogenic Pb can only develop in regions that have remained stable for long time periods, that is, only in cratons. In areas

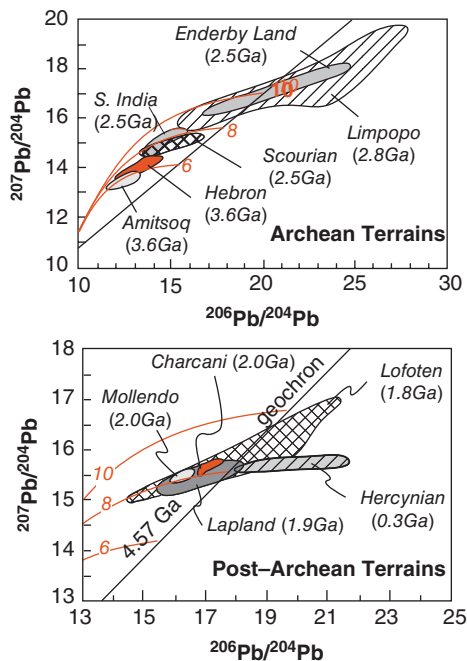


Figure 7.15 Pb isotope ratios in Archean and post-Archean granulite (i.e., lower crustal) terrains. the 4.57 Ga geochron and single stage growth curves for $\mu = 6$, $\mu = 8$, and $\mu = 10$ are also shown. While Archean terrains appear to be characterized by unradiogenic Pb, this is less true of post-Archean terrains. (Source: Replace with Adapted from Rudnick and Goldstein (1990). Reproduced with permission of Elsevier.)

where orogenies have occurred subsequent to crust formation, the Pb isotopic composition of the lower crust is rejuvenated through mixing with radiogenic Pb from upper crust and mantle-derived magmas.

Rudnick and Goldstein (1990) attempted to estimate the average Pb isotopic composition of the lower crust based on this orogenic age–Pb isotopic composition relationship. Their estimate is compared with other estimates for the Pb isotopic composition of the upper and lower crust in Figure 7.17. Rudnick and Goldstein concluded that while the Pb of the lower crust does lie to the left of the 4.57 Ga Geochron, it is not sufficiently unradiogenic to balance the unradiogenic Pb of the upper crust and upper mantle. Figure 7.17 also shows Halliday's (2004) average of a number of estimates of the Pb isotopic composition of the bulk silicate Earth. The average lies clearly to the right of the 4.57 Ga

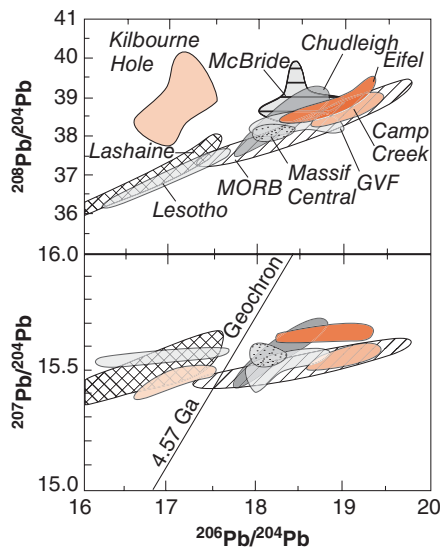


Figure 7.16 Pb isotope ratios in lower crustal xenoliths. Eifel is in Germany; GVF (Geronimo Volcanic Field), Kilbourne Hole and Camp Creek in the southwest US, McBride in Australia; and the Massif Central, in France. (Source: Replace with Adapted from Rudnick and Goldstein (1990). Reproduced with permission of Elsevier.)

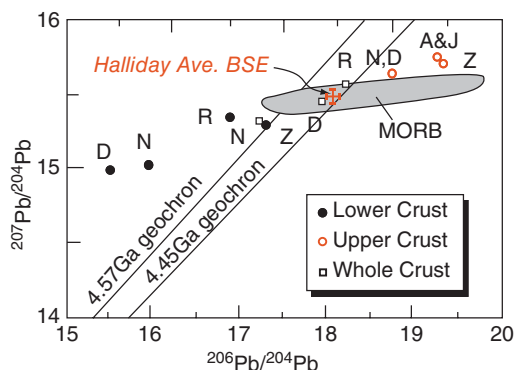


Figure 7.17 Estimates of the Pb isotopic composition of the crust: N: Newsom et al. (1986), D: Davies (1984), Z: Zartman and Doe (1981), R: Rudnick and Goldstein (1990). Also shown is Halliday's (2004) average of bulk silicate Earth estimates.

Geochron, but close to a 4.45 Ga Geochron. Thus, the apparent Pb isotopic composition of the Earth is consistent with evidence we discussed earlier that accretion of the Earth was not complete until roughly 100 Ma after the beginning of the Solar System.

7.3.3 Pb isotope ratios and the Th/U ratio of the crust

There have been a number of attempts to estimate the bulk composition of the continental crust. Isotope ratios can be used to check and refine estimates of these. Estimates of crustal composition are generally based on compilations of compositional data over wide, but nevertheless limited, areas of the continental crust. Model-based assumptions are often required to transform these limited data sets into estimates of the composition of the entire crust. For example, the well-known work of Taylor and McLennan (1985, 1995) is based largely on sampling of the Canadian Precambrian Shield and the assumption that the crust is ultimately andesitic in composition. Taylor and McLennan (1995) estimated the $^{232}\text{Th}/^{238}\text{U}$ ratio (κ) of the crust to be 3.87, a value that is surprisingly low given the value for the bulk Earth is 4.0 ± 0.2 and Th isotope ratios indicate that κ in the depleted mantle is ~2.5. Rudnick and Fountain (1995) estimated a value of 3.97, also surprisingly low, but perhaps not surprising since it was based in part of the work of Taylor and McLennan. If the mantle has lower κ than the bulk Earth, then mass balance would seem to require that the crust should have a high value than the bulk Earth. Furthermore, crustal rocks tend

to have higher $^{208}\text{Pb}^*/^{206}\text{Pb}^*$, suggesting κ has been higher in the crust than in the mantle for geologically long times.

Paul et al. (2003) used Asmeron and Jacobsen's (1993) estimate of the Pb composition of the riverine flux to estimate the Pb isotopic composition of upper crust and data from Rudnick and Goldstein (1990) to estimate the Pb isotope composition the lower crust. From this they calculated a κ_{Pb} for the crust of 4.26–4.30. This clearly implies the κ value of the crust must be higher than that estimated by Taylor and McLennan and Rudnick and Fountain. Indeed, when one considers that the crust is derived from the mantle, and the mantle source of crustal rocks have a κ equal to or lower than the bulk Earth value of ~4, this implies a κ substantially higher than ~4. Paul et al. used a mathematical model of the isotopic evolution of the Earth to estimate just how much higher. As is illustrated in Figure 7.18, the estimated that κ in the crust is 5.17. That value actually agrees well with an estimate of Wedepohl (1995). Notice that the model also correctly predicts a large difference between the κ_{Th} and κ_{Pb} in the depleted mantle, consistent with the observation of Galer and O'Nions (1985). The increase in κ_{Pb} in the depleted mantle in the model results from recycling crust Pb into the mantle through subduction.

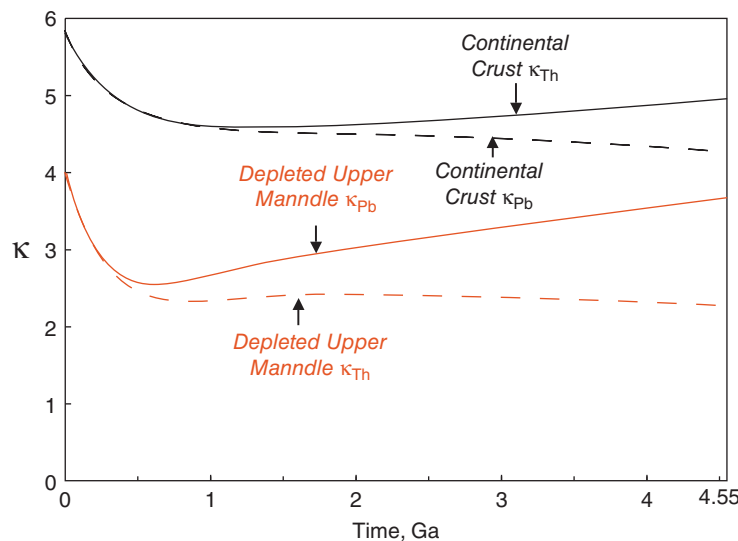


Figure 7.18 Computed evolution of κ and κ_{Pb} in the crust and depleted mantle. A present day κ_{Pb} in the crust of 4.3 requires a κ of 5.17, because some of the Pb now in the crust would have resided in the mantle, which has low κ . (Source: Paul et al., (2003). Reproduced with permission of John Wiley & Sons Ltd.)

7.4 OTHER APPROACHES TO CRUSTAL COMPOSITION AND EVOLUTION

As we have seen, samples of particulate material in rivers can be used to obtain estimates of upper crustal composition. However, because the Sm/Nd ratio changes little during production of sediment, these sediment samples also contain information on the age of the rocks they are derived from through Nd model ages (or crustal residence time). Sm/Nd and $^{143}\text{Nd}/^{144}\text{Nd}$ ratios in major rivers draining about 25% of the exposed continental crust (excluding Antarctica and Australia) as well as samples of loess and Aeolian dusts were analyzed by Goldstein et al. (a different Steve Goldstein than the Steve Goldstein of the Goldstein and Jacobsen papers) are shown in Figure 7.19. The Nd isotope ratios are fairly homogeneous. Sm/Nd ratios are quite uniform, illustrating a point that was already well known, namely that rare earth patterns of continental crustal material show relatively little variation. A further illustration of this point is shown in Figure 7.20. Virtually all crustal rocks have $^{147}\text{Sm}/^{144}\text{Nd}$ ratios at the extreme end of the range observed in mantle-derived

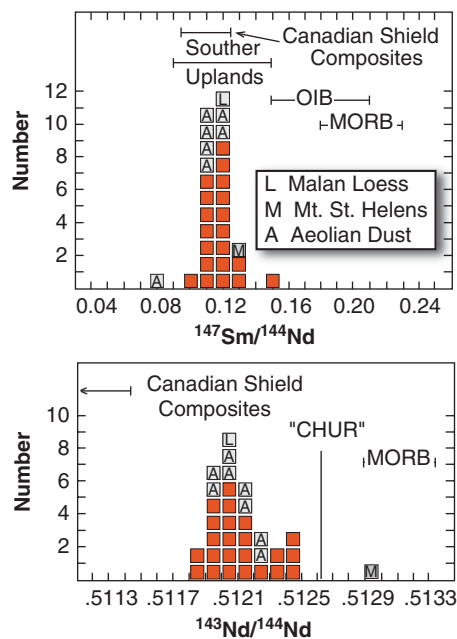


Figure 7.19 $^{147}\text{Sm}/^{144}\text{Nd}$ and $^{143}\text{Nd}/^{144}\text{Nd}$ ratios in major rivers, Aeolian dusts, and loess. (Source: Goldstein et al. (1984). Reproduced with permission of Elsevier.)

rocks, and the range of $^{147}\text{Sm}/^{144}\text{Nd}$ ratios in crustal material is small compared to the range observed in mantle-derived rocks. Figure 7.20 suggests there is a major fractionation of the Sm/Nd when crust is formed from the mantle, but thereafter processes within the crust tend to have only second-order effects on the Sm/Nd ratio. This is the main reason why crustal residence time calculated from $^{147}\text{Sm}/^{144}\text{Nd}$ and $^{143}\text{Nd}/^{144}\text{Nd}$ is such a robust parameter.

By studying sediments of various ages, we should be able to draw some inferences about the rates of continental growth. Goldstein et al. (1984) found that the mean crustal residence time (τ_{DM} , calculated from $^{147}\text{Sm}/^{144}\text{Nd}$ and $^{143}\text{Nd}/^{144}\text{Nd}$) of the river particulates they studied was 1.7 Ga, which they interpreted as the mean age of the crust being eroded. However, they estimated the mean crustal residence time of the entire sedimentary mass to be about 1.9 Ga. Figure 7.21 compares the stratigraphic age³ of sediments with their crustal residence ages. Note that in general we expect the crustal residence age will be somewhat older than the stratigraphic age. Only when a rock is eroded into the sedimentary mass immediately after its derivation from the mantle will its stratigraphic (τ_{ST}) and crustal residence age (τ_{CR}) be equal.

The top diagram illustrates the relationships between τ_{ST} and τ_{CR} that we would expect to see for various crustal growth scenarios, assuming there is a relationship between the amount of new material added to the continents and the amount of new material added to the sedimentary mass. If the continents had been created 4.0 Ga ago and if there had been no new additions to continental crust since that time, then the crustal residence time of all sediments should be 4.0 Ga regardless of stratigraphic age, which is illustrated by the line labeled "No new input." If, on the other hand, the rate of continent growth through time has been uniform since 4.0 Ga, then τ_{ST} and τ_{CR} of the sedimentary mass should lie along a line with slope of 1/2, which is the line labeled "Uniform Rate." The reason for this is as follows. If the sedimentary mass at any given time samples the crust in a representative fashion, then τ_{CR} of the sedimentary mass at the time of its deposition (at τ_{ST}) should be $(4.0 - \tau_{\text{ST}})/2$,⁴ that is, the mean time between the start of crustal

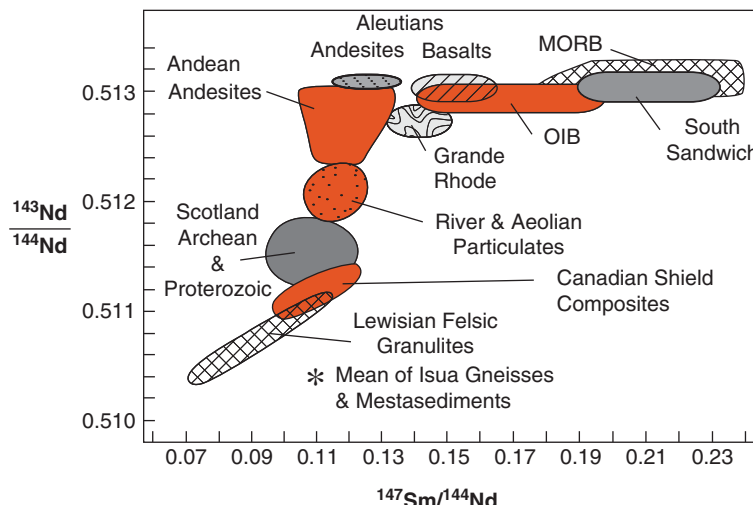


Figure 7.20 $^{147}\text{Sm}/^{144}\text{Nd}$ and $^{143}\text{Nd}/^{144}\text{Nd}$ in various crustal and mantle-derived rocks. (Source: Goldstein et al. (1984). Reproduced with permission of Elsevier.)

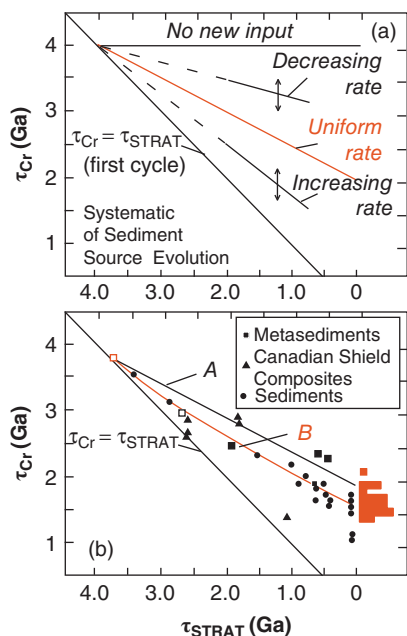


Figure 7.21 Relationship between stratigraphic age of sediments and the crustal residence age of material in sediments. See text for discussion. (Source: Goldstein et al. (1984). Reproduced with permission of Elsevier.)

growth (which we arbitrarily assume to be 4.0 Ga) and τ_{ST} . A scenario where the rate of crustal growth decreases with time is essentially intermediate between the one-time crust

creation at 4.0 and the uniform growth rate case. Therefore, we would expect the decreasing rate scenario to follow a trend intermediate between these two, for example, the line labeled “Decreasing Rate.” On the other hand, if the rate has increased with time, the τ_{CR} of the sedimentary mass would be younger than in the case of uniform growth rate, but still must be older than τ_{CR} , so this scenario should follow a path between the uniform growth rate case and the line $\tau_{\text{ST}} = \tau_{\text{CR}}$, for example, the line labeled “Increasing Rate.”

Line A in Figure 7.21b is the uniform growth rate line with a slope of 1/2. Thus the data seem to be compatible with a uniform rate of growth of the continental crust. However, the situation is complicated by various forms of recycling, including sediment-to-sediment and sediment-to-crystalline rock, and crust-to-mantle. Goldstein and O’Nions noted sedimentary mass is cannibalistic: sediments are eroded and redeposited. In general, the sedimentary mass follows an exponential decay function with a half-mass age of about 500 Ma. This means, for example, that half the sedimentary mass was deposited within the last 500 Ma, the other half of the sedimentary mass has a depositional age of over 500 Ma. Only 25% of sediments would have a depositional (“stratigraphic”) age older than 1000 Ma, and only 12.5% would have a stratigraphic age older than 1500 Ma, and so on. Line B represents

the evolution of the source of sediments for the conditions that the half-mass stratigraphic age is always 500 Ma and this age distribution is the result of erosion and re-deposition of old sediments. The line curves upward because in younger sediments consist partly of redeposited older sediments. In this process, τ_{ST} of this cannibalized sediment changes, but τ_{CR} does not. Goldstein and O'Nions noted their data could also be compatible with models, such as that of Armstrong, which have a near constancy of continental mass since the Archean if there was a fast but constantly decreasing rate of continent-to-mantle recycling.

We should emphasize that the τ_{CR} of sediments is likely to be younger than the mean age of the crust. This is so because sediments preferentially sample material from topographically high areas and topographically high areas tend to be younger than older areas of the crust (e.g., the shields or cratons) because young areas tend to be still relatively hot and therefore high (due to thermal expansion of the lithosphere).

7.5 SUBDUCTION ZONES

7.5.1 Geochemistry of two-component mixtures

Subduction-related magmatism is probably the principle way in which new material is added to the continental crust at present. Such magmas are, however, often mixtures of mantle-derived and crust-derived components. Thus, before exploring their isotope geochemistry, we need to consider the effects of mixing on isotope ratios.

When two components contribute material to magmas, we might expect that the proportion contributed by each might vary. If we plot the concentration of any two elements in different samples of this mixture against each other, they must lie on a straight line between the two end members. However, if we plot ratios of either elements or isotopes, they need not lie on a straight line. Indeed, in the general case they do not; rather they will define a curve whose equation is:

$$A \left(\frac{p}{P} \right) + B \left(\frac{p}{P} \right) \left(\frac{q}{Q} \right) + C \left(\frac{q}{Q} \right) + D = 0 \quad (7.1)$$

where ratios q/Q and p/P are the variables of the abscissa and ordinate respectively. If end

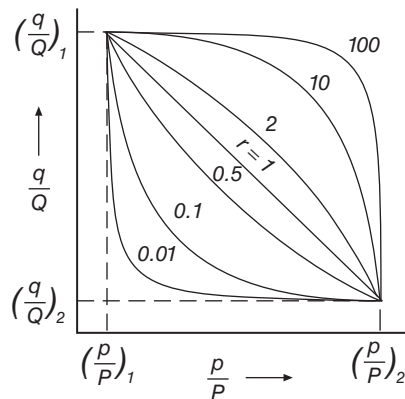


Figure 7.22 Plots of ratios of elements or isotopes, q/Q versus p/P for mixing of end members 1 and 2. The numbers along the curves are the values for r . (Source: Adapted from Langmuir et al., 1978.)

members are designated 1 and 2 and have ratios $(q/Q)_1$ and $(p/P)_1$, and $(q/Q)_2$ and $(p/P)_2$ respectively, then

$$A = Q_2 P_1 \left(\frac{q}{Q} \right)_2 - Q_1 P_2 \left(\frac{q}{Q} \right)_1 \quad (7.2)$$

$$B = Q_1 P_2 - Q_2 P_1 \quad (7.3)$$

$$C = Q_2 P_1 \left(\frac{p}{P} \right)_2 - Q_1 P_2 \left(\frac{p}{P} \right)_1 \quad (7.4)$$

$$D = Q_1 P_2 \left(\frac{p}{P} \right)_2 \left(\frac{q}{Q} \right)_2 - Q_2 P_1 \left(\frac{p}{P} \right)_1 \left(\frac{q}{Q} \right)_1 \quad (7.5)$$

The curvature of the mixing line will depend on the ratio r :

$$r = (Q_1 P_2) / (Q_2 P_1) \quad (7.6)$$

The greater the value of r , the greater the curvature. Only in the special case were $r = 1$ is the line straight. This is illustrated in Figure 7.22. This result is completely general and applies to mixing of river water and seawater, and so on as well as mixing of magmas.

Taking a concrete example, if our plot is $^{143}\text{Nd}/^{144}\text{Nd}$ versus $^{87}\text{Sr}/^{86}\text{Sr}$, then the curvature depends on the ratio of $(^{144}\text{Nd}_1/^{86}\text{Sr}_2)/(^{144}\text{Nd}_2/^{86}\text{Sr}_1)$. Since in most instances the amount of ^{144}Nd and ^{86}Sr is to a very good approximation proportional to total Nd and Sr, respectively, r is approximated by $\text{Nd}_1\text{Sr}_2/\text{Nd}_2\text{Sr}_1$. If we express this ratio

as $r = (\text{Nd/Sr})_1 / (\text{Nd/Sr})_2$ we see that the curvature depends on the ratio of the Nd/Sr ratio in the two end members. In mantle-derived rocks $\text{Sr/Nd} \sim 10$, so mixing curves typically show only modest curvature. In crustal rocks and sediments, deviations from $r = 1$ are more likely and curved mixing lines therefore more common.

Note that r will always be 1 where $Q = P$, that is, where the two denominators are the same. Consequently, on $^{207}\text{Pb}/^{204}\text{Pb} - ^{206}\text{Pb}/^{204}\text{Pb}$ plots mixing curves will always be straight lines because the denominators are the same (i.e., $Q = P = ^{204}\text{Pb}$).

Two component mixtures will also form straight lines when we plot a radiogenic isotope ratio vs. a parent-daughter ratio, that is, on isochron plots, for example, $^{87}\text{Sr}/^{86}\text{Sr} - ^{87}\text{Rb}/^{86}\text{Sr}$, because the denominators are the same. Thus mixing lines can be mistaken for isochrons and vice versa. One way to distinguish the two is a ratio-element plot. A ratio-element plot, for example $^{87}\text{Sr}/^{86}\text{Sr}$ versus Sr, will also in general be a curved line described by Eqn. 7.1 (because the denominators are ^{86}Sr and 1), but a ratio plotted against the inverse of the denominator, for example $^{87}\text{Sr}/^{86}\text{Sr} - 1/\text{Sr}$, will be a straight line (at least to the degree that ^{86}Sr is proportional to total Sr, which will be the case where the range in $^{87}\text{Sr}/^{86}\text{Sr}$ ratios is small). Such a plot can be a useful discriminator between isochrons and mixing lines because only in the latter case will $^{87}\text{Sr}/^{86}\text{Sr} - 1/\text{Sr}$ necessarily define a straight line (Figure 7.23). Again, this result

is completely general, and while the general principles have been illustrated with isotope ratios, they apply equally well to elemental ratios.

When the compositions of a magma or series of magmas appear to reflect mixing, we are often faced with having to decide whether (1) two mantle-derived magmas are mixing, (2) two distinct mantle sources are mixing, or (3) a mantle-derived magma is mixing with assimilated crust. In case (2), plots involving an elemental concentration will not fall on mixing lines because partial melting and fractional crystallization will change element concentrations. Isotope ratios will not be changed by magma genesis so a plot of two isotope ratios will describe a mixing line in case (2) as well as case (1).

Case (3), assimilation of crust by mantle-derived magmas presents a more difficult problem. Recognizing crustal assimilation in subduction zones magmas can be particularly difficult because many of geochemical effects characteristic of crustal assimilation can also result from the presence of subducted sediment component in such magmas. Plots of two isotope ratios will define a straight line in assimilation provided the process is simple mixing and does not involve simultaneous melting or crystallization. However, assimilation generally *does* involve melting and crystallization and produces more complicated ratio-ratio variations. Stable isotope ratios, oxygen in particular, are useful in recognizing

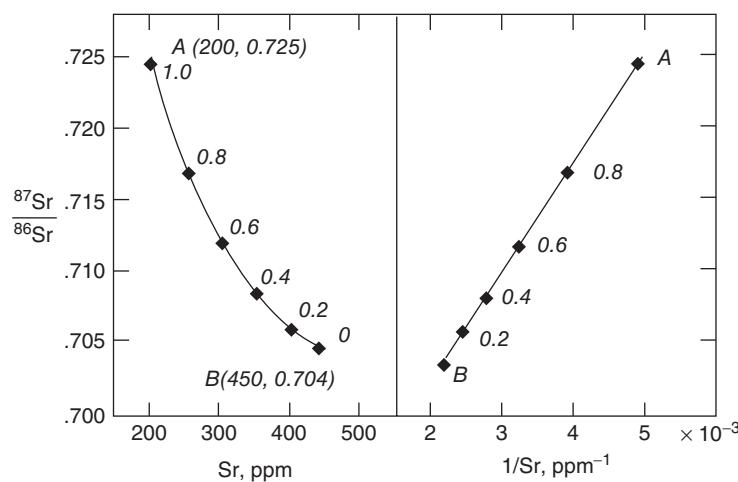


Figure 7.23 Mixing hyperbola formed by components A and B. (Source: Faure (1986). Reproduced with permission of John Wiley & Sons.)

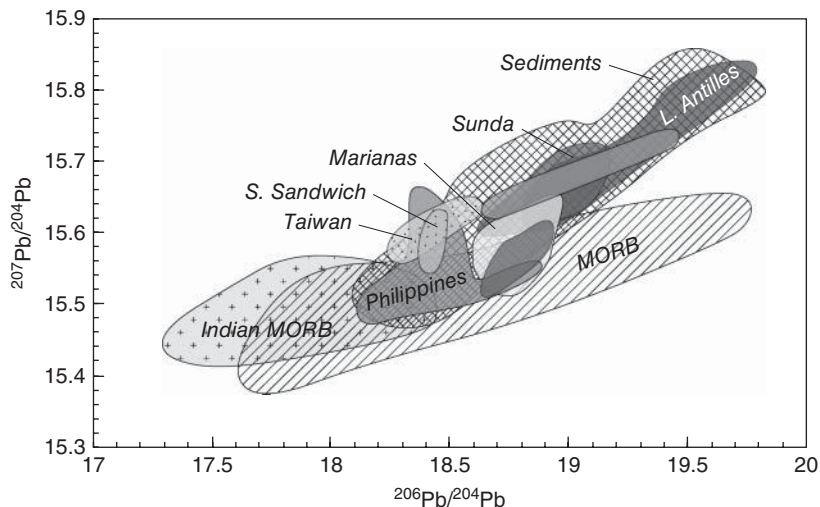


Figure 7.24 $^{206}\text{Pb}/^{204}\text{Pb}$ – $^{207}\text{Pb}/^{204}\text{Pb}$ for three arcs and the sediments available for subduction beneath them. In each case, the arcs define an array between MORB and the associated sediment.

assimilation. This is so because the mantle tends to have uniform stable isotope ratios and ones that differ from those in crustal rocks. We will postpone a full discussion of assimilation until Chapter 9.

7.5.2 Isotopic compositions of subduction-related magmas

As we noted, subduction zone magmatism is probably the principal mechanism by which new crust has been created in the Phanerozoic, and perhaps throughout geologic time. In addition, subduction zones are the regions in which oceanic crust and its veneer of sediment are recycled into the mantle. Given the obvious importance of subduction zones in the evolution of the Earth, it is worth briefly considering the isotope geochemistry of subduction-related magmas.

Island-arc and continental margins volcanics (IAV) are distinctive in many of their geochemical features. Isotopic studies have now demonstrated one reason for this: their sources contain a component of subducted oceanic crust and sediment. The first evidence to this effect was a study of Pb isotope ratios in the Lesser Antilles by Armstrong in 1971. Figure 7.24 compares Pb isotope ratios in a number of arcs to those of MORB and sediments. The similarity between the arc magmas and the sediments, first noted by Armstrong, is striking and certainly not coincidental.

The sediment, or rather some part of it, is being subducted to depths of 100 km beneath the arc where it enters the magma source region. In terms of their Sr-Nd systematics, however, island arcs overlap the MORB and OIB fields considerably (Figure 7.25), although they have some tendency to plot to the high $^{87}\text{Sr}/^{86}\text{Sr}$ side. This may be because the subducted oceanic crust is also an important source of Sr and Nd. The Nd of old (<150 Ma) oceanic crust will not be very different isotopically from that of modern MORB. However, hydrothermal activity at mid-ocean ridges results in isotopic exchange between basalt and seawater, shifting the $^{87}\text{Sr}/^{86}\text{Sr}$ of the oceanic crust to higher values (mean value of altered oceanic crust is probably in the range of 0.703–0.7035). One can also see from Figure 7.26, that Sr and Nd in island arc volcanics can qualitatively be described as a mixture of altered oceanic crust, depleted mantle, and sediment. In some cases, however, anomalous mantle, similar to that of mantle plumes, may also be involved.

Thus, arc magmas are themselves mixtures of mantle and crustal material, and continental margin volcanism, or accretion of intra-oceanic arcs, involves both additions of new material from the mantle and recycling of older crust. The proportion of sediment in arc magma sources can be estimated from mixing models (e.g., Figure 7.26) and is generally quite small, typically a percent or two or

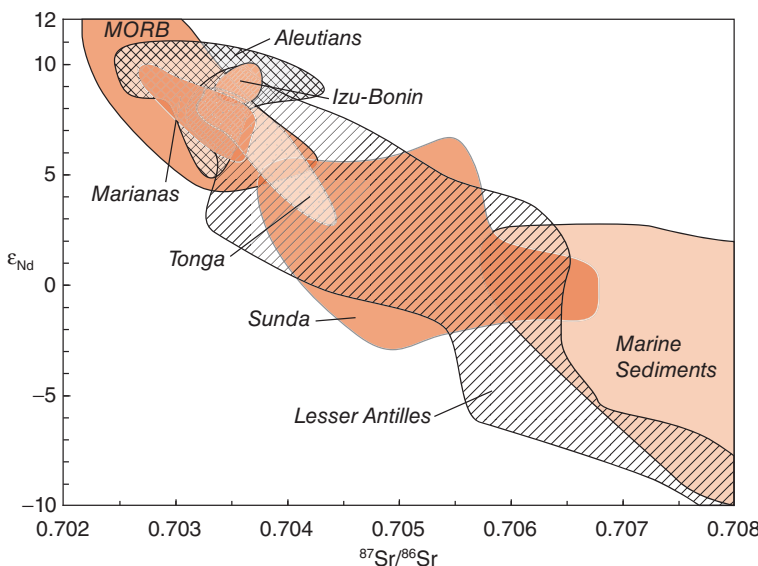


Figure 7.25 ϵ_{Nd} versus $^{87}\text{Sr}/^{86}\text{Sr}$ in intra-oceanic island arcs. Based on data in the GEOROC database.

less. Nevertheless, because sediment has much higher concentrations of Sr, Nd, and particularly Pb than mantle, significant proportions of these elements, and sometimes most of the Pb, are derived from the sediment. Continental margin magmas, such as those of the Andes, generally assimilate some of the crust through which they ascend, which results in further reworking, or high-level recycling, of continental crust.

Interestingly, the Lesser Antilles may be something of a present-day analogy to the isotopic pattern in the southwest USA that we discussed earlier (Figure 7.8). The arc is built perpendicular to the continental margin (an unusual situation). Archean crust occurs in the Guiana highland, which is drained by the Orinoco River, which has deposited a considerable volume of sediment in front of the arc. Because of the age of the drainage basin, the sediment of the Orinoco contains particularly radiogenic Pb and Sr and unradioactive Nd. Isotopic compositions in the sediment grade northward (Figure 7.27). This northward variation is mirrored by in the isotopic composition of arc lavas, and reflects a decreasing continental contribution with distance from the continent.

7.5.2.1 ^{10}Be in arc lavas

If further evidence of the presence of subducted sediment in arc magmas is needed,

it is provided by yet another isotopic system: ^{10}Be . We have discussed how ^{10}Be is created by spallation in the atmosphere. Because of its half-life is only 1.6 Ma, and cosmic rays penetrate solid matter so poorly, cosmogenic Be should not to be present in the interior of the Earth. Yet it is present in IAV (Figure 7.28). A skeptic might suppose that some unknown neutron reaction can create ^{10}Be in the Earth's interior. In addition, cosmogenic ^{10}Be in rain is rapidly absorbed onto clays, and that skeptic might suppose that even very young lavas might also absorb ^{10}Be . For these reasons, it was important to do control experiments by measuring ^{10}Be in non-arc lavas. As Figure 7.28 shows, ^{10}Be is not present in non-arc lavas. Thus the only reasonable interpretation of ^{10}Be in arc magmas is that it is derived from subducted sediment.

Not all arc lavas have ^{10}Be . For example, there is no ^{10}Be in lavas from the Lesser Antilles, where Pb and other isotopes suggest a significant contribution from sediment. The same is true of the Sunda arc. In both these arcs, however, the sediment pile is so thick that most sediment is accreted in a forearc wedge rather than subducted. In the Lesser Antilles, seismic and other studies of the forearc show that only the lowermost 100 m or so of sediment is carried into the subduction zone and possibly subducted. These are pre-Miocene

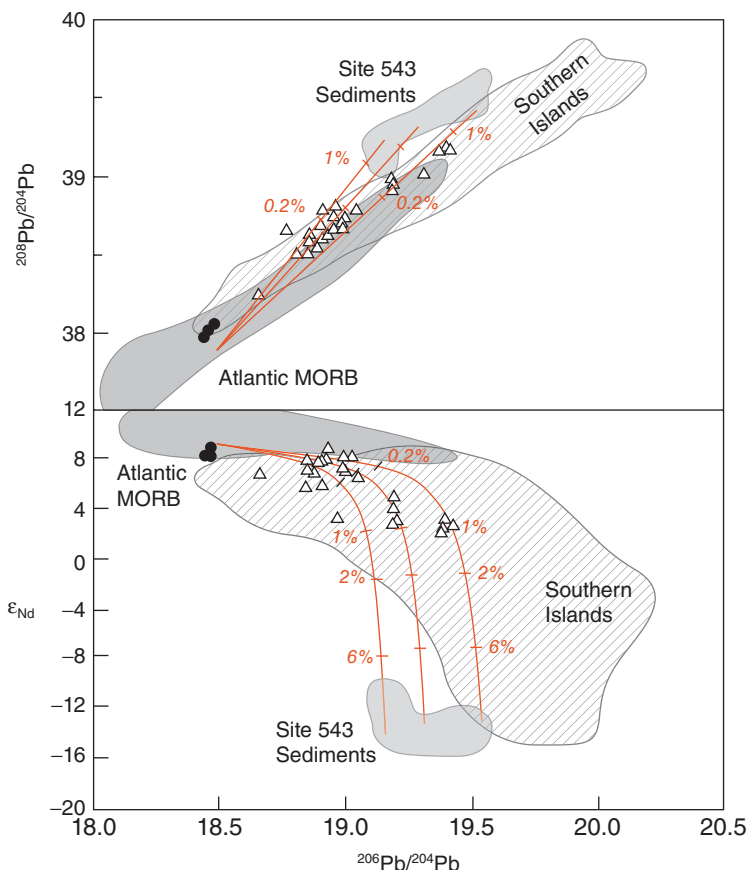


Figure 7.26 Pb and Nd isotopic compositions of lavas from the northern and southern parts of the Lesser Antilles arc compared with those of Site 543 sediments and Atlantic MORB. Data from the northern islands are shown as open triangles, basalts from Hole 543 are shown as solid circles. The solid lines represent mixing curves between depleted mantle (ave. MORB) and Site 543 sediments. Ticks show the percentage of sediments in the mixture. Compositions of the endmembers used for the calculation: (1) depleted mantle: Nd = 0.71 ppm, Pb = 0.023 ppm, $^{143}\text{Nd}/^{144}\text{Nd} = 0.5131$, $^{206}\text{Pb}/^{204}\text{Pb} = 18.5$, and $^{208}\text{Pb}/^{204}\text{Pb} = 37.9$; (2) for the sediment end members, Nd and Pb concentrations are those of the average of the entire Site 543 sedimentary pile and the isotopic compositions of the three end members are two samples from Site 543 and the average of Site 543. (Source: Carpentier et al. (2008). Reproduced with permission of Elsevier.)

sediments. Using our rule of thumb that a radioactive isotope will be gone after 5–10 half-lives, we can predict that sediment older than 8–16 Ma should have no ^{10}Be . Thus it is no surprise that ^{10}Be is not present in Lesser Antilles magmas.

7.5.2.2 Th isotope geochemistry of arc magmas

Another isotope system that has contributed significantly to our knowledge of island arc processes is the ^{230}Th - ^{238}U system. This system has been important in confirming the role of fluids in arc magma genesis. As we found

in Chapter 3, the equilibrium situation is that the activity of ^{230}Th is equal to the activity of ^{238}U , and hence the ratio ($^{230}\text{Th}/^{232}\text{Th}$) will be equal to the ($^{238}\text{U}/^{232}\text{Th}$) ratio. Equilibrium should characterize the mantle before melting (as well as old sediment). Because Th is more incompatible than U, the ($^{238}\text{U}/^{232}\text{Th}$) ratio in a melt should decrease, but the ($^{230}\text{Th}/^{232}\text{Th}$) ratio of a melt will be the same as that of its source. Thus, on a conventional plot of ($^{230}\text{Th}/^{232}\text{Th}$) against ($^{238}\text{U}/^{232}\text{Th}$), the melt should be driven to the left of the equiline. As we found in Chapter 6, this is what is observed in MORB and most OIB.

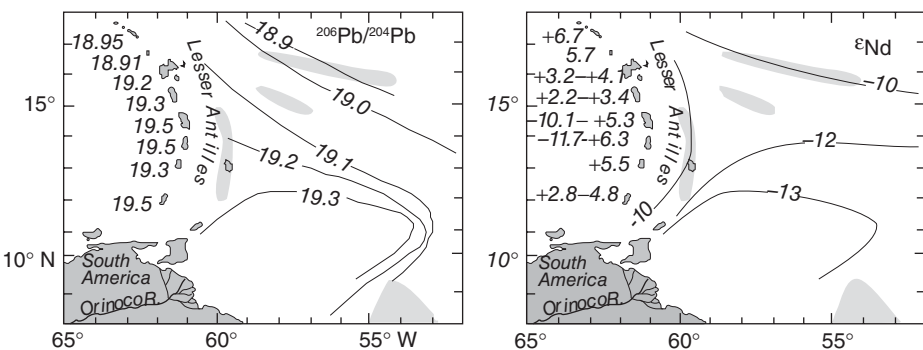


Figure 7.27 Contours of $^{206}\text{Pb}/^{204}\text{Pb}$ and ϵ_{Nd} in sediment in front of the Lesser Antilles island arc. Range or mean of these parameters in Lesser Antilles arc volcanics is written adjacent to each island. (Source: White and Dupré (1986). Reproduced with permission of John Wiley & Sons.)

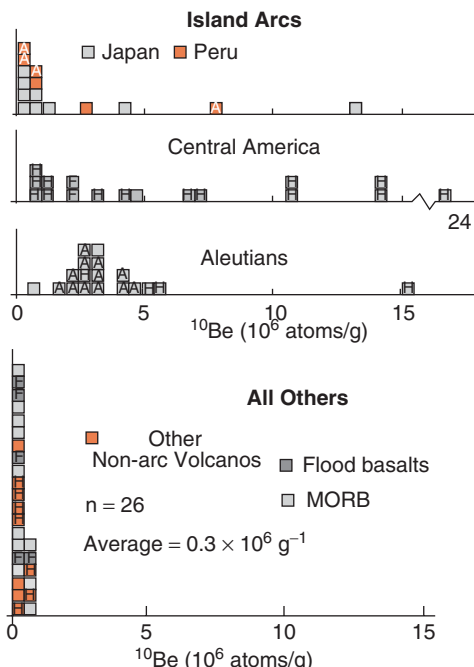


Figure 7.28 Comparison of ^{10}Be contents in arc (left) and non-arc (right) lavas (from Tera et al., 1986). “A” indicates sample from active volcano, “H” a historic eruption, and “F” (fresh) indicates collected during eruption. (Source: Tera et al. (1986). Reproduced with permission of Elsevier.)

As Figure 7.29 shows, although many arc magmas are close to equilibrium and some do plot to the left of the equiline, many some arcs have $(^{238}\text{U}/^{232}\text{Th}) - (^{230}\text{Th}/^{232}\text{Th})$ values that plot to the right of the equiline, that is, in arcs, U appears to be going in the melt more readily

than Th. The explanation of this is that U is enriched in the peridotitic mantle source of arc magmas by hydrous fluid transport from the lithospheric slab (the sediments and basalts of the oceanic crust). U is fairly soluble in water in its oxidized (6+) form; Th is quite insoluble. Thus hydrous fluids should transport U more readily than Th.

The idea that fluids might be important in transporting material from the slab to the magma genesis zone was proposed on other grounds (the abundance of water in these magmas and the enrichment in alkalis and alkaline earth trace elements, which are fairly soluble). The Th isotope studies provide confirming evidence of this idea.

7.6 RADIOGENIC ISOTOPES IN OCEANOGRAPHY

Oceans cover that portion of the Earth's surface not occupied by emergent continental crust and here too radiogenic isotope ratios have proved useful in understanding how the Earth works. In the context of oceanography, we can divide the radiogenic isotopes into two categories: those whose isotopic composition varies in the modern ocean due to their short residence times in seawater, and those whose isotopic composition is uniform in the modern ocean due to their long residence time in seawater. The former include Nd, Hf, and Pb isotope ratios, the latter Sr and, perhaps, Os isotope ratios. In this section, we'll briefly review the use of radiogenic isotopes in oceanography and paleoceanography. A longer and more detailed review can be found in Frank (2002).

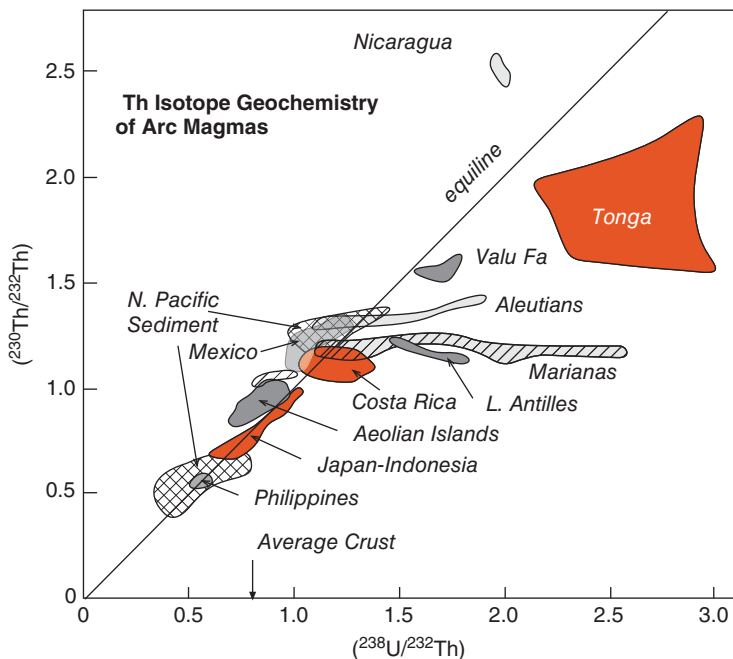


Figure 7.29 $(^{230}\text{Th}/^{232}\text{Th})$ versus $(^{238}\text{U}/^{232}\text{Th})$ in island arc magmas. (Source: McDermott and Hawkesworth (1991). Reproduced with permission of Elsevier.)

7.6.1 Oceanographic circulation and geochemical cycling

Ions enter seawater from a number of sources: rivers, submarine hydrothermal fluids, by diffusion out of sediments, and from dust particles that settle on the ocean surface. Isotopic variations in seawater in time and space can result from both variations in the relative strength of these fluxes and in their isotopic composition. The time required to erase or reduce compositional heterogeneity in the ocean is known as the *mixing time*, and is of the order of 10^3 years. However, this term is neither precisely defined nor precisely known (a reasonable, but not universally used, definition is the time required to reduce compositional variance by a factor of $1/e$). On the other hand, *residence time* in a steady-state system can be precisely defined as the ratio of the mass of an element in the ocean to the flux of that element into (or out of) the ocean. Nd, Hf, and Pb have short residence times not so much because of their insolubility as their particle reactivity: they are readily absorbed onto particles (both organic and inorganic) and removed from solution in this way. The residence time of Nd is in the range of 600–2000 years, that

of Hf is estimated at 1500–2000 years, and that of Pb is in the range of 50–400 years. Because these elements have residence times similar to or shorter than the mixing time, their isotopic composition varies in the ocean. Sr, on the other hand, has a residence time in the ocean of 2.4 million years and $^{87}\text{Sr}/^{86}\text{Sr}$ of seawater in the open ocean is uniform at 0.70925, although variations in this value occur in coastal waters. The residence time of Os in seawater is not entirely resolved; it may be as short as a few thousand years or as long as a few tens of thousands of years. The Os isotopic composition of deep ocean water appears to be constant within analytical error, but some variation is observed in surface waters. With the exception of Sr, all these elements are present in seawater at extremely low concentrations (parts per trillion and lower), so these isotopic analyses are extremely challenging.

Ocean circulation is ultimately driven by the pole-to-equator gradient in solar radiative energy or *insolation*. In response to this gradient, the atmosphere and oceans carry heat from low to high latitudes. The surface circulation of the ocean is driven by winds and this, combined with the Coriolis effect, results in

paired clockwise and counterclockwise gyres in the Northern and Southern Hemispheres, respectively, in the Pacific and Atlantic Oceans. Strong westward flowing equatorial currents occur between these gyres and, particularly in the Pacific, a usually smaller equatorial countercurrent runs eastward. The flow of this countercurrent greatly increases during El Niño events. Indian Ocean circulation has some of these aspects but is more complex and varies seasonally driven by the Indian monsoons.

In contrast, the deep circulation of the ocean is driven by density differences that depend on temperature and salinity. In the modern ocean, temperature has the dominant effect on density so that deep water is “formed,” that is acquires its characteristic temperature and salinity, at the high latitude and then flows equatorward at depth. This so-called “Great Conveyor Belt” begins in the North Atlantic, where water cooled in winter in the Norwegian, Greenland and Labrador Seas downwells to become North Atlantic Deep Water (NADW). As it flows south, it entrains Antarctic Bottom Water (AABW) from below and Antarctic Intermediate Water from above and joins the Antarctic Circumpolar Current, which makes it the largest current in the ocean in terms of volume transport, as part of the Circumpolar Deep Water (CDW). Antarctic Bottom Water, the coldest and densest water in the ocean, forms mainly in the Weddell Sea, during winter when extreme cooling and ice formation increase salinity and decrease temperature. This water then flows northward into all three oceans. The flow is balanced by southward flowing water at shallower depth. Traditionally, these water masses are identified by their temperature and salinity characteristics, which are “conservative” properties of the water mass in that once fixed at the surface, they can change only through mixing with other water masses. These water masses also have unique chemical properties as well, such as dissolved oxygen content, nutrient concentrations, and carbon isotope ratios, but these change over time, mainly due to biological activity. The water masses also acquire unique radiogenic isotope signatures because the isotopic composition of the sources of these elements varies geographically.

To a first approximation, the composition of seawater is “steady-state,” which means that

the fluxes of ions and other components to seawater are balanced by equal fluxes out of seawater, or *sinks*. For the elements of interest to us here, the primary sinks are absorption on particles, both organic and inorganic, precipitation in manganese nodules on the seafloor (although here again adsorption might be a better description of the actual chemical process), and biological precipitation of calcium carbonate. The latter is the dominant sink for Sr, while the remaining sinks dominate for Nd, Hf, Pb, and Os. While some of these radiogenic tracers are used to document modern ocean circulation, it is the incorporation of these elements into the components of ocean floor sediment that makes them particularly valuable as ocean water tracers because these sedimentary materials provide a historical record how the marine system has changed over time, including both changes in circulation and changes in sources of fluxes of these elements. These changes can then elucidate, among other things, past climate change.

7.6.2 Nd, Hf, Os, and Pb in the modern ocean

As noted previously, the greatest usefulness of the radiogenic tracers may be in reconstructing past ocean circulation, that is, paleoceanography. That, however, requires an understanding of the present distribution of these isotope ratios in the oceans. The first measurements of Nd isotope ratios in seawater were made over 30 years ago (Piepraga and Wasserburg, 1980), so that by now the Nd isotopic composition of seawater, which ranges from $\epsilon_{\text{Nd}} = -27$ to 1, is well characterized. Indeed, a database published by Lacan et al. (2012) contains 880 analyses. These are illustrated in Figure 7.30, which shows the frequency distribution of ϵ_{Nd} in the four oceans. The most radiogenic Nd occurs in the Atlantic and Arctic Oceans, with average ϵ_{Nd} of -11.4 ± 3.4 and -10.1 ± 1.7 , respectively. The least radiogenic Nd occurs in the Pacific, with average ϵ_{Nd} of -3.9 ± 1.8 and the Indian is intermediate, with average ϵ_{Nd} of -6.6 ± 2.5 . Peucker-Ehrenbrink et al. (2010) estimate the mean ϵ_{Nd} of seawater as -7.2 ± 0.5 . The radiogenic nature of Pacific Ocean Nd originally suggested hydrothermal inputs might be important (Piepraga and Wasserburg, 1980) because of the greater mid-ocean ridge magmatism and hydrothermal activity there,

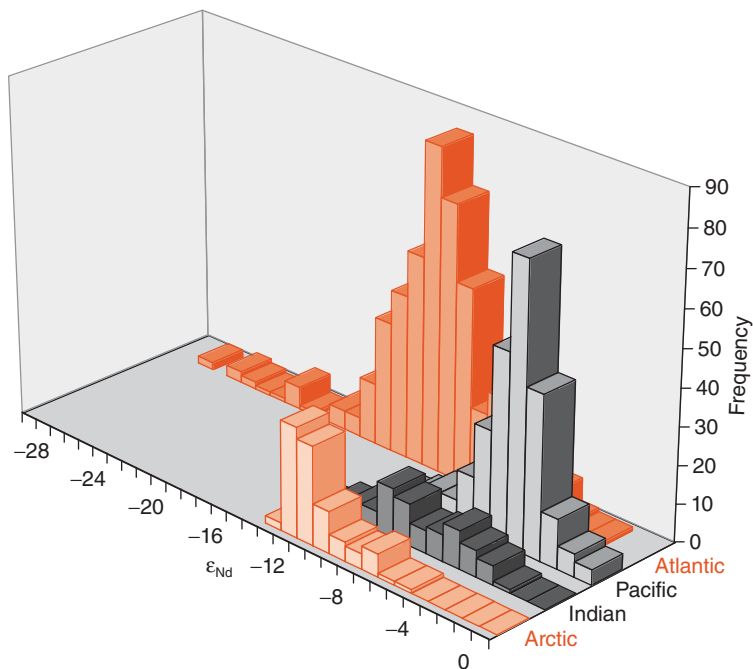


Figure 7.30 Histogram of ϵ_{Nd} dissolved in seawater, illustrating the radiogenic and unradiogenic nature of Pacific and Atlantic waters, respectively. Atlantic data includes water from the Mediterranean, which is relatively radiogenic. Data from compilation of Lacan et al. (2012).

but subsequent work shows the Nd dissolved in hydrothermal fluids is very quickly scavenged by particles, reducing the hydrothermal input to negligible levels (Halliday et al., 1992). The difference instead relates to the nature and age, and therefore isotopic composition, of geologic provinces supplying Nd to the ocean basins. The Pacific is surrounded by young volcanic arcs with relatively high ϵ_{Nd} while the Atlantic is surrounded by older tectonic blocks with lower ϵ_{Nd} , as is well demonstrated in the compilation of Jeandel et al. (2007). The most extremely unradiogenic Nd occurs in the Baffin Bay and the Labrador Sea, which are surrounded by extensive outcropping of Archean crust. Seawater in this region is a major source of NADW, which accounts for the particularly unradiogenic character of this water mass ($\epsilon_{\text{Nd}} \approx -14$). The unradiogenic nature of NADW is somewhat moderated as it flows southward, but it remains distinctive in the extreme South Atlantic where it mixes with Antarctic waters to become part of the CDW with ϵ_{Nd} of -8 to -9 (Stichel et al., 2012). Waters in the North Pacific tend to have the most radiogenic Nd. Surface waters show greater variability than

deep water. Attempts to reproduce the global pattern of ϵ_{Nd} in the oceans suggest that isotopic exchange between dissolved Nd and Nd in sedimentary particles on continental margins exerts an important control on isotopic composition (e.g., Albarède et al., 1997; Van der Flierd et al., 2004; Arsouze et al., 2009).

There are far fewer data on Hf isotopic composition as it has only recently become possible to directly measure Hf isotope ratios in seawater (e.g., Godfrey et al., 2009; Zimmermann et al., 2009a, 2009b). Measured values in Atlantic, Arctic, and Pacific seawater ranges from $\epsilon_{\text{Hf}} = 5.7$ to 8.6 . Figure 7.31 shows the relationship between ϵ_{Hf} and ϵ_{Nd} in seawater. The data fall along a distinctively lower slope than the terrestrial array (Figure 2.20), and mirror the slope observed in marine sediments and manganese nodules (White et al., 1986; Vervoort et al., 2011), which Albarède et al., (1998) termed the “seawater array.” As recognized early on, the discordance between the mantle and seawater arrays results from the difference in behavior of Nd and Hf in weathering (Patchett et al., 1984; White et al., 1986). Whereas Nd concentrates largely in clays and other fine-grained material, much of

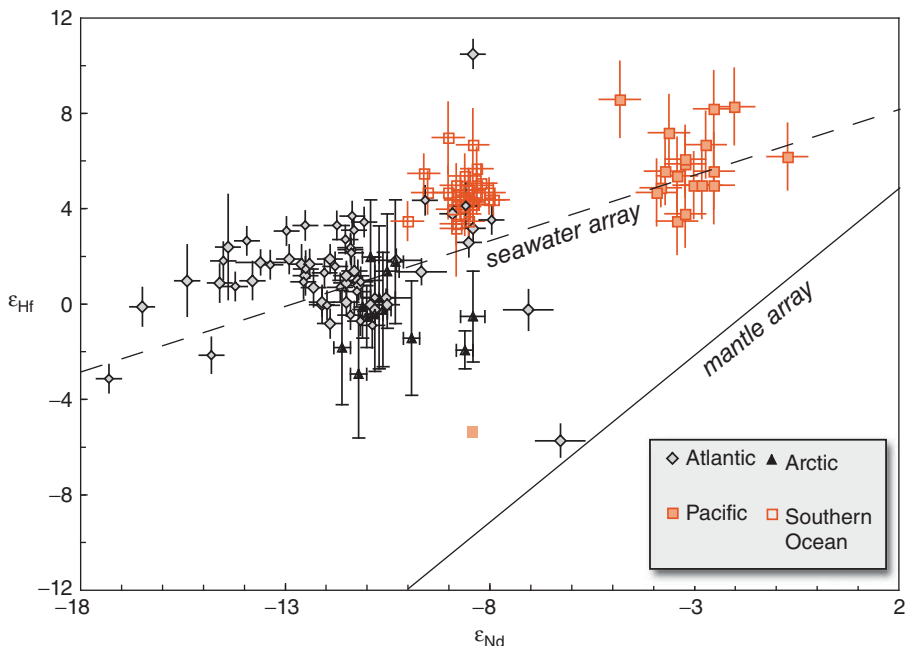


Figure 7.31 ϵ_{Hf} vs. ϵ_{Nd} in seawater. The “mantle array” is the correlation in mantle-derived rocks shown in Figure 2.20. The seawater array mirrors that observed in authigenic marine sediments (Vervoort et al., 2011). Data from Godfrey et al., (2009), Zimmermann et al. (2009a,b), Rickli et al. (2009, 2010) and Stichel et al. (2012).

the budget of Hf in sedimentary rocks is in zircon. Hf in zircon is very unradiogenic due to very low Lu/Hf. Zircon is a heavy mineral that resists mechanical weathering and transport, thus much of it remains in coarse-grained sediments of the continents and continental shelves. Clays and fine-grained accessory minerals, rich in Nd and radiogenic Hf, are more readily transported, by a combination of rivers, currents, and winds, to the deep ocean. This incongruent release of Hf appears to extend to Saharan dust carried to the Atlantic, as while Nd isotopic composition of surface waters is similar to that of dust, the Hf in surface waters is more radiogenic than the dust (Rickli et al., 2010). Hf isotope ratios appear to be less sensitive to ocean circulation changes, limiting the utility of ϵ_{Hf} as a stand-alone oceanographic tracer (Van der Flierdt et al., 2004).

The data also suggest two other differences between Hf and Nd in seawater. First, reduced variance in Hf isotopic composition is consistent with the longer residence time of Hf in seawater noted in the previous section. Second, the more radiogenic character of Hf, even at the high $\epsilon_{\text{Hf}} - \epsilon_{\text{Nd}}$ end of the array suggests

a greater proportion of “mantle” in seawater Hf supplied by ridge crest hydrothermal activity (White et al., 1986). Hf is present in river and ocean water mainly as $\text{Hf}(\text{OH})_4^-$ and as such is probably present primarily in colloids rather than in truly dissolved form. This colloidal Hf and Zr in river water is removed as the colloids aggregate and settle into the sediment and become during estuarine mixing (Bau and Koschinsky (2006)). Thus the radiogenic nature of Hf in seawater may reflect the very low flux of Hf from the continents rather than a particularly high flux from hydrothermal vents.

Pb isotope ratios present perhaps the greatest analytical challenge, because of the extremely low concentrations combined high blank levels that result from contamination with anthropogenic lead. Consequently, relatively few data exist and are reported as $^{207}\text{Pb}/^{206}\text{Pb}$ and $^{208}\text{Pb}/^{206}\text{Pb}$ ratios as ^{204}Pb levels are too low to measure accurately. The data that do exist show that even in deep Pacific water, the remotest and oldest seawater, anthropogenic lead dominates (Wu et al., 2010). Data on the natural Pb distribution in the ocean comes largely from manganese

nodules on the seafloor, into which seawater Pb is incorporated at high concentration. These data show $^{206}\text{Pb}/^{204}\text{Pb}$ ratios varying from about 18.5 to 19.3 (von Blanckenburg et al., 1996). As with Nd and Hf, the more “mantle-like” isotopic signatures are found in Pacific Ocean while more radiogenic, crustal-like signatures occur in the Atlantic, particularly the North Atlantic. Pb isotopes are well mixed in the Pacific and there is no evidence for the import of North Atlantic deep water-derived lead into either the Pacific or North Indian Ocean, a consequence of the short residence time of Pb in deep water (80–100 a). Rivers appear to be the major source of dissolved Pb in seawater, although dissolution of aeolian particulates may account for about 12% of the total flux and locally more (Henderson and Maier-Reimer, 2002). Although hydrothermal fluids are Pb-rich, they do not seem to be a significant source of seawater Pb as the Pb is quickly removed by particles in the fluid.

Osmium is, of course, an extremely rare element and this is certainly true in seawater, where the concentration is $\sim 10^{-8}$ ppm (10^{-14}g/g or $5 \times 10^{-14}\text{mol/kg}$). Osmium isotopic composition of deep water appears to be homogeneous within analytical error at $^{187}\text{Os}/^{188}\text{Os} = 1.067 \pm 0.011$ (Sharma et al., 1997; Levasseur et al., 1998; Woodhouse et al., 1999), which reflects a balance of a variety of sources. Interestingly, interplanetary dust particles and meteorites are a small but significant (5%) source of seawater Os. That source and hydrothermal systems developed on abyssal peridotite provide unradiogenic Os ($^{187}\text{Os}/^{188}\text{Os} \approx 0.13$) to balance radiogenic Os from the continents (e.g., Burton et al., 2010), which has an average $^{187}\text{Os}/^{188}\text{Os}$ of 1.4. Most of this continental Os is provided by rivers, but the aeolian flux is difficult to evaluate since loess has the same $^{187}\text{Os}/^{188}\text{Os}$ as seawater (Peucker-Ehrenbrink and Jahn, 2001). Chen et al. (2009) have reported $^{187}\text{Os}/^{188}\text{Os}$ ratios as low as 0.76 in Atlantic surface waters, which the authors interpret as reflecting recent anthropogenic inputs.

7.6.3 Radiogenic isotopes in paleoceanography

Neodymium isotope ratios have found particularly widespread use in studying ocean circulation changes associated with the

climatic oscillations of the Pleistocene. As we'll discuss in Chapter 10, the “Ice Ages” resulted from small variations in the Earth's orbit and rotation (the Milankovitch variations) that changed the amount of solar energy, or insolation, that reached high northern latitudes. This triggered a number of other changes that greatly amplified the small insolation signal into quite large changes in global climate. One of the most important of these amplifying factors was changes in ocean circulation, particularly in the North Atlantic and in production of North Atlantic Deep Water (NADW). As we found in the previous section, NADW has a uniquely unradiogenic Nd isotope signature, which can be imprinted on to the various authigenic components of ocean floor sediment, most notably ferromanganese nodules, crusts, and coatings on detrital and biogenic particles as the water mass flows southward. The latter can be selectively removed from the sediment by leaching with a complexing agent such as hydroxylamine hydrochloride or ethylenediaminetetraacetic acid (EDTA) and a stratigraphic history of the Nd isotopic composition of bottom water reconstructed. Figure 7.32 shows Nd isotopic variations of bottom water determined in this way from two localities, the Blake Ridge, off the coast of the southeastern USA, and the Cape Basin, southeast of the Cape of Good Hope. The longer Cape Basin record (Piotrowski et al., 2005: 2008) shows irregular variations through the Wisconsinan Ice Age that can be correlated with climatic and oceanographic events documented from sedimentological and stable isotope studies (we'll discuss these in Chapter 10). Both records exhibit a decrease in ϵ_{Nd} as the Wisconsinan ended, indicating a change to a circulation pattern similar to the present with a strong flow of NADW as ice volumes decreased (compare Figure 10.19). The NADW signal is stronger in the Blake Plateau record (Gutjahr et al., 2008, 2010) because, unlike in the Cape Basin, it is relatively undiluted with southern ocean waters.

Because lead has three radiogenic isotopes, it can be possible to identify multiple causative factors in isotope ratios variations. In the modern ocean, relatively warm ($\sim 10^\circ\text{C}$) but highly saline and therefore dense water flowing out of the Strait of Gibraltar plays an important role in North Atlantic

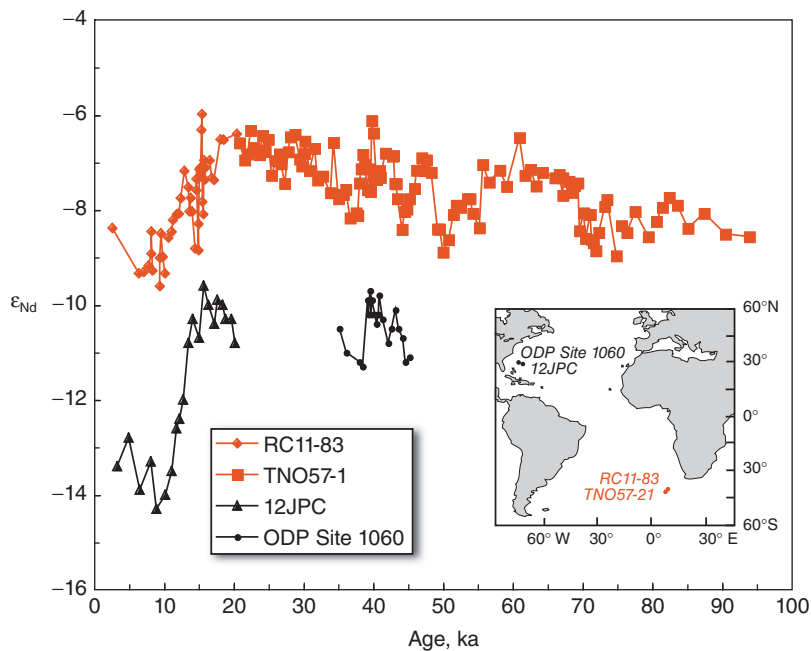


Figure 7.32 Variation in Nd isotopic composition of bottom water at two localities (locations shown in inset) as recorded by ferromanganese coatings on sedimentary particles in four cores. Data from Piotrowski et al. (2005), Gutjahr et al. (2008, 2010).

circulation and, ultimately, in production of NADW. Some of this Mediterranean Outflow Water (MOW) spreads out in the Central Atlantic at a depth of about 1000 m forming so-called Mediterranean Intermediate Water (MIW), while part of it flows north along the eastern Atlantic margin toward the Norwegian-Greenland Sea where its highly saline character preconditions NADW formation. Stichel et al. (2012) analyzed Nd and Pb isotope ratios in authigenic components of sediments of the Iberian continental margin. The Nd isotope ratios were compromised, probably by exchange with sediments carried downslope in the nepheloid layer, but Pb isotope revealed changes in both the isotopic composition of MOW and its outflow pattern over the last 23,000 years. Isotopic composition changes of the MOW were likely due to changing balances of riverine and aeolian Pb input to the Mediterranean; glacial climates were drier and likely favored a greater Aeolian input. Changes in outflow pattern could be linked to changes in NADW production discussed earlier.

On longer time scales, both Nd and Pb isotope ratios in manganese crusts suggest the present deep circulation of the Atlantic,

and the characteristic radiogenic Pb and unradiogenic Nd of deep water, has only been established within the last 8 Ma (O’Nions et al., 1998). The cause of the isotopic shift is unclear. Smaller shifts in ϵ_{Nd} are observed in the Pacific around 3–5 Ma, which corresponds to the closure of the Isthmus of Panama. O’Nions et al. (1998) speculate this may reflect the flow of NADW into the Pacific. The relatively unradiogenic nature of Pb in the North Pacific seems to have been maintained throughout the Cenozoic (Chen et al., 2013).

As we pointed out in Chapter 2, the Os isotopic composition of seawater has varied through time as a consequence of variation in the proportion of crustal, mantle, and crustal fluxes to seawater. As Figure 7.33 shows, there has been a particularly rapid increase in $^{187}\text{Os}/^{188}\text{Os}$, similar to that observed for $^{87}\text{Sr}/^{86}\text{Sr}$ (Figure 2.12). The likely cause of both is an increase of continental weathering flux resulting from Cenozoic mountain-building, most notably the rise of Himalayas, but also the Alps, Rockies, and Andes (Peucker-Ehrenbrink et al., 1995). It may also reflect a decreasing hydrothermal flux resulting from decreasing sea floor

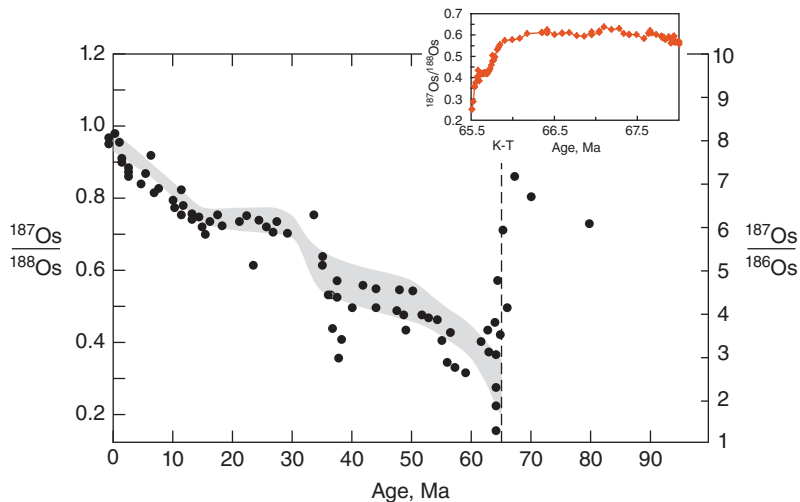


Figure 7.33 Os isotope composition of seawater over the last 80 Ma based on data in Peucker-Ehrenbrink et al. (1995) and Peucker-Ehrenbrink and Ravizza (2000). Gray field represents Peucker-Ehrenbrink et al.'s (1995) best estimates of seawater Os isotopic composition. Inset shows the data from the late Cretaceous Gubbio Formation of Robinson et al. (2009). K-T is the Cretaceous-Tertiary Boundary.

spreading rates. The geochemical behavior of both at the surface of the Earth is related to carbon, but while Sr is concentrated in carbonates, Os is concentrated in organic rich sediments.

Very low $^{187}\text{Os}/^{188}\text{Os}$ occurs exactly at the Cretaceous-Tertiary boundary (65.5 Ma). The inset shows a high-resolution study of the Gubbio Formation in Italy by Robinson et al. (2009). The lowest ratios occur right at the Cretaceous-Tertiary Boundary and are associated with elevated Ir, Os, and Pt concentrations, and are thus almost certainly due to chondritic Os ($^{187}\text{Os}/^{188}\text{Os} = 0.128$) delivered by the Chicxulub impactor. The study shows, however, that $^{187}\text{Os}/^{188}\text{Os}$ began to decline more than 500,000 years before the K-T boundary and similar declines are observed in several ODP cores. One possibility is that diagenetic remobilization has smeared out the impactor signal, but based on platinum group element concentrations, Robinson et al. concluded that in the Gubbio this affects $^{187}\text{Os}/^{188}\text{Os}$ no more than a meter (corresponding to roughly 70,000 years) from the boundary. The authors conclude the decline was a consequence of Deccan volcanism, although it is unclear whether the decline is a result of mantle Os released by Deccan volcanism or some indirect cause.

Osmium isotopes also show shorter-term variations reflecting the changing balance of crustal, cosmic, and mantle fluxes. Figure 7.34 shows the $^{187}\text{Os}/^{188}\text{Os}$ in cleaned foraminifera in sediment from ODP Site 578 in the Indian Ocean (Burton et al., 2010) and in bulk sediment in two cores from the southeastern Pacific (Oxburgh, 1998). Overall, there is good agreement between the two, though the Indian Ocean data show more variation, perhaps because of a component of detrital sediment in the Pacific cores, whereas foraminiferal calcite should contain only seawater-derived Os. Both data sets show minima at the last glacial maximum, approximately 20,000 years ago, and the previous one, approximately 150,000 to 160,000 years ago. Variations likely result from a decrease in the delivery of high $^{187}\text{Os}/^{188}\text{Os}$ continental weathering products to the ocean in the drier glacial climate. The $^{187}\text{Os}/^{188}\text{Os}$ also strongly, but not perfectly, anti-correlate with ε_{Nd} measured in foraminifera from Site 578 by Burton and Vance (2000). The previous glacial maximum in ε_{Nd} (note the scale is inverted) occurs somewhat later, around 135,000 years ago, than the $^{187}\text{Os}/^{188}\text{Os}$ minimum. Both Oxburgh (1998) and Burton et al. (2010) argue that the data are consistent with residence time (<12,000 years) that is closer

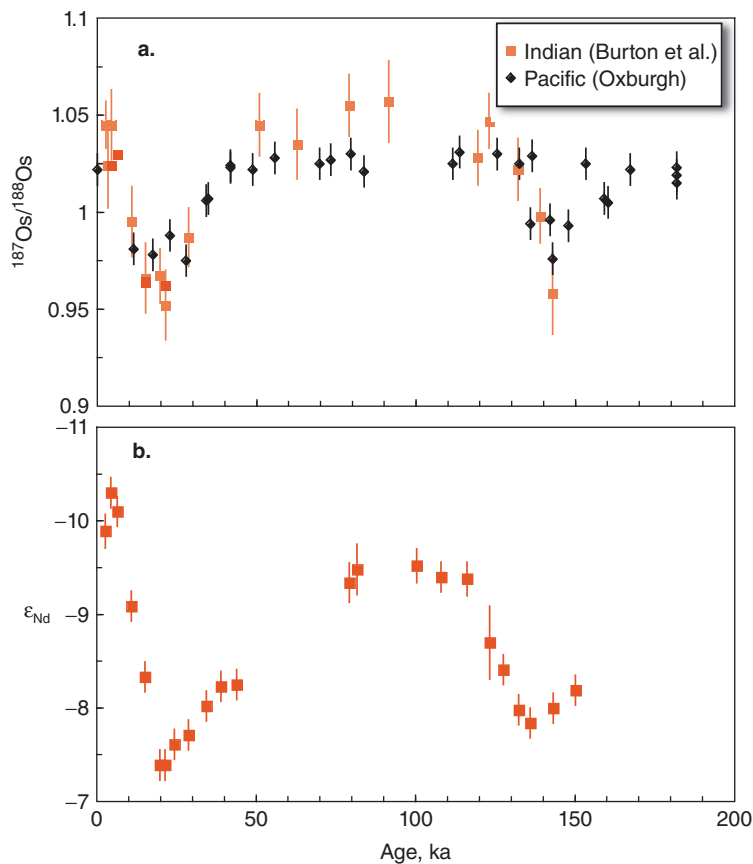


Figure 7.34 (a) $^{187}\text{Os}/^{188}\text{Os}$ from foraminifera in ODP Site 578 in the Indian Ocean (Burton et al., 2010) and bulk sediment in cores V19-54 and V19-55 in the Pacific (Oxburgh, 1998). (b) Nd isotope ratios in shells of the foram *G. menardii* from ODP Site 578 (Burton and Vance, 2000).

to the short end of the range of estimates (4000–40,000 years).

As Figure 2.12 shows, the $^{87}\text{Sr}/^{86}\text{Sr}$ of seawater has increased dramatically through the Cenozoic from about 0.7078–0.70925 at present. This changing isotopic composition results from changes in either the hydrothermal Sr flux, the riverine Sr flux or the $^{87}\text{Sr}/^{86}\text{Sr}$ of the riverine flux or some combination of these. Richter et al. (1992) argued that the changes are too great to be explained by the hydrothermal flux and that the most likely explanation relates to the rise of the Himalayas. In support of that hypothesis, they noted that the most rapid change in seawater $^{87}\text{Sr}/^{86}\text{Sr}$ occurred between 15 and 20 Ma, a time of exceptionally high erosion rates in the Himalayas. Sr in rivers draining the Himalayas is also exceptionally radiogenic. The Ganges, for example, has a $^{87}\text{Sr}/^{86}\text{Sr}$ of 0.725 while that of the Brahmaputra is

0.720 compared to a global average riverine $^{87}\text{Sr}/^{86}\text{Sr}$ of 0.7111 (Peucker-Ehrenbrink et al., 2010).

The long residence time of Sr in the ocean means that its isotopic composition is largely insensitive to variations in fluxes on the time scale of glacial-interglacial fluxes, but variations do occur on the time scales of several hundred thousand years. These shorter-term variations also cannot be accounted by changes in the hydrothermal flux and hence must be due to changes in the riverine flux or its isotopic composition. Capo and DePaolo (1990) noted the correlation between changes in seawater $^{87}\text{Sr}/^{86}\text{Sr}$ and climate proxies, such as $\delta^{18}\text{O}$ (we will discuss these in Chapter 10). Derry and France-Lanord (1996) suggested that in this case the connection between seawater $^{87}\text{Sr}/^{86}\text{Sr}$ might be the opposite of expected. They argued that reduced erosion rates but increased weathering intensity

during the Pliocene released proportionally more Sr minerals with high Rb/Sr like biotite and less from low Rb/Sr minerals such as calcite and plagioclase. The result was a decrease in the Himalayan riverine flux but an increase in its $^{87}\text{Sr}/^{86}\text{Sr}$ in the Pliocene.

NOTES

1. In brief, a *tonalite* is an alkali-poor, quartz-rich granite.
2. Units of km^3/yr are sometimes called Armstrong Units after Dick Armstrong and abbreviated (with tongue in cheek) as AU.
3. The stratigraphic age is the age of deposition of the sediment determined by conventional geochronological or geological means.

REFERENCES

- Albarède, F., Goldstein, S. L. and Dautel, D. 1997. The neodymium isotopic composition of manganese nodules from the Southern and Indian oceans, the global oceanic neodymium budget, and their bearing on deep ocean circulation. *Geochimica et Cosmochimica Acta*, 61: 1277–1291, doi: 10.1016/S0016-7037(96)00404-8.
- Albarède, F., Simonetti, A., Vervoort, J. D., Blichert-Toft, J. and Abouchami, W. 1998. A Hf-Nd isotopic correlation in ferromanganese nodules. *Geophysical Research Letters*, 25: 3895–3898, doi: 10.1029/1998GL900008.
- Allègre, C. J. and Rousseau, D. 1984. The growth of the continent through geological time studied by Nd isotope analysis of shales. *Earth and Planetary Science Letters*, 67: 19–34, doi: 10.1016/0012-821X(84)90035-9.
- Armstrong, R. L., 1968. A model for the evolution of strontium and lead isotopes in a dynamic Earth. *Reviews of Geophysics*, 6: 175–199.
- Armstrong, R. L., 1971. Isotopic and chemical constraints on models of magma genesis in volcanic arcs, *Earth and Planetary Science Letters*, 12: 137–142.
- Armstrong, R. L., 1981. Radiogenic isotopes: the case for crustal recycling on a near-steady-state no-continental-growth Earth. In: *The Origin and Evolution of the Earth's Continental Crust*, Moorbath, S. and Windley, B. F. (eds). pp. 259–287, London: The Royal Society.
- Arsouze, T., Dutay, J. C., Lacan, F. and Jeandel, C. 2009. Reconstructing the Nd oceanic cycle using a coupled dynamical-biogeochemical model. *Biogeosciences*, 6: 2829–2846, doi: 10.5194/bg-6–2829–2009.
- Asmeron, Y. and Jacobsen, S. B. 1993. The Pb isotopic evolution of the Earth: inferences from river water suspended loads. *Earth and Planetary Science Letters*, 115: 245–256.
- Bau, M. and Koschinsky, A. 2006. Hafnium and neodymium isotopes in seawater and in ferromanganese crusts: The “element perspective.” *Earth and Planetary Science Letters*, 241: 952–961, doi: 10.1016/j.epsl.2005.09.067.
- Ben Othman, D., White, W. M. and Patchett, J. 1989. The geochemistry of marine sediments, island arc magma genesis, and crust-mantle recycling, *Earth and Planetary Science Letters*, 94: 1–21.
- Bennett, V. C. and DePaolo, D. J. 1987. Proterozoic crustal history of the western United States as determined by neodymium isotope mapping. *Bulletin of the Geological Society of America*, 99: 674–685.
- Bennett, V. C., Brandon, A. D. and Nutman, A. P. 2007. Coupled ^{142}Nd - ^{143}Nd isotopic evidence for Hadean mantle dynamics, *Science*, 318: 1907–1910.
- Blichert-Toft, J. and Albarède, F. 2008. Hafnium isotopes in Jack Hills zircons and the formation of the Hadean crust. *Earth and Planetary Science Letters*, 265: 686–702, doi: 10.1016/j.epsl.2007.10.054.
- Boyet, M., Blichert-Toft, J., Rosing, M., Storey, M., Telouk, P. and Albarede, F. 2003. ^{142}Nd evidence for early Earth differentiation. *Earth and Planetary Science Letters*, 214: 427–442.
- Burton, K. W. and Vance, D. 2000. Glacial-interglacial variations in the neodymium isotope composition of seawater in the Bay of Bengal recorded by planktonic foraminifera. *Earth and Planetary Science Letters*, 176: 425–441, doi: 10.1016/S0012-821X(00)00011-X.
- Burton, K. W., Gannoun, A. and Parkinson, I. J. 2010. Climate driven glacial-interglacial variations in the osmium isotope composition of seawater recorded by planktic foraminifera. *Earth and Planetary Science Letters*, 295: 58–68, doi: 10.1016/j.epsl.2010.03.026.
- Condie, K. C. 1995. Episodic ages of greenstones: a key to mantle dynamics? *Geophysical Research Letters*, 22: 2215–2218.

4. One way to rationalize this equation is to think of newly deposited sediment at τ_{ST} as a 50-50 mixture of material derived from the mantle at 4.0 Ga and τ_{ST} . The equation for the T_{CR} of this mixture would be:

$$\tau_{\text{CR}} = \frac{4.0 + \tau_{\text{ST}}}{2}.$$

At time of deposition, its crustal residence age would have been: $\tau_{\text{CR}} = \frac{4.0 + \tau_{\text{ST}}}{2} - \tau_{\text{ST}} = \frac{4.0 \tau_{\text{ST}}}{2}$. You could satisfy yourself that a mixture of material having τ_{CR} of all ages between 4.0 Ga and τ_{ST} would have the same τ_{CR} as given by this equation.

- Condie, K. C. 1998. Episodic continental growth and supercontinents: a mantle avalanche connection? *Earth and Planetary Science Letters*, 163: 97–108, doi: 10.1016/s0012-821x(98)00178-2.
- Condie, K. C. and Aster, R. C. 2010. Episodic zircon age spectra of orogenic granitoids: The supercontinent connection and continental growth. *Precambrian Research*, 180: 227–236, doi: 10.1016/j.precamres.2010.03.008.
- Capo, R. C. and DePaolo, D. J. 1990. Seawater strontium isotopic variations from 2.5 million years ago to the present. *Science*, 249: 51–55.
- Caro, G., Bourdon, B., Birck, J.-L. and Moorbath, S. 2003. ^{146}Sm - ^{142}Nd evidence from Isua metamorphosed sediments for early differentiation of the Earth's mantle. *Nature*, 423: 428–432.
- Carpentier, M., Chauvel, C. and Mattielli, N. 2008. Pb-Nd isotopic constraints on sedimentary input into the Lesser Antilles arc system. *Earth and Planetary Science Letters*, 272: 199–211.
- Cates, N. L., Ziegler, K., Schmitt, A. K. and Mojzsis, S. J. 2013. Reduced, reused and recycled: Detrital zircons define a maximum age for the Eoarchean (ca. 3750–3780 Ma) Nuvvuagittuq Supracrustal Belt, Québec (Canada). *Earth and Planetary Science Letters*, 362: 283–293, doi: 10.1016/j.epsl.2012.11.054.
- Chappell, B. W. and White, A. 1974. Two contrasting granite types, *Pacific Geology*, 8: 173–174.
- Chen, C., Sedwick, P. N. and Sharma, M. 2009. Anthropogenic osmium in rain and snow reveals global-scale atmospheric contamination. *Proceedings of the National Academy of Sciences*, 106: 7724–7728, doi: 10.1073/pnas.0811803106.
- Chen, T.-Y., Ling, H.-F., Hu, R., Frank, M. and Jiang, S.-Y. 2013. Lead isotope provinciality of central North Pacific Deep Water over the Cenozoic. *Geochemistry, Geophysics, Geosystems*, 14: 1523–1537, doi:10.1002/ggge.20114.
- Chou, C.-L. 1978. Fractionation of siderophile elements in the Earth's upper mantle and lunar samples. *Proceedings of the Lunar and Planetary Science Conference*, 9: 163–165.
- Compston, W. and Pidgeon, R. T. 1986. Jack Hills, evidence of more very old detrital zircons in Western Australia, *Nature*, 321: 766–769.
- Davies, G. F. 1984. Geophysical and isotopic constraints on mantle convection: An interim synthesis. *Journal of Geophysical Research*, 89: 6017–6040.
- Debaille, V., O'Neill, C., Brandon, A. D., Haenecour, P., Yin, Q.-Z., Mattielli, N. and Treiman, A. H. 2013. Stagnant-lid tectonics in early Earth revealed by ^{142}Nd variations in late Archean rocks. *Earth and Planetary Science Letters*, 373: 83–92, doi: 10.1016/j.epsl.2013.04.016.
- Derry, L. A. and France-Lanord, C. 1996. Neogene Himalayan weathering history and river ^{87}Sr / ^{86}Sr : impact on the marine Sr record. *Earth and Planetary Science Letters*, 142: 59–74.
- Esser, B. K. and Turekian, K. K. 1993. The osmium isotopic composition of the continental crust. *Geochimica et Cosmochimica Acta*, 57: 3093–3104.
- Faure, G. 1986. *Principles of Isotope Geology*. New York: John Wiley & Sons, Inc.
- Frank, M. 2002. Radiogenic isotopes: tracers of past ocean circulation and erosional input. *Reviews of Geophysics*, 40: 1–1–1–38, doi: 10.1029/2000rg000094.
- Froude, D. O., Ireland, T. R., Kinny, P. D., Williams, I. S., Compston, W., Williams, I. R., and Myers, J. S. 1983. Ion microprobe identification of 4100–4200 Myr-old terrestrial zircons. *Nature*, 304: 616–618.
- Galer, S. J. G. and O'Nions, R. K. 1985. Residence time of thorium, uranium and lead in the mantle with implications for mantle convection. *Nature*, 316: 778–782.
- Garçon, M., Chauvel, C., France-Lanord, C., Limonta, M. and Garzanti, E. 2013. Removing the “heavy mineral effect” to obtain a new Pb isotopic value for the upper crust. *Geochemistry, Geophysics, Geosystems*, 14: doi: 10.1002/ggge.20219.
- Godfrey, L. V., Zimmermann, B., Lee, D. C., King, R. L., Vervoort, J. D., Sherrell, R. M. and Halliday, A. N. 2009. Hafnium and neodymium isotope variations in NE Atlantic seawater. *Geochemistry, Geophysics, Geosystems*, 10: Q08015, doi: 10.1029/2009gc002508.
- Goldstein, S. J. and Jacobsen, S. B. 1987. The Nd and Sr isotopic systematics of river-water dissolved material: implications for the sources of Nd and Sr in seawater. *Chemical Geology (Isotope Geoscience Section)*, 66: 245–272.
- Goldstein, S. J. and Jacobsen, S. B. 1988. Nd and Sr isotopic systematics of river-water suspended material: implications for crustal evolution. *Earth and Planetary Science Letters*, 87: 249–265.
- Goldstein, S. J., O'Nions, R. K. and Hamilton, P. J. 1984. A Sm-Nd isotopic study of atmospheric dusts and particulates from major river systems. *Earth and Planetary Science Letters*, 70: 221–236.
- Goldstein, S. L., O'Nions, R. K. and Hamilton, P. J. 1986. A Sm-Nd study of atmospheric dusts and particulates from major river systems, *Earth and Planetary Science Letters*, 70: 221–236.
- Gutjahr, M., Frank, M., Stirling, C. H., Keigwin, L. D. and Halliday, A. N. 2008. Tracing the Nd isotope evolution of North Atlantic Deep and Intermediate Waters in the western North Atlantic since the Last Glacial Maximum from Blake Ridge sediments. *Earth and Planetary Science Letters*, 266: 61–77, doi: 10.1016/j.epsl.2007.10.037.
- Gutjahr, M., Hoogakker, B. A. A., Frank, M. and McCave, I. N. 2010. Changes in North Atlantic Deep Water strength and bottom water masses during Marine Isotope Stage 3 (45–35 ka BP). *Quaternary Science Reviews*, 29: 2451–2461, doi: 10.1016/j.quascirev.2010.02.024.
- Halliday, A. N. 2004. Mixing, volatile loss and compositional change during impact-drive accretion of the Earth, *Nature*, 427: 505–509.

- Halliday, A. N., Davidson, J. P., Holden, P., Owen, R. M. and Olivarez, A. M. 1992. Metalliferous sediments and the scavenging residence time of Nd near hydrothermal vents. *Geophysical Research Letters*, 19: doi: 10.1029/92gl00393.
- Harrison, T. M., Blichert-Toft, J., Muller, W., Albarède, F., Holden, P. and Mojzsis, S. J. 2005. Heterogeneous Hadean hafnium: evidence of continental crust at 4.4 to 4.5 Ga. *Science*, 310: 1947–1950.
- Hawkesworth, C. J. and Kemp, A. I. S. 2006. Using hafnium and oxygen isotopes in zircons to unravel the record of crustal evolution. *Chemical Geology*, 226: 144–162.
- Hawkesworth, C. J., Dhuime, B., Pietranik, A. B., Cawood, P. A., Kemp, A. I. S. and Storey, C. D. 2010. The generation and evolution of the continental crust. *Journal of the Geological Society*, 167: 229–248, doi:10.1144/0016-76492009-072.
- Henderson, G. M. and Maier-Reimer, E. 2002. Advection and removal of ^{210}Pb and stable Pb isotopes in the oceans: a general circulation model study. *Geochimica et Cosmochimica Acta*, 66: 257–272, doi: 10.1016/S0016-7037(01)00779-7.
- Hurley, P. M., Hughes, H., Faure, G., Fairbairn, H. W. and Pinson, W. H. 1962, Radiogenic strontium-87 model of continent formation. *Journal of Geophysical Research*, 67: 5315–5334.
- Hurley, P. M., and Rand, J. R. 1969. Pre-drift continental nuclei, *Science*, 164: 1229–1242.
- Iizuka, T., Horie, K., Komiya, T., Maruyama, S., Hirata, T., Hidaka, H. and Windley, B. F. 2006. 4.2 Ga zircon xenocryst in an Acosta gneiss from northwestern Canada: Evidence for early continental crust. *Geology*, 34: 245–248, doi:10.1130/g22124.1.
- Jackson, M. G. and Carlson, R. W. 2012. Homogeneous superchondritic $^{142}\text{Nd}/^{144}\text{Nd}$ in the mid-ocean ridge basalt and ocean island basalt mantle. *Geochemistry, Geophysics, Geosystems*, 13: Q06011, doi:10.1029/2012gc004114.
- Jeandel, C., Arsouze, T., Lacan, F., Téchiné, P. and Dutay, J. C. 2007. Isotopic Nd compositions and concentrations of the lithogenic inputs into the ocean: A compilation, with an emphasis on the margins. *Chemical Geology*, 239, 156–164, doi: 10.1016/j.chemgeo.2006.11.013.
- Kemp, A. I. S., Wilde, S. A., Hawkesworth, C. J., Coath, C. D., Nemchin, A., Pidgeon, R. T. et al., 2010. Hadean crustal evolution revisited: New constraints from Pb-Hf isotope systematics of the Jack Hills zircons. *Earth and Planetary Science Letters*, 296: 45–56, doi:10.1016/j.epsl.2010.04.043.
- Kramers, J. D. and Tostikhin, I. N. 1997. Two terrestrial lead isotope paradoxes, forward transport modelling, core formation, and the history of the continental crust. *Chemical Geology*, 139: 75–110.
- Lacan, F., Tachikawa, K. and Jeandel, C. 2012. Neodymium isotopic composition of the oceans: A compilation of seawater data. *Chemical Geology*, 300–301, 177–184, doi:10.1016/j.chemgeo.2012.01.019.
- Langmuir, C. H., Vocke Jr, R. D., Hanson, G. N. and Hart, S. R. 1978. A general mixing equation with applications to Icelandic basalts. *Earth and Planetary Science Letters*, 37: 380–392.
- Levasseur, S., Birck, J.-L. and Allègre, C. J. 1998. Direct measurement of femtomoles of osmium and the $^{187}\text{Os}/^{186}\text{Os}$ ratio in seawater. *Science*, 282: 272–274, doi:10.1126/science.282.5387.272.
- McDermott, F., and Hawkesworth, C. 1991. Th, Pb, and Sr isotope variations in young island arc volcanics and oceanic sediments. *Earth and Planetary Science Letters*, 104: 1–15, doi: 10.1016/0012-821X(91)90232-7.
- Newsom, H. E., White, W. M., Jochum, K. P. and Hofmann, A. W. 1986. Siderophile and chalcophile element abundances in oceanic basalts, Pb isotope evolution and growth of the Earth's core, *Earth and Planetary Science Letters*, 80: 299–313.
- O'Neil, J., Carlson, R. W., Paquette, J.-L. and Francis, D. 2012. Formation age and metamorphic history of the Nuvvuagittuq Greenstone Belt. *Precambrian Research*, 220–221: 23–44, doi: 10.1016/j.precamres.2012.07.009.
- O'Neil, J., Carlson, R. L., Francis, D. and Stevenson, R. K. 2008. Neodymium-142 evidence for Hadean mafic crust. *Science*, 321: 1828–1831.
- O'Nions, R. K., Frank, M., von Blanckenburg, F. and Ling, H. F. 1998. Secular variation of Nd and Pb isotopes in ferromanganese crusts from the Atlantic, Indian and Pacific Oceans. *Earth and Planetary Science Letters*, 155: 15–28, doi: 10.1016/S0012-821X(97)00207-0.
- Oxburgh, R. 1998. Variations in the osmium isotope composition of sea water over the past 200,000 years. *Earth and Planetary Science Letters*, 159: 183–191, doi: 10.1016/S0012-821X(98)00057-0.
- Palmer, M. R. and Edmond, J. M. 1989. The strontium isotope budget of the modern ocean. *Earth and Planetary Science Letters*, 92: 11–26.
- Patchett, P. J., White, W. M., Feldmann, H., Kielinczuk, S. and Hofmann, A. W. 1984. Hafnium/rare earth element fractionation in the sedimentary system and crustal recycling into the Earth's mantle. *Earth and Planetary Science Letters*, 69: 365–378.
- Paul, D., White, W. M. and Turcotte, D. L. 2003. Constraints on the $^{232}\text{Th}/^{238}\text{U}$ ratio (κ) of the continental crust. *Geochemistry Geophysics Geosystems*, 4: doi: 10.1029/2002GC000497.
- Pegram, W. J., Esser, B. K., Krishnaswami, S. and Turekian, K. K. 1994. The isotopic composition of leachable osmium from river sediments. *Earth and Planetary Science Letters*, 128: 591–599.
- Peucker-Ehrenbrink, B. and Ravizza, G. 2000. The marine osmium isotope record. *Terra Nova*, 12: 205–219, doi: 10.1046/j.1365-3121.2000.00295.x.

- Peucker-Ehrenbrink, B. and Jahn, B.-M. 2001. Rhenium-osmium isotope systematics and platinum group element concentrations: Loess and the upper continental crust. *Geochemistry, Geophysics, Geosystems*, 2: 1061, doi: 10.1029/2001gc000172.
- Peucker-Ehrenbrink, B., Ravizza, G. and Hoffmann, A. W. 1995. The marine $^{187}\text{Os}/^{186}\text{Os}$ record of the past 80 million years. *Earth and Planetary Science Letters*, 130: 155–167.
- Peucker-Ehrenbrink, B., Miller, M. W., Arsouze, T. and Jeandel, C. 2010. Continental bedrock and riverine fluxes of strontium and neodymium isotopes to the oceans. *Geochemistry, Geophysics, Geosystems*, 11: Q03016, doi:10.1029/2009gc002869.
- Piepras, D. J. and Wasserburg, G. J. 1980. Neodymium isotopic variations in seawater. *Earth and Planetary Science Letters*, 50: 128–138, doi: 10.1016/0012–821X(80)90124–7.
- Piotrowski, A. M., Goldstein, S. L., Hemming, S. R. and Fairbanks, R. G. 2005. Temporal relationships of carbon cycling and ocean circulation at glacial boundaries. *Science*, 307: 1933–1938, doi: 10.1126/science.1104883.
- Piotrowski, A. M., Goldstein, S. L., Fairbanks, R. G. and Zylberman, D. R. 2008. Oscillating glacial northern and southern deep water formation from combined neodymium and carbon isotopes. *Earth and Planetary Science Letters*, 272: 394–405, doi: 10.1016/j.epsl.2008.05.011.
- Richter, F. M., Rowley, D. B. and DePaolo, D. J. 1992. Sr isotope evolution of seawater: the role of tectonics. *Earth and Planetary Science Letters*, 109: 11–23.
- Rickli, J., Frank, M. and Halliday, A. N. 2009. The hafnium-neodymium isotopic composition of Atlantic seawater. *Earth and Planetary Science Letters*, 280: 118–127, doi: 10.1016/j.epsl.2009.01.026.
- Rickli, J., Frank, M., Baker, A. R., Aciego, S., de Souza, G., Georg, R. B. and Halliday, A. N. 2010. Hafnium and neodymium isotopes in surface waters of the eastern Atlantic Ocean: Implications for sources and inputs of trace metals to the ocean. *Geochimica et Cosmochimica Acta*, 74: 540–557, doi: 10.1016/j.gca.2009.10.006.
- Rizo, H., Boyet, M., Blichert-Toft, J. and Rosing, M. T. 2013. Early mantle dynamics inferred from ^{142}Nd variations in Archean rocks from southwest Greenland. *Earth and Planetary Science Letters*, 377–378: 324–335, doi: 10.1016/j.epsl.2013.07.012.
- Rizo, H., Boyet, M., Blichert-Toft, J., O'Neil, J., Rosing, M. T. and Paquette, J.-L. 2012. The elusive Hadean enriched reservoir revealed by ^{142}Nd deficits in Isua Archaean rocks. *Nature*, 491: 96–100, doi: 10.1038/nature11565.
- Robinson, N., Ravizza, G., Coccioni, R., Peucker-Ehrenbrink, B. and Norris, R. 2009. A high-resolution marine $^{187}\text{Os}/^{188}\text{Os}$ record for the late Maastrichtian: Distinguishing the chemical fingerprints of Deccan volcanism and the KP impact event. *Earth and Planetary Science Letters*, 281: 159–168, doi: 10.1016/j.epsl.2009.02.019.
- Roth, A. S. G., Bourdon, B., Mojzsis, S. J., Touboul, M., Sprung, P., Guitreau, M. and Blichert-Toft, J. 2013. Inherited ^{142}Nd anomalies in Eoarchean protoliths. *Earth and Planetary Science Letters*, 361: 50–57, doi: 10.1016/j.epsl.2012.11.023.
- Rudnick, R. L. and Fountain, D. M. 1995. Nature and composition of the continental crust: a lower crustal perspective, *Reviews of Geophysics*, 33: 267–309.
- Rudnick, R. L. and Goldstein, S. L. 1990. The Pb isotopic compositions of lower crustal xenoliths and the evolution of lower crustal Pb, *Earth and Planetary Science Letters*, 98: 192–207, doi: 10.1016/0012–821X(90)90059–7.
- Rudnick, R. L. 1992. Xenoliths – samples of the lower crust. In: *Continental Lower Crust*, Fountain, D. M., Arculus, R. and Kay, R. W. (eds). pp. 269–316, Amsterdam: Elsevier.
- Scholl, D. W. and von Huene, R. 2009. Implications of estimated magmatic additions and recycling losses at the subduction zones of accretionary (non-collisional) and collisional (suturing) orogens. *Geological Society of London Special Publications*, 318: 105–125, doi:10.1144/sp318.4.
- Sharma, M., Papanastassiou, D. A. and Wasserburg, G. J. 1997. The concentration and isotopic composition of osmium in the oceans. *Geochimica et Cosmochimica Acta*, 61: 3287–3299, doi: 10.1016/S0016–7037(97)00210-X.
- Stichel, T., Frank, M., Rickli, J. r. and Haley, B. A. 2012. The hafnium and neodymium isotope composition of seawater in the Atlantic sector of the Southern Ocean. *Earth and Planetary Science Letters*, 317–318: 282–294, doi: 10.1016/j.epsl.2011.11.025.
- Taylor, S. R. and McLennan, S. M. 1985, *The Continental Crust: Its Composition and Evolution*, Oxford, Blackwell Scientific Publications, p. 312.
- Taylor, S. R. and McLennan, S. M. 1995, The geochemical evolution of the continental crust, *Reviews of Geophysics*, 33: 241–265.
- Taylor, D. J., McKeegan, K. D. and Harrison, T. M. 2009. Lu–Hf zircon evidence for rapid lunar differentiation. *Earth and Planetary Science Letters*, 279: 157–164, doi: 10.1016/j.epsl.2008.12.030.
- Tera, F., Brown, L., Morris, J. D., Sacks, I. S., Klein, J. and Middleton, R. 1986. Sediment incorporation in island-arc magmas: Inferences from ^{10}Be , *Geochimica et Cosmochimica Acta*, 50: 535–550.
- Touboul, M., Puchtel, I. S. and Walker, R. J. 2012. ^{182}W evidence for long-term preservation of early mantle differentiation products. *Science*, 335: 1065–1069, doi:10.1126/science.1216351.
- Touboul, M., Puchtel, I. S. and Walker, R. J. 2013. Tungsten isotope heterogeneities in Archean komatiites. *Mineralogical Magazine*, 77: 2348.
- Upadhyay, D., Scherer, E. E. and Mezger, K. 2009. ^{142}Nd evidence for an enriched Hadean reservoir in cratonic roots. *Nature*, 459: 1118–1121, doi: 10.1038/nature08089.

- Van de Flierdt, T., Frank, M., Lee, D.-C., Halliday, A. N., Reynolds, B. C. and Hein, J. R. 2004. New constraints on the sources and behavior of neodymium and hafnium in seawater from Pacific Ocean ferromanganese crusts. *Geochimica et Cosmochimica Acta*, 68: 3827–3843, doi: 10.1016/j.gca.2004.03.009.
- Vervoort, J. D., White, W. M. and Thorpe, R. 1994. Nd and Pb isotope ratios of the Abitibi greenstone belt: new evidence for very early differentiation of the Earth. *Earth and Planetary Science Letters*, 128: 215–229.
- Vervoort, J. D., Plank, T. and Prytulak, J. 2011. The Hf–Nd isotopic composition of marine sediments. *Geochimica et Cosmochimica Acta*, 75: 5903–5926, doi: 10.1016/j.gca.2011.07.046.
- Vervoort, J. D., Fisher, C. M. and Kemp, A. I. S. 2013. The myth of a highly heterogeneous Hf–Nd Eoarchean mantle and large early crustal volumes. *Mineralogical Magazine*, 77: 2409,
- von Blanckenburg, F., O’Nions, R. K. and Heinz, J. R. 1996. Distribution and sources of pre-anthropogenic lead isotopes in deep ocean water from Fe–Mn crusts. *Geochimica et Cosmochimica Acta*, 60: 4957–4963, doi: 10.1016/S0016-7037(96)00310-9.
- Wänke, H., Dreibus, G. and Jagoutz, E. 1984. Mantle geochemistry and accretion history of the Earth. In: *Archean Geochemistry*. Kröner, A. (ed.). Berlin: Springer.
- Wedepohl, K. H. 1995. The composition of the continental crust. *Geochimica et Cosmochimica Acta*, 59: 1217–1232.
- White, W. M., and Dupré, B. 1986. Sediment subduction and magma genesis in the Lesser Antilles: isotopic and trace element constraints. *Journal Geophysical Research*, 91: 5927–5941.
- White, W. M., Patchett, P. J. and BenOthman, D. 1986. Hf isotope ratios of marine sediments and Mn nodules: evidence for a mantle source of Hf in seawater. *Earth and Planetary Science Letters*, 79: 46–54.
- Willbold, M., Elliott, T. and Moorbat, S. 2011. The tungsten isotopic composition of the Earth’s mantle before the terminal bombardment. *Nature*, 477: 195–198, doi: 10.1038/nature10399.
- Willbold, M., Mojzsis, S. J. and Elliott, T. 2013. The $\epsilon_{182\text{W}}$ isotope composition of the ca. 3920 Ma Acosta Gneiss Complex. *Mineralogical Magazine*, 77: 2497,
- Woodhouse, O. B., Ravizza, G., Kenison Falkner, K., Statham, P. J. and Peucker-Ehrenbrink, B. 1999. Osmium in seawater: vertical profiles of concentration and isotopic composition in the eastern Pacific Ocean. *Earth and Planetary Science Letters*, 173: 223–233, doi: 10.1016/S0012-821X(99)00233-2.
- Wu, J., Rember, R., Jin, M., Boyle, E. A. and Flegal, A. R. 2010. Isotopic evidence for the source of lead in the North Pacific abyssal water. *Geochimica et Cosmochimica Acta*, 74: 4629–4638, doi: 10.1016/j.gca.2010.05.017.
- Zimmermann, B., Porcelli, D., Frank, M., Andersson, P. S., Baskaran, M., Lee, D.-C. and Halliday, A. N. 2009a. Hafnium isotopes in Arctic Ocean water. *Geochimica et Cosmochimica Acta*, 73: 3218–3233, doi: 10.1016/j.gca.2009.02.028.
- Zimmermann, B., Porcelli, D., Frank, M., Rickli, J. R., Lee, D.-C. and Halliday, A. N. 2009b. The hafnium isotope composition of Pacific Ocean water. *Geochimica et Cosmochimica Acta*, 73: 91–101, doi: 10.1016/j.gca.2008.09.033.

SUGGESTIONS FOR FURTHER READING

- Edmond, J. M. 1992. Himalayan tectonics, weathering processes, and the strontium isotope record in marine limestones. *Science*, 258: 1594–1597.
- Huang, Y., Chubakov, V., Mantovani, F., Rudnick, R. L. and McDonough, W. F. 2013. A reference Earth model for the heat-producing elements and associated geoneutrino flux. *Geochemistry, Geophysics, Geosystems*, 14: 2003–2029, doi: 10.1002/ggge.20129.
- Stumpf, R., Frank, M., Schönfeld, J. and Haley, B. A. 2010. Late Quaternary variability of Mediterranean Outflow Water from radiogenic Nd and Pb isotopes. *Quaternary Science Reviews*, 29: 2462–2472, doi: 10.1016/j.quascirev.2010.06.021.
- Vervoort, J. D., Patchett, P. J., Gehrels, G. E. and Nutmann, A. P. 1996. Constraints on early differentiation from hafnium and neodymium isotopes. *Nature*, 379: 624–627.
- White, W. M. 1989. Geochemical evidence for crust-to-mantle recycling in subduction zones, in *Crust/Mantle Recycling at Convergence Zones*, Gulen, S. R. H. A. L. (ed.) pp. 43–58, Dordrecht: Kluwer Academic Publishers.
- Zartman, R. E. and Doe, B. R. 1981. Plumbotectonics: The model. *Tectonophysics*, 75: 135–162.

PROBLEMS

1. If we view Indian Ocean water with ϵ_{Nd} of -6.6 as a simple mixture of Atlantic water with average ϵ_{Nd} of -11.4 and Pacific water with average ϵ_{Nd} of -3.9 (which it is not), what are the proportions of Atlantic and Pacific water in the mixture?

2. Suppose a dacitic magma containing 100 ppm Sr and 25 ppm Nd with $^{87}\text{Sr}/^{86}\text{Sr} = 0.7076$ and $\epsilon_{\text{Nd}} = -2$ mixes with a basaltic magma with 500 ppm Sr and 5 ppm Nd with $^{87}\text{Sr}/^{86}\text{Sr} = 0.7035$ and $\epsilon_{\text{Nd}} = +6$. Plot, at intervals of 10% addition of the dacitic magma, the Sr and Nd isotopic composition of the mixture. What is the value of r as defined in Eqn. 7.6?
3. If we assume that Sr in seawater ($^{87}\text{Sr}/^{86}\text{Sr} = 0.70925$) is a mixture of Sr from rivers ($^{87}\text{Sr}/^{86}\text{Sr} = 0.7119$) and Sr from mid-ocean ridge hydrothermal systems ($^{87}\text{Sr}/^{86}\text{Sr} = 0.7030$), what is the proportion of mid-ocean ridge derived Sr in seawater?
4. Average continental crust has $^{147}\text{Sm}/^{144}\text{Nd}$ of 0.112. Assuming that the average age of the crust is 2.2 Ga and that new crust when it forms has a ϵ_{Nd} of 0 (i.e., derived from a “chondritic” mantle), what should the average ϵ_{Nd} of crust be?
5. Assuming the continental crust has $^{147}\text{Sm}/^{144}\text{Nd}$ of 0.112 and an ϵ_{Nd} equal to that of the suspended load of rivers of -10.6 , what is the τ_{DM} model age of the crust?
6. The observable modern silicate Earth has today has $^{142}\text{Nd}/^{144}\text{Nd} = 1.141837$. The initial solar system $^{142}\text{Nd}/^{144}\text{Nd}$ was 0.141437. Assuming the Earth evolved with a constant $^{144}\text{Sm}/^{144}\text{Nd}$ from this initial value, what would its effective initial (at the formation of the solar system) $^{144}\text{Sm}/^{144}\text{Nd}$ be?
7. The present $^{142}\text{Nd}/^{144}\text{Nd}$ of the Nuvvaugittuq amphibolites is 1.141825. Assume that bulk silicate Earth today has $^{142}\text{Nd}/^{144}\text{Nd} = 1.141837$ and had the effective initial ratio that you calculated in Question 6. If the Nuvvaugittuq amphibolites formed from that bulk silicate Earth reservoir 200 million years after the start of the Solar System, what must their $^{144}\text{Sm}/^{144}\text{Nd}$ have been at the time they formed? What would have been the ratio of the $^{144}\text{Sm}/^{144}\text{Nd}$ to the bulk silicate Earth $^{144}\text{Sm}/^{144}\text{Nd}$ have been at that time (in other words, how fractionated would the Sm/Nd ratio have been)?
8. The (CI) chondritic concentration of W is 0.09 ppm while that of the bulk silicate Earth is 0.03 ppm. If the late accretionary veneer consisted of CI chondritic material with $\epsilon_{\text{W}} = -2$ and the silicate had $\epsilon_{\text{W}} = +0.13$ before addition of this material, what must the mass fraction of this late accretionary veneer have been?

Chapter 8

Stable isotope geochemistry I: Theory

8.1 INTRODUCTION

Stable isotope geochemistry is concerned with variations of the isotopic compositions of light elements arising from chemical fractionations rather than nuclear processes. The elements most commonly studied are H, Li, B, C, N, O, Si, S, and Cl. Of these, O, H, C, and S are by far the most important. These elements have several common characteristics:

- They have low atomic mass.
- The relative mass difference between the isotopes is large.
- They form bonds with a high degree of covalent character.
- The elements exist in more than one oxidation state (C, N, and S), form a wide variety of compounds (O), or are important constituents of naturally-occurring solids and fluids.
- The abundance of the rare isotope is sufficiently high (generally at least tenths of a percent) to facilitate analysis.

Elements *not* meeting these criteria show much smaller variations in isotopic composition. However, as new techniques offering greater sensitivity and higher precision have become available (in part through the use of the MC-ICP-MS), geochemists have begun to explore isotopic variations in 20 or so other elements, including Mg, Ca, Ti, Cr, Fe, Zn, Cu, Ge, Mo, Ti, Tl, and U. The largest isotopic variations observed in these elements are produced by biologically processes, but these are

still smaller than the former group of elements. Nevertheless, isotopic study of these elements has increased our understanding of the Earth and the Solar System in important ways and exploration of their isotope geochemistry continues. We will consider some of these elements as well as Li, B, Si, and Cl in Chapter 11.

Stable isotopes can be applied to a variety of problems. One of the most common is geothermometry. This use derives from the extent of isotopic fractionation varying inversely with temperature: fractionations are large at low temperature and small at high temperature. Another application is process identification. For instance, plants that produce “C₄” hydrocarbon chains (i.e., hydrocarbon chains four carbons long) as their primary photosynthetic products fractionate carbon differently to plants that produce “C₃” chains. This fractionation is retained up the food chain. This allows us to draw some inferences about the diet of fossil mammals from the stable isotope ratios in their bones. Sometimes stable isotopes are used as “tracers” much as radiogenic isotopes are. So, for example, we can use oxygen isotope ratios in igneous rocks to determine whether they have assimilated crustal material.

8.2 NOTATION AND DEFINITIONS

8.2.1 The δ notation

Variations in stable isotope ratios are typically in the parts per thousand range and hence are generally reported as *permil variations*,

δ , from some standard. Oxygen isotope fractionations are generally reported in permil deviations from SMOW (standard mean ocean water):

$$\delta^{18}\text{O} = \left[\frac{(^{18}\text{O}/^{16}\text{O})_{\text{sam}} - (^{18}\text{O}/^{16}\text{O})_{\text{SMOW}}}{(^{18}\text{O}/^{16}\text{O})_{\text{SMOW}}} \right] \times 10^3 \quad (8.1)$$

The same formula is used to report other stable isotope ratios. Hydrogen isotope ratios, δD , are reported relative to SMOW, carbon isotope ratios relative to Pee Dee Belemnite carbonate (PDB), nitrogen isotope ratios relative to atmospheric nitrogen, and sulfur isotope ratios relative to troilite in the Canyon Diablo iron meteorite. Cl isotopes are also reported relative to seawater; Li and B are reported relative to NIST (National Institute of Standards and Technology, formerly the National Bureau of Standards or NBS) standards. Unfortunately, a dual standard has developed for reporting O isotopes. Isotope ratios of carbonates are reported relative to the PDB carbonate standard. This value is related to SMOW by:

$$\delta^{18}\text{O}_{\text{PDB}} = 1.03086\delta^{18}\text{O}_{\text{SMOW}} + 30.86 \quad (8.2)$$

Table 8.1 lists the values for standards used in stable isotope analysis.

8.2.2 The fractionation factor

An important parameter in stable isotope geochemistry is the *fractionation factor*, α . It is defined as:

$$\alpha_{A-B} \equiv \frac{R_A}{R_B} \quad (8.3)$$

where R_A and R_B are the isotope ratios of two phases, A and B.

Table 8.1 Values of commonly analyzed stable isotope ratios.

Element	Notation	Ratio	Standard	Absolute Ratio
Hydrogen	δD	D/H ($^2\text{H}/^1\text{H}$)	SMOW	1.557×10^{-4}
Carbon	$\delta^{13}\text{C}$	$^{13}\text{C}/^{12}\text{C}$	PDB	1.122×10^{-2}
Nitrogen	$\delta^{15}\text{N}$	$^{15}\text{N}/^{14}\text{N}$	atmosphere	3.613×10^{-3}
Oxygen	$\delta^{18}\text{O}$	$^{18}\text{O}/^{16}\text{O}$	SMOW, PDB	2.004×10^{-3}
	$\delta^{17}\text{O}$	$^{17}\text{O}/^{16}\text{O}$	SMOW	3.71×10^{-4}
Sulfur	$\delta^{34}\text{S}$	$^{34}\text{S}/^{32}\text{S}$	CDT	4.43×10^{-2}

The fractionation of isotopes between two phases is often also reported as $\Delta_{A-B} = \delta_A - \delta_B$. The relationship between Δ and α is:

$$\Delta \approx (\alpha - 1)10^3 \text{ or } \Delta \approx 10^3 \ln \alpha \quad (8.4)$$

We derive it as follows. Rearranging eqn. 8.1, we have:

$$R_A = (\delta_A + 10^3)R_{\text{STD}}/10^3 \quad (8.5)$$

where R denotes an isotope ratio. Thus α may be expressed as:

$$\alpha = \frac{(\delta_A + 10^3)R_{\text{STD}}/10^3}{(\delta_B + 10^3)R_{\text{STD}}/10^3} = \frac{(\delta_A + 10^3)}{(\delta_B + 10^3)} \quad (8.6)$$

Subtracting 1 from each side and rearranging, and since δ is generally $\ll 10^3$, we obtain:

$$\alpha - 1 = \frac{(\delta_A - \delta_B)}{(\delta_B + 10^3)} \cong \frac{(\delta_A - \delta_B)}{10^3} = \Delta \times 10^{-3} \quad (8.7)$$

The second equation in (8.4) results from the approximation that for $x \approx 1$, $\ln x \approx x - 1$. As we will see, α is related to the equilibrium constant of thermodynamics by

$$\alpha_{A-B} = K^{1/n} \quad (8.8)$$

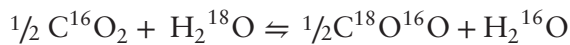
where n is the number of atoms exchanged.

8.3 THEORY OF MASS DEPENDENT ISOTOPIC FRACTIONATIONS

Isotope fractionation can originate from either *kinetic* or *equilibrium* effects or both. The former might be intuitively expected (since for example, we can readily understand that a lighter isotope will diffuse faster than a heavier one), but the latter may be somewhat surprising. After all, we were taught in introductory chemistry that oxygen is oxygen, and its properties are dictated by its electronic structure.

In the following sections, we will see that quantum mechanics predicts that mass affects the strength of chemical bonds and the vibrational, rotational, and translational motions of atoms. These quantum mechanical effects predict the small differences in the chemical properties of isotopes quite accurately. We shall now consider the manner in which isotope fractionations arise.

The electronic structures of all isotopes of an element are identical and since the electronic structure governs chemical properties, these properties are generally identical as well. Nevertheless, small differences in chemical behavior arise when this behavior depends on the frequencies of atomic and molecular motions. The energy of a molecule can be described in terms of several components: electronic, nuclear spin, translational, rotational, and vibrational. The first two terms are negligible and play no role in isotopic fractionations. The last three terms are the modes of motion available to a molecule and are the cause of differences in chemical behavior among isotopes of the same element. Of the three, vibration motion plays the most important role in isotopic fractionations. Translational and rotational motion can be described by classical mechanics, but an adequate description of vibrational motions of atoms in a lattice or molecule requires the application of quantum theory. As we shall see, *temperature-dependent equilibrium isotope fractionations arise from quantum mechanical effects on vibrational motions*. These effects are, as one might expect, generally small. For example, the equilibrium constant for the reaction:



is only about 1.04 at 25°C.

Figure 8.1 is a plot of the potential energy of a diatomic molecule as a function of distance between the two atoms. This plot looks broadly similar to one we might construct for two masses connected by a spring. When the distance between masses is small, the spring is compressed, and the potential energy of the system correspondingly high. At great distances between the masses, the spring is stretched and the energy of the system also high. At some intermediate distance, there is no stress on the spring, and the potential energy of the system is at a minimum (energy

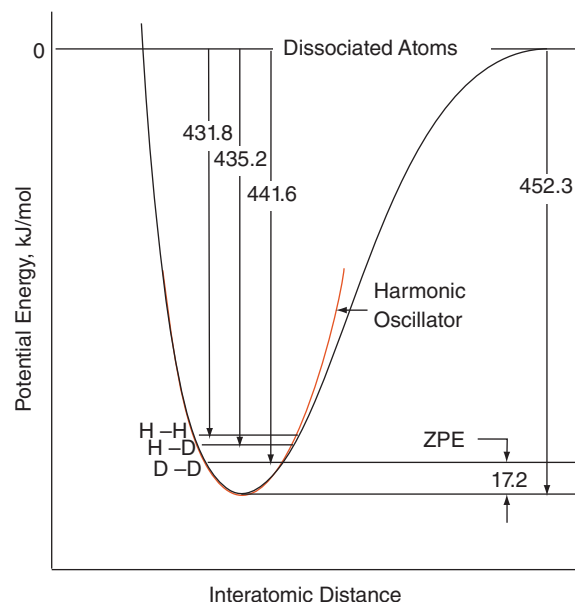


Figure 8.1 Energy-level diagram for the hydrogen atom. Fundamental vibration frequencies are 4405 cm^{-1} for H_2 , 3817 cm^{-1} for HD , and 3119 cm^{-1} for D_2 . The zero-point energy of H_2 is greater than that for HD , which is greater than that for D_2 . (Source: O’Neil (1986). Reproduced with permission of the Mineralogical Society of America.)

would be nevertheless be conserved because kinetic energy is at a maximum when potential energy is at a minimum). The diatomic oscillator, for example consisting of a Na and a Cl ion, works in an analogous way. At small interatomic distances, the electron clouds repel each other (the atoms are compressed); at large distances, the atoms are attracted to each other by the net charge on atoms. At intermediate distances, the potential energy is at a minimum. The energy and the distance over which the atoms vibrate are related to temperature.

In quantum theory, a diatomic oscillator cannot assume just any energy: only discrete energy levels may be occupied. The permissible energy levels, as we shall see, depend on mass. Quantum theory also tells us that even at absolute 0 the atoms will vibrate at a ground frequency v_0 . The system will have energy of $\frac{1}{2}hv_0$, where h is Planck’s constant. This energy level is called the *Zero Point Energy (ZPE)*. Its value depends on the electronic arrangements, the nuclear charges, and

the positions of the atoms in the molecule or lattice, all of which will be identical for isotopes of the same element. However, the energy also depends on the masses of the atoms involved, and thus will be different for different isotopes. *The vibrational frequency will be lower for a bond involving a heavier isotope of an element, which in turn lowers the vibrational energy of the molecule or crystal*, as suggested in Figure 8.1. *Thus bonds involving heavier isotopes will be stronger.* If a system consists of two possible atomic sites with different bond energies and two isotopes of an element available to fill those sites, *the energy of the system is minimized when the heavy isotope occupies the site with the stronger bond.* Thus, at equilibrium, the heavy isotope will tend to occupy the site with the stronger bond. This, in brief, is why equilibrium fractionations arise. Because bonds involving lighter isotopes are weaker and more readily broken, the lighter isotopes of an element participate more readily in a given chemical reaction. If the reaction fails to go to completion, which is often the case, this tendency gives rise to kinetic fractionations of isotopes. There are other causes of kinetic fractionations as well, and will consider them in due course. We will now consider in greater detail the basis for equilibrium fractionation, and see that they can be predicted from statistical mechanics.

8.3.1 Equilibrium fractionations

Urey (1947) and Bigeleisen and Mayer (1947) pointed out the possibility of calculating the equilibrium constant for isotopic exchange reactions from the *partition function*, q , of statistical mechanics. In the following discussion, bear in mind that quantum theory states that only discrete energies are available to an atom or molecule.

At equilibrium, the ratio of the number of molecules having internal energy E_i to the number having the zero point energy E_0 is:

$$\frac{n_i}{n_0} = g_i e^{-E_i/kT} \quad (8.9)$$

where n_0 is the number of molecules with ground-state or zero point energy, n_i is the number of molecules with energy E_i and k is Boltzmann's constant, T is the thermodynamic, or absolute, temperature, and g is a

statistical weight factor used to account for possible degenerate energy levels¹ (g is equal to the number of states having energy E_i). The average energy (per molecule) in a system is given by the *Boltzmann distribution function*, which is just the sum of the energy of all possible states times the number of particles in each state divided by the number of particles in all states:

$$\bar{E} = \frac{\sum_i n_i E_i}{\sum_i n_i} = \frac{\sum g_i E_i e^{-E_i/kT}}{\sum g_i e^{-E_i/kT}} \quad (8.10)$$

The denominator of this equation, which is the sum of all energy states accessible to the system is called the *partition function*, q :

$$q = \sum g_i e^{-E_i/kT} \quad (8.11)$$

Substituting 8.11 into 8.10, we can rewrite 8.10 in terms of the partial derivatives of q :

$$E = kT^2 \frac{\partial \ln q}{\partial T} \quad (8.12)$$

We will return to these equations shortly, but first let's see how all this relates to some parameters that are more familiar from thermodynamics and physical chemistry. It can also be shown (but we won't) from statistical mechanics that *entropy*² is related to energy and q by

$$S = \frac{U}{T} R \ln q \quad (8.13)$$

where R is the ideal gas constant and U is the internal energy of a system. We can rearrange this as:

$$U - TS = -R \ln q \quad (8.14)$$

and for the entropy and energy changes of a reaction, we have:

$$\Delta U - T \Delta S = -R \ln \prod q_n^\xi \quad (8.15)$$

where ξ in this case is the stoichiometric coefficient. In this notation, the stoichiometric coefficient is taken to have a negative sign for reactants (left side of reaction) and a positive sign for products (right side of reaction). The left hand side of this equation is simply the Gibbs Free Energy change of reaction under conditions of constant volume (as would be the case for an isotopic exchange reaction),

so that

$$\Delta G = -R \ln \prod_n q_n^{\xi} \quad (8.16)$$

The Gibbs Free Energy change is related to the equilibrium constant, K, by:

$$\Delta G = -RT \ln K \quad (8.17)$$

so the equilibrium constant for an isotope exchange reaction is related to the partition function as:

$$K = \prod_n q_n^{\xi} \quad (8.18)$$

For example, in the reaction involving exchange of ^{18}O between H_2O and CO_2 , the equilibrium constant is simply:

$$K = \frac{q_{\text{C}^{18}\text{O}^{16}\text{O}}^{1/2} q_{\text{H}_2^{16}\text{O}}}{q_{\text{C}^{16}\text{O}_2}^{1/2} q_{\text{H}_2^{18}\text{O}}} \quad (8.19)$$

The point of all this is simply that *the usefulness of the partition function is that it can be calculated from quantum mechanics, and from it we can calculate equilibrium fractionations of isotopes.*

The partition function involving energies of interest can be written as approximately:

$$q_{\text{total}} = q_{\text{trans}} q_{\text{rot}} q_{\text{vib}} \quad (8.20)$$

that is, the product of the translational, rotational and vibrational partition functions (we are ignoring contributions from anharmonic vibrations, rotational-vibrational interactions, and electronic energies). We should note here that since rotational and translations motions are not available to atoms in a solid, the partition function reduces to the vibrational partition function only.

It is convenient to treat these three modes of motion separately. Let's now do so.

8.3.1.1 Translational partition function

Writing a version of Eqn. 8.11 for translational energy, q_{trans} is expressed as:

$$q_{\text{trans}} = \sum_i g_{\text{tr},i} e^{-E_{\text{tr},i}/kT} \quad (8.21)$$

Now all that remains is to find an expression for translational energy and a way to do the summation. At temperatures above about 2 K, translational energy levels are so closely

spaced that they essentially form a continuum. The quantum translational energy of a particle in a cubical box is given by:

$$E_{\text{trans}} = \frac{n^2 h^2}{8 M d^2} \quad (8.22)$$

where n is the quantum energy level, h is Planck's constant, d is the length of the side of the cube, and M is mass of the particle. Substituting 8.22 into 8.21 and integrating:

$$q_{\text{trans}} = \int_0^\infty e^{-n^2 h^2 / 8 M d^2 k T} = \frac{(2 \pi M k T)^{1/2}}{h} d \quad (8.23)$$

gives an expression for q_{trans} for each dimension. The total three-dimensional translational partition function is then:

$$q_{\text{trans}} = \frac{(2 \pi M k T)^{3/2}}{h^3} V \quad (8.24)$$

where V is volume and is equal to d^3 . (It may seem odd that the volume should enter into the calculation, but since it is the ratio of partition functions that are important in equations such as 8.19, all terms in 8.24 except mass will eventually cancel.) If translation motion were the only component of energy, the equilibrium constant for exchange of isotopes would be simply the ratio of the molecular weights raised to the $3/2$ power. If we define the translational contribution to the equilibrium constant as K_{tr} as:

$$K_{\text{tr}} = \prod_i q_{\text{tr}}^{\xi} \quad (8.25)$$

K_{tr} reduces to the product of the molecular masses raised to three-halves of the stoichiometric coefficient:

$$K_{\text{tr}} = \prod_i \left(M_{\text{tr}}^{\xi} \right)^{3/2} \quad (8.26)$$

(note that M is the mass of the molecule, not the isotope). Thus the translational contribution to the partition function and fractionation factor is independent of temperature.

8.3.1.2 Rotational partition function

The allowed quantum *rotational* energy states are:

$$E_{\text{rot}} = \frac{j(j+1)h^2}{8\pi^2 I} \quad (8.27)$$

where j is the rotational quantum number and I is the moment of inertia. For a diatomic

molecule, $I = \mu d^2$, where d is the bond length and μ is reduced mass:

$$\mu = \frac{m_1 m_2}{m_1 + m_2} \quad (8.28)$$

where m_i is the atomic mass of atom i .

A diatomic molecule will have two rotational axes, one along the bond axis, the other perpendicular to it. Hence, in a diatomic molecule, j quanta of energy may be distributed $2j+1$ ways because there are two possibilities for every value of j except $j=0$, for which there is only one possible way. The statistical weight factor is therefore $2j+1$. Hence:

$$q_{rot} = \sum (2j+1) e^{-(j+1)b^2/8\pi^2IkT} \quad (8.29)$$

Again the spacing between energy levels is relatively small (except for hydrogen) and 8.29 may be evaluated as an integral. For a diatomic molecule, the partition function for rotation is given by:

$$q_{rot} = \frac{8\pi^2IkT}{\sigma b^2} \quad (8.30)$$

where σ is the symmetry number and is equal to the number of equivalent ways the molecule can be oriented in space. It is 1 for a heteronuclear diatomic molecule (such as CO or $^{18}\text{O}^{16}\text{O}$), and 2 for a homonuclear diatomic molecule such as $^{16}\text{O}_2$ or a symmetric tri-atomic molecule such as $^{16}\text{O}^{12}\text{C}^{16}\text{O}$ (more complex molecules will have higher symmetry numbers, for example, 12 for $^{12}\text{C}^1\text{H}_4$). Equation 8.30 also holds for linear polyatomic molecules with the symmetry factor equal to 2 if the molecule has a plane of symmetry (e.g., CO_2) and 1 if it does not.

For non-linear polyatomic molecules, the partition function is given by:

$$q_{rot} = \frac{8\pi^2(8\pi^3 I_A I_B I_C)^{1/2} (kT)^{3/2}}{\sigma b^3} \quad (8.31)$$

where I_A , I_B , and I_C are the principal moments of inertia. In calculating the rotational contribution to the equilibrium constant, all terms cancel except for moment of inertia and the symmetry factor, and the contribution of rotational motion to isotope fractionation is also independent of temperature.

For diatomic molecules, the equilibrium constant calculated from the ratios of

partition functions reduces to:

$$K_{rot} = \prod_i \left(\frac{I_i}{\sigma_i} \right)^{\xi_i} \quad (8.32)$$

In general, bond lengths are largely independent of the isotope involved, so the moment of inertia term may be replaced by the reduced masses:

$$K_{rot} \approx \prod_i \left(\frac{\mu_i}{\sigma_i} \right)^{\xi_i} \quad (8.32a)$$

8.3.1.3 Vibrational partition function

We will simplify the calculation of the vibrational partition function by treating the diatomic molecule as a harmonic oscillator (as Figure 8.1 suggests, this is a good approximation in most cases). In this case the quantum energy levels are given by:

$$E_{vib} = \left(n + \frac{1}{2} \right) \hbar v \quad (8.33)$$

where n is the vibrational quantum number and v is vibrational frequency. Unlike rotational and vibrational energies, the spacing between vibrational energy levels is large at geologic temperatures, so the partition function cannot be integrated. Instead, it must be summed over all available energy levels. Fortunately, the sum has a simple form: for diatomic molecules; the summation is simply equal to:

$$q_{vib} = \frac{e^{-hv/2kT}}{1 - e^{-hv/kT}} \quad (8.34)$$

For molecules consisting of more than two atoms, there are many vibrational motions possible. In this case, the vibrational partition function is the product of the partition functions for each mode of motion, with the individual partition functions given by 8.34. For a non-linear polyatomic molecule consisting of i atoms and the product is performed over all vibrational modes, ℓ , the partition function is given by:

$$q_{vib} = \prod_{\ell} \frac{e^{-hv_{\ell}/2kT}}{1 - e^{-hv_{\ell}/kT}} \quad (8.35)$$

where n is equal to 6 for *non-linear* polyatomic molecules and 5 for *linear* polyatomic molecules.

The vibrational energy contribution to the equilibrium constant for diatomic molecules is thus:

$$K_{vib} = \prod_i \left(\frac{e^{-hv_i/2kT}}{1 - e^{-hv_i/kT}} \right)^{\xi_i} \quad (8.36)$$

At room temperature and below, the exponential term in the denominator approximates to 0, and the denominator therefore approximates to 1, so the relation simplifies to:

$$q_{vib} \approx e^{-hv/2kT} \quad (8.37)$$

Thus at low temperature, the vibrational contribution to the equilibrium constant approximates to:

$$K_{vib} \approx \prod_{\ell} e^{-\xi_{\ell} h v_{\ell} / 2kT} \quad (8.38)$$

which has an exponential temperature dependence.

The full expression for the equilibrium constant calculated from partition functions for diatomic molecules is then:

$$K = \prod_i \left(M_i^{3/2} \left[\frac{I_i}{\sigma_i} \right] \frac{e^{-hv_i/2kT}}{1 - e^{-hv_i/kT}} \right)^{\xi_i} \quad (8.39)$$

This equation can be simplified through use of the Teller–Redlich spectroscopic theorem³ to:

$$K = \prod_i \left(\frac{m_i^{3r_i/2}}{\sigma_i} \frac{hv_i}{kT} \frac{e^{-hv_i/2kT}}{1 - e^{-hv_i/kT}} \right)^{\xi_i} \quad (8.40)$$

where r_i is the number of atoms being exchanged in the molecule.

Returning to our reaction between CO_2 and water, we can rearrange the equilibrium constant expression (8.19) as:

$$K = \frac{\left(q_{^{18}\text{O}}/q_{^{16}\text{O}} \right)_{\text{CO}_2}^{1/2}}{\left(q_{^{16}\text{O}}/q_{^{18}\text{O}} \right)_{\text{H}_2\text{O}}} \quad (8.41)$$

Thus, the equilibrium constant is the ratio of partition function ratios of the two isotopic versions of the two substances. We can see that the mass terms in Eqn. 8.40 will cancel in the computation and consequently we can omit them. The partition function ratio with

the mass terms omitted is sometimes referred to as the *reduced partition function*.

When theoretical calculations such as these are involved, isotope fractionation is also often expressed in terms of a β -factor defined as the ratio at equilibrium of the isotope ratio of the substance of interest to the isotope ratio of dissociated atoms:

$$\beta_{\text{H}_2\text{O}}^{^{18}\text{O}/^{16}\text{O}} \equiv \frac{\left(^{18}\text{O}/^{16}\text{O} \right)_{\text{H}_2\text{O}}}{\left(^{18}\text{O}/^{16}\text{O} \right)_\text{O}} \quad (8.42)$$

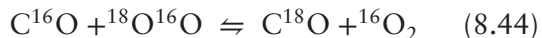
The denominator is the isotope ratio in a gas of monatomic oxygen and the numerator is the isotope ratio in water in equilibrium with it. The β factor for CO_2 would also have the isotope ratio of dissociated atoms in the denominator and thus in our example of CO_2 -water exchange, the denominators cancel so that:

$$\alpha = \frac{\beta_{\text{CO}_2}}{\beta_{\text{H}_2\text{O}}} \quad (8.43)$$

β -factors are closely related to the reduced partition function and are equal to it where the molecule of interest contains only one atom of the element of interest (this would be the case for water, for example, which contains only one oxygen atom). Where this is not the case, CO_2 for example, the β -factor differs from the reduced partition function by what Richet et al. (1977) termed an “excess factor,” which arises from our interest in atomic isotopic ratios rather than of isotopic molecular abundances. The reason for this will become clear in the following example.

8.3.1.4 Example of fractionation factor calculated from partition functions

To illustrate the use of partition functions in calculating theoretical fractionation factors, we will do the calculation for a very simple reaction: the exchange of ^{18}O and ^{16}O between O_2 and CO :



The choice of diatomic molecules greatly simplifies the equations. Choosing even a slightly more complex model, such as CO_2 would complicate the calculation because

there are more vibrational modes possible. Richet et al. (1977) and Chacko et al. (2001) provide examples of the calculation for more complex molecules.

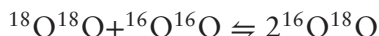
Let's first consider the relationship between the equilibrium constant and the fractionation factor for this reaction. The equilibrium constant for our reaction is:

$$K = \frac{[{}^{16}\text{O}_2][\text{C}^{18}\text{O}]}{[{}^{18}\text{O}{}^{16}\text{O}][\text{C}^{16}\text{O}]} \quad (8.45)$$

where we are using the brackets in the unusual chemical sense to denote concentration. We can use concentrations rather than activities or fugacities because the activity coefficient of a phase is independent of its isotopic composition. The fractionation factor, α , is defined as:

$$\alpha = \frac{({}^{18}\text{O}/{}^{16}\text{O})_{\text{CO}}}{({}^{18}\text{O}/{}^{16}\text{O})_{\text{O}_2}} \quad (8.46)$$

We must also consider the exchange reaction:



for which we can write a second equilibrium constant, K_2 . It turns out that when both reactions are considered, $\alpha \approx 2K$. The reason for this is as follows. The isotope ratio in molecular oxygen is related to the concentration of the two molecular species as:

$$\left(\frac{{}^{18}\text{O}}{{}^{16}\text{O}}\right)_{\text{O}_2} = \frac{[{}^{18}\text{O}{}^{16}\text{O}]}{[{}^{18}\text{O}{}^{16}\text{O}] + 2[{}^{16}\text{O}_2]} \quad (8.47)$$

$({}^{16}\text{O}_2)$ has 2 ${}^{16}\text{O}$ atoms, so it must be counted twice) whereas the ratio in CO is simply:

$$\left(\frac{{}^{18}\text{O}}{{}^{16}\text{O}}\right)_{\text{CO}} = \frac{[\text{C}^{18}\text{O}]}{[\text{C}^{16}\text{O}]} \quad (8.48)$$

Letting the isotope ratio equal R , we can solve 8.47 for $[{}^{18}\text{O}/{}^{16}\text{O}]$:

$$[{}^{18}\text{O}/{}^{16}\text{O}] = 2 \frac{[{}^{16}\text{O}_2]R_{\text{O}_2}}{1 - R_{\text{O}_2}} \quad (8.49)$$

and substitute it into 8.45:

$$K = \frac{(1 - R_{\text{O}_2})[\text{C}^{18}\text{O}]}{2R_{\text{O}_2}[\text{C}^{16}\text{O}]} = \frac{(1 - R_{\text{O}_2})R_{\text{CO}}}{2R_{\text{O}_2}} \quad (8.50)$$

Since the isotope ratio is a small number, the term $(1 - R) \approx 1$, so that:

$$K \cong \frac{R_{\text{CO}}}{2R_{\text{O}_2}} = \frac{\alpha}{2} \quad (8.51)$$

Relationships such as these are also why the β -factor can differ from the reduced partition function.

Now let's return to the problem of calculating K from the partition functions:

$$K = \frac{q_{{}^{16}\text{O}_2} q_{\text{C}^{18}\text{O}}}{q_{{}^{18}\text{O}{}^{16}\text{O}} q_{\text{C}^{16}\text{O}}} \quad (8.52)$$

where each partition function is the product of the translational, rotational, and vibrational partition functions. Since the reaction involves only diatomic molecules, we could simply use Eqn. 8.40. However, it is informative to see how the three separate modes of motion contribute to the overall equilibrium constant, so we will proceed by calculating the equilibrium constant for each mode of motion. The total equilibrium constant will then be the product of all three partial equilibrium constants.

For translational motion we noted the ratio of partition functions reduces to the ratio of molecular masses raised to the $3/2$ power. Hence:

$$\begin{aligned} K_{tr} &= \frac{q_{{}^{16}\text{O}_2} q_{\text{C}^{18}\text{O}}}{q_{{}^{18}\text{O}{}^{16}\text{O}} q_{\text{C}^{16}\text{O}}} = \left(\frac{M_{{}^{16}\text{O}_2} M_{\text{C}^{18}\text{O}}}{M_{{}^{18}\text{O}{}^{16}\text{O}} M_{\text{C}^{16}\text{O}}} \right)^{3/2} \\ &= \left(\frac{32 \times 30}{34 \times 28} \right)^{3/2} = 1.0126 \end{aligned} \quad (8.53)$$

We find that CO would be 12.6% richer in ${}^{18}\text{O}$ if translational motions were the only modes of energy available.

In the expression for the ratio of rotational partition functions, all terms cancel except the moment of inertia and the symmetry factors. The symmetry factor is 1 for all the molecules involved except ${}^{16}\text{O}_2$. In this case, the terms for bond length also cancel, so the expression involves only the reduced masses. So the expression for the rotational equilibrium constant becomes:

$$K_{rot} = \frac{q_{{}^{16}\text{O}_2} q_{\text{C}^{18}\text{O}}}{q_{{}^{18}\text{O}{}^{16}\text{O}} q_{\text{C}^{16}\text{O}}} = \left(\frac{\mu_{{}^{16}\text{O}_2} \mu_{\text{C}^{18}\text{O}}}{2\mu_{{}^{18}\text{O}{}^{16}\text{O}} \mu_{\text{C}^{16}\text{O}}} \right)$$

$$= \frac{1}{2} \left(\frac{\frac{16 \times 16}{16+16} \times \frac{12 \times 18}{12+18}}{\frac{18 \times 16}{18+16} \times \frac{12 \times 16}{12+16}} \right) = \frac{0.9916}{2} \quad (8.54)$$

(we'll ignore the 1/2, it will cancel out later when we calculate the fractionation factor). If rotation were the only mode of motion, CO would be 8‰ *poorer* in ^{18}O . Notice that both the translational and rotational equilibrium constants do not depend on temperature.

We'll do the calculation for low temperature, which will allow us to use Eqn. 8.38 to calculate the vibrational equilibrium constant:

$$\begin{aligned} K_{vib} &= \frac{q_{^{16}\text{O}_2} q_{\text{C}^{18}\text{O}}}{q_{^{18}\text{O}^{16}\text{O}} q_{\text{C}^{16}\text{O}}} \\ &= e^{\frac{-h(v_{^{16}\text{O}_2} + v_{\text{C}^{18}\text{O}} - v_{^{18}\text{O}^{16}\text{O}} - v_{\text{C}^{16}\text{O}})}{2kT}} \end{aligned} \quad (8.55)$$

Further, since we expect the difference in vibrational frequencies to be quite small, we may make the approximation $e^x = x + 1$. Hence:

$$\begin{aligned} K_{vib} &= 1 + \frac{-h}{2kT} \left[\left\{ v_{^{16}\text{O}_2} + v_{\text{C}^{18}\text{O}} \right\} \right. \\ &\quad \left. - \left\{ v_{^{18}\text{O}^{16}\text{O}} + v_{\text{C}^{16}\text{O}} \right\} \right] \end{aligned} \quad (8.56)$$

Let's make the simplification that the vibration frequencies are related to reduced mass as in a simple Hooke's Law harmonic oscillator:

$$\nu = \frac{1}{2\pi} \sqrt{\frac{\kappa}{\mu}} \quad (8.57)$$

where κ is the forcing constant and depends on the nature of the bond, and hence will be independent of isotopic composition. In this case, we may write:

$$\begin{aligned} \nu_{\text{C}^{18}\text{O}} &= \nu_{\text{C}^{16}\text{O}} \sqrt{\frac{\mu_{\text{C}^{16}\text{O}}}{\mu_{\text{C}^{18}\text{O}}}} = \nu_{\text{C}^{16}\text{O}} \sqrt{\frac{6.857}{7.2}} \\ &= 0.976 \nu_{\text{C}^{16}\text{O}} \end{aligned} \quad (8.58)$$

A similar expression may be written relating the vibrational frequencies of the oxygen molecule:

$$\nu_{^{16}\text{O}^{18}\text{O}} = 0.9718 \nu_{^{16}\text{O}_2}$$

Substituting these expressions in the equilibrium constant expression, we have:

$$K_{vib} = 1 + \frac{-h}{2kT} \left[v_{^{16}\text{O}_2} \{1 - 0.9718\} - v_{\text{C}^{16}\text{O}} \{1 - 0.976\} \right]$$

The measured vibrational frequencies of CO and O₂ are $6.50 \times 10^{13} \text{ sec}^{-1}$ and $4.74 \times 10^{13} \text{ sec}^{-1}$. Substituting these values and values for the Planck and Boltzmann constants, we obtain:

$$K_{vib} = 1 + \frac{5.544}{T} \quad (8.59)$$

At 300 K (room temperature), this evaluates to 1.0185.

We may now write the total equilibrium constant expression as:

$$\begin{aligned} K &= K_{tr} K_{rot} K_{vib} \\ &\cong \left(\frac{M_{^{16}\text{O}_2} M_{\text{C}^{18}\text{O}}}{M_{^{18}\text{O}^{16}\text{O}} M_{\text{C}^{16}\text{O}}} \right)^{3/2} \left(\frac{\mu_{^{16}\text{O}_2} \mu_{\text{C}^{18}\text{O}}}{2 \mu_{^{18}\text{O}^{16}\text{O}} \mu_{\text{C}^{16}\text{O}}} \right) \\ &\quad \times \left\{ 1 + \frac{h}{4\pi kT} \left[\left(\sqrt{\frac{\kappa}{\mu_{\text{C}^{16}\text{O}}}} - \sqrt{\frac{\kappa}{\mu_{\text{C}^{18}\text{O}}}} \right) \right. \right. \\ &\quad \left. \left. - \left(\sqrt{\frac{\kappa}{\mu_{^{16}\text{O}_2}}} - \sqrt{\frac{\kappa}{\mu_{^{18}\text{O}^{16}\text{O}}}} \right) \right] \right\} \end{aligned} \quad (8.60)$$

Evaluating this at 300 K we have:

$$K = 1.0126 \times \frac{0.9916}{2} \times 1.0185 = \frac{1.023}{2}$$

Since $\alpha = 2$ K, the fractionation factor is 1.023 at 300 K and would decrease by about 6 per mil per 100° temperature increase (however, we must bear in mind that our approximations hold only at low temperature; at high temperature equilibrium constants depend on the inverse square of temperature). This temperature dependence is illustrated in Figure 8.2. Thus CO would be 23 permil richer in the heavy isotope, ^{18}O , than O₂. This illustrates an important rule of stable isotope fractionations: *the heavy isotope goes preferentially in the chemical compound in which the element is most strongly bound*.

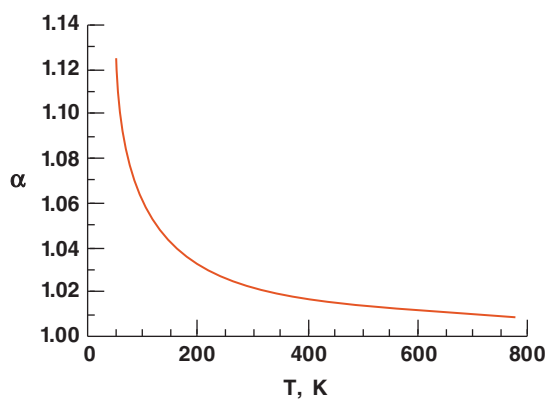


Figure 8.2 Fractionation factor, $\alpha = (^{18}\text{O}/^{16}\text{O})_{\text{CO}}/(^{18}\text{O}/^{16}\text{O})_{\text{O}_2}$, calculated from partition functions as a function of temperature.

Translational and rotational energy modes are, of course, not available to solids. Thus isotopic fractionations between solids are entirely controlled by the vibrational partition function. Fractionations between coexisting solids can be calculated as we have done above. A few decades ago, the task was daunting because the varieties of vibrational modes available to atoms in a lattice make the task computationally complex. With the computer power available today, theoretically computed fractionation factors are becoming more common. The lattice may be treated as a large polyatomic molecule having $3N-6$ vibrational modes, where N is the number of atoms in the unit cell. For large N , this approximates to $3N$.

Vibrational frequency and heat capacity are closely related because thermal energy in a crystal is stored as vibrational energy of the atoms in the lattice. Einstein and Debye independently treated the problem by assuming the vibrations arise from independent harmonic oscillations. Their models can be used to predict heat capacities in solids. The vibrational motions available to a lattice may be divided into two types, the first of which is “internal” or “optical” vibrations between individual radicals or atomic groupings within the lattice such as CO_3 , and $\text{Si}-\text{O}$. The vibrational frequencies of these groups can be calculated from the Einstein function and can be measured by optical spectroscopy. The second type are vibrations of the lattice as a whole,

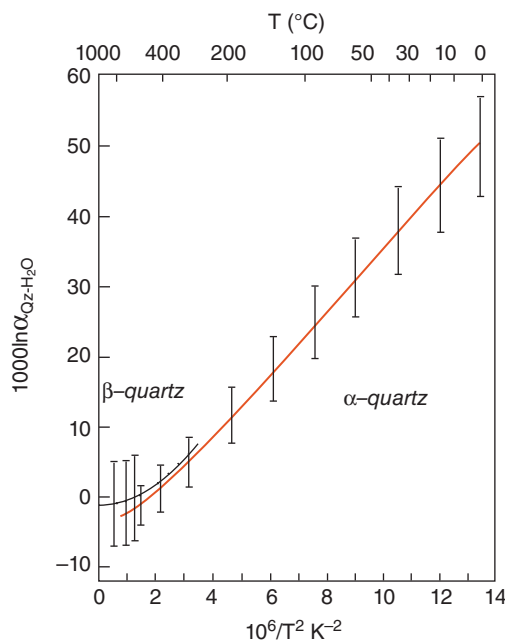


Figure 8.3 Calculated temperature dependencies of the fractionation of oxygen between water and quartz. (Source: Kawabe (1978). Reproduced with permission of Elsevier.)

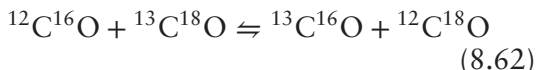
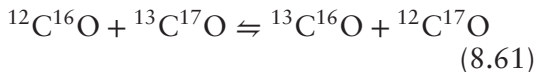
called “acoustical” vibrations, which can also be measured, but may also be calculated from the Debye function. From either calculated or observed vibrational frequencies, partition function ratios may be calculated, which in turn are directly related to the fractionation factor. Generally, the optical modes are the primary contribution to the partition function ratios. For example, for partitioning of ^{18}O between water and quartz, the contribution of the acoustical modes is less than 10%. The ability to calculate fractionation factors is particularly important at low temperatures where reaction rates are quite slow and experimental determination of fractionation therefore difficult. Figure 8.3 shows the calculated fractionation factor between quartz and water as a function of temperature. On the other hand, theoretically determined fractionation factors have the disadvantage that they generally assume perfect stoichiometry and crystallinity, whereas most natural crystals are chemically more complex. Thus, experimental determination of fractionation factor remains important.

8.3.1.5 Isotopologues and isotopic “clumping”

In the example we just considered, we were concerned only with how ^{18}O was distributed between CO and O_2 . However, the CO and O_2 will consist of a variety of molecules of distinct isotopic composition, or “isotopologues.” Indeed, there will be 12 such isotopologues: specifically $^{12}\text{C}^{16}\text{O}$, $^{12}\text{C}^{17}\text{O}$, $^{12}\text{C}^{18}\text{O}$, $^{13}\text{C}^{16}\text{O}$, $^{13}\text{C}^{17}\text{O}$, $^{13}\text{C}^{18}\text{O}$, $^{16}\text{O}_2$, $^{16}\text{O}^{17}\text{O}$, $^{16}\text{O}^{18}\text{O}$, $^{17}\text{O}_2$, $^{17}\text{O}^{18}\text{O}$, and $^{18}\text{O}_2$. The statistical mechanical theory we just considered predicts that the distribution of isotopes within a species will not be random but rather that some of these isotopologues will be thermodynamically favored, in particular the heavier isotopes of elements (^{13}C and ^{18}O) are more likely to be “clumped” together in a single molecule than to be randomly distributed among all molecules. The reason for this is that double heavy isotope substitution generally leads to a reduction in vibrational frequency and energy greater than twice that of single substitution. Thus, there is an energy advantage to bonding, or *clumping*, heavy isotopes together as opposed to simply distributing them randomly (Eiler, 2013).

As with the distribution of isotopes between chemical species, this *clumping* of isotopes within a species will be temperature dependent. We can use this as a geothermometer, and one that is independent of the isotopic composition of other phases. This, as we shall see in Chapter 11, is an important advantage.

Let's begin by considering the distribution of isotopes between the isotopologues of CO. There are six isotopologues and they can be related through the following two reactions:



(Since we can relate the six isotopologues through two reactions, we need only choose four of these isotopologues as the components of our system.) The equilibrium constant for reaction 8.62 can be calculated from:

$$K = \frac{q_{^{13}\text{C}^{16}\text{O}} q_{^{12}\text{C}^{18}\text{O}}}{q_{^{12}\text{C}^{16}\text{O}} q_{^{13}\text{C}^{18}\text{O}}} \quad (8.63)$$

A similar equation can be written for the equilibrium constant for 8.61. The individual partition functions can be calculated just as

described in the previous section. Doing so, we find that the two heaviest species, $^{13}\text{C}^{17}\text{O}$ and $^{13}\text{C}^{18}\text{O}$, will be more abundant than if isotopes were merely randomly distributed among the six isotopologues, that is, the heavy isotopes tend to “clump.” Wang et al. (2004) introduced a delta notation to describe this effect:

$$\Delta_i = \left(\frac{R_{i-e}}{R_{i-r}} - 1 \right) \times 1000 \quad (8.64)$$

where R_{i-e} is that ratio of the observed or calculated equilibrium abundance of isotopologue i to the isotopologue containing no rare isotopes and R_{i-r} is that same ratio if isotopes were distributed among isotopologues randomly. Thus, for example, in the system previously,

$$\Delta_{^{13}\text{C}^{18}\text{O}} = \left\{ \frac{\left([^{13}\text{C}^{18}\text{O}] / [^{12}\text{C}^{16}\text{O}] \right)_e}{\left([^{13}\text{C}^{18}\text{O}] / [^{12}\text{C}^{16}\text{O}] \right)_r} - 1 \right\} \times 1000 \quad (8.65)$$

Since R_{i-r} is the random distribution, it can be calculated directly as the probability of choosing isotopes randomly to form species. In the case of $^{13}\text{C}^{18}\text{O}$, it is:

$$R_{^{13}\text{C}^{18}\text{O}-r} = \left(\frac{[^{13}\text{C}^{18}\text{O}]}{[^{12}\text{C}^{16}\text{O}]} \right)_r = \frac{[^{13}\text{C}][^{18}\text{O}]}{[^{12}\text{C}][^{16}\text{O}]} \quad (8.66)$$

It gets a little more complex for molecules with more than two isotopes. In most cases, we are interested in combinations of isotopes rather than permutations, which is to say we don't care about order. This will not be the case for highly asymmetric molecules such as nitrous oxide, N_2O . The structure of this molecule is N-N-O and $^{14}\text{N}^{15}\text{N}^{16}\text{O}$ will have different properties than $^{15}\text{N}^{14}\text{N}^{16}\text{O}$, so in that case, order does matter. The CO_2 molecule is, however, symmetric and we cannot distinguish $^{16}\text{O}^{12}\text{C}^{18}\text{O}$ from $^{18}\text{O}^{12}\text{C}^{16}\text{O}$. Its random abundance would be calculated as:

$$\begin{aligned} R_{^{13}\text{C}^{16}\text{O}^{18}\text{O}-r} &= \left(\frac{[^{13}\text{C}^{16}\text{O}^{18}\text{O}]}{[^{12}\text{C}^{16}\text{O}_2]} \right)_r \\ &= \frac{2 [^{13}\text{C}] [^{16}\text{O}] [^{18}\text{O}]}{[^{12}\text{C}] [^{16}\text{O}]^2} \\ &= \frac{2 [^{13}\text{C}] [^{18}\text{O}]}{[^{12}\text{C}] [^{16}\text{O}]} \end{aligned} \quad (8.67)$$

The factor of 2 is in the denominator to take account of both $^{12}\text{C}^{16}\text{O}^{18}\text{O}$ and $^{12}\text{C}^{18}\text{O}^{16}\text{O}$.

As Wang et al. (2004) showed, value of Δ as defined in Eqn. 8.65 is related to the equilibrium constant (Eqn. 8.63) for the exchange reaction (Eqn. 8.61) as:

$$\Delta \approx -1000 \ln \frac{K}{K_r} \quad (8.68)$$

Since K_r refers to the case of random distribution of isotopes, it is equal to 1 and since K will have a value close to 1, we may use the approximation $\ln x \approx 1 - x$, so that 8.68 reduces to:

$$\Delta \approx (K - 1) \times 1000 \quad (8.69)$$

Figure 8.4 shows the Δ values calculated for three isotopologues of CO as a function of temperature by Wang et al. (2004). Δ values vary with the inverse of temperature, a direct consequence of the inverse temperature dependence of the vibrational equilibrium constant expressed in Eqn. 8.59. The calculations predict that at room temperature $^{13}\text{C}^{18}\text{O}$ and $^{13}\text{C}^{17}\text{O}$ concentrations will be 1–2 per mil above a purely random distribution of isotopes. Both are quite rare compared to the most abundant isotopologue, $^{12}\text{C}^{16}\text{O}$; the concentration of $^{13}\text{C}^{18}\text{O}$ will be less than 0.003%, that of $^{13}\text{C}^{17}\text{O}$ about 0.0004%.

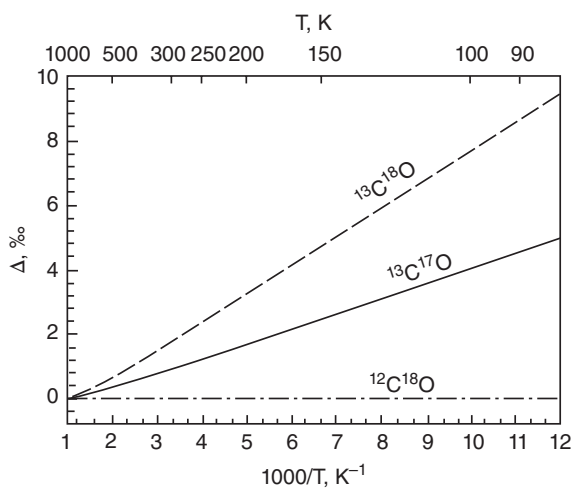


Figure 8.4 Predicted enrichment of isotopologues in CO_2 gas based on statistical mechanical calculations. (Source: Wang et al. (2004). Reproduced with permission of Elsevier.)

Very high precision and sensitivity is required to analyze the abundance of these isotopes and detect the small enrichment resulting from clumping.

CO is a relatively rare species in nature (on Earth anyway) and it is of limited geochemical interest, at least compared to CO_2 and its related forms such as carbonate and bicarbonate ions and, particularly, carbonate minerals. The latter are among the most common sedimentary minerals. Most form by precipitation from water (often biologically mediated), and the oxygen isotopic fractionation resulting from this precipitation reaction is temperature dependent. Thus, the isotopic composition of carbonates has proved to be a useful geothermometer and a very useful paleoclimatic tool. However, the isotopic composition of carbonate precipitated from water depends both on temperature and the isotopic composition of the water; calculating temperature thus requires knowing the isotopic composition of the water. In contrast, the relative abundance of carbonate isotopologues depends only on temperature and the isotopic composition of the carbonate. Since the latter is readily measured, temperature can be calculated from the abundance of the isotopologues, provided those can be measured.

The difficulty is two-fold. First, the abundance carbonate ion isotopologues containing two or more rare isotopes is very small; the most abundant will be $^{13}\text{C}^{18}\text{O}^{16}\text{O}_2$ with a relative abundance of about 67 ppm. Second, no analytical technique can directly measure the abundance of these rare isotopologues in carbonates. Carbonates are analyzed by first digesting the material in anhydrous phosphoric acid, which generates CO_2 gas. Carbon and oxygen isotopic compositions are then determined by analyzing the CO_2 as the CO_2^+ ion in a gas source mass spectrometer. Ghosh et al. (2006) showed that the abundance of $^{13}\text{C}^{18}\text{O}^{16}\text{O}$ isotopologue of analyzed CO_2 gas was proportional to the abundance of $^{13}\text{C}-^{18}\text{O}$ bonds in the carbonate. They found that the Δ value of the $^{13}\text{C}^{18}\text{O}^{16}\text{O}$ isotopologue in the CO_2 gas, referred to as Δ_{47} ,⁴ was about 0.2‰ higher than that of the carbonate, but this fractionation appears to be nearly constant. Analyzing both natural carbonate from corals known to have grown at different temperatures and

carbonates precipitated from laboratory solutions, Ghosh et al. (2006) showed Δ_{47} was inversely proportional to temperature as predicted by statistical mechanics (Figure 8.5). Ghosh et al. (2006) concluded that “clumped” isotopic analysis could be used as a geothermometer with a precision of about $\pm 2^\circ\text{C}$.

To further improve application of the clumping technique, workers from four laboratories (Dennis et al., 2011) proposed a method for standardizing and reporting clumped isotopic species to an absolute reference frame to avoid interlaboratory biases that result, among other things, from differences in fractionation that occur during acid digestion and ionization in the mass spectrometer. The approach involves standardization against prepared CO_2 gases whose Δ_{47} can be theoretically predicted. These include gases that vary in C and O isotopic composition that are equilibrated to a common temperature (typically 1000°C), and hence should have a common (and theoretically predicted) Δ_{47} , and a series of gases with the same isotopic composition equilibrated with water at a known temperature, and hence should also have theoretically predicted Δ_{47} values. The gases are then analyzed and the measured values regressed against theoretical

ones to provide calibration functions. We’ll consider specific examples of applications of the clumping technique in Chapter 11.

8.3.2 Kinetic fractionation

Kinetic effects are normally associated with fast, incomplete, or unidirectional processes like evaporation, diffusion and dissociation reactions. As an example, recall that temperature is related to the average kinetic energy. In an ideal gas, the average kinetic energy of all molecules is the same. The kinetic energy is given by:

$$E = \frac{1}{2}mv^2 \quad (8.70)$$

Consider two molecules of carbon dioxide, $^{12}\text{C}^{16}\text{O}_2$ and $^{13}\text{C}^{16}\text{O}_2$, in such a gas. If their energies are equal, the ratio of their velocities is $(45/44)^{1/2}$, or 1.011. Thus $^{12}\text{C}^{16}\text{O}_2$ can diffuse 1.1% further in a given amount of time at a given temperature than $^{13}\text{C}^{16}\text{O}_2$. This result, however, is largely limited to ideal gases, that is, low pressures where collisions between molecules are infrequent and intermolecular forces negligible. For the case of air, where molecular collisions are important, the

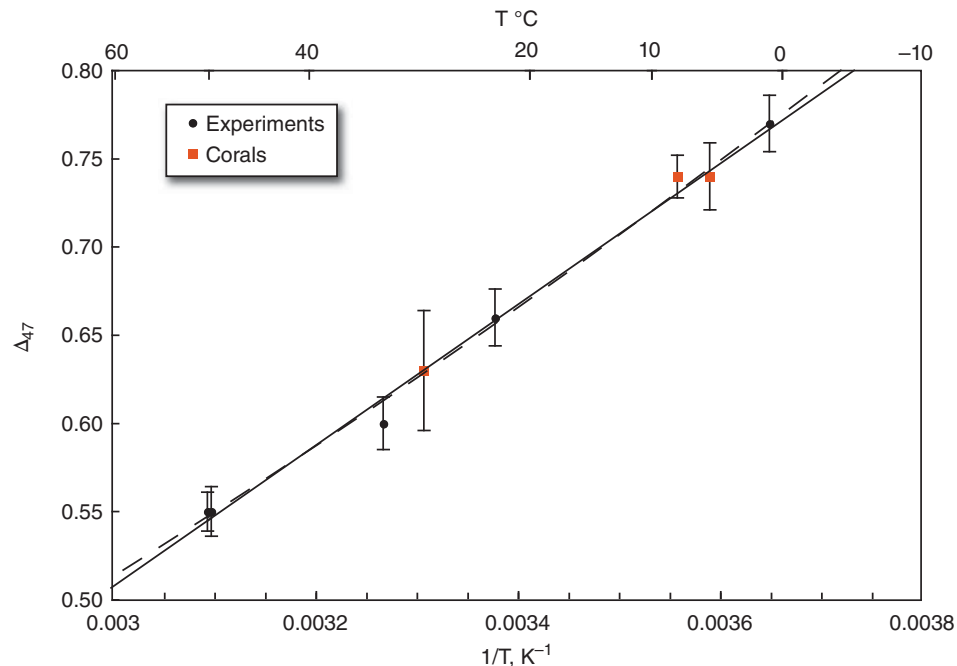


Figure 8.5 Data for Δ_{47} measured in experimental and natural carbonates by Ghosh et al. (2006) as a function of inverse temperature. Both $1/T$ (solid line) and a $1/T^2$ (dashed line) are fitted to the data.

ratio of the diffusion coefficients of the two CO₂ species is the ratio of the square roots of the reduced masses of CO₂ and air (mean molecular weight 28.8):

$$\frac{D_{12\text{CO}_2}}{D_{13\text{CO}_2}} = \frac{\sqrt{\mu_{13\text{CO}_2}}}{\mu_{12\text{CO}_2}} = \frac{17.561}{17.406} = 1.0044 \quad (8.71)$$

Hence we predict that gaseous diffusion would lead to only a 4.4‰ fractionation.

In addition, molecules containing the heavy isotope are more stable and have higher dissociation energies than those containing the light isotope. This can be readily seen in Figure 8.1. The energy required to raise the D₂ molecule to the energy where the atoms dissociate is 441.6 kJ/mole, whereas the energy required to dissociate the H₂ molecule is 431.8 kJ/mole. Therefore it is easier to break bonds such as H-H and C-H than D-D and C-D. Where reactions go to completion, this difference in bonding energy plays no role: isotopic fractionations will be governed by the considerations of equilibrium discussed in the previous section. *Where reactions do not achieve equilibrium the lighter isotope will be preferentially concentrated in the reaction products*, because of this effect of the bonds involving light isotopes in the reactants being more easily broken. Large kinetic effects are associated with biologically mediated reactions (e.g., bacterial reduction), because such reactions generally do not achieve equilibrium. Thus ¹²C is enriched in the products of photosynthesis in plants (hydrocarbons) relative to atmospheric CO₂, and ³²S is enriched in H₂S produced by bacterial reduction of sulfate.

We can express this in a more quantitative sense. The rate at which reactions occur is given by:

$$R = Ae^{-E_b/kT} \quad (8.72)$$

where A is a constant called the frequency factor and E_b is the barrier energy. Referring to Figure 8.1, the barrier energy is the difference between the dissociation energy, ε, and the zero-point energy. The constant A is independent of isotopic composition, thus the ratio of reaction rates between the HD molecule and the H₂ molecule is:

$$\frac{R_D}{R_H} = \frac{e^{-(\epsilon-1/2hv_D)kT}}{e^{-(\epsilon-1/2hv_H)kT}} \quad (8.73)$$

or

$$\frac{R_D}{R_H} = e^{(\nu_H-\nu_D)b/2kT} \quad (8.74)$$

Substituting for the various constants, and using the wavenumbers given in the caption to Figure 8.1 (remembering that ω = cv where c is the speed of light) the ratio is calculated as 0.24; in other words we expect the H₂ molecule to react four times faster than the HD molecule, a very large difference. For heavier elements, the rate differences are smaller. For example, the same ratio calculated for ¹⁶O₂ and ¹⁸O¹⁶O shows that the ¹⁶O will react about 15% faster than the ¹⁸O¹⁶O molecule.

The greater translational velocities of lighter molecules also allow them to break through a liquid surface more readily and hence evaporate more quickly than a heavy molecule of the same composition. The transition from liquid to gas in the case of water also involves breaking hydrogen bonds that form between the hydrogen of one molecule and an oxygen of another. This bond is weaker if ¹⁶O is involved rather than ¹⁸O, and thus is broken more easily, meaning H₂¹⁶O is more readily available to transform into the gas phase than H₂¹⁸O. Thus, water vapor above the ocean typically has δ¹⁸O around -13 per mil, whereas at equilibrium the vapor should only be about 9 per mil lighter than the liquid.

Let's explore this example a bit further. Kinetic fractionation of O isotopes between water and water vapor is an example of Rayleigh distillation (or condensation), as is fractional crystallization. Let A be the amount of the species containing the major isotope, H₂¹⁶O, and B be the amount of the species containing the minor isotope, H₂¹⁸O. The rate at which these species evaporate is proportional to the amount present:

$$dA = k_A A \quad (8.75a) \quad \text{and} \quad dB = k_B B \quad (8.75b)$$

Since the isotopic composition affects the reaction, or evaporation, rate, k_A ≠ k_B. We'll call this ratio of the rate constants α. Then

$$\frac{dB}{dA} = \alpha \frac{B}{A} \quad (8.76)$$

Rearranging and integrating, we have

$$\ln \frac{B}{B^\circ} = \alpha \ln \frac{A}{A^\circ} \quad \text{or} \quad \frac{B}{B^\circ} = \left(\frac{A}{A^\circ} \right)^\alpha \quad (8.77)$$

where A° and B° are the amount of A and B originally present. Dividing both sides by A/A°

$$\frac{B/A}{B^\circ/A^\circ} = \left(\frac{A}{A^\circ}\right)^{\alpha-1} \quad (8.78)$$

Since the amount of B makes up only a trace of the total amount of H_2O present, A is essentially equal to the total water present, and A/A° is essentially identical to f , the fraction of the original water remaining. Hence:

$$\frac{B/A}{B^\circ/A^\circ} = f^{\alpha-1} \quad (8.79)$$

Subtracting 1 from both sides, we have

$$\frac{B/A - B^\circ/A^\circ}{B^\circ/A^\circ} = f^{\alpha-1} - 1 \quad (8.80)$$

Comparing the left side of the equation to Eqn. 8.1, we see the per-mil fractionation is given by:

$$\delta = 1000(f^{\alpha-1} - 1) \quad (8.81)$$

Of course, the same principle applies when water condenses from vapor. Assuming a value of α of 1.01, δ will vary with f , the fraction of vapor remaining, as shown in Figure 8.6.

Even if the vapor and liquid remain in equilibrium throughout the condensation process,

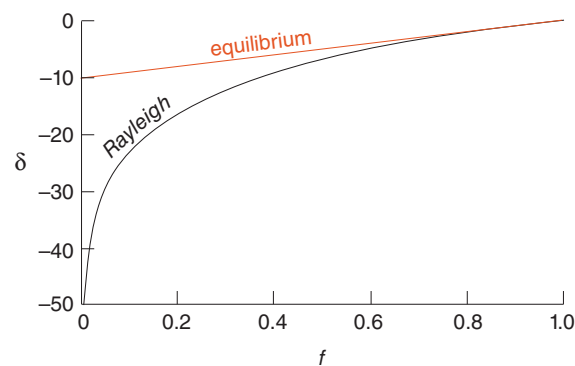


Figure 8.6 Fractionation of isotope ratios during Rayleigh and equilibrium condensation. δ is the per mil difference between the isotopic composition of original vapor and the isotopic composition as a function of f , the fraction of vapor remaining. (Source: White (2013). Reproduced with permission of John Wiley & Sons.)

the isotopic composition of the remaining vapor will change continuously. The relevant equation is:

$$\delta = \left(1 - \frac{1}{(1-f)/\alpha + f}\right) \times 1000 \quad (8.82)$$

The effect of equilibrium condensation is also shown in Figure 8.6.

It is important to bear in mind that kinetic fractionations often occur in combination with equilibrium fractionation. Although this example of Rayleigh condensation illustrates how kinetic effects can amplify equilibrium fractionations, kinetic effects can also counteract and partially or whole nullify equilibrium fractionations.

8.4 MASS INDEPENDENT FRACTIONATION

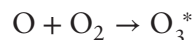
Most isotopic studies focus on the fractionation between the two most abundant isotopes of an element, for example, ^{16}O and ^{18}O . Some elements, however, have three or more isotopes. For example, O consists of ^{17}O , as well as ^{16}O and ^{18}O , although ^{17}O is an order of magnitude less abundant than ^{18}O (which is two orders of magnitude less abundant than ^{16}O). The reason for this focus is that, based on the theory we have just reviewed, mass fractionation should depend on mass difference. This is referred to as mass-dependent fractionation. The mass difference between ^{17}O and ^{16}O is half the difference between ^{18}O and ^{16}O , hence we expect the fractionation between ^{17}O and ^{16}O to be about half that between ^{18}O and ^{16}O . In the example of fractionation between CO and O_2 in the previous section, it is easy to show from equation 8.56 that through the range of temperatures we expect near the surface of the Earth (or Mars), that the ratio of fractionation factors $\Delta^{17}\text{O}/\Delta^{18}\text{O}$ should be ≈ 0.53 . In the limit of infinite temperature, $\Delta^{17}\text{O}/\Delta^{18}\text{O} \approx 0.52$. The empirically observed ratio for terrestrial fractionation (and also within classes of meteorites) is $\Delta^{17}\text{O}/\Delta^{18}\text{O} \approx 0.52$. Because the fractionation between ^{17}O and ^{16}O bears a simple relationship to that between ^{18}O and ^{16}O , the $^{17}\text{O}/^{16}\text{O}$ ratio is rarely measured. However, as we saw in Chapter 5, not all O isotope

variation in Solar System materials follows the expected *mass-dependent fractionation*. Furthermore, we saw that there is laboratory evidence that mass-independent fractionation can occur. Mass independent fractionation has subsequently been demonstrated to occur in nature, and indeed may provide important clues to Earth and Solar System processes and history, and we will return to this topic later.

Mass-independent fractionation is nevertheless rare. First observed in meteorites (Chapter 5), it has subsequently been observed in oxygen isotope ratios of atmospheric gases, most dramatically in stratospheric ozone (Figure 8.7), and more recently in sulfur isotope ratios of Archean sediments and modern sulfur-bearing aerosols in ice. The causes of mass-independent fractionation are incompletely understood and it seems likely there may be more than one cause. Only a brief discussion is given here, a fuller discussion of the causes of mass independent fractionation can be found in Thiemens (2006).

There is at least a partial theoretical explanation in the case of ozone (Heidenreich and Thiemens, 1986, Gao and Marcus, 2001). Their theory can be roughly explained as follows. Formation of ozone in the stratosphere typically involves the energetic collision of

monatomic and molecular oxygen, that is:



The ozone molecule thus formed is in a vibrationally excited state (designated by the asterisk) and, consequently, subject to dissociation if it cannot lose this excess energy. The excess vibrational energy can be lost either by collisions with other molecules, or by partitioning to rotational energy. In the stratosphere, collisions are comparatively infrequent hence repartitioning of vibrational energy represents an important pathway to stability. Because there are more possible energy transitions for asymmetric species such as $^{16}\text{O}^{16}\text{O}^{18}\text{O}$ and $^{16}\text{O}^{16}\text{O}^{17}\text{O}$ than symmetric ones such as $^{16}\text{O}^{16}\text{O}^{16}\text{O}$, the former can repartition its excess energy and form a stable molecule. At higher pressures, such as prevail in the troposphere, the symmetric molecule can readily lose energy through collisions, lessening the importance of the vibrational to rotational energy conversion. Gao and Marcus (2001) were able to closely match observed experimental fractionations, but their approach was in part empirical because a fully quantum mechanical treatment is not yet possible.

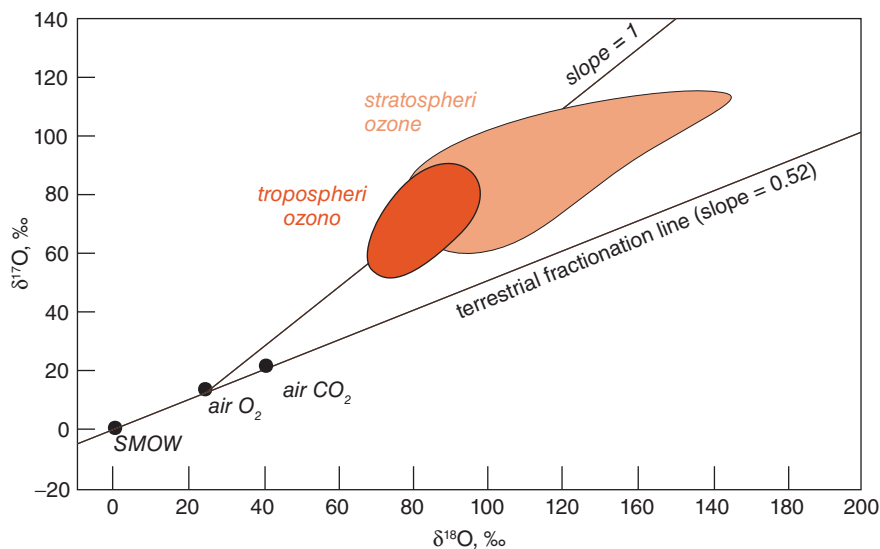


Figure 8.7 Oxygen isotopic composition in the stratosphere and troposphere show the effects of mass independent fractionation. A few other atmospheric trace gases show similar effects. Essentially all other material from the Earth and Moon plot on the *terrestrial fractionation line*. (Source: Johnson et al. (2001). Reproduced with permission of John Wiley & Sons.)

Theoretical understanding of mass-independent sulfur isotope fractionations is less advanced. Mass independent fractionations similar to those observed in Archean rocks (discussed in Chapter 11) have been produced in the laboratory by photo-dissociation (photolysis) of SO_2 and SO using deep ultraviolet radiation (wavelengths $< 220 \text{ nm}$). Photolysis at longer wavelengths does not produce mass independent fractionations. Current explanations therefore focus on ultraviolet photolysis. However, there as yet is no theoretical explanation of this effect and alternative explanations, including ones that involve the role in symmetry in a manner analogous to ozone, cannot be entirely ruled out.

8.5 HYDROGEN AND OXYGEN ISOTOPE RATIOS IN THE HYDROLOGIC SYSTEM

We noted earlier that isotopically light water has a higher vapor pressure, and hence lower boiling point than isotopically heavy water. Let's consider this in a bit more detail. Raoult's law states that the partial pressure, p , of a species above a solution is equal to its molar concentration in the solution times the standard state partial pressure, p^o , where the standard state is the pure solution. So for example:

$$p_{\text{H}_2^{16}\text{O}} = p_{\text{H}_2^{16}\text{O}}^o [\text{H}_2^{16}\text{O}] \quad (8.83\text{a})$$

and

$$p_{\text{H}_2^{18}\text{O}} = p_{\text{H}_2^{18}\text{O}}^o [\text{H}_2^{18}\text{O}] \quad (8.83\text{b})$$

Since the partial pressure of a species is proportional to the number of atoms of that species in a gas, we can define α , the fractionation factor between liquid water and vapor in the usual way:

$$\alpha_{l/v} = \frac{p_{\text{H}_2^{18}\text{O}}/p_{\text{H}_2^{16}\text{O}}}{[\text{H}_2^{18}\text{O}]/[\text{H}_2^{16}\text{O}]} \quad (8.84)$$

By solving 8.80a and 8.80b for $[\text{H}_2^{16}\text{O}]$ and $[\text{H}_2^{18}\text{O}]$ and substituting into 8.81 we arrive at the relationship:

$$\alpha_{l/v} = \frac{p_{\text{H}_2^{18}\text{O}}^o}{p_{\text{H}_2^{16}\text{O}}^o} \quad (8.85)$$

Interestingly enough, the fractionation factor for oxygen between water vapor and liquid

turns out to be just the ratio of the standard state partial pressures. The next question is how the partial pressures vary with temperature. According to classical thermodynamics, the temperature dependence of the partial pressure of a species may be expressed as:

$$\frac{d \ln P}{dT} = \frac{\Delta H}{RT^2} \quad (8.86)$$

where T is temperature, ΔH is the enthalpy or latent heat of evaporation, and R is the gas constant. Over a sufficiently small range of temperature, we can assume that ΔH is independent of temperature. Rearranging and integrating, we obtain:

$$\ln p = \frac{\Delta H}{RT} + \text{const} \quad (8.87)$$

We can write two such equations, one for $[\text{H}_2^{16}\text{O}]$ and one for $[\text{H}_2^{18}\text{O}]$. Dividing one by the other we obtain:

$$\ln \frac{p_{\text{H}_2^{18}\text{O}}^o}{p_{\text{H}_2^{16}\text{O}}^o} = A - \frac{B}{RT} \quad (8.88)$$

where A and B are constants. This can be rewritten as:

$$\alpha = ae^{-B/RT} \quad (8.89)$$

(where $a = e^A$). Over a larger range of temperature, ΔH is not constant. The fractionation factor in that case depends on the inverse square of temperature, so that the temperature dependence of the fractionation factor can be represented as:

$$\ln \alpha = A - \frac{B}{T^2} \quad (8.90)$$

Figure 8.8 shows water-vapor and ice-vapor fractionation factors for oxygen. Over a temperature range relevant to the Earth's surface, the fractionation factor for oxygen shows an approximately inverse dependence on temperature. Hydrogen isotope fractionation is clearly non-linear over a large range of temperature.

Given the fractionation between water and vapor, we might predict that there will be considerable variation in the isotopic composition of water in the hydrologic cycle, and indeed there is. Furthermore, these variations form the basis of estimates of paleotemperatures

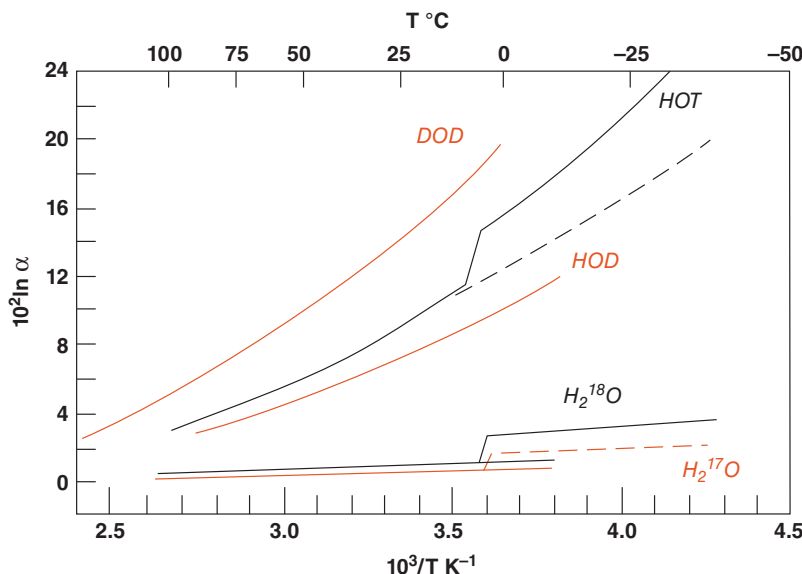


Figure 8.8 Temperature dependence of fractionation factors between vapor and water (solid lines) and vapor and ice (dashed lines) for various species of water. (Source: Adapted from van Hook, 1968.)

and past ice volumes. Let's now consider the question of isotopic fractionation in the hydro-sphere in greater detail.

As water vapor condenses, the droplets and vapor do not remain in equilibrium if the precipitation occurs and the droplets fall out of the atmosphere. So the most accurate description of the condensation process is Rayleigh distillation, which we discussed earlier. To a first approximation, condensation of water vapor will be a function of temperature. As air rises, it cools. You may have noticed the base elevation of clouds is quite uniform on a given day in a given locality. This elevation represents the isotherm where condensation begins. At that height, the air has become supersaturated, and condensation begins, forming clouds. Water continues to condense until equilibrium is again achieved. Further condensation will only occur if there is further cooling, which generally occurs as air rises. The point is that the parameter f , the fraction of vapor remaining, can be approximately represented as a function of temperature. To explore what happens when water vapor condenses, let's construct a simple hypothetical model of condensation and represent f as a hypothetical function of temperature such as:

$$f = \frac{T - 223}{50} \quad (8.91)$$

Since T is in kelvins, this equation means that f will be 1 at 273 K (0°C) and will be 0 at 223 K (-50°C). In other words, we suppose condensation begins at 0°C and is complete at -50°C . Now we also want to include temperature dependent fractionation in our model, so we will use Eqn. 8.86. Realistic values for the constant a and B are 0.9822 and -66.057J/mole respectively, so that 8.90 becomes:

$$\alpha = 0.9822 e^{66.057/RT} \quad (8.92)$$

Substituting 8.91, 8.92, and $R = 8.314\text{J/mol-K}$ into Eqn. 8.81, our model is:

$$\delta^{18}\text{O} = 10^3 \times \left[\left(\frac{T - 223}{50} \right)^{0.9822e^{7.9448T}-1} - 1 \right] \quad (8.93)$$

So we predict that the isotopic composition of water vapor should be a function of temperature. We can, of course, write an analogous equation for equilibrium condensation. Figure 8.9 shows the temperature dependence we predict for water vapor in the atmosphere as a function of temperature (we have assumed that the vapor begins with $\delta^{18}\text{O}$ of -10 before condensation begins).

Of course, ours is not a particular sophisticated model; we have included none of

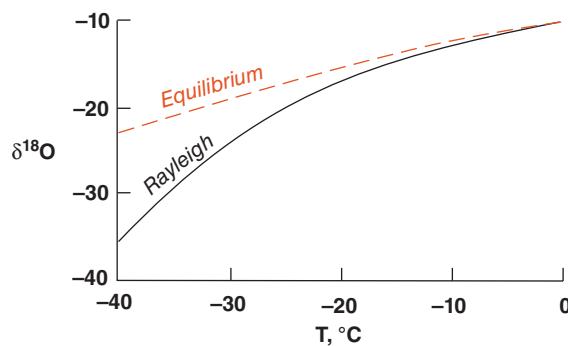


Figure 8.9 Calculated dependence of $\delta^{18}\text{O}$ on temperature based on eqn. 8.90. We assume the water vapor starts out 10 per mil depleted in $\delta^{18}\text{O}$.

the complexities of the real atmosphere. It is interesting to now look at some actual observations to compare with our model. Figure 8.10 shows the global variation in mean annual $\delta^{18}\text{O}$ in precipitation, which should be somewhat heavier than vapor, as a function of mean annual air temperature. The actual observations show a linear dependence on temperature and a somewhat greater range of $\delta^{18}\text{O}$ than our prediction. This reflects

both the *ad hoc* nature of our model and the complexities of the real system. We did not, for example, consider that some precipitation is snow and some rain, nor did we consider the variations that evaporation at various temperatures might introduce. It is also worth noting that monthly averages show considerable deviation from the trend of mean annual data shown in Figure 8.10.

Along with these factors, distance from the ocean also appears to be an important variable in the isotopic composition of precipitation. The further air moves from the site of evaporation (the ocean), the more water is likely to have condensed and fallen as rain, and therefore, the smaller the value of f . Topography also plays an important role in the climate, rainfall, and therefore in the isotopic composition of precipitation. Mountains force air up, causing it to cool and the water vapor to condense. Thus the water vapor in air that has passed over a mountain range will be isotopically lighter than air on the ocean side of a mountain range. These factors are illustrated in the cartoon in Figure 8.11.

Hydrogen as well as oxygen isotopes will be fractionated in the hydrologic cycle.

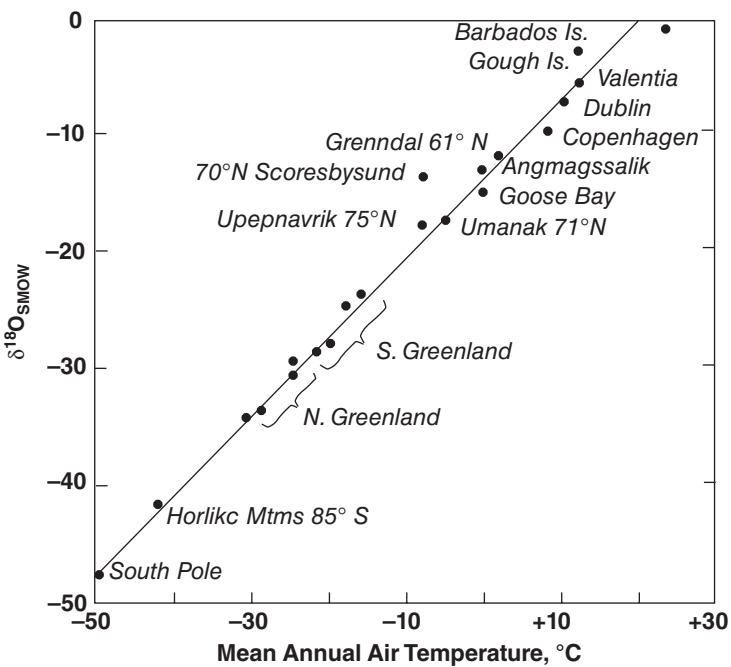


Figure 8.10 Variation of $\delta^{18}\text{O}$ in precipitation as a function of mean annual temperature. This relationship is approximately described as $\delta^{18}\text{O} = 0.69\text{T}^{\circ}\text{C} - 13.6$. (Source: Dansgaard (1964).)

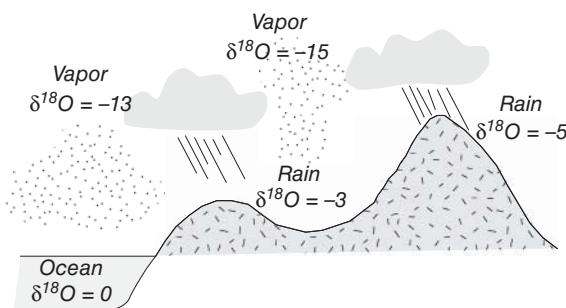


Figure 8.11 Cartoon illustrating the process of Rayleigh fractionation and the increasing fractionation of oxygen isotopes in rain as it moves inland.

Indeed, $\delta^{18}\text{O}$ and δD are well correlated in precipitation, as is shown in Figure 8.12. The fractionation of hydrogen isotopes, however, is greater because the mass difference is greater. The correlation shown in Figure 8.12 is known as the *Meteoric Water Line* (or sometimes the *Global Meteoric Water Line*) because local correlations between δD and $\delta^{18}\text{O}$ often define somewhat shallower slopes than the global trend shown in Figure 8.12).

The equation for the Meteoric Water Line is $\delta\text{D} = \delta^{18}\text{O} + 10$. As is apparent from both this equation and Figure 8.12, seawater (which by definition has $\delta\text{D} = \delta^{18}\text{O} = 0$) does not lie on this line. This reflects the role played by kinetic fractionation in evaporation, as we discussed in the Section 8.3.2.

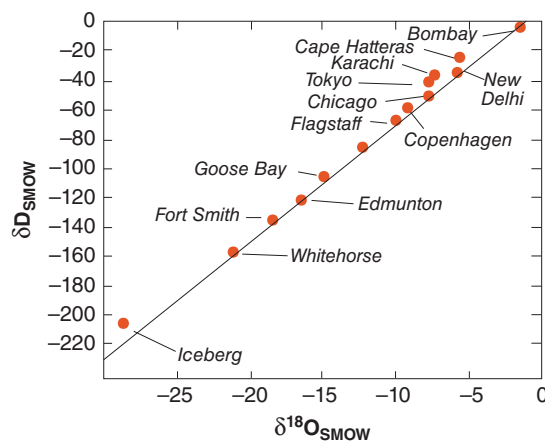


Figure 8.12 Northern Hemisphere variation in mean annual δD and $\delta^{18}\text{O}$ in precipitation and meteoric waters. The relationship between δD and $\delta^{18}\text{O}$ is approximately $\delta\text{D} = 8\delta^{18}\text{O} + 10$. (Source: Dansgaard (1964). CC-BY-4.0.)

Figure 8.13 shows the variation in oxygen isotopic composition of meteoric surface waters in the North America. The distribution is clearly not purely a function of mean annual temperature, and this illustrates the role of the factors discussed previously. We will return to the topic of the hydrologic system in Chapter 10 when we discuss paleoclimatology.

8.6 ISOTOPE FRACTIONATION IN THE BIOSPHERE

Biological processes often involve large isotopic fractionations, as we noted earlier. Indeed, biological processes are the most important cause of variations in the isotope composition of carbon, nitrogen, and sulfur. For the most part, the largest fractionations occur during the initial production of organic matter by the so-called primary producers, or *autotrophs*. These include all plants and many kinds of bacteria. The most important means of production of organic matter is photosynthesis, but organic matter may also be produced by chemosynthesis, for example, at mid-ocean ridge hydrothermal vents. Large fractions of both carbon and nitrogen occur during primary production. Additional fractionations also occur in subsequent reactions up through the food chain as *heterotrophs* consume primary producers, but these are generally smaller.

8.6.1 Carbon isotope fractionation during photosynthesis

The most important process producing isotopic fractionation of carbon is photosynthesis. Photosynthetic fractionation of carbon isotopes is primarily kinetic. The early work of Park and Epstein (1960) suggested fractionation occurred in several steps. Subsequent work has elucidated the fractionations involved in these steps, which we will consider in more detail here.

For terrestrial plants (those utilizing atmospheric CO_2), the first step is diffusion of CO_2 into the boundary layer surrounding the leaf, through the stomata, and finally within the leaf. The average $\delta^{13}\text{C}$ of various species of plants has been correlated with the stomatal conductance (Delucia et al., 1988), indicating that diffusion into the plant is indeed

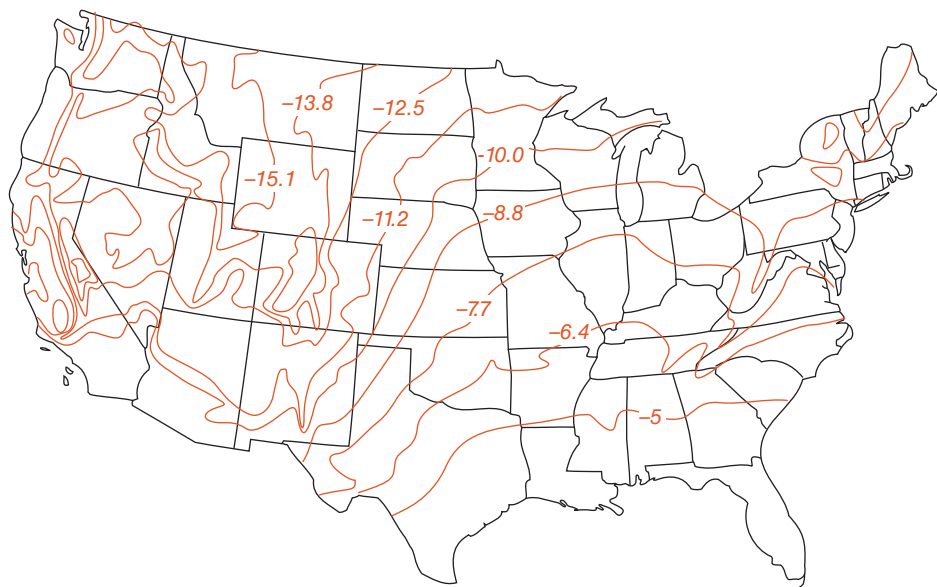
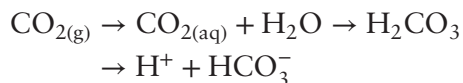


Figure 8.13 Variation of $\delta^{18}\text{O}$ in precipitation in the United States (computed from analysis of tap water). $\delta^{18}\text{O}$ depends on orographic effects, mean annual temperature, and distance from the sources of water vapor. (Source: Bowen et al. (2007). Reproduced with permission of John Wiley & Sons.)

important in fractionating carbon isotopes. On theoretical grounds, a 4.4‰ difference in the diffusion coefficients is predicted ($^{12}\text{CO}_2$ will diffuse more rapidly; Eqn. 8.71) so a fractionation of -4.4‰ is expected. Marine algae and aquatic plants can utilize either dissolved CO_2 or HCO_3^- for photosynthesis:



An equilibrium fractionation of $+0.9$ per mil is associated with dissolution ($^{13}\text{CO}_2$ will dissolve more readily), and an equilibrium $+7$ to $+12\text{‰}$ fractionation (depending on temperature) occurs during hydration and dissociation of CO_2 . Thus, we expect dissolved HCO_3^- to be about 8 – 12 per mil heavier than atmospheric CO_2 .

At this point, there is a divergence in the chemical pathways. Most plants use an enzyme called *ribulose bisphosphate carboxylase oxygenase* (RUBISCO) to catalyze a reaction in which *ribulose bisphosphate* reacts with one molecule of CO_2 to produce two molecules of 3-phosphoglyceric acid, a compound containing three carbon atoms, in a process called *carboxylation* (Figure 8.14).

Energy to drive this reaction is provided by another reaction, called *photophosphorylation*, in which electromagnetic energy is used to dissociate water, producing oxygen. The carbon is subsequently reduced, carbohydrate formed, and the ribulose bisphosphate regenerated. Such plants are called C_3 plants and this process is called the *Benson-Calvin*, or *Calvin*, cycle. C_3 plants constitute about 90% of all plants and comprise the majority of cultivated plants, including wheat, rice, and nuts. Algae and autotrophic bacteria also produce a three-carbon chain as the initial photosynthetic product. There is a kinetic fractionation associated with carboxylation of ribulose bisphosphate that has been determined by several methods to be -29.4‰ in higher terrestrial plants. Bacterial carboxylation has different reaction mechanisms and a smaller fractionation of about -20‰ . Thus for terrestrial plants a fractionation of about -34‰ is expected from the sum of the fractionation. The actual observed total fractionation is in the range of -20 to -30‰ .

The disparity between the observed total fractionation and that expected from the sum of the steps presented something of a conundrum. The solution appears to be a model

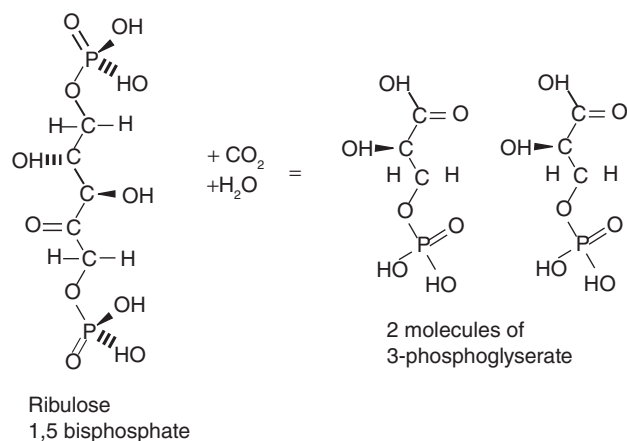


Figure 8.14 Ribulose bisphosphate (RuBP) carboxylation, the reaction by which C₃ plants fix carbon during photosynthesis. Bold solid bonds are in front of the plane of the paper, dashed ones behind. (Source: White (2013). Reproduced with permission of John Wiley & Sons.)

that assumes the amount of carbon isotope fractionation expressed in the tissues of plants depends on ratio the concentration of CO₂ inside plants to that in the external environment (e.g., Farquhar et al., 1982). In its simplest version, the model may be described by the equation:

$$\Delta = a + (c_i/c_a)(b - a) \quad (8.94)$$

where a is the isotopic fractionation due to diffusion into the plant, c_i is the interior CO₂ concentration, c_a is the ambient or exterior CO₂ concentration, and b is the fractionation occurring during carboxylation. According to this model, where an unlimited amount of CO₂ is available (i.e., when $c_i/c_a \approx 1$), carboxylation alone causes fractionation. At the other extreme, if the concentration of CO₂ in the cell is limiting (i.e., when $c_i/c_a \approx 0$), essentially all carbon in the cell will be fixed and therefore there will be little fractionation during this step and the total fractionation is essentially just that due to diffusion alone. Both laboratory experiments and field observations provide strong support for this model.

More recent studies have shown that Rubisco enzyme exists in at least two different forms and that these two different forms fractionate carbon isotopes to differing degrees. Form I, which is by far the most common, typically produces the fractionation mentioned earlier; fractionation produced by Form II, which appears to be restricted

to a few autotrophic bacteria and some dinoflagellates, can be as small as 17.8‰.

The other photosynthetic pathway is the Hatch–Slack cycle, used by the C₄ plants, which include hot-region grasses and related crops such as maize and sugarcane. These plants use *phosphoenol pyruvate carboxylase* (PEP) to initially fix the carbon and form oxaloacetate, a compound that contains four carbons (Figure 8.15). A much smaller fractionation, about –2.0 to –2.5‰ occurs during this step. In phosphoenol pyruvate carboxylation, the CO₂ is fixed in outer mesophyll cells as oxaloacetate and carried as part of a C₄ acid, either malate or asparatate, to inner bundle sheath cells where it is decarboxylated and refixed by RuBP (Figure 8.16). The environment in the bundle sheath cells is almost a closed system, so that virtually all the carbon carried there is refixed by RuBP. Consequently there is little fractionation during this step. C₄ plants have average $\delta^{13}\text{C}$ of –13‰. As in the case of RuBP photosynthesis, the fractionation appears to depend on the ambient concentration of CO₂. This dependence was modeled by Farquhar et al. (1983) as:

$$\Delta = a + (b_4 + b_3\phi - a)(c_i/c_a) \quad (8.95)$$

where a is the fractionation due to diffusion of CO₂ into the plant as above, b_4 is the fractionation during transport into bundle-sheath cells, b_3 is the fractionation during

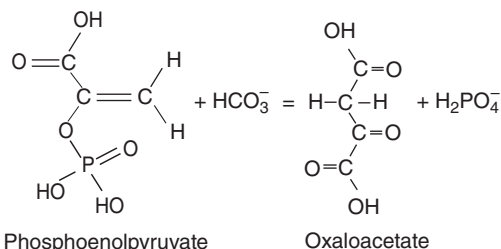


Figure 8.15 Phosphoenolpyruvate carboxylation, the reaction by which C₄ plants fix CO₂ during photosynthesis. (Source: White (2013). Reproduced with permission of John Wiley & Sons.)

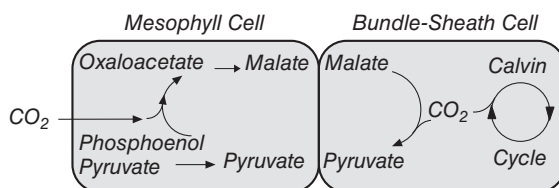


Figure 8.16 Chemical pathways in C₄ photosynthesis. (Source: Fogel and Cifuentes (1993). Reproduced with permission of Springer Science + Business Media.)

carboxylation (~−3‰), ϕ is the fraction CO₂ leaked from the plant.

A third group of plants, the CAM plants, have a unique metabolism called the “Crassulacean acid metabolism.” These plants generally use the C₄ pathway, but can use the C₃ pathway under certain conditions. They are generally adapted to arid environments and include pineapple and many cacti, they have $\delta^{13}\text{C}$ intermediate between C₃ and C₄ plants.

Terrestrial plants, which utilize CO₂ from the atmosphere, generally produce greater fractionations than marine and aquatic autotrophs, which utilize dissolved CO₂ and HCO₃[−], together referred to as *dissolved inorganic carbon* or DIC. As we noted earlier, there is about a +8‰ equilibrium fractionation between dissolved CO₂ and HCO₃[−]. Since HCO₃[−] is about 2 orders of magnitude more abundant in seawater than dissolved CO₂, many marine algae utilize this species, and hence tend to show a lower net fractionation during photosynthesis. Diffusion is slower in water than in air, so diffusion is often the rate-limiting step. Most aquatic plants

have some membrane-bound mechanism to pump DIC, which can be turned on when DIC is low (Sharkey and Berry, 1985). When DIC concentrations are high, fractionation in aquatic and marine plants is generally similar to that in terrestrial plants. When it is low and the plants are actively pumping DIC, the fractionation is less because most of the carbon pumped into cells is fixed. Thus carbon isotope fractionations can be as low as 5‰ in algae. The model describing this fractionation is:

$$\Delta = d + b_3(F_3/F_1) \quad (8.96)$$

where d is the equilibrium effect between CO₂ and HCO₃[−], b_3 is the fractionation associated with carboxylation, and (F_3/F_1) is the fraction of CO₂ leaked out of the cell. Though the net fractionation varies between species and depends on factors such as light intensity and moisture stress, higher C₃ plants have average bulk $\delta^{13}\text{C}$ values of −27‰; algae and lichens are typically −12 to 23‰.

In aquatic systems where the pH is lower than in seawater, CO₂ becomes a more important species and some algae can utilize this rather than HCO₃[−]. In those cases, the total fractionation will be greater. An interesting illustration of this and the effect of the CO₂ concentration on net fractionation is shown in Figure 8.17, which shows data on the isotopic composition of algae and bacteria in Yellowstone hot springs. Some fractionation is also associated with respiration (the oxidation of carbohydrate to CO₂), but the net effect of this is uncertain.

Not surprisingly, the carbon isotope fractionation in C fixation is also temperature dependent. Thus, higher fractionations are observed in cold-water phytoplankton than in warm water species. However, this observation also reflects a kinetic effect: there is generally less dissolved CO₂ available in warm waters because of the decreasing solubility at higher temperature (indeed, as we will see in Chapter 10, the effect of CO₂ concentration on fractionation in marine algae can be used to estimate ancient CO₂ levels). As a result, a larger fraction of the CO₂ is utilized and there is consequently less fractionation. Surface waters of the ocean are generally enriched in ¹³C because of uptake of ¹²C during photosynthesis (Figure 8.18). The degree of enrichment depends on the productivity: biologically

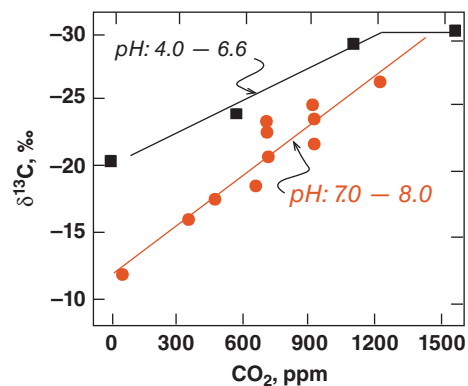


Figure 8.17 Dependence of $\delta^{13}\text{C}$ of algae and bacterial on CO_2 concentration from hydrothermal springs in Yellowstone National Park. Carbon isotope fractionation also depends on the pH of the water, because this determines the species of carbon used in photosynthesis. (Source: Fogel and Cifuentes (1993). Reproduced with permission of Springer Science + Business Media.)

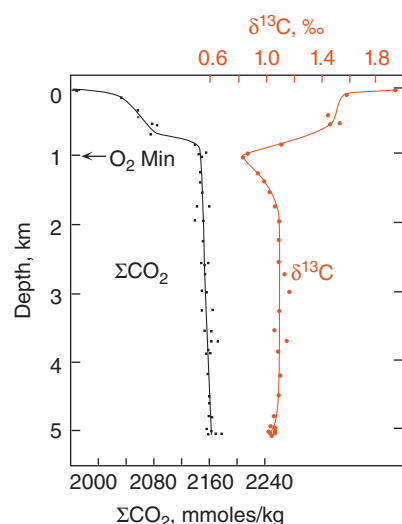


Figure 8.18 Depth profile of total dissolved inorganic carbon and $\delta^{13}\text{C}$ in the North Atlantic. (source: Adapted from Kroopnick et al., 1972.)

productive areas show greater enrichment. Deep water, on the other hand, is depleted in ^{13}C (perhaps it would be more accurate to say it is enriched in ^{12}C). Organic matter falls through the water column and is decomposed and “remineralized,” that is, converted to

inorganic carbon, by the action of bacteria, enriching deep water in ^{12}C . Thus biological activity acts to “pump” carbon, and particularly ^{12}C from surface to deep waters.

Nearly all organic matter originates through photosynthesis. Subsequent reactions convert the photosynthetically produced carbohydrates to the variety of other organic compounds utilized by organisms. Further fractionations occur in these reactions as discussed in Hayes (2001). Lipids (fats, waxes, etc.) in plants tend to be isotopically lighter (i.e., have lower $\delta^{13}\text{C}$) than other components (such as cellulose). The effect is usually small, a few per mil, compared to the fractionation during photosynthesis. These fractionations are thought to be kinetic in origin and may partly arise from organic C-H bonds being enriched in ^{12}C while organic C-O bonds are enriched in ^{13}C . ^{12}C is preferentially consumed in respiration (again, because bonds are weaker and it reacts faster), which would tend to enrich residual organic matter in ^{13}C . Thus, the carbon isotopic composition of organisms becomes more positive moving up the food chain.

Interestingly, although the energy source for chemosynthesis is dramatically different than for photosynthesis, the carbon-fixation process is similar and still involves the Calvin cycle. Not surprisingly then, carbon fractionation during chemosynthesis is similar to that during photosynthesis. Some chemosynthetic bacteria, notably some of the symbionts of hydrothermal vent organisms, have Rubisco Form II, and hence show smaller fractionations.

8.6.2 Nitrogen isotope fractionation in biological processes

Nitrogen is another important element in biological processes, being an essential component of all amino acids and proteins. As in the case of carbon, most of terrestrial nitrogen isotopic variation results from biological processes. These processes, however, are considerably more complex because nitrogen exists in more forms and more oxidation states. There are five important forms of inorganic nitrogen: molecular nitrogen (N_2), nitrate (NO_3^-), nitrite (NO_2^-), ammonia (NH_3), and ammonium (NH_4^+). Equilibrium isotope fractionations that can be quite large occur

Table 8.2 Nitrogen isotopic fractionation in the exogenic nitrogen cycle.

Reaction	Fractionation
N ₂ fixation	N ₂ → 2NH ₃ <2‰
	NH ₃ → NH ₄ ⁺ +19 to 33‰
Nitrification	NH ₄ ⁺ → NO ₃ ⁻ -15 to -35‰
Denitrification	NO ₃ ⁻ → N ₂ -5 to -30‰
Nitrate reduction	NO ₃ ⁻ → NH ₄ ⁺ -20 to -35‰

between these five forms. Except for the ammonium–ammonia reaction, the reactions between these forms are all redox reactions and they are predominantly biologically mediated. Significant kinetic fractionations occur during these biological mediated reactions. Table 8.2 summarizes net fractionations in the nitrogen cycle.

Heterotrophs, such as you and I, get their nitrogen from what they eat and there is only a slight difference, generally around 1 or 2‰, between animals and what they eat. Autotrophs, including algae, plants and bacteria, must assimilate nitrogen from the environment. Plants and algae cannot assimilate and utilize N₂; they must use some type of *fixed* nitrogen, which can be any of the remaining four forms listed earlier. The dirty work of converting nitrogen to ammonia (and from there to other forms of nitrogen), a process called *fixation*, is done by bacteria, including photosynthetic ones. This involves only a small fractionation of -3 to +1‰.

Reduced nitrogen (e.g., ammonia) is the form of nitrogen that is ultimately incorporated into organic matter, as NH₂ *amine* groups, by autotrophs. There is a fractionation of up to -20‰ when autotrophs uptake of ammonium (¹⁴N is taken up preferentially), the extent depending on the ammonium abundance. When ammonium is abundant, fractionation tends to be large, when it is not, most available ammonium is taken up and there is little fractionation (Figure 8.19). Most plants, including many marine algae, can utilize oxidized nitrogen, NO₃⁻ and NO₂⁻, as well as reduced nitrogen. In these cases, nitrogen must first be reduced by the action of reductase enzymes. δ¹⁵N fractionations of 0 to -24‰ have been measured for the assimilation of NO₃⁻.

There is a small fractionation when that ammonium is subsequently incorporated into organic molecules. There are two principle

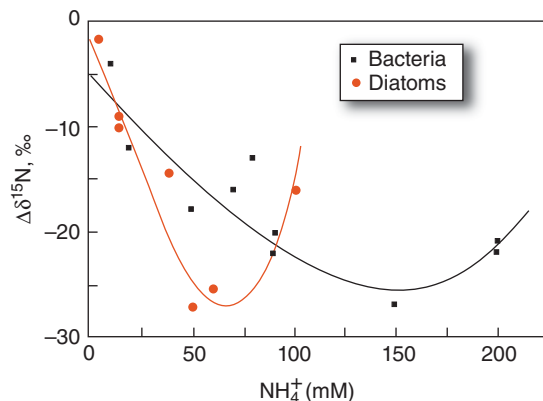


Figure 8.19 Dependence of nitrogen isotope fractionation by bacteria and diatoms on dissolved ammonium concentration. (Source: Fogel and Cifuentes (1993). Reproduced with permission of Springer Science + Business Media.)

reactions by which ammonia is incorporated into organic matter: formation of glutamate from α-ketoglutarate via the glutamate dehydrogenase reaction, and formation of glutamine from glutamate via the enzyme glutamine synthetase. A positive fractionation (i.e., the product is enriched in ¹⁵N) of +2 to +4 has been measured for the glutamate dehydrogenase reaction, and the fractionation for the glutamine synthetase reaction is also expected to be positive, because N is bound more strongly in the product than in ammonia.

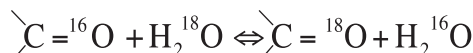
The net result of these various fractionations is that organic nitrogen is usually heavier than atmospheric nitrogen. The isotopic compositions of marine particulate nitrogen and non-nitrogen-fixing plankton are typically -3‰ to +12‰ δ¹⁵N. Terrestrial plants unaffected by artificial fertilizers generally have a narrower range of +6‰ to +13 per mil. Legumes (and a few other kinds of plants) are a special case. While they cannot fix nitrogen, they have symbiotic bacteria in their root nodules that can. As a result, legumes have distinctly lower δ¹⁵N than other terrestrial, in the range of -2 to +4‰. Marine blue-green algae range from -4 to +2, with most in the range of -4 to -2‰.

A caveat to all this is that most fixed nitrogen in modern ecosystems now derived, directly or indirectly, from artificial fertilizers.

These fertilizers contain ammonia derived from atmospheric N₂ through the Haber process, in which there is little isotopic fractionation. Consequently, modern plants, particularly those raised on artificial fertilizers, have lower δ¹⁵N.

8.6.3 Oxygen and hydrogen isotope fractionation by plants

Oxygen is incorporated into biological material from CO₂, H₂O, and O₂. However, both CO₂ and O₂ are in oxygen isotopic equilibrium with water during photosynthesis, and water is the dominant form. Therefore, the isotopic composition of plant water determines the oxygen isotopic composition of plant material. The oxygen isotopic composition of plant material seems to be controlled by exchange reactions between water and carbonyl oxygens (oxygens doubly bound to carbon):



Fractionations of +16 to +27‰ (i.e., the organically bound oxygen is heavier) have been measured for these reactions. Consistent with this, cellulose from most plants has δ¹⁸O of +27 ± 3‰. Other factors, however, play a role in the oxygen isotopic composition of plant material. First, the isotopic composition of water varies from δ¹⁸O ≈ -55‰ in Arctic regions to δ¹⁸O ≈ 0‰ in the oceans. Second, less than complete equilibrium may be achieved if photosynthesis is occurring at a rapid pace, resulting in less fractionation. Finally, some fractionation of water may occur during transpiration, with residual water in the plant becoming heavier.

Hydrogen incorporated into organic matter during photosynthesis is derived from meteoritic water, whose isotopic composition varies with distance from source and temperature (e.g., Figure 8.12). Hydrogen isotope fractionation during photosynthesis occurs such that the light isotope is strongly enriched in organic material. In marine algae, isotope fractionations of -100 to -150‰ have been observed, which is similar to that observed in terrestrial plants: -86 to -120‰. Among terrestrial plants, there appears to be a difference between C₃ and C₄ plants. The former

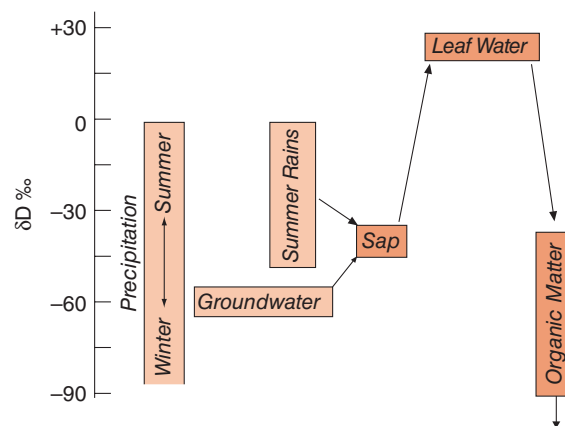


Figure 8.20 Isotopic Fractionations of hydrogen during primary production in terrestrial plants. (Source: Adapted White (1988). Reproduced with permission of Springer Science + Business Media.)

fractionations of -117 to -121‰, while fractionations -86 to -109‰ have been observed in C₄ plants. As a consequence, hydrogen isotopic compositions of organic matter show wide variations.

As is the case for oxygen, variations in the isotopic composition of available water and fractionation during transpiration are important in controlling the hydrogen isotopic composition of plants. This is illustrated in Figure 8.20.

8.6.4 Carbon and hydrogen isotopic composition of organic matter in sediments

Organic matter buried in sediment undergoes a series of diagenetic changes, some of which are biologically mediated (by bacteria) and some of which are abiotic. A complex, refractory⁵ substance called *kerogen* is the product the early stages of diagenesis. Sediments typically contain about a half a percent of such organic material. Little change in carbon and hydrogen isotopic composition occurs in early diagenesis; consequently, the δ¹³C and δD of kerogen are similar to the isotopic compositions of its source with δ¹³C typically in the range of -20 to -32‰ and δD in the range of -75 to -150‰. Subsequent heat and pressure transforms kerogen. This process produces coal from Type III kerogen, which is derived from cellulose-rich terrestrial organic matter accumulated in swamps and peat bogs.

Lipid-rich material derived from aquatic and marine algae and non-woody parts of terrestrial plants form Type I and II kerogens, which ultimately transforms to petroleum and natural gas. The transformations to coal and petroleum involve the progressive loss of hydrogen and oxygen, and hence decrease in H:C and O:C ratios of the material. Most of this likely occurs through generation and loss of H₂O and CO₂, but generation low molecular weight hydrocarbons that compose natural gas (methane, CH₄; ethane, C₂H₆; propane, C₃H₈; and butane, C₄H₁₀)⁶ can also occur. Fractionations tend to be small during this phase and petroleum liquids typically have $\delta^{13}\text{C}$ within 1‰ or of the kerogen that gave rise to them. Hydrogen isotopic fractionations also tend to be relatively small, although as Figure 8.21 shows, the δD of petroleum is skewed to lighter isotopic composition relative to kerogen. This is likely to be due mainly to the lipids, which tend to isotopically lighter contributing disproportionately to petroleum generation. Similarly small isotopic changes

occur in the generation of coal. These changes in isotopic composition are similar to or smaller than the isotopic heterogeneity of the kerogen itself. Thus carbon and hydrogen isotopic composition is used extensively in the petroleum industry as a tracer to determine the source rock of a petroleum reservoir.

As temperature increases beyond 100°C or so, hydrocarbons composing petroleum begin to break down, or “crack,” into lower molecular weight compounds and ultimately, into natural gas. Kinetic fractionations can become important during this phase as ¹³C forms stronger bonds. Consequently, gases generated, particularly methane, will be isotopically lighter than the precursor material. Clayton (1991) concluded that the effect of cracking is to increase $\delta^{13}\text{C}$ of oil by about 1.5‰ by 50% cracking. The isotopic composition of methane generated during the thermal cracking phase can have considerably lighter carbon and hydrogen than the oil. As Figure 8.22 shows, this *thermogenic* methane may have $\delta^{13}\text{C}$ as low as -60‰ and δD as low as -300‰.

Methane may also be produced by microbial processes. Some of these occur in anoxic sediments and soils during early diagenesis. Indeed, it is not uncommon to see bubbles of methane rising to the surface in small ponds from anoxic sediment accumulating beneath them. Methane is also generated in guts of animals, particularly ruminants such as cattle (but also humans). In all cases, the organisms actually producing the methane are a group of archaea called *methanogens*. They produce methane through two dominant pathways: CO₂ reduction by reaction with hydrogen, and fermentation. In the latter process, acetic acid (CH₃COOH) is broken down to produce CH₄ plus CO₂. Chemically, this *biogenic* methane is distinct from thermogenic methane discussed previously by the near absence of C₂ and higher alkanes in the latter. They are also isotopically distinct, as may be seen in Figure 8.22. Equilibrium fractionation between CO₂ and CH₄ is quite large. Richet et al. (1977) derived the following equation:

$$1000 \ln \alpha_{\text{CH}_4-\text{CO}_2} = 29.2 \left(\frac{1000}{T} \right) - 29.6 \quad (8.97)$$

According to this equation, α should rise from 1.05 to 1.08 as temperature falls from

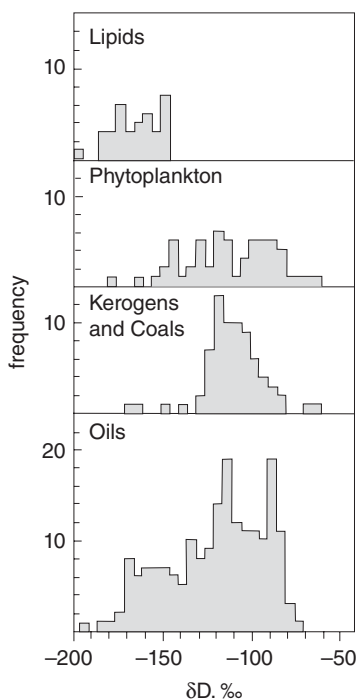


Figure 8.21 Hydrogen isotopic compositions of lipids, phytoplankton, and sedimentary organic matter. (Source: Adapted Schoell (1984). Reproduced with permission of Elsevier.)

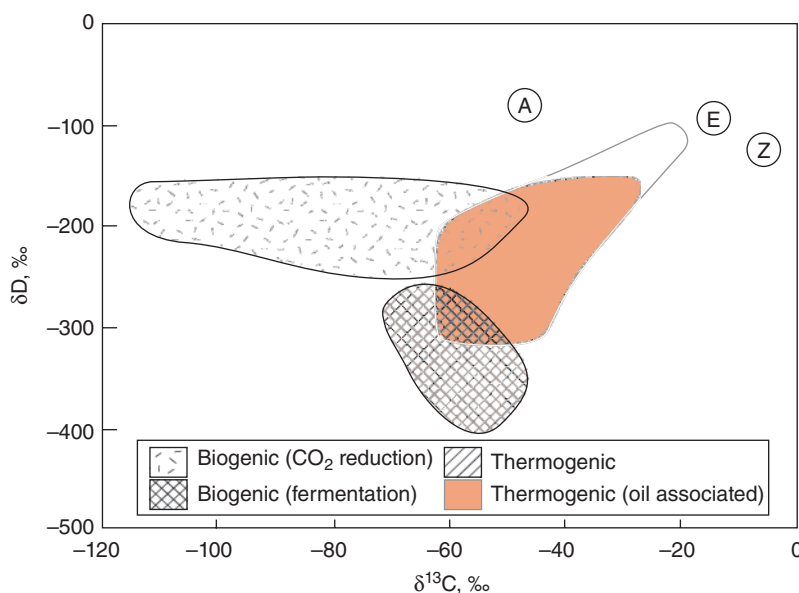


Figure 8.22 Carbon and hydrogen isotopic composition of methane. “Dry” refers to methane not associated with petroleum. “A” is the isotopic composition of atmospheric methane, “E” and “Z” are the isotopic compositions of abiotic methane from the East Pacific Rise (Welhan, 1988), and the Zimbales peridotite in the Philippines (Abrajano et al., 1988), respectively. These methanes have isotopic compositions close to that of mantle carbon. (Source: Adapted Schoell (1988) and Whiticar et al. (1986).)

100°C to 0°C. Thus at the ocean floor (~0°C), methane generated in equilibrium with seawater CO₂ would be expected to have $\delta^{13}\text{C}$ of around -80‰. Methane in marine sediments is most often somewhat heavier than this (Whiticar et al., 1986). Experiments by Botz et al. (1996) suggest why. In cultural experiments they found that fractionation between CO₂ and CH₄ was close to equilibrium values when microbial populations were stable and only a small fraction of the CO₂ was being converted to CH₄. Fractionation was less than equilibrium values when populations were growing and large fractions of available CO₂ (up to 30 or 40%) was converted to CH₄. Thus, as is the case in photosynthesis, kinetic factors may limit fractionation during methanogenesis. As Figure 8.22 shows, carbon isotope fractionation is generally smaller when methane is produced by fermentation, but hydrogen fractionation tends to be greater.

8.6.5 Biological fractionation of sulfur isotopes

Sulfur is a critical but minor component of living tissue (C:S atomic ratio is about

200). Plants take up sulfur as sulfate and subsequently reduce it to sulfide and incorporate it into cysteine (an amino acid with the composition HO₂CCH(NH₂)CH₂SH). There is apparently no fractionation of sulfur isotopes in transport across cell membranes and incorporation, but there is a fractionation of +0.5 to -4.5‰ in reduction process, referred to as *assimilatory sulfate reduction*. This is substantially less than the expected fractionation of about -20‰, suggesting that nearly all the sulfur taken up by primary producers is reduced and incorporated into tissue.

Sulfur, however, plays two other important roles in biological processes. First, sulfur in the form of sulfate can act as an electron acceptor or oxidant, and is utilized as such by sulfur-reducing bacteria. This process, in which H₂S is liberated, is called *dissimilatory sulfate reduction* and plays an important role in biogeochemical cycles, both as a sink for sulfur and source for atmospheric oxygen (because the sulfide is usually then buried in sediments). A large fractionation of +5 to -46‰ is associated with this

process. This process produces by far the most significant fractionation of sulfur isotopes, and thus governs the isotopic composition of sulfur in the exogene. Sedimentary sulfate typically has $\delta^{34}\text{S}$ of about +17, which is similar to the isotopic composition of sulfate in the modern oceans (+20), while sedimentary sulfide has a $\delta^{34}\text{S}$ of -18. The living biomass has a $\delta^{34}\text{S}$ of ≈ 0 .

The final important role of sulfur is a reductant. Sulfide is an electron acceptor used by some types of photosynthetic bacteria as well as other bacteria in the reduction of CO_2 to organic carbon. Most unique among these perhaps are the chemosynthetic bacteria of submarine hydrothermal vents. They utilize H_2S emanating from the vents as an energy source and form the base of the food chain in these unique ecosystems. A fractionation of +2 to -18‰ is associated with this process.

NOTES

1. The energy level is said to be “degenerate” if two or more states have the same energy level E_i .

2. Entropy is defined in the second law of thermodynamics, which states:

$$dS = \frac{dQ_{rev}}{T}$$

where Q_{rev} is heat gained by a system in a reversible process. Entropy can be thought of as a measure of the randomness of a system.

3. The Teller–Redlich Theorem relates the products of the frequencies for each symmetry type of the two isotopes to the ratios of their masses and moments of inertia:

$$\left(\frac{m_2}{m_1}\right)^{3/2} \frac{I_1}{I_2} \left(\frac{M_1}{M_2}\right)^{3/2} = \frac{hv_1/kT}{hv_2/kT}$$

where m is the isotope mass and M is the molecular mass. We need not concern ourselves with its details.

4. Two other CO_2 isotopologues also have mass 47, but their concentration is much, much lower than that of $^{13}\text{C}^{18}\text{O}^{16}\text{O}$.
5. “Refractory” in this context means resistant to oxidation or bacterial decomposition.
6. These compounds, in which the carbons are chained together, are called *alkanes* and are referred to by the number of carbons in the chain, e.g., C_2 = ethane.

REFERENCES

- Abrajano, T. A., Sturchio, N. C., Bohlke, J. K., Lyon, G. L., Poreda, R. J. and Stevens, C. M. 1988. Methane-hydrogen gas seeps, Zambales Ophiolite, Philippines: Deep or shallow origin? *Chemical Geology*, 71: 211–222, doi: 10.1016/0009-2541(88)90116-7.
- Bigeleisen, J. and Mayer, M. G. 1947. Calculation of equilibrium constants for isotopic exchange reactions, *Journal of Chemical Physics*, 15: 261–267.
- Botz, R., Pokojski, H.-D., Schmitt, M. and Thomm, M. 1996. Carbon isotope fractionation during bacterial methanogenesis by CO_2 reduction, *Organic Geochemistry*, 25: 255–262, doi: 10.1016/s0146-6380(96)00129-5.
- Bowen, G. J., Ehleringer, J. R., Chesson, L. A., Stange, E. and Cerling, T. E. 2007. Stable isotope ratios of tap water in the contiguous United States. *Water Resources, Research*, 43: W03419, doi: 10.1029/2006wr005186.
- Chacko, T., Cole, D. and Horita, J. 2001. Equilibrium oxygen, hydrogen and carbon isotope fractionation factors applicable to geologic systems. In: *Reviews in Mineralogy and Geochemistry v. 43: Stable Isotope Geochemistry*, Valley, J. W. and Cole, D. (eds). Chantilly, USA: Mineralogical Society of America.
- Clayton, C. J. 1991. Effect of maturity on carbon isotope ratios of oils and condensates. *Organic Geochemistry*, 17: 887–899, doi: 10.1016/0146-6380(91)90030-n.
- Dansgaard, W. 1964. Stable isotopes in precipitation, *Tellus*, 16: 436–463.
- DeLucia, E. H., Schlesinger, W. H. and Billings, W. D. 1988. Water relations and maintenance of Sierran conifers on hydrothermally altered rock. *Ecology*, 72: 48–51.
- Dennis, K. J., Affek, H. P., Passey, B. H., Schrag, D. P. and Eiler, J. M. 2011. Defining an absolute reference frame for “clumped,” isotope studies of CO_2 . *Geochimica et Cosmochimica Acta*, 75: 7117–7131.
- Eiler, J. M. 2013. The isotopic anatomies of molecules and minerals. *Annual Review of Earth and Planetary Sciences*, 41: 411–441, doi: 10.1146/annurev-earth-042711-105348.
- Estep, M. L. F. 1984. Carbon and hydrogen isotopic compositions of algae and bacteria from hydrothermal environments, Yellowstone National Park. *Geochimica et Cosmochimica Acta*, 48: 591–599, doi: 10.1016/0016-7037(84)90287-4.
- Farquhar, G. D. 1983. On the Nature of Carbon Isotope Discrimination in C_4 Species. *Functional Plant Biology*, 10: 205–226, doi: 10.1071/PP9830205.

- Farquhar, G. D., O'Leary, M. H. and Berry, J. A. 1982. On the Relationship Between Carbon Isotope Discrimination and the Intercellular Carbon Dioxide Concentration in Leaves. *Functional Plant Biology*, 9: 121–137, doi: 10.1071/PP9820121.
- Faure, G. 1986. *Principles of Isotope Geology*, 2nd edn, New York: John Wiley & Sons, Inc., 589 p.
- Ferronsky, V. I., and Polyakov, V. A. 1982. *Environmental Isotopes in the Hydrosphere*, 466 pp., Chichester: John Wiley & Sons, Ltd.
- Fogel, M. L. and Fuentes, M. L. 1993. Isotope Fractionation during Primary Production, in *Organic Geochemistry: Principles and Applications*, Engel, M. H. and Macko, S. A. (eds), p. 73–98, New York: Plenum.
- Gao, Y. Q. and Marcus, R. A. 2001. Strange and unconventional isotope effects in ozone formation, *Science*, 293: 259–263.
- Ghosh, P., Adkins, J., Affek, H., Balta, B., Guo, W., Schauble, E. A. et al., 2006. ^{13}C - ^{18}O bonds in carbonate minerals: A new kind of paleothermometer. *Geochimica et Cosmochimica Acta*, 70: 1439–1456, doi: 10.1016/j.gca.2005.11.014.
- Hayes, J. M. 2001. Fractionation of carbon and hydrogen isotopes in biosynthetic processes. In: *Reviews in Mineralogy and Geochemistry v. 43: Stable Isotope Geochemistry*, Valley, J. W. and Cole, D. (eds). Washington: Mineralogical Society of America.
- Hiedenreich, J. E. and Thiemens, M. 1986. A non-mass-dependent oxygen isotope effect in the production of ozone from molecular oxygen: The role of molecular symmetry in isotope chemistry. *Journal of Chemical Physics*, 86: 2129–2136.
- Johnson, D. G., Jucks, K. W., Traub, W. A. and Chance, K. V. 2001. Chance, Isotopic composition of stratospheric ozone, *Journal of Geophysical Research*, 105: 9025–9031.
- Kawabe, I. 1978. Calculation of oxygen isotopic fractionation in quartz-water system with special reference to the low temperature fractionation, *Geochimica et Cosmochimica Acta*, 42: 613–621.
- Kroopnick, P., Weiss, R. F. and Craig, H. 1972. Total CO₂, ^{13}C and dissolved oxygen- ^{18}O at Geosecs II in the North Atlantic. *Earth and Planetary Science Letters*, 16: 103–110.
- O'Neil, J. R. 1986, Theoretical and experimental aspects of isotopic fractionation. In: *Stable Isotopes in High Temperature Geologic Processes, Reviews in Mineralogy Volume 16*, J. W. Valley, (eds), Washington: Mineralogical Society of America, pp. 1–40.
- Park, R. and Epstein, S. 1960. Carbon isotope fractionation during photosynthesis, *Geochimica et Cosmochimica Acta*, 21: 110–126.
- Richet, P., Bottinga, Y. and Javoy, M. 1977. A review of hydrogen, carbon, nitrogen, oxygen, sulphur, and chlorine stable isotope fractionation among gaseous molecules. *Annual Review of Earth and Planetary Sciences*, 5: 65–110, doi: 10.1146/annurev.ea.05.050177.000433.
- Schoell, M. 1988. Multiple origins of methane in the Earth, *Chemical Geology*, 71: 1–10, doi: 10.1016/0009-2541(88)90101-5.
- Schoell, M. 1984. Recent advances in petroleum isotope geochemistry, *Organic Geochemistry*, 6: 645–663.
- Sharkey, T. D. and Berry, J. A. 1985. Carbon isotope fractionation of algae as influenced by an inducible CO₂ concentrating mechanism. In: *Inorganic Carbon Uptake by Aquatic Photosynthetic Organisms*, Lucas, W. J. and Berry, J. A. (eds). Rockville, MD: American Society of Plant Physiology.
- Thiemens, M. 2006. History and applications of mass-independent isotope effects. *Annual Reviews of Earth and Planetary Science*, 34: 217–262, doi: annurev.earth.34.031405.125026.
- Urey, H. 1947. The thermodynamic properties of isotopic substances, *Journal of the Chemical Society (London)*, 1947: 562–581.
- van Hook, W. A. 1968. Vapor pressures of the isotopic waters and ices. *The Journal of Physical Chemistry*, 72: 1234–1244, doi: 10.1021/j100850a028.
- Wang, Z., Schauble, E. A. and Eiler, J. M. 2004. Equilibrium thermodynamics of multiply substituted isotopologues of molecular gases. *Geochimica et Cosmochimica Acta*, 68: 4779–4797, doi: 10.1016/j.gca.2004.05.039.
- Welhan, J. A. 1988. Origins of methane in hydrothermal systems, *Chemical Geology*, 71: 183–198, doi: 10.1016/0009-2541(88)90114-3.
- White, J. W. C. 1988. Stable hydrogen isotope fractionation in plants: a review of current theory and some potential applications. In: *Stable Isotopes in Ecological Research*, Rundel, P. W., Ehleringer, J. R. and Nagy, K. A. (eds). New York: Springer Verlag.
- White, W. M. 2013. *Geochemistry*. Oxford: Wiley-Blackwell.
- Whiticar, M. J., Faber, E. and Schoell, M. 1986. Biogenic methane formation in marine and freshwater environments: CO₂ reduction vs. acetate fermentation—Isotope evidence. *Geochimica et Cosmochimica Acta*, 50: 693–709, doi: 10.1016/0016-7037(86)90346-7.

SUGGESTIONS FOR FURTHER READING

- Bowen, R. 1988. *Isotopes in the Earth Sciences*. Essex: Elsevier, 647 p.
- Bowen, G. J. 2010. Isoscapes: Spatial pattern in isotopic biogeochemistry. *Annual Review of Earth and Planetary Sciences*, 38: 161–187, doi: 10.1146/annurev-earth-040809-152429.

- Broecker, W. and Oversby, V. 1971. *Chemical Equilibria in the Earth*. New York: McGraw-Hill, 318 pp.
- Faure, G. 1986. *Principles of Isotope Geology*, 2nd edn, New York: John Wiley & Sons, 589 p.
- Ferronsky, V. I. and Polyakov, V. A. 1982. *Environmental Isotopes in the Hydrosphere*, 466 pp., Chichester: John Wiley & Sons, Ltd.
- Hoefs, J. 1988. *Stable Isotope Geochemistry*. 3rd edn, Berlin: Springer-Verlag, 241 p.
- O'Leary, M. H. 1981. Carbon isotope fractionation in plants. *Phytochemistry*, 20: 553–567.
- O'Leary, M. H. 1988. Carbon isotopes in photosynthesis. *BioScience*, 38: 328–336, doi: 10.2307/1310735.
- Sharp, Z. D. 2007. *Principles of Stable Isotope Geochemistry*. Upper Saddle River, NJ: Pearson Prentice Hall.

PROBLEMS

1. Using the statistical mechanical approach outlined in this chapter, calculate the fractionation factor $\Delta_{\text{CO-O}_2}$ for the $^{17}\text{O}/^{16}\text{O}$ ratio at 273 K. What is the expected ratio of fractionation of $^{17}\text{O}/^{16}\text{O}$ to that of $^{18}\text{O}/^{16}\text{O}$ at this temperature?
2. Show that at 300 K, equilibrium fractionation between O_2 and CO should lead to $\Delta^{17}\text{O}/\Delta^{18}\text{O} \approx 0.52$.
3. Derive a temperature dependent expression for the equilibrium constant in Eqn. 8.62:

$$K = \frac{q^{13}\text{C}^{16}\text{O} q^{12}\text{C}^{17}\text{O}}{q^{12}\text{C}^{16}\text{O} q^{13}\text{C}^{17}\text{O}}$$

What is the value at 300 K? What is the value at 1000 K?

4. Calculate the ratio $[^{13}\text{C}^{16}\text{O}^{18}\text{O}]/[^{12}\text{C}^{16}\text{O}_2]$ in CO_2 gas with a bulk isotopic composition of $\delta^{13}\text{C}_{\text{PDB}} = -6\text{\textperthousand}$ and $\delta^{18}\text{O}_{\text{SMOW}} = 0$. Assume that the standards have the isotopic compositions listed in Table 8.1.
5. Calculate the $\delta^{18}\text{O}$ of raindrops forming in a cloud after 80% of the original vapor has already condensed assuming: (1) the water initially evaporated from the ocean with $\delta^{18}\text{O} = 0$, (2) the liquid-vapor fractionation factor, $\alpha = 1.0092$.

Chapter 9

Stable isotope geochemistry II: High temperature applications

9.1 INTRODUCTION

Stable isotopes have a number of uses in high temperature geochemistry (i.e., igneous and metamorphic geochemistry). Perhaps the most important of these is geothermometry; that is, deducing the temperatures at which mineral assemblages equilibrated. This application makes use of the temperature dependency of fractionation factors. Other important applications include reconstructing ancient hydrothermal systems, detecting crustal assimilation in mantle-derived magmas, and tracing recycled crust in the mantle. These applications primarily involve O isotopes. Before discussing these subjects, let's briefly review the factors governing isotopic fractionation.

9.2 EQUILIBRIUM FRACTIONATIONS AMONG MINERALS

In Chapter 8, we found that the translational and rotation contributions to the partition function do not vary with temperature. In our example calculation at low temperature, we found the vibrational contribution varies with the inverse of absolute temperature. At higher temperature, the $e^{-hv/kT}$ term in Eqn. 8.35 becomes finite, this relationship breaks down, and the equilibrium constant becomes proportional to the inverse square of temperature:

$$\ln K = A + \frac{B}{T^2} \quad (9.1)$$

where A and B are constants. At infinite temperature, the fractionation is unity; that is, $\ln K \approx 0$. Because of the nature of this temperature dependency, fractionation of stable isotopes at mantle temperatures will usually be small and stable isotopes can be used as tracers, particularly in crustal assimilation and recycling, much as radiogenic isotopes are.

It must be emphasized that the simple calculations in Chapter 8 are applicable only to a gas whose vibrations can be approximated by a simple harmonic oscillator. Real gases show fractionations that are complex functions of temperature, with minima, maxima, inflections, and crossovers.

9.2.1 Compositional and structural dependence of equilibrium fractionations

The nature of the chemical bond is of primary importance in determining isotope fractionations. “*In general, bonds to ions with a high ionic potential and low atomic mass are associated with high vibrational frequencies and have a tendency to incorporate the heavy isotope preferentially*” (O’Neil, 1986). This point is illustrated by the *site-potential method* of estimating fractionation factors (Smyth, 1989). The site potential is simply the energy required (e.g., in electron volts) to remove an atom from its crystallographic site and is a measure of bond strength. Figure 9.1a shows that there is a strong correlation between the difference in oxygen site potential in minerals and the fractionation factor between

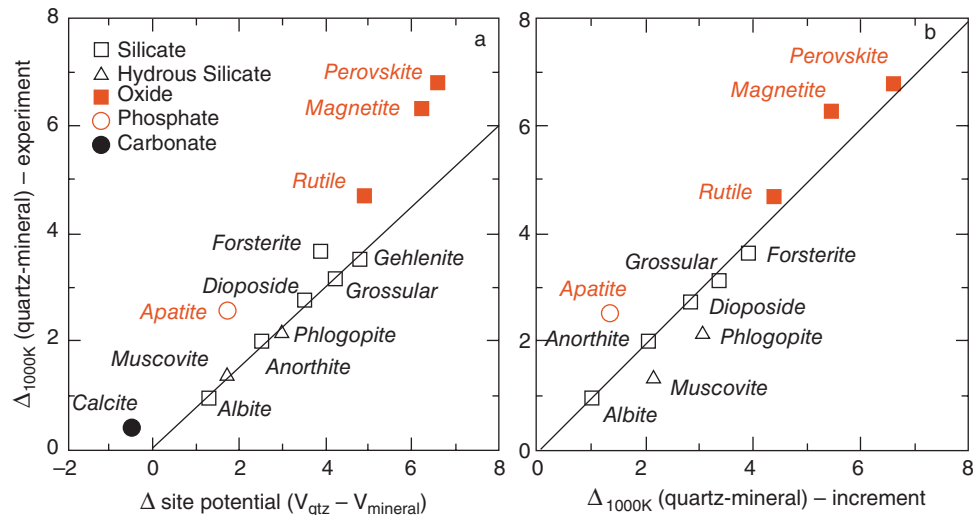


Figure 9.1 (a) Comparison of quartz-mineral fractionation factors estimated from the difference in oxygen site potential ($V_{\text{Qtz}} - V_{\text{mineral}}$) and experimentally observed fractionation factors at 1000 K. (b) Comparison of fractionation factors estimated through the increment method, which also considers cation mass, and experimentally observed fractionation factors at 1000 K. (Source: Adapted from Chacko, et al. (2001). Reproduced with permission of the Mineralogical Society of America.)

those two minerals. The solid line shows that silicates plot along a line with the equation $\Delta_{1000K}(\text{Qtz-mineral}) = 0.751(V_{\text{Qtz}} - V_{\text{mineral}})$. Oxides (and to a less extent, apatite and calcite) fall off this correlation. The deviation in the case of calcite and apatite probably reflects the more strongly covalent nature of oxygen bonds in those minerals. In the case of the oxides, it reflects the varying mass of the cation, as cation mass affects bond strength. In silicates, oxygens are primarily bound to Si and secondarily to other cations. However, in oxides such as rutile, perovskite, and magnetite, oxygen is bound primarily to Fe or Ti, which of course have very different masses to Si. The “increment method” of estimating fractionation factors (e.g., Zhang, 1999) takes account of the cation ion mass. As Figure 9.1b shows, this method produces an improved agreement of calculated and experimentally observed fractionation factors for the oxides.

Substitution of cations in a primarily ionic site in silicates has only a minor effect on fractionation factors. Thus, for example, we would expect relatively little O isotopic fractionation between K-feldspar and Na-feldspar. This turns out to be the case: the fractionation is of the order of 0.1 per mil at room

Table 9.1 Coefficients oxygen isotope fractionation at low temperatures $\Delta_{QZ-\phi} = A + B \times 10^6/T^2$.

ϕ	A	B
Feldspar	0	$0.97 + 1.04b^*$
Pyroxene	0	2.75
Garnet	0	2.88
Olivine	0	3.91
Muscovite	-0.60	2.2
Amphibole	-0.30	3.15
Biotite	-0.60	3.69
Chlorite	-1.63	5.44
Ilmenite	0	5.29
Magnetite	0	5.27

* b is the mole fraction of anorthite in the feldspar. This term therefore accounts for the compositional dependence discussed earlier. From Javoy (1977).

temperature. The substitution of Al for Si in plagioclase is somewhat more important (substitution of Ca for Na is much less important), leading to a 1.1 per-mil fractionation between anorthite and albite at room temperature. Table 9.1 lists the parameters for the temperature dependence of silicate and oxide fractionation factors at low temperatures.

Because oxygen occupies a generally similar lattice site in virtually all mantle and igneous minerals (it is covalently bonded to silicon and

ionically bonded to other cations such as Mg, Fe, Ca, etc.), fractionation of oxygen isotopes between these phases and during melting and crystallization are relatively small, although still measurable.

Carbonates tend to be very ^{18}O rich because O is bonded to a small, highly charged atom, C $^{4+}$. The fractionation relative to water, $\Delta^{18}\text{O}$ is about +30 for calcite. The cation (i.e., Ca or Mg in carbonate) has a secondary role (because of the effects of its mass on vibrational frequency). $\Delta^{18}\text{O}$ decreases to about 25 for Ba (about three times the mass of Ca).

Crystal structure usually plays a secondary role. The $\Delta^{18}\text{O}$ between aragonite and calcite is of the order of 0.5 per-mil. But there apparently is a large fractionation (10 per-mil) of C between graphite and diamond extrapolated to room temperature.

Pressure effects turn out to be small, 0.1 per mil at 2 GPa and less. The reason should be fairly obvious: there is no volume change in isotope exchange reactions, and pressure effects depend on volume changes. The volume of an atom is entirely determined by its electronic structure, which does not depend on the mass of the nucleus. On the other hand, there will be some minor fractionation that results from changes in vibrational frequency as crystals are compressed.

9.2.2 Geothermometry

One of the principal uses of stable isotopes is as geothermometers. Like conventional chemical geothermometers, stable isotope geothermometers are based on the temperature dependence of the equilibrium constant (Eqn 9.1). In actuality, the constants A and B in Eqn. 9.1 are slowly varying functions of temperature, such that K tends to zero at absolute 0, corresponding to complete separation, and to 1 at infinite temperature, corresponding to no isotope separation. We can obtain a qualitative understanding of why this is so by recalling that the entropy of a system increases with temperature. At infinite temperature, there is complete disorder, hence isotopes would be mixed randomly between phases (ignoring for the moment the slight problem that at infinite temperature there would be neither phases nor nuclei). At absolute 0, there is perfect order, hence no mixing of isotopes between phases. A and B are,

however, sufficiently invariant over a range of geologically interesting temperatures that as a practical matter they can be described as constants. We have also noted that at temperatures close to room temperature and below, the form of Eqn. 9.1 changes to $K \propto 1/T$.

Because of the dependence of the equilibrium constant on the inverse square of temperature, stable isotope geothermometry is employed primarily at low and moderate temperatures, that is, non-magmatic temperatures. At temperatures greater than 800°C or so (there is no exact cutoff), the fractionations are often too small for accurate temperatures to be calculated from them.

In principle, a temperature may be calculated from the isotopic fractionation between any phases provided the phases achieved equilibrium and the temperature dependence of the fractionation factor is known. Indeed, there are too many isotope geothermometers for all of them to be even mentioned here. We can begin by considering silicate systems. Figure 9.2 shows fractionation factors between various silicates and oxides as

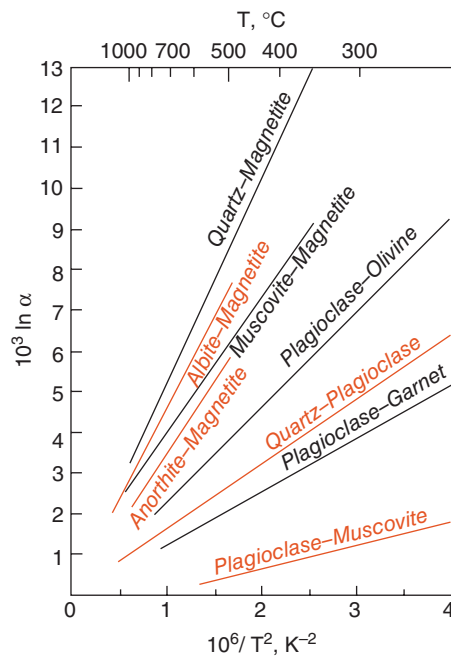


Figure 9.2 Calculated oxygen isotope fractionation for several mineral pairs as a function of temperature. (Source: from O'Neil (1986). Reproduced with permission of the Mineralogical Society of America.)

Table 9.2 Coefficients for oxygen isotope fractionations at elevated temperatures (600–1300°C).

	Cc	Ab	An	Di	Fo	Mt
Qz	0.38	0.94	1.99	2.75	3.67	6.29
Cc		0.56	1.61	2.37	3.29	5.91
Ab			1.05	1.81	2.73	5.35
An				0.76	1.68	4.30
Di					0.92	3.54
Fo						2.62

Coefficients are for mineral pair fractionations expressed as: $1000\alpha = B \times 10^6/T^2$ where B is given in the Table. Qz: quartz, Cc: calcite, Ab: albite, An: anorthite, Di: diopside, Fo: forsterite, Mt: magnetite. For example, the fractionation between albite and diopside is $1000\alpha_{Al-Di} = 1.81 \times 10^6/T^2$ (T in kelvins). (Chiba, et al. (1989). Reproduced with permission of Elsevier.)

a function of temperature. Tables 9.1 and 9.2 list coefficients A and B for temperature dependence of the fractionation factor between quartz and other common silicates and oxides when this temperature dependence is expressed as:

$$\Delta \cong 1000 \ln \alpha_{Qz-\phi} = A + \frac{B}{T^2} \times 10^6 \quad (9.2)$$

with temperature expressed in Kelvin. Recall that fundamental rule of thermodynamics states that if phases A and C and A and B are in equilibrium with each other, then C is also in equilibrium with B. Thus, Table 9.1 may be used to obtain the fractionation between any of the two phases shown.

The other isotope that has been used extensively for geothermometry of igneous and metamorphic rocks is sulfur. Its principal application has been in determining the temperature of deposition of sulfide ores, most of which precipitate from hydrous fluids. Sulfur may be present in fluids as any one of several species. Since isotope fractionation depends on bond strength, the predicted order of ^{34}S enrichment is: $\text{SO}_4^{2-} > \text{SO}_3^{2-} > \text{SO}_2 > \text{SCO} > \text{S}_x \sim \text{H}_2\text{S} \sim \text{HS}^{1-} > \text{S}^{2-}$ (Ohmoto and Rye, 1979). Figure 9.3 shows the temperature dependence of fractionation factors between H_2S and other phases, and Table 9.3 lists coefficients for the equation:

$$\Delta \cong 1000 \ln \alpha_{\phi-\text{H}_2\text{S}} = A + \frac{B}{T^2} \times 10^6 \quad (9.3)$$

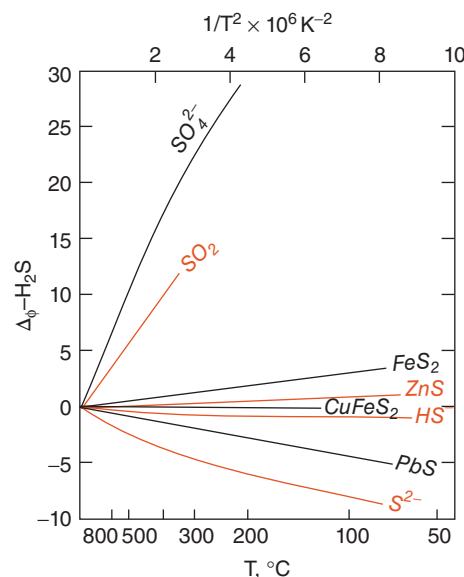


Figure 9.3 Relationship of S isotope fractionation between H_2S and other sulfur-bearing species and temperature. (Source: Ohmoto and Rye (1979). Reproduced with permission of John Wiley & Sons.)

Table 9.3 Coefficients for sulfur isotope fractionation $\Delta\phi-\text{H}_2\text{S} = A + B \times 10^6/T^2$ (T in kelvins).

ϕ	B	A	Range, °C
CaSO_4	6.0 ± 0.5	5.26	200–350
SO_2	-0.5 ± 0.5	4.7	350–1050
FeS	0.10 ± 0.05		200–600
FeS_2	0.4 ± 0.08		200–700
ZnS	0.10 ± 0.05		50–705
CuS	-0.4 ± 0.1		
Cu_2S	-0.75 ± 0.1		
CuFeS_2	-0.05 ± 0.08		200–600
SnS	-0.45 ± 0.1		
MoS_2	0.45 ± 0.1		
Ag_2S	-0.8 ± 0.1		
PbS	-0.63 ± 0.05		50–700

From Ohmoto and Rye (1979). Reproduced with permission of John Wiley & Sons.

CO_2 and other carbon-bearing species are ubiquitous in meteoric and hydrothermal waters. Carbonates often precipitate from such solutions and the fractionation between carbon-species provides yet another opportunity for geothermometry. Figure 9.4 shows carbon isotope fractionation factors between

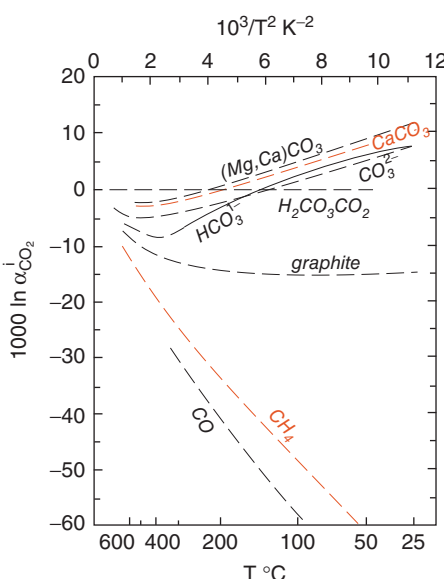


Figure 9.4 Fractionation factors for distribution of carbon isotopes between CO_2 and other carbon-bearing species as a function of temperature. (Source: Ohmoto and Rye (1979). Reproduced with permission of John Wiley & Sons.)

Table 9.4 Isotope fractionation factors of carbon compounds with respect to CO_2 $1000 \ln \alpha = A \times 10^8/T^3 + B \times 10^6/T^2 + C \times 10^3/T + D$.

ϕ	A	B	C	D	Range, °C
$\text{CaMg}(\text{CO}_3)_2$	-8.914	8.737	-18.11	8.44	≤ 600
$\text{Ca}(\text{CO}_3)$	-8.914	8.557	-18.11	8.24	≤ 600
HCO_3^{1-}	0	-2.160	20.16	-35.7	≤ 290
CO_3^{2-}	-8.361	-8.196	-17.66	6.14	≤ 100
H_2CO_3	0	0	0	0	≤ 350
CH_4	4.194	-5.210	-8.93	4.36	≤ 700
CO	0	-2.84	-17.56	9.1	≤ 330
C	-6.637	6.921	-22.89	9.32	≤ 700

From Ohmoto and Rye (1979). Reproduced with permission of John Wiley & Sons.

CO_2 and other carbon bearing species as a function of temperature. The figure includes fractionation factors both calculated from theory and observed vibrational frequencies (calcite, carbonate ion, carbon monoxide, methane) and empirical determined values (dolomite, bicarbonate ion, and carbonic acid). Table 9.4 lists coefficients for a third degree polynomial expression of temperature dependence.

9.2.2.1 The importance of equilibrium

All geothermometers are based on the apparently contradictory assumptions that complete equilibrium is achieved between phases during, or perhaps after, formation of the phases, but that the phases do not re-equilibrate at any subsequent time. The reason these assumptions can be made and geothermometry works at all is the exponential dependence of reaction rates on temperature. Isotope geothermometers have these same implicit assumptions about the achievement of equilibrium as other geothermometers.

There are a number of reasons why isotopic equilibrium might not be achieved. First, isotope geothermometers are applied to relatively low temperature situations where reaction rates are slower and equilibrium more difficult to attain. Second, kinetic fractionations may compete with equilibrium ones. If reactions do not run to completion, the isotopic differences may reflect kinetic effects as much as equilibrium effects. Third, a system may partially re-equilibrate at some lower temperatures during cooling. Fourth, free energies of isotope exchange reactions are low, meaning there is little chemical energy available to drive the reaction to equilibrium. Indeed, isotopic equilibrium probably often depends upon other reactions occurring that mobilize the element involved in the exchange. Finally, solid-state exchange reactions are particularly slow at temperatures well below the melting point. Equilibrium between solid phases will thus generally depend on reaction of these phases with a fluid. Of course, this is true of “conventional” chemical reactions as well, and metamorphism generally occurs in the presence of a fluid.

Figure 9.5 compares sphalerite–galena sulfur isotope temperatures with fluid-inclusion homogenization temperatures. Excluding the Pine Point data, the best fit to the data is fairly close to that expected from the fractionation factors listed in Table 9.3: $\Delta_{sp-gn} = 0.73 \times 10^6/T^2$. Many of the points fall off the expected curve, indicating disequilibrium. Ohmoto and Rye (1979) noted a number of factors that may contribute to the lack of fit, such as impure mineral separates used in the analysis; for example, 10% of the galena in sphalerite and vice versa would result in an estimated temperature of 215°C if the actual

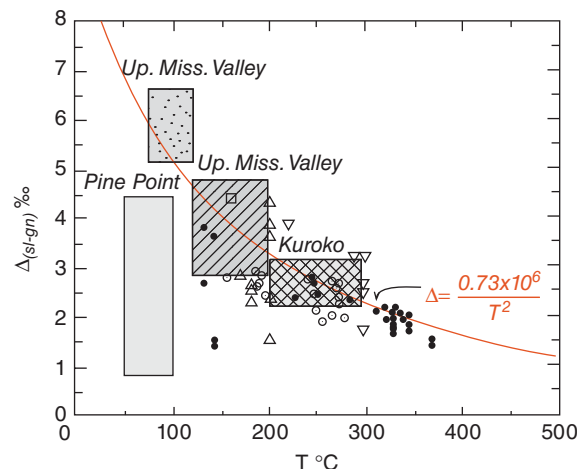


Figure 9.5 Comparison of temperatures determined from sphalerite–galena sulfur isotope fractionation with fluid-inclusion homogenization temperatures. J: Creede, CO, S: Sunnyside, O: Finlandia vein, C: Pasto Bueno, G: Kuroko. (Source: Ohmoto and Rye (1979). Reproduced with permission of John Wiley & Sons.)

equilibration temperature was 145°C. Different minerals may crystallize at different times and different temperatures in a hydrothermal system and, hence, would never be in equilibrium. In general, those minerals in direct contact with each other give the most reliable temperatures. Real disequilibrium may also occur if crystallization is kinetically controlled. The generally good fit to the higher temperature sulfides and poor fit to the low temperature ones suggests the temperature dependence of reaction kinetics may be the most important factor.

Isotope geothermometers do have several advantages over conventional chemical ones. First, as we have noted, there is no volume change associated with isotopic exchange reactions and hence little pressure dependence of the equilibrium constant (however, Rumble has suggested an indirect pressure dependence, wherein the fractionation factor depends on fluid composition which in turn depends on pressure). Second, whereas conventional chemical geothermometers are generally based on solid solution, isotope geothermometers can make use of pure phases such as SiO₂, and so on. Generally, any dependence on the composition of phases in

isotope geothermometers involved is of relatively second order importance. For example, isotopic exchange between calcite and water is independent of the concentration of CO₂ in the water. Compositional effects can be expected only where composition affects bonds formed by the element involved in the exchange. For example, we noted substitution of Al for Si in plagioclase affects O isotope fractionation factors because the nature of the bond with oxygen. The composition of a CO₂ bearing solution, however, should not affect isotopic fractionation between calcite and dissolved carbonate because the oxygen is bonded with C regardless of the presence of other ions (if we define the fractionation as between water and calcite, some effect is possible if the O in the carbonate radical exchanges with other radicals present in the solution).

9.3 STABLE ISOTOPE COMPOSITION OF THE MANTLE

Before we can use stable isotope ratios as indicators of crustal assimilation and tracers of crustal recycling, we need to define the stable isotopic composition of “uncontaminated” mantle. It is, however, important to recognize from the outset that, in a strict sense, there may be no such thing. We found in our consideration of radiogenic isotope ratios that no samples of “primitive” mantle have been recovered: the mantle, or at least that portion sampled by volcanism, has been pervasively processed. A very considerable amount of oceanic crust has been subducted during Earth’s history, perhaps accompanied by sediment. As we shall see, the stable isotopic composition of the oceanic crust is extensively modified by hydrothermal processes and low temperature weathering. Subduction of this material has the potential for modifying the stable isotopic composition of the mantle. Thus while we will attempt to use stable isotope ratios to identify “contamination” of mantle by subduction, we must recognize all of it may have been “contaminated” to some degree.

Other problems arise in defining the stable isotope composition of the mantle. We relied heavily on basalts as mantle samples in defining the radiogenic isotope composition of the mantle. We could do so because radiogenic isotope ratios are not changed in the magma

generation process. This will not be strictly true for stable isotope ratios, which can be changed by chemical processes. The effects of the melting process on most stable isotope ratios of interest are small, but not completely negligible. Degassing does significantly affect stable isotope ratios, particularly those of carbon and hydrogen, which compromises the value of magmas as a mantle sample. Once oxides begin to crystallize, fractional crystallization will affect oxygen isotope ratios, although the resulting changes are, as we shall see, only a few per mil even in extreme cases. Finally, weathering and hydrothermal processes can affect stable isotope ratios of basalts and other igneous rocks. Because hydrogen, carbon, nitrogen, and sulfur are all trace elements in basalts but are quite abundant at the Earth's surface, these elements are particularly susceptible to weathering effects. Even oxygen, which constitutes nearly 50% by weight of silicate rocks, is readily affected by weathering. Thus, we will have to proceed with some caution in using basalts as samples of the mantle for stable isotope ratios.

9.3.1 Oxygen

Assessing the oxygen isotopic composition of the mantle, and particularly the degree to which its oxygen isotope composition might vary, has proved to be more difficult than expected. One approach has been to use basalts as samples of mantle, as is done for radiogenic isotopes. Relatively little isotope fractionation occurs during partial melting, so the oxygen isotopic composition of basalt should be the same as that in the mantle source within a few tenths per mil. However, assimilation of crustal rocks by magmas and oxygen isotope exchange during weathering complicate the situation. An alternative is to use direct mantle samples such as xenoliths occasionally found in basalts, although these are considerably rarer than are basalts.

Figure 9.6 shows the oxygen isotope composition of olivine and clinopyroxene in 76 peridotite xenoliths analyzed by Matthey et al. (1994) using the laser fluorination technique. The total range of values observed is only about twice that expected from analytical error alone, suggesting the mantle is fairly homogeneous in its isotopic composition. The difference between co-existing olivines and

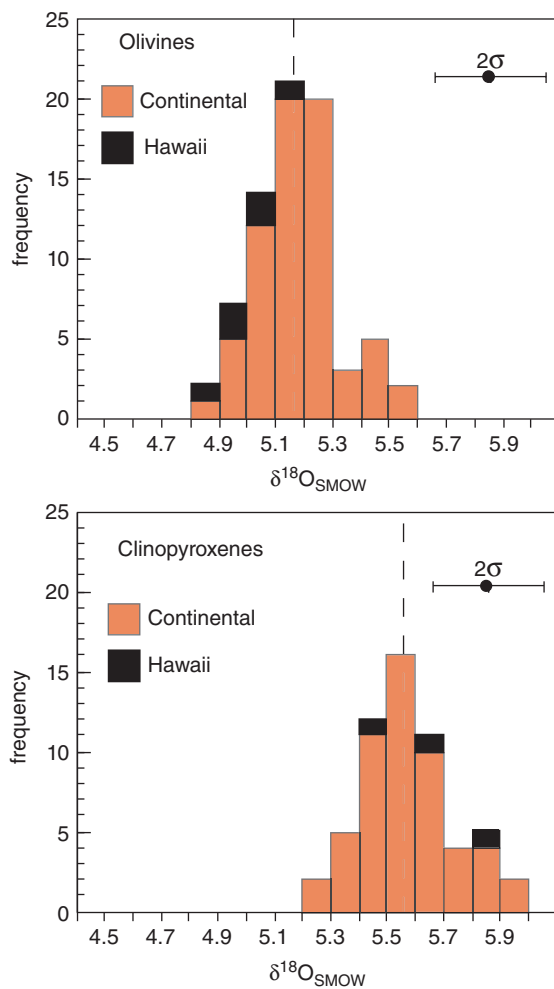


Figure 9.6 Oxygen isotope ratios in olivines and clinopyroxenes from mantle peridotite xenoliths. From Matthey et al. (1994).

clinopyroxenes averages about 0.5 per mil, which is consistent with the expected fractionation between these minerals at mantle temperatures. Matthey et al. (1994) estimated the bulk composition of these samples to be about +5.5 per mil.

Figure 9.7 shows the distribution of $\delta^{18}\text{O}$ in selected basalts from four different groupings. To avoid the weathering problems we discussed earlier, Harmon and Hoefs (1995) included only submarine basaltic glasses and basalts that had less than 0.75% water or had erupted historically in their compilation. There are several points worth noting in these data.

MORB are significantly more homogeneous than are other basalts. MORB have a mean

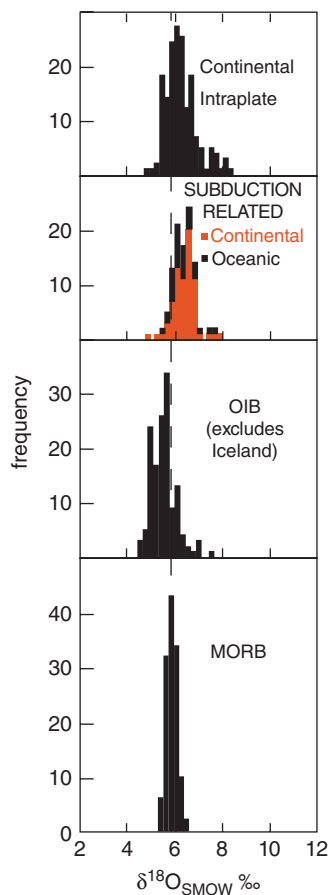


Figure 9.7 of MORB (+5.7). (Source: Harmon and Hoefs (1995). Reproduced with permission of Springer Science + Business Media.)

$\delta^{18}\text{O}_{\text{SMOW}}$ of +5.7‰ and a standard deviation of $\pm 0.2\text{‰}$. Thus, the depleted upper mantle appears to be a comparatively homogeneous and well-mixed reservoir for oxygen, just as it is for other elements. Oceanic island basalts, which presumably sample mantle plumes, are slightly less enriched in ^{18}O (mean $\delta^{18}\text{O}_{\text{SMOW}} = +5.5\text{‰}$) on average and are also more variable ($1\sigma = 0.5\text{‰}$). The histogram shown excludes Iceland, because Icelandic basalts are quite anomalous in their low $\delta^{18}\text{O}$ (mean $\sim 4.5\text{‰}$). This is in part due to assimilation of older basaltic crust that has equilibrated with meteoric water, which is quite ^{18}O -depleted at the latitude of Iceland, but there is also evidence that even primary Icelandic basalts are depleted in ^{18}O relative to MORB. Subduction-related basalts (i.e., island arc basalts and their

continental equivalents) are shifted to more positive $\delta^{18}\text{O}$ values. This may well reflect contributions from the subducting slab, and we shall explore this later in this chapter. Continental subduction-related basalts are more ^{18}O rich than their oceanic equivalents, most likely due to assimilation of continental crust. Finally, continental intraplate volcanics are more enriched in ^{18}O than are OIB, again suggestive of crustal assimilation.

9.3.2 Carbon

The stable isotopes of H, C, N, and S are much more difficult to analyze in igneous rocks. These elements are generally trace elements and are volatile. With rare exceptions, they have a strong tendency to exsolve from the melt and escape as gases as magmas approach the surface of the Earth. Not only are these elements lost during degassing but they also can be isotopically fractionated in the process. Thus, there is far less data on the isotopes of these elements in basalts and the meaning of this data is somewhat open to interpretation.

Most carbon in basalts is in the form of CO_2 , which has limited solubility in basaltic liquids at low pressure. As a result, basalts begin to exsolve CO_2 before they erupt. Thus, virtually every basalt sample has lost some carbon, and subareal basalts have lost virtually all carbon (as well as most other volatiles). Therefore, only basalts erupted beneath several km of water provide useful samples of mantle carbon. As a result, the data set is restricted to MORB, samples recovered from Loihi and the submarine part of Kilauea's East Rift Zone, and a few other seamounts.

The question of the isotopic composition of mantle carbon is further complicated by fractionation and contamination. There is a roughly 4‰ fractionation between CO_2 dissolved in basaltic melts and the gas phase, with ^{13}C enriched in the gas phase. If Rayleigh distillation occurs, that is if bubbles do not remain in equilibrium with the liquid, then the basalt that eventually erupts may have carbon that is substantially lighter than the carbon originally dissolved in the melt. Furthermore, MORB are pervasively contaminated with a very ^{13}C -depleted carbon. This carbon is probably organic in origin, and recent observations of an eruption on the East Pacific Rise suggest a source. Following the

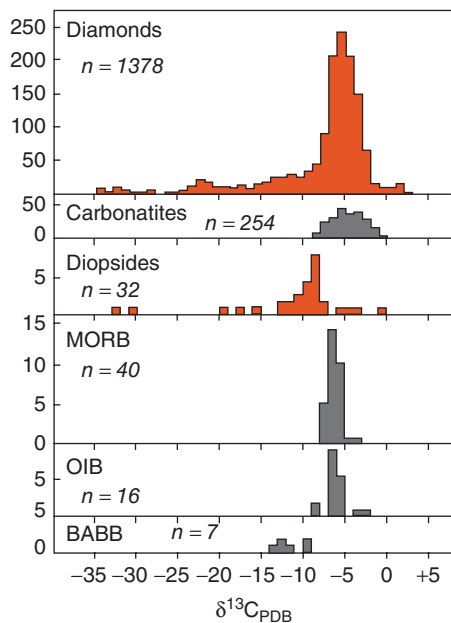


Figure 9.8 Carbon isotope ratios in mantle (dark gray) and mantle-derived materials (lighter gray). (Source: Matthey (1987). Reproduced with permission.)

1991 eruption at 9°30' N, there was an enormous “bloom” of bacteria stimulated by the release of H₂S. Bacterial mats covered everything. The remains of these bacteria may be the source of this organic carbon. Fortunately, it appears possible to avoid most of this contamination by the step-wise heating procedure now used by most laboratories. Most of the contaminant carbon is released at temperatures below 600°C, whereas most of the basaltic carbon is released above 900°C.

Figure 9.8 shows δ¹³C in various mantle and mantle-derived materials. MORB have a mean δ¹³C of -6.5 and a standard deviation of 1.7. Hawaiian basalts appear to have slightly heavier carbon. Xenoliths in oceanic island basalts are also slightly heavier than MORB. Whether this reflects a real difference in isotopic composition or merely the effect of fractionation is unclear. The most CO₂-rich MORB samples have δ¹³C of about -4. Since they are the least degassed, they presumably best represent the isotopic composition of the depleted mantle (Javoy and Pineau, 1991). If this is so, there may be little difference in carbon isotopic composition between MORB and oceanic islands sampled thus far (which

include only Hawaii, Reunion, and Kerguelen). Gases released in subduction zone volcanoes have δ¹³C that ranges from 0 to -10‰, with most values being in the range of -2 to -4‰, comparable to the most gas-rich MORB (Javoy, et al., 1986). Continental xenoliths are more heterogeneous in carbon isotopic composition than other groups, and the meaning of this is unclear. Carbonatites have somewhat lighter carbon than most MORB.

Diamonds show a large range of carbon isotopic compositions (Figure 9.8). Most diamonds have δ¹³C within the range of -2 to -8‰, hence similar to MORB. However, some diamonds have much lighter carbon. Based on the inclusions they contain, diamonds can be divided between peridotitic and eclogitic. Most peridotitic diamonds have δ¹³C close to -5‰, while eclogitic diamonds are much more isotopically variable. Most, though not all, of the diamonds with very negative δ¹³C are eclogitic. Many diamonds are isotopically zoned, indicating they grew in several stages.

Three hypotheses have been put forward to explain the isotopic heterogeneity in diamonds: primordial heterogeneity, fractionation effects, and recycling of organic carbon from the Earth’s surface into the mantle. Primordial heterogeneity seems unlikely for a number of reasons. Among these are the absence of very negative δ¹³C in other materials, such as MORB, and the absence of any evidence for primordial heterogeneity from the isotopic compositions of other elements. Boyd and Pillinger (1994) have argued that since diamonds are kinetically sluggish (witness their stability at the surface of the Earth, where they are thermodynamically out of equilibrium), isotopic equilibrium might not be achieved during their growth. Large fractionations might therefore occur due to kinetic effects. However, these kinetic fractionations have not been demonstrated, and fractionations of this magnitude (20‰ or so) would be surprising at mantle temperatures.

On the other hand, several lines of evidence support the idea that isotopically light carbon in some diamonds had its origin as organic carbon at the Earth’s surface. First, such diamonds are primarily of eclogitic paragenesis and eclogite is the high pressure equivalent of basalt. Subduction of oceanic crust continuously carries large amounts of basalt

into the mantle. Oxygen isotope heterogeneity observed in some eclogite xenoliths suggests these eclogites do indeed represent subducted oceanic crust. Second, the nitrogen isotopic composition of isotopically light diamonds is anomalous relative to nitrogen in other mantle materials yet similar to nitrogen in sedimentary rocks.

9.3.3 Hydrogen

Like carbon, hydrogen can be lost from basalts during degassing. On the one hand, the problem is somewhat less severe than for carbon because the solubility of water in basalt is much greater than that of CO₂. Basalts erupted beneath a kilometer of more of water probably retain most of their dissolved water. However, basalts, particularly submarine basalts, are far more readily contaminated with hydrogen (i.e., with water) than with carbon. Furthermore, the effect on hydrogen isotopic composition depends on the mode of contamination, as Figure 9.9 indicates. Direct addition of water or hydrothermal reactions will raise δD (because there is little fractionation during these processes), while low temperature weathering and hydration will lower δD , because hydrogen, rather than deuterium, is preferentially incorporated into alteration phases. Loss of H₂ and CH₄, which may partition into a CO₂ gas phase when it forms, could also affect the hydrogen isotopic composition

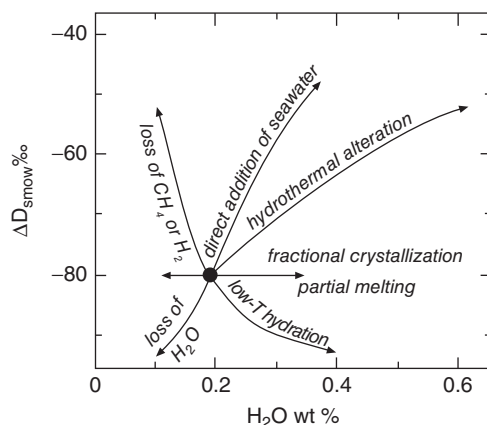


Figure 9.9 Effect of degassing and post-eruptive processes on the water content and δD of basalts. (Source: Kyser and O’Neil (1984). Reproduced with permission of Elsevier.)

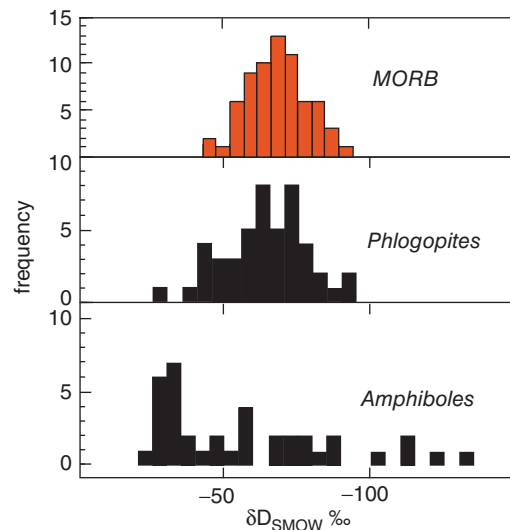


Figure 9.10 δD in MORB and in mantle phlogopites and amphiboles. The MORB and phlogopite data suggest the mantle has δD_{SMOW} of about -60 to -90 . (Source: Adapted from Hoefs, 1987.)

of basalts. However, the available evidence suggests that these species constitute only a small fraction of the hydrogen in basalts, so this effect is likely to be minor.

As Figure 9.10 indicates, MORB have mean δD_{SMOW} of about -67.5‰ and a standard deviation of $\pm 14\text{‰}$. How much of this variability reflects the processes shown in Figure 9.9 and how much reflects true heterogeneity in the mantle is unclear. Kyser (1986) has argued that mantle hydrogen is homogeneous with δD_{SMOW} of -80‰ . The generally heavier isotopic composition of MORB, he argues, reflects H₂O loss and other processes. However, Poreda, et al., (1986) found that δD in basalts from the Reykjanes Ridge south of Iceland correlated significantly with La/Sm and other trace element ratios, suggesting at least some of the isotopic variation of hydrogen in basalts reflects real variations in the mantle. Submarine basalts from Kilauea’s East Rift Zone have higher δD than MORB. Kyser and O’Neil (1984) argued that these higher values result from the addition of water to the magma in the rift zone. Hawaiian submarine basalts analyzed by Garcia et al. (1989) have δD very similar to MORB.

Hydrous minerals in xenoliths also provide a sample of mantle hydrogen. As Figure 9.10

shows, phlogopites have δD that is generally similar to that of MORB, though some lighter values also occur. Amphiboles have much more variable δD and have heavier hydrogen on average. Part of this difference probably reflects equilibrium fractionation. The fractionation between water and phlogopite is close to 0‰ in the temperature range 800–1000°C, whereas the fractionation between water and amphibole is about -15‰. However, equilibrium fractionation alone cannot explain either the variability of amphiboles or the deference between the mean δD of phlogopites and amphiboles. Complex processes involving amphibole formation that might include Rayleigh distillation may be involved in the formation of mantle amphiboles. This would be consistent with the more variable water content of amphiboles compared to phlogopites.

9.3.4 Nitrogen

Figure 9.11 summarizes the existing data on the nitrogen ratios in the crust and mantle. There are far less data than for other stable isotope ratios because of the low concentrations and pervasive contamination problems. The solubility of N₂ in basalts is very limited, though much of the nitrogen may be present as NH₄⁺, which is somewhat more soluble. Hence of volcanic rocks, once again only submarine basalts provide useful samples of mantle N. There are both contamination and analytical problems with determining nitrogen in basalts, which, combined with its low abundance (generally less than a ppm), mean that accurate measurements are difficult to make. Measurements of $\delta^{15}\text{N}_{\text{ATM}}$ in MORB range from about -2 to +12‰. The few available analyses of Hawaiian basalts range up to +20.

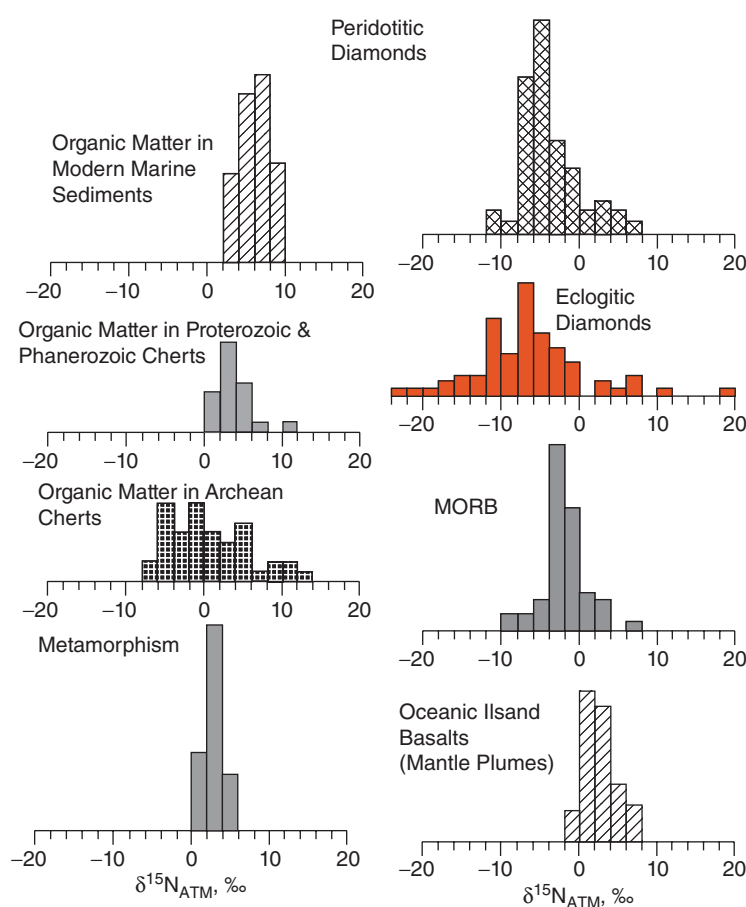


Figure 9.11 Isotopic composition of nitrogen in rocks and minerals of the crust and mantle. (Source: Modified from Marty and Dauphas (2003). Reproduced with permission of Elsevier.)

At present, it is very difficult to decide to what degree this variation reflects contamination (particularly by organic matter), fractionation during degassing, or real mantle heterogeneity. Perhaps all that can be said is that nitrogen in basalts appears to have positive $\delta^{15}\text{N}$ on average.

Diamonds can contain up to 2000 ppm of N and hence provide an excellent sample of mantle N. As can be seen in Figure 9.11, high $\delta^{13}\text{C}$ diamonds (the ones most common and usually of peridotitic paragenesis) have $\delta^{15}\text{N}$ that range from -12 to +5 and average about -3‰, which contrasts with the generally positive values observed in basalts. Low $\delta^{13}\text{C}$ diamonds have generally positive $\delta^{15}\text{N}$. Since organic matter and ammonia in crustal rocks generally have positive $\delta^{15}\text{N}$, this characteristic is consistent with the hypothesis that this group of diamonds is derived from subducted crustal material. However, since basalts appear to have generally positive $\delta^{15}\text{N}$, other interpretations are also possible. Fibrous diamonds, whose growth may be directly related to the kimberlite eruptions that carry them to the surface (Boyd et al., 1994), have more uniform $\delta^{15}\text{N}$, with a mean of about -5‰. Since there can be significant isotopic fractionations involved in the incorporation of nitrogen into diamond, the meaning of the diamond data is also uncertain, and the question of the nitrogen isotopic composition of the mantle remains an open one.

9.3.5 Sulfur

There are also relatively few sulfur isotope measurements on basalts, in part because sulfur is lost during degassing, except for those basalts erupted deeper than 1 km below sealevel. In the mantle, sulfur is probably predominantly or exclusively in the form of sulfide, but in basalts, which tend to be somewhat more oxidized, some of it may be present as SO_2 or sulfate. Equilibrium fractionation should lead to SO_2 being a few per mil lighter than sulfate. If H_2S is lost during degassing the remaining sulfur would become heavier; if SO_2 or SO_4^{2-} is lost, the remaining sulfur would become lighter. Total sulfur in MORB has $\delta^{34}\text{S}_{\text{CDT}}$ in the range of +1.3 to -1‰, with most values in the range 0 to +1‰. Sakai et al. (1984) found that sulfate in MORB, which constitutes 10–20% of total sulfur, was

3.5 to 9‰ heavier than sulfide. Basalts from Kilauea's East Rift Zone have a very restricted range of $\delta^{34}\text{S}$ of +0.5 to +0.8 (Sakai, et al., 1984).

Chaussidon et al. (1989) analyzed sulfides present as inclusions in minerals, both in basalts and in xenoliths, and found a wide range of $\delta^{34}\text{S}$ (-5 to +8‰). Low Ni sulfides in oceanic island basalts, kimberlites, and pyroxenites had more variable $\delta^{34}\text{S}$ than sulfides in peridotites and peridotite minerals. They argued there is a fractionation of +3‰ between sulfide liquid and sulfide dissolved in silicate melt. Carbonatites have $\delta^{34}\text{S}$ between +1 and -3‰ (Hoefs, 1987; Kyser, 1986). Overall, it appears the mantle has a mean $\delta^{34}\text{S}$ in the range of 0 to +1‰, which is very similar to meteorites that average about +0.1‰.

Chaussidon, et al. (1987) found that sulfide inclusions in diamonds of peridotitic paragenesis ($\delta^{13}\text{C} \sim -4\text{\textperthousand}$) had $\delta^{34}\text{S}$ of about +1‰ while eclogitic diamonds had higher, and much more variable $\delta^{34}\text{S}$ (+2 to +10‰). Eldridge et al. (1991) found that $\delta^{34}\text{S}$ in diamond inclusions was related to the Ni content of the sulfide. High Ni sulfide inclusions, which they argued were of peridotitic paragenesis, had $\delta^{34}\text{S}$ between +4‰ and -4‰. Low Ni sulfides, which are presumably of eclogitic paragenesis, had much more variable $\delta^{34}\text{S}$ (+14‰ to -10). These results are consistent with the idea that eclogitic diamonds are derived from subducted crustal material.

9.4 OXYGEN ISOTOPES IN MAGMATIC PROCESSES

As we found earlier, the equilibrium constant of isotope exchange reactions, K, is proportional to the inverse square temperature and consequently isotopic fractionation at high temperature is small. In magmatic systems, another factor limiting the fractionation of stable isotopes is the limited variety of bonds that O is likely to form. Most of the oxygen in silicates and in silicate liquids is not present as free ions, but is bound to silicon atoms to form silica tetrahedra, which will be linked to varying degrees depending on the composition of the mineral or the composition of the melt. The silica tetrahedra and the Si—O bonds in a silicate melt are essentially identical to those in silicate minerals. Thus, we would

expect the fractionation of oxygen isotopes between silicate liquids (magmas) and silicate minerals crystallizing from those liquids to be rather limited. We would expect somewhat greater fractionation when non-silicates such as magnetite (Fe_3O_4) crystallize. In general, crystallization of quartz will lead to a depletion of ^{18}O in the melt, crystallization of silicates such as olivine, pyroxene, hornblende, and biotite will lead to slight enrichment of the melt in ^{18}O , and crystallization of oxides such as magnetite and ilmenite will lead to a more pronounced enrichment of the melt in ^{18}O (however, oxides such as magnetite are generally only present at the level of a few percent in igneous rocks, which limits their effect). Crystallization of feldspars can lead to either enrichment or depletion of ^{18}O , depending on the temperature and the composition of the feldspar and the melt. Because quartz generally only crystallizes very late, the general effect of fractional crystallization on magma is generally to increase $\delta^{18}\text{O}$ slightly, generally not more than a few per mil. On the other hand, water-rock interaction at low to moderate temperatures at the surface of the Earth, produces much larger O isotopic changes, generally enriching the rock in ^{18}O . Consequently, crustal rocks show significant variability in $\delta^{18}\text{O}$.

As we have seen, the range of $\delta^{18}\text{O}_{\text{SMOW}}$ in the fresh, young basalts and other mantle materials is about +4.5 to +7. Because this range is narrow, and the range of those crustal materials is much greater, O isotope ratios are a sensitive indicator of crustal assimilation. Isotope ratios outside this range suggest, but do not necessarily prove, the magmas have assimilated crust (or that post-eruptional isotopic exchange has occurred).

9.4.1 Oxygen isotope changes during crystallization

The variation in O isotope composition produced by crystallization of magma will depend on the manner in which crystallization proceeds. The simplest, and most unlikely, case is *equilibrium* crystallization. In this situation, the crystallizing minerals remain in isotopic equilibrium with the melt until crystallization is complete. At any stage during crystallization, the isotopic composition of a mineral and the melt will be related by the fractionation

factor, α . Upon complete crystallization, the rock will have precisely the same isotopic composition as the melt initially had. At any time during the crystallization, the isotope ratio in the remaining melt will be related to the original isotope ratio as:

$$\frac{R_l}{R_0} = \frac{l}{f + \alpha(1-f)}; \quad \alpha = \frac{R_s}{R_l} \quad (9.4)$$

where R_l is the ratio in the liquid, R_s is the isotope ratio of the solid, R_0 is the isotope ratio of the original magma, f is the fraction of melt remaining. This equation is readily derived from mass balance, the definition of α , and the assumption that the O concentration in the magma is equal to that in the crystals; an assumption valid to about 10%. Since we generally do not work with absolute ratios of stable isotopes, it is more convenient to express 9.4, in terms of δ :

$$\Delta = \delta_{\text{melt}} - \delta_0 \cong \left[\frac{1}{f + \alpha(1-f)} - 1 \right] \times 1000 \quad (9.5)$$

where δ_{melt} is the value of the magma after a fraction $f-1$ has crystallized and δ_0 is the value of the original magma. For silicates, α is not likely to be much less than 0.998 (i.e., $\Delta = \delta^{18}\text{O}_{\text{melt}} - \delta^{18}\text{O}_{\text{xtals}} \leq 2$). For $\alpha = 0.999$, even after 99% crystallization, the isotope ratio in the remaining melt will change by only 1 per mil.

Fractional crystallization is a process analogous to Rayleigh distillation. Indeed, it is governed by the same equation (8.80), which we can rewrite as:

$$\Delta = 1000(f^{\alpha-1} - 1) \quad (9.6)$$

The key to the operation of either of these processes is that the product of the reaction (vapor in the case of distillation, crystals in the case of crystallization) is only instantaneously in equilibrium with the original phase. Once it is produced, it is removed from further opportunity to equilibrate with the original phase. This process is more efficient at producing isotopic variations in igneous rocks, but its effect remains limited because α is generally not greatly different from 1. Figure 9.12 shows calculated changes in the isotopic composition of melt undergoing fractional crystallization for various values of Δ ($\approx 1000(\alpha - 1)$). In

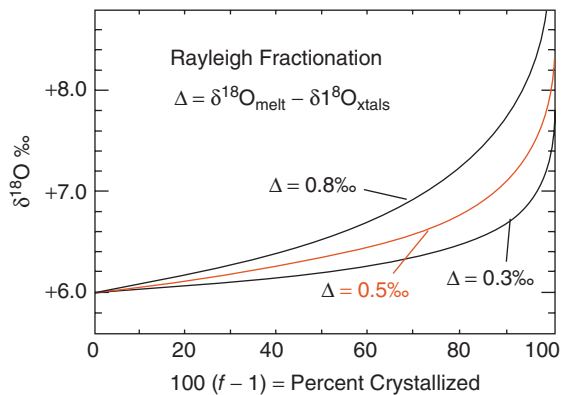


Figure 9.12 Plot of $\delta^{18}\text{O}$ versus fraction of magma solidified during Rayleigh fractionation, assuming the original $\delta^{18}\text{O}$ of the magma was +6. (Source: Taylor and Sheppard (1986). Reproduced with permission of the Mineralogical Society of America.)

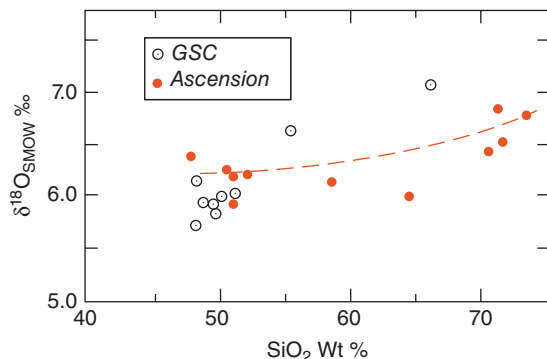


Figure 9.13 $\delta^{18}\text{O}$ as a function of SiO_2 in a tholeiitic suite from the Galapagos Spreading Center (GSC) (Muehlenbachs and Byerly, 1982) and an alkaline suite from Ascension Island (Sheppard and Harris, 1985). Dashed line shows model calculation for the Ascension suite. (Source: Adapted from Taylor and Sheppard, 1986.)

reality, Δ will change during crystallization because of (1) changes in temperature (2) changes in the minerals crystallizing, and (3) changes in the liquid composition. The changes will generally mean that the effective Δ will increase as crystallization proceeds. We would expect the greatest isotopic fractionation in melts crystallizing non-silicates such as magnetite and melts crystallizing at low temperature, such as rhyolites, and the least fractionation for melts crystallizing at highest temperature, such as basalts.

Figure 9.13 shows observed $\delta^{18}\text{O}$ as a function of temperature in two suites: one from a propagating rift on the Galapagos Spreading Center (GSC), the other from the island of Ascension. There is a net change in $\delta^{18}\text{O}$ between the most and least differentiated rocks in the GSC of about 1.3‰; the change in the Ascension suite is only about 0.5‰. These, and other suites, indicate the effective Δ is generally small, on the order of 0.1 to 0.3‰.

We can generalize the temperature dependence of stable isotopes by saying that at low temperature (ambient temperatures at the surface of the Earth up to the temperature of hydrothermal systems, 300–400°C), stable isotope ratios are changed by chemical processes. The amount of change can be used as an indication the nature of the process involved, and, under equilibrium conditions, of the temperature at which the process

occurred. At high temperatures (temperatures of the interior of the Earth or magmatic temperatures), chemical processes only minimally affect stable isotope ratios; they can therefore be used as tracers much as radiogenic isotope ratios are.

These generalizations lead to a final axiom: “igneous rocks whose oxygen isotopic compositions show significant variations from the primordial value (~6) must either have been affected by low temperature processes, or must contain a component that was at one time at the surface of the Earth” (Taylor and Sheppard, 1986).

Rocks that have equilibrated with water at the surface of the Earth, for example, sediments, tend to have $\delta^{18}\text{O}$ values significantly higher than +6. Water on the surface of the Earth typically has $\delta^{18}\text{O}$ significantly lower than +6 (0 for seawater, generally lower for meteoric water as we found in the last chapter). Interestingly, the δD values of sedimentary rocks and mantle-derived igneous rocks are rather similar (−50 to −85). This may be coincidental since the δD of sediments are controlled by fractionation between minerals and water, whereas δD of igneous rocks reflects the isotopic composition of mantle hydrogen (mantle water). On the other hand, it is possible that it is not coincidental. Plate tectonics results in the return of water-bearing rocks from the surface of the Earth to the

mantle (i.e., via subduction). It may well be that after 4.5 billion years, the subduction process essentially controls the isotopic composition of H in the upper mantle.

9.4.2 Combined fractional crystallization and assimilation

Because oxygen isotope ratios of mantle-derived magmas are uniform (with a few per mil) and generally different from rocks that have equilibrated with water at the surface of the Earth, oxygen isotopes are a useful tool in identifying and studying the assimilation of country rock by intruding magma. We might think of this process as simple mixing between two components: magma and country rock. In reality, it is always at least a three-component problem, involving country rock, magma, and minerals crystallizing from the magma. Magmas are essentially never superheated; hence the heat required to melt and assimilate surrounding rock can only come from the latent heat of crystallization of the magma. Approximately 1000 J/g would be required to heat rock from 150 to 1150°C and another 300 J/g would be required to melt it. If the latent heat of crystallization is 400 J/g, crystallization of 3.25 g of magma would be required to assimilate 1 g of cold country rock. Since some heat will be lost by simple conduction to the surface, we can conclude that the amount of crystallization will inevitably be greater than the amount of assimilation (the limiting case where mass crystallized equals mass assimilated could occur only at very deep layers of the crust where the rock is at its melting point to begin with). The change in isotopic composition of a melt undergoing the combined process of assimilation and fractional crystallization (AFC) is given by:

$$\delta_m - \delta_0 = \left([\delta_a - \delta_0] + \frac{\Delta}{R} \right) \{1 - f^{-R/(R-1)}\} \quad (9.7)$$

where R is the mass ratio of material assimilated to material crystallized, Δ is the difference in isotope ratio between the crystals and the magma ($\delta_{\text{magma}} - \delta_{\text{crystals}}$), f is the fraction of liquid remaining, δ_m is the $\delta^{18}\text{O}$ of the magma, δ_0 is the initial $\delta^{18}\text{O}$ of the magma, and δ_a is the $\delta^{18}\text{O}$ of the material being assimilated. (This equation is from DePaolo (1981) but differs slightly because we changed the

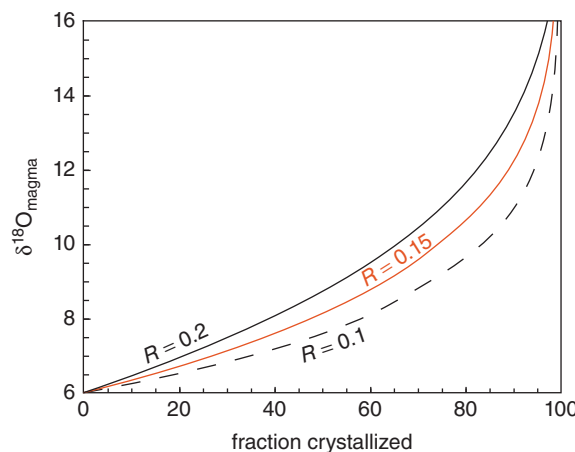


Figure 9.14 Variation in $\delta^{18}\text{O}$ of a magma undergoing AFC vs. fraction crystallized computed using equation 9.07. Initial $\delta^{18}\text{O}$ of the magma is +6, $\delta^{18}\text{O}$ of the assimilant is +18, $\Delta = +1$. R is the ratio of mass assimilated to mass crystallized.

definition of Δ .) The assumption is made that the concentration of oxygen is the same in the crystals, magma, and assimilant, which is a reasonable assumption. This equation breaks down at $R = 1$, but as discussed earlier, this is unlikely: R will always be less than 1. Figure 9.14 shows the variation of $\delta^{18}\text{O}$ of a magma with an initial $\delta^{18}\text{O} = 5.7$ as crystallization and assimilation proceed.

9.4.3 Combining radiogenic and oxygen isotopes

A more powerful tool for the study of assimilation processes can result if O isotopes are combined with a radiogenic isotope ratio such as $^{87}\text{Sr}/^{86}\text{Sr}$. There are several reasons for this. First, radiogenic isotopes and stable isotopes each have their own advantages. In the case of basaltic magmas, radiogenic elements, particularly Nd and Pb, often have lower concentrations in the magma than in the assimilant. This means a small amount of assimilant will have a large effect on the radiogenic isotope ratios. On the other hand, oxygen will be present in the magma and assimilant at nearly the same concentration, making calculation of the mass assimilated fairly straightforward. Also, it is easier to uniquely characterize the assimilant using both radiogenic and stable isotope ratios, as suggested in Figure 9.15.

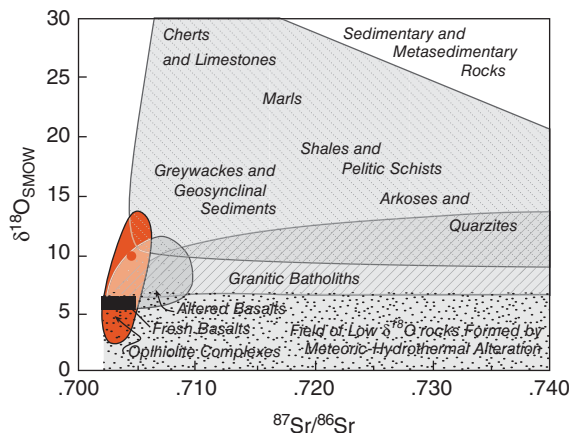


Figure 9.15 $\delta^{18}\text{O}$ versus $^{87}\text{Sr}/^{86}\text{Sr}$ showing range of isotopic composition in various terrestrial rocks. (Source: Taylor and Sheppard (1986). Reproduced with permission of the Mineralogical Society of America.)

The equation governing a radiogenic isotope ratio in a magma during AFC is different from 9.7 because we cannot assume the concentration of the element is the same in all the components. On the other hand, there is no fractionation between crystals and melt. The general equation describing the variation of the *concentration* of an element in a magma during AFC is:

$$\frac{C_m}{C_m^0} = f^{-z} + \left(\frac{R}{R-1} \right) \frac{C_a}{C_m^0} (1 - f^{-z}) \quad (9.8)$$

where C_m and the concentration of the element in the magma, C^0 is the original magma concentration, f is as defined for Eqn. 9.7 earlier, and z is as:

$$z = \frac{R + D - 1}{R - 1} \quad (9.9)$$

where D is the solid/liquid partition coefficient. The isotopic composition of the magma is given by (DePaolo, 1981):

$$\epsilon_m = \frac{\left(\frac{R}{R-1} \right) \frac{C_a}{z} (1 - f^{-z}) \epsilon_a + C_m^0 f^{-z} \epsilon^0}{\left(\frac{R}{R-1} \right) \frac{C_a}{z} (1 - f^{-z}) + C_m^0 f^{-z}} \quad (9.10)$$

where ϵ is the isotope ratio with subscripts m , a and 0 denoting the magma, the assimilant, and the original magma respectively and the other parameters are defined as in Eqns 9.8

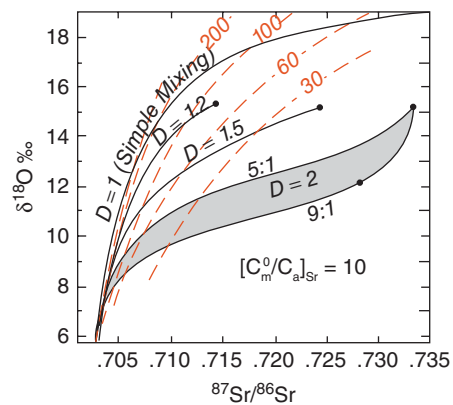


Figure 9.16 Variation of $\delta^{18}\text{O}$ with $^{87}\text{Sr}/^{86}\text{Sr}$ during AFC for a magma with an initial $\delta^{18}\text{O} = 5.7$ and $^{87}\text{Sr}/^{86}\text{Sr} = 0.703$, and an assimilant with $^{87}\text{Sr}/^{86}\text{Sr} = 0.735$ and $\delta^{18}\text{O} = +19$. All curves are for $R = 0.2(5 : 1)$, except for one with $D = 2$ for which $R = 0.11$ (labeled 9:1). Dashed red lines are calculated Sr concentrations (ppm) assuming an initial concentration of Sr in the magma of 500 ppm. Where $D = 1$, the problem simplifies to one of simple mixing. (Source: Taylor (1980). Reproduced with permission of Elsevier.)

and 9.9. Figure 9.16 shows calculated AFC curves on a plot of $\delta^{18}\text{O}$ versus $^{87}\text{Sr}/^{86}\text{Sr}$. Note that, except in the case where $D = 1$ where the problem simplifies to one of simple mixing, the mixing lines end at $f = 0.01$ (99% crystallized).

Figure 9.17 shows an actual case, the Adamello Massif in Italy. Actual analyses are plotted as dots with the concentrations of Sr in the sample shown adjacent to the dot. AFC lines are computed assuming the original magma had $\delta^{18}\text{O} = 5.6$, $^{87}\text{Sr}/^{86}\text{Sr} = 0.704$, and 750 ppm Sr, and the country rocks have $^{87}\text{Sr}/^{86}\text{Sr} = 0.736$, $\delta^{18}\text{O} = +13.6$, and 150 ppm Sr. Dashed lines are contours of calculated Sr concentrations in the magma. There is reasonably good agreement between the calculated model and the actual data, if we assume the bulk partition coefficient varied a bit (which would certainly be the case).

9.4.4 Sediment subduction versus assimilation

Magmas erupted and emplaced in subduction zones have unique geochemistry that is apparent in both their trace element and radiogenic

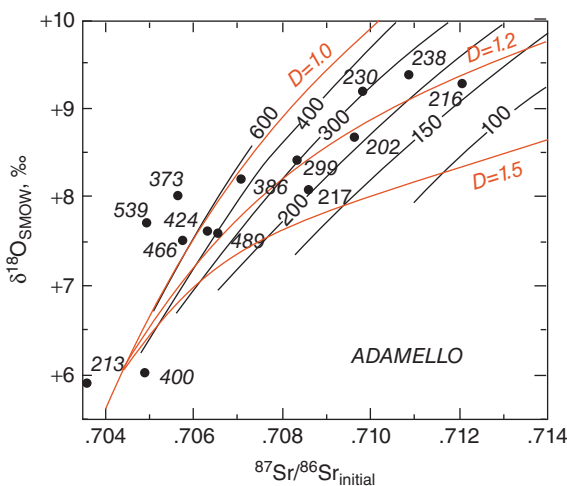


Figure 9.17 Variation of $\delta^{18}\text{O}$ with ${}^{87}\text{Sr}/{}^{86}\text{Sr}$ in the Adamello Massif in Italy compared with model AFC process using Eqns 9.7–9.10. (Source: Taylor and Sheppard (1986). Reproduced with permission of the Mineralogical Society of America.)

isotopic compositions. Most often, this unique geochemistry is taken as evidence that the sources of these magmas contain subducted sediments. However, in many instances, this interpretation is non-unique. The geochemical signature of subducted sediment is, in many respects, simply the signature of continental crust. In general, it is just as plausible that magmas have acquired this signature through assimilation of continental crust as by partial melting of a mantle containing subducted sediment. Magaritz et al. (1978) pointed out that by combining radiogenic isotope and oxygen isotope analyses, it is possible to distinguish between these two possibilities.

Magaritz et al. reasoned as follows. First, many continental materials have oxygen isotope ratios that are quite different from mantle values (e.g., Figure 9.18). Then they noted that all rocks have similar oxygen concentrations. Because of this, addition of 10% sediment with $\delta^{18}\text{O}$ of +20 to the mantle (+6) followed by melting of that mantle produces a magma with the same $\delta^{18}\text{O}$ (+8.4), as adding 10% sediment directly to the magma (i.e., in this case the magma also ends up with $\delta^{18}\text{O} = +8.4$). However, addition of 10% sediment to the mantle, followed by melting of that mantle produces a magma with a very different Sr isotope ratio than does adding 10% sediment

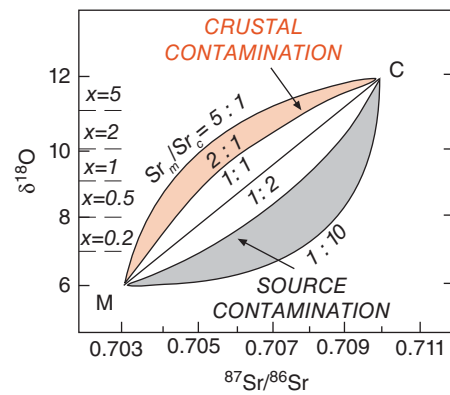


Figure 9.18 Mixing curves on a plot of $\delta^{18}\text{O}$ versus ${}^{87}\text{Sr}/{}^{86}\text{Sr}$. The labels on the lines refer to different ratios of Sr concentration in the two end-members. (Source: James (1981). Reproduced with permission of Annual Reviews, Inc.)

directly to the magma. The reason for this difference is that the Sr concentration of the magma is much higher (an order of magnitude or more higher) than that of the mantle. Thus addition of sediment to magma affects the Sr isotope ratio less than addition of sediment to the mantle. Indeed, most subduction-related magmas are richer in Sr (~400 ppm) than most continental materials and sediments; but sediments invariably have more Sr than does the mantle (10–40 ppm).

This point is illustrated in a more quantitative fashion in Figure 9.18. We discussed mixing trajectories earlier and noted that when two materials are mixed in varying proportions, a curve results on a plot of one ratio against another. The degree and sense of curvature depended on the ratio of the ratio of the two denominators in the two end-members. Since the concentration of oxygen is approximately the same in most rocks, the ratio of ${}^{16}\text{O}$ in the two end-members can be taken as 1. So, for example, in a plot of ${}^{87}\text{Sr}/{}^{86}\text{Sr}$ versus oxygen isotope ratio, the degree of curvature depends only on the ratio of Sr in the two end-members. In Figure 9.18, when the ratio of Sr in end-member M (magma or mantle) to Sr in end-member C (crust or sediment) is greater than 1, a concave downward mixing curve results. If that ratio is less than 1 (i.e., concentration of Sr in C is greater than in M), a concave upward curve results. Assimilation of crust by magma essentially corresponds to

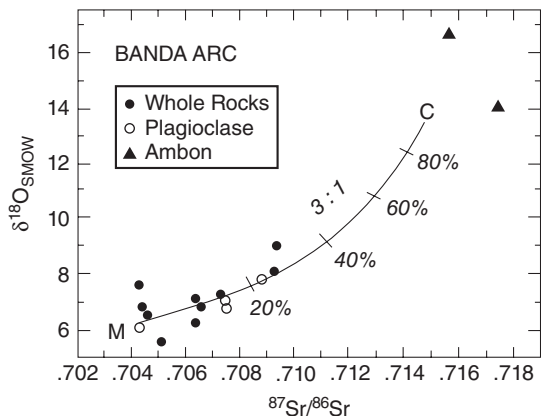


Figure 9.19 Oxygen and Sr isotopic composition of Banda arc magmas. Mixing curve constructed assuming a concentration ratio of $\text{Sr}_C/\text{Sr}_M = 3$. End member M has ${}^{87}\text{Sr}/{}^{86}\text{Sr} = 0.7035$ and $\delta^{18}\text{O} = +6$; end member C has ${}^{87}\text{Sr}/{}^{86}\text{Sr} = .715$ and $\delta^{18}\text{O} = +14$. Ticks indicate the percentage of end member C in the mixture. (Source: Adapted from Magaritz et al., 1978.)

the concave downward case ($\text{Sr}_M > \text{Sr}_C$) and mixing of subducted sediment and mantle corresponds to the concave upward case ($\text{Sr}_M < \text{Sr}_C$). Thus, these two processes are readily distinguished on such a plot.

Figure 9.19 shows the data of Magaritz et al. (1978) for the Banda arc. These data fall roughly along a mixing curve for $\text{Sr}_C/\text{Sr}_M = 3$. The samples are mainly basaltic andesites and andesites and have reasonably high Sr concentrations (150–500 ppm). Magaritz et al. (1978) argued that the apparent 3:1 concentration ratio between the C and M members was more consistent with mixing of pelitic sediments (which have 100–150 ppm Sr) with mantle than assimilation of crust by magma. The two triangles represent the isotopic composition of corderite-bearing lavas from the island of Ambon. The petrology and composition of these lavas suggest they are produced directly by melting of pelitic sediments in the deep crust. Thus their isotopic compositions were taken as potentially representative of the assimilant.

Considerable care must be exercised in the interpretation of oxygen isotope ratios in igneous rocks, particularly when the rocks come from a tropical region such as the Banda Arc. In such regions, rocks quickly begin to

react with water and primary phases in the groundmass are replaced with various secondary minerals. The isotopic composition of such minerals will be much higher (as high as $\delta^{18}\text{O} \approx +20$ to $+30$) than the original ones. Thus, the O isotopic composition of weathered igneous rocks will be higher than that of the original magma. Thus, in their study, Magaritz et al. (1978) also analyzed plagioclase phenocrysts. Phenocrysts generally weather less rapidly than does the groundmass and alteration effects can be easily identified visually, which is not always the case with the groundmass. So phenocrysts often provide a better measure of the oxygen isotopic composition of the original magma than does the whole rock. This is true even though there might have been a small equilibrium fractionation between the magma and the phenocryst.

The amount of subducted sediment implied by the mixing curve in Figure 9.19 is much greater than has been inferred to be involved in other arcs (about 1–3%). The Banda arc is directly adjacent to the Australian continent, so extensive involvement of sediment and crustal material is perhaps to be expected. On the other hand, the amount of sediment, or crustal material in the mixture is sensitive to assumptions about the oxygen isotope composition of that material. If the $\delta^{18}\text{O}$ of the crustal material is assumed to be $+22$ rather than $+14$, the calculated percentage of sediment involved would decrease by 50%.

The mean $\delta^{18}\text{O}$ of Marianas lavas is, in contrast to Banda, about $+6.2$ (Ito and Stern, 1986; Woodhead et al., 1987). This implies the amount of sediment involved in the source is less than 1%, which is consistent with the amount inferred from radiogenic isotope studies.

In a contrasting situation, James and Murcia (1984) used radiogenic and stable isotope systematics to argue for extensive assimilation of crust by magmas in the northern Andes. As shown in Figure 9.20, andesites from Nevado del Ruiz and Galeras volcanoes in Columbia define a steep array on plots of $\delta^{18}\text{O}$ vs. ${}^{87}\text{Sr}/{}^{86}\text{Sr}$ and ${}^{143}\text{Nd}/{}^{144}\text{Nd}$. Comparing this with Figure 9.18, we see that such steep arrays imply mixing between magma and crust rather than mantle and sediment. As we observed in the previous section, assimilation will inevitably be accompanied by fractionation crystallization. James and Murcia (1984)

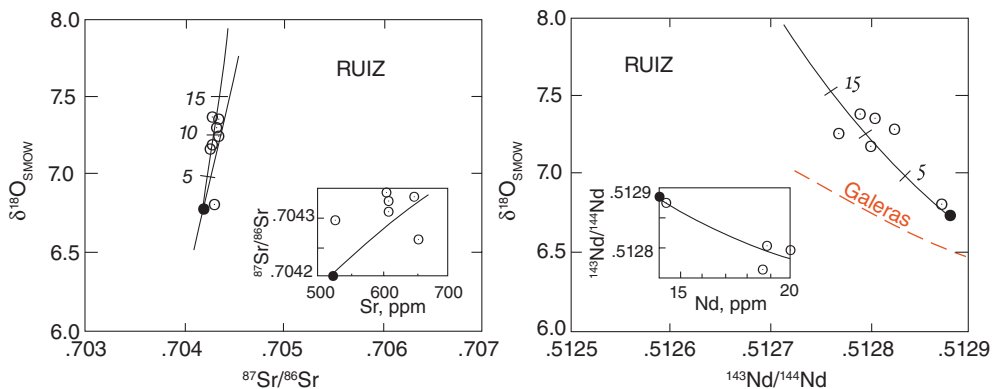


Figure 9.20 Sr, Nd, and O isotopes in lavas from Nevado del Ruiz Volcano in Columbia and an AFC model calculation. Dashed line shows AFC trajectory for another Colombian volcano, Galeras. (Source: James and Murcia, 1984.)

Table 9.5 Parameters for Ruiz assimilation model.

Original	Magma	Assimilant
$\delta^{18}\text{O}$	6.5‰	11‰
Δ	0.5‰	
${}^{87}\text{Sr}/{}^{86}\text{Sr}$	0.7041	0.710
β_{Sr}	0.2	
Sr, ppm	650	100
${}^{143}\text{Nd}/{}^{144}\text{Nd}$	0.51288	0.5122
Nd, ppm	20	20
β_{Nd}	0.2	
R	0.33	301

modeled this assimilation using the equations similar to 9.7–9.10 and the assumed concentrations listed in Table 9.5. The model fits the data reasonably well and implies assimilation of up to about 12% country rock. An R of 0.33 provided the best fit, though James and Murcia (1984) noted this parameter was not well constrained. A high value of R suggests the assimilation is occurring at moderate depth (<10 km), because it suggests only moderate input of heat in melting the country rock.

On a broader basis, Harmon et al. (1984) used O isotope ratios to show that extent of crustal assimilation in Andean magmas varies regionally and correlates with crustal thickness. The Andes are divided into three distinct volcanic provinces. In the north, the subduction zone is steeply dipping, and the volcanoes are located approximately 140 km over the Benioff zone. The crust in this *Northern Volcanic Zone* (NVZ), located in Columbia

and Ecuador, is approximately 40 km thick and is mainly Cretaceous and Cenozoic in age. Volcanics are primarily basaltic andesites and andesites. In the *Central Volcanic Zone* (CVZ), which extends from southern Peru to northern Chile and Argentina, the crust is 50–70 km thick and Precambrian to Paleozoic in age. The Benioff Zone lies approximately 140 km beneath these volcanoes. The volcanics range from andesite through rhyolite, and include extensive ignimbrites. The *Southern Volcanic Zone* (SVZ) is located in south-central Chile and overlies a shallower, more gently dipping Benioff Zone. These volcanoes lie roughly 90 km above the Benioff Zone and atop 30–35 km of Mesozoic and Cenozoic crust. Here, the volcanics are mainly basaltic, with minor andesite and dacite.

Figure 9.21 shows that $\delta^{18}\text{O}$ is most mantle-like in the SVZ, with a mean $\delta^{18}\text{O}$ of about +6.0, just slightly higher than the mean for MORB. ${}^{87}\text{Sr}/{}^{86}\text{Sr}$ ratios average about 0.704, just slightly higher than the mean for intra-oceanic arcs. The NVZ has higher $\delta^{18}\text{O}$, with a mean about +6.9, and somewhat higher ${}^{87}\text{Sr}/{}^{86}\text{Sr}$. $\delta^{18}\text{O}$ in the CVZ is highest, ranging from +7 to +14. This corresponds to the region of the thickest and oldest crust in the Andes. Volcanoes in the southern part of the CVZ, from 21–26°S, have apparently experienced the greatest assimilation. Minimum $\delta^{18}\text{O}$ values of around +7 in this region suggest that all magmas have assimilated at least some crust. Figure 9.22 shows an example of data from one volcano in the

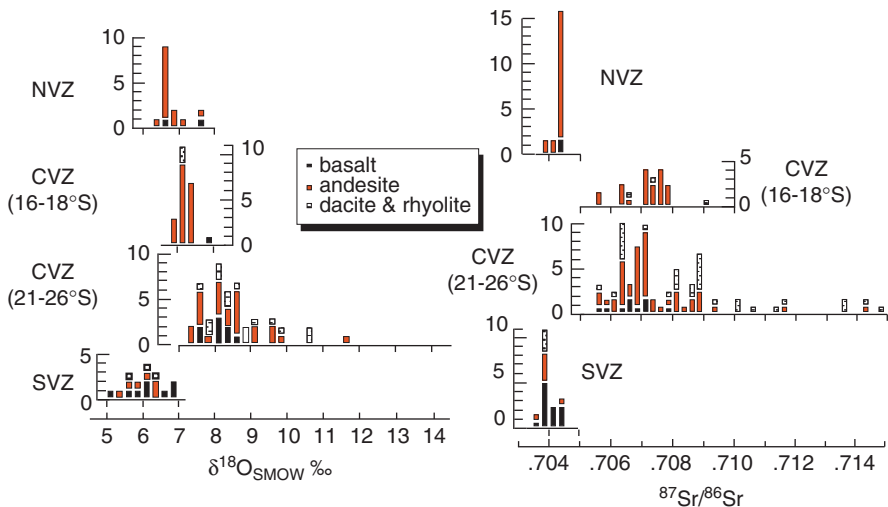


Figure 9.21 Oxygen and Sr isotope ratios in Andean volcanics. Dashed line shows the mean $\delta^{18}\text{O}$ of MORB. (Source: Harmon et al., 1984.)

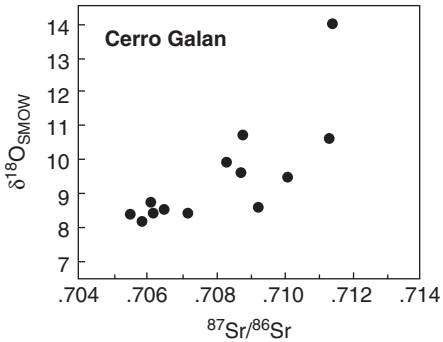


Figure 9.22 ${}^{87}\text{Sr}/{}^{86}\text{Sr}$ and $\delta^{18}\text{O}$ in Cerro Galan, and ignimbrite center in Northwest Argentina. (Source: Adapted from Harmon et al., 1984.)

CVZ, Cerro Galan in northwest Argentina. Sr and O isotope data define broad, slightly convex-upward array that is reminiscent of the AFC curves in Figure 9.16 for a value of $D \approx 2$.

9.4.5 Stable isotopes as indicators of crust-to-mantle recycling

The potential importance of the crust-to-mantle flux resulting from subduction was first pointed out by Armstrong in 1968. As we shall see, the oceanic crust undergoes substantial modification of its oxygen isotopic composition as a result of

the hydrothermal activity and metamorphism that occurs virtually simultaneously with formation of the oceanic crust and as a result of low-temperature reactions with seawater. The hydrothermal activity tends to lower the $\delta^{18}\text{O}$ of the middle and lower oceanic crust, while the low-temperature weathering raises the $\delta^{18}\text{O}$ of the upper oceanic crust. As we'll discuss in a subsequent section, there is little or no net change in oxygen isotope composition of the oceanic crust as a result of these processes. Thus subduction of the crystalline portion of the oceanic crust should have no net effect on the oxygen isotopic composition of the mantle as a whole, but it might increase isotopic heterogeneity.

The subduction process may influence the composition of the subcontinental lithosphere. As may be seen in Figure 9.23, eclogite¹ xenoliths from the Roberts Victor Mine (South Africa) kimberlite have remarkably variable oxygen isotope compositions (MacGregor and Manton (1986)). The range in $\delta^{18}\text{O}$ is similar to that of “mature” oceanic crust (i.e., subsequent to hydrothermal low temperature metamorphism), and contrasts with the homogeneity of olivines in peridotite xenoliths (Figure 9.6), many of which also come from kimberlites. Since eclogites are the high pressure equivalent of basalts, this suggests the eclogites come from subducted oceanic crust. Further evidence to this effect is the correlation observed between

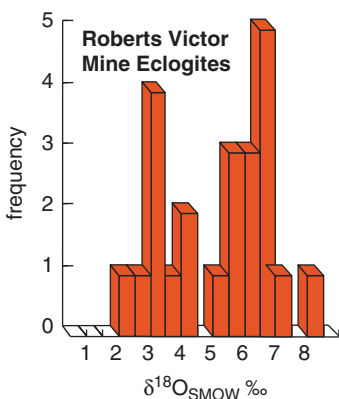


Figure 9.23 Oxygen isotope ratios in eclogite xenoliths from the Roberts Victor Mine kimberlite.

O isotope ratios, Sr isotope ratios, and K and Rb concentrations, as these will also be affected by metamorphism of the oceanic crust. Geobarometry indicates these eclogites last equilibrated at depths of 165–190 km. Radiogenic isotope evidence suggests they are 2.47 Ga old.

We examined the radiogenic isotope evidence for mantle heterogeneity in Chapter 6. One interpretation is that this heterogeneity

results from recycling of oceanic crust and sediment into the mantle. Since sediment, and, to a lesser degree, oceanic crust (as we shall see in the next section) differ in their oxygen isotopic compositions from normal mantle material, we might expect this recycling to produce variations in O isotope composition of basalts. As Figure 9.24 shows, this is indeed observed. EM2 basalts (defined by their radiogenic isotopic compositions as shown in Figures 6.13 and 6.14) show systematically higher $\delta^{18}\text{O}$ than MORB, while HIMU and low ${}^3\text{He}/{}^4\text{He}$ basalts (many HIMU basalts have low ${}^3\text{He}/{}^4\text{He}$) have systematically low $\delta^{18}\text{O}$. It is in EM2 basalts, such as those from Samoa the Society Islands, where the best evidence for a recycled sedimentary component is seen (e.g. Figure 6.16).

As we noted in Chapter 6, extremely radiogenic Sr was reported in lavas from Samoa by Jackson et al. (2007). Workman et al. (2008) found that $\delta^{18}\text{O}$ was well correlated with ${}^{87}\text{Sr}/{}^{86}\text{Sr}$ in these lavas (Figure 9.25), further strengthening the case that the Samoan plume contains anciently subducted sediment. One advantage of oxygen isotope ratios is that most rocks have rather similar oxygen concentrations. Thus, assuming isotopic

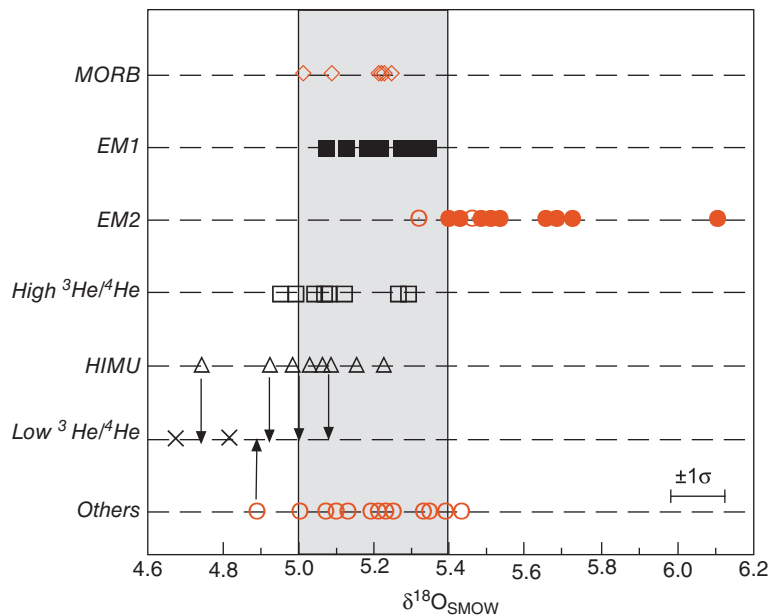


Figure 9.24 $\delta^{18}\text{O}$ in olivines from oceanic island basalts and MORB. See Section 6.4.1 for the definition of EM1, EM2, and HIMU. Shaded areas shows the range of $\delta^{18}\text{O}$ in upper mantle peridotites (e.g., Figure 21.6). (Source: Eiler et al. (1997). Reproduced with permission of Elsevier.)

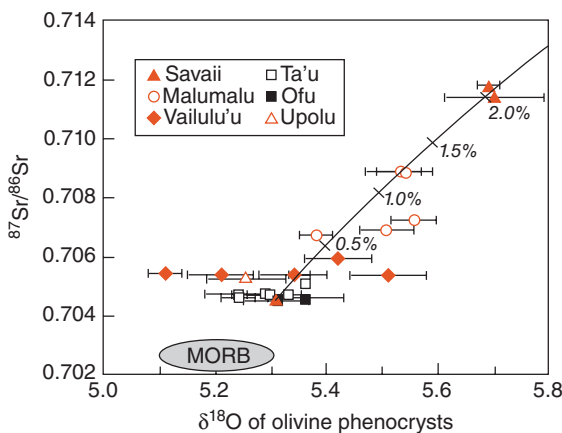


Figure 9.25 Oxygen and strontium isotope ratios in lavas from the Samoan archipelago (Savai'i and Upolu are islands, the remainder are seamounts). Also shown is the mixing curve of the sediment–mantle mixing model of Workman et al. (2008). (Source: Adapted from Workman et al., 2008.)

compositions of the end-members, we can easily calculate the fraction of each in a mixture. Workman et al. (2008) considered two models: one in which mantle (with olivine $\delta^{18}\text{O} = +5.2\text{\textperthousand}$ and ${}^{87}\text{Sr}/{}^{86}\text{Sr} \approx 0.7045$) mixes with anciently subducted upper continental crust ($\delta^{18}\text{O} = +10\text{\textperthousand}$, ${}^{87}\text{Sr}/{}^{86}\text{Sr} = 0.75$), the other in which depleted mantle mixes with anciently subducted marine sediment ($\delta^{18}\text{O} = +25\text{\textperthousand}$, ${}^{87}\text{Sr}/{}^{86}\text{Sr} = 0.75$). The curve for the latter mixing model is shown in Figure 9.25: up to about 2% sediment in the mixture would explain the isotopic compositions observed. Some Samoan lavas have even more radiogenic Sr, but those lack olivine phenocrysts and were not analyzed in this study. Extrapolating the model to those compositions implies their source contains 5–8% sediment.

Even among MORB there is a correlation between incompatible element enrichment and $\delta^{18}\text{O}$ (Figure 9.26). Since $\delta^{18}\text{O}$ should be effectively insensitive to the extent of partial melting and fractional crystallization, this correlation is likely to reflect a correlation between these properties in the MORB source. Since O isotope ratios can be changed only at low temperatures near the Earth's surface, Eiler and Schiano (2000) interpret this as evidence of a recycled component in MORB.

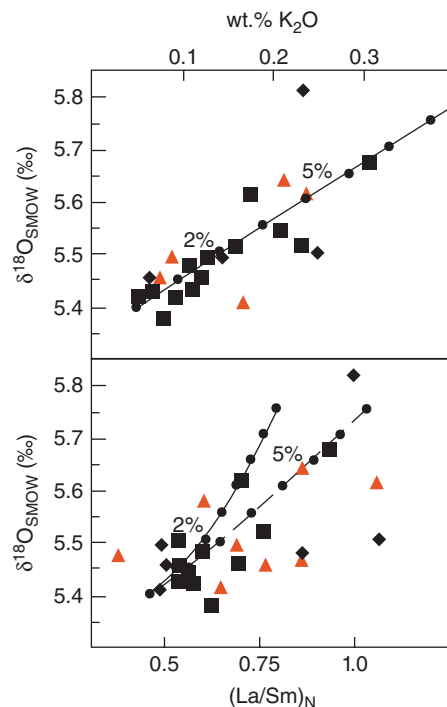


Figure 9.26 Relationship between $\delta^{18}\text{O}$ and K_2O and $(\text{La}/\text{Sm})_N$ (the chondrite-normalized La/Sm ratio) in MORB glass. Solid line shows the expected result if recycled altered oceanic crust is mixed with depleted peridotite and then melted 10%. Dashed line shows the expected result if a 10% melt of eclogitic recycled oceanic crust is mixed with a 10% melt of depleted peridotite. (Source: Eiler and Schiano (2000). Reproduced with permission of Nature Publishing Group.)

9.5 OXYGEN ISOTOPES IN HYDROTHERMAL SYSTEMS

9.5.1 Ridge crest hydrothermal activity and metamorphism of the oceanic crust

Early studies of “greenstones” dredged from mid-ocean ridges and fracture zones revealed they were depleted in ${}^{18}\text{O}$ relative to fresh basalts. Partitioning between various minerals, such as carbonates, epidote, quartz and chlorite, in these greenstones suggested they had equilibrated at about 300°C (Muehlenbachs and Clayton, 1972). This was the first, but certainly not the only, evidence that the oceanic crust underwent hydrothermal metamorphism at depth. Other clues included highly variable heat flow

at ridges and an imbalance in the Mg fluxes in the ocean. Nevertheless, the importance of hydrothermal processes was not generally recognized until the discovery of low temperature ($\sim 20^\circ\text{C}$) vents on the Galapagos Spreading Center in 1976 and high temperature (350°C) “black smokers” on the East Pacific Rise in 1979. Various pieces of the puzzle then began to fall rapidly into place and it was soon clear that hydrothermal activity was a very widespread and important phenomenon. Most of the oceanic crust is affected to some degree by this process, which also plays an important role in controlling the composition of seawater.

Hydrothermal metamorphism occurs because seawater readily penetrates the highly fractured and therefore permeable oceanic crust. A series of chemical reactions occurs as the seawater is heated, transforming it into the reduced, acidic, and metal-rich fluid. Eventually the fluid rises and escapes, forming the dramatic black smokers. Fluid in many “black smokers” vents at temperatures of about 350°C . This results from the density and viscosity minimum that occurs close to this temperature at pressures of 200–400 bars combined with a rapidly decreasing rock permeability above these temperatures.

Of the reactions that occur in the process, only one, namely oxygen isotope exchange, concerns us here. Seawater entering the oceanic crust has a $\delta^{18}\text{O}$ of 0, fresh igneous rock has a $\delta^{18}\text{O}$ of $\sim +5.7$. As seawater is heated, it will exchange O with the surrounding rock until equilibrium is reached. At temperatures in the range of $300\text{--}400^\circ\text{C}$ and for the mineral assemblage typical of greenschist facies basalt, the net water-rock fractionation is small³, 1 or 2‰. Thus isotopic exchange results in a decrease in the $\delta^{18}\text{O}$ of the rock and an increase in the $\delta^{18}\text{O}$ of the water. Surprisingly, there have only been a few oxygen isotope measurements of vent fluids; these indicate $\delta^{18}\text{O}$ of about +2.

At the same time hydrothermal metamorphism occurs deep in the crust, low-temperature weathering proceeds at the surface. This also involves isotopic exchange. However, for the temperatures ($\sim 2^\circ\text{C}$) and minerals produced by these reactions (smectites, zeolites, etc.), fractionations are quite large (something like 20‰). The result of these reactions is to increase the $\delta^{18}\text{O}$ of

the shallow oceanic crust and decrease the $\delta^{18}\text{O}$ of seawater. Thus, the effects of low temperature and high temperature reactions are opposing.

Muehlenbachs (1976) and Muehlenbachs and Furnas (2003) have argued that these opposing reactions actually buffered the isotopic composition of seawater at a $\delta^{18}\text{O}$ of ~ 0 . According to them, the net of low and high temperature fractionations was about +6, just the observed difference between the oceanic crust and the oceans. Thus, the oceanic crust ends up with an average $\delta^{18}\text{O}$ value about the same as it started with, and the net effect on seawater must be close to zero also. Could this be coincidental? One should always be suspicious of apparent coincidences in science, and they were.

Let’s think about this a little. Let’s assume the net fractionation is 6, but suppose the $\delta^{18}\text{O}$ of the ocean was -10 rather than 0. What would happen? Assuming a sufficient amount of oceanic crust available and a simple batch reaction with a finite amount of water, the net of high and low temperature basalt-seawater reactions would leave the water with $\delta^{18}\text{O}$ of $-10 + 6 = -4$. Each time a piece of oceanic crust is allowed to equilibrate with seawater, the $\delta^{18}\text{O}$ of the ocean will increase a bit. If the process is repeated enough, the $\delta^{18}\text{O}$ of the ocean will eventually reach a value of $6 - 6 = 0$. Actually, what is required of seawater-oceanic crust interaction to maintain the $\delta^{18}\text{O}$ of the ocean at 0‰ is a net increase in isotopic composition of seawater by perhaps 1–2‰. This is because low-temperature continental weathering has the net effect of decreasing the $\delta^{18}\text{O}$ of the hydrosphere. This is what Muehlenbachs and Clayton proposed.

The “half-time,” defined as the time required for the disequilibrium to decrease by half, for this process, has been estimated to be about 46 Ma. For example, if the equilibrium value of the ocean is 0‰ and the actual value is -2‰, the $\delta^{18}\text{O}$ of the ocean should increase to -1‰ in 46 Ma. It would then require another 46 Ma to bring the oceans to a $\delta^{18}\text{O}$ of -0.5‰ , and so on. Over long time-scales, this should keep the isotopic composition of oceanic crust constant. We’ll see in the next chapter that the oxygen isotopic composition of the ocean varies on times scales of thousands to tens of thousands of years

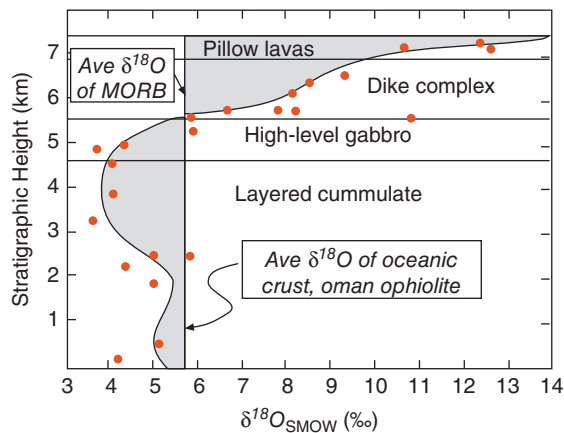


Figure 9.27 $\delta^{18}\text{O}$ of the Samail Ophiolite in Oman as a function of stratigraphic height. (Source: Gregory and Taylor (1981). Reproduced with permission of John Wiley & Sons.)

due to changes in ice volume. The isotopic exchange with oceanic crust is much too slow to dampen these short-term variations.

That water-rock interaction produces essentially no net change in the isotopic composition of the oceanic crust, and therefore of seawater was apparently confirmed by the first thorough oxygen isotope study of an ophiolite by Gregory and Taylor (1981). Their results for the Samail Ophiolite in Oman are shown in Figure 9.27. As expected, they found the upper part of the crust had higher $\delta^{18}\text{O}$ than fresh MORB and while the lower part of the section had $\delta^{18}\text{O}$ lower than MORB. Their estimate for the $\delta^{18}\text{O}$ of the entire section was +5.8, which is essentially identical to fresh MORB. At Ocean Drilling Project (ODP) Site 1256 in the equatorial eastern the oceanic crust was cored to a depth of 1500 m, just penetrating into the gabbroic layer. Oxygen isotope ratios show much the same pattern as the Samail ophiolite (Figure 9.28), with heavy oxygen in the volcanic zone and light oxygen in the dikes and gabbros. The shift in isotopic composition is coincident with a shift in the style of alteration from low- to high-temperature apparent from petrographic examination.

If the Muehlenbachs and Clayton hypothesis is correct, and assuming a steady-state tectonic environment, the $\delta^{18}\text{O}$ of the oceans

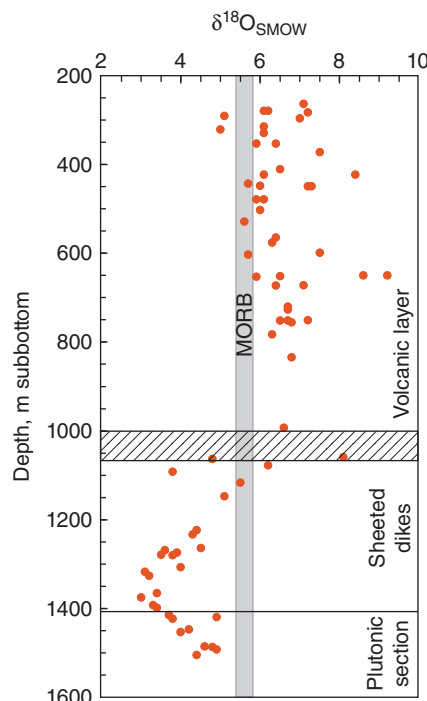


Figure 9.28 Oxygen isotope ratios measured in cores from ODP Site 1256 in the equatorial eastern Pacific. Cross-hatched area is the lava-dike transition zone. The volcanic section has mostly elevated $\delta^{18}\text{O}$ as a consequence of low-temperature interaction with seawater while the dikes and gabbros have mostly lowered $\delta^{18}\text{O}$ as a consequence of hydrothermal interaction. (Source: Gao et al. (2012). Reproduced with permission of John Wiley & Sons.)

should remain constant over geologic time. Whether it has or not, is controversial. Based on analyses of marine carbonates, Jan Veizer and his colleagues have argued that it is not (e.g., Veizer et al., 1999). The basis of their argument was that that $\delta^{18}\text{O}$ in marine carbonates increases over Phanerozoic time (Figure 9.29). More recently, however, Came et al. (2007) have used isotopic clumping analysis to calculate the isotopic composition of seawater from these Silurian and Carboniferous marine carbonates and found that seawater at the time indeed had values close to modern ones, implying the Muehlenbachs and Clayton hypothesis is correct. We'll consider this in more detail in Chapter 11.

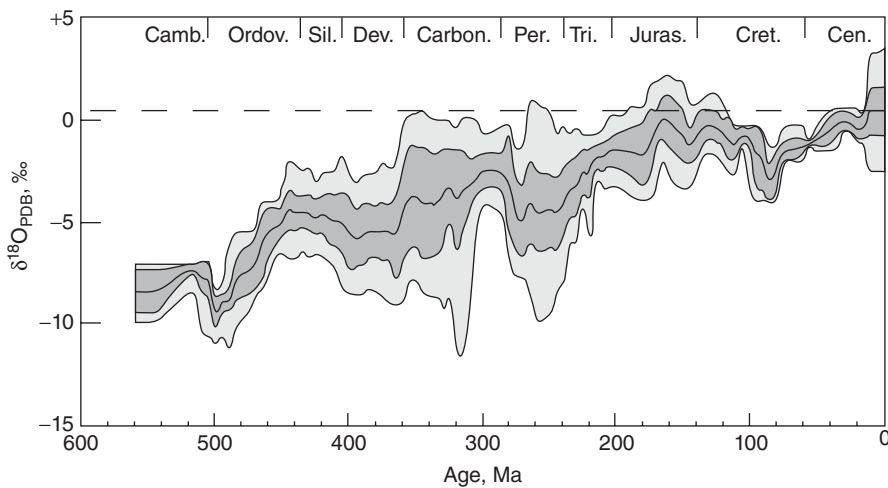


Figure 9.29 $\delta^{18}\text{O}$ in marine carbonates (brachiopods, belemnites, oysters, and foraminifera shells) over Phanerozoic time. (Source: Veizer et al. (1999). Reproduced with permission of Elsevier.)

9.5.2 Meteoric geothermal systems

Hydrothermal systems occur not only in the ocean, but just about everywhere that magma is intruded into the crust. In the 1950s a debate raged about the rate at which the ocean and atmosphere were created by degassing of the Earth's interior. W. W. Rubey assumed that water in hydrothermal systems such as Yellowstone was magmatic and argued that the ocean and atmosphere were created quite gradually through magmatic degassing. Rubey turned out to be wrong about hydrothermal systems. One of the first of many important contributions of stable isotope geochemistry to understanding hydrothermal systems was the demonstration by Craig (1963) that water in these systems was meteoric, not magmatic. The argument is based upon the data shown in Figure 9.30. For each geothermal system, the δD of the "chloride" type geothermal waters is the nearly same as the local precipitation and groundwater, but the $\delta^{18}\text{O}$ is shifted to higher values. The shift in $\delta^{18}\text{O}$ results from "high" temperature ($\sim 300^\circ\text{C}$) reaction of the local meteoric water with hot rock. However, because concentration of hydrogen in rocks is nearly 0 (more precisely because ratio of the mass of hydrogen in the water to mass of hydrogen in the reacting rocks is extremely high), there is essentially no change in the hydrogen isotopic composition of the water. If the water involved in these systems was

magmatic, it would not have the same δD as local meteoric water (though it is possible that these systems contain a few percent magmatic water).

Acidic, sulfide-rich water from these systems does have δD that is different from local meteoric water. This shift occurs when hydrogen isotopes are fractionated during boiling of geothermal waters. The steam produced is enriched in sulfide, accounting for their acidic character. The water than condenses from this steam the mixes with meteoric water to produce the mixing lines observed.

9.5.3 Water-rock reaction: Theory

Very often in geology it is difficult to observe the details of processes occurring today and our understanding of many of Earth processes comes from observing the effects these processes have had in the past, that is, the record they have left in the rocks. So it is with hydrothermal systems. In present systems, we very often can observe only the water venting, we cannot observe the reactions with rocks or the pattern of circulation. However, these, as well as temperatures involved and water-rock ratios, can be inferred from the imprint left by ancient hydrothermal systems.

Estimating temperatures at which ancient hydrothermal systems operated is a fairly straightforward application of isotope

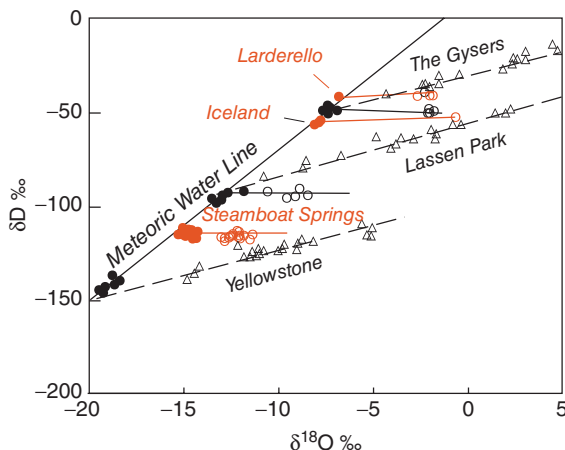


Figure 9.30 δD and $\delta^{18}\text{O}$ in meteoric hydrothermal systems. Closed circles show the composition of meteoric water in the vicinity of Yellowstone, Steamboat Springs (Colorado), Mt Lassen (California), Iceland, Larderello (Italy), and The Geysers (California), and open circles show the isotopic composition of chloride-type geothermal waters at those locations. Open triangles show the composition of acidic, sulfide-rich geothermal waters at those locations. Solid lines connect the meteoric and chloride waters, dashed lines connect the meteoric and acidic waters. The “Meteoric Water Line” shows the correlation between δD and $\delta^{18}\text{O}$ observed in precipitation shown in Figure 8.11. (Source: Craig (1963). Reproduced with permission of Consiglio Nazionale delle Ricerche.)

geothermometry, which we have already discussed. If we can measure the oxygen (or carbon or sulfur) isotopic composition of any two phases that were in equilibrium, and if we know the fractionation factor as a function of temperature for those phases, we can estimate the temperature of equilibration. We will focus now on water-rock ratios, which may also be estimated using stable isotope ratios.

For a closed hydrothermal system, we can write two fundamental equations. The first simply describes equilibrium between water and rock:

$$\Delta = \delta_w^f - \delta_r^f \quad (9.11)$$

where we use the subscript *w* to indicate water, and *r* to indicate rock. The superscript *f* indicates the final value. So Eqn. 9.10 just says that the difference between the final isotopic

composition of water and rock is equal to the fractionation factor (we implicitly assume equilibrium). The second equation is just a statement of mass balance for a closed system: the amount of the isotope present before reaction must be the same as after reaction:

$$c_w W \delta_w^i + c_r R \delta_r^i = c_w W \delta_w^f + c_r R \delta_r^f \quad (9.12)$$

where *c* indicates concentration (we assume concentrations do not change, which is valid for oxygen, but not generally valid for other elements), *W* indicates the mass of water involved, *R* the mass of rock involved, and the superscript *i* denotes the initial isotope ratio.

Substituting Eqn. 9.10 and rearranging, we derive the following equation:

$$\frac{W}{R} = \frac{\delta_r^f - \delta_r^i}{\delta_w^i - \delta_r^f - \Delta} \frac{c_r}{c_w} \quad (9.13)$$

The term on the left is the ratio of water to rock in the reaction. Notice that the right hand side does not include the final isotopic composition of the water, information that we would generally not have. The initial oxygen isotope composition of the water can be estimated in various ways. For example, we can determine the hydrogen isotopic composition (of rocks) and from that determine the oxygen isotope composition using the $\delta\text{D}-\delta^{18}\text{O}$ meteoric water line. The initial $\delta^{18}\text{O}$ of rock can generally be inferred from unaltered samples, and the final isotopic composition of the rock can be measured. The fractionation factor can be estimated if we know the temperature and the phases in the rock. For oxygen, the ratio of concentration in the rock to water will be close to 0.5 in all cases.

Equation 9.13 is for a closed system, that is, a batch reaction where we equilibrate *W* grams of water with *R* grams of rock. That is not very geologically realistic. In fact, a completely open system, where water makes one pass through hot rock, would be more realistic. In this case, we might suppose that a small parcel of water, *dW*, passes through the system and induces an incremental change in the isotopic composition of the rock, *dδr*. In this case, we can write:

$$R c_r d\delta_r = (\delta_w^i - [\Delta + \delta_r]) c_w dW \quad (9.14)$$

This equation states that the mass of isotope exchanged by the rock is equal to the mass

of isotope exchanged by the water (we have substituted $\Delta + \delta_r$ for δ). Rearranging and integrating, we have:

$$\frac{W}{R} - \ln \left(\frac{\delta_r^f - \delta_r^i}{-\delta_r^f + \delta_w^i - \Delta} + 1 \right) \frac{c_r}{c_w} \quad (9.15)$$

Thus, it is possible to deduce the water/rock ratio for an open system as well as a closed one.

Using this kind of approach, Gregory and Taylor (1981) estimated water/rock ratios of ≤ 0.3 for the gabbros of the Oman ophiolite. It should be emphasized, however, that this can be done with other isotope systems as well. For example, McCulloch et al. (1981) used Sr isotope ratios to estimate water/rock ratios varying from 0.5 to 40 for different parts of the Oman ophiolite.

9.5.4 The Skaergaard intrusion

A classic example of a meteoric hydrothermal system is the Early Tertiary Skaergaard intrusion in East Greenland. The Skaergaard has been studied for nearly 75 years as a classic mafic layered intrusion. Perhaps ironically, the initial motivation for isotopic study of the Skaergaard was determination of primary oxygen and hydrogen isotopic compositions of igneous rocks. The results, however, showed that the oxygen isotope composition of the Skaergaard has been pervasively altered by hydrothermal fluid flow. This was the first step in another important contribution of stable isotope geochemistry, namely the demonstration that most igneous intrusions have reacted extensively with water subsequent to crystallization.

Figure 9.31 shows a map of the Skaergaard with contours of $\delta^{18}\text{O}$ superimposed on it. Figure 9.32 shows a restored cross section of the intrusion with contours of $\delta^{18}\text{O}$. There are several interesting features. First, it is clear that circulation of water was strongly controlled by permeability. The impermeable basement gneiss experienced little exchange, as did the part of the intrusion beneath the contact of the gneiss with the overlying basalt. The basalt, which is typically highly fractured, is quite permeable and allowed water to flow freely through it and into the intrusion. Figures 9.31 and 9.32 define zones of low $\delta^{18}\text{O}$, which are the regions of hydrothermal

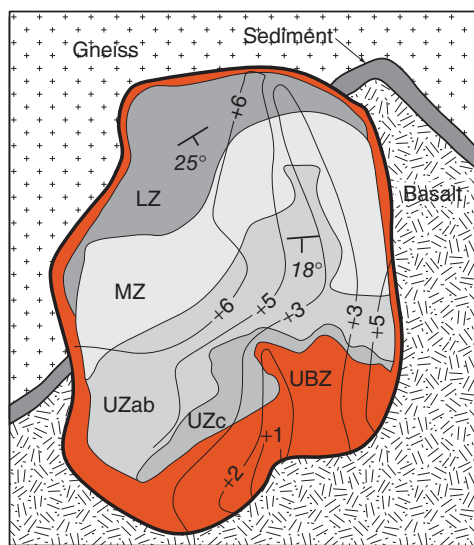


Figure 9.31 Oxygen isotope variations in the Skaergaard Intrusion. LZ, MZ, and UZ refer to the “lower zone,” “middle zone,” and “upper zone” of the intrusion, which dips 20–25° to the southeast. UBZ refers to the “upper border group.” The $\delta^{18}\text{O} = +6$ contour corresponds more or less to the trace of the gneiss–basalt contact through the intrusion (SW to NE). The gneiss is essentially impermeable, while the basalt is highly fractured. Thus most water flow was above this contact, and the gabbro below it retained its original “mantle” isotopic signature (+6). (Source: Taylor, 1974.)

upwelling. Water was apparently drawn into the sides of the intrusion and then rose above. This is just the sort of pattern observed with finite element models of fluid flow through the intrusion.

Calculated water-rock ratios for the Skaergaard were 0.88 in the basalt, 0.52 in the upper part of the intrusion and 0.003 for the gneiss, demonstrating the importance of the basalt in conduction the water into the intrusion and the inhibiting effect of the gneiss. Models of the cooling history of the intrusion suggest that each cm^3 of rock was exposed to between 10^5 and $5 \times 10^6 \text{ cm}^3$ of water over the 500,000 year cooling history of the intrusion. This would seem to conflict with the water/rock ratios estimated from oxygen isotopes. The difference is a consequence of each cm^3 of water flowing through many cm^3 of rock, but not necessarily reacting with it. Once water had flowed through enough grams

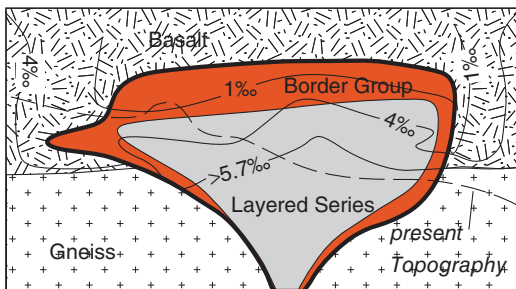


Figure 9.32 Restored cross section of the Skaergaard intrusion with contours of $\delta^{18}\text{O}$. (Source: Criss and Taylor (1986). Reproduced with permission of the Mineralogical Society of America.)

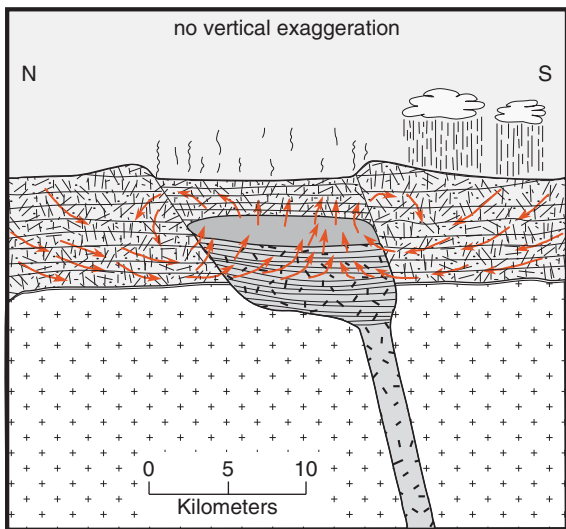


Figure 9.33 Cartoon illustrating the hydrothermal system in the Skaergaard intrusion. (Source: Taylor, 1974.)

of rock to come to isotopic equilibrium, it would not react further with the rock through which it subsequently flowed (assuming constant temperature and mineralogy). Thus, it is important to distinguish between W/R ratios calculated from isotopes, which reveal only the mass (or molar) ratio of water and rock in the net reaction, to flow models. Nevertheless, the flow models demonstrate that each gram of rock in such a system is exposed to an enormous amount of water. Figure 9.33 is a cartoon illustrating the hydrothermal system deduced from the oxygen isotope study.

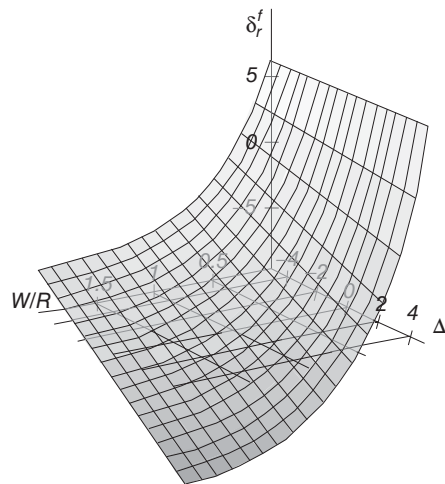


Figure 9.34 $\delta^{18}\text{O}_r^f$ as a function of W/R and Δ computed from Eqn. 9.16.

9.5.5 Oxygen isotopes and mineral exploration

Oxygen isotope studies can be a valuable tool in mineral exploration. Mineralization is very often (though not exclusively) associated with the region of greatest water flux, such as areas of upward moving hot water above intrusions. Such areas are likely to have the lowest values of $\delta^{18}\text{O}$. To understand this, let's solve Eqn. 9.15, the final value of $\delta^{18}\text{O}$:

$$\delta_r^f = (\delta_r^i - \delta_w^i - \Delta) e^{-(\text{W}/\text{R})(c_w/c_r)} + \delta_w^i + \Delta \quad (9.16)$$

If we assume a uniform initial isotopic composition of the rocks and the water, then all the terms on the right hand side are constants except W/R and Δ , which is a function of temperature. Thus the final values of $\delta^{18}\text{O}$, that is, the values we measure in an area such as the Skaergaard, are functions of the temperature of equilibration, and an exponential function of the W/R ratio. Figure 9.34 shows $\delta^{18}\text{O}_r^f$ plotted as a function of W/R and δ , where $\delta^{18}\text{O}_r^i$ is assumed to be +6 and $\delta^{18}\text{O}_w^i$ is assumed to be -13.

Figure 9.35 shows another example of the $\delta^{18}\text{O}$ imprint of an ancient hydrothermal system: the Bohemia mining district in Lane County, Oregon, where Tertiary volcanic rocks of the Western Cascades have been intruded by a series of dioritic plutons. Approximately \$1,000,000 worth of gold was removed from the region between 1870 and 1940. $\delta^{18}\text{O}$ contours form a bull's

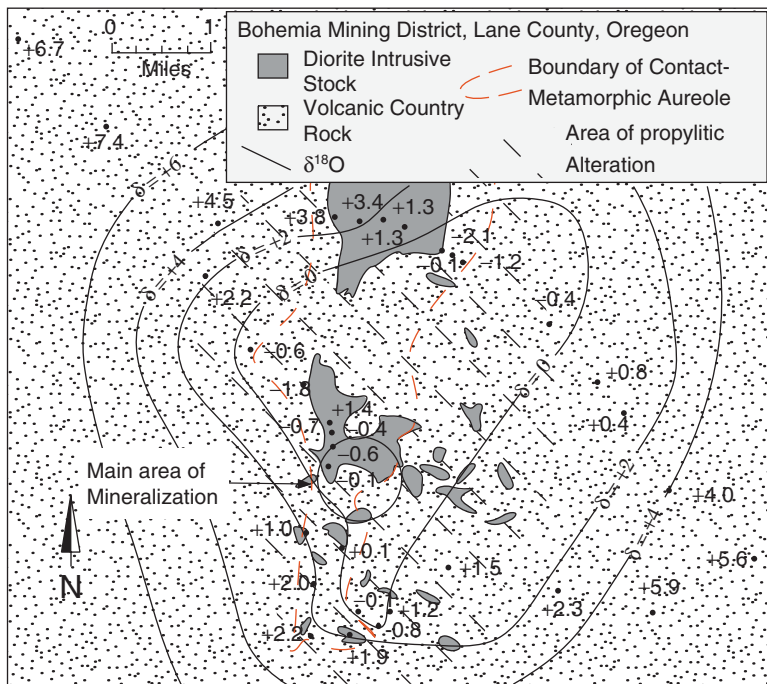


Figure 9.35 $\delta^{18}\text{O}$ variations in the Bohemia mining district, Oregon. Note the bull's eye pattern of the $\delta^{18}\text{O}$ contours. (Source: Taylor, 1974.)

eye pattern, and the region of low $\delta^{18}\text{O}$ corresponds roughly with the area of propylitic (i.e., greenstone) alteration. Notice that this region is broader than the contact metamorphic aureole. The primary area of mineralization occurs within the $\delta^{18}\text{O} < 0$ contour. In this area relatively large volumes of gold-bearing hydrothermal solution, cooled, perhaps mixing with groundwater, and precipitated gold. This is an excellent example of the value of oxygen isotope studies to mineral exploration. Similar bull's eye patterns are found around many other hydrothermal ore deposits.

the most complex. This complexity arises in part because there are five common valence states in which sulfur can occur in the Earth, +6 (e.g., BaSO_4), +4 (e.g., SO_2), 0 (e.g., S), -1 (e.g., FeS_2), and -2 (H_2S). Significant equilibrium isotopic fractionations occur between each of these valence states. Sulfur in each of these valence states forms a variety of compounds, and fractionations can occur between these as well. Finally, sulfur is important in biological processes and fractionations in biologically mediated oxidations and reductions are often different from fractionations in the abiological equivalents.

There are two major reservoirs of sulfur on the Earth that have uniform sulfur isotopic compositions: the mantle, which has $\delta^{34}\text{S}$ of ~ 0 and in which sulfur is primarily present in reduced form, and seawater, which has $\delta^{34}\text{S}$ of +20 and in which sulfur is present as SO_4^{2-} . Sulfur in sedimentary, metamorphic, and igneous rocks of the continental crust may have $\delta^{34}\text{S}$ that is both greater and smaller than these values (Figure 9.36). All of these can be sources of sulfide in ores, and further fractionation may occur during transport and deposition of sulfides. Thus,

9.6 SULFUR ISOTOPES AND ORES

9.6.1 Introduction

A substantial fraction of all economically valuable metal ores are sulfides. These have formed in a great variety of environments and under a great variety of conditions. Sulfur isotope studies have been very valuable in sorting out the genesis of these deposits. Of the various stable isotope systems we will consider in this book, sulfur isotopes are undoubtedly

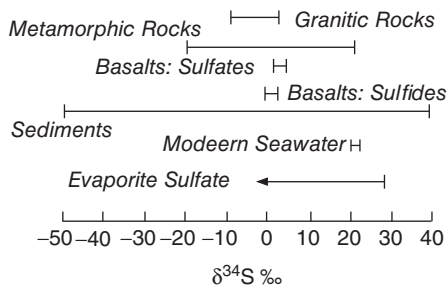


Figure 9.36 $\delta^{34}\text{S}_{\text{CDT}}$ in various geologic materials (Source: Hoefs, 1987. Reproduced with permission of Springer Science + Business Media.)

the sulfur isotope geochemistry of sulfide ores is remarkably complex.

9.6.2 Sulfur isotope fractionations in magmatic processes

Sulfur is present in peridotites as trace sulfides, and that is presumably its primary form in the mantle. At temperatures above about 400°C, H₂S and SO₂ are the stable forms of sulfur in fluids and melts. In basaltic melts, sulfur occurs predominantly as dissociated H₂S: HS⁻. It is unlikely that significant fractionation occurs between these forms during melting. Indeed, as we have seen, the mean $\delta^{34}\text{S}$ in basalts (~+0.1) is close to the value in meteorites, which is presumably also the mantle value. The solubility of H₂S in silicate melts is related to the Fe content, decreasing with decreasing Fe. The solubility of H₂S in basalt appears to be only slightly less than that of water, so that under moderate pressure, essentially all sulfur will remain dissolved in basaltic liquids.

As basalts rise into the crust, cool, and crystallize, several processes can affect the oxidation state and solubility of sulfur and the produce isotopic fractionations. First, the decreasing pressure results in some of the sulfide partitioning into the gas (or fluid) phase. In addition, H₂ can be lost from the melt through diffusion. This increases the f_{O_2} of the melt, and as result, some of the sulfide will be oxidized to SO₂, which is very much less soluble in silicate melts than H₂S. Decreasing Fe content as a consequence of fractional crystallization will also decrease the solubility of S in the melt, increasing its concentration

in a coexisting fluid or gas phase. Isotope fractionation will occur between the three species (dissolved HS⁻, H₂S, SO₂). The isotopic composition of the fluid (gas) will differ from that of the melt, and can be computed as:

$$\delta^{34}\text{S}_{\text{fluid}} = \delta^{34}\text{S}_{\text{melt}} - \Delta_{\text{HS}^-} + \Delta_{\text{SO}_2} \left(\frac{R}{R+1} \right) \quad (9.17)$$

where Δ_{HS} is the fractionation factor between HS⁻ and H₂S, Δ_{SO_2} is the fractionation factor between H₂S and SO₂, and R is the mole fraction ratio SO₂/H₂S and is given by:

$$R = \frac{X_{\text{SO}_2}}{X_{\text{H}_2\text{S}}} = \frac{K v_{\text{H}_2\text{S}} f_{\text{O}_2}^{3/2}}{P_f v_{\text{H}_2\text{O}} X_{\text{H}_2\text{O}} v_{\text{SO}_2}} \quad (9.18)$$

where v are the fugacity or activity coefficients, P_f is the fluid pressure (generally equal to total pressure), f_{O_2} is oxygen fugacity, and K is the equilibrium constant for the reaction:

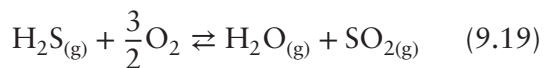


Figure 9.37 shows the sulfur isotope fractionation between fluid and melt calculated from Eqns 9.17 and 9.18 as a function of function of temperature and f_{O_2} for P_{H₂O} = 1 kB. At the temperatures and f_{O_2} of most basalts, sulfur will be present primarily as H₂S in the fluid (gas phase) and HS⁻ in the melt. The fractionation between these species is small (~0.6‰), so the isotopic composition of fluid phase will not be very different that of the melt. For rhyolites and dacites, a significant fraction of the sulfur can be present as SO₂, so that greater fractionation between melt and fluid is possible.

An interesting feature of these equations is that the fractionation between fluid and melt depends on the water pressure. Figure 9.37 is valid only for P_{H₂O} = 1 kB. A decrease in P_f or X_{H₂O} (the mole fraction of water in the fluid) will shift the SO₂/H₂S equal concentration boundary and the $\delta^{34}\text{S}$ contours to lower f_{O_2} . Conversely, an increase in the water content will shift the boundary toward higher f_{O_2} .

Both the eruptions of El Chichón in 1983 and Pinatubo in 1991 released substantial amounts of SO₂, which resulted in global climate cooling. The SO₂-rich nature of these eruptions is thought to result from mixing of a mafic, S-bearing magma with a more oxidized

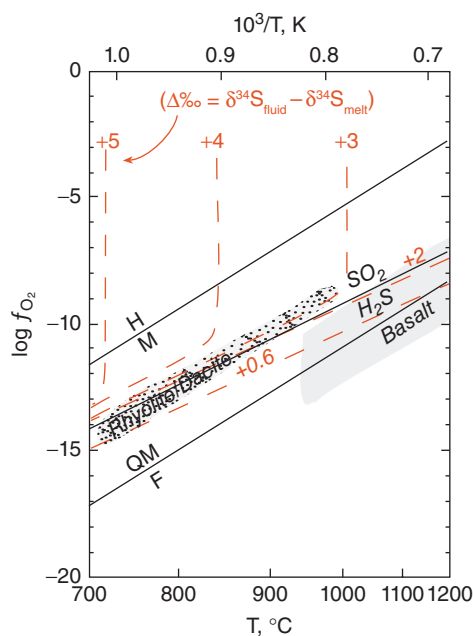


Figure 9.37 Fractionation of sulfur isotopes between fluid and melt (shown by dashed curves) as a function of oxygen fugacity and temperature for $P_{H_2O} = 1 \text{ kB}$. Solid lines show equal concentration boundaries for quartz + magnetite \rightleftharpoons fayalite (QM-F), $H_2S \rightleftharpoons SO_2$, and Magnetite \rightleftharpoons Hematite (M-H).
(Source: Ohmoto and Rye (1979). Reproduced with permission of John Wiley & Sons.)

dacitic magma, which resulted in oxidation of the sulfur, and consequent increase of SO_2 in the fluid phase. There are a number of other processes that affect the solubility and oxidation state of sulfur in the melt, and hence isotopic fractionation. Wall rock reactions could lead to either oxidation or reduction of sulfur; crystallization of sulfides or sulfates could cause relatively small fractionations and additionally affect the SO_2/H_2S ratio of the fluid. Depending on the exact evolutionary path taken by the magma and fluid, $\delta^{34}\text{S}$ of H_2S may be up to $-13\text{\textperthousand}$ lower than that of the original magma. Thus, variations in the isotopic composition of sulfur are possible even in a mantle-derived magma whose initial $\delta^{34}\text{S}$ was that of the mantle ($\sim 0\text{\textperthousand}$). Variability of sulfur isotopic compositions do, however, give some indication of the f_{O_2} history of a magma. Constant $\delta^{34}\text{S}$ of magmatic sulfides suggests f_{O_2} remained below the SO_2/H_2S

boundary; variability in isotopic composition suggests a higher f_{O_2} .

9.6.3 Sulfur isotope fractionation in hydrothermal systems

Although some sulfide ore deposits are magmatic, most were deposited by precipitation from aqueous solution at low to moderate temperature. At temperatures below about 400°C , sulfide species (H_2S and HS^-) are joined by sulfate (SO_4^{2-} , HSO_4^{1-} , KSO_4^{1-} , $NaSO_4^{1-}$, $CaSO_4$, and $MgSO_4$) as the dominant forms of aqueous sulfur. The ratio of sulfide to sulfate will depend on the oxidation state of the fluid. Small fractionations occur among the various sulfide and sulfate species, but there is a major fractionation between sulfide and sulfate. Neglecting the small fractionation between H_2S and HS^- and among sulfate species, $\delta^{34}\text{S}_{H_2S}$ of the fluid can be expressed as:

$$\delta^{34}\text{S}_{H_2S} = \delta^{34}\text{S}_{fluid} - \Delta_{SO_4^{2-}} \times \left(\frac{R'}{R' + 1} \right) \quad (9.20)$$

where $\Delta_{SO_4^{2-}}$ is the fractionation between H_2S and SO_4^{2-} and R' is the molar ratio of sulfide to sulfate:

$$R' = \frac{\Sigma SO_4^{2-}}{\Sigma H_2S} \quad (9.21)$$

In general, R' will be a function of f_{O_2} , pH, fluid composition and temperature. Figure 9.38 shows the difference between $\delta^{34}\text{S}$ in sulfide and $\delta^{34}\text{S}$ in the total fluid as a function of pH and f_{O_2} . Only under conditions of low pH and low f_{O_2} , will the $\delta^{34}\text{S}$ of pyrite (FeS_2) be the same as the $\delta^{34}\text{S}$ of the fluid from which it precipitated. For conditions of relatively high f_{O_2} or high pH, substantial differences between the $\delta^{34}\text{S}$ of pyrite and the $\delta^{34}\text{S}$ of the fluid from which it precipitated are possible. Figure 9.39 shows the difference between $\delta^{34}\text{S}$ in sulfide and $\delta^{34}\text{S}$ in the total fluid as a function of the sulfate/sulfide ratio (R') and temperature. When the fluid is sulfide dominated, the $\delta^{34}\text{S}$ of the sulfide and that of the bulk fluid will necessarily be nearly identical. For conditions where the concentrations of sulfate and sulfide are similar, large fractionations between sulfides and fluids from which they precipitate are possible.

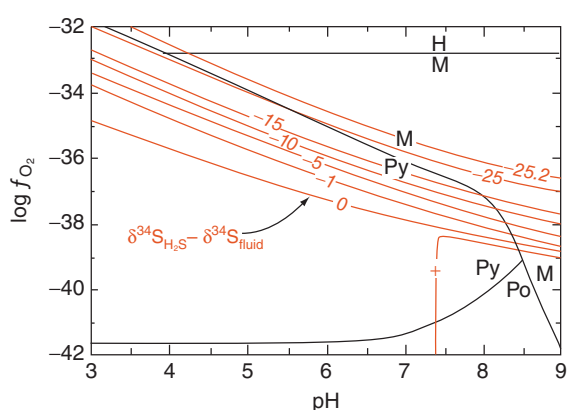


Figure 9.38 Difference in $\delta^{34}\text{S}$ between H_2S and bulk fluid as a function of pH and f_{O_2} at 250°C . Equal concentration boundaries are shown for magnetite-hematite (M-H), magnetite-pyrite (M-Py), magnetite-pyrrhotite (M-Po), and pyrite-pyrrhotite (Py-Po). (Source: Ohmoto and Rye (1979). Reproduced with permission of John Wiley & Sons.)

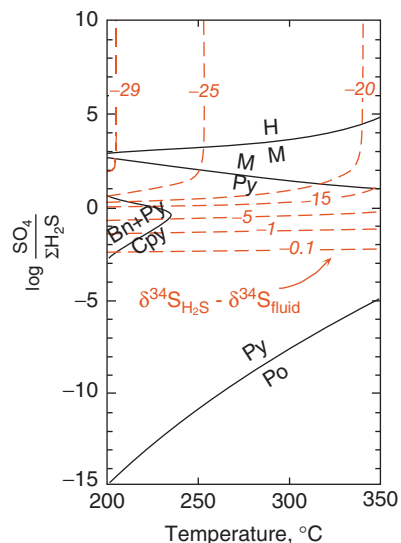


Figure 9.39 Difference in $\delta^{34}\text{S}$ between H_2S and bulk fluid as a function of temperature and sulfate/sulfide ratio in a pH neutral fluid. Equal concentration boundaries M: magnetite, H: hematite, Py: pyrite, Po: pyrrhotite, Bn: bornite (Cu_5FeS_4), Cp: chalcopyrite. (Source: Ohmoto and Rye (1979). Reproduced with permission of John Wiley & Sons.)

At magmatic temperatures, reactions generally occur rapidly and most systems appear to be close to equilibrium. This will not necessarily be the case at lower temperatures because of the strong dependence of reaction rates on temperature. While isotopic equilibration between various sulfide species and between various sulfate species seems to be readily achieved at moderate and low temperatures, isotopic equilibration between sulfate and sulfide appears to be more difficult to achieve. Sulfate-sulfide reaction rates have been shown to depend on pH (reaction is more rapid at low pH) and, in particular, on the presence of sulfur species of intermediate valences. Equilibration is much more rapid when such intermediate valence species are present. Presumably, this is because reaction rates between species of adjacent valence states (e.g., sulfate and sulfite, SO_3^{2-}) are rapid, but reaction rates between widely differing valence states (e.g., sulfate and sulfide) are much slower.

Low temperatures also lead to kinetic, rather than equilibrium, fractionations. As we saw, kinetic fractionation factors result from different isotopic reaction rates. Interestingly enough, the rates for oxidation of H_2^{32}S and H_2^{34}S appear to be nearly identical. This leads to the kinetic fractionation factor, α_k , of 1.000 ± 0.003 , whereas the equilibrium fractionation between H_2S and SO_4 will be 1.025 at 250°C and 1.075 at 25°C . Thus, sulfate produced by oxidation of sulfide can have $\delta^{34}\text{S}$ identical to that of the original sulfide. Kinetic fractionations for the reverse reaction, namely reduction of sulfate, are generally larger. The fractionation observed is generally less than the equilibrium fractionation and depends on the overall rate of reduction: the fractionation approaches the equilibrium value when reaction rate is slow. Disequilibrium effects have also been observed in decomposition of sulfide minerals. Figure 9.40 illustrates some interesting possible effects that can arise as a result of disequilibrium.

If there is disequilibrium between sulfate and sulfide in solution, it is likely equilibrium will not be achieved between mineral pairs involving pyrite and chalcopyrite (CuFeS_2) even when isotopic equilibrium is attained between other sulfides such as galena (PbS), sphalerite (ZnS), and pyrrhotite (FeS). This is because precipitation of the former involves

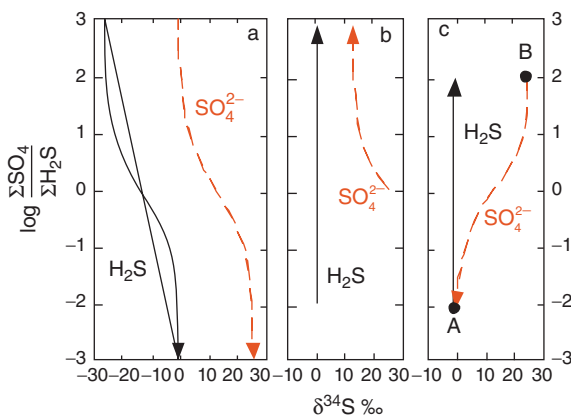
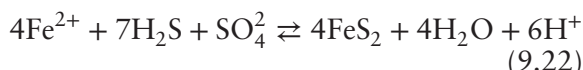


Figure 9.40 Isotopic relationships between coexisting H_2S and SO_4^{2-} as a function of sulfate/sulfide ratio. (a) Equilibrium conditions at 250°C where $\delta^{34}\text{S}_{\text{fluid}} = 0\text{‰}$. (b) Non-equilibrium oxidation of H_2S . Isotopic composition of H_2S remains constant, but that of sulfate changes due to addition of sulfate derived from non-equilibrium oxidation of H_2S . (c) Non-equilibrium mixing of H_2S -rich fluid A and SO_4^{2-} -rich fluid B. $\delta^{34}\text{S}_{\text{H}_2\text{S}}$ remains constant (equilibrium fractionation is achieved during reduction), but $\delta^{34}\text{S}_{\text{SO}_4^{2-}}$ varies due to addition of sulfate derived from oxidation of sulfide. (Source: Ohmoto and Rye (1979). Reproduced with permission of John Wiley & Sons.)

reactions such as:



whereas the latter involve only simple combinations, for example:



9.6.4 Isotopic composition of sulfide ores

A number of important sulfide deposits were apparently produced by reduction of sulfate that was ultimately derived from seawater. The expected isotopic compositions of such deposits are shown in Figure 9.41. The isotopic composition of these sulfides depends on the reduction mechanism, temperature, and whether the system was open or closed to sulfate and sulfide. At temperatures less than 50°C, the only mechanism for reduction of sulfate is bacterial. Optimal temperatures for

such reduction are around 30–50°C. Deep euxinic basins such as the Black Sea are good examples of systems that are open to SO_4 but closed to H_2S and where reduction is bacterial. In these cases, reduction occurs slowly at the bottom, but SO_4 is continuously supplied from the water mass above. In such environments, sulfides appear to have a $\delta^{34}\text{S}$ of 40 to 60‰ less than that of contemporaneous seawater (the sulfur isotopic composition of seawater has varied through time). A good example of such a deposit is the Kupferschiefer in Germany, where the most common $\delta^{34}\text{S}$ is about -40‰, which is about 50‰ less than Permian seawater (+10‰).

In systems closed to SO_4 but open to H_2S , the process is similar to Rayleigh distillation. This would be the case, for example, where sulfate reduction occurs much more rapidly than sulfate is supplied to the system, but sulfide is effectively lost from the system by crystallization of sulfide minerals. The composition of the sulfate, as a function of the fraction of sulfate remaining, f , is given by:

$$\delta^{34}\text{S}_{\text{SO}_4^{2-}} = \delta^{34}\text{S}_{\text{SO}_4^{2-}}^0 + 1000(f^{1-\alpha} - 1) \quad (9.24)$$

The composition of the sulfide at any time, t , is related to that of sulfate by:

$$\delta^{34}\text{S}_{\text{H}_2\text{S}}^t = \delta^{34}\text{S}_{\text{SO}_4^{2-}}^t - 1000(\alpha - 1) \quad (9.25)$$

where α is the effective sulfate-sulfide fractionation factor. The effective fractionation factor for reduction may be greater than the equilibrium one because of the more rapid reaction of ^{32}S species than ^{34}S ones. A typical value of α under these circumstances might be 1.025.

Systems closed to both species are analogous to equilibrium crystallization. In either case, the $\delta^{34}\text{S}$ of both sulfide and sulfate increases during the reduction process. Systems closed to SO_4 characteristically show a spread in $\delta^{34}\text{S}$ that is skewed toward positive values, have $\delta^{34}\text{S}$ that increases in the later stages, and have both minimum and modal values that are approximately 25‰ lower than the original sulfate (e.g., contemporaneous seawater). Examples are the White Pine and Zambian copper deposits, which apparently formed in shallow marine or brackish environments.

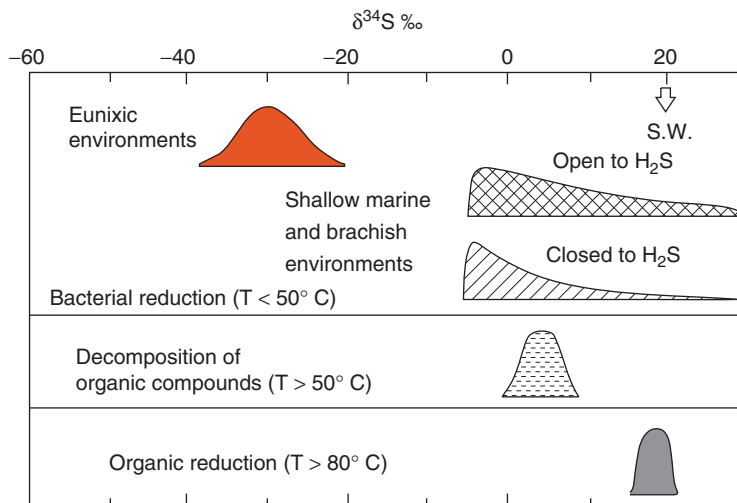
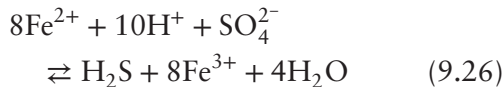


Figure 9.41 Expected distribution of $\delta^{34}\text{S}$ values for sulfide ores produced by sulfate reduction of seawater having an isotopic composition of $\delta^{34}\text{S} = +20\text{\textperthousand}$. (Source: Ohmoto and Rye (1979). Reproduced with permission of John Wiley & Sons.)

At temperatures above 50°C , thermal decomposition of sulfur-bearing organic compounds produces H_2S . The $\delta^{34}\text{S}$ values of such H_2S are typically $15\text{\textperthousand}$ less than that of seawater. This reduction is accelerated by the presence of S species of intermediate valence. The extent of isotopic fractionation in this process decreases with increasing temperature and is effectively nil above 80°C .

In ridge crest hydrothermal systems, seawater sulfate is reduced by reactions with Fe^{2+} such as:



Reduction most likely occurs at temperatures above 250°C (sulfide was not produced in basalt-seawater experiments below this temperature), and it is likely that equilibrium is achieved in this process. Modern seawater has a $\delta^{34}\text{S}$ of $+20$, and values of H_2S between $-5\text{\textperthousand}$ and $+20\text{\textperthousand}$ are expected (the latter corresponds to complete reduction of sulfate). Consistent with this prediction, sulfide in active seafloor hydrothermal vents has a $\delta^{34}\text{S}$ of $+3.5$. This process produces the class of ores referred to either as *stratabound sulfides* or *volcanogenic massive sulfides*. Isotopic compositions of some example deposits are shown in Figure 9.42, along with the composition of contemporaneous seawater. They

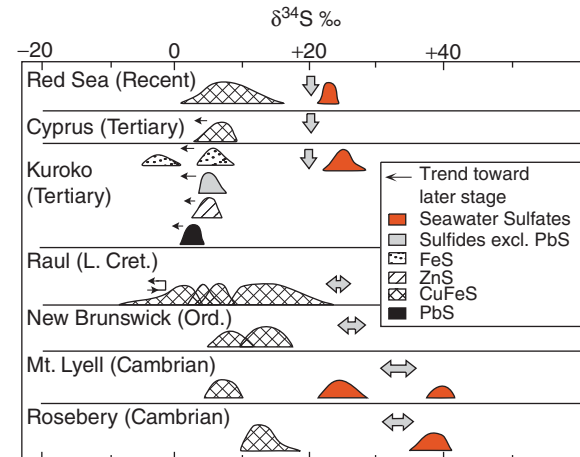


Figure 9.42 $\delta^{34}\text{S}$ in volcanogenic massive sulfide deposits. Arrows show the isotopic composition of contemporaneous seawater sulfate. (Source: Ohmoto and Rye (1979). Reproduced with permission of John Wiley & Sons.)

typically have $\delta^{34}\text{S}$ approximately $17\text{\textperthousand}$ lower than contemporaneous seawater.

The isotopic compositions of several example porphyry copper deposits are shown in Figure 9.43. The sulfides in these generally have $\delta^{34}\text{S}$ between -3 and $+1\text{\textperthousand}$, which is close to the mantle value, and the fractionation between sulfides and coexisting sulfates

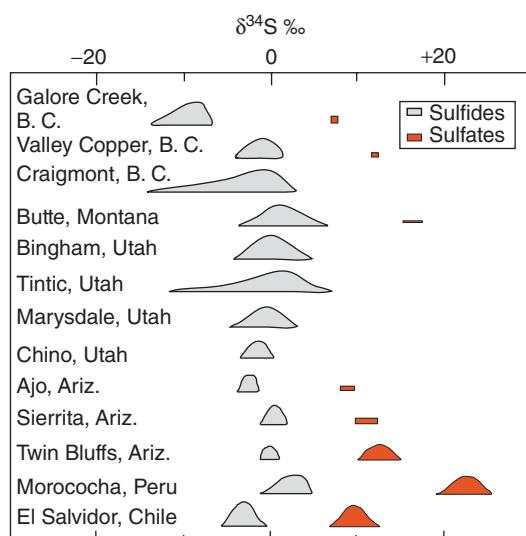


Figure 9.43 $\delta^{34}\text{S}$ in porphyry copper sulfides and sulfates. (Source: Ohmoto and Rye (1979). Reproduced with permission of John Wiley & Sons.)

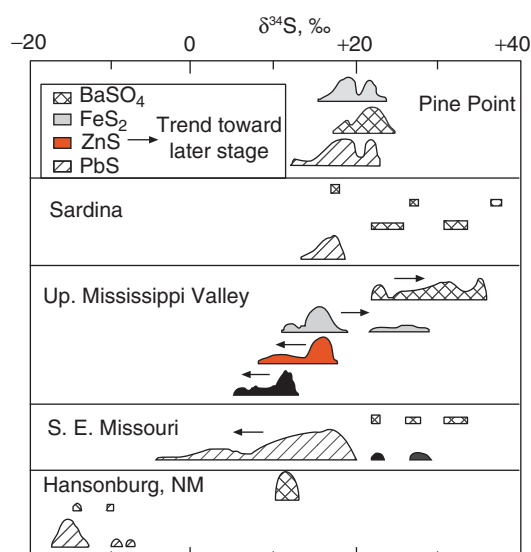


Figure 9.44 Sulfur isotope ratios in some Mississippi Valley-type Pb and Zn deposits. (Source: Ohmoto and Rye (1979). Reproduced with permission of John Wiley & Sons.)

suggest equilibration temperatures between 450 and 650°C, which is generally in good agreement with other temperature estimates. The isotopic compositions indicate the sulfur was derived from igneous sources, either as magmatic fluids or by dissolution of igneous sulfides. The low $\delta^{34}\text{S}$ of Galore Creek is lower than most others and suggests the oxidation state of the magma was high or that some sedimentary sulfide was incorporated. The high $\delta^{34}\text{S}$ of Morococha suggests some sulfur was derived from the evaporites found in the surrounding country rock. H and O isotopic compositions in these deposits are generally inconsistent with water being of magmatic derivation. It is possible these isotope ratios reflect overprint of meteoric water circulation after mineralization.

Mississippi Valley type deposits are carbonate-hosted lead and zinc sulfides formed under relatively low temperature conditions. Figure 9.44 shows the sulfur isotope ratios of some examples. They can be subdivided into Zn-rich and Pb-rich classes. The Pb-rich and most of the Zn-rich deposits were formed between 70 and 120°C, while some of the Zn-rich deposits, such as those of the Upper Mississippi Valley, were formed at temperatures up to 200°C. Co-existing sulfides of the Pb-poor Upper Mississippi

Valley deposits are in isotopic equilibrium, whereas sulfur isotope equilibrium was most often not achieved in Pb-rich deposits. In the former, $\delta^{34}\text{S}$ values are quite uniform over a large area, suggesting the ore-forming fluid supplied both metals and sulfides and transported them over long distances. The high positive $\delta^{34}\text{S}$ suggests the sulfur was ultimately derived from ancient seawater, perhaps from formation water or evaporites in deep sedimentary basins, and reduced by reaction with organic compounds.

$\delta^{34}\text{S}$ is correlated with Pb isotope ratios in galenas of the S.E. Missouri district. This, and the variability of $\delta^{34}\text{S}$, suggests there was more than one source of the sulfur and lead. Isotopically heavy sulfur was apparently carried with the metal by the ore-forming fluid while the isotopically light sulfur was derived from pyrite in the host rock. In Pine Point, sulfide may have been locally produced by reaction between sulfate-bearing fluids and organic matter in sediment. Local production of sulfide shortly before ore deposition may help to account for the lack of isotopic equilibrium in this deposit, since time is an element in the attainment of isotopic equilibrium.

Figure 9.45 illustrates a generalized model for the genesis of Mississippi Valley type deposits. In most instances, metals and sulfur

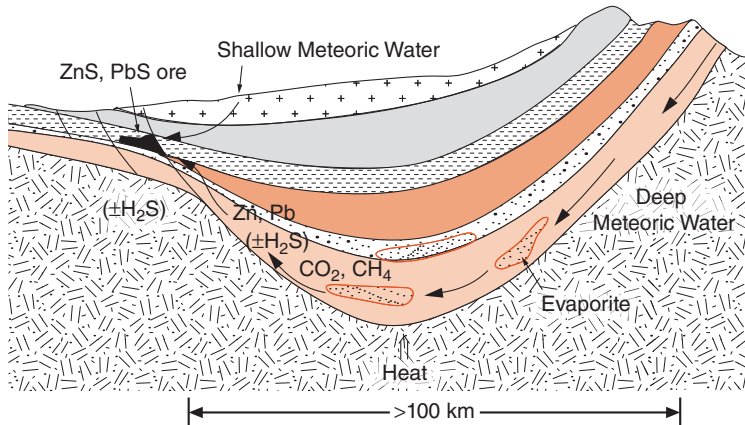


Figure 9.45 Cartoon illustrating the essential features of the genesis of Mississippi Valley sulfide ores. (Source: Ohmoto (1986). Reproduced with permission of the Mineralogical Society of America.)

appear to have been derived distant from sedimentary units, perhaps particularly from evaporites, by hot, deep-circulating meteoric water. In North America, most of these seem to have formed during or shortly after the late Paleozoic Appalachian-Ouchita-Marathon Orogeny. Mixing of the hot saline fluids with low salinity ground water was probably the immediate cause of metal precipitation in most instances. In others, such as Pine-Point, local reduction of sulfate in the fluids to sulfide may have caused precipitation.

NOTES

- Eclogite is a rock consisting primarily of Na-rich pyroxene and garnet that forms only at

high pressures. Compositionally these eclogites are similar to basalts, as are most.

- While this is typical, temperatures of 400°C or so have also been found. Most low-temperature vents waters, such as those on the GSC appear to be mixtures of 350°C hydrothermal fluid and ambient seawater, with mixing occurring at shallow depth beneath the seafloor. Although hydrothermal fluids with temperatures substantially above 400°C have not been found, there is abundant evidence from metamorphosed rocks that water-rock reactions occur at temperatures up to 700°C.
- While the mineral-water fractionation factors for quartz and carbonate are in the range of +4–+6 at these temperatures, the fractionation factor for anorthite and chlorite are close to zero, and that for magnetite is negative.

REFERENCES

- Boyd, S. R. and Pillinger, C. T. 1994. A preliminary study of $^{15}\text{N}/^{14}\text{N}$ in octahedral growth form diamonds. *Chemical Geology*, 116: 43–59, doi: 10.1016/0009-2541(94)90157-0.
- Boyd, S. R., Pineau, F. and Javoy, M. 1994. Modelling the growth of natural diamonds. *Chemical Geology*, 116: 29–42.
- Came, R. E., Eiler, J. M., Veizer, J., Azmy, K., Brand, U. and Weidman, C. R. 2007. Coupling of surface temperatures and atmospheric CO₂ concentrations during the Palaeozoic era. *Nature*, 449: 198–201, doi: 10.1038/nature06085.
- Chacko, T., Cole, D. and Horita, J. 2001. Equilibrium oxygen, hydrogen and carbon isotope fractionation factors applicable to geologic systems. In: *Stable Isotope Geochemistry*, Valley, J. W. (ed.). pp. 1–61. Washington: Mineralogical Society of America.
- Chaussidon, M., Albarède, F. and Sheppard, S. M. F. 1989. Sulphur isotope variations in the mantle from ion microprobe analyses of micro-sulphide inclusions. *Earth and Planetary Science Letters*, 92: 144–156.
- Chaussidon, M., Albarède, F. and Sheppard, S. M. F. 1987. Sulphur isotope heterogeneity in the mantle from ion microprobe measurements of sulphide inclusions in diamonds. *Nature*, 330: 242–244.
- Chiba, H., Chacko, T., Clayton, R. N. and Goldsmith, J. R. 1989. Oxygen isotope fractionations involving diopside, forsterite, magnetite, and calcite: application to geothermometry. *Geochimica et Cosmochimica Acta*, 53: 2985–2995.

- Craig, H., 1963. The isotopic composition of water and carbon in geothermal areas. In: *Nuclear Geology on Geothermal Areas*, Tongiorgi, E. (ed.). p. 17–53, Pisa: Consiglio Nazionale delle Ricerche Laboratorio di Geologia Nucleare.
- Criss, R. E. and Taylor, H. P. 1986. Meteorichydrothermal systems. In: *Stable Isotopes in High Temperature Geological Processes, Reviews in Mineralogy* 16, Valley, J. W., Taylor H. P. and O'Neil, J. R. (eds). p. 373–424, Washington: Mineralogical Society of America.
- DePaolo, D. J. 1981. Trace element and isotopic effects of combined wallrock assimilation and fractional crystallization. *Earth and Planetary Science Letters*, 53: 189–202, doi: 10.1016/0012-821X(81)90153-9.
- Eiler, J. M. and Schiano, P. 2000. Oxygen-isotope evidence for recycled crust in the sources of mid-ocean ridge basalts, *Nature*, 403: 530–533.
- Eiler, J. M., Farley, K. A., Valley, J. W., Hauri, E., Craig, H., Hart, S. R. and Stolper, E. 1997. Oxygen isotope variations in oceanic basalt phenocrysts, *Geochimica et Cosmochimica Acta*, 61: 2281–2293.
- Eldridge, C. S., Compston, W., Williams, I. S., Harris, J. W. and Bristow, J. W. 1991. Isotope evidence for the involvement of recycled sediment in diamond formation. *Nature*, 353: 649–653.
- Gao, Y., Vils, F., Cooper, K. M., Banerjee, N., Harris, M., Hoefs, J., et al. 2012. Downhole variation of lithium and oxygen isotopic compositions of oceanic crust at East Pacific Rise, ODP Site 1256. *Geochemistry, Geophysics, Geosystems*, 13: Q10001, doi:10.1029/2012gc004207.
- Garcia, M. O., Muenow, D. W., Aggrey, K. E. and O'Neil, J. R. 1989. Major element, volatile, and stable isotope geochemistry of Hawaaian submarine tholeiitic glasses, *Journal of Geophysical Research*, 94: 10525–10538.
- Gregory, R. T. and Taylor, H. P. 1981. An oxygen isotope profile in a section of Cretaceous oceanic crust, Samail Ophiolite, Oman: Evidence for $\delta^{18}\text{O}$ buffering of the oceans by deep (>5 km) seawater-hydrothermal circulation at mid-ocean ridges, *Journal of Geophysical Research*, 86: 2737–2755.
- Harmon, R. S. and Hoefs, J. 1995. Oxygen isotope heterogeneity of the mantle deduced from global $\delta^{18}\text{O}$ systematics of basalts from different geotectonic settings. *Contributions to Mineralogy and Petrology*, 120: 95–114, doi: 10.1007/bf00311010.
- Harmon, R. S., Barreiro, B. A., Moorbat, S., Hoefs, J., Francis, P. W. et al., 1984. Regional O-, S-, and Pb-isotope relationships in late Cenozoic calc-alkaline lavas of the Andean Cordillera, *Journal Of the Geological Society, London*, 141: 803–822.
- Hoefs, J. 1987, *Stable Isotope Geochemistry*, 3rd edn. Berlin: Springer Verlag, 241 p.
- Ito, E. and Stern, R. J. 1986. Oxygen and strontium isotopic investigations of subduction zone volcanism: the case of the Volcano Arc and the Marianas Island arc, *Earth and Planetary Science Letters*, 76: 312–320.
- Jackson, M. G., Hart, S. R., Koppers, A. A. P., Staudigel, H., Konter, J., Blusztajn, J., et al. 2007. The return of subducted continental crust in Samoan lavas. *Nature*, 448: 684–687, doi: 10.1038/nature06048.
- James, D. E. and Murcia, A. 1984. Crustal contamination in northern Andean volcanics, *Journal of the Geological Society of London*, 141: 823–830.
- James, D. E. 1981. The combined use of oxygen and radiogenic isotopes as indicators of crustal contamination. *Annual Reviews of Earth and Planetary Sciences*, 9: 311–344.
- Javoy, M. and Pineau, F. 1991. The volatile record of a “popping” rock from the Mid-Atlantic Ridge at 14° N: chemical and isotopic composition of the gas trapped in the vesicles, *Earth and Planetary Science Letters*, 107: 598–611.
- Javoy, M., Pineau, F. and Delorme, H. 1986, Carbon and nitrogen isotopes in the mantle, *Chemical Geology*, 57: 41–62.
- Javoy, M. 1977, Stable isotopes and geothermometry. *Journal of the Geological Society of London*, 133: 609–639.
- Kyser, K. T. and O'Neil, J. R. 1984. Hydrogen isotopes systematics of submarine basalts, *Geochimica Cosmochimica Acta*, 48: 2123–2133.
- Kyser, K. T. 1986, Stable isotope variations in the mantle. In: *Stable Isotopes in High Temperature Geological Processes*, Valley, J. W., Taylor, B. E. and O'Neil, J. R. (eds). p. 141–164, Washington: Mineralogical Society of America.
- MacGregor, I. D. and Manton, W. I. 1986. Robert Victor Eclogites: ancient oceanic crust, *Journal of Geophysical Research*, 91: 14063–14079.
- Magaritz, M., Whitford, D. J. and James, D. E. 1978. Oxygen isotopes and the origin of high $^{87}\text{Sr}/^{86}\text{Sr}$ andesites, *Earth and Planetary Science Letters*, 40: 220–230.
- Mattey, D. P. 1987. Carbon isotopes in the mantle. *Terra Cognita*, 7: 31–38.
- Mattey, D., Lowry, D. and Macpherson, C. 1994. Oxygen isotope composition of mantle peridotite. *Earth and Planetary Science Letters*, 128: 231–241, doi: 10.1016/0012-821X(94)90147-3.
- Marty, B. and Dauphas, N. 2003. The nitrogen record of crust-mantle interaction and mantle convection from Archean to present. *Earth and Planetary Science Letters*, 206: 397–410 (Elsevier).
- McCulloch, M. T., Gregory, R. T., Wasserburg, G. J. et al., 1981. Sm-Nd, Rb-Sr and $^{18}\text{O}/^{16}\text{O}$ isotopic systematics in an oceanic crustal section: evidence for the Samail ophiolite, *Journal of Geophysical Research*, 86: 2721.
- Muehlenbachs, C. and Furnas, H. 2003. Ophiolites as faithful records of the oxygen isotope ratio of ancient seawater: the Solund-Stavfjord Ophiolite Complex as a Late Ordovician example. In: *Ophiolites in Earth History*. London: Geological Society of London.
- Muehlenbachs, K. and Byerly, G. 1982. ^{18}O enrichment of silicic magmas caused by crystal fractionation at the Galapagos Spreading Center, *Contributions to Mineralogy and Petrology*, 79: 76–79.

- Muehlenbachs, K. and Clayton, R. 1972. Oxygen isotope geochemistry of submarine greenstones, *Canadian Journal of Earth Sciences*, 9: 471–478.
- Muehlenbachs, K., 1976. Oxygen isotope composition of the oceanic crust and its bearing on seawater, *Journal of Geophysical Research*, 81: 4365–4369.
- O’Neil, J. R., 1986. Theoretical and experimental aspects of isotopic fractionation. In: *Stable Isotopes in High Temperature Geologic Processes, Reviews in Mineralogy Volume 16*, Valley, J. W., Taylor, H. P. and O’Neil, J. R. (eds), Washington: Mineralogical Society of America, pp. 1–40.
- Ohmoto, H. and Rye, R. O. 1979. Isotopes of sulfur and carbon. In: *Geochemistry of Hydrothermal Ore Deposits*, H. Barnes (ed.). New York: John Wiley & Sons, Inc..
- Ohmoto, H. 1986. Stable isotope geochemistry of ore deposits, in *Stable Isotopes in High Temperature Geological Processes, Reviews in Mineralogy 16*, Valley, J. W., Taylor, H. P. and O’Neil, J. R. (eds). p. 491–560, Washington: Mineralogical Society of America.
- Poreda, R., Schilling, J. G. and Craig, H. 1986, Helium and hydrogen isotopes in ocean-ridge basalts north and south of Iceland, *Earth and Planetary Science Letters*, 78: 1–17.
- Sakai, H., Des Marais, D. J., Ueda, A. and Moore, J. G. 1984. Concentrations and isotope ratios of carbon, nitrogen, and sulfur in ocean-floor basalts, *Geochimica et Cosmochimica Acta*, 48: 2433–2442.
- Šoštaric, S. B., Palinkaš, L. A., Topa, D., Spangenberg, J. E. and Prochaska, W. 2011. Silver–base metal epithermal vein and listwaenite types of deposit Crnac, Rogozna Mts., Kosovo. Part I: Ore mineral geochemistry and sulfur isotope study. *Ore Geology Reviews*, 40: 65–80, doi: 10.1016/j.oregeorev.2011.05.002.
- Sheppard, S. M. F. and Harris, C. 1985. Hydrogen and oxygen isotope geochemistry of Ascension Island lavas and granites: variation with fractional crystallization and interaction with seawater. *Contributions to Mineralogy and Petrology*, 91: 74–81.
- Smyth, J. R., 1989. Electrostatic characterization of oxygen site potentials in minerals, *Geochimica et Cosmochimica Acta*, 53: 1101–1110.
- Taylor, H. P. and S. M. F. Sheppard, 1986. Igneous rocks: I. Processes of isotopic fractionation and isotope systematics, in *Stable Isotopes in High Temperature Geological Processes*, Valley, J. W., Taylor, H. P. and O’Neil, J. R. (eds). p. 227–271, Washington: Mineralogical Society of America.
- Taylor, H. P. Jr., 1968. The oxygen isotope geochemistry of igneous rocks, *Contributions to Mineralogy and Petrology*, 19: 1–71.
- Taylor, H. P. Jr., 1974. The application of oxygen and hydrogen studies to problems of hydrothermal alteration and ore deposition, *Economic Geology*, 69: 843–883.
- Taylor, H. P., 1980. The effects of assimilation of country rocks by magmas on $^{18}\text{O}/^{16}\text{O}$ and $^{87}\text{Sr}/^{86}\text{Sr}$ systematics in igneous rocks, *Earth and Planetary Science Letters*, 47: 243–254.
- Veizer, J., Ala, D., Azmy, K., Bruchschen, P., Buhl, D., Bruhn, F. et al. 1999. $^{87}\text{Sr}/^{86}\text{Sr}$, $\delta^{13}\text{C}$, and $\delta^{18}\text{O}$ evolution of Phanerozoic seawater. *Chemical Geological*, 161: 59–88.
- Woodhead, J. D., Harmon, R. S. and Fraser, D. G. 1987. O, S, Sr, and Pb isotope variations in volcanic rocks from the Northern Mariana Islands: implications for crustal recycling in intra-oceanic arcs, *Earth and Planetary Science Letters*, 83: 39–52.
- Workman, R. K., Eiler, J. M., Hart, S. R. and Jackson, M. G. 2008. Oxygen isotopes in Samoan lavas: Confirmation of continent recycling. *Geology*, 36: 551–554, doi: 10.1130/g24558a.1.
- Zhang, Y.-F., 1999. Calculation of oxygen isotope fractionation in minerals. *Episodes*, 22: 99–106.

SUGGESTIONS FOR FURTHER READING

- Alt, J. C. 2003. Stable isotopic composition of upper oceanic crust formed at a fast spreading ridge, ODP Site 801. *Geochemistry, Geophysics, Geosystems*, 4: 8908, doi: 10.1029/2002gc000400.
- Bottinga, Y. 1969. Carbon isotope fractionation between graphite, diamond, and carbon dioxide. *Earth and Planetary Science Letters*, 5: 301–307.
- Chaussidon, M., Sheppard, S. M. F. and Michard, A. 1991, Hydrogen, sulfur and neodymium isotope variations in the mantle beneath the EPR at 12°50'N. In: *Stable Isotope Geochemistry: A Tribute to Samuel Epstein*, Taylor, H. P., O’Neil, J. R. and Kaplan, I. R. (eds). p. 325–338, San Antonio: Geochemical Society.
- Des Marais, D. J. and Moore, J. G. 1984. Carbon and its isotopes in mid-oceanic basaltic glasses, *Earth and Planetary Science Letters*, 69: 43–57.
- Hofmann, A. W. and White, W. M. 1982. Mantle Plumes from ancient oceanic crust, *Earth and Planetary Science Letters*, 57: 421–436.
- Javoy, M., Pineau, F. and Demaiffe, D. 1984. Nitrogen and carbon isotopic composition in the diamonds of Mbaji Mayi (Zaire). *Earth and Planetary Science Letters*, 68: 399–412.
- Marty, B. and Jambon, A. 1987. C/3He in volatile fluxes from the solid Earth: implications for carbon geodynamics. *Earth and Planetary Science Letters*, 83: 16–26.
- Pineau, F. and Javoy, M. 1983. Carbon isotopes and concentrations in mid-ocean ridge basalts. *Earth and Planetary Science Letters*, 62, 239–257.

- Porcelli, D. R., O’Nions, R. K., Galer, S. J. G., Cohen, A. S. and Mattey, D. P. 1992. Isotopic relationships of volatile and lithophile trace elements in continental ultramafic xenoliths. *Contributions to Mineralogy and Petrology*, 110: 528–538.
- Trull, T., Nadeau, S., Pineau, F., Polv e, M. and Javoy, M. 1993. C-He systematics in hotspot xenoliths: Implications for mantle carbon contents and recycling. *Earth and Planetary Science Letters*, 118: 43–64.
- Valley, J. W. and Cole, D. R. (eds) 2001. *Stable Isotope Geochemistry, Reviews in Mineralogy Vol. 43*. Washington: Mineralogical Society of America.
- Wallmann, K. 2001. The geological water cycle and the evolution of marine $\delta^{18}\text{O}$ values. *Geochimica et Cosmochimica Acta*, 65: 2469–2485.

PROBLEMS

1. Šoštaric et al. (2011) measured the following $\delta^{34}\text{S}$ data on sphalerite (ZnS)-galena (PbS) pairs in a hydrothermal silver-base metal ore deposit in the Rogozna Mountains of Kosovo. Using the coefficients in Table 9.3, calculate the equilibration temperature for each pair.

	Sphalerite $\delta^{34}\text{S}$	Galena $\delta^{34}\text{S}$
3/2/V	2.9	0.4
3/6/V	4.2	1.7
12/1/V	4.2	1.2
6/1/IV	4.9	2.3
6/4/IV	4.3	2.9

2. Make a plot using Eqn. 9.7 similar to Figure 9.14 comparing AFC evolution where $\Delta = 0$ and $\Delta = +2$. Use a value of $R = 0.15$ in both cases and an initial $\delta^{18}\text{O} = 6$.
3. Plot the evolution of $\delta^{18}\text{O}$ versus $^{87}\text{Sr}/^{86}\text{Sr}$ in a magma undergoing assimilation-fractional crystallization. Assume the magma initially has $\delta^{18}\text{O} = 6\text{\textperthousand}$ and $^{87}\text{Sr}/^{86}\text{Sr} = 0.703$, that the assimilant has $\delta^{18}\text{O} = +18$ and $^{87}\text{Sr}/^{86}\text{Sr} = 0.720$. Use Sr concentrations for the initial magma and the assimilant of 500 and 100 ppm, respectively.
4. Figure 9.28 shows that $\delta^{18}\text{O}$ reaches a minimum at Site 1256 of $-3\text{\textperthousand}$ just above the base of the sheeted dike complex. Assuming that the bulk fractionation factor, Δ between water and rock is $+1.5\text{\textperthousand}$ and that the initial $\delta^{18}\text{O}$ of the water and rock is 0 and $+5.7\text{\textperthousand}$, respectively, estimate the effective water/rock ratio that these rocks experienced.
5. The fractionation between HS^- and H_2S has a temperature dependence of $\Delta = -0.06 \times 10^6/T^2$; that between SO_2 and H_2S is $\Delta = -0.5 + 4.7 \times 10^6/T^2$. Estimate the $\delta^{34}\text{S}$ of pyrrhotite (FeS) crystallizing in equilibrium with an H_2S fluid that in turn is equilibrium with magmatic sulfur with $\delta^{34}\text{S}$ at 850°C whose mole fraction ratio $\text{SO}_2/\text{H}_2\text{S}$ (R) is 0.1.
6. What would the R (mole fraction ratio $\text{SO}_2/\text{H}_2\text{S}$) have to be for pyrite to precipitate with $\delta^{34}\text{S} = +4.9$ from a magma at 700°C whose bulk $\delta^{34}\text{S}$ is 0? (Assume that the pyrite is in equilibrium with an H_2S fluid in equilibrium with the magma.) What is the $\delta^{34}\text{S}$ of that fluid? Comparing your result with Figure 9.37, roughly estimate the $\log f_{\text{O}_2}$ of the magma.

Chapter 10

Stable isotope geochemistry III: Low temperature applications

10.1 STABLE ISOTOPES IN PALEONTOLOGY, ARCHEOLOGY, AND THE ENVIRONMENT

10.1.1 Introduction

The isotopic composition of a given element in living tissue depends on: (1) the source of that element (e.g., atmospheric CO₂ versus dissolved CO₂; seawater O₂ versus meteoric water O₂), (2) the processes involved in initially fixing the element in organic matter (e.g., C₃ versus C₄ photosynthesis), and (3) subsequent fractionations as the organic matter passes up the food web. Besides these factors, the isotopic composition of fossil material will depend on any isotopic changes associated with diagenesis, including microbial decomposition. In this section, we will see how this may be inverted to provide insights into the food sources of fossil organisms, including man. This, in turn, provides evidence about the environment in which these organisms lived.

10.1.2 Isotopes and diet: You are what you eat

In Chapter 8 we saw that isotope ratios of carbon and nitrogen are fractionated during primary production of organic matter. Terrestrial C₃ plants have δ¹³C values between −23 and −34‰, with an average of about −27‰. The C₄ pathway involves a much smaller fractionation, so that C₄ plants have δ¹³C between −9 and −17‰, with an average of about −13‰. Marine plants, which

are all C₃, can utilize dissolved bicarbonate as well as dissolved CO₂. Seawater bicarbonate is about 8.5‰ heavier than atmospheric CO₂; as a result, marine plants average about 7.5‰ heavier than terrestrial C₃ plants. In contrast to the relatively (but not perfectly) uniform isotopic composition of atmospheric CO₂, the carbon isotopic composition of seawater carbonate varies due to biological processes. Because the source of the carbon they fix is more variable, the isotopic composition of marine plants is also more variable. Finally, marine cyanobacteria (blue-green algae) tend to fractionate carbon isotopes less during photosynthesis than do true algae, so they tend to average 2–3‰ higher in δ¹³C.

Nitrogen isotopes are, as we saw, also fractionated during primary uptake. Based on their source of nitrogen, plants may also be divided into two types: those that can utilize N₂ directly and those that utilize only “fixed” nitrogen as ammonia and nitrate. The former include the legumes (e.g., beans, peas, etc.) and marine cyanobacteria. The legumes, which are exclusively C₃ plants, utilize both N₂ (through symbiotic nitrogen-fixing bacteria in their roots) and fixed nitrogen, and have an average δ¹⁵N of +1‰, whereas modern nonleguminous plants average about +3‰. However, it seems likely that prehistoric nonleguminous plants were more positive, averaging perhaps +9‰, because the isotopic composition of present soil nitrogen has been affected by the use of chemical fertilizers. For both groups, there

was probably a range in $\delta^{15}\text{N}$ of ± 4 or 5\textperthousand , because the isotopic composition of soil nitrogen varies and there is some fractionation involved in uptake. Marine plants have $\delta^{15}\text{N}$ of $+7 \pm 5\text{\textperthousand}$, whereas marine cyanobacteria have $\delta^{15}\text{N}$ of $-1 \pm 3\text{\textperthousand}$. Figure 10.1 summarizes the isotopic composition of nitrogen and carbon in the various classes of photosynthetic organisms (autotrophs).

DeNiro and Epstein (1978) studied the relationship between the carbon isotopic composition of animals and their diet. (Most of the animals in this study were perhaps of little direct paleontological interest, being small and soft-bodied. DeNiro and Epstein studied small animals for a practical reason: they are easier to analyze than a large animal such as a horse.) Figure 10.2 shows that there is little further fractionation of carbon by animals and thus the carbon isotopic composition of animal tissue closely reflects that of their diet. DeNiro and Epstein (1978) estimated that carbon in animal tissue is on average about 1\textperthousand heavier than their diet. Mice, although not analyzed whole and not shown in Figure 10.2, were also included in the study. Various tissues from mice had $\delta^{13}\text{C}$ within $\pm 2\text{\textperthousand}$ of their diet, so the relationships in Figure 10.2 extend to vertebrates as well. DeNiro and Epstein found that the same species has a different isotopic composition when fed a different diet. Conversely, different species had similar

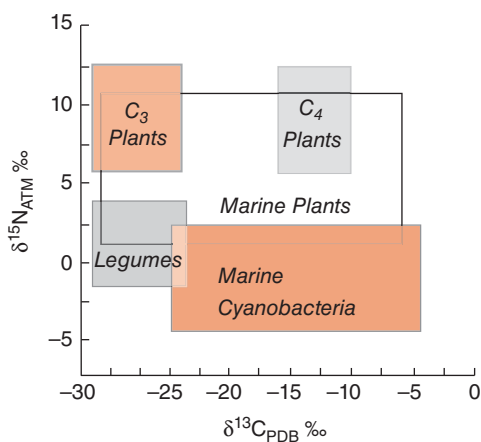


Figure 10.1 Relationship between $\delta^{13}\text{C}$ and $\delta^{15}\text{N}$ among the principal classes of autotrophs. (Source: DeNiro (1987). Reproduced with permission of American Scientist.)

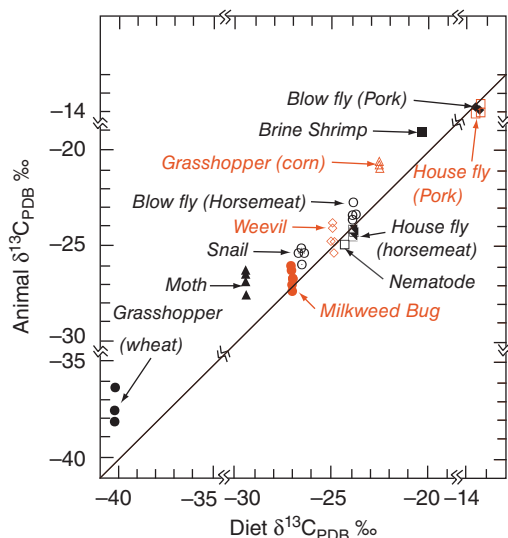


Figure 10.2 Relationship between $\delta^{13}\text{C}$ in animals and that of their diets. When a species was given more than one diet, that diet is shown in parentheses. (Source: DeNiro and Epstein (1978). Reproduced with permission of Elsevier.)

isotopic compositions when fed the same diet. Thus, diet seems to be the primary control on the isotopic composition of animals. Subsequent work by McCutchan et al. (2003) found an average shift in $\delta^{13}\text{C}$ of animals relative to their diet of $+0.5 \pm 0.13$.

The small fractionation between animal tissue and diet is a result of the slightly weaker bond formed by ^{12}C compared to ^{13}C . The weaker bonds are more readily broken during respiration, and, not surprisingly, the CO_2 respired by most animals investigated was slightly lighter than their diet. Thus, only a small fractionation in carbon isotopes occurs as organic carbon passes up the food chain, about $+1\text{\textperthousand}$ at each step in the chain. Terrestrial food chains are usually not more than three trophic levels long, implying a maximum further fractionation of $+3\text{\textperthousand}$. Marine food chains can have up to seven trophic levels, implying a maximum carbon isotope difference between primary producers and top predators of 7\textperthousand . These differences are smaller than the range observed in primary producers. In a similar study, DeNiro and Epstein (1981) found that $\delta^{15}\text{N}$ of animal tissue is related to the $\delta^{15}\text{N}$ of the animal's diet, but is typically $3\text{--}4\text{\textperthousand}$ higher than that of the diet.

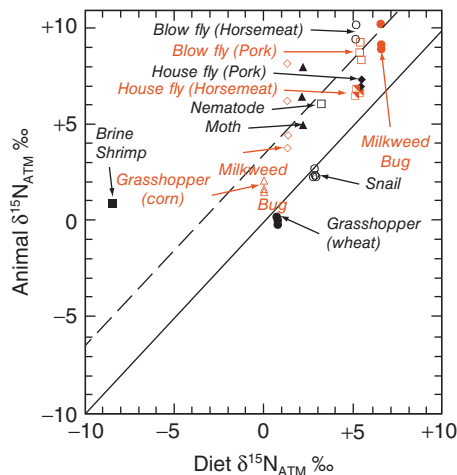


Figure 10.3 Relationship between $\delta^{15}\text{N}$ in animals and that of their diet. Animals typically have 3–4‰ heavier nitrogen than their diet. Dashed line is the isotopic composition plus 3.5‰. When a species was given more than one diet, that diet is shown in parentheses. (Source: DeNiro and Epstein (1981). Reproduced with permission of Elsevier.)

(Figure 10.3). Thus, in contrast to carbon, significant fractionation of nitrogen isotopes will occur as nitrogen passes up the food chain.

Schoeninger and DeNiro (1984) studied the carbon and nitrogen isotopic composition of bone collagen in animals. Their findings reflected just the relationships expected from the work of DeNiro and Epstein (1978, 1981): in primary herbivores, carbon in bone collagen was a few per mil heavier than the isotopic composition of plants, and $\delta^{15}\text{N}$ increased by about 3‰ at each trophic level. More recent work by McCutchan et al. (2003) found that the trophic shift in $\delta^{15}\text{N}$ was $+1.4 \pm 0.21\text{‰}$ for carnivores raised on invertebrates, $+3.3 \pm 0.26\text{‰}$ for carnivores raised on other high-protein diets and was $+2.2 \pm 0.30\text{‰}$ for herbivores. Marine vertebrates tend to have more positive $\delta^{15}\text{N}$ than do their terrestrial counterparts because they generally feed at a higher trophic level. The primary producers in the ocean are generally microscopic algae. Most marine herbivores are also small (zooplankton); there are very few marine vertebrate herbivores (anchovies are an example). As we noted, marine food chains are longer than terrestrial ones and, since nitrogen isotope fractionation occurs at

each level, the top marine predators have more positive $\delta^{15}\text{N}$ than terrestrial top predators. These relationships are summarized in Figure 10.4.

Apatite in bone appears to undergo isotopic exchange with meteoric water once it is buried, but bone collagen and tooth enamel appear to be robust and retain their original isotopic compositions. Tooth enamel, in which carbon is present as carbonate, however, is systematically 12–15‰ heavier than carbon in organic tissue. (Such a fractionation is, of course, expected, and consistent with the observation that carbonate is always heavier than organic carbon.) Collagen typically has carbon about 4‰ heavier than diet. These results mean that the nitrogen and carbon isotopic composition of fossil bones and teeth can be used to reconstruct the diet of fossil animals.

10.1.3 Carbon isotopes and the evolution of horses and grasslands

Horses (Family Equidae) have been around for 58 million years. Beginning in the early Miocene, a major radiation took place and the number of genera in North America increased from three at 25 Ma to 12 at 10 Ma. It subsequently fell at the end of the Miocene, and the last North American species became extinct in the Holocene. A major change in dental morphology, from low-crowned to high crowned, accompanied the Miocene radiation. For nearly 100 years, the standard textbook explanation of this dental change was that associated with a change in feeding from leaf browsing to grass grazing. Grasses contain enough silica to make them quite abrasive, thus a high crowned tooth would last longer in a grazing animal and would therefore be favored in horse's evolution as it switched food sources. The change in horse diet was thought to reflect the evolution of grassland ecosystems (or biomes). This line of reasoning led to the conclusion that grasslands first became important biomes in the Miocene.

Carbon isotope ratios provide the first opportunity to test this hypothesis. Grasses of tropical and temperate regions are almost exclusively C₄ plants. C₃ grasslands occur only in high latitude regions. In the North American prairie, for example, C₃ grasslands become important only north of

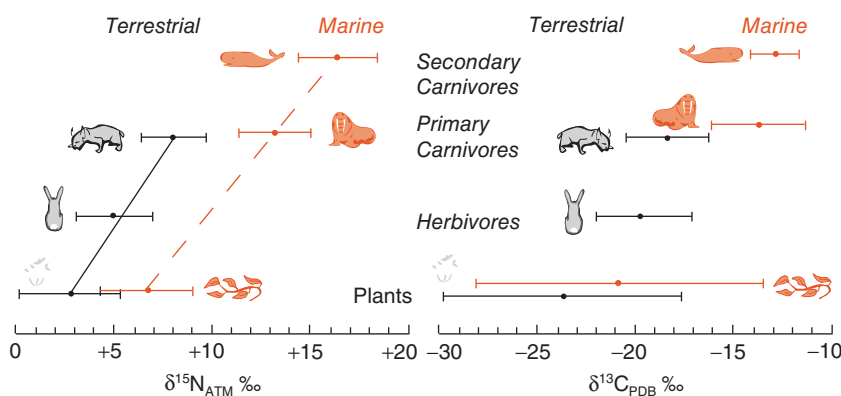


Figure 10.4 Values of $\delta^{13}\text{C}$ and $\delta^{15}\text{N}$ in various marine and terrestrial organisms. (Source: Schoeninger and DeNiro (1984). Reproduced with permission of Elsevier.)

the US-Canadian border (Figure 10.5). The appearance of grasslands inferred from the evolution of horse teeth implies a change from a predominantly C_3 to a predominantly C_4 photosynthetic pathway and a corresponding shift in the $\delta^{13}\text{C}$ of the biomass in these regions. Since the carbon isotopic composition of animals reflects that of their diet, and since the $\delta^{13}\text{C}$ of dental enamel appears to record the $\delta^{13}\text{C}$ of the animal, the change in horse dentition should also be reflected in a change in the carbon isotopic composition of

those teeth if the change in dentition were related to a change in diet.

Wang et al. (1994) carried out such a test by analyzing the carbon isotopic composition of dental enamel from fossil horse teeth of Eocene through Pleistocene age. They found a sharp shift in the isotopic composition of the teeth consistent with a change in diet from C_3 to C_4 vegetation, but it occurred later than the change in dental morphology (Figure 10.6). The change in dental morphology begins in the mid-Miocene (about 18 Ma), while shift in $\delta^{13}\text{C}$ occurs at around 7 Ma. This leads to an interesting dilemma. Which change, morphology or carbon isotopic composition actually reflects the appearance of the grassland biome? It is possible that the change in dental morphology is unrelated to the evolution of grasslands? If that is the case, it is difficult to understand the change in dental morphology. Alternatively, grasslands may have appeared in mid-Miocene and only subsequently become dominated by C_4 grasses.

If the latter interpretation is correct, it raises the question of what evolutionary pressure caused the change from C_3 to C_4 photosynthesis in tropical and temperate grasses. An important observation in that respect is that C_4 grasslands appear to have become important in both North America and Asia at about the same time (7 Ma). Indeed, the first evidence for a shift from C_3 dominant to C_4 dominant ecosystems came from an observed change in the $\delta^{13}\text{C}$ of soil carbonate in Pakistan (Quade et al., 1989). Quade et al. (1989) first interpreted this as a response to the uplift of the Tibetan Plateau and the

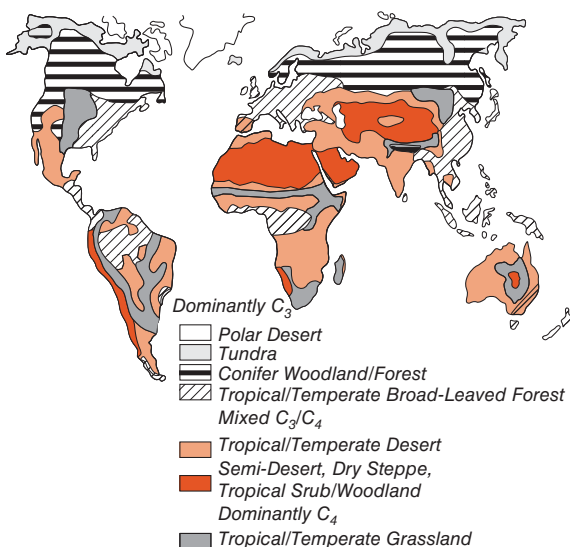


Figure 10.5 Present global distribution of C_3 and C_4 vegetation. (Source: Cerling and Quade (1993). Reproduced with permission of John Wiley & Sons.)

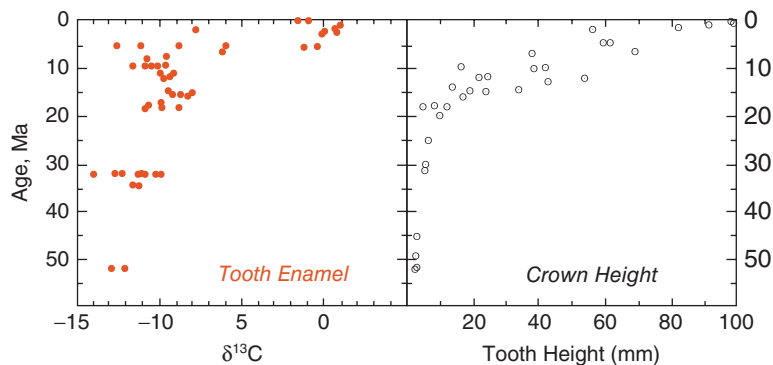


Figure 10.6 $\delta^{13}\text{C}$ and crown height in North American fossil horses as a function of age. (Source: Wang et al. (1994). Reproduced with permission of Elsevier.)

development of the Monsoon. However, other evidence, including oxygen isotope data from Pakistani soil carbonates, suggests the Monsoons developed about a million years earlier (at about 8 Ma). The synchronicity of the C_4 grass becoming dominant in the grasslands in Asia and North America (Figure 10.7) suggests a global cause, while the Monsoons are a regional phenomenon. Furthermore, subsequent ^{14}C studies of the teeth of horses and other mammals revealed that, at least in Tibet, uplift of the plateau was associated with a shift from C_4 to C_3 vegetation (Wang et al., 2006).

Though there has been some speculation that the C_4 photosynthetic pathway may have evolved as early as the Cretaceous, the oldest direct fossil evidence for C_4 plants (plants with enlarged bundle-sheath cells) is late Miocene;

that is, the same age as the observed $\delta^{13}\text{C}$ increase. Thus the isotopic shift may date the evolution of C_4 photosynthesis. C_4 photosynthesis involves only relatively minor modification of plant enzymes and structures and it occurs in diverse, distantly related families. It may, therefore, have evolved independently in many families (Ehleringer, et al. 1991). This also suggests some global environmental change that favored C_4 photosynthesis.

Several groups suggested that the appearance of C_4 grasses reflects a drop in the concentration of atmospheric CO_2 in the Miocene. In the C_3 photosynthetic pathway, Rubisco can catalyze not only the fixation of carbon in phosphoglycerate, but also the reverse reaction where CO_2 is released, a process called photorespiration. When concentrations of CO_2 are high, the forward reaction is favored and the C_3 pathway is more efficient overall than the C_4 pathway. At low CO_2 concentrations, however, the C_4 pathway, in which CO_2 is first transported into bundle-sheath cells, is more efficient, as the concentration in bundle-sheath cells is maintained at around 1000 ppm (Figure 10.8). Thus, under present conditions, C_4 plants have a competitive advantage. At higher CO_2 conditions, C_3 plants are more efficient. There is some evidence that Eocene CO_2 concentrations were much higher than present (perhaps 800 ppm as opposed to 250 ppm pre-Industrial Revolution), and that concentrations dropped dramatically during the Miocene (however, other isotope evidence, which we will discuss in a subsequent section, suggests the drop in

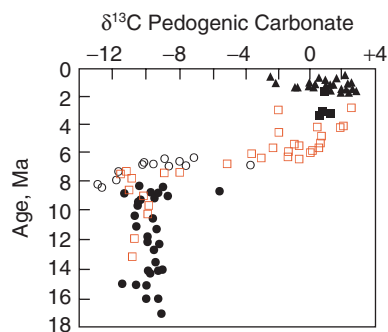


Figure 10.7 $\delta^{13}\text{C}$ in carbonates from paleosols of the Potwar Plateau in Pakistan. The change in $\delta^{13}\text{C}$ may reflect the evolution of C_4 plants. (Source: Quade et al. (1989). Reproduced with permission of Nature Publishing Group.)

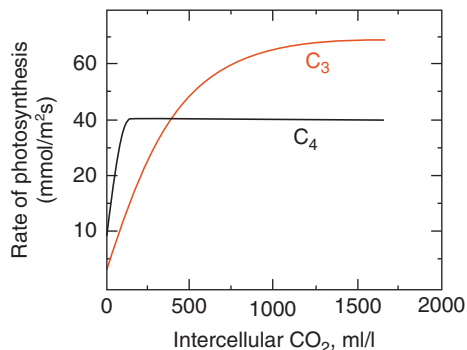


Figure 10.8 Rate of photosynthesis as a function of intercellular CO₂ concentrations in C₄ and C₃ plants. At concentrations of atmospheric CO₂ that prevailed before the Industrial Revolution, C₄ plants would have had a competitive advantage. At concentrations above the present level, C₃ plants are more efficient. (Source: Ehleringer et al. (1991). Reproduced with permission of Elsevier.)

CO₂ concentrations occurred in the Eocene). Such a drop would give C₄ plants a competitive advantage. This would be particularly true in the warm climates where C₄ plants dominate because the rate of photorespiration is temperature dependent.

An interesting epilogue to these studies is that of MacFadden et al., (1999) who analyzed both carbon isotopes and abrasion patterns of six species of early Pliocene (~5 Ma) horses from Florida. All six species bore the high-crowned dental hallmark of grazers. Some species grazed solely on C₄ grasses, but others, notably including *D. mexicanus*, a close relative of the modern horse, browsed C₃ shrubs and trees. The high crowned dental morphology had been inherited from their ancestors and when the species switched back to eating browse, its teeth did not change. This is an example that evolution is often “irreversible.”

10.1.4 Isotopes, archeology, and paleodiets

The differences in nitrogen and carbon isotopic composition of various foodstuffs and the preservation of these isotope ratios in bone collagen provides a means of determining what ancient peoples ate. The Tehuacan valley in the state of Puebla, Mexico contains a remarkable archeological record of

human habitation going back nearly 10,000 years. Consequently, it had been the subject of classic studies on the origins of Western Hemisphere agriculture by R. S. MacNeish in the 1960s. The first inhabitants, the Ajeroado phase, were small bands of nomadic hunter-gathers. The first evidence for plant cultivation came in the El Riego phase with evidence of experimentation with plantings of squash, chili, amaranth, and possibly wild maize (teosinte). DeNiro and Epstein (1981) analyzed the isotopic composition of bone collagen from human remains of Tehuacan inhabitants and found that maize (a C₄ plant) became an important part of their diet as early as 4000 BC, whereas archeological investigations had concluded maize did not become important in their diet until perhaps 1500 BC (Figure 10.9a). In addition, there seemed to be steady increase in the dependence on legumes (probably beans) from 6000 BC to 1000 AD and a more marked increase in legumes in the diet after 1000 AD (Figure 10.9b).

A dependence on C₄ vegetation, or on herbivores that fed on it, is certainly not new in human history. Carbon isotopic studies have shown that human ancestors *Australopithecus africanus* and *Homo ergaster* had diets of which was on average 25% derived from C₄ plants (Lee-Thorp et al., 2000; van der Merwe et al., 2003). The fraction of diet derived from C₄ plants was highly variable: from nearly 0–50% for different individuals. The dependence of C₄-derived nutrition is consistent with the idea that human evolution involved, in part, leaving the forests (which are composed entirely of C₃ plants) and moving out into the savannah, which dominated by C₄ grasses. δ¹³C of both plant biomarkers (organic chemicals that can be associated with a specific biological source) in Gulf of Aden sediments and of soil increased over the last 3 Ma, indicating an expansion of East African grasslands. deMenocal (2011) points out that there is a particularly rapid change in these δ¹³C values occurs around 2.6 Ma, which coincides with the appearance of the genus *Homo* and the extinction of *Australopithecus afarensis* (“Lucy”).

Mashed grain and vegetable charred onto potsherds provides an additional record of the diets of ancient peoples. Hasdorff and DeNiro (1985) found that vegetable matter subjected to conditions similar to burial in

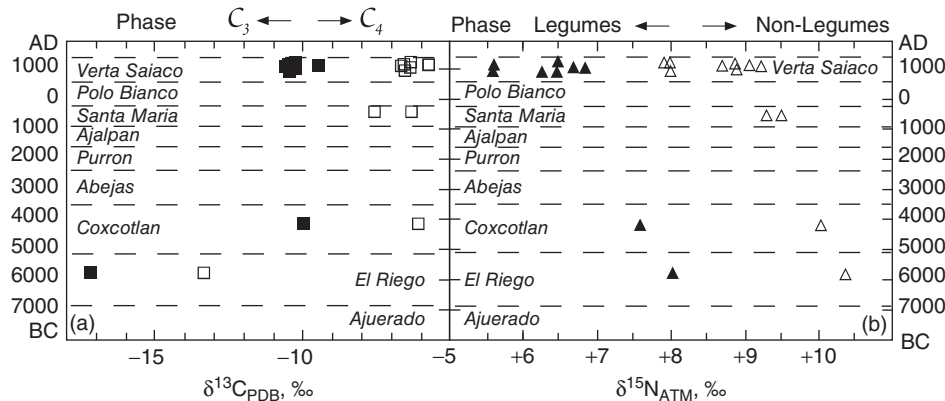


Figure 10.9 $\delta^{13}\text{C}$ and $\delta^{15}\text{N}$ in human bone collagen (open symbols) and calculated values in the diet (closed symbols) of the Tehuacan Indians as a function of age. The $\delta^{13}\text{C}$ data indicate a predominance of C_4 plants (probably maize) in all phases after the El Riego period. The $\delta^{15}\text{N}$ data indicate the importance of legumes in the diet became increasingly important with time. (Source: DeNiro and Epstein (1981). Reproduced with permission of Elsevier.)

soil underwent large shifts in $\delta^{15}\text{N}$ and $\delta^{13}\text{C}$ but did not undergo such shifts if the vegetable matter was burned or charred. The carbonization (charring, burning) process itself produced only small (2 or 3‰) fractionations. Since these fractionations are smaller than the range of isotopic compositions in various plant groups, they are of little significance. In the process of cooking, plant remains can become charred onto the pots in which they are cooked. Since potsherds are among the most common artifacts recovered in archaeological sites, this provides a second value means of reconstructing the diets of ancient peoples.

Figure 10.10 summarizes the results obtained in a number of studies of bone collagen and potsherds (DeNiro, 1987). Studies of several historical populations, including Eskimos and the Tlinglit Indians of the Northwest USA, were made as a control. The isotope data show that the diet of Neolithic Europeans consisted entirely of C_3 plants and herbivores feeding on them, in contrast to the Tehuacan Indians, who depended mainly on C_4 plants. Prehistoric peoples of the Bahamas and Denmark depended both on fish and on agriculture. In the case of Mesolithic Denmark, other evidence indicates the crops were C_3 , and the isotope data bear this out. Although there is no corroborating evidence, the isotope data suggest the Bahamians also depended on C_3 rather than C_4 plants. The

Bahamians had lower $\delta^{15}\text{N}$ because the marine component of their diet came mainly from coral reefs. Nitrogen fixation is particularly intense on coral reefs, which leads to ^{15}N depletion of the water, and consequently, of reef organisms. A limitation of this approach, however, is that animals derive their nitrogen from proteins they consume. Protein-poor foods, such as potatoes, which can provide a significant proportion of dietary calories, are effectively invisible to nitrogen isotope analysis.

A taste for “seafood,” including freshwater fish, seems to be one way in which the earliest fully modern human of Europe differed from Neanderthals. The former arrived in Europe about 40,000 years ago, and rapidly displaced the Neanderthals, who had been there for the previous 100,000 years or more. Carbon and nitrogen isotopic compositions of Neanderthal bone collagen over that time suggests they hunted herbivores who fed on C_3 plants (there were no edible C_4 plants in Europe). Bone collagen of Paleolithic modern humans from Europe has higher $\delta^{15}\text{N}$ and lower $\delta^{13}\text{C}$ than that of Neanderthals they displaced. Comparison of human isotopic compositions with those of possible prey species, such as bison, ibex, and red deer, led Richards and Trinkaus (2009) to conclude that humans must have included significant amounts of aquatic or marine foods in their diet. This is particularly true of bones found at Pećstra cu

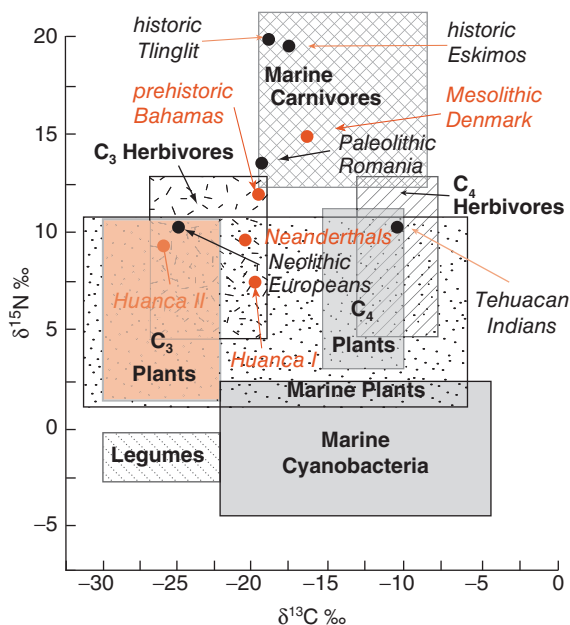


Figure 10.10 $\delta^{13}\text{C}$ and $\delta^{15}\text{N}$ of food stuffs and diets reconstructed from bone collagen and vegetable matter charred onto pots by DeNiro and colleagues. The Huanca people were from the Upper Mantaro Valley of Peru. Data from pot sherds of the Huanca I period (AD 1000–1200) suggest both C₃ and C₄ plants were cooked in pots, but on C₃ plants during the Huanca II period (AD 1200–1470). Also shown in the average bone collagen 13 Neanderthals from Europe and a 40,000 year old modern human from Pećstra cu Oase, Romania (Richards and Trinkaus, 2009). (Source: DeNiro (1987). Reproduced with permission of American Scientist.)

Oase, Romania, which at 40,000 years, are the oldest dated modern human remains found in Europe to date.

Oxygen in combination with strontium isotope ratios has also proved useful in archeological research. An excellent example is the case of the “Iceman,” the remains of a copper age human that had been frozen and mummified in an Alpine glacier for 5200 years before his discovery in 1991. The body was discovered by Austrian hikers near the crest of the Alps and Austrian authorities took custody of it, but it actually had been found just across the border in Italy. Consequently, there were questions as to whether the Iceman was Austrian or Italian, as well as

a jurisdictional dispute between the Austrian and the Italians. Müller et al. (2003) analyzed oxygen, carbon, and strontium, and lead isotope ratios in the Iceman’s bones and teeth. The isotopic composition of tooth enamel is fixed in childhood, whereas bone material is renewed continually and hence its isotopic composition reflects the environment over the last several years of life. Rain falling on the Italian side of the Alps is derived from the relatively warm Mediterranean and is isotopically heavier than the rain in Austria, derived from the relatively cold North Atlantic. The Iceman’s tooth enamel and bones had $\delta^{18}\text{O}_{\text{SMOW}}$ close to −11, implying he grew up and lived most of his adulthood in the Eisack/Isarco, Rienz, Hohlen, or Non valleys of the Italian side. Comparison of Sr and Pb isotopic compositions of the Iceman’s bones with rocks outcropping in the region confirm his Italian origin and suggest that the Feldthurns archeological site in the Eisack valley was most likely his home.

10.1.5 Carbon isotopes and the earliest life

We saw in Chapter 8 that carbon fixation, whether through chemosynthesis or photosynthesis, produces a large negative isotopic fractionation of carbon. This large fractionation occurs in the Benson–Calvin cycle that is common to all autotrophs. Consequently, $\delta^{13}\text{C}$ values of −20‰ or less in reduced carbon compounds are generally interpreted as evidence of biologic origin of those compounds. Schidlowski (1988) first reported $\delta^{13}\text{C}$ as low as −26‰ in samples from Godthåbsfjord region of West Greenland that are definitely older than 3.5 Ga. In 1996, Mojzsis and others reported $\delta^{13}\text{C}$ between −20 and −50‰ in graphite inclusions in grains of apatite in 3.85 Ga in banded-iron formations (BIFs) from Akilia Island in that same area of West Greenland (book cover photo). In 1999, Røsing reported $\delta^{13}\text{C}$ of −19‰ from graphite in turbiditic and pelagic metasedimentary rocks from the Isua greenstone belt in the same area (Figure 10.11). These rocks are thought to be older than 3.7 Ga.

Schidlowski (1988), Mojzsis et al. (1996), and Røsing (1999) all interpreted these negative $\delta^{13}\text{C}$ as evidence of a biogenic origin of the carbon, and therefore that life existed

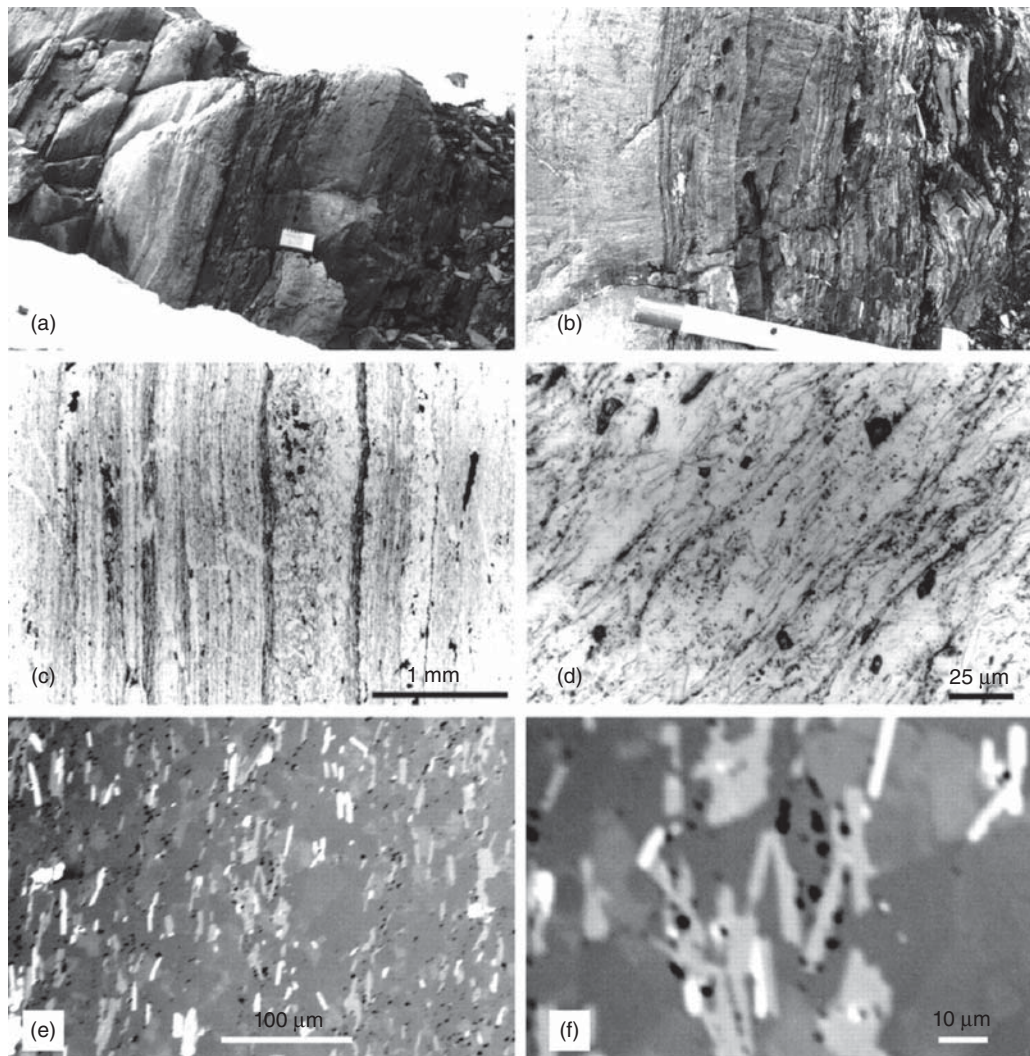


Figure 10.11 Photographs and photomicrographs of the turbidite sediments from Isua, West Greenland. E and F are electron microscope photographs of graphite globules in the samples. (Source: Røsing (1999). Reproduced with permission of AAAS.)

on Earth at this time. This is older than the earliest physical fossil evidence of life, which occurs in rocks 3.5 Ga old. Furthermore, the earliest part of this time coincides with the *late heavy bombardment* of the Moon, and a similar asteroid bombardment is thought to have affected the Earth at this time – presumably, making life difficult for any organisms that did exist. Perhaps not surprisingly then, the interpretation of life older than 3.7 Ga has been controversial.

There are several reasons for the controversy, but all ultimately relate to the extremely complex geological history of the area. The

geology of the Godthåbsfjord region includes not only the early Archean Isua greenstone belt and Itsaq gneiss complex, but also rocks of middle and late Archean age as well. Most rocks are multiply and highly deformed and metamorphosed and the exact nature, relationships, and structure of the precursor rocks are difficult to decipher.

Røsing et al. (1996) demonstrated that at least some of the carbonates sampled by Schidlowski (1988) cross-cut pre-existing lamination and argued that they are veins deposited by metamorphic fluid flow. Van Zuilen et al. (2003) argue that the graphite

originated by thermal decomposition of siderite, in reactions such as:



followed by disproportionation of the CO:



The difference in $\delta^{13}\text{C}$ they observed between the graphite and carbonate phases, roughly 5–10‰, is consistent with equilibrium fractionation in the range of 300–600°C.

On Akilia Island, the locality studied by Mojzsis et al. (1996), the predominant Amitsoq gneisses are metamorphosed dioritic to granitic plutons that surround fragments of metasedimentary rocks that include conglomerates, BIFs, metacherts, and felsic metasediments with graded bedding. The precursors are thought to have been deposited in a shallow marine environment; they were subsequently metamorphosed to nearly granulite facies. Both the ortho- and paragneisses were intruded by the mafic Ameralik dikes, which are now amphibolites. The region was again deformed, folded and metamorphosed in the late Archean. Structural relationships are unclear and although some dates are as old as 3.87 Ga, the age of the metasediments is far less clear. Indeed, the apatites themselves have Pb-Pb ages of 1.5 Ga, but it is unclear whether this is a crystallization or metamorphic age. Even if this is a recrystallization age, it is possible that (1) the depositional age of the metasediments is as young as 3.6 or 3.7 Ga and (2) the apatites and their graphite inclusions are secondary and grew during the early Archean metamorphism.

Samples studied by Røsing (1999) come from some of the least deformed rocks in the region. The rocks have been metamorphosed only to schist facies and original sedimentary structures are apparent. The $\delta^{13}\text{C}$ in these rocks is fairly uniform, and distinctly more negative than $\delta^{13}\text{C}$ of graphite (−11‰) and carbonate (−2.5‰) from carbonate veins in the region. Røsing argues that not only that the negative $\delta^{13}\text{C}$ is evidence of a biogenic origin of the carbon, but, from sedimentological considerations, that source of the carbon was photosynthetic planktonic organisms. Røsing (1999) reported a Sm-Nd age of 3.78 ± 0.81 Ga for the sediments and the volcanic rocks upon which they were deposited, although

the scatter in the isochron is relatively large. Cross-cutting intrusive rocks, however, are well dated at 3.71 Ga and provide a minimum age.

While Røsing's data do perhaps reflect the best case for life from the Isua area, this age remains 160 Ma younger than the age claimed by Mojzsis et al. (1996). Furthermore, $\delta^{13}\text{C}$ values are not as negative as the data of Mojzsis (1996) and it remains unclear whether the fractionation of ~16.5‰ between the graphite and local carbonate might have resulted from abiologic processes.

10.1.6 Tracing methane contamination in drinking water

While rarely abundant, methane is ubiquitous on the surface of the Earth. It is present in the atmosphere (present concentration: 1.8 ppm) where it is an important greenhouse gas. As we noted in Chapter 8, biogenic methane is produced naturally by methanogens in reducing environments such as swamps and anoxic marine sediments, as well as in landfills, rice paddies, and in the guts of animals by fermentation and reduction of CO_2 . Thermogenic methane, which is the main component of natural gas, is produced in buried organic-rich sediments by thermal cracking of hydrocarbons. The latter represents an increasingly important resource for an energy-hungry world. Natural gas has the advantage of producing significantly less CO_2 and far fewer pollutants such as nitrogen and sulfur oxides, hydrocarbons, particulates, and so on that cause, acid rain, smog, and have adverse effects on human health. In this sense, it is a clean fuel. In the past, natural gas has been recovered (“produced” in industrial jargon) from porous reservoir rocks from which it can readily be pumped, often as a by-product of petroleum production. New technologies including horizontal drilling and hydrofracturing (in which water and sand is forced into the formation at high pressure to increase porosity), however, have enabled production of natural gas from impermeable source rocks, typically shales, where it has been trapped for millions or hundreds of millions of years. Whereas in the conventional petroleum and natural gas production, a limited number of wells are concentrated atop natural subsurface reservoirs where gas and

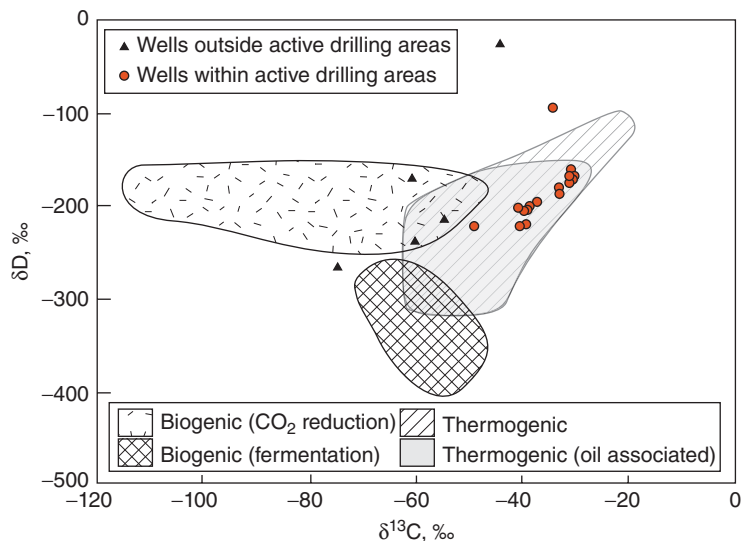


Figure 10.12 Isotopic composition of methane in rural drinking water in Pennsylvania and New York compared with fields for methane of various sources from Figure 8.22. Data from Osborne et al. (2011).

petroleum has concentrated in “traps,” “shale gas” is recovered by drilling many wells over broad areas. Hydrofracturing combined with this broad dispersal of wells has raised a number of environmental concerns, particularly in relatively densely populated areas, such as the northeastern USA.

One of these concerns is the presence of methane in drinking water. Methane is not toxic in the usual sense, but it is a potential explosion and asphyxiation hazard. Residents have complained of methane in their drinking water (and indeed, there are anecdotal reports of residents igniting water flowing from their faucets) and filed lawsuits against the gas companies. Gas companies respond that methane occurs naturally in soil and rocks through which groundwater flows, and that therefore methane in drinking water is not necessarily a result of drilling operations. Osborn et al. (2011) sampled water from 60 residential water wells in New York and Pennsylvania. They found measurable methane was present in 85% of these wells. However, in water wells more than 1 km distant from a natural gas well, methane concentrations averaged 1.1 mg/L whereas concentrations averaged 19.3 mg/L in water wells within 1 km of a natural gas well. More significantly, in water wells near natural gas wells, $\delta^{13}\text{C}$ of methane averaged $-37\text{\textperthousand}$ whereas in those not near natural

gas wells $\delta^{13}\text{C}$ averaged $-54\text{\textperthousand}$. Figure 10.12 compares the carbon and hydrogen isotopic compositions in these samples with fields for methane from various sources (Figure 8.22). Water samples taken near natural gas wells fall within the field of thermogenic methane while those from other wells generally fall within the biogenic field. Clearly, thermogenic methane from natural gas wells is contaminating water in nearby wells. It should be pointed out, however, that (1) in many wells where the presence of thermogenic methane could be documented from isotopic compositions, methane concentrations were not elevated above background levels, and (2) the study showed that in a few wells with elevated methane, the methane was of biogenic origin and not due to contamination by natural gas drilling.

10.2 STABLE ISOTOPES IN PALEOCLIMATOLOGY

10.2.1 Introduction

At least since the classic work of Louis Agassiz in 1840, geologists have contemplated the question of how the Earth’s climate might have varied in the past. But until 1947, they had no means of quantifying paleotemperature changes. In that year, two papers were published; one by Jacob Bigeliesen and Maria

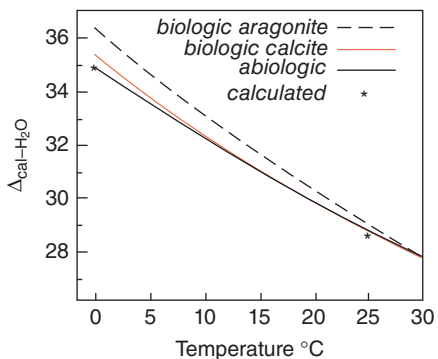


Figure 10.13 Fractionation of oxygen isotopes between calcium carbonate and water as a function of temperature for biologically precipitated calcite (mollusks), biologically precipitated aragonite, and abiologically precipitated calcite (Epstein et al., 1953; Craig, 1965). Also shown are the calculated fractionation factors from Urey (1947) for 0°C and 25°C.

Meyer, entitled “Calculation of equilibrium constants for isotopic exchange reactions” and one by Harold Urey entitled “The thermodynamic properties of isotopic substances,” which effectively initiated the field of stable isotope geochemistry. Urey calculated the temperature dependence of oxygen isotope fractionation between calcium carbonate and water and proposed that the isotopic composition of carbonates could be used as a paleothermometer (Urey, 1947). Urey’s post-doctoral associate Samuel Epstein and several students tested Urey’s idea by growing mollusks in water of various temperatures (Epstein et al., 1953). They found the following empirical relationship:

$$\Delta = \delta^{18}\text{O}_{\text{cal}} - \delta^{18}\text{O}_{\text{water}} = 15.36 - 2.673(16.52 + T)^{0.5} \quad (10.1)$$

This equation was in good, though not exact, agreement with the theoretical prediction of Urey (Figure 10.13). The field of paleothermometry began with a paper based on these principles by J. M. McCrae (1950).

10.2.2 The record of climate change in deep sea sediments

It is perhaps ironic that while glaciers are a continental phenomenon, our best record

of them is from the oceans. In part, this is because each period of continental glaciation largely destroys the record of the previous one. In contrast, deep-sea sediments are generally not disturbed by glaciation. Thus, while much was learned by studying the effects of Pleistocene glaciation in Europe and North America, much was left unresolved: questions such as the precise chronology, cause, temperatures, and ice volumes (ice area could of course be determined, but this is only part of the problem). The questions of temperature chronology were largely resolved through isotopic studies of deep-sea biogenic sediments. Dating of coral reefs provided the best estimates of ice volume. These, as we shall see, provided the essential clue as to cause. While that question too has been largely resolved, the details are still being worked out.

The principles involved in paleoclimatology are simple. As Urey formulated it, the isotopic composition of calcite secreted by organisms should provide a record of paleo-ocean temperatures because the fractionation of oxygen isotopes between carbonate and water is temperature dependent. In actual practice, the problem is somewhat more complex because the isotopic composition of the shell, or test, of an organism will depend not only on temperature, but also on the isotopic composition of water in which the organism grew, vital effects (i.e., different species may fractionate oxygen isotopes somewhat differently), and post-burial isotopic exchange with sediment pore water. As it turns out, the latter two are usually not very important for carbonates, at least for late Tertiary/Quaternary sediments, but the former is.

10.2.3 The quaternary δ¹⁸O record

The first isotopic work on deep-sea sediment cores with the goal of reconstructing the temperature history of Pleistocene glaciations was by Emiliani (1955), who was then a student of Urey at the University of Chicago. Emiliani analyzed δ¹⁸O in foraminifera from piston cores from the world ocean. Remarkably, many of Emiliani’s findings are still valid today, albeit in modified form. He concluded that the last glacial cycle had ended about 16,000 years ago, and found that temperature increased steadily between that time and about 6000 years ago. He also recognized

14 other glacial–interglacial cycles over the last 600,000 years (we now recognize only about six major glacial intervals over this time), and found that these were global events, with notable cooling even in low latitudes. He concluded that bottom water in the Atlantic was 2°C cooler, but that bottom water in the Pacific was only 0.8°C cooler during glacial periods. He also concluded that the fundamental driving force for Quaternary climate cycles was variations in the Earth's orbital parameters.

Emiliani had the field of oxygen isotope paleoclimatology virtually to himself until about 1970. In retrospect, it is remarkable how much Emiliani got right. By that time, others saw the value of this approach and got into the act. Their work resulted in significant modifications to some of Emiliani's conclusions. One of the main improvements was simply refining the time scale using paleomagnetic stratigraphy and, later, some of the geochronological tools we discussed earlier in this book (^{10}Be , Th isotopes, etc.). In his initial work, Emiliani had only ^{14}C dating available to him, and he dated older sections simply by extrapolating sedimentation rates based on ^{14}C dating.

Another important modification to Emiliani's work was a revision of the magnitude of temperature variations. Emiliani had realized that the isotopic composition of the ocean would vary between glacial and interglacial times as isotopically light water was stored in glaciers, thus enriching the oceans in ^{18}O . Assuming a $\delta^{18}\text{O}$ value of about $-15\text{\textperthousand}$ for glacial ice, Emiliani estimated that this factor accounted for about 20% of the observed variations. The remainder he attributed to the effect of temperature on isotope fractionation. However, Shackleton and Opdyke (1973) argued that storage of isotopically light water in glacial ice was actually the main effect causing oxygen isotopic variations in biogenic carbonates, and that the temperature effect was only secondary. Their argument was based on the observation that nearly the same isotopic variations occurred in both planktonic (surface-dwelling) and benthic (bottom dwelling) foraminifera. Because of the way in which the deep water of the ocean is formed and circulates, Shackleton and Opdyke argued that deep-water temperature should not vary much between glacial and interglacial cycles.

Analyzing tests of both benthic and planktonic organisms allowed a better calculation of temperature changes. The isotopic composition of tests of benthic organisms, that is, those growing in deep water, could be used to determine the change in seawater isotopic composition. This would allow a more precise calculation of surface water temperature change from the isotopic composition of planktonic tests (shells of organisms growing in surface water).

Nevertheless, the question of just how much of the variation is deep-sea carbonate sediments is due to ice build-up and how much is due to the effect of temperature on fractionation continued to be debated. After Shackleton and Opdyke's work, climate modeling suggested deep-water temperatures might indeed vary, though probably not as much as Emiliani had calculated. It is now clear that the average $\delta^{18}\text{O}$ of glacial ice is less than $-15\text{\textperthousand}$, as Emiliani had assumed. Typical values for Greenland ice are -30 to $-40\text{\textperthousand}$ (relative to SMOW) and as much as $-50\text{\textperthousand}$ for Antarctic ice.

If the exact isotopic composition of ice and the ice volume were known, it would be a straightforward exercise to calculate the effect of continental ice build-up on ocean isotopic composition. For example, the present volume of continental ice is $27.5 \times 10^6 \text{ km}^3$, while the volume of the oceans is $1350 \times 10^6 \text{ km}^3$. Assuming glacial ice has a mean $\delta^{18}\text{O}$ of $-30\text{\textperthousand}$ relative to SMOW, we can calculate the $\delta^{18}\text{O}$ of the hydrosphere as $-0.6\text{\textperthousand}$ (neglecting freshwater reservoirs, which are small). At the height of the Wisconsin Glaciation, the volume of glacial ice is thought to have increased by $42 \times 10^6 \text{ km}^3$, corresponding to a lowering of sea level by 125 m. If the $\delta^{18}\text{O}$ of ice was the same then as now ($\sim -30\text{\textperthousand}$), we can readily calculate that the $\delta^{18}\text{O}$ of the ocean would have increased by $1.59\text{\textperthousand}$. This is illustrated in Figure 10.14.

To see how much this affects estimated temperature changes, we can use Craig's¹ (1965) revision of the Epstein calcite-water geothermometer:

$$T^\circ\text{C} = 16.9 - 4.2\Delta_{\text{cal-water}} + 0.13(\Delta_{\text{cal-water}})^2 \quad (10.2)$$

According to this equation, the fractionation should be $33\text{\textperthousand}$ at 20°C . At 14°C , the fractionation is $31.5\text{\textperthousand}$. If a glacial foram

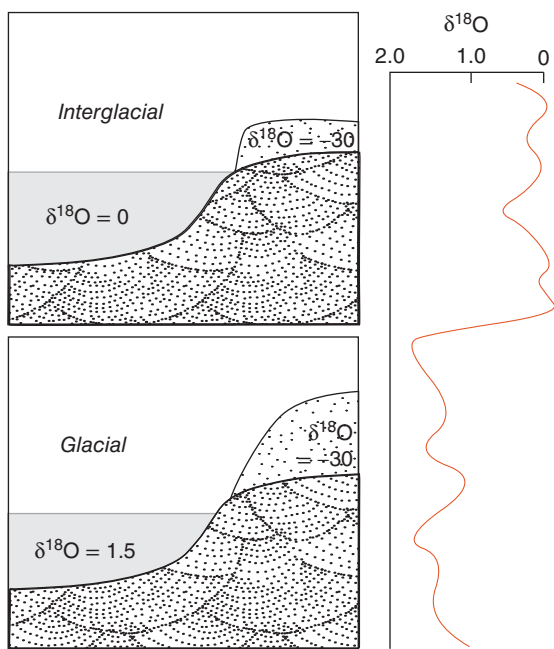


Figure 10.14 Cartoon illustrating how $\delta^{18}\text{O}$ of the ocean changes between glacial and interglacial periods. (Source: White (2003). Reproduced with permission of John Wiley & Sons.)

shell were 2‰ lighter, Emiliani would have made a correction of 0.5‰ for the change in oxygen isotopic composition of seawater and attributed the remainder of the difference, 1.5‰, to temperature. He would have concluded that the ocean was 6°C cooler. However, if the change in the isotopic composition of seawater is actually 1.5‰, leaving only a 0.5‰ difference due to temperature, the calculated temperature difference is only about 2°C. Thus the question of the volume of glacial ice, and its isotopic composition needed to be resolved before $\delta^{18}\text{O}$ in deep-sea carbonates could be used to calculate paleotemperatures. It is now generally assumed that the $\delta^{18}\text{O}$ of the ocean changed by 1.5‰ between glacial and interglacial periods, but second order local variations also occur (due to evaporation and precipitation), leaving some uncertainty in exact temperatures. Comparison of sea-level curves derived from dating of terraces and coral reefs indicate that each 0.011‰ variation in $\delta^{18}\text{O}$ represents a 1 m change in sea-level.

By now, thousands of deep-sea cores have been analyzed for oxygen isotope ratios.

Though most reveal the same general picture, the $\delta^{18}\text{O}$ curve varies from core to core. In addition to the changing isotopic composition of the ocean, the $\delta^{18}\text{O}$ in a given core will depend on several other factors. (1) The temperature in which the organisms grew. (2) The faunal assemblage, as the exact fractionation will vary from organism to organism. For this reason, $\delta^{18}\text{O}$ analyses are often performed on a single species. However, these “vital effects” are usually small, at least for planktonic foraminifera. (3) Local variations in water isotopic composition. This is important in the Gulf of Mexico, for example. Melt-water released at the end (termination) of glacial stages flooded the surface of the Gulf of Mexico with enough isotopically light melt-water to significantly change its isotopic composition relative to the ocean as a whole. (4) Sedimentation rate varies from core to core, so that $\delta^{18}\text{O}$ as a function of depth in the core will differ between cores. Changes in sedimentation rate at a given locality will distort the appearance of the $\delta^{18}\text{O}$ curve. (5) Bioturbation, that is, burrowing activity of seafloor animals, which may smear the record.

10.2.4 The cause of quaternary glaciations

For these reasons, correlating from core to core and can sometimes be difficult and constructing a “standard” $\delta^{18}\text{O}$ record is a non-trivial task. Nevertheless, it is the first step in understanding the global climate change signal. Figure 10.15 shows the global $\delta^{18}\text{O}$ record constructed by averaging five cores (Imbrie, et al., 1984). A cursory examination of the global curve shows a periodicity of approximately 100,000 years. The same periodicity was apparent in Emiliani’s initial work and led him to conclude that the glacial-interglacial cycles were due to variations in the Earth’s orbital parameters. These are often referred to as the Milankovitch cycles, after M. Milankovitch, a Serbian astronomer who argued they caused the ice ages in the early part of the twentieth century².

Three parameters describe these variations: e : eccentricity, ϵ : obliquity (tilt), and precession : $\epsilon \sin \omega$, where ω is the longitude of perihelion (perihelion is the Earth’s closest approach to the Sun). The *eccentricity*

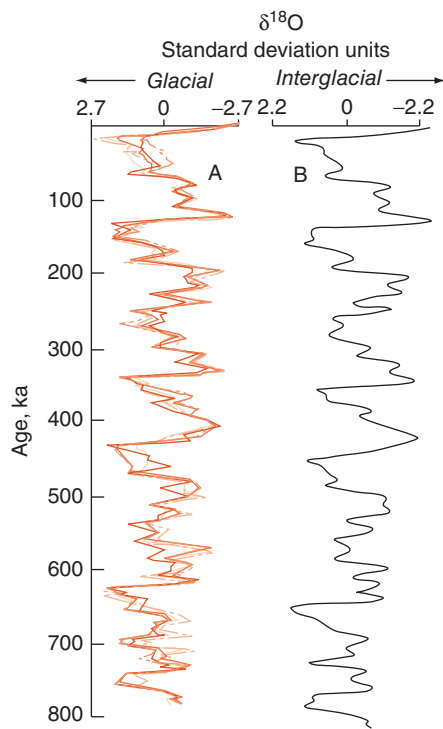


Figure 10.15 A. “Stacking of five cores” selected by Imbrie et al. (1984). Because the absolute value of $\delta^{18}\text{O}$ varies in from core to core, the variation is shown in standard deviation units. B. Smoothed average of the five cores in A. (Source: After Imbrie et al., 1984.)

(i.e., the degree to which the orbit differs from circular) of the Earth’s orbit about the Sun, and the degree of tilt, or *obliquity*, of the Earth’s rotational axis vary slightly. Precession refers to the change in the direction in which the Earth’s rotational axis tilts when it is closest to the Sun (perihelion). These variations, which are illustrated in Figure 10.16, affect the pattern of solar radiation, or *insolation*, that the Earth receives. Changes in these parameters have negligible effect on the total insolation, but they do affect the pattern of insolation. For example, tilt of the rotational axis determines seasonality, and the latitudinal gradient of insolation. It is this gradient that drives atmospheric and oceanic circulation. If the tilt is small, seasonality will be reduced (cooler summers, warmer winters). Precession relative to the eccentricity of the Earth’s orbit also affects seasonality. For example, the Earth is presently closest to the Sun in January. As a result, Northern Hemisphere

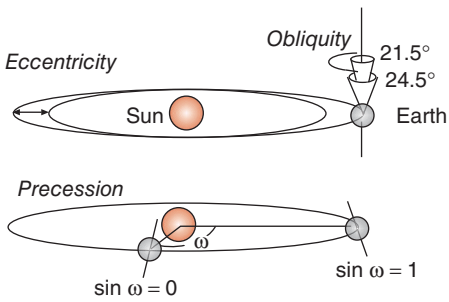


Figure 10.16 Cartoon illustrating the “Milankovitch parameters.” The eccentricity is the degree the Earth’s orbit departs from circular. Obliquity is the tilt of the Earth’s rotation axis with respect to the plane of the ecliptic. Obliquity varies between 21.5° and 24.5° . Precision is the variation in the direction of tilt at the Earth’s closest approach to the Sun (perihelion). The parameter ω is the angle between the Earth’s position on June 21 (summer solstice), and perihelion. (Source: White (2013). Reproduced with permission of John Wiley & Sons.)

winters (and Southern Hemisphere summers) are somewhat milder than they would be otherwise. For a given latitude and season, precession will result in a $\pm 5\%$ difference in insolation. While the Earth’s orbit is only slightly elliptical, and variations in eccentricity are small, these variations are magnified because insolation varies with the inverse square of the Earth-Sun distance. These variations can change the insolation and the average annual equator-to-pole gradient.

Variation in tilt approximates a simple sinusoidal function with a period of 41,000 yrs. Variations in eccentricity can be approximately described with characteristic period of 100,000 years. In actuality variation in eccentricity is more complex, and is more accurately described with periods of 400,000, 123,000, 85,000, and 58,000 yrs. Similarly, variation in precession has characteristic periods of 23,000 and 19,000 yrs.

While Emiliani suspected $\delta^{18}\text{O}$ variations were related to variations these “Milankovitch” parameters, the first quantitative approach to the problem was that of Hayes et al. (1976). They applied Fourier analysis to the $\delta^{18}\text{O}$ curve, a mathematical tool that transforms a complex variation such as that in Figure 10.15 to the sum of a

series of simple sine functions. Hayes et al. then used spectral analysis to show that much of the spectral power of the $\delta^{18}\text{O}$ curve occurred at frequencies similar to those of the Milankovitch parameters. The most elegant and convincing treatment, however, was that of Imbrie (1985). Imbrie's treatment involved several refinements and extension of the earlier work of Hayes et al. (1976). First, he used improved values for Milankovitch frequencies. Second, he noted these Milankovitch parameters might vary with time, as might the climate system's response to them. The Earth's orbit and tilt are affected by the gravitational field of the Moon and other planets. In addition, other astronomical events, such as bolide impacts, can affect them. Thus, Imbrie treated the first and second 400,000 years of Figure 10.15 separately. The power spectrum for these two parts of the $\delta^{18}\text{O}$ curve is shown in Figure 10.17.

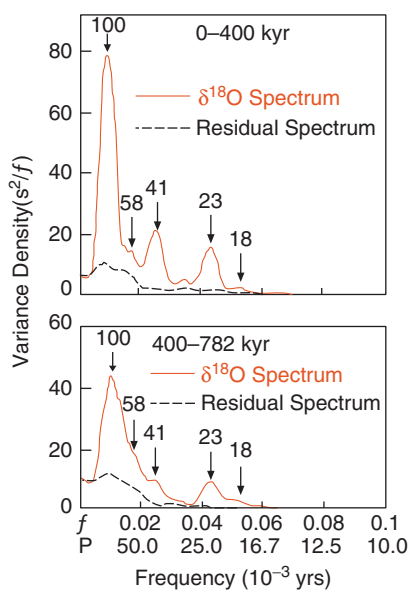


Figure 10.17 Power spectrum of the composite $\delta^{18}\text{O}$ curve shown in Figure 10.13 as a function of frequency. Peaks in the spectrum correspond with the frequencies of the variations of the Milankovitch parameters. The residual spectrum shows the variance remaining after subtracting a phase and gain model based on the Milankovitch parameters. The upper figure shows the power spectrum for 0–400 kyr BP, the lower figure for the period 400–782 kyr. (Source: After Imbrie, 1985.)

Imbrie observed that climate does not respond instantaneously to forcing. For example, maximum temperatures are not reached in Ithaca until mid or late July, 3–4 weeks after the maximum insolation, which occurs on June 21. Thus, there is a *phase* difference between the forcing function (insolation) and climatic response (temperature). Imbrie also pointed out that the climate might respond differently to different forcing functions. As an example, he used temperature variations in the Indian Ocean, which respond both to annual changes in insolation and to semiannual changes in ocean upwelling. The response to these two forcing functions differs in different localities. The extent to which climate responds to a particular forcing function is the *gain*. The phase lag may also differ from locality to locality. Mathematically, the climatic response can be expressed as:

$$y = g_1(x_1 - \phi_1) + g_2(x_2 - \phi_2) \quad (10.3)$$

where y is the climatic response (temperature) x_1 and x_2 are the two forcing functions (insolation and upwelling), g_1 and g_2 are the gains associated with them and ϕ_1 and ϕ_2 are the phase lags).

Imbrie (1985) constructed a model for response of global climate (as measured by the $\delta^{18}\text{O}$ curve) in which each of the six Milankovitch forcing functions was associated with a different gain and phase. The values of gain and phase for each parameter were found statistically by minimizing the residuals of the power spectrum (Figure 10.17). Table 10.1 gives the essential parameters of the model. σ_x is the strength of each forcing function, and σ_y is the strength of the response (given in meters of sea level reduction), k is the coefficient of coherency, g is the gain (σ_y/σ_x), and ϕ_1 is the phase difference between input function and the climatic response. The resulting model is shown in comparison with the data for the past 400,000 years and the next 25,000 years in Figure 10.18. The model has a correlation coefficient, r , of 0.88 with the data. Thus about r^2 , or 77%, of the variation in $\delta^{18}\text{O}$, and therefore presumably in ice volume, can be explained Imbrie's Milankovitch model. The correlation for the period 400,000–782,000 yrs is somewhat poorer, around 0.80, but nevertheless impressive. Imbrie's work has,

Table 10.1 Gain and phase model of Imbrie (1985).

Frequency band	σ_y (m)	σ_x (u)	k (m/u)	g ka	ϕ
e ₁₂₃	19.5	0.167	0.58	68	-5
e ₉₅	19.3	0.250	0.83	64	-3
e ₅₉	12.2	0.033	0.79	292	-12
ϵ	15.0	0.394	0.92	35	-9
p_{23}	13.0	0.297	0.95	42	-6
p_{18}	5.3	0.154	0.81	28	-3

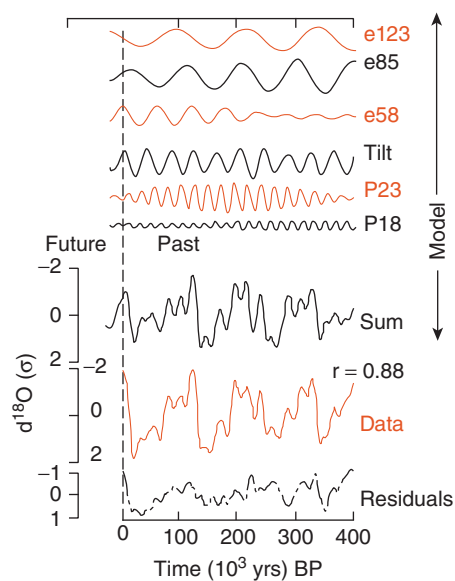


Figure 10.18 Gain and phase model of Imbrie relating variations in eccentricity, tilt, and precession to the oxygen isotope curve. Top shows the variation in these parameters over the past 400,000 and next 25,000 years. Bottom shows the sum of these functions with appropriated gains and phases applied and compares them with the observed data. (Source: After Imbrie (1985).)

of course, not been the last word on this and models of this type have become more sophisticated in succeeding decades (summarized, for example, in reviews by Berger, 1992; Ruddiman, 2006; and Berger, 2013).

Since variations in the Earth's orbital parameters do not affect the average annual insolation the Earth receives, but only its pattern in space and time, one might ask how this could cause glaciation. The key factor seems to be the insolation received during summer

by high northern latitudes. This is, of course, the area where large continental ice sheets develop. The Southern Hemisphere, except for Antarctica, is largely ocean, and therefore not subject to glaciation. Glaciers apparently develop when summers are not warm enough to melt the winter's accumulation of snow.

Nevertheless, the total variation in insolation is small, and not enough by itself to cause the climatic variations observed. Apparently, there are feedback mechanisms at work that serve to amplify the fundamental Milankovitch forcing function. One of these feedback mechanisms was identified by Agassiz, and that is ice albedo, or reflectance. Snow and ice reflect much of the incoming sunlight back into space. Thus as glaciers advance, they cause further cooling. Any additional accumulation of ice in Antarctica, however, does not result in increased albedo, because the continent is fully ice covered even in non-glacial time, hence the dominant role of northern hemisphere insolation in driving climate cycles. Establishing the role of other feedback mechanisms is a matter of much current research. Isotope geochemistry provides some interesting insights into two of these; ocean circulation and carbon dioxide, and we discuss them in the subsequent sections.

10.2.5 Carbon isotopes, ocean circulation, and climate

As we noted, the Milankovitch variations change only the distribution of solar energy received by the Earth, not the total amount. If this were the only factor in climate change, we would expect that the glaciation in the Southern and Northern Hemispheres would be exactly out of phase. This, however, is not the case. Thus, there must be feedback mechanisms at work capable of producing globally synchronous climate variation. Broecker, (1984 and subsequent papers) argued that one of these was the deep circulation of the ocean.

The role of surface ocean in climate is well understood: for example, the south-flowing California Current keeps the West Coast of the USA relatively dry and maintains more moderate temperatures in coastal regions than they would otherwise be. The role of the deep, or *thermohaline*, circulation of the oceans is less obvious, but perhaps no less important.

Whereas the surface ocean circulation is wind-driven, the deep circulation is driven by density, which is in turn controlled by temperature and salinity.

In the present ocean, most deep ocean water masses “form” in high latitudes. Once these deep-water masses form, they do not return to the surface for nearly a thousand years. The principal site of deep-water formation today is the Southern Ocean where the Antarctic Intermediate Water (AAIW) is formed in the Antarctic Convergence and Antarctic Bottom Water (AABW), the densest of ocean water masses, is formed near the coast of Antarctica, particularly in the Weddell Sea. A lesser amount of deep water is also formed in the Labrador, Greenland, and Norwegian Seas of the far northern Atlantic when warm, salty water from the Gulf of Mexico and the Mediterranean is strongly cooled during winter; this water mass is called North Atlantic Deep Water (NADW). After formation, this water sinks to the bottom of the ocean and flows southward. Today, it is the deepest and densest water mass in the North Atlantic. In the South Atlantic, the somewhat cold and denser AABW flows northward beneath the NADW, which is in turn overlain by AAIW.

Formation of deep water thus involves loss of thermal energy by the ocean to the atmosphere and the present thermohaline circulation of the oceans keeps high latitude climates milder than they would otherwise be. In particular, energy extracted from the Atlantic Ocean water in the formation of NADW keeps the European climate relatively mild.

We saw in Chapter 8 that $\delta^{13}\text{C}$ is lower in deep water than in surface water (Figure 8.18). This results from biological cycling: photosynthesis in the surface waters discriminates against ^{13}C , leaving the dissolved inorganic carbon of surface waters with high $\delta^{13}\text{C}$, while oxidation of falling organic particles rich in ^{12}C lowers $\delta^{13}\text{C}$ in deep water: in effect, ^{12}C is “pumped” from surface to deep water more efficiently than ^{13}C . $\delta^{13}\text{C}$ values in the deep water are not uniform, varying with the “age” of the deep water: the longer the time since the water was at the surface, the more enriched it becomes in ^{12}C and the lower the $\delta^{13}\text{C}$. Since this is also true of total inorganic carbon and nutrients such as PO_4 and NO_3 , $\delta^{13}\text{C}$ correlates negatively with nutrient and ΣCO_2 concentrations. NADW has high $\delta^{13}\text{C}$ because it

contains water that was recently at the surface (and hence depleted in ^{12}C by photosynthesis). Deep water is not formed in either the Pacific or the Indian Oceans; all deep waters in those oceans flow in from the Southern Ocean. Hence deep water in the Pacific, being rather “old” has low $\delta^{13}\text{C}$. AABW is a mixture of young NADW, which therefore has comparably high $\delta^{13}\text{C}$, and recirculated Pacific deep water and hence has lower $\delta^{13}\text{C}$ than NADW. Thus, these water masses can be distinguished on the basis of $\delta^{13}\text{C}$.

Examining $\delta^{13}\text{C}$ in benthic foraminifera in cores from a variety of locations, Oppo and Fairbanks (1987) concluded that production of NADW was lower during the last glacial maximum and increased to present levels in the interval between 15,000 and 5000 years ago. Figure 10.19 shows an example of data from core RC13–229, located in the South Atlantic. $\delta^{13}\text{C}$ values decrease as $\delta^{18}\text{O}$ increases. As we saw in the previous sections, $\delta^{18}\text{O}$ in marine carbonates is a measure of glacial ice volume and climate. As the climate warmed at the end of the last glacial interval, $\delta^{13}\text{C}$ values in bottom water in the South Atlantic increased, reflecting an increase in the proportion of NADW relative

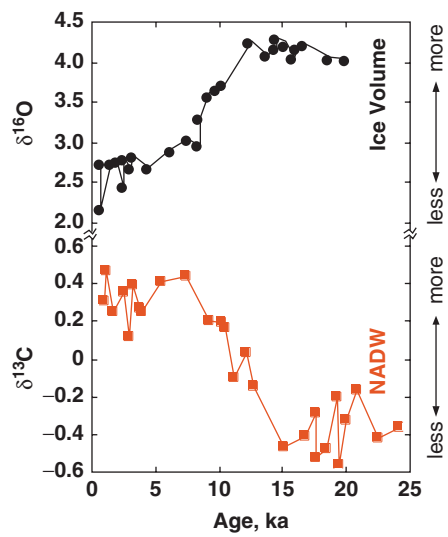


Figure 10.19 Variation in $\delta^{18}\text{O}$ and $\delta^{13}\text{C}$ in benthic foraminifera from core RC13–229 from the eastern South Atlantic. $\delta^{13}\text{C}$ data suggest the proportion of NADW in this region increased as the climate warmed. Data from Oppo and Fairbanks (1987).

to AABW in this region. From $\delta^{13}\text{C}$ variations in Mediterranean and Central Atlantic cores, Oppo and Fairbanks (1987) also concluded that the production of MIW was greater during the last glacial maximum. Thus the mode of ocean circulation apparently changes between glacial and interglacial times; this change may well amplify the Milankovitch signal.

Subsequent carbon isotope studies of benthic foraminifera have established that deep circulation in the Atlantic was much different than it is today (Figure 10.20). Rather than formation of cold, dense NADW (characterized by heavy carbon) in the far northern Atlantic, a less dense water mass called “Glacial North Atlantic Intermediate Water” or GNAIW formed further south in the Atlantic. Rather than sinking to the

bottom of the North Atlantic, it sunk only to depths of 1500 m or so and flowed southward above the north-flowing glacial AABW, characterized by light carbon, which penetrated all the way into the North Atlantic. Today, production of NADW releases heat to the atmosphere, warming it. In the absence of NADW production in glacial times, the North Atlantic region, and Europe in particular, would have been much colder. This is further evidence that NADW production in an important positive feedback amplifying the primary “Milankovitch” signal.

10.2.6 The tertiary marine $\delta^{18}\text{O}$ record

Imbrie's (1985) analysis suggests that the climate system's response to Milankovitch forcing has changed significantly even

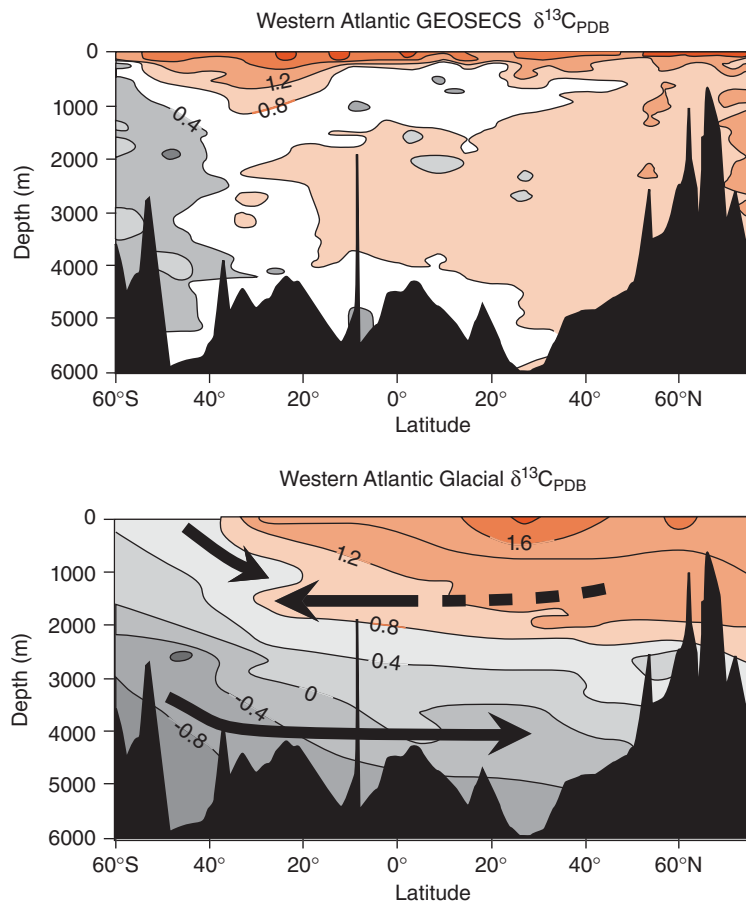


Figure 10.20 Cross-section of $\delta^{13}\text{C}$ the North Atlantic today and during glacial times. As discussed in the text, different water masses have different $\delta^{13}\text{C}$ signatures. (Source: Curry and Oppo (2005). Reproduced with permission of John Wiley & Sons.)

over the last 800,000 years. The present glacial-interglacial cycles began only 2 million years ago, yet the orbital variations responsible for Milankovitch forcing should be more or less stable over tens of millions of years. They should provide a steady and, hence, predictable pacing of climate change. Indeed, this pattern can be seen in high-resolution marine isotopic records, such as Figure 10.21. The amplitude of the isotopic variations,

however, have not been constant, but rather have increased with time, particularly since the beginning of the Pliocene (about 5 million years ago). Interestingly, the importance of eccentricity and obliquity in forcing climate appears to have changed over time. During the Pliocene and early Pleistocene the 41,000 yr obliquity component appears to be dominant, and this appears to be the case in the early Oligocene (~30–35 Ma) as well

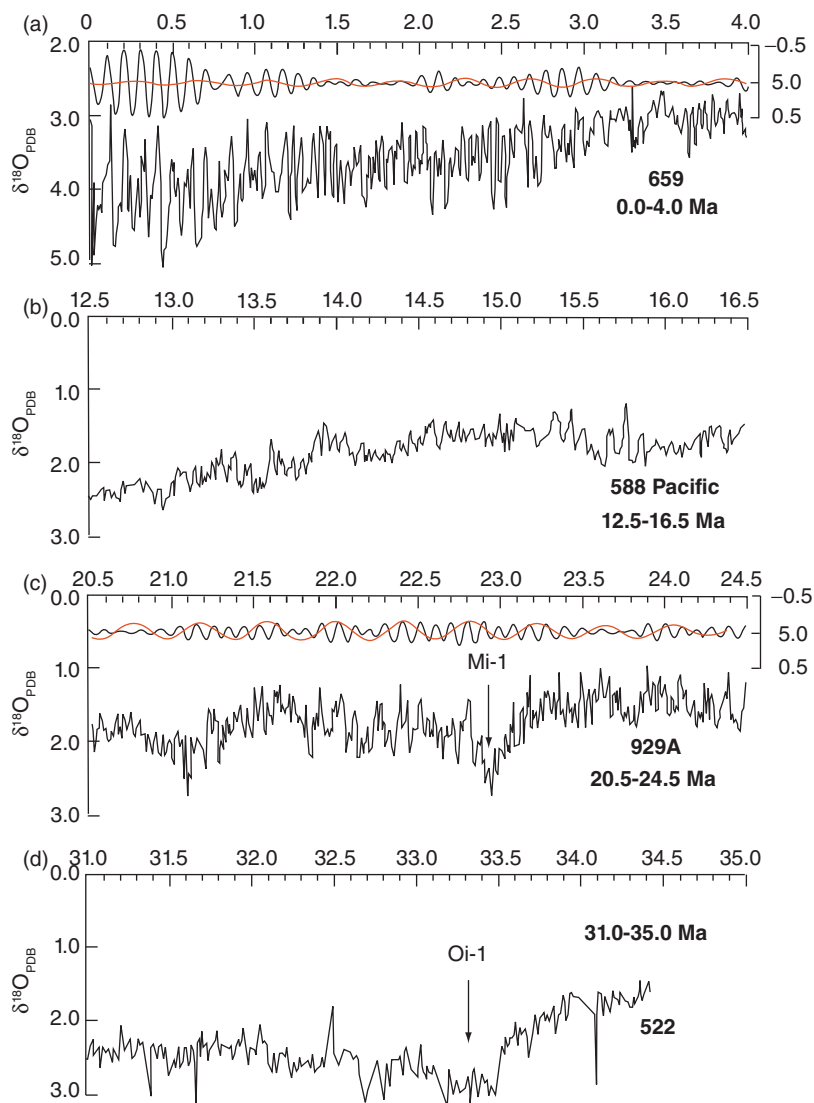


Figure 10.21 Variation in $\delta^{18}\text{O}$ in benthic foraminifera in the Tertiary. Data are from Ocean Drilling Program Sites 659 in the eastern equatorial Atlantic, 588 in the southwest Pacific, 929 in the western equatorial Atlantic, 522 in the South Atlantic, and 659 in the Southern Ocean. The upper curves in (a) and (c) represent Gaussian band-pass filters designed to isolate variance associated with the 400- (gray) and 100-ky eccentricity cycles. Note that $\delta^{18}\text{O}$ is relative to PDB, rather than SMOW. This is conventional for carbonates. (Source: From Zachos et al., 2001.)

(Zachos et al., 2001). In the last half of the Pleistocene the 100,000 yr component of eccentricity appears to be dominant. These differences do not reflect differences in the strength of the Milankovitch signal, but rather global climate's sensitivity to it. In addition to the Milankovitch-related wiggles, one also sees a clear trend toward higher $\delta^{18}\text{O}$ with time, suggesting general global cooling.

Longer-term changes in Tertiary climate resulted from factors other than astronomical forcing. Some of these changes were driven by plate tectonics and include widening of the North Atlantic, opening and widening of the Tasmanian and Drake Passages, allowing for winds and currents in the Southern Ocean to circle the globe unrestricted; collision of India with Asia and subsequent uplift of the Himalayas and Tibetan Plateau; uplift of Panama and closure of the Central American Seaway. Two other factors are the growth of polar ice sheets, which did not exist when the Tertiary began and a decline in atmospheric CO_2 , which we will discuss in a subsequent section.

Superimposed on the general increase in $\delta^{18}\text{O}$ are some important “events” in which $\delta^{18}\text{O}$ changes more rapidly. Going backward through time, these include the shifts that mark the onset of Pleistocene glaciation, the rapid increase in $\delta^{18}\text{O}$ from mid-Miocene through Pliocene, a brief (~ 200 ky) excursion, referred to as Mi-1, to more positive $\delta^{18}\text{O}$ that coincided with the Oligocene/Miocene boundary (~ 23 Ma) and is thought due to a brief expansion of Antarctic ice volume. This event was followed by a series of intermittent but smaller glaciations. Another sharp change, referred to as Oi-1, occurred just above the Eocene/Oligocene boundary (34.0 Ma) and reflects the sudden appearance of large continental ice sheets on Antarctica. This in turn may have been due to reorganization of the oceanic and atmospheric circulation as evidenced by global wide shifts in the distribution of marine biogenic sediments.

Studies of spatially distributed cores suggest that global temperatures were some 2°C warmer during the Eocene than at present. Perhaps more significantly, the latitudinal gradient in temperature may have been only half the present one. This suggests oceanic and atmospheric circulation was different from the present, and on the whole much more efficient

at transporting heat from equator to poles. Why this was so remains unclear.

The Eocene–Oligocene shift is thought to represent the beginning of present system where temperature variations dominate thermohaline circulation in the oceans, and initiation of extensive East Antarctic glaciation. As we found in the previous section, deep ocean water masses are formed at high latitudes and are dense mainly because they are cold. Typically deep water today has a temperature between 2 and -2°C . Before the Eocene, deep water appears to have been much warmer, and thermohaline circulation may have been dominated by salinity differences. (The formation of Mediterranean Intermediate Water, which forms as a result of evaporative increase in salinity, can be viewed as a remnant of this salinity-dominated circulation.) It was probably not until late Miocene that the present thermohaline circulation was completely established. Even subsequent to that time, important variations may have occurred, as we have seen.

The mid-Miocene increase in $\delta^{18}\text{O}$ probably represents the expansion of the Antarctic ice sheets to cover West Antarctica. This interpretation is supported by δD analyses of sediment pore water. Even though pore water exchanges with sediment, water dominates the deuterium budget so that δD values are approximately conservative (diffusion also affects δD , but this effect can be corrected for). An increase of about 10‰ δD occurs between mid and late Miocene, which is thought to reflect the accumulation of deuterium-depleted water in Antarctic ice sheets.

10.2.7 Continental isotopic records

Climate change has left an isotopic record on the continents as well as in the deep sea. As with the deep-sea records, it is the isotopic composition of H_2O that is the paleoclimatic indicator. The record may be left directly in ice, in carbonate precipitated from water, or in clays equilibrated with water. We will consider examples of all of these in this section.

As we noted with the deep-sea carbonate record, the preserved isotopic signal can be a function of several variables. Continental records tend to be even more difficult to interpret than marine ones. All the isotopic records we will consider record in some fashion the

isotopic composition of precipitation in a given region. The isotopic composition of precipitation depends on a host of factors:

1. The isotopic composition of the oceans (the ice volume effect).
2. The isotopic composition of water in the source area (the $\delta^{18}\text{O}$ of surface water in the ocean varies by a per mil or more because of evaporation, precipitation and freezing and is correlated with salinity).
3. Temperature and isotopic fractionation in the source area (when water evaporates a temperature dependence isotopic fraction occurs; kinetic affects will also occur, and will depend on the vigor of mixing of water at the sea surface; higher wind speeds and more turbulent mixing will reduce the kinetic fractionation).
4. Atmospheric and oceanic circulation patterns (as we saw in Chapter 8, the isotopic composition of water vapor is a function of the fraction of vapor remaining, which is not necessarily a simple function of temperature; changes in atmospheric and oceanic circulation may also result in changes in the source of precipitation in a given region).
5. Temperature in the area where the precipitation falls, as this determines the fractionation between vapor and water.
6. Seasonal temperature and precipitation patterns. The isotopic record might reflect water falling during only part of the year, and the temperature recorded may therefore be that of only a single season rather than an annual average. For example, even in a wet area such as Ithaca, NY, recharge of groundwater occurs mainly in winter; during summer, evaporation usually exceeds precipitation.
7. Evaporation of water or sublimation of ice. The isotopic record might be that of water remaining after some has evaporated. Since evaporation involves isotopic fractionation, the preserved isotopic record will not necessarily be that of the precipitation that falls.

All of these are climatic factors and are subject to change between glacial and interglacial periods. Changes in these factors do not mean that the stable isotope record in a given region is not recording climatic changes, but they do

mean that the climatic changes recorded might not be global ones.

10.2.8 Vostok and EPICA Antarctic ice cores

Climatologists recognized early on that continental ice preserves a stratigraphic record of climate change. Some of the first ice cores recovered for the purpose of examining the climatic record and analyzed for stable isotopes were taken from Greenland in the 1960s (e.g., Camp Century Ice Core). Subsequent cores have been taken from Greenland, Antarctica, and various alpine glaciers. The alpine glaciers generally give isotopic records of only a few thousand years, but are nevertheless useful, recording events such as the Little Ice Age. The Greenland and Antarctic cores provide a much longer record. Very long ice cores that covered 150,000 years were first recovered by the Russians from the Vostok station in Antarctica in the 1980s (e.g., Jouzel, et al., 1987) and were deepened over the next 20 years, eventually reaching back 400,000 years. Drilling was halted in 2003 out of concern for intersecting and contaminating the body of water beneath the ice, known as Lake Vostok. Attention then shifted to the EPICA (European Project for Ice Coring in Antarctica) project, which recovered 3270 m of ice core, extending back through eight glacial cycles and more than 800,000 years.

Hydrogen isotopes show a much larger range and much greater temperature-dependent fractionation than oxygen, so in ice, interest centers on δD . Figure 10.22 compares the EPICA δD record with the marine $\delta^{18}\text{O}$ record. As may be seen, there is good agreement between the marine $\delta^{18}\text{O}$ record and the EPICA δD record back to ~800 ky B.P. The lowermost 60 m of ice, however, appear to have been deformed and do not provide a reliable record. The core also provides a record of atmospheric CO_2 , O_2 , N_2 , and $\delta^{18}\text{O}_{\text{O}_2}$ from gas trapped in bubbles and we will return to this in a subsequent section.

Jouzel et al. (2007) converted δD to temperature variations based on a $6.2\text{‰}/^\circ\text{C}$ relationship between δD and temperature in Antarctic snow and on simulations using Global Circulations Models that incorporate water isotopes using simple Rayleigh fractionation models of the sort we considered

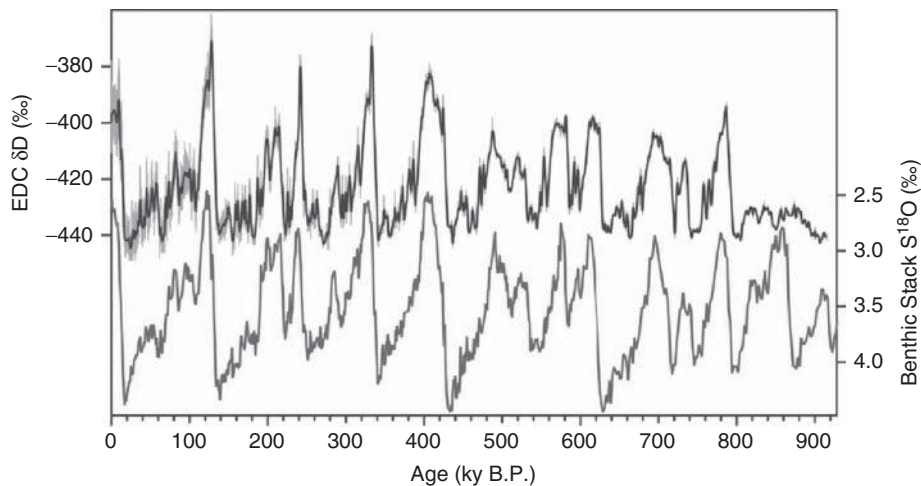


Figure 10.22 Climate record of the upper 2700 m of the EPICA Ice core. The upper curve shows δD in the Vostok ice core. The lower curve shows the marine benthic carbonate $\delta^{18}\text{O}$ curve. (Source: Jouzel, et al. (2007). Reproduced with permission of AAAS.)

in Chapter 8. Their results are shown in Figure 10.23.

Spectral analysis of the Vostok and EPICA isotope records shows strong peaks in variance at 41 kyr (the obliquity frequency) and at the 23 kyr precessional frequency. Thus the ice core data appear to confirm the importance of Milankovitch climatic forcing. It is interesting and significant that even in this core, taken at 78°S , it is primarily insolation at 65°N that is the controlling influence. There are, however, some differences between the ice record and the marine record, and we will consider these further in a subsequent section.

10.2.9 Ice records from Greenland: GRIP, GISP, and NGRIP

To complement the remarkable record of the Antarctic ice cores, drilling was begun in the late 1980s on two deep ice cores at the summit of the Greenland ice cap. A core drilled by a European consortium project, called GRIP (Greenland Ice Core Project), was located exactly on the ice divide; a core by a US consortium, called GISP2 (Greenland Ice Sheet Project), was drilled 28 km to the west of the GRIP site. Flow and deformation of ice in the lower parts of these cores compromised the climate record beyond 110,000 yrs BP. Consequently, in 2003 a second core was completed by the European consortium, located several

hundred km to the northwest of the GRIP site, called NGRIP, penetrated over 3000 m and successfully recovered a record of the entire last glacial cycle. Because snowfall rates are higher in Greenland than they are in central Antarctica, the record covers less time. On the other hand, they provide more detailed climate records of the Holocene and the last glacial cycle. They also provide a record of climate in the Northern Hemisphere, and in the North Atlantic, the region that undoubtedly holds the key to Quaternary glacial cycles. Over roughly the past 120,000 years, there is a good correlation between the NGRIP record and marine $\delta^{18}\text{O}$ and Antarctic ice records.

Records are most detailed for the last glacial interval, spanning the period from roughly 110,000 years ago to 14,000 years ago. This time was also much more variable in addition to being colder on average. In particular, there are cold periods that end with rapid warming on time scales of a few decades. The transition back to cold episodes was much slower. These rapid fluctuations in climate are known as Dansgaard–Oeschager events and can be correlated to $\delta^{18}\text{O}$ variations in high-resolution (i.e., high sedimentation rate) sediment cores from the North Atlantic. As may be seen in Figure 10.23, the warming events correlate with isotopic (temperature) maxima in Antarctica, suggesting coupling of

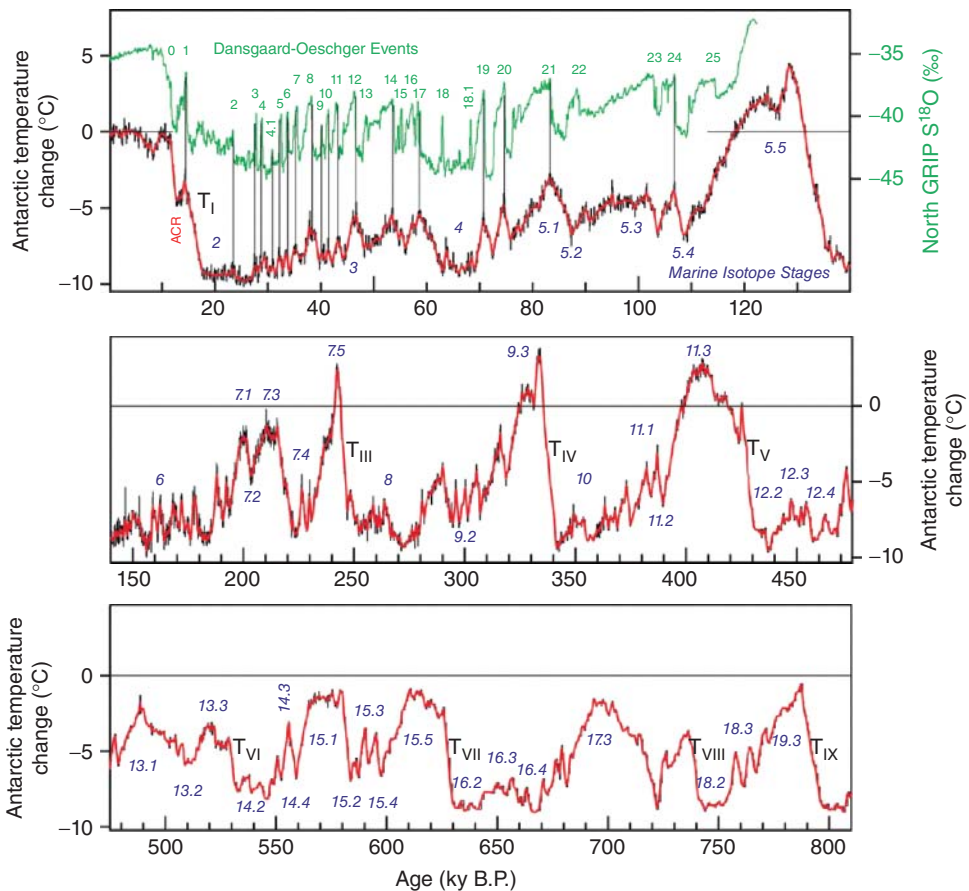


Figure 10.23 Antarctic temperature variation calculated from the EPICA ice core compared to the $\delta^{18}\text{O}$ record from the NGRIP ice core from Greenland. (Source: Jouzel et al. (2007). Reproduced with permission of AAAS.)

climate between the two hemispheres. The causes of these events are still unclear, but changes in the North Atlantic ocean circulation, perhaps triggered by an influx of fresh water, are suspected.

A number of other chemical and physical parameters are being or have been measured in the Greenland ice cores. One of the more important finding to date is that cold periods were also dusty periods (again, this had previously been suspected from marine records). Ice formed in glacial intervals has higher concentrations of ions such as Ca^{2+} and Na^+ derived from sea salt and calcite and other minerals in soils in arid regions, indicating higher atmospheric dust transport during glacial periods, reflecting conditions that were both dustier and windier. Windier conditions could well result if thermohaline circulation was reduced, as the pole to equator temperature gradient

would increase. Atmospheric dust may be an important feedback in the climate cycle: dust can act as nuclei for water condensation, increasing cloud cover and cooling the climate (Walker, 1995). It may also serve as feedback in another way. In parts of the ocean far from continents wind-blown dust is a significant source of Fe, whose abundance locally limits biological productivity. Increased winds during the last glacial period may have fertilized the ocean with Fe, effectively turning up the biological pump and drawing down atmospheric CO_2 . On the negative side, the abundance of dust and aerosols compromises the record of atmosphere gases such as CO_2 that trapped air bubbles provide in the much cleaner Antarctic ice. It's easy to understand why, particularly for CO_2 . CaCO_3 will react with aerosols in the trapped in the ice such as H_2SO_4 and HNO_3 (produced from SO_2 and

NO_2 released by volcanic eruptions and other natural processes) to produce CO_2 . Thus, the Greenland ice cores have not been useful in reconstructing changes in atmospheric CO_2 .

10.2.10 Speleotherm and related climate records

Calcite precipitating from groundwater, such as in veins or stalactites and stalagmites (collectively called speleotherms) and flowstone in caves provide yet another climate record, as the isotopic composition of the calcite reflects that of the precipitation. A distinct advantage of these records is that, unlike ice and marine sediment records, they can be accurately dated by U-Th decay series disequilibrium (Chapter 3). There are disadvantages as well. First, growth rates can be slow (1 mm/yr to less than 1 $\mu\text{m}/\text{yr}$) and discontinuous, limiting resolution. Second, the relationship between the isotopic composition of this calcite and climate is complex, depending not only on temperature, but also the amount of precipitation and its isotopic composition and the amount of evaporation. Third, the latter depend on local and regional climate variations that can differ significantly from global trends. This, of course, is an advantage if regional, rather than global, climate variations are the principal interest, and indeed much of the research of speleotherms focuses on local and regional climate variations.

One of the first and most significant of these records was that of vein calcite in Devil's Hole in Nevada. Devil's Hole is an open fault zone near a major groundwater discharge area in the southern basin and range in southwest Nevada (Devil's Hole is located in the next basin east from Death Valley). The fissure is lined with calcite that has precipitated from supersaturated groundwater over the past 500,000 years. A 36 cm long core was recovered by SCUBA divers and analyzed by Winograd, et al. (1992) for $\delta^{18}\text{O}$ and dated using U-Th disequilibrium determined by mass spectrometry.

Overall, the Devil's Hole record is strongly similar to the SPECMAP marine record, but there are some significant differences, most notably Termination II, the end of the penultimate glacial epoch, in the Devil's Hole record preceded that in the SPECMAP record by about 13 ka (140 ka vs. 127 ka). This was an

important point because Termination³ II in the SPECMAP record corresponds with a peak in Northern Hemisphere summer insolation. Subsequently, Spötl et al. (2002) determined an age from Termination II of 135 ka based on dating of flowstone in Spannagel Cave in the Austrian Alps.

Part of the issue related to dating of the SPECMAP marine record, as well as Antarctic ice records. Age control on these records is quite poor beyond the limit of ^{14}C dating. Indeed, ages in this part of the SPECMAP record were “tuned” to the orbital insolation forcing; that is, the match between Northern Hemisphere summer insolation and SPECMAP $\delta^{18}\text{O}$ was an assumption, not an observation. Subsequent studies of $\delta^{18}\text{O}$ and sea-level rise in ancient reef corals from Barbados, the Bahamas, and Tahiti revealed that Termination II occurred at 135–137 ka, some 8–10 thousand years before the Northern Hemisphere insolation peak (Henderson et al., 2000; Gallup et al., 2002; Thomas et al., 2009).

The 135–137 ka age refers to the mid-point of the warming and deglaciation event. By combining a U-Th disequilibrium dated $\delta^{18}\text{O}$ record from a high resolution speleotherm from Corchia Cave in Italy with $\delta^{18}\text{O}$ marine sediment record from the Iberian margin, the likely source of precipitation in Italy, Drysdale et al. (2009) determined that Termination II began at 141 ± 2.5 ka, well before the Northern Hemisphere insolation peak at 127 ka. They pointed out, however, that the timing coincides well with increasing high latitude Southern Hemisphere insolation. The idea that Southern Hemisphere insolation may have been any important driver of Termination II is consistent with observation that the warming signal in Antarctic Ice records leads the marine record by several thousand years. Drysdale et al. also argued that the timing supported the proposal that obliquity variations controlled the timing of glacial terminations (Huubers and Wunsch, 2005).

Differences between the Devil's Hole and the marine isotopic records nonetheless persist. The most likely explanation in that the Devils Hole record reflects regional climate changes (Grootes, 1993). Subsequently, based on analysis of sediment cores from the California margin Herbert et al. (2001) argued that the Devil's Hole record reflected circulation

changes in the eastern North Pacific. Specifically, they found coastal waters systematically warmed 10,000 to 15,000 years sooner than deglaciations over the last 500,000 years. They argued the cause was a collapse of the California Current, which carries relatively cool water southward along the coast of the western USA, allowed warmer waters from the south (the Davidson counter current) to intrude further north. This in turn was driven by atmospheric circulation changes induced by the Laurentide Ice Sheet.

10.2.11 Soils and paleosols

The concentration of CO_2 dissolved in soil solutions is very much higher than in the atmosphere, reaching 1% by volume. As a result, soil water can become supersaturated with respect to carbonates. In soils where evaporation exceeds precipitation, soil carbonates form. The carbonates form in equilibrium with soil water, but the isotopic composition of soil water tends to be heavier than that of mean annual precipitation. There are two reasons for this. First, soil water enriched in ^{18}O relative to meteoric water due to preferential evaporation of isotopically light water molecules. Second, rain (or snow) falling in wetter, cooler seasons is more likely to run off than during warm seasons. Thus, there is a strong correlation between $\delta^{18}\text{O}$ in soil carbonate and meteoric water, though soil carbonates tend to be about 5‰ more enriched than expected from the calcite-water fractionation (Figure 10.24). Because of this correlation, the isotopic composition of soil carbonate may be used as a paleoclimatic indicator.

Figure 10.25 shows one example of $\delta^{18}\text{O}$ in paleosol carbonates used in this way. The same Pakistani paleosol samples analyzed by Quade et al. (1989) for $\delta^{13}\text{C}$ (Figure 10.7) were also analyzed for $\delta^{18}\text{O}$. The $\delta^{13}\text{C}$ values recorded a shift toward more positive values at 7 Ma, which apparently reflect the appearance of C_4 grasslands. The $\delta^{18}\text{O}$ shows a shift to more positive values at around 8 Ma, or a million years before the $\delta^{13}\text{C}$ shift. Quade et al. interpreted this as due to an intensification of the Monsoon system at that time, and interpretation consistent with marine paleontological evidence.

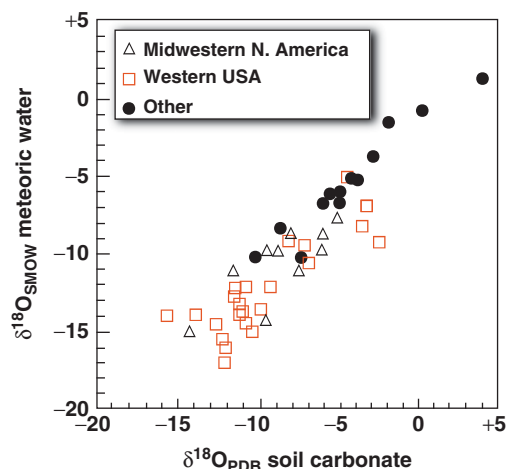


Figure 10.24 Relationship between $\delta^{18}\text{O}$ in local average meteoric water and soil carbonate. (Source: Cerling and Quade (1993). Reproduced with permission of John Wiley & Sons.)

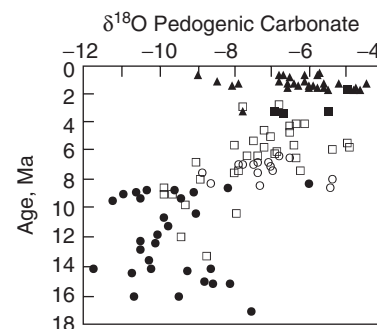


Figure 10.25 $\delta^{18}\text{O}$ in paleosol carbonate nodules from the Potwar Plateau in northern Pakistan. Different symbols correspond to different overlapping sections that were sampled. (Source: Quade et al. (1989). Reproduced with permission of Nature Publishing Group.)

Clays, such as kaolinites, are another important soil constituent. Savin and Epstein (1970) showed that during soil formation, kaolinite and montmorillonite form in approximate equilibrium with meteoric water so that their $\delta^{18}\text{O}$ values are systematically shifted by +27‰ relative the local meteoric water, while δD are shifted by about 30‰. Thus kaolinites and montmorillonites define a line parallel to the meteoric water line (Figure 10.26), the so-called kaolinite line.

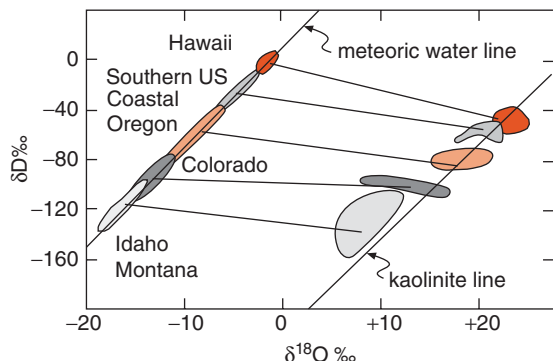


Figure 10.26 Relationship between δD and $\delta^{18}\text{O}$ in modern meteoric water and kaolinites. Kaolinites are enriched in ^{18}O by about 27‰ and ^2H by about 30‰. (Source: Lawrence and Taylor (1972). Reproduced with permission of Elsevier.)

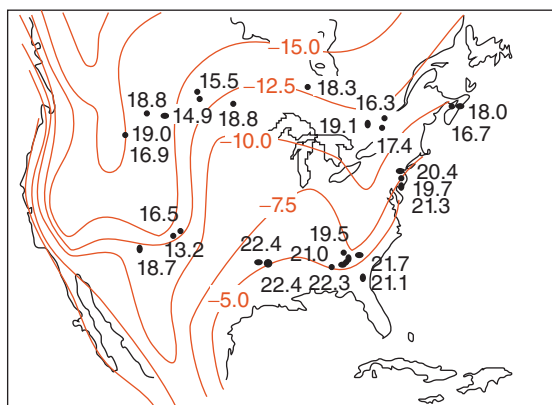


Figure 10.27 $\delta^{18}\text{O}$ in Cretaceous kaolinites from North America compared with contours of $\delta^{18}\text{O}$ (value shown in outline font) of present-day meteoric water. (Source: Lawrence and Meaux (1993). Reproduced with permission of John Wiley & Sons.)

From this observation, Lawrence and Taylor (1972) and Taylor (1974) reasoned that one should be able to deduce the isotopic composition of rain at the time ancient kaolinites formed from their δD values. Since the isotopic composition of precipitation is climate dependent, as we have seen, ancient kaolinites provide another continental paleoclimatic record.

Lawrence and Meaux (1993) conclude, however, that most ancient kaolinites have exchanged hydrogen subsequent to their formation, and therefore are not a good paleoclimatic indicator (this conclusion is, however, controversial). On the other hand, they conclude that oxygen in kaolinite does preserve the original $\delta^{18}\text{O}$, and that can, with some caution, be used as a paleoclimatic indicator. Figure 10.27 compares the $\delta^{18}\text{O}$ of ancient Cretaceous North American kaolinites with the isotopic composition of modern precipitation. If the Cretaceous climate were the same as the present one, the kaolinites should be systematically 27‰ heavier than modern precipitation. For the southeastern USA, this is approximately true, but the difference is generally less than 27‰ for other kaolinites, and the difference decreases northward. This indicates these kaolinites formed in a warmer environment than the present one. Overall, the picture provided by Cretaceous kaolinites confirms what has otherwise been deduced about Cretaceous climate: the Cretaceous climate was generally warmer, and

the equator to pole temperature gradient was lower.

10.3 THE CARBON CYCLE, ISOTOPES, AND CLIMATE

10.3.1 The short-term carbon cycle and anthropogenic impacts

There is considerable reason to believe that the Earth's climate is linked to atmospheric CO_2 concentrations. There are several lines of evidence for this. First, and perhaps, most importantly, is the observation that CO_2 gas is transparent to visible radiation but strongly absorbs infrared radiation. Most of the energy the Earth receives from the Sun is the visible part of the spectrum. The Earth loses an equal amount of energy in the form of infrared radiation (if it did not, the Earth's surface would continually get hotter). Atmospheric CO_2 absorbs this outgoing radiation and acts as an insulating layer, keeping the Earth warmer than it otherwise would be. In principle anyway, the higher the atmospheric CO_2 concentration, the warmer the Earth's surface will be. This is the familiar greenhouse hypothesis, first proposed by Savant Ahrrenius in 1896 in a paper entitled "On the Influence of Carbonic Acid in the Air upon the Temperature of the Ground." At that time, there were neither the temperature records nor data on changes in atmospheric

CO_2 concentration. Consequently, no one paid much attention to this until oceanographer Roger Revelle and physicist Hans Suess of the Scripps Institution of Oceanography became interested in the problem in the 1950s and convinced their colleague Charles Keeling to begin making regular measurements of atmospheric CO_2 concentration.

As Figure 10.28 indicates, carbon cycles rapidly between five reservoirs on the surface of the Earth. Of the total carbon in these five reservoirs, atmospheric CO_2 is only a small part. Roughly equal amounts of carbon are present in the terrestrial biosphere, the atmosphere, and the surface ocean, with somewhat more being present in soil carbon. The bulk of the surficial carbon, about 50 times as much as in the atmosphere, is dissolved in the deep ocean (mainly as HCO_3^-). The fluxes of carbon to and from the atmosphere are large relative to the amount of CO_2 in the atmosphere; indeed nearly 25% of the atmospheric CO_2 "turns over" in a year. The balance of these fluxes controls the concentration of atmospheric CO_2 . The isotopic composition varies between these reservoirs, primarily due to the fractionation during photosynthesis.

In the last several hundred years, man has affected the carbon cycle through burning of fossil fuels and clearing of forests. Both these activities can be viewed as fluxes of carbon to the atmosphere, the former from sedimentary

organic carbon, the latter from the terrestrial biosphere. The carbon flux from fossil fuel burning increased significantly over the twentieth century and is presently around 9 Gt per year, a reasonably well-known value, and is growing; the deforestation flux is uncertain, but 2 Gt per year is a commonly cited figure. This has resulted in a roughly 0.5% per year annual increase in the concentration of CO_2 in the atmosphere (Figure 10.29), as determined by a global system of monitoring stations (the first of which were installed by Charles Keeling in the late 1950s at Mauna Loa and the South Pole). This is equivalent to an average increase in the mass of atmospheric CO_2 reservoir of about 3 Pg/yr⁴ since 1960. This increase in atmospheric CO_2 is only about 60% of the fossil fuel flux and 49% of the total estimated anthropogenic carbon flux. Thus, roughly 3–5 Pg of carbon are "missing" in the sense they are going into some reservoir other than the atmosphere, presumably the ocean or terrestrial biosphere.

Both sources of the anthropogenic carbon flux, biospheric carbon released by deforestation and sedimentary organic carbon released by burning fossil fuels, have highly negative $\delta^{13}\text{C}$ (the isotopic composition of fossil fuel burned has varied over time from $\delta^{13}\text{C} \approx -24\text{\textperthousand}$ in 1850 to $\delta^{13}\text{C} \approx -28\text{\textperthousand}$ at present as coal has been partly replaced by oil and gas). Thus, we might expect to see a decrease

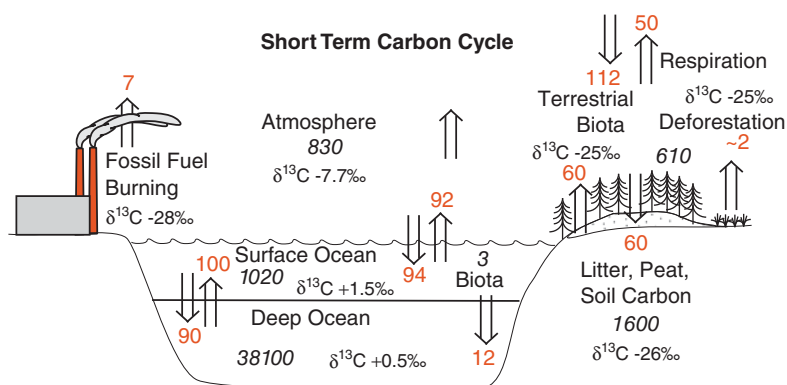


Figure 10.28 The Carbon Cycle. Numbers in black italic show the amount of carbon (in 10^{15} grams or gigatons, Gt) in the atmosphere, oceans, terrestrial biosphere, and soil (including litter, debris, etc.). Fluxes (gray) between these reservoirs (arrows) are in 10^{15} g C/yr . Also shown in the approximate isotopic composition of each reservoir. Magnitudes of reservoirs and fluxes are principally from Siegenthaler and Sarimento (1993) and Falkowski et al. (2000), isotopic compositions are from Heimann and Maier-Reimer (1996).

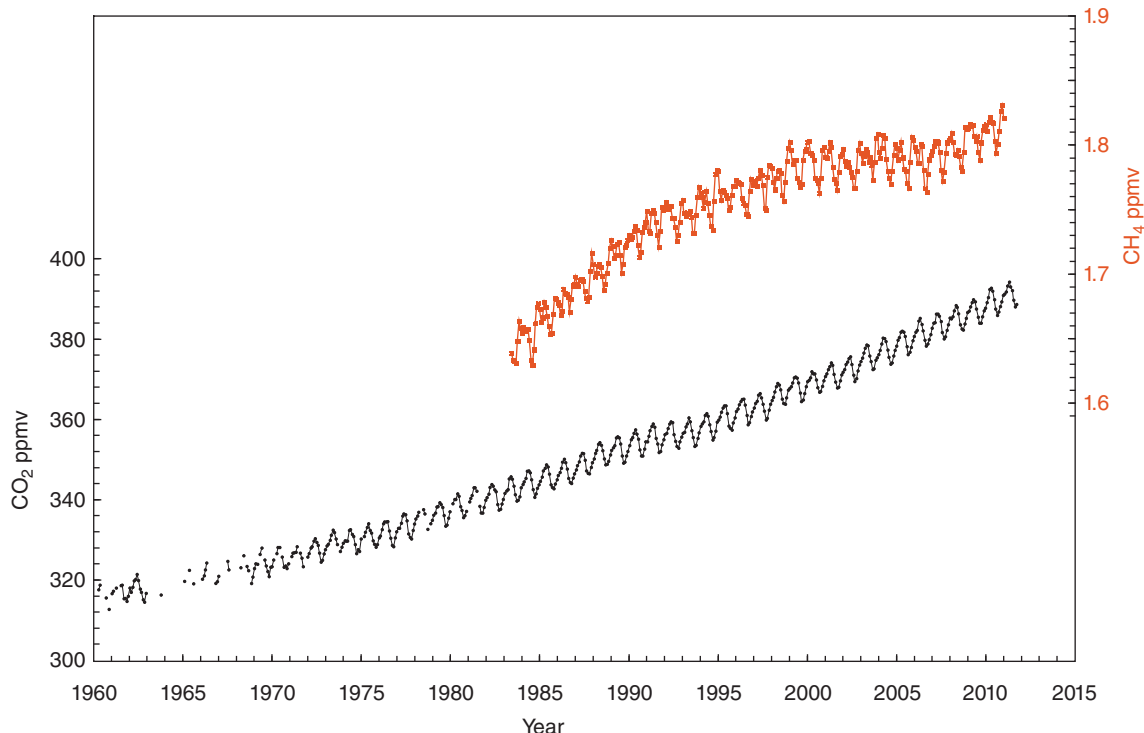


Figure 10.29 Atmospheric CO₂ and CH₄ concentrations (ppm volume) measurements at Mauna Loa, Hawaii, begun by C. D. Keeling in 1958. Annual cycles reflect the effects of seasonal changes in photosynthesis. Data from the Scripps CO₂ program (<http://scrippsco2.ucsd.edu>) NOAA-ESRL Global Monitoring System (<http://noaa.gov/gmd>).

in the $\delta^{13}\text{C}$ of atmospheric CO₂ with time. This is indeed observed. First, Figure 10.30 shows the $\delta^{13}\text{C}$ of atmospheric CO₂ measured at Mauna Loa over the period 1990–2013. There is a clear decrease in $\delta^{13}\text{C}$ over time. Superimposed on the temporal decrease are seasonal variations reflecting uptake of a light carbon (making atmospheric carbon heavier) in the spring as photosynthesis increases and release of light carbon the fall as respiration becomes dominant over photosynthesis. On a longer time-scale, measurements of $\delta^{13}\text{C}$ in ice cores, compliment the direct measurements (Figure 10.31) and show that $\delta^{13}\text{C}$ of atmospheric CO₂ was approximately constant over the first half of the last millennium, increased slightly around 1600 (perhaps related to the little ice age), then began to decline around the time of the Industrial Revolution. The decline is greater (up to a factor of 2 greater) than that expected from burning of fossil fuel alone, which is one line of evidence that there has been a significant destruction of the terrestrial biosphere over the last 200 years.

To what degree the “missing” CO₂ (i.e., that fraction of CO₂ produced by burning fossil fuel and terrestrial biosphere destruction that has not accumulated in the atmosphere) has been taken up by the oceans or by terrestrial reservoirs remains an incompletely resolved question. Accurate predictions of future increases in atmospheric CO₂ require an answer, because storage of carbon in these two reservoirs is quite different. Once stored in the oceans, most carbon is unlikely to re-enter the atmosphere soon. However, increases in the terrestrial biomass or detritus and soil carbon may be unique, short-lived phenomena and, furthermore, may be susceptible to continued human intervention and climate change.

Several teams of investigators have attempted use of $\delta^{13}\text{C}$ changes in the atmosphere and ocean to determine what has happened to the balance of the anthropogenic carbon. Because of the rapid decline of $\delta^{13}\text{C}$ in atmospheric CO₂, the oceans and atmosphere are out of isotopic equilibrium. The

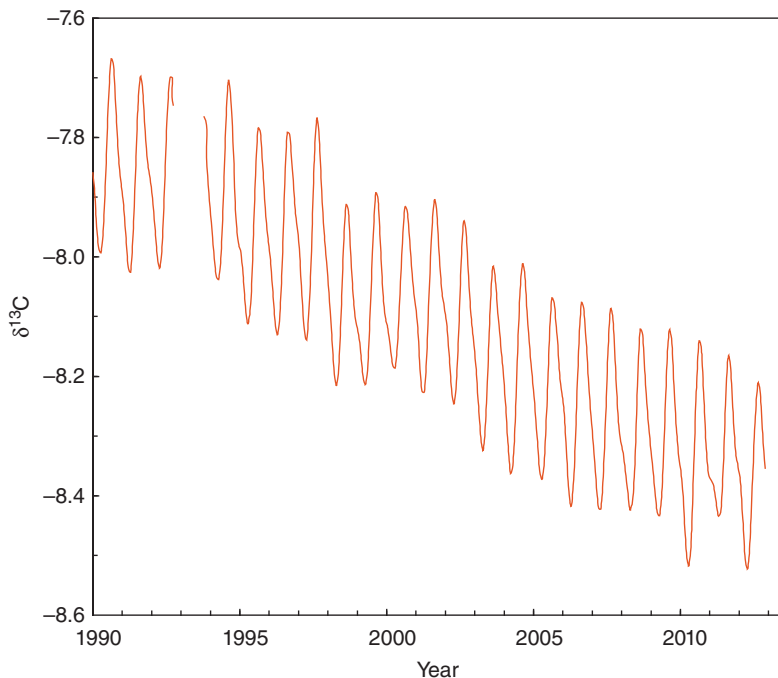


Figure 10.30 Monthly variation in carbon isotopic composition of atmospheric CO_2 measured at Mauna Loa, Hawaii between 1990 and 2013. Data from the NOAA-ESRL Global Monitoring System.

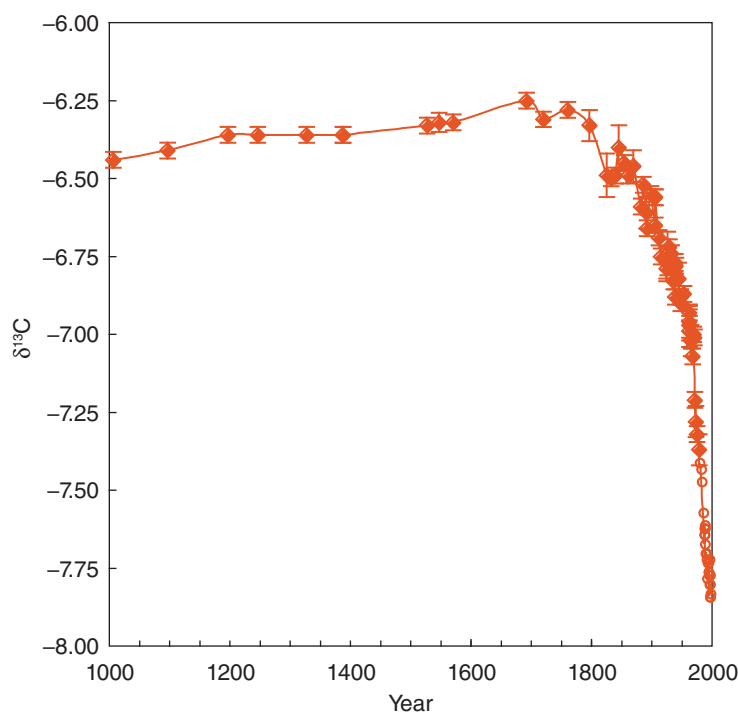


Figure 10.31 Variation in $\delta^{13}\text{C}$ in an ice from the Law Ice Dome, Antarctica (filled diamonds) and air samples from Cape Grim, Tasmania (open circles). Data from Francey et al. (1999).

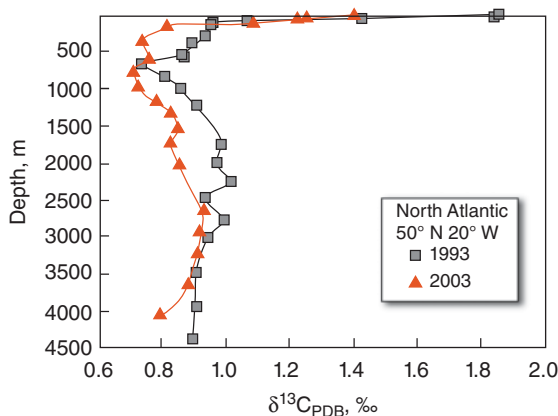


Figure 10.32 $\delta^{13}\text{C}$ as a function of water depth in the North Atlantic as sampled in 1993 and again in 2003. (Source: Quay et al. (2007). Reproduced with permission of John Wiley & Sons.)

extent of this disequilibrium depends on the rate of air-ocean exchange of CO_2 and can be used to estimate the rate of ocean uptake. Another approach is to examine the depth-integrated changes in $\delta^{13}\text{C}$ over time. Figure 10.32 shows the change in $\delta^{13}\text{C}$ with depth in the North Atlantic between 1993 and 2003. The anthropogenic signal has penetrated to the base of the water column in this region (the North Atlantic is unusual in this respect because of the sinking of NADW; the anthropogenic signal is not observed at depth in the Pacific or Indian Oceans). Based on observations such as these, Quay et al. (2007) estimated that the North Atlantic was taking up 0.32 Pg C/yr.

Other approaches have been aimed at estimating the total ocean uptake. The small concentration gradient between hemispheres (as indicated by the similar CO_2 concentrations at Mauna Loa and the South Pole) requires that much of the anthropogenic CO_2 be taken up in the Northern Hemisphere. Based on global isotopic measurements of $\delta^{13}\text{C}$ in the atmosphere, Keeling et al. (1989) concluded that the uptake by the oceans was 2.2 Gt/year in 1980. In their model, the hemispheric gradient is explained by a large Northern Hemisphere oceanic sink. By comparing seasonal and latitudinal variations in atmospheric $\delta^{13}\text{C}$, Ciais et al. (1995) concluded that the terrestrial biosphere north of 30°N took up 3.6 Gt/yr in 1992–1993, while the global ocean took

up only 1.82 Gt/yr in these years. Heimann and Maier-Reimer (1996) also used the rate of $\delta^{13}\text{C}$ change in the ocean to estimate an oceanic uptake rate of 2.1 ± 0.9 Gt/yr. They also pointed out the importance of the riverine carbon flux to the ocean, which previous workers had neglected. Using a box diffusion ocean model to match both the observed $\delta^{13}\text{C}$ and nuclear bomb-related ^{14}C changes, Quay et al. (2003) estimated an oceanic CO_2 uptake rate of 1.7 ± 0.2 Pg C/yr between 1970 and 1990. Joos et al. (1999) used atmospheric CO_2 and $\delta^{13}\text{C}$ records over the last millennium to reconstruct temporal variability in the terrestrial and oceanic carbon sink. They concluded that there was considerably interannual variability in oceanic CO_2 uptake, which correlates with El Niño-Southern Oscillation cycles (during El Niño conditions ocean uptake is higher). They found that interannual variations in the oceanic sink for the 1980–1996 period were around ± 1 Gt C/yr and currently averages around 2 Gt C/yr. The variability of ocean and biosphere uptake might explain why there is so much uncertainty in the estimates of these fluxes. Summarizing a variety of studies and approaches, Gruber et al. (2009) estimated the ocean uptake at 2.2 ± 0.3 Gt/yr.

An ocean uptake of 2 Gt per year leaves at least additional 3 Gt per year, more than the deforestation flux, that is apparently being taken up by the terrestrial biosphere. Ciais et al. (1995) concluded most of this occurs in Northern Hemisphere temperate and polar regions. Since most of the fossil fuel burning occurs in the Northern Hemisphere, we would expect the concentration of CO_2 to be slightly higher at Mauna Loa than at the South Pole. This is indeed the case; however, Ciais et al. found that the hemispheric gradient was less than that predicted by most models of atmospheric CO_2 transport, indicating much of the missing CO_2 must be taken up in the Northern Hemisphere.

It would appear then that expansion of the Northern Hemisphere terrestrial biosphere at least balances, and likely exceeds, deforestation, which now occurs mainly in the tropics. There are several possible explanations for this. These are as follows.

1. As agriculture became more efficient in the twentieth century, land cleared for

- agriculture in Europe and North America in previous centuries has been abandoned and is returning to forest.
2. Average global temperature has increased by over 0.5°C over the last century, perhaps as a result of rising atmospheric CO_2 concentrations. This temperature increase may be producing an expansion of boreal forests.
 3. Pollution, particularly by nitrates emitted when fossil fuel is burned, may be fertilizing and enhancing growth of the biosphere.
 4. As we saw in Chapter 8, plants photosynthesize more efficiently at higher CO_2 concentrations, so increasing atmospheric CO_2 concentrations can, in principle, stimulate plant growth. Since most plant growth is generally limited by availability of nutrients such as phosphate and nitrate rather than CO_2 , it is unclear whether such stimulation would actually occur. However, higher CO_2 concentrations may allow plants to close their stomata somewhat. Stomata, through which leaves exchange gas with the atmosphere, are pathways both for CO_2 into the leaf and for H_2O out of the leaf. Closing the stomata somewhat would reduce water loss and therefore may allow plants to survive in drier climates, leading to an expansion of forests into grasslands and grasslands into deserts.

10.3.2 The quaternary carbon isotope record and glacial cycles

In our discussion of Quaternary climate cycles, we noted the need for feedback mechanisms to amplify the Milankovitch signal and mentioned that atmospheric CO_2 concentration might be one of these. Early evidence that atmospheric CO_2 concentration might vary between glacial and interglacial epochs came from carbon isotope studies of deep-sea cores. Shackleton (1977) found that seawater $\delta^{13}\text{C}$ increased during glacial times. He attributed this isotopic change to an increase in the terrestrial biomass that would occur as a result of, among other things, increasing land area due to falling sea level (there is more biological productivity per square meter on land than in the ocean). This would draw down atmospheric CO_2 and perhaps provide

the necessary feedback to amplify orbital forcing of climate change. Further evidence of varying atmospheric CO_2 came from the first measurement of CO_2 concentrations in air bubbles in ice cores beginning in the late 1970s and early 1980s. The best of these records have come from the Antarctic ice cores from the Vostok and EPICA ice cores. The most recent of these efforts is shown in Figure 10.33. There is a remarkable similarity between temperatures deduced from δD of the ice and the measured CO_2 in the bubbles. Also interesting is that over the past 450,000 years, CO_2 in each interglacial interval reaches about the same 280–300 ppm level as in the recent, pre-industrial past. Interglacial CO_2 levels appear to be lower in the 450,000–750,000 year interval. During cold intervals, atmospheric CO_2 decreases by 100 ppm, or more than 35%, to 180 ppm than during interglacial periods. In the Antarctic ice records, air temperatures appear to rise several hundred years before CO_2 rises when glacial epochs end (i.e., at “terminations”), implying that climate change is somehow forcing CO_2 .

It is clear that CO_2 is following climate and acting as a positive feedback. But what is the mechanism by which atmospheric CO_2 concentrations change in glacial cycles? Changes in seawater temperature (CO_2 is more soluble in water at lower temperature), changes in ocean volume, changes the terrestrial biosphere as Shackleton suggested, high latitude peat deposits and soil carbon, the efficiency of the oceanic biological pump, and the vertical circulation, or “ventilation,” of the oceans have all been suspected as being part of the feedback system. Research over the last 30 years, including carbon isotope studies, suggests that changes in ocean circulation linked to climate-related changes in atmospheric circulation may be the most important of these effects.

Even from the early data, it was apparent that CO_2 had risen quite rapidly at the end of the last glaciation. The rapid changes in both atmospheric CO_2 and the larger difference in $\delta^{13}\text{C}$ between ocean and atmosphere during glacial periods suggested to Broecker (1982) that the ocean must somehow be involved since it is a much larger carbon reservoir and exchanges relatively quickly with the atmosphere. He noted that one

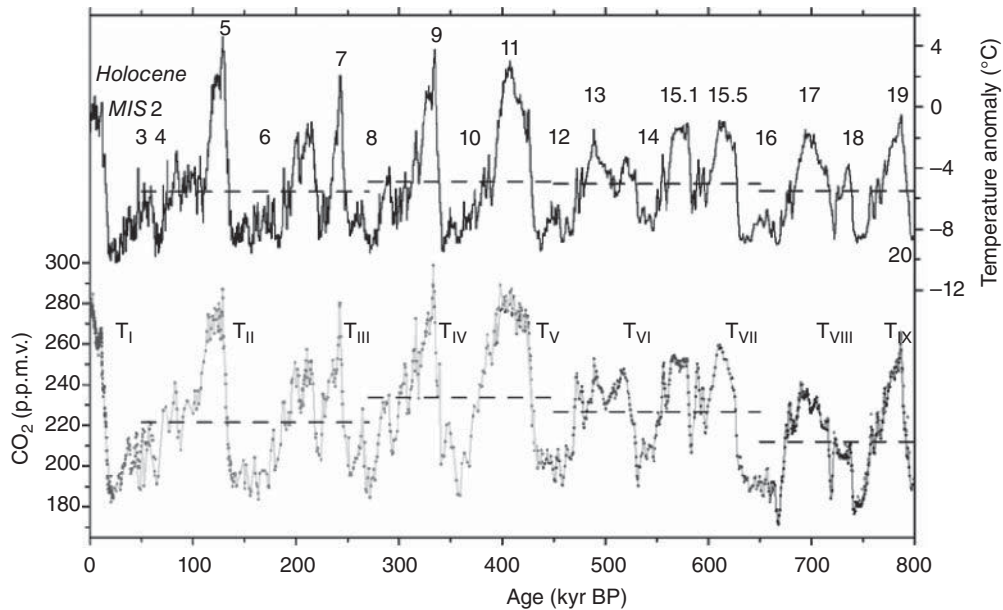


Figure 10.33 Comparison of CO_2 in bubbles (gray shows analytical uncertainties) in the EPICA ice core with temperatures calculated from δD . (Source: Lüthi et al. (2008). Reproduced with permission of Nature Publishing Group.)

obvious mechanism, changing the solubility of CO_2 in the ocean due to changing temperature (solubility of CO_2 increases with decreasing temperature), would produce only about a 20 ppm decrease in atmospheric CO_2 during glacial times, and about half this would be offset by decreasing volume of the oceans. Broecker suggested the changes in atmospheric CO_2 resulted from changing biological productivity in the oceans, in other words, the effectiveness of the biological pump. He suggested that as sea level rose, phosphorus was removed by biological processes from the ocean and deposited on continental shelves. Because the water column is short above continental shelves, there is less opportunity for falling organic matter to be recycled before being incorporated in the sediment. He supposed that phosphorus is the limiting nutrient in the oceans; lowering its concentration would decrease marine biological productivity and thereby allow the concentration of CO_2 in the atmosphere to rise.

Boyle (1988) proposed a different mechanism for changing atmospheric CO_2 , but one that nevertheless involved the oceans. In his model, the primary driving factor is a redistribution of nutrients and metabolic CO_2 in the ocean so that they are concentrated in

deep rather than in intermediate waters as in the present ocean. As the concentrations of CO_2 in the bottom water increase, pH drops and calcium carbonate sediment on the deep ocean floor dissolves. This, in turn, increases pH and ocean alkalinity, allowing it to dissolve more CO_2 from the atmosphere. Following on this idea, Toggweiler (1999) and Toggweiler et al. (2006) suggests that this redistribution of CO_2 reflects differences in ocean circulation in the Southern Ocean as well as the North Atlantic. Toggweiler (1999) suggested that reduced ventilation of deep water reduced atmospheric CO_2 by 21 ppm, that an additional 36 ppm reduction occurs due to the consequent carbonate dissolution and increase in ocean alkalinity, and that cold water temperatures further reduced atmospheric CO_2 by 23 ppm (CO_2 is more soluble in water at lower temperatures). Toggweiler et al. (2006) suggested specifically the ocean circulation changes result from a climate-driven migration of the westerly winds in the Southern Ocean. In the present interglacial climate, these most intense Westerlies are located south of the Antarctic polar front. As a result of a phenomenon called Ekman transport, these winds drive water away from Antarctica, and as a result, water rises, or “upwells” from

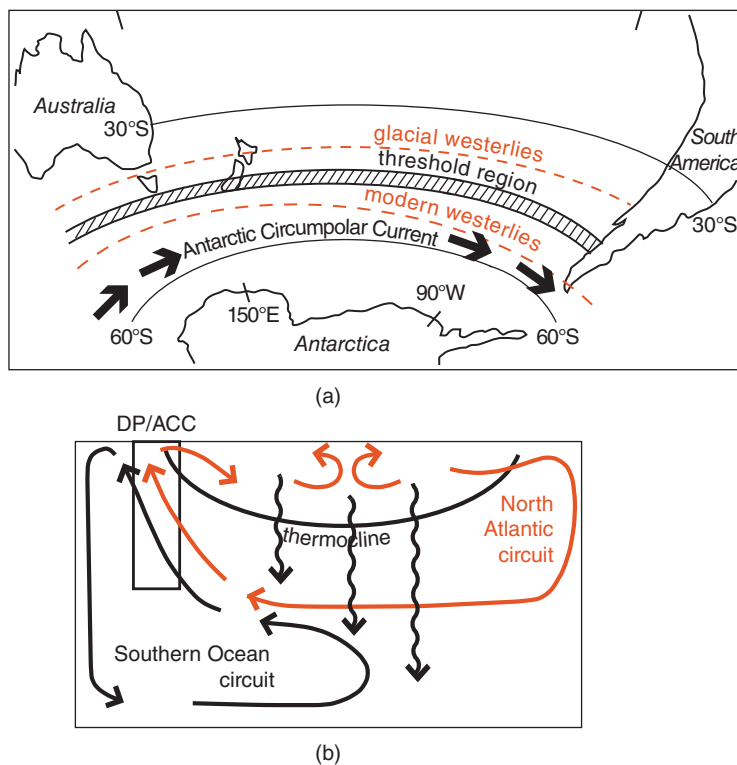


Figure 10.34 (a) Map showing the position of the strongest Westerlies today and at the Last Glacial Maximum in relation to the Antarctic Circumpolar Current (ACC). The Westerlies are pushed to these limits by the positive feedback between atmospheric temperature and CO₂. The threshold, which extends into the Indian and Atlantic, is the northernmost zone where the Westerlies can induce strong upwelling. b. Schematic diagram of simplified deep circulation of the ocean. Respired CO₂ accumulates during glacial periods in the deep southern domain because the southern circulation was inactive or very weak. The box labeled “DP/ACC” depicts the ocean’s main upwelling zone along the southern flank of the ACC in the latitude band of Drake Passage (DP). (Source: Toggweiler et al. (2006). Reproduced with permission of John Wiley & Sons.)

depth (Figure 10.34a). This upwelling allows CO₂ built-up by respiration in the deep ocean to vent to the atmosphere, keeping atmospheric CO₂ concentrations high. As climate cools in glacial periods, these winds migrate northward where they produce considerable less upwelling. The result is that water in the “Southern Circuit” (Figure 10.34b) circulates slowly during glacial periods, allowing respired CO₂ to accumulate.

Many of the mechanisms by which climate could drive changes in CO₂ involve biology, that is, photosynthesis and respiration. Because of the large fractionation of carbon isotopes associated with photosynthesis, these mechanisms predict changes in δ¹³C in the oceans and atmosphere. For example, looking at Figure 10.28, we can see that since

the terrestrial biosphere has lower δ¹³C than the atmosphere, storage of carbon in the biosphere should raise atmospheric δ¹³C. On the other hand, since the oceans have higher δ¹³C than the atmosphere, transfer of carbon from the atmosphere to the ocean should lower atmospheric δ¹³C, though the effect would be smaller. Slow ventilation of deep water, as proposed by Toggweiler (1999) should not only increase CO₂ in deep water, it should lower its δ¹³C. Hodell et al. (2003) demonstrated sharp gradients in ocean water δ¹³C between 2100 and 2700 m depth during glacial periods over the last 1.1 Ma from analysis of benthic foraminifera (Figure 10.35). The gradient in δ¹³C reflects much greater accumulation and storage of respiration CO₂ in the deep and intermediate waters of the Southern Ocean and is

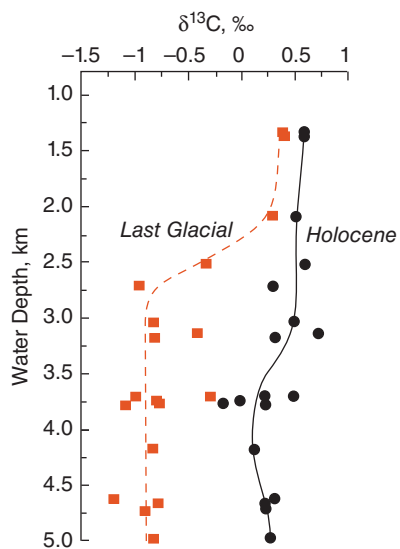
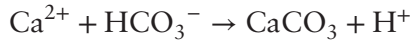


Figure 10.35 Comparison of modern and glacial period in $\delta^{13}\text{C}$ in shells of the benthic forams of the *Cibicidoides* genus recovered from cores from the South Atlantic. (Source: Hodell et al. (2003). Reproduced with permission of John Wiley & Sons.)

consistent with the proposals of Toggweiler (1999) and Toggweiler et al. (2006). Hodell et al. (2000) also found that the carbonate compensation depth (CCD), the depth below which carbonate sediment is not found in the ocean because it dissolves faster than it builds up, rose and fell in a manner consistent with the proposals of Boyle (1988) and Toggweiler (1999).

$\delta^{13}\text{C}$ of atmospheric CO_2 for the past 22,000 years has been measured in bubbles in the EPICA ice core by Elsig et al. (2009) and Lourantou et al. (2010) and is shown in Figure 10.36. Over the last 6000 years, atmospheric CO_2 concentrations increased by 10 ppm or so while $\delta^{13}\text{C}$ decreased slightly. Elsig et al. (2009) suggested this was due to a combination of desertification of the Sahara plus anthropogenic land-use change (i.e., development of agriculture). In the interval from about 10,000 years ago to about 7500 years ago, CO_2 decreased slightly while $\delta^{13}\text{C}$ increased relatively rapidly. The principle effect here was most likely expansion of the terrestrial biosphere to previously glaciated areas and storage of isotopically light carbon in peat and soil at high latitudes. Changes in carbonate compensation and growth of coral

reefs (to keep up with rising sea level) likely also had an influence. Coral reef growth, perhaps counter-intuitively, has the effect of increasing atmospheric CO_2 . Reef organisms effectively precipitate calcite through the reaction:



Consequently, reef growth decreases ocean alkalinity and pH, allowing the oceans to dissolve less CO_2 .

Prior to 11,000 years ago, the variation in $\delta^{13}\text{C}$ is more complex. Over this period, $\delta^{13}\text{C}$ correlates with the slope of the atmospheric CO_2 curve rather than its value, such that $\delta^{13}\text{C}$ is low when CO_2 concentration is rising rapidly. An initial increase in atmospheric CO_2 and decrease in $\delta^{13}\text{C}$ marks the end of the last glacial maximum around the time of Heinrich Event 1 (Heinrich events, first identified as layers of ice-raftered debris in sediment cores from the North Atlantic, are now understood to be events where the North American ice sheet destabilized and sent great flotillas of icebergs into the North Atlantic.) This is followed by a period when $\delta^{13}\text{C}$ increased and atmospheric CO_2 concentrations stabilized during the Bølling–Allerød period, a time recognized from pollen records of Europe as one of rapidly moderating climate and ice sheet retreat. Following this, $\delta^{13}\text{C}$ again decreased and atmospheric CO_2 increased in the Younger Dryas period, a time recognized from European pollen records as a return to cold, almost glacial, conditions. Lourantou et al. (2010) concluded from this record that changes in Southern Ocean ventilation played the dominant role changing atmospheric CO_2 , but changes in marine productivity, North Atlantic circulation, and the terrestrial biosphere were involved as well. The initial increase in atmospheric CO_2 is likely due to more rapid ventilation of the Southern Ocean in a poleward shift in Westerlies as suggested by Toggweiler et al. (2006), but reduced ocean productivity also played a role. During the Bølling–Allerød, production of North Atlantic Deep Water intensified, enhancing warming in the North Atlantic region. In response, expansion of the Northern Hemisphere terrestrial biosphere to higher latitudes and consequent build-up of carbon and peat eventually caused $\delta^{13}\text{C}$ to decrease

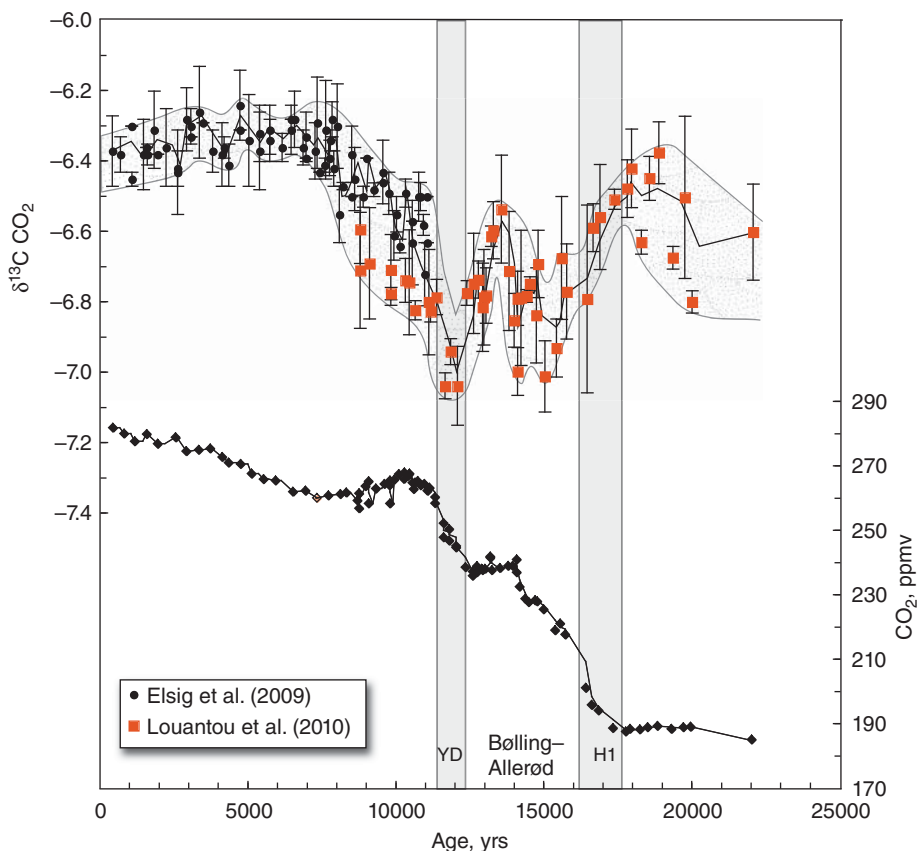


Figure 10.36 $\delta^{13}\text{C}$ in carbon dioxide and carbon dioxide concentrations in the EPICA Dome C ice core from Antarctica. Data from Elsig et al. (2009) and Louantou et al. (2010). Curve through the data is a three-point running mean. YD: Younger Dryas, H1: Heinrich Event 1.

and the increase in atmospheric CO_2 to stall. Meltwater from retreating glaciers flooded the North Atlantic in the Younger Dryas shut down NADW production, producing locally cooler conditions but resulting in more vigorous Southern Ocean overturn, driving up atmospheric CO_2 and increasing its $\delta^{13}\text{C}$.

10.3.3 The long-term carbon cycle

On geologic times scales, our carbon cycle model must be augmented by three reservoirs: sedimentary carbonate, sedimentary organic carbon, and the mantle, as well as fluxes between these reservoirs and the oceans and atmosphere. This long-term model is shown in Figure 10.37, where the anthropogenic perturbations have been removed. The most important thing to notice is that there is much more carbon in the carbonate and sedimentary organic carbon reservoirs than in

all the reservoirs in Figure 10.28 combined. However, the fluxes to and from the sedimentary reservoirs are small, so they play little role in short-term ($<1\text{ Ma}$) atmospheric CO_2 variations (at least in natural ones: we could properly consider fossil fuel burning as a flux from sedimentary organic carbon to the atmosphere). We should also point out that only a small fraction of the sedimentary organic carbon is recoverable fuel; most is present as minor amounts (typically 0.5% or less) of kerogen and other refractory organic compounds in sediments. Even greater amounts of carbon are probably stored in the mantle, though the precise amount is difficult to estimate. An order of magnitude figure might be $125\text{--}500\text{ ppm CO}_2$ in mantle, which implies a total inventory of $1.3\text{--}5 \times 10^8\text{ Gt}$, or nearly 10^6 times the amount in the atmosphere. Again, the flux from the mantle to the atmosphere, which results from

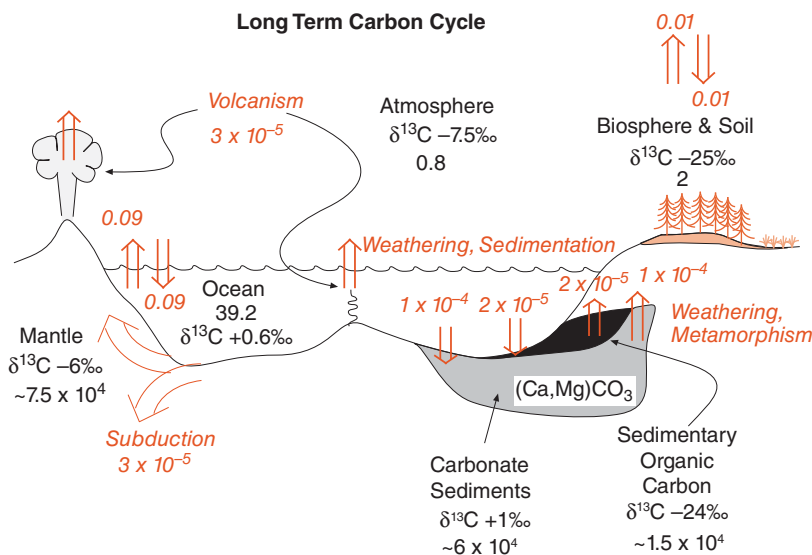


Figure 10.37 The long-term carbon cycle. Roman (black) numbers show the amount of carbon (in 10^{18} grams) in the reservoirs. Fluxes between these reservoirs (arrows) are shown in (gray) italics in units of 10^{18} g/yr. Values are the pre-Industrial Revolution state of the system. Uncertainties on many of the masses and fluxes are large. Also shown are estimates of the carbon isotopic composition.

volcanism, is small, so the mantle plays no role in short-term atmospheric CO_2 variations. On long time scales ($>10^6$ yr), however, it is the fluxes to and from sediments and the mantle that control the atmospheric CO_2 concentration.

10.3.3.1 The tertiary carbon isotope record of cooling and extinction

Figure 10.39, later, shows $\delta^{13}\text{C}$ and $\delta^{18}\text{O}$ in benthic forams from 40 DSDP and ODP drill cores selected to represent, as best as possible, global means. On these time scales, the main influences $\delta^{13}\text{C}$ are changes in biological productivity and ocean circulation, burial and erosion of carbon in sediments, and the volcanic flux. Recall that organic carbon has strongly negative $\delta^{13}\text{C}$ – burial of organic carbon will drive the marine system toward more positive values, erosion of organic carbon will drive it to negative values. Volcanic CO_2 has $\delta^{13}\text{C}$ of -6 , very similar to the atmospheric value, so changes in the volcanic flux will have a minimal effect on the isotopic composition of system. The fractionation between dissolved carbonate and precipitated carbonate is fairly small, so both erosion and burial of carbonate also have only a small effect on $\delta^{13}\text{C}$ of the system. There are a number of interesting

features of this record. Let's consider these in chronological sequence.

First, there is a decline in $\delta^{13}\text{C}$ around the Cretaceous-Tertiary boundary. This is not well shown in Figure 10.38 because the curve has been smoothed, but does show up well in detailed studies, such as that of d'Hondt et al. (1998). Figure 10.39 shows $\delta^{13}\text{C}$ values in carbonate from DSDP site 528. The data show a sharp drop in $\delta^{13}\text{C}$ at the K-T boundary. This is consistent with a strong reduction in bioproductivity, and consequently, a drop in the burial rate of organic carbon. The marine system appears to have partially recovered within a million years, and completely recovered within 3 million years.

The next notable event is the so-called Late Paleocene Thermal Maximum at 55 Ma. A sharp drop ($\sim 2.5\text{\textperthousand}$) in $\delta^{13}\text{C}$ coincides with an increase in $\delta^{18}\text{O}$ that corresponds to an increase in deep ocean temperature of $5\text{--}6^\circ\text{C}$ that occurred within 10,000 years. Recovery occurred over 500,000 years. There are a variety of hypotheses as to the cause of this event, but perhaps the most interesting and provocative is that warming of ocean deep water (which in Figure 10.38 can be seen to be occurring through the late Paleocene) eventually destabilized methane hydrates in continental shelf sediments. The

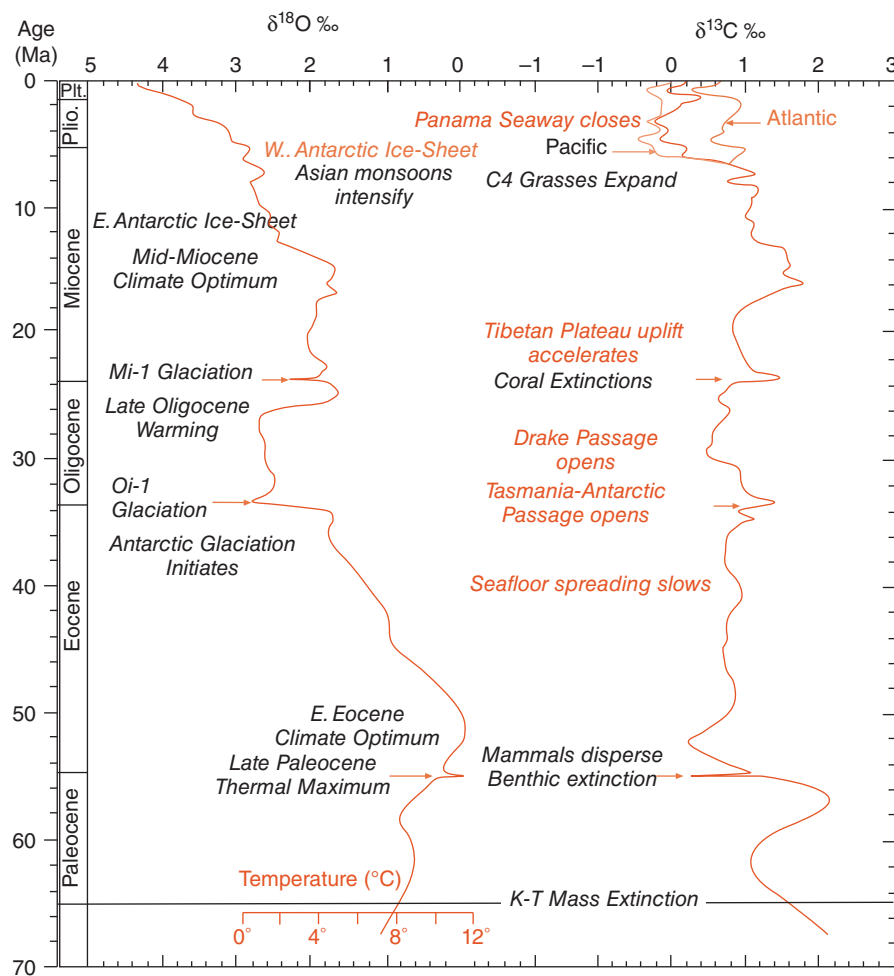


Figure 10.38 $\delta^{13}\text{C}$ and $\delta^{18}\text{O}$ in marine benthic foraminifera. Data are a compilation from many cores. In the Late Miocene, $\delta^{13}\text{C}$ of Pacific and Atlantic bottom waters diverge, and these are shown as separate curves. Also shown are significant climatic, tectonic, and biologic events (Source: Modified from Zachos et al., 2001.)

resulting release of methane to the atmosphere both drove ocean-atmosphere $\delta^{13}\text{C}$ to lighter mean values and dramatically increased global temperatures as a consequence of the strong greenhouse effect of methane and its oxidation product, CO_2 . The oceans became significantly more acidic at this time as evidenced by a much shallower carbonate compensation depth, which strongly suggests higher atmospheric CO_2 . This event was accompanied by shifts in the diversity and distribution of fauna and flora, notably including a migration of warm-climate mammals to high latitudes. At the same time, up to 50% of species of deep-sea benthic foraminifera species became extinct, even though they

had survived previous crises such as the K-T impact without significant extinction.

The next events are the Oi-1 and Mi-1 glaciations both of which reflect brief extremes in Antarctic ice-volume and temperature. The positive shifts in $\delta^{18}\text{O}$ are indicative of global cooling, while the positive shift in $\delta^{13}\text{C}$ suggests an increase in burial of organic carbon or a decrease in its erosion, either of which would have decreased CO_2 in the ocean-atmosphere system and thereby contributed to the cooling.

The final interesting feature is a roughly 1% decrease in $\delta^{13}\text{C}$ in the late Miocene. This could result from either a decrease in organic carbon burial, an increase in organic carbon

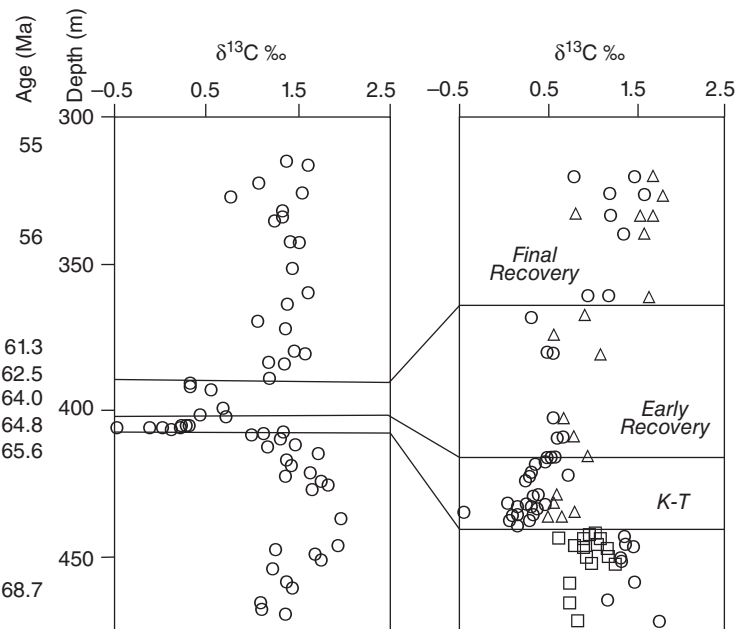


Figure 10.39 $\delta^{13}\text{C}$ in fine ($<25\ \mu\text{m}$) carbonate (circles) and planktonic foraminifera from DSDP Site 528 in the South Atlantic. (Source: d'Hondt (1998). Reproduced with permission of AAAS.)

erosion, or an increase in volcanism. There is no evidence of the latter; furthermore, all of these should have resulted in an increase in atmospheric CO_2 . However, there is independent evidence from boron isotopes, which we will consider in the follow chapter, and $\delta^{13}\text{C}$ in alkenones from marine phytoplankton, which we'll discuss in the following section, that atmospheric CO_2 concentrations have been fairly stable at 200–300 ppm since the late Oligocene (this contrasts with much higher concentrations prior to 35 Ma). Derry and France-Lanord (1996) proposed this decrease reflects a decrease in the fractionation between organic and inorganic carbon due lower atmospheric CO_2 levels. As we found in Chapter 8, if plants should fix a greater proportion of the CO_2 in their cell interiors, as they might at low atmospheric CO_2 then net fractionation should decrease. Again, however, other evidence suggests that atmospheric CO_2 concentration was more or less constant through the Miocene.

10.3.3.2 Paleo-atmospheric CO_2 concentrations from $\delta^{13}\text{C}$ in organic carbon

Ice cores provide information on atmospheric CO_2 concentrations back nearly a

million years. But what role has atmospheric CO_2 concentrations played in climate variations in the Tertiary and earlier periods? What part of early Tertiary warmth can be attributed to higher atmospheric CO_2 ? The need to predict the climatic consequences of fossil fuel burning and build-up of atmospheric CO_2 make these questions important.

One method of determining paleo- CO_2 concentrations arises from an observed relationship between $\delta^{13}\text{C}_{\text{org}}$ of marine phytoplankton and the concentration of dissolved inorganic CO_2 (Degens et al., 1968; Degens, 1969). We saw in Chapter 8 that the fractionation of carbon isotopes during photosynthesis is related to CO_2 concentrations (e.g., Figure 8.17). The reason for this, in simple terms, is that when more CO_2 is available, plants are more selective and therefore show a greater preference for ^{12}C . Thus in principle at least, $[\text{CO}_{2\text{aq}}]$ can be estimated from measurements $\delta^{13}\text{C}_{\text{org}}$. Atmospheric CO_2 can then be calculated from the equilibrium between $\text{CO}_{2\text{aq}}$ and $\text{CO}_{2\text{g}}$; that equilibrium depends on temperature, which must also be estimated. There are other complications, however, and variety of studies contributed to developing a useful proxy for atmospheric CO_2 concentrations from $\delta^{13}\text{C}$ of marine organic matter

over the next few decades, including Rau (1994) and Jasper and Hayes (1994). These efforts culminated in the work of Pagani et al. (1999).

Complicating factors including diagenetic effects on the organic matter and a dependence of the fractionation on species, cell geometry, and growth rate. Some of these problems can be overcome by focusing on a single organic compound such as the C₃₇ alkanadienone, as suggested by Jasper and Hayes (1994). This molecule, a 37-long hydrocarbon chain including a ketone bond and two unsaturated (i.e., doubly bonded) carbons, is particularly resistant to diagenetic change (indeed, it survives in petroleum). It is produced by a specific group of haptophyte algae (e.g., coccolithophoroids such as *Emiliania huxleyi*) whose cell physiology and geometry is rather similar, and which live in the upper 100 m of the water column, which should be in near-equilibrium with atmospheric CO₂. According to the photosynthesis model of Farquhar (1982), which we presented in Chapter 8, the isotopic fractionation during photosynthesis depends on the ratio of concentration of CO₂ in the atmosphere to that in the cell interior. We might expect that this ratio will depend on the photosynthetic rate: at high rates, there will be a draw-down of CO₂ in the cell interior. Pagani et al. (1999) assumed that the carbon fractionation during photosynthesis obeyed the following simple relationship:

$$\Delta = a - \frac{b}{[\text{CO}_2]_{aq}} \quad (10.4)$$

where b depends on physiological factors affecting fractionation, particularly growth rate. Experiments by Bidigare et al. (1997, 1999) determined the value of a and showed that b correlated strongly with dissolved phosphate concentration; the latter is not surprising since photosynthesis rates in marine phytoplankton are well known to be limited by nutrient availability in most areas. The problem, of course, is nutrient levels in the geologic past are not directly known. Pagani et al. (1999) essentially finessed this issue by focusing on samples in oligotrophic (i.e., nutrient limited) areas of the ocean, such as DSDP site 588 in the Coral Sea.

The other thing that must be known in order to determine Δ is the carbon isotopic composition of dissolved CO₂; Pagani

et al. (1999) determined this from the isotopic composition of planktonic foraminifera shells in the same layer. Combining paleotemperature estimates based on δ¹⁸O discussed in the previous section with estimated [CO₂]_{aq} estimated using Eqn. 10.4, they estimated atmospheric CO₂ through most of the Miocene and late Oligocene (Figure 10.40). The results were surprising because they showed that CO₂ has been near its pre-industrial modern level throughout most of the Miocene. Thus, the cooling that occurred in the late Miocene seen in Figure 10.39 was not due to decreasing atmospheric CO₂ as was widely suspected. P_{CO₂} does appear to have declined sharply at the Oligocene-Miocene boundary, coinciding with a known glacial event, but otherwise there is little relationship to apparent climate change over this period. As we shall see in the next chapter, boron isotopic measurements largely confirm these results.

We should also caution that these results do not negate the now well-established control that CO₂ exerts on climate. We have seen that atmospheric CO₂ correlates strongly with temperature through the Pleistocene climate extremes. And, as we shall see, atmospheric CO₂ was higher in the early Tertiary and Cretaceous when climate was warm. As of 2013, atmospheric CO₂ stood at over 397 ppmv.

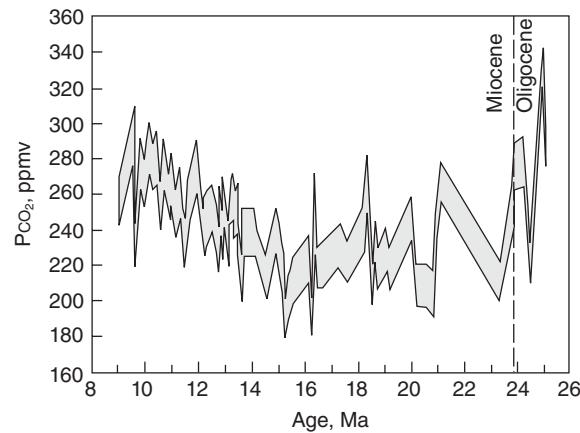


Figure 10.40 Atmospheric CO₂ concentration during the Miocene calculated from the difference between δ¹³C in diunsaturated alkenones and carbonate in sediments from DSDP site 588 by Pagani et al. (1999). Gray area falls between maximum and minimum values calculated using different assumptions.

That this is higher than it has been at any time over the last 25 million years is very much reason for concern.

10.3.3.3 The phanerozoic carbon isotope record and models of atmospheric CO₂

Figure 10.41 shows the Phanerozoic variation of δ¹³C and δ³⁴S in marine carbonates, both of which presumably record the isotopic composition of seawater at the time of deposition. (This long-term record misses some short-term events, such as dramatic negative shifts in δ¹³C associated with the Permo-Triassic and Cretaceous-Tertiary extinctions that are captured by detailed sampling such as that shown in Figure 10.39.) The record does reveal a gradual increase in δ¹³C and decrease in δ³⁴S through much of the Paleozoic and a more dramatic increase in δ¹³C (and decrease in δ³⁴S) associated with the expansion of land plants and high rates of burial of organic carbonic in the Carboniferous.

We expect the isotopic compositions of carbon and sulfur to be linked because burial and erosion of reduced sediment (organic carbon and sulfide) affect the concentration of

atmospheric oxygen. As a simple consequence of mass balance, photosynthesis and subsequent burial of organic carbon increases δ¹³C in the ocean-atmosphere system and also increases atmospheric O₂ concentration. The latter enhances sulfide oxidation. Sulfide (and other forms of reduced sulfur) is isotopically light, so when it is oxidized to sulfate and added to the ocean, it lowers seawater δ³⁴S. This mechanism accounts for the shift to more positive δ¹³C and more negative δ³⁴S in the Carboniferous, when the terrestrial biota rapidly expanded and organic carbon (later to become coal) accumulated in vast swamps in what would become North America and parts of Europe and Asia.

The sedimentary record of δ³⁴S and δ¹³C has given rise to various attempts to model the variation of atmospheric CO₂ and O₂ though geologic time. Berner, et al. (1983) (often referred to as the BLAG model) pointed out that silicate weathering is another important control on atmospheric CO₂ as it removes CO₂ from the ocean-atmosphere system through weathering reactions such as

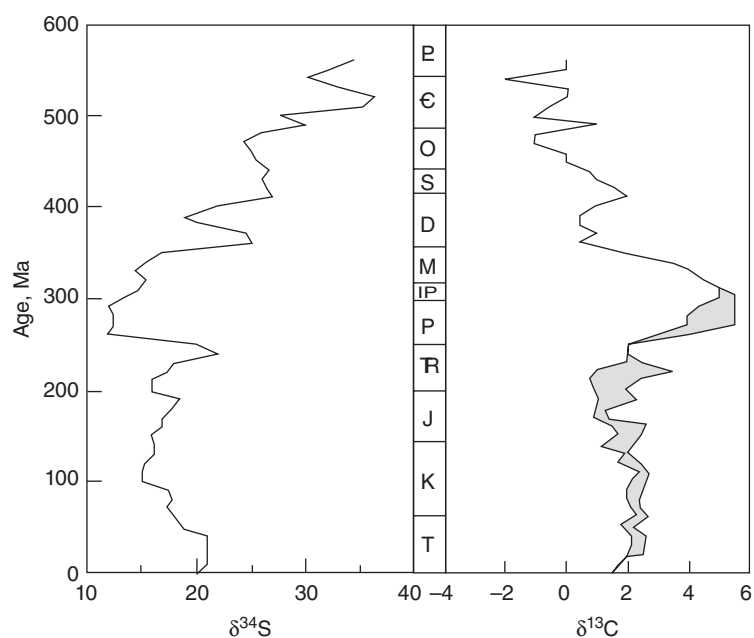
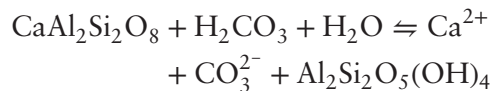
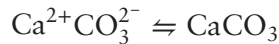


Figure 10.41 Isotopic compositions of carbon and sulfur in the oceans through Phanerozoic time. (Source: δ³⁴S adapted from Kampschulte and Strauss (2004); δ¹³C adapted from the compilation of Berner (2006a).)

and subsequent precipitation of carbonate from seawater:



Berner (1991) developed these ideas further in the GEOCARB model and its subsequent versions (e.g., Berner and Kothavala, 2001; Berner, 2006a,b). We'll consider only the gross aspects of this complex model here. The following is based mainly on Berner (2006a,b).

Berner considered the fluxes between the ocean-atmosphere, carbonate, and organic carbon reservoirs (Figure 10.42). He assumed that the system was in steady-state at any given time, an assumption justified by the small size of the atmosphere-ocean reservoir compared to the sedimentary ones. Thus one can write the following equation:

$$F_{\text{wc}} + F_{\text{mc}} + F_{\text{wg}} + F_{\text{mg}} = F_{\text{bc}} + F_{\text{bg}} \quad (10.5)$$

where F is a flux, subscript w denotes weathering, subscript m magmatic or metamorphic release of carbon, subscript b burial, subscript c the carbonate reservoir, and subscript g denotes organic sediments. Equation 10.5 states the steady-state condition that the rate of release of carbon from organic or carbonate sediment through metamorphism, magmatism, and weathering equals the rate burial of organic carbon and carbonate sediment. The isotopic composition of the oceans and atmosphere depends on these fluxes:

$$\delta_o F_{\text{bc}} + (\delta_o - \delta_c) F_{\text{bg}} = \delta_o (F_{\text{wc}} + F_{\text{mc}}) + \delta_g (F_{\text{wg}} + F_{\text{mg}}) \quad (10.6)$$

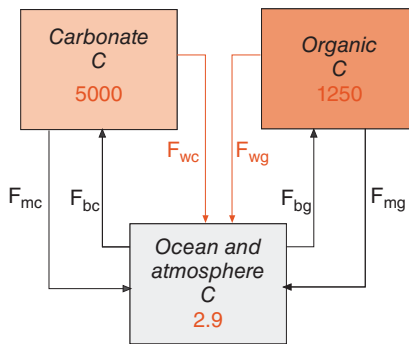


Figure 10.42 Simple model of carbon flow considered by Berner (1991). Masses of carbon are given in units of 10^{18} moles. Fluxes are described in the text. (Source: After Berner, 1991.)

where the subscript o denotes the ocean and $\alpha_c \parallel \text{I} \parallel$ is the fractionation during photosynthesis. Because the isotopic composition of the oceans ($\delta^{13}\text{C}_o$) through time can be estimated from $\delta^{13}\text{C}$ in carbonate (e.g., Figure 10.41), Eqn. 10.6 provides a constraint on these fluxes.

Berner and Kothavala (2006) expressed rate of uptake of CO_2 via the weathering of Ca and Mg silicates over time (F_{wsi}) as:

$$\begin{aligned} F_{\text{wsi}} &= F_{\text{bc}} - F_{\text{wc}} \\ &= f_B(T, \text{CO}_2) f_R(t) f_E(t) f_{AD}(t)^{0.65} F_{\text{wsi}}(0) \end{aligned} \quad (10.7)$$

where f_B is the feedback factor for silicates expressing the dependence of weathering on temperature and on CO_2 , f_R is the mountain uplift factor (ratio of land relief at time t to present relief), f_E is a factor expressing the dependence of weathering on soil biological activity due to land plants (= 1 at present), f_{AD} is the change in the ratio river discharge at time t to present river discharge due to change in paleogeography (a function of change in both land area and river runoff; the power of 0.65 reflects dilution of dissolved load at high runoff), and $F_{\text{wsi}}(0)$ is the present weathering uptake of CO_2 .

The weathering feedback works in two ways (Volk, 1987). First of all, global surface temperatures should correlate with atmospheric CO_2 concentrations. Since weathering reaction rates are, in principle, temperature dependent, Berner reasoned that weathering would be more rapid when temperatures, and hence atmospheric CO_2 concentrations, are higher (these same assumptions are present in the BLAG model). Second, Berner assumes that higher atmospheric CO_2 leads to greater rates of photosynthesis and biological activity. This enhances weathering through greater production of biological acids and nutrient uptake. (One might also speculate that atmospheric CO_2 might directly speed weathering since protons generated by dissociation of carbonic acid plays a key role in weathering. However, the dissolved CO_2 in groundwater comes primarily from respiration by soil organisms rather than the atmosphere. Hence increasing atmospheric CO_2 would not directly affect weathering rates.) The weathering feedback function can

be formulated as the product of these two factors:

$$f_B(T, \text{CO}_2) = f(T)f(\text{CO}_2) \quad (10.8)$$

The temperature dependence is contains the usual Arrhenius exponential relationship:

$$\begin{aligned} f(T) = & e^{E/RT(t)-E/RT(0)} \\ & \times [1 - \rho(T(t) - T(0))]^{0.65} \end{aligned} \quad (10.9)$$

where R is the gas constant, E is the activation energy for the weathering reaction, and ρ is the coefficient expressing the effect of temperature on global river runoff. The temperature difference is in turn dependent of atmospheric CO_2 levels, solar irradiation (W_s),⁵ and the effect of changes in paleogeography on temperature (λ):

$$T(t) - T(0) = \gamma \ln \left(\frac{\text{CO}_2(t)}{\text{CO}_2(0)} \right) - W_s(t) + \lambda(t) \quad (10.10)$$

where γ is the “greenhouse” coefficient and is computed from atmospheric global circulation models. f_{CO_2} is expressed as:

$$f(\text{CO}_2) = \left[\frac{\text{CO}_2(t)}{\text{CO}_2(0)} \right]^{-0.5} \quad (10.11)$$

before vascular plants (which first appeared in the mid-Silurian about 425 Ma but only became important in the Devonian), and after vascular plants as:

$$f(\text{CO}_2) = \left[\frac{\text{CO}_2(t) \text{CO}_2(0)}{1 + \text{CO}_2(t)/\text{CO}_2(0)} \right] \quad (10.12)$$

where ϕ is a fertilization factor that expresses the dependency of photosynthesis rates on with CO_2 concentration and has a value near 0.4 (e.g., Figure 10.8).

Other fluxes in Eqns 10.5–10.7 are complex function of geological and biological history (e.g., volcanism, continental land area, biological productivity, and evolution) and much of the work in constructing this model comes from estimating how these have varied from the geologic record. Berner then calculated the magmatic and weathering fluxes, and

substituting these into Eqns 10.5 and 10.6, calculated the burial fluxes in 1 million year steps. From values of F_{wc} and F_{bc} , he solved for $f\text{CO}_2(t)$ in Eqn. 10.7 and then for $\text{CO}_2(t)$. This new value of $f\text{CO}_2(t)$ was then used to iterate the calculation until a constant $f\text{CO}_2(t)$ was obtained.

From this, new values for the mass of the reservoirs and their isotopic composition were calculated using mass balance equations such as:

$$dC/dt = F_{\text{bg}} - (F_{\text{wc}} + F_{\text{mc}}) \quad (10.13)$$

and

$$d(\delta_c C)/dt = \delta_o F_{\text{bc}} - \delta_c (F_{\text{wm}} + F_{\text{mc}}) \quad (10.14)$$

The results of the latest version of the model (Berner, 2006b), which distinguishes weathering of volcanic and non-volcanic rocks (the former are richer in Ca and Mg and hence more effective at removing atmospheric CO_2) shown in Figure 10.43. The results correspond more or less with what is known from the geologic record about temperature changes during the Phanerozoic. To begin with, the Early Paleozoic was warm compared with the late Precambrian, which was a time of several major glaciations. The early Paleozoic

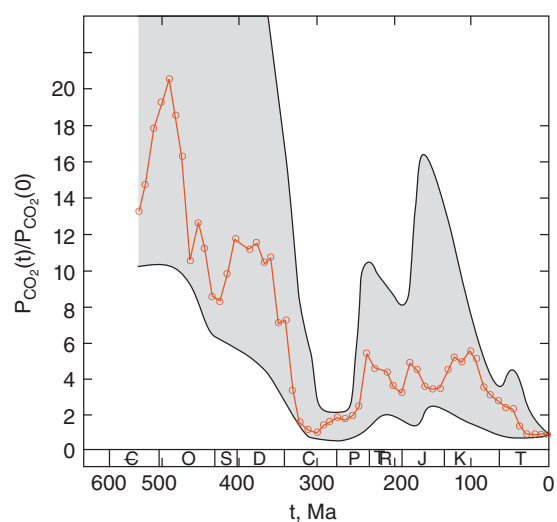


Figure 10.43 Concentration of atmospheric carbon dioxide over the Phanerozoic. Open circles with the solid line is the GEOCARBULF model of Berner (2006b). Errors on the model are shown as gray and are taken from Berner and Kothavala (2001).

warms implies a significantly greater greenhouse effect than as present because the Sun was some 5% less bright then. The late Paleozoic, on the other hand, was cool, and the time of the last major glacial epoch before the late Tertiary/Quaternary glaciation. The Cretaceous is well known as a remarkably warm period. Berner's model shows generally high CO₂ during warm periods of the early Paleozoic, low CO₂ (resulting from organic carbon burial in the Carboniferous) associated with glaciation in the late Paleozoic, and high CO₂ (associated with volcanism, among other things) in the warm Cretaceous. Thus if the model is correct, it substantiates the widely held assumption that atmospheric CO₂ concentrations strongly influence global temperature. The model has undoubtedly grown more realistic and accurate of its two decades of development, but just how accurate these estimates are remains to be seen. It would be far preferable to have CO₂ proxies, such as the δ¹³C of alkenones discussed in the previous

section and boron isotopes discussed in the next chapter, for pre-Tertiary times.

NOTES

1. Harmon Craig was also a student of Harold Urey.
2. While Milankovitch was a strong and early proponent of the idea that variations in the Earth's orbit caused ice ages, he was not the first to suggest it. J. Croll of Britain first suggested it in 1864, and published several subsequent papers on the subject.
3. The ends of glacial epochs are called *Terminations*. They are quantitatively defined as the mid-point in the δ¹⁸O rise and are numbered successively backward in time.
4. Pg = pentagrams or 10¹⁵g. This is also referred to as a gigatons; 1 Pg = 1 gigaton.
5. As was pointed out in Chapter 1, the Sun has grown about 30% brighter over geologic time.

REFERENCES

- Arrhenius, S. 1896. Ueber den Einfluss des Atmosphärischen Kohlensäuregehalts auf die Temperatur der Erdoberfläche. *Proceedings of the Royal Swedish Academy of Science*, 22: 1–101.
- Berger, A. L. 1992. Astronomical theory of Paleoclimates and the last glacial-interglacial cycle. *Quaternary Science Reviews*, 11: 571–581, doi: 10.1016/0277-3791(92)90014-Y.
- Berger, W. H. 2013. On the Milankovitch sensitivity of the Quaternary deep-sea record. *Climate of the Past*, 9: 2003–2011, doi: 10.5194/cp-9-2003-2013.
- Berner, R. A. and Kothavala, Z. 2001. Geocarb III: A revised model of atmospheric CO₂ over phanerozoic time. *American Journal of Science*, 301: 182–204, 10.2475/ajs.301.2.182.
- Berner, R. A., Lasaga, A. C. and Garrels, R. M. 1983. The carbonate-silicate geochemical cycle and its effect on atmospheric carbon dioxide over the past 100 million years. *American Journal of Science*, 1983: 641–683.
- Berner, R. A. 1991. Atmospheric CO₂ levels over Phanerozoic time. *Science*, 249: 1382–1386.
- Berner, R. A. 2006a. GEOCARBSULF: A combined model for Phanerozoic atmospheric O₂ and CO₂. *Geochimica et Cosmochimica Acta*, 70: 5653–5664, 10.1016/j.gca.2005.11.032.
- Berner, R. A. 2006b. Inclusion of the weathering of volcanic rocks in the GEOCARBSULF model. *American Journal of Science*, 306: 295–302, doi: 10.2475/05.2006.01.
- Bidigare, R. R., Fluegge, A., Freeman, K. H., Hanson, K. L., Hayes, J. M., Hollander, D. et al. 1997. Consistent fractionation of 13C in nature and in the laboratory: Growth-rate effects in some haptophyte algae. *Global Biogeochemical Cycles*, 11: 2 doi: 11:279–292, 10.1029/96gb03939.
- Bidigare, R. R., Fluegge, A., Freeman, K. H., Hanson, K. L., Hayes, J. M., Hollander, D. et al. 1999. Correction to “Consistent fractionation of 13C in nature and in the laboratory: Growth-rate effects in some haptophyte algae.” *Global Biogeochemical Cycles*, 13: 251 doi: 252, 10.1029/1998gb900011.
- Boyle, E. A. 1988. Vertical oceanic nutrient fractionation and glacial/interglacial CO₂ cycles. *Nature*, 331: 55–56.
- Broecker, W. S. 1982. Glacial to Interglacial changes in ocean chemistry. *Progress in Oceanography*, 11: 151–197.
- Broeker, W. S. 1984. Terminations. In: *Milankovitch and Climate*, Berger, A., Imbrie, J., Hayes, J., Kukla, G. and Satzman, B. (eds). pp. 687–689. Dordrecht: D. Reidel Publishing Co.
- Cerling, T. E. and Quade, J. 1993. Stable carbon and oxygen in soil carbonates, in *Climate Change in Continental Isotopic Records*, *Geophysical Monograph* 78, Swart, P. K., Lohmann, K., C., McKenzie, J. and Savin, S. (eds). . Washington: AGU .
- Ciaias, P., Tans, P. P., Trolier, M., White, J. W. C. and Francey, R. J. 1995. A large northern hemisphere terrestrial CO₂ sink indicated by the ¹³C/¹²C ratio of atmospheric CO₂. *Science*, 269: 1098–1102.
- Craig, H. 1965, Measurement of oxygen isotope paleotemperatures, in *Stable Isotopes in Oceanographic Studies and Paleotemperatures*, E. Tongiorgi (ed.). p. 161–182, Pisa: CNR Lab. Geol. Nucl..

- Curry, W. B. and Oppo, D. W. 2005. Glacial water mass geometry and the distribution of $\delta^{13}\text{C}$ of ΣCO_2 in the western Atlantic Ocean. *Paleoceanography*, 20: PA1017, doi: 10.1029/2004PA001021.
- d'Hondt, S., Donaghay, S., Zachos, J. C., Luttenberg, D. and Lindinger, M. 1998, Organic carbon fluxes and ecological recovery from the Cretaceous-Tertiary mass extinction. *Science*, 282: 276–278.
- Degens, E. T. 1969. Biogeochemistry of stable carbon isotopes. In: *Organic Geochemistry*, Eglington, G. and Murphy, M. T. J. (eds). New York: Springer-Verlag.
- Degens, E. T., Guillard, R. R. L., Sackett, W. M. and Hellbust, J. A. 1968. Metabolic fractionation of carbon isotopes in marine plankton - I: temperature and respiration experiments. *Deep Sea Research*, 15: 1–9.
- deMenocal, P. B. 2011, Climate and human evolution. *Science*, 331: 540–542, doi: 10.1126/science.1190683.
- DeNiro, M. J. and Epstein, S. 1978, Influence of diet on the distribution of carbon isotopes in animals. *Geochimica et Cosmochimica Acta*, 42: 495–506.
- DeNiro, M. J. and Epstein, S. 1981, Influence of diet on the distribution of nitrogen isotopes in animals. *Geochimica et Cosmochimica Acta*, 45: 341–351.
- DeNiro, M. J. 1987. Stable isotopy and archaeology. *American Scientist*, 75: 182–191.
- Derry, L. A. and France-Lanord, C. 1996. Neogene growth of the sedimentary organic carbon reservoir. *Paleoceanography*, 11: 265–275.
- Drysdale, R. N., Hellstrom, J. C., Zanchetta, G., Fallick, A. E., Sánchez Goñi, M. F., Couchoud, I., et al. 2009. Evidence for obliquity forcing of glacial termination II. *Science*, 325: 1527–1531, doi: 10.1126/science.1170371.
- Ehleringer, J. R., Sage, R. F., Flanagan, L. B. and Pearcy, R. W. 1991, Climate change and the evolution of C_4 photosynthesis. *Trends in Ecology and Evolution*, 6: 95–99.
- Elsig, J., Schmitt, J., Leuenberger, D., Schneider, R., Eyer, M., Leuenberger, M. et al., 2009. Stable isotope constraints on Holocene carbon cycle changes from an Antarctic ice core. *Nature*, 461: 507–510.
- Emiliani, C., 1955. Pleistocene temperatures. *Journal of Geology*, 63: 538–578.
- Epstein, S., Buchbaum, H. A. and Lowenstam, H. A. 1953. Revised carbonate-water isotopic temperature scale. *Geological Society of America Bulletin*, 64: 1315–1326.
- Falkowski, P., Scholes, R. J., Boyle, E., Canadell, J., Canfield, D., Elser, J., et al. 2000. The global carbon cycle: A test of our knowledge of Earth as a system. *Science*, 290: 291–296, doi: 10.1126/science.290.5490.291.
- Farquhar, G. D., O'Leary, M. H. and Berry, J. A. 1982. On the relationship between carbon isotope discrimination and the intracellular carbon dioxide concentration in leaves. *Australian Journal of Plant Science*, 9: 121–137.
- Francey, R. J., Allison, C. E., Etheridge, D. M., Trudinger, C. M., Enting, I. G., Leuenberger, M., et al. 1999. A 1000-year high precision record of $\delta^{13}\text{C}$ in atmospheric CO_2 . *Tellus B*, 51: 170–193, doi: 10.1034/j.1600–0889.1999.t01–1-00005.x.
- Gallup, C. D., Cheng, H., Taylor, F. W. and Edwards, R. L. 2002. Direct determination of the timing of sea level change during termination II. *Science*, 295: 310–313, doi: 10.1126/science.1065494.
- Grootes, P. M. 1993. Interpreting continental oxygen isotope records. In: *Climate Change in Continental Isotopic Records*, Geophysical Monograph 78, Swart, P. K., Lohmann, K. C., McKenzie, J. and Savin, S. (eds). p. 37–46. Washington: AGU.
- Gruber, N., Gloor, M., Mikaloff Fletcher, S. E., Doney, S. C., Dutkiewicz, S., Follows, M. J., et al. 2009. Oceanic sources, sinks, and transport of atmospheric CO_2 . *Global Biogeochemical Cycles*, 23: GB1005, doi: 10.1029/2008gb003349.
- Hasdorff, C. A. and DeNiro, M. J. 1985. New isotope method used to reconstruct prehistoric plant production and cooking practices. *Nature*, 315: 489–491.
- Hayes, J. D., Imbrie, J. and Shackleton, N. J. 1976, Variations in the Earth's orbit: pacemaker of the ice ages, *Science*, 194: 1121–1132.
- Heimann, M. and Maier-Reimer, E. 1996. On the relations between the oceanic uptake of CO_2 and its carbon isotopes. *Global Biogeochemical Cycles*, 10: 89–110.
- Henderson, G. M. and Slowey, N. C. 2000. Evidence from U-Th dating against Northern Hemisphere forcing of the penultimate deglaciation. *Nature*, 404: 61–66, doi: 10.1038/35003541.
- Herbert, T. D., Schuffert, J. D., Andreasen, D., Heusser, L., Lyle, M., Mix, A., et al. 2001. Collapse of the California current during glacial maxima linked to climate change on land. *Science*, 293: 71–76, doi: 10.1126/science.1059209.
- Hodell, D. A., Charles, C. D. and Sierro, F. J. 2000. Late Pleistocene evolution of the ocean's carbonate system. *Earth and Planetary Science Letters*, 192: 104–124.
- Hodell, D. A., Venz, K. A., Charles, C. D. and Ninnemann, U. S. 2003, Pleistocene vertical carbon isotope and carbonate gradients in the South Atlantic sector of the Southern Ocean. *Geochemistry, Geophysics, Geosystems*, 4: 1004 10.1029/2002gc000367.
- Huybers, P. and Wunsch, C. 2005. Obliquity pacing of the late Pleistocene glacial terminations. *Nature*, 434: 491–494, doi: 10.1038/nature03401.
- Imbrie, J. 1985, A theoretical framework for the Pleistocene ice ages. *Journal Of the Geological Society, London*, 142: 417–432.
- Imbrie, J., Hayes, J. D., Martinson, D. G., McIntyre, A., Mix, A. et al., 1984, The orbital theory of Pleistocene climate: support from a revised chronology of the marine $\delta^{18}\text{O}$ record. In: *Milankovitch and Climate, Part 1*, Berger, A. L., Imbrie, J., Hayes, J., Kukla, G. and Saltzman, B. (eds). p. 269–305. Dordrecht: D. Reidel .

- Jasper, J. P. and Hayes, J. M. 1994. Reconstruction of paleoceanic P_{CO_2} levels from carbon isotopic compositions of sedimentary biogenic components. In: *Carbon Cycling in the Glacial Ocean: Constraints on the Ocean's Role in Global Change*, Zahn, R., Pedersen, T. F., Kaminski, M. A. and Labeyrie, L. (eds). p. 323–341. Berlin: Springer-Verlag.
- Joos, F., Meyer, R., Bruno, M. and Leuenberger, M. 1999. The variability in the carbon sinks as reconstructed for the last 1000 years. *Geophysical Research Letters*, 26: 1437–1440, doi: 10.1029/1999gl900250.
- Jouzel, C., Lorius, C., Perfit, J. R., Genthon, C., Barkov, N. I., Kotlyakov, V. M. and Petrov, V. N. 1987. Vostok ice core: a continuous isotope temperature record over the last climatic cycle (160,000 years), *Nature*, 329: 403–403.
- Jouzel, J., Masson-Delmotte, V., Cattani, O., Dreyfus, G., Falourd, S., Hoffmann, G. et al., 2007. Orbital and millennial Antarctic climate variability over the past 800,000 years. *Science*, 317: 793–796.
- Kampschulte, A. and Strauss, H. 2004. The sulfur isotopic evolution of Phanerozoic seawater based on the analysis of structurally substituted sulfate in carbonates, *Chemical Geology*, 204: 255–286, 10.1016/j.chemgeo.2003.11.013.
- Keeling, C. D., Bacastow, R. B., Carter, A. F., Piper, S. C., Whorf, T. P., Heimann, M., Mook, W. G. et al. 1989. A three dimensional model of atmospheric CO_2 transport based on observed winds, 1, Analysis of observational data. In: *Aspects of Climate Variability in the Pacific and the Western Americas*, *Geophysical Monograph* 55, Peterson, D. H. (ed.). pp. 165–237. Washington: AGU.
- Lawrence, J. R. and Taylor, H. P. 1972. Hydrogen and oxygen isotope systematics in weathering profiles, *Geochimica et Cosmochimica Acta*, 36: 1377–1393.
- Lawrence, J. R. and Meaux, J. R. 1993. The stable isotopic composition of ancient kaolinites of North America, in *Climate Change in Continental Isotopic Records*, *Geophysical Monograph* 78, Swart, P. K., Lohmann, K. C., McKenzie, J. and Savin, S. (eds), p. 249–261. Washington: AGU.
- Lee-Thorp, J., Thackeray, J. F. and van der Merwe, N. 2000. The hunters and the hunted revisited. *Journal of Human Evolution*, 39: 565–576, 10.1006/jhev.2000.0436.
- Lourantou, A., Lavrič, J. V., Köhler, P., Barnola, J.-M., Paillard, D., Michel, E. et al., 2010. Constraint of the CO₂ rise by new atmospheric carbon isotopic measurements during the last deglaciation, *Global Biogeochemical Cycles*, 24: GB2015, doi:10.1029/2009gb003545.
- Luthi, D., Le Floch, M., Bereiter, B., Blunier, T., Barnola, J.-M., Siegenthaler, U. et al., 2008. High-resolution carbon dioxide concentration record 650,000–800,000 years before present. *Nature*, 453: 379–382.
- MacFadden, B. J., Solounias, N. and Cerling, T. E. 1999. Ancient diets, ecology, and extinction of 5-million-year-old horses from Florida. *Science*, 283: 824–827.
- McCutchan, J. H., Lewis, W. M., Kendall, C. and McGrath, C. C. 2003. Variation in trophic shift for stable isotope ratios of carbon, nitrogen, and sulfur. *Oikos*, 102: 378–390.
- Mojzsis, S. J., Arrhenius, G., McKeegan, K. D., Harrison, T. M., Nutman, A. P. and Friend, C. R. L. 1996. Evidence for life on Earth before 3800 million years ago. *Nature*, 384: 55–59.
- Müller, W., Fricke, H., Halliday, A. N., McCulloch, M. T. and Warthro, J.-A. 2003. Origin and migration of the alpine Iceman. *Science*, 302: 862–866.
- Oppo, D. W. and Fairbanks, R. G. 1987. Variability in the deep and intermediate water circulation of the Atlantic Ocean during the past 25,000 years: Northern Hemisphere modulation of the Southern Ocean. *Earth and Planetary Science Letters*, 86: 1–15.
- Osborn, S. G., Vengosh, A., Warner, N. R. and Jackson, R. B. 2011. Methane contamination of drinking water accompanying gas-well drilling and hydraulic fracturing. *Proceedings of the National Academy of Sciences*, 108: 8172–8176.
- Pagani, M., Arthur, M. A. and Freeman, K. 1999. Miocene evolution of atmospheric carbon dioxide. *Paleoceanography*, 14: 273–292.
- Quade, J., Cerling, T. E. and Bowman, J. R. 1989. Development of Asian monsoon revealed by marked ecological shift during the latest Miocene in northern Pakistan. *Nature*, 342: 163–166.
- Quay, P., Sonnerup, R., Stutsman, J., Maurer, J., Körtzinger, A., Padin, X. A. and Robinson, C. 2007. Anthropogenic CO₂ accumulation rates in the North Atlantic Ocean from changes in the $^{13}C/^{12}C$ of dissolved inorganic carbon. *Global Biogeochemical Cycles*, 21: GB1009, doi: 10.1029/2006gb002761.
- Quay, P., Sonnerup, R., Westby, T., Stutsman, J. and McNichol, A. 2003. Changes in the $^{13}C/^{12}C$ of dissolved inorganic carbon in the ocean as a tracer of anthropogenic CO₂ uptake. *Global Biogeochemical Cycles*, 17: 1004, doi: 10.1029/2001gb001817.
- Rau, G. 1994. Variations in sedimentary organic δC as a proxy for past changes in ocean and atmospheric CO₂ reconstructions. In: *Carbon Cycling in the Glacial Ocean: Constraints on the Ocean's Role in Global Change*, Zahn, R., Pedersen, T. F., Kaminski, M. A. and Labeyrie, L. (eds). pp. 309–321. Berlin: Springer-Verlag.
- Richards, M. P. and Trinkaus, E. 2009. Isotopic evidence for the diets of European Neanderthals and early modern humans. *Proceedings of the National Academy of Sciences U.S.A.*, 106: 16034–16039, doi: 10.1073/pnas.0903821106.
- Røsing, M. 1999. ^{13}C -depleted carbon microparticles in >3700 Ma sea-floor sedimentary rocks from West Greenland. *Science*, 283: 674–676.
- Røsing, M., Rose, M. N., Bridgwater, D. and Thomsen, H. S. 1996. Earliest part of Earth's stratigraphic record: a reappraisal of the >3.7 Ga Isua (Greenland) supracrustal sequence. *Geology*, 24: 43–46.

- Ruddiman, W. F. 2006. Orbital changes and climate. *Quaternary Science Reviews*, 25: 3092–3112, doi:10.1016/j.quascirev.2006.09.001.
- Savin, S. M. and Epstein, S. 1970. The oxygen and hydrogen isotope geochemistry of clay minerals. *Geochimica et Cosmochimica Acta*, 34: 25–42.
- Schidlowski, M. 1988. A 3800-million year isotopic record of life from carbon in sedimentary rocks. *Nature*, 333: 313–318.
- Schoeninger, M. J. and DeNiro, M. J. 1984. Nitrogen and carbon isotopic composition of bone collagen from marine and terrestrial animals. *Geochimica et Cosmochimica Acta*, 48: 625–639.
- Shackleton, N. J. 1977. Carbon-13 in *Uvigerina*: tropical rainforest history and the Pacific carbonate dissolution cycles. In: *The Fate of Fossil Fuels in the Oceans*, Anderson, N. R. and Malahoff, A. (eds). New York: Plenum.
- Shackleton, N. J. and Opdyke, N. D. 1973. Oxygen isotope and paleomagnetic stratigraphy of an equatorial Pacific core V28–238: oxygen isotope temperatures and ice volumes on a 10^5 and 10^6 year time scale, *Quaternary Research*, 3: 39–55.
- Siegenthaler, U. and Sarmiento, J. L. 1993. Atmospheric carbon dioxide and the ocean. *Nature*, 365: 119–125.
- Spötl, C., Mangini, A., Frank, N., Eichstädter, R. and Burns, S. J. 2002. Start of the last interglacial period at 135 ka: Evidence from a high Alpine speleothem. *Geology*, 30: 815–818, doi: 10.1130/0091-7613(2002)030<0815:sotlip>2.0.co;2.
- Taylor, H. P. 1974. The application of oxygen and hydrogen studies to problems of hydrothermal alteration and ore deposition. *Economic Geology*, 69: 843–883.
- Thomas, A. L., Henderson, G. M., Deschamps, P., Yokoyama, Y., Mason, A. J., Bard, E., et al. 2009. Penultimate deglacial sea-level timing from uranium/thorium dating of Tahitian corals. *Science*, 324: 1186–1189, doi: 10.1126/science.1168754.
- Toggweiler, J. R., Russell, J. L. and Carson, S. R. 2006. Midlatitude westerlies, atmospheric CO₂, and climate change during the ice ages. *Paleoceanography*, 21: PA2005, 10.1029/2005pa001154.
- Toggweiler, J. R. 1999. Variation of atmospheric CO by ventilation of the ocean's deepest water. *Paleoceanography*, 14: 571–588, doi: 10.1029/1999pa900033.
- Urey, H. C. 1947. The thermodynamics of isotopic substances, *Journal of the Chemical Society*, 1947: 562–581.
- van der Merwe, N. J., Thackeray, J. F., Lee-Thorp, J. A. and Luyt, J. 2003. The carbon isotope ecology and diet of Australopithecus africanus at Sterkfontein, South Africa. *Journal of Human Evolution*, 44: 581–597, doi: 10.1016/s0047-2484(03)00050-2.
- van Zijl, M. A., Lepland, A., Teranes, J., Finarelli, J., Whalen, M. and Arrhenius, G. 2003. Graphite and carbonates in the 3.8 Ga old Isua supracrustal belt, southern West Greenland. *Precambrian Research*, 136: 331–348.
- Volk, T. 1987. Feedbacks between weathering and atmospheric CO₂ over the last 100 million years. *American Journal of Science*, 287: 763–779.
- Walker, J. C. G. 1995. There is more to climate than carbon dioxide. *U.S. National Report to International Union of Geodesy and Geophysics*. Ann Arbor: American Geophysical Union.
- Wang, Y., Deng, T. and Biasatti, D. 2006. Ancient diets indicate significant uplift of southern Tibet after ca. 7 Ma. *Geology*, 34(4): 309–312.
- Wang, Y., Cerling, T. E. and MacFadden, B. J. 1994. Fossil horses and carbon isotopes: new evidence for Cenozoic dietary, habitat, and ecosystem changes in North America. *Palaeogeography, Palaeoclimatology, Palaeoecology*, 107: 269–279.
- Winograd, I., Coplen, T. B., Landwehr, J. M., Riggs, A. C., Ludwig, K. R. et al., 1992. Continuous 500,000 year climate record from vein calcite in Devils Hole, Nevada. *Science*, 258: 255–260.
- Zachos, J. C., Pagani, M., Sloan, L., Thomas, E. and Billups, K. 2001. Trends, rhythms, and aberrations in global climate 65 Ma to present, *Science*, 292: 686–693.

SUGGESTIONS FOR FURTHER READING

- Amiot, R., Lécuyer, C., Buffetaut, E., Escarguel, G., Fluteau, F. and Martineau, F. 2006. Oxygen isotopes from biogenic apatites suggest widespread endothermy in Cretaceous dinosaurs, *Earth and Planetary Science Letters*, 246: 41–54, 10.1016/j.epsl.2006.04.018.
- Barnola, J. M., Raynaud, D., Korotkevich, Y. S. and Lorius, C. 1987. Vostok ice core provides 160,000 year record of atmospheric CO₂, *Nature*, 329: 409–414.
- Broecker, W. S. and Denton, G. H. 1989. The role of ocean-atmosphere reorganizations in glacial cycles, *Geochimica et Cosmochimica Acta*, 53: 2465–2501.
- Cerling, T. E. 1984. The stable isotopic composition of modern soil carbonate and its relationship to climate, *Earth and Planetary Science Letters*, 71: 229–240.
- Cerling, T. E., Wang, Y. and Quade, J. 1993. Expansion of C₄ ecosystems as an indicator of global ecological change in the late Miocene, *Nature*, 361: 344–345.
- Dansgaard, W., Jonhsen, S. J., Clauson, H. B., Dahl-Jensen, D., Gundestrup, N. S., Hammer, C. U., et al. 1993. Evidence for general instability in past climate from a 250-kyr ice-core record. *Nature*, 364: 218–220.

- Edmond, J. M., Palmer, M. R., Measures, C. I., Grant, B. and Stallard, R. F. 1995. The fluvial geochemistry and denudation rate of the Guayana Shield in Venezuela, Columbia, and Brazil. *Geochimica et Cosmochimica Acta*, 59: 3301–3326.
- Goericke, R. and Fry, B. 1994. Variations of marine phytoplankton $\delta^{13}\text{C}$ with latitude, temperature, and dissolved CO_2 in the world ocean. *Global Biogeochemical Cycles*, 8: 85–90.
- Grootes, P. M., Stuiver, M., White, J. W. C., Johnsen, S. and Jouzel, J. 1993. Comparison of oxygen isotope records from the GISP2 and GRIP Greenland ice cores. *Nature*, 366: 552–554.
- Holser, W. T. 1984. Gradual and abrupt shifts in ocean chemistry during Phanerozoic time. In: *Patterns of Change in Earth Evolution*, Holland, H. D. and Trendall, A. (eds). Princeton University Press, Princeton.
- Leuenberger, M., Siegenthaler, U. and Langway, C. C. 1992. Carbon isotopic composition of atmospheric CO_2 during the last ice age from an Antarctic ice core. *Nature*, 357: 488–490.
- McCrea, J. M. 1950. On the isotopic chemistry of carbonates and a paleotemperature scale. *Journal of Chemical Physics*, 18: 849–857.
- Rau, G. H., Froelich, P. N., Takahashi, T. and DesMarais, D. J. 1991. Does sedimentary organic $\delta^{13}\text{C}$ record variations in ocean $[\text{CO}_{2\text{aq}}]$? *Global Biogeochemical Cycles*, 6: 335–347.
- Schlesinger, W. H. 1991. *Biogeochemistry*. San Diego: Academic Press.
- Shackleton, N. J. and Kennett, J. P. 1975. Paleotemperature history of the Cenozoic and the initiation of Antarctic glaciation: oxygen and carbon isotope analyses in DSDP sites 277, 279, and 281. *Deep Sea Drilling Project Initial Reports*, 29: 743–755.
- Tans, P. P., Berry, J. A. and Keeling, R. F. 1993. Oceanic $^{13}\text{C}/^{12}\text{C}$ observations: a new window on ocean CO_2 uptake. *Global Biogeochemical Cycles*, 7: 353–368.
- Taylor, K. C., Lamorey, G. W., Doyle, G. A., Alley, R. B., Grootes, P. M., Mayewski, P. A., et al. 1993. The flickering switch of late Pleistocene climate change. *Nature*, 361: 432–436.

PROBLEMS

- Assuming that in a certain species of C_3 plant the fractionation of carbon isotopes during carboxylation is $-29.4\text{\textperthousand}$, the fractionation due to diffusion of CO_2 into the plant is $-4.4\text{\textperthousand}$, and the concentration of CO_2 in the interior of the cell is 150 ppm, what will the fractionation, Δ , be for exterior CO_2 concentrations of 150, 250, 360, and 600 ppm?
- Do a search of the scientific literature (using a tool such as Google Scholar, Scopus, or Web of Science) and find a recent paper where light stable isotopes have been used in an archeological or paleontological study. Describe the study and the role of isotope geochemistry in it.
- Glaciers presently constitute about 2.1% of the water at the surface of the Earth and have a $\delta^{18}\text{O}_{\text{SMOW}}$ of ≈ -30 . The oceans ($\delta^{18}\text{O}_{\text{SMOW}} = 0$) contain essentially all remaining water. If the mass of glaciers were to increase by 50%, how would the isotopic composition of the ocean change (assuming the isotopic composition of ice remains constant)?
- The mass of the oceans is 1.4×10^{21} g, that of the atmosphere is 5.1×10^{18} kg. During Pleistocene interglacial periods atmospheric CO_2 concentration was typically 290 ppmv (parts per million by volume) and a typical glacial atmospheric CO_2 concentration was 180 ppmv. If the interglacial concentration of dissolved CO_2 in the ocean was 2100 mmoles/kg, how much would the glacial concentration of dissolved CO_2 in the ocean have to be if all the CO_2 missing from the atmosphere had dissolved in the ocean? Assume a molecular weight for the atmosphere of 28.9.
- The data in Figure 10.36 indicates that at the end of the last glacial period, atmospheric CO_2 rose from 190 ppm to 270 ppm in 7000 years. Assuming all this CO_2 was derived from the ocean, how much greater must the ocean-to-atmosphere flux have been during this period than the present flux of about 92 Gt C/yr? (Assume a molecular weight for the atmosphere of 28.9 and note that the present flux is in gigatons of *carbon* rather than CO_2 .)
- How does Eqn. 10.4 compare to Eqn. 8.94? What physical assumptions and mathematical manipulations need be made to reconcile the two?

Chapter 11

Unconventional isotopes and approaches

11.1 INTRODUCTION

Traditional stable isotope geochemistry, the field developed by Harold Urey and his colleagues and students, focused on simple isotope ratios of light elements that can be analyzed in a gas source mass spectrometer: $^2\text{H}/^1\text{H}$, $^{13}\text{C}/^{12}\text{C}$, $^{15}\text{N}/^{14}\text{N}$, $^{18}\text{O}/^{16}\text{O}$, and $^{34}\text{S}/^{32}\text{S}$. Over the past decade or two, stable isotope geochemistry has expanded in three important new directions.

First, geochemists have begun to exploit the tendency of isotopes of pairs of elements, particularly carbon and oxygen, to “clump” in thermodynamically preferred isotopologues. We introduced the theoretical basis of this approach in Chapter 8. In this chapter, we explore some examples of the uses and applications of this approach. A review by Eiler (2013) provides other examples.

Second, by analyzing additional isotope ratios of oxygen and sulfur, specifically $^{17}\text{O}/^{16}\text{O}$ and $^{33}\text{S}/^{32}\text{S}$, mass-independent fractionations were discovered in terrestrial materials in the past decade or so. As we found in Chapter 8, both equilibrium and kinetic effects should produce fractionations whose magnitude depends on the relative mass difference between the isotopes of interest; this is known as mass-dependent fractionation. However, reactions induced by relatively high-energy photons in the atmosphere can produce fractionations in which the magnitude of fractionation is independent of the mass difference between isotopes. Studying these mass-independent fractionations have

led to important new insights into Earth processes and evolution.

Third, the list of elements of interest has greatly expanded, including both light elements such as Li and B, which we would expect to experience relatively large fractionations, but also heavier metals and gases such as Mg, Si, Cl, Ca, Fe, Cu, Zn, Se, Mo, Tl, Hg, and U, which experience smaller, but nonetheless measurable fractionations. A variety of techniques are used in analysis including thermal ionization (for example, boron can be analyzed as the heavy ion Cs_2BO_2^+), gas source mass spectrometry (Cl), multi-collector ICP-MS, and ion probe techniques. The theoretical principles are the same as we discussed in Chapter 8: heavier isotopes will enter the phase with the stronger bond and the extent of fractionation depends on temperature. The largest fractionations will occur where the element is partitioned between phases in which the element’s atomic environment is very different or its oxidation state changes. Biologically mediated reactions produce some of the largest fractionations for these elements, particularly Fe, Cu, and Zn, just as was the case for traditional elements C, N, and S. The list of these “non-traditional” stable isotopes is sufficiently long that we have space here only to “highlight” some of the more fascinating insights these studies have provided. More details on these elements can be found in Volume 55 of *Reviews in Mineralogy: Geochemistry of Non-Traditional Stable Isotopes* (Johnson et al., 2004). These non-traditional stable isotopes are summarized in Table 11.1.

Table 11.1 Values of non-conventional stable isotope ratios.

Element	Notation	Ratio	Standard	Absolute Ratio
Lithium	$\delta^7\text{Li}$	${}^7\text{Li} / {}^6\text{Li}$	NIST L-SVEC	12.1735
Boron	$\delta^{11}\text{B}$	${}^{11}\text{B} / {}^{10}\text{B}$	NIST 951	4.0436
Magnesium	$\delta^{26}\text{Mg}$	${}^{26}\text{Mg} / {}^{24}\text{Mg}$	DSM3	0.13979
Silicon	$\delta^{30}\text{Si}$	${}^{30}\text{Si} / {}^{28}\text{Si}$	NBS28 (NIST-RM8546)	0.033532
	$\delta^{29}\text{Si}$	${}^{29}\text{Si} / {}^{28}\text{Si}$		0.050804
Chlorine	$\delta^{37}\text{Cl}$	${}^{37}\text{Cl} / {}^{35}\text{Cl}$	seawater (SMOC) NIST-SRM 975	0.31963 0.31977
Calcium	$\delta^{44/42}\text{Ca}$	${}^{44}\text{Ca} / {}^{42}\text{Ca}$	NIST SRM 915a	0.310163
	$\delta^{44/40}\text{Ca}$	${}^{44}\text{Ca} / {}^{40}\text{Ca}$		0.021518
	$\delta^{43/42}\text{Ca}$	${}^{43}\text{Ca} / {}^{42}\text{Ca}$		0.208655
Iron	$\delta^{56}\text{Fe}$	${}^{56}\text{Fe} / {}^{54}\text{Fe}$	IRMM-14	15.698
	$\delta^{57}\text{Fe}$	${}^{57}\text{Fe} / {}^{54}\text{Fe}$		0.363255
Copper	$\delta^{65}\text{Cu}$	${}^{65}\text{Cu} / {}^{63}\text{Cu}$	NIST 976	0.44562
Zinc	$\delta^{68}\text{Zn}$	${}^{68}\text{Zn} / {}^{64}\text{Zn}$	JMC3-0749L	0.37441
	$\delta^{66}\text{Zn}$	${}^{66}\text{Zn} / {}^{64}\text{Zn}$		0.56502
Molybdenum	$\delta^{97/95}\text{Mo}$	${}^{97}\text{Mo} / {}^{95}\text{Mo}$	various*	0.5999
	$\delta^{98/95}\text{Mo}$	${}^{98}\text{Mo} / {}^{95}\text{Mo}$		1.5157

*No interlaboratory standard has been agreed upon. Based on data listed in Coplen et al. (2002).

11.2 APPLICATIONS OF ISOTOPIC CLUMPING

We introduced the theory behind isotopic “clumping” studies in Chapter 8. Here, we’ll consider applications to geothermometry and paleoclimatology. A significant advantage of clumped isotope geothermometry is that, assuming equilibrium was achieved between a carbonate mineral and the water from which it precipitated and no subsequent disturbance of the system, both paleotemperatures and the isotopic composition of the water can be determined from analysis of the carbonate. This is because the Δ_{47} parameter (a measure of the abundance of the ${}^{13}\text{C}{}^{18}\text{O}{}^{16}\text{O}$ isotopologue relative to a purely stochastic distribution we introduced in Chapter 8) is a function only of the equilibrium temperature for a given mineral. Once the equilibrium temperature is known, then the $\delta^{18}\text{O}$ and $\delta^{13}\text{C}$ of the water can be calculated from the $\delta^{18}\text{O}$ and $\delta^{13}\text{C}$ of the carbonate (e.g., Eqn. 10.1).

We saw in Chapter 10 how oxygen and hydrogen isotope geothermometry has successfully determined the cause of the Pleistocene “Ice Ages” and reconstructed climate variation through the Cenozoic. Qualitative proxies such as fossils and glacial sediments indicate that dramatic climate variations also occurred in the Mesozoic and, particularly, the Paleozoic: there is evidence of glaciation in the Carboniferous that was as severe as

the Pleistocene as well as evidence for perhaps less severe glaciation in the Late Ordovician, with intervening periods that appear to have been significantly warmer than the present. Such warmer temperatures would be consistent with much higher modeled atmospheric CO_2 concentrations in the Paleozoic (such as shown in Figure 10.43). However, oxygen isotope geothermometry based on carbonate fossils suggests that variations of tropical sea surface temperatures were relatively small over this time. Conventional isotope geothermometry, however, necessarily requires assumptions about the oxygen isotopic composition of seawater of the time. For the Pleistocene and even the Tertiary, the isotopic composition of seawater is readily constrained (as discussed in Chapter 10). This is not so easily done for periods earlier in Earth’s history. Veizer et al. (1999) argued, based on analysis of marine carbonate fossils, that $\delta^{18}\text{O}$ increased from a mean value of about $-8\text{\textperthousand}$ in the Cambrian to a present value close to 0\textperthousand . Muehlenbachs, however, has argued that seawater $\delta^{18}\text{O}$ has been buffered by ridge-crest hydrothermal activity to values close to 0 throughout Earth’s history (Muehlenbachs, 1976; Muehlenbachs and Furnas, 2003; Chapter 9).

To address these issues, Came et al. (2007) analyzed carbon and oxygen isotopes of Silurian brachiopods from Anticosti Island,

Canada, and Carboniferous (Pennsylvanian) molluscs from Oklahoma; both of these localities were tropical at the time. Came et al. applied clumped isotope geothermometry to determine the temperatures of seawater in which they grew. Although all samples appeared to be well preserved based on various criteria, some proved to have been diagenetically altered, yielding unreasonably high temperatures and anomalous $\delta^{13}\text{C}$ and $\delta^{13}\text{O}$ seawater values. The remaining samples yielded growth temperatures of $24.9 \pm 1.7^\circ\text{C}$ for the Carboniferous, and $34.9 \pm 0.4^\circ\text{C}$ for the Silurian. The Carboniferous temperatures are similar to or slightly lower than those of modern tropical seas, while the Silurian temperatures are significantly warmer. The authors point out that these temperature differences are consistent with models of atmospheric CO_2 during the Paleozoic: CO_2 was substantially higher in the Silurian than in the both the Carboniferous and the present. Came et al. also calculated $\delta^{18}\text{O}_{\text{SMOW}}$ of seawater for both times and obtained values of $-1.2 \pm 0.1\text{\textperthousand}$ and $-1.6 \pm 0.5\text{\textperthousand}$, values quite close to the modern one (the present seawater $\delta^{18}\text{O}_{\text{SMOW}}$ is, of course, 0, but is $\sim -1.5\text{\textperthousand}$ if Antarctic and Greenland ice is included). The results suggest that the $\delta^{18}\text{O}$ of seawater has been approximately constant, at least through the Phanerozoic, and that the low values of $\delta^{18}\text{O}$ observed for Paleozoic carbonates by Veizer et al. (1999) appear to reflect a combination of higher seawater temperatures and, predominately, diagenetic alteration of the carbonates.

A second example addresses the question of whether or not dinosaurs were warm-blooded, a question that has lingered for over 150 years. Reptiles are, of course, cold-blooded (ectotherms) and often spend the early hours of the day warming themselves in the Sun before becoming active. For the largest dinosaurs, the sauropods, the problem was less keeping warm than keeping cool. Because of their enormous mass, which exceeded 9 tons in some cases, their internal temperatures might have exceeded 40°C if they could not efficiently shed metabolically generated internal heat. Eagle et al. (2010) analyzed the carbonate component from tooth apatite, $\text{Ca}_5(\text{PO}_4,\text{CO}_3)_3(\text{OH},\text{CO}_3,\text{F},\text{Cl})$, in five modern animal species: elephant, rhino, crocodile, alligator, and sand shark, whose estimated

body temperatures ranged from 37 to 23.6°C . They found that Δ_{47} of the carbonate component released by phosphoric acid digestion showed the same relationship to temperature as for inorganic calcite (Chapter 8). The teeth of two fossil mammoths also analyzed yielded temperatures of $38.4 \pm 1.8^\circ\text{C}$, within error of the body temperatures of modern elephants. Tooth dentin of the mammoths, however, yielded lower temperatures, but both $\delta^{18}\text{O}$ and rare earth patterns of the phosphate component suggested the dentin has suffered diagenetic alteration. Eagle et al. (2011) then analyzed tooth enamel from Jurassic sauropods. Teeth from the Tendaguru Beds of Tanzania of three *Brachiosaurus* fossils yielded temperatures of $38.2 \pm 1^\circ\text{C}$ and two fossils of *Diplodocinae* yielded temperatures of $33.6 \pm 4^\circ\text{C}$. Three *Camarasaurus* teeth from the Morrison Formation in Oklahoma yielded temperatures of $36.9 \pm 1^\circ\text{C}$, while one from Howe Quarry in Wyoming yielded a lower temperature of $32.4 \pm 2.4^\circ\text{C}$. These temperatures are $5\text{--}12^\circ\text{C}$ higher than modern crocodilians and, with the exception of the Howe Quarry tooth, within error of modern mammals. They are also $4\text{--}7^\circ\text{C}$ lower than predicted for animals of this size if they did not somehow thermoregulate. The authors note that this does not prove that dinosaurs were endotherms, but it does indicate that a “combination of physiological and behavioral adaptations and/or a slowing of metabolic rate prevented problems with overheating and avoided excessively high body temperatures.” In modern mammals, tooth enamel is produced only in youth. If this was also true of sauropods, it indicates that they maintained high body temperatures during youth, consistent with observations of bone structure that suggests high growth rates.

For the third example, we fast-forward 200 million years to the Pliocene of East Africa, the time and place of the emergence of the genus *Homo*. Abundant hominid fossils and artifacts of Plio-Pleistocene age have been found in the Turkana Basin, part of the East African Rift in Kenya. This area presently is among the hottest 1% of land on the planet with a mean annual temperature of almost 30°C . Much of the basin is occupied by a saline lake, Lake Turkana, and the surround land is quite arid. But what was the climate there like as our genus evolved from Australopithecine

ancestors? Some paleoclimatic proxies derived from fossil pollen assemblages suggest that late Pliocene temperatures were cooler than present, while other proxies and models suggest an even warmer climate. To resolve this, Passey et al. (2010) applied clumped isotope geothermometry to paleosol carbonates of Pliocene and Pleistocene age from the Turkana Basin. Before doing so, however, they demonstrated that temperatures calculated from Δ_{47} in modern soil carbonates did in fact reflect the climate in which they formed. They found good agreement between calculated temperatures from soil carbonates and mean annual temperatures in tropical regions, although in temperate latitudes (such as California), soil carbonate clumped isotope temperatures correlated with mean warm season temperature rather than mean annual temperature. That's not surprising since we expect soil carbonates to form only with evaporation exceeds precipitation, and in temperate latitudes that occurs

in summer. Passey et al. (2010) also measured modern soil temperatures at 50 cm depth in the Turkana Basin and found that they typically were 4°C higher than mean average air temperature.

The results of this study are shown in Figure 11.1a. Calculated clumped isotope paleosol temperatures range from 28–41°C and average 33°C, quite similar to the average modern soil temperature of 35°C measured by Passey et al. There is no secular trend apparent over the period from 4–0.5 Ma. Calculated $\delta^{18}\text{O}_{\text{SMOW}}$ and measured $\delta^{13}\text{C}_{\text{PDB}}$ values are shown in Figure 11.1b. There is a hint of an increase in $\delta^{13}\text{C}_{\text{PDB}}$ through time, consistent with an increasing component of C_4 grasses in the flora. $\delta^{18}\text{O}$ appears constant through the Pliocene but steadily increased through the Pleistocene, consistent with the results of an earlier study of Turkana Basin paleosols (Cerling et al., 1988). There are several possible causes of the increase in $\delta^{18}\text{O}$,

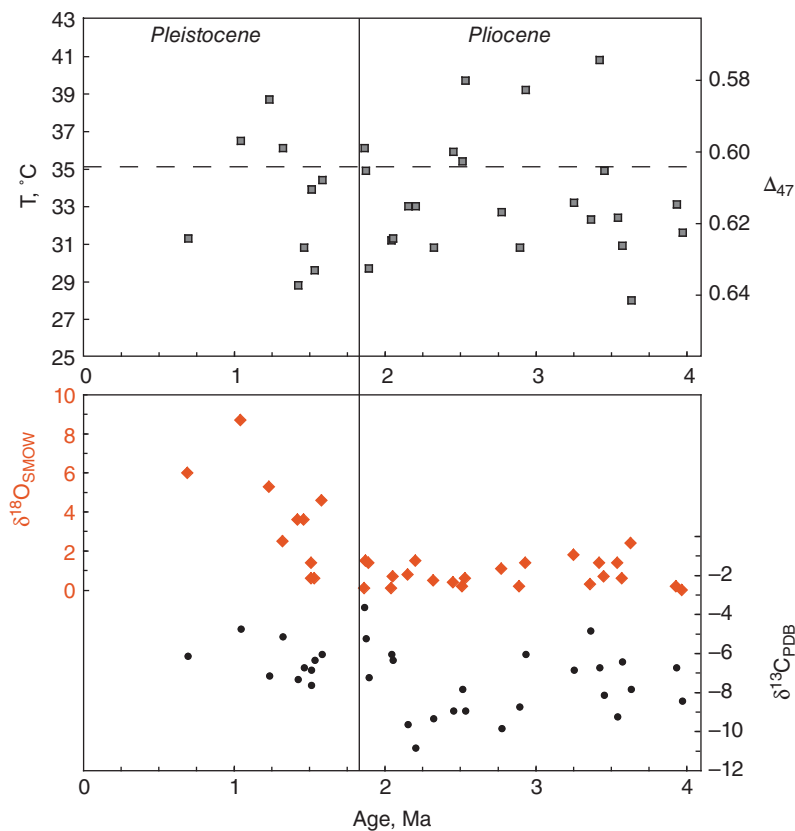


Figure 11.1 (a) Δ_{47} and calculated soil temperatures of paleosols from the Turkana Basin, Kenya. Dashed line shows the average modern soil temperature at a depth of 50 cm. (b) Measured $\delta^{13}\text{C}_{\text{PDB}}$ and calculated $\delta^{18}\text{O}_{\text{SMOW}}$ of Turkana Basin paleosols. Data from Passey et al. (2010).

including changes in basin hydrology and regional atmospheric and oceanic circulation. The interpretation consistent with other paleoclimatic indicators from the area is that the Turkana Basin, while equally hot, was less arid in the Pliocene than at present. Regardless, the results show that our genus originated in one of the hottest climates on the planet, which on the one hand, may explain our preference for warm weather, and on the other, makes our adaption to extremely cold climates all the more remarkable.

11.3 MASS INDEPENDENT ISOTOPE FRACTIONATIONS

11.3.1 Mass-independent fractionation of oxygen in the atmosphere

In Chapters 5 and 8, we found that oxygen isotopes exhibit mass independent fractionations in meteorites and in atmospheric ozone. Mass independent fractionations of oxygen isotopes also occur in other atmospheric species, as may be seen in Figure 11.2. Atmospheric nitrates show particularly strong mass independent fractionation. Nitrate forms in the atmosphere in a variety of ways. Some mechanisms are homogeneous phase reactions (i.e., they result from reactions entirely in the gas phase) with ozone or the OH molecule. Others are heterogeneous phase reactions, involving both gaseous and liquid phases such as water droplets. Fractionations are larger in the heterogeneous reactions than the homogeneous ones. There is a seasonal variation in the isotopic composition of atmospheric nitrate, such that fractionation is greater in winter months because of the greater cloudiness in winter (more water droplets), and hence greater contribution of heterogeneous phase reactions in winter. The nitrate, dissolved in water droplets as nitric acid, is washed out of the atmosphere by rain and into streams, soil, and so on. The signature of mass independent isotope fractionation then propagates through entire ecosystems, providing a tracer of nitrate for scientific studies.

Atmospheric sulfur oxides also exhibit mass independent isotope fractionation. Sulfur makes its way into the atmosphere in a number of ways: volcanic emission of H_2S and SO_2 , biomass burning (both anthropogenic and natural), and oxidation of dimethyl sulfide ($\text{C}_2\text{H}_6\text{S}$), which is emitted by marine

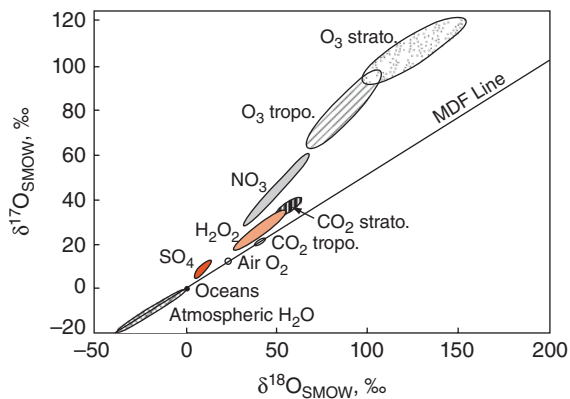
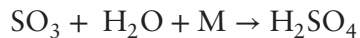


Figure 11.2 Oxygen isotopic composition of atmospheric oxygen-bearing species. (Source: Thiemens and Shaheen (2014). Reproduced with permission of Elsevier.)

plankton. Once in the atmosphere, the various forms of sulfur are oxidized to SO_3 and then to sulfate (SO_4^{2-}). As with NO_2 oxidation, this last step may be either a homogeneous reaction in the gas phase, such as:



where M is another gas phase molecule, or a heterogeneous reaction in which sulfate is produced in solution (in a water droplet) by reaction with H_2O_2 or O_3 . Interestingly, only the heterogeneous phase reactions result in mass independent fractionation, with the ozone oxidation pathway producing a much larger fractionation than the peroxide one. Once formed, the sulfate retains its mass independent fractionated signature on at least million year time-scales (except under conditions of high acidity). This allows tracing of sulfur pathways through the atmosphere and biosphere on geologic time-scales. For example, sulfate salts in the dry valleys of Antarctica were shown to be derived in part from atmospheric oxidation of marine dimethyl sulfide.

Perhaps the most interesting application to come out of mass independent fractionation of sulfates is a measure of paleo-cloudiness. Again, as with the nitrates, mass independent fractionations are greatest when the oxidation occurs in solution. Consequently, more abundant droplets in the atmosphere result in a greater average extent of mass independent fractionation of sulfates. Turning that around, greater mass independent fractionation of

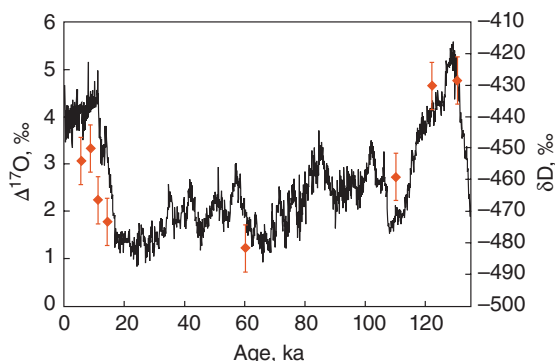


Figure 11.3 $\Delta^{17}\text{O}$ in sulfates (diamonds) in ice from the Vostok ice core compared with δD of the ice. Greater mass independent fractionation implies a drier climate during glacial periods. Data from Alexander et al. (2002). (Source: From Alexander et al. (2002). Reproduced with permission of John Wiley & Sons.)

oxygen in sulfates implies greater cloudiness. Figure 11.3 shows that mass independent oxygen isotope fractionation in sulfates in Vostok ice follows the δD curve. This is consistent with other evidence suggesting glacial period were drier, with fewer clouds.

11.3.2 Mass independent sulfur isotope fractionation and the rise of atmospheric oxygen

Sulfur isotope fractionations in the modern Earth are usually mass dependent and $\delta^{33}\text{S}$ and $\delta^{36}\text{S}$ are related to variations in $\delta^{34}\text{S}$ as

$$\delta^{33}\text{S} = 0.515 \times \delta^{34}\text{S} \quad \text{and} \quad \delta^{36}\text{S} = 1.90 \times \delta^{34}\text{S}$$

Some processes can produce mass independent fractionations. Let's define the quantities $\Delta^{33}\text{S}$ and $\Delta^{36}\text{S}$ as:

$$\Delta^{33}\text{S} = \delta^{33}\text{S} - 0.515 \times \delta^{34}\text{S} \quad (11.1)$$

and

$$\Delta^{36}\text{S} = \delta^{36}\text{S} - 1.90 \times \delta^{34}\text{S} \quad (11.2)$$

Mass independent fractionation of sulfur isotopes has been reported from sulfate aerosols from large volcanic eruptions, such as the 1991 eruption of Pinatubo, but not for smaller eruptions (Savarino, et al. 2003). The mechanism also appears to involve photolysis of SO_2 by ultraviolet light. Large plinian eruptions loft ash and aerosols into the stratosphere, whereas the products of smaller

eruptions are confined to the troposphere, into which relatively little UV penetrates.

In the modern Earth mass independent fractionation of sulfur is rare and appears to occur only in sulfur lofted into the stratosphere by these largest volcanic eruptions. However, Farquhar et al. (2000) found that many sulfides (primarily pyrite) in sediments and metasediments formed prior to 2500 Ma have positive $\Delta^{33}\text{S}$ and negative $\Delta^{36}\text{S}$ while hydrothermal sulfide ores and sedimentary sulfates (mainly barite) have negative $\Delta^{33}\text{S}$ and positive $\Delta^{36}\text{S}$ (Figure 11.4). During the Archean, $\Delta^{33}\text{S}$, that is, deviations from mass-dependent fractionation, of over 3‰ occurred. Farquhar et al. found smaller deviations, up to $1/2$ ‰ in rocks from the period 2500–2000 Ma. They found no significant deviations from mass dependent fractionation in rocks younger than 2000 Ma.

This raises the obvious question of what process or processes operated during the Archean that could produce mass independent fractionation? Why is this process now rare? As mentioned in Chapter 8, mass independent isotope fractionation has been observed during laboratory photolysis of SO_2 and SO using ultraviolet light. This, together with the observation that ozone and molecular oxygen absorb ultraviolet radiation, provides a possible explanation. Modern volcanic eruptions loft vast quantities of SO_2 into the atmosphere and Archean eruptions likely did as well. If the Archean atmosphere lacked O_2 and O_3 , ultraviolet radiation could penetrate deeply into it and photodissociate SO_2 . According to experiments, these reactions produce sulfate with negative $\Delta^{33}\text{S}$ and elemental sulfur with positive $\Delta^{33}\text{S}$. The sulfate would dissolve in rain and ultimately find its way into the oceans. Some of this would precipitate as barite, BaSO_4 . Some sulfate would be reduced in hydrothermal systems and precipitate as metal sulfides. Both these processes occur in modern oceans. The S would form particulate S_8 and also be swept out of the atmosphere by rain and ultimately incorporated into sediments, where it would react to form sedimentary sulfides. The latter also requires an absence of O_2 in the atmosphere since elemental S in the modern atmosphere is quickly oxidized.

Mass independent fractionation in Archean sulfur thus provides evidence that the early atmosphere lacked free oxygen. This is

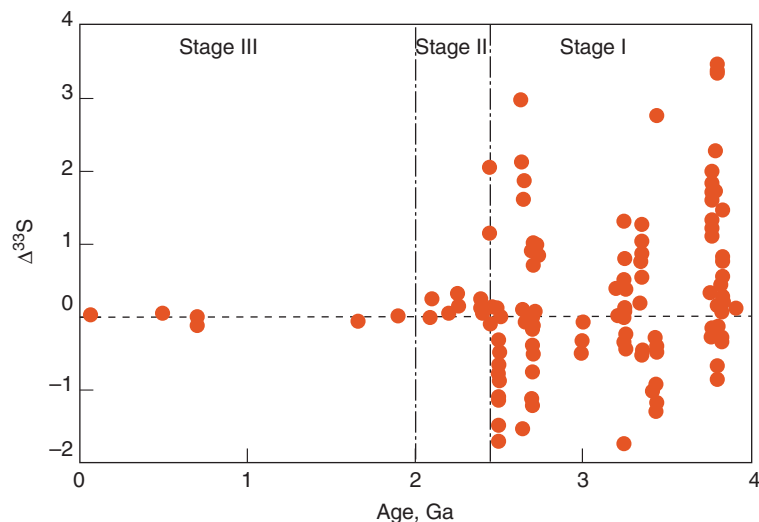


Figure 11.4 $\Delta^{33}\text{S}$ in sulfur through time. During Stage 1 (prior to 2.45 Ga), extensive mass independent fractionation occurred as evidenced by $\Delta^{33}\text{S}$ up to 3.5‰, indicating the lack of atmospheric oxygen. During Stage 2 (2.45 – 2.0 Ga), limited amounts of atmospheric oxygen absorbed most UV radiation and limited mass independent fractionation to <0.5‰. Higher levels of atmospheric oxygen, perhaps 10% of present levels or more, in Stage 3 (since 2.0 Ga) effectively eliminate UV radiation and mass independent fractionation. (Source: Farquhar and Wing (2003). Reproduced with permission of Elsevier.)

consistent with other evidence, such as the oxidation state of paleosols and detrital minerals, that the atmosphere did not contain significant amounts of O_2 until the early Proterozoic, about 2.4 billion years ago. Farquhar and Wing (2003), Kasting and Catling (2003), and Canfield (2005) provide excellent reviews on this topic.

Mass independent fractionation of sulfur has also been found in sulfide inclusions in diamond, which exhibit $\Delta^{33}\text{S}$ values up to +0.6‰ (Farquhar et al., 2002). The diamonds in question, from the Orapa kimberlite in Botswana, are of the “eclogitic” type, which also exhibit highly negative $\delta^{13}\text{C}$ and highly variable $\delta^{15}\text{N}$ (Chapter 8), suggesting an ancestry of subducted sedimentary organic matter. Dating of silicate inclusions in some eclogitic diamonds give Archean ages. Thus the Archean atmospheric sulfur had worked its way into the mantle. Mass-independent fractionated sulfur has been also reported from late Archean volcanogenic massive sulfides (VMS) and komatiite-hosted NiS deposits (Bekker et al., 2009) – the latter indicating that atmospheric sulfur found its way into magmatic systems, most likely through assimilation of crust and

earlier-formed VMS deposits. Recently Cabral et al. (2013) reported mass independent fractionations in sulfide inclusions in olivines of basaltic lavas from Mangaia, Cook Islands. These are shown in Figure 11.5 along with the compositions of sulfide inclusions in diamonds reported by Farquhar et al. (2002). Mangaia, as we saw in Chapter 6, has the most extreme of the St. Helena or HIMU-type OIB Pb and Sr isotopic signatures. Again, there is no known mechanism for producing mass independent fractionation of sulfur other than in the atmosphere, and that occurred almost exclusively in the Archean and earliest Proterozoic. Thus, this sulfur appears to be sedimentary sulfur transported into the mantle through subduction and only returned to the Earth’s surface 2.5 Ga or more later. It provides dramatic confirmation that material of surficial origin is indeed transported deep within the Earth and returned to the surface through mantle plumes.

11.4 ISOTOPES OF IRON AND MOLYBDENUM

Additional insights into the oxygenation of the atmosphere and ocean have come from the

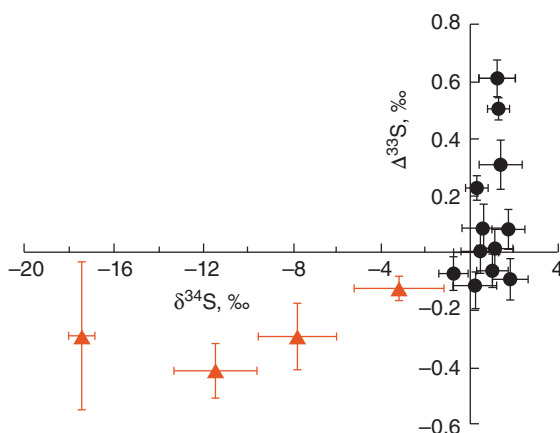


Figure 11.5 Sulfur isotope composition of sulfide inclusions in diamond (black circles) (Farquhar et al., 2002) and olivines from basaltic lavas of Mangaia, Cook Islands (diamonds) (Cabral, et al., 2013). Three of four of the Mangaia sulfides appear to form a mixing trend to a component with low $\delta^{34}\text{S}$ and low $\Delta^{33}\text{S}$. Another Mangaia inclusion of secondary origin had $\Delta^{33}\text{S} \approx 0$. (Source: Cabral et al. (2013). Reproduced with permission of Nature Publishing Group.)

isotopes of iron and molybdenum, metals that never form gases under conditions prevailing on Earth. Both Fe and Mo are transition metals that exist in several oxidation states. Both are bioessential elements. Iron plays a variety of roles in life, from photosynthesis in plants to oxygen transport in animals. Molybdenum is essential in bacterial nitrogen fixation (i.e., conversion of N_2 to NH_3 ; recall that only bacteria are capable of nitrogen fixation) and is an important component of many key enzymes, both in bacteria and eukaryotes such as you and I. In the modern ocean, these two elements behave very differently. In most environments at the surface of the Earth, iron is in the Fe^{3+} state and is highly insoluble. This, and its rapid uptake by phytoplankton, keeps its concentration in the ocean quite low and variable, near $1 \times 10^{-9}\text{M}$, despite being the most abundant element in the Earth. The reduced form of iron, Fe^{2+} is much more soluble. Molybdenum at the surface of the Earth is generally in the Mo^{6+} state and forms the highly soluble molybdate ion (MoO_4^{2-}) in aqueous solution. Consequently, its concentration in the ocean is about $1 \times 10^{-7}\text{M}$ and varies only

in proportion to total dissolved solids (i.e., salinity). In reducing environments, Mo can be reduced to the IV form where it can form molybdenum sulfide or molybdenum-iron sulfide phases.

11.4.1 Fe isotopes and the great oxidation event

Fe has four stable isotopes: ^{54}Fe , ^{56}Fe , ^{57}Fe , and ^{58}Fe , whose abundances are 5.85%, 91.74%, 2.12%, and 0.28%, respectively (Coursey et al., 2011). Most research has focused on the ratio of the two most abundant isotopes, $^{56}\text{Fe}/^{54}\text{Fe}$, expressed as $\delta^{56}\text{Fe}$; some studies also report $^{57}\text{Fe}/^{54}\text{Fe}$ as $\delta^{57}\text{Fe}$ and $^{57}\text{Fe}/^{56}\text{Fe}$ as $\delta^{57/56}\text{Fe}$. δ values are most commonly reported relative to the IRMM-14 standard whose isotopic composition is $^{56}\text{Fe}/^{54}\text{Fe} = 15.698$, $^{57}\text{Fe}/^{54}\text{Fe} = 0.36325$ and $^{58}\text{Fe}/^{54}\text{Fe} = 0.04823$, although some workers use average igneous rocks as the standard to define $\delta^{56}\text{Fe}$ (i.e., $\delta^{56}\text{Fe}_{\text{igneous rocks}} \equiv 0$; e.g., Johnson et al., 2008). Here, we will discuss iron isotopes relative to the IRMM standard, that is, $\delta^{56}\text{Fe}_{\text{IRMM-14}}$. Since all variations in iron isotopes observed to date fall along mass-dependent fractionation trends, we will consider only $\delta^{56}\text{Fe}$ (where only $\delta^{57}\text{Fe}$ values were reported, these have been converted to $\delta^{56}\text{Fe}$ using $\delta^{56}\text{Fe} = \delta^{57}\text{Fe} \times 0.668$; values reported relative to average igneous rock have been converted using $\delta^{56}\text{Fe}_{\text{IRMM-14}} = \delta^{56}\text{Fe}_{\text{igneous rocks}} + 0.014\text{\textperthousand}$).

Variation of $\delta^{56}\text{Fe}$ is shown in Figure 11.6. Igneous rocks show only very limited variation. Ninety-four published analyses of whole rock peridotite samples have a mean $\delta^{56}\text{Fe}_{\text{IRMM-14}}$ of $0.00\text{\textperthousand}$, with a standard deviation of $\pm 0.11\text{\textperthousand}$. This value likely represents the composition of the bulk silicate Earth. Larger variations occur in individual peridotite minerals. The average of 97 high precision analyses of oceanic basalts (mainly from Teng et al., 2013) is slightly heavier, $\delta^{56}\text{Fe}_{\text{IRMM-14}} = +0.11\text{\textperthousand}$ with a standard deviation of $0.03\text{\textperthousand}$. The difference between basalts and peridotites is consistent with a small ($\Delta^{56}\text{Fe} \approx -0.2\text{\textperthousand}$) fractionation between olivine and silicate liquid during partial melting and fractional crystallization (e.g., Weyer et al., 2005; Teng et al., 2008) and with the observation that the most depleted peridotites typically have the lightest

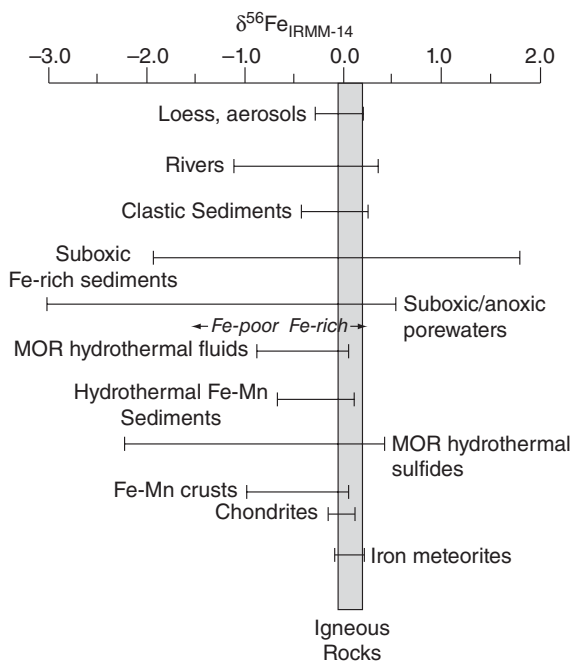


Figure 11.6 Variation of $\delta^{56}\text{Fe}$ in terrestrial materials and meteorites.

Fe (Williams et al., 2005). Granitoid igneous rocks are slightly heavier and more variable, $\delta^{56}\text{Fe} = +0.16 \pm 0.07\text{\textperthousand}$.

Data summarized by Craddock and Dauphas (2011) show that carbonaceous and ordinary chondrites have uniform $\delta^{56}\text{Fe}$ values of $-0.010 \pm 0.010\text{\textperthousand}$ and $-0.01 \pm 0.010\text{\textperthousand}$, respectively; enstatite chondrites appear to be just slightly heavier, with $\delta^{56}\text{Fe}$ of $+0.020 \pm 0.010\text{\textperthousand}$. On average, SNC meteorites (from Mars) have $\delta^{56}\text{Fe}$ of $-0.012 \pm 0.066\text{\textperthousand}$ and HED meteorites (from 4Vesta) have $\delta^{56}\text{Fe}$ of $0.019 \pm 0.027\text{\textperthousand}$, while lunar basalts have a mean $\delta^{56}\text{Fe}$ of $+0.105 \pm 0.127\text{\textperthousand}$, ($0.073\text{\textperthousand}$ if high-Ti basalts are excluded, which are slightly heavier), very similar to terrestrial basalts (Weyer et al., 2005). Thus the three other planetary bodies from which we have samples, the Moon, Vesta, and Mars, have Fe isotopic compositions that are nearly identical to each other and nearly indistinguishable from those of ordinary and carbonaceous chondrites. Iron meteorites have a mean and standard deviation $\delta^{56}\text{Fe}$ of $+0.050 \pm 0.101\text{\textperthousand}$; magmatic iron meteorites (those derived from asteroidal cores) have $\delta^{56}\text{Fe}$ of $+0.045 \pm 0.042\text{\textperthousand}$ and are thus just slightly heavier than chondrites

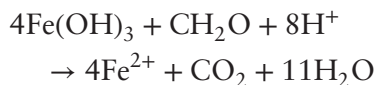
(Poitrasson et al., 2005). Several experimental studies have found that the equilibrium fractionation between metal and silicate liquid at high temperature and pressure is quite small, with $\Delta^{56}\text{Fe}_{\text{metal-silicate}} < 0.05\text{\textperthousand}$ (Poitrasson et al., 2005; Hin et al., 2012) and cannot account for even the small (but statistically significant) difference in $\delta^{56}\text{Fe}$ between iron meteorites and chondrites. The small difference in $\delta^{56}\text{Fe}$ between peridotites (presumably representing bulk silicate Earth) and chondrites is also statistically significant (although not above the 5% level) and could also not result from equilibrium fractionation during core formation. It is possible, however, that some as yet unrecognized form of kinetic fractionation could account for the difference; if so that could provide clues to the details of the core formation process.

Looking at Figure 11.6, we see that most materials having $\delta^{56}\text{Fe}$ significantly different than 0 have negative $\delta^{56}\text{Fe}$. This includes high temperature hydrothermal fluids from mid-ocean ridges. While most fluid samples have $\delta^{56}\text{Fe}$ closer to 0, Fe-poor fluids can have $\delta^{56}\text{Fe}$ as low as $-0.8\text{\textperthousand}$. The relationship to concentration suggests the fractionation results from precipitation of Fe oxides and pyrites, with the isotopically lightest fluids being those from which the most Fe has precipitated (Johnson et al., 2008).

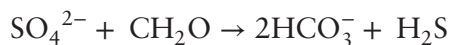
The largest iron isotopic variation is observed in sediments and low-temperature fluids and is principally due to the relatively large equilibrium fractionation ($\sim +3\text{\textpercent}$) associated with oxidation of Fe^{2+} to Fe^{3+} . However, Fe^{3+} produced by oxidative weathering of igneous and high-grade metamorphic rocks is immobile, consequently, isotopically heavy Fe^{3+} remains bound in the solid phase in minerals such as magnetite, iron-bearing clays, and iron oxy-hydroxides. Thus weathering in an oxidative environment produces little net change in Fe isotopic composition. Weathering in a reducing environment, as would have occurred in the early Archean, also produces little fractionation because there is no change in oxidation state. In the transition from anoxic early Archean world to the modern oxic one significant pools of both Fe^{2+} and Fe^{3+} would have existed, creating the potential for more significant variations in $\delta^{56}\text{Fe}$. The rise of atmospheric oxygen is, of course, a period of great significance in Earth

history and therefore of great interest to earth scientists. We now consider the insights iron isotopes provide into this period.

Johnson et al. (2008) argue that most of the fractionation evident in Figure 11.6 must be biologically mediated, although coordination changes and abiotic oxidation and reduction may contribute small fractionations. Two biological processes are important in reducing ferric iron in anoxic environments: dissimilatory iron reduction (DIR) and bacterial sulfate reduction (BSR). Both of these reactions occur only in the absence of free oxygen. In DIR, iron is the electron receptor in the oxidation of organic carbon, which can be written as:

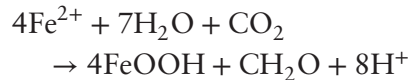


In BSR, sulfur is the electron receptor in organic carbon oxidation:



Iron is then reduced by reaction with sulfide and precipitated as iron sulfide (e.g., pyrite). Of these pathways, DIR produces the largest decrease in $\delta^{56}\text{Fe}$. In the Archean, ferric iron would have been rare or absent. However, many scientists believe that anoxygenic photosynthesis evolved before oxygenic

photosynthesis. Anoxygenic photosynthesis is performed today by green and purple bacteria that oxidize reduced sulfur in the course of reducing carbon. In the Archean, ferrous iron was likely a more abundant reductant than sulfide and may have been used by early photosynthetic life in reactions such as:



The fractionation associated with this reaction is thought to be similar to abiotic iron oxidation. Photosynthesis thus would have provided a supply of ferric iron to feed an iron cycle operating in parallel to the early carbon cycle.

Figure 11.7 shows the variation of $\delta^{56}\text{Fe}$ in various sedimentary materials over earth history. As we noted earlier, a variety of evidence, including sulfur isotope ratios, indicates that the atmosphere lacked significant levels of O_2 until about 2.4 billion years ago. Between 2.4 and 2.2 Ga, a number of changes are observed: detrital pyrite and uraninite disappear from sediments, so-called red beds (sandstones consisting of quartz coated with hematite) appear, sulfates such as gypsum appear in evaporite sequences, and paleosols become Fe-rich, indicating soil Fe was in the immobile Fe^{3+} form, all suggesting significant levels of atmospheric

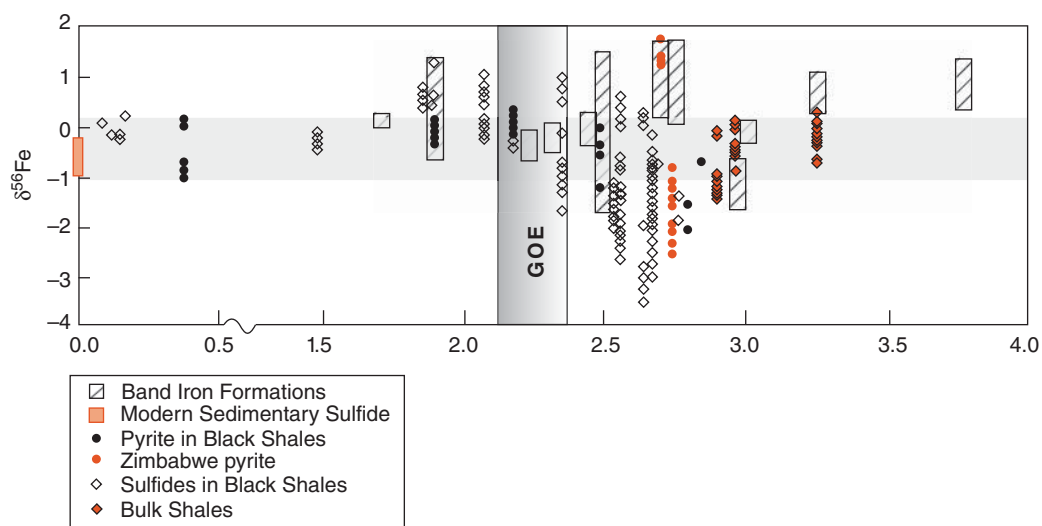


Figure 11.7 Variation of ^{56}Fe in sediments through geologic time. Modified from Anbar and Rouxel (2007) and Johnson et al., (2008) with additional data of Planavsky et al. (2012). Gray bar shows the time of the rise of atmospheric oxygen, or the “Great Oxidation Event” (GOE). (Source: Adapted from Anbar and Rouxel, 2007. Adapted from Johnson et al. 2008.)

oxygen. Figure 11.7 shows that iron isotope ratios became distinctly more variable around 2.8 billion years ago. A variety of works have argued that this indicates that significant pools of Fe^{3+} were already available by then, well ahead of the rise of atmospheric O_2 (e.g., Johnson et al., 2008).

Even in the early Archean, elevated $\delta^{56}\text{Fe}$ values are observed in banded iron formations. Banded iron formations (BIFs) are marine sediments, typically consisting of layers of iron oxide (usually hematite or magnetite, although in some cases the iron is concentrated in clays or carbonates) alternating with layers of chert. They are thought to have formed when ferrous iron-rich deep ocean water upwelled to the surface, was oxidized and precipitated, with the layering reflecting cyclic, perhaps annual, changes in upwelling. The ferrous iron was oxidized to ferric iron and precipitated. Oxidation could have occurred through anoxygenic photosynthesis (Kappler et al., 2005) or through reaction with dissolved oxygen in the surface water produced by photosynthesis. The former might be the best explanation for the smaller 3.7–3.8 billion year old BIF found in Isua, Greenland, but oxygenic photosynthesis may have been involved in the massive BIFs of the later Archean, such as the Hamersley deposit in Australia or the Mesoproterozoic deposits near Lake Superior in North America.

The positive $\delta^{56}\text{Fe}$ of BIFs in the Archean and the first half of the Proterozoic is consistent with partial oxidation of a large pool of dissolved Fe^{2+} , suggesting the deep oceans lacked dissolved oxygen. In the late Archean and early Proterozoic, $\delta^{56}\text{Fe}$ values in BIFs became less variable, perhaps because oxidation of available Fe^{2+} was more complete. The positive $\delta^{56}\text{Fe}$ in BIFs is complimented by negative $\delta^{56}\text{Fe}$ in black shales and pyrites, consistent with DIR of ferric iron. Both suggest that the surface waters of the ocean may have contained small by significant amounts of dissolved oxygen at this time. Further insights into the oxygenation of the oceans and atmosphere come from Mo isotopes, which we explore in the following paragraphs.

11.4.2 Mo isotopes and oxygenation of the oceans

Mo has seven stable isotopes: ^{92}Mo , ^{94}Mo , ^{95}Mo , ^{96}Mo , ^{97}Mo , ^{98}Mo , and ^{100}Mo , whose

abundances are 14.77%, 9.27%, 15.90%, 16.68%, 9.56%, 24.19%, 9.67%, respectively (Coursey et al., 2011). All of these are relatively abundant, but isobaric interferences with Zr make analysis of ^{92}Mo , ^{94}Mo , and ^{96}Mo difficult. Early studies reported the $^{97}\text{Mo}/^{95}\text{Mo}$ ratio expressed as $\delta^{97/95}\text{Mo}$ but more recent studies generally reported the $^{98}\text{Mo}/^{95}\text{Mo}$ ratio, expressed either as $\delta^{98/95}\text{Mo}$ or $\delta^{98}\text{Mo}$, since the variation in this ratio is larger. To date, there is no evidence of mass independent fractionation of molybdenum isotopes, so that $\delta^{98/95}\text{Mo} \approx 1.5 \times \delta^{97/95}\text{Mo}$. No widely accepted interlaboratory standard exists, although seawater, thought to have homogenous Mo isotopic composition, provides a basis for comparison (seawater $\delta^{98/95}\text{Mo} = 2.45 \pm 0.11$; Nakagawa et al., 2008). $\delta^{98/95}\text{Mo}$ shows about 5‰ variation in terrestrial materials (Figure 11.8). Although small nucleosynthetic-related anomalies have been observed in meteorites (e.g., Burkhardt et al., 2011), their isotopic composition is otherwise fairly uniform and similar to that of terrestrial igneous rocks, with no systematic variations between meteorite classes (Becker

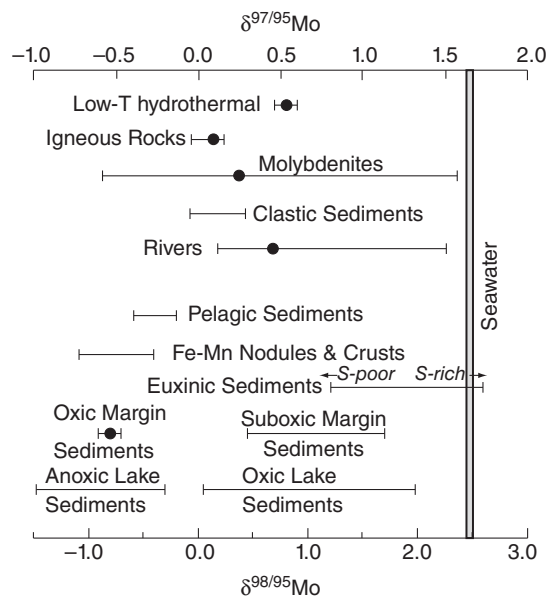


Figure 11.8 Molybdenum isotopic variations in the modern Earth. Much of the range in seawater and igneous rocks may be the results of analytical error and interlaboratory bias. (Source: Adapted from Anbar, 2004.)

and Walker, 2003). There appears to be little variation in igneous rocks, whose average $\delta^{98/95}\text{Mo}$ is +0.07‰, suggesting little fractionation in high-temperature processes. However, only eight analyses of igneous rocks (two granites and six Kamchatka basalts analyzed by Seibert et al., 2003) have been reported, so the igneous rock and bulk silicate Earth values are not well defined. Molybdenites (MoS_2) are somewhat more variable; the mean value of 60 analyses is +0.4‰ and Dahl et al. (2011) suggest this value, rather than the igneous rock mean, is representative of the continental crust. Clastic sedimentary rocks have similar isotopic compositions and show similarly small variation. Rivers have positive $\delta^{98/95}\text{Mo}$ with a flux-weighted average of about +0.7‰ (Archer and Vance, 2008). This suggests some fractionation occurs during weathering, with light isotopes preferentially incorporated into secondary minerals or absorbed onto their surfaces. Analysis of low temperature hydrothermal fluids at a single site suggests they have a similar $\delta^{98/95}\text{Mo}$ of about +0.8‰ (McManus et al., 2002).

The isotopic composition of seawater appears to be uniform throughout the open ocean, which is expected given that the residence time of Mo in the ocean (~800 ka) is much longer than the mixing time. However, the $\delta^{98/95}\text{Mo}$ of seawater is +2.3‰, about 1.5‰ higher than Mo delivered to the oceans by rivers. Clearly then, Mo isotope fractionation must be occurring in the marine system. Mn-Fe nodules and crusts have $\delta^{98/95}\text{Mo}$ of -0.5 to -1‰ and Barling et al. (2001) inferred that the low $\delta^{98/95}\text{Mo}$ of the nodules and high $\delta^{98/95}\text{Mo}$ of seawater results from preferential adsorption of isotopically light Mo onto crusts. This fractionation has subsequently been confirmed experimentally. A small fractionation (0.25‰) also occurs through preferential biological uptake of light Mo. In part because only a relatively small fraction of available Mo is biologically utilized, this fractionation probably plays little role in producing the isotopic variations seen in Figure 11.8.

Mo in marine sediments deposited under euxinic conditions,¹ such as the Black Sea or the Cariaco Basin, has isotopic compositions close to that of seawater; that is, the fractionation appears to be 0. This may at first seem surprising, since a fractionation associated

with valence state change is expected. There are two reasons for this. First, under euxinic conditions, such as prevail in the modern Black Sea beneath 200 m or so, dissolved Mo is scavenged nearly completely, limiting the potential for isotopic fractionation. Furthermore, rather than being immediately reduced under such conditions, Mo is first transformed from oxymolybdate to oxythiomolybdate ions ($\text{MoO}_{4-x}\text{S}_x^{2-}$) by substituting sulfur atoms for oxygen atoms (Helz et al., 1996). Fractionations do occur between these species, but they tend to be small. The oxythiomolybdate ion is very particle reactive and readily absorbed onto surfaces, particularly of organic particles, and scavenged from seawater in that way. Only after incorporation into sediments is Mo reduced to Mo^{4+} (Helz et al., 1996). In contrast, Mo in sediments deposited under oxygen-poor, but not euxinic, conditions have an average isotopic composition of $\delta^{98/95}\text{Mo} \approx +1.6\text{\textperthousand}$ (Brucker et al., 2009). In these environments, which are typical of some continental shelves, sediment pore waters become reducing and sulfidic within the first few tens of cm of the surface; and Mo in the pore water precipitates as Mo-Fe sulfide. Pore waters are isotopically heavy (up to +3.5‰), and both the data on pore waters and sediments suggest a moderate fractionation of about -0.7‰ (McManus et al., 2002). The precipitation results in a concentration gradient such that Mo concentration in pore water decreases with depth. Consequently, Mo from seawater diffuses into the sediment and such sediment thus represents a sink for Mo dissolved in seawater.

In the modern ocean, where oxic conditions prevail and Mo is a conservative element with uniform isotopic composition, about 30–50% of seawater Mo is removed by adsorption on Mn-Fe nodules and crusts under oxic conditions. A roughly similar amount is removed by sulfide precipitation in pore water and a much smaller fraction, 5–15%, removed by precipitation under euxinic conditions (see Problem 1 at the end of this chapter). Of these three removal mechanisms, only oxic adsorption involves a significant isotopic fractionation. Because light isotopes are preferentially absorbed, seawater is isotopically heavy. At times in the past, however, when anoxic or euxinic conditions prevailed, Mo should have had an

isotopic composition close to that of rivers ($\delta^{98/95}\text{Mo} \approx +0.7\text{\textperthousand}$). Consequently, Mo isotopes in ancient sediments should provide information on the oxidation state of ancient oceans (Anbar and Rouxel, 2007).

Because the isotopic composition of euxinic sediments appears to be identical to that of seawater, the Mo isotopic composition of sediments deposited under euxinic conditions, such as black shales, can be used to trace the isotopic composition of seawater through time. Voegelin et al. (2009) showed that non-skeletal carbonates also incorporate Mo with only small isotopic fractionation, thus carbonates are also used as paleo-oceanographic tracers. In both black shales and carbonates any fractionations will likely result in a lower $\delta^{98/95}\text{Mo}$ in the sediment, thus it is the maximum $\delta^{98/95}\text{Mo}$ that most likely represents the seawater value. Figure 11.9 shows the variation of Mo isotope ratios in marine sediments – principally organic-rich shales and carbonates through geologic time. The Mesoarchean record is sparse, but $\delta^{98/95}\text{Mo}$ in sediments deposited prior to 2.7 Ga are low, lower than the modern river average and within the range of molybdenites and close to igneous rock values. This suggests an absence of fractionation during both weathering and deposition, which is consistent with an oxygen-free atmosphere and ocean. Beginning at about 2.7 Ga, however, $\delta^{98/95}\text{Mo}$ began to rise and reached values of about 1.5‰ by 2.5 Ga (e.g., Voegelin,

et al., 2010). Czaja et al. (2012) found a negative correlation between $\delta^{56}\text{Fe}$ and $\delta^{98/95}\text{Mo}$ in carbonates and shales from the late Archean Transvaal Basin of South Africa (Figure 11.10). Based on a dispersion/reaction model, they argue that the correlation results as dissolved Fe^{2+} is oxidized in the photic zone of the ocean by photosynthetically produced O_2 . As a consequence $\text{Fe}(\text{OH})_3$ precipitates with positive $\delta^{56}\text{Fe}$ and adsorbs isotopically light Mo on its surfaces. The residual dissolved Fe^{2+} and Mo, which has negative $\delta^{56}\text{Fe}$ and positive $\delta^{98/95}\text{Mo}$ is incorporated into carbonates. According to their model, O_2 concentrations in photic zone of the basin reached about 12% of that of the modern ocean. However, they argue that the atmosphere at the time may well have been essentially O_2 free, with concentrations near 10^{-5} of present levels.

Throughout the subsequent Proterozoic, $\delta^{98/95}\text{Mo}$ remained below +1.4‰. These values are consistent with the idea that while the Proterozoic atmosphere contained significant amounts of O_2 , perhaps 10% of present levels, much of the deep ocean remained anoxic or euxinic. For example, Kendall et al (2009) calculated that 30–70% of Mo was removed from the ocean in euxinic sedimentation around 1.1 billion years ago (compared to 5–15% today) and Dahl et al. (2011) concluded that the seawater $\delta^{98/95}\text{Mo}$ value of about +1‰ in the late Proterozoic (750 Ma) implies that euxinic bottom water covered 1–4% of the seafloor, 20–80 times

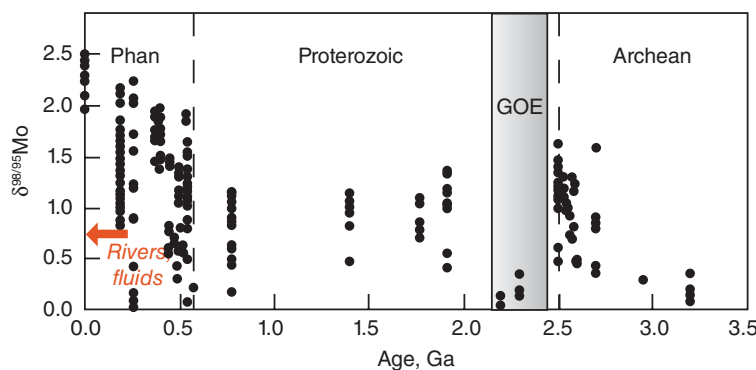


Figure 11.9 Variation of $\delta^{98/95}\text{Mo}$ in marine black shales and carbonates through geologic time. Because any fractionation is likely to result in lower $\delta^{98/95}\text{Mo}$ in the sediment, it is the maximum values that most likely represent seawater composition. The data suggest that limited amounts of O_2 were present in the oceans by the late Archean and that O_2 levels did not reach modern levels until the Phanerozoic. (Source: Adapted from Duan et al., 2010.)

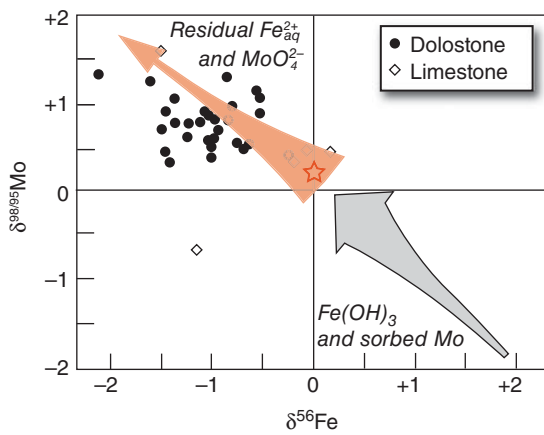


Figure 11.10 Correlated $\delta^{98/95}\text{Mo}$ and $\delta^{56}\text{Fe}$ in late Archean carbonates from the Transvaal Basin. Modelling suggests the correlation results from oxidization of dissolved Fe^{2+} in the photic zone of the ocean, followed by precipitation of $\text{Fe}(\text{OH})_3$ and adsorption of dissolved Mo. Residual Fe incorporated in carbonate is isotopically light Fe while residual Mo is isotopically heavy. (Source: Czaja et al. (2012). Reproduced with permission of Elsevier.)

more than the modern ocean. Dahl et al. (2010) suggest that $\delta^{98/95}\text{Mo}$ subsequently increased in two steps – the first was around the Proterozoic-Phanerozoic boundary, which is also the time of the first multi-cellular animals, when $\delta^{98/95}\text{Mo}$ briefly increases from Proterozoic values of 1.1–1.2‰ to about 1.8‰ before decreasing to 1.4‰. Dahl et al. (2010) interpret this as an increase in atmospheric oxygen from Proterozoic levels of a few percent of present values to 10–14% of present values in the early Phanerozoic. A second increase occurred sometime between the mid-Silurian and the mid-Devonian when $\delta^{98/95}\text{Mo}$ increased to about +2‰. This second event correlates with both the diversification of vascular plants and the expansion of large predatory fish and Dahl et al. (2010) interpret it as indicative of a rise in atmospheric O_2 levels to more than 40% of the present value. Although the oceans appear to be well oxygenated through most of the subsequent Phanerozoic, occasional anoxic events occurred, such as the end Permian event and Toarcian event of the early Jurassic, resulting in brief excursions to lower $\delta^{98/95}\text{Mo}$.

Based on the constant $\delta^{98/95}\text{Mo}$ of Fe-Mn crusts, the seawater $\delta^{98/95}\text{Mo}$ value appears to have remained the same as the modern value throughout the Cenozoic (Siebert et al., 2003).

11.5 ISOTOPES OF COPPER AND ZINC

Like Fe and Mo, Cu, and Zn are transition metals and, as such, tend to form a greater variety of bonds than the alkali and alkaline earth metals. Copper is significantly siderophile and much, perhaps most, of the Earth's inventory is in its core, whereas Zn is not and most or all the Earth's inventory is in the mantle and crust. Both are, however, chalcophile and most ores of Zn and Cu consist of sulfides or secondary minerals produced from sulfides. Both are somewhat volatile, Zn much more so than Cu. The 50% nebular condensation temperature of Cu is 1037 K, that of Zn is 726 K, similar to that of Pb. In addition, Zn forms volatile complexes such as ZnCl_2 that partition into volcanic gas phases. Zn exists essentially in only one valence, 2+; copper exists mainly in cupric form (the 2+ valence state) in low temperature, oxidizing environments at the surface of the Earth and it is predominantly in the cuprous (+1 valence state) form at high temperature and in reducing environments. More rarely, Cu occurs as the native metal (i.e., the 0 valence²). On the whole, oxidation and reduction do not play a major role in Cu and Zn isotope fractionation, in contrast to Fe and Mo. Copper and zinc are slightly to moderately incompatible elements, meaning their concentrations are higher in the crust than in the mantle and their concentrations tend to increase during fractional crystallization of mafic magmas. Like Fe and Mo, both Cu and Zn are bio-utilized and the largest isotopic fractionations occur as a consequence of biological processes.

11.5.1 Cu isotopes

Former Saudi oil minister, Sheik Ahmed Zaki Yamani once said, “The Stone Age didn’t end for lack of stone.” Instead it ended when people learned to smelt copper and work it into tools and weapons as the Copper Age began. When people found that they could make stronger tools by alloying the copper with tin the Bronze Age succeeded the Copper Age. In

a different sense, the age of copper continues; because of its high conductivity and stability as a metal, we make very extensive use of it for wiring and piping. Copper remains the third most produced metal (over 15,000 tons per year), following iron and aluminum. Perhaps no material has played as large a role for such a length of time in human civilization as copper.

Copper has two isotopes, ^{63}Cu and ^{65}Cu with abundances of 69.15% and 30.85%, respectively (Coursey et al., 2009). Data are reported as $\delta^{65}\text{Cu}$ relative to the NIST SRM976³ standard, whose $^{65}\text{Ce}/^{63}\text{Cu}$ ratio is listed in Table 11.1. Copper isotope variations in meteorites and terrestrial materials are summarized in Figure 11.11. Cu isotope ratios vary significantly in meteorites. Among chondrites, $\delta^{65}\text{Cu}$ varies between classes; among carbonaceous chondrites, $\delta^{65}\text{Cu}$ decreases with increasing petrologic grade from $-0.09\text{\textperthousand}$ for CI1 to $-1.45\text{\textperthousand}$ for CV3. $\delta^{65}\text{Cu}$ in ordinary chondrites shows a smaller range, -0.5 to $-0.1\text{\textperthousand}$ and increases in order H, L, LL. Luck et al. (2005) found that $\delta^{65}\text{Cu}$ correlated with oxygen isotope ratios and with Ni/Cu ratios; Moynier et al. (2007) showed that $\delta^{65}\text{Cu}$ also correlated negatively with Ni and Zn isotopic compositions. Luck et al. (2005) and Moynier et al. (2007) interpret these variations as resulting from fractionations between silicate, metal, sulfide, and gas phases in the solar nebula followed by sorting of these components and subsequent mixing in parent bodies. Even larger variations are observed in iron meteorites, which range from $\delta^{65}\text{Cu} = -9.23\text{\textperthousand}$ to $\delta^{65}\text{Cu} = +1\text{\textperthousand}$, although most fall within a narrower range of -2.5 to $+0.25\text{\textperthousand}$ (Williams and Archer, 2011; Bishop et al., 2012). These variations result from a number of factors including metal-silicate fractionation during segregation ($\Delta^{65}\text{Cu}_{\text{met.}-\text{sil.}} \approx -0.5\text{\textperthousand}$), fractionation between solid and liquid metal phases, and fractionation between metal and sulfide phases ($\Delta^{65}\text{Cu}_{\text{met.}-\text{sulf.}} \approx +0.64\text{\textperthousand}$). However, the observed variations greatly exceed those expected from equilibrium fractionations alone. Williams and Archer suggested they reflect kinetic effects during exsolution of sulfide from the metal phases, including more rapid diffusion of the lighter Cu isotope, ^{63}Cu . Lunar basalts have $\delta^{65}\text{Cu} = +0.5\text{\textperthousand}$, heavier than the silicate

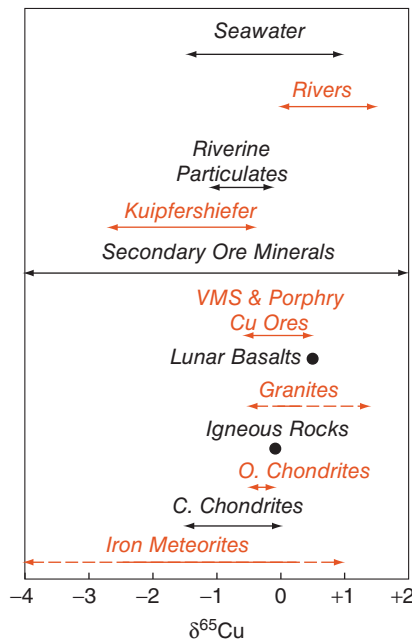


Figure 11.11 Cu isotope ratios in terrestrial, lunar, and meteoritic materials.

Earth, which Herzog et al. (2009) attributed to igneous fractionation.

The very few data that have been published on ultramafic and basaltic rocks (e.g., Ben Othman et al., 2006) suggest that the $\delta^{65}\text{Cu}$ of the bulk silicate Earth is in the range of 0 to $0.1\text{\textperthousand}$. Li et al. (2009) found that $\delta^{65}\text{Cu}$ in most granites from the Lachlan Fold Belt of Australia varied between -0.15 and $+0.21\text{\textperthousand}$, and that mean values for S- and I-type granites were indistinguishable at around 0\textperthousand . Two granites had heavier isotopic compositions (up to $+1.5\text{\textperthousand}$) and two had significantly lighter compositions (down to $-0.45\text{\textperthousand}$), which Li et al. interpreted as a consequence of possible hydrothermal and secondary alteration. Thus, in igneous silicate rocks, $\delta^{65}\text{Cu}$ is nearly constant at $0 \pm 0.2\text{\textperthousand}$ implying copper isotope fractionations among silicate minerals and melts are quite limited. Sediments and marine sedimentary particles tend to have slightly heavier isotopic compositions: $\delta^{65}\text{Cu} = +0.08$ to $+0.35\text{\textperthousand}$ (Maréchal et al., 1999).

Not surprisingly, greater fractionations are observed when phases other than silicates are involved. Ehrlich et al. (2004) found that the fractionation during experimental precipitation of covellite (CuS) from copper sulfate

solution varied with temperature as:

$$\Delta_{Cu^{2+}-CuS}(\text{‰}) = \frac{0.26 \pm 0.02 \times 10^6}{T^2} + 0.08 \pm 0.25 \quad (11.3)$$

This reaction involves both precipitation and reduction (from Cu²⁺ to Cu¹⁺) and results in the reduced precipitate being isotopically lighter than the solution. However, the temperature range of their experiments was small (10–40°C). Pekala et al. (2011) reacted Cu²⁺ solutions with pyrite and pyrrhotite at temperatures from 40 to 200°C. Subsequent microscopic investigation showed the pyrite and pyrrhotite being replaced by covellite, chalcocite (Cu₂S), and bornite (Cu₅FeS₄). At temperatures up to 150°C, the observed fractionation followed that predicted by Eqn. 11.3, but was greater than predicted (about 2.5‰) at 200°C. Pekala et al. argued that reduction was the key step controlling the isotopic fractionation. Fernandez and Borrok (2009) reacted pyrite, chalcopyrite, and sphalerite (ZnS) with acidic, oxidized solutions and found that the leached Cu was up to 2‰ heavier than that in the sulfide minerals. Thus, during both dissolution and precipitation, copper sulfides are isotopically lighter than Cu²⁺ in solution. Seo et al. (2007) carried out theoretical quantum mechanical calculations of fractionation factors and found that fractionation between sulfide and chloride species in hydrothermal fluids, such as (CuCl₂)⁻ and (Cu(HS)₂)⁻ should be quite small. Larger fractionations appear possible if high temperature vapor phase species such as Cu₃Cl₃ or (CuCl₂)²⁻ were involved.

As we noted, most copper ores are sulfides. Two of the main types of copper ores, volcanogenic massive sulfides and porphyry coppers, form by precipitation of sulfides from hydrothermal solution (seawater is the primary water source in the former, magmatic water in the latter). Most primary copper sulfides minerals in these types of deposits, such as chalcopyrite (CuFeS₂) and cubanite (CuFe₂S₃), have δ⁶⁵Cu in a relatively narrow range 0 ± 0.5‰, similar to igneous rocks and the bulk silicate Earth (Larson et al., 2003; Rouxel et al., 2004; Markl et al., 2006; Mathur et al., 2009). Since the copper in these deposits is derived from igneous rocks or magmas, this implies that the fractionations involved in their formation are generally

small. Native copper has isotopic compositions within this same range (Larson et al., 2003). Rouxel et al. (2004) found that primary chalcopyrite and cubanite in mid-ocean ridge active hydrothermal chimneys defined a wider range of -0.43 to +3.62‰. Chalcopyrite from massive sulfide deposits and inactive vents is consistently depleted in δ⁶⁵Cu relative to chalcopyrite in active vents (consistent with the experimental studies mentioned earlier). Secondary minerals found at inactive vents and in massive sulfide piles, which included atacamite (Cu₂Cl(OH)₃) and bornite showed more variable compositions (-2 to +4.7‰). Rouxel et al. argued that the relatively wide range of δ⁶⁵Cu in primary sulfides resulted from secondary minerals being redissolved by hydrothermal fluids as the systems evolved and the copper reprecipitated as primary sulfides. Thus, they reasoned, the oxidation of primary sulfides was the major cause of copper isotope fractionation in these systems.

A much wider variation in δ⁶⁵Cu, -17 to +10‰, is observed in secondary minerals that typically develop during weathering of sulfides in the near-surface (Mathur et al., 2009). Mathur et al. (2009) found that Cu in the enriched supergene⁴ zones is typically 0.4 to 5‰ heavier than primary ore deposit (the hypogene). Markl et al. (2006) found that relict primary chalcopyrite were typically isotopically depleted with δ⁶⁵Cu down to -3‰; secondary cuprous minerals such as cuprite (Cu₂O) were isotopically heavy (δ⁶⁵Cu : +0.4 to 1.65‰) and secondary cupric mineral such as malachites (CuCO₃(OH)₂) were also usually isotopically heavy, but showed a wider range than cuprous minerals (δ⁶⁵Cu : -1.5 to +2.4‰).

Sediment-hosted stratiform copper deposits are another important class of copper ore deposits. These form when relatively low temperature fluids (<120°C) dissolve copper and other metals from rocks then precipitate them within existing sedimentary formations. The Kupferschiefer, a Permian organic- and carbonate-rich shale (a bituminous marl), that extends over much of northern Europe, is a classic example. Mildly oxidizing fluids leached Cu and other metals including Zn, Pb, and Ag from the underlying red sandstones, carrying them into the overlying shale. Reaction with organic matter in the shale reduced the fluids, which resulted in

precipitation of the metals as sulfides. This mineralization likely occurred when rifting associated with the opening of the Tethys Ocean resulted in higher heat flow. $\delta^{65}\text{Cu}$ in the principal copper minerals, which include bornite, chalcolite, digenite (Cu_9S_5), and covellite, range from about -2.7 to 0\textperthousand , but most fall within the narrow range of $-0.4 \pm 0.36\text{\textperthousand}$ (Asael et al., 2009). In a similar stratiform copper deposit developed in Cambrian sediments of the Timna Valley, Israel, copper sulfides have much lighter isotopic compositions $-2.0 \pm 0.4\text{\textperthousand}$. Asael et al. (2009) explained the difference in terms of temperature, pH, and oxidation state of the fluids. In the Timna valley, the deposit formed under mildly oxidizing conditions (E_{H} values of 0.5 – 0.6), low temperature and mildly acidic ($\text{pH} < 6$) conditions. In that case, copper is in the cupric form and the principal species of dissolved copper is CuCl^+ . Thus sulfide precipitation involves reduction of copper to the cuprous form. In contrast, the Kuipferschiefer fluids were hotter (100°C), more reduced ($E_{\text{H}} 0.4$ to 0.5) and more neutral ($\text{pH } 6.3$), and the dissolved copper was in the cuprous form, principally as the $(\text{CuCl}_3)^{2-}$ ion, and little fractionation occurred upon precipitation.

Although toxic at high concentrations and used as a fungicide and algaecide, copper is an important micronutrient and plays a role in photosynthesis, membrane activity, and protein synthesis. Pokrovsky et al. (2008) found that no isotopic fractionation occurred during copper uptake by cultured diatoms and photosynthetic and non-photosynthetic bacteria. Fractionation did occur during adsorption of Cu onto bacterial cell surfaces at low pH (1.8–3.5), with ^{63}Cu being preferentially adsorbed ($\Delta^{65}\text{Cu}_{\text{ad-sol.}} \approx -1.2\text{\textperthousand}$). The opposite fractionation ($\Delta^{65}\text{Cu}_{\text{ad-sol.}} \approx +1\text{\textperthousand}$) occurred during adsorption of Cu on gibbsite and goethite surfaces at pH 4–6. In contrast, terrestrial plants do appear to fractionate copper isotopes. Weinstein et al. (2011) found that grasses and sedges preferentially take up ^{63}Cu and that copper isotopes in these plants became progressively lighter the further they were transported within the plant with fractionations of up to 1\textperthousand relative to the growth medium. One analyzed mussel had $\delta^{65}\text{Cu}$ of $+0.09\text{\textperthousand}$, which is about 1 per mil lighter than seawater, and one sample of human blood had $\delta^{65}\text{Cu}$ of $+0.3\text{\textperthousand}$ (Maréchal et al., 1999).

$\delta^{65}\text{Cu}$ in rivers is isotopically heavy compared to silicate rocks, varying from $+0.02$ to $+1.45\text{\textperthousand}$, with a discharge-weighted average of $+0.68\text{\textperthousand}$. In comparison, riverine particulate matter is isotopically light ($\delta^{65}\text{Cu} : -0.24$ to $-1.02\text{\textperthousand}$) (Vance et al., 2008). Seawater has somewhat variable isotopic composition ($\delta^{65}\text{Cu} : +0.9$ to $-1.5\text{\textperthousand}$), but the variation is not systematic with depth, even though Cu concentrations typically show surface water depletion and deep-water enrichment (Bermin et al., 2006; Vance et al., 2008). Vance et al. (2008) suggested that adsorption on particle surfaces controls the Cu isotopic composition of rivers and seawater, with ^{63}Cu preferentially adsorbed on particle surfaces. This would seem require the opposite fractionation as that observed by Pokrovsky et al. (2008), who observed preferential adsorption of ^{65}Cu . The apparent discrepancy is likely due to Pokrovsky's experiments being carried out with pure water, whereas seawater and river water contain abundant organic ligands that complex most of the dissolved Cu. As we learned in Chapter 8, the heavy isotope goes preferentially into the strongest bond. In pure water, where dissolved copper can form only weak aquo-complexes with water molecules, surface complexes are the stronger bond; in natural waters, bonds with dissolved organic ligands are stronger than surface complexes.

11.5.2 Zn isotopes

Zinc has five isotopes: ^{64}Zn (48.27%), ^{66}Zn (27.98%), ^{67}Zn (4.10%), ^{68}Zn (19.02%), and ^{70}Zn (0.63%) (Coursey et al., 2011). The $^{66}\text{Zn}/^{64}\text{Zn}$ and $^{68}\text{Zn}/^{64}\text{Zn}$ are of most interest and are reported as $\delta^{66}\text{Zn}$ and $\delta^{68}\text{Zn}$. Early results were reported relative to a solution made from Johnson-Matthey Company (JMC) metal stock by workers at ENS Lyon. The supply of this standard has been exhausted, but despite this, most data continue to be reported relative to the JMC-0749 standard, so all values mentioned here are relative to that standard, that is, $\delta^{66}\text{Zn}_{\text{JMC}}$. Some recent results have been reported relative to the Institute for Reference Materials and Measurements standard IRMM-3702, whose isotopic composition is $^{66}\text{Zn}/^{64}\text{Zn} = 0.56397 \pm 30$, $^{67}\text{Zn}/^{64}\text{Zn} = 0.08217 \pm 4$, $^{68}\text{Zn}/^{64}\text{Zn} = 0.37519 \pm 35$, and $^{70}\text{Zn}/^{64}\text{Zn} = 0.01242 \pm 2$, and this may become the future

convention. Data reported relative to the IRMM standard can be converted as $\delta^{66}\text{Zn}_{\text{JMC}} = \delta^{66}\text{Zn}_{\text{IRMM-3702}} + 0.3\text{\textperthousand}$. Zn isotopic fractionations reported to date are mass dependent (i.e., $\delta^{66}\text{Zn}$, $\delta^{67}\text{Zn}$ and $\delta^{68}\text{Zn}$ are correlated) so we will focus only on $\delta^{66}\text{Zn}$.

Data on terrestrial igneous rocks is limited; basalts range from $\delta^{66}\text{Zn}_{\text{JMC}} = +0.17$ to $+0.48\text{\textperthousand}$, with an average of $+0.31\text{\textperthousand}$ (Ben Othman et al., 2006; Herzog et al., 2009; Paniello et al., 2012; Telus et al., 2012). The standard deviation is $0.08\text{\textperthousand}$, which is comparable to analytical precision and suggests igneous fractionation of Zn isotopes is quite small. A value of $\delta^{66}\text{Zn}_{\text{JMC}} = +0.31 \pm 0.08\text{\textperthousand}$, thus, presumably represents the composition of the bulk silicate Earth. Granitoid rocks have a similar range and average $\delta^{66}\text{Zn} = +0.26\text{\textperthousand}$ with no apparent difference between A, I, and S-type granites; pegmatites, however, are about $+4\text{\textperthousand}$ isotopically heavier than granites, ranging from $\delta^{66}\text{Zn} \sim 0.53$ to $+0.88\text{\textperthousand}$ (Telus et al., 2012). This likely results from preferential fractionation of heavy Zn isotopes into the hydrous fluids involved in pegmatite formation (Telus et al., 2012), suggesting in turn that Zn is more strongly bound in these fluids, probably primarily to chloride complexes, than it is in silicate magmas. The range of $\delta^{66}\text{Zn}$ in most siliciclastic sediments overlaps that of igneous ones (Maréchal et al., 1999; 2000), suggesting there is little Zn isotope fractionation in weathering.

Zinc in carbonaceous chondrites is slightly isotopically heavy, with $\delta^{66}\text{Zn}_{\text{JMC}}$ varying from $+0.16$ to $+0.52\text{\textperthousand}$ and averaging about $0.37\text{\textperthousand}$. $\delta^{66}\text{Zn}$ increases in the order CO-CV, CM, CI and correlates with chemical parameters suggesting the variation results from mixing between isotopically heavy and light components in the solar nebula (Luck et al., 2005). Ordinary chondrites are more variable, with $\delta^{66}\text{Zn}_{\text{JMC}}$ ranging from -1.3 to $+0.76\text{\textperthousand}$, and averaging $+0.1\text{\textperthousand}$, similar to the bulk silicate Earth value. Zinc in EH enstatite chondrites is fairly uniform and similar to the silicate Earth, with $\delta^{66}\text{Zn}_{\text{JMC}}$ ranging from $+0.15$ to $+0.31\text{\textperthousand}$; $\delta^{66}\text{Zn}_{\text{JMC}}$ is more variable and heavier in the EL group, ranging from $+0.01$ to $+0.63\text{\textperthousand}$ in EL3 chondrites and from $+2.26$ to $+7.35\text{\textperthousand}$ in the EH6 group (Moynier et al., 2011). The EL chondrites tend to be

volatile element-depleted; the heavy Zn isotopic compositions suggest this depletion resulted from evaporation, particularly in the EL6 group. HED achondrites (meteorites from Vesta) tend to be slightly isotopically heavy compared to Earth (Paniello et al., 2009). Aubrites, reduced achondrites related to enstatite chondrites, have isotopically light Zn ($\delta^{66}\text{Zn}_{\text{JMC}} = -7.08$ to $-0.37\text{\textperthousand}$). These very light compositions suggest their zinc is derived from condensation from a vapor (Moynier et al., 2011). In irons, $\delta^{68}\text{Zn}$ varies from -0.6 to $+3.7\text{\textperthousand}$. $\delta^{66}\text{Zn}_{\text{JMC}}$ correlates positively with $\delta^{65}\text{Cu}$ in IIIA irons, probably as a result of fractional crystallization of metal, silicate, and sulfide from a metal-rich magma. The widest range is seen in the IAB-IIICD group (thought to represent impact melts rather than asteroid cores) and probably reflects complex interaction between the metallic liquid and the asteroid regolith (Luck et al., 2005). $\delta^{66}\text{Zn}_{\text{JMC}}$ in SNC (Martian) meteorites average $+0.25\text{\textperthousand} \pm 0.05$, but the range, $+0.13$ to $+0.35\text{\textperthousand}$, completely overlaps that of terrestrial basalts, suggesting the Earth and Mars have similar Zn isotopic compositions (Paniello et al. 2012).

Most lunar basalts are isotopically heavy and fall in the range of $+0.46$ to $+1.9\text{\textperthousand}$, averaging $+1.43 \pm 0.32\text{\textperthousand}$ with no apparent difference between high- and low-Ti lunar basalts. Pyroclastic beads as well as two basalts are isotopically much lighter with $\delta^{66}\text{Zn}_{\text{JMC}}$ as low as $-5.4\text{\textperthousand}$ (Herzog et al., 2009; Paniello et al., 2012). The light isotopic compositions in pyroclastic beads and in some basalts likely represents condensation of isotopically light Zn from volcanic gases emitted during eruption. Partitioning of Zn into a vapor phase (probably as ZnCl_2) is consistent with the observation of strong Zn enrichment in fumarole gases in terrestrial volcanoes (e.g., Symonds et al., 1987). Heavier values that occur in regolith and soil samples most likely result from sputtering and impact effects (Paniello et al., 2012). The distinctly heavy isotopic composition of lunar zinc is best explained by evaporative loss of Zn during the Moon's formation. Zinc, as we noted earlier, is volatile and is depleted in lunar basalts by 1 to 2 orders of magnitude compared to terrestrial ones. Paniello et al. (2012) found that the Moon's zinc concentration and isotopic composition can be explained if roughly

80–90% of the zinc was lost by evaporation with a vapor/melt fractionation factor of $\alpha = 0.999$. Lunar zinc isotope ratios thus support the giant impact model of the Moon's formation.

Some of the largest variation in $\delta^{66}\text{Zn}$ occurs in sulfide minerals, which range from -0.43 to $+1.33\text{\textperthousand}$. John et al. (2008) found that ^{66}Zn in ridge crest hydrothermal fluids from a variety of sites in the Pacific and Atlantic ranged from 0.0 to $+1.04\text{\textperthousand}$, with isotopic composition correlating with temperature. High temperature ($>350^\circ\text{C}$) vent fluids had ^{66}Zn close to the basalt value ($\sim 0.3\text{\textperthousand}$), while Zn in lower temperature fluids ($<250^\circ\text{C}$) tended to be isotopically heavier. John et al. argued that the variations reflected subsurface precipitation of isotopically light sphalerite (ZnS) as vent fluids cooled. Zn can also be incorporated into other sulfides such as chalcopyrite, which are isotopically light as or lighter than sphalerite.

A significant fraction of Zn dissolved in natural waters is present in the form of complexes, both organic and inorganic. Indeed, in many natural waters, the majority of dissolved Zn may be organically complexed; in seawater about 50% of the remaining Zn will be complexed with inorganic ligands such as carbonate and chloride. Black et al. (2011) calculated fractionation factors between zinc metal and aqueous species using partition functions. They predict that Zn-aquo complexes⁵ should be $1.6\text{\textperthousand}$ heavier ($\Delta^{66/64}\text{Zn}_{\text{aq-met}} = +1.6$) than Zn metal at 25°C . Fractionation factors for sulfate and citrate complexes were predicted to be slightly greater, while the fractionation between tetrachloro-zinc, $[\text{ZnCl}_4]^{2-}$, and metal should be smaller, around $+0.8\text{\textperthousand}$. Based on their calculations, we would expect Zn to become heavier in the order chloro-complexed < aquo-complexed < sulfate-complexed \approx citrate-complexed in aqueous solution. Fujii et al. (2010) experimental determined the fractionation between chloro- and aquo-complexed Zn dissolved in HCl solution to be of similar magnitude to those predicted by Black et al. (2010). In systems involving water, therefore, speciation may introduce significant Zn isotope fractionations.

Data on zinc isotopes in seawater is very limited and the Zn isotopic budget of seawater has yet to be worked out. $\delta^{66}\text{Zn} \approx +0.3\text{\textperthousand}$

in a single sample of English Channel water, while in the upper 400 m of North Pacific seawater, $\delta^{66}\text{Zn}$ varied from -0.15 to $+0.15\text{\textperthousand}$ and correlated negatively with $\delta^{65}\text{Cu}$ (Bermin et al., 2006). Although Zn concentrations are strongly depleted in surface water due to biological uptake, that study found no apparent correlation between $\delta^{66}\text{Zn}$ and Zn concentration. Zn in eight deep water samples from the Pacific and Indian Oceans appears to be slightly heavy compared to surface water and somewhat more isotopically uniform, with $\delta^{66}\text{Zn}$ varying from $+0.22$ to $+0.64\text{\textperthousand}$ and averaging $\delta^{66}\text{Zn} = 0.45 \pm 0.14\text{\textperthousand}$ (Bermin, 2006). Manganese nodules have $\delta^{66}\text{Zn}$ that range from $+0.53$ to $+1.16\text{\textperthousand}$ and average $0.90\text{\textperthousand}$ (Maréchal et al., 2000). Thus there is an apparent positive fractionation of Zn isotopes in Mn nodule formation. John et al. (2008) estimate that the riverine and atmospheric inputs to seawater are relatively light $^{66}\text{Zn} \approx 0.1$ to $0.3\text{\textperthousand}$; however, the principal source of Zn in seawater is hydrothermal fluids, which, as we found earlier, are isotopically variable, although perhaps somewhat heavier than the riverine source on average.

Pichat et al., (2003) found that $\delta^{66}\text{Zn}$ in sediments from ODP core 849 from the eastern equatorial Pacific, whose age ranged from 3 to 174 ka, showed a general decrease with time, varying from $+0.31$ to $+1.34\text{\textperthousand}$. Superimposed on this decrease was a weak periodic variation with periodicities of 35.3 and 21.2 ka. The material in the core was primarily biogenic: carbonate tests of coccolithophorids and foraminifera (and indeed, the analysis was restricted to the carbonate fraction of the sediment). The 21.2 ka periodicity corresponds closely to the mean periodicity of the precession periodicity of the Milankovitch variations (Chapter 10). Pichat et al. thus interpreted these variations as climatic effects of oceanic circulation (specifically equatorial upwelling) and biological productivity.

Zinc is a remarkably important element in biology. It is the second most abundant transition metal, following iron, in organisms. It is found in all classes of enzymes as well as in transcription factors (proteins that bind to DNA sequences, effectively turning genes on and off). It is important in protein synthesis and membrane activity, conversion of CO_2 to bicarbonate ion and vice versa (in both plants and animals), brain activity, leaf

formation, digestion, and so on. Nevertheless data on Zn isotope fractionation in organisms is fairly limited at present (this will undoubtedly change in the future). In hydroponic⁶ growth experiments with tomatoes, lettuce, and rice, Weiss et al. (2005) found that roots of these plants preferentially took up isotopically heavy Zn from the growing solutions and that the shoots of the plants were isotopically light compared to the roots (by up to 0.5‰). Simple growth experiments of Moynier et al. (2009) with lentils (beans) and bamboo confirmed the preferential transport of isotopically light Zn up the plant and into the leaves – suggesting the process is at least partially controlled by diffusion. Fractionations observed in bamboo were up to 1‰. John et al. (2007) found that experimentally grown marine diatoms preferentially took up isotopically light Zn and that the fractionation depended on Zn concentrations. At low concentrations, the fractionation was about −0.2‰ but at higher concentrations it was −0.8‰. The difference likely reflects two biochemical pathways being used to transport Zn into cell interiors: a high-affinity mechanism associated with a small isotopic fractionation predominates at low concentrations but becomes saturated at higher concentrations, where the low-affinity mechanism becomes dominant. In contrast, Andersen et al., (2011) found that Zn in cleaned diatoms tests from sediment core tops from the Southern Ocean was isotopically heavy, with $\delta^{66}\text{Zn}$ ranging from +0.7 to +1.5‰. $\delta^{66}\text{Zn}$ correlated negatively with Zn concentrations in the tests and biogenic silica accumulation rates in the sediment. Assuming that Zn concentrations in the tests correlates with Zn concentrations in surface seawater in which the diatoms grew, this suggests surface seawater becomes isotopically heavier as it becomes progressively Zn-depleted by biological uptake. Because autotrophs such as plants and diatoms preferentially take up Zn²⁺ rather than organically complexed Zn, and because there is isotopic fractionation between species in solution, the degree to which fractionations in biological systems reflect fractionations between dissolved Zn species rather than biochemical processes will require further study. Zn isotope ratios in animals is remarkably variable, from −0.4 to 0.8‰; human blood appears to be

more uniform and isotopically heavy ($\delta^{66}\text{Zn}$ + 0.3 to +0.4‰) (Cloquet et al., 2008; Marèchal et al., 1999).

11.6 ISOTOPES OF BORON AND LITHIUM

Although there are a few earlier works in the literature, there was little interest in the isotopic composition of boron and lithium until about 25 years ago. This are perhaps several reasons for this: both elements have low abundances in the Earth, they have only one valance state in nature, and analysis was challenging because neither B nor Li form gaseous species that could be analyzed in the conventional gas-source mass spectrometers and the fractionation produced in thermal ionization mass spectrometers would exceed the natural ones. The development of new analytical techniques overcame the analytical issues in the 1980s and the fields of boron and lithium isotope geochemistry have developed rapidly.

Though both lithium and boron can occur as stoichiometric components of minerals, these minerals have limited occurrence, and they generally substitute for other elements in silicates. Boron is relatively abundant in seawater with a concentration of 4.5 ppm. Lithium is somewhat less abundant, with a concentration of 0.17 ppm. Both are “conservative” species in seawater, which is to say they are always present in a constant ratio to salinity. In silicate rocks, the concentration of boron ranges from a few tenths of a ppm or less in fresh basalts and peridotites to several tens of ppm in clays. Lithium concentrations in these materials typically range from a few ppm to a few tens of ppm. Boron has two isotopes: ^{10}B and ^{11}B whose abundances are 19.9% and 80.1%, respectively (Coursey et al., 2011). The $^{11}\text{B}/^{10}\text{B}$ is reported as per mil variations, $\delta^{11}\text{B}$, from the NIST SRM 951 standard. Li also has two isotopes: ^6Li and ^7Li whose abundances are 7.59% and 92.41%, respectively (Coursey et al., 2011). The $^7\text{Li}/^6\text{Li}$ ratio is reported as per mil variation, $\delta^7\text{Li}$, from the NIST SRM 8545 Li_2CO_3 (L-SVEC) standard (Table 11.1). Prior to 1996, Li isotope ratios were often reported as $\delta^6\text{Li}$, i.e., deviations from the $^6\text{Li}/^7\text{Li}$ ratio. However, the standard used was the same, so that for variations less than about 10‰, $\delta^7\text{Li} \approx -\delta^6\text{Li}$; at higher deviations, a more exact conversion

is necessary, that is, $-38.5\text{‰} \delta^6\text{Li} = 40\text{‰} \delta^7\text{Li}$. The analytical precision for most of the Li isotope data now in the literature is about 1‰, but recent advances, particularly the use of multiple-collector inductively coupled plasma mass spectrometers, has reduced uncertainty to as little as 0.2‰.

11.6.1 Boron isotopes

In nature, boron has a valence of +3 and is almost always bound to oxygen or hydroxyl groups in either trigonal (e.g., BO_3) or tetrahedral (e.g., B(OH)_4^-) coordination (the only exception is boron bound to fluorine, e.g., BF_3). Since the bond strengths and vibrational frequencies of trigonal and tetrahedral forms differ, we can expect that isotopic fractionation will occur between these two forms. This is confirmed by experiments that show a roughly 20‰ fractionation between B(OH)_3 and B(OH)_4^- , with ^{11}B preferentially found in the B(OH)_3 form. In solution, the reaction between trigonal and tetrahedral boron is quite fast, implying equilibrium can be expected and that the isotopic fractionation should reflect this equilibrium.

In natural aqueous solutions boron occurs as both boric acid, B(OH)_3 , and the borate ion, B(OH)_4^- , the dominant species being determined by pH. At a pH of around 9 and above B(OH)_4^- dominates and B(OH)_3 dominates at a lower pH. In seawater, which has a pH in the range of 7.6–8.1, about 80–90% of boron will be in the B(OH)_3 form. Most fresh waters are a little more acidic so B(OH)_3 will be more dominant; only in highly alkaline solutions, such as saline lakes, will B(OH)_4^- be dominant. The most common boron mineral in the crust is tourmaline ($\text{Na(Mg,Fe,Li,Al)}_3\text{Si}_6\text{O}_{18} (\text{BO}_3)_3(\text{OH,F})_4$), in which boron is present in BO_3 groups. In clays, boron appears to occur primarily as B(OH)_4^- , most likely substituting for silica in tetrahedral layers. The coordination of boron in common igneous minerals is uncertain, possibly substituting for Si in tetrahedral sites. Boron is an incompatible element in igneous rocks and is very fluid-mobile. It is also readily adsorbed onto the surfaces of clays. There is an isotopic fractionation between dissolved and adsorbed B of -20 to -30‰ (i.e., adsorbed B is ^{11}B poor), depending on pH and temperature (Palmer et al., 1987).

Figure 11.12 illustrates the variation in B isotopic composition in geologic materials. Spivack and Edmond (1987) found the $\delta^{11}\text{B}$ of seawater was uniform within analytical error and was confirmed by Foster et al. (2010) who determined a $\delta^{11}\text{B}$ value of $39.61 \pm 0.04\text{‰}$. Fresh MORB have a mean $\delta^{11}\text{B}$ of $-4.25 \pm 2.1\text{‰}$. Oceanic island basalts (OIB) have slightly lighter $\delta^{11}\text{B}$ (e.g., Chaudron and Jambon, 1994). Bulk chondrites have $\delta^{11}\text{B}$ similar to MORB, which presumably is approximately the bulk silicate Earth value. However, meteoritic materials can have quite variable $\delta^{11}\text{B}$ as a consequence of a variety of processes, including cosmogenic production and decay of ^{10}Be both in the early Solar System and subsequent exposure of the meteorites to cosmic rays. The average B

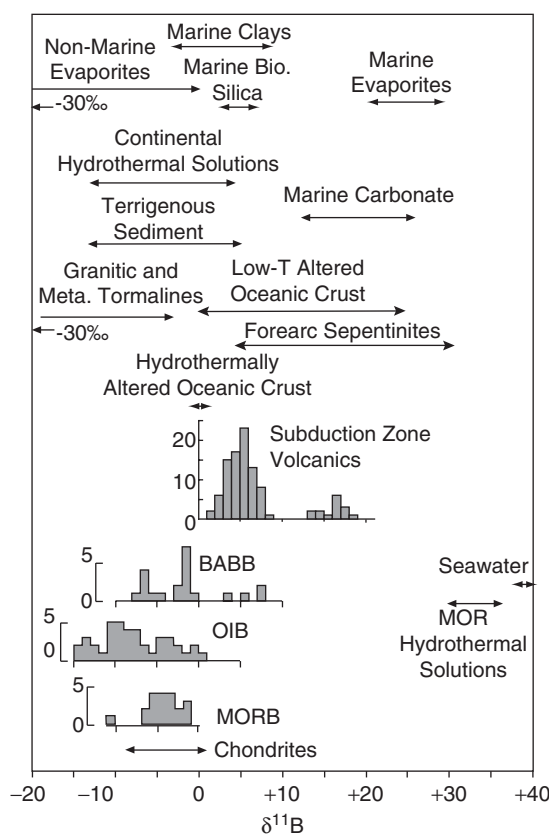


Figure 11.12 Boron isotopic composition in crystalline rocks (MORB: mid-ocean ridge basalts; OIB: oceanic island basalts; BABB: back-arc basin basalts, IAV: island arc volcanics), sediments, groundwater, freshwater, salt lakes, seawater, and mid-ocean ridge hydrothermal solutions.

isotopic composition of the continental crust probably lies between -13 and $-8\text{\textperthousand}$ (Chaussidon and Abarède, 1992).

Perhaps the most remarkable aspect of B isotope geochemistry is the very large fractionation of B isotopes between the oceans and the solid Earth. It was recognized very early that some of this difference reflected the fractionation that occurred during adsorption of boron on clays (e.g., Schwarcz et al., 1969). However, as we noted earlier, this fractionation is only about $30\text{\textperthousand}$ or less, whereas the difference between the continental crust and seawater is close to $50\text{\textperthousand}$. Furthermore, the net effect of hydrothermal exchange between the oceanic crust and seawater is to decrease the $\delta^{11}\text{B}$ of seawater (Spivack and Edmond, 1987). This large $\delta^{11}\text{B}$ difference is a consequence of the ocean not being a simple equilibrium system but rather a kinetically controlled open one. Since most processes operating in the ocean appear to preferentially remove ^{10}B from the ocean, seawater is driven to an extreme ^{11}B -rich composition. Ishikawa and Nakamura (1993) noted that ancient limestones and cherts have more negative $\delta^{11}\text{B}$ than their modern equivalents, calcareous and siliceous oozes, and suggested that further fractionation occurs during diagenesis.

Another large fractionation occurs during evaporation and precipitation. Rose-Koga et al. (2006) found that boron in rain and snow is substantially lighter than seawater with $\delta^{11}\text{B}$ ranging from -10 to $+34\text{\textperthousand}$. They estimate a seawater–vapor fractionation of $+25.5\text{\textperthousand}$.

Spivack and Edmond (1987) investigated the exchange of boron between seawater and oceanic crust. Boron is readily incorporated into the alteration products of basalt, so that even slightly altered basalts show a dramatic increase in B concentration and an increase in $\delta^{11}\text{B}$, with altered oceanic crust having $\delta^{11}\text{B}$ in the range of 0 to $+25\text{\textperthousand}$. Smith et al. (1995) estimated that average altered oceanic crust contains 5 ppm B (compared to 0.31 ppm in fresh oceanic crust; White and Klein, 2013) and $\delta^{11}\text{B}$ of $+3.4\text{\textperthousand}$. During high temperature interaction between seawater and oceanic crust, Spivack and Edmond (1987) concluded that boron was quantitatively extracted from the oceanic crust by hydrothermal fluids. The $\delta^{11}\text{B}$ of these fluids is slightly lower than that of seawater. They inferred that the B in

these fluids is a simple mixture of seawater- and basalt-derived B and that little or no isotopic fractionation was involved. Analysis of hydrothermally altered basalts recovered by the Ocean Drilling Project generally confirm these inferences, as they are boron-poor and have $\delta^{11}\text{B}$ close to 0 (Ishikawa and Nakamura, 1992).

Island arc volcanics (IAV) have distinctly more positive $\delta^{11}\text{B}$ than either MORB or OIB. This may in part reflect the incorporation of subducted marine sediment and altered oceanic crust into the sources of island arc magmas (e.g., Palmer, 1991), but a more important factor is likely to be fractionation of B isotopes during dehydration of the subducting slab, in which ^{11}B is strongly partitioned into the fluid phase (You et al., 1995). This process begins at quite shallow depths in the subduction zone, in the forearc region, where fluids released from the overlying slab serpentinate the forearc mantle and enrich it in ^{11}B , producing forearc serpentinites with $\delta^{11}\text{B}$ as high as $+30\text{\textperthousand}$. By the time the slab reaches the sub-arc magmagenesis region, fluids released are less ^{11}B -rich, such that island arc volcanics typically have $\delta^{11}\text{B}$ of around $+5\text{\textperthousand}$. As Figure 11.12 shows, the distribution of $\delta^{11}\text{B}$ in island arc volcanics is distinctly bimodal, with modes at $+5\text{\textperthousand}$ and $+16\text{\textperthousand}$. All samples with $\delta^{11}\text{B} > 12$ are from the South Sandwich arc. Tonarinni et al. (2011) interpret these very high values as a consequence of subduction erosion of the forearc region; that is, they suggest the strongly ^{11}B -enriched serpentinites of the forearc are being carried into the magmagenesis zone.

The differences in $\delta^{11}\text{B}$ between oceanic island basalts (OIB) and MORB is perhaps more problematic. Though no experimental or theoretical studies have been carried out, it seems unlikely that significant fractionation of boron isotopes will occur during melting of the mantle, both because the temperatures are high, and because the atomic environment of B in silicate melts is probably similar to that in silicate solids. Thus, as we found was the case for O isotopes, B isotope fractionation probably occurs only at the surface of the Earth, and the difference between OIB and MORB must somehow reflect surface processes. Chaussidon and Marty (1995) argued that the boron isotopic composition of the mantle is that of OIB

(−10‰) and that the higher $\delta^{11}\text{B}$ of MORB reflects contamination of MORB magmas by altered oceanic crust. This seems unlikely for several reasons. First, although there are still relatively few data available, MORB appear to be relatively homogeneous in their boron isotopic composition. This means assimilation would have to be systematic and pervasive and that all MORB magmas would have to assimilate roughly the same amount of material. Both of these seem highly improbable. Second, there is little or no other evidence for pervasive assimilation of oceanic crust by MORB magmas. Third, oceanic island basalts have an opportunity to assimilate not only altered oceanic crust, but also overlying sediment. Yet, according to the Chaussidon and Marty (1995) hypothesis, they are not systematically contaminated. Although they are not *systematically* contaminated, there is evidence of *occasional* assimilation of oceanic crust and/or sediment by oceanic island basalt magmas from both B and Os isotope geochemistry. This may explain some of the lower $\delta^{11}\text{B}$ values in OIB seen in Figure 11.4 (Chaussidon and Jambon, 1994).

The alternative explanation for the lower $\delta^{11}\text{B}$ in OIB is that they contain a component of material recycled into the mantle, through subduction, from the surface of the Earth. The idea that mantle plumes, and the OIB magmas they produce, contain material recycled from the surface of the Earth has been suggested on other grounds, as we saw in Chapter 6. As we noted earlier significant fractionation of B isotopes occurs during sediment dehydration during subduction (You et al., 1994). The fluid produced will be enriched in ^{11}B , leaving the sediment and oceanic depleted in ^{11}B . Thus the effect of subduction zone processes will be to lower the $\delta^{11}\text{B}$ of oceanic crust and sediment carried into the deep mantle.

One of the more interesting applications of boron isotopes has been determining the paleo- $p\text{H}$ of the oceans. Boron is readily incorporated into carbonates, with modern marine carbonates having B concentrations in the range of 15–60 ppm. In modern foraminifera, $\delta^{11}\text{B}$ is roughly 20‰ lighter than the seawater in which they grow. This fractionation seems to result from the kinetics of B co-precipitation in CaCO_3 , in which incorporation of B in carbonate is preceded by surface adsorption

of $\text{B}(\text{OH})_4^-$ (Vengosh et al., 1991; Heming and Hanson, 1992).

The reaction between $\text{B}(\text{OH})_3$, and $\text{B}(\text{OH})_4^-$ in seawater may be written as:



The equilibrium constant for this reaction is:

$$-\text{pK}^{app} = \ln \frac{\text{B}(\text{OH})_4^-}{\text{B}(\text{OH})_3} - \text{pH} \quad (11.5)$$

The relative abundance of these two species is thus pH dependent. Furthermore, we can easily show that the isotopic composition of these two species must vary if the isotopic composition of seawater is constant. From mass balance we have:

$$\delta^{11}\text{B}_{\text{SW}} = \delta^{11}\text{B}_3 f + \delta^{11}\text{B}_4 (1-f) \quad (11.6)$$

where f is the fraction of $\text{B}(\text{OH})_3$ (and $1-f$ is therefore the fraction of $\text{B}(\text{OH})_4^-$), $\delta^{11}\text{B}_3$ is the isotopic composition of $\text{B}(\text{OH})_3$, and $\delta^{11}\text{B}_4$ is the isotopic composition of $\text{B}(\text{OH})_4^-$. If the isotopic compositions of the two species are related by a constant fractionation factor, Δ_{3-4} , we can write 11.6 as:

$$\begin{aligned} \delta^{11}\text{B}_{\text{SW}} &= \delta^{11}\text{B}_3 f + \delta^{11}\text{B}_4 - \delta^{11}\text{B}_{4f} \\ &= \delta^{11}\text{B}_4 - \Delta_{3-4} f \end{aligned} \quad (11.7)$$

Solving for $\delta^{11}\text{B}_4$, we have:

$$\delta^{11}\text{B}_4 = \delta^{11}\text{B}_{\text{SW}} + \Delta_{3-4} f \quad (11.8)$$

Thus, assuming a constant fractionation factor and isotopic composition of seawater, the $\delta^{11}\text{B}$ of the two B species will depend only on f , which, as we can see in Eqn. 11.5, will depend on pH.

If the mechanism for incorporation of B in carbonate suggested by Vengosh et al. (1991) is correct, the fractionation of $^{11}\text{B}/^{10}\text{B}$ between calcite and seawater will be pH dependent. There is still some debate as to as to the exact mechanism of boron incorporation in carbonate, in particular whether only borate ion or both boric acid and borate ion can be incorporated. Regardless of the exact mechanism, the isotopic composition of boron in carbonate precipitated from seawater has been shown to be a strong function of pH (Sanyal et al., 1996), allowing, in principle,

the reconstruction of paleo-seawater pH from carbonates. There are some additional factors that must be considered: (1) different carbonate-secreting species may fractionate B isotopes slightly differently, perhaps because they alter the pH of their micro-environment, or perhaps because $\text{B}(\text{OH})_3$ is also utilized to varying degrees, (2) the fractionation factor is temperature dependent, and (3) the B isotopic composition of seawater may vary with time. Nevertheless, if care is exercised to account for “vital” effects and variation in the isotopic composition and temperature of seawater, the B isotopic composition of marine biogenic carbonate preserved in sediment should reflect the pH of the water from which they were precipitated.

The pH of seawater, in turn, is largely controlled by the carbonate equilibrium and depends, therefore, on the partial pressure of CO_2 in the atmosphere. Thus, if the pH of ancient seawater can be determined, it should be possible to estimate p_{CO_2} of the ancient atmosphere. Given the concern about the relation of future climate to future p_{CO_2} , it is obviously interesting to know how these factors related in the past.

Pearson and Palmer (2000) measured $\delta^{11}\text{B}$ in foraminiferal carbonate extracted from Ocean Drilling Program (ODP) cores and from this calculated pH based on Eqns 11.5–11.8. To minimize the effect of temperature on the fractionation factor, they restricted their study to cores from regions that were tropical at the time of deposition. To minimize vital effects, they used only one species of planktonic foraminifera for the Neogene period, *G. trilobus* (also known as *G. sacculifer*), which is thought to incorporate B with no vital effect. For the Paleogene, they used six species where the vital effect was arguably minimal. They argue that changes in the B isotopic composition of seawater should be slow to occur since the residence time of B in seawater is roughly 20 million years. Nevertheless, they account for a small variation, roughly 1.7‰, in seawater $\delta^{11}\text{B}$ over Tertiary time. The results suggest dramatically lower seawater pH and dramatically higher p_{CO_2} in the Paleogene. The apparent variation in p_{CO_2} is qualitatively consistent with what is known about Tertiary climate change – namely that a long-term cooling trend began in the early to middle Eocene. In contrast to the Paleogene,

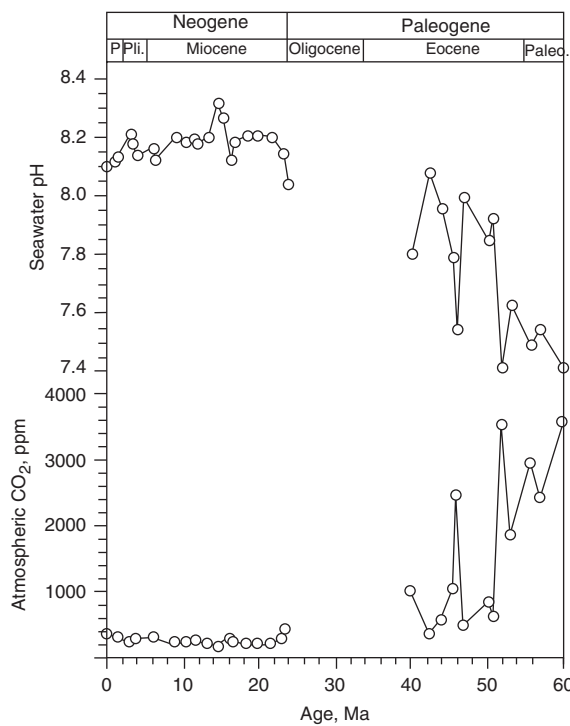


Figure 11.13 Top graph shows the variation pH of surface seawater during Tertiary time as inferred from $\delta^{11}\text{B}$ in shells of planktonic foraminifera in ODP cores. Bottom graph shows the concentration of atmospheric CO_2 calculated from seawater pH. (Source: Adapted from Pearson and Palmer, 2000.)

Figure 11.13 shows that the Neogene is characterized by atmospheric p_{CO_2} near or slightly below modern pre-industrial levels. The results are remarkably consistent with estimates of paleo- CO_2 by Pagani et al. (1999) based on $\delta^{13}\text{C}$ of C_{37} alkadienone which also indicate low atmospheric CO_2 levels through the Neogene and higher ones in the Paleogene (Figure 10.31). As we noted in Chapter 10, the low values through the Neogene are surprising, given the evidence for cooling through the Neogene, particularly over the last 10–15 Ma (e.g., Figure 10.39). It suggests some factor other than the greenhouse effect must account for the Neogene cooling.

On a more limited time-scale, Höönsch and Hemming (2005) investigated $\delta^{11}\text{B}$ over the last two glacial cycles (0–140 and 300–420 ka). In that study, they controlled for temperature by analyzing the Mg/Ca ratio of the carbonate shells, which is known to be strongly temperature dependent. Their

calculated pH values ranged from 8.11–8.32, which in turn correspond to a p_{CO_2} range of ~180–~325 ppm. These calculated p_{CO_2} values are in good agreement with CO_2 concentrations measured in bubbles in the Vostok ice core (Figure 10.34). Hönisch et al. (2009) extended the boron isotope-based p_{CO_2} record through the Pleistocene. They were particularly interested in the mid-Pleistocene time when the dominant orbital forcing frequency switched from 40,000 years to 100,000 years. They found that whereas over the last 400,000 years p_{CO_2} has varied from 180 and 300 ppmv in glacial and interglacial periods, respectively, the variation had been 210 and 280 ppmv in the early Pleistocene. The calculated average p_{CO_2} of the early and late Pleistocene are 248 and 241 ppmv,

respectively, and statistically indistinguishable. Thus a decrease in p_{CO_2} does not seem to be responsible for the more severe glaciations of the late Pleistocene.

Pearson et al. (2009), working with foraminifera from a well-preserved Paleogene section in Tanzania determined p_{CO_2} over the Eocene–Oligocene transition, a time of great interest because it was then that Antarctic glaciation began. Some had suspected that a drop in p_{CO_2} below 750 ppmv may have been responsible for the cooling that led to formation of the ice sheet. Their $\delta^{11}\text{B}$ results suggest that p_{CO_2} did dip below this level near this boundary, but recovered in the early Oligocene before declining again (Figure 11.14).

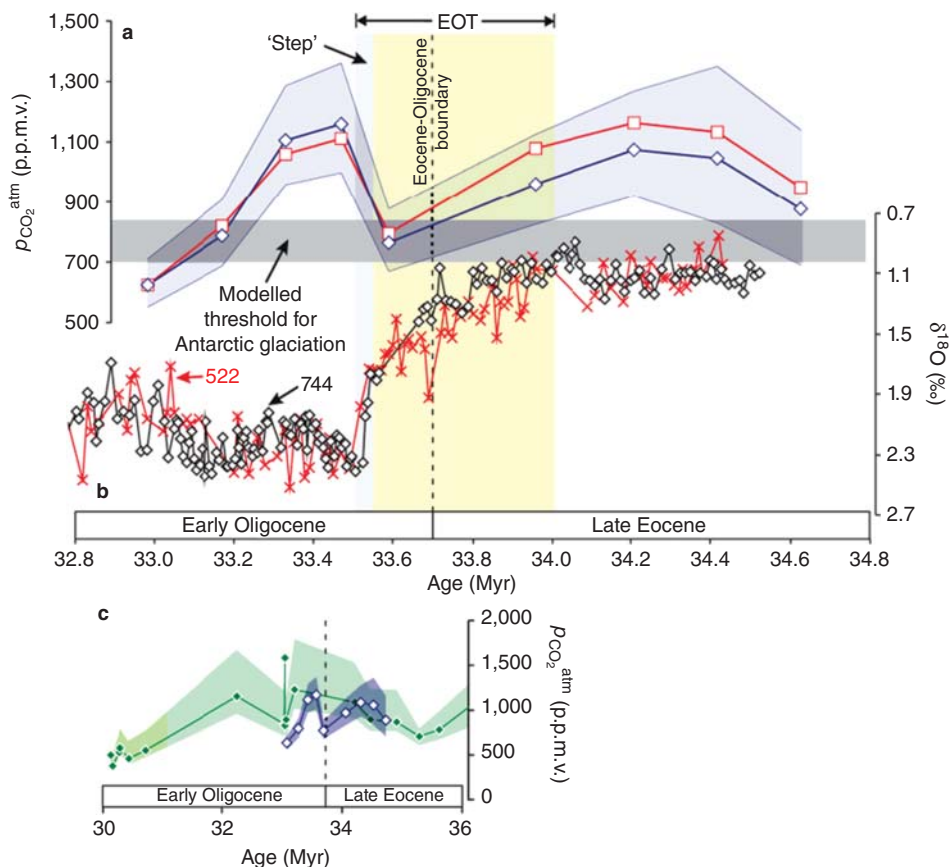


Figure 11.14 (a) p_{CO_2} (\pm uncertainty from $\delta^{11}\text{B}$ measurements at 95% confidence; diamond symbols calculated assuming varying $[\text{CO}_3^{2-}]$, star symbols are for constant $[\text{CO}_3^{2-}]$). The gray band is the assumed threshold for Antarctic glaciation. (b) Deep-sea oxygen isotopes from DSDP site 522 (crosses) and ODP site 744 (diamonds). (c) $\delta^{11}\text{B}$ proxy measurements compared to alkenone proxy estimates (filled diamond symbols with pale shaded band for maximum and minimum). (Source: Pearson et al. (2009). Reproduced with permission of Nature Publishing Group.)

Although still somewhat controversial, paleo-seawater pH reconstruction based on boron isotopes has become better grounded in the last few years. Some of the controversy centered around the lack of experimental determination of the fractionation factor between $\text{B}(\text{OH})_3$ and $\text{B}(\text{OH})_4^-$ (Pagani et al., 2005; Zeebe 2005). This has been partially resolved by Klochko et al. (2006) who experimentally determined the fractionation factor, α , to be 1.0272 ± 0.0006 and independent of temperature. This value differs from the theoretically estimated value of 1.0194, which had previously been used for paleo-oceanographic calculations. However, the theoretical is hampered by uncertainties in measured vibrational frequencies, and attempts to calculate it *ab initio* from molecular orbital theory result in uncertainties that are too large to be useful. In addition to this, there are other uncertainties in the mechanism of incorporation of boron into carbonate and the associated fractionation factor, and uncertainties in how $\delta^{11}\text{B}$ in seawater has varied with time, and the requirement of high precision measurement of B isotope ratios. Foster (2008) has shown that paleo- CO_2 determined from foraminifera in cores from the Caribbean agree well with CO_2 in the Vostok ice core using the experimentally determined fractionation factor.

11.6.2 Li isotopes

Terrestrial lithium isotopic variation is dominated by the strong fractionation that occurs between minerals, particularly silicates, and water. Indeed, this was first demonstrated experimentally by Urey in the 1930s. This fractionation in turn reflects the chemical behavior of Li. The ionic radius of Li^{1+} is small (78 pm) and Li readily substitutes for Mg^{2+} , Fe^{2+} , and Al^{3+} in crystal lattices, mainly in octahedral sites. It is tetrahedrally coordinated in aqueous solution by four water molecules (the solvation shell) to which it is strongly bound, judging from the high solvation energy. These differences in atomic environment, differences in binding energies, the partly covalent nature of bonds, and the low mass of Li all lead to strong fractionation of Li isotopes.

Modern study of Li isotope ratios began with the work of Chan and Edmond (1988). They found that the isotopic composition

of seawater was uniform within analytical error with a $\delta^7\text{Li}$ value of $+33\text{\textperthousand}$ (which has subsequently been revised to $+31\text{\textperthousand}$ based on more accurate techniques). Subsequent work suggests that $\delta^7\text{Li}$ in seawater might vary by as much as 4%, but the degree to which this variation reflects analytical error and inter-laboratory biases remains unclear, as the residence time of Li in the ocean (1.5–3 Ma) is much longer than the mixing time.

Fresh MORB have $\delta^7\text{Li}$ of $+3.8 \pm 1.3\text{\textperthousand}$ (White and Klein, 2013), a range not much larger than that expected from analytical error alone. Oceanic island basalts (OIB) have on average higher $\delta^7\text{Li}$: $+4.9 \pm 1.2\text{\textperthousand}$. The highest $\delta^7\text{Li}$ occurs on islands characterized by particularly radiogenic Pb (the so-called HIMU OIB group), such as on some islands of the Cook-Austral chain. Here, $\delta^7\text{Li}$ may be as high as $+8\text{\textperthousand}$. This may reflect a recycled crustal component in their sources (e.g., Vlastelic et al., 2009). High precision analyses of whole carbonaceous and ordinary chondrites have a narrow range of values with a mean of $2.96 \pm 0.77\text{\textperthousand}$; enstatite chondrites appear to be systematically lighter, with a mean of $1.69 \pm 0.73\text{\textperthousand}$ (Pogge von Strandmann, et al., 2011). Individual components of meteorites are more variable. The mean $\delta^7\text{Li}$ of fertile, unaltered and unmetasomatized peridotites is $+3.5 \pm 0.5\text{\textperthousand}$, which is presumably the value of the bulk silicate Earth, is essentially indistinguishable from that of carbonaceous and ordinary chondrites (Pogge von Strandmann, et al., 2011). Other peridotites exhibit a larger range: -15 to $+10\text{\textperthousand}$.

There appears to be little relationship between $\delta^7\text{Li}$ and other geochemical parameters in igneous rocks, such as MgO concentration, suggesting Li experiences little isotopic fractionation during fractional crystallization, and perhaps also partial melting (Tomasca et al., 1999; Teng et al., 2004). However, Pogge von Strandmann et al. (2011) found a correlation between $\delta^7\text{Li}$ and $\delta^{26}\text{Mg}$ in peridotites xenoliths, which they attribute to kinetic isotope fractionation occurring during transport from the mantle. Alpine eclogites can have distinctly light isotopic compositions. These rocks are thought to be fragments of basaltic oceanic crust deeply subducted and metamorphosed then subsequently rapidly exhumed during the Alpine orogeny. Their light isotopic compositions

presumably reflect preferential partitioning of ${}^7\text{Li}$ into the fluid produced as the rocks were dehydrated during metamorphism. $\delta^7\text{Li}$ in granites ranges from about -5 to $+10\text{\textperthousand}$, with an average of $+1.7\text{\textperthousand}$. Based on this and analysis of other crustal materials, Teng et al. (2009) estimate the average continental crust to have $\delta^7\text{Li} = +1.2\text{\textperthousand}$.

Oceanic crust altered by seawater at low temperatures takes up Li from solution and has high $\delta^7\text{Li}$ compared to fresh basalt. In hydrothermal reactions, however, Li is lost from basalt into the solution and hydrothermal fluids can Li concentrations up to 50 times greater than seawater. ${}^7\text{Li}$ is extracted more efficiently than ${}^6\text{Li}$ during this process, so hydrothermally altered basalt can have $\delta^7\text{Li}$ as low as $-2\text{\textperthousand}$. Serpentinites (hydrothermally altered peridotite) can have even lower $\delta^7\text{Li}$. Because they extract Li from oceanic crust so completely, hydrothermal solutions have Li isotopic compositions intermediate between MORB despite this fractionation.

The average $\delta^7\text{Li}$ of island arc volcanics, $+4.05 \pm 1.5\text{\textperthousand}$ is only slightly higher than that of MORB. This is somewhat surprising since other isotopic evidence clearly demonstrates island arc magmas contain components derived from subducted oceanic crust and sediment. Furthermore, while $\delta^7\text{Li}$ have been shown in some cases to correlate with chemical and isotopic indicators of a subduction component, this is not always the case.

It seems nevertheless likely that the subduction process has profoundly influenced the isotopic composition of the mantle over time. As a consequence of fractionation occurring during weathering, seawater is strongly enriched in ${}^7\text{Li}$. This enrichment is imprinted upon the oceanic crust as it reacts with seawater. When the oceanic crust is returned to the mantle during subduction, the mantle becomes progressively enriched in ${}^7\text{Li}$. The continental crust, on the other hand, becomes progressively depleted in ${}^7\text{Li}$ over time. Elliot et al. (2004) calculate that this process has increased $\delta^7\text{Li}$ in the mantle by 0.5 to 1\textperthousand and decreased $\delta^7\text{Li}$ of the continental crust by 3\textperthousand over geologic time.

As is the case for boron, seawater represents one extreme of the spectrum of isotopic compositions in the Earth (Figure 11.15). During mineral-water reactions, the heavier isotope, ${}^7\text{Li}$, is preferential partitioned into

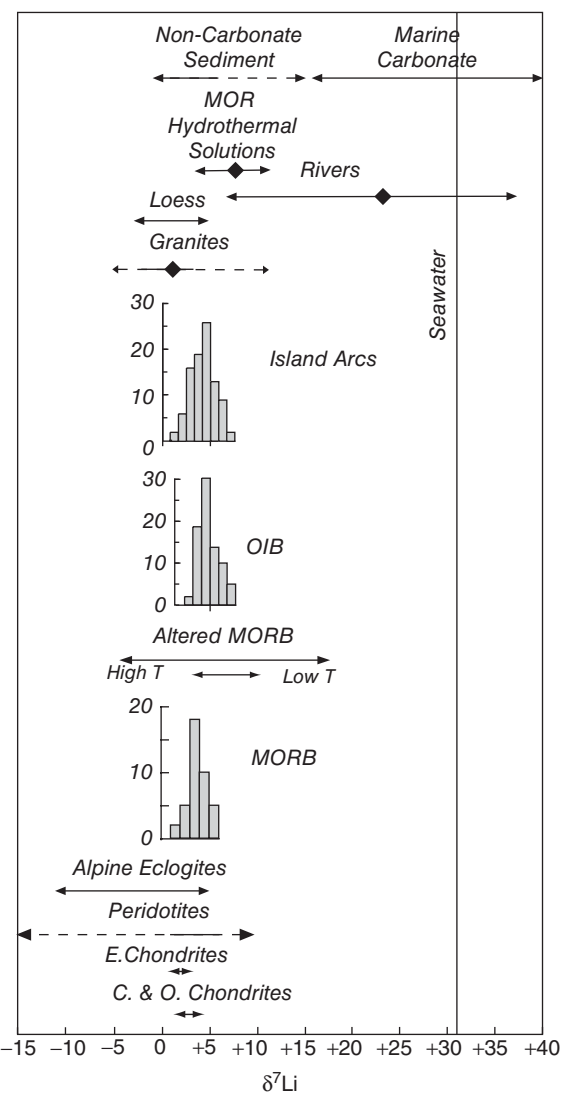


Figure 11.15 Li isotopic composition of terrestrial and meteoritic materials. Diamonds represent average values.

the solution. Weathering on the continents results in river water being isotopically heavy, $+23.5\text{\textperthousand}$ on average and the suspended load of rivers which have $\delta^7\text{Li} \approx +2$ (Teng et al., 2004). The riverine flux is slightly smaller than the hydrothermal one, which has an average $\delta^7\text{Li}$ of $+8\text{\textperthousand}$ and the total inputs to seawater are on average about $+15\text{\textperthousand}$. Thus, seawater is some 16 per mil heavier than average river water, so additional fractionation must occur in the marine environment. This includes adsorption on particles (although Li is less prone to absorption than most other metals), authigenic clay formation,

and low temperature alteration of oceanic crust. Misra and Froehlich (2012) estimate that authigenic clay formation accounts for about 70% of Li removal, with low-temperature alteration of the oceanic crust accounting for the remainder and that the net fractionation factor for these processes is $-16\text{\textperthousand}$, consistent with other observations and experiments. $\delta^7\text{Li}$ in shale ranges from -3 to $+5\text{\textperthousand}$. Marine carbonate sediments, which tend

to be Li-poor, typically have higher $\delta^7\text{Li}$ than non-carbonate sediment.

Misra and Froehlich (2012) compiled lithium isotopic analyses of Cenozoic foraminifera and have shown the $\delta^7\text{Li}$ of seawater has increased by 9\textperthousand over this period. Although not identical, it tracks the rise in $^{87}\text{Sr}/^{86}\text{Sr}$ and $^{187}\text{Os}/^{188}\text{Os}$ remarkably well (Figure 11.16). Misra and Froehlich attribute the change in all three ratios to changes in

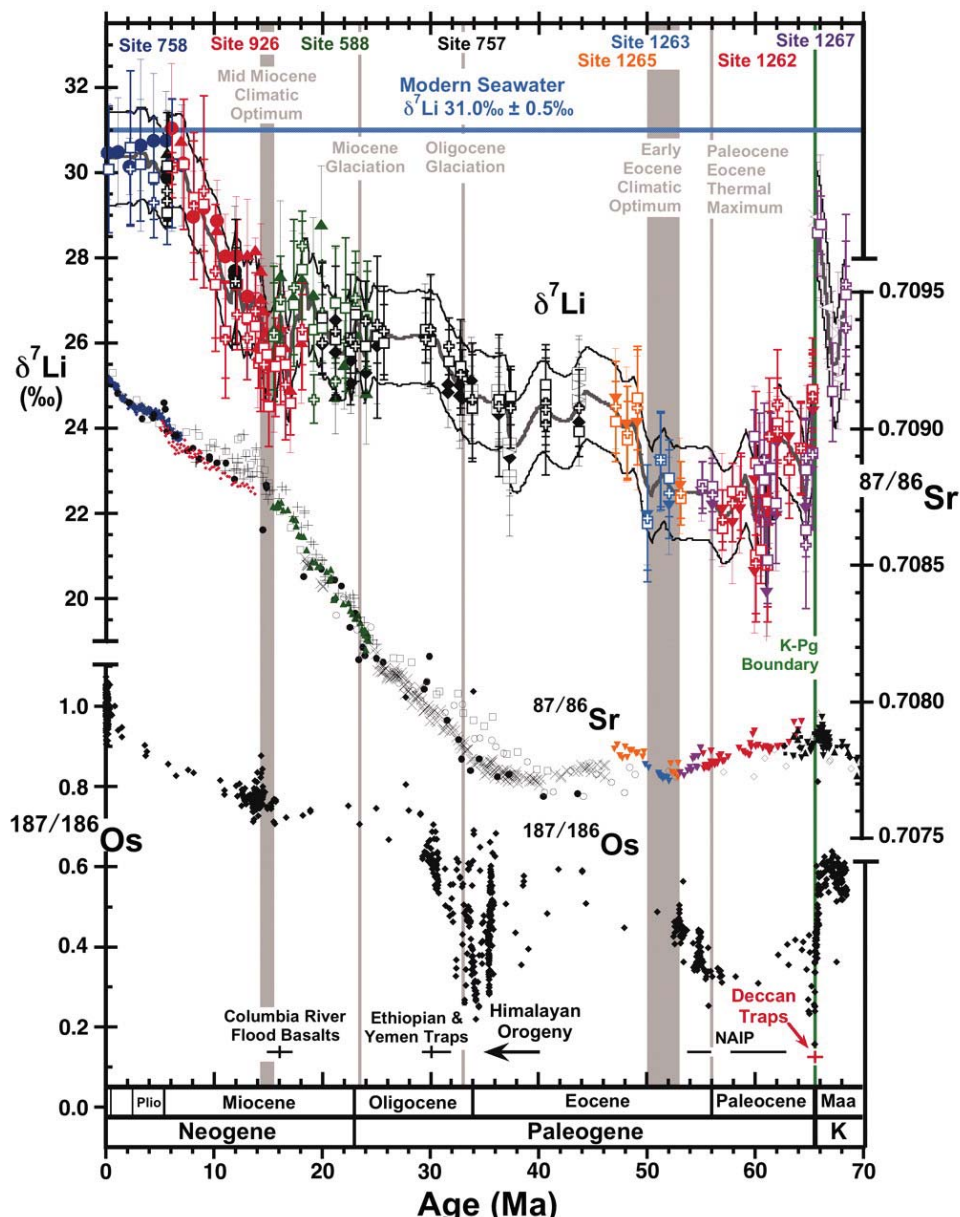


Figure 11.16 $\delta^7\text{Li}$, $^{87}\text{Sr}/^{86}\text{Sr}$, and $^{187}\text{Os}/^{188}\text{Os}$ in seawater over the Cenozoic. (Source: Misra and Froehlich (2012). Reproduced with permission of AAAS.)

weathering of the continents due primarily to changes in tectonism over the Cenozoic, which has seen the rise of the Rocky Mountains, the Andes, the Himalayas, and the Alps. As they point out, low-lying terrains where removal of weathering products is transport-limited, especially those in the tropics, undergo congruent weathering and Li isotope ratios in rivers that drain such terrains reflect those of the bedrocks. Rivers draining mountainous terrains, which undergo high weathering and denudation rates with incongruent weathering, are ${}^7\text{Li}$ -enriched.

Silicate weathering plays an important role in drawing down atmospheric CO_2 . Misra and Froehlich (2012) note the overall similarity of these curves to that of ocean bottom water $\delta^{18}\text{O}$, which records decreasing temperature and increasing ice volume. They suggest “ $\delta^7\text{Li}_{\text{sw}}$ might provide alternative estimates of atmospheric CO_2 consumption by the silicate weathering.”

Rudnick et al. (2004) found that a saprolite⁷ developed on granite had a lighter isotopic composition (as light as $-6.8\text{\textperthousand}$) than the granite ($+2.3\text{\textperthousand}$). ${}^7\text{Li}$ decreased with decreasing Li concentration in a manner consistent with leaching of Li by Rayleigh fractionation during weathering with a $\Delta_{\text{residue-solution}}$ of $-3\text{\textperthousand}$. Far more negative values were observed in saprolite developed on a diabase, with ${}^7\text{Li}$ as low as $-20\text{\textperthousand}$. Again, Li decreased with decreasing concentration consistent with Rayleigh fractionation, but the saprolite also likely gained Li from isotopically heavy groundwater.

Diffusion can also fractionate Li isotopes. As we found in Chapter 8, lighter isotopes of an element will diffuse faster than heavier isotopes. The relatively large mass difference between ${}^7\text{Li}$ and ${}^6\text{Li}$ (17%) results in substantially faster diffusion of ${}^6\text{Li}$. Richter et al. (1999) found that the ratio of diffusion coefficients for isotopes of an ion diffusing in molten silicates obeyed the relation:

$$\frac{D_1}{D_2} = \left(\frac{m_2}{m_1} \right)^{\beta} \quad (11.9)$$

where β is an empirical parameter determined experimentally. Richter et al. (2003) found that the value of β was 0.215 for Li, implying 3% faster diffusion of ${}^6\text{Li}$. In molten basalt-rhyolite diffusion experiments

this more rapid diffusion of ${}^6\text{Li}$ produced isotopic variations as great as $40\text{\textperthousand}$ over 10 mm distances in 15 hours. Comparable isotopic variations have been observed in nature. Teng et al. (2006) observed that the isotopic composition of Li diffusing out of a pegmatite into surrounding amphibolite decreased from $+7.6$ to $-19.9\text{\textperthousand}$ over a distance of 10 m. Because of its small ionic size and charge, Li diffuses more readily than most other elements. Indeed, Richter et al. (2009) found it diffused two orders of magnitude faster than Ca. This rapid diffusion also contributes to the large potential for the diffusional isotopic fractionation.

11.7 ISOTOPES OF MAGNESIUM AND CALCIUM

Calcium and magnesium are alkaline earth elements and exist in nature almost exclusively in the +2 valance state. Magnesium is the third most abundant element on Earth; calcium is the fifth. Both are lithophile, mobile, and fairly soluble (they are among the most abundant cations in natural waters), and both are conservative ions in seawater, which is to say their concentrations vary only in proportion to salinity. Both are bio-essential elements and are taken up by organisms in significant quantities, but abundant enough that they are rarely, if ever, biolimiting. Mg is incorporated into the chlorophyll molecule and is involved in energy metabolism and protein synthesis. Ca is widely used by organisms in structural tissues such as bones and shells, and plays key roles in regulating a variety of cellular processes and in intercellular communication, such as neurotransmission. These elements form carbonates more readily than most other elements and these carbonates form a significant fraction of the sedimentary mass.

11.7.1 Mg isotopes

Mg has three stable isotopes: ${}^{24}\text{Mg}$, ${}^{25}\text{Mg}$, and ${}^{26}\text{Mg}$ with relative abundances of 78.99%, 10.00%, and 11.01%, respectively (Coursey et al., 2011). We have already seen that ${}^{26}\text{Mg}$ is the radiogenic product of the short-lived radionuclide, ${}^{26}\text{Al}$, and that the ${}^{26}\text{Al}-{}^{26}\text{Mg}$ is the most important chronometer of events in the early Solar System. However, variations in ${}^{26}\text{Mg}$ due to radioactive decay are restricted

to the earliest formed objects in the Solar System, CAIs and chondrules; subsequently formed objects, such as meteorite parent bodies and planets, appear to be homogeneous with respect to radiogenic ^{26}Mg , and our focus in this chapter will be on variations in Mg isotope ratios resulting from chemical fractionations.

By convention, the isotope ratios of interest are $^{25}\text{Mg}/^{24}\text{Mg}$ and $^{26}\text{Mg}/^{24}\text{Mg}$ and these are reported in the usual notation indicating per mil deviations from a standard, $\delta^{25}\text{Mg}$ and $\delta^{26}\text{Mg}$, respectively. There has, however, been some evolution in this notation. Initially, interest in Mg isotopes focused exclusively on radiogenic ^{26}Mg and the symbol $\delta^{26}\text{Mg}$ referred to variations in ^{26}Mg due to decay of ^{26}Al and not to mass fractionation. Mass fraction effects were expressed as $\Delta^{25}\text{Mg}$ (per mil deviations of $^{25}\text{Mg}/^{24}\text{Mg}$). In order to be consistent with notation used for other elements, current notation uses $\delta^{26}\text{Mg}$ to refer to variations due to mass fractionation, $\delta^{26}\text{Mg}^*$ refers to radiogenic variations in ^{26}Mg , and $\Delta^{25}\text{Mg}$ is reserved for mass independent fractionations in a manner exactly analogous to $\Delta^{17}\text{O}$ and $\Delta^{33}\text{S}$. However, no mass independent fractionations of Mg isotopes have yet been observed in terrestrial materials, and $\delta^{25}\text{Mg} \approx$

0.52 $\delta^{26}\text{Mg}$. Prior to 2003, Mg isotope data was reported relative to a purified magnesium metal standard, NIST-SRM 980; however, that standard proved to be isotopically heterogeneous and the current standard is a solution designated DSM3, derived from Mg extracted from the Dead Sea. Data can be approximately converted using $\delta^{26}\text{Mg}_{\text{DSM3}} = \delta^{26}\text{Mg}_{\text{SRM980}} + 3.405$ (the exact conversion is given by Young and Galy, 2004). Our discussion here will exclusively use on $\delta^{26}\text{Mg}_{\text{DSM3}}$.

Schauble (2011) has calculated fractionation factors for a variety of minerals as well as aqueous solution from partition function using the theoretical approach described in Chapter 8. These can be approximated using the following polynomial approximation:

$$1000 \ln \alpha = \frac{A}{T^6} + \frac{B}{T^4} + \frac{C}{T^2} \quad (11.9)$$

where T is thermodynamic temperature and A , B , and C are constants unique to each pair of phases. Calculated values are shown plotted as a function of temperature in Figure 11.17. The results indicate that we expect heavy Mg isotopes to partition in the order aluminosilicates/oxides > silicates > water > carbonate. Particularly strong fractionation is predicted to occur at low temperature between

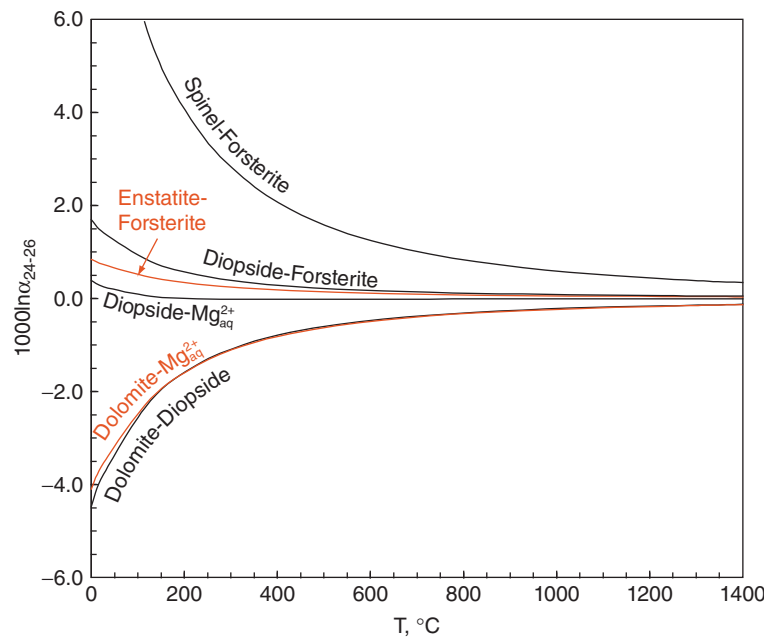


Figure 11.17 $^{26}\text{Mg}/^{24}\text{Mg}$ fractionation factors for a variety of minerals as well as Mg^{2+} ion in aqueous solution calculated from the polynomial equation given by Schauble (2011).

water and/or silicates and carbonate, with the carbonate becoming isotopically light. At higher temperatures, fractionation among mantle silicates (olivine and pyroxenes) is predicted to be quite small, with Δ values less than 0.1‰ above 800°C; however, significant fractionation of >0.5‰ is predicted to occur between silicates and non-silicates such as spinel, even at temperatures above 1000°C. The coordination of Mg in spinel is, of course, quite different than in silicates, so a relatively large fractionation is not surprising.

Figure 11.18 shows the variation of $\delta^{26}\text{Mg}$ in terrestrial materials and bulk meteorites. Fresh peridotites have $\delta^{26}\text{Mg} = -0.22 \pm 0.07\text{\textperthousand}$ and show no resolvable variation with composition. This value presumably represents the isotopic composition of the bulk silicate Earth and is indistinguishable from the average value for basalts ($-0.26 \pm 0.07\text{\textperthousand}$), which also show no systematic variation with composition. Chondrites have a mean $\delta^{26}\text{Mg}$ of $-0.28 \pm 0.06\text{\textperthousand}$ and show no systematic variations between classes (Teng et al., 2010a; Pogge von Strandmann et al., 2011). This suggests Mg isotope fractionations at high temperature and in magmatic systems are, overall, insignificant and is consistent with our expectations based on Schauble's (2011) calculated partition coefficients.

In spite of the apparent uniformity in Mg isotopic composition of bulk mantle samples and basalts, measurable variations on the mineral grain scale have been observed. Young et al. (2009) demonstrated $\delta^{26}\text{Mg}$ differences between spinel (MgAl_2O_4) and olivine in San Carlos peridotite xenoliths of up to 0.88‰ (spinel being isotopically heavier), which were consistent with theoretically predicted fractionations at 800°C. Spinel abundances are generally quite low in peridotites (<1% in those studied by Young et al.), so it would contribute only negligibly to Mg isotope fractionation during melting. Nevertheless, Mg isotope fractionation between spinel-olivine pairs has potential as a geothermometer when the analyses can be done with sufficient precision. Differences between olivine and pyroxenes were smaller, on the order of 0.2–0.3‰, but still larger than the theoretically expected fractionation, suggesting Mg isotopic disequilibrium. Teng et al. (2011) reported correlated variation in $\delta^{26}\text{Mg}$ and $\delta^{56}\text{Fe}$ in olivine fragments of a Hawaiian

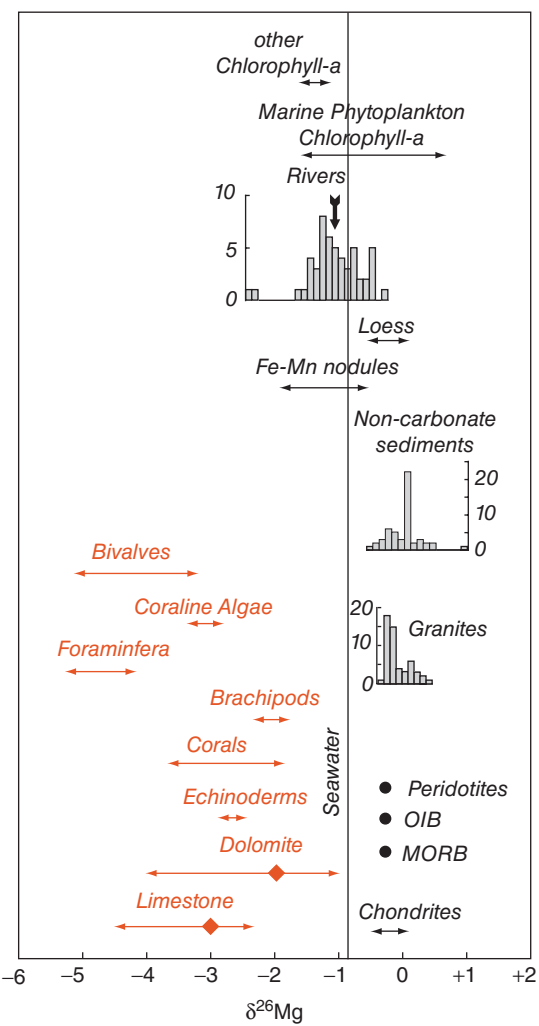


Figure 11.18 Magnesium isotopes in terrestrial materials. The 2σ variation in peridotites, seawater, OIB, and MORB are less than the size of the symbols. Data for peridotites, MORB, OIB, and chondrites are from Teng et al. (2010). Flux-weighted average riverine $\delta^{26}\text{Mg}$ is shown by the arrow and is from Tipper et al. (2006).

basalt, with $\delta^{56}\text{Fe} = -3.3 \times \delta^{26}\text{Mg}$. The variation (total variation in $\delta^{26}\text{Mg}$ was up to 0.4‰) correlated with the $\text{Mg}/(\text{Mg}+\text{Fe})$ ratio of the olivines and Teng et al. (2011) interpreted the variations are resulting from diffusion-driven fractionation as the olivine re-equilibrated with the surrounding cooling magma.

In contrast to basalts and peridotites, continental materials and natural waters show measurable variation in $\delta^{26}\text{Mg}$. Granites vary

in $\delta^{26}\text{Mg}$ from -0.3 to $0.44\text{\textperthousand}$. This variation is unrelated to SiO_2 content and hence apparently reflects variation in source composition, which can include sediments and deep crustal materials, rather than igneous differentiation. Li et al. (2009) found that S-type (derived from melting of metasediments) and I-type (derived from melting of meta-igneous rocks) has a relatively narrow range of isotopic compositions and were on average only slightly isotopically heavier than the bulk silicate Earth. A-type granites from China, derived by deep crustal anatexis, tended to be heavier and more isotopically variable. Granites from the Peninsular Range (Baja California) are even heavier, with $\delta^{26}\text{Mg}$ up to $+0.44\text{\textperthousand}$ (Shen et al., 2009). The mean $\delta^{26}\text{Mg}$ of granites is $-0.08\text{\textperthousand}$, somewhat heavier than the bulk silicate Earth value.

Non-carbonate sediments show a wider variation of $\delta^{26}\text{Mg}$ from about -0.5 to $+0.9\text{\textperthousand}$ and have an average $\delta^{26}\text{Mg}$ of 0\textperthousand . The greatest variation, however, is between carbonate and silicate materials; there is essentially no overlap between carbonate and silicate materials, which is consistent with the large difference in coordination and bonding of Mg and predicted fractionation factors. There is considerable variation among carbonates, which range from $\delta^{26}\text{Mg}$ of $-1\text{\textperthousand}$ to $-5\text{\textperthousand}$. Some or much of this variation appears to be mineralogically controlled with $\delta^{26}\text{Mg}$ decreasing in the order of dolomite > aragonite > high magnesium calcite > low magnesium calcite (Hippler et al., 2009). Skeletal carbonates appear to show additional variation related to phylum, although within foraminifera interspecific variation in appears limited (Pogge von Strandmann, 2008). For the most part, Mg isotopic variations in skeletal carbonate appear to be independent of temperature and salinity.

Rivers also show a wide isotopic variation that reflects the $\delta^{26}\text{Mg}$ of their drainage basin: most rivers have $\delta^{26}\text{Mg}$ in the range of $-1.5\text{\textperthousand}$ to $+0.5\text{\textperthousand}$, but those draining carbonate terrains can have $\delta^{26}\text{Mg} < -2\text{\textperthousand}$. Major rivers show much less isotopic variation, however. Tipper et al. (2006) calculated a flux-weighted mean composition of $-1.09\text{\textperthousand}$. Seawater is isotopically uniform at $\delta^{26}\text{Mg} = -0.82 \pm 0.01\text{\textperthousand}$ within analytical precision (Foster et al., 2010), which is expected given

the long residence time of Mg in seawater. The Mg isotopic variations observed in sediments and waters suggest that significant fractionation occurs during weathering. Consistent with this, Teng et al. (2010b) observed $\delta^{26}\text{Mg}$ values of up to $+0.65\text{\textperthousand}$ in saprolite developed on a diabase with $\delta^{26}\text{Mg}$ of $-0.29\text{\textperthousand}$. The data were consistent with Rayleigh fractionation occurring during weathering as light Mg^{2+} is progressively released to solution with heavier Mg remaining in the solid weathering products. The apparent fractionation factor for the process was $+0.4\text{\textperthousand}$. In summary then, little or no fractionation of Mg isotopes occurs during igneous processes. During weathering, secondary minerals become progressively isotopically heavier as isotopically light Mg goes into solution. Carbonates precipitating from solution are particularly isotopically light and their precipitation will tend to drive solutions to more positive values.

Rivers are the principal source of Mg to the oceans; comparing the isotopic compositions of rivers ($-1.09\text{\textperthousand}$) with that of the ocean ($-0.82\text{\textperthousand}$), it is clear that if the ocean is in steady-state (specifically, its $\delta^{26}\text{Mg}$ is not changing with time), then significant fractionation of Mg isotopes must occur in the marine environment. The principal Mg sink in the oceans is ridge-crest hydrothermal activity, which is thought to remove 50–100% of Mg from the oceans. High temperature hydrothermal systems remove Mg quantitatively from seawater – the vent fluids contain no Mg. In that case, then, there can be no isotopic fractionation. Low temperature systems are less efficient at removing Mg, and hence there is potential for isotopic fractionation. No Mg isotope measurements of low temperature submarine systems have been reported (although one hydrothermal fluid from Iceland had a measured $\delta^{26}\text{Mg}$ of $+0.85\text{\textperthousand}$), so the impact of low temperature systems on seawater $\delta^{26}\text{Mg}$ is unclear. Another sink for Mg is biogenic carbonate (mainly calcite) precipitation. The average $\delta^{26}\text{Mg}$ of deep-sea calcareous oozes is $-1.03\text{\textperthousand}$ (Rose-Koga and Albarède, 2010), quite close to the riverine value. This similarity of isotopic composition to the riverine source of marine Mg, together with the low Mg concentration of calcareous ooze ($\sim 0.06\%$), means biogenic carbonate precipitation has little effect on the

Mg isotopic mass balance in the oceans. Two other potentially important sinks are dolomite precipitation and exchange reactions with clays (in which Mg^{2+} in solution replaces Ca^{2+} and other ions in clays), although the latter is likely to be minor. Unfortunately, there are as yet no empirical or theoretical of fractionation factors for ion exchange reactions with clays, but both exist for dolomite precipitation. Dolomites show a fairly wide range of Mg isotopic compositions, but using the mean $\delta^{26}Mg$ value of $-2\text{\textperthousand}$, Tipper et al. (2006) estimate that 87% of seawater Mg is removed by hydrothermal systems and 13% by dolomite precipitation.

Over the long term, Mg isotopic composition of seawater depends on (1) the riverine flux and its Mg isotopic composition, which in turn depends on the weathering rates, (2) the hydrothermal flux, which in turn depends on the rate of seafloor-spreading, and (3) the rate of dolomite formation. All three of these factors are likely to vary over geologic time. The question of rates of dolomite formation is interesting because judging from the amount of dolomite in the sedimentary mass, the present rate of formation appears to be slow compared to the geologic past. While the rates of seafloor spreading over the last 100 Ma can be constrained from magnetic anomaly patterns, the degree to which these rates have varied are nonetheless debated and independent constraints would be useful. Finally, weathering rates depend on both climate (temperature, precipitation) and atmospheric CO_2 concentrations (Chapter 10). There is intense interest in how these factors have varied. If the Mg isotopic composition of seawater through geologic time could be established, it could be potentially useful in addressing all these issues. The $\delta^{26}Mg$ of foraminiferal shells appears to be independent of temperature and water chemistry and thus might provide a record of $\delta^{26}Mg$ through time. However, it must first be established that Mg isotopic compositions of forams (or any other potential recorder of seawater $\delta^{26}Mg$) do not change through diagenesis. The question of inter-species differences would also have to have to be addressed. There are a host of other issues as well. For example, what controls Mg isotopic fractionation during weathering, what controls isotopic fractionation during dolomite formation, and so on?

11.7.2 Calcium isotopes

Calcium has six stable isotopes: ^{40}Ca , ^{42}Ca , and ^{43}Ca , ^{44}Ca , ^{46}Ca , and ^{48}Ca with relative abundances of 96.94%, 0.647%, 0.135%, 2.086%, 0.0004%, and 0.187%, respectively (Coursey et al., 2011). ^{40}Ca is the principal decay product of ^{40}K (89.5% of ^{40}K decays). However, because ^{40}Ca is vastly more abundant than ^{40}K , variation in ^{40}Ca due to radioactive decay is generally less than 0.01% (K-rich/Ca-poor materials, such as salt deposits, are an exception). Chemical fractionations of Ca isotope ratios are thus the principal interest. Unfortunately, there are several ways of reporting calcium isotope variations. The older convention is to measure the $^{44}Ca/^{40}Ca$ ratio and reported it as $\delta^{44}Ca$ (or $\delta^{44}Ca$). There are two difficulties with this approach: (1) the $^{44}Ca/^{40}Ca$ ratio is small, ~ 0.02 , and is difficult to measure accurately, and (2) some variation in ^{40}Ca abundance results from radioactive decay of ^{40}K . The latter point is illustrated by a study by Ryu et al. (2011), who found that $\delta^{44/40}Ca$ in various minerals of the Boulder Creek granodiorites varied by $8.8\text{\textperthousand}$ (K -feldspar had the highest $\delta^{44/40}Ca$) while $\delta^{44/42}Ca$ values varied only by $0.5\text{\textperthousand}$. Consequently, a second convention has emerged, which is to measure the $^{44}Ca/^{42}Ca$ ratio, reported as $\delta^{44/42}Ca$. Because Ca is such an abundant element, relatively little is sacrificed by measuring the less abundant isotopes.

A consensus has not entirely emerged on what standard value should be used for the delta notation. Many labs report values relative to the NIST SRM 915a $CaCO_3$ standard, whose isotope ratios are listed in Table 11.1. However, there are exceptions to this convention; UC Berkeley reports ratios relative to bulk silicate Earth, whose composition relative to NIST SRM 915a is $\delta^{44/40}Ca_{SRM915a} = +0.97\text{\textperthousand}$, $\delta^{43/40}Ca_{SRM915a} = +0.88\text{\textperthousand}$, and $\delta^{44/42}Ca_{SRM915a} = +0.46\text{\textperthousand}$. Other labs report values relative to seawater, whose isotopic composition is $\delta^{44/40}Ca_{SRM915a} = 1.88 \pm 0.04\text{\textperthousand}$ and $\delta^{44/42}Ca_{SRM915a} = 0.94 \pm 0.07\text{\textperthousand}$ (Hippler et al., 2003). SRM 915a is no longer available and has been replaced by SRM 915b whose $\delta^{44/40}Ca_{SRM915a} = +0.72 \pm 0.04\text{\textperthousand}$ and $\delta^{42/44}Ca = +0.34 \pm 0.02\text{\textperthousand}$. Delta values in the following discussion are relative to SRM915a. Studies to date suggest that all observed calcium isotope fractionations are

mass dependent: in other words, $\delta^{44/40}\text{Ca}$, $\delta^{43/42}\text{Ca}$, and $\delta^{44/42}\text{Ca}$ are strongly correlated and the other two ratios can be predicted from measuring any one (excepting any *radiogenic* variations in ^{40}Ca). Consequently, $\delta^{44/42}\text{Ca} \cong 0.476 \times \delta^{44/40}\text{Ca}$. An overview of calcium isotopic composition of terrestrial and extraterrestrial materials is shown in Figure 11.19.

Simon and DePaolo (2010) found that the Earth, Moon, Mars, and differentiated asteroids (4-Vesta and the angrite and aubrite parent bodies) have $\delta^{44/40}\text{Ca}$ indistinguishable from primitive ordinary chondritic meteorites, while enstatite chondrites are 0.5‰ enriched and primitive carbonaceous chondrites 0.5‰ depleted relative to ordinary chondrites. They speculate that the variations observed in enstatite and carbonaceous chondrites reflect fractionation during high temperature evaporation and condensation in the early solar nebula. These initial variations were averaged out in during accretion of large bodies such as asteroids and planets.

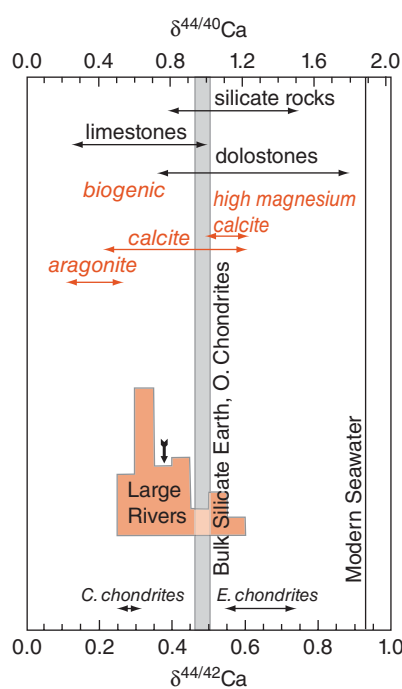


Figure 11.19 Ca isotopic composition of terrestrial and meteoritic materials. Isotopic compositions of biogenic carbonates are shown in red. Arrow shows the average composition of continental runoff of Tipper et al. (2010).

To date, there has been only a limited effort to investigate Ca isotope fractionations in terrestrial igneous rocks; $\delta^{44/40}\text{Ca}$ values compiled by DePaolo (2004) show a range of nearly 0.7‰, some of which reflects variable amounts of radiogenic ^{40}Ca ; the small number of igneous rock $\delta^{44/42}\text{Ca}_{\text{SRM915a}}$ values in the literature range from +0.31‰ to +0.80‰. Individual minerals show greater variation. As noted earlier, minerals from a single granodiorite studied by Ryu et al. (2011) varied by 0.5‰. Huang et al (2010) found that $\delta^{42/44}\text{Ca}$ in orthopyroxene was 0.38‰ higher than in clinopyroxene in Kilbourne Hole peridotites xenoliths and 0.25‰ higher in San Carlos peridotite xenoliths. They estimated the $\delta^{44/40}\text{Ca}_{\text{SRM915a}}$ of the Earth's mantle to be +1.05‰ ($\delta^{44/42}\text{Ca}_{\text{SRM915a}} = +0.50\text{\textperthousand}$), slightly higher than the average ratios they measured in basalts ($\delta^{44/40}\text{Ca}_{\text{SRM915a}} = +0.97 \pm 0.04\text{\textperthousand}$) and slightly higher than the UC Berkeley bulk silicate Earth value ($\delta^{44/40}\text{Ca}_{\text{SRM915a}} = +0.97\text{\textperthousand}$).

Huang et al. (2011) analyzed Hawaiian lavas and found that $\delta^{42/44}\text{Ca}_{\text{SRM915a}}$ in lavas of Koolau volcano (Oahu) were much lower, 0.34–0.40‰, and found that calcium isotope ratios correlated inversely with $^{87}\text{Sr}/^{86}\text{Sr}$ (Figure 11.20) and with Sr/Nb ratios, but not with other trace element ratios. Huang et al. argued that the calcium isotope variations and these correlations reflected the presence of marine carbonates in ancient recycled oceanic crust that makes up part of the Hawaiian mantle plume (e.g., Hofmann and White, 1982; Sobolev et al., 2005).

High temperature hydrothermal fluids have a $\delta^{44/40}\text{Ca}_{\text{SRM915a}}$ of +0.95‰, well within the range of the isotopic composition of MORB; thus, there appears to be no significant isotopic fractionation between hydrothermal fluids and oceanic crust (Amini et al., 2008). However, hydrothermal systems also involve precipitation of anhydrite and Amini et al. (2008) found the fractionation factor ($\Delta^{44/40}\text{Ca}$) for anhydrite precipitation in oceanic crust to be -0.5‰. In addition, aragonite precipitates within the oceanic crust at low temperatures with similar fractionation factors (-0.34‰). Thus, the effect of seawater interaction with the oceanic crust is to drive seawater to heavier isotopic compositions.

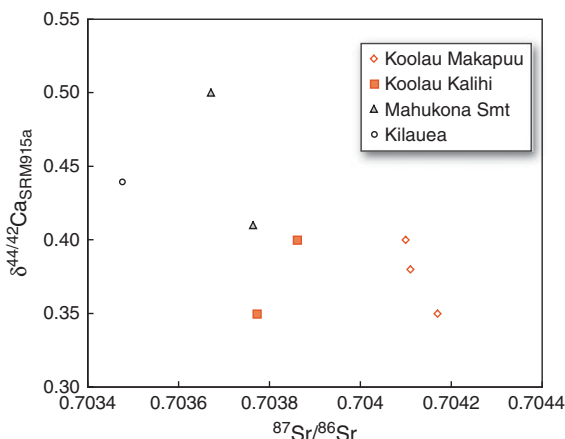


Figure 11.20 $\delta^{44/42}\text{Ca}_{\text{SRM}915\text{a}}$ versus ${}^{87}\text{Sr}/{}^{86}\text{Sr}$ in Hawaiian lavas analyzed by Huang et al. (2011). Huang et al. interpreted this correlation as mixing between recycled sedimentary carbonate and mantle. (Source: Data from Huang et al. (2011).)

Several studies have shown that there is apparently little fractionation during physical weathering, at least during early stages. In laboratory dissolution experiments Ryu et al. (2011) found that $\delta^{44/42}\text{Ca}$ of solutions produced in the experiments varied due to incongruent dissolution, but that little mass fractionation occurred. Hindshaw et al. (2011) found that soils that have developed over the last 150 years in front of the retreating Damma glacier in Switzerland have Ca isotopic ratios identical to the granite on which they had developed. In contrast to purely physical weathering, significant fractionations occur when biology is involved. Plants preferentially take up lighter Ca isotopes. Weigand et al. (2005) found that calcium uptake by Hawaiian Ohia trees has $\Delta^{44/40}\text{Ca}$ fractionation factors of -1 to $-2\text{\textperthousand}$; on the other hand, twigs and leaves are about $0.5\text{\textperthousand}$ heavier than the Ca in xylem. As a result of this preferential uptake of light Ca isotopes by the flora, the soil solutions become isotopically heavier (e.g., Cenki-Tok et al. 2009). In the marine environment, autotrophs such as the alga *Emiliania huxleyi* also preferentially utilize isotopically light Ca. *E. huxleyi* is a coccolithophorid and secretes a test, or shell, composed of calcite plates or *coccoliths*, which constitute about half the calcium carbonate precipitated from the ocean. Such

precipitation is, of course, an important part of the global calcium cycle and we consider this later in this section.

Significant fractionation occurs in precipitation of calcium carbonate from solution. Marriott et al. (2004) found the $\Delta^{44/42}\text{Ca}$ fractionation factor for inorganic calcite precipitation had a temperature dependence of $0.008 \pm 0.005\text{\textperthousand}/^\circ\text{C}$ ($\Delta^{44/40}\text{Ca} = 0.015\text{\textperthousand}/^\circ\text{C}$). Gussone et al. (2005) found that the fractionation factor for aragonite was about $0.6\text{\textperthousand}$ lower than for calcite at any given temperature, but that the temperature dependence of the fractionation factor for aragonite was similar to that of calcite. In addition to temperature, the fractionation factor appears to depend on CO_3^{2-} concentration, precipitation rate, and Mg^{2+} concentration, with less fractionation in the precipitation of high-magnesium calcite.

Most calcium carbonate precipitation is biogenic. Gussone et al. (2006) found that the fractionation factor for precipitation of *E. huxleyi* coccoliths was greater than that for inorganic precipitation but that the temperature dependence of the $\Delta^{44/40}\text{Ca}$ fractionation factor ($0.027 \pm 0.006\text{\textperthousand}/^\circ\text{C}$) was similar to the temperature dependence for inorganic calcite precipitation. Growth rate, carbonate concentrations, and other factors appeared to have little effect on the fractionation factor. They also noted that the isotopic composition of the whole organism is essentially identical to that of the calcite coccoliths and therefore that the fractionation apparently occurs during uptake of Ca from seawater rather than during calcite precipitation.

Ca isotope fractionation by planktonic foraminifera, which also secrete calcite tests, does not show simple temperature dependence. While Gussone et al. (2003) found that $\Delta^{44/40}\text{Ca}$ exhibited a temperature dependence of $0.24\text{\textperthousand}/^\circ\text{C}$ in laboratory-grown *Globigerinoides sacculifer*, subsequent studies at lower salinity found no temperature dependence (Gussone et al., 2009). Sime et al. (2005) found no significant temperature dependence in the Ca isotopic composition of tests of 12 planktonic species recovered from deep-sea core tops. It appears that any temperature-dependence of Ca isotope fractionation in planktonic foraminifera fractionation is masked by other factors such as salinity and kinetic fractionations related to growth rate (Kisakürek et al., 2011).

Table 11.2 Calcium isotope fractionation in biogenic carbonate.

Organism	Fractionation Factors	
	$\Delta^{44/40}\text{Ca}$	$\Delta^{44/42}\text{Ca}$
Bivalves (calcite)	-1.50	-0.71
Foraminifera (calcite)	-0.94	-0.45
Coccolithophorids (calcite)	-1.30	-0.62
Brachiopods (calcite)	-0.85	-0.40
Sponges (aragonite)	-1.50	-0.71
Pteropod snails (aragonite)	-1.40	-0.67
Scleractinian corals (aragonite)	-1.10	-0.52

Temperature dependence of the fractionation factor in benthic foraminifera also appears weak, particularly below 5°C (Gussone and Flippstone, 2010). Table 11.2 lists the approximate fractionation factors for biogenic carbonate precipitation. Scleractinian corals (e.g., reef-building corals) are anomalous in that although they precipitate aragonite, fractionation factors are similar to

those for calcite secreting organisms (Böhm et al., 2006).

In animals, Ca isotope systematics are complex. The isotopic composition of soft tissues (muscle, blood) appears to track that of diet, although with considerable variability (Figure 11.21). In chickens, for example, Skulan and DePaolo (1999) found that $\delta^{44/40}\text{Ca}$ varied by more than 3‰ between blood, muscle, egg white, and egg yolk, with egg white and egg yolk differing by nearly 2‰. Mineralized tissues (bones, shell, and teeth) were on average about 1.3‰ lighter than soft tissues. Subsequent studies (e.g., Chu et al., 2006) have generally confirmed this effect. The data suggest that in animals there is little Ca isotopic fractionation in uptake but a large fractionation in mineralized tissue formation. Soft tissues are more variable and this variability likely reflects both fast cycling and short residence times of calcium ion in soft tissues as well as two-way exchange of Ca between soft and mineralized tissues. In addition, Reynard et al. (2010) found that in sheep, ewes had $\delta^{42/44}\text{Ca}$ about 0.14‰ heavier than rams.

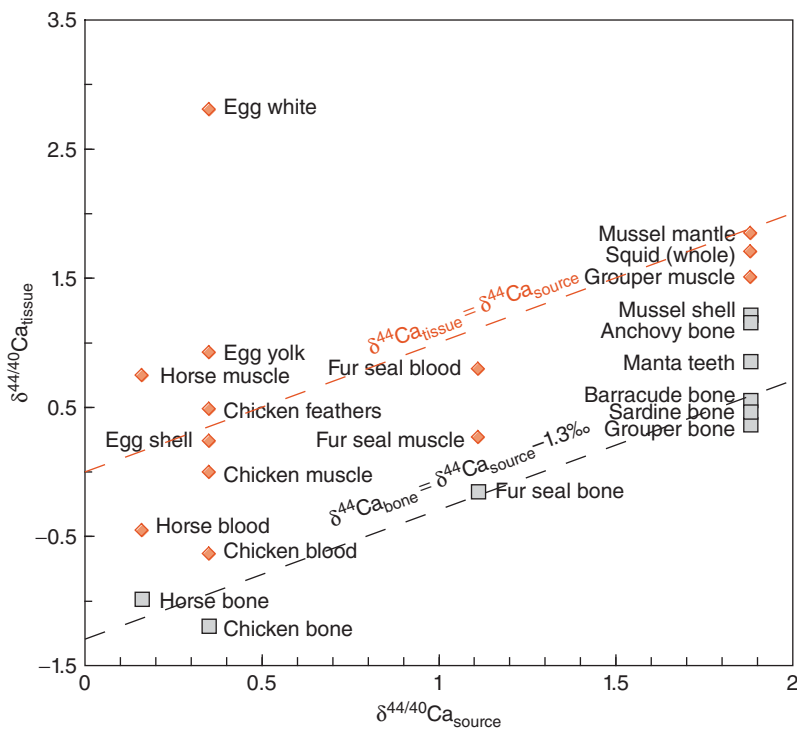


Figure 11.21 Relationship between $\delta^{44/40}\text{Ca}$ in diet and soft and mineralized tissues in animals.
(Source: Skulan and DePaolo (1999). Reproduced with permission of National Academy of Sciences, U.S.A.)

Noting the very light isotopic composition of sheep's milk relative to their diet (Chu et al., 2006), they attributed this sexual difference to lactation in ewes.

Farkaš et al. (2007) attempted to deduce the Ca isotopic history of seawater over Phanerozoic time from the isotopic composition of marine carbonates and phosphates (Figure 11.22). The results suggest that $\delta^{44/42}\text{Ca}$ has increased by $\sim 0.33\text{\textperthousand}$ over the last 500 Ma, although the path has been bumpy. An increase in the Carboniferous was followed by a return to lower values in the Permian and Triassic. Although details are unclear because of sparse data coverage, values again increased in the second half of the Mesozoic and declined again in Paleogene before increasing to present values in the Neogene. Farkaš et al. concluded that not only must have Ca fluxes changed over time (there is independent evidence from fluid inclusions in evaporites that seawater Ca concentrations have changed with time), but fractionation factors must have changed as well. They proposed that this varying fractionation reflected variation in the dominant mineralogy in marine carbonate precipitations:

oscillating between calcite and aragonite. In their hypothesis, that in turn reflected variation in the oceanic Mg/Ca ratio: low Mg/Ca favors calcite while high Mg/Ca favors aragonite. They suggest that the Mg/Ca ratio was in turn controlled by tectonic processes, specifically variable rates of oceanic crust production that modulated the hydrothermal calcium and magnesium flux to and from the oceans. Sime et al. (2007) reconstructed the marine Ca isotope record over the last 24 million years using planktonic foraminifera. They concluded that variations in $\Delta^{44/42}\text{Ca}$ during calcite precipitation were insufficient to account for the variation in $\delta^{42/44}\text{Ca}$ observed (about $0.1\text{\textperthousand}$), although they played a role and that variations of $\pm 0.05\text{\textperthousand}$ in the isotopic composition of weathering flux was required.

11.8 SILICON ISOTOPES

Silicon, which is the third or fourth most abundant element on Earth (depending on how much may be in the core), has three isotopes: ^{28}Si (92.23%), ^{29}Si (4.69%), and ^{30}Si (3.09%) (Coursey et al., 2011). By convention, $^{29}\text{Si}/^{28}\text{Si}$ and $^{30}\text{Si}/^{28}\text{Si}$ ratios are reported as

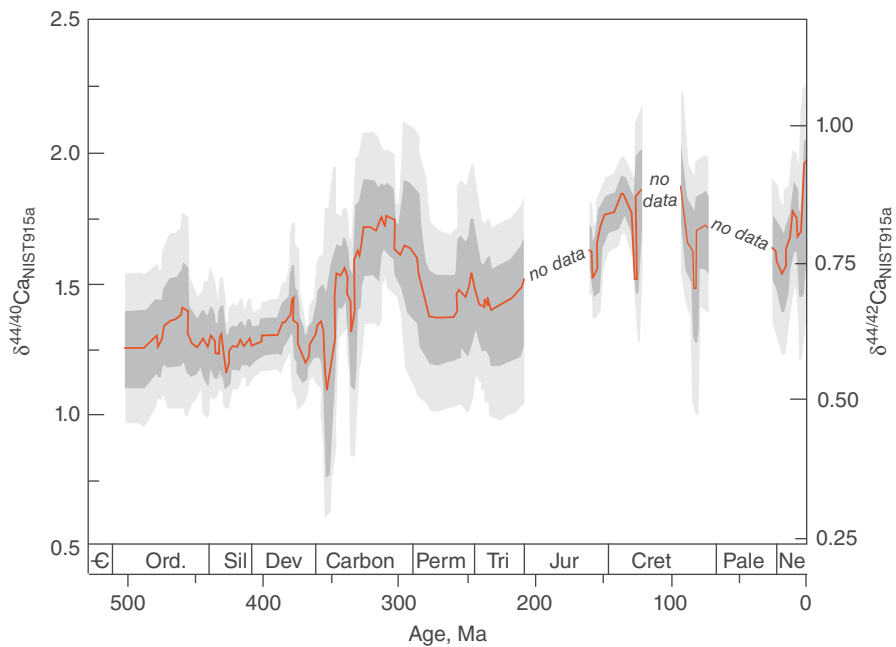


Figure 11.22 Ca isotopic composition of seawater over the last 500 Ma calculated from the isotopic composition of marine carbonates and phosphates. Thick line shows a 10-point moving average; dark and light grey regions show the 1σ and 2σ bounds, respectively. (Source: Farkaš et al. (2007). Reproduced with permission of Elsevier.)

$\delta^{29}\text{Si}$ and $\delta^{30}\text{Si}$ relative to the standard NBS28 (NIST-RM8546) whose isotopic composition is ${}^{30}\text{Si}/{}^{28}\text{Si} = 0.033532$ and ${}^{29}\text{Si}/{}^{28}\text{Si} = 0.0508204$ (Coplen et al., 2002). The first study of silicon isotope geochemistry is 60 years old (Reynolds and Verhoogen, 1953), but the field has rapidly expanded only since the advent of the high-precision multi-collector-ICP-MS in the last decade or so, and some aspects of Si isotope geochemistry are not yet fully understood. To date, all reported $\delta^{29}\text{Si}$ and $\delta^{30}\text{Si}$ are consistent with mass-dependent fractionation, so we will consider only $\delta^{30}\text{Si}$.

Figure 11.23 provides an overview of the Si isotopic composition of terrestrial and extraterrestrial materials. Silicon isotope geochemistry has relevance to a wide variety of issues in earth science. The first, and arguably the most fundamental of these, is the parental material of the Earth and the composition of the Earth's core. As we saw in Chapter 5, the Earth and Moon uniquely share a common oxygen isotopic composition with enstatite chondrites. This has led some to suggest that enstatite chondrites provide a better model for the Earth's composition than carbonaceous or ordinary chondrites (e.g., Javoy et al., 2010). Estimates of the $\delta^{30}\text{Si}$ of the bulk silicate Earth vary from $-0.29 \pm 0.08\text{\textperthousand}$ (Savage et al., 2010) and $-0.28 \pm 0.05\text{\textperthousand}$ (Fitoussi et al., 2009) to $-0.38\text{\textperthousand}$ (Chakrabarti and Jacobsen, 2010). Excepting the latter estimate,⁸ this value falls outside the range observed in ordinary and carbonaceous chondritic meteorites (-0.36 to $-0.56\text{\textperthousand}$) and much outside that of enstatite chondrites (-0.58 to $-0.67\text{\textperthousand}$) (Chakrabarti and Jacobsen, 2010; Armytage et al., 2011). The Moon appears to have the same Si isotopic composition as the silicate Earth (Fitoussi and Bourdon, 2012; Armytage et al., 2012). There is wide agreement that the difference in Si isotopic composition between meteorites (representing nebular material parental to the Earth) and the bulk silicate Earth reflects isotopic fractionation of Si between the core and silicate Earth. Observational differences of Si isotopic composition between metal and silicate phases in enstatite chondrites (Ziegler et al., 2010), experimental data (Shahar et al., 2011), and theoretical calculations (Schauble et al., 2007) indicate that the fractionation of Si isotopes between

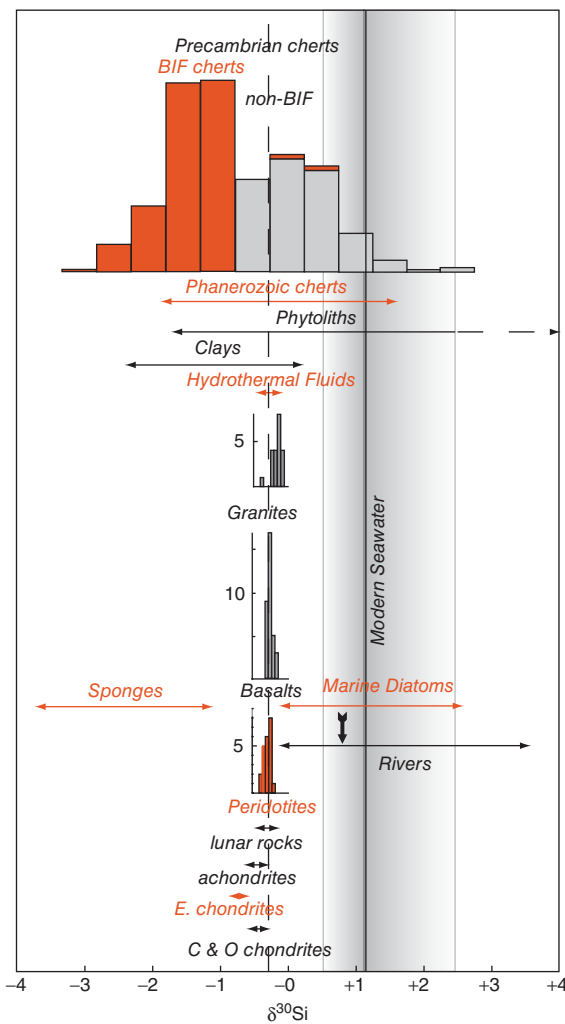


Figure 11.23 Silicon isotopic composition of terrestrial and solar system materials. Dashed line is the estimated $\delta^{30}\text{Si}$ of the bulk silicate Earth. “C & O chondrites” are carbonaceous and ordinary chondrites; “E chondrites” are enstatite chondrites; gray area shows the range of $\delta^{30}\text{Si}$ in seawater; solid line is estimated average seawater composition. Arrow shows estimated average composition of rivers. Precambrian cherts from compilation of Chakrabarti et al., 2012).

metal and silicate can be expressed as:

$$\Delta^{30}\text{Si}_{\text{silicate-metall}} \cong \frac{7.5 \times 10^6}{T^2} \quad (11.10)$$

This equation tells us that isotopically light Si preferentially partitions into the metal phase (i.e., the core) and the extent of fractionation decreases with temperature.

We don't know exactly the temperature of equilibration, but assuming a difference in $\delta^{30}\text{Si}$ between the bulk silicate Earth and carbonaceous or chondrites of $-0.15\text{\textperthousand}$, Armytage et al. (2011) concluded that the core contains ~ 8.7 wt% Si while Ziegler et al. (2010) concluded the core contains at least 6% Si. This amount of Si would be consistent with geophysical observations, such as seismic velocity and moment of inertia, which constrain the density of the core and require that it contain a few percent of an element lighter than Fe or Ni. Fitoussi and Bourdon (2012) calculate that to account for the much greater difference in $\delta^{30}\text{Si}$ between the Earth and Moon and enstatite chondrites, the Earth's core would have to contain 28 wt% Si, an amount much greater than allowed by geophysical constraints. The similarity of $\delta^{30}\text{Si}$ of the Moon and silicate Earth implies that the Earth's core had mostly segregated before the Moon-forming impact and the $\delta^{30}\text{Si}$ in silicates from proto-Earth and the impactor were homogenized in the aftermath of the impact (Armytage et al., 2012). Considering Si, Cr, Ni, and O isotopic compositions, Fitoussi and Bourdon (2012) suggest that the Earth-Moon composition could be accounted for if the parental material were a mix of carbonaceous and ordinary chondritic material with the addition of 15% of enstatite chondrite.

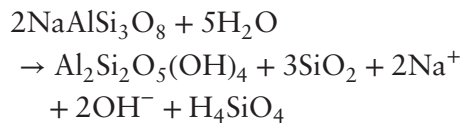
The average $\delta^{30}\text{Si}$ of mantle-derived ultramafic xenoliths is $-0.30 \pm 0.04\text{\textperthousand}$, that of basalts is $-0.28 \pm 0.03\text{\textperthousand}$, and that of granitic rocks is $-0.23 \pm 0.13\text{\textperthousand}$. This implies that there is a slight fractionation associated with melting and fractional crystallization, with lighter silicon isotopes partitioning preferentially into SiO_2 -poor mafic minerals such as olivine. Savage et al. (2012) found that $\delta^{30}\text{Si}$ in igneous rocks depended on SiO_2 composition approximately as:

$$\delta^{30}\text{Si}(\text{\textperthousand}) = 0.0056 \times [\text{SiO}_2] - 0.568 \quad (11.12)$$

Savage et al. (2012) also found a slight variation in $\delta^{30}\text{Si}$ in granites that related to their petrogenesis: S-type granites (those derived by melting of sedimentary precursors and with $\text{Al}_2\text{O}_3/(\text{CaO}+\text{Na}_2\text{O}+\text{K}_2\text{O}) > 1$) had slightly lighter $\delta^{30}\text{Si}$ than either I-type (derived from melting of igneous precursors) or A-type (derived by fractional crystallization of a mafic parent magma) granites. Compared to other

processes, however, Si isotope fractionation in igneous processes is quite small; for example, in the course of evolution from basaltic to andesitic, the $\delta^{30}\text{Si}$ of a magma would increase by only $\sim 0.06\text{\textperthousand}$, an amount only slightly greater than present analytical precision. This, of course, should not be surprising because (1) temperatures involved are high, (2) the oxidation state of Si does not vary, and (3) the atomic environments of Si in silicate minerals and melts do not differ greatly.

At lower temperatures and where another form of Si is involved (silicic acid: H_4SiO_4), fractionations are (not surprisingly) greater. Igneous minerals at the surface of the Earth undergo weathering reactions such as:



Thus, when albite reacts with water, Si partitions between residual clay (kaolinite in this example), quartz, and silicic acid in aqueous solution. This is an overall reaction that involves a variety of intermediate steps and phases and furthermore occurs rather slowly. Thus determining the fractionation factors for such reactions experimentally is difficult. Méheut et al. (2007) used a theoretical approach to calculate a $\Delta^{30}\text{Si}$ kaolinite-quartz fractionation factor of $-1.6\text{\textperthousand}$ at 25°C . Experimental estimates of the fractionation of between dissolved H_4SiO_4 and biogenic opaline silica indicate that $\Delta^{30}\text{Si}_{\text{opal-diss. Si}} \approx -1.1\text{\textperthousand}$ (De La Rocha et al., 1997). Other studies indicate little fractionation in the transformation of opal to quartz, so we can infer that the fractionation between kaolinite and dissolved silica should be $\sim -2.5\text{\textperthousand}$. Consequently, we expect that weathering of silicate rocks to produce isotopically light clays and an isotopically heavy solution. In addition, some of the silica released into solution by weathering can be absorbed on the surface of oxides and hydroxides in soils such as ferrihydrite and goethite. Delstanche et al. (2009) experimentally determined fractionation factors for adsorption of Si on ferrihydrite as $\Delta^{29}\text{Si}_{-\text{ferri-solu.}} \approx -0.81\text{\textperthousand}$ and $\Delta^{29}\text{Si}_{-\text{geoth.-solu.}} \approx -0.54\text{\textperthousand}$. Assuming mass-dependent fractionation these imply ^{30}Si fractionation factors of $\Delta^{30}\text{Si}_{-\text{ferri-solu.}} \approx -1.59\text{\textperthousand}$ and $\Delta^{30}\text{Si}_{\text{geoth.-solu.}} \approx -1.06\text{\textperthousand}$. This

adsorption drives dissolved silica further toward isotopically heavy compositions. The solubility of silica is quite limited; concentrations in rivers are typically less than 10 ppm. Consequently, isotopic fractionation between dissolved silica and solid phases has a smaller effect on the isotopic composition of solid phases than the solution.

In addition to being the key ingredient in silicate rocks and minerals, silicon is also extensively bio-utilized. Terrestrial plants take-up silicic acid from the soil solution and incorporate it in various tissues, where it appears to increase rigidity, increase photosynthetic efficiency, limit loss of water by evapotranspiration, and increase the resistance to pathogens and grazing by herbivores, including insects. The “phytoliths” formed in this process consist of hydrated opaline silica and vary widely in silicon isotopic composition. Ding et al. (2009) suggest the latter is due to Rayleigh fractionation during precipitation of the phytoliths from plant fluids with an apparent fractionation factor of $\Delta^{30}\text{Si}_{\text{phyto-solu.}} \approx +2\text{\textperthousand}$. This follows a fractionation during uptake of H_4SiO_4 from the soil solution by roots of $\Delta^{30}\text{Si}_{\text{roots-soil}} \approx -1.2\text{\textperthousand}$. Thus, silica utilization by plants drives the soil solution towards heavier isotopic compositions.

In view of the fractionations during weathering and uptake by the terrestrial biota, it is not surprising to find that rivers are isotopically heavy, with $\delta^{30}\text{Si}$ ranging from -0.1 to $+3.4\text{\textperthousand}$ and averaging about $+0.8\text{\textperthousand}$ (De La Rocha et al., 1997; Georg et al., 2006; Ding et al., 2011). Isotopic compositions vary not only between different rivers, but also over time in individual rivers. Georg et al. (2006) found that $\delta^{30}\text{Si}$ correlated positively with dissolved Si concentration and inversely with discharge and base cation flux. They suggest that the higher $\delta^{30}\text{Si}$ are associated with active clay mineral formation during slow seepage of water through soils and low river discharge.

Dissolved silica reaching the oceans is extensively bio-utilized and can be bio-limiting. Marine organisms utilizing silica include sponges and planktonic protists such as diatoms, silicoflagellates, and radiolarians. Of these, sponges appear to fractionate silica the most. De La Rocha (2003) found that $\delta^{30}\text{Si}$ in modern sponge spicules range from -1.2 to $-3.7\text{\textperthousand}$ and fractionation factors $\Delta^{30}\text{Si}_{\text{sponge-sw}}$ averaged $-3.8 \pm 0.8\text{\textperthousand}$.

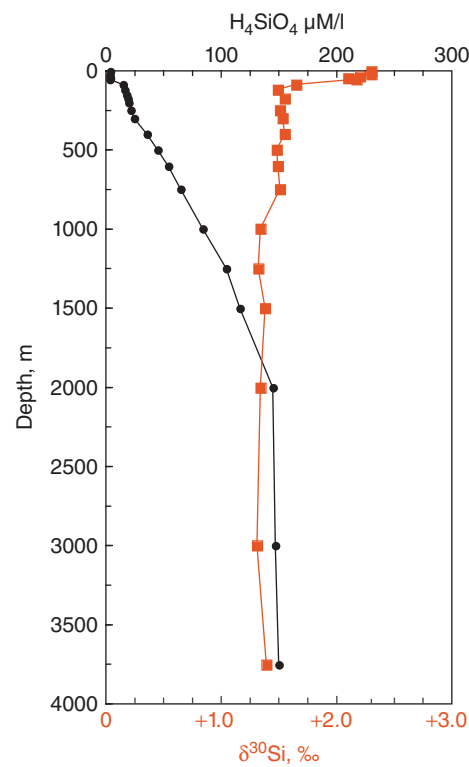


Figure 11.24 Variation of $\delta^{30}\text{Si}$ and dissolved silica concentration with depth in the equatorial Pacific. Data from Beucher et al. (2008).

Diatoms, which account for some 75% of primary productivity in the oceans, are far more important in the marine silica cycle. These organisms live in the surface waters and build tests (or shells) of opaline silica. As a consequence, dissolved silica is depleted in the surface waters (Figure 11.24). As their remains sink, the tests tend to redissolve and consequently deep waters are enriched in dissolved silica. As we noted previously, experiments suggest a fractionation factor, that is, $\Delta^{30}\text{Si}_{\text{opal-dissolv.}}$, of about $-1.1\text{\textperthousand}$ during formation of diatom tests, and as a consequence, surface waters are typically enriched in ^{30}Si . Curiously, Demarest et al. (2009) found that the fractionation during partial dissolution of diatoms tests was just the opposite: the solution became isotopically lighter and the residual tests isotopically heavier with a $\Delta^{30}\text{Si}_{\text{opal-dissolv.}} \approx +0.55\text{\textperthousand}$. Thus in both precipitation and dissolution of diatom tests, the lighter isotope reacts more readily (see Problem 4).

Because $\delta^{30}\text{Si}$ in oceans is tightly coupled with biological productivity and hence the carbon cycle, there is much interest in using silicon isotopes in understanding the modern silica cycle and using $\delta^{30}\text{Si}$ in siliceous biogenic sediments to reconstruct productivity variations in the ancient oceans. To date, only a few such studies have been carried out, and interpretation of these variations remains somewhat equivocal. Improved understanding of the silica cycle in the modern ocean is needed before $\delta^{30}\text{Si}$ can be used as a paleo-oceanographic proxy.

The silicon isotopic composition of seawater through time has been controlled by (1) the isotopic composition of the sources of dissolved Si and (2) their relative fluxes and (3) fractionations occurring during removal of Si from seawater. The principal fluxes are (a) weathering of continents (i.e., rivers), (b) submarine hydrothermal vents and (c) dissolved Si diffusing out of sediments. Variations in the Si isotopic composition of seawater are recorded in cherts, which are ubiquitous throughout the sedimentary record. Modern cherts are derived primarily from biogenic opal produced by diatoms, which became important in the sedimentary record in the Mesozoic, and radiolarians, which first appeared in the Cambrian. Such silica-utilizing organisms were absent in the Precambrian (except for sponges in the latest Proterozoic), yet cherts are found throughout the Precambrian. Many Precambrian cherts appear to have formed secondarily through reaction of sedimentary and igneous rocks with Si-rich diagenetic fluids and do not provide a record of $\delta^{30}\text{Si}$ in seawater. Other Precambrian cherts, however, likely formed through direct abiogenic precipitation from H_4SiO_4 -saturated seawater and/or hydrothermal fluids (in the absence of silica-secreting organisms, dissolved silica concentrations in Precambrian oceans were likely much higher). Chakrabarti et al. (2012) found that banded iron formations (BIFs), which typically consists of alternating Fe-rich and SiO_2 -rich layers, have lighter Si isotopic compositions than non-BIF Precambrian cherts (Figure 11.23), which they argue is due to a greater hydrothermal component in BIF cherts. They found that $\delta^{30}\text{Si}$ of Archean cherts progressively increased with time, consistent with increasing input of dissolved

Si from weathering of growing continents and decreasing hydrothermal activity over this period. Submarine hydrothermal activity is associated with mid-ocean ridge and island-arc volcanism and a decrease with time is, of course, what we expect for an Earth that is slowly cooling. Maximum $\delta^{30}\text{Si}$ occurred at around 1.5 Ga in the Mesoproterozoic, after which $\delta^{30}\text{Si}$ appears to decrease again. The cause of the latter decrease is not yet fully understood, but this study makes clear that understanding how $\delta^{30}\text{Si}$ has varied through time will help us understand the evolution of the Earth.

11.9 CHLORINE ISOTOPES

Chlorine has two isotopes ^{35}Cl and ^{37}Cl whose abundances are 75.76% and 24.24%, respectively (Coursey et al. 2011). It is most commonly in the -1 valance state and strongly electropositive, forming predominantly ionic bonds, but in the rare circumstance of strongly oxidizing conditions it can have valances up to +7. Chlorine is relatively volatile, and has a strong propensity to dissolve in water; consequently much of the Earth's inventory is in the oceans. Since the oceans are a large and isotopically uniform reservoir of chlorine (Godon et al., 2004), isotope ratios are reported as $\delta^{37}\text{Cl}$ relative to seawater chloride (formally called Standard Mean Ocean Chloride or SMOC denoted as $\delta^{37}\text{Cl}_{\text{SMOC}}$), whose $^{37}\text{Cl}/^{35}\text{Cl}$ is 0.319627 (Coplen et al., 2002). NIST-SRM 975 is the commonly used reference standard, whose isotopic composition is $^{73}\text{Cl}/^{35}\text{Cl} = 0.31977$ ($\delta^{37}\text{Cl}_{\text{SMOC}} = +0.52\%$).⁹

Relatively few Cl isotopic analyses of meteorites have been reported. Sharp et al. (2007) reported $\delta^{37}\text{Cl}$ of +1.21‰ in Orgueil (CV1), +0.46‰ in Murchison (CM2) and -0.38‰ in Allende (CV3); components of meteorites such as water-soluble extracts and sodalite ($\text{Na}_8\text{Al}_6\text{Si}_6\text{O}_{24}\text{Cl}_{12}$) show greater variability. Because the oceans and evaporites, which both have $\delta^{37}\text{Cl}$ of ~0‰, likely contain more than 80% and possibly more than 90% of the Earth's chlorine inventory, the $\delta^{37}\text{Cl}$ of the Earth is probably close to 0‰. Sharp et al. (2010a) found that $\delta^{37}\text{Cl}$ in lunar materials ranged from -0.7–+24‰. They argued that both the positive value and the large spread resulted from fractionation during

volatilization and loss of metal chlorides during eruption of the basalts. That in turn, they suggested, indicated the Moon is hydrogen poor because formation of magmatic HCl lessens the fractionation during degassing in terrestrial basalts.

Schauble et al. (2003) calculated theoretical fractionation factors for chlorine. They found (not surprisingly) that the largest fractionation occurred between chlorine of different oxidation states. Predicted chloride-chlorate (ClO_2), and chloride-perchlorate (ClO_4^-) fractionation factors are as great as 27 and 73‰ at 298 K, with ^{37}Cl concentrating in the oxidized forms; however, naturally occurring chlorine in these oxidized forms is extremely rare and plays essentially no role in the natural chlorine cycle. Among chlorides, they predicted that ^{37}Cl will preferentially partition into organic molecules (by 5–9‰ at 295 K) and into salts and silicates where it is bound to divalent metals (e.g., FeCl_2) in preference to monovalent ones (such as NaCl) by 2–3‰ at 298 K. ^{37}Cl should also concentrate in silicates relative to brines by 2–3‰ at surface temperature. They also calculated $\Delta_{\text{Cl}_2-\text{HCl}} = +2.7\text{\textperthousand}$ and $\Delta_{\text{HCl}-\text{NaCl}} = +1.45\text{\textperthousand}$. Experiments by Eggenkamp et al. (1995) produced the following fractionation factors: $\Delta_{\text{NaCl-soln}} = +0.26\text{\textperthousand}$, $\Delta_{\text{KCl-soln}} = -0.09\text{\textperthousand}$, and $\Delta_{\text{MgCl}_{2.6}\text{H}_2\text{O-soln}} = -0.6\text{\textperthousand}$. These fractionations are consistent with the observed narrow range and mean value of $\delta^{37}\text{Cl}$ in halite evaporites (−0.9 to +0.9‰ and +0.06‰, respectively) and slightly lighter composition of potash (KCl) facies evaporites (average −0.3‰) (Eastoe et al., 2007). Liebscher et al. (2006) experimentally determined fractionations between NaCl solutions and aqueous vapor at 450°C at pressures close to the critical point and found that $\Delta^{37}\text{Cl}_{\text{vapor-liquid}}$ values were within ±0.2‰ of 0. Sharp et al. (2010b) experimentally determined the fractionation between HCl vapor and gas and found $\Delta^{37}\text{Cl}_{\text{HClvapor-HClliquid}} \approx +1.7\text{\textperthousand}$, consistent with theoretical prediction.

Figure 11.25 summarizes $\delta^{37}\text{Cl}$ variations in natural materials. As noted earlier, seawater is isotopically homogeneous within analytical error or nearly so.¹⁰ Phanerozoic marine evaporites are fairly homogeneous, with a mean and standard deviation of −0.08 and 0.33‰, respectively. Eastoe et al., (2007)

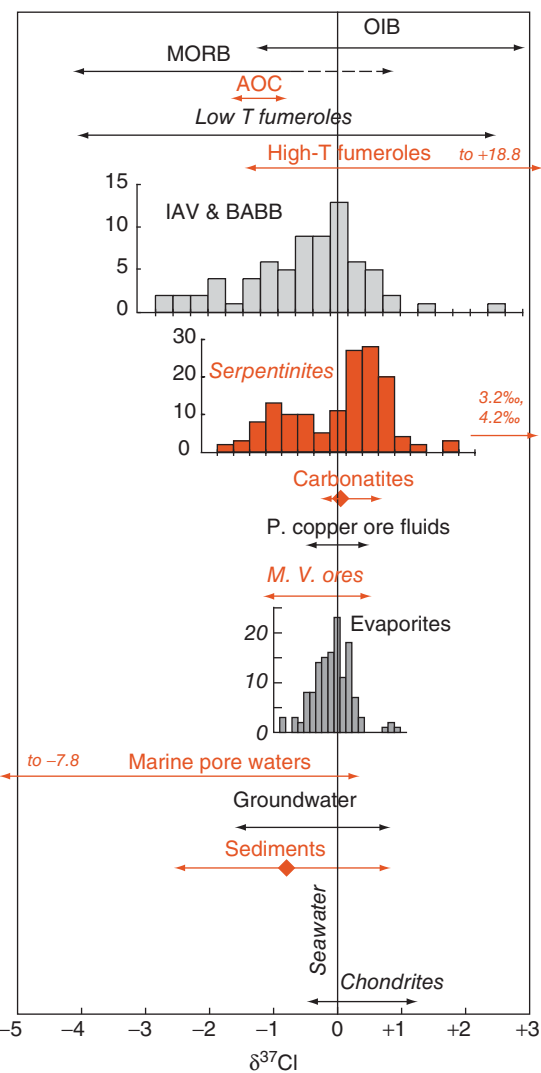


Figure 11.25 Chlorine isotope variations in terrestrial materials and meteorites. AOC is altered oceanic crust; P. copper ores are porphyry copper ores and M.V. ores are Mississippi Valley type deposits (Chapter 9).

found small but significant variations in $\delta^{37}\text{Cl}$ of evaporite deposits between basins, which they attributed to contribution from non-marine sources, but found no systematic variation with basin size or age, other than a potash (KCl) facies being slightly lighter than halite facies, consistent with theoretically predicted fractionation. This suggests that the Cl isotopic composition of seawater has been uniform over the Phanerozoic. Both groundwaters and sediments of various types, including metasediments, also exhibited only limited variation in $\delta^{37}\text{Cl}$.

In the surficial environment, the largest variation in $\delta^{37}\text{Cl}$ appears to be in fumarole gases and fluids and in marine pore waters, particularly pore waters expelled through accretionary prisms. Somewhat surprisingly, low temperature fumarole effluents (those with measured temperatures $<100^\circ\text{C}$) show less variability than high temperature ones, although those with the highest temperatures ($>400^\circ\text{C}$) have more uniform $\delta^{37}\text{Cl}$ ($1.0 \pm 1.3\text{\textperthousand}$). Since the fractionations between HCl gas and Cl^- in solutions should be $<2\text{\textperthousand}$, the large variations are surprising. Sharp et al. (2010b) attributed them to a kind of Rayleigh distillation process in which ^{37}Cl partitions into HCl-bearing gas phase from which a ^{37}Cl -poor solution then partially recondenses further enriching the remaining gas in ^{37}Cl . The extremely light $\delta^{37}\text{Cl}$ observed in pore fluids in accretionary prisms (Ransom et al., 1995; Wei et al., 2008) appears to result from fractionation between serpentinites and fluid, as serpentinite clasts and muds recovered from the Marianas fore-arc have $\delta^{37}\text{Cl}$ up to $+1.5\text{\textperthousand}$. Nevertheless, the fractionation required to generate these isotopically light fluids seem surprisingly large compared to the fractionation factors of $2\text{--}3\text{\textperthousand}$ estimated theoretically by Schauble et al. (2003) by analogy to chloride salts. It may be that this analogy is a poor one. Barnes et al. (2008) suggested the fractionation occurs as result of transformation of serpentine from the lizardite to the antigorite or chrysotile structure. Schauble et al. (2003) suggested that the discrepancy may reflect changes in the bonding structure around dissolved Cl^- with temperature, pressure, and solute composition making extrapolation of room temperature results difficult.

The range in $\delta^{37}\text{Cl}$ mantle-derived volcanic rocks exceeds that of materials from the Earth's surface except for high-temperature fumaroles and pore fluids. This is surprising as for most other stable isotope systems, the variation is greatest in surface materials, which is what we would expect due to (1) higher temperatures in the mantle and (2) the smaller range of atomic environments in mantle minerals. MORB have $\delta^{37}\text{Cl}$ as low as $-4\text{\textperthousand}$, but the upper limit is in question. Michael and Cornell (1998) showed that many MORB have assimilated chlorine, apparently by assimilating brines and

hydrothermally altered oceanic crust. They argued that samples with K/Cl ratios lower than 12.5 had assimilated seawater chlorine. Bonifacie et al. (2008) showed that $\delta^{37}\text{Cl}$ in MORB correlated positively with Cl concentration (and negatively with K/Cl) and concluded (1) that this trend was indeed a result of assimilation of seawater-derived Cl brines, (2) even samples with K/Cl higher than 12.5 might be contaminated and (3) the $\delta^{37}\text{Cl}$ of MORB was probably less than $-1.5\text{\textperthousand}$. Layne et al. (2009) subsequently reported MORB from the Lau Basin with $\delta^{37}\text{Cl}$ as low as $-4\text{\textperthousand}$. Although it is clear that some MORB have assimilated Cl, $\delta^{37}\text{Cl}$ appears to correlate with $^{206}\text{Pb}/^{204}\text{Pb}$ in low-Cl MORB (Figure 11.26), suggesting at least some of the variation in $\delta^{37}\text{Cl}$ is due to mantle heterogeneity.

OIB also show a considerable range in $\delta^{37}\text{Cl}$ (John et al., 2010) and, as Figure 11.26 shows, there is a relationship between $\delta^{37}\text{Cl}$ and $^{206}\text{Pb}/^{204}\text{Pb}$ that suggests a systematic variation in $\delta^{37}\text{Cl}$ between mantle reservoirs established from radiogenic isotope ratios (Chapter 6). Basalts from St. Helena, which have high $^{206}\text{Pb}/^{204}\text{Pb}$ characteristic of HIMU, have low $\delta^{37}\text{Cl}$, while Pitcairn and Reunion, which have low $^{206}\text{Pb}/^{204}\text{Pb}$ characteristic of EMI, have intermediate $\delta^{37}\text{Cl}$. The Society Islands, which have high $^{87}\text{Sr}/^{86}\text{Sr}$ and intermediate $^{206}\text{Pb}/^{204}\text{Pb}$ characteristic of the EMII reservoir appears to have the highest $\delta^{37}\text{Cl}$. Carbonatites, which are presumably derived from the subcontinental mantle lithosphere, have an average $\delta^{37}\text{Cl}$ of $+0.14\text{\textperthousand}$ and show only limited variation about this mean.

The origin of such large $\delta^{37}\text{Cl}$ variations in the mantle is difficult to understand. Since fractionation factors decrease with temperature, we can be confident that these variations did not originate within the mantle, but rather must have originated in a relatively low temperature environment at or near the surface of the Earth. Interaction between the oceanic crust and seawater at mid-ocean ridges produces only limited variation in $\delta^{37}\text{Cl}$. High temperature hydrothermal vent fluids have $\delta^{37}\text{Cl}$ that is homogeneous and not different from seawater within analytical error, although low-temperature off axis basement fluids are lighter and more variable (-2.09 to $-0.12\text{\textperthousand}$). Altered basalts from Hole 504B are only slightly heavier than fresh MORB, with $\delta^{37}\text{Cl}$ from -1.30 to $-0.8\text{\textperthousand}$.

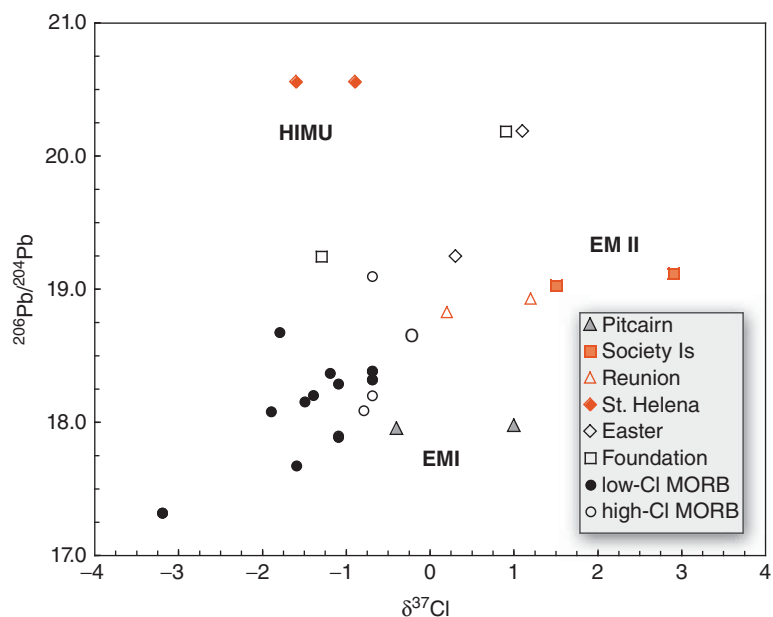


Figure 11.26 Chlorine and lead isotope ratios in oceanic island basalts and MORB. Chlorine isotope data from John et al. (2011), Bonifacie et al. (2008) and Layne et al. (2010).

(Bonifacie et al., 2007). Greater fractionation appears to occur when peridotites react with seawater-derived fluids. Altered peridotites recovered from mid-ocean ridges and associated fractures have $\delta^{37}\text{Cl}$ ranging from -2.44 to $+1.75\text{\textperthousand}$, with talc systematically lighter than serpentine (Barnes et al., 2009). Marine sediments overlying the oceanic crust vary only from -1.8 to $+0.7\text{\textperthousand}$. Further reaction between mantle peridotite and fluids may occur in subduction zones. As we noted earlier, fluids expelled through accretionary prisms in subduction zones have extremely light $\delta^{37}\text{Cl}$ and serpentinite muds and clasts can have $\delta^{37}\text{Cl}$ ranging from -0.22 to $1.61\text{\textperthousand}$ (Barnes et al., 2008). Subduction-related volcanics also exhibit a large range in $\delta^{37}\text{Cl}$: -2.6 to $+2.4\text{\textperthousand}$. Nevertheless, the combined range of $\delta^{37}\text{Cl}$ in MORB and OIB exceeds all of these variations. Understanding them will undoubtedly lead to important new insights into the origin of mantle reservoirs.

NOTES

1. In the terminology of Anbar and Rouxel (2007), *euxinic* refers to conditions when water contains measurable amounts of H_2S ,

while anoxic refers to conditions without O_2 but also without H_2S .

2. Native copper was first mined and exploited by primitive societies lacking smelting technology. One example is the Keweenaw native copper of Michigan, exploited by Native Americans of the region as their sole source of metal for tools and ornamental objects.
3. NIST stands for the U.S. National Institute of Standards and Technology and was formerly known as the National Bureau of Standards, hence NBS is sometimes seen in place of NIST. SRM stands for standard reference material.
4. This zone of weathering that typically occurs above an ore deposit is referred to as the *supergene*; the unweathered ore deposit is referred to as the *hypogene*. Because of oxidation, dissolution, and reprecipitation, parts of the supergene can be enriched in metals such as copper relative to the hypogene.
5. An *aquo-complex* is one in which the ion is bound to water molecules (i.e., $[\text{Zn}(\text{H}_2\text{O})]^{2+}$). These water molecules are also referred to as the *solvation shell*. While all ions in solution have solvation shells and form aquo-complexes, their existence is ignored in many chemical and thermodynamic treatments. Thus, Zn^{2+} is effectively synonymous with $[\text{Zn}(\text{H}_2\text{O})]^{2+}$.

6. Hydroponics is a method of growing plants from a solution without soil.
7. Saprolite is highly weathered rock that constitutes the base of a soil profile (the C horizon).
8. Here we exclude the value of Chakrabarti and Jacobsen (2010) and adopt a $\delta^{30}\text{Si}$ value for the bulk silicate Earth of $-0.29\text{\textperthousand}$ because the values of international analytical standards reported by Chakrabarti and Jacobsen (2010)
-
-
-
-
9. The supply of this standard has been exhausted and it has been superseded by NIST-SRM 975a, whose $^{37}\text{Cl}/^{35}\text{Cl} = 0.31970$.
10. The sole reported exception is water from the upper current of the Bosphorus, which has a $\delta^{37}\text{Cl}_{\text{SMOC}}$ of $+0.4\text{\textperthousand}$ (Eastoe et al., 2007).

REFERENCES

- Alexander, B., Savarino, J., Barkov, N., Delmas, R. J. and Thiemens, M. H. 2002. Climate driven changes in the oxidation pathways of atmospheric sulfur. *Geophysical Research Letters*, 29: 301–304.
- Amini, M., Eisenhauer, A., Böhm, F., Fietzke, J., Bach, W., Garbe-Schönberg, D., et al., 2008. Calcium isotope ($\delta^{44/40}\text{Ca}$) fractionation along hydrothermal pathways, Logatchev field (Mid-Atlantic Ridge, $14^{\circ}45'\text{N}$). *Geochimica et Cosmochimica Acta*, 72: 4107–4122.
- Anbar, A. D. 2004. Molybdenum stable isotopes: observations, interpretations, and directions. In: *Geochemistry of Non-traditional Stable Isotopes*, Johnson, C. M., Beard, B. L. and Albarède, F. (eds). Washington: MSA.
- Anbar, A. D. and Rouxel, O. 2007. Metal stable isotopes in paleoceanography, *Annual Reviews of Earth and Planetary Sciences*, 35: 717–746, doi:10.1146/annurev.earth.34.031405.125029.
- Andersen, M. B., Vance, D., Archer, C., Anderson, R. F., Ellwood, M. J. and Allen, C. S. 2011. The Zn abundance and isotopic composition of diatom frustules, a proxy for Zn availability in ocean surface seawater. *Earth and Planetary Science Letters*, 301: 137–145.
- Archer, C. and Vance, D. 2008. The isotopic signature of the global riverine molybdenum flux and anoxia in the ancient oceans. *Nature Geoscience*, 1: 597–600, doi: 10.1038/ngeo282.
- Armytage, R. M. G., Georg, R. B., Savage, P. S., Williams, H. M. and Halliday, A. N. 2011. Silicon isotopes in meteorites and planetary core formation. *Geochimica et Cosmochimica Acta*, 75: 3662–3676, doi: 10.1016/j.gca.2011.03.044.
- Armytage, R. M. G., Georg, R. B., Williams, H. M. and Halliday, A.N. 2012. Silicon isotopes in lunar rocks: Implications for the Moon's formation and the early history of the Earth. *Geochimica et Cosmochimica Acta*, 77: 504–514, doi: 10.1016/j.gca.2011.10.032.
- Asael, D., Matthews, A., Oszczepalski, S., Bar-Matthews, M. and Halicz, L. 2009. Fluid speciation controls of low temperature copper isotope fractionation applied to the Kupferschiefer and Timna ore deposits. *Chemical Geology*, 262: 147–158.
- Barling, J., Arnold, G. L. and Anbar, A. D. 2001. Natural mass-dependent variations in the isotopic composition of molybdenum. *Earth and Planetary Science Letters*, 193: 447–457.
- Barnes, J. D., Sharp, Z. D. and Fischer, T. P. 2008. Chlorine isotope variations across the Izu-Bonin-Mariana arc. *Geology*, 36: 883–886.
- Barnes, J. D., Paulick, H., Sharp, Z. D., Bach, W. and Beaudoin, G. 2009. Stable isotope ($\delta^{18}\text{O}$, δD , $\delta^{37}\text{Cl}$) evidence for multiple fluid histories in mid-Atlantic abyssal peridotites (ODP Leg 209). *Lithos*, 110: 83–94, doi: 10.1016/j.lithos.2008.12.004.
- Becker, H. and Walker, R. J. 2003. Efficient mixing of the solar nebula from uniform Mo isotopic composition of meteorites. *Nature*, 425: 152–155.
- Bekker, A., Barley, M. E., Fiorentini, M. L., Rouxel, O. J., Rumble, D. and Beresford, S. W. 2009. Atmospheric sulfur in Archean komatiite-hosted nickel deposits. *Science*, 326: 1086–1089, doi: 10.1126/science.1177742.
- Ben Othman, D., Luck, J. M., Bodinier, J. L., Arndt, N. T. and Albarède, F. 2006. Cu–Zn isotopic variations in the Earth's mantle. *Geochimica et Cosmochimica Acta*, 70: A46.
- Bermin, J. 2006. Determination of the isotopic composition of Cu and Zn in seawater. PhD dissertation, University of London.
- Bermin, J., Vance, D., Archer, C. and Statham, P. J. 2006. The determination of the isotopic composition of Cu and Zn in seawater. *Chemical Geology*, 226: 280–297.
- Beucher, C. P., Brzezinski, M. A. and Jones, J. L. 2008. Sources and biological fractionation of silicon isotopes in the Eastern Equatorial Pacific. *Geochimica et Cosmochimica Acta*, 72: 3063–3073.
- Bishop, M. C., Moynier, F., Weinstein, C., Fraboulet, J.-G., Wang, K. and Foriel, J. 2012. The Cu isotopic composition of iron meteorites. *Meteoritics and Planetary Science*, 47: 268–276.
- Black, J. R., Kavner, A. and Schauble, E. A. 2011. Calculation of equilibrium stable isotope partition function ratios for aqueous zinc complexes and metallic zinc. *Geochimica et Cosmochimica Acta*, 75: 769–783.
- Böhm, F., Gussone, N., Eisenhauer, A., Dullo, W.-C., Reynaud, S., and Paytan, A., 2006. Calcium isotope fractionation in modern scleractinian corals. *Geochimica et Cosmochimica Acta*, 70: 4452–4462.

- Bonifacie, M., Jendrezejewski, N., Agrinier, P., Coleman, M., Pineau, F. and Javoy, M. 2007. Pyrohydrolysis-IRMS determination of silicate chlorine stable isotope compositions. *Application to oceanic crust and meteorite samples. Chemical Geology*, 242: 187–201.
- Bonifacie, M., Jendrezejewski, N., Agrinier, P., Humler, E., Coleman, M. and Javoy, M. 2008. The chlorine isotope composition of Earth's mantle. *Science*, 319: 1518–1520.
- Brucker, R. L. P., McManus, J., Severmann, S. and Berelson, W. M. 2009. Molybdenum behavior during early diageneisis: insights from Mo isotopes. *Geochemistry, Geophysics, Geosystems*, 10: Q06010, doi: 10.1029/2008gc002180.
- Burkhardt, C., Kleine, T., Oberli, F., Pack, A., Bourdon, B. and Wieler, R. 2011. Molybdenum isotope anomalies in meteorites: Constraints on solar nebula evolution and origin of the Earth. *Earth and Planetary Science Letters*, 312: 390–400.
- Cabral, R. A., Jackson, M. G., Rose-Koga, E. F., Koga, K. T., Whitehouse, M. J., Antonelli, M. A., et al. 2013. Anomalous sulphur isotopes in plume lavas reveal deep mantle storage of Archaean crust. *Nature*, 496: 490–493, doi: 10.1038/nature12020.
- Came, R. E., Eiler, J. M., Veizer, J., Azmy, K., Brand, U. and Weidman, C. R. 2007. Coupling of surface temperatures and atmospheric CO₂ concentrations during the Palaeozoic era. *Nature*, 449: 198–201.
- Canfield, D. E. 2005. The early history of atmospheric oxygen: Homage to Robert M. Garrels. *Annual Reviews of Earth and Planetary Sciences*, 33: 1–36, doi:10.1146/annurev.earth.33.092203.122711.
- Cenki-Tok, B., Chabaux, F., Lemarchand, D., Schmitt, A. D., Pierret, M. C., Viville, D., et al. 2009. The impact of water–rock interaction and vegetation on calcium isotope fractionation in soil- and stream waters of a small, forested catchment (the Strengbach case). *Geochimica et Cosmochimica Acta*, 73: 2215–2228.
- Cerling, T. E., Bowman, J. R. and O'Neil, J. R. 1988. An isotopic study of a fluvial-lacustrine sequence: The Plio-Pleistocene koobi flora sequence, East Africa. *Palaeogeography, Palaeoclimatology, Palaeoecology*, 63: 335–356.
- Chakrabarti, R. and Jacobsen, S.B. 2010. Silicon isotopes in the inner Solar System: Implications for core formation, solar nebular processes and partial melting. *Geochimica et Cosmochimica Acta*, 74: 6921–6933, doi: 10.1016/j.gca.2010.08.034.
- Chakrabarti, R., Knoll, A. H., Jacobsen, S. B. and Fischer, W. W. 2012. Si isotope variability in Proterozoic cherts. *Geochimica et Cosmochimica Acta*, 91: 187–201, doi: 10.1016/j.gca.2012.05.025.
- Chan, L.-H. and Edmond, J. M. 1988. Variation of lithium isotope composition in the marine environment: a preliminary report. *Geochimica et Cosmochimica Acta*, 52: 1711–1717.
- Chaussidon, M. and Jambon, A. 1994. Boron content and isotopic composition of oceanic basalts: geochemical and cosmochemical implications. *Earth and Planetary Science Letters*, 121: 277–291.
- Chaussidon, M. and Marty, B. 1995. Primitive boron isotope composition of the mantle. *Science*, 269: 383–266.
- Chaussidon, M. and Albarède, F. 1992. Secular boron isotope variations in the continental crust: an ion microprobe study. *Earth and Planetary Science Letters*, 108: 229–241.
- Chu, N.-C., Henderson, G. M., Belshaw, N. S. and Hedges, R. E. M. 2006. Establishing the potential of Ca isotopes as proxy for consumption of dairy products. *Applied Geochemistry*, 21: 1656–1667.
- Cloquet, C., Carignan, J., Lehmann, M. and Vanhaecke, F. 2008. Variation in the isotopic composition of zinc in the natural environment and the use of zinc isotopes in biogeosciences: a review. *Analytical and Bioanalytical Chemistry*, 390: 451–463.
- Coplen, T. B., Böhlke, J. K., Bièvre, P. D., Ding, T., Holden, N. E., Hopple, J. A and et al. 2002. Isotope-abundance variations of selected elements (IUPAC Technical Report). *Pure and Applied Chemistry*, 74: 1987–2017, doi:0.1351/pac200274101987.
- Coursey, J. S., Schwab, D. J., Tsai, J. J. and Dragoset, R. A. 2009. *Atomic weights and isotopic compositions with relative atomic masses [Online]*. Gaithersburg, MD: NIST Physical Measurement Laboratory. Available at: www.nist.gov/pml/data/comp.cfm 2012] (accessed July 11, 2014).
- Coursey, J. S., Schwab, D. J., Tsai, J. J. and Dragoset, R. A. 2011. *Atomic Weights and Isotopic Compositions with Relative Atomic Masses [Online]*. Gaithersburg, MD: U.S. National Institute of Standards and Technology Physical Measurement Laboratory. Available at: www.nist.gov/pml/data/comp.cfm 2011 (accessed July 11, 2014).
- Craddock, P. R. and Dauphas, N. 2011. Iron isotopic compositions of geological reference materials and chondrites. *Geostandards and Geoanalytical Research*, 35: 101–123.
- Czaja, A. D., Johnson, C. M., Roden, E. E., Beard, B. L., Voegelin, A. R., Nägler, T. F., et al. 2012. Evidence for free oxygen in the Neoarchean Ocean based on coupled iron–molybdenum isotope fractionation. *Geochimica et Cosmochimica Acta*, 86: 118–137.
- Dahl, T. W., Canfield, D. E., Rosing, M. T., Frei, R. E., Gordon, G. W., Knoll, A. H. and Anbar, A. D. 2011. Molybdenum evidence for expansive sulfidic water masses in ~750 Ma oceans. *Earth and Planetary Science Letters*, 311: 264–274.
- Dahl, T. W., Hammarlund, E. U., Anbar, A. D., Bond, D. P. G., Gill, B. C., Gordon, G. W., et al. 2010. Devonian rise in atmospheric oxygen correlated to the radiations of terrestrial plants and large predatory fish. *Proceedings of the National Academy of Sciences*, 107: 17911–17915.
- De La Rocha, C. L. 2003. Silicon isotope fractionation by marine sponges and the reconstruction of the silicon isotope composition of ancient deep water. *Geology*, 31: 423–426.
- De La Rocha, C. L., Brzezinski, M. A. and DeNiro, M. J. 1997. Fractionation of silicon isotopes by marine diatoms during biogenic silica formation. *Geochimica et Cosmochimica Acta*, 61: 5051–5056.

- Delstanche, S., Opfergelt, S., Cardinal, D., Elsass, F., Andre, L. and Delvaux, B. 2009. Silicon isotopic fractionation during adsorption of aqueous monosilicic acid onto iron oxide. *Geochimica et Cosmochimica Acta*, 73: 923–934, doi: 10.1016/j.gca.2008.11.014.
- Demarest, M. S., Brzezinski, M. A. and Beucher, C. P. 2009. Fractionation of silicon isotopes during biogenic silica dissolution. *Geochimica et Cosmochimica Acta* 73: 5572–5583.
- DePaolo, D. J. 2004. Calcium isotopic variations produced by biological, kinetic, radiogenic, and nucleosynthetic processes. In: *Geochemistry of Non-Traditional Stable Isotopes*, Johnson, C. M., Beard, B. L. and Albarède, F. (eds). Washington, DC: Mineralogical Society of America.
- Ding, T. P., Gao, J. F., Tian, S. H., Wang, H. B. and Li, M. 2011. Silicon isotopic composition of dissolved silicon and suspended particulate matter in the Yellow River, China, with implications for the global silicon cycle. *Geochimica et Cosmochimica Acta*, 75: 6672–6689.
- Ding, T. P., Zhou, J. X., Wan, D. F., Chen, Z. Y., Wang, C. Y. and Zhang, F. 2008. Silicon isotope fractionation in bamboo and its significance to the biogeochemical cycle of silicon. *Geochimica et Cosmochimica Acta*, 72: 1381–1395.
- Duan, Y., Anbar, A. D., Arnold, G. L., Lyons, T. W., Gordon, G. W. and Kendall, B. 2010. Molybdenum isotope evidence for mild environmental oxygenation before the Great Oxidation Event. *Geochimica et Cosmochimica Acta*, 74: 6655–6668.
- Eagle, R. A., Schauble, E. A., Tripathi, A. K., Tütken, T., Hulbert, R. C. and Eiler, J. M. 2010. Body temperatures of modern and extinct vertebrates from ^{13}C - ^{18}O bond abundances in bioapatite. *Proceedings of the National Academy of Sciences*, 107: 10377–10382, doi:10.1073/pnas.0911115107.
- Eagle, R. A., Tütken, T., Martin, T. S., Tripathi, A. K., Fricke, H. C., Connely, M., et al. 2011. Dinosaur body temperatures determined from isotopic (^{13}C - ^{18}O) ordering in fossil biominerals. *Science*, doi: 10.1126/science.1206196.
- Eastoe, C. J., Peryt, T. M., Petrychenko, O. Y. and Geisler-Cussey, D. 2007. Stable chlorine isotopes in Phanerozoic evaporites. *Applied Geochemistry*, 22: 575–588, doi: 10.1016/j.apgeochem.2006.12.012.
- Eggenkamp, H. G. M., Kreulen, R. and Koster Van Groos, A. F. 1995. Chlorine stable isotope fractionation in evaporites. *Geochimica et Cosmochimica Acta*, 59: 5169–5175.
- Ehrlich, S., Butler, I., Halicz, L., Rickard, D., Oldroyd, A. and Matthews, A. 2004. Experimental study of the copper isotope fractionation between aqueous Cu(II) and covellite, CuS. *Chemical Geology*, 209: 259–269, doi: 10.1016/j.chemgeo.2004.06.010.
- Eiler, J. M. 2013. The isotopic anomalies of molecules and minerals. *Annual Review of Earth and Planetary Sciences*, 41: 411–441, doi: doi:10.1146/annurev-earth-042711-105348.
- Elliott, T., Jeffcoate, A. and Bouman, C. 2004. The terrestrial Li isotope cycle: light-weight constraints on mantle convection, *Earth and Planetary Science Letters*, 220: 231–245.
- Farkaš, J., Böhm, F., Wallmann, K., Blenkinsop, J., Eisenhauer, A., van Geldern, R., et al., 2007. Calcium isotope record of Phanerozoic oceans: Implications for chemical evolution of seawater and its causative mechanisms. *Geochimica et Cosmochimica Acta*, 71: 5117–5134.
- Farquhar, J. and Wing, B. A. 2003. Multiple sulfur isotopes and the evolution of atmospheric oxygen. *Earth and Planetary Science Letters*, 213: 1–13.
- Farquhar, J., Wing, B. A., McKeegan, K. D., Harris, J. W., Cartigny, P. and Thiemens, M. 2002. Mass-independent fractionation sulfur of inclusions in diamond and sulfur recycling on early Earth. *Science*, 298: 2369–2372.
- Farquhar, J., Bao, H. and Thiemens, M. 2000. Atmospheric influence of Earth's earliest sulfur cycle, *Science*, 289: 756–758.
- Fernandez, A. and Borrok, D. M. 2009. Fractionation of Cu, Fe, and Zn isotopes during the oxidative weathering of sulfide-rich rocks. *Chemical Geology*, 264: 1–12.
- Fitoussi, C. and Bourdon, B. 2012. Silicon isotope evidence against an enstatite chondrite Earth. *Science*, 335: 1477–1480, doi: 10.1126/science.1219509.
- Fitoussi, C., Bourdon, B., Kleine, T., Oberli, F. and Reynolds, B. C. 2009. Si isotope systematics of meteorites and terrestrial peridotites: implications for Mg/Si fractionation in the solar nebula and for Si in the Earth's core. *Earth and Planetary Science Letters*, 287: 77–85, doi: 10.1016/j.epsl.2009.07.038.
- Foster, G. L., Pogge von Strandmann, P. A. E. and Rae, J. W. B. 2010. Boron and magnesium isotopic composition of seawater. *Geochemistry, Geophysics, Geosystems*, 11: Q08015, doi: 10.1029/2010GC003201.
- Foster, G. L. 2008. Seawater pH, pCO_2 and $[\text{CO}_2^3]$ variations in the Caribbean Sea over the last 130kyr: A boron isotope and B/Ca study of planktic foraminifera, *Earth and Planetary Science Letters*, 271: 254–266, 10.1016/j.epsl.2008.04.015.
- Fujii, T., Moynier, F., Telouk, P. and Abe, M. 2010. Experimental and theoretical investigation of isotope fractionation of zinc between aqua, chloro, and macrocyclic complexes. *The Journal of Physical Chemistry A*, 114: 2543–2552.
- Georg, R. B., Reynolds, B. C., Frank, M. and Halliday, A. N. 2006. Mechanisms controlling the silicon isotopic compositions of river waters. *Earth and Planetary Science Letters*, 249: 290–306, doi: 10.1016/j.epsl.2006.07.006.
- Godon, A., Jendrezejewski, N., Eggenkamp, H. G. M., Banks, D. A., Ader, M., Coleman, M. L. and Pineau, F. 2004. A cross-calibration of chlorine isotopic measurements and suitability of seawater as the international reference material. *Chemical Geology*, 207: 1–12.
- Gussone, N. and Filipsson, H. L. 2010. Calcium isotope ratios in calcitic tests of benthic foraminifers. *Earth and Planetary Science Letters*, 290: 108–117, doi: 10.1016/j.epsl.2009.12.010.

- Gussone, N., Höönsch, B., Heuser, A., Eisenhauer, A., Spindler, M. and Hemleben, C. 2009. A critical evaluation of calcium isotope ratios in tests of planktonic foraminifers. *Geochimica et Cosmochimica Acta*, 73: 7241–7255, doi: 10.1016/j.gca.2009.08.035.
- Gussone, N., Böhm, F., Eisenhauer, A., Dietzel, M., Heuser, A., Teichert, B. M. A., et al., 2005. Calcium isotope fractionation in calcite and aragonite. *Geochimica et Cosmochimica Acta* 69: 4485–4494, doi: 10.1016/j.gca.2005.06.003.
- Gussone, N., Eisenhauer, A., Heuser, A., Dietzel, M., Bock, B., Böhm, F., et al. 2003. Model for kinetic effects on calcium isotope fractionation ($\delta^{44}\text{Ca}$) in inorganic aragonite and cultured planktonic foraminifera. *Geochimica et Cosmochimica Acta*, 67: 1375–1382, doi: 10.1016/s0016-7037(02)01296-6.
- Gussone, N., Langer, G., Thoms, S., Nehrke, G., Eisenhauer, A., Riebesell, U. and Wefer, G. 2006. Cellular calcium pathways and isotope fractionation in *Emiliania huxleyi*. *Geology*, 34: 625–628, doi: 10.1130/g22733.1.
- Helz, G. R., Miller, C. V., Charnock, J. M., Mosselmans, J. F. W., Patrick, R. A. D., Garner, C. D. and Vaughan, D. J. 1996 Mechanism of molybdenum removal from the sea and its concentration in black shales: EXAFS evidence. *Geochimica et Cosmochimica Acta*, 60: 3631–3642, doi: 10.1016/0016-7037(96)00195-0.
- Heming, N. G. and Hanson, G. N. 1992. Boron isotopic composition and concentration in modern marine carbonates. *Geochimica et Cosmochimica Acta*, 56: 537–543.
- Herzog, G. F., Moynier, F., Albarède, F. and Bereznay, A. A. 2009. Isotopic and elemental abundances of copper and zinc in lunar samples, Zagami, Pele's hairs, and a terrestrial basalt. *Geochimica et Cosmochimica Acta*, 73: 5884–5904.
- Hin, R. C., Schmidt, M. W. and Bourdon, B. 2012. Experimental evidence for the absence of iron isotope fractionation between metal and silicate liquids at 1 GPa and 1250–1300°C and its cosmochemical consequences. *Geochimica et Cosmochimica Acta*, 93: 164–181, doi: 10.1016/j.gca.2012.06.011.
- Hindshaw, R. S., Reynolds, B. C., Wiederhold, J. G., Kretzschmar, R. and Bourdon, B. 2011. Calcium isotopes in a proglacial weathering environment: Damma glacier, Switzerland. *Geochimica et Cosmochimica Acta*, 75: 106–118, doi: 10.1016/j.gca.2010.09.038.
- Hippler, D., Buhl, D., Witbaard, R., Richter, D. K. and Immenhauser, A. 2009. Towards a better understanding of magnesium-isotope ratios from marine skeletal carbonates. *Geochimica et Cosmochimica Acta*, 73: 6134–6146, doi: 10.1016/j.gca.2009.07.031.
- Hippler, D., Schmitt, A.-D., Gussone, N., Heuser, A., Stille, P., Eisenhauer, A. and Nägler, T. F. 2003. Calcium isotopic composition of various reference materials and seawater. *Geostandards Newsletter*, 27: 13–19.
- Hofmann, A. W. and White, W. M. 1982. Mantle plumes from ancient oceanic crust. *Earth and Planetary Science Letters*, 57: 421–436.
- Höönsch, B. and Hemming, N. G. 2005. Surface ocean pH response to variations in pCO₂ through two full glacial cycles. *Earth and Planetary Science Letters*, 236: 305–314, 10.1016/j.epsl.2005.04.027.
- Höönsch, B., Hemming, N. G., Archer, D., Siddall, M. and McManus, J. F. 2009. Atmospheric carbon dioxide concentration across the Mid-Pleistocene transition, *Science*, 324: 1551–1554, 10.1126/science.1171477.
- Huang, S., Farkaš, J. and Jacobsen, S. B. 2010. Calcium isotopic fractionation between clinopyroxene and orthopyroxene from mantle peridotites. *Earth and Planetary Science Letters*, 292: 337–344, doi: 10.1016/j.epsl.2010.01.042.
- Huang, S., Farkaš, J. and Jacobsen, S. B. 2011. Stable calcium isotopic compositions of Hawaiian shield lavas: Evidence for recycling of ancient marine carbonates into the mantle. *Geochimica et Cosmochimica Acta*, 75: 4987–4997.
- Ishikawa, T. and Nakamura, E. 1992. Boron isotope geochemistry of the oceanic crust from DSDP/ODP Hole 504B. *Geochimica et Cosmochimica Acta*, 56: 1633–1639.
- Ishikawa, T. and Nakamura, E. 1993. Boron isotope systematics of marine sediments. *Earth and Planetary Science Letters*, 117: 567–580.
- Javoy, M., Kaminski, E., Guyot, F., Andrault, D., Sanloup, C., Moreira, M., et al. 2010. The chemical composition of the Earth: Enstatite chondrite models. *Earth and Planetary Science Letters*, 293: 259–268.
- John, S. G., Geis, R. W., Saito, M. A. and Boyle, E. A. 2007. Zinc isotope fractionation during high-affinity and low-affinity zinc transport by the marine diatom *Thalassiosira oceanica*. *Limnology and Oceanography*, 56: 2710–2714.
- John, S. G., Rouxel, O. J., Craddock, P. R., Engwall, A. M. and Boyle, E. A. 2008. Zinc stable isotopes in seafloor hydrothermal vent fluids and chimneys. *Earth and Planetary Science Letters*, 269: 17–28.
- John, T., Layne, G. D., Haase, K. M. and Barnes, J. D. 2010. Chlorine isotope evidence for crustal recycling into the Earth's mantle. *Earth and Planetary Science Letters*, 298: 175–182.
- Johnson, C. M., Beard, B. L. and Roden, E. E. 2008. The iron isotope fingerprints of redox and biogeochemical cycling in modern and ancient Earth *Annual Reviews of Earth and Planetary Sciences*, 36: 457–493, doi: 10.1146/annurev.earth.36.031207.124139.
- Johnson, C. M., Beard, B. L. and Albarede, F. 2004. *Geochemistry of Non-Traditional Stable Isotopes*. Washington: Mineralogical Society of America.
- Kappler, A., Pasquero, C., Konhauser, K. O. and Newman, D. K. 2005. Deposition of banded iron formations by anoxygenic phototrophic Fe(II)-oxidizing bacteria. *Geology*, 33: 865–868, doi: 10.1130/g21658.1.
- Kasting, J. F. and Catling, D. 2003. Evolution of a Habitable Planet, *Annual Reviews of Astronomy and Astrophysics*, 41: 429–463.

- Kendall, B., Creaser, R. A., Gordon, G. W. and Anbar, A. D. 2009. Re-Os and Mo isotope systematics of black shales from the Middle Proterozoic Velkerri and Wollogorang Formations, McArthur Basin, northern Australia. *Geochimica et Cosmochimica Acta*, 73: 2534–2558.
- Kisakürek, B., Eisenhauer, A., Böhm, F., Hathorne, E. C. and Erez, J. 2011. Controls on calcium isotope fractionation in cultured planktic foraminifera, *Globigerinoides ruber* and *Globigerinella siphonifera*. *Geochimica et Cosmochimica Acta*, 75: 427–443.
- Klochko, K., Kaufman, A. J., Yao, W., Byrne, R. H. and Tossell, J. A. 2006. Experimental measurement of boron isotope fractionation in seawater. *Earth and Planetary Science Letters*, 248: 276–285, doi: 10.1016/j.epsl.2006.05.034.
- Larson, P. B., Maher, K., Ramos, F. C., Chang, Z., Gaspar, M. and Meinert, L. D. 2003. Copper isotope ratios in magmatic and hydrothermal ore-forming environments. *Chemical Geology*, 201: 337–350.
- Layne, G. D., Kent, A. J. R. and Bach, W. 2009. $\delta^{37}\text{Cl}$ systematics of a backarc spreading system: The Lau Basin. *Geology*, 37: 427–430, doi: 10.1130/g25520a.1.
- Li, W., Jackson, S. E., Pearson, N. J., Alard, O. and Chappell, B. W. 2009. The Cu isotopic signature of granites from the Lachlan Fold Belt, SE Australia. *Chemical Geology*, 258: 38–49, doi: 10.1016/j.chemgeo.2008.06.047.
- Liebscher, A., Barnes, J. and Sharp, Z. 2006. Chlorine isotope vapor–liquid fractionation during experimental fluid-phase separation at 400°C/23MPa to 450°C/42MPa. *Chemical Geology*, 234: 340–345.
- Luck, J.-M., Othman, D. B. and Albarède, F. 2005. Zn and Cu isotopic variations in chondrites and iron meteorites: Early solar nebula reservoirs and parent-body processes. *Geochimica et Cosmochimica Acta*, 69: 5351–5363.
- Maréchal, C. N., Nicolas, E., Douchet, C. and Albarède, F. 2000. Abundance of zinc isotopes as a marine biogeochemical tracer. *Geochemistry, Geophysics, Geosystems*, 1: 1–15.
- Maréchal, C. N., Télouk, P. and Albarède, F. 1999. Precise analysis of copper and zinc isotopic compositions by plasma-source mass spectrometry. *Chemical Geology*, 156: 251–273.
- Markl, G., Lahaye, Y. and Schwinn, G. 2006. Copper isotopes as monitors of redox processes in hydrothermal mineralization. *Geochimica et Cosmochimica Acta*, 70: 4215–4228.
- Marriott, C. S., Henderson, G. M., Belshaw, N. S. and Tudhope, A. W. 2004. Temperature dependence of $\delta^7\text{Li}$, $\delta^{44}\text{Ca}$ and Li/Ca during growth of calcium carbonate. *Earth and Planetary Science Letters*, 222: 615–624.
- Mathur, R., Titley, S., Barra, F., Brantley, S., Wilson, M., Phillips, A., Munizaga, F., Maksaev, V., Vervoort, J. and Hart, G. 2009. Exploration potential of Cu isotope fractionation in porphyry copper deposits. *Journal of Geochemical Exploration*, 102: 1–6.
- McManus, J., Nägler, T. F., Siebert, C., Wheat, C. G. and Hammond, D. E. 2002. Oceanic molybdenum isotope fractionation: Diagenesis and hydrothermal ridge-flank alteration. *Geochemistry, Geophysics, Geosystems*, 3, 1078: doi: 10.1029/2002gc000356.
- Méheut, M., Lazzeri, M., Balan, E. and Mauri, F. 2007. Equilibrium isotopic fractionation in the kaolinite, quartz, water system: Prediction from first-principles density-functional theory. *Geochimica et Cosmochimica Acta*, 71: 3170–3181.
- Michael, P. J. and Cornell, W. C. 1998. Influence of spreading rate and magma supply on crystallization and assimilation beneath mid-ocean ridges: Evidence from chlorine and major element chemistry of mid-ocean ridge basalts. *Journal of Geophysical Research*, 103: 18325–18356.
- Misra, S. and Froelich, P. N. 2012. Lithium Isotope History of Cenozoic Seawater: Changes in Silicate Weathering and Reverse Weathering. *Science*, 335: 818–823.
- Moynier, F., Blichert-Toft, J., Telouk, P., Luck, J.-M. and Albarède, F. 2007. Comparative stable isotope geochemistry of Ni, Cu, Zn, and Fe in chondrites and iron meteorites. *Geochimica et Cosmochimica Acta*, 71: 4365–4379.
- Moynier, F., Paniello, R. C., Gounelle, M., Albarède, F., Beck, P., Podosek, F. and Zanda, B. 2011. Nature of volatile depletion and genetic relationships in enstatite chondrites and aubrites inferred from Zn isotopes. *Geochimica et Cosmochimica Acta*, 75: 297–307.
- Moynier, F., Pichat, S., Pons, M.-L., Fike, D., Balter, V. and Albarède, F. 2009. Isotopic fractionation and transport mechanisms of Zn in plants. *Chemical Geology*, 267: 125–130.
- Muehlenbachs, C. and Furnas, H. 2003. Ophiolites as faithful records of the oxygen isotope ratio of ancient seawater: the Solund-Stavfjord Ophiolite Complex as a Late Ordovician example. *Ophiolites in Earth History*. London: Geological Society of London.
- Muehlenbachs, K. 1976. Oxygen isotope composition of the oceanic crust and its bearing on seawater. *Journal of Geophysical Research*, 81: 4365–4369.
- Nakagawa, Y., Firduus, M. L., Norisuye, K., Sohrin, Y., Irisawa, K. and Hirata, T. 2008. Precise Isotopic Analysis of Mo in Seawater Using Multiple Collector-Inductively Coupled Mass Spectrometry Coupled with a Chelating Resin Column Preconcentration Method. *Analytical Chemistry*, 80: 9213–9219.
- Pagani, M., Arthur, M. A. and Freeman, K. H. 1999. Miocene evolution of atmospheric carbon dioxide. *Paleoceanography*, 14: 273–292, doi: 10.1029/1999pa900006.
- Pagani, M., Lemarchand, D., Spivack, A. J. and Gaillardet, J. 2005. A critical evaluation of the boron isotope-ph proxy: The accuracy of ancient ocean pH estimates, *Geochimica et Cosmochimica Acta*, 69: 953–961.
- Palmer, M. R. 1991. Boron-isotope systematics of Halmahera arc (Indonesia) lavas: evidence for involvement of the subducted slab. *Geology*, 19: 215–217.

- Palmer, M., Spivack, M. and Edmond, J. M. 1987. Temperature and pH controls over isotopic fractionation during adsorption of boron on marine clay. *Geochimica et Cosmochimica Acta*, 51: 2319–2323.
- Paniello, R. C., Day, J. M. D. and Moynier, F. 2012. Zinc isotopic evidence for the origin of the Moon. *Nature*, 490: 376–379.
- Paniello, R. C., Moynier, F., Podosek, F. A. and Beck, P. 2009. Zinc isotopic composition of achondrites. *72nd Meeting of the Meteoritical Society, 2009 Nancy, France*. Meteoritical Society: A166.
- Passey, B. H., Levin, N. E., Cerling, T. E., Brown, F. H. and Eiler, J. M. 2010. High-temperature environments of human evolution in East Africa based on bond ordering in paleosol carbonates. *Proceedings of the National Academy of Sciences*, 107: 11245–11249.
- Pearson, P. N., Foster, G. L. and Wade, B. S. 2009. Atmospheric carbon dioxide through the Eocene–Oligocene climate transition. *Nature*, 461: 1110–1113.
- Pearson, P. N. and Palmer, M. R. 2000. Atmospheric carbon dioxide concentrations over the past 60 million years. *Nature*, 406: 695–699.
- Pekala, M., Asael, D., Butler, I. B., Matthews, A. and Rickard, D. 2011. Experimental study of Cu isotope fractionation during the reaction of aqueous Cu(II) with Fe(II) sulphides at temperatures between 40 and 200°C. *Chemical Geology*, 289: 31–38.
- Pichat, S., Douchet, C. and Albarède, F. 2003. Zinc isotope variations in deep-sea carbonates from the eastern equatorial Pacific over the last 175 ka. *Earth and Planetary Science Letters*, 210: 167–178.
- Planavsky, N., Rouxel, O. J., Bekker, A., Hofmann, A., Little, C. T. S. and Lyons, T. W. 2012. Iron isotope composition of some Archean and Proterozoic iron formations. *Geochimica et Cosmochimica Acta*, 80: 158–169.
- Pogge von Strandmann, P. A. E. 2008. Precise magnesium isotope measurements in core top planktic and benthic foraminifera. *Geochemistry, Geophysics, Geosystems*, 9: Q12015, doi: 10.1029/2008gc002209.
- Pogge von Strandmann, P. A. E., Elliott, T., Marschall, H. R., Coath, C., Lai, Y.-J., Jeffcoate, A. B. and Ionov, D. A. 2011. Variations of Li and Mg isotope ratios in bulk chondrites and mantle xenoliths. *Geochimica et Cosmochimica Acta*, 75: 5247–5268, doi:10.1016/j.gca.2011.06.026.
- Poirrasson, F., Levasseur, S. and Teutsch, N. 2005. Significance of iron isotope mineral fractionation in pallasites and iron meteorites for the core–mantle differentiation of terrestrial planets. *Earth and Planetary Science Letters*, 234: 151–164.
- Pokrovsky, O. S., Viers, J., Emnova, E. E., Kompantseva, E. I. and Freydier, R. 2008. Copper isotope fractionation during its interaction with soil and aquatic microorganisms and metal oxy(hydr)oxides: Possible structural control. *Geochimica et Cosmochimica Acta*, 72: 1742–1757.
- Ransom, B., Spivack, A. J. and Kastner, M. 1995. Stable Cl isotopes in subduction-zone pore waters: Implications for fluid–rock reactions and the cycling of chlorine. *Geology*, 23: 715–718.
- Reynard, L. M., Henderson, G. M. and Hedges, R. E. M. 2010. Calcium isotope ratios in animal and human bone. *Geochimica et Cosmochimica Acta*, 74: 3735–3750.
- Reynolds, J. H. and Verhoogen, J. 1953. Natural variations in the isotopic constitution of silicon. *Geochimica et Cosmochimica Acta*, 3: 224–234.
- Richter, F. M., Dauphas, N. and Teng, F.-Z. 2009. Non-traditional fractionation of non-traditional isotopes: Evaporation, chemical diffusion and Soret diffusion. *Chemical Geology*, 258: 92–103.
- Richter, F. M., Liang, Y. and Davis, A. M. 1999. Isotope fractionation by diffusion in molten oxides. *Geochimica et Cosmochimica Acta*, 63: 2853–2861, doi:10.1016/s0016-7037(99)00164-7.
- Rose-Koga, E. F. and Albarède, F. 2010. A data brief on magnesium isotope compositions of marine calcareous sediments and ferromanganese nodules. *Geochemistry, Geophysics, Geosystems*, 11: Q03006, doi:10.1029/2009GC002899.
- Rose-Koga, E. F., Sheppard, S. M. F., Chaussidon, M. and Carignan, J. 2006. Boron isotopic composition of atmospheric precipitations and liquid–vapour fractionations. *Geochimica et Cosmochimica Acta*, 70: 1603–1615, doi:10.1016/j.gca.2006.01.003.
- Rouxel, O., Fouquet, Y. and Ludden, J. N. 2004. Copper isotope systematics of the lucky strike, rainbow, and Logatchev sea-floor hydrothermal fields on the Mid-Atlantic Ridge. *Economic Geology*, 99: 585–600.
- Rudnick, R. L., Tomascak, P. B., Njo, H. B. and Gardner, L. R. 2004. Extreme lithium isotopic fractionation during continental weathering revealed in saprolites from South Carolina. *Chemical Geology*, 212: 45–57, doi:10.1016/j.chemgeo.2004.08.008.
- Ryu, J.-S., Jacobson, A. D., Holmden, C., Lundstrom, C. and Zhang, Z. 2011. The major ion, $\delta^{44/40}\text{Ca}$, $\delta^{44/42}\text{Ca}$, and $\delta^{26/24}\text{Mg}$ geochemistry of granite weathering at pH = 1 and T = 25°C: power-law processes and the relative reactivity of minerals. *Geochimica et Cosmochimica Acta*, 75: 6004–6026, doi: 10.1016/j.gca.2011.07.025.
- Sanyal, A., Hemming, N. G., Broecker, W. S., Lea, D. W., Spero, H. J. and Hanson, G. N. 1996. Oceanic pH control on the boron isotopic composition of foraminifera; evidence from culture experiments. *Paleoceanography*, 11: 513–517.
- Savage, P. S., Georg, R. B., Armytage, R. M. G., Williams, H. M., and Halliday, A. N., 2010. Silicon isotope homogeneity in the mantle. *Earth and Planetary Science Letters*, 295: 139–146.
- Savage, P. S., Georg, R. B., Williams, H. M., Turner, S., Halliday, A. N. and Chappell, B. W. 2012. The silicon isotope composition of granites. *Geochimica et Cosmochimica Acta*, 92: 184–202, doi: 10.1016/j.gca.2012.06.017.

- Savarino, J., Bekki, S., Cole-Dai, J. and Thiemens, M. H. 2003. UV induced mass-independent sulfur isotope fractionation in stratospheric volcanic sulfate. *Geophysical Research Letters*, 30: 11–14.
- Schauble, E. A. 2011. First-principles estimates of equilibrium magnesium isotope fractionation in silicate, oxide, carbonate and hexaaquamagnesium(2+) crystals. *Geochimica et Cosmochimica Acta*, 75, 844–869; doi:10.1016/j.gca.2010.09.044.
- Schauble, E. A., Georg, R. B. and Halliday, A. N. 2007. Silicate metal fractionation of silicon isotopes at high pressure and temperature. *Eos Trans. AGU Fall Meet. Suppl.*, 88 (52): V42A-07.
- Schauble, E. A., Rossman, G. R. and Taylor Jr, H. P. 2003. Theoretical estimates of equilibrium chlorine-isotope fractionations. *Geochimica et Cosmochimica Acta*, 67: 3267–3281, doi: 10.1016/s0016-7037(02)01375-3.
- Schwarcz, H. P., Agyei, E. K. and McMullen, C. C. 1969. Boron isotopic fractionation during clay adsorption from sea-water. *Earth and Planetary Science Letters*, 6: 1–5.
- Seo, J. H., Lee, S. K. and Lee, I. 2007. Quantum chemical calculations of equilibrium copper (I) isotope fractionations in ore-forming fluids. *Chemical Geology*, 243: 225–237.
- Shahar, A., Hillgren, V. J., Young, E. D., Fei, Y., Macris, C. A. and Deng, L. 2011. High-temperature Si isotope fractionation between iron metal and silicate. *Geochimica et Cosmochimica Acta*, 75: 7688–7697, doi: 10.1016/j.gca.2011.09.038.
- Sharp, Z. D., Barnes, J. D., Brearley, A. J., Chaussidon, M., Fischer, T. P. and Kamenetsky, V. S. 2007. Chlorine isotope homogeneity of the mantle, crust and carbonaceous chondrites. *Nature*, 446: 1062–1065 doi: 10.1038/nature05748.
- Sharp, Z. D., Barnes, J. D., Fischer, T. P. and Halick, M. 2010a. An experimental determination of chlorine isotope fractionation in acid systems and applications to volcanic fumaroles. *Geochimica et Cosmochimica Acta*, 74: 264–273, doi: 0.1016/j.gca.2009.09.032.
- Sharp, Z. D., Shearer, C. K., McKeegan, K. D., Barnes, J. D. and Wang, Y. Q. 2010b. The chlorine isotope composition of the moon and implications for an anhydrous mantle. *Science*, 329: 1050–1053, doi: 10.1126/science.1192606.
- Shen, B., Jacobsen, B., Lee, C.-T. A., Yin, Q.-Z., Morton, D. M. and Sleep, N. H. 2009. The Mg Isotopic Systematics of Granitoids in Continental Arcs and Implications for the Role of Chemical Weathering in Crust Formation. *Proceedings of the National Academy of Sciences*, 106: 20652–20657.
- Siebert, C., Nägler, T. F., von Blanckenburg, F. and Kramers, J. D. 2003. Molybdenum isotope records as a potential new proxy for paleoceanography. *Earth and Planetary Science Letters*, 211: 159–171.
- Sime, N. G., De La Rocha, C. L., and Galy, A. 2005. Negligible temperature dependence of calcium isotope fractionation in 12 species of planktonic foraminifera. *Earth and Planetary Science Letters*, 232: 51–66.
- Sime, N. G., De La Rocha, C. L., Tipper, E. T., Tripathi, A., Galy, A. and Bickle, M. J. 2007. Interpreting the Ca isotope record of marine biogenic carbonates. *Geochimica et Cosmochimica Acta*, 71: 3979–3989.
- Simon, J. I. and DePaolo, D. J. 2010. Stable calcium isotopic composition of meteorites and rocky planets. *Earth and Planetary Science Letters*, 289: 457–466, doi: 10.1016/j.epsl.2009.11.035.
- Skulan, J. and DePaolo, D. J. 1999. Calcium isotope fractionation between soft and mineralized tissues as a monitor of calcium use in vertebrates. *Proceedings of the National Academy of Sciences*, 96: 13709–13713.
- Smith, H. J., Spivack, A. J., Staudigel, H. and Hart, S. R. 1995. The boron isotopic composition of altered oceanic crust, *Chemical Geology*, 126: 119–135.
- Sobolev, A. V., Hofmann, A. W., Sobolev, S. V. and Nikogosian, I. K., 2005. An olivine-free mantle source of Hawaiian shield basalts. *Nature* 434: 590–597.
- Spivack, A. and Edmond, J. M. 1987. Boron isotope exchange between seawater and the oceanic crust. *Geochimica et Cosmochimica Acta*, 51: 1033–1044.
- Symonds, R. B., Rose, W. I., Reed, M. H., Lichte, F. E. and Finnegan, D. L. 1987. Volatilization, transport and sublimation of metallic and non-metallic elements in high temperature gases at Merapi Volcano, Indonesia. *Geochimica et Cosmochimica Acta*, 51: 2083–2101, doi: 10.1016/0016-7037(87)90258-4.
- Telus, M., Dauphas, N., Moynier, F., Tissot, F. o. L. H., Teng, F.-Z., Nabelek, P. I., Craddock, P. R. and Groat, L. A. 2012. Iron, zinc, magnesium and uranium isotopic fractionation during continental crust differentiation: The tale from migmatites, granitoids, and pegmatites. *Geochimica et Cosmochimica Acta*, 97: 247–265.
- Teng, F.-Z., Dauphas, N. and Helz, R. T. 2008. Iron isotope fractionation during magmatic differentiation in Kilauea Iki Lava Lake. *Science*, 320: 1620–1622, doi:10.1126/science.1157166.
- Teng, F.-Z., Dauphas, N., Helz, R. T., Gao, S. and Huang, S. 2011. Diffusion-driven magnesium and iron isotope fractionation in Hawaiian olivine. *Earth and Planetary Science Letters*, 308: 317–324, doi: 10.1016/j.epsl.2011.06.003.
- Teng, F.-Z., Dauphas, N., Huang, S. and Marty, B. 2013. Iron isotopic systematics of oceanic basalts. *Geochimica et Cosmochimica Acta*, 107: 12–26, doi: 10.1016/j.gca.2012.12.027.
- Teng, F.-Z., McDonough, W. F., Rudnick, R. L. and Walker, R. J. 2006. Diffusion-driven extreme lithium isotopic fractionation in country rocks of the Tin Mountain pegmatite. *Earth and Planetary Science Letters*, 243: 701–710, doi:10.1016/j.epsl.2006.01.036.
- Teng, F.-Z., Li, W.-Y., Ke, S., Marty, B., Dauphas, N., Huang, S., Wu, F.-Y. and Pourmand, A. 2010a. Magnesium isotopic composition of the Earth and chondrites. *Geochimica et Cosmochimica Acta*, 74, 4150–4166, doi: 10.1016/j.gca.2010.04.019.

- Teng, F.-Z., Li, W.-Y., Rudnick, R. L. and Gardner, L. R. 2010b. Contrasting lithium and magnesium isotope fractionation during continental weathering. *Earth and Planetary Science Letters*, 300: 63–71, doi:10.1016/j.epsl.2010.09.036.
- Teng, F.-Z., McDonough, W. F., Rudnick, R. L., Dalpe, C., Tomascak, P. B., Chappell, B. W. and Gao, S. 2004. Lithium isotopic composition and concentration of the upper continental crust. *Geochimica et Cosmochimica Acta*, 68: 4167–4178.
- Thiemens, M. 2006. History and Applications of Mass-Independent Isotope Effects, *Annual Reviews of Earth and Planetary Sciences*, 34: 217–262.
- Thiemens, M. H. and Shaheen, R. 2014. 5.6 - Mass-independent isotopic composition of terrestrial and extraterrestrial materials. In: Treatise on Geochemistry, 2nd Edn. Holland, H. D. and Turekian, K. K. (eds). Oxford: Elsevier
- Tipper, E. T., Galy, A., Gaillardet, J., Bickle, M. J., Elderfield, H. and Carder, E. A. 2006. The magnesium isotope budget of the modern ocean: Constraints from riverine magnesium isotope ratios. *Earth and Planetary Science Letters*, 250: 241–253, doi: 10.1016/j.epsl.2006.07.037.
- Tomascak, P. B., Tera, F., Helz, R. T. and Walker, R. J. 1999. The absence of lithium isotope fractionation during basalt differentiation: new measurements by multicollector sector ICP-MS. *Geochimica et Cosmochimica Acta*, 63: 907–910, doi:10.1016/s0016-7037(98)00318-4.
- Tonarini, S., Leeman, W. P. and Leat, P. T. 2011. Subduction erosion of forearc mantle wedge implicated in the genesis of the South Sandwich Island (SSI) arc: Evidence from boron isotope systematics. *Earth and Planetary Science Letters*, 301: 275–284, doi: 10.1016/j.epsl.2010.11.008.
- Vance, D., Archer, C., Bermin, J., Perkins, J., Statham, P. J., Lohan, M. C., et al. 2008. The copper isotope geochemistry of rivers and the oceans. *Earth and Planetary Science Letters*, 274: 204–213.
- Veizer, J., Ala, D., Azmy, K., Bruchschen, P., Buhl, D., Bruhn, F., et al. 1999. $^{87}\text{Sr}/^{86}\text{Sr}$, $\delta^{13}\text{C}$, and $\delta^{18}\text{O}$ evolution of Phanerozoic seawater. *Chemical Geology*, 161: 59–88.
- Vengosh, A., Kolodny, Y., Starinsky, A., Chivas, A. and McCulloch, M. 1991. Coprecipitation and isotopic fractionation of boron in modern biogenic carbonates. *Geochimica et Cosmochimica Acta* 55: 2901–2910.
- Vlastelic, I., Koga, K., Chauvel, C., Jacques, G. and Telouk, P. 2009. Survival of lithium isotopic heterogeneities in the mantle supported by HIMU-lavas from Rurutu Island, Austral Chain. *Earth and Planetary Science Letters*, 286: 456–466, doi: 10.1016/j.epsl.2009.07.013.
- Voegelin, A. R., Nägler, T. F., Beukes, N. J. and Lacassie, J. P. 2010. Molybdenum isotopes in late Archean carbonate rocks: Implications for early Earth oxygenation. *Precambrian Research*, 182: 70–82.
- Voegelin, A. R., Nägler, T. F., Samankassou, E. and Villa, I. M. 2009. Molybdenum isotopic composition of modern and Carboniferous carbonates. *Chemical Geology*, 265: 488–498.
- White, W. M. and Klein, E. 2013. Composition of the oceanic crust. In: Treatise on Geochemistry Volume 3, The Crust, 2nd Edn, Rudnick, R. L. (ed.). Amsterdam: Elsevier.
- Wei, W., Kastner, M. and Spivack, A. 2008. Chlorine stable isotopes and halogen concentrations in convergent margins with implications for the Cl isotopes cycle in the ocean. *Earth and Planetary Science Letters*, 266: 90–104.
- Weinstein, C., Moynier, F. D. R., Wang, K., Paniello, R., Foriel, J., Catalano, J. and Pichat, S. 2011. Isotopic fractionation of Cu in plants. *Chemical Geology*, 286: 266–271, doi: 10.1016/j.chemgeo.2011.05.010.
- Weiss, D. J., Mason, T. F. D., Zhao, F. J., Kirk, G. J. D., Coles, B. J. and Horstwood, M. S. A. 2005. Isotopic discrimination of zinc in higher plants. *New Phytologist*, 165: 703–710.
- Weyer, S., Anbar, A. D., Brey, G. P., Münker, C., Mezger, K. and Woodland, A. B. 2005. Iron isotope fractionation during planetary differentiation. *Earth and Planetary Science Letters*, 240: 251–264.
- Wiegand, B. A., Chadwick, O. A., Vitousek, P. M. and Wooden, J. L. 2005. Ca cycling and isotopic fluxes in forested ecosystems in Hawaii. *Geophysical Research Letters*, 32: L11404, doi: 10.1029/2005GL022746.
- Williams, H. M. and Archer, C. 2011. Copper stable isotopes as tracers of metal–sulphide segregation and fractional crystallisation processes on iron meteorite parent bodies. *Geochimica et Cosmochimica Acta*, 75: 3166–3178.
- Williams, H. M., Peslier, A. H., McCammon, C., Halliday, A. N., Levasseur, S., Teutsch, N. and Burg, J. P. 2005. Systematic iron isotope variations in mantle rocks and minerals: The effects of partial melting and oxygen fugacity. *Earth and Planetary Science Letters*, 235: 435–452.
- You, C.-F. 1994. Comment on “Boron content and isotopic composition of oceanic basalts: geochemical and cosmochemical implications” by M. Chaussidon and A. Jambon. *Earth and Planetary Science Letters*, 128: 727–730.
- You, C. F., Spivack, A. J., Gieskes, J. M., Rosenbauer, R. and Bischoff, J. L. 1995. Experimental study of boron geochemistry: implications for fluid processes in subduction zones. *Geochimica et Cosmochimica Acta*, 59: 2435–2442.
- Young, E. D. and Galy, A. 2004. The isotope geochemistry and cosmochemistry of magnesium. In: *Geochemistry of Non-traditional Stable Isotopes*, Johnson, C. M., Beard, B. L. and Albarède, F. (eds). Washington, DC: MSA.
- Young, E. D., Tonui, E., Manning, C. E., Schauble, E. and Macris, C. A. 2009. Spinel–olivine magnesium isotope thermometry in the mantle and implications for the Mg isotopic composition of Earth. *Earth and Planetary Science Letters*, 288: 524–533.
- Zeebe, R. 2005. Stable boron isotope fractionation between dissolved $\text{B}(\text{OH})_3$ and $\text{B}(\text{OH})_4^-$, *Geochimica et Cosmochimica Acta*, 69: 2753–2766.

Ziegler, K., Young, E. D., Schauble, E. A. and Wasson, J. T. 2010. Metal–silicate silicon isotope fractionation in enstatite meteorites and constraints on Earth’s core formation. *Earth and Planetary Science Letters*, 295: 487–496.

SUGGESTIONS FOR FURTHER READING

- Chan, L. H., Edmond, J. M., Thompson, G. and Gillis, K. 1992. Lithium isotopic composition of submarine basalts: implications for the lithium cycle of the oceans. *Earth and Planetary Science Letters*, 108: 151–160.
- Chan, L.-H. and Frey, F. A. 2003. Lithium isotope geochemistry of the Hawaiian plume: results from the Hawaii Scientific Drilling Project and Koolau Volcano. *Geochemistry Geophysics Geosystems*, 4: doi: 10.1029/2002GC000365.
- Elliott, T., Thomas, A., Jeffcoate, A. and Niu, Y. 2006. Lithium isotope evidence for subduction-enriched mantle in the source of mid-ocean-ridge basalts, *Nature*, 443: 565–568.
- Gao, Y. Q. and Marcus, R. A. 2001. Strange and unconventional isotope effects in ozone formation, *Science*, 293: 259–263.
- Heuser, A. and Eisenhauer, A. 2008. The Calcium Isotope Composition ($\delta^{44/40}\text{Ca}$) of NIST SRM 915b and NIST SRM 1486. *Geostandards and Geoanalytical Research*, 32: 311–315, doi:10.1111/j.1751-908X.2008.00877.x.
- Johnson, D. G., Jucks, K. W., Traub, W. A. and Chance, K. V. 2001. Isotopic composition of stratospheric ozone. *Journal of Geophysical Research*, 105: 9025–9031.
- Seitz, H.-M., Brey, G. P., Zipfel, J., Ott, U., Weyer, S., Durali, S. and Weinbruch, S. 2007. Lithium isotope composition of ordinary and carbonaceous chondrites, and differentiated planetary bodies: Bulk solar system and solar reservoirs. *Earth and Planetary Science Letters*, 260: 582–596, doi: 10.1016/j.epsl.2007.06.019.
- Simon, J. I., DePaolo, D. J. and Moynier, F. 2009. Calcium isotope composition of meteorites, Earth, and Mars. *The Astrophysical Journal*, 702: 707.
- Spivack, A. J., You, C.-F. and Smith, H. J. 1993. Foraminiferal boron isotope ratios as a proxy for surface ocean pH over the past 21 Myr. *Nature*, 363: 149–151.
- Tipper, E. T., Gaillardet, J., Galy, A., Louvat, P., Bickle, M. J. and Capmas, F. 2010. Calcium isotope ratios in the world’s largest rivers: A constraint on the maximum imbalance of oceanic calcium fluxes. *Global Biogeochemical Cycles*, 24: GB3019, doi: 10.1029/2009GB003574.
- Tomascak, P. B. 2004. Developments in the understanding and application of lithium isotopes in the Earth and planetary sciences. In: *Geochemistry of Non-Traditional Stable Isotopes*, Johnson, C. M., Beard, B. L. and Albarede, F. (eds). Washington: Mineralogical Society of America.
- Wiechert, U. and Halliday, A. N. 2007. Non-chondritic magnesium and the origins of the inner terrestrial planets. *Earth and Planetary Science Letters*, 256: 360–371, doi: 10.1016/j.epsl.2007.01.007.

PROBLEMS

1. The present ocean has a $\delta^{98/95}\text{Mo}$ of +2.3‰ and that the input to the ocean is 90% from rivers ($\delta^{98/95}\text{Mo} = +0.7\text{\textperthousand}$) and 10% from hydrothermal fluid ($\delta^{98/95}\text{Mo} = +0.8\text{\textperthousand}$). Let’s assume that removal of Mo from the oceans occurs only through oxic adsorption onto Mn-Fe crusts from seawater and authigenic Fe-Mo-S deposition reducing continental margin. Assume the fractionation for oxic adsorption (Δ_{Oxic}) is -3.0‰ and that removal by sulfide precipitation under anoxic conditions in sediments (Δ_{Anoxic}) is -0.6‰, what fraction of the removal occurs through oxic adsorption?
2. The following are constants for the polynomial function approximating fractionation factors (Eqn. 11.9) between the listed phase and Mg_g given by Schubale (2011):

	A	B	C
Dolomite	1.667×10^{14}	-1.2954×10^{10}	2.1154×10^6
Mg ²⁺ _{aq}	2.3453×10^{14}	-1.9796×10^{10}	2.5007×10^6

- (a) Calculate the fractionation dolomite–Mg_{aq}²⁺ fractionation factor at 15 and 25°C.
- (b) Assuming that rivers are the only source of Mg to seawater and that they have $\delta^{26}\text{Mg}$ of -1.1‰ and that hydrothermal activity and dolomite formation are the only sinks, and

that seawater is in steady state with $\delta^{26}\text{Mg} = -0.82\text{\textperthousand}$. If there is no fractionation in hydrothermal removal, use the fractionation factor you calculated previously for 20°C to determine what fractionation of seawater Mg is removed by dolomite formation. What would the isotopic composition of this dolomite be?

- (c) Using the fraction of Mg removal by dolomite formation you calculated in (b), how would the $\delta^{26}\text{Mg}$ of seawater change if the temperature increased from 15° to 25°C?

3. Calcium has six stable isotopes, more than any other element with atomic number under 40.

- (a) Why?
(b) Why does ^{40}Ca constitute more than 96% of calcium?

4. The fractionation factor for the precipitation of opal by diatoms is $\Delta^{30}\text{Si}_{\text{opal-dissolv.-}} \approx -1.1\text{\textperthousand}$, while that for the dissolution of diatoms tests is $\Delta^{30}\text{Si}_{\text{opal-dissolv.-}} \approx +0.55\text{\textperthousand}$; in other words, ^{28}Si appears to go preferentially into the reactant in both reactions. What does this suggests controls the fractionation? Justify your answer.

Chapter 12

Noble gas isotope geochemistry

12.1 INTRODUCTION

The noble gases are those elements on the extreme right of the Periodic Table. The name is derived from their unreactive character, a consequence of having outer electron orbitals filled. Isotopes of all six noble gases are produced to some degree by nuclear processes. ^4He is, of course, produced by alpha decay while ^{40}Ar is produced by electron capture decay of K. Isotopes of Kr and Xe are produced by U fission, while Rn consists of only short-lived isotopes of the U and Th decay series. In addition, ^{129}Xe is the decay product of the extinct radionuclide ^{129}I (half-life: 15.8 Ma) and the heavy Xe isotopes were produced by fission of the extinct nuclide ^{244}Pu (half-life 82 Ma). While neon isotopes are not produced directly by radioactive decay, significant variations occur in Ne isotopes as a consequence of reaction between “fissogenic” neutrons and magnesium as well as between alpha particles and ^{18}O . Finally, cosmic ray interactions can also produce isotopic variations in the noble gases, as we have already seen. Cosmic ray interactions produce a great many nuclides (Chapter 4), but because noble gases are so rare the effects are more significant than for other elements. In addition to nuclear processes, noble gas isotope ratios also vary as a consequence of mass-dependent fractionations. The processes that produced these fractionations mainly occurred in the young Solar System and Earth and provide important insights into that very early episode of history,

as was recognized more than half a century ago (Damon and Kulp, 1958).

In the following sections, we will consider the data on He, Ne, Ar, Kr, and Xe separately (radon nuclides are too short-lived to be of interest here) and examine how noble gases and their isotope ratios vary in Solar System materials as this provides an essential background for understanding noble gas isotope variations on this planet. In later sections we will see how all the noble gases can be used together to inform broad theories of Earth’s formation, structure and evolution. Much more detail on noble gas geochemistry can be found in books by Ozima and Podosek (2002) and Porcelli et al. (2002).

12.1.1 Noble gas chemistry

Although the noble gases almost never form chemical bonds in nature (the recent discovery of ArH in Crab Nebula supernova remnant is the exception (Barlow et al., 2013), and they can be induced to do so in laboratory experiments and Xe *may* be reactive in nature at high pressure), they nonetheless differ in their solubility in liquids (including water, oil, and magma), ionization potential, polarizability, diffusivity, and the extent to which they absorb onto solid surfaces. Noble gas solubility is a complex function of a variety of factors including temperature, pressure, and salinity, but under typical surface conditions, water solubility increases with increasing atomic number. Varying temperature dependence of

noble gas solubility in water enables dissolved noble gas concentrations in groundwater to be used as a paleothermometer (e.g., Kipfer et al., 2002). In magma, solubility decreases with atomic weight (i.e., He is the most soluble, Xe the least). In equilibration between water and petroleum, the heavier noble gases appear to partition into the petroleum phase more extensively than the lighter noble gases. As one might expect, diffusivity increases with decreasing atomic weight. Being a particularly small and electrically neutral atom, He diffuses particularly rapidly. Even at modest temperatures of the upper crust (150°C), radiogenic ${}^4\text{He}$ will diffuse too rapidly out of minerals to be retained. Nevertheless, on the scale of the whole crust, significant transport of even He occurs only through advection. The heavier noble gases, Xe in particular, can be strongly absorbed onto mineral surfaces. For example, Yang and Anders (1982) found mineral/gas distribution coefficients for chromite and carbon decreased from 0.1 for Xe to 0.6×10^{-3} for Ne. Helium has the highest first ionization potential of all elements (2373 kJ/mol) and ionization potential drops with increasing atomic number such that the ionization potential of krypton (1351 kJ/mol) is only a little higher than that of hydrogen (1312 kJ/mol) and the ionization potential of xenon (1170 kJ/mol) is well below that of hydrogen.

The atmosphere is the largest terrestrial reservoir of most noble gases (He is the exception) and is well mixed and consequently isotopically homogeneous (concentration of the noble gases are listed in Table 12.1). Concentrations of noble gases in rocks and minerals are extremely low and recovering them in sufficient quantities to determine their isotopic

composition is a trick rivaling Moses' producing water from rock. The first part of the trick is to choose the right rock. Because they readily escape to the atmosphere when lavas erupt subaerially, data on isotopic composition of noble gases in the mantle are restricted to samples from deep wells and hot springs, submarine-erupted basalts, fluid inclusions in minerals that crystallized at depth (including xenoliths and in some cases phenocrysts), and, in the case of Iceland, subglacially erupted basalts. When basalts are erupted under several kilometers of water or ice, the solubility of noble gases is such that at least some of the gases remain in the melt and are trapped in the quenched glassy rims and vesicles of pillow basalts. Several approaches can then be used to extract the noble gases from rocks and minerals. First, the rock or mineral can be fused in vacuum, allowing noble gases to be collected, cryogenically separated, and analyzed in a mass spectrometer. Second, the sample can be step-heated, terminating with complete fusion, with each temperature-release fraction analyzed separately, much as is done in ${}^{40}\text{Ar}/{}^{39}\text{Ar}$ dating (Chapter 3). Third, the sample may be crushed in vacuum, which releases only those gases trapped in vesicles and fluid inclusions. The remaining material can then be step-heated to release gases trapped in the crystalline structure or glass. Finally, samples may be attacked or etched with acids, an approach largely restricted to meteorites. In some cases, distinct compositions result from different release strategies for the same sample, that in turn reflects multiple origins of the gas (but we don't have space to go into that detail of the craft).

12.1.2 Noble gases in the Solar System

Figure 12.1 shows the relative abundances of the noble gases in various Solar System materials. Noble gas geochemistry divides these into two basic patterns: *solar* and *planetary*, terms we will use throughout this chapter. The former include the spectroscopically measured “solar” abundances in the Sun itself and the solar wind (as determined from spacecraft measurements), even though the latter shows small depletions in the light noble gases. This reflects some elemental fractionation in the acceleration of elements into the solar wind as well as fractionation in the

Table 12.1 Abundances of noble gases in the atmosphere and Sun.

Element	Atmosphere	Sun
He	5.24×10^{-6}	2.288×10^9
Ne	1.818×10^{-5}	2.146×10^6
Ar	0.0934	1.025×10^5
${}^8\text{Kr}$	1.14×10^{-6}	55.15
Xe	8.7×10^{-8}	5.391
Rn	$\sim 6 \times 10^{-20}$	

Atmospheric concentrations are mixing ratio, i.e., molar concentrations; solar concentrations are molar concentrations relative to Si $\equiv 1 \times 10^6$.

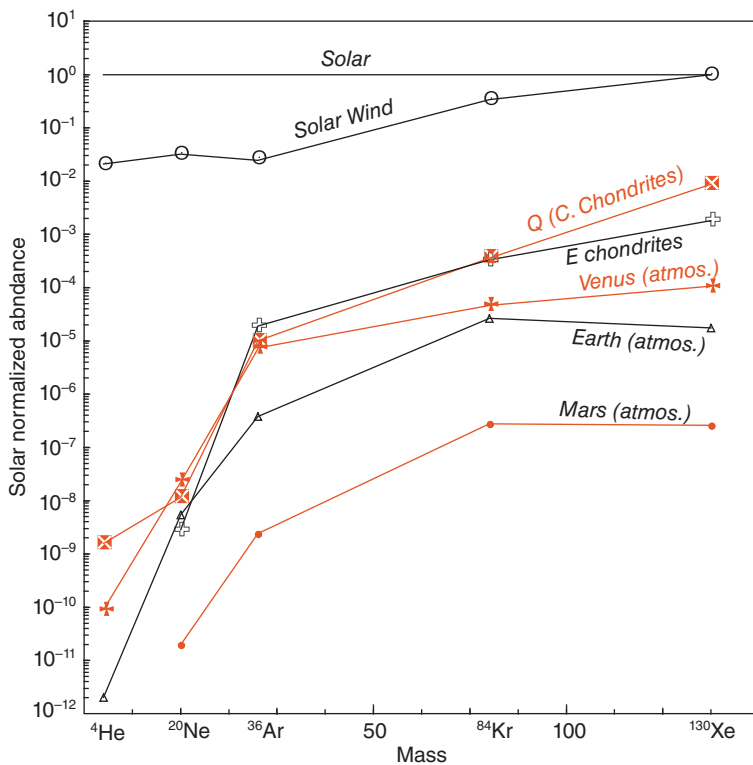


Figure 12.1 Abundance patterns of noble gases in the Solar System. *Planetary* patterns, which include the atmospheres of the terrestrial planets as well as gases in chondrites, show depletions in the light noble gases relative to the *Solar* patterns of the Sun and solar wind. Based on data in Hunten et al. (1988), Busemann et al. (2000); Pepin and Porcelli (2002), Ozima and Podosek (2002), and Wieler (2002).

retention of these gases in various target materials such as foils deployed in spacecraft and lunar soils. *Solar* abundance patterns also occur as a component of the noble gas inventory of meteorites and in interplanetary dust particles. Solar gases in these materials originate through solar wind implantation and are released by heating at relatively low temperatures. The remaining *planetary* patterns show much stronger depletions in the light relative to the heavy noble gases, particularly He and Ne. Planetary patterns are observed in both terrestrial planet atmospheres and as the major component of the noble gas inventory of meteorites. Step heating and successive leaching reveals carbonaceous chondrites contain a variety of noble gases components, including solar gases (implanted by the solar wind) and cosmogenic nuclides (Figure 5.16), but the most abundant components have planetary type patterns. One of most ubiquitous of these planetary components is released by

leaching with oxidizing acids such as HNO_3 and HClO_4 . The carrier of these noble gases, called “Q,” appears to be carbon-rich component present in the matrix and in coatings on chondrules, but its exact nature is unclear (the so-called “P1” component in meteorites appears to be essentially the same as “Q”). In contrast to ordinary chondrites, which are gas-poor, at least some enstatite chondrites also contain a significant inventory of noble gases, and their abundance patterns are basically similar to that of the Q component of carbonaceous chondrites. These planetary abundance patterns suggest a fractionation process operating in the early Solar System in which noble gases were lost from planets and planetary embryos in proportion to atomic mass. The atmospheres of Earth and Mars share this planetary pattern for the light noble gases, but whereas meteorites have Kr/Xe ratios less than the solar value, the atmospheres of Earth and Mars have solar or greater than solar

Table 12.2 Solar System noble gas isotopic compositions.

	Solar Wind	Q (chondrites)	Earth Atm.	Mars Atm.
$^4\text{He}/^3\text{He}$	2.16×10^3 [†]	6.28×10^3	7.225×10^5	–
$^{21}\text{Ne}/^{22}\text{Ne}$	0.0329	0.0294	0.0296	–
$^{20}\text{Ne}/^{22}\text{Ne}$	13.78	10.7	9.8	10.1
$^{38}\text{Ar}/^{36}\text{Ar}$	0.1828	0.1882	0.1876	0.244
$^{40}\text{Ar}/^{36}\text{Ar}$	0.0003 [§]	0.78 [£]	296.16 [*]	2400
$^{84}\text{Kr}/^{82}\text{Kr}$	4.882	4.955	4.946	4.869
$^{86}\text{Kr}/^{82}\text{Kr}$	1.476	1.534	1.51	1.463
$^{124}\text{Xe}/^{130}\text{Xe}$	0.0293	0.0281	0.0234	0.0239
$^{128}\text{Xe}/^{130}\text{Xe}$	0.5083	0.5077	0.4715	0.4658
$^{129}\text{Xe}/^{130}\text{Xe}$	6.286	6.436	6.50	16.03
$^{131}\text{Xe}/^{130}\text{Xe}$	4.996	5.056	5.213	5.060
$^{132}\text{Xe}/^{130}\text{Xe}$	6.047	6.177	6.61	6.313
$^{136}\text{Xe}/^{130}\text{Xe}$	1.797	1.954	2.176	2.242

[†]Based on Genesis mission measurements; the primordial Solar System value is inferred from the Jovian atmosphere to be 6.021×10^3 .

^{*}Mark et al. (2011).

[§]Inferred primordial value from Ozima and Podosek (2006).

[£]Lowest value observed by Busemann et al. (2000)

Based on data from Busemann et al. (2000), Pepin and Porcelli (2002), Ozima and Podesek (2006), and Heber et al., (2009).

Kr/Xe ratios, which is interpreted as a Xe depletion. This is sometimes called as the “missing xenon” problem or “xenon paradox.” Xe appears less depleted in the Venusian atmosphere, but noble gas abundances in the Venusian atmosphere are less well constrained than those of the terrestrial and Martian atmospheres. We’ll return to the xenon paradox at the end of the Chapter.

Noble gases show far greater isotopic variability in the Solar System than the other elements we have considered thus far. Significant isotopic variations occur even among chondritic meteorites and bulk isotopic compositions in meteorites differ from those of the Sun. There are several reasons for this. First, as we found in Chapter 5, presolar grains are present in some primitive carbonaceous chondrites and contain isotopically heterogeneous noble gases synthesized in a variety of stellar environments (e.g., red giants, supernovae), although these form only a small fraction of noble gas inventories in meteorites. Second, meteorites can also acquire solar noble gases through solar wind implantation. Third, cosmic ray-induced nuclear reactions produce additional variability in meteorites and planetary surfaces. Fourth, radiogenic nuclides such as ^4He , ^{40}Ar , ^{129}Xe , and so on are present in variable proportions depending on parent/daughter ratios. Fifth, fusion reactions in

the young Sun increased its $^3\text{He}/^4\text{He}$ ratio. Finally, noble gases in meteorites (and planetary atmospheres) appear to have undergone mass-dependent fractionation as a result of processes occurring in the solar nebula or during planetesimal formation.

Table 12.2 lists the isotopic composition of noble gases in a variety of Solar System materials. Only isotope ratios for the solar wind are available – it is not possible to measure most isotope ratios in the Sun directly.¹ While there is likely some mass dependent isotopic fractionation between the outer convective regions of the Sun and the solar wind, these are likely small (Wieler, 2002). Isotope ratios of planetary gases, including those in meteorites and the atmospheres of Earth and Mars, differ from solar values in being variably enriched in radiogenic isotopes (e.g., ^{21}Ne , ^{40}Ar). Further, planetary noble gases are isotopically heavier than solar ones with isotope ratios exhibiting mass dependent fractionations of solar-wind ratios (Pepin, 2006).

Understanding why planetary noble gas isotope ratios exhibit such large fractionations relative to solar values remains a significant problem in noble gas geochemistry. Hydrodynamic escape under the influence of gravity appears to be the only reasonable mechanism that can explain both the observed elemental and isotopic fractionations observed in

noble gases (Pepin, 2006). The basic idea is that even heavy noble gases could be entrained by the escape of a hot, light gas such as hydrogen or methane. This is resisted by gravity, so that the extent to which a species is entrained and escapes depends on its mass. Where and when this occurred is unclear. Ozima et al. (1998) proposed it occurred through Rayleigh fractionation during dissipation of the solar nebula, driven perhaps by intense UV radiation from the young Sun or a neighboring star. Such a general model would explain the compositional and isotopic similarity of planetary atmospheres and meteorites. Pepin (1991, 2003) suggested instead that the fractionation occurred during hydrodynamic escape of methane from transient atmospheres of planetesimals. In that case, the energy source would have been heating by short-lived radionuclides. On larger planets and planetary embryos, further fractionations could occur during hydrodynamic escape of primitive atmospheres, driven either by UV radiation from the Sun or energy released by impacts. In the case of Mars, further fractionation of noble gas isotope ratios might have occurred as the atmosphere was lost by solar wind sputtering once the magnetic field ceased (Pepin, 2006).

Helium isotope ratios vary between solar and planetary noble gases for an additional reason. The primordial $^4\text{He}/^3\text{He}$ ratio of the Solar System is taken to be the isotopic composition of the Jovian atmosphere as measured by the Galileo spacecraft, which is 6.021×10^3 . Ratios approaching this value have been also measured in carbonaceous chondrites (Busemann et al, 2000). The $^4\text{He}/^3\text{He}$ ratio in the solar wind, and presumably the Sun, is much lower: 2.28×10^3 . This difference is a consequence of deuterium burning in the young Sun. Deuterium burning, which produces ^3He , occurs during the T-Tauri phase of stars when stellar temperatures reach 10^6 K and while the star is still accreting mass, and before the *p-p* chain and other “main sequence” fusion reactions have initiated. Importantly, this process is thought to occur while the nebula is still present and before terrestrial planets have fully accreted (although perhaps after the giant planets had formed) and largely consumes the deuterium in the star, so that subsequent ^3He production is limited. Furthermore, while heat is

transported by radiation in the interior of main sequence stars, in the deuterium-burning phase, heat is transported throughout the star by convection. Consequently, ^3He produced by deuterium burning deep within a T-Tauri star would be convectively mixed to the surface and incorporated in the solar wind, but not in a main-sequence star. T-Tauri stars have particularly strong stellar winds (orders of magnitude greater than the present solar wind). Thus ^3He produced by deuterium burning would have been blown back into the solar nebula by these strong T-Tauri stellar winds where it could be implanted in dust and acquired by growing planets. If the Earth’s He inventory consists of He implanted in accreting solids by these early stellar winds, its $^3\text{He}/^4\text{He}$ ratio would be significantly higher than if it were primordial. We’ll return to this question in a later section.

12.2 HELIUM

12.2.1 He in the atmosphere, crust, and oceans

Helium is, of course, produced by alpha decay. Essentially all of this is from the U and Th decay series; the amount produced by other alpha emitters such as ^{147}Sm is insignificant. Decay of ^{238}U eventually produces eight ^4He , ^{235}U produces seven, and ^{232}Th produces six. This decay also accounts for ~80% of heat production in the Earth, with the decay of ^{40}K producing the remaining ~20%. The specific heat production of U and Th are $4.12 \times 10^{-4} \mu\text{W/mol}$ and $1.14 \times 10^{-4} \mu\text{W/mol}$. Combining these we can estimate that the ratio of ^4He production to heat production is about $10^{12} \text{ }^4\text{He atoms/W}$. In units commonly used in noble gas studies, this translates to $3.7 \times 10^{-8} \text{ cm}^3 \text{ STP/J}$ (STP denotes standard temperature and pressure, 25°C and 1 atm; under these conditions, 1 M of gas occupies $2.24 \times 10^4 \text{ cm}^3$). Both ^3He and ^4He are also produced by nuclear reactions on Li such as $^6\text{Li}(n, \alpha)^3\text{He}$ with neutrons produced by α reactions with O, Mg, and Si. Small amounts of He are also generated by cosmic-ray interactions (including ^3He produced by decay of cosmogenic ^3H), as we found in Section 4.1.4, but this “cosmogenic” He is a trivial fraction of total He production in the Earth. As a consequence of both alpha decay and these reactions, the $^3\text{He}/^4\text{He}^2$ production ratio in the

crust is in the range of 0.4 to 1×10^{-8} (Ballentine and Burnard, 2002) and ratios in this range are typical of continental crust. The production ratio is lower in the mantle (due to lower Li concentrations) and any “nucleogenic” ${}^3\text{He}$ in that reservoir is trivial compared to primordial ${}^3\text{He}$.

The atmospheric ${}^3\text{He}/{}^4\text{He}$ ratio of 1.384×10^{-6} is well above the crustal production ratio and reflects continued release of primordial ${}^3\text{He}$ from the solid Earth. Helium is unique in that it is the only element for which the Earth is not a closed system. Its mass is sufficiently low that it can be accelerated to escape velocity in the upper atmosphere. As a consequence, the Earth continually “bleeds” helium to space, and since ${}^3\text{He}$ has only $\frac{3}{4}$ the mass of ${}^4\text{He}$, ${}^3\text{He}$ is lost even more readily than ${}^4\text{He}$ ³ (the Earth also gains small amounts of He by capture of solar wind: “auroral precipitation”). Consequently, the atmospheric concentration is low, 5.2 ppmv,⁴ despite its being the second most abundant element in the Sun and the cosmos. The residence time of He in the atmosphere is estimated to be 10^6 to 10^7 years (see Problem 12.1). Given its short residence time, even this low concentration implies that He in the atmosphere must be continually replenished by He from the solid Earth.

The uniform atmospheric isotope ratio provides a useful standard and reference value for He isotope ratios. He isotope ratios are often reported relative to the atmospheric value as:

$$\left(\frac{{}^3\text{He}}{{}^4\text{He}}\right)_{R/R_A} = \frac{\left({}^3\text{He}/{}^4\text{He}\right)_{\text{sample}}}{\left({}^3\text{He}/{}^4\text{He}\right)_{\text{atmosphere}}} \quad (12.1)$$

with the ratio on the left-hand-side usually denoted simply as the R/R_A . In these units, crustal rocks generally have He isotope ratios in the range of 0.01 to 0.1, mantle-derived rocks have values in the range of 5–50, the primordial value is 120 and the ratio in the present solar wind is 336 (Figure 12.2). Low values in the crust reflect degassing of He that occurred during its formation and the subsequent production of ${}^4\text{He}$ by radioactive decay. Higher ${}^3\text{He}/{}^4\text{He}$ in mantle-derived rocks indicates that the mantle has not been entirely degassed and retains some fraction of its initial, or primordial, inventory of helium. The isotopic composition of He in the atmosphere thus reflects the isotopic composition of He

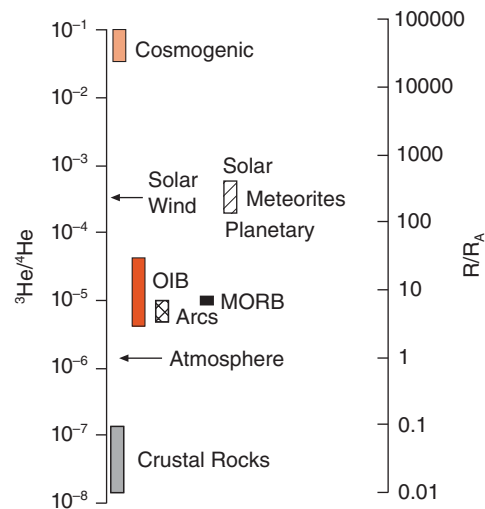


Figure 12.2 Summary of He isotope variations in the Earth and Solar System. The R/R_A scale give the ${}^3\text{He}/{}^4\text{He}$ ratio relative to the atmospheric value. (Source: White (2013). Reproduced with permission of John Wiley & Sons.)

leaking from the solid Earth, and is therefore intermediate between the crust and mantle values.

Within the crust, He diffuses out of minerals and accumulates in pore fluids (principally water). Helium concentrations in water in equilibrium with the atmosphere (so-called air-saturated water or ASW) are around 2×10^{-12} mol/g. In old groundwaters, concentrations range as high as 10^{-7} mol/g, illustrating this accumulation. In some cases, radiogenic production within the aquifer can explain the observed concentrations, but in other cases, such as the Great Artesian Aquifer of Australia, groundwater appears to accumulate He at rates comparable to the entire production within the continental crust beneath it, about 1.5×10^{-6} mol·m⁻²·yr⁻¹ (Torgensen and Clark, 1985). In regions of continental extension and magmatism (the two are often associated), such as the Rhine Graben and Pannonian Basin in Europe, the Rio Grande Rift in the Western USA, and the Subei Basin in China, much higher He concentrations in crustal fluids, including water, petroleum, and natural gas, are observed. These are always associated with R/R_A ratios well above the crustal value of ~0.1 (e.g., O’Nions and Oxburgh, 1988; Ballentine et al., 2002), and

usually above 1 Ra. The elevated R/R_A values are indicative of a flux of He from the mantle. That in turn likely reflects partial melting of the mantle and transport of He and other gases through the crust in fluids.

Tritium, ^3H , is produced by cosmic ray interactions in the atmosphere and decays to ^3He with a half-life of 12.4 yrs. Tritium produced in this way reacts to form H_2O and enters the hydrologic cycle, ultimately entering the oceans. In the ocean, the $^3\text{H}/^4\text{He}$ ratio has been used to determine rates of mixing of water masses in and above the thermocline (e.g., Jenkins, 1987; Schlosser and Winckler, 2002). Deep water masses are typically old enough so that any ^3H has decayed and this approach is no longer useful. However, deep water masses typically show elevated $^3\text{He}/^4\text{He}$ ratios as a consequence of mantle degassing. Indeed, the first evidence that the Earth continues to degas primordial He came from the observation of elevated $^3\text{He}/^4\text{He}$ in deep water of the Pacific (Clark et al., 1969). Subsequent work has shown that most of this He enters the ocean via hydrothermal systems at mid-ocean ridges, with smaller contribution from submarine volcanism associated with island arcs and oceanic island chains. Based on the distribution of ^3He in the deep ocean and an ocean circulation model, Bianchi et al (2010) estimated the ^3He flux from the oceans as $527 \pm 102 \text{ mol/yr}$, about half the flux originally estimated by Craig et al. (1975). Assuming a $^3\text{He}/^4\text{He}$ ratio of this helium equal to the average value in MORB (see the following), this corresponds to a total He flux of $4.11 \times 10^7 \text{ mol/yr}$ through the oceans.

Very high $^3\text{He}/^4\text{He}$ ratios have been found in slowly accumulating deep ocean sediments. These high ratios result from the presence of interplanetary dust particles (IDP). The particles themselves have $^3\text{He}/^4\text{He}$ ratios of $\sim 170 R/R_A$. There is a constant rain of these particles over the entire Earth surface, but they are a significant component of sediment only at extremely slow accumulation rates, such as occur in the central Pacific. In those cases, bulk sediment $^3\text{He}/^4\text{He}$ may exceed R/R_A of 50. If one assumes that accumulation rates of IDP's are constant, $^3\text{He}/^4\text{He}$ ratios can be used to determine sedimentation rates. On the other hand if accumulation rates are not constant, $^3\text{He}/^4\text{He}$ ratios provide a record of cosmic

events such as asteroid or comet breakup (Schlosser and Winckler, 2002).

12.2.2 He in the mantle

Before we examine the data, we must consider a couple of caveats. First, because some loss of He is almost inevitable even during submarine eruptions and ^4He is continually generated by alpha decay, the $^3\text{He}/^4\text{He}$ ratio measured from lava may be lower than that of the mantle source, especially in old samples. Second, subaerial samples exposed to cosmic rays can contain cosmogenic He, in which case the $^3\text{He}/^4\text{He}$ could be higher than that of the mantle source. The importance of both these effects increases with the age of the sample.

MORB are, of course, inevitably erupted under water and the data set on He isotope ratios in MORB is relatively rich. Furthermore, there is so little He in the atmosphere and dissolved in seawater that any atmospheric contamination is usually negligible, or readily corrected for (in contrast to the other noble gases). The OIB data set is largely restricted to basalts erupted on seamounts and from submarine fissures of some oceanic islands and to xenoliths and phenocrysts found in the lavas. Figure 12.3 summarizes these data. There are several observations: first, the ratio in MORB, and presumably therefore the depleted upper mantle, is higher than the atmospheric value, with a mean R/R_A value of MORB of 8.8 ± 2.5 ($^{4\text{He}}/^{3\text{He}} = 82, 100$) and a median value of 8.1. Second, $^3\text{He}/^4\text{He}$ is relatively uniform in MORB. Most of the samples with $R/R_A > 10$ come from parts of the ridge close to oceanic islands and are thus likely influenced by mantle plumes.

In contrast, $^3\text{He}/^4\text{He}$ values in OIB are more variable and may be either higher or lower than in MORB, although most are higher (Graham, 2002). Figure 12.4 shows the isotopic composition of He in basalts from a variety of mantle plumes plotted as a function of plume flux estimates of Davies (1988) and Sleep (1990). As may be seen, there is no obvious relationship between plume flux and He isotopic composition.

Overall, there is little correlation between He isotope ratios and other isotope ratios, such as $^{87}\text{Sr}/^{86}\text{Sr}$, as is illustrated in Figure 12.5 (although correlations often exist within

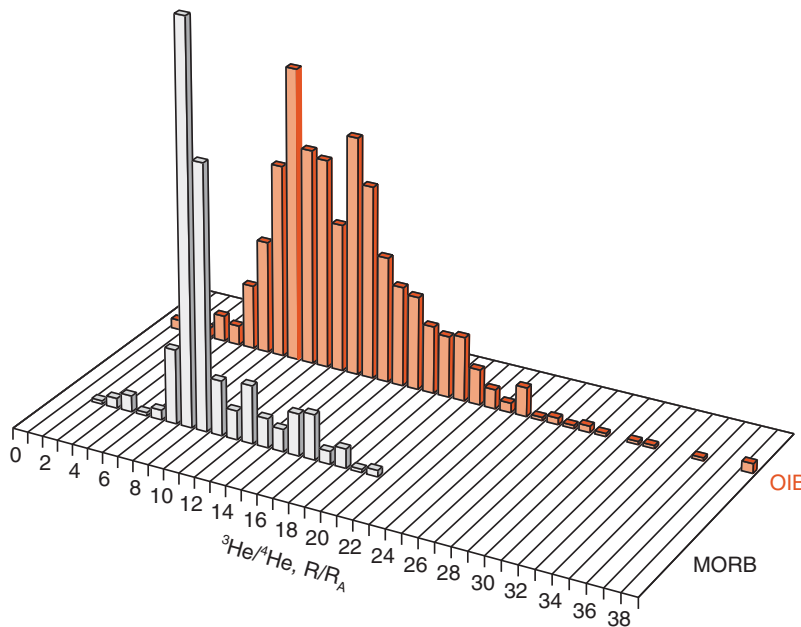


Figure 12.3 Comparison of ${}^3\text{He}/{}^4\text{He}$ analyses of 573 MORB and 759 OIB from the PetDB and GEOROC databases. (Source: White (2010). Reproduced with permission of Annual Reviews, Inc.)

individual oceanic islands, e.g., Kurz et al., 1987). The highest ${}^3\text{He}/{}^4\text{He}$ ratios are associated with intermediate ${}^{87}\text{Sr}/{}^{86}\text{Sr}$, ${}^{143}\text{Nd}/{}^{144}\text{Nd}$, and Pb isotope ratios (Kurz et al., 1982; Hanan and Graham, 1996; Class and Goldstein, 2005). These high ${}^3\text{He}/{}^4\text{He}$ ratios suggest that this material has been substantially less degassed than material with lower or higher ${}^{87}\text{Sr}/{}^{86}\text{Sr}$ ratios. This observation is consistent with the idea that the Earth has lower ${}^{87}\text{Sr}/{}^{86}\text{Sr}$ and higher ${}^{143}\text{Nd}/{}^{144}\text{Nd}$ than chondrites as a consequence of collisional erosion because we expect the primitive mantle, which in the eroded Earth model, would have ${}^{87}\text{Sr}/{}^{86}\text{Sr}$ in the range of 0.703 to 0.704 to be the least outgassed and have the highest ${}^3\text{He}/{}^4\text{He}$ (Jackson et al., 2010). The lower ${}^3\text{He}/{}^4\text{He}$ in OIB with more extreme ${}^{87}\text{Sr}/{}^{86}\text{Sr}$, ${}^{143}\text{Nd}/{}^{144}\text{Nd}$, and Pb isotope ratios is consistent with the idea that those isotopic signatures reflect subduction recycling of oceanic crust and sediment (Hofmann and White, 1982; Jackson et al., 2007).

Judging from He trapped in fluid inclusions in phenocrysts and xenoliths, the subcontinental lithospheric mantle typically has R/R_A values that range from 5 to 8, i.e., well above the atmospheric and crustal values but lower

than MORB. A few xenoliths have ratios slightly higher than MORB. Higher ratios are observed in lavas associated with mantle plumes (such as Yellowstone and Afar shown in Figure 12.4). R/R_A values as high as 13 have been reported from the 250 million year old Siberian flood basalts (Basu et al., 1995) as well as the Deccan flood basalts (Basu et al., 1993), and up to ~24 in fluid inclusions from 380 Ma alkaline magmatic rocks from the Kola Peninsula. The highest reported values in any lavas, R/R_A ≈ 50 were reported from early Tertiary picrites from Baffin Island and West Greenland (Starkey et al., 2009). The Siberian Traps represent one of the greatest known outpouring of lava in the planet's history and thought to have formed as the head of a large deep mantle plume reached the near-surface. The Baffin Island province is associated with the beginnings of the Icelandic mantle plume and the Deccan Province is associated with the beginning of the Reunion mantle plume.

Extreme ${}^3\text{He}/{}^4\text{He}$ ratios, up to 1000 R/R_A, have been reported from diamonds. Since these ratios are well above the Solar System initial value (~ 120 R/R_A, ${}^4\text{He}/{}^3\text{He} = 6.024 \times 10^3$), they must reflect some sort of

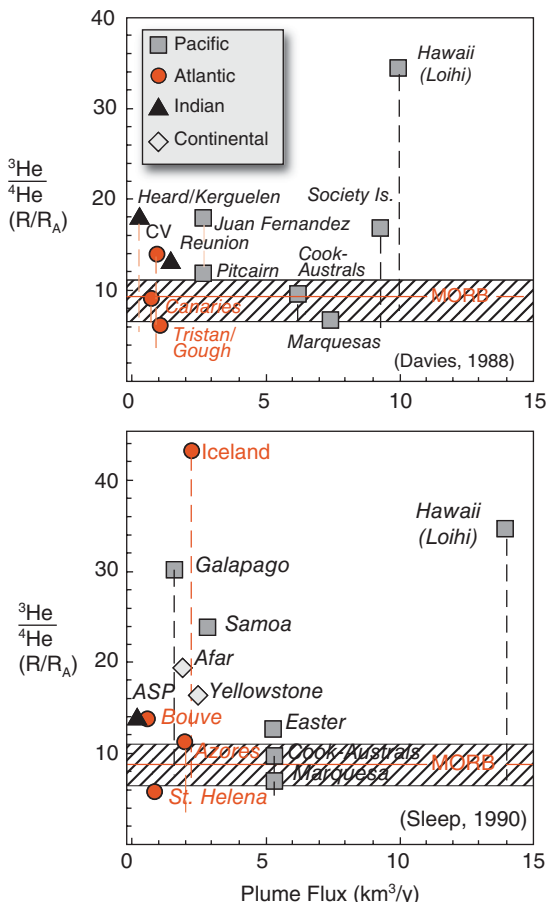


Figure 12.4 Helium isotope ratios in plume-derived basalts and MORB as a function of plume flux. There is no apparent relationship between plume flux and He isotope ratios. ASP = Amsterdam-St. Paul. (Source: Adapted from Graham, 2002.)

nucleogenic production of ${}^3\text{He}$ (e.g., Ozima and Zashu, 1983; Zandik et al., 1987). In some instances where the diamonds may be from alluvial placer deposits, cosmogenic production could be the explanation. In other cases, however, cosmogenic production can be ruled out production through α -n reactions is suspected, but a fully satisfactory explanation has not been given.

He isotope ratios in island arc volcanics are generally somewhat lower than those in MORB. If only the maximum values in each arc are considered (because low values could reflect crustal or atmospheric contamination or radiogenic in-growth) the range is 4.5 to 8.9 R/R_A ; the overall mean is 5.37 (Hilton et al., 2002). Values lower than MORB likely

reflect radiogenic He from subducting oceanic crust and sediment. If this radiogenic component has R/R_A of ~ 0.1 , then it is nonetheless clear that the primary source of He in island arcs is depleted mantle, an observation consistent with the idea that island arc volcanics are primarily derived from the mantle wedge above the subducting slab. Back arc basin basalts range from MORB-like values in the Mariana Trough, to values higher than MORB (up to 28.1 R/R_A in the Rochambeau Bank of Lau Basin) in the Lau, North Fiji, and Manus Basins (Lupton et al. 2009). These higher ratios suggest a mantle plume component. There is independent evidence of a plume contribution in the North Lau Basin from shear-wave splitting measurements, which suggest southward flow from the Samoan mantle plume into the basin (Smith et al., 2001). Hilton et al. (2002) estimate the global ${}^4\text{He}$ flux from island arc volcanism as $1.2 \times 10^7 \text{ mol/yr}$, or about 3.7% of the total flux from the solid Earth.

The generally higher ${}^3\text{He}/{}^4\text{He}$ ratios in mantle plumes provide evidence that they are derived from a part of the mantle that has been less degassed than the mantle that gives rise to MORB. The latter is generally assumed to be the upper mantle or asthenosphere. Simple logic suggests (but doesn't prove) that the deep mantle should have experienced less melting and degassing than the upper mantle (because melting and degassing can occur only near the surface). Hence, high He isotope ratios in plume-derived basalts are often cited as evidence that plumes come from the deep mantle (however, simple logic might be misleading). Low ${}^3\text{He}/{}^4\text{He}$ ratios in some plumes, such as Tristan and St Helena, could reflect the presence or predominance of material recycled from the Earth's surface, such as oceanic crust, in these plumes.

12.3 NEON

Neon isotope ratios vary in the Earth as a consequence of two processes: (1) mass dependent fractionation, a consequence of mass differences between ${}^{20}\text{Ne}$, ${}^{21}\text{Ne}$, and ${}^{22}\text{Ne}$ affecting behavior, and (2) production through nuclear reactions. The former mainly occurred in the early days of the Earth and Solar System as we'll discuss in Section 12.7. The latter results mainly from $\alpha - n$ reactions

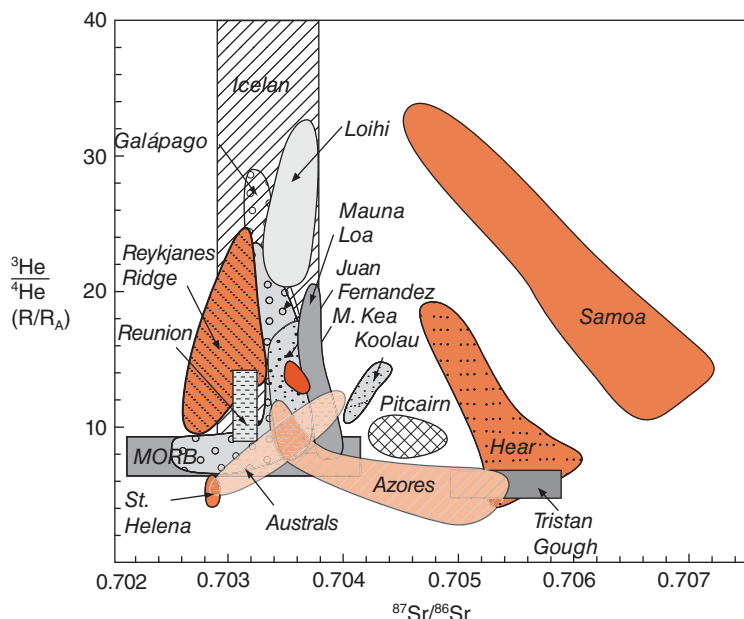


Figure 12.5 Relationship between ${}^3\text{He}/{}^4\text{He}$ and ${}^{87}\text{Sr}/{}^{86}\text{Sr}$ in MORB and OIB. (Source: Adapted from Graham, 2002.)

such as ${}^{17}\text{O}(\alpha, \text{n}){}^{20}\text{Ne}$, ${}^{18}\text{O}(\alpha, \text{n}){}^{21}\text{Ne}$, ${}^{24}\text{Mg}(\text{n}, \alpha){}^{21}\text{Ne}$, and ${}^{19}\text{F}(\alpha, \text{n}){}^{22}\text{Ne}$ with the alpha particles derived from decay of U and Th and neutrons derived either from other α -n reactions or, more rarely, ${}^{238}\text{U}$ fission. While these reactions produce all three Ne isotopes, the largest effect is on ${}^{21}\text{Ne}$ reflecting both low abundance as well as production (${}^{21}\text{Ne}$ is far less abundant, 0.26% of Ne, than other Ne isotopes). The abundances of the other two isotopes are not significantly affected by these reactions in the mantle, but because of higher fluorine concentrations, there is minor but significant production of ${}^{22}\text{Ne}$ in the crust.

Figure 12.6 provides a summary of Ne isotopic variations. The first observation is that the atmospheric ${}^{20}\text{Ne}/{}^{22}\text{Ne}$ ratio is lower than that of the solar wind and meteoritic components (Table 12.2), as well as mantle Ne. Since neither ${}^{20}\text{Ne}$ nor ${}^{22}\text{Ne}$ are created in significant amounts by nuclear processes, the explanation for this difference must reflect chemical processes. Indeed, after accounting for a small amount of nucleogenic ${}^{21}\text{Ne}$ in the atmosphere derived from the solid Earth, the relative differences in ${}^{21}\text{Ne}/{}^{22}\text{Ne}$ and ${}^{20}\text{Ne}/{}^{22}\text{Ne}$ between the solar wind and the atmosphere are those expected for mass dependent fractionation, that is, depletion of

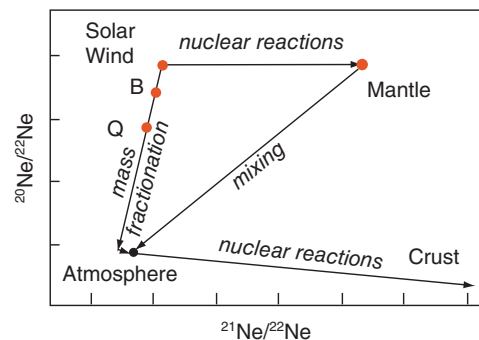


Figure 12.6 Schematic illustration of the isotopic variation of terrestrial Ne. Atmospheric ${}^{21}\text{Ne}/{}^{22}\text{Ne}$ is lower than solar wind Ne by about half as much as ${}^{20}\text{Ne}/{}^{22}\text{Ne}$, the ratio expected for mass-dependent fractionation. The meteoritic Q and B components (see also Figure 5.16) also lie on this mass-dependent fractionation line. Mantle Ne appears to have ${}^{20}\text{Ne}/{}^{22}\text{Ne}$ similar to the solar wind value. ${}^{21}\text{Ne}$ production in the solid Earth by (α, n) and (n, α) reactions increases the ${}^{21}\text{Ne}/{}^{22}\text{Ne}$ by varying amounts, depending on the U/Ne ratio. Samples of Ne from the solid Earth are invariably contaminated by atmospheric Ne, which drives compositions back toward the atmospheric value.

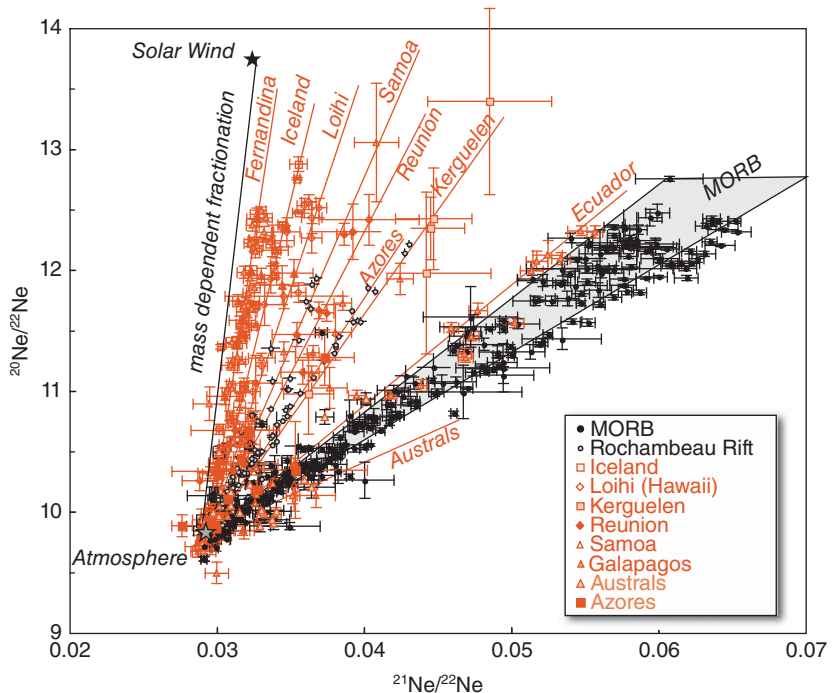


Figure 12.7 Ne isotope variations in oceanic basalts and xenoliths. Data from Trieloff et al. (2000), Trieloff et al. (2002), Poreda and Farley (1992), Tucker et al. (2012), Jackson et al. (2010), Valbracht et al. (1996), Valbracht et al. (1997), Madureira et al. (2005), Moreira et al. (1998), Hanyu et al. (2011), Mukhopadhyay (2012), Pető et al. (2013), Kurz et al. (2009), and Parai et al. (2012).

Ne isotopes from the atmospheric reservoir in proportion to mass. Trapped Ne in meteorites, including Q, also shows depletion in light isotopes compared to the solar wind (e.g., Figure 5.17), although meteoritic Ne is not as depleted in light isotopes as is the atmosphere. In contrast to the atmosphere, Ne from the Earth's mantle appears to have $^{20}\text{Ne}/^{22}\text{Ne}$ ratios similar to that of the solar wind. We'll consider theories to explain this difference in a later section.

12.3.1 Neon in the solid earth

Given that the continental crust has been created by magmatism, it is not surprising to find that it has been extensively degassed and hence highly depleted in noble gases. Because of this, nucleogenic Ne is a greater fraction of Ne in the crust than in the atmosphere or mantle. Thus, $^{21}\text{Ne}/^{22}\text{Ne}$ in crustal fluids (water, natural gas) can be an order of magnitude greater than the atmospheric value. As is the case with He, Ne isotope ratios can be used to trace the origin and age of ground water.

Figure 12.7 shows Ne isotopic variations in oceanic basalts (including xenoliths in oceanic island basalts). The data form a variety of arrays that terminate at one end close to the atmospheric value and extend to more "solar-like" $^{20}\text{Ne}/^{22}\text{Ne}$ and nucleogenic $^{21}\text{Ne}/^{22}\text{Ne}$. These arrays reflect ubiquitous mixing with air (the Ne/He ratio is higher in the atmosphere than in rocks, making the latter more subject to contamination). The $^{21}\text{Ne}/^{22}\text{Ne}$ ratio is in part a function of the U-Th/Ne ratio in the mantle source region: high U-Th/Ne leads to higher $^{21}\text{Ne}/^{22}\text{Ne}$ through nucleogenic production. We see that MORB generally have higher $^{21}\text{Ne}/^{22}\text{Ne}$ than OIB, implying higher U-Th/Ne, consistent with the idea suggested by the He data that the MORB reservoir is more degassed than the OIB one. The MORB data scatter somewhat suggesting some heterogeneity in the U-Th/Ne ratio. The Rochambeau Rift and Galapagos data form two distinct arrays, one MORB-like, one more OIB-like. In the Rochambeau Rift case, this is consistent with the idea of Samoan plume material invading

the Lau Basin. In the Galapagos, the arrays are consistent with differences in Sr, Nd, and Pb isotope ratios of the volcanoes sampled, with Volcan Ecuador and Volcan Wolf having more MORB-like compositions than Volcan Fernandina. The Austral Islands are exceptional in that their neon appears to be more rather than less nucleogenic than MORB. In this respect, He and Ne isotopes of the Australs are consistent, as $^{3}\text{He}/^{4}\text{He}$ ratios in the Australs are lower than in MORB in contrast to most OIB (Figure 12.5).

Perhaps the most significant implication of the data, however, is that Ne in the atmosphere is isotopically distinct from that in the Earth's interior. The maximum reported reliable $^{20}\text{Ne}/^{22}\text{Ne}$ in oceanic basalts is 12.8 (higher ratios have been reported from xenoliths, but these have high analytical uncertainty), which is less than the solar value of 13.78. However, Yokochi and Marty (2004) reported values as high as 13.05 ± 0.20 inclusions from Devonian alkaline magmatic rocks from the Kola Peninsula (the same release fraction had an R/R_A of 13.5). Since there is potential atmospheric contamination in all these data, it is possible that the $^{20}\text{Ne}/^{22}\text{Ne}$ ratio of the high $^{20}\text{Ne}/^{22}\text{Ne}$ end-member of all these arrays is solar. Thus Ne in the Earth's interior appears to have a solar-like isotopic composition. After correcting for atmospheric Ne, it is possible to interpret the OIB data in terms of just two components: a solar-like primordial mantle composition and a ^{21}Ne -rich degassed MORB component, which also has a solar-like $^{20}\text{Ne}/^{22}\text{Ne}$. Some have argued that the MORB source has a lower, more planetary-like $^{20}\text{Ne}/^{22}\text{Ne}$ ratio than the OIB source. The maximum $^{20}\text{Ne}/^{22}\text{Ne}$ observed in MORB (12.75) is slightly lower than the highest precisely measured $^{20}\text{Ne}/^{22}\text{Ne}$ ratio in OIB and is well above the $^{20}\text{Ne}/^{22}\text{Ne}$ of trapped components (e.g., Q) in chondrites, but similar to the chondritic Ne-B component.

Since alpha particles are, of course, ^{4}He nuclei, radiogenic production of ^{4}He and nucleogenic production of ^{21}Ne are closely linked, with an estimated production $^{21}\text{Ne}/^{4}\text{He}$ ratio of 4.5×10^{-8} (Honda and McDougall, 1998). $^{21}\text{Ne}^*/^{4}\text{He}^*$ ratios (where, as usual, the asterisk denotes the radio/nucleogenic component) observed in MORB and OIB vary considerably,

probably due to elemental fractionation during and after eruption: He is more soluble in magma than is neon and hence is less likely to be lost by degassing. On the other hand, it is much more subject to diffusive loss. The two samples with best preserved initial gas contents, the DICE 10 sample from Iceland (a subglacially erupted glassy basalt) and the 2πD43 sample (a gas-rich “popping rock”) from the Mid-Atlantic Ridge, have $^{21}\text{Ne}^*/^{4}\text{He}^*$ ratios of 4.5×10^{-8} and 7.2×10^{-8} , respectively, close to the expected ratio. We'll see in a subsequent section that we can use these ratios to estimate Ne/He ratios in the mantle.

12.4 ARGON

Argon has three isotopes: ^{36}Ar , ^{38}Ar , and ^{40}Ar . The latter constitutes 99.6% of atmospheric Ar. Argon geochronology, certainly the most significant aspect of Ar isotope ratios, was discussed in Chapter 3. Here we review the geochemical aspects and implications of Ar isotope variations in the Earth. Comparing the atmospheric $^{40}\text{Ar}/^{36}\text{Ar}$ ratio of 296 to the primordial one of $\sim 3 \times 10^{-4}$, we see that atmospheric Ar is almost exclusively radiogenic. Furthermore, we infer that atmospheric Ar must owe its origin to degassing of the Earth's interior (since there is no potassium in the atmosphere) plus release of radiogenic ^{40}Ar produced by decay of ^{40}K in the crust. Since the half-life of ^{40}K is ~ 1.4 Ga, most of this Ar must have been degassed after the Earth formed. Depending on the assumed K concentration in the Earth, something like 50–67% of the radiogenic Ar produced since the Earth formed is now in the atmosphere. As we shall see, higher $^{40}\text{Ar}/^{36}\text{Ar}$ ratios are observed in well gases, fluid inclusions, and submarine basalts.

The atmospheric $^{38}\text{Ar}/^{36}\text{Ar}$ ratio of 0.1876 is higher than the solar wind value of 0.1828. Since nuclear processes produce neither isotope to a significant degree, the difference is most likely due to mass fractionation, as is apparently the case with the $^{20}\text{Ne}/^{22}\text{Ne}$ ratio. One might then suspect that the $^{38}\text{Ar}/^{36}\text{Ar}$ ratio in the Earth's interior would differ from the atmospheric value, as is the case for neon. However, Raquin and Moreira (2009) found that both OIB and MORB had $^{38}\text{Ar}/^{36}\text{Ar}$ ratios identical to the atmospheric value within analytical error. It may

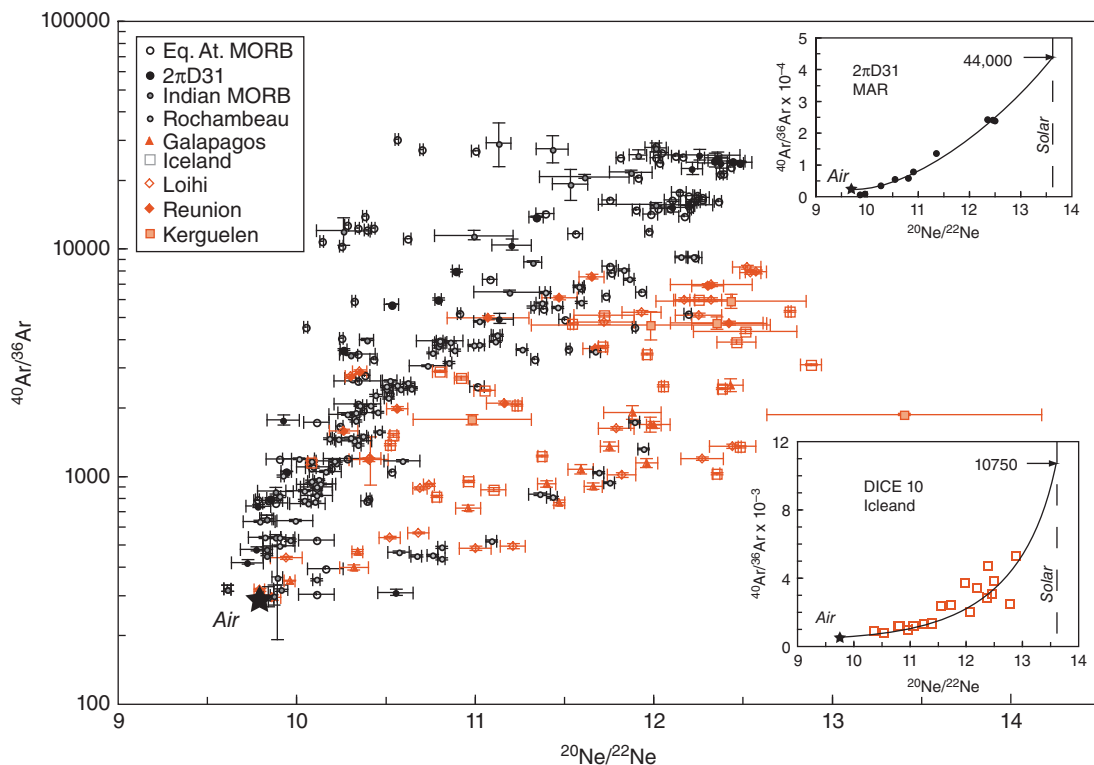


Figure 12.8 $^{40}\text{Ar}/^{36}\text{Ar}$ as plotted against $^{20}\text{Ne}/^{22}\text{Nd}$ in MORB, OIB, and related xenoliths. Variation within suites generally reflects atmospheric contamination. It is apparent that MORB have higher $^{40}\text{Ar}/^{36}\text{Ar}$ than OIB. Examples of mixing hyperbolae are shown for samples from the Mid-Atlantic Ridge (2πD31) and Iceland (DICE 10). One approach to determining the $^{40}\text{Ar}/^{44}\text{Ar}$ of mantle end-member is to assume that it has a solar $^{20}\text{Ne}/^{22}\text{Ne}$ ratio. Under this assumption, the MORB sample has $^{40}\text{Ar}/^{36}\text{Ar}$ of 44,000 and the Iceland sample has $^{40}\text{Ar}/^{36}\text{Ar}$ of 10,750.

be that this reflects subduction recycling of atmospheric Ar into the mantle as it appears that, unlike He and Ne, the heavier noble gases can pass through the subduction barrier (Sarda, 2004). Alternatively, future improvements in analytical precision may reveal a difference between atmospheric and mantle $^{38}\text{Ar}/^{36}\text{Ar}$ ratios.

Figure 12.8 shows $^{40}\text{Ar}/^{36}\text{Ar}$ plotted against $^{20}\text{Ne}/^{22}\text{Ne}$. The variation within individual sample suites largely reflects atmospheric contamination. Argon constitutes 0.93% of the atmosphere, so atmospheric contamination is a particularly important issue in assessing the Ar isotopic composition of the Earth's interior. Consequently, it is generally the maximum value observed in a suite of analyses of sample that is of greatest interest, but even the maximum ratio might reflect the effects of contamination. One approach, used by, for example, Moreira et al. (1998)

and Mukhopadhyay (2012), is to assume that the magmatic end-member has a solar $^{20}\text{Ne}/^{22}\text{Ne}$ ratio (assumed by them to be 13.6; subsequent measurements show it to be 13.78). A mixing hyperbola can then be fitted to the data to determine the $^{40}\text{Ar}/^{36}\text{Ar}$ ratio at $^{20}\text{Ne}/^{22}\text{Ne}$ ratio = 13.6. As Figure 12.8 shows, in the Iceland case this value is 10,750 while in the MORB case it is 44,000. In the MORB case, the value estimated in this way is close to the maximum value observed in MORB (40,000; Burnard et al., 1998). Ballentine et al. (2008) inferred a similar value for the mantle end-member of CO₂ well gas⁵ from the Bravo Dome of northeast New Mexico, USA. In the Iceland case, the estimated $^{40}\text{Ar}/^{36}\text{Ar}$ is somewhat higher than any value observed in Iceland or any other oceanic island (8340 from Loihi, Hawaii). Of course, the magmatic end-member could have lower $^{20}\text{Ne}/^{22}\text{Ne}$ than the solar value, so this

approach gives the maximum $^{40}\text{Ar}/^{36}\text{Ar}$. Nevertheless, it is clear then that there is a quite significant difference in $^{40}\text{Ar}/^{36}\text{Ar}$ between the MORB and OIB reservoirs (we should note that neither, however, is likely to have a homogeneous $^{40}\text{Ar}/^{36}\text{Ar}$ ratio). The difference is consistent with the inference made already from He and Ne isotopes that the MORB source reservoir appears to be more degassed than the OIB one and Ar in the MORB source reservoir is more dominated by the radiogenic component.

Ratios of K, U, and Th concentrations vary to only a limited extent in most terrestrial reservoirs, with K/U \sim 13,000 and Th/U \sim 4. Consequently, we would expect the production rates of $^4\text{He}/^{40}\text{Ar}$ to be similar in such reservoirs. The production ratio has, however, increased over time due to the short half-life of ^{40}K relative to ^{238}U and ^{232}Th , so that for a given K/U and Th/U ratio in a closed system, the $^4\text{He}^*/^{40}\text{Ar}^*$ ratio is a function of age, increasing from \sim 1.7 for a reservoir the age of the Solar System to a present production rate of 4.65. In principle then, the $^4\text{He}^*/^{40}\text{Ar}^*$ ratio could be used to deduce either the length of time the system has been closed if a fixed K/U ratio is assumed or the K/U ratio if a reservoir age is assumed. Unfortunately, however, as is true of He/Ne ratios, fractionation during and after eruption and degassing can change the He/Ar ratio and MORB and OIB show a large range of values. The two samples with best-preserved initial gas contents, the DICE 10 sample from Iceland and the 2BD43 sample from the Mid-Atlantic Ridge, have $^4\text{He}^*/^{40}\text{Ar}^*$ ratios of \sim 2.5 and \sim 1.5, respectively in release fractions with the highest $^{20}\text{Ne}/^{22}\text{Ne}$ ratios. Assuming, questionably, that these values actually represent those of the mantle, Iceland values would be consistent with a reservoir age of \sim 2.5 Ga, while the MORB values suggest a reservoir age close to that of the Solar System. Alternatively, the lower MORB values could reflect a higher K/U ratio. Using the value of 19,000 that Arevalo et al. (2009) calculated for average MORB, the reservoir age decreases to 3 Ga. However, White and Klein (2013) and Gale et al. (2013) calculated lower K/U ratios of 16,500 and 12,300, respectively. Hanyu et al. (2011) found that basalts from the Australs have $^4\text{He}^*/^{40}\text{Ar}^*$ ratios in the least fractionated release fractions of 10–15. Assuming a

reservoir age of \sim 2 Ga, this implies a much lower K/U ratio of \sim 3000. These samples also have low $^{40}\text{Ar}/^{36}\text{Ar}$ (<2000) compared to other OIB and MORB. Assuming coherent behavior between the alkalis Rb and K, the low K/U ratio would be consistent with the low $^{87}\text{Sr}/^{86}\text{Sr}$ and high $^{206}\text{Pb}/^{204}\text{Pb}$ observed in these basalts. We should be cautious, however, not to conclude too much from $^4\text{He}^*/^{40}\text{Ar}^*$ ratios – firm inferences can be made only for closed systems, which mantle reservoirs certainly are not (indeed, we found in Chapter 6 that the MORB source reservoir is perhaps better treated as an open system). Perhaps the only useful inferences are that these reservoirs are old and the HIMU reservoir – the source of Australs basalts, has a lower K/U than other reservoirs.

12.5 KRYPTON

Krypton has six stable isotopes: ^{78}Kr , ^{80}Kr , ^{82}Kr , ^{83}Kr , ^{84}Kr , and ^{86}Kr . The two lightest together constitute less than 3% of Kr; ^{84}Kr is the most abundant (57%) and the remaining isotopes have abundances between 11 and 17%. There is some production of ^{86}Kr by fission of ^{238}U and ^{244}Pu (1% and 0.1% yields, respectively, compared to respective ^{136}Xe yields of 6.3% and 5.6% for fission of these nuclides). ^{84}Kr is also produced by fission, but the yield is seven times lower than that of ^{86}Kr . Krypton isotopic variations resulting from such fission have so far only been resolved in U-rich minerals. Krypton isotopic compositions of oceanic basalts are not resolvably different, perhaps due to atmospheric contamination, but Holland et al. (2009) reported Kr isotopic variations in well gas from the Bravo Dome, NM in the southwestern USA. The well gas Kr isotope ratios differ from the atmospheric value (Figure 12.9), and the difference can't entirely be attributed to nuclear processes (the data shown have been corrected for production by U-fission in the crust). The well gas is variably contaminated by the atmosphere so that the data define a mixing line between air and a component that is more similar to Kr in carbonaceous chondrites. As Figure 12.9 indicates, Kr in carbonaceous chondrites is isotopically “heavy” relative to the solar wind and the difference appears to be consistent with mass-dependent fractionation. However, the atmosphere lies off the

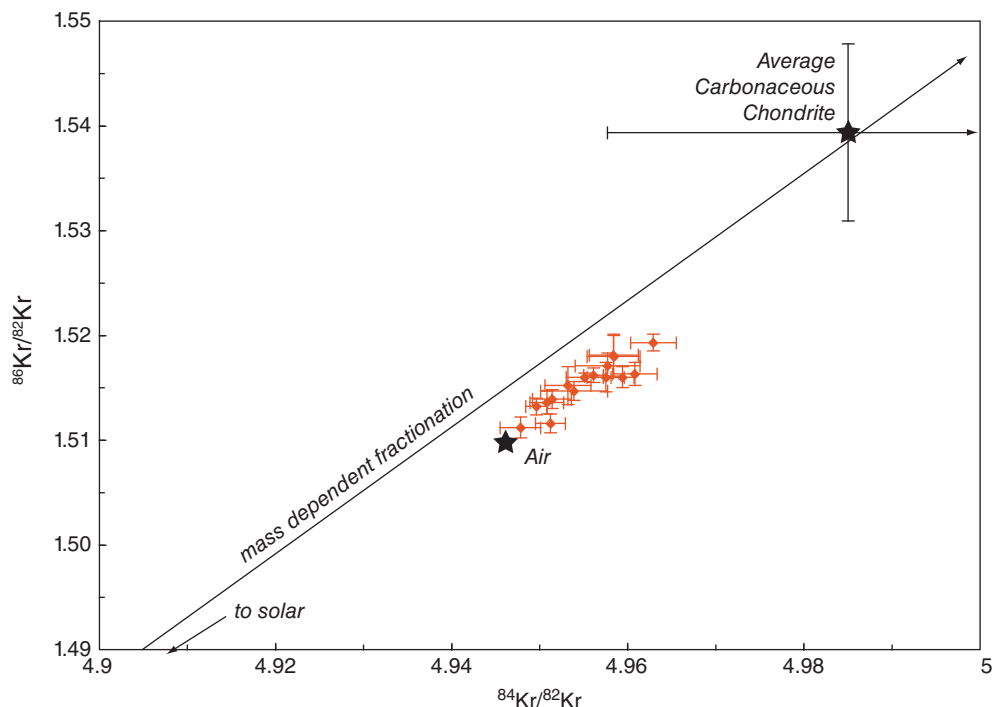


Figure 12.9 Kr isotopic composition of the atmosphere and well gas from the Bravo Dome, NM (data from Holland et al., 2009). This data is corrected for U fission in the crust. Average carbonaceous chondrites lie close to a mass-dependent fractionation line from the composition of solar wind. (Source: Data from Holland et al. 2009.)

mass-dependent fractionation line for reasons that are unclear (correcting for fissogenic production would shift the atmosphere even further from the mass dependent fractionation line). As we have seen, Ne in the atmosphere and chondrites is also fractionated relative to the solar wind. Interestingly, while mantle Ne is more similar to solar Ne than is the atmosphere, the reverse is true for Kr: mantle Kr plots away from the solar value and is more similar to planetary Kr.

12.6 XENON

Xenon has nine stable isotopes: ^{124}Xe , ^{126}Xe , ^{128}Xe , ^{129}Xe , ^{130}Xe , ^{131}Xe , ^{132}Xe , ^{134}Xe , and ^{136}Xe , of which several are produced by decay of extant and extinct radionuclides and as such its isotopic composition is particularly rich in information about Earth's history. Unfortunately, xenon presents an even more difficult analytical challenge than the other noble gases for several reasons. First, its concentration is far lower. The usual normalizing Xe isotope, ^{130}Xe , is 2 to 3 orders of

magnitude less abundant than ^3He and ^{22}Ne and 3 to 4 orders of magnitude less abundant than ^{36}Ar . Furthermore, while He and Ar isotope ratios vary by an order of magnitude and more, Xe isotopic variations are in the percent to tens of percent range, requiring higher precision analysis. Finally, Xe turns out to be a very “stubborn” gas, readily absorbing onto walls of sampling vessels and analytical equipment, greatly complicating analysis. Additionally, as is the case for Ne and Ar, atmospheric contamination is virtually ubiquitous. One consequence of this is that there are far fewer data on Xe isotopes than on the other noble gases, although with analytical advances these data are becoming more common.

The two lightest Xe isotopes, ^{124}Xe and ^{126}Xe , each constitute only about 0.09% of Xe; ^{128}Xe constitutes only 1.9%. These three, together with ^{130}Xe (4.1%), are the only Xe isotopes not significantly produced by nuclear processes. The atmosphere is depleted in the light non-radiogenic Xe isotopes relative to the solar wind (Figure 12.10). The extent of depletion is correlated with mass:

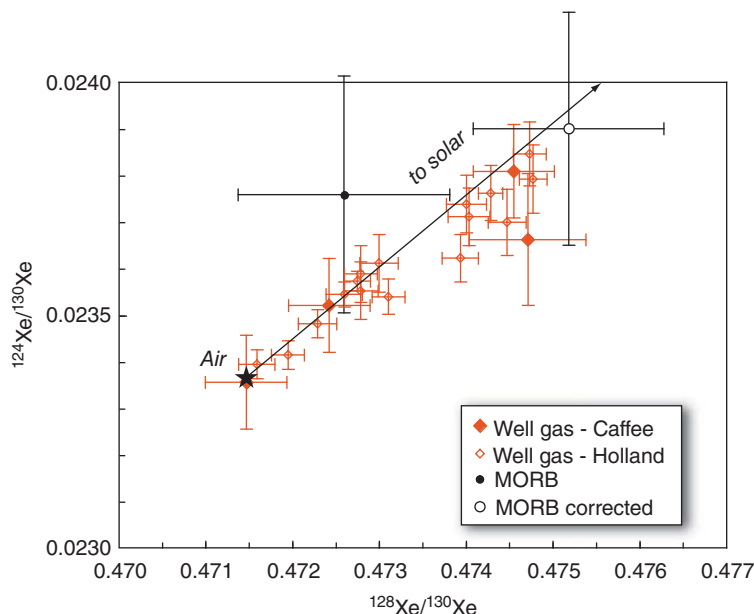


Figure 12.10 $^{124}\text{Xe}/^{130}\text{Xe}$ and $^{128}\text{Xe}/^{130}\text{Xe}$ in CO_2 well gases from the western US (Sheep Mountain and McElmo Dome, CO and Bravo Dome, NM) and Caroline, Australia from Caffee et al., (1999) and Holland et al. (2009) and the average of 32 analyses of gas-rich MORB from the Mid-Atlantic Ridge (Kunz et al., 1998). Both solar and chondritic Xe plots are above and to the right of the graph (arrow). The open black circle is Pepin and Porcelli's (2006) recomputed average of the Kunz et al. MORB data that excludes the least reliable analyses. The McElmo Dome sample has an atmospheric composition; the remaining samples have compositions that are more “solar” in character than air. The isotopic difference between air and solar is consistent with mass-dependent fractionation.

^{124}Xe is about three times more depleted relative to ^{130}Xe than is ^{128}Xe ; consequently mass-dependent fractionation is the suspected cause, as it was with the other noble gases. Unfortunately, because of their very low abundance, the lightest Xe isotopes are rarely included in analyses. ^{124}Xe and ^{128}Xe data from the Earth’s interior that does exist, data from CO_2 well gases and from a few particularly gas-rich MORB samples, indicates that Xe in the Earth’s interior is not as light isotope-depleted as the atmosphere (Figure 12.10). Because both the well and MORB gas are probably somewhat contaminated by atmospheric Xe, the true mantle isotope ratios may be more “solar” in composition than the analyzed compositions. Again, this is the same as we observe for Ne.

The remaining Xe isotopes have relative abundances of 9% or more and are more easily analyzed, at least by comparison. Even in the most gas-rich submarine lavas concentrations only reach 10^{-11} cc STP/g. All are affected by nuclear processes: ^{129}Xe is

the product of the extinct radionuclide ^{129}I (half-life 15.7 Ma) while ^{131}Xe through ^{136}Xe are the products of spontaneous fission of ^{238}U and ^{244}Pu . As we found in Chapter 5, ^{129}Xe excesses were discovered in meteorites in 1960; a few years later Butler et al. (1963) reported excess ^{129}Xe relative to atmospheric Xe in Bravo Dome CO_2 well gas, which they attributed to decay of ^{129}I in the early Earth. They stated what, at the time, was a surprising conclusion: “This would mean that outgassing of the Earth’s interior is incomplete and that ... ^{129}Xe and possibly other daughter products are presently being added to the Earth’s atmosphere and upper crust.” Subsequently, Staudacher and Allègre (1982) reported elevated $^{129}\text{Xe}/^{130}\text{Xe}$ in MORB relative to the atmosphere, demonstrative that the convecting mantle has a different Xe isotopic composition from the atmosphere. Since the half-life of ^{129}Xe is only ~16 Ma, the difference between the atmospheric and mantle $^{129}\text{Xe}/^{130}\text{Xe}$ ratio must have been established very early in Earth’s history, within at most the

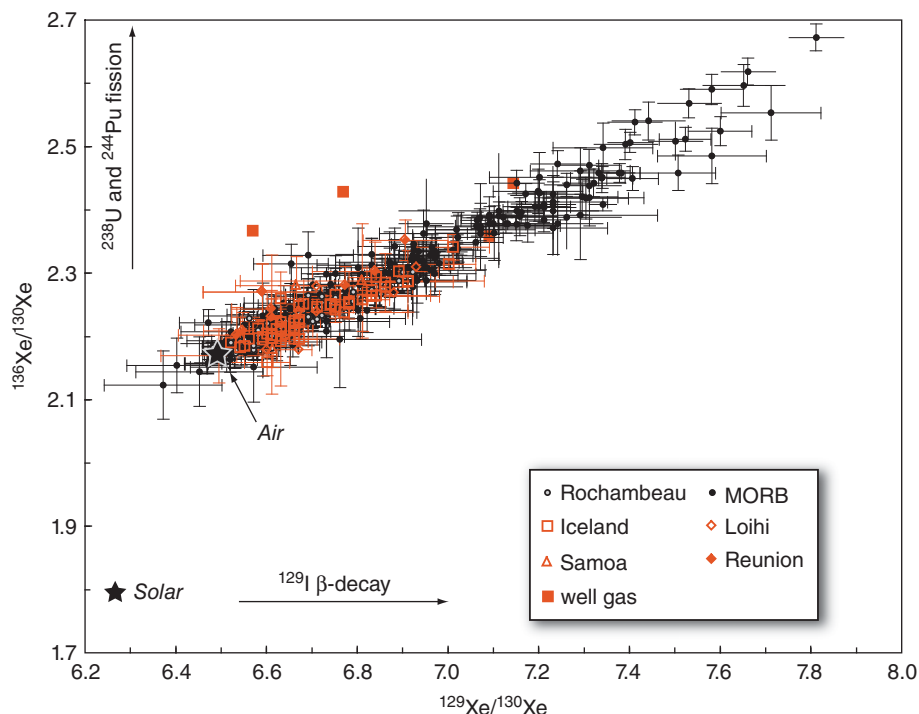


Figure 12.11 $^{129}\text{Xe}/^{130}\text{Xe}$ and $^{136}\text{Xe}/^{130}\text{Xe}$ in mantle-derived rocks and well gases. The MORB and OIB data are well correlated. Excesses in MORB are typically greater than observed in OIB. Two of the well gases (Caroline, Australia and Bravo Dome, MN, USA) fall off the trend, probably due to a contribution of crustal uranogenic ^{136}Xe . Uncertainties in the well gas data are smaller than the symbol.

first 100 Ma. Although they (Staudacher et al., 1986) failed to find excess ^{129}Xe in xenoliths from Hawaii and Reunion, many subsequent studies of OIB and related xenoliths clearly demonstrate excess ^{129}Xe in OIB sources (e.g., Poreda and Farley, 1992; Trieloff et al, 2000). However, maximum $^{129}\text{Xe}/^{130}\text{Xe}$ ratios in OIB are invariably lower than those found in MORB (Figure 12.11); that in turn implies OIB are derived from a source that had a lower $^{129}\text{I}/^{130}\text{Xe}$ ratio than MORB. This is consistent with the conclusion drawn from the other noble gas that the OIB source is less degassed than the MORB one. This difference must have been established very early in Earth's history, given the 15.7 Ma half-life of ^{129}I .

Excesses in the heavy Xe isotopes relative to atmospheric, attributed to ^{238}U fission, were recognized in U-bearing minerals in the late 1940s and also in well gas by Butler et al. (1963). Staudacher and Allègre (1982) reported excesses of $^{134}\text{Xe}/^{130}\text{Xe}$, and $^{136}\text{Xe}/^{130}\text{Xe}$ in MORB relative to the atmosphere and subsequent studies have confirmed

these excesses in both MORB and OIB, as is shown in Figure 12.11, confirming fissogenic Xe in the Earth's mantle. Staudacher and Allègre claimed some of the excess in the heavy Xe isotopes was due to decay of extinct ^{244}Pu (half-life: 82 Ma), since these anomalies correlate with $^{129}\text{Xe}/^{130}\text{Xe}$. However, discriminating the ^{244}Pu fission contribution from that of ^{238}U is difficult. Ratios of fission yields for ^{238}U are $^{131}\text{Xe}/^{132}\text{Xe} = 0.155 \pm 0.006$, $^{134}\text{Xe}/^{132}\text{Xe} = 1.458 \pm 0.033$, and $^{136}\text{Xe}/^{132}\text{Xe} = 1.76 \pm 0.033$, with the absolute yield for ^{132}Xe being $3.6 \pm 0.4\%$. The branching ratio of fission relative to total decay of ^{238}U is $\lambda_{sf}/\lambda_{238} = 5.45 \times 10^{-7}$ (in other words, almost all decays occur through α -decay; less than one in a million decays occur through fission). Fission yields for ^{244}Pu are $^{131}\text{Xe}/^{132}\text{Xe} = 0.278 \pm 0.017$, $^{134}\text{Xe}/^{132}\text{Xe} = 1.041 \pm 0.016$, and $^{136}\text{Xe}/^{132}\text{Xe} = 1.12 \pm 0.016$ with an absolute yield of ^{132}Xe of $5 \pm 0.4\%$ and a branching ratio $\lambda_{sf}/\lambda_{244} = 1.25 \times 10^{-3}$. Although the chondritic initial $^{244}\text{Pu}/^{238}\text{U}$

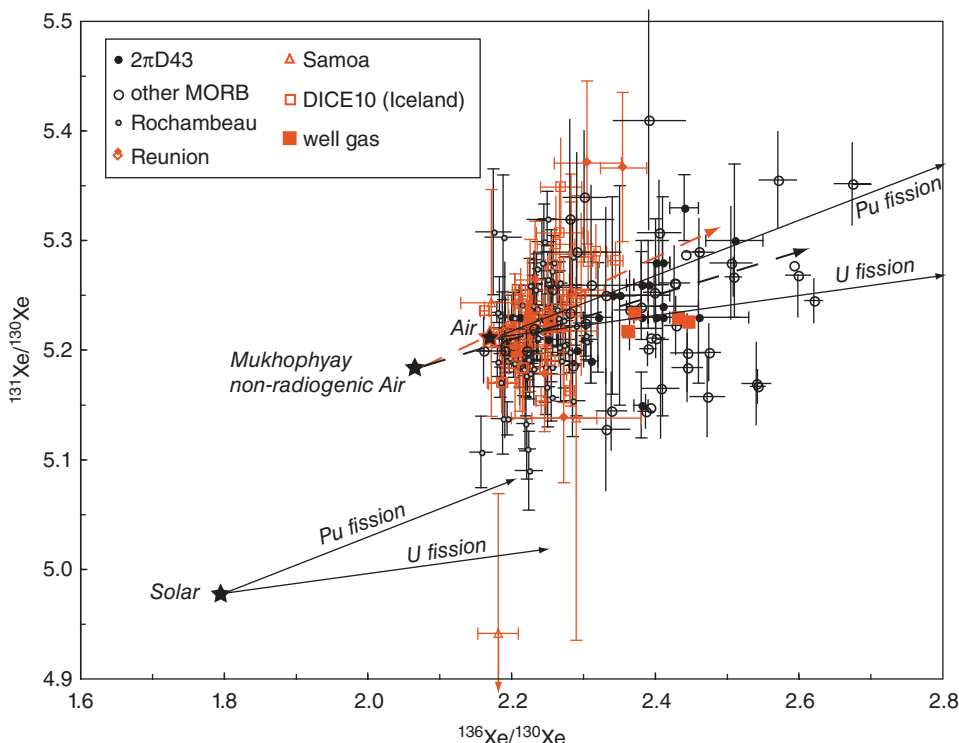


Figure 12.12 $^{131}\text{Xe}/^{130}\text{Xe}$ and $^{136}\text{Xe}/^{130}\text{Xe}$ in mantle-derived rocks and well gases. Solid arrows show the isotopic evolution of solar and atmospheric Xe resulting from ^{244}Pu and ^{238}U fission. Dashed black and red arrows show the regression slopes calculated by Mukhopadhyay (2012) for MORB sample 2πD43 and Icelandic sample DICE10, respectively.

ratio was low (~ 0.0068 ; Table 5.1), the higher branching ratio and yield means that in a chondritic reservoir, ^{244}Pu would produce about 30 times as much Xe as ^{238}U over the history of the Solar System. Given that the ^{244}Pu half-life is significantly longer than that of ^{129}Xe , its certainly reasonable to expect it was present in the early Earth, but that existence cannot be established from ^{136}Xe and ^{134}Xe excesses alone.

The biggest difference in fissogenic production is between ^{136}Xe and ^{131}Xe : ^{244}Pu produces relatively less ^{136}Xe and more than twice as much ^{131}Xe than ^{238}U . Based on precise analyses of $^{131}\text{Xe}/^{130}\text{Xe}$ and $^{136}\text{Xe}/^{130}\text{Xe}$ in the so-called “popping rock,”⁶ Kunz et al. (1988) were able to more clearly demonstrate a ^{244}Pu fissogenic component in the MORB source. They inferred that ^{244}Pu fission accounts for about 30% of the fissogenic xenon excesses in the mantle. Subsequent high-precision studies tend to confirm a contribution from ^{244}Pu , as is shown in

Figure 12.12. While this figure clearly suggests a component of Xe from Pu fission, deconvolving ^{238}U and ^{244}Pu is problematic for several reasons. First, all samples most likely contain an atmospheric component. Second, as Figure 12.10 shows, atmospheric Xe is fractionated relative to both mantle Xe and solar Xe; furthermore, atmospheric Xe contains a radiogenic component derived from degassing of the Earth’s interior. Thus determining the primordial, non-radiogenic mantle Xe isotopic composition is problematic. Finally, analytical errors are relatively large and there is consequently considerable scatter in the data.

Several studies have attempted to deconvolve the various components in the mantle Xe between primordial, atmospheric, Pu fissogenic, and U fissogenic, but some assumptions are inevitably required and the results vary with the assumptions made. For example, Kunz et al. (1988) assume an initial Xe isotopic composition of the mantle that can be

derived from the $^{129}\text{Xe}/^{130}\text{Xe}$ - $^{136}\text{Xe}/^{130}\text{Xe}$ and $^{131}\text{Xe}/^{130}\text{Xe}$ - $^{136}\text{Xe}/^{130}\text{Xe}$ correlations observed in MORB (e.g., Figures 12.11 and 12.12). Effectively, this assumes no “solar” Xe component in the mantle. From this, they concluded that $32 \pm 10\%$ of the ^{136}Xe excess in MORB relative to the atmosphere was derived from ^{244}Pu decay. Caffee et al. (1999), however, use the $^{124}\text{Xe}/^{130}\text{Xe}$ - $^{128}\text{Xe}/^{130}\text{Xe}$ variation in well gas (Figure 12.10) to argue for a more “solar” initial Xe isotopic composition for the mantle and calculate that 41% of the ^{136}Xe in MORB is derived from Pu fission. Comparing the “popping rock” from the Mid-Atlantic Ridge with subglacial Iceland sample DICE 10, Mukhopadhyay (2012) showed that analyses from the Icelandic sample fell along a higher $^{131}\text{Xe}/^{130}\text{Xe}$ and $^{136}\text{Xe}/^{130}\text{Xe}$ slope than did analyses from the MORB sample; these are shown in Figure 12.12. The scatter in the data is considerable, but Mukhopadhyay found the difference was significant at the 99% confidence level. He calculated that 5–43% of the ^{136}Xe in MORB was produced by ^{244}Pu fission, depending on the initial composition assumed. Regardless of the initial composition assumed, he calculated the Icelandic sample had significantly greater amounts, 47–99%, of ^{136}Xe derived from ^{244}Pu fission. This result is consistent with the idea drawn from other noble gases that the Iceland source, as well as other OIB sources, is less degassed than the MORB source because while ^{238}U has continued to produce ^{136}Xe throughout Earth’s history, ^{136}Xe derived from ^{244}Pu would have been produced only in the first few hundred million years of Earth’s history.

Data on other MORB samples, particularly MORB from the equatorial Mid-Atlantic Ridge analyzed by Tucker et al. (2012) show considerably more scatter, plotting both well above and below the $2\pi\text{D43}$ regression line, implying variable contributions from ^{244}Pu and ^{238}U fission and perhaps less distinction between the MORB and OIB sources. Tucker et al. (2012) also found that those MORB that contain a HIMU component (Chapter 6) based on radiogenic Pb isotopic compositions, appears to have less radiogenic ^{129}Xe and ^{244}Pu -derived ^{136}Xe than other MORB. They argued that this reflects a larger component recycled from the surface (through subduction) in the HIMU reservoir than in other

ones, consistent with $^3\text{He}/^4\text{He}$ ratios lower than MORB observed in HIMU OIB.

Analytical technology has only recently enabled Xe isotopic analyses of sufficient precision to resolve the effects of radioactive decay and mass-dependent fractionation. Thus there is reason to believe this field will advance particularly rapidly in the coming years.

12.7 IMPLICATIONS OF NOBLE GAS ISOTOPE RATIOS FOR THE ORIGIN AND EVOLUTION OF THE EARTH

Noble gases provide particularly useful constraints on two aspects of the Earth: the nature and relationship of chemical reservoirs in the mantle and Earth’s formation and earliest history. In this section we’ll summarize those constraints and the theories that have been developed to explain them. It goes without saying that these theories must also take into account other chemical and physical information about the Earth and about noble gases in the Solar System. Table 12.3 summarizes the *inferred* noble gas isotopic compositions of the atmosphere and the principal mantle reservoirs, namely the upper mantle, that gives rise to MORB and the OIB source reservoir, which we infer to be the source of mantle plumes and located in the deep mantle. For comparison, Table 12.3 also lists solar and chondritic noble gas isotope ratios from Table 12.2. As we discussed in Section 12.1.2, noble gases are isotopically heterogeneous in chondritic meteorites, and furthermore, meteorites differ in noble gas isotopic composition from the solar wind. Consequently, unlike the elements we considered in previous chapters, it is not possible to readily infer the noble gas isotopic composition of the primitive Earth. Indeed, as we shall see, the primitive Earth may well have been an isotopically heterogeneous mix of solar and planetary components, and some of the isotopic variation we observe today may still reflect that initial isotopic heterogeneity.

12.7.1 Mantle reservoirs of noble gases in the modern Earth

We begin by noting that, in Table 12.3 and following discussion, the terms “upper mantle” and “deep mantle” do not necessarily correspond to seismically defined regions. For example, the seismically defined “upper mantle” is the region above the 660 km

Table 12.3 Noble gas isotopic composition of terrestrial and other reservoirs.

	Air	Upper Mantle	Deep Mantle	Solar	C. Chondrites (Q)
${}^3\text{He}/{}^4\text{He}$ (R/R _A)	≡ 1	8.8 ± 2.5	5–50	334	120
${}^{21}\text{Ne}/{}^{22}\text{Ne}$	0.0296	0.06*	0.042*	0.0329	0.0294
${}^{20}\text{Ne}/{}^{22}\text{Ne}$	9.8	12.75*	13*	13.78	10.7
${}^{40}\text{Ar}/{}^{36}\text{Ar}$	298.56	$\sim 40,000^\ell$	8000–12000 $^\ell$	$3 \times 10^{-4\dagger}$	~ 0.78
${}^{38}\text{Ar}/{}^{36}\text{Ar}$	0.1876	0.1896 ± 0.0031	0.1882 ± 0.0007	0.1828	0.1880
${}^{84}\text{Kr}/{}^{82}\text{Kr}$	4.946	4.963 ‡	—	4.882	4.955
${}^{86}\text{Kr}/{}^{82}\text{Kr}$	1.51	0.152 ‡	—	1.476	1.534
${}^{124}\text{Xe}/{}^{130}\text{Xe}$	0.0234	0.0239 ‡	—	0.0293	0.0281
${}^{128}\text{Xe}/{}^{130}\text{Xe}$	0.4715	0.4752 ‡	—	0.5083	0.5077
${}^{129}\text{Xe}/{}^{130}\text{Xe}$	6.50	7.81*	7.00*	6.286	6.436
${}^{131}\text{Xe}/{}^{130}\text{Xe}$	5.21	5.41*	5.35*	4.996	5.056
${}^{132}\text{Xe}/{}^{130}\text{Xe}$	6.61	7.01*	6.76*	6.047	6.177
${}^{136}\text{Xe}/{}^{130}\text{Xe}$	2.176	2.55*	2.674*	1.797	1.954

“Upper Mantle” based on data from MORB and well gas.

“Lower Mantle” based on data from OIB and large igneous provinces.

* Maximum observed or inferred value.

‡ Maximum observed or inferred value.

$^\ell$ Air, solar and chondritic values from Table 12.2.

† Maximum observed value in Bravo Dome well gas.

velocity discontinuity. Our geochemically defined “upper mantle” likely includes that region (less the continental lithosphere), but it may extend much deeper. Our geochemically defined “deep mantle” is the source region of mantle plumes, but it may constitute only a part of the seismically defined lower mantle. We also note that both these reservoirs may be internally heterogeneous and as such the values listed in Table 12.3 may only be typical ones.

Comparing noble gas isotope ratios of the mantle reservoirs in Table 12.3, we see that the upper mantle is generally enriched in isotopes produced by radioactive decay or other nuclear processes: ${}^4\text{He}$, ${}^{21}\text{Ne}$, ${}^{40}\text{Ar}$, ${}^{129}\text{Xe}$, and the heavy fissogenic Xe isotopes. The simplest way to explain all these differences is that the upper mantle has lost more of its initial inventory of noble gases than the deep mantle; that is, it has experienced a greater extent of degassing so that the radiogenic isotopes are more dominant. An alternative interpretation is that He and other noble gases are less incompatible, that is, partition less readily into the melt, than U and Th and therefore that melt extraction decreases the (U+Th)/He and K/Ar ratios and consequently melt-depleted mantle should have higher ${}^3\text{He}/{}^4\text{He}$ than more primitive mantle. Recent experimental work shows that this is indeed a possibility (e.g., Heber et al., 2007). Further, it demonstrates that extraction of noble gases during melting

is incomplete; implying that subduction of recycled oceanic lithosphere need not have extremely low ${}^3\text{He}/{}^4\text{He}$. Thus, the lower mantle could retain relatively high ${}^3\text{He}/{}^4\text{He}$ despite a flux of subducted oceanic crust into it (e.g., Albarède, 1998; Gonnerman and Mukhopadhyay, 2009). Nevertheless, the coincidence of melt-depleted Sr, Nd, and Hf signatures with degassed He, Ne, Ar, and Xe signatures in MORB do suggest melt removal is an important mechanism of degassing. Further, as we discuss next, Xe isotope data limit how much recycled material could be present in the relatively undegassed deep mantle reservoir.

There are some exceptions to this pattern of difference between MORB and OIB: most notably, “HIMU”-type OIB (Chapter 6) tend to have lower ${}^3\text{He}/{}^4\text{He}$ ratios than MORB. The Australs, the only HIMU islands for which Ne and Ar data are available, also have more nucleogenic Ne than MORB, as well as relatively low ${}^{20}\text{Ne}/{}^{22}\text{Ne}$ and low ${}^{40}\text{Ar}/{}^{36}\text{Ar}$ ratios (although the latter in particular could just reflect atmospheric contamination). Low ${}^3\text{He}/{}^4\text{He}$ is also observed in Tristan da Cunha and appears to be present, along with higher ${}^3\text{He}/{}^4\text{He}$ values, in basalts from other islands such as the Azores and Pitcairn. As we found in Chapter 6, there is clear evidence of a recycled component in at least some OIB, and this could well explain the examples of low ${}^3\text{He}/{}^4\text{He}$ because we expect material recycled from the surface to be thoroughly degassed. It

may also explain the relatively low $^{40}\text{Ar}/^{36}\text{Ar}$ because it appears that atmospheric heavy rare gases can be subducted and recycled into the mantle (Sarda, 2004).⁷ Thus, the source of OIB appears to be heterogeneous (an inference supported by isotope ratios we considered in Chapter 6), and includes both more primitive, relatively undegassed material as well as components recycled from the surface. Here we will focus on primarily on the less degassed, relatively primitive component.

The high $^3\text{He}/^4\text{He}$ ratio in many OIB has long been cited as evidence that the OIB reservoir is located in the deep mantle on the simple logic that a deep mantle, being furthest from the surface, is least likely to experience degassing (e.g., Kurz et al., 1982). There have been a variety of ideas of just what this gas-rich reservoir is and how big it is, its composition and extent of degassing. Allègre et al. (1986) and Porcelli and Wasserburg (1995) assume mass fractions of $\frac{2}{3}$ and $\frac{3}{4}$, respectively, essentially equating it with the seismically defined lower mantle (i.e., region below 660 km). Tolstikhin and Hofmann (2005) assume a much smaller volume, namely the lowermost 200 km region of the mantle known as D' (D-double-prime). In the Tolstikhin and Hofmann model D' slowly supplies noble gases to overlying mantle plume sources through diffusion and convective entrainment.

Porcelli and Halliday (2001), among others, have suggested the core may be a major reservoir of noble gases, He in particular, which then leak into the lower mantle. This idea depends on how noble gases partition between silicate and metal liquids. Relatively low-pressure experiments by Matsuda et al. (1993) suggest the partition coefficients are low, but preliminary diamond anvil experiments at higher pressures by Jephcoat et al. (2008) suggest the possibility of much higher partition coefficients. Regardless, if the core formed in the presence of a dense, primitive atmosphere, then the gas pressures may have been sufficiently high that some significant amount of gas could still be incorporated into the core even partition coefficients are low. Since the core should have low concentrations of radioactive parents, U, Th, and K, any noble gases in the core can be expected to have near-primordial isotopic compositions. One exception is iodine, which recent experiments

suggest has a metal/silicate partition coefficient greater than 1 (Armytage et al., 2013), which would lead to high $^{129}\text{Xe}/^{130}\text{Xe}$ ratios in the core. At this point, all that can be said is that the possibility that the core is a significant reservoir of noble gases is speculative, but one that cannot presently be ruled out.

12.7.1.1 *He, Ar, and Ne Budgets*

Noble gas budgets present a far more difficult challenge than those for lithophile elements for several reasons. First, as we earlier noted, chondrites provide no strong constraints on either isotopic compositions or concentrations in the bulk Earth. Second, degassing and atmospheric contamination badly degrades information in both basalts and xenoliths (the mantle sample) and even well gases. However, since the concentrations of K, U, and Th are at least somewhat constrained in the Earth and mantle, we can estimate the production rates and inventories of the radiogenic and nucleogenic daughters, ^{40}Ar , ^4He , and ^{21}Ne . In the case of argon, we also know how much ^{40}Ar is in the atmosphere and, as we previously noted, most of this is radiogenic. We can use this in a mass balance calculation to estimate how much Ar has been lost from the mantle. Because the He is lost from the atmosphere, we cannot do a similar mass balance, but the rate at which He is lost from the mantle to the atmosphere provides some useful constraints. Because the production of ^4He and ^{21}Ne are closely linked, we can also place constraints on the Ne budget. We'll begin by considering the Ar mass balance, then examine the He and Ne budgets.

^{40}Ar mass balance (e.g., Allègre et al., 1986; 1996) constrains the mass of the mantle that has been degassed. Exact concentrations are difficult to know, except in the atmosphere, so these are “back of the envelope” calculations; the results are nonetheless instructive. For example, assuming a bulk silicate Earth K concentration of 240 ppm (McDonough and Sun, 1995), we can calculate that 3.34×10^{18} moles of radiogenic ^{40}Ar have been produced in the Earth over the last 4.5 Ga. The atmosphere contains 1.69×10^{18} moles of ^{40}Ar , which is essentially entirely radiogenic. This implies that ~51% of the radiogenic ^{40}Ar is in the atmosphere. Using the Rudnick and Gao (2003) estimate of 1.8% K_2O in the

continental crust and assuming a mean K/Ar age of the crust of 1 Ga, we can calculate that there should be 7.56×10^{16} moles ^{40}Ar in the crust, or only a little over 2% of the Earth's budget. Using other estimates of the crustal K concentration and perhaps a somewhat older K-Ar age of the crust, we might be able to increase the amount of ^{40}Ar in the crust to 4 or 5%, but no more. Thus, under these assumptions more than 45% of the radiogenic Ar must be in the mantle.

We can change these numbers somewhat by changing assumptions. For example, Lyubetskaya and Korenaga (2007) estimate the bulk silicate Earth K concentration at only 190 ppm. Such a lower concentration would be consistent with the collisional erosion hypothesis we discussed in Chapter 6 to explain the Earth's non-chondritic $^{142}\text{Nd}/^{144}\text{Nd}$. This implies a ^{40}Ar inventory in the Earth of $2.64 \times 10^{18}\text{M}$, of which 64% would be in the atmosphere and 2.8% in the crust, leaving ~33% in the mantle.

Now let's calculate how much of this ^{40}Ar could be in the "upper mantle" (i.e., MORB source) reservoir. One way to approach this is to note that the ^3He flux into the oceans from mid-ocean ridge volcanism is 527 mole/yr. Using the average MORB $^4\text{He}/^3\text{He}$ of 82,100, this is 4.33×10^7 ^4He moles/yr. If we assume a $^4\text{He}^*/^{40}\text{Ar}^*$ production rate of 2 (corresponding to a reservoir age of ~2 Ga, then the ^{40}Ar flux from oceanic crust creation is 2.17×10^7 mole/yr (essentially all ^4He and ^{40}Ar in MORB is radiogenic). The oceanic crust production rate is $20\text{ km}^3/\text{yr}$ and assuming a density of 2800 kg/m^3 , this translates to $5.6 \times 10^{16}\text{g/yr}$. From this we calculate a ^{40}Ar concentration of $3.86 \times 10^{10}\text{mole/g}$ in the magma. Assuming MORB is produced by 10% melting of the mantle, this implies a mantle concentration of an order of magnitude lower, or about $3.86 \times 10^{-11}\text{mole/g}$. If the MORB source occupies only mantle above the 660 km discontinuity, this would amount to 4.17×10^{16} moles or only about 1.3 to 1.6% of the Earth's total $^{40}\text{Ar}^*$, depending on the assumed K concentration. If the MORB source occupies the entire mantle, this amounts to 1.55×10^{17} moles or about 4.6 to 5.9% of the Earth's Ar inventory. An alternative approach is to use the concentrations in the popping rock measured by Moreira et al.

(1998), which was about $1.4 \times 10^{-9}\text{moles/g}$ ^{40}Ar . Using the same 10% melting assumption, this implies the upper mantle contains 4.5–5.7% of the Earth's ^{40}Ar . If the entire mantle has this concentration, it represents 16.8–21.2% of the Earth's inventory.

In summary, it appears that a significant fraction of the radiogenic ^{40}Ar must be stored in mantle reservoir (an observation first made by Damon and Kulp, 1958), and much of this in a reservoir having a substantially higher ^{40}Ar concentration than the depleted mantle. This reservoir is most likely located in the deep mantle. We can also ask how long has this ^{40}Ar been building up?, which is equivalent to asking what the K-Ar age of the mantle is. We can do this by solving equation 2.2 for t . The whole mantle has 2.64 to 3.34×10^{18} moles of ^{40}Ar , depending on which value of K concentration we use for the bulk silicate Earth (190 vs 240 ppm). Depending on whether we use these K concentrations, thus assuming an undepleted mantle composition, or subtract the amount in the crust (34 to 45% of the total), we calculate an age of between 3.95 Ga and 2.78 Ga. In other words, most of the degassing of the mantle occurred early in Earth's history. Since we know that some Ar is currently being lost through degassing at mid-ocean ridges and oceanic islands, this "age" likely underestimates the length of time that the reservoir containing the "missing Ar" has been accumulating the $^{40}\text{Ar}^*$.

It is also instructive to consider the budget for a non-radiogenic isotope such as ^{36}Ar . In this case, there is no easy way to estimate the ^{36}Ar content of the bulk silicate Earth, but we do know how much ^{36}Ar is in the atmosphere and we can estimate how much is in the MORB source. There are 5.73×10^{15} moles of ^{36}Ar in the atmosphere. Moreira et al. (1998) measured $1.79 \times 10^{-14}\text{moles/g}$ in the popping rock, which translates to a mantle concentration of $1.79 \times 10^{-15}\text{moles/g}$ assuming again 10% melting. At these concentrations, the mantle above the 660 km discontinuity would contain 1.93×10^{13} moles moles, or just 0.3% of the amount in the atmosphere. If this concentration characterizes the entire mantle, it still amounts to only 1.2% of the amount in the atmosphere. Since we have already concluded that at least part of the lower mantle must be less degassed than the MORB reservoir, its concentration is likely to

be higher, but nonetheless it would appear that the entire mantle has lost much of its inventory of non-radiogenic noble gas isotopes. Halliday (2013) estimates that 97% or more the Earth's ^{36}Ar inventory is in the atmosphere.

Turning to helium, it is interesting to compare the rate at which ^4He is being lost from the upper mantle to the rate at which it is being created. As we noted earlier, Bianchi et al. (2011) estimated the degassing flux at mid-ocean ridges at 527 M/yr ^3He . Using the average $^3\text{He}/^4\text{He}$ of 8.8 R/R_A ($^4\text{He}/^3\text{He} = 8.21 \times 10^4$), we calculate a ^4He flux of 4.33×10^7 . Provided we know its mass and uranium and thorium concentration, the rate at which ^4He is being produced is easily calculated as:

$$\frac{d^4\text{He}}{dt} = {}^{238}\text{U} \left\{ 8\lambda_{238} + 7\frac{{}^{235}\text{U}}{{}^{238}\text{U}}\lambda_{235} + 6\kappa\lambda_{232} \right\} M_R \quad (12.2)$$

where ${}^{238}\text{U}$ is the (molar) concentration and M_R is the reservoir mass, in this case the depleted mantle. Salters and Stracke (2004) estimated the U concentration of the depleted mantle as 4.7 ppb and κ as 2.91, which corresponds to a production rate of 1.8×10^{-19} moles/g/yr. Taking the mass of the depleted mantle as the seismically defined upper mantle (1.08×10^{27} g), the production rate is 1.94×10^{-8} moles/yr. In this case, the “degassing efficiency,” the ratio of loss to production is 22.3%. Workman and Hart estimated a lower U concentration for the depleted mantle (3.2 ppb), which would imply a degassing efficiency of 33%. Since the geochemical evidence is that subduction-related magmas are derived largely from depleted mantle, we should add to this number the flux from subduction zone volcanoes, which Porcelli and Ballentine (2002) estimate at 0.6 to 2.3×10^7 moles/yr, which would imply a degassing efficiency as high as 34%.

We can also use Eqn. 12.2 to calculate the total mantle radiogenic ^4He production. Using the McDonough and Sun (1995) U concentration of 20 ppb less the amount in the crust (1.3 ppm; Rudnick and Gao, 2003) and a mantle mass of 4×10^{27} g, this is 2×10^9 moles/yr. If we consider that degassing occurs only at mid-ocean ridges, then the degassing efficiency is 2.2%. This rises only to

2.8% if we use the bulk silicate Earth concentrations of Lyubetskaya and Korenaga (2007). Of course, volcanism elsewhere also degasses the mantle. Porcelli and Ballentine estimate that rate of degassing through oceanic island volcanism at 0.4 to 7.3×10^7 moles/yr. Considering all volcanic degassing, and using the Lyubetskaya and Korenaga (2007) U and Th concentrations, the mantle ^4He degassing efficiency would reach a maximum of 8.9%, so we can conclude that ^4He must be accumulating in the mantle. In contrast, the rate at which heat is being lost from the mantle (~ 30 TW) is substantially greater than it is being produced (~ 12 TW, using McDonough and Sun concentrations, 8.7 TW using Lyubetskaya and Korenaga concentrations). O’Nions and Oxburgh (1983) first pointed out this dichotomy between the loss of He and heat from the Earth.

We can also place some constraints on the evolution of $^3\text{He}/^4\text{He}$ in the less degassed reservoir sampled by mantle plumes. Let’s first suppose that such a reservoir is undegassed and primordial and has the U and Th concentrations of the bulk silicate Earth. Using a primordial $^3\text{He}/^4\text{He}$ ratio of 120 R/R_A ($^4\text{He}/^3\text{He} = 6021$) and the highest value measured in plume material of 50 R/R_A ($^4\text{He}/^3\text{He} = 6021$) in 60 million year old primitive basalts produced by melting of the Iceland mantle plume and now found on Baffin Island (Starkey et al., 2009), the ratio of $^4\text{He}^*/^3\text{He}$ is then:

$$\frac{^4\text{He}^*}{^3\text{He}} = \left(\frac{^4\text{He}}{^3\text{He}} \right)_{\text{today}} - \left(\frac{^4\text{He}}{^3\text{He}} \right)_0 = 8430 \quad (12.3)$$

Assuming 20 ppb and 80 ppb U and Th concentrations, respectively (McDonough and Sun, 1995), this reservoir would produce 1.54×10^{-9} moles/g ^4He over 4.5 Ga. From these values we can calculate a ^3He concentration of 1.82×10^{-13} moles/g. This concentration assumes a closed system, that is, no loss of He over 4.5 Ga and is therefore a *minimum* initial concentration. Porcelli and Ballentine (2003) using a similar approach but different values, calculate a concentration of 1.26×10^{-13} moles/g for the Icelandic source. For comparison, the CI chondrite He concentration is 56 nL/g or 2.5×10^{-9} moles/g (Palme and O’Neill, 2003). Assuming an initial $^3\text{He}/^4\text{He}$ of 120 R/R_A,

we can calculate a concentration ${}^3\text{He}$ 3.16×10^{-13} moles/g, implying a terrestrial concentration of 0.39 times CI chondrites. Halliday (2013) estimated the primordial terrestrial ${}^3\text{He}$ concentration at 1.6 to 1.9×10^{-13} moles/g, which compares to his estimated “chondritic” concentration of 3.8×10^{-13} moles/g, corresponding to a factor of ~ 3 depletion. Given the uncertainties, the similarity in these values is more surprising than the difference.

How much of this He could be in the depleted mantle, assuming it occupies only the region above 660 km? We noted the present estimated U concentrations of 3.2–4.7 ppb U, but of course these have decreased through time from the presumed initial primordial values. This depletion is likely a complex function of time, but building a simple model is nonetheless instructive. We could suppose that U concentration decreases exponentially from a primordial concentration of 20 ppb to a present one of 4.7 ppb. In this case, the depleted mantle would have generated 1.42×10^{-9} moles/g ${}^4\text{He}^*$. Using Eqn. 12.2, we can calculate a ${}^3\text{He}$ concentration of 1.87×10^{-14} moles/g, or about an order of magnitude less than what we estimated for “primordial mantle.” If we assume the upper mantle attained its present low U concentration 4.5 billion years ago, in which case we estimate a concentration of 5×10^{-15} moles/g ${}^3\text{He}$. In both cases, however, we assume closed system evolution of ${}^4\text{He}$ and ignore losses through degassing, so these are overestimates. Taking account of the “degassing efficiency” of ${}^4\text{He}$ calculated earlier, the actual concentration would be a factor of 3 lower, assuming steady-state degassing. If the depleted mantle occupies only the mantle above 660 km, only 0.25–0.75% of the Earth’s ${}^3\text{He}$ is in this reservoir. Porcelli and Ballentine (2003), using a different approach, estimate the depleted mantle ${}^3\text{He}$ concentration at $2\text{--}7.6 \times 10^{-15}$ moles/g, which overlaps with the above estimates, while Porcelli and Elliott (2008) estimate a lower concentration of 1.44×10^{-15} moles/g.

It seems unlikely that either degassing of He or depletion of U and Th in the mantle has been steady state, particularly since these processes should be linked to heat production in the Earth and creation of the continental crust, both of which have declined over time.

Porcelli and Elliott (2008) considered a variety of models where the degassing flux is a function the rate melting beneath mid-ocean ridges and proportional to the mantle He concentration. They assume the melting rate declines exponentially over time, so that the flux can be expressed as:

$$\dot{F}(t) = -\alpha e^{-\beta t} [{}^3\text{He}(t)]_M \quad (12.4)$$

where $\dot{F}(t)$ is the ${}^3\text{He}$ degassing flux at time t , α is flux of mantle passing through the MOR melting regime, β is constant describing the rate of decrease of melting through time and $[{}^3\text{He}(t)]_M$ is the mantle helium concentration at time t . They assume that fractions of He and U removed from the mantle by melting are the same. An important conclusion they derive from these models is that any present reservoir with ${}^3\text{He}/{}^4\text{He}$ of 50 R/R_A must have been isolated from the depleted mantle and have remained closed to He loss since at least 3 Ga, and likely longer. While the “isolation time” depends on the assumed initial helium concentration, it is largely insensitive to the initial ${}^3\text{He}/{}^4\text{He}$ ratio.

Honda and McDougall (1998) pointed out that we can use the coupled production of radiogenic ${}^4\text{He}$ and nucleogenic ${}^{21}\text{Ne}$ to estimate time-integrated ${}^3\text{He}/{}^{22}\text{Ne}$ ratios. As we noted earlier the ${}^{21}\text{Ne}^*/{}^4\text{He}^*$ production ratio (we again use the asterisk to designate radio/nucleogenic) is constant at about 4.5×10^{-8} . Knowing that, we can calculate the ${}^3\text{He}/{}^{22}\text{Ne}$ ratio as follows:

$$\begin{aligned} {}^3\text{He}/{}^{22}\text{Ne} \\ = \frac{({}^3\text{He}/{}^4\text{He})_m - ({}^3\text{He}/{}^4\text{He})_i}{({}^{21}\text{Ne}^*/{}^4\text{He}^*)/({}^{21}\text{Ne}^*/{}^{22}\text{Ne})_m} \end{aligned} \quad (12.5)$$

where the subscripts m and i denote the measured and initial ratios, respectively, and ${}^{21}\text{Ne}^*/{}^4\text{He}^*$ is the production rate (assumed to be 4.5×10^{-8}). We need values for the measured and primordial ratios of ${}^3\text{He}/{}^4\text{He}$ as well as the ${}^{21}\text{Ne}^*/{}^{22}\text{Ne}$ ratio. The value we assume for the initial ${}^3\text{He}/{}^4\text{He}$ depends on whether we assume that the mantle’s initial inventory of He was primordial planetary He ($\text{R/R}_A = 120$) or solar (i.e., post-deuterium burning, $\text{R/R}_A = 335$). Our result will depend on our assumption, but as we shall see, not strongly.

To determine the ${}^{21}\text{Ne}^*/{}^{22}\text{Ne}$ ratio we assume that the initial ${}^{21}\text{Ne}/{}^{22}\text{Ne}$ falls on the

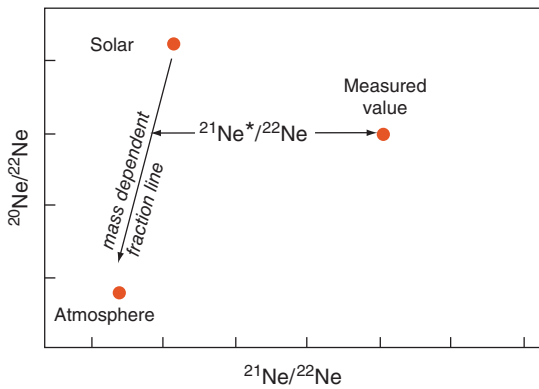


Figure 12.13 Cartoon illustrating the computation of the $^{21}\text{Ne}^*/^{22}\text{Ne}$ ratio. The initial ratio is assumed to lie on a mass dependent fractionation line passing through the solar isotopic composition. The $^{21}\text{Ne}^*/^{22}\text{Ne}$ ratio is the offset from that line.

mass dependent fractionation line passing through the solar value. The $^{21}\text{Ne}^*/^{22}\text{Ne}$ ratio is then the difference between the measured $^{21}\text{Ne}/^{22}\text{Ne}$ and the value of $^{21}\text{Ne}/^{22}\text{Ne}$ on the fractionation line corresponding to the measured $^{20}\text{Ne}/^{22}\text{Ne}$. This is illustrated in Figure 12.13. We then compute the $^3\text{He}/^{22}\text{Ne}$ ratio using Eqn. 12.4.

We also need to consider that most if not all samples have experienced some degree of atmospheric contamination. We can correct for this assuming we know something about the mantle end-member composition. We could, for example, assume the $^{20}\text{Ne}/^{22}\text{Ne}$ is solar. We could then plot calculated $^3\text{He}/^{22}\text{Ne}$ against $^{20}\text{Ne}/^{22}\text{Ne}$ and by extrapolating to the solar value determined the mantle $^3\text{He}/^{22}\text{Ne}$ for each array. This is shown in Figure 12.14. The MORB data show a particularly good correlation and extrapolate to a $^3\text{He}/^{22}\text{Ne}$ ratio of 10.92 ± 0.75 at a $^{20}\text{Ne}/^{22}\text{Ne}$ ratio of 13.78. This is indistinguishable from the value of 10.2 that Honda and McDougall (1998) obtained for the popping rock data alone using a slightly different approach. This result makes the assumption of a solar $^3\text{He}/^4\text{He}$ ratio ($R/R_A = 336$); had we instead used the primordial value, we would obtain a slightly higher $^3\text{He}/^{22}\text{Ne}$ of 11.43. Our result also depends on our assumed end-member $^{20}\text{Ne}/^{22}\text{Ne}$. Taking this to be the maximum observed ratio of 12.75, we obtain a $^3\text{He}/^{22}\text{Ne}$ of 8.08.

$^3\text{He}/^{22}\text{Ne}$ ratios calculated for the Loihi, Iceland, and Galapagos data sets (using solar $^3\text{He}/^4\text{He}$ and $^{20}\text{Ne}/^{22}\text{Ne}$ ratios) are much lower: 5.28 ± 0.71 , 2.17 ± 0.18 , and

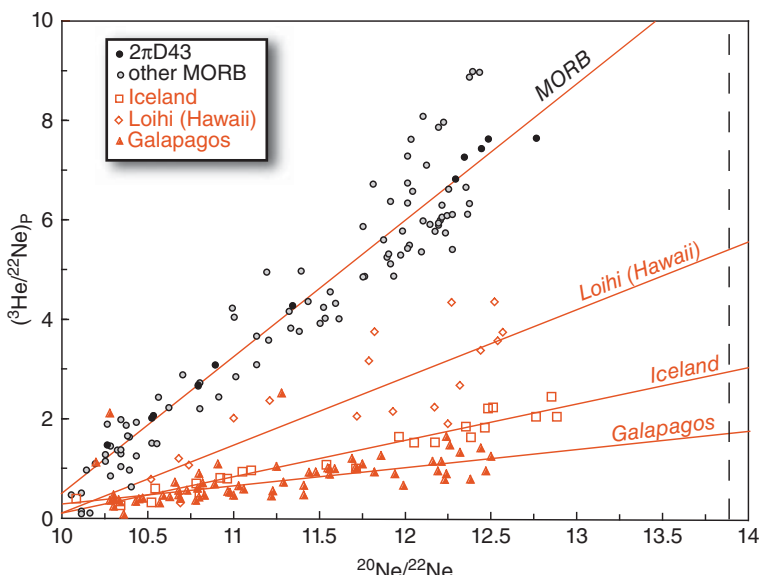


Figure 12.14 Calculated primordial $^3\text{He}/^{22}\text{Ne}$ ratios as a function of observed $^{20}\text{Ne}/^{22}\text{Ne}$. Linear trends reflect atmospheric contamination. Extrapolating to an assumed mantle $^{20}\text{Ne}/^{22}\text{Ne}$ such as the solar value (dashed line) provides the mantle $^3\text{He}/^{22}\text{Ne}$ ratio.

1.68 ± 0.37 , respectively. The Loihi result is indistinguishable from the value of 6.0 ± 1.4 for a different Hawaiian data set. Honda and McDougall observed that the Hawaiian $^{20}\text{Ne}/^{22}\text{Ne}$ ratio is close to the solar value (solar $^3\text{He}/^{22}\text{Ne} \approx 5.4$; solar wind = 3.5), which appears to be confirmed by Loihi data, but the Iceland and Galapagos $^3\text{He}/^{22}\text{Ne}$ ratios are less than solar. All, however, are well above the “planetary” ratio ($^3\text{He}/^{22}\text{Ne} \approx 0.2$ in Q). One explanation for less than solar values is the mantle source contains a mixture of “solar” and “planetary” noble gases, because the latter has $^3\text{He}/^{22}\text{Ne}$ less than solar (Figure 12.1). The higher than solar $^3\text{He}/^{22}\text{Ne}$ in MORB is difficult to explain in terms of Solar System components, but Honda and McDougall noted that He is more soluble in magma than is Ne and suggested that the MORB source may have obtained its high $^3\text{He}/^{22}\text{Ne}$ as a consequence of degassing of an early magma ocean.

12.7.1.2 Fluxes between the mantle reservoirs

Several studies have proposed that noble gases are supplied to the degassed upper mantle from the relatively undegassed deep mantle reservoir (e.g., Kellogg and Wasserburg, 1990; O’Nions and Tolstikhin, 1994). Perhaps the best developed of these is the work of Kellogg and Wasserburg (1990) who developed such a model for He that was subsequently extended to other noble gases by Porcelli and Wasserburg (1995). Kellogg and Wasserburg noted that mantle plumes represent a flux from the deep to the upper mantle. Any noble gases not incorporated into melts of these plumes and subsequently degassed become part of the upper mantle reservoir. They estimated the noble gas flux between mantle reservoirs for a range of fluxes and degassing efficiencies of plumes. This model seems quite reasonable from a physical perspective and these models are readily reconciled with He, Ar, and perhaps Ne isotope systematics, but other differences in noble gas isotope ratios between MORB and OIB suggest that the reservoirs have been largely isolated for much of Earth’s history and exchange between them must be limited. One of these observations is the difference in $^3\text{He}/^{22}\text{Ne}$ ratio we calculated previously (which O’Nions and Tolstikhin assumed was the same in both reservoirs).

As Honda and McDougall (1998) pointed out, the calculated ratio is the *time-integrated* one and the differences could not survive if there were large fluxes of noble gas between these reservoirs. Xe is also revealing. In Porcelli and Wasserburg’s (1995) mode, upper mantle noble gas isotope ratios evolve to their present values through degassing, subduction recycling of atmospheric gas, radioactive decay, and a flux from the deep mantle to the upper mantle. The model requires higher $^{129}\text{Xe}/^{130}\text{Xe}$ in the deep mantle reservoir than in the upper mantle. Data produced since that time, however, strongly suggest that the opposite is the case and that $^{129}\text{Xe}/^{130}\text{Xe}$ is greater in the upper mantle than in the deep mantle (Figure 12.11). Another observation is the difference between the apparent fractions of Pu- and U-fissogenic Xe in the two reservoirs (Figure 12.12), which, as Mukhopadhyay (2012) points out, also seems to require long-term isolation of the two reservoirs.

On the other hand, it seems clear that mantle plumes from the deep mantle do intrude the upper mantle as the Kellogg and Wasserburg model reflects. Furthermore, there is evidence of mixing between plume-derived and the upper mantle gases along ridges (e.g., Poreda et al., 1986). Thus complete isolation of reservoirs would require a degassing efficiency of 1 in the Kellogg and Wasserburg model, which seems somewhat unlikely because it required complete melt extraction from the entire plume. It may be the initial differences in noble gas signatures of these reservoirs were greater and have been slowly reduced over time through this process.

12.7.2 Formation of the Earth and evolution of the atmosphere

How the Earth acquired its inventory of highly volatile elements, which includes the noble gases as well as H, C, and N, is a question of long-standing great interest in geochemistry. Here we briefly summarize some of the salient observations and review some of the more recent theories.

- Our first observation is that noble gases are highly depleted in the Earth relative to the Sun and primitive chondrites, but not as depleted as one might expect from their extremely low condensation temperatures.

This is illustrated in Figure 12.15, which plots the concentrations of the elements in the silicate Earth relative to CI chondrites as a function of their 50% condensation temperature. Most elements with condensation temperatures less than 1500 K plot along a trajectory of decreasing concentration with decreasing condensation temperature, with the exception of siderophile elements such as the platinum group elements, Fe, Ni, Ag, and so on. Depletion of these elements is readily explained by their concentration in the Earth's core. The trend of the non-siderophile elements would predict that the noble gases should be depleted by factors of over 100, but actual depletion factors are smaller, range from about 2 for Kr to about 40 for Ar and show no relationship to condensation temperature. The noble gases are also significantly less depleted than either carbon or nitrogen. The origin of the noble gas inventory in chondrites is itself a problem, since these meteorites appear to have formed at temperatures well above the condensation temperatures of the noble gases. As we noted earlier, some of this inventory resulted from solar wind implantation, but the "planetary" gases, such as Q, were acquired in some other way, perhaps absorption on to carbonaceous material.

- A second observation is most of the Earth's non-radiogenic noble gas inventory (except for He) is in the atmosphere. Estimates of the fraction of noble gases in the mantle range from ~15% of the Earth's Xe (Marty, 2012) to 0.6% of the Earth's Ne (Halliday, 2013). In contrast, somewhere between 33 and 47% of the Earth's radiogenic ^{40}Ar remains in the mantle. This difference provides an important constraint on the timing and mechanisms of degassing of the Earth's interior. The overall abundance of noble gases in the Earth is similar to the planetary pattern observed in chondrites (Figure 12.1) with the exception of Xe.
- Terrestrial noble gases show variable mass dependent fractionations from both solar and chondritic compositions. Atmospheric Ne is enriched in heavy isotopes by more than 100‰/amu relative to solar, Ar by 13‰/amu, Kr by 6‰/amu, while Xe is enriched by more than 30‰/amu.

- Mantle noble gases differ from atmospheric ones both in the extent to which they are fractionated relative to solar values, and in being richer in radiogenic and nucleogenic isotopes ^{21}Ne , ^{40}Ar , ^{129}Xe , and ^{131}Xe - ^{136}Xe . Ne and Xe non-radiogenic isotope ratios are more similar to solar values than is the atmosphere, while the opposite is the case for Kr. There is no resolvable difference between mantle and atmospheric ^{38}Ar / ^{36}Ar . However, even after correction for nucleogenic contributions, the difference between Xe (and perhaps Kr) isotope ratios cannot be entirely explained by mass dependent fractionations.
- Variation in radiogenic Xe isotope ratios in terrestrial reservoirs require different I/Xe and Pu/Xe ratios over the first 100 million years of Solar System history. This requires either that the atmosphere was created by extensive early degassing of the mantle or that atmospheric Xe is derived from a fundamentally different cosmic source than mantle Xe.
- Differences in noble gas radiogenic/nucleogenic isotope ratios between the upper and deep mantle reservoir indicate the two reservoirs have different degassing histories. Differences in radiogenic Xe isotopes requires that this difference in degassing history extends to the earliest episode of Earth's history and possibly earlier. It furthermore requires that exchange between the two reservoirs has been limited since then (e.g., Ozima et al., 1985).

How to explain these observations remains a matter of some debate, although there is fairly broad agreement in some areas. First, both "solar" and "planetary" noble gases, which differ in both abundance patterns and isotopic composition resulting from mass dependent fractionation, apparently contributed to the Earth's noble gas inventory (e.g., Marty, 2012; Mukhopadhyay, 2012; Halliday, 2013). These components appear to be inhomogeneously distributed in the Earth. In particular, the atmosphere appears to be derived primarily from planetary gases while mantle noble gases have a larger fraction of solar noble gases. It is also possible that noble gases in the deep mantle (the less degassed

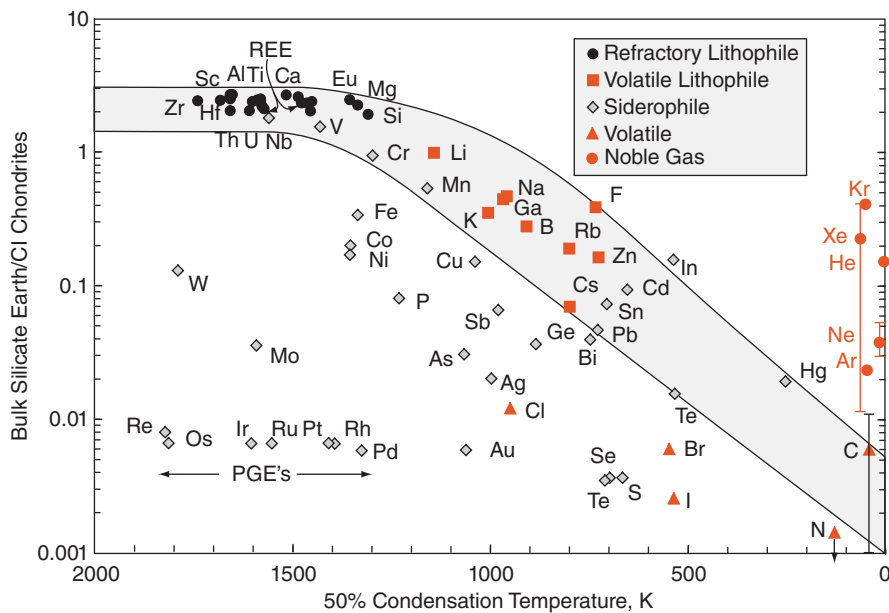


Figure 12.15 Chondrite-normalized abundances of the elements in the silicate Earth as a function of 50% nebular condensation temperature. Gray regions show the general trend of decreasing abundance with decreasing condensation temperature. Most elements plotting below the trend are siderophile and likely concentrated in the Earth core. The noble gases are an exception to the pattern. (Source: Modified from White (2013) with noble gas data from Halliday (2013) and Marty (2012). Error bars on Ne, Xe, and C show the range of their estimates. Adapted from White, 2013.)

OIB source) are richer in the solar component than are noble gases in the depleted upper mantle MORB source (Mukhopadhyay, 2012). Since meteorites, and hence presumably their parent bodies, contain both planetary and solar noble gases, the mix of solar and planetary gases can be explained by accretion of chondritic planetesimals alone (e.g., Marty, 2012).

Albarède (2009) note the lack of isotopic fractionation of moderately volatile elements such as Zn and K argues against a scenario in which the Earth lost its volatile component by hydrodynamic escape⁸ following the Moon-forming collision. He argues that the terrestrial planets are likely to have initially accreted from very volatile-poor material, which is consistent with the relationship between elemental abundance and condensation temperature in Figure 12.15 and nebular models which suggests that radiation from the young Sun would have cleared the inner nebula of gas before elements more volatile than the alkalis condensed. In this model, more volatile elements, including atmospheric noble gases were added 100 million years or

so later by accretion of veneer of carbonaceous chondrite-like asteroids that initially formed near the orbits of the giant planets. If the atmosphere is largely derived from this late accretionary veneer, it requires that the noble gas isotopic composition of late accreting material was isotopically distinct. In the model proposed by Tokstikhin and Hofmann (2005) late accreting material was enriched by implantation of solar gases by the very strong solar winds of the young Sun. This material made up a primitive crust, which then, because of high density, sunk to the base of the mantle where it remains.

Mixing of solar and planetary gases fails to explain the Earth's Xe, and possible Kr, deficiency and some aspects of Xe isotopic compositions. Several explanations have been proposed. One of these is the addition of a small fraction of cometary material (Dauphas, 2003; Halliday, 2013). Comets originate in the outer regions of the Solar System where temperatures are cold enough for water, methane and other gases to form and trap heavy noble gases. Above 30 K, argon and krypton are trapped more efficiently than

xenon, leading to fractionated noble gas patterns. While comets have quite different hydrogen isotopic compositions and hydrogen/argon ratios than the Earth and hence are an unlikely source of the Earth's water (Drake and Righter, 2002), cometary ices are so enriched in noble gases that addition of as little as a millionth of the mass of the Earth of cometary material could explain the noble gas abundance pattern of the Earth, as well as the peculiar features of terrestrial Kr isotopic composition (Owen et al., 1992; Dauphas, 2003; Halliday, 2013). This amount of cometary material would have contributed negligibly to the inventory of other volatile elements such as water and carbon. Another possible explanation is suggested by high pressure experiments showing that reactions with oxygen to form XeO_2 that can be incorporated in silicates at high pressure. This suggests the "missing Xe" might be stored in the deep Earth, particularly if these reactions involve isotopic fractionation (Sanloup, et al., 2011).

Shcheka and Keppler (2012) proposed a different explanation based on solubility of noble gas in Mg-perovskite (MgSiO_3) in high-pressure experiments. They documented high solubility of Ar, up to 1 wt%, and somewhat lower Kr solubility, 0.1–0.3 wt%, but much lower solubility of Xe, 0.03%. They hypothesized that noble gases are incorporated in oxygen vacancies in Mg-perovskite and that the high Ar solubility results from the similarity between the Ar atomic radius (164 pm) and the O^{2-} site radius (~130 pm). The Xe atomic radius is much larger (196 pm) and is thus not easily accommodated in O vacancies. They proposed that a significant fraction of the Earth's primordial inventory of Ar, and to a lesser degree Kr, could have been sequestered in Mg-perovskite crystallizing from a magma ocean in the young Earth. Around the same time, "most of the primary atmosphere was lost by hydrodynamic escape due to high surface temperatures, intense ultraviolet radiation from the early Sun and meteorite impacts" – as has widely been proposed by others (e.g., Pepin and Porcelli, 2002; Pepin, 2006). Once the mantle had solidified and solid state convection begun, mantle degassing was able to replenish lost Ar and Kr, but not Xe according to their hypothesis.

In addition to inhomogeneous accretion of three components (solar, planetary, and cometary) noble gas isotopic composition appears to reflect processes occurring in the young Earth. Radiogenic mantle Xe suggests the mantle experienced extensive outgassing prior to about 4.45 Ga. In addition, the isotopically heavy nature of atmospheric Ne is difficult to explain by mixing of solar and planetary components alone. Partial hydrodynamic escape of an early primitive atmosphere may explain this (e.g., Pepin, 2006). The Moon-forming impact might explain both the loss of the primitive atmosphere and early mantle degassing.

These processes do not seem able to explain the isotope fractionation observed in terrestrial xenon, which is depleted in light Xe isotopes compared to "planetary" or "solar" Xe (Figures 12.10 and 12.16). The comparatively large fractionations of such a heavy gas suggest ionization is involved (Marty, 2012). Xe has a lower ionization potential than other noble gases as well as gases such as CO_2 , CH_4 , N_2 , and H_2O thought to comprise the Earth's early atmosphere. This has led to the suggestion that extreme UV radiation resulted in loss of light Xe isotopes, either in nebular materials accreted to the Earth or from the atmosphere of the young Earth. Ancient atmospheric Xe trapped in Archean barite and hydrothermal quartz from Australia have isotopic compositions that are more solar-like than the modern atmosphere (Figure 12.16), whereas trapped Ne and Kr are atmospheric (Pujol et al., 2009; 2011). This suggests the possibility that atmospheric Xe loss, preferentially of the light isotopes, due to solar UV irradiation continued through at least the first two billion years or more of Earth's history.

No single model of the Earth's formation entirely explains all the observations on noble gas geochemistry we have reviewed in this chapter. Thus, there is plenty of work left for isotope geochemists of the future. Nevertheless, our understanding of the formation and evolution of the Earth has greatly advanced in the last three or so decades since data on the isotopic composition of noble gases in the Earth's interior began to accumulate. We have every reason to expect that our understanding will greatly increase over the next few decades.

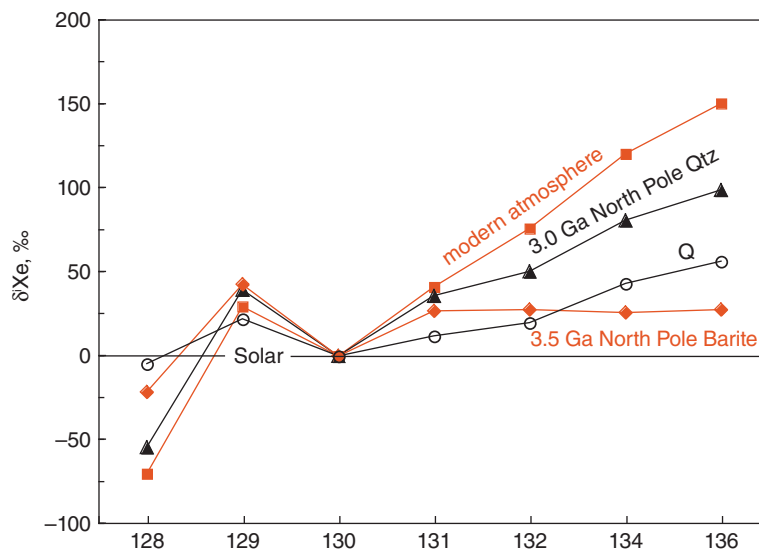


Figure 12.16 Fractionation of Xe isotopes shown as $\delta^{139}\text{Xe}$ ($(^{139}\text{Xe} / ^{130}\text{Xe}_{\text{sample}} / ^{139}\text{Xe} / ^{130}\text{Xe}_{\text{solar}} - 1) \times 1000$) relative to the solar wind value plotted vs. ^{139}Xe for xenon from 3.5 Ga barites (Pujol, 2009) and 3.0 Ga fluid inclusions in quartz (Pujol et al., 2011) from the North Pole area of western Australia, the modern atmosphere, and the meteoritic Q component. The North Pole samples have been corrected for fissogenic Xe and the barite sample for radiogenic production from double electron capture decay of ^{130}Ba ($t_{1/2} = 6 \times 10^{20}$ yrs). All show excess ^{129}Xe relative to solar due to decay of extinct ^{129}Xe . The modern atmosphere is fractionated relative to solar by about 33‰ per mass unit, whereas the 3.0 Ga quartz inclusions is fractionated by ~24‰ per mass unit and the 3.5 Ga barite by only ~12‰ per mass unit. This suggests atmospheric Xe became increasingly fractionated through time.

NOTES

1. Solar energetic particles (SEP), produced by solar flares, were previously thought to be isotopically distinct. However, their distinct isotopic character has been shown to result from fractionation during implantation (Wieler et al., 2007).
2. The usual convention in isotope geochemistry is to place the radiogenic isotope, ^4He in the numerator, as in Table 11.2. Perhaps because ^3He is often of more interest than ^4He , the usual convention for He is to ignore the convention and place ^3He in the numerator. This, however, is not universal and the $^4\text{He}/^3\text{He}$ ratio is sometimes reported instead. In the rest of this chapter, we will adopt the anti-convention convention and use $^3\text{He}/^4\text{He}$. Expressed in this way, it is similar to ratios of light stable isotopes, such as $^{18}\text{O}/^{16}\text{O}$, with the less abundant isotope in the numerator.
3. Creationists have claimed that He cannot escape from the Earth's atmosphere because thermal velocities of He in the upper atmosphere are below escape velocity. They argue that since ^4He is steadily produced by decay, ^4He should steadily accumulate in the atmosphere if it does not escape. The atmospheric abundance, they argue, therefore fixes the age of the Earth to be young (<40,000 yrs). This argument is flawed because thermal escape, sometimes called Jean's escape, in which He is accelerated to escape velocity through thermal collisions, is the least important of three principal He escape mechanisms. Most important appears to be the "polar wind" in which He is first ionized, then accelerated along magnetic field lines that allow flow outward at the poles. The third mechanism is acceleration by interaction with the solar wind. Satellite observations confirm the loss of He in this manner, but because of the role played by the solar wind, which varies dramatically in time, the exact flux out of the atmosphere remains somewhat uncertain, with consequent uncertainty in atmospheric residence time. H and O are also lost through this "polar wind," but those losses are trivial in proportion to the terrestrial inventories of H and O.
4. parts per million by volume. This is effectively a molar concentration.

5. This CO₂, which is a major source of industrial CO₂, is thought to have originated from decarbonation of limestone sediments driven by intrusion of basaltic magma. The noble gases appear to be derived from the intruding magma. Helium isotope ratios in the gas range to greater than 4 R/R_A.
6. This sample, known as 2πD43, was recovered from a depth of 3500 m at 14°N on from the Mid-Atlantic Ridge by dredge from the Russian research vessel *Akademik Boris Petrov*. The lava was so gas-rich that when brought on board pressure within the vesicles was sufficient to explode the samples, causing them to pop. The high gas content has allowed particularly precise isotopic analysis of magmatic gases.
7. However, neither atmospheric Ne nor He are subducted to a significant extent (Ballentine and Holland, 2008), so neither He nor Ne isotope ratios can be explained in this way.
8. In hydrodynamic escape, light atoms or molecules such as H₂ or He at high temperature can reach velocities allowing them to escape from the atmosphere (Jean's escape) and in doing so "drag" heavier atoms or molecules, Ar for example, that have not attained escape velocity along with them.

REFERENCES

- Albarède, F. 1998. Time-dependent models of U-Th-He and K-Ar evolution and the layering of mantle convection. *Chemical Geology*, 145: 413–430.
- Albarède, F. 2009. Volatile accretion history of the terrestrial planets and dynamic implications. *Nature*, 46: 1227–1233,
- Allègre, C. J., Hofmann, A. W. and O'Nions, R. K. 1996. Constraints on the evolution of Earth's mantle from rare gas systematics. *Nature*, 303: 762–766.
- Allègre, C. J., Staudacher, T. and Sarda, P. 1986. Rare gas systematics: formation of the atmosphere, evolution and structure of the Earth's mantle, *Earth and Planetary Science Letters*, 81: 127–150.
- Arevalo, R., Jr., McDonough, W. F. and Luong, M. 2009. The K/U ratio of the silicate Earth: Insights into mantle composition, structure and thermal evolution. *Earth and Planetary Science Letters*, 278: 361–369, doi: 10.1016/j.epsl.2008.12.023.
- Armytage, R. M. G., Jephcoat, A. P., Bouhifd, M. A. and Porcelli, D. 2013. Metal-silicate partitioning of iodine at high pressures and temperatures: Implications for the Earth's core and ¹²⁹Xe budgets. *Earth and Planetary Science Letters*, 373: 140–149, doi: 10.1016/j.epsl.2013.04.031.
- Ballentine, C. J. and Burnard, P. G. 2002. Production, release and transport of noble gases in the continental crust. *Reviews in Mineralogy and Geochemistry*, 47: 481–538, doi:10.2138/rmg.2002.47.12.
- Ballentine, C. J. and Holland, G. 2008. What CO₂ well gases tell us about the origin of noble gases in the mantle and their relationship to the atmosphere. *Philosophical Transactions of the Royal Society A*, 366: 4183–4203, doi: 10.1098/rsta.2008.0150.
- Ballentine, C. J., Burgess, R. and Marty, B. 2002. Tracing fluid origin, transport and interaction in the crust. *Reviews in Mineralogy and Geochemistry*, 47: 539–614, doi:10.2138/rmg.2002.47.13.
- Barlow, M. J., Swinyard, B. M., Owen, P. J., Cernicharo, J., Gomez, H. L., Ivison, R. J., et al. 2013. Detection of a noble gas molecular ion, ³⁶ArH⁺, in the Crab Nebula. *Science*, 342: 1343–1345, doi:10.1126/science.1243582.
- Basu, A. R., Poreda, R. J., Renne, P. R., Teichmann, F., Vasiliev, Y. R., Sobolev, N. V. and Turrin, B. D. 1995. High-³He plume origin and temporal-spatial evolution of the Siberian Flood basalts. *Science*, 269: 822–825, doi: 10.2307/2888490.
- Basu, A. R., Renne, P. R., DasGupta, D. K., Teichmann, F. and Poreda, R. J. 1993. Early and late alkali igneous pulses and a high-³He plume origin for the Deccan Flood basalts. *Science*, 261: 902–906, doi: 10.2307/2882121.
- Bianchi, D., Sarmiento, J. L., Gnanadesikan, A., Key, R. M., Schlosser, P. and Newton, R. 2010. Low helium flux from the mantle inferred from simulations of oceanic helium isotope data. *Earth and Planetary Science Letters*, 297: 379–386, doi: 10.1016/j.epsl.2010.06.037.
- Burnard, P., Graham, D. and Turner, G. 1997. Vesicle-specific noble gas analyses of "popping rock": implications for primordial noble gases in Earth. *Science*, 276: 568–571.
- Busemann, H., Baur, H. and Wieler, R. 2000. Primordial noble gases in "phase Q" in carbonaceous and ordinary chondrites studied by closed-system stepped etching. *Meteoritics and Planetary Science*, 35: 949–973, doi: 10.1111/j.1945-5100.2000.tb01485.x.
- Butler, W. A., Jeffery, P. M., Reynolds, J. H. and Wasserburg, G. J. 1963. Isotopic variations in terrestrial xenon. *Journal of Geophysical Research*, 68: 3283–3291.
- Coffee, M. W., Hudson, G. B., Velsko, C., Huss, G. R., Alexander, E. C. and Chivas, A. R. 1999. Primordial noble gases from Earth's mantle: identification of a primitive volatile component. *Science*, 285: 2115–2118, doi:10.1126/science.285.5436.2115.

- Clarke, W. B., Beg, M. A. and Craig, H. 1969. Excess ${}^3\text{He}$ in the sea: Evidence for terrestrial primodal helium. *Earth and Planetary Science Letters*, 6: 213–220, doi: 10.1016/0012-821X(69)90093-4.
- Class, C. and Goldstein, S. 2005. Evolution of helium isotopes in the Earth's mantle. *Nature*, 436: 1107–1112, doi: 10.1038/nature0390.
- Craig, H., Clarke, W. B. and Beg, M. A. 1975. Excess ${}^3\text{He}$ in deep water on the East Pacific Rise. *Earth and Planetary Science Letters*, 26: 125–132, doi: 10.1016/0012-821X(75)90079-5.
- Damon, P. E. and Kulp, J. L. 1958. Inert gases and the evolution of the atmosphere. *Geochimica et Cosmochimica Acta*, 13: 280–292, doi: 10.1016/0016-7037(58)90030-9.
- Dauphas, N. 2003. The dual origin of the terrestrial atmosphere. *Icarus*, 165: 326–339, doi: 10.1016/S0019-1035(03)00198-2.
- Davies, G. F. 1988. Ocean bathymetry and mantle convection, 1, large-scale flow and hotspots, *Journal of Geophysical Research*, 93: 10467–10480.
- Drake, M. J. and Righter, K. 2002. Determining the composition of the Earth. *Nature*, 416: 39–44.
- Gale, A., Dalton, C. A., Langmuir, C. H., Su, Y. and Schilling, J.-G. 2013. The mean composition of ocean ridge basalts. *Geochemistry, Geophysics, Geosystems*, doi: 10.1029/2012gc004334.
- Gonnermann, H. M. and Mukhopadhyay, S. 2009. Preserving noble gases in a convecting mantle. *Nature*, 459: 560–563.
- Graham, D. W. 2002. Noble gas isotope geochemistry of mid-ocean ridge and ocean island basalts: Characterization of mantle source reservoirs. *Reviews in Mineralogy and Geochemistry*, 47: 247–317, doi: 10.2138/rmg.2002.47.8.
- Halliday, A. N. 2013. The origins of volatiles in the terrestrial planets. *Geochimica et Cosmochimica Acta*, 105: 146–171, doi: 10.1016/j.gca.2012.11.015.
- Hanyu, T., Tatsumi, Y. and Kimura, J.-I. 2011. Constraints on the origin of the HIMU reservoir from He–Ne–Ar isotope systematics. *Earth and Planetary Science Letters*, 307: 377–386, doi: 10.1016/j.epsl.2011.05.012.
- Heber, V. S., Brooker, R. A., Kelley, S. P. and Wood, B. J. 2007. Crystal-melt partitioning of noble gases (helium, neon, argon, krypton, and xenon) for olivine and clinopyroxene. *Geochimica et Cosmochimica Acta*, 71: 1041–1061, doi: 10.1016/j.gca.2006.11.010.
- Heber, V. S., Wieler, R., Baur, H., Olinger, C., Friedmann, T. A. and Burnett, D. S. 2009. Noble gas composition of the solar wind as collected by the Genesis mission. *Geochimica et Cosmochimica Acta*, 73: 7414–7432, doi: 10.1016/j.gca.2009.09.013.
- Hilton, D. R., Fischer, T. P. and Marty, B. 2002. Noble gases and volatile recycling at subduction zones. *Reviews in Mineralogy and Geochemistry*, 47: 319–370, doi: 10.2138/rmg.2002.47.9.
- Hofmann, A. W. and White, W. M. 1982. Mantle plumes from ancient oceanic crust. *Earth and Planetary Science Letters*, 57: 421–436.
- Holland, G., Cassidy, M. and Ballentine, C. J. 2009. Meteorite Kr in Earth's mantle suggests a late accretionary source for the atmosphere. *Science*, 326: 1522–1525, doi: 10.1126/science.1179518.
- Jephcoat, A. P., Bouhifd, M. A. and Porcelli, D. 2008. Partitioning experiments in the laser-heated diamond anvil cell: volatile content in the Earth's core. *Philosophical Transactions of the Royal Society A*: 366: 4295–4314, doi: 10.1098/rsta.2008.0226.
- Hanan, B. B. and Graham, D. W. 1996. Lead and helium isotope evidence from oceanic basalts for a common deep source of mantle plumes. *Science*, 272: 991–995.
- Hunten, D. M., Pepin, R. O. and Owen, T. C. 1988. Planetary atmospheres. In: *Meteorites and the Early Solar System*, Kerridge, J. F. and Matthews, M. S. (eds). Tuscon: University of Arizona Press.
- Honda, M. and McDougall, I. 1998. Primordial helium and neon in the Earth – A speculation on early degassing. *Geophysical Research Letters*, 25: 1951–1954, doi: 10.1029/98gl01329.
- Jackson, M. G., Carlson, R. W., Kurz, M. D., Kempton, P. D., Francis, D. and Blusztajn, J. 2010. Evidence for the survival of the oldest terrestrial mantle reservoir. *Nature*, 466: 853–856, doi: 10.1038/nature09287.
- Jackson, M. G., Hart, S. R., Koppers, A. A. P., Staudigel, H., Konter, J., Blusztajn, J., Kurz, M. and Russell, J. A. 2007. The return of subducted continental crust in Samoan lavas. *Nature*, 448: 684–687, doi: 10.1038/nature06048.
- Jenkins, W. J. 1987. ${}^3\text{H}$ and ${}^3\text{He}$ in the Beta Triangle: Observations of gyre ventilation and oxygen utilization rates. *Journal of Physical Oceanography*, 17: 763–783.
- Kellogg, L. H. and Wasserburg, G. J. 1990. The role of plumes in mantle helium fluxes. *Earth and Planetary Science Letters*, 99: 276–289, doi: 10.1016/0012-821X(90)90116-F.
- Kipfer, R., Aeschbach-Hertig, W., Peeters, F. and Stute, M. 2002. Noble gases in lakes and ground waters. *Reviews in Mineralogy and Geochemistry*, 47: 615–700, doi: 10.2138/rmg.2002.47.14.
- Kunz, J., Staudacher, T. and Allègre, C. J. 1998. Plutonium-Fission Xenon Found in Earth's Mantle. *Science*, 280: 877–880, doi: 10.1126/science.280.5365.877.
- Kurz, M. D., Jenkins, W. J., Schilling, J. G. and Hart, S. R. 1982. Helium isotopic variations in the mantle beneath the central North Atlantic Ocean. *Earth and Planetary Science Letters*, 58: 1–14.
- Kurz, M. D., Curtice, J., Fornari, D., Geist, D. and Moreira, M. 2009. Primitive neon from the center of the Galapagos hotspot. *Earth and Planetary Science Letters*, 286: 23–34, doi: 10.1016/j.epsl.2009.06.008.

- Kurz, M. D., Garcia, M. O., Frey, F. A. and O'Brien, P. A. 1987. Temporal helium isotopic variations within Hawaiian volcanoes: Basalts from Mauna Loa and Haleakala. *Geochimica et Cosmochimica Acta*, 51: 2905–2914, doi: 10.1016/0016-7037(87)90366-8.
- Lupton, J. E., Arculus, R. J., Greene, R. R., Evans, L. J. and Goddard, C. I. 2009. Helium isotope variations in seafloor basalts from the Northwest Lau Backarc Basin: Mapping the influence of the Samoan hotspot. *Geophysical Research Letters*, 36: L17313, doi: 10.1029/2009GL039468.
- Lyubetskaya, T. and Korenaga, J. 2007. Chemical composition of Earth's primitive mantle and its variance: 1. Method and results. *Journal of Geophysical Research*, 112: B03211, doi: 10.1029/2005jb004223.
- Madureira, P., Moreira, M., Mata, J. and Allègre, C. J. 2005. Primitive neon isotopes in Terceira Island (Azores archipelago). *Earth and Planetary Science Letters*, 233: 429–440, doi: 10.1016/j.epsl.2005.02.030.
- Mark, D. F., Stuart, F. M. and de Podesta, M. 2011. New high-precision measurements of the isotopic composition of atmospheric argon. *Geochimica et Cosmochimica Acta*, 75: 7494–7501, doi: 10.1016/j.gca.2011.09.042.
- Marty, B. 2012. The origins and concentrations of water, carbon, nitrogen and noble gases on Earth. *Earth and Planetary Science Letters*, 313: 56–66, doi: 10.1016/j.epsl.2011.10.040.
- Matsuda, J., Sudo, M., Ozima, M., Ito, K., Ohtaka, O. and Ito, E. 1993. Noble gas partitioning between metal and silicate under high pressures. *Science*, 259: 788–790, doi: 10.1126/science.259.5096.788.
- McDonough, W. F. and Sun, S.-S. 1995. The composition of the Earth. *Chemical Geology*, 120: 223–253.
- Moreira, M., Kunz, J. and Allègre, C. 1998. Rare gas systematics in popping rock: isotopic and elemental compositions in the upper mantle. *Science*, 279: 1178–1181, doi: 10.1126/science.279.5354.1178.
- Mukhopadhyay, S. 2012. Early differentiation and volatile accretion recorded in deep-mantle neon and xenon. *Nature*, 486: 101–104, doi: 10.1038/nature11141.
- O'Nions, R. K. and Oxburgh, E. R. 1983. Heat and helium in the Earth. *Nature*, 306: 429–431.
- O'Nions, R. K. and Oxburgh, E. R. 1988. Helium, volatile fluxes and the development of continental crust. *Earth and Planetary Science Letters*, 90: 331–347.
- O'Nions, R. K. and Tolstikhin, I. N. 1994. Behaviour and residence times of lithophile and rare gas tracers in the upper mantle. *Earth and Planetary Science Letters*, 124: 131–138.
- Owen, T., Bar-Nun, A. and Kleinfeld, I. 1992. Possible cometary origin of heavy noble gases in the atmospheres of Venus, Earth, and Mars. *Nature*, 358: 43–46.
- Ozima, M. and Podosek, F. A. 2002. *Noble Gas Geochemistry*. Cambridge, Cambridge University Press.
- Ozima, M., Wieler, R., Marty, B. and Podosek, F. A. 1998. Comparative studies of solar, Q-Gases and terrestrial noble gases, and implications on the evolution of the Solar Nebula. *Geochimica et Cosmochimica Acta*, 62: 301–314, doi: 10.1016/S0016-7037(97)00339-6.
- Ozima, M. and Zashu, S. 1983. Primitive helium in diamonds. *Science*, 219: 1067–1068, doi: 10.1126/science.219.4588.1067.
- Palme, H. and O'Neill, H. S. C. 2003. Cosmochemical estimates of mantle composition. In: *The Mantle and Core*, Heinrich, D. H. and Karl, K. T. (eds). Amsterdam: Elsevier.
- Parai, R., Mukhopadhyay, S. and Standish, J. J. 2012. Heterogeneous upper mantle Ne, Ar and Xe isotopic compositions and a possible Dupal noble gas signature recorded in basalts from the Southwest Indian Ridge. *Earth and Planetary Science Letters*, 359–360: 227–239, doi: 10.1016/j.epsl.2012.10.017.
- Pépin, R. O. 1991. On the origin and early evolution of terrestrial planet atmospheres and meteoritic volatiles. *Icarus*, 92: 2–79, doi: 10.1016/0019-1035(91)90036-S.
- Pépin, R. O. and Porcelli, D. 2002. Origin of noble gases in the terrestrial planets. *Reviews in Mineralogy and Geochemistry*, 47: 191–246, doi: 10.2138/rmg.2002.47.7.
- Pépin, R. O. and Porcelli, D. 2006. Xenon isotope systematics, giant impacts, and mantle degassing on the early Earth. *Earth and Planetary Science Letters*, 250: 470–485, doi: 10.1016/j.epsl.2006.08.014.
- Pépin, R. O. 2003. On noble gas processing in the solar accretion disk. *Space Science Reviews*, 106: 211–230, doi: 10.1023/a:1024693822280.
- Pépin, R. O. 2006. Atmospheres on the terrestrial planets: Clues to origin and evolution. *Earth and Planetary Science Letters*, 252: 1–14, doi: 10.1016/j.epsl.2006.09.014.
- Pető, M. K., Mukhopadhyay, S. and Kelley, K. A. 2013. Heterogeneities from the first 100 million years recorded in deep mantle noble gases from the Northern Lau Back-arc Basin. *Earth and Planetary Science Letters*, 369–370: 13–23, doi: 10.1016/j.epsl.2013.02.012.
- Porcelli, D. and Ballentine, C. J. 2002. Models for distribution of terrestrial noble gases and evolution of the atmosphere. *Reviews in Mineralogy and Geochemistry*, 47: 411–480, doi: 10.2138/rmg.2002.47.11.
- Porcelli, D., Ballentine, C. and Weiler, R. (eds) 2002. *Noble Gases in Geochemistry and Cosmochemistry*. Washington: Mineralogical Society of America.
- Porcelli, D. and Elliott, T. 2008. The evolution of He Isotopes in the convecting mantle and the preservation of high $^3\text{He}/^4\text{He}$ ratios. *Earth and Planetary Science Letters*, 269: 175–185, doi: 10.1016/j.epsl.2008.02.002.
- Porcelli, D. and Halliday, A. N. 2001. The core as a possible source of mantle helium. *Earth and Planetary Science Letters*, 192: 45–56, doi: 10.1016/S0012-821X(01)00418-6.
- Porcelli, D. and Wasserburg, G. J. 1995. Mass transfer of helium, neon, argon, and xenon through a steady-state upper mantle. *Geochimica et Cosmochimica Acta*, 59: 4921–4937, doi: 10.1016/0016-7037(95)00336-3.
- Poreda, R., Schilling, J. G. and Craig, H. 1986. Helium and hydrogen isotopes in ocean-ridge basalts north and south of Iceland. *Earth and Planetary Science Letters*, 78: 1–17.

- Poreda, R. J. and Farley, K. A. 1992. Rare gases in Samoan xenoliths. *Earth and Planetary Science Letters*, 113: 129–144.
- Pujol, M., Marty, B. and Burgess, R. 2011. Chondritic-like xenon trapped in Archean rocks: A possible signature of the ancient atmosphere. *Earth and Planetary Science Letters*, 308: 298–306, doi: 10.1016/j.epsl.2011.05.053.
- Pujol, M., Marty, B., Burnard, P. and Philippot, P. 2009. Xenon in Archean barite: Weak decay of ^{130}Ba , mass-dependent isotopic fractionation and implication for barite formation. *Geochimica et Cosmochimica Acta*, 73: 6834–6846, doi: 10.1016/j.gca.2009.08.002.
- Raquin, A. and Moreira, M. 2009. Atmospheric $^{38}\text{Ar}/^{36}\text{Ar}$ in the mantle: Implications for the nature of the terrestrial parent bodies. *Earth and Planetary Science Letters*, 287: 551–558, doi: 10.1016/j.epsl.2009.09.003.
- Rudnick, R. L. and Gao, S. 2003. Composition of the Continental Crust. In: *The Crust, Volume 3: Treatise on Geochemistry*, Rudnick, R. L. (ed.). Oxford: Pergamon.
- Salters, V. J. M. and Stracke, A. 2004. Composition of the depleted mantle. *Geochemistry, Geophysics, Geosystems*, 5: doi: 10.1029/2003GC000597.
- Sanloup, C., Schmidt, B. C., Gudfinnsson, G., Dewaele, A. and Mezouar, M. 2011. Xenon and argon: A contrasting behavior in olivine at depth. *Geochimica et Cosmochimica Acta*, 75: 6271–6284, doi: 10.1016/j.gca.2011.08.023.
- Sarda, P. 2004. Surface noble gas recycling to the terrestrial mantle. *Earth and Planetary Science Letters*, 228: 49–63.
- Schlosser, P. and Winckler, G. 2002. Noble gases in ocean waters and sediments. *Reviews in Mineralogy and Geochemistry*, 47: 701–730, doi: 10.2138/rmg.2002.47.15.
- Shcheka, S. S. and Keppler, H. 2012. The origin of the terrestrial noble-gas signature. *Nature*, 490: 531–534, doi: 10.1038/nature11506.
- Sleep, N. H. 1990. Hotspots and mantle plumes: Some phenomenology. *Journal of Geophysical Research*, 95: 6715–6736.
- Smith, G. P., Wiens, D. A., Fischer, K. M., Dorman, L. M., Webb, S. C. and Hildebrand, J. A. 2001. A complex pattern of mantle flow in the Lau Backarc. *Science*, 292: 713–716, doi: 10.1126/science.1058763.
- Starkey, N. A., Stuart, F. M., Ellam, R. M., Fitton, J. G., Basu, S. and Larsen, L. M. 2009. Helium isotopes in early Iceland plume picrites: Constraints on the composition of high $^3\text{He}/^4\text{He}$ mantle. *Earth and Planetary Science Letters*, 277: 91–100, doi: 10.1016/j.epsl.2008.10.007.
- Staudacher, T. and Allègre, C. J. 1982. Terrestrial xenology. *Earth and Planetary Science Letters*, 60: 389–406, doi: 10.1016/0012–821X(82)90075–9.
- Staudacher, T., Kurz, M. D. and Allègre, C. J. 1986. New noble-gas data on glass samples from Loihi Seamount and Hualalai and on dunite samples from Loihi and Réunion Island. *Chemical Geology*, 56: 193–205, doi: 10.1016/0009–2541(86)90003–3.
- Tolstikhin, I. and Hofmann, A. W. 2005. Early crust on top of the Earth's core. *Physics of the Earth and Planetary Interiors*, 148: 109–130, doi: 10.1016/j.pepi.2004.05.011.
- Torgersen, T. and Clarke, W. B. 1985. Helium accumulation in groundwater, I: An evaluation of sources and the continental flux of crustal ^4He in the Great Artesian Basin, Australia. *Geochimica et Cosmochimica Acta*, 49: 1211–1218, doi: 10.1016/0016-7037(85)90011-0.
- Trieloff, M., Kunz, J. and Allègre, C. J. 2002. Noble gas systematics of the Réunion mantle plume source and the origin of primordial noble gases in Earth's mantle. *Earth and Planetary Science Letters*, 200: 297–313, doi: 10.1016/S0012–821X(02)00639–8.
- Trieloff, M., Kunz, J., Clague, D. A., Harrison, D. and Allègre, C. J. 2000. The nature of pristine noble gases in mantle plumes. *Science*, 288: 1036–1038, doi: 10.1126/science.288.5468.1036.
- Tucker, J. M., Mukhopadhyay, S. and Schilling, J.-G. 2012. The heavy noble gas composition of the depleted MORB mantle (DMM) and its implications for the preservation of heterogeneities in the mantle. *Earth and Planetary Science Letters*, 355–356: 244–254, doi: 10.1016/j.epsl.2012.08.025.
- Valbracht, P. J., Honda, M., Matsumoto, T., Mattielli, N., McDougall, I., Ragettli, R. and Weis, D. 1996. Helium, neon and argon isotope systematics in Kerguelan ultramafic xenoliths: implications for mantle source signatures. *Earth and Planetary Science Letters*, 138: 29–38, doi: 10.1016/0012–821X(95)00226–3.
- Valbracht, P. J., Staudacher, T., Malahoff, A. and Allègre, C. J. 1997. Noble gas systematics of deep rift zone glasses from Loihi Seamount, Hawaii. *Earth and Planetary Science Letters*, 150: 399–411, doi: 10.1016/S0012–821X(97)00094–0.
- White, W. M. 2010. Oceanic Island Basalts and Mantle Plumes: The Geochemical Perspective. *Annual Review of Earth and Planetary Sciences*, 38: 133–160, doi: 10.1146/annurev-earth-040809–152450.
- White, W. M. and Klein, E. 2013. Composition of the Oceanic Crust. In: *Treatise on Geochemistry Volume 3. The Crust*. 2nd Edn, Rudnick, R. L. (ed.). Amsterdam: Elsevier.
- Wieler, R. 2002. Noble gases in the Solar System. *Reviews in Mineralogy and Geochemistry*, 47: 21–70, doi: 10.2138/rmg.2002.47.2.
- Wieler, R., Grimberg, A. and Heber, V. S. 2007. Consequences of the non-existence of the “SEP” component for noble gas geo-and cosmochemistry. *Chemical Geology*, 244: 382–390, doi: 10.1016/j.chemgeo.2007.06.026.
- Workman, R. and Hart, S. R. 2005. Major and trace element composition of the depleted MORB mantle (DMM). *Earth and Planetary Science Letters*, 231: 53–72, doi: 10.1016/j.epsl.2004.12.005.
- Yang, J. and Anders, E. 1982. Sorption of noble gases by solids, with reference to meteorites. III. Sulfides, spinels, and other substances; on the origin of planetary gases. *Geochimica et Cosmochimica Acta*, 46: 877–892, doi: 10.1016/0016-7037(82)90044-8.

- Yokochi, R. and Marty, B. 2004. A determination of the neon isotopic composition of the deep mantle. *Earth and Planetary Science Letters*, 225: 77–88, doi: 10.1016/j.epsl.2004.06.010.
- Zadnik, M. G., Smith, C. B. and Begemann, F. 1987. Crushing a terrestrial diamond: ${}^3\text{He}/{}^4\text{He}$ higher than solar. *Meteoritics*, 22: 540–541.

SUGGESTIONS FOR FURTHER READING

- Davies, G. F. 1999. Geophysically constrained mantle mass flows and the ${}^{40}\text{Ar}$ budget: a degassed lower mantle? *Earth and Planetary Science Letters*, 166: 149–162.
- Farley, K. A. and Craig, H. 1992. Atmospheric argon contamination of oceanic island basalt olivine phenocrysts. *Geochimica et Cosmochimica Acta*, 58: 2519–2526.
- Farley, K. A. and Poreda, R. J. 1993. Mantle neon and atmospheric contamination. *Earth and Planetary Science Letters*, 114: 325–339.
- Farley, K. A., Natland, J. H. and Craig, H. 1992. Binary mixing of enriched and undegassed (primitive?) mantle components (He, Sr, Nd, Pb) in Samoan lavas. *Earth and Planetary Science Letters*, 111: 183–199.
- Marty, B. and Jambon, A. 1987. C^3He in volatile fluxes from the solid Earth: implications for carbon geodynamics. *Earth and Planetary Science Letters*, 83: 16–26, doi: 10.1016/0012-821X(87)90047-1.
- Ozima, M. and Alexander, E. C. 1976. Rare gas fractionation patterns in terrestrial samples and the Earth atmosphere evolution model. *Reviews of Geophysics and Space Physics*, 14: 386.
- Ozima, M. 1994. Noble gas state in the mantle. *Reviews of Geophysics*, 32: 405–426.
- Ozima, M., Podosek, F. A. and Igarashi, G. 1985. Terrestrial xenon isotope constraints on the early history of the Earth. *Nature*, 315: 471–474.
- Staudacher, T. and Allègre, C. J. 1988. Recycling of oceanic crust and sediments: the noble gas subduction barrier. *Earth and Planetary Science Letters*, 89: 173–183.

PROBLEMS

1. Assume that the atmosphere is steady state and that the isotopic composition of He lost from the top of the atmosphere equals that entering it from the solid Earth. Using the ${}^3\text{He}/{}^4\text{He}$ of the atmosphere given in Table 11.2, the He flux and isotopic from the oceans given in Section 11.2, and assuming that the flux from the continents has an isotopic composition of $R/R_A = 0.01$, calculate the total flux to the atmosphere. What is the fraction from the crust and oceans?
2. Repeat the calculation of total flux in Problem 1, but assume that ${}^3\text{He}$ preferentially escapes from the top of the atmosphere such that the ratio of ${}^3\text{He}/{}^4\text{He}$ escaping is 10% higher than the atmospheric concentration (i.e., R/R_A escaping = 1.1).
3. Using the flux you calculated in Problem 1, the atmospheric concentration of 5.2 ppmv, an atmospheric mass of 5.1×10^{21} g, what is the residence time of ${}^4\text{He}$ in the atmosphere?
4. Assuming a terrestrial concentration of U and Th to be 16 and 64 ppb, respectively, what is the current production rate of ${}^4\text{He}$ in the Earth? How does this compare with the rate of ${}^4\text{He}$ loss to the atmosphere you calculated in Problem 1?
5. The Earth loses heat at a rate of 44 TW, about 16 TW of which is radiogenic, the remainder representing the loss of primordial heat. Assuming the ${}^3\text{He}/{}^4\text{He}$ ratio of the atmosphere represents the ratio of which these isotopes are lost from the solid Earth and that all ${}^4\text{He}$ is radiogenic and all ${}^3\text{He}$ is primordial, how do the rates of loss of radiogenic He and heat compare?

Appendix

Mass spectrometry

A.1 SAMPLE EXTRACTION AND PREPARATION

Isotopic analysis can be performed on minerals, rocks, soil, tissue, gases, and liquids – just about anything. In view of the broad possibilities, we will only cover a few generalities here. In most instances, the element to be analyzed must be first isolated and purified before it can undergo isotopic analysis in a mass spectrometer. Purification is necessary to avoid isobaric interferences and well as to enhance ionization efficiency. This can be done in a number of ways:

- Dissolving the sample and then chemically purifying it (a process that often involves chromatography).
- Reacting the sample with a reagent to produce a gas. For example, oxygen isotopic analysis of silicates involves reacting the sample with a fluorine compound such as bromine pentafluoride to produce CO₂ gas; in the case of carbonates, the process is similar but the reagent is phosphoric acid. Purification is then achieved either cryogenically, or more commonly, using a gas chromatograph. For organic compounds, pyrolysis (thermal decomposition) may precede such reactions.
- Heating or fusing a sample in vacuum to release a gas. This is the usual method for noble gases. Individual gas components are separated cryogenically.
- Noble gases contained in vesicles and inclusions can be released by crushing in vacuum.

- If the sample is a liquid, the element of interest can be extracted chromatographically from the solution.

With instruments in which the analyte is a gas or a liquid, a chromatograph can be used to select a specific compound, for example the alkenones discussed in Chapter 10. This technique is termed compound-specific isotopic analysis.

Micro-analytical techniques in which solids can be directly analyzed have become increasingly important in the last several decades. The first of these is secondary ion mass spectrometry (SIMS), in which an ion beam (generally Cs or O) is fired at a polished surface to produce secondary ions that are then swept into the mass spectrometer. An alternative approach is laser ablation in which a finely focused laser is fired at a polished surface ablating a small pit. The “debris” consists of very fine particles that are swept up by a carrier gas, generally argon and carried into the mass spectrometer. A variation of this technique is laser fluorination, in which a laser is focused on a small spot of the sample in the presence of fluorine gas, producing a reaction that releases the element of interest (e.g., oxygen or argon).

A.2 THE MASS SPECTROMETER

In most cases, isotopic abundances are measured by mass spectrometry. One exception is, as we have seen, short-lived radioactive isotopes, the abundances of which are determined by measuring their decay rate, and in

fission track dating, where the abundance of ^{238}U is measured, in effect, by inducing fission. Another exception is spectroscopic measurement of isotope ratios in the Sun and stars. Frequencies of electromagnetic emissions of the lightest elements are sufficiently dependent on nuclear mass that emissions from different isotopes can be resolved. This approach is useful in astronomy not only because it is the only possibility, but also because isotope ratios of stars show very large variations. This technique is not sufficiently precise for most geochemical problems. A mass spectrometer is simply a device that can separate atoms or molecules according to their mass. There are a number of different kinds of mass spectrometers operating on different principles. Undoubtedly, the vast majority of mass spectrometers are used by chemists for qualitative or quantitative analysis of organic compounds. We will focus exclusively, however, on mass spectrometers used for isotope ratio determination. Most isotope ratio mass spectrometers are of a similar design, the magnetic-sector, or Nier mass spectrometer,¹ a schematic of which is shown in Figure A.1. It consists of three essential parts: an ion source, a mass analyzer and a detector. There are, however, several variations on the design of the Nier mass spectrometer. Some of these modifications relate to the specific task of the instrument; others are evolutionary improvements. We will first consider the Nier mass spectrometer, and then briefly consider a few other kinds of mass spectrometers.

A.2.1 The ion source

As its name implies, the job of the ion source is to provide a stream of energetic ions to the mass analyzer. Ions are most often produced by either *thermal ionization*, for solid-source

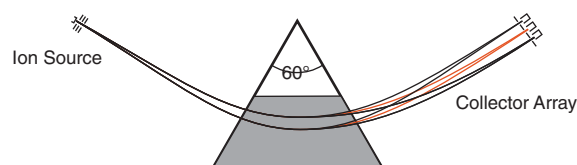


Figure A.1 The magnetic sector or Nier mass spectrometer. This instrument uses a 60° magnetic sector, but 90° magnetic sectors are also sometimes used.

mass spectrometers, *electron bombardment*, for gas-source mass spectrometers, or by inductively exciting a carrier gas into a plasma state in the case of inductively coupled plasma–mass spectrometers (ICP-MS).

In *thermal ionization mass spectrometry* (TIMS), used for metals such as Sr, Nd, and Pb, a solution containing the element of interest is dried or electroplated onto a “filament,” a thin ribbon of high-temperature metal, such as Re, Ta, or W, welded to supports. The ribbon is placed in the instrument and heated under vacuum by passing an electric current of several amperes through it, the sample evaporates, and some fraction of the atoms, depending on the element, ionize. The alkali metals ionize quite easily; the ionization efficiency for Cs, for example, approaches 100%. For some other elements, it can be 0.1% or less. In some cases, multiple filaments are used to achieve higher ionization efficiency. Ions produced in this way may be either the pure metal, for example Sr^+ , or a radical such as OsO_4^- .

Ionization efficiency can sometimes be increased by using a suitable substrate with a high work function. The greater energy required to evaporate the atom results in a higher likelihood of its also being ionized. Tantalum oxide, for example, is a good substrate for analysis of Sr. Ionization efficiency can also be increased by altering the chemical form of the element of interest so that its evaporation temperature is increased (ionization is more likely at higher temperatures). For example, when a silica gel suspension is loaded along with Pb, the evaporation temperature of Pb is increased by several hundred degrees, and the ionization efficiency improved by orders of magnitude. Finally, the sample may be loaded in a particular chemical form in order to (1) form a positive rather than negative ion (*or vice versa*) and (2) provide a molecule of high mass, such as cesium metaborate where boron is the element of interest, to minimize mass fractionation, or to promote or inhibit the formation of oxides.

Electron bombardment is used when the analyte is a gas, such as CO_2 , H_2 , or N_2 . The gas is introduced slowly into the evacuated source through a small orifice. In this case, a current is passed through a filament, normally Re, giving off electrons that strike the analyte molecules, and ionize them by knocking off one of the electrons. Except for noble gases,

the ion is generally a polyatomic species such as H_2^+ or CO_2^+ .

Most thermal ionization mass spectrometers employ a turret source in which a number of samples (typically 6 to 20) can be loaded. The turret is rotated to bring each sample into position for analysis. Gas source mass spectrometers often employ automated gas inlet systems, which allow for automated analysis of many samples. They also have so-called dual inlet systems that allow for rapid switching between a sample and a standard gas, insuring both are analyzed under similar conditions allowing correction for instrumental mass fractionation and other effects.

A third type of ion source is an *inductively coupled plasma* (ICP), which is slowly replacing thermal ionization for many applications. An ICP operates by passing a carrier gas, generally Ar, through an induction coil in which an electric current alternates at radio frequencies. This excites the gas into $\sim 7000^\circ\text{K}$ plasma, in which the gas is completely ionized. The analyte is aspirated, generally as a solution, into the plasma and is ionized by the plasma. Alternatively, the sample can be introduced into the gas stream as an aerosol produced by laser ablation. The ions flow through an orifice into mass spectrometer. Initially, quadrupole mass spectrometers, which are commonly used for analysis of organic compounds, were employed for these instruments. However, quadrupoles cannot achieve the same level of accuracy as magnetic sector instruments, although they are widely used for elemental analysis. Magnetic sector ICP-MS instruments came on the market a decade after quadrupole ICP-MS instruments and now achieve accuracies competitive with thermal ionization instruments. Combined with their generally higher ionization efficiency and hence higher sensitivity, they produce results that are superior to thermal instruments for several elements. As they continue to develop they may entirely replace thermal ionization instruments. More information on ICP-MS can be found in Vanhaecke and Degryse (2012).

In secondary ion mass spectrometry (SIMS), the sample is introduced directly into the evacuate source chamber and ions produced by *ion sputtering*, in which an ion beam is fired at the sample surface to produce secondary ions. The advantage of this technique is that very

small areas, with diameters of the order of tens of microns and less, can be analyzed. The amount of analyte ions produced, however, is small, so this approach is most useful when the element of interest is at high concentration (Pb and Hf in zircon, or oxygen in silicates, for example). Even in this case, however, precision is generally lower than with other techniques.

Another method of ion production is *resonance ionization*. In this technique, a laser, tuned to a frequency appropriate for ionization of the element of interest, is fired at the sample.

After the ions are produced, they are accelerated by an electrostatic potential, typically in the range of 5–20 kV for magnetic sector mass spectrometers. The ions move through a series of slits between charged plates. The charge on the plates also serves to collimate the ions into a beam. Generally the potential on the plates can be varied somewhat; in varying the potential on the plates, one attempts to maximize the beam intensity by “steering” as many ions as possible through the slits. Thus the source produces a narrow beam of nearly mono-energetic ions (secondary ions are not mono-energetic and must be energy-filtered, which we will discuss next).

A.2.2 The mass analyzer

The function of the mass analyzer is two-fold. The main purpose is to separate the ions according to their mass (strictly speaking, according to their mass/charge ratio). But as is apparent in Figure A.2, the mass analyzer of a sector mass spectrometer also acts as a lens, focusing the ion beam on the detector.

A charged particle moving in a magnetic experiences a force

$$\mathbf{F} = q\mathbf{v} \times \mathbf{B} \quad (\text{A.1})$$

where \mathbf{B} is the magnetic field strength, \mathbf{v} is the particle velocity, and q is its charge (bold is used to denote vector quantities). Note that force is applied perpendicular to the direction of motion (hence it is more properly termed a torque), and it is also perpendicular to the magnetic field vector. Since the force is always directed perpendicular to the direction of motion, the particle begins to move in a circular path. The motion is thus much like swinging a ball at the end of a string, and we

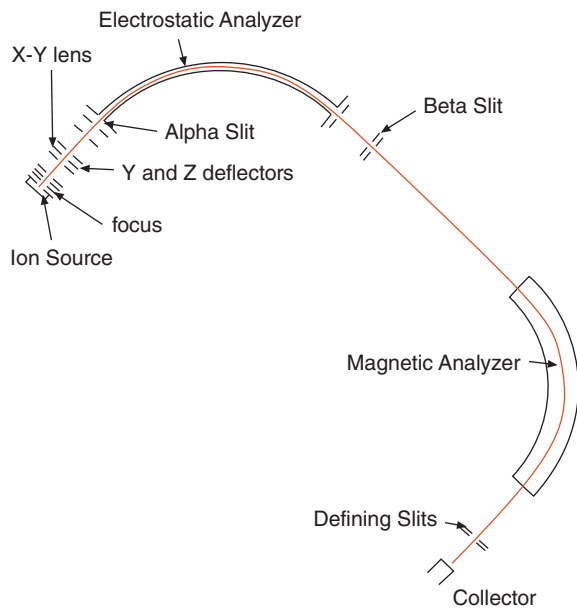


Figure A.2 A double-focusing or Nier-Johnson mass spectrometer with both magnetic and electrostatic sectors. (Source: Majer, 1977.)

can use equation for a centripetal force:

$$F = m \frac{v^2}{r} \quad (\text{A.2})$$

This can be equated with the magnetic force:

$$m \frac{v^2}{r} = qv \times B \quad (\text{A.3})$$

The velocity of the particle can be determined from its energy, which is the accelerating potential, V , times the charge:

$$Vq = \frac{1}{2}mv^2 \quad (\text{A.4})$$

Solving A.4 for v^2 , and substituting in Eqn. A.3 yields (in non-vector form):

$$2 \frac{V}{r} = \sqrt{\frac{2Vq}{m}} B \quad (\text{A.5})$$

Solving A.5 for the mass/charge ratio:

$$\frac{m}{q} = \frac{B^2 r^2}{2V} \quad (\text{A.6})$$

relates the mass/charge ratio, the accelerating potential, the magnetic field, and the radius of

curvature of the instrument. If B is in gauss, r in cm, and V in volts, this equation becomes:

$$\frac{m}{q} = 4.825 \times 10^{-5} \frac{B^2 r^2}{V} \quad (\text{A.7})$$

with m in unified atomic mass units and q in units of electronic charge. For a given set of conditions, a heavier particle will move along a curve having a longer radius than a lighter one. In other words, the lighter isotopes experience greater deflections in the mass analyzer.

A typical radius is 27 cm for a TIMS instrument, which typically operating potential is 8 to 10 kV. Instruments with smaller radii are used in gas source mass spectrometers for light elements such as C, O, and Ar and larger radii are used in SIMS instruments where it is necessary to separate isobaric interferences. Masses are selected for analysis by varying the magnetic field (note that in principle we could also vary the accelerating potential; however, doing so has a second order effect on beam intensity, which is undesirable), generally in the range of a few thousand gauss for a TIMS instrument.

It was shown in the 1950s that if the ions entered the magnetic field at an angle of 26.5° rather than at 90°, the effective radius of the mass analyzer doubles (i.e., a 27 cm instrument will have an effective radius of 54 cm). This design trick, employed in all modern mass spectrometers, results in higher resolution (better separation between the masses at the collector). An additional advantage of this “extended geometry” is that the ion beam is focused in the z direction (up-down) in addition to the x - y direction. This is an important effect because it allows the entire ion beam to enter the detector, which in turn allows the use of multiple detectors. In addition, modern mass spectrometers have further modifications to the magnet pole faces to produce a linear focal plane, which is helpful in the multiple collectors currently in use.

Collisions of ions with ambient gas result in velocity and energy changes and cause the beam to broaden. To minimize this, the analyzer is evacuated to 10^{-6} to 10^{-9} torr ($= 1 \text{ mm Hg} \approx 10^{-3} \text{ atm}$). Somewhat lower vacuums can be tolerated in the ion source. Where very high resolution is required or the ion beam is not initially mono-energetic, as in SIMS or ICP-MS instruments, an energy filter is

employed. This is simply an electrostatic field. The electric field force is not proportional to velocity, as it the magnetic field. Instead, ions are deflected according to their energy. The radius of curvature is given by:

$$R = \frac{2V}{V_2} \quad (\text{A.8})$$

where V_2 is the electrostatic potential of the energy filter and V is the energy of the ions (equal to the accelerating potential). Instruments employing both mass and energy filters are sometimes called *double-focusing* instruments. An example is shown in Figure A.2.

A.2.3 The detector

In general, ions are “collected,” or detected, at the focal plane of the mass spectrometer in one of two ways. The most common method, particularly for high precision mass spectrometers, is with a “Faraday cup,” which is shown schematically in Figure A.3. As the name implies, this is a metal cup, generally a few millimeters wide and several centimeters deep (the depth is necessary to prevent ions and electrons from escaping). After passing through a narrow slit, ions strike the Faraday cup and are neutralized by electrons flowing to the cup from ground. The ion current into the cup is determined by measuring the voltage developed across a resistor as electrons flow to the cup to neutralize the ion current. The voltage is amplified, converted to a digital signal, and sent to a computer that controls data acquisition. In most mass spectrometers,

the resistor has a value of 10^{11} ohms. Since $V=I\Omega$, an ion current of 10^{-11} A will produce a voltage of 1 V. Typical ion currents are on the order of 10^{-15} to 10^{-10} A. In the design of the collector, care must be exercised that ions or free electrons produced when the ion strikes the cup cannot escape from the cup.

Most modern mass spectrometers now employ a number of Faraday cups arrayed along the focal plane so that several isotopes can be collected simultaneously. The spacing of the Faraday cups varies from element to element. Positioning of cups can be done using stepping motors under computer control. In some cases, fixed cups are used and electric fields are used to deflect specific masses into the cups.

When ion currents are weak, a “multiplier” is used as the detector. These increase the signal-to-noise ratio, but at some cost in precision. In an electron multiplier, illustrated in Figure A.4, the ion strikes a charged dynode. The collision produces a number of free electrons, which then move down a potential gradient. Each one of the electrons strikes a second electrode, again producing a number of free electrons. This process continues through a series of 10 or so electrodes to produce a cascade or shower of electrons. The net effect is an amplification of the signal of typically 100. An alternative is a Daly detector (named for its inventor), illustrated in Figure A.5. Ions strike a charged electrode, producing electrons as in the electron multiplier. These electrons then strike a fluorescent screen producing light, which is later converted to electrical signal. The net effect is also an amplification of a factor of 100.

Multipliers may be used in either “analog” or “pulse count” mode. In analog model, the ion beam current is simply amplified and measured. In pulse count mode, rather than measuring the ion beam current, individual ions are counted. When an ion strikes the

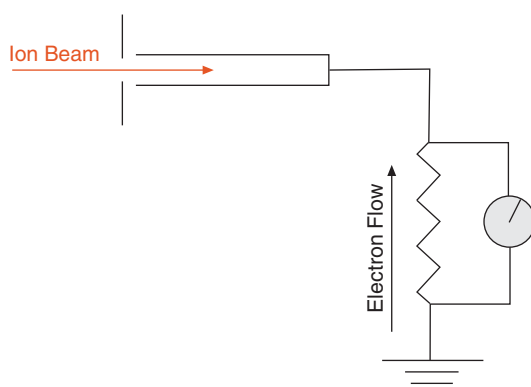


Figure A.3 Schematic drawing of a Faraday cup configured for positive ions. Electron flow would reverse for negative ions.

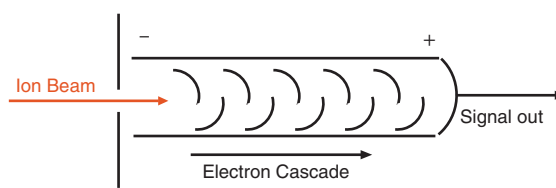


Figure A.4 Schematic of an electron multiplier.

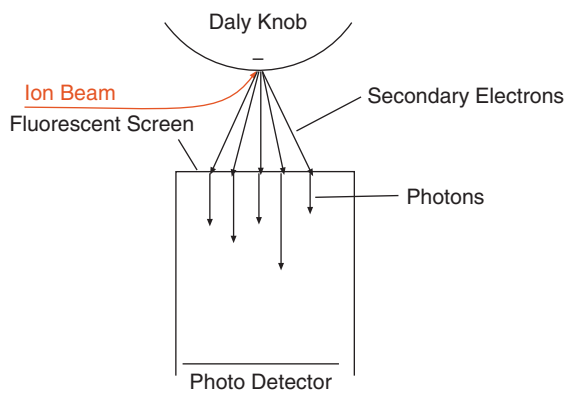


Figure A.5 Schematic of the Daly Detector.

detector, an electrical “pulse” is produced. In pulse count mode, these pulses are counted by specialized electronics. Pulse count mode is useful only at low beam intensities; at higher ion beam intensities, an analog detector, such as the Faraday cup, provides superior results.

A.3 ACCELERATOR MASS SPECTROMETRY

Traditionally, cosmogenic nuclides have been measured by counting their decays. In the past few decades, the utility of these cosmogenic nuclides in geochemistry and geochronology has been greatly enhanced by the advent of accelerator mass spectrometers, providing both more precise results from old applications (e.g., ^{14}C dating) and new applications

(identifying subducted sediment with ^{10}Be). Mass spectrometry is a much more efficient method of detecting atoms than counting their decays in most instances. For example, the $^{14}\text{C}/^{12}\text{C}$ ratio in the atmosphere is 10^{-12} . One gram of this carbon produces about 15 beta decays per minute. But this gram contains about 10^{10} atoms of ^{14}C . Even at an efficiency of ion production and detection of only 1%, 70 μg of carbon can produce an ion beam that will result in detection of 36,000 atoms ^{14}C per hour. It would take 65 years for the same amount of carbon to produce 36,000 beta decays. However, there are some severe limitations with conventional mass spectrometry in measuring very small isotope ratios (down to 10^{-15}). Two problems must be overcome: limitations of resolution, and isobaric interferences. Conventional mass spectrometers have resolutions of only about a ppm at Δm of 1 u, and a fraction of a ppm at Δm of 2 u. What this means is that for every 10^6 or 10^7 , ^{12}C atoms that arrived at the ^{12}C position in the detector, about 1 ^{12}C atom will arrive at the ^{14}C position. If the $^{14}\text{C}/^{12}\text{C}$ ratio is 10^{-14} , some 10^7 more ^{12}C would be detected at the ^{14}C position than ^{14}C atoms!

The techniques involved in accelerator mass spectrometry vary with the element of interest, but most applications share some common features that we will briefly consider. Figure A.6 is an illustration of the instrument at the National Ocean Sciences Accelerator Mass Spectrometer Facility at Woods Hole Oceanographic Institution. We will consider

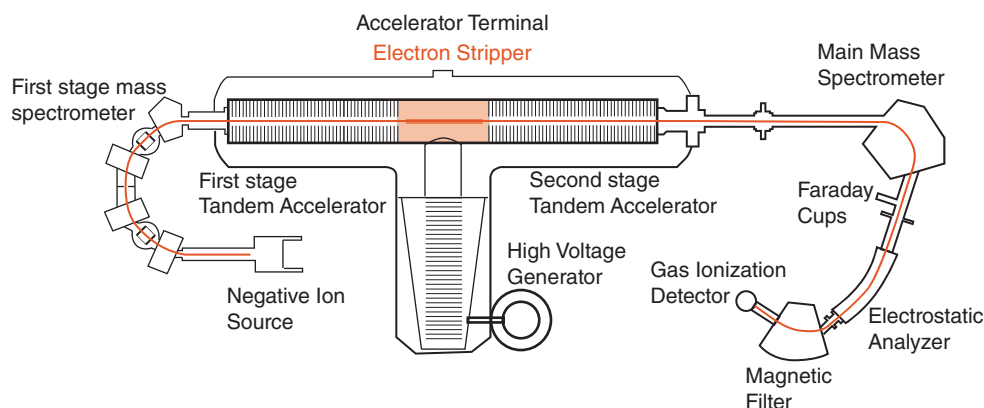


Figure A.6 The accelerator mass spectrometer at National Ocean Sciences Accelerator Mass Spectrometer Facility at Woods Hole Oceanographic Institution. Gray line shows the ion path through the instrument. (Source: Adapted from an image of Woods Hole Oceanographic Institution.)

its application in ^{14}C analysis as an example. A beam of C^- is produced by sputtering a graphite target with Cs^+ ions. There are several advantages in producing, in the initial stage, negative ions, the most important of which in this case is the instability of the negative ion of the principal atomic isobar, ^{14}N . The ions are then accelerated to 40keV (a higher energy than conventional mass spectrometers) and separated with the first stage magnet, so that only ions with m/q of 12–14 enter the accelerator. In the first stage of the tandem accelerator, the negative ions are accelerated toward the positive charge of the accelerator terminal at 2.5 MeV. Electrons are then stripped from the atoms in the electron stripper through high-energy collisions with Ar gas to produce C^{4+} ions. The reason for producing multiply charged ions is that there are no known stable molecular ions with charge greater than +2. Thus the production of multiply charged ions effectively separates ^{14}C ions from molecular isobaric ions such as $^{12}\text{CH}_2$. The now positively charged ions accelerate away from the positive charge of the accelerator terminal and pass through the main mass spectrometer. Following this, ^{12}C and ^{13}C are detected by Faraday cups, while ^{14}C continues through an electrostatic filter (which selects for ion energy E/q) and a magnetic filter (which selects for momentum) before entering the detector. The final detector distinguishes ^{14}C from residual ^{14}N , ^{12}C , and ^{13}C by the rate at which they lose energy through interaction with a gas.

A.4 ANALYTICAL STRATEGIES

Isotopic variations in nature are very often quite small. For example, variations in Nd (neodymium) isotope ratios are measured in parts in 10,000. There are exceptions, of course. He and Os isotope ratios, as well as Ar isotope ratios, can vary by orders of magnitude, as can Pb in exceptional circumstances (minerals rich in uranium). These small variations necessitate great efforts in precise measurements. In this section we will briefly discuss some of the methods employed in isotope geochemistry to reduce analytical error.

One technique used universally to reduce analytical errors is to make a *large number of measurements*. Thus a value for the $^3\text{He}/^4\text{He}$ ratio reported in a paper will actually be

the mean of perhaps 100 individual ratios measured during a “run” or analysis. Any short-term drift or noise in the instrument and its electronics, as well as in the ion beam intensity, will tend to average out. The use of *multiple collectors* and simultaneous measurement of several isotopes essentially eliminates errors resulting from fluctuations in ion beam intensity. This, however, introduces other errors related to the relative gains of the amplifiers, which then require correction. A final way to minimize errors is to *measure a large signal*. The inherent uncertainty in measuring x number of counts is \sqrt{x} . Thus the inherent uncertainty in measuring 100 atoms is 10%, but the uncertainty in measuring 1,000,000 atoms is only 0.1%. These “counting statistics” are the ultimate limit in analytical precision, but they come into play only for very small sample sizes.

A.4.1 Correcting mass fractionation

One of the most important sources of error in solid source mass spectrometry results from the tendency of the lighter isotopes of an element to evaporate more readily than the heavier isotopes (Chapter 8). This means that the ion beam will be richer in light isotopes than the sample remaining on the filament. As the analysis proceeds, the solid will become increasingly depleted in light isotopes and the ratio of a light isotope to a heavy one will continually decrease. This effect can produce variations up to a percent or so per mass unit (though it is generally much less). This would be fatal for Nd, for example, where natural isotopic variations are much less than a percent, if there were no way to correct for this effect. Fortunately, a correction can be made. The trick is to measure the ratio of two isotopes that are not radiogenic; that is a ratio that should not vary in nature. For Sr, for example, we measure the ratio of $^{86}\text{Sr}/^{88}\text{Sr}$. By convention, we assume that the value of this ratio is equal to 0.11940. Any deviation from the value is assumed to result from mass fractionation in the mass spectrometer. The simplest assumption about mass fractionation is that it is linearly dependent on the difference in mass of the isotopes we are measuring. In other words, the fractionation between ^{87}Sr and ^{86}Sr should be half that between ^{88}Sr and ^{86}Sr . So if we know how much the $^{86}\text{Sr}/^{88}\text{Sr}$ has fractionated from the “true” ratio, we can

calculate the amount of fractionation between ^{87}Sr and ^{86}Sr . Formally, we can write the *linear mass fractionation law* as:

$$\alpha(u, v) = \left[\frac{R_{uv}^N}{R_{uv}^M} - 1 \right] / \Delta m_{uv} \quad (\text{A.9})$$

where α is the fractionation factor between two isotopes u and v , Δm is the mass difference between u and v (e.g., 2 for 86 and 88), R^N is the “true” or “normal” u/v isotope ratio (e.g., 0.11940 for 86/88), and R^M is the measured ratio. The correction to the ratio of two other isotopes (e.g., $^{87}\text{Sr}/^{86}\text{Sr}$) is then calculated as:

$$R_{ij}^C = R_{ij}^M (1 + \alpha(i, j) \Delta m_{ij}) \quad (\text{A.10})$$

where R^C is the corrected ratio and R^M is the measured ratio of i to j and

$$\alpha(i, j) = \frac{\alpha(u, v)}{1 - \alpha(u, v) \Delta M_{vj}} \quad (\text{A.11})$$

If we choose isotopes v and j to be the same (e.g., to both be ^{86}Sr), then $\Delta m_{vj} = 0$ and $\alpha(i, j) = \alpha(u, v)$. (A convention that is unfortunate in terms of these equations, however, is that we speak of the 86/88 ratio, when we should speak of the 88/86 ratio (=8.37521).) Using the 88/86 ratio, the “normalization” equation for Sr becomes:

$$\begin{aligned} \left(\frac{^{87}\text{Sr}}{^{86}\text{Sr}} \right)^c &= \left(\frac{^{87}\text{Sr}}{^{86}\text{Sr}} \right)^M \\ &\times \left[1 + \left\{ \frac{8.37521}{(^{88}\text{Sr}/^{86}\text{Sr})^M} - 1 \right\} \right] / 2 \end{aligned} \quad (\text{A.12})$$

A more accurate description of mass fractionation is the *power law*. The fractionation factor is:

$$\alpha = \left[\frac{R_{uv}^N}{R_{uv}^M} \right]^{1/\Delta m_{uv}} - 1 \quad (\text{A.13})$$

The corrected ratio is computed as:

$$R_{ij}^C = R_{ij}^M [1 + \alpha]^{\Delta m_{ij}} \quad (\text{A.14})$$

or:

$$\begin{aligned} R_{ij}^C &= R_{ij}^M \left[1 + \alpha \Delta m_{ij} + \frac{1}{2} \Delta m_{ij} (\Delta m_{ij} - 1) \alpha^2 \right. \\ &\quad \left. + \dots \right] \end{aligned} \quad (\text{A.15})$$

Since α is a small number, higher order terms may be dropped.

Finally, it is claimed that the power law correction is not accurate and that the actual fractionation is described by an *exponential law*, from which the fractionation factor may be computed as:

$$\alpha = \frac{\ln [R_{uv}^N / R_{uv}^M]}{m_j \ln(m_u / m_v)} \quad (\text{A.16})$$

and the correction is:

$$\begin{aligned} R_{ij}^C &= R_{ij}^M \left(\frac{m_i}{m_j} \right)^{m_i} \\ &= R_{ij}^M \left[1 + \alpha \Delta m_{ij} - \alpha \frac{m_{ij}^2}{2m_j} + \alpha^2 \frac{m_{ij}^2}{2} + \dots \right] \end{aligned} \quad (\text{A.17})$$

The exponential law appears to provide the most accurate correction for mass fractionation. However, all of these laws are empirical rather than theoretical. The processes of evaporation and ionization are complex, and there is yet no definitive theoretical treatment of mass fractionation during this process.

For stable isotopes where the objective to discover the extent of natural fractionation, as well as for Pb, which has only one non-radiogenic isotope, this approach cannot obviously cannot be used. As we noted, gas source mass spectrometers used for light stable isotopes are designed to minimize instrumental fractionation and furthermore they can quickly switch from sample to standard and back. A correction for any instrumental mass fractionation can be made based on the difference between the measured and “true” isotopic composition of the standard. This approach is not practical for either TIMS or ICP-MS instruments, but there are several other approaches possible. First, standards can be analyzed intermittently and a correction applied to samples based on the observed mass fractionation in the standards; this was the traditional approach used for Pb isotopes. Second, for light elements such as Li or B, one can analyze a polyatomic molecule containing a much heavier element, increasing atomic mass and hence decreasing fractionation. Two other alternatives are available. In the first of these, for elements with three or more isotopes, a “spike” consisting of two or more

isotopes of the element in proportions very different from the natural ones can be added to the analyte. Knowing the precise composition of the spike, the amount of spike added, and that the “natural” isotopic composition must be related to that of standard by mass fractionation, the true isotopic composition of the analyte can be calculated (e.g., Krabbenhoft et al., 2010). This approach is used quite successfully for Pb, but requires separate analysis of spiked and unspiked fractions (e.g., Galer, 1999). Finally, for ICP-MS analyses, the “spike” can consist of isotopes of an element with masses similar to that of the element of interest. For example, Maréchal et al. (1999) used Cu (with isotopes ^{63}Cu and ^{65}Cu) to correct for isotopic fractionation during analysis of Zn (isotopes ^{64}Zn , ^{66}Zn , ^{67}Zn , ^{68}Zn , and ^{70}Zn). This approach must be used with some caution, however, since different elements in the same solution can fractionate to different extents (White et al., 2000).

A.4.2 Deconvolution of results

If the analyte is a polyatomic species, measured abundances of isotopologues must be deconvoluted to obtain the isotopic composition of the element or elements of interest. For example, carbon and oxygen are commonly analyzed as CO_2 , of which there are 12 isotopologues (excluding those containing ^{14}C). For example, ions detected in the collector set for m/z of 46 can be $^{12}\text{C}^{18}\text{O}^{16}\text{O}$, $^{13}\text{C}^{17}\text{O}^{16}\text{O}$, or $^{12}\text{C}^{17}\text{O}^{17}\text{O}$. Of course, isotopologues of ^{17}O are not very abundant, and those containing two ^{17}O atoms will be rare indeed, so mass 46 will consist mainly of $^{12}\text{C}^{18}\text{O}^{16}\text{O}$, but a correction must nevertheless be made. We do not *a priori* know the isotopic composition of either carbon or oxygen, but by solving a series of simultaneous equations, we can nevertheless deduce both if we assume their isotopic compositions are related to standards by mass dependent fractionation laws previously. Another example is that of Nd, which is often analyzed as NdO^+ . $^{134}\text{Nd}^{16}\text{O}^+$ has a mass of 160, but so does $^{143}\text{Nd}^{17}\text{O}^+$ and $^{142}\text{Nd}^{18}\text{O}^+$. This situation is further complicated by mass fractionation that occurs during analysis. Nevertheless, if one assumes that all Nd and O non-radiogenic isotopes are in their natural proportions, calculation of the $^{143}\text{Nd}/^{144}\text{Nd}$ is possible by solving a

series of simultaneous equations. These calculations are often built into the software (or can be added) of the computers that control the instruments, so they are largely invisible to the user.

A.4.3 Isotope dilution analysis

Determining precise ages generally requires that we not only determine isotope ratios precisely, but that we also determine parent-daughter ratios precisely. In essence, this means we need to determine the concentrations of the parent and daughter elements. The mass spectrometer is designed for isotope ratio analysis, but with a technique called isotope dilution, we can use it for determining concentrations of elements. It is easiest to explain the technique by taking a concrete example. We can start with the simplest possible example, that of a mono-isotopic element such as Cs. All natural Cs is ^{133}Cs . However, ^{135}Cs is a U fission product with a half-life of 2.3 million years; on the scale of laboratory time, we can consider it to be stable. We take a known amount of rock containing an unknown amount of Cs in it and add a known amount of pure ^{135}Cs “spike” to it. If we separate the Cs from the rock and analyze it in the mass spectrometer, the ratio of ^{135}Cs to ^{133}Cs we observe will be directly proportional to the ratio of the amount of ^{135}Cs we add to the rock to the amount of ^{133}Cs in the rock to begin with. In other words:

$$\frac{^{135}\text{Cs}}{^{133}\text{Cs}} = \frac{\text{moles } ^{135}\text{Cs added}}{\text{moles } ^{133}\text{Cs in rock}} \quad (\text{A.18})$$

Since we know how much ^{135}Cs we added, we can easily calculate the moles of ^{133}Cs in the rock. We can calculate the Cs concentration in ppm from this simply by multiplying by the atomic weight and dividing by the weight of rock we used in our analysis. This is the isotope dilution technique.

The general case is slightly more complex because neither the natural element nor the “spike” will be mono-isotopic. Let’s take a second concrete example. Suppose we want to know the concentration of Rb in a rock. Rb has two isotopes, ^{85}Rb and ^{87}Rb . We make the assumption that the proportion of these two isotopes will not vary in nature. ^{85}Rb constitutes 72.165% and ^{87}Rb 27.835% of

all Rb; the $^{87}\text{Rb}/^{85}\text{Rb}$ ratio is thus 0.3857. Now suppose we have available a “spike” containing 99% ^{87}Rb and 1% ^{85}Rb . Adding a known amount of spike to the rock, and analyzing the isotopic composition, the measured $^{87}\text{Rb}/^{85}\text{Rb}$ will be equal to:

$$\left(\frac{^{87}\text{Rb}}{^{85}\text{Rb}}\right)_M = \frac{[^{87}\text{Rb}]_N + [^{87}\text{Rb}]_S}{[^{85}\text{Rb}]_N + [^{85}\text{Rb}]_S} \quad (\text{A.19})$$

where $(^{87}\text{Rb}/^{85}\text{Rb})_M$ is the measured ratio and $[^{87}\text{Rb}]_N$ is the moles of “natural” ^{87}Rb in the rock, $[^{87}\text{Rb}]_S$ is the moles of ^{87}Rb in the spike we added, and so on.

We can rearrange Eqn. A.19 as:

$$[^{87}\text{Rb}]_N = \frac{[^{85}\text{Rb}]_S \{R_M(^{85}\text{Rb}/^{87}\text{Rb})_S - 1\}}{1 - R_M(^{85}\text{Rb}/^{87}\text{Rb})_N} \quad (\text{A.20})$$

where R_M is $(^{87}\text{Rb}/^{85}\text{Rb})_M$ and $(^{85}\text{Rb}/^{87}\text{Rb})_N$ is the natural isotope ratio and $(^{85}\text{Rb}/^{87}\text{Rb})_S$ is the ratio in the spike. Note that $[^{87}\text{Rb}]_S$ would more conveniently be expressed as the (molar) concentration times the weight of spike added. To find the concentration of ^{87}Rb , we would simply divide by the weight of the sample. To form the $^{87}\text{Rb}/^{86}\text{Sr}$ ratio, we would carry out an isotope dilution analysis for Sr, and calculate the amount of ^{86}Sr using an equation similar to A.20. If our spike is a solution containing both Rb and Sr (which is the usual case), when we divide the equation for ^{87}Sr by the equation from ^{86}Sr , the terms for the weight of spike and weight of sample cancel; that is, weighing error is eliminated.

If we are primarily interested in the concentration of an element such as Rb, rather than the $^{87}\text{Rb}/^{86}\text{Sr}$ ratio, we can rewrite Eqn. A.19 in an alternative form if we let $[^{87}\text{Rb}]_N = N \ ^{87}\text{Rb}$ where N is the total number of atoms (or moles) of Rb in the rock and ^{87}Rb is now the relative abundance of ^{87}Rb in “natural” Rb, that is, 0.27835. Similarly, $[^{87}\text{Rb}]_S = S \ ^{87}\text{Rb}$ where S is the total number of moles of “spike” Rb added to the sample. Equation A.19 then becomes:

$$\left(\frac{^{87}\text{Rb}}{^{85}\text{Rb}}\right)_M = \frac{N^{87}\text{Rb}_N + S^{87}\text{Rb}_S}{N^{85}\text{Rb}_N + S^{85}\text{Rb}_S} \quad (\text{A.21})$$

which we can rearrange as:

$$N = S \left[\frac{^{87}\text{Rb}_S - ^{85}\text{Rb}_S R_M}{^{85}\text{Rb}_N R_M - ^{87}\text{Rb}_N} \right] \quad (\text{A.22})$$

To convert to moles to weight in grams, we multiply the right side by the atomic weight of natural Rb. If our spike concentration is in grams, we would divide by the atomic weight of Rb in the spike:

$$N = S \left[\frac{^{87}\text{Rb}_S - ^{85}\text{Rb}_S R_M}{^{85}\text{Rb}_N R_M - ^{87}\text{Rb}_N} \right] \frac{AW_N}{AW_S} \quad (\text{A.23})$$

Once again, it is convenient to express S , the amount spike Rb added, as the concentration times the weight. And to obtain the concentration of Rb in the rock rather than the weight, we would divide by the weight of the sample:

$$Rb \ conc = \left[\frac{^{87}\text{Rb}_S - ^{85}\text{Rb}_S R_M}{^{85}\text{Rb}_N R_M - ^{87}\text{Rb}_N} \right] \times \frac{AW_N}{SW_S} \frac{\text{spike wt} \times \text{spike conc}}{\text{sample wt}} \quad (\text{A.24})$$

For elements consisting of more than two isotopes, it is possible to include corrections for mass fractionation in the isotope dilution calculation (e.g., Hofmann, 1971).

NOTES

1. It was developed by Alfred Nier of the University of Minnesota in the 1930s. Nier used his instrument to determine the isotopic abundances of many of the elements. In the course of doing so, however, he observed variations in the ratios of isotopes of a number of stable isotopes as well as Pb isotopes and hence was partly responsible for the fields of stable and radiogenic isotope geochemistry. He also was the first to use a mass spectrometer for geochronology, providing the first radiometric age of the solar system. In the 1980s he was still designing mass spectrometers, this time miniature ones which could fly on spacecraft on interplanetary voyages. These instruments provided measurements of the isotopic composition of atmospheric gases of Venus and Mars. Nier died in 1994.

REFERENCES

- Dickin, A. 1995. *Radiogenic Isotope Geochemistry*. Cambridge: Cambridge University Press.
- Elmore, D. and Phillips, F. M. 1987. Accelerator mass spectrometry measurements of long-lived radioisotopes. *Science*, 236: 543–550.
- Faure, G. 1986. *Principles of Isotope Geology*. New York: John Wiley & Sons, Inc.
- Galer, S. J. G. 1999. Optimal double and triple spiking for high precision lead isotopic measurement. *Chemical Geology*, 157: 255–274.
- Hofmann, A. 1971. Fractionation corrections for mixed-isotope spikes of Sr, K, Pb. *Earth and Planetary Science Letters*, 10: 397–402.
- Krabbenhöft, A., Eisenhauer, A., Böhm, F., Vollstaedt, H., Fietzke, J., Liebetrau, V., et al. 2010. Constraining the marine strontium budget with natural strontium isotope fractionations ($^{87}\text{Sr}/^{86}\text{Sr}$, $\delta^{88}/^{86}\text{Sr}$) of carbonates, hydrothermal solutions and river waters. *Geochimica et Cosmochimica Acta*, 74: 4097–4109, doi: 10.1016/j.gca.2010.04.009.
- Majer, J. R. 1977. *The Mass Spectrometer*. London: Wykeham Publications.
- Maréchal, C. N., Télouk, P. and Albarede, F. 1999. Precise analysis of copper and zinc isotopic compositions by plasma-source mass spectrometry. *Chemical Geology*, 156: 251–273, doi: 10.1016/s0009-2541(98)00191-0.
- Muzikar, P., Elmore, D. and Granger, D. E. 2003. Accelerator mass spectrometry in geologic research. *Geological Society of America Bulletin*, 115: 643–654, doi: 10.1130/0016-7606(2003)115<0643:amsigr>2.0.co;2.
- Vanhaecke, F. and Degryse, P. (eds) 2012. *Isotopic Analysis: Fundamentals and Applications Using ICP-MS*. Weinheim: Wiley-VCH.
- Wasserburg, G. J., Jacobsen, S. B., DePaolo, D. J., McCulloch, M. T. and Wen, T. 1981. Precise determination of Sm/Nd ratios, Sm and Nd isotopic abundances in standard solutions. *Geochimica et Cosmochimica Acta* 45: 2311–2324.
- White, W. M., Albarede, F. and Telouk, P. 2000. High-precision analysis of Pb isotope ratios by multi-collector ICP-MS. *Chemical Geology*, 167: 257–270.
- Wunderlich, R. K., Hutcheon, I. D., Wasserburg, G. J. and Blake, G. A. 1992. Laser-induced isotopic selectivity in the resonance ionization of Os. *International Journal of Mass Spectrometry and Ion Processes*, 115: 123–155.

PROBLEMS

- How long will a $^{143}\text{Nd}^+$ ion spend traversing a 2 m mass spectrometer flight tube if it has been accelerated by a potential of 10 kV?
- What magnetic field (in gauss) is required to steer a $^{87}\text{Sr}^+$ atom through a 90° sector, 30 cm radius mass spectrometer when the accelerating potential is set to 10 kV?
- If the magnetic field in the mass spectrometer described earlier is set to intensity you have calculated, what would be the spacing in mm between a faraday cup collecting $^{87}\text{Sr}^+$ and one collecting $^{86}\text{Sr}^+$?
- Show that the equation:

$$(^{87}\text{Sr}/^{86}\text{Sr})_{\text{true}} = \sqrt{\frac{87''}{86'} \frac{87'}{88''}} \times 8.37521$$

corrects for both mass fractionation and differences in amplifier gain between two Faraday cups. $87''$ is the measured signal intensity of ^{87}Sr in cup 2, $87'$ is the measured signal intensity in cup 1.

- Suppose you measure a $^{87}\text{Sr}/^{86}\text{Sr}$ ratio of 0.70326 with a mass spectrometer. To monitor mass fractionation, you also measured $^{86}\text{Sr}/^{88}\text{Sr}$ and found a value of 0.12010. Assume the true value of $^{86}\text{Sr}/^{88}\text{Sr}$ is 0.11940.
 - What is the true $^{87}\text{Sr}/^{86}\text{Sr}$ ratio according to the linear mass fractionation law?
 - What is the true $^{87}\text{Sr}/^{86}\text{Sr}$ ratio according to the power mass fractionation law?

Index

- absolute age of wood, 103
absolute solar system
 chronology, 136
acapulcoites, 126, 129
Acasta gneisses, 206
accelerator mass spectrometry
 (AMS), 102, 104,
 459–460
Acfer (CH3) chondrite, 150
achondrites, 126, 128, 138
 primitive, 126
 Shallowater aubrite, 132
acopulcite, 133
Acopoluco acopulcite, 133
acoustical vibrations, 255
Adamello Massif, 292
Agassiz, Louis, 1, 326
 ^{26}Al , 106–108
ALHA78132 achondrite, 138
alkaline earth elements, 48
allanite $((\text{Ca}, \text{Ce}, \text{Y}, \text{La})_2(\text{Al}, \text{Fe}^{+3})_3(\text{SiO}_4)_3(\text{OH}))$, 91
Allende (CV3), 126
 CAI's, 127–128, 138
 acid-dissolution residues of,
 148
 $^{26}\text{Al}-^{26}\text{Mg}$, 134–136
 importance as a heat source,
 134
 systematics for two different
 meteorites, 135
alpha-counting, 86
alpha decay, 13
amoeboid olivine aggregates
 (AOAs), 125, 136
amphiboles, 287
Andean magmas, 295
Andrew Bain Fracture Zone, 187
Angra dos Reis, 128

angrites, 126, 128
angular momentum,
 nuclear, 14
annealing of fission tracks, 115,
 116
 zircon (ZrSiO_4), 118
anomalous W isotopic
 compositions, 138
anorthosites, 139
Antarctic Bottom Water
 (AABW), 233
Antarctic Circumpolar Current,
 233
Antarctic Convergence and
 Antarctic Bottom Water
 (AABW), 333
Antarctic Intermediate Water
 (AAIW), 333
apatite ($\text{Ca}_5(\text{PO}_4)_3(\text{OH})$), 73
apparent isochrons, 64
aragonite, 49
 $^{40}\text{Ar}/^{39}\text{Ar}$ dating, 39, 43–47
 complications affecting, 44–45
 isochrons, 45–47
 $^{40}\text{Ar}/^{36}\text{Ar}$ ratio, 45, 422
Archean crust, 214
Archean Isua supracrustals, 209
archeology and isotopes,
 321–323
Ar diffusional loss, 45
argon, 430–432
Arrhenius relation, 117
arsenides, 63
asphaltenes, 64
assimilation and fractional
 crystallization (AFC),
 291–292
assimilatory sulfate reduction,
 273

asteroids
 239 Nenetta, 126
 3819 Robinson, 126
tungsten and silver isotopes in,
 140
 4 Vesta, 126, 129
Asuka 881394, 128
Asymptotic Giant Branch stars
 (AGB), 147–148
atmospheric carbon, 102
atmospheric CO_2 , 356–358
atmospheric specific activity, 103
atomic masses, 4
atomic theory, 2–3
authigenic celadonite, 49
autotrophs, 265

baddeleyite (ZrO_2), 73, 91
Banda arc magmas, 294
barrier energy, 259
basalts, 49, 139
 basaltic achondrite, 128
 oceanic island basalts (OIB),
 163–164
Bastar craton of India, 209
batch melting, 193
 ^{10}Be , 106–108, 146
 constant production rate for,
 108
 dating, 106–107
 as a function of depth, 107
 production of, 104
Becker, H., 2
Benioff zone, 295
Benson-Calvin cycle, 266,
 323
benthic foraminifera, 106, 328,
 333–335, 349–350, 352
benzene (C_6H_6), 102

- beta decay, 13–14, 14, 16, 39, 176
 neutrinos and, 176
 Big Bang phenomenon, 16, 18
 binding energies, 4
 in liquid-drop model, 6–7
 per nucleon, 4
 biosphere, isotope fractionation in, 265–274
 biological fractionation of sulfur isotopes, 273–274
 carbon and hydrogen isotopic composition of organic matter in sediments, 271–273
 carbon isotope fractionation during photosynthesis, 265–269
 nitrogen isotope fractionation in biological processes, 269–271
 oxygen and hydrogen isotope fractionation by plants, 271
 biotite, 73
 black smokers, 299
 blueschist facies rocks, 60–61
 blue supergiant, 23
 Bohr, Neils, 2, 6
 Boltwood, Bertram, 2, 32
 Boltzmann distribution function, 249
 bomb-produced radionuclides in hydrology, 108–110
 Borexino detector, 178
 boron isotopes, 384–390
 Bothe, W., 2
Bouvante achondrite, 128
 branching ratio, 39
 brown dwarfs, 20
 bulk partition coefficient, 194
 buoyancy flux, 179
- Ca-bearing minerals, 49
 calcite flowstone, 89
 calcium-aluminum inclusions (CAIs), 125
 ages of, 128, 133–137, 140
 $^{26}\text{Al}/^{27}\text{Al}$ ratios, 134, 146, 150
 ^{10}Be in, 146
 compositions, 153
Efremovka, 127
 Sr, Mo, Ba, Nd, and Sm
 isotopic compositions of, 151
 as U-Pb dating targets, 127
 calcium isotopes, 397–401
 CALIB program, 104
- calibration of ^{14}C , 104
 Calvin cycle, 266
 Cape of Good Hope, 236
 capture cross section, 11, 43
 carbonaceous chondrites, 125, 138, 152
 noble gases of, 146, 421–423
 U/Pb ratio in, 168
 carbon and hydrogen isotopic composition of organic matter in sediments, 271–273
 carbonates, 87, 89
 ion isotopologues, 257
 isotopic composition of, 257
 carbon-12 atom, 4
 carbon-burning phase, 22
 carbon cycle
 long-term, 351–359
 short-term, 342–347
 carbon-14 dating, 2, 89, 102–103
 of groundwater, 108
 moraines, 114
 short half-life, 102
 to waters less than 25,000 years old, 108
 carbon isotope fractionation during photosynthesis, 265–269
 of algae and autotrophic bacteria, 266, 268
 fractionation occurring during carboxylation, 267
 of marine algae and aquatic plants, 266
 observed total fractionation *vs* expected fractionation, 266–267
 stomatal conductance, 265
 of terrestrial plants, 265–266
 carbon isotopes, 265–269, 318–321
 composition of mantle, 284–286
 and earliest life, 323–325
 ocean circulation, and climate, 332–334
 carboxylation, 266
 Ca-rich plagioclase, 45
 Cenozoic mountain-building, 237
 Central Volcanic Zone (CVZ), 295
 CERN's Large Hadron Collider, 101
 Chadwick, James, 2
 chalcophile elements, 61
 Chandrasekhar mass, 25
- characteristic penetration depth, 112
 charcoal, 89
Chassigny, 126, 144
 chemical abrasion technique, 81
 Chicxulub impactor, 238
 chlorine isotopes, 405–408
 chlorophyll porphyrin, 64
 chondrites, 125, 138, 207
 $^{40}\text{Ar}/^{39}\text{Ar}$ ages, 129
 carbonaceous (C), 125
 chondritic Hf/W ratio, 137
 chondrules of, 125, 128, 135–136
 CI, 125
 enstatite, 125
 late accretionary veneer of, 140
 Nd isotopic variations, 143
 $^{142}\text{Nd}/^{144}\text{Nd}$ ratio, 141
 ordinary, 125
 petrographic grade, 126
Ste. Marguerite, 128
Tuxtuac, 131
 $^{182}\text{W}/^{183}\text{W}$, 163
Zag, 132
 chondritic uniform reservoir (CHUR), 53, 54, 211
 model age of a system, 55
 chronometer, 12
 C_3 & C_4 hydrocarbons, 246, 266–268
 CI chondrites, 125
 Circumpolar Deep Water (CDW), 233
 ^{36}Cl , 106–108
 ages of moraine boulders from Bloody Canyon, 114
 $^{36}\text{Cl}/\text{Cl}$ ratio, 109–110
 dating of glacial deposits, 113–114
 hydrologic flow parameters, 111
 means of production, 109
 Clayton, R., 152
 Clayton's self-shielding hypothesis, 153
 CI chondrites, 125
 clinopyroxene, 48, 194
 closure depths, 119–120
 closure temperatures
 for K-Ar, 129
 U-Th-He system, 83
 ^{35}Cl spallation reactions, 114
 clumping of isotopes, 256–258
 applications, 366–369

- CM2 chondrites, 147
 characteristics of presolar grains in, 149
- CNO cycle, 21–22
- $^{13}\text{C}^{18}\text{O}$, 256
- CO, isotopologues of, 257
- CO₂ concentrations, 1
- coincidence counting, 102
- Cold Bokkeveld* chondrite, 138
- collisional erosion hypothesis, 53, 144
- concordia diagram, 78–79
 Tera-Wasserburg, 76
 concordant, 78
 definition, 78
 for Pb loss during a metamorphic event, 79
 Pa-Th, 92
 U-Pb, 92–93
 of zircons, 80–82
- constant activity model, 94
- constant flux–constant sedimentation model, 94–95
- constant flux model, 94
- constant initial concentration model, 94
- constant rate of supply model, 94
- constant sedimentation model, 94
- continental crust, 173
 Acasta gneisses, 206
 assimilation, effects of, 189
 Cretaceous-Tertiary boundary, 238
 crustal composition and evolution, 224–226
 evolution of κ and κ_{Pb} , 223
 growth of, 212–215
 Hadean crustal protoliths, 206
 Hadean eon, 206–212
 half-mass stratigraphic age, 226
 Hf in crustal rocks, 220
 isotopic composition of, 217–223
 marine sediments, 220
 mass of, 174
 mass ratio of continental crust to depleted mantle, 173
 mechanisms of crustal growth, 205–206
 Nd and Hf isotopic approaches to crustal evolution, 215–217
 $^{143}\text{Nd}/^{144}\text{Nd}$, 224–225
 $^{143}\text{Nd}/^{144}\text{Nd}$ ratio, 173–174
 $^{143}\text{Nd}/^{144}\text{Nd}$ ratio of, 173–174
 O– ϵ_{Hf} relationship, 216
- $^{187}\text{Os}/^{188}\text{Os}$, 236, 238
 $^{187}\text{Os}/^{186}\text{Os}$ ratio, 221
- Pb isotope ratios and Th/U ratio, 223
- Proterozoic crust, 216
- rate of continent-to-mantle recycling, 226
- relationships between τ_{ST} and τ_{CR} , 224
- rock formation, 215
- sedimentary mass, 225
- $^{147}\text{Sm}/^{144}\text{Nd}$ ratio of, 174
- $^{147}\text{Sm}/^{144}\text{Nd}$ ratios, 224–225
- subduction zones, 226–231
- tectonic erosion of, 182
- U/Pb ages of juvenile igneous rocks, 214
- continental flood basalts, 191, 193
- continental isotopic records, 336–337
- continental volcanism, 206
- conventional meteorite chronology, 128
- $^{13}\text{C}^{18}\text{O}^{16}\text{O}$ isotopologue, 257
- copper isotopes, 378–381
- corderite-bearing lavas, 294
- Coriolis effect, 232
- Cornell Electron Storage Ring, 101
- corundum (Al_2O_3), 150
- cosmic ray exposure ages of meteorites, 154
- cosmic ray flux, 101
- cosmic ray-induced spallation, 111
- cosmic rays in the atmosphere, 101–102
 ^{10}Be , ^{26}Al , and ^{36}Cl , 106–108
 tritium (^3H), 108
- cosmochronology
 conventional methods, 126–129
 extinct radionuclides, 129–145
 origin of short-lived nuclides, 145–146
- cosmogenic nuclides, 101–114
- cosmogenic-produced radionuclides in hydrology, 108–110
 erosion rates, 113
- cosmological nucleosynthesis, 17–18
 quarks and anti-quarks, behavior of, 18
- coulombic (electrostatic) force, 3
- country rock, 291
- CO₂-water exchange, 252
- Crassulacean acid metabolism, 268
- Cretaceous kaolinites, 342
- crustal residence age, 56
- cummingtonite amphibolites, 208
- Dalgety Downs* chondrite, 138
- dalton, 3
- Dalton, John, 2
- Darcy's law, 195
- dating silicate-metal fractionation, 137
- DAWN mission of NASA, 126, 129, 138
- de Broglie Equation, 5
- de Broglie wavelength, 5
- decay constants, 36–37
- decay counting, 86
- Deccan volcanism, 238
- deep water, 269, 333
 CO₂ in, 349
 $^3\text{He}/^4\text{He}$ ratios, 425
 ocean circulation in, 236
- osmium isotopic composition of, 236
- Pb isotope ratios in, 235
- record of climate change in deep sea sediments, 327
- temperature, 328
- warming of, 336, 352
- Zn in, 383
- delta δ notation, 246–247, 256
- densities of fission track, 115
 induced, 116
 spontaneous, 116–117
 spontaneous vs induced, 117
- depleted mantle model age, 56
- detector efficiency, 87
- detrital zircons, 214
 crystallization age histogram of, 217
- Jack Hills zircons, 210
- deuterium burning, 20, 423
- deviations, 37–38
- Devonian sediments, 110
- deVries events, 103
- Dhurmsala* chondrite, 138
- diamonds, 148, 150
 $\delta^{13}\text{C}$, 285, 288
 fibrous, 288
- isotopic heterogeneity in, 285
- Re-Os dating of, 63–64
- diatomic molecule, 250–251, 252

- diatomic oscillator, 248
 diet and isotopes, 316–318
 differentiated meteorites, 125
 diogenites, 126
 dissimilatory sulfate reduction, 273
 dissolved inorganic carbon (DIC), 268
 dissolved load of rivers, 220
 distribution coefficient, defined, 193
 Dodson's closure temperature equation, 119
D'Orbigny angrite, 128, 136
 DUPAL anomaly, 187, 188
 early-enriched reservoir (EER), 143
 Earth
 chondritic Sm/Nd ratio of, 53
 continental crust. *see* continental crust
 continental crust
 cosmic rays in the atmosphere, 101–102
 formation and evolution of, 444–447
⁴He abundance in, 112, 424
 ϵ_{Hf} and ϵ_{Nd} , 59
 incompatible lithophile elements of, 144
 magnetic field, 103
 mantle array, 165
 mantle-derived magmas, 163
 mathematical model of
 isotopic evolution of, 223
 Nd isotopic composition of, 173
¹⁴²Nd/¹⁴⁴Nd ratio, 141
¹⁴³Nd/¹⁴⁴Nd ratio of, 52
 oceanic crust, 205
 Pb, geochemical behavior of, 73
 Pb isotope system, 166–172, 222
 Pb-Pb age of, 168
 primitive mantle, 163
 radiogenic isotope geochemistry of mantle, 163–172
 relative abundances of lithophile elements, 163
 reservoirs of sulfur, 305
 Sm/Nd ratio of, 140–142, 165, 175
¹⁴⁷Sm/¹⁴⁴Nd ratio of, 52
 solar wind, 103
 Sr-Nd-Hf system, 163–166
 U/Pb ratio of chondrites, 167
 ϵ_{W} *vs* age the giant impact, 141
¹⁸²W/¹⁸⁴W, 206
 eclogite, 182
Efremovka CAI, 127
 Einstein function, 255
 electromagnetic spectra, 8
 electron capture, 14–15
 electroweak, 14
 El Niño events, 233
 EM I and EM II mantle reservoirs, 183–184
 energetic collisions, 144
 enstatite chondrite, 125
 entropy and energy changes of a reaction, 249
 EPICA (European Project for Ice Coring in Antarctica) project, 337
 e-process, 23
 epsilon notation, 52
 ϵ_{Nd} , 52–54
 ϵ_{Hf} , 57
 ϵ_{W} , 137
 epsilon ϵ_{Nd} , 52–53, 59
 equilibrium condensation, 260
 equilibrium constant, 250
 for exchange of isotopes, 250
 equilibrium crystallization, 289
 equilibrium fractionations, 249–258
 example of fractionation factor calculated from partition functions, 252–254
 of isotopes, 250
 isotopologues and isotopic “clumping,” 256–258
 rotational partition function, 250–252
 translational partition function, 250
 vibrational partition function, 251–252
 equilibrium fractionations among minerals, 277–282
 compositional and structural dependence, 277–279
 geothermometry, 279–282
 equiline, 91
 equipoint, 90
 erosion rates of
 cosmogenic-produced radionuclides, 113
 error on the slope, 38
 eruption age, 91, 96
 eruption window, 96
 ethylenediaminetetraacetic acid (EDTA), 236
 eucrites, 126, 128
 even-even nuclides, 12
 even-odd effect, 7–9
 excess Ar, 44–45
 identifying, 46
 excess factor, 252
 exhumation rates, 119
 explosive nucleosynthesis, 17, 25–27
 p-process, 26–27
 r-process, 25–26
 exposure ages of meteorites, 154
 extinct radionuclides, 15, 129–145
²⁶Al–²⁶Mg, 134–136
 in Earth, 136
¹⁸²Hf–¹⁸²W, 136–140
¹²⁹I, 129
 identified in meteorites, 130
¹²⁹I–¹²⁹Xe, 131–133
⁵³Mn, 130
¹⁰⁷Pd–¹⁰⁷Ag, 133–134
²⁴⁴Pu, 131–133
 short-lived radionuclides in the early Solar System, 131
¹⁴⁶Sm/¹⁴²Nd, 140–145
 stable isotope of Mn, 130
¹²⁹Xe, 129
- feeding zone of Earth accretion, 140
 fibrous diamonds, 288
 Fish Canyon Tuff, 117
 fission decay, 15–16
 fission tracks, 114–121, 132
 activation energies, 117–118
 analytical procedures, 115–117
 annealing of, 115
 apatite fission track ages *vs* altitude for metamorphic rocks of the Higher Himalaya, 120
 closure temperatures, 118–119
 in context of K-Ar dating, 118
 dating, basis for, 115
 densities, 115
 etching procedures for dating, 116
 induced track density, 116
 interpreting ages of, 117–119
 interpreting track length, 119–120
 neutron-induced fission, 116

- in a polished and etched zircon, 115
- problems of partial annealing, 119
- relation between percentage of tracks annealed, temperature, and time, 118
- of uranium atoms, 114–117
- fixation, 270
- fixed nitrogen, 270
- fossil reef corals, ^{230}Th dating of, 89
- FOZO, 185
- fractional crystallization, 289
- fractionation factors, 247, 253, 302
- experimental determination of, 255
- between quartz and water, 255
- temperature dependencies of, 255, 263–264
- topography and, 264
- fractionation of isotopes, 247
- mass-independent fractionation, 369–371
- frequency factor, 259
- FUN anomalies, 151
- Galapagos Archipelago, 188–189
- Galapagos Spreading Center (GSC), 290, 299
- galena (PbS), 73, 308, 311
- gamma decay, 12–13
- gamma ray frequency, 12
- garnets, 54, 194
- garnet-bearing lithologies, 183
- garnet-mica schist from Snow Peak in northern Idaho, 60
- garnet peridotite facies, 196
- partition coefficient of Lu in, 51
- Sm-Nd isochron of, 54
- gas proportional counter, 102
- Gast, Paul, 161
- Genesis mission of NASA, 153
- Geochron*, 167, 170, 222
- geochronology, 32
- calculation of isochron, 37–39
- isochron dating, 36
- geology, principal objective of, 161
- geoneutrinos, 176–178
- geothermometry, 279–282
- Giant Impact Hypothesis, 140
- Gibbs Free Energy change of reaction, 249–250
- Gibeon* (IVA iron), 134
- GISP2 (Greenland Ice Sheet Project), 338
- glacial cycles, 347–351
- glaucophane ($\text{Na}_2\text{Mg}_3\text{Al}_2\text{Si}_8\text{O}_{22}(\text{OH})_2$), 61
- Global Meteoric Water Line, 265
- global warming, 1, 342–347
- glutamate dehydrogenase reaction, 270
- graphite presolar grains, 148–149, 150
- Great Artesian Aquifer, 110
- Great Conveyer Belt, 233
- Great Nebula in Orion, 145
- greenhouse hypothesis, 342
- Greenland ice cores, 338–340
- GRIP (Greenland Ice Core Project), 338
- groundwater, 108–110, 301, 305, 326, 393, 406, 420, 424
- age of, 110
- calcite precipitating, 340
- carbon-14 dating of, 108
- CO_2 in, 357
- determination of age, 110
- Pleistocene chronology and dating of, 106
- Gujba* (CB3), 128
- Hadean eon, 206–212
- Hadean crustal protoliths, 206
- $^{176}\text{Hf}/^{177}\text{Hf}$ ratio, 207
- late accretionary veneer, evidence of, 206–207
- ^{142}Nd evidence of Hadean crust formation, 207–210
- $^{142}\text{Nd}/^{144}\text{Nd}$ ratios, 207–208
- $\varepsilon_{^{142}\text{Nd}}$ values in amphibolites, 208
- trace element depletions, 209
- from zircons, 210–212
- half-time, 299
- Hawaiian archipelago, 189
- Hawaiian basalts, 65, 193
- Hawaii* OIB, 180
- H chondrites, 128–129
- mass-dependent fractionation line (MDFL) with, 153
- HD molecule, 259
- ^4He , 4
- He burning, 21
- HED achondrites, 126, 138
- He/H ratio, 17, 20
- helium, isotopes of
- erosion rates from cosmogenic ^{3}He , 112–113
- in Haleakala volcano, 113
- ^4He , 110–111
- upward mobility of, 110
- in the Earth, 423–427
- helium burning, 152
- Hertzsprung–Russell diagram of relationship between luminosity and surface temperature, 19
- Hess, Victor, 101
- heterotrophs, 265, 270
- $^{177}\text{Hf}/^{176}\text{Hf}$ ratio, 166
- Hf isotope ratios
- in river water, 235
- in Saharan dust, 235
- in seawater, 234
- $^{182}\text{Hf}-^{182}\text{W}$ constraints, 136–140
- HIMU reservoir, 185
- H_2 molecule, 259
- Holocene stratigraphy, 104
- homogeneous solar nebula, 126
- Hooke's Law harmonic oscillator, 254
- Hooray sandstone, 110
- horses (Family Equidae), evolution of, 318–321
- hot spots, 179
- howardites, 126
- human evolution, 321
- hydrocarbons, Re-Os dating of, 64–65
- hydrogen and oxygen isotope ratios in hydrologic system, 262–265
- delta $\delta^{18}\text{O}$ precipitation, 264
- hydrogen burning, 19
- hydrogen isotope fractionation, 262, 271–272
- hydrogen isotopic composition of mantle, 286–287
- hydrogenous sediments, 59
- hydrologic cycle, 264
- hydrothermal metamorphism, 298–300
- hydrous minerals of xenoliths, 286
- hydroxylamine hydrochloride, 236
- IAB irons, 129
- Ibitira*, 128
- icelandic basalts, 284
- Iceland oceanic plateau, 206
- Iceman and isotopes, 323
- β -factors, 252–253
- igneous rocks, 290
- ilmenite, 289

- increment method of estimating fractionation factors, 278
- Indian Ocean circulation, 233
- Indian Ocean MORB, 187
- inherited Ar, 45
- intermediate nuclides, 93
- interplanetary dust particles (IDPs), 150
- interstellar space, nucleosynthesis in, 27–28
- inverse beta decay reaction, 176
- inverse isochron plot, 46
- iron isotopes, 371–375
- iron meteorites, 63, 128
- isobars, 3, 7, 14
- isochron, calculation of, 37–39
- error on the intercept, 38
 - error on the slope, 38
 - intercept, 38
 - mean squared weighted deviations (MSWD), 39
 - regression slope, 38
 - slope, 38
- isochron dating, 36
- isochrons
- $^{40}\text{Ar}/^{39}\text{Ar}$, 45–47
 - dating, 36
 - equation, 36
- ISOPLOT, 39
- isotones, 3, 8
- isotope dilution analysis, 462–463
- isotope geochemistry, 3, 8. *see also* noble gas isotope geochemistry; stable isotope geochemistry
- applications of, 2
 - core-mantle boundary, 175
 - growth of, 1
 - isotopic fractionations, 33
 - isotopic homogenization of a system, 37
 - isotropic coulomb field, 9
 - production rates in terrestrial rocks, 112
 - role in transforming geology, 1
- isotope ratio in molecular oxygen, 253
- isotopic “clumping,” 256–258
- isotopic composition of carbonates, 257
- isotopic composition of continental crust, 217–223
- Archean lower crustal terrains, 221
 - of lower crust, 221–223
- $^{143}\text{Nd}/^{144}\text{Nd}$ ratios, 218
- orogenic age–Pb isotopic composition relationship, 222
- sediments and rivers, 218–221
- $^{87}\text{Sr}/^{86}\text{Sr}$ ratios, 218, 220
- isotopic composition of melt, 289
- isotopic disequilibrium, 194
- isotopic heterogeneity, 151
- isotopologues, 256–258
- Isthmus of Panama, 237
- Isua gneisses, 206
- I-type granites, 216
- $^{129}\text{I}-^{129}\text{Xe}$ decay system, 131–133
- I-Xe system, 133
- Jack Hills zircons, 83, 210–211
- detrital zircons, 210
 - Hf isotope composition of, 212
- juvenile crust in orogens, 214
- Juvinas achondrite, 138
- KamLAND detector, 176–178
- kaolinite line, 341
- kaolinites, 341–342
- K-Ar ages, 128
- K-Ar-Ca system, 39–47
- $^{40}\text{Ar}/^{39}\text{Ar}$ dating, 39, 43–47
 - Ar diffusion flux, 41
 - branched decay, 39
 - cooling rate, 42
 - diffusion, cooling rates, and closure temperatures, 40–42
 - diffusion “flux,” 41
 - diffusion radius, 41
 - $^{40}\text{K}/^{40}\text{Ar}$ ratio, 40
 - $^{40}\text{K}/^{40}\text{Ca}$ ratio, 40
 - radiogenic Ar, 41
 - radiogenic daughter production, 39
- Karroonda chondrite, 138
- Karoo flood basalts, 193
- K-bearing minerals, 49
- Kelvin, Lord, 32
- Kepler, Johannes, 27
- Kerguelen oceanic plateau, 191
- Kerguelen OIB, 180
- Kerguelen plume, 189
- kerogen, 271
- K-feldspar, 48
- Khariar syenites, 209–210
- Kilauea’s East Rift Zone, 284, 288
- kinetic energy, 258
- kinetic fractionations, 152, 258–260, 272
- of O isotopes, 259
- komatiites, 63, 65, 207
- krypton, 432–433
- Kurz, M. D., 112
- LaPlace operator, 5
- Large Magellanic Cloud, 27
- large slow-shear wave velocity (LLSVPs), 171–172
- laser-ablation inductively coupled mass spectrometry (LA-ICP-MS), 82
- Law of Constant Proportions, 2
- lawsonite ($\text{CaAl}_2\text{Si}_2\text{O}_7(\text{OH})_2 \cdot \text{H}_2\text{O}$), 61
- legumes, 270
- Lewis Cliff 86010 angrite, 128, 136
- liquid-drop model, 6–7, 15
- liquid scintillation counting, 102
- lithium isotopes, 384–385, 390–393
- lithophile, 61
- lodranites, 126, 129
- low shear wave velocities provinces (LLSVPs), 145
- ^{176}Lu , 151
- Lu-Hf system, 37, 56–61, 170
- advantages of, 57, 58
 - analytical problems with, 57
 - calibration experiment on, 57
 - comparison with U-Pb isochrons of Proterozoic dolorites, 57
 - decay rate of a nuclide, 57
 - Hf in felsic crystalline rocks, 59
 - ϵ_{Hf} value, 57, 59
 - ionic radii, 56
 - ionization efficiency, 57
 - isochron for a garnet-mica schist from northern Idaho, 60
 - isochron plot, 57–58
 - isotopic analysis of Hf, 57
 - $^{176}\text{Lu}-^{176}\text{Hf}$ internal isochron age, 58
 - $^{167}\text{Lu}/^{177}\text{Hf}$ ratio in chondrites, 58
 - odd-odd nuclei, 56
 - range of Lu/Hf ratios in common rocks and minerals, 58–59
 - similarity between Sm-Nd system and, 59
 - systematics of chondrite meteorites, 58
 - “terrestrial” decay constant of Söderlund and Scherer, 57

mafic protolith, 211
 magic numbers, 7–8
 magmatic irons, 126
 magnesium isotopes, 393–397
 magnetic moment, 9–10
 magnetite, 289
 main sequence stars, 19
 manganese nodule, 107
 growth of, 94
 isotopic compositions of, 233–237
 ^{230}Th dating of, 94
 mantle
 array, 165, 180
 carbon isotopic composition of, 284–286
 chemistry, geographic variations in, 187–189
 contamination of, 282
 fluxes between reservoirs, 444
 fractionated Hf/W ratios, 207
 He in, 425–427
 hydrogen isotopic composition of, 286–287, 290
 metasomatism, 182, 191
 nitrogen isotopic composition of, 287–288
 oxygen isotopic composition of, 283–284
 reservoirs of noble gases, 437–444
 stable isotope geochemistry of, 282–288
 sulfur isotopic composition of, 288
 xenoliths, 183
 mantle plume reservoirs
 common component of plumes, 186
 deep recycling of oceanic crust and, 181–182
 EM II reservoir, 183–184
 evolution of, 180–187
 Hf-Nd isotopic systematics of the mantle array, 184
 Iceland and Azores mantle plumes, 187
 Morgan’s plume model, 179
 parent-daughter ratios, 181
 partial melting, effect of, 182
 Pb/Ce ratio, 183
 plumes and zoo, 179–180
 ridge-crest hydrothermal activity, effects of, 185
 subducted sediments, 182
 s-wave velocities, 181
 tectonic erosion of continental crust and, 182
 Marianas lavas, 294

marine continent-derived sediments, 59
 marine sediments, determining age of, 107
 mass accumulation rate, 95
 mass balance equation, 173, 193
 mass decrement of an atom, 4
 mass-dependent fractionation, 261
 mass-dependent fractionation line (MDFL), 153
 mass-depth function, 94–95
 mass-energy equivalence, 4
 mass fraction of depleted mantle (DMM), 174
 mass independent fractionation, 260–262
 of ozone, 261
 sulfur isotope fractionations, 262
 mass-independent O fractionation, 152–153
 massive stars, 22
 mass spectrometry
 accelerator, 459–460
 analytical strategies, 460–463
 detector, 458–459
 ion source, 455–456
 mass analyzer, 456–458
 mass spectrometer, 454–455
 sample extraction and preparation, 454
 Masuda–Coryell plots, 52
 Mayer–Jensen coupling, 10
 mean squared weighted deviations (MSWD), 39
 Mediterranean Intermediate Water (MIW), 237
 Mediterranean Outflow water (MOW), 237
 melting and melt extraction, models of, 194
 Spiegelman and Elliot model of melt transport, 194–198
 melts crystallizing non-silicates, 290
 metabasalts, 206
 meta-igneous protolith, 216
 metal-silicate fractionation, 138
 metamict, 80
 metasediments, 206
 meteoric geothermal systems, 301
 Meteoric Water Line, 265
 meteorites
 age of CAIs from CV3, 128
 age of metamorphism of, 128
 achondrite, 128
 differentiated, 125
 exotic components in, 151
 exposure ages of, 154
 graphite interstellar grains in, 150
 HED, 126
 iron, 128
 I-Xe ages of, 133
 Martian, 144
 measurements of, 73
 $^{142}\text{Nd}/^{144}\text{Nd}$ ratio, 141
 neon alphabet soup and “pre-solar” noble gases in, 146–148
 oxygen isotope variations in, 151–152
 Pd/Ag ratio in iron, 133
 primitive, 125
 SNC, 126
 stardust and isotopic anomalies in, 146–151
 thermal metamorphism in, 126
 U-Pb ages of chondritic and achondritic, 127
 variation of $^{134}\text{Xe}/^{132}\text{Xe}$ and $^{136}\text{Xe}/^{132}\text{Xe}$ in, 132
 methanogens, 272
 40–39 method, 43
 Mg isotopic compositions, 150
 MgO-rich lavas, 63
 mica, 48
 mid-ocean ridge basalts (MORB), 164, 166, 170–171, 178–179, 181, 187, 193, 198, 218, 300, 437
 carbon isotopic composition of mantle, 285
 measurements of $\delta^{15}\text{N}_{\text{ATM}}$ in, 287–288
 oxygen isotopic composition of mantle, 283–284
 Milankovitch parameters, 1, 330
 mineral exploration, oxygen isotopes and, 304–305
 Mississippi Valley type deposits, 311
 mixing time, 232
 $^{53}\text{Mn}/^{52}\text{Cr}$ ratio, 130–131
 Mn–Fe oxides, 88
 molecular clocks, 32
 molecular masses, ratio of, 253
 molybdenum isotopes, 375–378
 monazite, 73
 Moon, formation of, 139
 giant impact from, 206
 homogeneous isotopic composition of lunar materials, 139

- Moon, formation of (*continued*)
 minimum age of, 140
 $^{142}\text{Nd}/^{144}\text{Nd}$ ratios, 144
 moraines, 114
 in Bloody Canyon of Mono Basin, 114
 Multi-collector secondary ionization mass spectrometers (MC-SIMS), 81
 muons, 102, 112
Murchison chondrite, 138
Murray chondrite, 138
 Nakhrites, 126
Nanton (IAB-IICD) iron meteorite, 167
 Nd isotope system, 50, 164–165, 173, 224
 Nd isotope ratios, 237
 variations of bottom water, 236
 Nd model age, 56
 $^{142}\text{Nd}/^{144}\text{Nd}$ anomalies, 209–210
 $^{142}\text{Nd}/^{144}\text{Nd}$ ratio, 53, 165, 207–208
 chondrites, 141
 Earth, 141
 meteorites, 141
 Moon, 144
 $^{143}\text{Nd}/^{144}\text{Nd}$ ratio
 of continental crust, 173–174
 of the Earth, 52, 54
 vs time plot, 56
 Neanderthal bone collagen, 322
 Ne burning, 22
 neon, 427–430
 alphabet soup in meteorites, 146–148
 Ne-E(H), 147
 Ne-E(L), 147
 neutral current reaction, 176
 neutrinos, 14, 151
 neutrons, 3
 capture, 24, 26
 excess number, 6–7
 neutron-induced fission, 116
 neutron-neutron pairing energy, 11
 neutron-poor isotopes, 151
 neutron-rich e-process material, 151
 NGRIP, 338
 NH_2 amine groups, 270
 nitrogen isotope fractionation in biological processes, 269–271
 equilibrium isotope fractionations, 269–270
 forms of inorganic nitrogen, 269
 in marine blue-green algae, 270
 nitrogen isotopic composition of mantle, 287–288
 $^{14}\text{N}(\text{n}, \text{p})^{14}\text{C}$ reaction, 102
 $^{15}\text{N}^{14}\text{N}^{16}\text{O}$, 256
 noble gas isotope geochemistry
 abundances of noble gases, 420
 argon, 430–432
 He, Ar, and Ne Budgets, 439–444
 helium, 423–427
 implications in evolution of Earth, 437–447
 krypton, 432–433
 neon, 427–430
 in Solar System, 420–423
 Xenon, 433–437
Nogoya chondrite, 138
 non-chondritic Sm/Nd, 54
 non-conventional stable isotope ratios, 366
 non-linear polyatomic molecules, partition function of, 251
 non-magmatic irons, 126, 129
 North Atlantic Deep Water (NADW), 233, 234, 236, 333, 351
 ocean circulation, 236
 outflow pattern, 237
 unradiogenic nature of, 234, 236
 Northern Hemisphere Regression Line, 187
 Northern Hemisphere terrestrial biosphere, 346–347
 Northern Volcanic Zone (NVZ), 295
 Norwegian-Greenland Sea, 237
 nuclear binding force, 4
 nuclear decay, 12
 nuclear forces, 3–6
 nuclear magnetic resonance (NMR), 10
 nuclear magnetons, 9
 nuclear mass, 3
 nuclear physics
 atomic masses and binding energies, 4
 collective model, 11–12
 definitions and units, 3
 early development of atomic and nuclear theory, 2–3
 liquid-drop model, 6–7
 nucleons, nuclei, and nuclear forces, 3–6
 shell model of the nucleus, 7–11
 nuclear spin, 8–9, 9
 nuclear theory, 2–3
 nucleosynthesis, 16–28
 cosmological, 17–18
 definition, 16
 explosive, 17, 25–27
 in interstellar space, 27–28
 observations, 16
 stellar, 17–25
 nucleus, angular momentum and magnetic moment of, 8
 nuclides
 ^{10}Be , ^{26}Al , and ^{36}Cl , 106–108
 cosmogenic, 101–114
 cosmogenic and
 bomb-produced radionuclides in hydrology, 108–110
 cosmogenic production of, 139
 decay series, 85
 even-even, 12
 half-lives of daughter, 84
 from hydrogen, helium, and carbon burning in main sequence, 21
in-situ produced cosmogenic nuclides, 110–114
 intermediate, 93
 odd-even, 9, 10, 24
 s-process, 142
 U decay series, 193
Nuevo Laredo achondrite, 128
Nuvvaugittuq Belt, 208
Nuvvaugittuq supracrustal belt, 208–209
NWA2364 CAI, 127
NWA 5697 chondrite, 128
 Ocean Drilling Project (ODP), 300
 oceanic crust, 205
 accretion of, 205–206
 balancing depleted mantle and, 172–179
 hydrothermal metamorphism of, 298–300
 mass ratio of continental crust to depleted mantle, 173
 partial melting, effect of, 182
 oceanic island basalts (OIB), 163–164, 186, 284
 Eu anomalies, 184
Hawaii, 180
Kerguelen, 180

- noble gas isotope ratios, 238–239
- Pb isotope systematics of, 169
- Society*, 180
- St. Helena*, 180
- oceanic lithospheric enrichment, 182–183
- oceanographic circulation and geochemical cycling, 232–233
- oceanography, 104, 231–240
- $^{16}\text{O}^{12}\text{C}^{18}\text{O}$, 256–257
- odd-even nuclides, 9, 10
- odd-odd nuclei, 10
- in Lu-Hf system, 56
- oligarchic growth, 140
- olivine, 194
- O isotopes in, 283
- Ontong-Java oceanic plateau, 191, 206
- $^{18}\text{O}^{16}\text{O}$ molecule, 259
- open system nature of oceans, 50
- ordinary chondrite, 125
- Orgueil* (CI1) chondrite, 136, 138
- neon isotopic compositions in, 147
 - SiC grains in, 147
- orthopyroxene, 194
- Os isotope composition, 182
- deep ocean water, 232
 - ratios, 61–63, 64
- osmiridium (OsIr), 62
- osmium, 61, 236
- in deep water, 236
 - $^{187}\text{Os}/^{186}\text{Os}$ continental weathering products, 238
 - in seawater, 238
- Os-Nd isotope systematics, 191, 193
- $^{186}\text{Os}/^{188}\text{Os}$ ratio, 65
- $^{187}\text{Os}/^{188}\text{Os}$ ratios, 61–63, 191
- oxygen isotope fractionation between K-feldspar and Na-feldspar, 278
- carbonate-water, 327
- during crystallization, 289–290
- at high temperature, 277–280
- water rock, 298–305
- at low temperatures, 278–280
- mass-independent fractionation, 369–370
- by plants, 271
- oxygen isotope heterogeneity in eclogites, 286
- oxygen isotopes in hydrothermal systems, 298–305
- metamorphism of oceanic crust, 298–300
- meteoric geothermal systems, 301
- $\delta^{18}\text{O}$, 300–301
- oxygen isotopes and mineral exploration, 304–305
- ridge crest hydrothermal activity, 298–300
- Skaergaard intrusion, 303–304
- water-rock reaction, theory, 301–303
- oxygen isotopes in magmatic processes, 288–298
- calculated Sr concentrations, 292
 - combined fractional crystallization and assimilation, 291
 - combining radiogenic and oxygen isotopes, 291–292
- during crystallization of feldspars, 289–291
- crystallization of quartz and silicates, 289
- sediment subduction *vs* assimilation, 292–296
- silica tetrahedra and Si – O bonds, 288–289
- solid/liquid partition coefficient, 292
- stable isotopes as indicators of crust-to-mantle recycling, 296–298
- variation in $\delta^{18}\text{O}$ of a magma, 291
- oxygen isotope variations and nebular processes, 151–154
- oxygen isotopic composition of mantle, 283–284
- MORB, 283–284
- olivine and clinopyroxene, 283
- total range of values observed, 283
- Pacific Ocean MORB, 187
- pairing effects, 10–11
- paleo-atmospheric CO₂, 354–356
- paleoclimatology, 104
- paleoclimatology, stable isotopes in, 326–342
- record of climate change in deep sea sediments, 327
- paleodiets and isotopes, 321–323
- Paleolithic cave paintings and engravings, 89
- paleoceanography, radiogenic isotopes in, 236–240
- paleosols, 341
- Appalachian-Ouchita-Marathon Orogeny, 312
- Lachlan Fold Belt, 216
- parent-daughter ratio, $R_{P/D}$, 36, 166, 170
- Hf isotope compositions, 210
- in mantle, 164
 - in radiogenic isotope ratios, 190
 - radiogenic isotope ratio *vs*, 227
- Spiegelman and Elliot model of melt transport, 195
- subduction zone processing effects, 185
- of Th-Pb system, 77
- time-integrated, 175, 178
- partition function, 249–254
- $^{231}\text{Pa}-^{235}\text{U}$ dating, 91–93
- dependence of $(^{231}\text{Pa})/^{235}\text{U}$ ratio on age, 92
- Pauli Exclusion Principle, 8
- Pb, geochemical behavior of, 73
- ^{210}Pb dating, 93–95
- measured on sediment samples from Tehuantepec Gulf, Mexico, 95
- Pb isotope ratios, 33
- in Archean and post-Archean granulite, 222
 - in deep Pacific water, 235
 - evolution of, 183
 - in lower crustal xenoliths, 222
 - of marine sediment, 220
 - in modern marine sediments, 219
 - in rivers, 236
 - silicate Earth, 212
- Pb isotope system, 166–172
- of crust, 221
 - Earth, Pb-Pb age of, 168
 - first-order, 170
 - of lower crust, 221
 - magma flux of mantle plumes, 171
- Pb isotope systematics of oceanic island basalts (OIB), 169
- ratios, 167
- Pb-Pb age, 74–77
- Pb-Pb isochron, 75
- $^{207}\text{Pb}/^{204}\text{Pb}$ ratio, 183–184, 187, 218
- ^{107}Pd , 133–134
- half-life of, 133
- $^{107}\text{Pd}-^{107}\text{Ag}$, 133–134

- Pee Dee Belemnite carbonate (PDB), 247
 pelitic sediments, 294
 peralkaline lava, 91, 93
 per-mil fractionation, 260
 PHEM, 186
 phenocrysts, 294
 phlogopite (Mg-rich mica), 191
 phosphates, 128
 phosphoenol pyruvate carboxylase (PEP), 267
 phosphoenolpyruvate carboxylation, 268
 3-phosphoglyceric acid, 266
 photodisintegrates, 22
 photo-dissociation (photolysis), 152, 262, 370
 photophosphorylation, 266
 pion, 3, 5–6, 102
 plagioclase, 48, 240
 Planck's constant, 5, 250
 planetesimals, 138
 planktonic foraminifera, 106
 platinoid metal deposits, 62
 platinum group metals (PGM), 62
 Pleistocene climate change, 89, 326–332, 336–340
 PoCl_3 , 95
 pole-to-equator gradient in solar radiative energy, 232
 polycyclic aromatic hydrocarbons, 64
 polygenetic hypothesis, 17
 ^{210}Po - ^{210}Pb dating, 95–96
 polonium-lead disequilibrium, 96
 porphyrins, 64
 porphyry copper deposits, 310
 potential function $V(r)$, 5
 pp process, 20
 p-process, 26–27
 pre-solar noble gases in meteorites, 146–148
 pre-solar grains, isotopic composition of, 148–150
 primitive achondrites, 126, 129
 primitive mantle, 175, 179, 186, 282
 primitive meteorites, 125
 protactinium, 91
 Proterozoic crust, 216
 protogalaxies, 20
 proton-proton pairing energy, 11
 ^{190}Pt - ^{186}Os decay, 65
 ^{244}Pu , 15, 131–133, 419, 432–437
 pyrochlore ($\text{Na}, \text{Ca})_2\text{Nb}_2\text{O}_6(\text{OH},\text{F})$), 91
 quantum mechanics, 248
 quantum translational energy of a particle, 250
 quartzites, 82
 quartz-mineral fractionation, 278
 quaternary carbon isotope record, 347–351
 quaternary glaciations, 329–332
 quaternary $\delta^{18}\text{O}$ record, 327–329
 ^{226}Ra dating, 93
 radioactive cosmogenic nuclides, 101
 radioactive decay, 12–16
 alpha decay, 13
 basic equation of, 12, 84
 beta decay, 13–14
 electron capture, 14–15
 gamma decay, 12–13
 of nuclide in a rock, 113–114
 spontaneous fission, 15–16
 radioactive disequilibrium, 193, 194
 U-series disequilibria, 200
 radioactive equilibrium, 84
 before melting, 194
 radioactive isotope geochemistry
 basic equations, 33–35
 decay of ^{87}Rb to ^{87}Sr , 35
 U-Th-Pb system, 35
 radiocarbon dates to calendar years, 105
 radiogenic isotope geochemistry of mantle
 balancing depleted mantle and crust, 172–179
 of Earth, 163–172
 geographic variations in mantle chemistry, 187–189
 mantle plume reservoirs, 179–187
 subcontinental lithosphere, 189–193
 time-integrated and time-averaged, 162–163
 U-series isotopes and melt generation, 193–198
 radiogenic ^{206}Pb and ^{207}Pb , 74
 radionuclides, 34
 cosmogenic and bomb-produced, 108–110
 extinct, 129–145
 ^{129}I , 129, 434–435
 short-lived, 129, 145–146
 short-lived, origin of, 145–146
 Raoult's law, 262
 rare earths
 concentrations in the CI carbonaceous chondrite Orgueil, 52
 inner electron shells, 50
 ionic radii, 51
 mafic minerals, 51
 normalizing process of, 52
 Periodic Table, 51
 relative concentrations of, 51
 valence state of, 51
 ^{226}Ra - ^{230}Th whole rock isochron, 93
 Rayleigh condensation, 260
 Rayleigh distillation, 259, 263, 284, 287, 289
 ^{87}Rb decay constant, 37
 Rb/Sr fractionations, 162
 ^{87}Rb / ^{86}Sr ratio, time-integrated and time-averaged, 162–163
 Rb-Sr system, 170
 chemistry and geochronology, 48–49
 deviations from closed system behavior, 47–48
 disadvantage of, 49
 in the Earth, 49
 Hurley estimate, 213
 isotopic composition of daughter, 48
 range in parent/daughter ratio, 47
 ratio of parent to daughter, 47
 Rb/Sr dating, 49
 resetting during metamorphism, 213
 Sr isotope chronostratigraphy, 49–50
 recombination era, 18
 red giant, 20
 red giant phase, 21
 red giant/supernova injection hypothesis, 146
 reduced nitrogen, 270
 reduced partition function, 252
 reef-building corals, 89
 glacial maximum of, 90
 refractory calcium-aluminum inclusions, 125
 Re-Os geochronology, 48, 63–65
 dating of diamonds, 63–64
 dating of hydrocarbons, 64–65
 differences in compatibility, 63

- ^{190}Pt - ^{186}Os decay, 65
 Re/Os ratios, 191
 Re-Os system. *see also* Re-Os geochronology
 decay system, 61–63
 metal-silicate partition coefficients, 62
 Os isotope ratios, 61–63
 Re/Os ratio of the mantle, 62
 valences and ionic radii, 61
 reservoir effects, 103
 reservoir rock, 64
 residence time, 108, 232, 239
 Reunion mantle plume, 192
 ribulose bisphosphate carboxylase oxygenase (RUBISCO), 266–267
 ridge crest hydrothermal activity, 298–300
 Roberts Victor Mine (South Africa) kimberlite, 190, 296
 rotational motion of molecules, 248
 rotational partition function, 250–252
 r-process, 25–26
 nuclides, 151
 RuBP photosynthesis, 267
 Samail ophiolite, 300
 Schrödinger Equation, 8
 for a three-dimensional harmonic oscillator, 9
 seawater
 array, 234
 of Baffin Bay region, 234
 carbon isotope ratios in, 268–269
 Hf isotope ratios in, 234
 in ice ages, 104–106
 isotopic equilibrium, 87
 isotopic variations in, 232
 of Labrador Sea, 234
 mean ε_{Nd} of, 233
 Nd isotopic composition of, 233
 Os isotope composition of seawater, 238
 oxygen isotope exchange, 299
 Pb isotope ratios in, 235–236
 residence time of Os in, 232
 Sr in, 50, 220
 ^{87}Sr / ^{86}Sr ratio, 50
 sulfate, 310
 ^{234}U - ^{238}U ratio, 86–88
 sedimentary rocks, 49
 sedimentation rate, 106–107
 sediment subduction *vs* assimilation, 292–296
 “see through” open system behavior, 56, 76
 seismic tomography, 171
 seismic velocities, 179
 semi-total Pb isochron diagram, 76
 shale, isotopic ratios of, 162
Shallowater aubrite, 132
 absolute age of, 133
 shell model of the nucleus, 7–11
 capture cross section, 11
 even-odd effect, 7–9
 magic numbers, 7–8
 pairing effects, 10–11
 Shergottites, 126, 144
 shielding effect, 27
 short-lived radionuclides, 129
 origin of, 145–146
 SHRIMP, 83
 SiC presolar grains, 148–149
 Mo isotope anomalies in, 150
 siderophile elements, 61
 Si isotopic compositions, 149
 silicate Earth, 62, 165, 174
 heterogeneous tungsten isotopic composition, 207
 near-chondritic ^{187}Os / ^{188}Os ratio of, 62
 Pb isotope ratios, 212, 222
 siderophile abundances in, 207
 U/Pb ratio in, 168
 silicate-metal fractionation, 137
 silicon burning. *see* e-process
 silicon isotopes, 401–405
 Skaergaard intrusion, 303–304
 ^{146}Sm - ^{142}Nd , 140–145
 Sm-Nd chronometer, 54
 Sm-Nd geochronology, 48
 ^{147}Sm / ^{144}Nd ratio, 165
 of Earth, 52, 54, 175
 ^{147}Sm / ^{144}Nd ratios
 in crustal growth, 224–225
 Sm-Nd system, 50–56, 191
 crystallization of a terrestrial magma ocean, 53
 epsilon ε_{Nd} , 52–53, 59
 ionic radii, 51
 isochron based on six garnet fractions, 55
 model ages and crustal residence times, 55–56
 partition coefficient of Lu in garnet, 51
 relative concentrations of rare earths, 51
 similarity between Lu-Hf system and, 59
 ^{147}Sm / ^{144}Nd ratio of the Earth, 52
 SN 1987A, 27
 SNC meteorites, 126, 138
 Society OIB, 180
 Solar System, 16–17, 53, 83, 125, 126, 135, 206
 ^{26}Al / ^{27}Al ratios, 136
 formation of iron cores within small planetary bodies, 133–134
 generation of the solar wind, 153
 ^{176}Hf / ^{177}Hf of, 58
 models of planetary accretion, 167
 Moon, formation of, 139
 noble gas isotopes, 420–423
 ^{16}O -rich nature of Sun, 153
 short-lived radionuclides in the early, 131, 145–146
 solar wind, 103
 stars, 19
 Sun, 19
 South African kimberlites, 117
 Southern Volcanic Zone (SVZ), 295
 South Pacific Isotope and Thermal (SOPITA) anomaly, 188
 Southwest Indian Ridge (SWIR), 187
 spallation reactions, 101, 106, 146
 of ^{40}Ar , 109
 ^{35}Cl , 114
 cosmic ray-induced, 111
 specific activity, 102
 atmospheric, 103
 of ^{14}C , 103
 speleotherms, 340–341
 spelothems, 89
 sphalerite–galena sulfur isotope temperatures, 281
 sphene (CaTiSiO_5), 48, 73, 118
 Spiegelman and Elliot model of melt transport, 194–198
 conservation equation for each parent-daughter pair, 195
 of decompression melting beneath mid-ocean ridges and oceanic islands, 195
 effective velocity of element, 196
 melting rate, 195

- partition coefficients for Th and U, 197
 porosity and depth, relationship, 195–196
 relative effective velocities, 197
 spin-orbit interaction, 10
 spontaneous fission, 15–16
 spontaneous fission tracks, 116–117
 vs induced fission tracks, 117
 s-process nuclide, 142, 147
 Sr in seawater, 50
 Sr isotope chronostratigraphy, 49–50
 Sr isotope geochemistry, principles of, 161
 Sr-Nd-Hf system, 163–166, 180
 Sr-Nd-Pb isotopic compositions, 185
 Sr partition coefficient, 48
 $^{87}\text{Sr}/^{86}\text{Sr}$, 49, 161–163, 295
 of riverine flux, 239
 in seawater, 50
 vs $\delta^{18}\text{O}$, 291–293
 in continental crust, 212, 218, 220
St. Helena OIB, 180, 185
St. Marguerite, 136
 stable chlorine, 109–110
 stable cosmogenic nuclides, 111
 stable isotope geochemistry, 1, 2
 commonly studied elements, 246–247
 equilibrium fractionations among minerals, 277–282
 fractionation factor, 247
 hydrogen and oxygen isotope ratios in hydrologic system, 262–265
 isotope fractionation in biosphere, 265–274
 isotopic fractionation, 246
 of mantle, 282–288
 mass independent fractionation, 260–262
 δ notation, 246–247
 oxygen isotopes in hydrothermal systems, 298–305
 oxygen isotopes in magmatic processes, 288–298
 in paleontology, archeology, and the environment, 312–326
 stable isotopes as indicators of crust-to-mantle recycling, 296–298
- stable isotopes in paleoclimatology, 326–342
 sulfur isotopes and ores, 305–312
 theory of mass dependent isotopic fractionations, 247–260
 stable nuclei, 3
 standard mean ocean water (SMOW), 247
 stellar nucleosynthesis, 17–25
 astronomical background, 18–20
 e-process, 23
 hydrogen, helium, and carbon burning in main sequence, 20–23
 s-process, 23–25
 stoichiometric coefficient, 249
 stratabound sulfides, 310
 strong force, 3
 subcontinental lithosphere, 189–193
 assimilation of continental crust, effects of, 189
 isotopic heterogeneity of, 190
 partial melts, 191
 xenoliths, 189–190
 subduction erosion, 217
 process of, 183
 subduction-related basalts, 284
 subduction-related volcanism, 206
 subduction zone magmatism, 214
 subduction zones, 226–231
 Nd, Hf, Os, and Pb in modern ocean, 233–236
 oceanographic circulation and geochemical cycling, 232–233
 Suess effect, 103
 sulfur isotope fractionation, 280
 mass-independent fractionation, 370–371
 sulfur isotopes, 274
 sulfur isotopes and ores, 305–312
 hydrothermal systems, sulfur isotope fractionations in, 307–309
 isotopic composition of sulfide ores, 309–312
 magmatic processes, sulfur isotope fractionations in, 306–307
 reservoirs on Earth, 305
- in ridge crest hydrothermal systems, 310
 solubility of H₂S in silicate melts, 306
 sulfur isotopic composition of mantle, 288
 sunspot cycle, 103
 supernova debris, injection of, 150–151
 supernova explosion, 25
 surface circulation of ocean, 232–233
 surface tension, 15
 suspended load, 220
- Tardree rhyolite of Ireland, 117
 Taylor Series expansion, 35
 Teller–Redlich spectroscopic theorem, 252
 temperature-dependent equilibrium isotope fractionations, 248
 Tera-Wasserburg diagram, 76
 terrigenous sediments, 59
 tertiary marine $\delta^{18}\text{O}$ record, 334–336
 theory of mass dependent isotopic fractionations, 247–260
 equilibrium fractionations, 249–258
 Theo's flow, 209
Thera, 140
 thermal ionization mass spectrometry (TIMS), 81–82, 465
 thermal metamorphism in meteorites, 126
 thermochronology, 83, 115
 thermogenic methane, 272
 thermohaline, 332
 Thomson, J. J., 2
 three-dimensional harmonic oscillator, Schrödinger Equation for, 9
 three-dimensional translational partition function, 250
 $^{230}\text{Th}-^{238}\text{U}$ dating, 88–91
 of allanite crystals, 91
 applications, 89
 crystallizing magma with homogeneous ($^{230}\text{Th}/^{232}\text{Th}$) and ($^{238}\text{U}/^{232}\text{Th}$) ratios, 90
 equilibrium situation, 90
 of fossil reef corals, 89
 isochron on a commendite lava from Kenya, 91
 of magma, 91

- ^{230}Th - ^{238}U mineral isochron, 93
 ^{230}Th / ^{238}U ratio, 193
 in melting, 197
 ^{232}Th / ^{238}U ratio, 35, 77
 time-averaged Rb/Sr ratio, 162–163
 time-integrated Lu/Hf, 166
 time-integrated Rb/Sr ratio, 162–163
 time-integrated Th/U ratio, 170, 178
 titanite, 73. *see* sphene (CaTiSiO_5)
 Toba volcano, 91
Toluca metal, 138
 tooth enamel, isotopic composition of, 323
 total U-Pb isochrons, 76–77
 of lunar samples, 76
 regression analysis, 76–77
 ^{238}U - ^{206}Pb , ^{235}U - ^{207}Pb , and ^{207}Pb - ^{206}Pb methods, 76
 tracer studies, 33
 tracing methane contamination in drinking water, 325–326
 track length of fission tracks, 119–120
 translational motion, 248
 translational partition function, 250
 triple alpha process, 21
 Tristan da Cunha mantle plume, 189, 192
 tritium (^3H), 108
 precipitation at Ottawa, 109
 troilite, 167
 tunneling, 13
 two-error regression algorithm, 38
 type I, II, and III kerogen, 271–272
 Type Ib/c supernovae, 151
 Type II supernovae, 20, 151
 Type I supernovae, 23
 ^{238}U decay, 13, 15
 ^{235}U decay constant, 37
 U-decay series dating, 83–96
 basic principles, 84–86
 carbonates, case of, 87
 in a closed system, 84
 decay counting, 86
 equilibrium state, 86
 half-lives and decay constants, 84
 half-lives and decay constants of long-lived U and Th daughters, 86
 parent decay, 84
 ^{231}Pa - ^{235}U dating, 91–93
 ^{210}Pb dating, 93–95
 ^{210}Po - ^{210}Pb dating, 95–96
 ^{226}Ra dating, 93
 rate of marbles dropping into a hopper, demonstration, 86
 supported and unsupported abundances, 87
 ^{230}Th - ^{238}U dating, 88–91
 ^{234}U - ^{238}U dating, 86–88
 U-doped glass standard, 117
 U-enrichment of oceanic crust, 185
 U half-lives, re-evaluation of, 74
 underplating of continents, 206
 unstable cosmogenic nuclide, rate of change of abundance, 154
 U-Pb concordia diagram, 92–93
 ^{238}U / ^{204}Pb ratio, 35, 78
 ^{238}U / ^{206}Pb ratio, 35, 78
 uranium-bearing minerals, 73
 urelites, 126
Usercalc, 196, 198
 U-series isotopes and melt generation, 193–198
 U-Th-He system, 83
 U-Th-Pb dating, 72
 U-Th-Pb system, 35, 72
 chemistry of U, Th, and Pb, 72–73
 measurements of meteorites, 73
 parameters of, 74
 uranium decay constant, 73–74
 ^{238}U / ^{235}U ratio constant, 73–74
 ^{238}U / ^{232}Th ratio, 197
 ^{234}U - ^{238}U dating, 86–88
 ^{238}U / ^{235}U ratio, 35
 in CAIs, 127
 Vetreny komatiites, 207
 vibrational equilibrium constant, 257
 vibrational frequencies of oxygen molecule, 254–255
 vibrational partition function, 251–252, 254
 vibration motion, 248
 volcanogenic massive sulfides, 310
 Vostok and EPICA Antarctic ice cores, 337–338
 water, isotopic composition of, 257
 water masses, properties of, 233
 water-rock reaction, theory, 301–303
 water-rock ratios for Skaergaard, 303
 wavelengths, 5
 weathering feedback, 357–358
 white dwarfs, 20
 winonaites, 126
 W isotopic composition, 138, 140
 wood, absolute age of, 103
 W boson particles, 14
 ^{182}W / ^{183}W ratio, 137–138
 Xe-HL, 148
 xenoliths, 65, 163, 189, 296
 continental, 285
 hydrous minerals in, 286
 in oceanic island basalts, 285
 Os isotope ratios in, 191
 oxygen isotopic composition of, 283
 xenon, 15, 147, 433–437
 s-process-only isotopes of, 147
 Xe-S, isotopic composition of, 148
 xenotime (YPO_4), 73
 X-winds, 146, 153
 Zero Point Energy (ZPE), 248, 249, 259
 zeta method, 116–117
 zinc isotopes, 381–384
 zircon (ZrSiO_4), 59–60, 73, 91, 206, 213
 annealing, 118
 Archean crust, 214
 bearing quartzites, 82
 concordia diagram of, 80–82
 crystallization age of, 208
 crystallization ages, 80
 dating, 77–83, 82, 86
 detrital, 208, 210, 212, 214, 216–217
 distribution of zircon
 crystallization ages, 214
 effect, 59
 from Finnish tonalite, 81
 geochronology, 76
 Hadean crust from, 210–212
 Hf in, 235
 ion probe ages of, 83
 isotopic composition of, 81
 Jack Hills, 83, 210
 Lu/Hf ratios, 210–212, 216, 220
 in mafic rocks, 208

zircon ($ZrSiO_4$) (*continued*)
mechanical and chemical
stability of, 82
metamict regions of, 81
metamorphism ages, 80
multiple episodes of open
system behavior, 81
Pb gain in, 80

Pb loss during a metamorphic
event, 78–79, 81
radiation damage to crystal
lattice, 80
range of 4100–4260 Ma,
82
resistance characteristics of,
77

in river water, 235
step-wise dissolution of, 81
thermal ionization analysis of,
81
zoning in, 83
Zn-rich deposits, sulfur isotopes
in, 311
zone of weathering, 75

WILEY END USER LICENSE AGREEMENT

Go to www.wiley.com/go/eula to access Wiley's ebook EULA.